3 MM SPECTRAL LINE SURVEYS OF THE HIGH MASS STAR FORMING REGIONS SAGITTARIUS B2(N-LMH) AND ORION-KL

BY

DOUGLAS NATHANIEL FRIEDEL

B.S., Clarkson University, 1999
B.S., Clarkson University, 1999

DISSERTATION

Submitted in partial fulfillment of the requirements
for the degree of Doctor of Philosophy in Astronomy
in the Graduate College of the
University of Illinois at Urbana-Champaign, 2005

Urbana, Illinois

Abstract

There are over 135 different molecular species known to exist in the interstellar medium, and more are found every year. However, how these different molecular species form in the depths of space is a mystery. A few can be explained, but for most, including the most abundant molecule in the universe H_2, the formation mechanism is not well understood. Part of the problem with understanding these formation mechanisms is that conditions in the interstellar medium currently cannot be recreated in the lab, and thus direct experimentation is not possible. Another issue is that the physical conditions and spatial distributions for many of the observed molecular species are not well constrained.

In order to fill in some of the blanks for the second issue, spectral line surveys of two high mass star forming regions (Sgr B2(N-LMH) and Orion-KL) were conducted. These surveys provide not just the spectra of these regions, but also measurements of the spatial scales and temperatures of the observed species, thus constraining the mechanisms by which these species form. Additionally, observations of two comets were carried out in an attempt to link the chemistry of high mass star forming regions with that of the presolar nebula.

The second chapter of this dissertation describes the methods and techniques used to analyze the data. The third chapter gives the results of the analysis of the data from the Sgr B2(N-LMH) line survey, where most large, saturated molecular species were constrained to a very small region in the cloud, with the exception of a single transition of C_2H_5OH which is found to be widespread. The fourth chapter gives the initial survey results for Orion-KL, a region where large N bearing species and large O bearing species occupy different spatial regions, thus giving insight into differing N and O chemistry in the interstellar medium. A more thorough analysis of the data from Orion-KL will be carried out in the future. The fifth chapter gives the results of observations of two nearby comets during the summer of 2004.

To my wife.

Acknowledgments

First, I would like to thank my wife, Heather, for her unwaivering support and tolerating my trips to conferences and innumerable observing runs.

I would also like to thank my advisor Prof. Lewis Snyder for his many years of guidance. I am also grateful to my thesis committee Prof. Ed Sutton, Prof. Leslie Looney, and Prof. Brian Fields for their input and numerous helpful discussions.

I would like to thank Dr. Anthony Remijan, Dr. Susanna Widdicus Weaver, and Dr. David Meier for countless discussions on interstellar chemistry, data reduction, and everyday life. I am grateful to Dr. Barry Turner for obtaining the 12 meter data.

Table of Contents

List of Tables

List of Figures

Chapter 1

Introduction

1.1 Why Spectral Line Surveys?

Spectral line surveys provide powerful tools to analyze the coupled dynamical and chemical evolution of molecular clouds. In a survey, many lines of a single species are observed at similar sensitivities, diminishing the errors associated with derived quantities. For example, a particular problem arises in deriving accurate abundances due to overlapping identifications of molecular species. Surveys provide the best means of avoiding this problem by revealing intensity changes in lines of a given species.

The surveys in this dissertation, of the high mass star forming regions Sgr B2(N-LMH) and Orion-KL, will provide additional information due to their unique nature. The data were taken with both an interferometer (BIMA Array) and a single-element radio telescope (NRAO 12 meter) which together yield information on multiple spatial scales. This allows for constraints to be placed not only on the spatial distribution of molecular species but on their potential formation mechanisms as well. These regions were chosen because they are well known sources of a large number of molecular species (e.g., Turner, 1989, 1991; Mehringer et al., 1997; Liu et al., 2001, 2002; Martín-Pintado et al., 2001; Remijan et al., 2003).

1.2 Observations on Multiple Spatial Scales

The surveys utilize data from both the Berkeley-Illinois-Maryland Association (BIMA) Array[1] (ten 6.1 meter elements) and the single-element NRAO 12 meter[2] radio telescope. Unlike previous surveys which only utilized a single type of instrument (array or single element), the surveys in this dissertation are able to sample multiple spatial scales of the source. The NRAO 12 meter observations have a primary beam $\sim 65''$, at 3 mm, while the synthesized beam of the BIMA Array in C configuration, is $\sim 25'' \times 6''$ (for Sgr B(2N-LMH)) and $\sim 13'' \times 8''$ (for Orion-KL) at 3 mm. A

[1] Operated by the University of California, Berkeley, the University of Illinois, and the University of Maryland with support from the National Science Foundation.

[2] NRAO is operated by the Associated Universities, Inc., under contract with the National Science Foundation.

single-element telescope is best for detecting large scale, extended emission, but poor at detecting compact sources due to beam dilution. An array is insensitive to structures larger than an angular size determined by the minimum spacing of its elements, and thus resolves out large scale structure. For the BIMA Array, this is ∼10 times the size of the synthesized beam (Wright, 1996)[3]. This feature is very important to astrochemistry because the location of a particular molecular species may indicate its formation mechanism. Molecules formed by low temperature gas phase reactions and those formed and desorbed at low temperature on grains will be primarily extended in emission. On the other hand those that need warmer temperatures to desorb from the surface and those formed in warm gas phase reactions will be detected in the warmer compact cores of the sources. Thus, a single element telescope would be most sensitive to molecules formed in low temperature gas phase and grain surface reactions, while an array would be most sensitive to molecules formed in warm cores (either in gas phase reactions or initially on a grain and then desorbed from the surface).

1.3 Interstellar Chemistry-How Much Do We Really Know?

We know very little of chemistry in the interstellar medium (ISM). There are over 135 known molecular species that have been detected in the ISM[4], and for most of these species how they formed is still a mystery. For some simple species such as CO, N_2, O_2, C_2H_2, and C_2H_4 gas phase reactions can explain their formation (Charnley et al., 1995; Charnley, 1997, 2001). However, this is not the case for the most abundant molecule in the universe, H_2. It's gas phase formation rates are so low that it is unlikely that the bulk of H_2 formed in this way (Duley & Williams, 1985). The currently accepted theory is that H_2 forms on the surfaces of interstellar dust grains (Gould & Salpeter, 1963; Hollenbach & Salpeter, 1971). However, this process is not well understood and numerous models and lab experiments have been carried out over the past ∼40 years in order to better understand this process (e.g., Gould & Salpeter, 1963; Hollenbach & Salpeter, 1971; Duley, 1996; Parneix & Brechignac, 1998; Pirronello et al., 1997; Takahashi, 1999; Cazaux & Tielens, 2002; Cuppen & Herbst, 2005).

Additionally many more complex species have been observed with such large abundances they cannot be formed by gas phase chemical reactions alone (e.g., Miao & Snyder, 1997). These larger and more complex molecular species are also thought to be formed on grain surfaces. H is thought to be very mobile on cold grain surfaces and thus an H atom can traverse a grain and potentially react with other atoms or molecules. Hydrogenation of heavy atoms (anything heavier than H) and molecules can happen with very high efficiency on grains (Watson & Salpeter, 1972). This could explain molecules such as methanol (CH_3OH). The formation of simple hydrogenated species has been tested in the lab with good results. Hiraoka et al. (1998a,b) have shown that methane (CH_4),

[3]BIMA Memoranda Series (Wright, 1996) is available at: http://bima.astro.umd.edu/memo/memo45.ps.

[4]See http://www.cv.nrao.edu/∼awootten/allmols.html or D. R. Lide (2004) (http://www.hbcpnetbase.com §14, Interstellar Molecules) for a complete list.

formaldehyde (H_2CO), and CH_3OH can form on 13 K CO ice sprayed with H. Also O'Neill et al. (2002) concluded that only a small fraction of CO sticking to grains would need to be hydrogenated to CH_3OH in order to explain observations toward diffuse clouds. It has also been theorized that CH_3OH can form in hot post-shock gas, a case likely for the Orion compact ridge region (Hartquist et al., 1995; Latter & Charnley, 1996).

While H may be mobile at low temperatures (~10 K) other atoms and radicals are not. However, if the grain temperature is raised (e.g., via weak shocks) C, O, CH, CH_3, NH_2, and CH_3 can become highly mobile on grain surfaces, possibly leading to more complex species (Widicus Weaver, 2005a). Additionally, other reaction schemes have been proposed to explain the large observed abundances of species such as methyl formate ($HCOOCH_3$), which cannot be formed by single atom addition reactions (Horn et al., 2004). Photoprocessing, radical-radical, and radical recombination reactions are some of the possibilities (Allen & Robinson, 1975; Hasegawa et al., 1992; Hasegawa & Herbst, 1993; Shalabiea & Greenberg, 1994; Ruffle & Herbst, 2000, 2001).

Forming the molecules on grain surfaces is only part of the problem, as the molecules need to be released into the gas phase in order to be detected by radio telescopes. These release mechanisms need to be strong enough to break any bonds the molecules have with the grain surface, but weak enough to not destroy the molecule in the process. In the case of exothermic reactions, the energy released may be enough to liberate the newly formed molecule from the grain surface. However, this is likely to apply to only a small percentage of reactions. Other desorption mechanisms that have been proposed include spot heating by cosmic rays, grain-grain collisions, heating by newly formed stars, and shocks (Shalabiea & Greenberg, 1994; Hartquist et al., 1995).

While much progress has been made toward understanding chemistry in the ISM there is still much that is currently unknown or untestable in the lab and to date no model can explain the observed abundances of more than a handful of species.

1.4 Future Applications of the Surveys

The results of the Sgr B2(N-LMH) and Orion-KL spectral line surveys can help to constrain formation models. For the first time source size measurements of all observed species from the Sgr B2(N-LMH) region will be presented, and these measurements will constrain where each molecular species is present and on what scale. In combination with the measured rotation temperatures, insight can be gained into the physical conditions (e.g., hot dense core[5], warm envelope, cold medium), and thus formation mechanisms, where the molecular species are present. A structural analysis of the species detected in Orion-KL can give insight into the differing formation mechanisms of N versus O bearing species and thus hot core versus grain mantle evaporation/shock formation mechanisms.

No discussion of interstellar chemistry would be complete without mentioning the chemistry of low mass star forming regions and the early solar nebula. It is not known if the diversity of interstellar chemistry observed in high mass star forming regions such as Sgr B2(N-LMH) and

[5]Hot cores are defined as having $n(H_2)\sim\times10^7$ cm^{-3} and temperatures of at least 100-200 K (Remijan et al., 2003).

Orion-KL also exists around lower mass stars (hot corinos), such as the Sun, when they form. Comets are thought to have preserved some of the most pristine material from the early solar nebula. The observations of many molecular species in comets can give insight into the chemical processes that occurred during the comet's formation and how these processes differ from those seen in high mass star forming regions. In order to properly model the chemistry of comets, the abundances of each observed species must be calculated. However, the standard (Haser) model for calculating these quantities does not trace the changing physical conditions in cometary comae very well. A new method (which traces the changing physical conditions) for calculating the abundances of molecular species in comets has recently been developed by Friedel et al. (2005a), and results from observations of two comets using this method (VTOV model) are given in this dissertation.

Chapter 2

Methods

2.1 Introduction

This chapter describes the methods used in the data analysis of this dissertation. Included are the formalisms used for calculating column densities, opacities, beam filling factors, source sizes, and partition functions. In addition, a detailed description of the propagation of uncertainties through the calculations is presented.

2.2 Calculating Column Densities

Calculating accurate column densities for simple and complex molecular species is important since they are critical to the understanding of the role of each method of molecular formation. Hopefully future formation models will be able to reproduce these quantities. For example, Charnley et al. (1992) and Miao & Snyder (1997) invoke grain chemistry in order to explain the observed quantities of C_2H_5CN in Orion-KL and Sgr B2(N-LMH). However no model to date has been able to reproduce these observed quantities.

2.2.1 Emission Features

For emission features there are many different ways to calculate the total column density, $\langle N_T \rangle$, including large velocity gradient models (e.g., de Vicente et al., 1997), rotational temperature diagrams (e.g., Friedel et al., 2005b), statistical equilibrium methods (e.g., Remijan et al., 2004c), and directly from individual transitions (e.g., Miao et al., 1995). For the work in this dissertation the best methods to use are the rotational temperature diagram (RTD) method and calculating $\langle N_T \rangle$ from individual transitions (when too few transitions were detected in order to use the RTD method). With the assumption of LTE, to calculate $\langle N_T \rangle$ from a single transition for an array, we have (e.g., Friedel et al., 2005b; Remijan et al., 2005)

$$\frac{N_u}{g_u} = \frac{2.04 W C_\tau}{B \theta_a \theta_b S \mu^2 \nu^3} \frac{T_r}{T_r - T_b} \times 10^{20} \text{ cm}^{-2} \tag{2.1}$$

and for a single element radio telescope (e.g., Snyder et al., 2001)

$$\frac{N_u}{g_u} = \frac{1.67WC_\tau}{B^* S\mu^2 \nu} \frac{T_r}{T_r - T_b} \times 10^{14} \text{ cm}^{-2} \tag{2.2}$$

and

$$\langle N_T \rangle = \frac{N_u}{g_u} Q_{rv} e^{E_u/T_r}. \tag{2.3}$$

Here W is the integrated line intensity in Jy beam^{-1} km s^{-1} or K km s^{-1}, respectively, Q_{rv} is the rotational-vibrational partition function (see §2.5), E_u is the upper state energy of the transition in K, T_r is the rotational temperature in K, C_τ is the opacity correction factor (see §2.3), B is the beam filling factor (see §2.4), $B^* = \eta_M^* B$, where η_M^* is the corrected main beam efficiency, θ_a and θ_b are the FWHM Gaussian synthesized beam axes in arcseconds, $S\mu^2$ is the product of the line strength and the square of the relevant dipole moment in Debye^2, ν is the transition frequency in GHz, N_u/g_u is the upper state column density divided by its statistical weight ($2J$+1), and T_b is the total background continuum temperature.

The RTD method is an extension of the method for single transitions. It is a plot of the natural log of equation (2.1) or (2.2) versus E_u. A weighted least squares fit to this plot will yield the rotation temperature (the negative inverse of the slope of the line) and N_u/g_u at E_u=0 (the y axis intercept). $\langle N_T \rangle$ can then be calculated from equation (2.3), using the above quantities. The use of this method does have some caveats and pitfalls which are described in Snyder et al. (2005) (see Appendix F). The primary pitfall that can be of concern with this work is the use of a few weak ($\sim$3-4 σ) lines of some species in the analysis. These weak lines may just be noise spikes at frequencies coincident with expected transitions. The inclusion of these weak lines can skew the results; however every effort has been made to be sure of the identification of all lines used in the analysis.

2.2.2 Absorption Features

For absorption features the total beam averaged column density can be calculated from (Lucas & Liszt, 1993; Greaves & Nyman, 1996)

$$\langle N_T \rangle = \frac{8.0 Q_r e^{E_l/T_r} \int \tau dv}{S\mu^2 (1 - e^{-h\nu/kT_r})} \times 10^{12} \text{ cm}^{-2}, \tag{2.4}$$

where Q_r is the rotational partition function as the temperatures are too low to populate any vibrational states, E_l is the lower state energy, and the opacity, τ, is defined in §2.3.

2.3 Opacity

High optical depth ($\tau > 1$) can greatly reduce the observed intensity of a spectral line. From Rohlfs & Wilson (2000) the opacity at the line center can be calculated from

$$T_{MB} = (1 - e^{-\tau})(J(T_r) - J(2.73\text{ K}) - T_C)$$

giving

$$\tau = -ln\left[1 - \frac{T_{MB}}{J(T_r) - J(2.73\text{ K}) - T_C}\right], \tag{2.5}$$

where $T_{MB} = T_R^*/\eta_M$ is the main beam brightness temperature of the line, $J(T)$ is defined as (Rohlfs & Wilson, 2000)

$$J(T) = \frac{h\nu}{k}\frac{1}{e^{h\nu/kT} - 1}\text{ K}, \tag{2.6}$$

$J(2.73)$ is the cosmic microwave background, and T_C is the continuum brightness temperature. For observations not done in a temperature scale one can convert from Jy beam^{-1} to K using (Rohlfs & Wilson, 2000)

$$T = \frac{1.22 I_0}{B\theta_a\theta_b\nu^2}\text{ K}, \tag{2.7}$$

where I_0 the is peak intensity of the line in Jy beam^{-1}. For emission lines the optical depth correction factor, C_τ can then be calculated from (Goldsmith & Langer, 1999)

$$C_\tau = \frac{\tau}{1 - e^{-\tau}}. \tag{2.8}$$

This factor is then applied to the column density equation (2.1) or (2.2).

2.4 Beam Filling Factor

Another item that needs to be considered when calculating column densities is the beam filling factor. The beam filling factor accounts for the drop in peak intensity, in temperature units, when the source is smaller than the beam. As an example take a source that is a $2'' \times 2''$ Gaussian being observed by a telescope with a $60''$ Gaussian beam. The flux from this 4.532 arcsec^2 source gets spread over the 4079.12 arcsec^2 beam. This acts to reduce the peak intensity by a factor of $\sim$900. This drop in peak intensity happens for both single element telescopes and interferometers. By adding in a beam filling factor to the column density equation we can correct for this drop in peak intensity. The beam filling factor is calculated as (Ulich & Haas, 1976)

$$B = \frac{\Theta_S^2}{\Theta_S^2 + \Theta_B^2}, \tag{2.9}$$

where Θ_S^2 is the source size in arcsec^2 and Θ_B^2 is the size of the beam in arcsec^2. Figure 2.1 shows the beam filling factor and the log of its inverse (the log of the multiplicative factor that $1/B$ applies

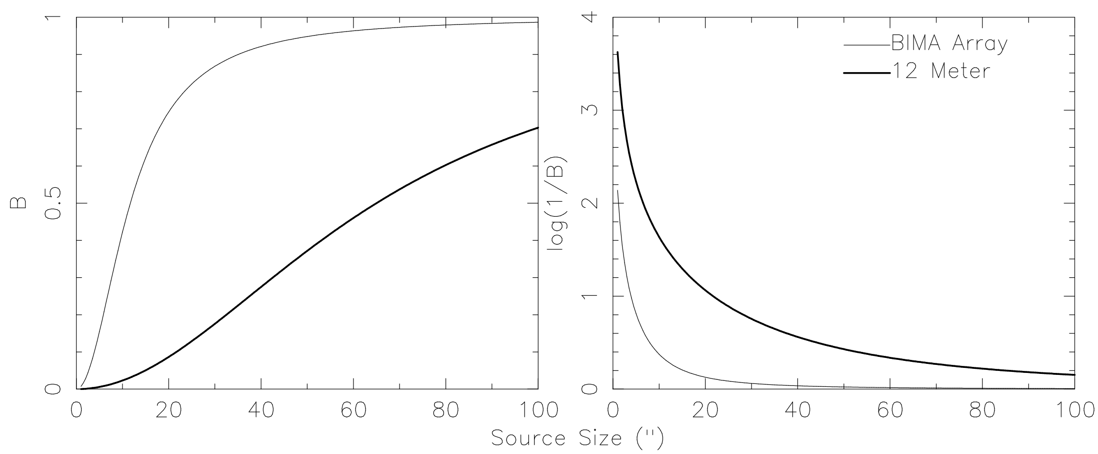

Figure 2.1 The beam filling factor (B) and its inverse. The abscissa is source size in arcsec. The plot of $\log(1/B)$ shows how much correcting for the source size can affect the column density.

to the column density) as a function of source size. The heavy line is for the 12 meter telescope at 98 GHz (FWHM=65″), and the normal line is for the BIMA Array with a synthesized beam of 24″×5.7″(a typical Sgr B2(N-LMH) beam size). For source sizes much larger than the beam ($\Theta_S^2 \gg \Theta_B^2$) $B = 1$, for sources just filling the beam ($\Theta_S^2 = \Theta_B^2$) $B = 0.5$, and as the source size gets much smaller than the beam ($\Theta_B^2 \gg \Theta_S^2 \rightarrow 0$) $B \rightarrow 0$. Note how much the column density can increase ($1/B$ factor, right hand plot) as source size decreases.

2.4.1 Determining Source Sizes

In order to properly calculate the beam filling factor one must know the size of the source. There are several ways of calculating, or at least estimating, the source size. The main methods are outlined below.

Image Space

Measuring the source size in image space is the easiest to visualize since it works directly from a map. The primary challenge is that the true source size comes from a deconvolution of the source in the map and the synthesized beam (which depends on the u-v sampling). The MIRIAD (Sault et al., 1995) task IMFIT does a good job at fitting single (and in some cases multiple sources) from an image. Difficulty can arise if the signal-to-noise is not high (<6), if the size of the source measured on the map is not well constrained, or if the source size is large compared to the synthesized beam. In the Sgr B2(N-LMH) line survey fitting with IMFIT was problematic.

U-*V* Space

Another method for measuring source size is fitting in the u-v plane. This method assumes that the source has a Gaussian shape on the sky. Since the Fourier transform of a Gaussian is Gaussian the analysis is straightforward. Chapter 7 of Rohlfs & Wilson (2000) gives a detailed explanation of how source sizes can be determined in u-v space. The MIRIAD task UVANM was developed and used to measure source sizes for nearly all of the lines in the Sgr B2(N-LMH) survey.

Clean Components

The last method of source size determination described here is the analysis of the clean component map. The clean component map is created by the MIRIAD task CLEAN and is essentially a map of the model emission/absorption peaks (i.e. single pixels). Analysis of clean component maps can be problematic, especially if the signal-to-noise ratio is less than ~6. However, it may at times give insight into structure much smaller than the synthesized beam. In Figure 2.2 the two Sgr B2(N) components (at v_{LSR}'s of 64 and 72 km s^{-1}), separated by only 5$''$, can be seen. While the clean component maps do not offer conclusive proof that the different velocity components come from different regions, when they are combined with previous observations that show the different cores at higher resolution (see e.g. Hollis et al., 2003) they can help determine if a line may be another velocity component of a nearby line.

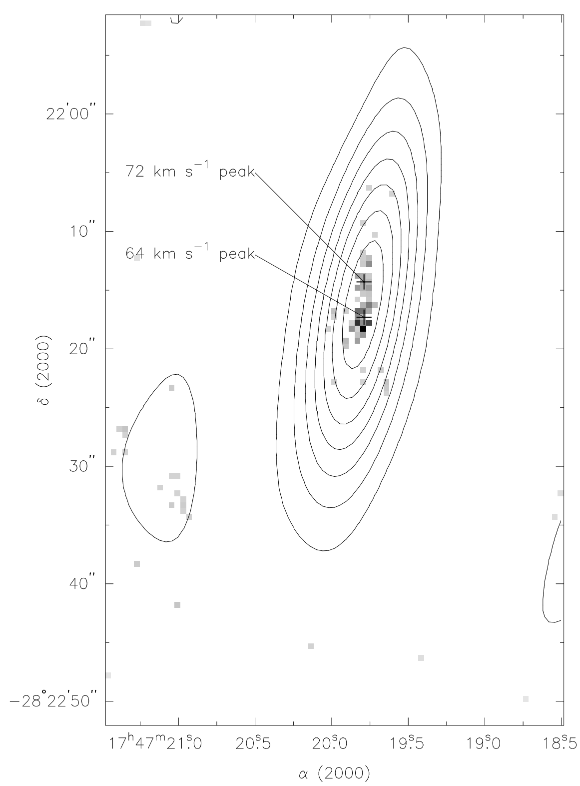

Figure 2.2 A map of the clean components of C_2H_5CN in grey scale pixels overlayed with a contour map of a cleaned and restored map. The two Sgr B2(N-LMH) components can be seen in the clean component map while they are lost in the contour map.

Comparison of Methods

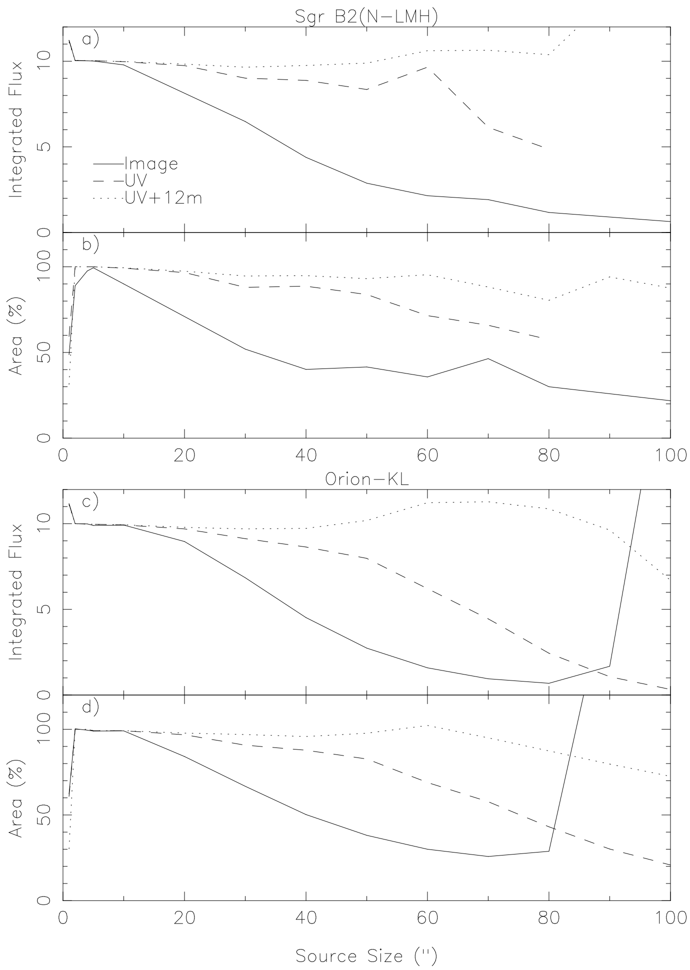

Figure 2.3 The ability to recover source size and flux. The abscissa is input source size in arcsec. The input integrated flux is 10 Jy. a) shows the recovered integrated flux for sources at Sgr B2(N-LMH). The solid line denotes how much integrated flux was measured in the final image, the dashed lines denotes how much integrated flux was measured in *u*-*v* space, and the dotted line denoted how much integrated flux was measured in *u*-*v* space including data from the 12 meter. b) shows the measured area of the source compared to the input source size (in %). c) and d) are the same as a) and b) except for a source at the position of Orion-KL.

Figure 2.3 illustrates how well specific source size measurement methods recover the true nature of the source. For all plots the solid line represents measurements made in the image plane by IMFIT, the dashed line represents measurements made in the *u*-*v* plane by UVANM, and the dotted line represents measurements made in the *u*-*v* plane with the addition of single element data. All models used the typical BIMA Array in its C configuration. Panel a) shows the recovered integrated flux on the ordinate and source size, in arcsec, on the abscissa for sources located at the position of Sgr B2(N-LMH) on the sky ($\delta \sim -28.5°$, $\sim 24.4'' \times 6.3''$ synthesized beam). All sources have the same integrated flux (10 Jy). Note that all three methods do equally well out to a source size of $\sim$10$''$, but by the time the source size reaches 20$''$ the flux recovered in the image plane is below 80% that of the original and drops off from there. The u-v plane measurements do better and recover over 80% of the flux out to source sizes of $\sim 60''$, but beyond that, due to the lack of short spacings between elements, an increasing percentage of the flux is not recovered. The addition of single element data helps and allows good recovery out to $\sim 80''$, but it too eventually fails due to the lack of short spacings. Panel b) shows the measured source size (as an area), as a percentage of the input source size (as an area), for each method. Note that IMFIT has trouble for sources even as small as $15''$ across, beyond this source size the area measured is less than 80% of the input size. Measurements in the u-v plane recover >80% of the area out to $\sim 55''$ but drops off beyond this source size. The addition of the single element data allows for good measurements (better than 80% recovery) out to $\sim 100''$. Panels c) and d) are the same as a) and b) except for a source at the position of Orion-KL on the sky ($\delta \sim -5°$, $\sim 13.7'' \times 9.4''$ synthesized beam). Note that these are specific cases for the observations discussed in this dissertation and cannot be generalized.

In general the measurement of source sizes is not trivial and a combination of all the methods described here was used in the analysis of the line survey data. All source sizes reported in this work are the FWHM of the Gaussian on the sky.

2.5 Partition Functions

Table 2.1 gives the rotational partition function (column (2)) for the species detected in this survey. This general form of the rotational partition functions is the high temperature limit (valid for $T_r \geq 50$ K). For those molecules detected in cooler emission regions or in absorption where the rotational temperature is on the order of 10 K, the partition function must be determined by directly summing over all states. From McQuarrie (2000) for linear molecules

$$Q_r = \sum_{J=0}^{\infty}(2J+1)e^{-\frac{B}{kT_r}J(J+1)} \tag{2.10}$$

and for symmetric tops

$$Q_r = \frac{1}{\sigma}\sum_{J=0}^{\infty}(2J+1)e^{-\frac{A}{kT_r}J(J+1)}\sum_{K=-J}^{+J}e^{-(A-C)\frac{K^2}{kT_r}}, \tag{2.11}$$

where A, B, and C are the rotational constants in Hz, J is the rotational quantum number, K is the quantum number for the projection of angular momentum along the axis of symmetry, k is the Boltzmann constant ($k = 2.083 \times 10^{10}$ Hz K^{-1}), and σ is the symmetry number[1]. The low temperature case for asymmetric top molecules is much more complex and must be solved numerically. The only asymmetric top molecule that was detected in absorption is CH_3OH. In this case the low temperature partition function is taken from Pickett et al. (1998).

[1]The symmetry number is the number of ways that a molecule can be rotated to give a mirror image of itself (McQuarrie, 2000).

When calculating column densities and relative abundances, it has been traditional to use only the rotational part of the partition function (e.g., Remijan et al., 2003, 2004a). The vibrational part of the partition function has generally only been employed when vibrationally excited transitions of a species have been detected (see e.g. Nummelin & Bergman, 1999; Mehringer et al., 2004; Remijan et al., 2005). In general the vibrational part of the partition function should be included in the analysis, *even if* vibrationally excited transitions were not detected[2]. This is because, while the lowest lying vibrationally excited state of many simple species are over 1000 K above ground, for many larger species the lowest lying vibrational states can be very low. For example l-C_3H has its lowest vibrationally excited state only 39 K above ground, HC_3N has 3 vibrationally excited states below 720 K (all of which have been detected in the Orion Survey), and the asymmetric top $(CH_3)_2CO$ (acetone) has 2 vibrationally excited states below 200 K (Müller et al., 2001; Groner et al., 2005). Thus, at temperatures commonly seen in hot cores, these low lying states will contain a significant population, which needs to be included in the column density.

The addition of the vibrational part of the partition function is rather straightforward. From Widicus Weaver et al. (2005)

$$Q_{rv} \approx \sum_{i=0}^{n} e^{-E_i/T_r} Q_r, \tag{2.12}$$

where Q_{rv} is the rotational-vibrational partition function, n is the number of vibrationally excited states in the calculation, and E_i is the energy above ground of the vibrationally excited state. Note that for $n = 0$ this reduces to just $Q_{rv} = Q_r$. Column (3) of Table 2.1 gives the known vibrational energies (below 1000 K) for each species. Most of the species listed have vibrational states above 1000 K, however at hot core temperatures, these states will contribute a negligible amount to the column density. In addition to the energies listed in column (3) there are combination bands (whose energies are the sum of any two or more of the energies listed in column (3)) and overtones (integer multiples of the energies listed in column (3)), which need to be taken into account. Both of these types have been detected in several species, such as C_2H_3CN (overtones) (Nummelin & Bergman, 1999, and this work) and HC_3N (overtones and combinations) (Remijan et al., 2005, and this work). To include overtones and combination bands, additional terms need to be added to equation (2.12) with the energy of the overtone or combination.

Figure 2.4 shows the effect of including the vibrational part of the partition function on the overall partition function for $(CH_3)_2CO$. The ordinate is partition function value and the abscissa is rotational temperature in K. The dashed line indicates Q_r for each temperature while the solid line indicates Q_{rv}. For low temperatures (< 100 K) the difference is not large;, however the difference increases rapidly for higher rotation temperatures. Columns (4) and (5) of Table 2.1 show the effect of including the vibrational part of the partition function for each molecule. Both Q_r and Q_{rv} are taken at 150 K.

One must be careful when calculating partition functions for molecules with one or more internal

[2]Rotational transitions of vibrationally excited states are cataloged for only a few states of a few species. Thus transitions of vibrationally excited states may be in spectra, but their identity may not be known.

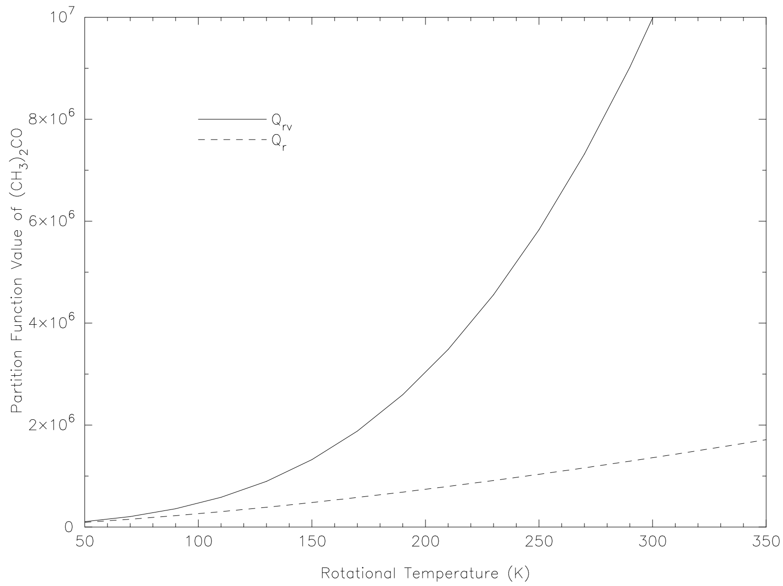

Figure 2.4 The effect of including the vibrational partition function for $(CH_3)_2CO$ is shown. The ordinate is partition function value and the abscissa is rotational temperature in K. The dashed line indicates Q_r for each temperature while the solid line indicates Q_{rv}.

rotors where the ground state energy between the torsional states is noticeable (e.g. CH_3OH has a 14 K difference between the ground state energies of the A and E torsional states). Under normal hot core conditions the energy difference is insignificant and the partition function is just two times that for the A torsional state (Turner, 1991). However, in the extremes (i.e. cold dark clouds and very warm hot cores) the partition function must be calculated for each torsional state separately. For cold dark clouds the effect is obvious, the higher energy torsional state may not be populated. But for hot cores the effect is not as obvious, until you look at the energies of the vibrational states. The 14 K energy difference between the A and E ground torsional states grows to a $\sim$120 K difference between the A and E torsional states of the first vibrationally excited state. With such a difference in energy the partition function and column density for each torsional state must be calculated separately and then combined.

Table 2.1. Partition Functions and Vibrationally Excited Energies[a]

Species	Rotational Partition Function (Q_r)	Vibrational Energies (K)	Q_r(150 K)	Q_{rv}(150 K)	Refs.
l-C_3H	$1.86T$	39.1,287.8,431.6	279.2	611.5	1,2
C_2H	$0.48T$	534.5	72.0	74.0	3
C_2H_3CN	$5.10T^{3/2}$	344,489,820,982	9253.6	10738.9	4,5
C_2H_3CHO	$4.30T^{3/2}$	225.8,470.4,811.3,853.0	7899.6	10661.0	2,6
C_2H_5CN	$7.17T^{3/2}$	297,306,544,784	1.3×10^4	1.8×10^4	2,7
t-C_2H_5OH	$3.68T^{3/2}$	295.6,369.7,602.7	1.2×10^4	1.5×10^4	8
g^+-C_2H_5OH	$1.84T^{3/2}$	335.2,423.7,602.7[b]	1.2×10^4	1.5×10^4	8
g^--C_2H_5OH	$1.84T^{3/2}$	400.3,423.5,602.7[b]	1.2×10^4	1.4×10^4	8
C_2S	$3.22T$	387.4	483.0	522.3	9
CH_3CN	$0.98T^{3/2}$	520.7	1800.4	1856.3	2
CH_3CCH	$1.04T^{3/2}$	471.8,910.6	1910.6	2000.8	2,6
CH_3CHO	$4.60T^{3/2}$	216,732	8450.7	11145.77	2
$(CH_2)_2O$	$7.58T^{3/2}$	[c]			2,3
$(CH_3)_2CO$	$8.18T^{3/2}$[d]	115,180,554,696,762	4.8×10^5	1.3×10^6	2,10
$(CH_3)_2O$	$2.86T^{3/2}$[d]	292,348,601	1.7×10^5	2.2×10^5	2,11
CH_2NH	$0.38T^{3/2}$	[c]			2
CH_3OH	$1.20T^{3/2}$	300.5,423.6[e,f]	2263.5	2776.0	3
CN[e]	$0.38T$	[c]			6,12
CO[e]	$0.36T$	[c]			6,12
CS	$0.86T$	[c]			3
HC_5N	$15.64T$	157.5,387.0,669.6,853.0,923.5	2346.6	4074.4	3,13
HC_3N[e]	$4.57T$	320.8,717.8,954.0	685.5	783.8	3
HCN[e]	$0.49T$	[c]			3
HCO	$0.58T$	[c]			2,6
HCO^+	$0.48T^{3/2}$	[c]			2,6
$HCOOCH_3$	$12.45T^{3/2}$	187,457,478	2.3×10^4	3.5×10^4	2,14
HCOOH	$1.71T^{3/2}$	899,918	3137.1	3151.8	3
HCS^+	$1.00T$	[g]			2,6
HDO	$0.03T^{3/2}$	[c]			2,6
H_2C_3S	$7.00T^{3/2}$	[c]			2,3
H_2CO	$0.55T^{3/2}$	[c]			2,6
H_2CS	$1.15T^{3/2}$	469.0	2112.7	2209.4	2,6
HNC[e]	$0.46T$	667.8	71.7	72.6	3
HNCO	$1.50T^{3/2}$	830.5,944.1	2769.2	2785.3	3,6
N_2H^+	$0.25T^{3/2}$	988	37.5	37.6	2,6
NH_2D	$0.70T^{3/2}$	[c,h]			2,6
NH_2CHO	$5.60T^{3/2}$	415.3,812.8,866.0	1.0×10^4	1.1×10^4	15
OCS[e]	$3.43T$	748.6	513.7	517.2	3
SO_2[e]	$2.30T^{3/2}$	744.8	4164.7	4193.8	3
SO	$0.98T$	[c]	435.0	435.6	3

Table 2.1—Continued

Species	Rotational Partition Function (Q_r)	Vibrational Energies (K)	Q_r(150 K)	Q_{rv}(150 K)	Refs.
SiO[e]	$0.96T$	[c]	143.9	144.1	3
SiS	$2.30T$	[c]			6,12

[a]Only vibrationally excited states below 1000 K are listed, because even at hot core temperatures the population of vibrationally excited states above 1000 K will be less than 10% of the total.

[b]No energy was given for this mode for gauche C_2H_5OH. Values are assumed to be at least that for trans C_2H_5OH.

[c]Lowest vibrationally excited state lies above 1000 K

[d]In order to calculate the column density one needs to multiply by 64/2 and weight the integrated intensity by the spin weight of the transition (see Friedel et al. (2005b) (Appendix I))

[e]Isotopomers are assumed to have the same energies for their vibrationally excited states, unless otherwise noted.

[f]The energies refer to the first vibrational state of the A and E torsional states.

[g]No vibrational energies could be found in the literature, but the lowest state is likely to be above 1000 K.

[h]Assumed the same as NH_3.

References. — (1) Yamamoto et al. (1990b); (2) Jacox (2005); (3) Müller et al. (2001); (4) Nummelin & Bergman (1999); (5) Halverson et al. (1948); (6) Pickett et al. (1998); (7) Mehringer et al. (2004); (8) Senent et al. (2000); (9) Nakajima et al. (2002); (10) Groner et al. (2005); (11) Groner et al. (2002); (12) Mizushima (1975); (13) Fischer & Ross (2003); (14) Oesterling et al. (1999); (15) McNaughton et al. (1999)

2.6 Propagation of Uncertainties

When calculating the column density one must be sure to include the correct uncertainties from all measurements. With so many factors the calculation of the uncertainty in a column density can be rather complex. In the case of emission features the quantities from equation (2.1) or equation (2.2) that contain measurable uncertainties are W, C_τ, B, T_r, and T_b. These uncertainties[3] can be easily calculated from uncertainty propagation formalisms and give

$$\left(\frac{\delta N_u/g_u}{N_u/g_u}\right) = \left(\left(\frac{\delta W}{W}\right)^2 + \left(\frac{\partial f}{\partial T_r}\delta T_r\right)^2 + \left(\frac{\partial f}{\partial T_b}\delta T_b\right)^2 + \left(\frac{\delta B}{B}\right)^2 + \left(\frac{\delta C_\tau}{C_\tau}\right)^2\right)^{1/2}, \quad (2.13)$$

where

$$\left(\frac{\delta W}{W}\right) = \left(\left(\frac{\delta I}{I}\right)^2 + \left(\frac{\delta v}{v}\right)^2\right)^{1/2}, \quad (2.14)$$

[3]In all instances the uncertainties are considered to be uncorrelated.

where I is the intensity and v is the line width and

$$f = \frac{T_r}{T_r - T_b}$$

giving

$$\frac{\partial f}{\partial T_r} = \left(-\frac{T_r}{(T_r - T_b)^2} + \frac{1}{T_r - T_b}\right) \text{ and } \frac{\partial f}{\partial T_b} = \frac{T_r}{(T_r - T_b)^2}.$$

The uncertainties in B, δB, can be calculated from equation (2.9) giving

$$\delta B = \delta\Theta_S \left(\frac{\partial B}{\partial \Theta_S}\right) = 2\delta\Theta_S \left(\frac{\Theta_S}{\Theta_S^2 + \Theta_B^2} - \frac{\Theta_S^3}{(\Theta_S^2 + \Theta_B^2)^2}\right). \tag{2.15}$$

Similarly δC_τ can be calculated from equation (2.8) giving

$$\delta C_\tau = \delta\tau \left(\frac{\partial C_\tau}{\partial \tau}\right) = \delta\tau \left(\frac{1}{1 - e^{-\tau}} - \frac{\tau e^{-\tau}}{(1 - e^{-\tau})^2}\right), \tag{2.16}$$

where

$$\begin{aligned} \delta\tau &= \left(\delta T_{MB}^2 \left(\frac{\partial \tau}{\partial T_{MB}}\right)^2 + \delta x^2 \left(\frac{\partial \tau}{\partial x}\right)^2\right)^{1/2} \\ &= \left(\delta T_{MB}^2 \left(\frac{1}{x\left(1 - \frac{T_{MB}}{x}\right)}\right)^2 + \delta T_C^2 \left(\frac{T_{MB}}{x^2\left(1 - \frac{T_{MB}}{x}\right)}\right)^2\right)^{1/2}, \end{aligned} \tag{2.17}$$

where $x = (J(T_r) - J(2.73) - T_C)$ and $\delta x = (\delta J(T)^2 + \delta T_C^2)^{1/2}$.

For $\langle N_T \rangle$ calculated from individual transition the uncertainty in equation (2.13) is the uncertainty for $\langle N_T \rangle$. This is because the temperature in these situations is assumed, so Q_{rv} and the exponential term in equation (2.3) will have no uncertainties. However for $\langle N_T \rangle$ calculated by the RTD method the uncertainties for each point are given by equation (2.13) while the uncertainty in $\langle N_T \rangle$ is given by

$$\left(\frac{\delta N_T}{N_T}\right) = \left(\left(\frac{\delta Q_{rv}}{Q_{rv}}\right)^2 + \left(\frac{\delta a}{a}\right)^2\right)^{1/2}, \tag{2.18}$$

where a and δa are the intercept and its uncertainty from the weighted least squares fit and

$$\left(\frac{\delta Q_{rv}}{Q_{rv}}\right)^2 = \left(\frac{\delta T}{T}\right)^2 \tag{2.19}$$

for linear and diatomic molecules and

$$\left(\frac{\delta Q_{rv}}{Q_{rv}}\right)^2 = \left(\frac{1.5\delta T}{T}\right)^2 \tag{2.20}$$

for all others. The uncertainties from the vibrational part of the partition function are ignored since their contribution would be negligible.

For absorption features using equation (2.4) the uncertainty is given by

$$\left(\frac{\delta N_T}{N_T}\right) = \left(\left(\frac{\delta \tau}{\tau}\right)^2 + \left(\frac{\delta v}{v}\right)^2\right)^{1/2}. \tag{2.21}$$

Chapter 3

Sagittarius B2(N-LMH) Line Survey

3.1 Introduction

This chapter presents the full analysis of the BIMA Array/NRAO 12 meter telescope $\lambda = 3$ mm spectral line survey of Sagittarius B2(N-LMH). The initial results of this survey were presented in Friedel et al. (2004) (see Appendix C). A detailed description of the source and observations are given with the initial results. Additional spectral bands that were covered only by the BIMA Array have been added to the analysis (see Figure 2 of Friedel et al. (2004)).

The analysis takes into account that the velocity structure in and around the Sgr B2(N-LMH) region is rather complex. Several species have velocity components at not only the systemic velocity of $\sim$64 km s^{-1}, but also at $\sim$72 and $\sim$52 km s^{-1}. Hollis et al. (2003) determined that the source of the $\sim$72 km s^{-1} velocity component is a secondary hot core $\sim 5''$ north of Sgr B2(N-LMH) (as seen in Figure 2.2). The source of the $\sim$52 km s^{-1} velocity feature is less clear. In general the emission from this feature has very large linewidths, indicating it may come from an outflow or it may be from rotation of a disk (see e.g. Hollis et al., 2003, and references therein).

3.2 Data

The spectra from the bands covered by both instruments are presented in Figures 3.17(a-l)[1], LSR velocities of 64 km s^{-1} for the BIMA Array and 65 km s^{-1} for the 12 meter[2] were used in order to derive the frequency scale (Mehringer et al., 1997). Data obtained by the BIMA Array are presented in the top panel while data obtained by the 12 meter are presented in the lower panel. The spectra from the bands only covered by the BIMA Array are presented in Figures 3.18(a-e)[1]. The dashed lines on all BIMA Array spectra denote spectral window edges and the "I" bars, in both the 12 meter and BIMA Array data, denote 1σ rms noise levels. Transitions and unidentified lines (U lines) that are labeled in bold have velocity components at both 64 km s^{-1} and one or

[1]Due to the size of these figures and tables they appear at the back of this chapter.

[2]The difference in rest velocities is smaller then the channel spacing and will not affect the analysis or results of the data.

both of ∼72 or ∼52 km s^{-1}. In the cases where the secondary component is not obviously related to the main component the secondary component is denoted by a line out of the side of the main label.

Table 3.1 summarizes the molecular detections of the survey. The first column lists the molecule, the second and third columns list the number of detected transitions by the BIMA Array for the bands also covered by the 12 meter and those exclusively covered by the array, the fourth column lists the number of detected transitions by the 12 meter, the fifth column lists the total number of transitions detected for each species and the last column lists the reference for the molecular information for each species. Table 3.14[1] lists the molecular transitions grouped by molecule. The first column lists the rest frequency of the transition, along with the 2σ standard deviation. The second column lists the quantum numbers of the transition. The third and fourth columns list the intensity and line width[3] of each line observed by the BIMA Array. If the transition was not detected, a 1σ upper limit has been set for the intensity. The fifth and sixth columns list the beam size and opacity for the BIMA Array observations. The seventh and eighth columns list the intensity and line width of each line observed by the 12 meter. The ninth and tenth columns list the beam size and opacity for the 12 meter observations. The eleventh column lists the upper energy level of each transition. The twelfth column lists the product of the line strength and the square of the relevant dipole moment. The thirteenth column lists the measured source size for each transition. Table 3.15[1] lists the detected unidentified (U) lines. The first column lists the rest frequency (based on the LSR velocity of Sgr B2(N-LMH)). The second and third columns list the peak intensity and line width of each line from the BIMA Array. The fourth and fifth columns list the peak intensity and line width of each line from the 12 meter. If a line was undetected by one of the telescopes, a 1σ upper limit has been set for the intensity. The sixth column lists the measured source size for each U line. Note that at the distance of Sgr B2(N-LMH) (∼7.1 kpc) each arcsecond on the sky is ∼7100 AU or ∼3.4×10^{-2} pc.

Tables 3.16[1] and 3.17[1] list the transitions with ∼72 km s^{-1} and ∼52 km s^{-1} velocity components, respectively. The first column lists the rest frequency of the main line (at 64km s^{-1}) The second column lists the upper energy of the transition. The third column lists the V_{LSR} of the component. The fourth, fifth, and sixth columns list the intensity, line width and opacity of the transitions from the BIMA Array. The seventh, eighth, and ninth columns list the intensity, line width, and opacity of the transitions from the 12 meter. The tenth column lists the measured source size of the transition. Table 3.18[1] lists the U lines which appear to have components at ∼72 km s^{-1}. The first column gives the rest frequency of the main line. The second column lists the V_{LSR} of the component. The third and fourth columns list the intensity and line width from the BIMA Array observations. The fifth and sixth columns list the intensity and line width from the 12 meter observations. The seventh column lists the measured source size of the line.

[3]Intensities and line widths were obtained by a least squares fit to the line profiles.

Table 3.1. Summary of Molecules Detected Toward Sgr B2(N-LMH)

Species	Detected Transitions: BIMA	Additional BIMA Bands	12 meter	Total	Reference
l-C_3H[a]	1	0	0	1	1,2,3
C_2H	0	1	0	1	3
C_2H_3CN	17	1	3	18	4
C_2H_5CN	13	27	8	40	5
C_2H_5OH	15	2	4	17	5
C_2S	0	0	2	2	6,7
CH_3CHO	0	2	0	2	3
CH_3CN	6	0	6	6	8
$CH_3^{13}CN$	6	0	6	6	8
$(CH_3)_2CO$	0	5	0	5	9
$(CH_3)_2O$	6	18	4	24	10
CH_3OH	2	3	2	5	11
$^{13}CH_3OH$	0	2	0	2	11
CH_2NH[a]	0	1	0	1	3
^{13}CN[a]	3	0	3	3	12
^{13}CO	1	0	1	1	13
$C^{18}O$	0	1	0	1	3
H39α	0	0	1	1	14
HC_5N	0	0	1	1	3,15
HC_3N	2	6	1	8	16
$H^{13}CCCN$	1	1	0	2	3
$HC^{13}CCN$	1	1	1	2	16
$HCC^{13}CN$	1	1	1	2	16
$H^{13}CN$[a]	1	0	1	1	17
$HC^{15}N$	1	0	1	1	17
HCO[a]	0	0	1	1	3,18
$H^{13}CO^+$	1	0	1	1	19
$HC^{17}O^+$	1	0	1	1	20
$HCOOCH_3$	18	5	14	23	21
HCOOH	4	0	4	4	22
HNC	0	1	0	1	3
$HN^{13}C$[a]	1	0	1	1	3,23
HNCO	2	4	2	6	3,24
NH_2CHO[a]	2	2	2	4	25
NH_2D[a]	2	0	2	2	3,26,27
$^{15}NNH^+$	1	0	1	1	3,15
$OC^{34}S$	1	0	1	1	3,17

Table 3.1—Continued

	Detected Transitions				
Species	BIMA	Additional BIMA Bands	12 meter	Total	Reference
SiO	1	0	1	1	28
SO	1	0	1	1	29
^{34}SO	1	0	1	1	29
SO_2	2	1	1	3	30
U	73	40	24	125	···
Totals	188	125	104	330	

[a]Number of detected lines does not include hyperfine components.

References. — (1) Gottlieb et al. (1986) (2) Yamamoto et al. (1990b); (3) Pickett et al. (1998); (4) Gerry et al. (1979); (5) Lovas (1982); (6) Yamamoto et al. (1990a); (7) Murakami (1990); (8) Boucher et al. (1980); (9) Groner et al. (2002); (10) Groner et al. (1998); (11) Xu & Lovas (1997); (12) Bogey et al. (1984); (13) Lovas & Tiemann (1974); (14) Lilley & Palmer (1968); (15) Francis Lovas, private communication 2003; (16) Lafferty & Lovas (1978); (17) Lovas (1978); (18) Snyder et al. (1985); (19) Woods et al. (1981); (20) Guelin et al. (1982); (21) Oesterling et al. (1999); (22) Willemot et al. (1980); (23) Frerking et al. (1979); (24) Winnewisser et al. (1976); (25) Johnson et al. (1972); (26) Bester et al. (1983); (27) Shah & Wootten (2001); (28) Lovas & Krupenie (1974); (29) Tiemann (1974); (30) Lovas (1985)

3.3 Results and Discussion

Table 3.2 gives a summary of the results for each species. The molecular species are listed in the first column. The second column lists the average measured source size. The third column lists the rotation temperature calculated from the rotation temperature diagrams or, if there were not enough points for a diagram to be useful, the average rotation temperature, of all species, is reported and is used in the calculations. The fourth and fifth columns list the total source averaged column densities from the BIMA Array and 12 meter, respectively. The sixth and seventh columns list the abundance of the species relative to H_2 ($\langle N_T \rangle$=7.1×10^{26} cm^{-2}) for the BIMA Array and 12 meter column densities listed. The H_2 column density was calculated from Kuan et al. (1996) but using the continuum source size measured in this survey (2.3×10^{-10} sr) (see §3.3.21) in place of the source size used in their calculations, since their source size was an estimate. Tables 3.3 and 3.4 summarize the results for the 72 km s^{-1} and 52 km s^{-1} velocity components. The first three columns are identical to Table 3.2. The fourth and seventh columns list the column densities from the BIMA Array and 12 meter data, respectively. The fifth and eighth columns list the abundance of the species relative to H_2 and the sixth and ninth columns list the ratio of the column density of the velocity component relative to the main component (64 km s^{-1}). The H_2 column density was assumed to be the same for each of the velocity components. Note that all upper limits use the 1 σ rms noise level of the associated window as the intensity and 7 km s^{-1} as the line width. The upper limits also include corrections for beam response to source size.

The following sections detail the results for each molecular species (except for l-C_3H, C_2S, CH_3CHO, $(CH_3)_2CO$, CH_3HN, HCO, and HCOOH, because little can be concluded beyond what is given in Table 3.2). The 64 km s^{-1} component is discussed first, followed by any secondary velocity components detected. Eleven species that are seen only in absorption or a combination of absorption and emission (C_2H, CH_3OH, ^{13}CO, $C^{18}O$, $H^{13}CN$, $HC^{15}N$, $H^{13}CO^+$, $HC^{17}O^+$, HNC, $HN^{13}C$, and SiO) are discussed together in §3.3.21. Constraints on the identification of the unidentified lines from this survey are discussed in §3.3.20.

Table 3.2. 64 km s^{-1} Source Sizes, Rotation Temperatures, and Column Densities

Molecular Species	Size ($''$)	T_{rot}[a] (K)	$\langle N_T \rangle$ (cm^{-2}) BIMA	$\langle N_T \rangle$ (cm^{-2}) 12 meter	[X] BIMA	[X] 12 meter
l-C_3H	2.7(8)	163	$1.2(10) \times 10^{16}$	$< 1.1 \times 10^{16}$	$1.7(14)\times10^{-11}$	$<1.5\times10^{-11}$
C_2H_3CN	3.3(5)	306(88)	$9.6(66) \times 10^{17}$	$8.6(25) \times 10^{17}$	$1.5(14)\times10^{-9}$	$1.2(4)\times10^{-9}$
C_2H_5CN	2.7(2)	163(19)	$3.1(8) \times 10^{18}$	...	$4.4(11)\times10^{-9}$	...
		208(20)	...	$2.3(5) \times 10^{18}$	...	$3.2(7)\times10^{-9}$
C_2H_5OH	2.1(1)	148(64)	$3.1(17) \times 10^{18}$	$4.2(16) \times 10^{18}$	$4.4(24)\times10^{-9}$	$5.9(24)\times10^{-9}$
(extended)	~78	50	...	$1.4(1)\times10^{16}$	...	...
C_2S	>32.3(31)	50	$< 2.0 \times 10^{14}$	$9.8(6) \times 10^{13}$	...	...
CH_3CHO	2.1(7)	163	$5.9(41) \times 10^{17}$	...	$8.3(58)\times10^{-10}$	...
CH_3CN	4.1(2)	181(15)	[b]	$2.9(4) \times 10^{17}$	...	$4.1(6)\times10^{-10}$
$CH_3^{13}CN$	3.4(3)	~132	$\sim 1.0 \times 10^{17}$		$\sim1.4\times10^{-10}$	
		153(8)	...	$4.2(3) \times 10^{16}$	...	$5.9(5)\times10^{-11}$
$(CH_3)_2CO$	2.2(14)	163	$1.7(10) \times 10^{18}$	...	$2.4(14)\times10^{-9}$	...
$(CH_3)_2O$	2.3(3)	134(27)	$2.1(7) \times 10^{18}$	$6.3(24) \times 10^{18}$	$3.0(10)\times10^{-9}$	$8.9(34)\times10^{-9}$
CH_3OH	3.1(2)	163	$3.3(18) \times 10^{18}$	$9.0(13) \times 10^{18}$	$4.0(25)\times10^{-9}$	$1.3(2)\times10^{-8}$
$^{13}CH_3OH$	3.3(4)	163	$1.9(14) \times 10^{17}$	...	$2.7(20)\times10^{-10}$	...
CH_2NH	3.0(3)	163	$4.6(16) \times 10^{17}$	...	$6.5(23)\times10^{-10}$	...
^{13}CN	...	4.6	$3.7(7) \times 10^{14}$	...	[c]	...
$C^{18}O$	3.1(4)	163	$3.3(13) \times 10^{18}$	...	$4.6(18)\times10^{-9}$	...
HC_5N	1.9(5)	163	$< 2.4 \times 10^{16}$	$5.6(30) \times 10^{16}$	$<3.4\times10^{-11}$	$7.9(42)\times10^{-11}$
HC_3N	2.7(3)	541(140)	$2.2(12) \times 10^{17}$	$3.1(13) \times 10^{17}$	$3.1(17)\times10^{-10}$	$4.4(18)\times10^{-10}$
$H^{13}CCCN$	1.8(5)	163	$1.5(10) \times 10^{16}$	$< 3.4 \times 10^{17}$	$2.1(14)\times10^{-11}$	$<4.8\times10^{-10}$
$HC^{13}CCN$	2.6(7)	163	$4.0(25) \times 10^{15}$	$3.4(9) \times 10^{16}$	$5.6(35)\times10^{-12}$	$4.8(13)\times10^{-11}$
$HCC^{13}CN$	2.5(6)	163	$4.3(29) \times 10^{15}$	$3.8(10) \times 10^{16}$	$6.1(41)\times10^{-12}$	$5.4(14)\times10^{-11}$
HCO	> 31	50	$< 5.8 \times 10^{15}$	$1.8(1) \times 10^{15}$	...	...
$HCOOCH_3$	2.2(2)	163	$2.5(7) \times 10^{18}$	$3.9(14) \times 10^{18}$	$3.5(10)\times10^{-9}$	$5.4(20)\times10^{-9}$
HCOOH	2.4(6)	163	$3.1(4) \times 10^{17}$	$1.5(4) \times 10^{18}$	$4.4(6)\times10^{-10}$	$2.1(6)\times10^{-9}$
HNCO	2.2(4)	133(40)	$8.8(80) \times 10^{18}$	$2.2(9) \times 10^{18}$	$1.2(11)\times10^{-8}$	$3.1(13)\times10^{-9}$
NH_2CHO	2.5(8)	198(89)	$9.0(68) \times 10^{18}$	$6.6(35) \times 10^{18}$	$1.3(10)\times10^{-8}$	$9.3(49)\times10^{-9}$
NH_2D(ortho)	2.8(3)	163	$7.5(45) \times 10^{17}$	$2.2(6) \times 10^{18}$	$1.1(6)\times10^{-9}$	$3.1(9)\times10^{-9}$
NH_2D(para)	2.6(4)	163	$3.8(16) \times 10^{17}$	$3.0(13) \times 10^{17}$	$5.4(21)\times10^{-10}$	$4.2(18)\times10^{-10}$
N_2H^+	2.4(3)	163	$1.8(6) \times 10^{15}$	$8.0(28) \times 10^{15}$	$2.5(9)\times10^{-12}$	$1.1(4)\times10^{-11}$
$OC^{34}S$	2.7(3)	163	$2.7(8) \times 10^{17}$	$5.3(14) \times 10^{17}$	$3.8(11)\times10^{-10}$	$7.5(20)\times10^{-10}$
SO	4.8(2)	163	$1.9(2) \times 10^{17}$	$1.4(1) \times 10^{18}$	$2.7(3)\times10^{-10}$	$2.0(1)\times10^{-9}$
SO(wide)	...	163	$4.0(6) \times 10^{17}$	...	...	...
^{34}SO	1.3(12)	163	$\sim 7.9 \times 10^{17}$	$\sim 7.4 \times 10^{17}$	$\sim1.1\times10^{-9}$	$\sim1.0\times10^{-9}$
SO_2	1.4(6)	188(98)	$\sim 2.7 \times 10^{19}$	$\sim 1.3 \times 10^{19}$	$\sim3.8\times10^{-8}$	$\sim1.8\times10^{-8}$

[a]Rotation temperatures given with no uncertainty are assumed.

[b]Due to very high opacity, a column density was not determined.

[c]There were too many weak overlapping components to obtain a fit so no column density could be calculated.

Table 3.3. 72 km s^{-1} Source Sizes, Rotation Temperatures, and Column Densities

Molecular Species	Size ($''$)	T_{rot}[a] (K)	BIMA $\langle N_T \rangle$(cm^{-2})	BIMA [X]	BIMA $\frac{\langle N_{74} \rangle}{\langle N_{64} \rangle}$	12 meter $\langle N_T \rangle$(cm^{-2})	12 meter [X]	12 meter $\frac{\langle N_{74} \rangle}{\langle N_{64} \rangle}$
C_2H_3CN	3.0(2)	163	$1.5(5) \times 10^{17}$	$2.1(7)\times10^{-10}$	0.14(13)	$1.1(2) \times 10^{17}$	$1.5(3)\times10^{-11}$	0.14(5)
C_2H_5CN	3.1(4)	154(47)	$5.3(30) \times 10^{17}$	$7.5(44)\times10^{-10}$	0.17(11)	$5.0(26) \times 10^{17}$	$7.0(37)\times10^{-10}$	0.22(12)
C_2H_5OH	3.6(6)	163	$4.5(25) \times 10^{16}$	$6.3(35)\times10^{-11}$	$\sim$0.01	$< 5.9 \times 10^{17}$	$<8.3\times10^{-10}$	< 0.14
CH_3OH	4.0(6)	163	$1.4(6) \times 10^{18}$	$2.0(9)\times10^{-9}$	0.42(29)	$1.2(3) \times 10^{18}$	$1.7(4)\times10^{-9}$	0.13(4)
$^{13}CH_3OH$	2.3(9)	163	$1.2(10) \times 10^{17}$	$1.7(14)\times10^{-10}$	$\sim$0.63	...	...	...
CH_2NH	4.4(2)	163	$7.5(33) \times 10^{16}$	$1.1(5)\times10^{-10}$	0.16(9)	...	...	...
$C^{18}O$	3.8(7)	163	$1.1(4) \times 10^{19}$	$1.5(6)\times10^{-8}$	3.33(179)	...	...	...
HC_3N	2.8(6)	163	$1.5(13) \times 10^{16}$	$2.1(18)\times10^{-11}$	$\sim$0.07	...	...	...
$HC^{13}CCN$	1.8(8)	163	$\sim 3.0 \times 10^{16}$[b]	$\sim4.2\times10^{-11}$	7.50(469)	[c]	...	...
$HCC^{13}CN$	2.8(6)	163	$8.6(61) \times 10^{15}$	$1.2(9)\times10^{-11}$	2.00(196)	[c]	...	...
$HCOOCH_3$	2.5(8)	163	$5.5(35) \times 10^{17}$	$7.7(49)\times10^{-10}$	0.22(15)	$1.2(5) \times 10^{18}$	$1.7(7)\times10^{-9}$	0.32(18)
HCOOH	4.1(4)	163	$< 2.6 \times 10^{16}$	$<3.7\times10^{-11}$	0.08(1)	$8.8(44) \times 10^{17}$	$1.2(6)\times10^{-9}$	0.59(33)
NH_2CHO	2.1(3)	163	$7.2(27) \times 10^{16}$	$1.0(4)\times10^{-10}$	$8.1(68)\times10^{-3}$	$1.2(3) \times 10^{17}$	$1.7(4)\times10^{-10}$	0.18(10)

[a]Rotation temperatures given with no uncertainty are assumed.

[b]Column density is approximate due to large uncertainties.

[c]Column density could not be determined as velocity component could not be reliably separated from main component.

Table 3.4. 52 km s^{-1} Source Sizes, Rotation Temperatures, and Column Densities

Molecular Species	Size ($''$)	T_{rot}[a] (K)	BIMA $\langle N_T \rangle$(cm^{-2})	BIMA [X]	BIMA $\frac{\langle N_{52} \rangle}{\langle N_{64} \rangle}$	12 meter $\langle N_T \rangle$(cm^{-2})	12 meter [X]	12 meter $\frac{\langle N_{52} \rangle}{\langle N_{64} \rangle}$
C_2H_5CN	2.7(7)	163	$3.5(25) \times 10^{17}$	$4.9(35)\times10^{-10}$	0.11(9)	$4.5(33) \times 10^{17}$	$6.3(46)\times10^{-10}$	0.20(15)
CH_3OH	3.1(2)	163	$6.5(49) \times 10^{18}$	$9.2(69)\times10^{-9}$	1.97(183)	$7.1(17) \times 10^{17}$	$1.0(2)\times10^{-9}$	0.08(2)
$HC^{13}CCN$	2.0(5)	163	$\sim 1.9 \times 10^{16}$[b]	$\sim2.7\times10^{-11}$	4.75(297)	[c]	...	...
$HCC^{13}CN$	2.0(5)	163	$\sim 2.1 \times 10^{16}$[b]	$\sim3.0\times10^{-11}$	4.88(329)	[c]	...	...

[a]Rotation temperatures are assumed.

[b]Column density is approximate due to large uncertainties.

[c]Column density could not be determined as velocity component could not be reliably separated from main component.

3.3.1 C_2H_3CN (Vinyl Cyanide)

A total of 18 C_2H_3CN transitions (2 ground state (gs) and 16 vibrationally excited state (ves)) were detected in this survey, one of which is severely blended with a transition of CH_3OH. An average source size of 3.4(5)″ was found for this molecule. This yields a total column density of $9.6(66) \times 10^{17}$ cm^{-2} with a rotation temperature of 306(88) K from the BIMA Array data. There are fewer points on the diagram than detected transitions because several of the transitions are degenerate in both energy and frequency. Since only three of the transitions were detected by the 12 meter, the BIMA Array rotation temperature was adopted. Together with the average source size, the 12 meter data yield a total column density of $8.6(25) \times 10^{17}$ cm^{-2}. Figure 3.1 shows the C_2H_3CN rotation temperature diagram for the main velocity component[4]. These column densities

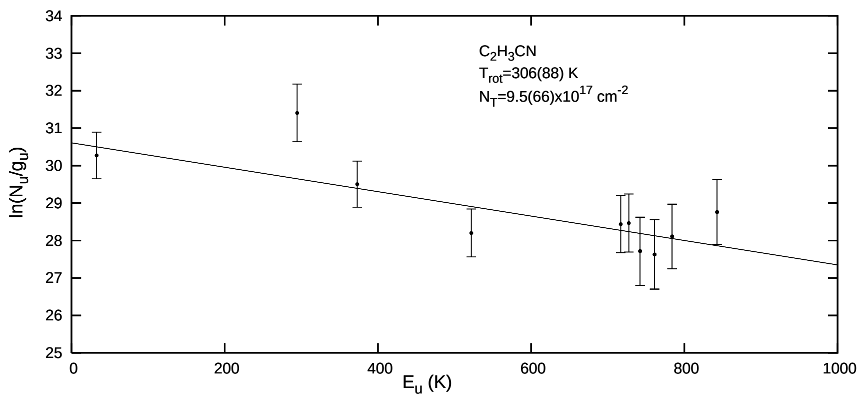

Figure 3.1 C_2H_3CN rotation temperature diagram from BIMA Array data. The abscissa is the upper state energy of the transition in K and the ordinate is the log of the normalized column density. The line is the weighted least squares fit to the data.

agree, within the uncertainties, with those reported by Nummelin & Bergman (1999). While the rotation temperature reported here is much lower, it also agrees within the uncertainties. Also the source size reported in Nummelin & Bergman (1999) is significantly smaller than that reported here. A two temperature component fit, utilized by Nummelin & Bergman (1999), was not needed for the data reported here,possibly due to the much smaller number of lines observed in this survey.

Five of the C_2H_3CN transitions (1 gs and 4 ves) have velocity components near 72 km s^{-1}. Using the average rotation temperature of 163 K and average source size of 3.0(2)″ total column densities of $1.5(5) \times 10^{17}$ cm^{-2} and $1.1(2) \times 10^{17}$ cm^{-2} are found from the BIMA Array and 12 meter data, respectively.

3.3.2 C_2H_5CN (Ethyl Cyanide)

A total of 40 C_2H_5CN transitions (15 gs and 25 ves) were detected in this survey. When calculating the column density and rotation temperature of C_2H_5CN one must be careful of degeneracies. In the ground vibrational state, the *A* and *E* torsional states are degenerate. However, in the first and

[4]All error bars on the rotation temperature diagrams are 2 σ unless otherwise noted.

second excited states (and likely with higher states also) the A and E torsional states are no longer degenerate. Thus, one needs to either divide all of the ground state integrated intensities by 2 and also multiply the partition function by 2 or multiply the integrated intensities of the vibrationally excited transitions by 2 to take the degeneracies into account. From source size fits in the u-v plane an average source size of 2.7(2)″ was found for C_2H_5CN. Rotation temperature diagrams yield total column densities and rotation temperatures of $3.1(8) \times 10^{18}$ cm^{-2} and 163(19) K from the BIMA Array data and $2.3(5) \times 10^{18}$ cm^{-2} and 208(20) K from the 12 meter data. Figure 3.2 shows the C_2H_5CN rotation temperature diagram from the BIMA Array. The points denoted with a □ have low E_u and high $S\mu^2$ and are optically thick and are not used in any calculations. Figure 3.3 shows the C_2H_5CN rotation temperature diagram from the 12 meter data. The column densities

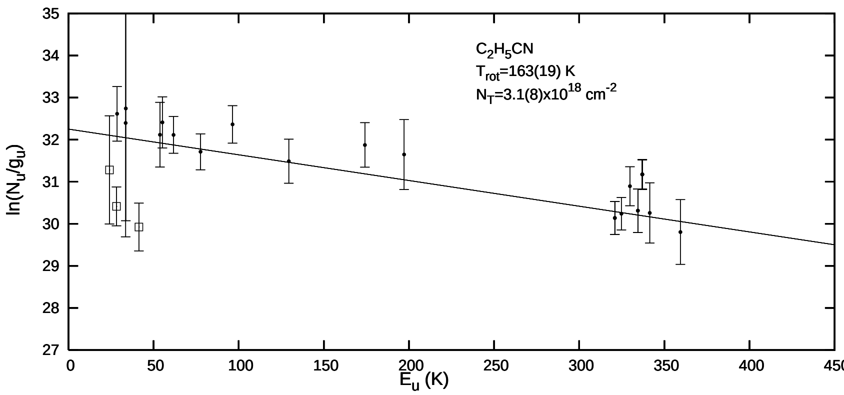

Figure 3.2 C_2H_5CN rotation temperature diagram from the BIMA Array. The abscissa is the upper state energy of the transition in K, and the ordinate is the log of the normalized column density. The line is the weighted least squares fit to the data. The points indicated with a □ are highly optically thick and were not used in the calculation.

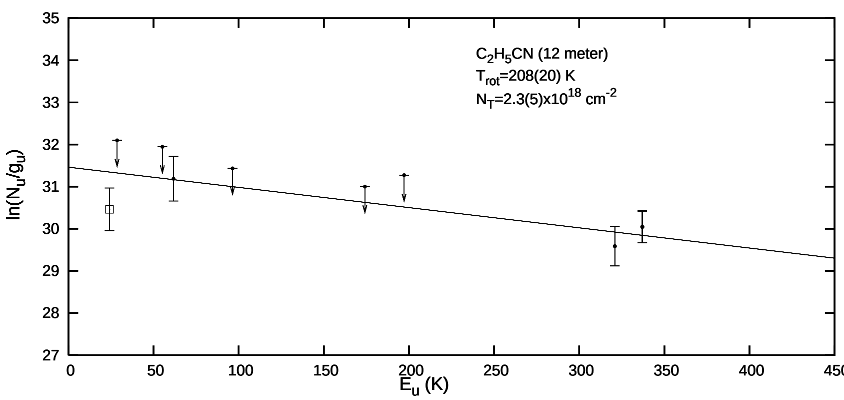

Figure 3.3 C_2H_5CN rotation temperature diagram from the 12 meter. The abscissa is the upper state energy of the transition in K, and the ordinate is the log of the normalized column density. The line is the weighted least squares fit to the data. The points indicated by arrows are 1 σ upper limits on the transitions not detected by the 12 meter.

from this survey are almost two orders of magnitude higher than those reported in Mehringer et al. (2004) and this is most likely due to the source size correction used in this survey.

Thirty one of the detected C_2H_5CN transitions (14 gs and 17 ves) have components at ~72 km s^{-1}. Using the average measured source size of 3.1(4)″ a total column density of $5.3(30) \times 10^{17}$ cm^{-2} and a rotation temperature of 154(47) K are found from the BIMA Array data. Using this source size and rotation temperature, the 12 meter data yields a total column density of $5.0(26) \times 10^{17}$ cm^{-2}. These column densities are an order of magnitude higher than those reported in Mehringer et al. (2004), for this velocity component, and the difference is most likely due to the source size correction used in this survey. Figure 3.4 shows the rotation temperature diagram for the 72 km s^{-1} velocity component of C_2H_5CN.

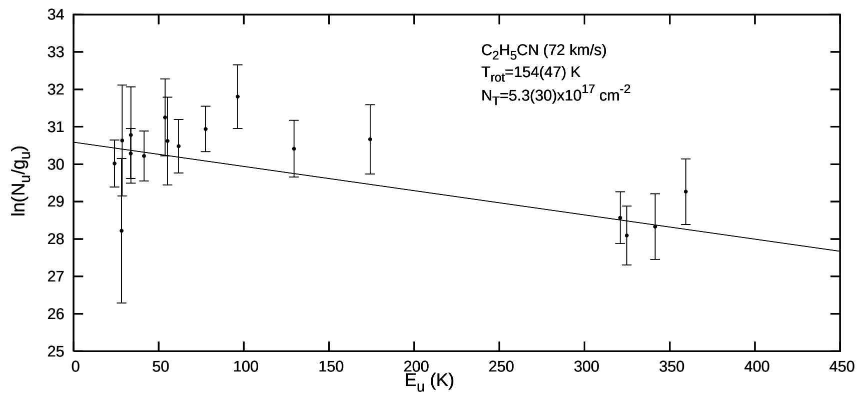

Figure 3.4 BIMA Array 72 km s^{-1} C_2H_5CN velocity component rotation temperature diagram. The abscissa is the upper state energy of the transition in K, and the ordinate is the log of the normalized column density. The line is the weighted least squares fit to the data.

Fifteen of the detected C_2H_5CN transitions (4 gs and 11 ves) have velocity components at ~52 km s^{-1}. Using the average source size of 2.7(7)″ and a rotation temperature of 163 K total column densities of $3.5(25) \times 10^{17}$ cm^{-2} and $4.5(33) \times 10^{17}$ cm^{-2} are found from the BIMA Array and 12 meter data, respectively.

3.3.3 C_2H_5OH (Ethanol)

This survey detected a total of 17 ground state C_2H_5OH transitions. C_2H_5OH has three torsional states (*trans*, *gauch+*, and *gauch-*) each with slightly different ground state energies. These energy differences grow with the vibrational states (although the two *gauch* states stay nearly identical). Thus the column densities of the states must be calculated separately and then summed together[5]. From source size fitting in the *u-v* plane an average source size of 2.1(1)″ is found. The rotation temperature diagram shown in Figure 3.5 yields a total column density of $3.1(17) \times 10^{18}$ cm^{-2} and rotation temperature of 148(64) K from the BIMA Array data. Using this temperature and source size the 12 meter data give a total column density of $4.2(16) \times 10^{18}$ cm^{-2}. The transition denoted by a □ in the diagram has a very low upper state energy (~9 K) and appears to have a significant extended component that can be seen in the order of magnitude difference in intensity between the

[5]Since only ground state transitions were detected in this work all torsional states were used in the analysis, but the application of the vibrational partition function was done separately and the results summed together.

12 meter and BIMA Array spectra. This difference is due to the fact that the BIMA Array filters out the large scale component that contributes almost all of the 12 meter flux. The size of this component from fitting in the *u*-*v* plane is estimated to be at least 78″. Using a rotation temperature of 50 K (Hollis et al., 2003) the 12 meter data give a total column density of $1.4(1)\times10^{16}$ cm^{-2} for this extended component. These column densities are nearly three orders of magnitude higher than

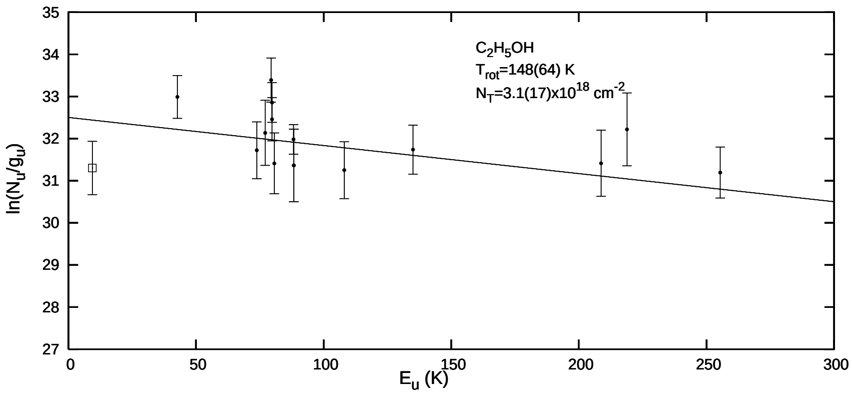

Figure 3.5 C_2H_5OH rotation temperature diagram. The abscissa is the upper state energy of the transition in K, and the ordinate is the log of the normalized column density. The line is the weighted least squares fit to the data. The point indicated with a □ is highly extended and was not used in the calculation.

those reported in Nummelin et al. (2000) (hereafter N00) and the rotation temperature reported here is a factor of two higher. The column density difference is likely due to the lower reported temperature in N00 and the source size correction in this survey.

Eight of the detected C_2H_5OH transitions have components at 72 km s^{-1}. Using the average source size of 3.6(6)″ and a rotation temperature of 163 K the BIMA Array data yields a total column density of $4.5(25)\times10^{16}$ cm^{-2}. Using this source size and temperature the 12 meter data yields an upper limit of $< 5.9\times10^{17}$ cm^{-2}.

3.3.4 CH_3CN (Methyl Cyanide)

A total of six ground state transitions of CH_3CN were detected in this survey. Due to the very high opacity of the BIMA Array data, a normal analysis was not feasible. Using an average source size of 4.1(2)″, Figure 3.6 shows the rotation temperature diagram from the 12 meter data. From this a total column density of $2.9(4)\times10^{17}$ cm^{-2} and a rotation temperature of 181(15) K are found. This column density and source size agree rather well with those reported by N00. The rotation temperatures however do not agree. This may be due to the much larger range of energies reported by N00, including transitions within the first vibrational state and K values up to 12 within the ground vibrational state.

A total of six $CH_3^{13}CN$ transitions were detected in this survey. An average source size of 3.4(3)″ was measured for these transitions. Figure 3.7 shows the rotation temperature diagram for the BIMA Array data, and Figure 3.8 shows the rotation temperature diagram for the 12 meter data. Transitions denoted with a □ have either a high opacity or are severely blended with other

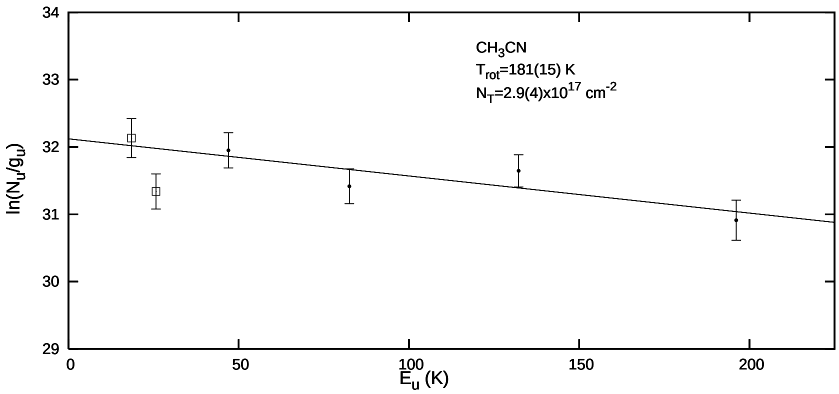

Figure 3.6 CH_3CN rotation temperature diagram from the 12 meter data. The abscissa is the upper state energy of the transition in K, and the ordinate is the log of the normalized column density. The line is the weighted least squares fit to the data. The points indicated with a □ are strongly blended and are not used in the calculations.

transitions and were not used in the analysis. A total column density of $\sim 1.0 \times 10^{17}$ cm^{-2} and rotation temperature of ∼132 K are found from the BIMA Array data, and a total column density of $4.2(3) \times 10^{16}$ cm^{-2} and rotation temperature of 153(8) K are found from the 12 meter data.

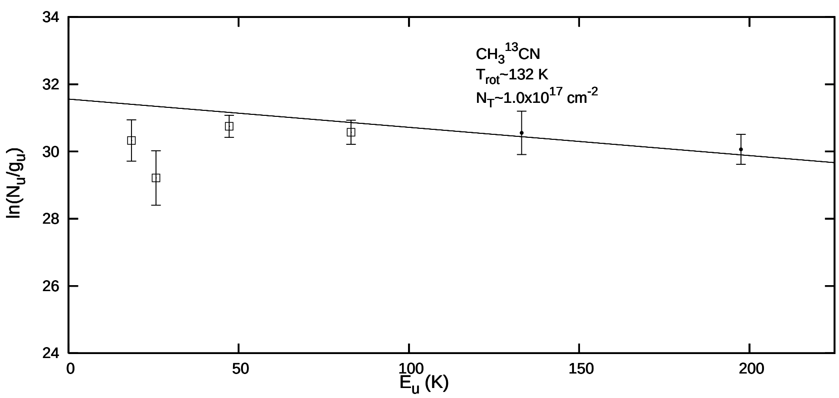

Figure 3.7 $CH_3^{13}CN$ rotation temperature diagram from the BIMA Array data. The abscissa is the upper state energy of the transition in K, and the ordinate is the log of the normalized column density. The line is the weighted least squares fit to the data. The points indicated with a □ are highly optically thick or strongly blended and are not used in the calculation.

The column densities and rotation temperatures reported here are lower than those reported by N00. As with CH_3CN these differences are most likely due to the much larger energy range in N00.

From the column densities the $^{12}C/^{13}C$ ratio for this species is of 6.8(10). It is also possible that the 12 meter and BIMA Array are sampling different populations of CH_3CN. The lower energy transitions may have significant extended components seen by the 12 meter but resolved out by the BIMA Array.

Due to the large line width and blending of transitions, no components at any velocity other than 64 km s^{-1} were reliably fit. In the case of unresolved velocity components the column densities calculated are overestimates.

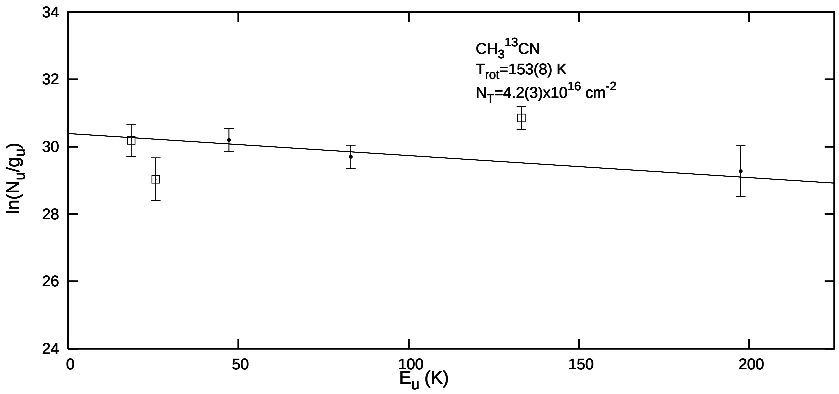

Figure 3.8 $CH_3^{13}CN$ rotation temperature diagram from the 12 meter data. The abscissa is the upper state energy of the transition in K, and the ordinate is the log of the normalized column density. The line is the weighted least squares fit to the data. The points indicated with a □ are highly optically thick or strongly blended and are not used in the calculation.

3.3.5 $(CH_3)_2O$ (Dimethyl Ether)

In this survey a total of 24 degenerate and nondegenerate ground state $(CH_3)_2O$ transitions were detected. From source size fitting in the u-v plane an average source size of 2.3(3)″ was found. Figure 3.9 shows the rotation temperature diagram of $(CH_3)_2O$ from the BIMA Array data. The total column density from the diagram is $2.1(7)\times10^{18}$ cm^{-2} with a rotation temperature of 134(27) K. Using this temperature and source size the 12 meter data yield a column density of $6.3(24)\times10^{18}$ cm^{-2}. N00 reported a column density several orders of magnitude lower than that reported here, the difference being due to the source size correction used in this survey. No emission features were detected at either 72 km s^{-1} or 52 km s^{-1}, although the $(CH_3)_2O$ features were weak and emission from these other velocity components could have been below the 3 σ detection limit. Friedel et al. (2004) speculated that $(CH_3)_2O$ may have extended structure, however the u-v source size analysis indicates a compact distribution.

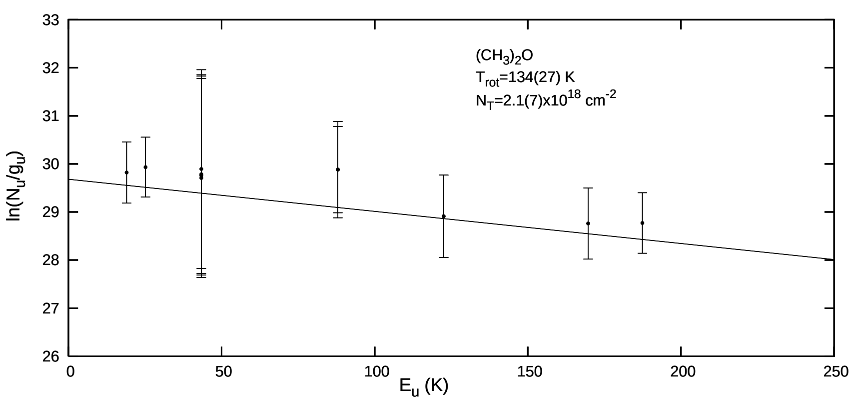

Figure 3.9 $(CH_3)_2O$ rotation temperature diagram from the BIMA Array data. The abscissa is the upper state energy of the transition in K, and the ordinate is the log of the normalized column density. The line is the weighted least squares fit to the data.

3.3.6 CH_3OH (Methanol)

A total of five (4 gs and 1 ves) transitions of CH_3OH, one of which is blended with a transition of C_2H_3CN, were detected in this survey. Using an average measured source size of 3.1(2)″ and a temperature of 163 K a total column density of $3.3(18) \times 10^{18}$ cm^{-2} is found from the BIMA Array data and $9.0(13) \times 10^{18}$ cm^{-2} from the 12 meter data. These column densities and the source size agree well with those reported in N00.

Two of the CH_3OH transitions have components at ∼72 km s^{-1}. Using an average source size of 4.0(6)″ and a rotation temperature of 163 K, total column densities of $1.4(6) \times 10^{18}$ cm^{-2} and $1.2(3) \times 10^{18}$ cm^{-2} are found from the BIMA Array and 12 meter data, respectively. Also two of the CH_3OH transitions have components at ∼52 km s^{-1}, and using a source size of 3.1(2)″ and a rotation temperature of 163 K total column densities of $6.5(49) \times 10^{18}$ cm^{-2} and $7.1(17) \times 10^{17}$ cm^{-2} are found from the BIMA Array and 12 meter data, respectively.

Two transitions of $^{13}CH_3OH$ were detected by the BIMA Array in the extra bands. Using a measured source size of 3.3(3)″ and a temperature of 163 K, the total column density of $1.9(14) \times 10^{17}$ cm^{-2} is found. This gives a $^{12}C/^{13}C$ ratio of 17.6(167). Given the uncertainties in this column density and that reported in N00, they are in agreement. One of the $^{13}CH_3OH$ transitions has a component at ∼72 km s^{-1}, and using a source size of 2.3(9)″ and rotation temperature of 163 K a total column density of $1.9(14) \times 10^{17}$ cm^{-2} is found.

3.3.7 ^{13}CN (Cyanogen Radical)

Two multiplets of ^{13}CN transitions were detected in this survey. Only one of these multiplets, from the BIMA Array data, could be reliably fit with Gaussians. Using the continuum source size, since these transitions were seen in absorption, and a temperature of 4.6 K (see §3.3.21) the BIMA Array data yield a total column density of $3.7(7) \times 10^{14}$ cm^{-2}. A reliable fit could not be found for the 12 meter data, thus no column densities could be calculated. Due to the low signal to noise and complex hyperfine structure of these transitions no other velocity components were detected, although they could be hidden by the hyperfine structure or they could be below the detection limit.

3.3.8 H39α

The 12 meter detected the only recombination line in this survey. The BIMA Array also detected the line, but towards Sgr B2(M) rather than Sgr B2(N-LMH). This is not surprising, as the majority of HII emission comes from the main core (Gaume et al., 1995; de Pree et al., 1995, 1996). A source size of 2.4(5)″ was measured for the recombination line, although there was indication of multiple sources.

3.3.9 HC_5N (Cyanodiacetylene)

The 12 meter detected the only HC_5N transition in the survey. Using a measured source size of $1.9(5)''$[6] and a temperature of 163 K, the total column density from the 12 meter is $5.6(30) \times 10^{16}$ cm^{-2} and the upper limit from the BIMA Array is $< 2.4 \times 10^{16}$ cm^{-2}. It is possible that this identification is incorrect as the $J = 40 - 39$ transition has a very high upper energy and is more likely to be detected by the array than by the 12 meter. High energy transitions will be primarily excited in the core and not in an extended region.

3.3.10 HC_3N (Cyanoacetylene)

A total of eight transitions (1 gs and 7 ves) of HC_3N were detected in this survey. Source sizes of the transitions measured in the *u*-*v* plane were well correlated with upper energy. The lowest upper energy transition has the largest source size, and the source size dropped with increasing upper energy with an average source size of $2.7(3)''$. The lowest upper energy transition ($J = 10 - 9$) also has indications of an extended component on the order of $20''$, although without a measurement from the 12 meter the actual size of the extended component is uncertain. Several of the transitions also have indications of weak emission from Sgr B2(M). Figure 3.10 shows the rotation temperature diagram from HC_3N. Note that the lowest energy transition appears optically thick and is not used in the calculations. The fit yields a total column density of $2.2(12) \times 10^{17}$ cm^{-2} and a rotation temperature of 541(140) K. Using this source size and rotation temperature the 12 meter observations yield a column density of $3.1(13) \times 10^{17}$ cm^{-2}.

It is possible that the lines of the ground and vibrationally excited states occupy different spatial regions which may be why the rotation temperature is so high compared to that of other compact species. This is supported by the fact that the line width of all ground state transitions (including isotopologues) appear to be near 7 km s^{-1}, while the typical line width of the vibrationally excited state lines is 2-3 times that. If a rotation temperature of 163 K is assumed, the ground state line yields a total column density of $6.1(9)\times10^{15}$ cm^{-2}. Four of the HC_3N transitions have components at $\sim$72 km s^{-1}. Using an average source size of $2.8(6)''$ and a rotation temperature of 163 K, the BIMA Array data yield a total column density of $1.5(13) \times 10^{16}$ cm^{-2}.

Two transitions of each of the three ^{13}C isotopologues of HC_3N were detected. Both transitions of $H^{13}CCCN$ are from vibrationally excited states while the transitions from the other two isotopomers are ground state transitions. Using an average source size of $1.8(5)''$ and rotation temperature of 163 K for $H^{13}CCCN$, a total column density of $1.5(10) \times 10^{16}$ cm^{-2} is found from the BIMA Array data and an upper limit of $< 3.4 \times 10^{17}$ cm^{-2} is found from the 12 meter data. For $HC^{13}CCN$ an average source size of $2.6(7)''$ and rotation temperature of 163 K yield total column densities of $4.0(25) \times 10^{15}$ cm^{-2} and $3.4(9) \times 10^{16}$ cm^{-2} from the BIMA Array and 12 meter data, respectively. For $HCC^{13}CN$ an average source size of $2.5(6)''$ and rotation temperature of 163 K

[6]Although the BIMA Array did not detect this transition above 3 σ, source size fitting in the *u*-*v* plane was still possible.

yield total column densities of $4.3(29) \times 10^{15}$ cm^{-2} and $3.8(10) \times 10^{16}$ cm^{-2} from the BIMA Array and 12 meter data, respectively. The large column density of $H^{13}CCCN$ with respect to the other isotopomers is likely due to the much smaller source size for $H^{13}CCCN$. Thus, since both transitions of $H^{13}CCCN$ are from vibrationally excited states, it is likely that these transitions occupy the same, smaller, spatial region as the vibrationally excited transitions of HC_3N.

All detected transitions of $HC^{13}CCN$ and $HCC^{13}CN$ have components at $\sim$72 km s^{-1}. Using measured source sizes of 1.8(8)″ and 2.8(6)″ and a rotation temperature of 163 K, the BIMA Array data yield column densities of $\sim 3.0 \times 10^{16}$ cm^{-2} and $8.6(61) \times 10^{15}$ cm^{-2}, respectively. The $\sim$72 km s^{-1} velocity component could not be reliably separated from the main components in the 12 meter data, thus column densities could not be calculated.

For all detected isotopologues of HC_3N the 12 meter data and column densities suggest an extended ground state component that is resolved out by the BIMA Array. This is supported by the column densities reported by N00, which are also larger than those from the array.

In order to obtain a $^{12}C/^{13}C$ ratio one must add up all three variations of HC_3N containing ^{13}C (or multiply one of them by three). This yields a ratio less than one (0.67), an unlikely value. This indicates that the main isotope of HC_3N may also be optically thick in the ground state and thus the ratio is underestimated. The argument for high opacity is further supported by the fact that the transition is not centered at 64 km s^{-1} but rather closer to 60 or 61 km s^{-1}. This shift could be induced by opacity/self absorption at the peak of the line.

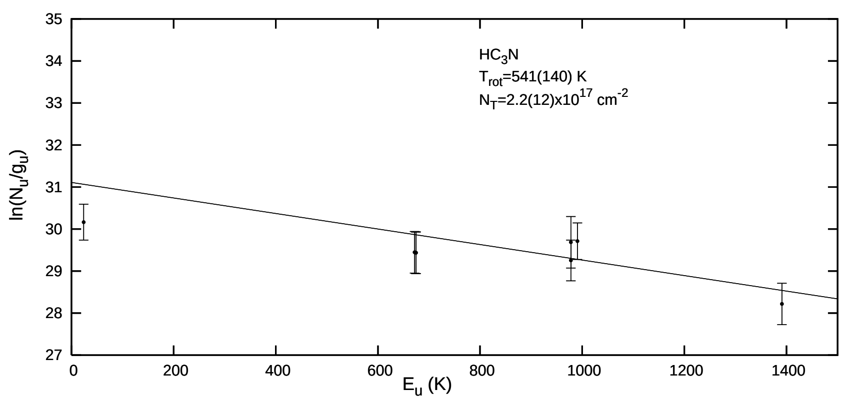

Figure 3.10 HC_3N rotation temperature diagram. The abscissa is the upper state energy of the transition in K, and the ordinate is the log of the normalized column density. The line is the weighted least squares fit to the data.

3.3.11 $HCOOCH_3$ (Methyl Formate)

This survey detected a total of 23 ground state $HCOOCH_3$ transitions. Even though a large number of transitions were detected, their upper energy ranged from 19.7 K to 59.1 K which is too small of a spread in energy to construct a meaningful rotation temperature diagram. Using an average source size of 2.2(2)″ and a temperature of 163 K, the BIMA Array data yield a total column density of $2.5(7) \times 10^{18}$ cm^{-2} and the 12 meter data yield a total column density of $3.9(14) \times 10^{18}$ cm^{-2}.

Seven of the $HCOOCH_3$ transitions have a component at $\sim$72 km s^{-1}. With an average source size of 2.5(8)$''$ and a rotation temperature of 163 K, total column densities of $5.5(35) \times 10^{17}$ cm^{-2} and $1.2(5) \times 10^{18}$ cm^{-2} are found from the BIMA Array and 12 meter data, respectively. Since $HCOOCH_3$ transitions are in A and E pairs, it is possible that more of the transitions have components at $\sim$72 km s^{-1} that are hidden by the 64 km s^{-1} component of the other line in the pair. As for many of the species in this survey the column densities reported here are orders of magnitude higher than those reported by N00. The difference is most likely from the source size correction and vibrational partition function used in this survey.

3.3.12 HNCO (Isocyanic Acid)

Six ground state transitions of HNCO were detected in this survey. HNCO has an average source size of 2.2(4)$''$. However the $5_{0,5}-4_{0,4}$ transition (the lowest energy transition detected) has a significant extended component at least 74$''$ in size. Figure 3.11 shows the rotation temperature diagram of HNCO from the BIMA Array data[7]. From the fit the total column density is $8.8(80) \times 10^{18}$ cm^{-2} with a temperature of 133(40) K. Using this temperature and average source size the 12 meter data yield a total column density of $2.2(9) \times 10^{18}$ cm^{-2}. No other velocity components were detected for HNCO. However the high velocity wing of the $5_{0,5} - 4_{0,4}$ transition from the 12 meter data is truncated and the BIMA Array data indicates severe self absorption. Thus HNCO may have other velocity components that went undetected by this survey. The column densities reported by N00

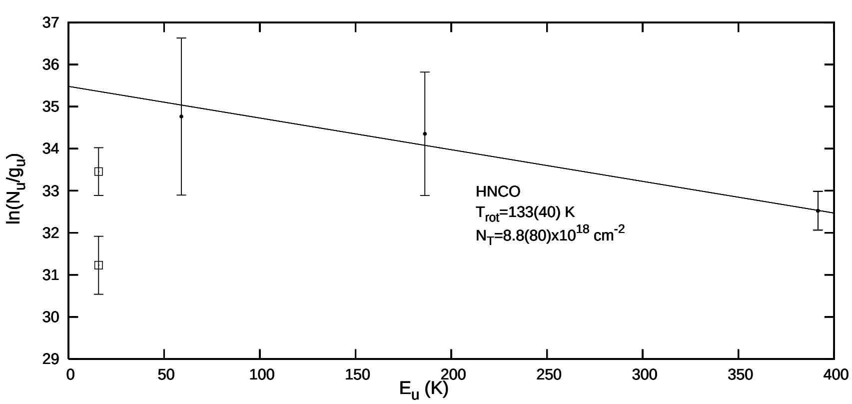

Figure 3.11 HNCO rotation temperature diagram. The abscissa is the upper state energy of the transition in K, and the ordinate is the log of the normalized column density. The line is the weighted least squares fit to the data. The points denoted by a □ are optically thick and are not used in any calculations. Note the error bars are 1 σ for this plot.

are orders of magnitude lower than those reported here, the difference being due to the source size correction. The rotation temperatures also do not agree. This may be due to the relatively small number of transitions detected in this survey, giving few points to fit for the temperature.

[7]Due to their size the error bars are 1 σ for this plot. Also with only a few points the fit may not be reliable

3.3.13 NH_2CHO (Formamide)

Only four ground state NH_2CHO transitions were detected by this survey. Measurements in u-v space give an average source size of 2.5(8)″ for NH_2CHO. Figure 3.12 shows the rotation temperature diagram. The fit to the BIMA Array data gives a total column density of $9.0(68) \times 10^{18}$ cm^{-2} and a rotation temperature of 198(89) K. Using this temperature and source size, the 12 meter data has a total column density of $6.6(35) \times 10^{18}$ cm^{-2}. One NH_2CHO transition has a velocity component at ∼72 km s^{-1} with a source size of 2.1(3)″. Using this with a rotation temperature of 163 K yields column densities of $7.2(27) \times 10^{16}$ cm^{-2} and $1.2(3) \times 10^{17}$ cm^{-2} from the BIMA Array and 12 meter data, respectively. The main velocity component rotation temperature agrees well with

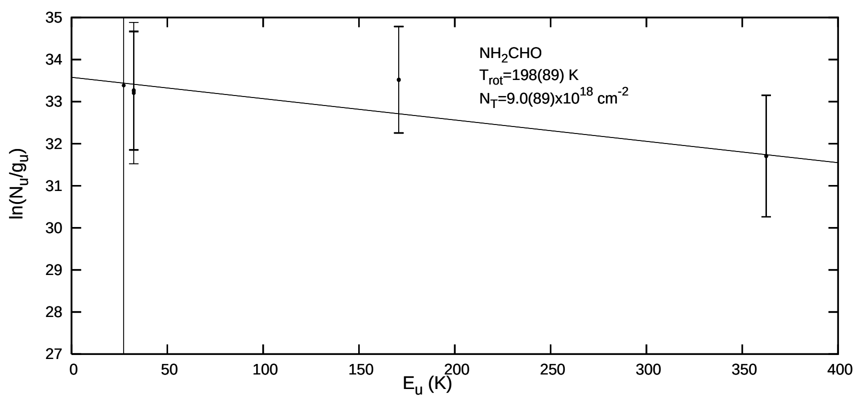

Figure 3.12 NH_2CHO rotation temperature diagram. The abscissa is the upper state energy of the transition in K, and the ordinate is the log of the normalized column density. The line is the weighted least squares fit to the data. Note that the error bars are 1 σ for this plot.

that reported by N00, but the column density reported here is much larger due to the source size correction used in this survey.

3.3.14 NH_2D (Deuterated Ammonia)

Two ground state NH_2D transitions were detected in this survey. The ortho state has a source size of 2.8(3)″, and the para state has a source size of 2.6(4)″. Using a temperature of 163 K and the appropriate source size, the ortho state has total column density of $7.5(45) \times 10^{17}$ cm^{-2} from the BIMA Array data and $2.2(6) \times 10^{18}$ cm^{-2} from the 12 meter data, and the para state has a total column density of $3.8(16) \times 10^{17}$ cm^{-2} from the BIMA Array data and $3.0(13) \times 10^{17}$ cm^{-2} from the 12 meter data. These column densities give an ortho to para ratio of 2.0(14) and 7.3(37) for the BIMA Array and 12 meter respectively. These two ratios do not agree. This may be due to a triplet of $HCOOCH_3$ transitions, detected by the BIMA Array, that may be buried in the NH_2D ortho line, adding to its intensity in the 12 meter data. No other velocity components were detected for NH_2D.

3.3.15 ^{15}NNH$^+$

A single ground state transition of $^{15}N_2H^+$ was detected by this survey and has a source size of $2.4(3)''$. Using this source size and a rotation temperature of 163 K, the BIMA Array data give a total column density of $1.8(6) \times 10^{15}$ cm^{-2}, and the 12 meter data give a total column density of $8.0(28) \times 10^{15}$ cm^{-2}. The difference between the column densities may be due to either low S/N or extended components, especially since the 12 meter has a larger line width, indicating missing flux from the BIMA Array observations. This is not surprising as cations are not expected to reside in dense hot cores, as they react easily with other molecules, but rather should reside in less dense outer layers. The slight velocity offset also indicates that ^{15}NNH$^+$ is not directly related to the primary core.

3.3.16 OC^{34}S (Carbonyl Sulfide)

One transition of OC^{34}S was detected in this survey. Using a temperature of 163 K and a source size of $2.7(3)''$ the BIMA Array data give a total column density of $2.7(8) \times 10^{17}$ cm^{-2}, and the 12 meter data give a total column density of $5.3(14) \times 10^{17}$ cm^{-2}. Sulphur bearing species are the only molecules known to have stronger emission from Sgr B2(M) (compared to Sgr B2(N-LMH))(e.g. Sutton et al., 1991). While the BIMA Array did not detect noticeable emission from OC^{34}S from Sgr B2(M), this source is close to the half power point of the BIMA Array main beam, and thus any weak emission from Sgr B2(M) may be below the detection limit. The slight difference in column density between the 12 meter and BIMA Array data may be due to such emission. Note also that the 12 meter data line width is larger than BIMA Array data line width. Given the low upper energy of the transition, it may be coming from extended structure. The column densities reported here are roughly two orders of magnitude larger than those reported by N00. The difference is likely to be due to the source size correction and larger assumed temperature in this survey. No other velocity components of OC^{34}S were detected in this survey.

3.3.17 SO (Sulphur Monoxide)

A single ground state transition of SO was detected in this survey. The BIMA Array detected two spectral components (one wide, the other narrow), both centered near 64 km s^{-1}. The 12 meter data were best fit with a single Gaussian with a line width between that of the wide and narrow BIMA Array components. Using a temperature of 163 K and a measured source size of $4.8(2)''$ the narrow component has a total column density of $1.9(2) \times 10^{17}$ cm^{-2}, and using a measured source size of $3.1(3)''$, the wide component has a total column density of $4.0(6) \times 10^{17}$ cm^{-2}. Using this temperature and source size the 12 meter data have a total column density of $1.4(1) \times 10^{18}$ cm^{-2}. The lack of detection of the wide component by the 12 meter suggests it may be even more compact than the source size fit suggests. The 12 meter column density is noticeably larger than that of the BIMA Array. This is due to the fact that Sgr B2(M), just beyond the FWHM of the 12 meter beam, contains a significant quantity of SO, which can be seen in the BIMA Array maps. Also the low E_u of the transition indicated that it may have a significant extended component. The source size and total column density from the BIMA Array data agree well with that reported by N00, and the sum of the column densities from Sgr B2(N-LMH) and Sgr B2(M) reported in N00 agree well with the 12 meter column density.

Additionally a single transition of ^{34}SO was detected in this survey. Using a measured source size of 1.3(12)″ and a rotation temperature of 163 K, the BIMA Array data yield a total column density of $\sim 7.9 \times 10^{17}$ cm^{-2}, and the 12 meter data yield a total column density $\sim 7.4 \times 10^{17}$ cm^{-2}. This may be an over estimate of the column densities as the source size fit and thus the column densities have large uncertainties. Given these uncertainties the column density reported here agrees with that reported by N00. No other velocity components were detected for either isotopologue, although the large line width of SO could mask emission at ~72 or ~52 km s^{-1}.

3.3.18 SO_2 (Sulphur Dioxide)

A total of three ground state SO_2 transitions were detected by this survey. The transitions have an average source size of 1.4(6)″. Figure 3.13 shows the rotation temperature diagram[8]. Most of the uncertainty in the points comes from the uncertainty in the source size. The total column density from the BIMA Array data is $\sim 2.7 \times 10^{19}$ cm^{-2} with a rotation temperature of 188(98) K. Using this temperature and source size the 12 meter data yield a total column density of $\sim 1.3 \times 10^{19}$ cm^{-2}. These column densities are very high and are due to the rather small source size measured. The column densities would be better constrained with the observation of more SO_2 transitions, especially those with large S/N. These column densities are slightly higher that those

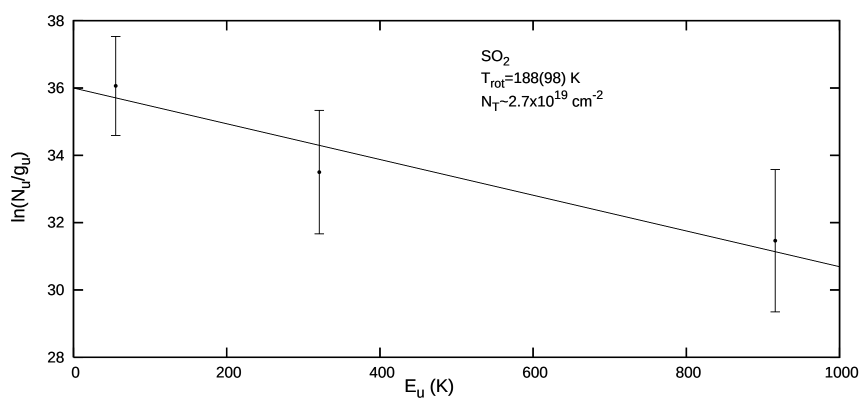

Figure 3.13 SO_2 rotation temperature diagram. The abscissa is the upper state energy of the transition in K, and the ordinate is the log of the normalized column density. The line is the weighted least squares fit to the data. Note the error bars are 1 σ for this plot.

reported by N00, and the difference may be attributed to the noticeably smaller source size used in this survey. No other velocity components were detected for this species.

[8]The error bars are 1 σ for this plot. Also with only 3 points the fit may not be reliable.

3.3.19 Velocity Component Ratios

The ratios of column densities of the ~72 and ~52 km s^{-1} velocity components to the main component (columns (6) and (9) from Tables 3.3 and 3.4) suggest that these components originate from sources with lower masses or that these components are at a different evolutionary stage than the main component. This latter hypothesis is supported by the ratios of HC^{13}CCN and HCC^{13}CN, which are higher than 1. This indicates that these regions may be more similar to dark clouds, such as TMC-1, where carbon chain molecules abound, rather than to hot molecular cores. Note that the 72/64 km s^{-1} ratio given for HC_3N uses the column density from the vibrationally excited transitions. If just the ground state transition is used the ratio becomes 1.8(15) which is in agreement with the other isotopomers of this species. The C^{18}O ratio is also larger than 1, however in this case this may be due to poor fits of the blended 64/72 km s^{-1} components.

3.3.20 U Lines

The initial results of this survey in Friedel et al. (2004) had a total of 120 U lines. Of these 120 U lines, 35 (29%) have since been identified as either other velocity components of previously identified lines or other U lines or as the potential identification listed in column (6) of Table 5 from Friedel et al. (2004). Most of the latter type are from vibrationally excited states of well known species such as C_2H_3CN and C_2H_5CN.

With the inclusion of the extra bands observed by the BIMA Array the total number of U lines in this survey is 125. Many of these are expected to be vibrationally excited states of well known species whose first vibrationally excited states have not been cataloged (e.g., $HCOOCH_3$ and $(CH_3)_2O$) or of higher, uncataloged, vibrational states of molecules where the lowest vibrational state(s) is/are known, (e.g., C_2H_3CN, C_2H_5CN, and $(CH_3)_2CO$). The remainder of this section is devoted to attempting to classify/identify these 125 U lines.

Frequency Relations

Given the large number of unidentified lines it is entirely possible that some of the transitions are related (i.e. come from the same molecular species). For linear, symmetric top, and asymmetric top molecules the rotational transition frequencies for a given molecule can be calculated. For diatomic and linear molecules the frequencies are given by (Bernath, 1995)

$$\nu = 2B(J+1) \text{ MHz}, \tag{3.1}$$

where B is the rotational constant in MHz. For symmetric tops the frequencies are given by (Bernath, 1995)

$$\nu = 2B(J+1) - 4D_J(J+1)^3 - 2D_{JK}(J+1)K^2 \text{ MHz}, \tag{3.2}$$

where D_J and D_{JK} are centrifugal distortion constants, which are small compared to B. Since symmetric top transitions are confined to K ladders and since the most probable ladder to detect is

$K = 0$, the frequency difference between transitions in this ladder reduces to equation (3.1), except in the case of an extraordinarily large D_J. Asymmetric tops are more difficult to characterize and usually require numerical analysis to complete most of the transitions. The transitions follow the following selection rules ($\Delta J = 0, \pm 1$)(Bernath, 1995)
a-type

$$\Delta K_a = 0(\pm 2, \pm 4, ...)$$
$$\Delta K_c = \pm 1(\pm 3, \pm 5, ...)$$

b-type

$$\Delta K_a = \pm 1(\pm 3, \pm 5, ...)$$
$$\Delta K_c = \pm 1(\pm 3, \pm 5, ...)$$

c-type (if $\mu_c \neq 0$)

$$\Delta K_a = \pm 1(\pm 3, \pm 5, ...)$$
$$\Delta K_c = 0(\pm 2, \pm 4, ...)$$

where the values in parenthesis are much weaker transitions than the initial values. The most likely transitions to be detected are a-type transitions with $\Delta K_a = 0$ or c-type with $\Delta K_c = 0$. b-type transition are generally weaker than either a-type or c-type since μ_b is generally smaller than μ_a or μ_c and thus are less likely to be detected. In these cases the frequencies can be calculated with equation (3.1) (Bernath, 1995).

For vibrationally excited states the frequencies can be calculated with (Bernath, 1995)

$$\nu = 2B(J+1) - 4D_v(J+1)^3 \text{ MHz}, \tag{3.3}$$

where D_v is the vibrational centrifugal distortion constant, which for lower vibrational states is very small when compared to B, thus equation (3.3) reduces to equation (3.1). This is a simplified description of how to calculate the frequencies of transitions, for a more detailed explanation see Bernath (1995).

Thus the most probable transitions to detect, for all types of molecules, can be calculated with equation (3.1); if two or more U lines are from the same molecular species then the ratio of their frequencies will be the ratio of their upper J values. The Sgr B2(N-LMH) U-line frequencies were run through a script to look for rational ratios of the frequencies. The script used a tolerance of 1 part in 100,000 (1 MHz), to allow for potentially related transitions with larger distortion constants to be matched, and allowed matches from $J = 3$ to $J = 20$. Table 3.5 lists the eleven potential matches. The first column lists the match number, the second and third columns list the frequencies in MHz of the matching lines, the fourth and fifth columns list the upper J quantum number associated with each frequency, and the sixth column lists the potential B value in MHz, calculated from equation (3.1).

Table 3.5. Potentially Related U Lines

Match Number	ν_1 (MHz)	ν_2 (MHz)	(J_1)	(J_2)	B (MHz)
1[a]	86,386.3	106,322.0	13	16	3322.5
2[a]	86,459.3	106,411.6	13	16	3325.3
3	86,956.1	110,143.3	15	19	2898.5
4	87,016.5	106,353.0	9	11	4834.2
5[a]	89,814.7	106,654.8	16	19	2806.7
6[a]	90,069.1	106,957.1	16	19	2814.6
7	90,128.5	106,514.5	11	13	4096.7
8[a]	90,517.3	108,620.7	5	6	9051.7
9[a]	90,517.3	108,620.7	10	12	4525.8
10[a]	90,517.3	108,620.7	15	18	3017.2
11	106,411.6	112,011.7	19	20	2800.2

[a]Frequency ratio matches with tolerance of 3.9×10^{-6}, or 1 channel width.

Of the eleven potential matches, numbers 1, 2, 5, 6, 8, 9, and 10 met higher tolerance constraints (3.9×10^{-6}, equivalent to the width of one channel). There are no missing transitions (i.e. no other J's that should have been detected were missing) from any matches except number 5. In this case the $J = 20$ transition should appear at 112,268.2 MHz but is missing. Thus number 5 may not be a match. Also, obviously at most one of match numbers 8, 9, and 10 can be correct. The intensity and width of the lines also needs to be taken into account when considering whether 2 lines are related. The line width should not vary much (only a factor of 2 or so at most)[9] between the pairs of lines. Match numbers 1, 4, 5, 6, and 11 are still likely candidates when this is taken into account. Thus there are a few U-line pairs that may be from the same molecules.

Potential Identifications

Four of the U lines reported in Friedel et al. (2004) (89.8147, 89.9931, 90.0783, and 109.9596 GHz) have been identified as potential transitions of Methyl Glycolate (CH_3OCOCH_2OH) by Widicus Weaver (2005b), but have yet to be confirmed. Also of note are the U-lines at the frequencies 91.0156, 91.0186, and 91.0212 GHz. These lines look similar to the profiles of transitions from double rotor molecules, such as $(CH_3)_2O$ and $(CH_3)_2CO$. These frequencies do not match any listed frequency for either of these species, but they may be from an uncataloged vibrational state of either species, a previously undetected species, or they may just be coincidental and not related

[9]This applies for weaker lines as the rms noise level will contribute a significant amount of uncertainty to the line width that may not be accounted for in the Gaussian fit. For stronger lines ($> 5\sigma$) the line width should not deviate by more than a factor of 1.5 from one line to the next.

Table 3.6. U lines Also Seen Toward Orion-KL

Hot Core (GHz)	Compact Ridge (GHz)
86,034.3	86,034.3
86,915.5	89,731.9
106,629.9	89,829.6
106,654.8	112,011.7
110,104.7	
112,011.7	

at all.

In order to further attempt to identify the U lines, the frequencies of the U lines have been compared with those from the Orion-KL survey. Since the Orion-KL region shows chemical differentiation between its components (one is N rich, while the other is O rich), if a U line from the Sgr B2(N-LMH) survey is seen toward only one of the Orion-KL components, then its identification can be constrained to be more likely a N or O bearing species. Table 3.6 lists the U lines that are common between this survey and the Orion-KL survey. The first column lists those U lines common with the hot core (N rich) region, and the second column lists those common with the compact ridge (O rich) region. Two of the U lines (86,034.3 and 112,011.7 GHz) are common to both the hot core and compact ridge, indicating that they may come from one of the few molecular species common to both sources (such as CH_3OH, HC_3N, or simple species)(see §4).

One U line of note is at 90.0378 GHz. This line was first seen in Turner (1989) and is seen in this survey, by both instruments, with a significant intensity (~2 Jy beam^{-1}) and with a second velocity component at ~72 km s^{-1}. However, there is no indication of this line toward Orion-KL. Thus, the origin of this line is either a species that is not present in Orion-KL or is from a high energy vibrationally excited state that is populated in Sgr B2(N-LMH) but not Orion-KL. If the parent species of this line is N bearing then the first solution is more likely than the latter since the rotation temperatures for N bearing species in Orion-KL are equivalent to or higher than those seen in Sgr B2(N-LMH) (see § 4.4). On the other hand if the parent species is O bearing then either solution is a possibility as the rotation temperatures for many of the O bearing species in Orion-KL are lower than those seen in Sgr B2(N-LMH).

Source Sizes

For a large number of the U lines the measured source size is roughly that of identified transitions coming from the compact hot cores, thus indicating their potential origin. However for many of the other U lines the measured source size is much smaller than that of the average identified transition. These U lines ($< 2.0''$ in size), while likely to be associated with a hot core, may be from high energy (vibrationally excited or ground state) transitions that require the higher density and temperature of the innermost part of the core in order to be excited. Also of note are the handful of U lines that show indications of large scale emission. These U lines must come from lower lying states ($<$ 50 K) in order to be so wide spread.

3.3.21 Absorption Lines of Simple Species

When looking at transitions that are primarily in absorption (those with very low E_u), it becomes evident that there are local velocity components in addition to those seen in emission in more complex species. Additionally these species also show absorption at LSR velocities ranging from +30 to -105 km s^{-1}. These are line of sight (LOS) absorption features caused by intervening low temperature clouds between Sgr B2(N-LMH) and the Earth.

In order to calculate the column densities of the absorption lines, using equation (2.4), the continuum temperature and continuum size need to be calculated. Table 3.7 lists the continuum parameters for Sgr B2(N-LMH) and Sgr B2(M)[10]. Column (1) lists the frequency in GHz, column (2) lists the synthesized beam, columns (3) and (6) list the continuum intensity in Jy beam^{-1} for N and M, respectively, columns (4) and (7) list the continuum source size in arcsec, and columns (5) and (8) list the continuum temperature in K (calculated using equation (2.7)). Note that Sgr B2(N-LMH) has two continuum components of roughly equal intensity (in Jy beam^{-1}), but when converted to K the smaller source is an order of magnitude stronger than the larger component. Thus the smaller component the primary contributor of the continuum. Table 3.8 lists the transition parameters of the transitions detected in absorption. Column (1) lists the molecular species, column (2) lists the quantum numbers of the transition, column (3) lists the transition frequency, columns (4) and (5) list the upper and lower energies of the transitions, respectively, column (6) lists $S\mu^2$ and columns (7), (8), & (9) lists the partition function for 3, 4.6, and 60 K.

Local Velocity Components

The local (to Sgr B2(N-LMH)) velocity structure includes features with $v_{LSR} > 40$ km s^{-1} and is seen toward both Sgr B2(N-LMH) and Sgr B2(M). While the BIMA Array was able to observe both Sgr B2(N-LMH) and Sgr B2(M) as separate objects, the 12 meter observed them in the same beam. Thus all 12 meter data presented here are a composite from both structures. Hollis et al. (2004) describes the local environment around Sgr B2(N-LMH) based on observations of glycolaldehyde (CH_2OHCHO). Surrounding the cores is thought to be a warm ($\sim$50 K) envelope on the order of $50''$ across, where CH_2OHCHO was seen purely in emission. Around this warm envelope is a much cooler ($\sim$8 K) and larger halo, where CH_2OHCHO is seen in both emission and absorption (depending on how well the beam coupled to the source). Due to the size of the envelope the emission features will most likely be resolved out by the BIMA Array but easily detectable by the

[10]This source is included because it is the field of view of both instruments.

Table 3.7. Sgr B2 Continuum Properties

Frequency (GHz)	$\theta_a \times \theta_b$ ($'' \times ''$)	Sgr B2(N-LMH)[a] I_0[b] (Jy/bm)	Size ($''$)	T_A^*/η_M (K)	Sgr B2(M) I_0[b] (Jy/bm)	Size ($''$)	T_A^*/η_M (K)
86.2	27.4×6.5	3.4	3.5(6)/11.0(6)	48.4(155)/7.7(5)	7.2	7.1(4)	30.0(26)
86.8	47.9×6.4	2.2	2.8(6)/13.0(11)	46.6(195)/3.3(4)	5.6	6.1(5)	27.1(40)
90.0	24.5×6.2	3.1	2.5(3)/11.2(2)	77.0(178)/6.7(1)	7.5	5.8(3)	41.1(35)
106.6	21.0×5.1	4.7	3.2(5)/13.1(9)	43.3(88)/7.2(2)	9.4	5.0(2)	46.7(30)
108.0	19.3×5.4	4.0	3.5(7)/14.0(6)	44.4(126)/6.1(2)	7.3	4.8(4)	40.2(55)
110.0	32.7×4.8	5.0	3.6(4)/9.0(2)	42.5(87)/9.5(3)	6.7	4.3(5)	40.6(84)
112.3	18.1×5.4	3.9	3.3(5)/15.2(7)	40.5(11)/5.8(2)	7.0	4.9(3)	36.5(16)

[a]Sgr B2(N-LMH) has two components of roughly equal intensity.

[b]All I_0 values have been primary beam corrected.

Table 3.8. Molecular Parameters of Lines Seen in Absorption Toward Sgr B2(N-LMH).

Molecular Species	Transition	Frequency (MHz)	E_u (K)	E_l (K)	$S\mu^2$ (D^2)	Q_r 3 K	4.6 K	50 K
C_2H	1-0	87,316.9250 (40)[a]	4.2	0.0	0.64	1.82	2.56	28.95
CH_3OH	$0_{0,0} - 1_{-1,1}$	108,893.9290 (150)	13.1	7.9	0.97	6.39[b]	12.13[b]	571.65[b]
^{13}CO	1-0	110,201.3700 (200)	5.3	0.0	0.01	1.54	2.12	23.02
$C^{18}O$	1-0	109,782.1730 (20)	5.3	0.0	0.01	1.54	3.39	23.10
$H^{13}CN$	1-0	86,340.1840 (600)[a]	4.0	0.0	8.91	1.83	2.59	29.29
$HC^{15}N$	1-0	86,054.9610 (600)	4.1	0.0	8.91	1.84	2.59	29.38
$H^{13}CO^+$	1-0	86,745.3920 (780)	4.2	0.0	10.89	1.83	2.48	29.15
$HC^{17}O^+$	1-0	86,754.3290 (10000)	4.2	0.0	10.89	1.82[c]	2.57[c]	29.03[c]
HNC	1-0	90,663.5930 (90)	4.3	0.0	9.30	1.77	2.48	27.91
$HN^{13}C$	1-0	87,090.8590 (920)[a]	4.2	0.0	7.28	1.82	2.57	29.04
SiO	2-1	86,846.8910 (560)	6.3	2.1	19.20	3.24	4.76	57.90

[a]Only the frequency of the strongest hyperfine component is reported.

[b]Estimated from Pickett et al. (1998) at 9.375 K.

[c]Estimated from Q_r of HCO^+ and $HC^{18}O^+$.

12 meter. The 12 meter spectra all show significant emission features, while the BIMA Array sees little (usually only a wing) of the emission. The only exception to this is $HC^{17}O^{+}$ which has such a low abundance that the emission feature seen by the 12 meter is rather weak, while the BIMA Array sees no emission. The cooler halo surrounding the envelope will produce features that are purely in absorption, as is seen in the spectra from both instruments.

For the emission components a rotation temperature of 60 K is found to be the best fit for all species (with the exception of ^{13}CO which required a temperature of 90 K). For the local absorption components a temperature of ~4.6 K was found to be the best fit for all species. All emission components were assumed to fill the respective beams, while the absorption components were assumed to match the size of the continuum sources. In order to get reliable fits for the 12 meter data, a large scale (i.e. beam filling) low level continuum source of ~0.5 K was needed (in addition to the CMB), which would be resolved out by the BIMA Array. This is not unreasonable as there is significant large scale structure in the region (e.g. de Vicente et al., 2000). Table 3.9 lists the local velocity components detected toward Sgr B2(N-LMH) and Sgr B2(M) by the BIMA Array. Column (1) lists the synthesized beam size, columns (2) and (6) list the central velocity of the component in km s^{-1}, columns (3) and (7) list the intensity in Jy $beam^{-1}$, columns (4) and (8) list the linewidth of the component in km s^{-1}, and columns (5) and (9) list the total beam averaged column density in cm^{-2}. Table 3.10 lists the same information for the 12 meter observations.

As can be seen from Tables 3.9 and 3.10 the bulk of the emission comes from a single velocity component at ~64 km s^{-1}. However the absorption has many components. The primary absorption components are near ~54, ~64, ~72, and ~85-90 km s^{-1}. Not all of these absorption components can be seen with every species. This may be due to the fact that the absorption lines are very wide and thus may mask each other, especially for those lines that saturate the continuum. The absorption component with a v_{LSR} ~85-90 km s^{-1} is only seen toward Sgr B2(N-LMH), indicating that while the other absorption components are very wide spread, this component is extended but only around the Sgr B2(N-LMH) region. Figure 3.14 shows a rough diagram of the local velocity structure of the region. Temperatures and velocities are given for each structure. Solid outlines indicate emission features while dashed lines indicate absorption features. Note that this diagram is not to scale.

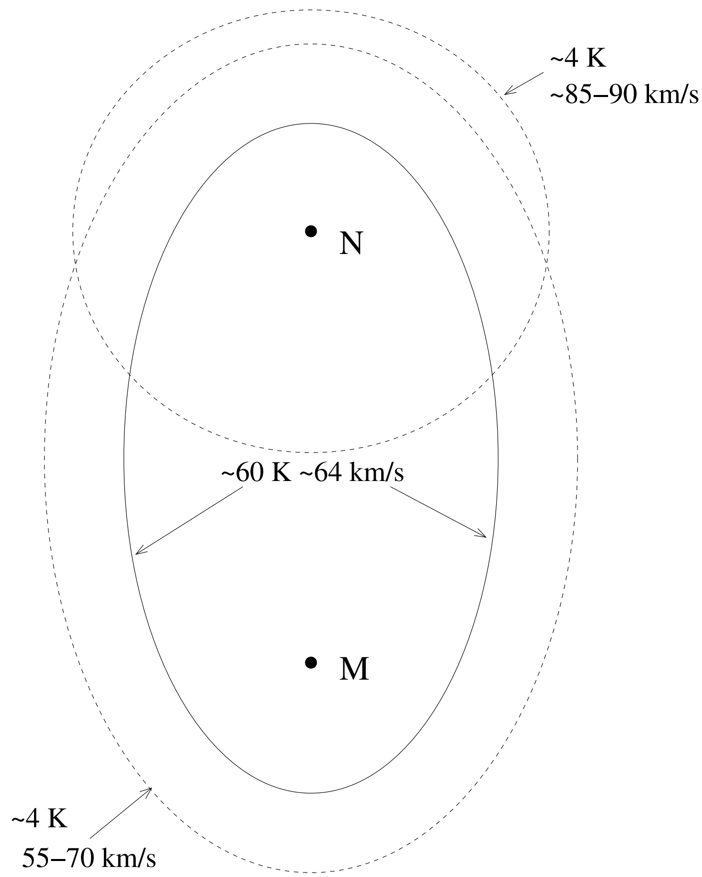

Figure 3.14 Diagram of the large scale Sgr B2 velocity components. For each component a rough outline of its boundaries is given as well as the associated velocity and an estimate of the temperature. Emission components are denoted by solid outlines while absorption components are denoted by dashed outlines. Note that this diagram is not to scale.

Table 3.9. Local Velocity Components of Sgr B2(N) and (M) from the BIMA Array

	Sgr B2(N)				Sgr B2(M)			
$\theta_a \times \theta_b$ ($'' \times ''$)	Velocity (km/s)	I_0 (Jy/bm)	Δv (km/s)	$\langle N_T \rangle$ (cm^{-2})	Velocity (km/s)	I_0 (Jy/bm)	Δv (km/s)	$\langle N_T \rangle$ (cm^{-2})
				$H^{13}CO^+$				
48.6×6.3	61.3[a]	-1.3(3)	17.6(16)	3.6(14)×10^{13}	61.3(13)	-5.0(3)	13.8(20)	2.6(8)×10^{14}
48.6×6.3	71.8[a]	-1.2(2)	21.2(58)	3.8(16)×10^{13}	71.8(13)	-4.3(8)	8.1(12)	1.0(5)×10^{14}
48.6×6.3	84.4(14)	-1.5(3)	7.4(14)	1.8(8)×10^{13}	...	...	...	...
				SiO				
25.5×6.5	55.8(49)	-1.9(59)	11.2(126)	~7.0×10^{13}	59.1(13)	-6.5(4)[b]	10.7(10)	>1.5×10^{15}
25.5×6.5	69.3(82)	-2.6(6)	20.0(544)	~2.8×10^{14}	70.1(13)	-6.2(4)[b]	11.3(11)	>1.6×10^{15}
25.5×6.5	83.9(25)	-2.6(41)	10.3(70)	~1.4×10^{14}	...	...	...	...
				$H^{13}CN$				
24.8×6.9	40.4(14)	2.4(4)	9.6(18)	8.6(22)×10^{14}	...	...	...	...
24.8×6.9	56.1(20)	-2.1(1)	25.0(70)	2.4(11)×10^{14}	55.6(14)	-4.4(6)	10.4(16)	3.5(15)×10^{14}
24.8×6.9	76.4(14)	-1.7(3)	13.3(49)	9.3(50)×10^{13}	70.0(14)	-5.4(2)	15.7(29)	6.6(36)×10^{14}
24.8×6.9	85.8(14)	-2.5(6)	5.8(09)	~9.7×10^{13}	82.7(14)	3.0(6)	4.2(7)	3.6(9)×10^{14}
				$HC^{15}N$				
31.3×6.5	52.1(14)	1.5(2)	15.7(29)	4.0(9)×10^{14}	...	...	...	...
31.3×6.5	65.1(14)	-2.1(3)	6.6(12)	3.7(18)×10^{13}	61.5(26)	-4.0(12)	11.1(30)	1.6(11)×10^{14}
31.3×6.5	71.8(14)	-0.5(3)	4.4(35)	~3.6×10^{12}	69.9(26)	-3.0(17)	9.6(28)	8.3(78)×10^{13}
31.3×6.5	83.9(14)	-1.5(2)	8.9(19)	1.6(6)×10^{13}	...	...	...	...

Table 3.9—Continued

$\theta_a \times \theta_b$ ($'' \times ''$)	Sgr B2(N) Velocity (km/s)	Sgr B2(N) I_0 (Jy/bm)	Sgr B2(N) Δv (km/s)	Sgr B2(N) $\langle N_T \rangle$ (cm^{-2})	Sgr B2(M) Velocity (km/s)	Sgr B2(M) I_0 (Jy/bm)	Sgr B2(M) Δv (km/s)	Sgr B2(M) $\langle N_T \rangle$ (cm^{-2})
				$HC^{17}O^+$				
24.6×6.9	...	...	...	...	57.5(20)	-0.4(3)	5.9(48)	$\sim 3.6 \times 10^{12}$
24.6×6.9	64.8(13)	-0.8(1)	12.8(21)	$1.4(4) \times 10^{13}$	67.6(13)	-1.4(1)	12.2(24)	$3.2(7) \times 10^{13}$
24.6×6.9	80.4(13)	-0.6(1)	8.9(21)	$7.2(25) \times 10^{12}$	...	...	...	...
				$HN^{13}C$				
25.4×6.7	61.6(13)	-2.7(26)	13.0(15)	$\sim 1.9 \times 10^{14}$	62.8(13)	-6.9(0.3)[b]	9.6(8)	$>1.2 \times 10^{15}$
25.4×6.7	71.2[a]	-1.7(10)	15.7(285)	$\sim 7.2 \times 10^{13}$	71.2(13)	-5.2(6)	7.9(8)	$\sim 4.3 \times 10^{14}$
25.4×6.7	82.5(19)	-2.6(23)	10.1(28)	$\sim 1.2 \times 10^{14}$	...	...	...	...
25.4×6.7	120.1(30)	-0.4(1)	31.8(74)	$2.4(9) \times 10^{13}$	...	...	...	...
				C_2H				
33.7×6.2	64.7(13)[c]	-2.7(1)	19.9(8)	$8.9(23) \times 10^{15}$[d]	65.9(13)	-7.1(2)[b]	15.0(4)	$>3.4 \times 10^{16}$[d]
33.7×6.2	82.1(13)	-1.2(2)	7.1(13)	$4.2(13) \times 10^{14}$	...	...	...	...
				^{13}CO				
19.8×5.1	37.1(11)	4.2(2)	15.2(9)	$7.7(6) \times 10^{17}$	36.8(11)	3.0(7)	5.6(15)	$4.2(15) \times 10^{16}$
19.8×5.1	53.6(11)	2.8(3)	12.8(22)	$2.4(6) \times 10^{17}$	56.0(11)	21.9(4)	15.7(3)	$8.9(8) \times 10^{18}$
20.1×5.1	66.0(11)	-4.5(4)	7.7(8)	$\sim 5.2 \times 10^{16}$	63.1(11)	-17.2(5)	8.0(3)	$3.2(1) \times 10^{17}$
20.1×5.1	72.5(11)	3.2(4)	4.0(6)	$1.4(3) \times 10^{17}$	...	...	...	...
20.1×5.1	82.0(11)	1.7(7)	1.5(7)	$2.8(17) \times 10^{16}$	...	...	...	...
20.1×5.1	82.9(11)	4.1(2)	34.5(15)	$1.7(1) \times 10^{18}$	...	...	...	...
20.1×5.1	90.9(11)	-3.5(4)	5.5(8)	$2.1(11) \times 10^{16}$	88.6(11)	4.5(6)	8.0(12)	$4.1(8) \times 10^{17}$

Table 3.9—Continued

$\theta_a \times \theta_b$ ($'' \times ''$)	Sgr B2(N) Velocity (km/s)	I_0 (Jy/bm)	Δv (km/s)	$\langle N_T \rangle$ (cm^{-2})	Sgr B2(M) Velocity (km/s)	I_0 (Jy/bm)	Δv (km/s)	$\langle N_T \rangle$ (cm^{-2})
				$C^{18}O$				
21.9×5.1	···	···	···	···	58.2(11)	6.6(12)	17.2(15)	$1.2(2)\times10^{18}$
21.9×5.1	67.4(10)	2.5(5)	7.4(6)	$3.3(13)\times10^{18}$	62.2(11)	4.8(13)	6.7(17)	$3.4(12)\times10^{17}$
21.9×5.1	77.6(5)	4.0(2)	22.5(25)	$1.1(4)\times10^{19}$	···	···	···	···
				HNC, J=1-0				
24.7×6.2	···	···	···	···	38.8(13)	-1.2(3)	6.4(34)	$1.4(9)\times10^{13}$
24.7×6.2	44.0(13)	1.6(1)	7.2(7)	$2.0(2)\times10^{14}$	···	···	···	···
24.7×6.2	53.4(13)	-2.0(2)	4.4(6)	$2.6(14)\times10^{13}$	50.7(13)	6.0(7)	4.7(6)	$4.8(9)\times10^{14}$
24.7×6.2	66.5(13)	-2.6(1)	20.6(21)	$2.2(20)\times10^{14}$	61.2(13)	-6.7(2)	16.9(27)	$3.7(8)\times10^{14}$
24.7×6.2	···	···	···	···	73.0(13)	-4.7(8)	6.8(10)	$1.2(6)\times10^{14}$
24.7×6.2	83.8(13)	-3.2(2)	11.0(7)	$\sim1.5\times10^{14}$	86.1(13)	2.3(2)	14.1(14)	$4.3(6)\times10^{14}$
				CH_3OH				
20.5×5.3	···	···	···	···	61.1(11)	-5.6(14)	2.6(8)	$9.4(60)\times10^{15}$
20.5×5.3	65.3(11)	-2.6(3)	13.0(23)	$2.3(12)\times10^{16}$	67.4(11)	-6.9(9)	6.4(12)	$4.1(25)\times10^{16}$
20.5×5.3	81.9(11)	-2.3(3)	10.6(23)	$7.0(30)\times10^{15}$	···	···	···	···

[a]Velocity was fixed in order to obtain an adaquite fit.

[b]Intensity and column density are approximate as the line completely absorbs the continuum.

[c]Optically thick fit - hyperfine components not in proportion.

[d]Base on the strongest optically thin hyperfine component.

Table 3.10. Composite Local Velocity Components of Sgr B2(N) and (M) from the 12 Meter

Velocity (km/s)	I_0 (Jy/bm)	Δv (km/s)	θ ($''$)	$\langle N_T \rangle$ (cm^{-2})
		$H^{13}CO^+$		
58.8(14)	-15.8(50)	9.3(9)	73	$1.5(10)\times10^{13}$
63.4(14)	25.6(36)	23.2(11)	73	$5.2(10)\times10^{14}$
66.8(14)	-23.2(37)	12.4(15)	73	$3.5(23)\times10^{13}$
92.7(17)	4.3(2)	24.8(26)	73	$4.2(5)\times10^{13}$
		SiO		
59.0(13)	-22.1(42)	11.3(12)	73	$4.4(21)\times10^{13}$
65.2(13)	37.2(29)	31.6(11)	73	$8.7(13)\times10^{14}$
68.4(13)	-25.9(31)	11.8(10)	73	$5.9(25)\times10^{13}$
94.8(13)	2.5(8)	11.0(33)	73	$1.3(5)\times10^{13}$
112.7(24)	3.9(2)	31.5(54)	73	$5.6(10)\times10^{13}$
		$H^{13}CN$		
56.5(14)	-34.5[a]	16.3	74	$1.6(2)\times10^{14}$
64.0(14)[b]	28.0[a]	27.6	74	$\sim1.5\times10^{15}$
69.0(14)	-30.5[a]	16.2	74	$1.3(1)\times10^{14}$
99.0(14)	3.0(3)	16.1(19)	74	$4.2(6)\times10^{13}$
117.0(14)	2.6[a]	4.1	74	$\sim9.2\times10^{12}$
		$HC^{15}N$		
61.6(14)	5.6(13)	22.9(22)	74	$4.2(11)\times10^{13}$
63.2(14)	-5.5(13)	10.8(15)	74	[c]
81.6(14)	-2.2(3)	5.9(14)	74	$\sim5.3\times10^{12}$
92.4(18)	0.8(2)	8.6(46)	74	$3.3(20)\times10^{12}$
		$HC^{17}O^+$		
56.3(33)	1.5(11)	9.3(77)	74	$\sim5.4\times10^{12}$
		$HN^{13}C$		
60.2(13)	-13.4(40)	8.7(13)	73	$2.7(20)\times10^{13}$
64.0(13)	20.2(20)	25.6(09)	73	$6.7(7)\times10^{14}$
67.4(13)	-14.2(32)	9.8(16)	73	$3.2(22)\times10^{12}$

Table 3.10—Continued

Velocity (km/s)	I_0 (Jy/bm)	Δv (km/s)	θ ($''$)	$\langle N_T \rangle$ (cm^{-2})
		^{13}CO		
59.3(11)	90.3(9)	12.0(1)	57	$4.9(2)\times10^{17}$
72.4(11)	84.5(7)	9.8(1)	57	$3.6(1)\times10^{17}$
75.3(11)	170.5(7)	37.9(1)	57	$3.2(1)\times10^{18}$
118.9(11)	9.5(3)	12.5(5)	57	$3.2(2)\times10^{16}$

[a]Gaussian fit is approximate.

[b]Optically thick fit - hyperfine components not in proportion.

[c]An opacity and thus a column density could not be calculated for this line.

Line of Sight Velocity Components

The line of sight (LOS) velocity components, $v_{LSR} < 40$ km s^{-1}, have been extensively studied (e.g. Huttemeister et al., 1993; Tieftrunk et al., 1994; Greaves, 1995; Greaves & Nyman, 1996; Vastel et al., 2002). The velocity components can be broken up into six distinct components, listed in Table 3.11 and shown in Figure 3.15, from Vastel et al. (2002). The first column lists the source name and the second column lists the v_{LSR} range of the source.

All of these features are thought to extend over at least 50$''$ (Greaves & Williams, 1994). The rotation temperature in these sources is very low, often just above the 2.7 K cosmic microwave background (Tieftrunk et al., 1994; Greaves & Williams, 1994). On the other hand, the kinetic temperature averages around 20 K, with values as high as 70 K in regions near the Galactic center (Tieftrunk et al., 1994; Greaves, 1995). The density is thought to vary across the sources, with lower values ($n(H_2)< 200$ cm^{-3}) near the edges with the density peaking in the center ($\sim 2 \times 10^4$ cm^{-3}) and with an average value of $\sim$ 200 cm^{-3} (Greaves, 1995; Greaves & Nyman, 1996). Although there is no active star formation in these regions, they are not considered to be dark clouds since they are associated with spiral arms and Galactic center bar structures (Greaves & Nyman, 1996). For the analysis of the spectral features produced by these sources, a rotation temperature of 3 K is being adopted for both emission and absorption features, which is similar to values measured by Tieftrunk et al. (1994). Note that no LOS velocity components of the lowest energy CH_3OH transition were seen in this survey because there was no coverage of those frequencies.

Table 3.12 lists the LOS velocity components detected toward Sgr B2(N-LMH) and Sgr B2(M) by the BIMA Array. Column (1) lists the synthesized beam size, columns (2) and (6) list the central velocity of the component in km s^{-1}, columns (3) and (7) list the intensity in Jy beam^{-1},

Table 3.11. Sources of Velocity Structure Along the Line of Sight Towards Sgr B2

Source	v_{LSR} (km s^{-1})
Scutum arm	$+30 \leftrightarrow +35$
Sagittarius arm	$+5 \leftrightarrow +20$
Orion arm	$-5 \leftrightarrow +5$
4 kpc	$-30 \leftrightarrow -15$
3 kpc	$-50 \leftrightarrow -35$
X2 orbit	$-110 \leftrightarrow -55$

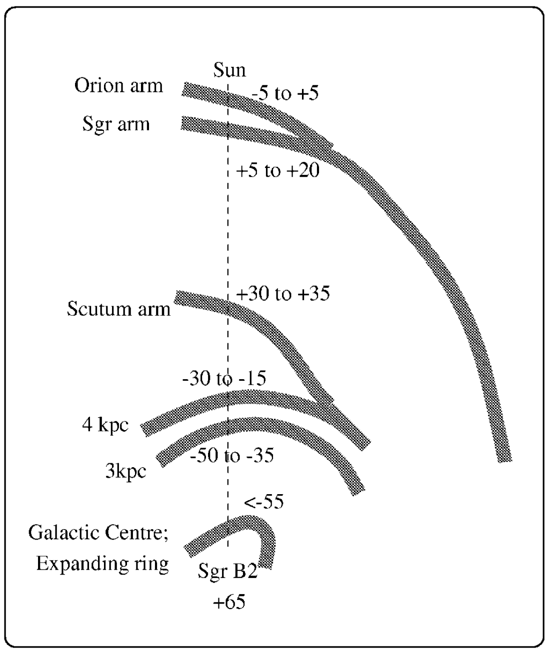

Figure 3.15 Sources of the line of sight emission and absorption features seen toward Sgr B2. The dark bands are the sources of the features and are labeled both by name and what velocity component they produce. From Vastel et al. (2002). Note this is not to scale.

columns (4) and (8) list the linewidth of the component in km s^{-1}, and columns (5) and (9) list the total beam averaged column density in cm^{-2}. Table 3.13 lists the same information for the 12 meter data.

Table 3.12. Line of Sight Velocity Components Detected Toward Sgr B2(N) and (M) by the BIMA Array

	Sgr B2(N)				Sgr B2(M)			
$\theta_a \times \theta_b$ ($'' \times ''$)	Velocity (km/s)	I_0 (Jy/bm)	Δv (km/s)	$\langle N_T \rangle$ (cm^{-2})	Velocity (km/s)	I_0 (Jy/bm)	Δv (km/s)	$\langle N_T \rangle$ (cm^{-2})
				$H^{13}CO^+$				
48.7×6.4	-105.9(14)	-1.4(17)	1.5(18)	$\sim$1.8×10^{12}	···	···	···	···
48.7×6.4	-81.7(14)	-0.8(3)	2.4(9)	1.4(9)×10^{12}	···	···	···	···
48.7×6.4	-39.2(14)	-1.0(2)	3.8(8)	3.0(11)×10^{12}	-41.3(13)	-3.2(5)	3.2(6)	2.0(6)×10^{13}
48.6×6.3	4.7(14)	-1.0(1)	15.7(24)	1.2(3)×10^{15}	1.4(13)	-2.5(8)	2.1(9)	9.3(56)×10^{12}
48.6×6.3	···	···	···	···	13.2(20)	-1.3(2)	32.0(43)	6.4(13)×10^{13}
48.6×6.3	22.4(22)	-0.4(1)	10.5(50)	2.9(17)×10^{12}	···	···	···	···
				SiO				
25.5×6.5	-14.9(24)	-0.5(6)	4.0(54)	$\sim$2.9×10^{12}	···	···	···	···
25.5×6.5	10.4(36)	-0.9(3)	24.4(87)	3.5(20)×10^{13}	8.0(13)	-1.7(1)	38.6(30)	3.3(4)×10^{14}
				$H^{13}CN$				
24.3×6.9	-106.9(14)	-1.1(4)	1.9(7)	3.8(24)×10^{12}	-102.4(14)	-1.2(3)	3.5(9)	1.4(6)×10^{13}
24.3×6.9	3.9(14)	-1.1(2)	9.4(20)	1.9(7)×10^{13}	2.0(14)	-2.9(22)	7.3(29)	$\sim$9.2×10^{13}
24.3×6.9	14.6(14)	-0.8(2)	3.2(10)	4.4(20)×10^{12}	9.6(224)	-0.5(8)	13.2(276)	$\sim$2.2×10^{13}
24.3×6.9	···	···	···	···	35.5(14)	-0.7(2)	9.6(45)	2.2(13)×10^{13}
				$HN^{13}C$				
25.4×6.7	···	···	···	···	-101.9(13)	-0.8(2)	5.3(17)	1.0(5)×10^{13}
25.4×6.7	5.2(13)	-0.6(1)	12.4(30)	8.0(28)×10^{12}	2.6(13)	-2.9(2)	4.0(4)	3.4(6)×10^{13}

Table 3.12—Continued

$\theta_a \times \theta_b$ ($'' \times ''$)	Sgr B2(N) Velocity (km/s)	Sgr B2(N) I_0 (Jy/bm)	Sgr B2(N) Δv (km/s)	Sgr B2(N) $\langle N_T \rangle$ (cm^{-2})	Sgr B2(M) Velocity (km/s)	Sgr B2(M) I_0 (Jy/bm)	Sgr B2(M) Δv (km/s)	Sgr B2(M) $\langle N_T \rangle$ (cm^{-2})
				C_2H				
33.9×6.2	-106.3(13)	-1.0(3)	3.5(11)	$8.7(41)\times10^{13}$	-97.5(13)	-1.2(2)	16.1(28)	$7.9(20)\times10^{14}$
33.9×6.2	-40.1(13)	-0.9(2)	4.3(12)	$9.4(37)\times10^{13}$	-40.9(13)	-3.2(4)	2.0(3)	$3.4(10)\times10^{14}$
33.7×6.2	-25.7(16)	-0.6(1)	15.8(36)	$2.1(7)\times10^{14}$	-21.5(13)	-2.0(2)	10.4(15)	$9.3(20)\times10^{14}$
33.7×6.2	3.4(13)	-1.1(1)	17.0(22)	$4.8(11)\times10^{14}$	5.3(13)	-2.6(2)	20.1(20)	$2.6(4)\times10^{15}$
				^{13}CO				
19.9×5.1	-105.6(11)	-3.2(5)	3.7(6)	$9.7(34)\times10^{15}$	-102.5(11)	-3.9(12)	2.0(7)	$1.2(7)\times10^{16}$
19.9×5.1	...	...	...	...	-101.9(28)	-1.4(4)	23.3(71)	$4.3(20)\times10^{16}$
19.9×5.1	-93.1(11)	-1.3(6)	2.0(11)	$1.3(9)\times10^{15}$	...	...	...	...
19.9×5.1	-80.0(11)	-3.3(5)	3.7(7)	$1.1(4)\times10^{16}$	...	...	...	...
19.9×5.1	-74.3(11)	-2.8(5)	3.4(8)	$6.6(26)\times10^{15}$	-76.2(11)	-5.8(30)	1.4(9)	$\sim1.7\times10^{16}$
19.8×5.1	...	...	...	...	-58.7(11)	-6.6(11)	2.5(5)	$4.0(21)\times10^{16}$
19.8×5.1	-47.3(11)	-4.1(4)	4.5(7)	$1.7(12)\times10^{16}$	-49.2(11)	-8.3(10)	3.0(5)	$\sim6.1\times10^{16}$
19.8×5.1	...	...	...	...	-48.0(15)	3.1(5)	25.1(34)	[a]
19.8×5.1	...	...	...	...	-45.5(11)	-11.9(10)[b]	2.8(4)	$>2.6\times10^{17}$
19.8×5.1	-40.4(11)	-5.2(4)[b]	4.9(6)	$>7.8\times10^{16}$	-41.1(11)[b]	-13.0(9)	3.9(4)	$>3.6\times10^{17}$
19.8×5.1	-25.2(11)	-5.1(13)[b]	1.4(4)	$>2.2\times10^{15}$	-25.6(11)	-4.3(7)	5.8(11)	$4.1(13)\times10^{16}$
19.8×5.1	-20.2(11)	-3.4(5)	3.4(5)	$7.5(36)\times10^{15}$	-19.4(11)	-7.0(10)	2.6(4)	$5.2(29)\times10^{16}$
19.8×5.1	2.1(11)	-1.1(4)	5.1(21)	$2.2(14)\times10^{15}$	4.7(11)	-3.2(5)	10.2(19)	$4.8(14)\times10^{16}$
19.8×5.1	11.0(11)	-3.0(3)	9.2(10)	$1.6(5)\times10^{16}$	...	...	...	...
19.8×5.1	...	...	...	...	27.5(11)	3.4(11)	2.3(9)	$1.9(10)\times10^{16}$
				$C^{18}O$				
14.0×5.0	-45.6(3)	-2.0(4)	3.2(8)	$3.1(13)\times10^{15}$	-46.2(11)	-6.1(5)	2.0(2)	$3.3(10)\times10^{16}$
14.0×5.0	-41.3(2)	-2.6(4)	1.4(3)	$2.0(8)\times10^{15}$	-41.4(11)	-7.5(4)	1.9(1)	$\sim4.3\times10^{16}$

Table 3.12—Continued

$\theta_a \times \theta_b$	Sgr B2(N)				Sgr B2(M)			
($'' \times ''$)	Velocity (km/s)	I_0 (Jy/bm)	Δv (km/s)	$\langle N_T \rangle$ (cm^{-2})	Velocity (km/s)	I_0 (Jy/bm)	Δv (km/s)	$\langle N_T \rangle$ (cm^{-2})
HNC								
24.5×6.2	-105.9(13)	-2.1(1)	6.1(5)	$1.4(4)\times10^{13}$	-103.0(13)	-4.7(3)	8.0(10)	$1.2(3)\times10^{14}$
24.5×6.2	-92.2(13)	-0.9(2)	2.0(6)	$1.4(6)\times10^{12}$	-93.3(13)	-1.9(3)	8.3(25)	$3.0(11)\times10^{13}$
24.5×6.2	-80.0(13)	-1.5(2)	4.0(6)	$5.5(17)\times10^{12}$	...	...	...	...
24.5×6.2	-73.4(13)	-1.7(1)	6.0(6)	$9.8(26)\times10^{12}$	-76.8(13)	-1.6(5)	2.7(9)	$7.6(38)\times10^{12}$
24.5×6.2	-46.4(13)	-5.5[c]	0.6	[a]	-45.9(13)	-3.3(5)	2.4(5)	$1.8(6)\times10^{13}$
24.5×6.2	-39.8(13)	-2.4(2)	4.5(4)	$1.4(5)\times10^{13}$	-40.7(13)	-6.0(5)[b]	3.3(3)	$>2.9\times10^{14}$
24.5×6.2	-26.1(13)	-0.7(2)	4.6(13)	$2.4(11)\times10^{12}$	-26.3(13)	-2.1(4)	5.0(18)	$2.0(9)\times10^{13}$
24.5×6.2	-20.2(13)	-1.9(7)	1.6(7)	$3.0(24)\times10^{12}$	-20.5(13)	-2.9(4)	5.1(14)	$3.0(10)\times10^{13}$
24.5×6.2	-15.7(13)	0.5(1)	8.5(24)	$1.2(4)\times10^{13}$	...	...	...	...
24.5×6.2	0.4(13)	-1.3(5)	7.4(19)	$8.3(5)\times10^{12}$	-0.8(13)	-4.4(17)	5.5(12)	$6.8(60)\times10^{13}$
24.5×6.2	9.8(14)	-2.0(1)	14.9(23)	$3.2(10)\times10^{13}$	6.8(13)	-4.8(5)	10.6(53)	$1.6(9)\times10^{14}$
24.5×6.2	...	...	...	...	18.4(22)	-3.2(7)	10.8(33)	$7.7(34)\times10^{13}$
24.7×6.2	27.8(13)	-1.2(1)	6.7(9)	$6.8(18)\times10^{12}$	31.5(13)	-5.6(4)	4.5(5)	$1.2(7)\times10^{14}$

[a] An opacity and thus a column density could not be calculated for this line.

[b] Intensity and column density are approximate as the line completely absorbs the continuum.

[c] Gaussian fit is approximate.

Table 3.13. Line of Sight Velocity Components Detected Toward Sgr B2(N) and (M) by the 12 Meter

Velocity (km/s)	I_0 (Jy/bm)	Δv (km/s)	θ ($''$)	$\langle N_T \rangle$ (cm^{-2})
		$H^{13}CO^+$		
-106.8(14)	-2.0(5)	2.2(6)	73	$1.8(5)\times10^{12}$
-75.2(14)	-1.4(3)	5.1(13)	73	$2.8(7)\times10^{12}$
-41.4(14)	-2.2(4)	3.7(7)	73	$3.3(7)\times10^{12}$
3.2(14)	-2.8(5)	8.6(14)	73	$1.1(2)\times10^{13}$
14.2(19)	-1.9(2)	13.5(36)	73	$1.0(3)\times10^{13}$
		$H^{13}CN$		
-107.6(14)	-2.3(2)	2.5(5)	74	$5.4(12)\times10^{12}$
1.8(14)	-1.1[a]	18.1	74	$1.6(2)\times10^{13}$
		^{13}CO		
-106.7(11)	10.2(5)	7.2(4)	57	$7.1(5)\times10^{15}$
-88.3(11)	3.7(8)	2.4(7)	57	$8.6(31)\times10^{14}$
-84.7(11)	4.9(5)	28.6(29)	57	$1.4(2)\times10^{16}$
-83.3(11)	8.2(8)	3.9(6)	57	$3.1(6)\times10^{15}$
-79.1(11)	4.5(8)	2.8(7)	57	$1.2(4)\times10^{15}$
-59.0(11)	6.4(7)	2.4(3)	57	$1.5(2)\times10^{15}$
-47.8(11)	16.4(5)	4.8(2)	57	$7.6(4)\times10^{15}$
-41.7(11)	32.0(6)	4.4(1)	57	$1.4(1)\times10^{16}$
-26.5(11)	7.6(3)	21.0(19)	57	$1.6(2)\times10^{16}$
-6.1(11)	6.2(5)	10.0(24)	57	$6.0(15)\times10^{15}$
-2.3(11)	13.8(13)	3.5(3)	57	$4.7(6)\times10^{15}$
4.8(17)	24.0(264)	9.1(29)	57	$\sim2.1\times10^{16}$
7.5(11)	6.1(12)	1.5(4)	57	$8.8(29)\times10^{14}$
13.6(45)	24.6(68)	13.7(115)	57	$3.3(29)\times10^{16}$
23.1(11)	16.9(68)	5.8(9)	57	$9.5(41)\times10^{15}$
31.5(11)	21.3(13)	11.5(7)	57	$2.4(2)\times10^{16}$

[a]Gaussian fit is approximate.

Greaves & Nyman (1996) has previously conducted a survey of the LOS transitions using the SEST 15 meter radio telescope. Given the calibration uncertainties as well as uncertainties from Gaussian fits, the results reported here agree with those reported by Greaves & Nyman (1996).

Figure 3.16 shows all the velocity components seen in this survey. The ordinate is molecular species, and the abscissa is the v_{LSR} of the line. Triangles denote Sgr B2(N-LMH) features from the BIMA Array. Boxes denote Sgr B2(M) features from the BIMA Array. Open circles denote features detected by the 12 meter. Red points denote emission components and the error bars denote the uncertainties of the fits. Vertical lines indicate common velocities seen across several species: green are seen in both Sgr B2(N-LMH) and Sgr B2(M), red are seen only in Sgr B2(N-LMH) and dashed black are seen only in Sgr B2(M).

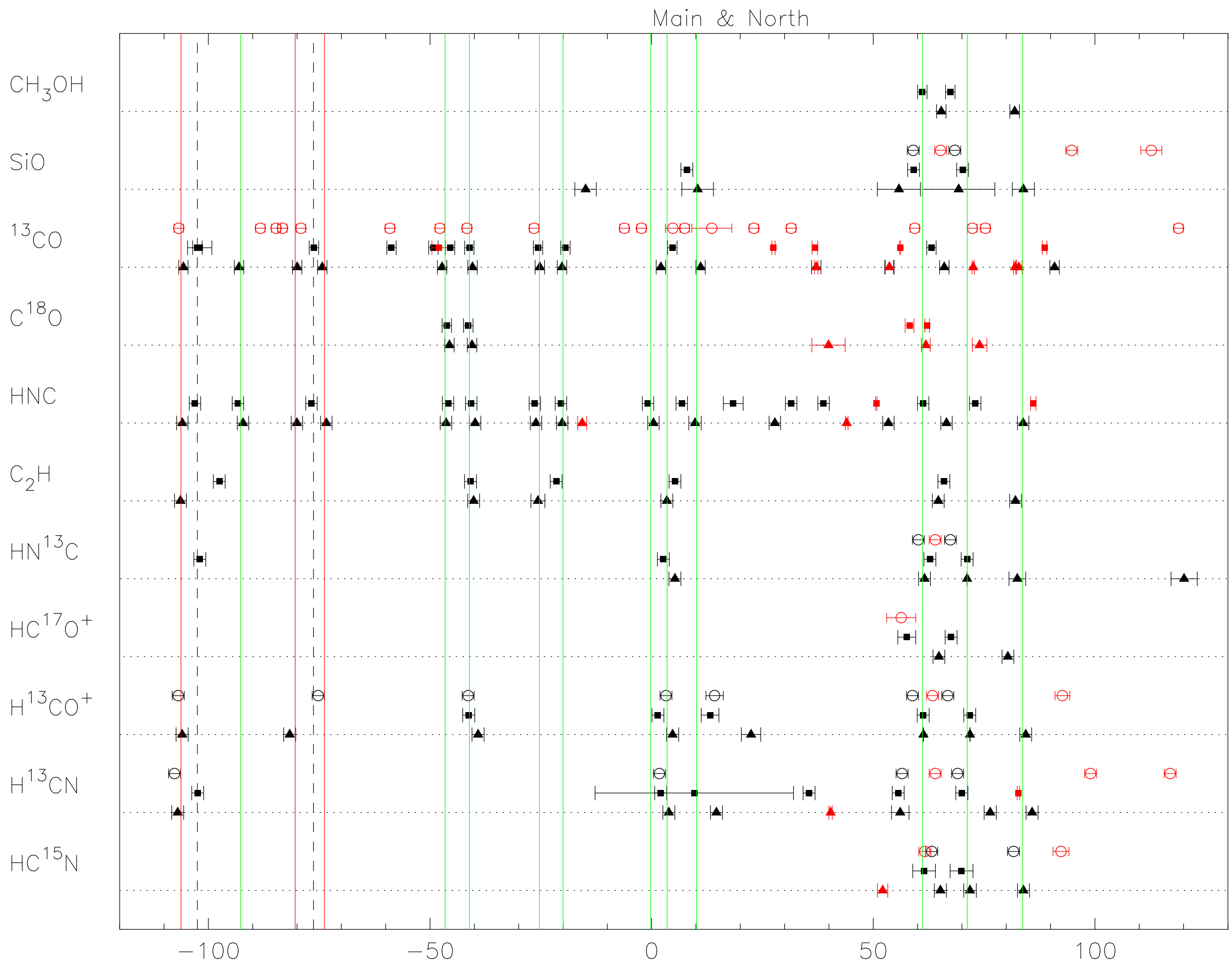

Figure 3.16 Velocity components toward Sgr B2(N-LMH) and Sgr B2(M); both line of sight and local components are included. The ordinate is molecular species, and the abscissa is the v_{LSR} of the line. Triangles denote Sgr B2(N-LMH) features from the BIMA Array. Boxes denote Sgr B2(M) features from the BIMA Array. Open circles denote features detected by the 12 meter. Red points denote emission components, and the error bars denote uncertainties of the fits. Vertical lines indicate common velocities seen across several species: green are seen in both Sgr B2(N-LMH) and Sgr B2(M), red are seen only in Sgr B2(N-LMH) and dashed black are seen only in Sgr B2(M).

3.3.22 Line Statistics

This spectral line survey detected a total of 331 spectral features associated with the 64 km s^{-1} main core of Sgr B2(N-LMH). Of these lines, 206 of these lines have been identified, leaving 125 as unidentified lines. This gives a spectral line density of 6.92 per 100 MHz: 4.31 from identified lines and 2.61 from U lines. A total of 86 spectral features were detected at a v_{LSR} of ~72 km s^{-1} (73 identified and 13 unidentified), and a total of 24 (all identified) transitions were detected at a v_{LSR} of ~52 km s^{-1}.

There are a total of ~15,500 spectral channels in this survey. Assuming Gaussian statistics and independent channels, one would expect 42 of these to be above 3 σ and 1 above 4 σ just from random noise. Thus some of the very narrow lines detected at the ~3 σ level may not be real.

3.4 Conclusions and Future Work

This survey presents accurate source size measurements (for the first time) and column densities for many complex molecular species. These source sizes and column densities will help future models of interstellar molecular formation by indicating what species exist where and on what scale and in what ratios to each other. A total of 331 spectral lines were detected (not including velocity components other than the systemic velocity of 64 km s^{-1}), of which 206 have been identified (from 40 molecular species and isotopologues and one recombination line) and 125 are unidentified. This gives a total line density (per 100 MHz) of 6.92 (4.31 from identified lines and 2.61 from U lines).

The simple molecular species (generally those with 3 or fewer atoms) and CH_3OH all appear to have very extended components (on the order of at least 30″). Many of the species show both emission and absorption components at several velocity components, both locally to Sgr B2(N-LMH) and along the line of sight. These species most likely form from low temperature gas phase reactions such as ion-molecule reactions. The single exception is a low temperature CH_3OH transition, which shows several local absorption features (no line of sight components were detected because they were beyond the frequency coverage of this survey). CH_3OH in this region is likely to form on grains via H atom addition to CO rather than in hot post shock gas, since the presence of strong shocks on the large scale have not been seen toward Sgr B2(N-LMH)[11]. Its presence in an extended envelope suggests that it may be easily liberated from grain surfaces once it has formed.

All of the complex molecular species appear to exist primarily in the hot core with source sizes of ~3.1″. The exception is a single, low energy transition of C_2H_5OH, which has a very large (>70″) extended component. C_2H_5OH similarly to CH_3OH is thought to form on grain surfaces and not in gas phase reactions. This indicates that H atom addition on grain surfaces can happen at very low temperatures in extended, cool clouds, as was suggested by laboratory experiments by Hiraoka et al. (1998a,b). It may be possible that other complex saturated species (such as $HCOOCH_3$ and $(CH_3)_2CO$) may also have extended components. Observations of very

[11]Weak large scale shocks have been detected toward the Galactic center (Martín-Pintado et al., 2001).

low temperature transitions (<10 K) of these species should be carried out in order to verify this hypothesis. These observations need to be conducted either with enough *u*-*v* coverage to detect large scale structure or with a combination of array and single dish instruments.

The source sizes of the U lines were also measured, and an analysis was conducted to determine if there are any frequency relations among the lines. Of the 125 U lines 9 pairs of lines have potential relationships, meaning that each pair could originate from the same molecular species. In general many of the U lines have source sizes similar to those of complex hot core molecules, suggesting they might originate from such species. Others have noticeably smaller source sizes, indicating that they might be from high energy transitions (either vibrationally excited or ground state) and a few had extended components, suggesting they originate from low lying states of previously undetected species or low lying but uncataloged vibrationally excited states of known species. Additionally four U lines have been potentially identified as methyl glycolate, and three others follow the pattern of a double rotor species and may be related.

Many species, both simple and complex, have emission components at velocities other than the systemic velocity of Sgr B2(N-LMH). Emission components were seen in complex species at $\sim$72 and $\sim$52 km s^{-1}. The $\sim$72 km s^{-1} component originates from a second core 5$''$ north of the main core. This second core may be at a different evolutionary stage than the main core, as indicated by the much higher abundances of carbon chain molecules in this secondary core. The origin of the $\sim$52 km s^{-1} velocity component is much less clear and may require higher spatial resolution observations in order to see its origins. Some possibilities are a rotating disk or an outflow (Hollis et al., 2003, and references therein). Most simple species show absorption lines (emission lines in the case of ^{13}CO) from large scale cooler clouds both around the Sgr B2 complex and along the line of sight. Most of the local components surround both the Sgr B2(N-LMH) and Sgr B2(M) cores, while one component at $\sim$85-90 km s^{-1} appears to be around only Sgr B2(N-LMH).

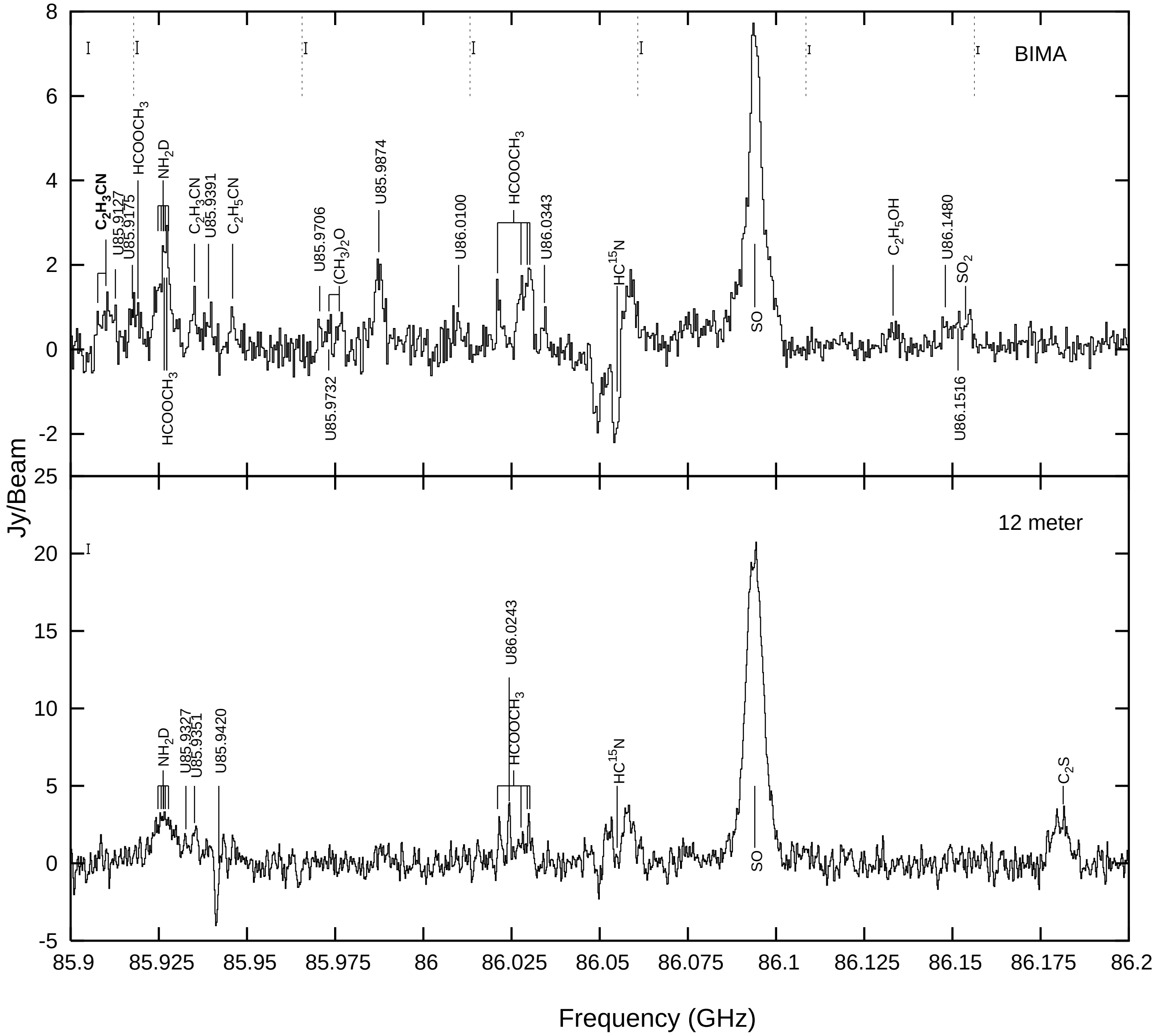

Figure 3.17 Continuum subtracted spectra from the Sgr B2(N-LMH) line survey. The top spectrum is from the BIMA Array. The vertical dashed lines denote where two spectral windows meet. The bars next to the window edges denote the rms noise level of each window. The bottom spectrum is from the NRAO 12 meter and matches the BIMA frequency range.

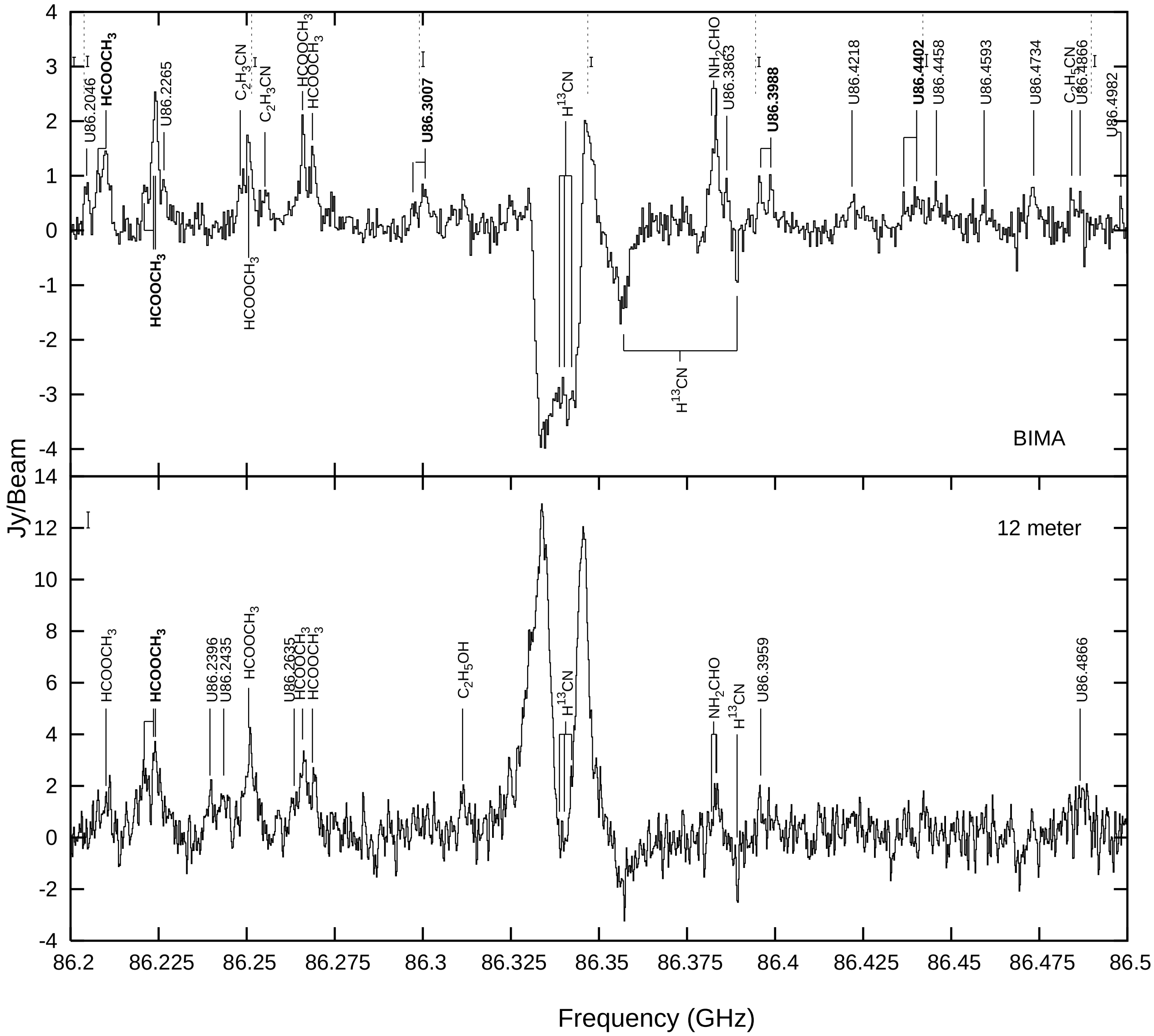
BIMA
12 meter
Jy/Beam
Frequency (GHz)
U86.2046
HCOOCH3
U86.2265
C2H3CN
HCOOCH3
U86.3007
H13CN
NH2CHO
U86.3863
U86.3988
U86.4218
U86.4402
U86.4458
U86.4593
U86.4734
C2H5CN
U86.4866
U86.4982
U86.2396
U86.2435
U86.2635
C2H5OH
U86.3959

Fig. 3.17b

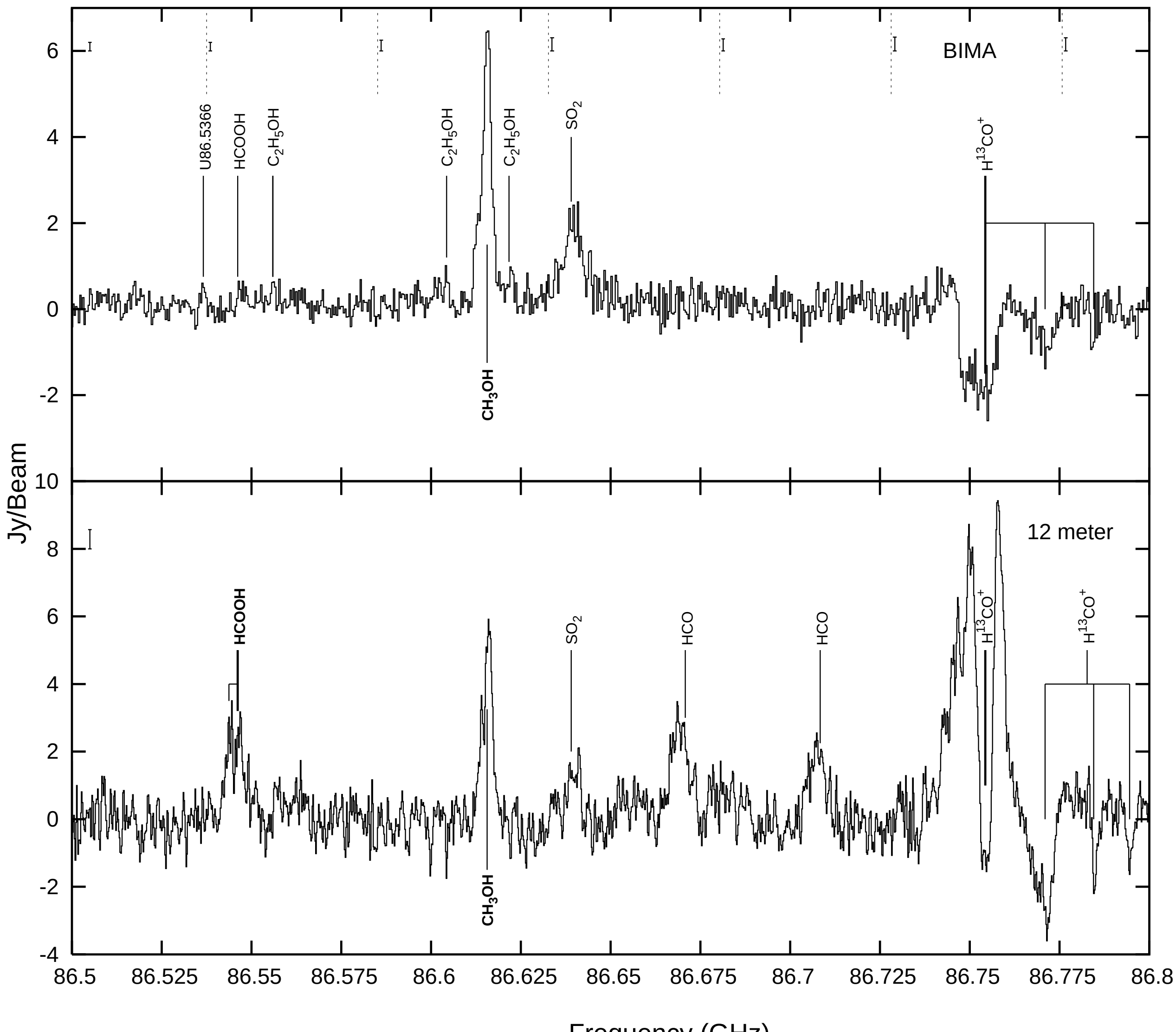

BIMA
12 meter
Jy/Beam
Frequency (GHz)
U86.5366
HCOOH
C2H5OH
CH3OH
SO2
H13CO+
HCO

Fig. 3.17c

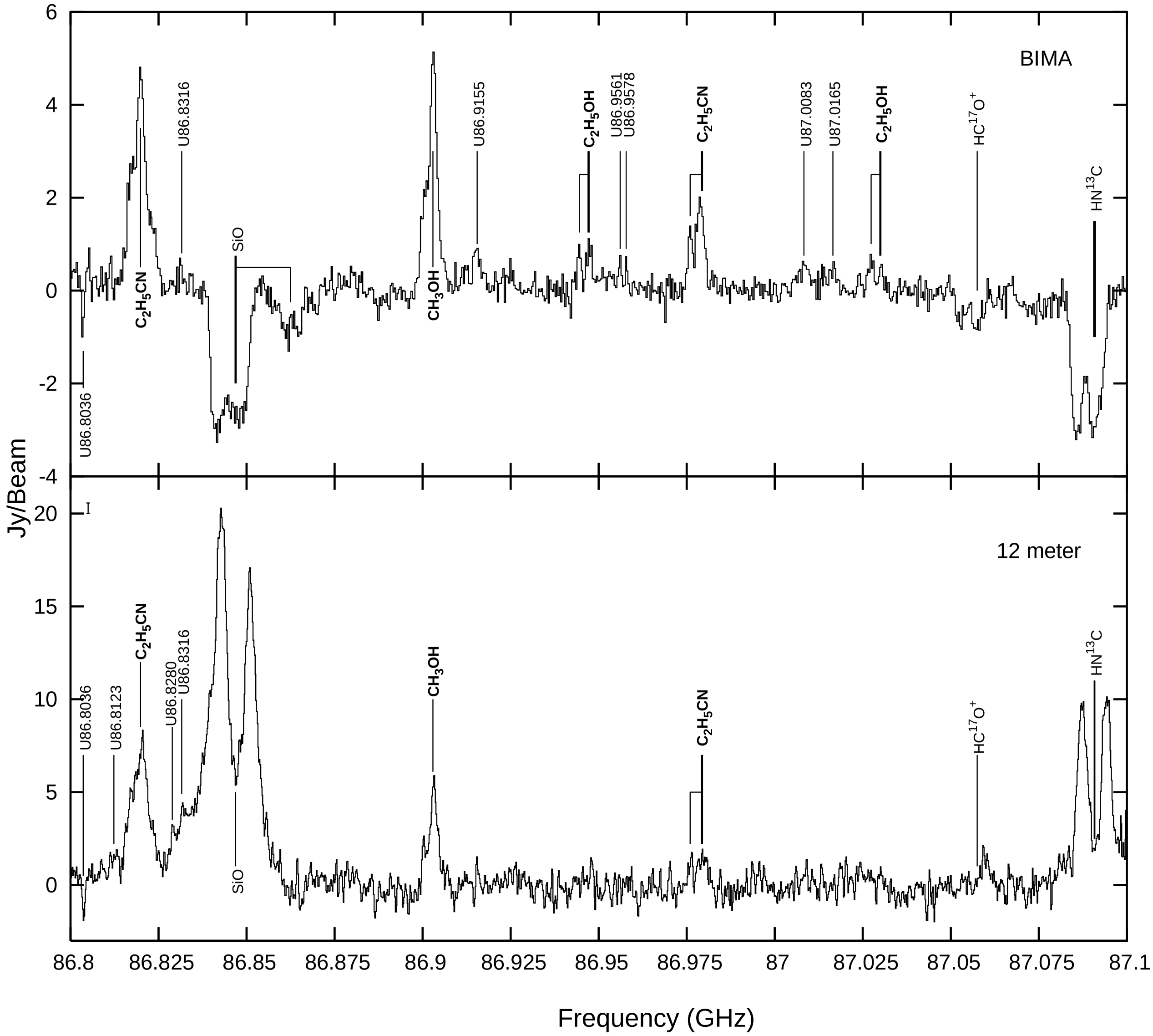
BIMA
12 meter
Jy/Beam
Frequency (GHz)
U86.8036
U86.8123
C_2H_5CN
U86.8280
U86.8316
SiO
CH_3OH
U86.9155
C_2H_5OH
U86.9561
U86.9578
U87.0083
U87.0165
$HC^{17}O^+$
$HN^{13}C$

Fig. 3.17d

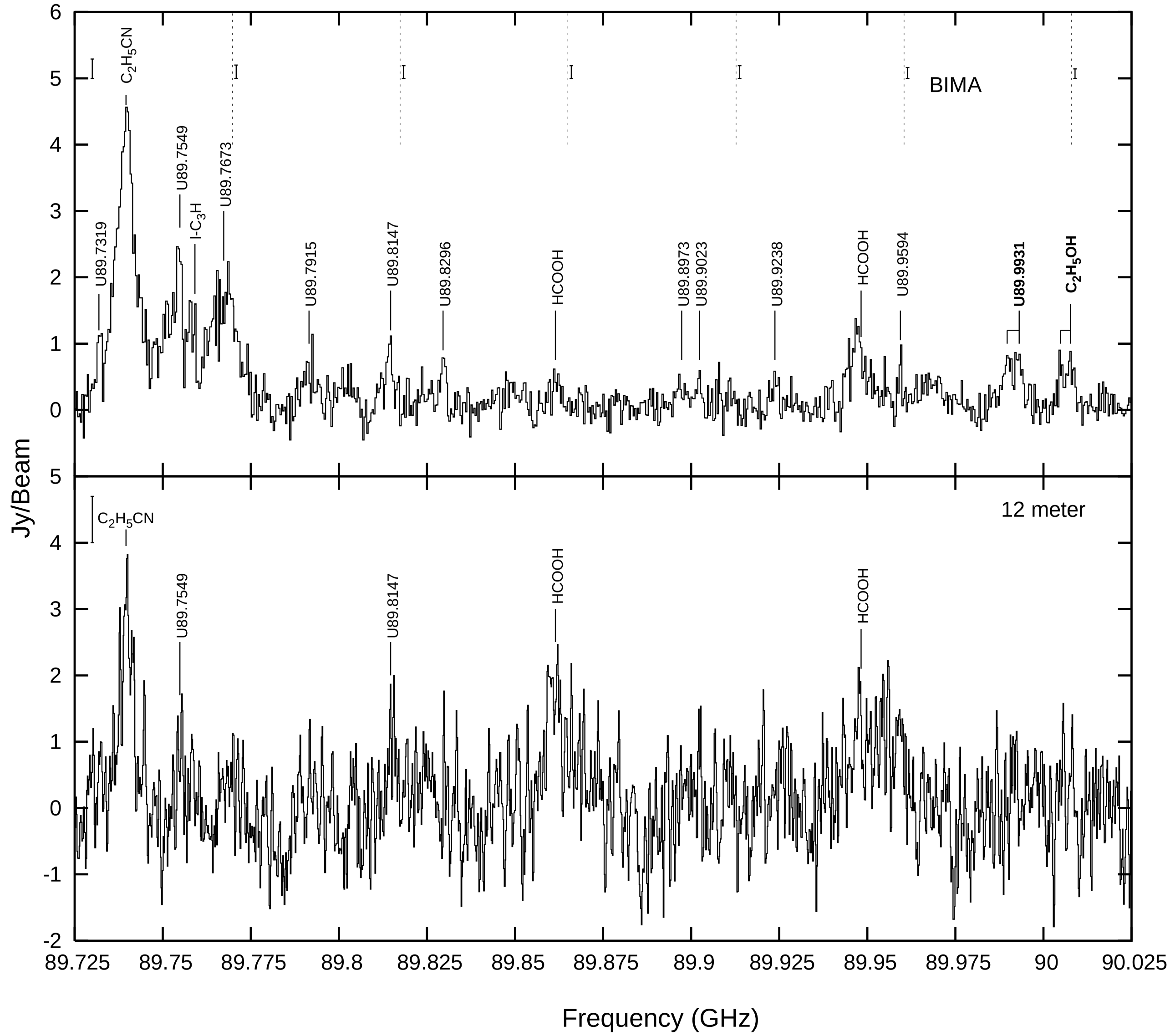

BIMA
12 meter
Jy/Beam
Frequency (GHz)
U89.7319
C_2H_5CN
U89.7549
l-C_3H
U89.7673
U89.7915
U89.8147
U89.8296
HCOOH
U89.8973
U89.9023
U89.9238
U89.9594
U89.9931
C_2H_5OH

Fig. 3.17e

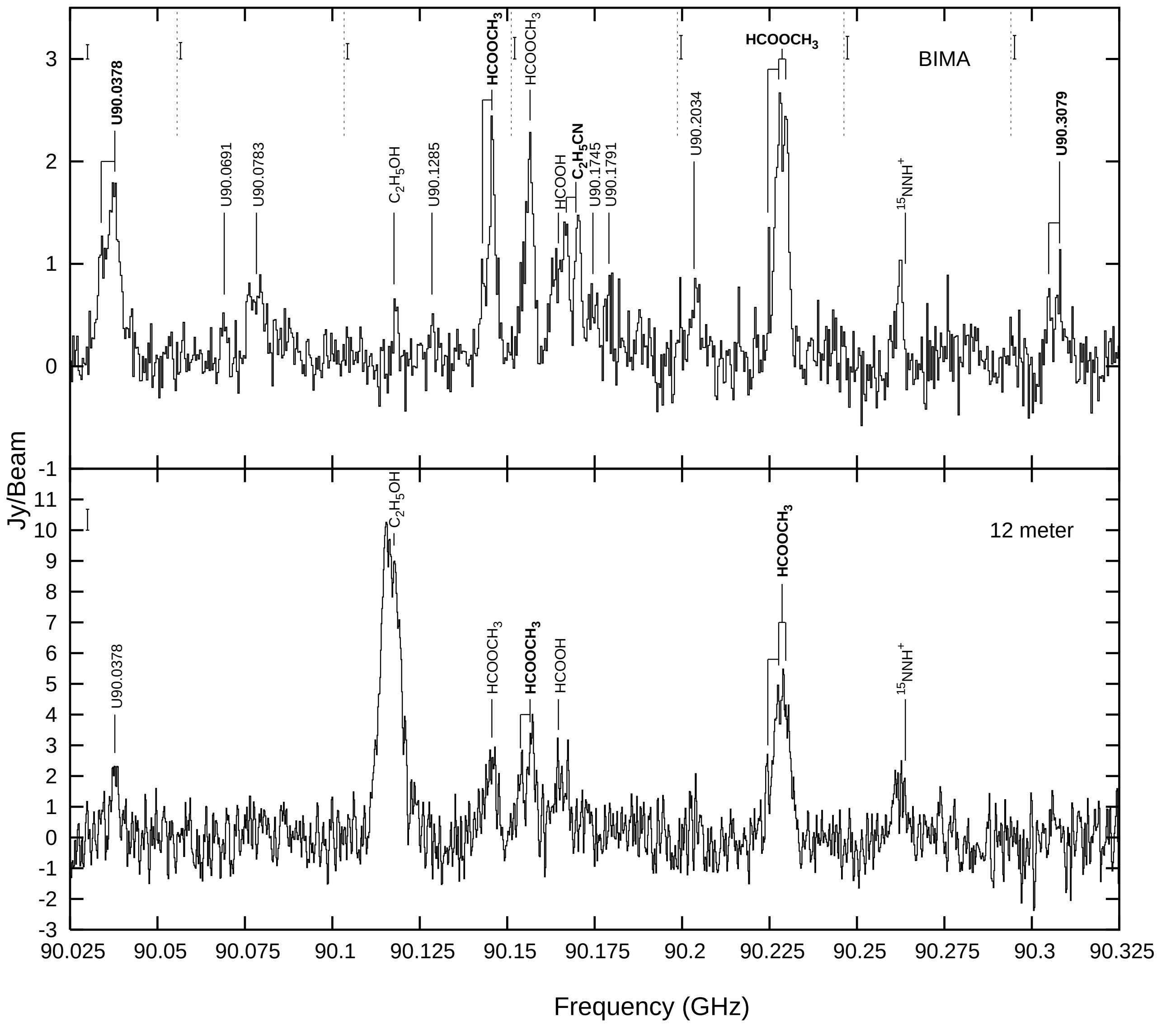
BIMA
12 meter
U90.0378
U90.0691
U90.0783
C_2H_5OH
U90.1285
$HCOOCH_3$
$HCOOCH_3$
HCOOH
C_2H_5CN
U90.1745
U90.1791
U90.2034
$HCOOCH_3$
$^{15}NNH^+$
U90.3079
Jy/Beam
Frequency (GHz)

Fig. 3.17f

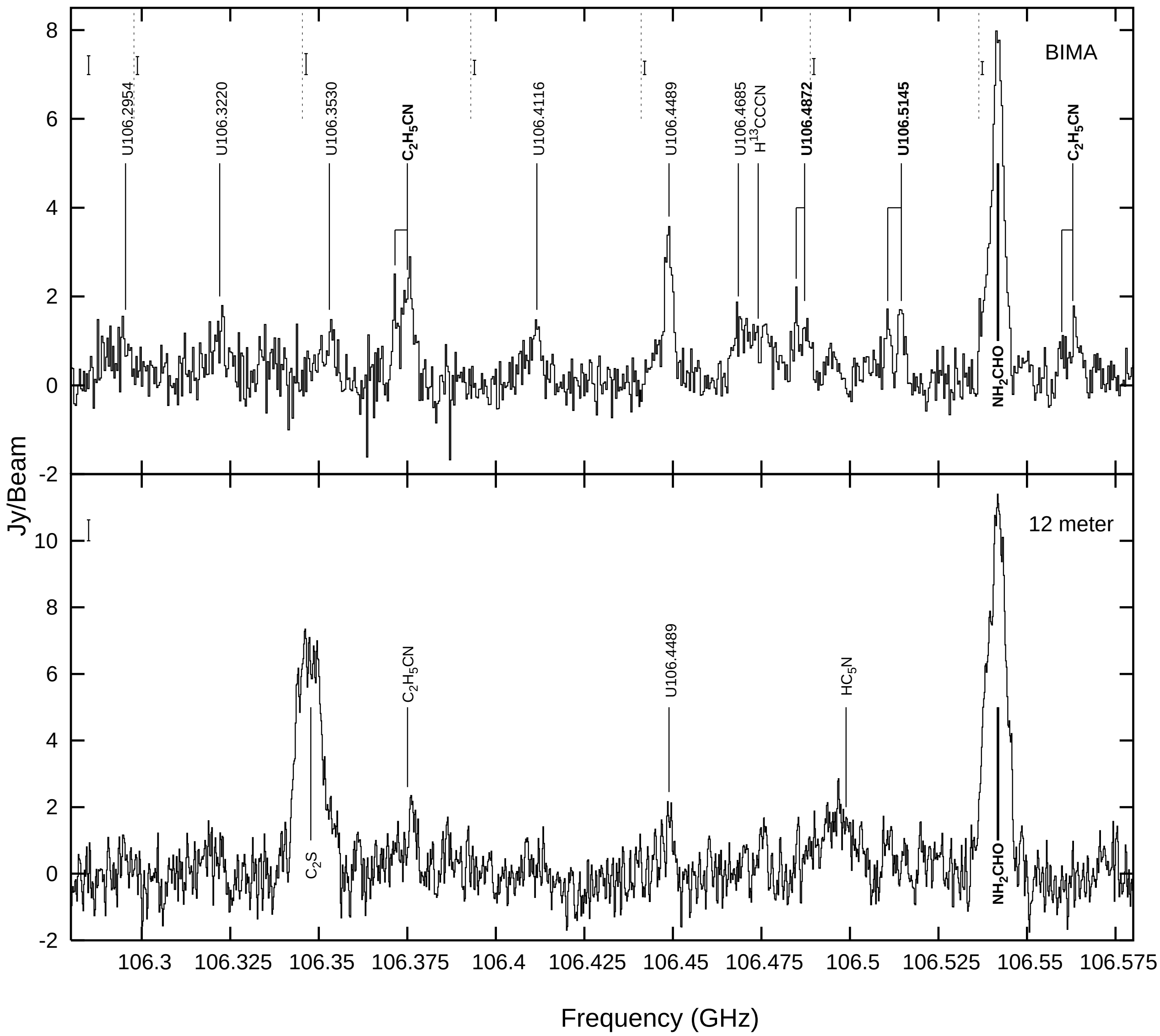
BIMA
12 meter
Jy/Beam
Frequency (GHz)
U106.2954
U106.3220
U106.3530
C2H5CN
U106.4116
U106.4489
U106.4685
H13CCCN
U106.4872
U106.5145
NH2CHO
C2S
HC5N
106.3
106.325
106.35
106.375
106.4
106.425
106.45
106.475
106.5
106.525
106.55
106.575

Fig. 3.17g

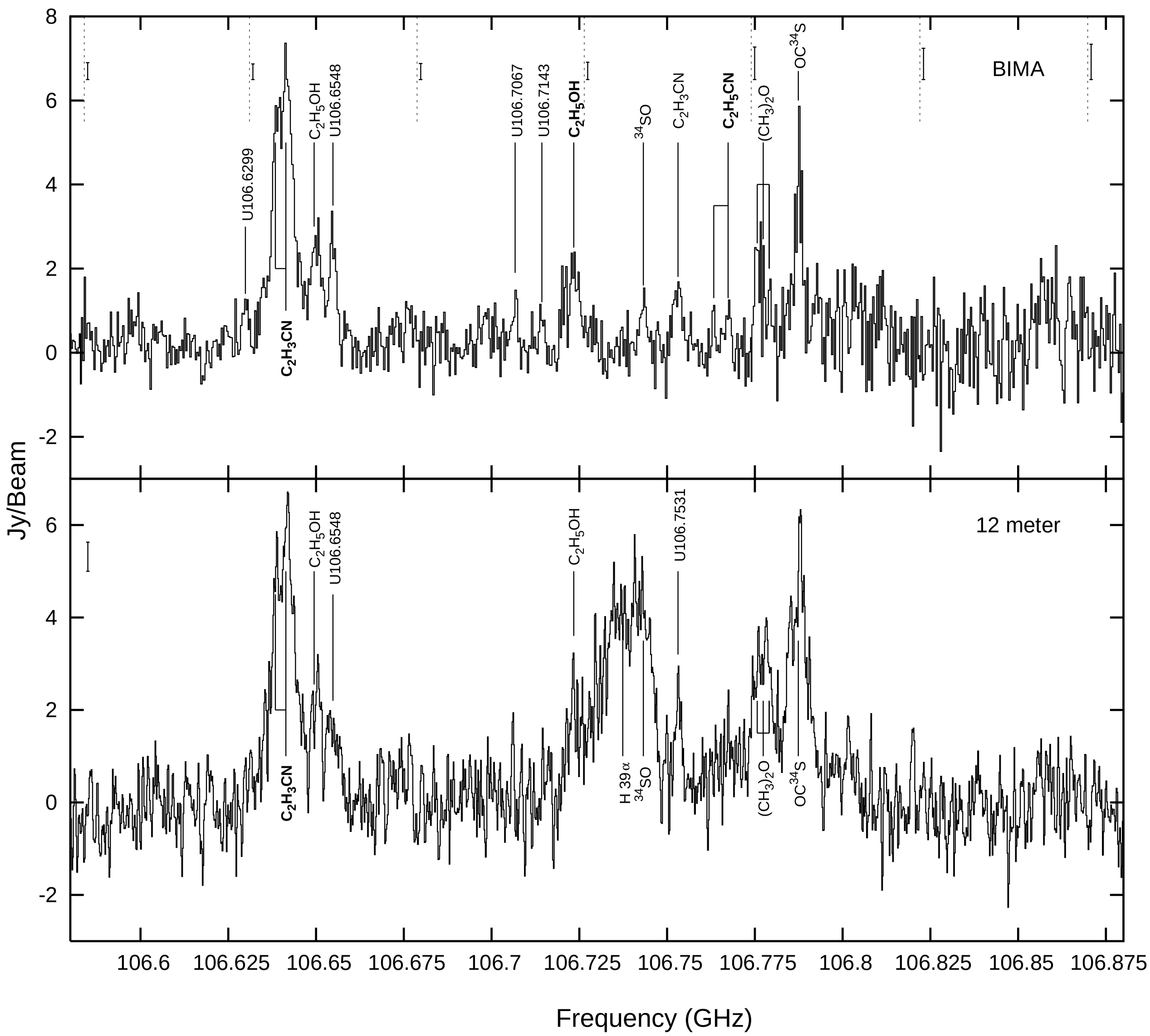
Jy/Beam
BIMA
12 meter
U106.6299
C2H3CN
C2H5OH
U106.6548
U106.7067
U106.7143
C2H5OH
34SO
C2H3CN
C2H5CN
(CH3)2O
OC34S
H 39α
U106.7531
Frequency (GHz)

Fig. 3.17h

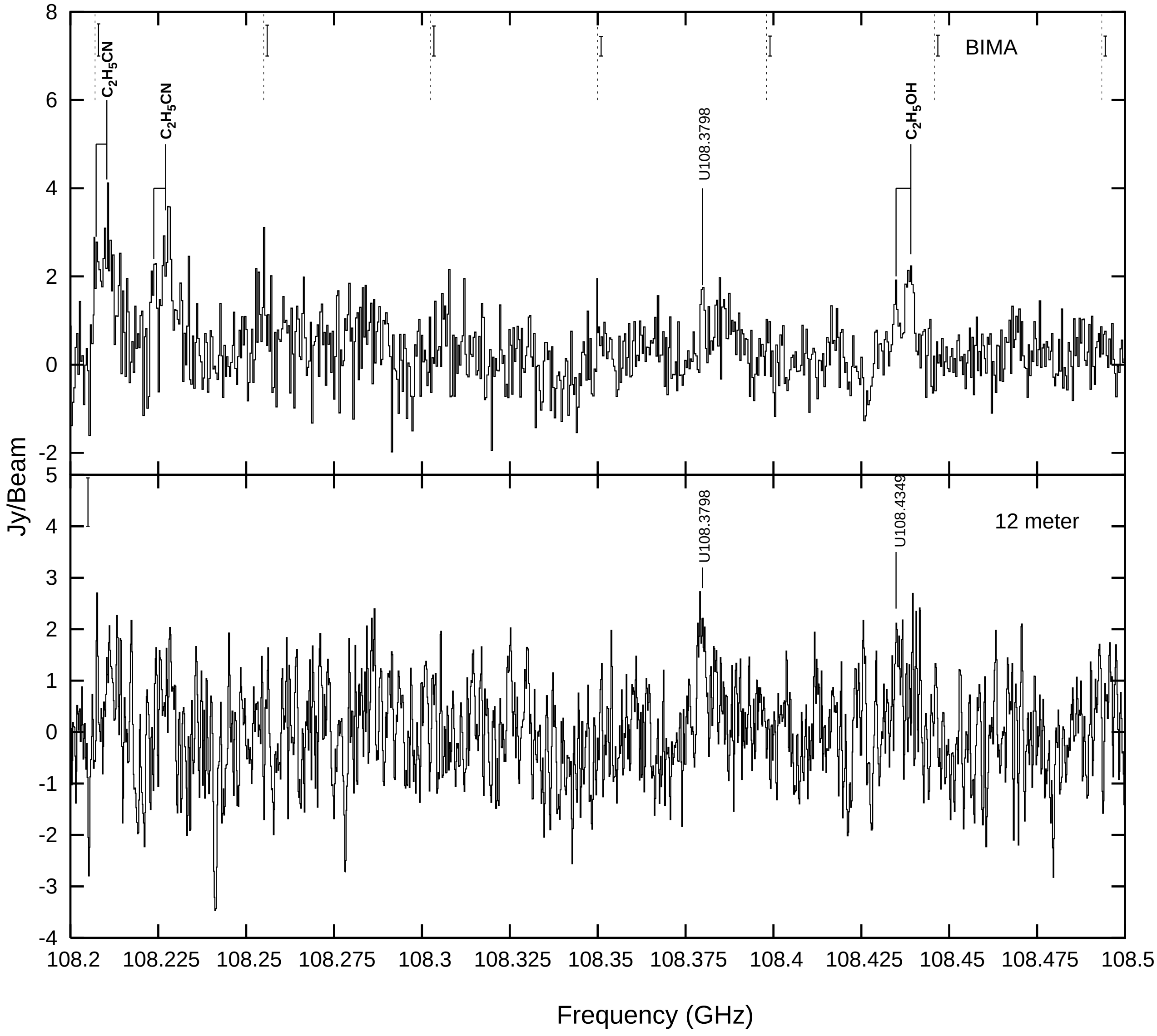

BIMA
12 meter
C_2H_5CN
C_2H_5CN
U108.3798
C_2H_5OH
U108.3798
U108.4349
Jy/Beam
Frequency (GHz)

Fig. 3.17i

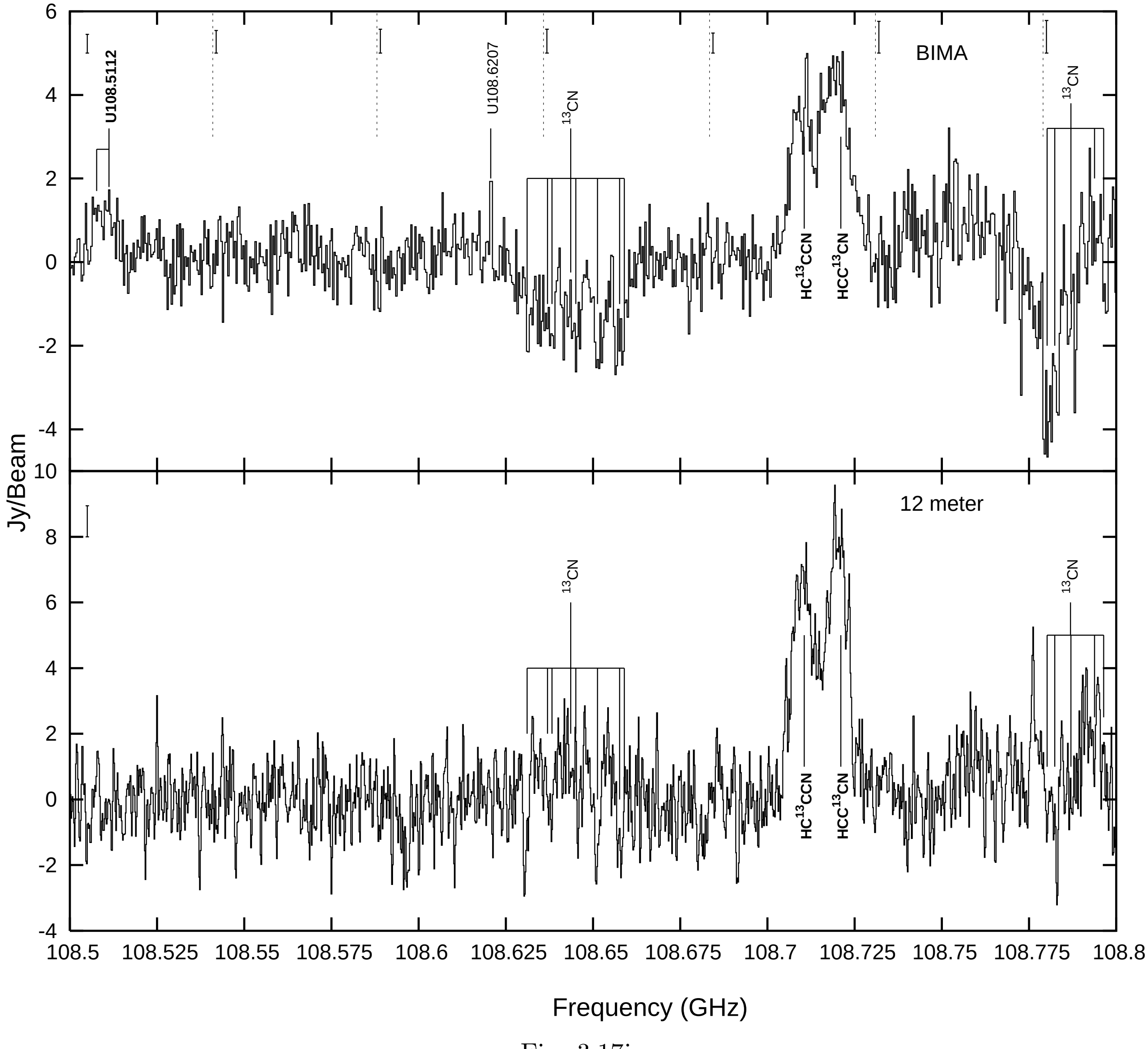

BIMA
12 meter
U108.5112
U108.6207
^{13}CN
HC^{13}CCN
HCC^{13}CN
Jy/Beam
Frequency (GHz)
108.5
108.525
108.55
108.575
108.6
108.625
108.65
108.675
108.7
108.725
108.75
108.775
108.8

Fig. 3.17j

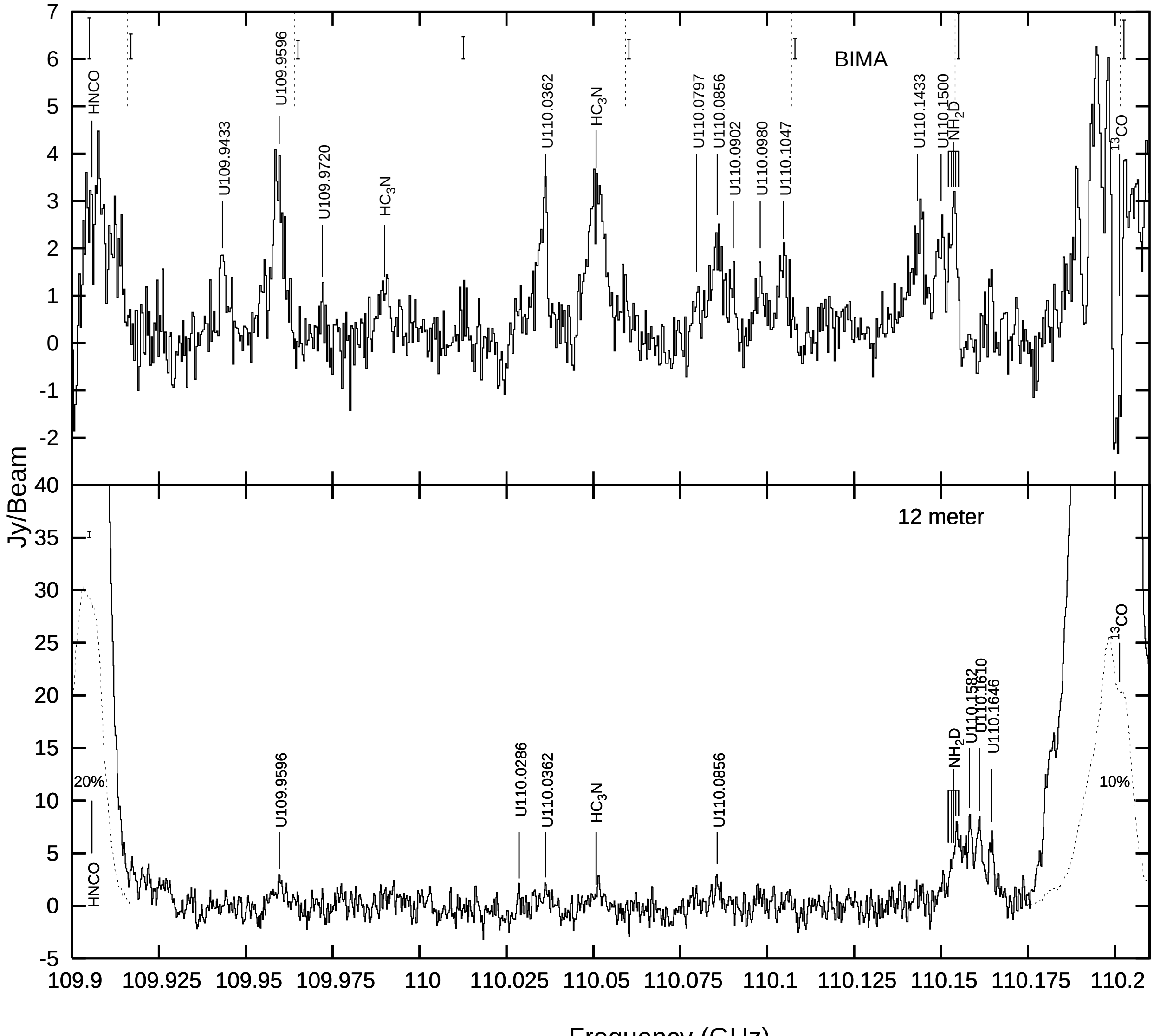
BIMA
12 meter
Jy/Beam
Frequency (GHz)
HNCO
U109.9433
U109.9596
U109.9720
HC_3N
U110.0362
U110.0797
U110.0856
U110.0902
U110.0980
U110.1047
U110.1433
U110.1500
NH_2D
^{13}CO
20%
10%
U110.0286
U110.1582
U110.1610
U110.1646

Fig. 3.17k

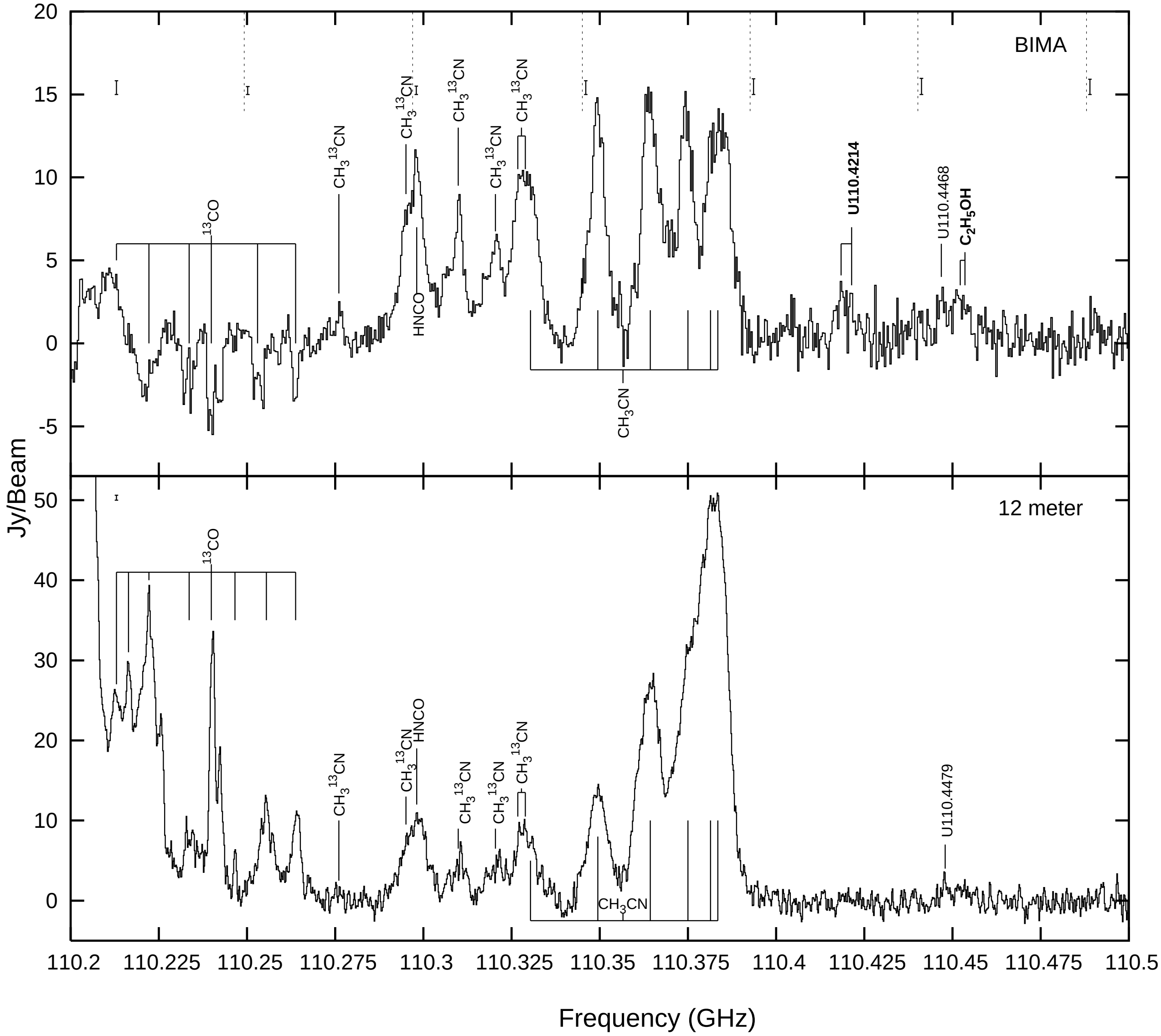
BIMA
12 meter
Jy/Beam
Frequency (GHz)
^{13}CO
$CH_3^{13}CN$
HNCO
CH_3CN
U110.4214
U110.4468
C_2H_5OH
U110.4479
Fig. 3.17l

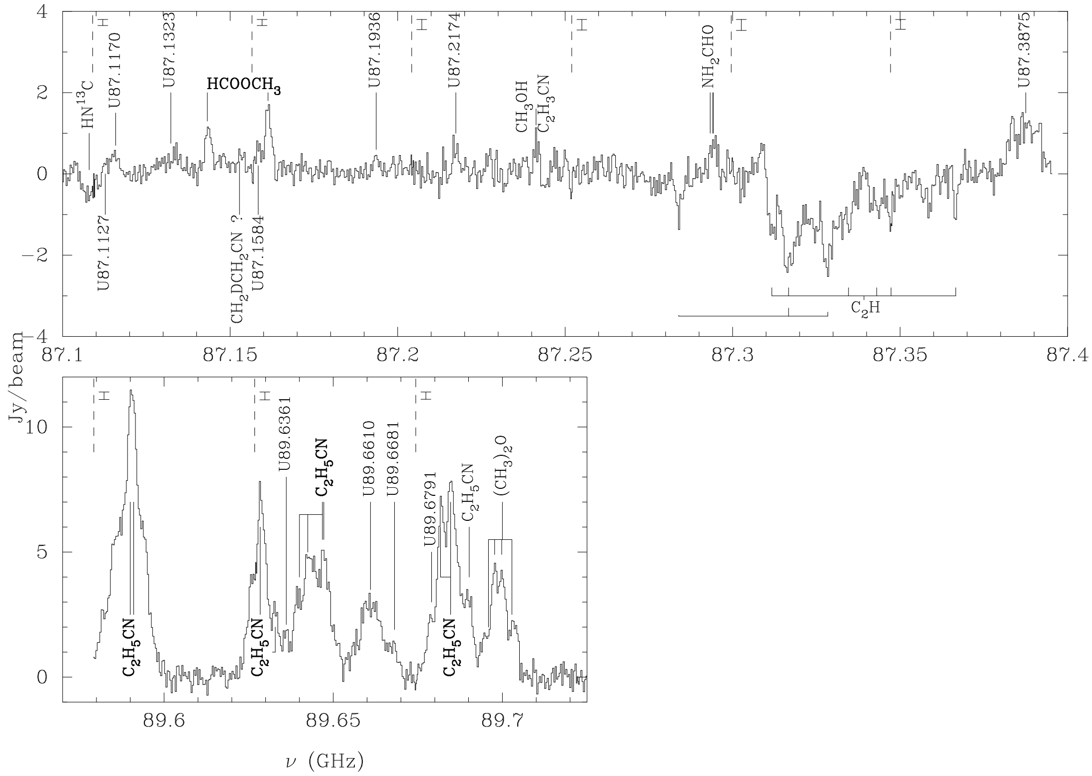

Figure 3.18 BIMA Array Spectra of frequencies not covered by the 12 meter. The axes and labels are the same as for Figure 3.17.

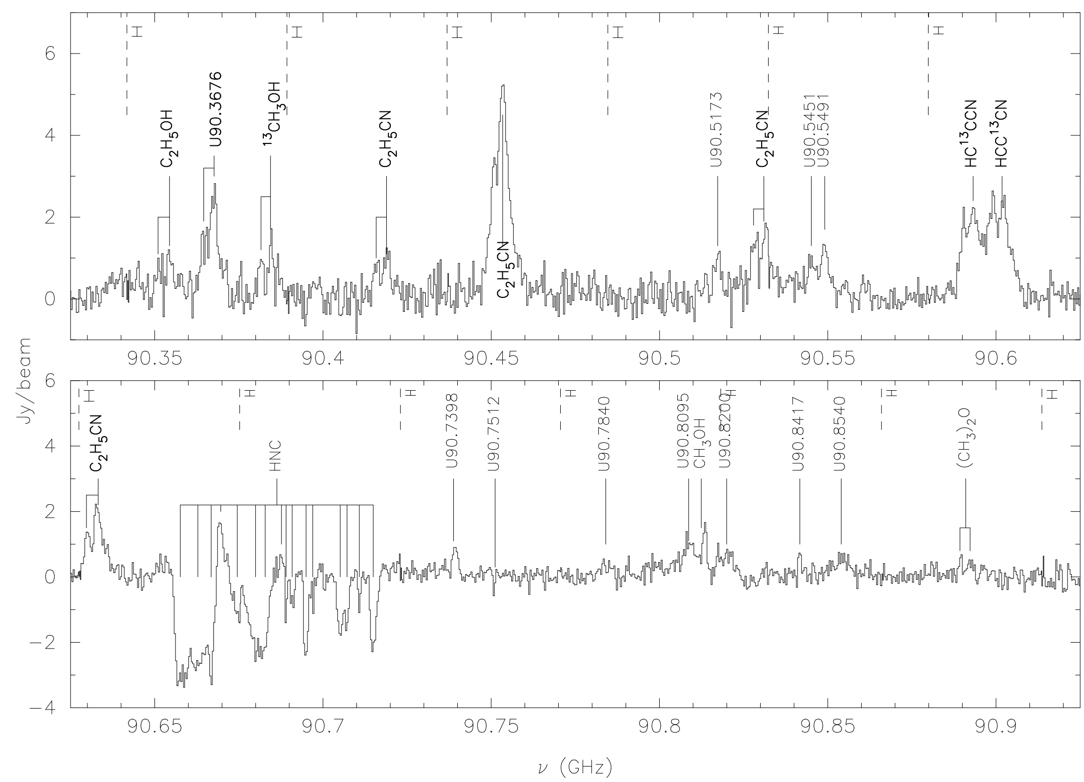

Fig. 3.18b

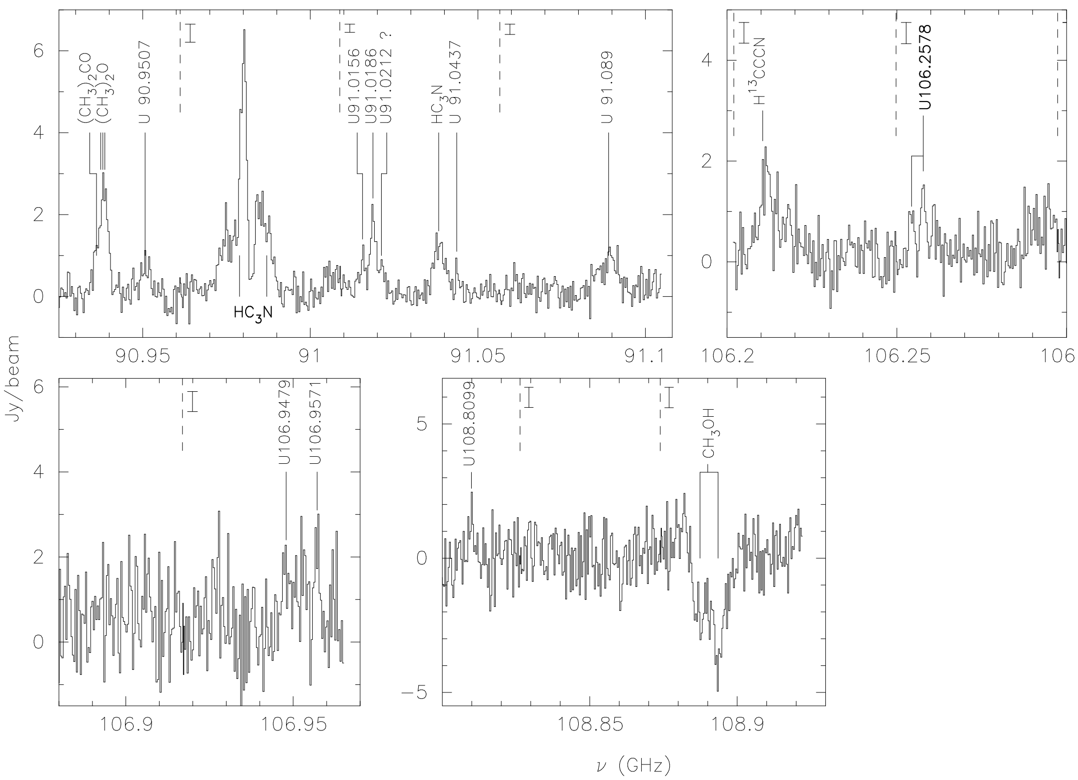

Fig. 3.18c

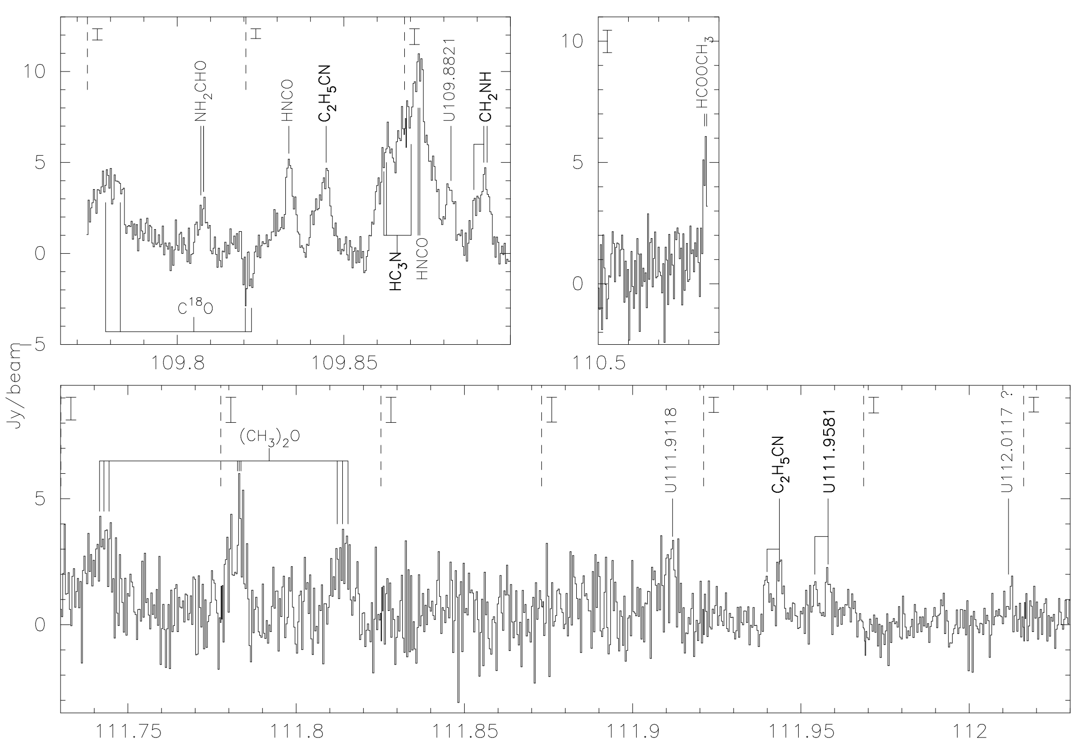

Fig. 3.18d

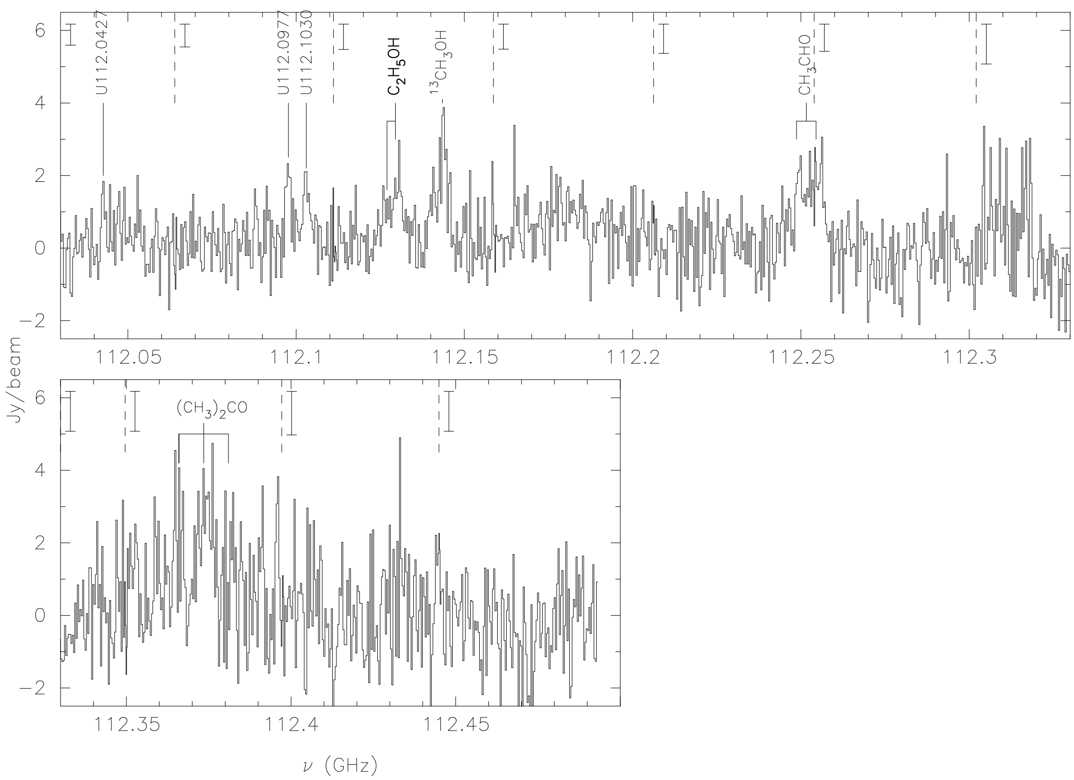

U112.0427
U112.0977
U112.1030
C2H5OH
13CH3OH
CH3CHO
(CH3)2CO
Jy/beam
ν (GHz)

Fig. 3.18e

Table 3.14. Detected Transitions

Rest Frequency (MHz)[a]	Transition[b]	BIMA Array I_0 (Jy/bm)	BIMA Array Δv (km/s)	BIMA Array $\theta_a \times \theta_b$ ($'' \times ''$)	BIMA Array τ	12 meter telescope I_0 (Jy/bm)	12 meter telescope Δv (km/s)	12 meter telescope θ ($''$)	12 meter telescope τ	E_u (K)	$\langle S_{i,j}\mu^2 \rangle$ (D^2)	Source Size ($''$)
l-C_3H ($\nu_4^2\Sigma^\mu$) $N_J = 4_{\frac{7}{2}} - 3_{\frac{5}{2}}$												
89,759.3280 (480)[d]	$F = 4 - 3$	1.0(8)	7.0(56)	30.8×6.2	0.12	< 0.7	···	71		49.9	18.45	2.7(8)
89,759.8490 (480)[d]	$F = 3 - 2$	···	···	30.8×6.2	0.09	< 0.7	···	71		49.9	13.74	2.7(8)
C_2H $N_J = 1_{\frac{3}{2}} - 0_{\frac{1}{2}}$												
87,284.1560 (30)	$F = 1 - 1$	[c]	···	33.9×6.2		···	···			4.2	0.04	···
87,316.9250 (40)	$F = 2 - 1$	[c]	···	33.9×6.2		···	···			4.2	0.40	···
87,328.6240 (60)	$F = 1 - 0$	[c]	···	33.9×6.2		···	···			4.2	0.20	···
C_2H_3CN												
$\nu = 0$												
86,248.3660 (50)	$32_{5,28} - 33_{4,29}$[e]	0.8(1)	6.6(17)	23.9×6.6	0.05	< 0.6	···	74		294.6	4.68	···
106,641.3940 (170)	$11_{1,10} - 10_{1,9}$	6.7(2)	11.7(19)	20.6×5.2	0.34	6.1(2)	10.7(9)	60	···	32.9	147.71	2.7(3)
$^1\nu_{11}$												
85,987.1760 (110)	$9_{2,7} - 8_{2,6}$	1.9(2)	10.5(12)	31.9×6.5	0.13	< 0.6	···	74		373.1	124.45	2.1(7)
$^1\nu_{15}$												
106,753.0890 (270)	$11_{1,10} - 10_{1,9}$	1.5(2)	8.8(13)	20.7×5.2	0.07	2.2(3)	6.1(9)	60	0.00	522.0	158.75	2.2(3)
$^2\nu_{11}$												
85,909.7910 (310)	$9_{5,5} - 8_{5,4}$[d]	1.0(2)	10.9(34)	32.1×6.5	0.02	< 0.6	···	74		761.1	90.57	2.0(10)
85,909.7910 (310)	$9_{5,4} - 8_{5,3}$[d]	···	···	32.1×6.5	···	···	···	74		761.1	90.57	2.0(10)
85,910.5640 (300)	$9_{4,6} - 8_{4,5}$[d]	···	···	32.1×6.5	···	···	···	74		742.2	105.08	2.0(10)
85,910.6320 (300)	$9_{4,5} - 8_{4,4}$[d]	···	···	32.1×6.5	···	···	···	74		742.2	105.08	2.0(10)
85,917.1870 (320)	$9_{6,4} - 8_{6,3}$[d]	0.9(2)	6.9(18)	32.1×6.5	0.03	< 0.6	···	74		784.1	72.77	···
85,917.1870 (320)	$9_{6,3} - 8_{6,2}$[d]	···	···	32.1×6.5	···	···	···	74		784.1	72.77	···
85,925.2410 (310)	$9_{3,7} - 8_{3,6}$	[f]	···	32.3×6.5		< 0.6	···			727.5	116.40	···

Table 3.14—Continued

Rest Frequency (MHz)[a]	Transition[b]	BIMA Array I_0 (Jy/bm)	BIMA Array Δv (km/s)	BIMA Array $\theta_a \times \theta_b$ ($''\times''$)	BIMA Array τ	12 meter telescope I_0 (Jy/bm)	12 meter telescope Δv (km/s)	12 meter telescope θ ($''$)	12 meter telescope τ	E_u (K)	$\langle S_{i,j}\mu^2 \rangle$ (D^2)	Source Size ($''$)
85,929.6550 (360)	$9_{7,3} - 8_{7,2}$	f	···	32.3×6.5		< 0.6	···			811.3	51.67	···
85.929.6550 (360)	$9_{7,2} - 8_{7,1}$	f	···	32.3×6.5		< 0.6	···			811.3	51.67	···
85,934.5720 (310)	$9_{3,6} - 8_{3,5}$	1.0(2)	6.9(14)	32.3×6.5	0.06	2.1(2)	6.9(10)	74	0.00	727.5	116.40	2.5(8)
85,945.9680 (420)	$9_{8,2} - 8_{8,1}$[d]	0.9(2)	5.0(13)	32.3×6.5	0.03	< 0.6	···	74		842.7	27.49	2.4(8)
85,945.9680 (420)	$9_{8,1} - 8_{8,0}$[d]	···	···	32.3×6.5	···	···	···	74		842.7	27.49	2.4(8)
86,254.8480 (320)	$9_{2,7} - 8_{2,6}$	0.6(1)	12.2(27)	25.0×6.9	0.04	< 0.6	···	74		717.1	124.45	1.5(14)
87,241.3930 (1030)	$13_{3,10} - 14_{2,13}$	g	···	25.0×6.7		···	···			748.6	1.81	2.9(3)
						C_2H_5CN						
$\nu = 0$												
86,484.2300 (400)	$29_{3,27} - 28_{4,24}$	0.5(1)	5.9(32)	27.6×6.4	0.11	< 0.6	···	74		197.1	6.2	0.9(4)
86,819.8510 (130)	$10_{1,10} - 9_{1,9}$	4.3(5)	7.9(10)	48.1×6.4	2.32	5.3(3)	8.7(16)	73	0.00	24.1	146.7	4.2(3)
89,590.0315 (4000)	$10_{4,7} - 9_{4,6}$	2.0(4)	8.1(11)	30.2×6.3	0.51	···	···			41.4	124.5	3.0(2)
89,591.0159 (4000)	$10_{4,6} - 9_{4,5}$	2.0(4)	8.1(11)	30.2×6.3	0.51	···	···			41.4	124.5	3.0(2)
89,628.4468 (1000)	$10_{3,8} - 9_{3,7}$	7.1(2)	10.4(12)	30.8×6.2	3.49	···	···			33.6	134.9	2.9(9)
89,684.7134 (3400)	$10_{3,7} - 9_{3,6}$	7.6(1)	13.8(11)	31.2×6.2	3.49	···	···			33.65	134.9	3.0(2)
90,169.6330 (260)	$20_{2,18} - 19_{3,17}$	1.5(1)	6.6(9)	26.6×5.2	0.35	< 0.7	···	71		96.4	6.1	1.0(6)
90,418.9167 (1000)	$15_{1,14} - 14_{2,13}$	1.0(2)	9.5(27)	47.4×6.1	0.22	···	···			53.76	6.8	2.2(5)
90,453.3528 (3400)	$10_{2,8} - 9_{2,7}$	3.1(1)	8.5(10)	46.7×6.1	0.92	···	···			28.2	142.3	3.2(3)
90,530.9512 (1000)	$23_{3,20} - 23_{2,21}$	1.4(1)	13.2(25)	46.0×6.2	0.32	···	···			129.4	26.0	2.3(22)
106,375.0030 (200)	$15_{3,12} - 15_{2,13}$	2.4(2)	10.9(13)	22.4×5.2	0.43	2.0(2)	7.6(14)	60	0.00	61.7	13.2	1.9(4)
106,562.9160 (320)	$27_{3,24} - 26_{4,23}$	1.3(2)	9.6(14)	19.5×5.6	0.21	< 0.6	···	60		174.1	7.2	1.8(4)
108,210.3860 (170)	$11_{1,11} - 10_{0,10}$	2.7(3)	13.8(35)	25.7×5.2	0.47	< 0.9	···	59		28.6	11.0	2.4(5)
108,227.0930 (200)	$14_{3,11} - 14_{2,12}$	2.6(4)	13.0(26)	25.7×5.2	0.45	< 0.9	···	59		55.2	12.1	1.8(8)
111,943.5641 (3600)	$18_{2,17} - 18_{1,18}$	2.4(2)	6.2(7)	18.8×5.6	0.38	···	···			77.6	9.6	2.3(22)
$\nu_b = 1$												
86,978.8645 (30)	$10_{1,10} - 9_{1,9}A$	1.0(1)	9.5(9)	24.4×6.6	0.52	0.8(1)	10.1(16)	73	0.00	321.0	123.78	···
86,978.8844 (30)	$10_{1,9} - 9_{1,8}E$	1.0(1)	9.5(9)	24.4×6.6	0.52	0.8(1)	10.1(16)	73	0.00	321.0	123.52	···

Table 3.14—Continued

Rest Frequency (MHz)[a]	Transition[b]	BIMA Array I_0 (Jy/bm)	BIMA Array Δv (km/s)	BIMA Array $\theta_a \times \theta_b$ ($''\times''$)	BIMA Array τ	12 meter telescope I_0 (Jy/bm)	12 meter telescope Δv (km/s)	12 meter telescope θ ($''$)	12 meter telescope τ	E_u (K)	$\langle S_{i,j}\mu^2\rangle$ (D^2)	Source Size ($''$)
89,647.8334 (30)	$10_{6,4}-9_{6,3}A$	0.5(1)	12.5[h]	30.8×6.2	0.26	···	···			358.0	94.9	2.5(4)
89,647.8349 (30)	$10_{6,5}-9_{6,4}E$	0.5(1)	12.5[h]	30.8×6.2	0.26	···	···			358.0	94.9	2.5(4)
89,647.8650 (30)	$10_{6,4}-9_{6,3}E$	0.5(1)	12.5[h]	30.8×6.2	0.26	···	···			358.0	94.9	2.5(4)
89,690.1630 (20)	$10_{3,8}-9_{3,7}E$	1.6(1)	12.3(15)	31.2×6.2	0.96	···	···			329.81	134.9	2.0(7)
89,690.2930 (20)	$10_{3,8}-9_{3,7}A$	1.6(1)	12.3(15)	31.2×6.2	0.96	···	···			329.81	134.9	2.0(7)
89,739.3806 (20)	$10_{4,6}-9_{4,5}A$	1.0(1)	22.6(10)	30.9×6.3	0.52	0.7(1)	15.7(11)	71	0.00	337.1	102.07	3.1(4)
89,739.9347 (20)	$10_{4,6}-9_{4,5}E$	1.0(1)	22.6(10)	30.9×6.3	0.52	0.7(1)	15.7(11)	71	0.00	337.1	102.07	3.1(4)
89,740.5796 (20)	$10_{4,7}-9_{4,6}A$	1.0(1)	22.6(10)	30.9×6.3	0.52	0.7(1)	15.7(11)	71	0.00	337.1	102.07	3.1(4)
89,741.1004 (20)	$10_{4,7}-9_{4,6}E$	1.0(1)	22.6(10)	30.9×6.3	0.52	0.7(1)	15.7(11)	71	0.00	337.1	107.07	3.1(4)
90,633.2200 (30)	$10_{3,7}-9_{3,6}E$	0.9(1)	15.0(12)	24.7×6.2	0.44	···	···			324.8	134.9	2.8(4)
90,633.2306 (30)	$10_{2,8}-9_{2,7}A$	0.9(1)	15.0(12)	24.7×6.2	0.44	···	···			324.8	142.3	2.8(4)
$\nu_t=1$												
89,640.9102 (20)	$10_{4,7}-9_{4,6}A$	0.6(2)	12.5[h]	30.8×6.2	0.26	···	···			348.7	124.5	2.5(4)
89,641.2683 (20)	$10_{4,7}-9_{4,6}E$	0.6(2)	12.5[h]	30.8×6.2	0.26	···	···			348.7	124.5	2.5(4)
89,641.5900 (20)	$10_{4,6}-9_{4,5}A$	0.6(2)	12.5[h]	30.8×6.2	0.26	···	···			348.7	124.5	2.5(4)
89,641.7464 (20)	$10_{4,6}-9_{4,5}E$	0.6(2)	12.5[h]	30.8×6.2	0.26	···	···			348.7	124.5	2.5(4)
89,646.6645 (30)	$10_{5,6}-9_{5,5}E$	0.6(2)	12.5[h]	30.8×6.2	0.26	···	···			359.4	111.2	2.5(4)
89,646.8027 (30)	$10_{5,6}-9_{5,5}A$	0.6(2)	12.5[h]	30.8×6.2	0.26	···	···			359.4	111.2	2.5(4)
89,646.8077 (30)	$10_{5,5}-9_{5,4}A$	0.6(2)	12.5[h]	30.8×6.2	0.26	···	···			359.4	111.2	2.5(4)
89,647.2179 (30)	$10_{5,5}-9_{5,4}E$	0.6(2)	12.5[h]	30.8×6.2	0.26	···	···			359.4	111.2	2.5(4)
90,366.4838 (20)	$10_{2,8}-9_{2,7}A$	1.3(1)	8.4(14)	47.5×6.2	0.70	···	···			334.5	119.24	2.5(7)
90,367.0302 (20)	$10_{2,8}-9_{2,7}E$	1.3(1)	8.4(14)	47.5×6.2	0.70	···	···			334.5	119.24	2.5(7)
109,843.6289 (30)	$12_{1,11}-11_{1,10}A$	2.3(5)	10.5(15)	21.6×5.0	0.96	···	···			341.4	176.5	1.7(4)
109,844.7027 (30)	$12_{2,11}-11_{2,10}E$	2.3(5)	10.5(15)	21.6×5.0	0.96	···	···			341.4	172.8	1.7(4)

Table 3.14—Continued

Rest Frequency (MHz)[a]	Transition[b]	BIMA Array I_0 (Jy/bm)	Δv (km/s)	$\theta_a \times \theta_b$ ($'' \times ''$)	τ	12 meter telescope I_0 (Jy/bm)	Δv (km/s)	θ ($''$)	τ	E_u (K)	$\langle S_{i,j}\mu^2 \rangle$ (D^2)	Source Size ($''$)
						C_2H_5OH[i]						
86,132.9200 (60)	$18^+_{4,14} - 18^-_{3,16}$	0.5(1)	10.0(36)	25.5×6.4	0.23	< 0.6	···	74		218.9	6.12	···
86,311.2673 (32)	$5^+_{2,4} - 4^+_{2,3}$	< 0.3	···	24.5×6.9	···	1.8(1)	6.0(5)	74	0.00	73.7	5.03	···
86,555.9124 (28)[d]	$5^+_{4,2} - 4^+_{4,1}$	0.7(2)	4.4(13)	27.6×6.4	0.15	< 0.6	···	73		88.3	4.20	2.1(1)
86,556.0115 (28)[d]	$5^+_{4,1} - 4^+_{4,0}$	···	···	27.6×6.4	0.15	···	···	73		88.3	4.20	2.1(1)
86,604.2917 (28)	$5^+_{3,3} - 4^+_{3,2}$	0.9(1)	4.3(8)	27.6×6.4	0.46	< 0.6	···	73		79.8	4.07	2.2(21)
86,621.7341 (28)	$5^+_{3,2} - 4^+_{3,1}$	0.9(1)	6.4(10)	27.6×6.4	0.46	< 0.6	···	73		79.8	4.07	3.4(32)
86,947.1200 (270)	$15_{2,13} - 15_{1,14}$	0.9(2)	7.2(15)	25.2×6.5	0.45	< 0.6	···	73		108.1	22.56	···
87,029.9919 (30)	$5^+_{2,3} - 4^+_{2,2}$	0.6(1)	4.2(11)	24.6×6.9	0.28	< 0.6	···	73		73.8	5.02	1.0(2)
90,007.6927 (110)	$13^-_{0,13} - 13^+_{1,13}$	0.7(1)	8.8(19)	23.2×6.7	0.31	< 0.7	···	71		135.0	11.11	2.0(3)
90,117.6000 (90)	$4_{1,4} - 3_{0,3}$	0.6(1)	4.7(11)	23.6×6.6	0.26					9.4	5.35	4.5(7)
						9.9(2)	21.5(5)	71	0.01	9.4	5.35	>78
90,354.3735 (80)	$21_{1,20}1 - 21_{2,20}0$	1.1(2)	6.8(13)	47.5×6.2	0.53	···	···	60	0.00	255.4	25.06	2.5(7)
106,649.4400 (310)	$13_{1,12} - 13_{0,13}$	2.7(2)	11.4(16)	20.6×5.2	1.35	2.5(2)	7.8(13)	60	0.00	79.4	10.14	2.2(5)
106,723.4100 (180)	$9_{2,8} - 9_{1,9}$	2.1(2)	9.1(16)	20.6×5.2	0.85	1.7(2)	10.4(17)	59		42.7	7.66	2.1(6)
106,767.1764 (20)	$6^-_{1,5} - 5^-_{1,4}$	1.0(2)	5.2(14)	20.7×5.2	0.32	< 0.6	···	60		80.7	7.91	···
108,438.592 (60)	$13_{3,10} - 13_{2,11}$	2.2(1)	7.8(6)	19.6×5.2	0.88	< 0.6	···	57		88.2	18.19	1.8(10)
110,452.1777 (74)	$21_{3,18} - 21_{2,19}$	2.3(3)	8.5(28)	31.5×4.8	0.87	< 0.6	···			208.7	33.93	3.4(3)
112,129.5204 (30)	$12_{3,9} - 12_{2,10}$	1.9(3)	9.4(30)	18.1×5.4	0.64	···	···			77.1	13.24	2.1(4)
						C_2S						
86,181.4130 (100)	$J_N = 6_7 - 5_6$	< 0.2	···	24.9×6.5	···	2.8(2)	18.7(12)	74	0.00	23.3	49.1	32.3(31)
106,347.7420 (100)	$J_N = 9_8 - 8_7$	< 0.5	···	22.4×5.2	···	7.1(3)	22.4(6)	60	0.01	24.5	75.5	47.1(45)
						CH_3CHO						
112,248.7220 (60)	$6_{1,6} - 5_{1,5}A$	1.9(2)[j]	12.5(16)	18.4×5.3	0.52	···	···			21.1	37.94	1.9(4)

Table 3.14—Continued

Rest Frequency (MHz)[a]	Transition[b]	BIMA Array I_0 (Jy/bm)	BIMA Array Δv (km/s)	BIMA Array $\theta_a \times \theta_b$ ($''\times''$)	BIMA Array τ	12 meter telescope I_0 (Jy/bm)	12 meter telescope Δv (km/s)	12 meter telescope θ ($''$)	12 meter telescope τ	E_u (K)	$\langle S_{i,j}\mu^2\rangle$ (D^2)	Source Size ($''$)
112,254.5120 (60)	$6_{-1,6} - 5_{-1,5}$	1.9(2)	12.5(16)	18.4×5.3	0.52	···	···			21.1	36.88	2.7(6)
					CH_3CN							
110,330.3470 (23)[k]	$J_K = 6_5 - 5_5$	6.1(4)	16.4(3)	20.0×5.0	[l]	3.3(3)	20.9(1)	57	0.01	196.1	28.07	3.9(1)
110,349.4730 (16)	$J_K = 6_4 - 5_4$	12.9(4)	16.4(3)	31.5×4.8	[l]	12.5(2)	20.9(1)	57	0.01	132.2	51.03	3.3(1)
110,364.3570 (11)	$J_K = 6_3 - 5_3$	14.8(4)	16.4(3)	31.5×4.8	[l]	26.8(2)	20.9(1)	57	0.01	82.5	68.90	4.1(4)
110,374.9920 (9)	$J_K = 6_2 - 5_2$	12.7(4)	16.4(3)	31.5×4.8	[l]	27.1(3)	20.9(1)	57	0.01	47.0	81.66	4.6(1)
110,381.3760 (10)	$J_K = 6_1 - 5_1$	8.5(5)	16.4(3)	31.5×4.8	[l]	16.1(8)	20.9(1)	57	0.01	25.7	89.31	4.5(1)
110,383.5040 (10)	$J_K = 6_0 - 5_0$	8.8(4)	16.4(3)	31.5×4.8	[l]	36.5(8)	20.9(1)	57	0.01	18.5	91.87	4.5(1)
					$CH_3^{13}CN$							
110,276.0470 (460)	$J_K = 6_5 - 5_5$	1.2(2)	17.2(4)	20.0×5.0	[l]	0.6(2)	15.4(4)	57	0.00	197.5	28.07	1.9(5)
110,295.0700 (340)	$J_K = 6_4 - 5_4$	3.2(9)	17.2(4)	20.0×5.0	[l]	5.3(2)	15.4(4)	57	0.00	133.1	51.03	2.6(3)
110,309.8670 (290)	$J_K = 6_3 - 5_3$	6.8(4)	17.2(2)	20.0×5.0	[l]	4.5(2)	15.4(4)	57	0.00	83.0	68.90	2.5(2)
110,320.4350 (290)	$J_K = 6_2 - 5_2$	5.4(2)	17.2(4)	20.0×5.0	0.91	4.4(2)	15.4(4)	57	0.00	47.2	81.66	2.7(1)
110,326.7770 (300)[k]	$J_K = 6_1 - 5_1$	1.6(6)	17.2(4)	20.0×5.0	0.33	1.5(4)	15.4(4)	57	0.00	25.7	89.31	3.9(1)
110,328.8900 (310)[k]	$J_K = 6_0 - 5_0$	4.3(11)	17.2(4)	20.0×5.0	0.11	4.9(8)	15.4(4)	57	0.00	18.5	91.87	3.9(1)
					$(CH_3)_2CO$							
90,936.2080 (12)	$7_{3,5} - 6_{2,4}$EE	1.1(3)	12.5(21)	32.3×6.0	0.02	···	···			19.7	34.77	2.0(6)
112,365.9870 (130)	$11_{0,11} - 10_{1,10}$AE	0.8(1)	13.1(17)	20.0×5.1	0.02	···	···			33.5	89.20	2.0(6)
112,366.0320 (110)	$11_{0,11} - 10_{1,10}$EA	0.8(1)	13.1(17)	20.0×5.1	0.02	···	···			33.5	89.20	2.0(6)
112,373.5480 (90)	$11_{0,11} - 10_{1,10}$EE	3.3(4)	13.1(17)	20.0×5.1	0.02	···	···			33.5	89.20	2.0(6)
112,381.0290 (140)	$11_{0,11} - 10_{1,10}$AA	1.6(2)	13.1(17)	20.0×5.1	0.02	···	···			33.5	89.20	2.0(6)
					$(CH_3)_2O$							
85,973.2490 (80)	$13_{2,12} - 12_{3,9}$AA	0.3(1)	5.6(15)	31.9×6.5	0.02	< 0.6	···	74		88.0	2.81	1.9(10)

Table 3.14—Continued

Rest Frequency (MHz)[a]	Transition[b]	BIMA Array I_0 (Jy/bm)	BIMA Array Δv (km/s)	BIMA Array $\theta_a \times \theta_b$ ($'' \times ''$)	BIMA Array τ	12 meter telescope I_0 (Jy/bm)	12 meter telescope Δv (km/s)	12 meter telescope θ ($''$)	12 meter telescope τ	E_u (K)	$\langle S_{i,j}\mu^2 \rangle$ (D^2)	Source Size ($''$)
85,976.1310 (80)	$13_{2,12} - 12_{3,9}$EE	0.8(2)	5.6(15)	31.9×6.5	0.02	< 0.6	···	74		88.0	2.81	2.0(19)
90,889.2530 (50)	$15_{3,12} - 14_{4,11}$AA	0.3(1)	5.1(13)	24.4×6.5	0.01	···	···			122.5	3.61	···
90,892.2540 (40)	$15_{3,12} - 14_{4,11}$EE	0.5(1)	5.1(13)	24.4×6.5	0.01	···	···			122.5	3.61	2.8(27)
90,938.7000 (20)	$6_{0,6} - 5_{1,5}$AE	0.3(0)	7.4(11)	32.3×6.0	0.03	···	···			19.0	5.37	2.3(8)
90,937.5050 (20)	$6_{0,6} - 5_{1,5}$AA	0.5(1)	7.4(11)	32.3×6.0	0.03	···	···			19.0	5.37	2.3(8)
90,938.7010 (20)	$6_{0,6} - 5_{1,5}$EA	0.2(0)	7.4(11)	32.3×6.0	0.03	···	···			19.0	5.37	2.3(8)
90,938.1030 (20)	$6_{0,6} - 5_{1,5}$EE	1.3(1)	7.4(11)	32.3×6.0	0.03	···	···			19.0	5.37	2.3(8)
106,775.6790 (80)	$9_{1,8} - 8_{2,7}$AA	0.9[k]	7.0	32.2×5.0	0.02	1.1(1)	15.7(13)	60	0.00	43.4	3.66	3.6(3)
106,777.3710 (60)	$9_{1,8} - 8_{2,7}$EE	1.4[k]	7.0	32.2×5.0	0.02	1.7(1)	15.7(13)	60	0.00	43.4	3.66	2.5(11)
106,779.0580 (60)	$9_{1,8} - 8_{2,7}$AE	0.5[k]	7.0	32.2×5.0	0.02	0.6(1)	15.7(13)	60	0.00	43.4	3.66	1.7(6)
106,779.0660 (60)	$9_{1,8} - 8_{2,7}$EA	0.4[k]	7.0	32.2×5.0	0.02	0.4(1)	15.7(13)	60	0.00	43.4	3.66	1.7(6)
111,741.5920 (40)	$19_{3,16} - 19_{2,17}$AE	0.6(1)	18.4(26)	24.5×5.1	0.02	···	···			187.4	25.98	1.4(12)
111,742.9840 (30)	$19_{3,16} - 19_{2,17}$EE	1.6(2)	18.4(26)	24.5×5.1	0.02	···	···			187.4	25.98	1.4(12)
111,744.3770 (50)	$19_{3,16} - 19_{2,17}$AA	1.0(1)	18.4(26)	24.5×5.1	0.02	···	···			187.4	25.98	1.4(12)
111,741.5920 (40)	$19_{3,16} - 19_{2,17}$EA	0.4(0)	18.4(26)	24.5×5.1	0.02	···	···			187.4	25.98	1.4(12)
111,782.5960 (30)	$7_{0,7} - 6_{1,6}$AA	1.0(1)	15.8(21)	24.7×5.1	0.02	···	···			25.2	6.8	1.7(6)
111,783.6290 (20)	$7_{0,7} - 6_{1,6}$EA	0.4(0)	15.8(21)	24.7×5.1	0.02	···	···			25.2	6.8	1.7(6)
111,783.6280 (20)	$7_{0,7} - 6_{1,6}$AE	0.6(1)	15.8(21)	24.7×5.1	0.02	···	···			25.2	6.8	1.7(6)
111,783.1120 (20)	$7_{0,7} - 6_{1,6}$EE	1.6(1)	15.8(21)	24.7×5.1	0.02	···	···			25.2	6.8	1.7(6)
111,812.2370 (40)	$18_{3,15} - 18_{2,16}$AE	0.2(0)	16.5(3.4)	24.7×5.1	0.03	···	···			169.7	24.14	2.1(6)
111,812.2380 (40)	$18_{3,15} - 18_{2,16}$EA	0.2(0)	16.5(3.4)	24.7×5.1	0.03	···	···			169.7	24.14	2.1(6)
111,815.3820 (50)	$18_{3,15} - 18_{2,16}$AA	0.2(0)	16.5(3.4)	24.7×5.1	0.03	···	···			169.7	24.14	2.1(6)
111,813.8100 (30)	$18_{3,15} - 18_{2,16}$EE	0.2(0)	16.5(3.4)	24.7×5.1	0.03	···	···			169.7	24.14	2.1(6)
						CH_3OH						
86,615.6020 (140)	$7_{2,6} - 6_{3,3}$A−	6.6(1)	8.3(5)	27.6×6.4	2.64	4.2(2)	10.6(3)	73	0.00	102.7	1.36	2.7(2)
86,902.9470 (140)	$7_{2,5} - 6_{3,4}$A+	4.7(15)	6.7(9)	25.2×6.5	1.50	5.9(1)	7.4(4)	73	0.00	102.7	1.36	3.5(2)
87,241.2660 (530)	$14_{1,13} - 14_{1,14}$A+	[m]	···			···	···			260.1	0.1	3.1(2)

Table 3.14—Continued

Rest Frequency (MHz)[a]	Transition[b]	BIMA Array I_0 (Jy/bm)	BIMA Array Δv (km/s)	BIMA Array $\theta_a \times \theta_b$ ($''\times''$)	BIMA Array τ	12 meter telescope I_0 (Jy/bm)	12 meter telescope Δv (km/s)	12 meter telescope θ ($''$)	12 meter telescope τ	E_u (K)	$\langle S_{i,j}\mu^2\rangle$ (D^2)	Source Size ($''$)
90,812.3870 (2320)	$20_{-3,17}-19_{-2,17}, \nu=1$	1.3(2)	3.5(7)	24.1×6.4	0.22	···	···			558.8	13.20	2.2(21)
108,893.9290 (150)	$0_{0,0}-1_{-1,1}$E	[c]	···			···	···			13.1	0.97	···
				$^{13}CH_3OH$								
90,384.3570 (370)	$13_{1,13}-12_{2,10}$A+	1.6(2)	4.6(8)	47.5×6.2	0.22	···	···			218.7	4.28	3.4(4)
112,143.5460 (210)	$3_{1,3}-4_{0,4}$A+	2.2(7)	2.1(8)	18.1×5.4	0.23	···	···			28.0	3.01	3.3(3)
				CH_2NH								
109,891.9950 (790)	$8_{1,7}-7_{2,6}, F=7-6$	1.3(1)	8.1(22)	21.6×5.0	0.16	···	···			122.6	1.11	3.0(3)
109,893.0690 (820)	$8_{1,7}-7_{2,6}, F=8-7$	1.5(2)	8.1(22)	21.6×5.0	0.19	···	···			122.6	1.26	3.0(3)
109,892.1200 (780)	$8_{1,7}-7_{2,6}, F=9-8$	1.7(2)	8.1(22)	21.6×5.0	0.21	···	···			122.6	1.43	3.0(3)
				^{13}CN								
	N_{J,F_1,F_2}											
108,631.1210 (1000)	$1_{1,0}-0_{0,1}$	0.5(1)	11.2(8)	18.9×3.5		[n]	···	59		5.2	2.10	···
108,636.9230 (1000)	$1_{1,1}-1_{0,1}$	1.4(1)	11.2(8)	18.9×3.5		[n]	···	59		5.2	2.10	···
108,638.2120 (1000)	$1_{1,1}-0_{1,0}$	0.5(1)	11.2(8)	18.9×3.5		[n]	···	59		5.2	2.10	···
108,643.5900 (1000)	$1_{1,2}-0_{1,1}$	0.6(1)	11.2(8)	18.9×3.5		[n]	···	59		5.2	2.10	···
108,645.0640 (2000)	$1_{1,1}-0_{1,1}$	0.4(1)	11.2(8)	18.9×3.5		[n]	···	59		5.2	2.10	···
108,645.0640 (2000)	$1_{1,0}-0_{1,1}$	0.5(1)	11.2(8)	18.9×3.5		[n]	···	59		5.2	2.10	···
108,651.2970 (1000)	$1_{1,2}-0_{0,1}$	2.3(2)	11.2(8)	18.9×3.5		[n]	···	59		5.2	2.10	···
108,657.6460 (1000)	$1_{1,2}-0_{1,2}$	1.8(1)	11.2(8)	18.9×3.5		[n]	···	59		5.2	2.10	···
108,658.9480 (1000)	$1_{1,1}-0_{1,2}$	0.6(1)	11.2(8)	18.9×3.5		[n]	···	59		5.2	2.10	···
108,780.2010 (1000)	$1_{2,3}-0_{1,2}$	[n]	···	20.8×5.2		[n]	···	59		5.2	4.21	···
108,782.3740 (1000)	$1_{2,2}-0_{1,1}$	[n]	···	20.8×5.2		[n]	···	59		5.2	4.21	···
108,786.9820 (1000)	$1_{2,1}-0_{1,0}$	[n]	···	20.8×5.2		[n]	···	59		5.2	4.21	···
108,793.7530 (1000)	$1_{2,1}-0_{1,1}$	[n]	···	20.8×5.2		[n]	···	59		5.3	4.21	···

Table 3.14—Continued

Rest Frequency (MHz)[a]	Transition[b]	BIMA Array I_0 (Jy/bm)	Δv (km/s)	$\theta_a \times \theta_b$ ($'' \times ''$)	τ	12 meter telescope I_0 (Jy/bm)	Δv (km/s)	θ ($''$)	τ	E_u (K)	$\langle S_{i,j}\mu^2 \rangle$ (D^2)	Source Size ($''$)
108,796.4000 (1000)	$1_{2,2} - 0_{1,2}$	[n]	···	20.8×5.2		[n]	···	59		5.3	4.21	···
					^{13}CO							
110,201.3700 (200)	$J = 1 - 0$	[c]	···			[c]	···	57		5.3	0.01	···
					$C^{18}O$							
109,782.1730 (20)	$1 - 0$	2.5(5)	7.4(16)	21.9×5.1	0.31	···	···		0.00	5.3	0.01	3.1(4)
					H39α							
106,737.3630	Recom. Line	< 0.4	···	20.6×5.2		4.0(2)	43.2(54)	60		···	···	2.4(3)
					HC_5N							
106,498.9110 (80)	$J = 40 - 39$	< 0.4	···	19.5×5.6		1.7(1)	34.1(26)	60	0.00	103.6	749.96	1.9(5)
					HC_3N							
90,978.9890 (30)	$10 - 9$	5.8(3)	6.7(3)	32.4×5.9	0.29	···	···			23.9	138.68	4.4(3)
90,987.0050 (580)	$10 - 9\ ^1\nu_5\ \ell = 1e$	1.9(2)	14.0(29)	32.4×5.9	0.09	···	···			977.7	137.29	2.0(7)
91,038.3070 (610)	$10 - 9\ ^1\nu_5\ \ell = 1f$	1.2(1)	14.7(16)	32.4×5.9	0.05	···	···			977.7	137.29	2.3(6)
109,861.9990 (460)	$12 - 11\ ^2\nu^7\ \ell = 0$	2.8(2)	15.6(23)	21.6×5.0	0.09	···	···			671.8	166.42	2.5(2)
109,862.8280 (550)	$12 - 11\ ^2\nu_7\ \ell = 2e$	2.7(2)	15.6(23)	21.6×5.0	0.09	···	···			674.4	161.80	2.5(2)
109,870.1880 (480)	$12 - 11\ ^2\nu_7\ \ell = 2f$	2.7[o]	15.6	21.6×5.0	0.09	···	···			674.4	161.80	2.5(2)
109,990.0000 (2000)	$12 - 11\ ^1\nu_6\ ^1\nu_7\ \ell = 1e-$	1.3(1)	10.0(13)	18.9×5.4	0.04	< 0.6	···	57		1391.0	166.00	1.0(9)
110,050.7650 (184)	$12 - 11\ ^3\nu_7\ \ell = 1e$	3.1(2)	18.2(13)	18.9×5.4	0.10	1.6(3)	8.3(20)	57	0.00	990.7	165.27	2.6(7)
					$H^{13}CCCN$							
106,210.6721 (42)	$12 - 11\ ^1\nu_7\ \ell = 1f$	1.2(2)	6.5(15)	22.7×5.2	0.30	···	···			351.2	165.16	2.2(15)

Table 3.14—Continued

Rest Frequency (MHz)[a]	Transition[b]	BIMA Array I_0 (Jy/bm)	BIMA Array Δv (km/s)	BIMA Array $\theta_a \times \theta_b$ ($'' \times ''$)	BIMA Array τ	12 meter telescope I_0 (Jy/bm)	12 meter telescope Δv (km/s)	12 meter telescope θ ($''$)	12 meter telescope τ	E_u (K)	$\langle S_{i,j}\mu^2 \rangle$ (D^2)	Source Size ($''$)
106,474.1000 (10000)	$12-11\ ^2\nu_7$	1.1(1)	33.0(58)	19.5×5.6	0.18	< 0.6	···	60		673.0	166.00	1.8(4)
$HC^{13}CCN$												
90,593.1598 (210)	$10-9$	1.3(7)	6.7(2)	24.2×6.2	0.30	···	···			23.9	138.68	2.7(5)
108,710.5230 (240)	$12-11$	2.5(3)	6.7(2)	18.9×5.5	0.39	6.9(2)	20.3(9)	59	0.00	33.9	166.42	1.9(11)
$HCC^{13}CN$												
90,601.7932 (122)	$10-9$	1.3(8)	6.7(2)	24.2×6.2	0.30	···	···			23.9	138.68	1.7(14)
108,721.0077 (144)	$12-11$	2.5(3)	6.7(2)	18.9×5.5	0.43	8.1(2)	19.2(7)	59	0.00	33.9	166.42	2.6(4)
$H^{13}CN$ $J=1-0$												
86,338.7670 (600)	$F=1-1$	[c]	···	24.5×6.9		[c]	···	74		4.0	8.91	···
86,340.1840 (600)	$F=2-1$	[c]	···	24.5×6.9		[c]	···	74		4.0	8.91	···
86,342.2740 (600)	$F=0-1$	[c]	···	24.5×6.9		[c]	···	74		4.0	8.91	···
$HC^{15}N$												
86,054.9610 (600)	$J=1-0$	[c]	···	31.9×6.5		[c]	···	74		4.1	8.91	···
HCO $N_{K_a,K_c} = 1_{0,1} - 0_{0,0}, J = \frac{3}{2} - \frac{1}{2}$												
86,670.8200 (800)	$F=2-1$	< 0.3	···	48.1×6.4		2.8(4)	19.7(26)	73	0.00	4.2	1.86	> 31
86,708.3500 (800)	$F=1-0$	< 0.3	···	48.1×6.4		2.1(2)	17.8(28)	74	0.00	4.2	1.86	> 38
$H^{13}CO^+$												
86,754.3290 (780)	$J=1-0$	[c]	···	48.1×6.4		[c]	···	73		4.2	10.89	···

Table 3.14—Continued

Rest Frequency (MHz)[a]	Transition[b]	BIMA Array I_0 (Jy/bm)	Δv (km/s)	$\theta_a \times \theta_b$ ($''\times''$)	τ	12 meter telescope I_0 (Jy/bm)	Δv (km/s)	θ ($''$)	τ	E_u (K)	$\langle S_{i,j}\mu^2\rangle$ (D^2)	Source Size ($''$)
$HC^{17}O^+$												
87,057.5000 (10000)	$J = 1 - 0$	[c]	···	24.6×6.9		[c]	···	73		4.2	10.89	···
$HCOOCH_3$												
85,919.0860 (280)	$7_{6,1} - 6_{6,0}$E	0.7(2)[p]	6.8(12)	31.9×6.5	0.17	< 0.6	···	74		40.4	5.00	···
85,926.5080 (220)	$7_{6,2} - 6_{6,1}$E	0.7(2)[p,q]	6.8(12)	31.9×6.5	0.17	< 0.6	···	74		40.4	5.00	2.9(6)
85,927.2300 (240)	$7_{6,2} - 6_{6,1}$A	0.7(2)[p,q]	6.8(12)	31.9×6.5	0.17	< 0.6	···	74		40.4	5.00	2.9(6)
85,927.2360 (240)	$7_{6,1} - 6_{6,0}$A	0.7(2)[p,q]	6.8(12)	31.9×6.5	0.17	< 0.6	···	74		40.4	5.00	2.9(6)
86,021.0080 (260)	$7_{5,2} - 6_{5,1}$E	1.2(2)	5.6(11)	31.9×6.5	0.30	2.6(4)	3.6(6)	74	0.00	33.1	9.20	1.7(5)
86,027.6740 (220)	$7_{5,3} - 6_{5,2}$E	1.5(2)	7.8(20)	31.9×6.5	0.39	1.2(3)	5.9(10)	74	0.00	33.1	9.20	1.2(11)
86,029.4450 (240)	$7_{5,3} - 6_{5,2}$A	1.2(2)	4.2(14)	31.9×6.5	0.30	1.2(3)	5.9(10)	74	0.00	33.1	9.20	1.7(15)
86,030.2120 (240)	$7_{5,2} - 6_{5,1}$A	1.8(3)	4.4(9)	31.9×6.5	0.50	1.2(4)	5.9(10)	74	0.00	33.1	9.20	1.7(15)
86,210.0790 (240)	$7_{4,4} - 6_{4,3}$A	1.3(1)	8.2(10)	24.9×6.5	0.33	1.7(2)	8.3[h]	74	0.00	27.2	12.70	2.1(8)
86,223.5480 (260)	$7_{4,3} - 6_{4,2}$E	1.5(1)	7.1(16)	24.9×6.5	0.40	1.2(3)	8.3[h]	74	0.00	27.2	12.60	2.6(6)
86,224.1060 (220)	$7_{4,4} - 6_{4,3}$E	1.3(1)	3.7(8)	24.9×6.5	0.33	1.7(2)	8.3[h]	74	0.00	27.2	12.60	2.6(6)
86,250.5760 (240)	$7_{4,3} - 6_{4,2}$A	1.5(1)	7.8(13)	24.9×6.5	0.40	3.1(2)	14.4(10)	74	0.00	27.2	12.70	1.5(11)
86,265.8260 (240)	$7_{3,5} - 6_{3,4}$A	1.7(2)	6.3(12)	24.5×6.9	0.46	2.9(2)	8.4(7)	74	0.00	22.4	15.30	···
86,268.6590 (220)	$7_{3,5} - 6_{3,4}$E	1.3(2)	8.6(20)	24.5×6.9	0.33	2.5(2)	5.2(20)	74	0.00	22.6	15.20	1.9(11)
87,143.1980 (140)	$7_{3,4} - 6_{3,3}$E	1.1(1)	7.7(10)	25.0×6.7	0.27	···	···			22.6	15.20	1.9(2)
87,161.3130 (120)	$7_{3,4} - 6_{3,3}$A	1.7(1)	7.4(6)	24.7×6.8	0.45	···	···			22.6	15.3	1.0(9)
90,145.6340 (240)	$7_{2,5} - 6_{2,4}$E	2.0(1)	9.1(9)	23.6×6.6	0.51	2.3(2)	13.6(14)	71	0.00	19.7	17.30	1.7(16)
90,156.5110 (260)	$7_{2,5} - 6_{2,4}$A	1.9(1)	11.1(8)	26.6×6.2	0.48	3.3(3)	8.2(10)	71	0.00	19.7	17.30	2.8(5)
90,227.5950 (260)[d]	$8_{0,8} - 7_{0,7}$E	4.4(8)	7.7(5)	26.6×6.2	0.58	2.8(15)	14.0(9)	71	0.00	20.1	21.00	1.8(10)
90,229.6470 (280)[d]	$8_{0,8} - 7_{0,7}$A	···	···	26.6×6.2	0.58	3.0(13)	14.0(9)	71	0.00	20.0	21.00	2.5(12)
110,535.1820 (140)[d]	$9_{7,3} - 8_{7,2}$E	5.4(18)	4.8(14)	32.7×4.8	0.27	···	···			59.1	9.60	2.6(6)
110,535.1840 (140)[d]	$9_{7,2} - 8_{7,1}$E	···	···	32.7×4.8	0.27	···	···			59.1	9.60	2.6(6)
110,535.9550 (130)[d]	$9_{7,3} - 8_{7,2}$A	···	···	32.7×4.8	0.27	···	···			59.1	9.60	2.6(6)

Table 3.14—Continued

Rest Frequency (MHz)[a]	Transition[b]	BIMA Array I_0 (Jy/bm)	BIMA Array Δv (km/s)	BIMA Array $\theta_a \times \theta_b$ ($'' \times ''$)	BIMA Array τ	12 meter telescope I_0 (Jy/bm)	12 meter telescope Δv (km/s)	12 meter telescope θ ($''$)	12 meter telescope τ	E_u (K)	$\langle S_{i,j}\mu^2 \rangle$ (D^2)	Source Size ($''$)
						HCOOH						
86,546.1800 (200)	$4_{1,4} - 3_{1,3}$	0.5(1)	9.4(22)[k]	27.6×6.4	0.16	2.4(2)	10.8(22)	73	0.00	13.6	7.26	1.5(10)
89,861.4800 (200)	$4_{2,3} - 3_{2,2}$	0.4(1)	14.1(24)	23.9×6.2	0.12	2.3(4)	8.5(17)[k]	71	0.00	23.5	5.80	2.6(4)
89,948.2100 (200)	$4_{3,2} - 3_{3,1}$	1.3(1)	9.2(28)	23.9×6.2	0.44	1.8(1)	7.2(7)	71	0.00	39.4	3.39	1.9(6)
90,164.6200 (200)	$4_{2,2} - 3_{2,1}$	0.9(1)	13.5(40)	26.6×6.2	0.28	1.9(2)	17.8(21)	71	0.00	23.5	5.80	⋯
						HNC						
90,633.5930 (90)	1-0	[c]	⋯	24.7×6.2		⋯	⋯			4.3	9.3	⋯
						$HN^{13}C$ $J = 1 - 0$						
87,090.7350 (920)	$F = 0 - 1$	[c]	⋯	24.6×6.9		[c]	⋯	73		4.2	7.28	⋯
87,090.8590 (920)	$F = 2 - 1$	[c]	⋯	24.6×6.9		[c]	⋯	73		4.2	7.28	⋯
87,090.9420 (920)	$F = 1 - 1$	[c]	⋯	24.6×6.9		[c]	⋯	73		4.2	7.28	⋯
						HNCO						
109,833.4890 (60)	$5_{3,3} - 4_{3,2}$	2.4(3)	8.8(9)	21.6×5.0	0.97	⋯	⋯			391.6	8.21	1.8(7)
109,833.4890 (60)	$5_{3,2} - 4_{3,1}$	2.4(3)	8.8(9)	21.6×5.0	0.97	⋯	⋯			391.6	8.21	1.8(7)
109,872.3370 (300)	$5_{2,4} - 4_{2,3}$	3.6(1)	26.1(16)	21.6×5.0	2.67	⋯	⋯			186.2	10.78	1.5(6)
109,872.7650 (300)	$5_{2,3} - 4_{2,2}$	3.6(1)	26.1(16)	21.6×5.0	2.67	⋯	⋯			186.2	10.78	1.5(6)
109,905.7530 (100)	$5_{0,5} - 4_{0,4}$	2.9(4)	24.4(74)	21.8×5.0	⋯	151.2(12)	26.5(2)	57	0.04	15.8	12.8	2.3(10)
		1.7(12)	6.3(56)	21.8×5.0	⋯	23.6(22)	6.8(8)	57	0.01			>74
110,298.0980 (80)[k]	$5_{1,4} - 4_{1,3}$	8.5(8)	17.6(14)	20.0×5.0	2.96	8.4(6)	15.0(10)	57	0.00	59.0	12.3	2.3(2)

Table 3.14—Continued

Rest Frequency (MHz)[a]	Transition[b]	BIMA Array I_0 (Jy/bm)	BIMA Array Δv (km/s)	BIMA Array $\theta_a \times \theta_b$ ($'' \times ''$)	BIMA Array τ	12 meter telescope I_0 (Jy/bm)	12 meter telescope Δv (km/s)	12 meter telescope θ ($''$)	12 meter telescope τ	E_u (K)	$\langle S_{i,j}\mu^2 \rangle$ (D^2)	Source Size ($''$)
					NH_2CHO							
	$7_{1,6} - 7_{0,7}$											
86,381.9540 (80)	$F = 7 - 7$	0.7[k]	7.5(20)	24.5×6.9	0.14	0.4[k]	7.2(28)	74	0.00	32.5	1.46	1.6(7)
86,383.2490 (30)[d]	$F = 8 - 8$	1.5(3)	7.5(20)	24.5×6.9	0.18	1.6(3)	7.2(28)	74	0.00	32.5	1.69	1.6(7)
86,383.4350 (50)[d]	$F = 6 - 6$	···	···	24.5×6.9	0.13	···	···	74	0.00	32.5	1.28	1.6(7)
	$25_{3,22} - 25_{3,23}$											
87,293.3010 (10)	$F = 25 - 25$	0.3(1)	7.2(20)	34.1×6.2	0.06	···	···			362.3	2.38	···
87,294.1580 (10)	$F = 26 - 26$	0.3(1)	7.2(20)	34.1×6.2	0.06	···	···			362.3	2.49	···
87,294.1930 (10)	$F = 24 - 24$	0.3(1)	7.2(20)	34.1×6.2	0.05	···	···			362.3	2.30	···
106,541.8110 (800)	$5_{2,3} - 4_{2,2}$	7.8(2)	10.8(4)	19.5×5.6	5.54	10.9(4)	14.3(6)	60	0.00	27.2	54.92	3.0(4)
	$17_{2,15} - 16_{3,14}$											
109,807.9420 (0)	$F = 16 - 15$	0.8(1)	9.7(12)	21.9×5.1	0.10	···	···			170.8	0.77	1.3(10)
109,807.8960 (0)	$F = 18 - 7$	0.9(1)	9.7(12)	21.9×5.1	0.11	···	···			170.8	0.82	1.3(10)
109,807.1390 (10)	$F = 17 - 16$	0.8(1)	9.7(12)	21.9×5.1	0.10	···	···			170.8	0.73	1.3(10)
					NH_2D							
Ortho	$1_{0,1} - 1_{1,1}$											
85,924.7470 (400)	$F = 0 - 1$	0.1(0)[q]	18.0(24)	31.9×6.5	0.02	0.3(0)	26.0(14)	74	0.00	20.7	0.36	2.7(8)
85,925.6840 (400)	$F = 2 - 1$	0.2(0)[q]	18.0(24)	31.9×6.5	0.04	0.4(0)	26.0(14)	74	0.00	20.7	0.45	2.7(8)
85,926.2630 (200)	$F = 0 - 0$	0.0(0)[q]	18.0(24)	31.9×6.5		0.0(0)	26.0(14)	74		20.7	0.00	2.7(8)
85,926.2630 (200)	$F = 1 - 1$	0.5(1)[q]	18.0(24)	31.9×6.5	0.12	1.2(1)	26.0(14)	74	0.00	20.7	1.34	2.7(8)
85,926.2630 (200)	$F = 2 - 2$	0.1(0)[q]	18.0(24)	31.9×6.5	0.02	0.2(0)	26.0(14)	74	0.00	20.7	0.27	2.7(8)
85,926.8580 (400)	$F = 1 - 2$	0.2(0)[q]	18.0(24)	31.9×6.5	0.04	0.4(0)	26.0(14)	74	0.00	20.7	0.45	2.7(8)
85,927.7210 (400)	$F = 1 - 0$	0.1(0)[q]	18.0(24)	31.9×6.5	0.02	0.3(0)	26.0(14)	74	0.00	20.7	0.36	2.7(8)
Para	$1_{0,1} - 1_{1,1}$											
110,152.0840 (400)	$F = 0 - 1$	0.5(2)	4.4(10)	18.9×5.4	0.08	0.7(3)	2.3(6)	57	0.00	21.2	0.36	2.6(4)
110,152.9950 (400)	$F = 2 - 1$	0.6(2)	4.4(10)	18.9×5.4	0.09	0.9(4)	2.3(6)	57	0.00	21.2	0.45	2.6(4)

Table 3.14—Continued

Rest Frequency (MHz)[a]	Transition[b]	BIMA Array I_0 (Jy/bm)	BIMA Array Δv (km/s)	BIMA Array $\theta_a \times \theta_b$ ($''\times''$)	BIMA Array τ	12 meter telescope I_0 (Jy/bm)	12 meter telescope Δv (km/s)	12 meter telescope θ ($''$)	12 meter telescope τ	E_u (K)	$\langle S_{i,j}\mu^2 \rangle$ (D^2)	Source Size ($''$)
110,153.5990 (200)	$F = 0 - 0$	0.0(0)	4.4(10)	18.9×5.4		0.0(0)	2.3(6)	57		21.2	0.00	2.6(4)
110,153.5990 (200)	$F = 1 - 1$	1.8(6)	4.4(10)	18.9×5.4	0.31	2.8(12)	2.3(6)	57	0.00	21.2	1.34	2.6(4)
110,153.5990 (200)	$F = 2 - 2$	0.3(1)	4.4(10)	18.9×5.4	0.05	0.5(2)	2.3(6)	57	0.00	21.2	0.27	2.6(4)
110,154.2220 (400)	$F = 1 - 2$	0.6(2)	4.4(10)	18.9×5.4	0.09	0.9(4)	2.3(6)	57	0.00	21.2	0.45	2.6(4)
110,155.0530 (400)	$F = 1 - 0$	0.5(2)	4.4(10)	18.9×5.4	0.08	0.7(3)	2.3(6)	57	0.00	21.2	0.36	2.6(4)
						$^{15}NNH^+$						
90,263.8330 (600)	$J = 1 - 0$	1.0(1)	6.3(10)	26.6×6.2	0.29	1.9(1)	14.2(14)	71	0.00	4.5	11.56	2.4(3)
						$OC^{34}S$						
106,787.3800 (1600)	$J = 9 - 8$	3.8(5)	10.1(14)	32.2×5.0	0.78	4.8(2)	19.2(9)	60	0.00	26.3	4.60	2.7(3)
						SiO						
86,846.8910 (560)	$J = 2 - 1$	[c]	···	25.2×6.5		[c]	···	73		6.3	19.20	···
						SO						
86,093.9380 (340)	$J_K = 2_2 - 1_1$	4.6(3)	10.2(7)	24.9×6.5	0.43	19.8(1)	20.6(2)	74	0.00	19.3	3.60	4.8(2)
		3.1(3)	34.0(22)	24.9×6.5	0.27							
						^{34}SO						
106,743.2440 (1400)	$J_N = 2_3 - 1_2$	1.2(3)	6.7(16)	20.6×5.2	1.27	2.0(4)	14.3(27)	61	0.00	20.9	3.63	1.3(12)
						SO_2						
86,153.7090 (250)	$39_{9,31} - 40_{8,32}$	0.8(2)	4.0(13)	24.9×6.5	0.70	< 0.6	···	74		916.1	15.91	0.9(8)
86,639.0400 (1000)	$8_{3,5} - 9_{2,8}$	2.0(1)	20.7(19)	48.1×6.4	1.70	1.5(2)	13.0(17)	73	0.00	55.2	3.02	1.9(6)
90,548.1600 (30)	$25_{3,23} - 24_{4,20}$	1.2(2)	10.7(21)	23.5×6.3	1.16	···	···			320.8	8.68	1.0(9)

Table 3.14—Continued

Rest Frequency (MHz)[a]	Transition[b]	BIMA Array I_0 (Jy/bm)	BIMA Array Δv (km/s)	BIMA Array $\theta_a \times \theta_b$ ($'' \times ''$)	BIMA Array τ	12 meter telescope I_0 (Jy/bm)	12 meter telescope Δv (km/s)	12 meter telescope θ ($''$)	12 meter telescope τ	E_u (K)	$\langle S_{i,j}\mu^2 \rangle$ (D^2)	Source Size ($''$)

[a]Frequency uncertainty is 95% (2σ) confidence level.

[b]Transitions are J_{K_a,K_c} unless otherwise noted.

[c]Multiple emission and absorption components detected.

[d]These transitions were blended and were fit with a single Gaussian.

[e]This transition may be blended with the $\sim$72 km s^{-1} $7_{4,3} - 6_{4,2}A$ transition of $HCOOCH_3$.

[f]These transitions are too blended with $HCOOCH_3$ and NH_2D to be fit with Gaussians.

[g]This transition is blended with the $14_{1,13} - 14_{1,14}$ transition of CH_3OH.

[h]Line width was fixed in order to get an adequate intensity fit.

[i]For EtOH a "+"=gauche+ and a "-"=gauche- state.

[j]These transitions were forced to have the same line width and intensity.

[k]Intensity and line width were approximated because the least squares Gaussian fitting did not give a satisfactory fit.

[l]Opacity could not be calculated for this transition.

[m]This transition is blended with the $13_{3,10} - 14_{2,13}$ transition of C_2H_3CN.

[n]A reliable fit could not be found.

[o]Extracted base on other HC_3N transitions.

[p]Due to confusion from transitions from NH_2D the intensity and line width of these transitions were extrapolated from the other detected $HCOOCH_3$ transitions.

[q]The integrated line intensity of this transition may be smaller than the reported value due to blending with transitions of C_2H_3CN.

Table 3.15. Detected Unidentified Lines

Rest Frequency (MHz)	BIMA Array I_0 (Jy/bm)	BIMA Array Δv (km/s)	12 meter telescope I_0 (Jy bm^{-1})	12 meter telescope Δv (km s^{-1})	Source Size ($''$)
85,912.7[a]	0.9[b]	1.7	< 0.6	···	4.4(43)
85,932.7[a]	< 0.3	···	1.2(6)	3.9(28)	2.6(25)
85,939.1	0.7(2)	10.5(54)	< 0.6	···	2.2(14)
85,942.0[a]	< 0.3	···	-4.2(8)	3.1(6)	3.1(4)
85,970.6[a]	0.7(6)	3.3(30)	< 0.6	···	···
85,973.2	0.4[b]	5.7	< 0.6	···	1.9(11)
86,010.0	0.8(4)	5.1(32)	< 0.6	···	1.8(17)
86,024.3[a]	< 0.3	···	4.1(8)	2.7(6)	1.3(5)
86,034.3	0.8(4)	5.1(32)	< 0.6	···	2.0(10)
86,148.0	0.5(4)	5.3(48)	< 0.6	···	3.4(8)
86,151.6	0.6(2)	17.3(140)	< 0.6	···	···
86,204.6	0.9(2)	5.4(20)	< 0.6	···	~0.5
86,226.5	0.7(2)	13.2(74)	< 0.6	···	2.3(2)
86,239.6	< 0.2	···	1.7(4)	8.1(34)	···
86,243.5	< 0.2	···	1.6(4)	10.6(46)	···
86,263.5	< 0.2	···	1.4(4)	10.0(56)	···
86,300.7	0.7(2)	12.5(40)	< 0.6	···	1.4(12)
86,386.3	0.9(4)	4.6(24)	< 0.6	···	1.7(16)
86,398.8	0.8(2)	7.4(26)	< 0.6	···	···
86,421.8	0.6(2)	6.7(32)	< 0.6	···	2.0(10)
86,440.2	0.5(2)	17.8(76)	< 0.6	···	···
86,445.8	0.6(2)	9.9(46)	< 0.6	···	···
86,459.3	0.5(4)	5.2(46)	< 0.6	···	···
86,473.4[c]	0.7(2)	8.9(26)	< 0.6	···	···
86,486.6	0.6[b]	3.2	1.3(2)	24.2(72)	2.7(7)
86,498.2[a]	0.7[b]	1.9	< 0.6	···	1.6(6)
86,536.6	0.6(2)	4.8(28)	< 0.6	···	···
86,812.3	< 0.3	···	1.6(2)	10.7(34)	···
86,831.6	0.8[b]	2.5	1.7[b]	6.0	2.0(5)
86,915.5	0.8(2)	9.5(30)	< 0.6	···	···
86,956.1[a]	0.7(2)	3.6(12)	< 0.6	···	2.8(10)
86,957.8[a]	0.8(2)	2.2(10)	< 0.6	···	2.4(6)
87,008.3	0.5(2)	14.5(40)	< 0.6	···	···
87,016.5	0.5(2)	8.5(28)	< 0.6	···	···
87,112.7	0.3(2)	4.0(29)	···	···	···
87,117.0	0.5(1)	9.6(27)	···	···	···
87,132.3	0.4(1)	26.9(46)	···	···	4.3(2)
87,152.9	0.5(1)	10.0(27)	···	···	···

Table 3.15—Continued

Rest Frequency (MHz)	BIMA Array I_0 (Jy/bm)	BIMA Array Δv (km/s)	12 meter telescope I_0 (Jy bm^{-1})	12 meter telescope Δv (km s^{-1})	Source Size ($''$))
87,158.4	0.7(1)	5.5(11)	···	···	···
87,193.6	0.4(1)	7.3(21)	···	···	···
87,217.4	0.7(2)	7.0(20)	···	···	···
87,387.5	1.2(1)	33.5(28)	···	···	3.4(7)
89,636.1	1.8(3)	6.2(17)	···	···	···
89,661.0	2.9(1)	27.9(17)	···	···	2.2(8)
89,668.1	0.8(2)	8.3(27)	···	···	···
89,679.1	2.3(2)	11.8(19)	···	···	1.6(15)
89,731.9	0.9(4)	7.1(36)	< 0.7	···	2.0(13)
89,754.9	1.6(8)	4.8(26)	1.2(6)	5.3(32)	1.4(13)
89,767.3	1.7(2)	32.6(54)	< 0.7	···	3.2(7)
89,791.5	0.6(2)	18.4(82)	< 0.7	···	···
89,814.7	0.8(2)	11.9(40)	1.1(4)	8.8(32)	~0.8
89,829.6	0.8(4)	5.9(26)	< 0.7	···	···
89,897.3	0.3(2)	15.4(14)	< 0.7	···	···
89,902.3	0.5(4)	5.4(42)	< 0.7	···	···
89,923.8	0.4(2)	9.1(60)	< 0.7	···	···
89,959.4[a]	0.8(4)	3.4(20)	< 0.7	···	1.2(11)
89,993.1	0.8(2)	7.5(26)	< 0.7	···	···
90,037.8[c]	1.7(2)	12.1(40)	2.2(4)	8.2(20)	2.0(5)
90,069.1	0.5(2)	6.3(34)	< 0.7	···	2.8(27)
90,078.3	0.8(2)	18.5(38)	< 0.7	···	···
90,128.5	0.5(2)	4.8(32)	< 0.7	···	···
90,174.5	0.6(2)	11.8(62)	< 0.7	···	1.6(12)
90,179.1	0.7(2)	7.4(36)	< 0.7	···	···
90,203.4[c]	0.7(2)	13.2(36)	< 0.7	···	2.1(20)
90,307.9	0.6(2)	12.0(66)	< 0.7	···	···
90,367.6	2.6(2)	8.4(14)	···	···	2.6(7)
90,517.3	1.0(2)	10.0(18)	···	···	···
90,545.1	1.0(2)	8.1(21)	···	···	~0.7
90,549.1	1.2(2)	10.7(21)	···	···	···
90,739.3	0.9(2)	6.3(16)	···	···	2.4(19)
90,751.2	-0.6[b]	0.1	···	···	···
90,784.0	0.4(1)	13.0(41)	···	···	···
90,809.5	0.8(1)	33.0(41)	···	···	···
90,820.0	0.7(1)	16.1(28)	···	···	···
90,841.7[a]	0.8(2)	3.0(7)	···	···	···
90,854.0	0.5(1)	24.2(36)	···	···	···
90,950.7	0.7(1)	15.3(30)	···	···	···

Table 3.15—Continued

Rest Frequency (MHz)	BIMA Array I_0 (Jy/bm)	BIMA Array Δv (km/s)	12 meter telescope I_0 (Jy bm^{-1})	12 meter telescope Δv (km s^{-1})	Source Size ($''$))
91,015.6	0.9(2)	8.9(25)	···	···	2.3(8)
91,018.6	2.0(3)	5.6(11)	···	···	2.1(9)
91,021.2	0.7(2)	8.8(39)	···	···	···
91,043.7[a]	1.0(4)	1.9(10)	···	···	2.0(12)
91,089.0	0.9(1)	26.9(32)	···	···	2.5(3)
106,257.8	1.5(2)	4.9(9)	···	···	~35.7[gh]
106,295.4	1.0(4)	9.1(56)	< 0.6	···	2.8(3)[d]
106,322.0	1.0(2)	22.9(84)	< 0.6	···	···
106,353.0	0.9(2)	17.3(66)	1.0(4)	4.0(18)	···
106,411.6	1.4(4)	7.3(30)	< 0.6	···	1.0(9)
106,448.9	3.4(4)	7.7(14)	1.8(6)	5.5(20)	···
106,468.5	0.8(6)	10.6(74)	< 0.6	···	2.1(20)
106,487.2	1.1(2)	13.9(46)	< 0.6	···	1.6(8)
106,514.5	1.8(4)	5.9(18)	< 0.6	···	1.5(11)
106,629.9	1.2(4)	6.6(30)	< 0.6	···	1.4(13)
106,654.8	2.8(4)	6.4(14)	1.7(4)	12.2(42)	2.6(3)
106,706.7	1.2(6)	5.4(32)	< 0.6	···	2.0(19)
106,714.3	1.0(6)	4.5(36)	< 0.6	···	2.5(6
106,947.9	1.7(5)	11.0(43)	···	···	~1.1
106,957.1	2.6(7)	5.1(15)	···	···	1.8(7)
108,379.8	1.9(12)	3.5(24)	2.3(6)	6.6(20)	···
108,511.2	1.3(6)	7.4(62)	< 0.9	···	1.3(11)
108,620.7[a]	2.2(8)	1.8(10)	< 0.9	···	1.8(7)
108,809.9	1.7(6)	4.7(18)	···	···	3.4(4)
109,882.1	3.1(3)	8.9(12)	···	···	2.0(3)
					~29.6
109,943.3	2.0(4)	5.0(16)	< 0.6	···	1.0(9)
109,959.6	3.5(4)	10.5(16)	2.1(6)	8.1(44)	···
109,972.0	0.9(6)	4.1(30)	< 0.6	···	···
110,028.6[a]	< 0.5	···	2.4(16)	1.3(10)	1.4(13)
110,036.2	3.5[b]	3.3	1.5(8)	5.9(36)	1.8(10)
110,079.7	0.9(4)	6.7(40)	< 0.6	···	1.8(17)
110,085.6	2.0(4)	13.3(38)	1.9(8)	6.3(26)	···
110,090.2	1.2(6)	4.7(28)	< 0.6	···	···
110,098.0	1.2(4)	10.8(28)	< 0.6	···	1.3(12)
110,104.7	1.7(4)	10.8(38)	< 0.6	···	···
110,143.3	2.5[b]	16.7	< 0.6	···	···
110,150.0	2.2(6)	7.8(26)	< 0.6	···	···

Table 3.15—Continued

Rest Frequency (MHz)	BIMA Array I_0 (Jy/bm)	BIMA Array Δv (km/s)	12 meter telescope I_0 (Jy bm^{-1})	12 meter telescope Δv (km s^{-1})	Source Size ($''$))
110,158.2	< 1.0	···	5.1	31.8	>64.0
110,161.0[a]	< 1.0	···	3.5(14)	2.6(12)	···
110,164.6[a]	< 1.0	···	4.5(12)	3.1(12)	2.2(3)
110,421.4[a]	2.8(18)	2.9(24)	< 0.6	···	2.2(6)
110,446.8	2.6(8)	6.4(26)	< 0.6	···	···
110,447.9	< 0.97	···	2.6(10)	4.9(20)	3.0(3)[d]
111,911.8	2.7(2)	8.9(7)	···	···	···
111,958.1	2.0(3)	4.6(7)	···	···	~0.4
112,011.7	0.8(2)	15.5(50)	···	···	1.4(13)
112,042.7	1.8(5)	3.1(10)	···	···	1.8(6)
112,097.7	2.2(4)	5.0(11)	···	···	2.5(5)[d]
112,103.0	1.7(3)	8.8(20)	···	···	1.5(10)

[a]This feature is a questionable detection because its line width is <4 km s^{-1}; hence it may be due to interference.

[b]Intensity and line width were approximated because the least squares Gaussian fitting did not give a satisfactory fit.

[c]Previously detected U line.

[d]Multiple spatial components seen in u-v data.

Table 3.16. 72 km s^{-1} Sgr B2(N-LMH) Velocity Components

Rest Frequency (MHz)	E_u (K)	V_{LSR} (km/s)	BIMA Array I$_0$ (Jy/bm)	BIMA Array Δv (km/s)	BIMA Array τ	12 meter telescope I$_0$ (Jy/bm)	12 meter telescope Δv (km/s)	12 meter telescope τ	Source Size ($''$)
C_2H_3CN									
$\nu = 0$									
106,641.3940	32.9	72.4(4)	4.3(9)	6.6(12)	0.73	4.0(4)	6.6(7)	0.48	3.0(2)
$^2\nu_{11}$									
85,909.7910	761.1	72.7(7)	0.2[a]	3.4	0.05	< 0.6	···		2.2(9)
85,909.7910	761.1	72.7(7)	0.2[a]	3.4	0.05	< 0.6	···		2.2(9)
85,910.5640	742.2	72.7(7)	0.2[a]	3.4	0.07	< 0.6	···		2.2(9)
85,910.6320	742.2	72.7(7)	0.2[a]	3.4	0.07	< 0.6	···		2.2(9)
C_2H_5CN									
$\nu = 0$									
86,819.8510	24.1	72.9(8)	2.5(2)	10.2(1.4)	0.58	5.3(3)	13.0(19)	0.59	3.3(7)
89,590.0315	41.4	73.4(14)	1.5(1)	21.8(4.5)	0.29	···	···		2.7(3)
89,591.0159	41.4	73.4(14)	1.5(1)	21.8(4.5)	0.29	···	···		2.7(3)
89,628.4468	33.6	73.8(9)	3.2(3)	9.5(1.4)	0.77	···	···		4.0(3)
89,684.7134	33.7	74.0(2)	5.1(6)	6.2(0.6)	1.94	···	···		3.9(3)
90,169.6330	96.4	73.1(6)	1.2(3)	6.8(1.6)	0.22	< 0.7	···		1.7(7)
90,418.9167	53.8	74.3(10)	0.9(2)	6.2(2.4)	0.16	···	···		1.5(14)
90,453.3528	28.2	76.3(16)	0.7(5)	8.2(4.9)	0.12	···	···		4.3(7)
90,530.9512	129.4	74.0(8)	1.2(2)	7.5(1.7)	0.22	···	···		2.7(10)
106,375.0030	61.7	73.9(1)	1.9(3)	3.9(1.6)	0.27	< 0.6	···		1.3(10)
106,562.9160	174.1	72.8(8)	0.9(2)	5.8(1.9)	0.12	< 0.6	···		2.8(7)
108,210.3860	28.6	72.5(7)	1.8(8)	4.3(2.3)	0.24	< 0.9	···		1.6(6)
108,227.0930	55.2	73.4(6)	2.1(7)	3.9(1.6)	0.28	< 0.9	···		1.6(8)
111,943.5641	77.6	73.7(3)	1.9(2)	5.2(0.8)	0.24	···	···		1.6(9)
$\nu_b = 1$									
86,978.8645	321.0	73.9(6)	0.7(1)	4.4(8)	0.27	0.8(2)	3.9(10)	0.09	···
86,978.8844	321.0	73.9(6)	0.7(1)	4.4(8)	0.27	0.8(2)	3.9(10)	0.09	···
89,647.8334	358.0	76.1(21)	0.4(1)	15.1(39)	0.14	···	···		···
89,647.8349	358.0	76.1(21)	0.4(1)	15.1(39)	0.14	···	···		···
89,647.8650	358.0	76.1(21)	0.4(1)	15.1(39)	0.14	···	···		···
90,633.2200	324.8	75.5(0.4)	0.5(1)	4.8(11)	0.18	···	···		2.5(5)
90,633.2306	324.8	75.5(0.4)	0.5(1)	4.8(11)	0.18	···	···		2.5(5)

Table 3.16—Continued

Rest Frequency (MHz)	E_u (K)	V_{LSR} (km/s)	BIMA Array I$_0$ (Jy/bm)	BIMA Array Δv (km/s)	BIMA Array τ	12 meter telescope I$_0$ (Jy/bm)	12 meter telescope Δv (km/s)	12 meter telescope τ	Source Size ($''$)
$\nu_t = 1$									
89,640.9102	348.7	76.1(21)	0.5(1)	15.1(39)	0.18	···	···		···
89,641.2683	348.7	76.1(21)	0.5(1)	15.1(39)	0.18	···	···		···
89,641.5900	348.7	76.1(21)	0.5(1)	15.1(39)	0.18	···	···		···
89,641.7464	348.7	76.1(21)	0.5(1)	15.1(39)	0.18	···	···		···
89,646.6645	359.4	76.1(21)	0.5(1)	15.1(39)	0.18	···	···		···
89,646.8027	359.4	76.1(21)	0.5(1)	15.1(39)	0.18	···	···		···
89,646.8077	359.4	76.1(21)	0.5(1)	15.1(39)	0.18	···	···		···
89,647.2179	359.4	76.1(21)	0.5(1)	15.1(39)	0.18	···	···		···
109,843.6289	341.4	74.3(10)	0.9(4)	6.7(20)	0.25	···	···		2.0(10)
109,844.7027	341.4	74.3(10)	0.9(4)	6.7(20)	0.25	···	···		2.0(10)
C_2H_5OH									
86,947.1200	108.1	73.0(4)	1.0(2)	3.7(10)	0.13	< 0.6	···		···
87,029.9919	73.8	72.9(5)	0.7(1)	6.7(12)	0.09	< 0.6	···		11.8(110)
90,007.6927	135.0	73.6(7)	0.6(1)	5.5(15)	0.07	< 0.7	···		···
90,354.3735	255.4	75.5(10)	0.8(2)	6.5(18)	0.09	···	···		···
106,767.1764	80.7	74.9(3)	1.3(4)	2.2(8)	0.12	< 0.6	···		2.3(3)
108,438.5492	88.2	74.2(2)	1.6(2)	5.0(6)	0.14	< 0.6	···		4.0(5)
110,452.1777	208.7	73.7	2.9(7)	4.8(13)	0.25	< 0.6	···		4.3(2)
112,129.5204	77.1	72.8(22)	1.1(3)	8.6(47)	0.09	···	···		2.7(5)
CH_3OH									
86,615.6020	102.7	72.8(6)	1.9(1)	7.8(11)	0.22	2.5(1)	3.0(2)	0.18	1.5(14)
86,902.9470	102.7	72.1(5)	2.1(1)	8.0(9)	0.24	2.9(1)	5.5(4)	0.20	4.0(6)
$^{13}CH_3OH$									
90,384.3570	218.7	73.1(6)	1.0(2)	6.5(15)	0.31	···	···		2.3(9)
CH_2NH									
109,891.9950	122.6	72.2(15)	0.7(2)	7.2(16)	0.04	···	···		4.4(2)
109,892.1200	122.6	72.2(15)	0.9(2)	7.2(16)	0.05	···	···		4.4(2)
109,893.0690	122.6	72.2(15)	0.8(2)	7.2(16)	0.04	···	···		4.4(2)
$C^{18}O$									
109,782.1730	5.3	75.3(10)	4.0(2)	22.5(25)	0.35	···	···		3.8(7)

Table 3.16—Continued

Rest Frequency (MHz)	E_u (K)	V_{LSR} (km/s)	BIMA Array I$_0$ (Jy/bm)	BIMA Array Δv (km/s)	BIMA Array τ	12 meter telescope I$_0$ (Jy/bm)	12 meter telescope Δv (km/s)	12 meter telescope τ	Source Size ($''$)
				HC_3N					
90,978.9890	23.9	75.0(15)	1.5(2)	20.8(39)	0.32	···	···		2.8(6)
109,861.9990	671.8	74.6(6)	1.1(4)	5.2(22)	0.28	···	···		···
109,862.8280	674.4	74.6(6)	1.0(4)	5.2(22)	0.25	···	···		···
109,870.1880	674.4	74.6(6)	1.0(4)	5.2(22)	0.27	···	···		···
				$HC^{13}CCN$					
90,593.1598	23.9	73.7(7)	1.8(11)	9.4(10)	1.57	···	···		1.8(8)
108,710.1598	33.9	[b]	3.5(5)	9.4(10)[c]	···	[d]	···		···
				$HCC^{13}CN$					
90,601.7923	23.9	73.7(7)	1.8(12)	9.4(10)	0.41	···	···		2.8(6)
108,721.0077	33.9	[b]	3.8(6)	9.4(10)[c]	0.68	[d]	···		···
				$HCOOCH_3$					
86,210.0790	27.2	71.9	0.9(1)	7.4(14)	0.26	< 0.6	···		3.3(5)
86,223.5480	27.2	74.1(5)	0.5(1)	4.7(12)	0.12	1.1(1)	14.9(20)	0.00	···
86,224.1060	27.2	74.1(5)	0.5(1)	4.7(12)	0.12	1.1(1)	14.9(20)	0.00	···
87,161.3130	22.6	74.0(5)	0.7(1)	5.5(11)	0.19	···	···		···
90,145.6340	19.7	73.1(5)	0.8(2)	4.1(13)	0.21	[d]	···		1.0(9)
90,156.5110	19.7	73.0(4)	[d]	···		2.3(3)	5.3(11)	0.00	2.1(5)
90,227.5950	20.1	74.3	1.3(2)	1.6(3)	0.36	2.2(4)	2.2(5)	0.00	2.0(19)
				HCOOH					
86,546.1800	13.6	72.6(8)	< 0.2	···		2.4(3)	8.5(15)	0.00	4.1(4)
				NH_2CHO					
106,541.8110	27.2	74.1(3)	1.7(2)	6.5(14)	0.51	3.6(5)	8.1(10)	0.00	2.1(3)

[a] The line intensity and width are approximate due to poor Gaussian fitting.

[b] Unable to obtain reliable fit on velocity, thus the value is assumed to be the same as the previous transition.

[c] Unable to obtain reliable fit on line width, thus the value is assumed to be the same as the previous transition.

[d] Unable to obtain a reliable Gaussian fit.

Table 3.17. 52 km s^{-1} Sgr B2(N-LMH) Velocity Components

Rest Frequency (MHz)	E_u (K)	V_{LSR} (km/s)	BIMA Array I$_0$ (Jy/bm)	BIMA Array Δv (km/s)	BIMA Array τ	12 meter telescope I$_0$ (Jy/bm)	12 meter telescope Δv (km/s)	12 meter telescope τ	Source Size ($''$)
C_2H_5CN (EtCN)									
$\nu = 0$									
86,819.8510	24.1	53.5(1.5)	1.5(0.1)	11.8(2.6)	0.24	2.9(7)	15.8(58)	0.00	2.2(6)
89,590.0315	41.4	50.8(1.2)	1.4(0.2)	16.4(1.8)	0.20	···	···		2.6(3)
89,591.0159	41.4	50.8(1.2)	1.4(0.2)	16.4(1.8)	0.20	···	···		2.6(3)
89,628.4468	33.6	49.3(0.6)	2.6(0.2)	10.0(2.5)	0.55	···	···		3.2(5)
$\nu_b = 1$									
89,647.8334	358.0	50.6(29)	0.1[a]	7.9	0.04	···	···		···
89,647.8349	358.0	50.6(29)	0.1[a]	7.9	0.04	···	···		···
89,647.8650	358.0	50.6(29)	0.1[a]	7.9	0.04	···	···		···
$\nu_t = 1$									
89,640.9102	348.7	50.6(29)	0.1[a]	7.9	0.04	···	···		···
89,641.2683	348.7	50.6(29)	0.1[a]	7.9	0.04	···	···		···
89,641.5900	348.7	50.6(29)	0.1[a]	7.9	0.04	···	···		···
89,641.7464	348.7	50.6(29)	0.1[a]	7.9	0.04	···	···		···
89,646.6645	359.4	50.6(29)	0.1[a]	7.9	0.04	···	···		···
89,646.8027	359.4	50.6(29)	0.1[a]	7.9	0.04	···	···		···
89,646.8077	359.4	50.6(29)	0.1[a]	7.9	0.04	···	···		···
89,647.2179	359.4	50.6(29)	0.1[a]	7.9	0.04	···	···		···
CH_3OH									
86,615.6020	102.7	59.6(2)	1.1(2)	2.3(7)	0.27	1.7(4)	2.7(3)	0.00	2.7(2)
86,902.9470	102.7	57.5(67)	0.9(6)	10.9(77)	0.13	0.5(2)	4.6(17)	0.00	3.5(2)
$HC^{13}CCN$									
90,953.1598	23.9	57.9(50)	1.3(8)	18.3(69)	0.62	···	···		2.0(5)
108,710.1598	33.9	57.9(50)	2.3(1)	18.3(69)	0.85	[b]	···		2.0(5)
$HCC^{13}CN$									
90,601.7923	23.9	57.9(50)	1.3(8)	18.3(69)	0.62	···	···		2.0(5)
108,721.0077	33.9	57.9(50)	2.5(1)	18.3(69)	0.98	[b]	···		2.0(5)

[a]Intensity and line width are approximate due to poor Gaussian line fit.

[b]The velocity wings of these transitions were too blended with the main line to obtain a reliable Gaussian fit.

Table 3.18. Unidentified Lines with 72 km s^{-1} Velocity Components

Rest Frequency (MHz)	V_{LSR} (km/s)	BIMA Array I$_0$ (Jy/bm)	BIMA Array Δv (km/s)	12 meter telescope I$_0$ (Jy/bm)	12 meter telescope Δv (km/s)	Source Size ($''$)
86,300.7	76.2(7)	0.4(2)	5.0(38)	< 0.6	···	···
86,398.8[a]	74.1(7)	0.9(2)	5.2(18)	1.9(6)	3.3(14)	···
86,440.2[b]	76.8(7)	0.6(4)	1.9(12)	< 0.6	···	···
89,993.1	75.3(6)	0.8(2)	10.3(36)	< 0.7	···	3.1(8)
90,037.8	77.0(6)	1.0(2)	11.6(50)	< 0.7	···	1.5(6)
90,307.9	74.3(6)	0.6(4)	4.1(34)	< 0.7	···	2.3(18)
90,367.6	74.2(11)	1.4(2)	8.8(22)	···	···	2.9(17)
106,257.8	73.9(6)	1.0(2)	4.9(13)	···	···	2.1(2)[c]
106,487.2[b]	70.8(5)	1.5(8)	1.9(10)	< 0.6	···	···
106,514.5	74.7(5)	1.5(4)	5.7(22)	< 0.6	···	···
108,511.2	73.7(5)	1.3(4)	9.1(68)	< 0.9	···	1.0(11)
110,421.4	72.1(5)	2.9(10)	9.4(46)	< 0.6	···	···
111,958.1	74.5(6)	1.4(2)	7.9(14)	···	···	2.0(4)

[a]Previously detected U line.

[b]This feature is a questionable detection because its line width is <4 km s^{-1}; hence it may be due to interference.

[c]Multiple spatial components seen in *u*-*v* data.

Chapter 4

Orion-KL Line Survey

4.1 Introduction

Orion-KL (Kleinmann & Low, 1967) is the closest massive star forming region to the Sun at a distance of ∼480 pc (Genzel et al., 1981). It has long been the target of searches for complex molecular species (e.g., Liu et al., 2001, 2002; Remijan et al., 2003), maser studies (e.g., Doeleman et al., 1999; Horiuchi & Kameya, 2000), polarization studies (e.g., Rao et al., 1998), mapping projects (e.g., Welch et al., 1981; Wright et al., 1996), and spectral line surveys (e.g., Johansson et al., 1984; Sutton et al., 1985; Turner, 1989, 1991; Blake et al., 1996; Schilke et al., 2001). Of these numerous spectral line surveys only two, Turner (1989, 1991) and Johansson et al. (1984), were in the 3mm region (70-115 GHz and 70-91 GHz respectively), and both were done with single element telescopes. Interferometric observations of the region have shown that most of the detected molecular lines have come from either the Hot Core (Blake et al., 1996) (α(J2000)=05^{h}35^{m}14^s.5, δ(J2000)=$-5°22'30''$) or the Compact Ridge (Liu et al., 2001, 2002)(α(J2000)=05^{h}35^{m}14^s.2, δ(J2000)=$-5°22'41''$) which are separated in projection by only ∼5800 AU. Large oxygen bearing species (such as methyl formate ($HCOOCH_3$), dimethyl ether ($(CH_3)_2O$), and formic acid ($HCOOH$)) are observed primarily toward the compact ridge (e.g. Liu et al., 2002), while large nitrogen bearing species (such as vinyl cyanide (C_2H_3CN) and ethyl cyanide (C_2H_5CN)) are located toward the hot core (e.g. Blake et al., 1987). There are two other notable sources in the region (Blake et al., 1987), the extended ridge, whose angular extent is unknown and is most likely resolved out by the BIMA Array, and the plateau whose angular extent is ∼20″. Each of these four regions is characterized by slightly different linewidths, rest velocities and excitation temperatures. Table 4.1 lists the parameters of the sources in Orion-KL. The first column lists the source, the second column lists the v_{LSR} of the source, the third column lists the typical linewidth, and the fourth column lists the approximate source size (from Blake et al. (1987)).

The hot core is thought to be a dense cloud close (within 2-3″) to the main heating (infrared) source of the region (Blake et al., 1987; Liu et al., 2002, and references therein). Thus the species seen toward the hot core most likely come from a hot, dense environment. Contrasting this, the compact ridge is thought to be the interaction of an outflow with the ambient molecular material,

Table 4.1. Orion-KL Source Parameters[a]

Source	v_{LSR} (km s^{-1})	Δv (km s^{-1})	Size ($''$)
Hot Core	3-5	5-10	$\leq$10
Compact Ridge	7-8	3-5	$\leq$30[b]
Extended Ridge	9	4	$\leq$20
Plateau	7-8	$\geq$20	unknown

[a]Taken from Blake et al. (1987).

[b]Many molecules have been seen to emit from a region $\sim 8'' \times 15''$ in size (e.g., Liu et al., 2002).

and the species seen toward this source are thought to be released off of grain surfaces or form in or behind the shock front (Blake et al., 1987).

This chapter presents the spectra and initial results of the BIMA Array spectral line survey of the Orion-KL region from 80-115.9 GHz. The single-element 12 meter data are presented in Turner (1989, 1991).

4.2 Observations

The observations with the BIMA Array were carried out in C configuration (minimum baseline of 8 meters and maximum baseline of 61 meters) from 2002 October to 2003 November. The array was operating in cross-correlation (double-sideband) mode with a sideband rejection of better than 20 dB. The correlator was configured to have four 50 MHz wide windows in each sideband with 128 channels per window. This resulted in a channel spacing of 391 kHz ($\sim 1.4 - 1.1$ km s^{-1}) for all observations. Saturn was used as the flux density calibrator, and 0423-013 and 0609-157 were used to calibrate the antenna based gains. The absolute amplitude calibration of 0423-013 and 0609-157 from the flux density calibrators is accurate to within ~20%. The passbands were automatically calibrated during data acquisition. The data were calibrated, continuum subtracted,[1] and imaged using the MIRIAD software package.

4.3 Data

A total of 975 spectral lines (620 identified and 355 unidentified) were detected toward the hot core, and 790 spectral lines (518 identified 272 unidentified) were detected toward the compact

[1]The continuum was subtracted from each window separately and variations within the calibration uncertainties of 20% were seen from window to window across the band.

ridge. Figures 4.23(a-dp)[2] show the spectra from this survey. The upper panels show the hot core spectra while the lower panels show the compact ridge spectra. The ordinate gives the intensity in Jy beam^{-1}, and the abscissa gives the frequency in GHz. A v_{LSR} of 8 km s^{-1} was used to derive the frequency axis for the compact ridge spectra, and a v_{LSR} of 5 km s^{-1} was used to derive the frequency axis for the hot core spectra (Blake et al., 1987). The dashed lines denote window edges, and the "I" bars give the 1 σ rms noise level for each window. Spectral lines are labeled either with their identification or with U (unidentified) and the frequency. Spectral lines that are unlabeled originate from the other component (and are identified there) and appear in both spectra because of the size and shape of the synthesized beam.

Table 4.2 gives a summary of all the molecular species detected in this survey. The first column gives the molecular species, and the second and third columns list the number of lines detected for each species toward the hot core and compact ridge, respectively. All molecular parameters are from Pickett et al. (1998), Müller et al. (2001), and/or Francis Lovas, private communication, 2003. Tables 4.5[2] and 4.6[2] give the results for individual species for the hot core and compact ridge respectively. The first column lists the frequency in MHz; the second column lists the quantum numbers. The third and fourth columns list the intensity in Jy beam^{-1} and linewidth in km s^{-1}. The fifth column lists the synthesized beam size, and the sixth and seventh columns list the upper energy, in K, and $S\mu^2$, in D^2, of the transition. Table 4.7[2] lists the unidentified lines from both the hot core and compact ridge. The first and fourth columns give the frequencies of the U lines in MHz for the hot core and compact ridge, respectively. The second and fifth columns give the intensity of the lines for each source, and the third and sixth columns give the linewidth for the lines for each source.

A strict 3 σ minimum for the intensity was imposed on all line identifications. In general, weak spectral features that were not at least two channels wide were not assumed to be real toward the hot core. However, since the average linewidths of several species (e.g., $(CH_3)_2O$ and $HCOOCH_3$) toward the compact ridge are less than two channels, weak, single channel lines from this source were assumed to be real. Section 4.4.16 discusses the statistics of these weak lines. All intensities and linewidths are from Gaussian fits to the line profiles, and all uncertainties in the tables are 1 σ unless otherwise noted.

[2]Due to the size of the spectra and tables they appear at the back of this chapter.

Table 4.2. Summary of Molecules Detected Toward Orion-KL

Species	Hot Core	Compact Ridge
C_2H	4	4
C_2H_3CHO	1	0
C_2H_3CN	86	0
C_2H_5CN	220	0
C_2H_5OH	11	21
CH_3CCH	2	4
CH_3CHO	0	13
CH_3CN	30	11
$^{13}CH_3CN$	7	7
$CH_3^{13}CN$	9	5
$(CH_3)_2CO$	54	0
$(CH_3)_2O$	0	120
CH_3OH	40	60
$^{13}CH_3OH$	7	14
$(CH_2)_2O$	0	4
CN	7	0
CO	1	1
$C^{18}O$	1	1
^{13}CO	1	1
CS	1	1
^{13}CS	1	1
$C^{33}S$	1	1
$C^{34}S$	1	1
HC_3N	32	10
$H^{13}CCCN$	1	0
$HC^{13}CCN$	3	0
$HCC^{13}CN$	4	0
HCN	1	1
$H^{13}CN$	1	1
$HC^{15}N$	1	1
HCO^+	1	1
$H^{13}CO^+$	1	1
$HCOOCH_3$	0	177
HCOOH	1	5
HCS^+	0	1
HDO	1	1
H_2CS	0	5
H_2C_3S	2	0
H_2CO	1	0
HNC	1	1
HNCO	14	12
NH_2CHO	7	0

Table 4.2—Continued

Species	Hot Core	Compact Ridge
NH_2D	3	2
NNH^+	0	1
$^{15}N^{15}NH^+$	0	1
OCS	3	3
$O^{13}CS$	2	0
$OC^{33}S$	1	0
$OC^{34}S$	3	3
SO	4	4
^{33}SO	1	1
^{34}SO	4	3
SO_2	26	7
$^{34}SO_2$	7	2
$SO^{17}O$	3	0
SiO	2	2
^{30}SiO	1	1
^{29}SiO	1	1
^{28}SiO	1	1
SiS	2	0

4.4 Initial Results

This section gives the results of the initial analysis of the data. Note that source size corrections, opacity corrections, and vibrational partition functions have not been applied to the data at this stage. Large N bearing species (e.g., C_2H_3CN) were detected only toward the hot core region while simple N bearing species, CH_3CN, and HC_3N were detected toward both the hot core and compact ridge. The most complex O bearing species were detected only toward the compact ridge, while simple O bearing species and and alcohols were detected toward both sources and, surprisingly, $(CH_3)_2CO$ was detected only toward the hot core. Additionally the simple species (both N and O bearing) and C_2H_3CN, HC_3N, and C_2H_5CN also appear to have components associated with the plateau region (this assignment is due to components with large linewidths).

4.4.1 C_2H_3CN (Vinyl Cyanide)

A total of 86 transitions (9% of all hot core transitions) of C_2H_3CN were detected in this survey toward the hot core, of which 23 are from vibrationally excited states. Many of these transitions show two linewidth components, one narrow and the other wide, indicating that C_2H_3CN is present in both the hot core and plateau regions. Figure 4.1 shows the rotation temperature diagram for the narrow components giving a total column density of $4.8(3)\times10^{16}$ cm^{-2} and a rotation temperature of 469(62) K. Figure 4.2[3] shows the rotation temperature diagram for the large linewidth component giving a total column density of 1.0(1)$\times 10^{16}$ cm^{-2} and a rotation temperature of 226(91) K. A lower rotation temperature is possible since the fit relies on only two points above 60 K.

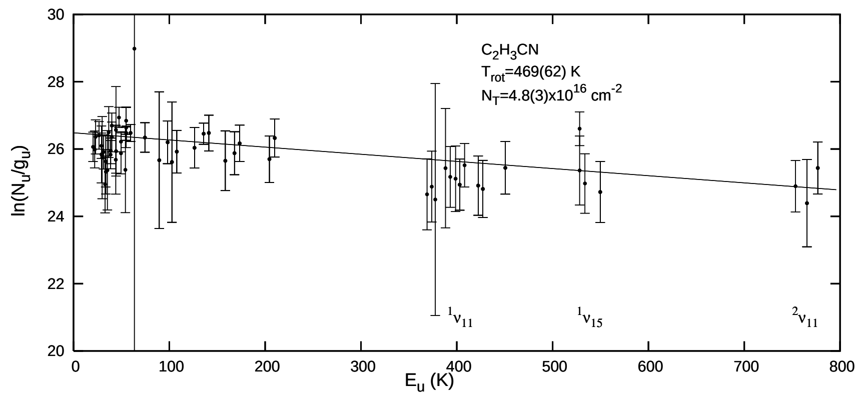

Figure 4.1 Rotation temperature diagram of C_2H_3CN from the hot core. The abscissa is the upper state energy of the transition in K, and the ordinate is the log of the normalized column density. The line is the weighted least squares fit to the data.

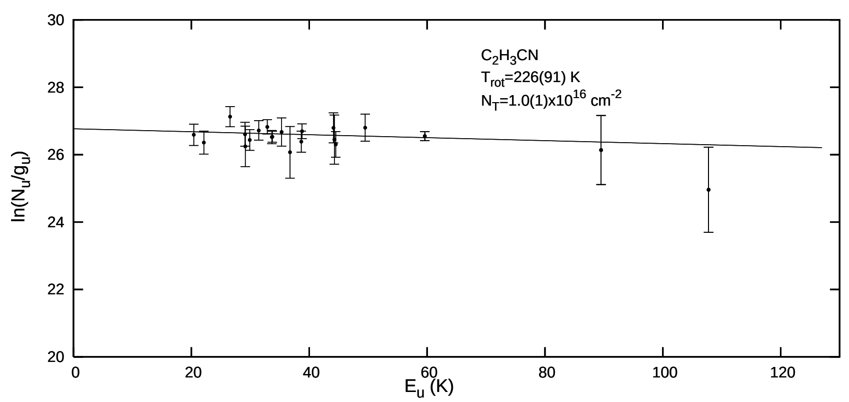

Figure 4.2 Rotation temperature diagram of large linewidth C_2H_3CN components from the hot core. The abscissa is the upper state energy of the transition in K, and the ordinate is the log of the normalized column density. The line is the weighted least squares fit to the data.

4.4.2 C_2H_5CN (Ethyl Cyanide)

C_2H_5CN has 220 detected lines, the largest of any species in this survey. This represents 23% of all hot core lines and 98 these lines are from vibrationally excited states. C_2H_5CN, like C_2H_3CN, has two linewidth components for many of its transitions, indicating sources in both the hot core and plateau regions. Figure 4.3 shows the rotation temperature diagram for the narrow components, and gives a total column density of 7.5(2)$\times 10^{16}$ cm^{-2} and a rotation temperature of 314(7) K. Figure 4.4 shows the rotation temperature diagram for the large linewidth component, and gives a total column density of 3.5(1)$\times 10^{16}$ cm^{-2} and a rotation temperature of 118(2) K.

[3]All error bars in the diagrams are 2 σ, unless otherwise noted.

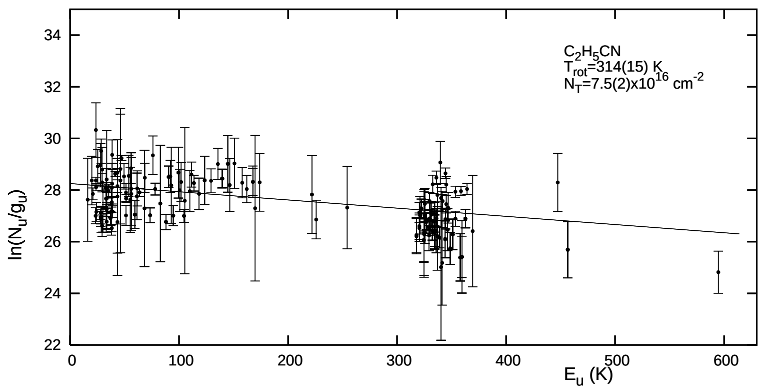

Figure 4.3 Rotation temperature diagram of C_2H_5CN from the hot core. The abscissa is the upper state energy of the transition in K, and the ordinate is the log of the normalized column density. The line is the weighted least squares fit to the data.

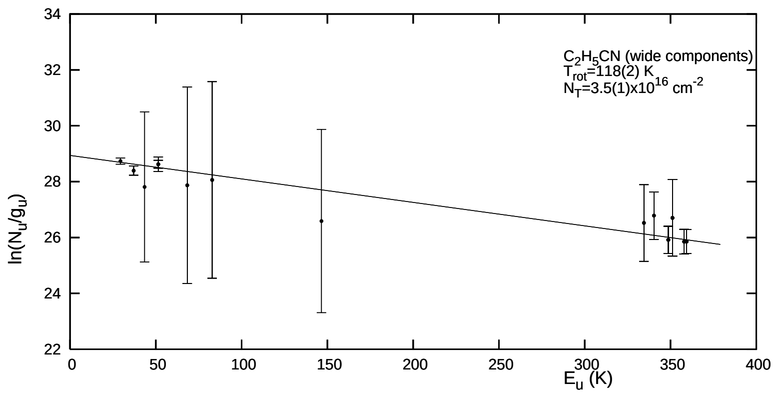

Figure 4.4 Rotation temperature diagram of large linewidth C_2H_5CN components from the hot core. The abscissa is the upper state energy of the transition in K, and the ordinate is the log of the normalized column density. The line is the weighted least squares fit to the data.

4.4.3 C_2H_5OH (Ethanol)

Hot Core

Since C_2H_5OH is a large O bearing species, it is surprising that a significant number of C_2H_5OH transitions were detected toward the hot core. This may indicate that alcohols (C_2H_5OH and CH_3OH, which is also seen toward both components) have similar formation mechanisms that are different from other large O bearing species. From the rotation temperature diagram shown in Figure 4.5 a total column density of $1.1(2)\times10^{16}$ cm^{-2} with a rotation temperature of 305(47) K are found. The diagram does show indications of the need for a two temperature fit, one for the low temperature transitions and one for the higher temperature transitions, as has been utilized in the past for other sources (e.g., Nummelin et al., 2000).

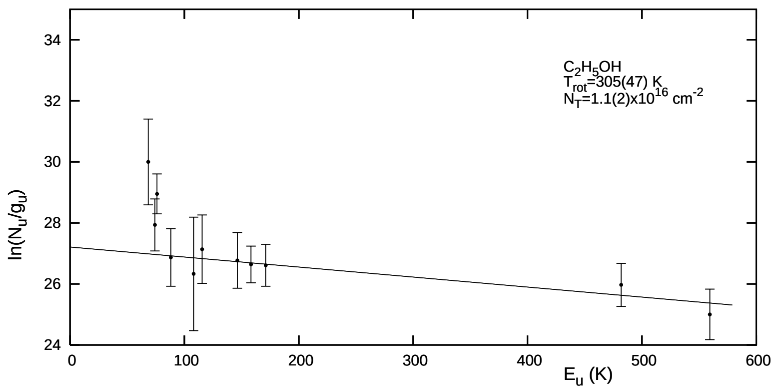

Figure 4.5 Rotation temperature diagram of C_2H_5OH from the hot core. The abscissa is the upper state energy of the transition in K, and the ordinate is the log of the normalized column density. The line is the weighted least squares fit to the data.

Compact Ridge

Nearly twice as many C_2H_5OH transitions were detected toward the compact ridge compared to the hot core. From the rotation temperature diagram shown in Figure 4.6 a total column density and rotation temperature of $2.0(3)\times10^{16}$ cm^{-2} and 81(7) K are found.

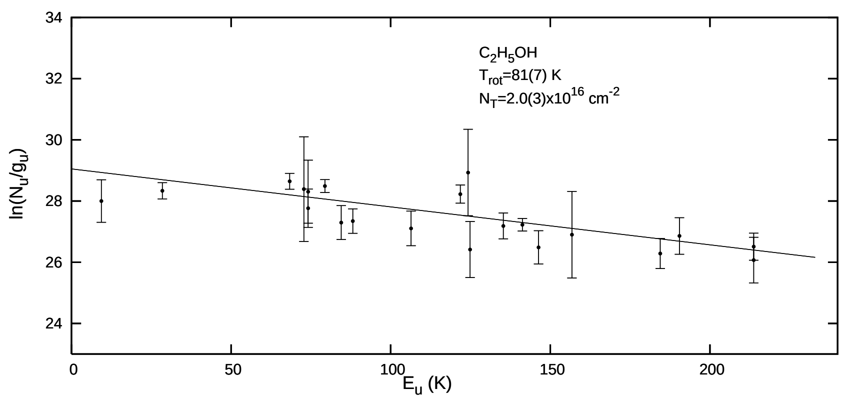

Figure 4.6 Rotation temperature diagram of C_2H_5OH from the compact ridge. The abscissa is the upper state energy of the transition in K, and the ordinate is the log of the normalized column density. The line is the weighted least squares fit to the data.

4.4.4 CH_3CHO (Acetaldehyde)

All detected CH_3CHO transitions were seen toward the compact ridge, and from the rotation temperature diagram shown in Figure 4.7 a total column density of $6.8(15)\times10^{15}$ cm^{-2} and a rotation temperature of ~332 K are found. However the fit to the points relies heavily on a single transition above 200 K which may not be from CH_3CHO since no other transitions above ~50 K were detected. Thus the total column density and rotation temperature are rough estimates of the true value.

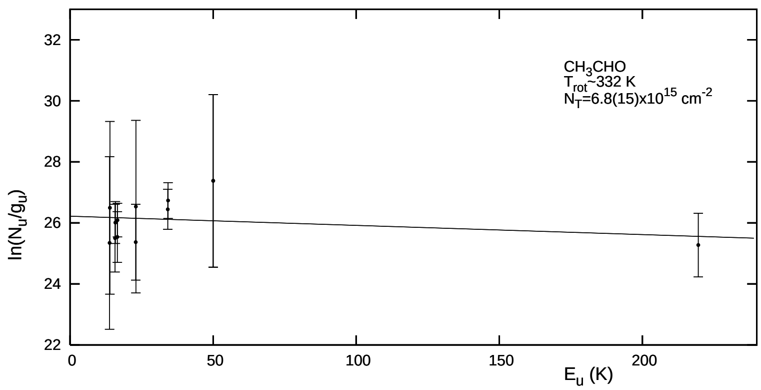

Figure 4.7 Rotation temperature diagram of CH_3CHO from the compact ridge. The abscissa is the upper state energy of the transition in K, and the ordinate is the log of the normalized column density. The line is the weighted least squares fit to the data.

4.4.5 CH_3CN (Methyl Cyanide)

Hot Core

Thirty ground state and vibrationally excited state CH_3CN transitions were detected toward the hot core as were many $^{13}CH_3CN$ and $CH_3^{13}CN$ transitions. Figure 4.8 shows the rotation temperature diagram for CH_3CN giving a total column density of $1.8(1)\times10^{16}$ cm^{-2} and a rotation temperature of 228(1) K. Using this temperature, total column densities for $^{13}CH_3CN$ and $CH_3^{13}CN$ of $1.4(5)\times10^{15}$ cm^{-2} and $1.4(1)\times10^{15}$ cm^{-2} are found, respectively. Note that there is significant scatter in the points in the diagram. This is likely due to opacity at the low temperature end and due to the large number of overlapping transitions, which were difficult to fit, at the high temperature end. The low energy transitions also have large linewidth components, indicating emission from the plateau region as well as the hot core. Enough transitions of CH_3CN were detected that an analysis via the statistical equilibrium method may be possible (e.g., Remijan et al., 2004c).

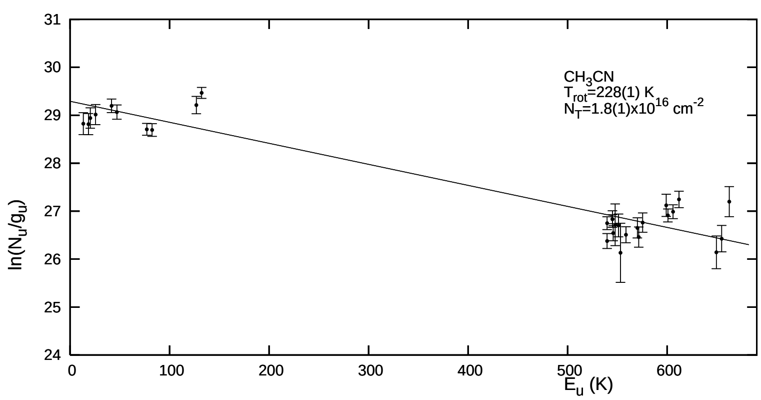

Figure 4.8 Rotation temperature diagram of CH_3CN from the hot core. The abscissa is the upper state energy of the transition in K, and the ordinate is the log of the normalized column density. The line is the weighted least squares fit to the data.

Compact Ridge

Only the ground state transitions of CH_3CN and its isotopologues were detected toward the compact ridge. This makes CH_3CN the largest and most complex N bearing species detected toward the compact ridge and indicates that CH_3CN may have a formation mechanism that differs from other large N bearing species. No rotation temperature diagrams could be constructed from the fits to the data. Thus a rotation temperature of 200 K was assumed, and total column densities of 4.1×10^{15} cm^{-2}, 1.2×10^{15} cm^{-2}, and 4.5×10^{14} cm^{-2} were found for CH_3CN, $^{13}CH_3CN$, and $CH_3^{13}CN$, respectively.

4.4.6 $(CH_3)_2CO$ (Acetone)

Friedel et al. (2005b) (see Appendix I) reported the first detection of $(CH_3)_2CO$ toward the hot core region and the first detection of vibrationally excited $(CH_3)_2CO$ in the ISM. This species is the only known large O bearing species seen exclusively toward the hot core (there were no $(CH_3)_2CO$ transitions detected above 3 σ toward the compact ridge). This indicates that $(CH_3)_2CO$ has a different formation mechanism than other large O bearing species such as its structural relative $(CH_3)_2O$ and $HCOOCH_3$. Figure 4.9 shows the rotation temperature diagram for $(CH_3)_2CO$. The diagram gives a total column density of $2.0(3)\times10^{16}$ cm^{-2} with a rotation temperature of 176(48) K.

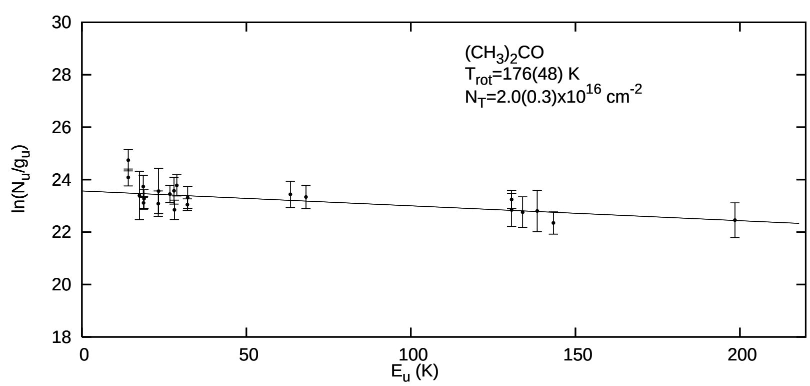

Figure 4.9 Rotation temperature diagram of $(CH_3)_2CO$ from the hot core. The abscissa is the upper state energy of the transition in K, and the ordinate is the log of the normalized column density. The line is the weighted least squares fit to the data. This figure is from Friedel et al. (2005b)

4.4.7 $(CH_3)_2O$ (Dimethyl Ether)

A total of 120 $(CH_3)_2O$ transitions (15% of all compact ridge transitions) were detected in this survey toward the compact ridge. Figure 4.10 shows the rotation temperature diagram for $(CH_3)_2O$. This species, like $(CH_3)_2CO$, has little scatter among the points, and has a total column density and rotation temperature of $7.2(1)\times10^{16}$ cm^{-2} and 84(1) K.

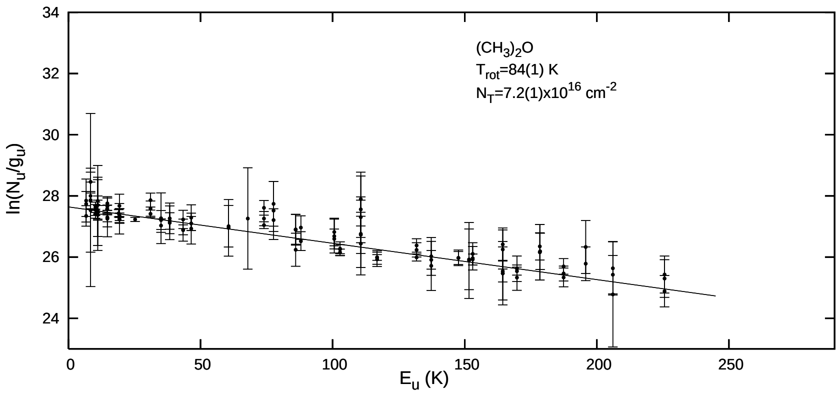

Figure 4.10 Rotation temperature diagram of $(CH_3)_2O$ from the compact ridge. The abscissa is the upper state energy of the transition in K, and the ordinate is the log of the normalized column density. The line is the weighted least squares fit to the data.

4.4.8 CH_3OH (Methanol)

Hot Core

CH_3OH was one of the few large molecular species detected toward both the hot core and compact ridge. Although it is an O bearing species, it is not surprising that it was detected toward the hot core since it is one of the most widespread species in the ISM. The rotation temperature diagram shown in Figure 4.11 shows significant scatter. However this scatter may be reduced when beam filling factors and opacity corrections are applied. From the diagram a total column density of $5.2(4)\times10^{17}$ cm^{-2} and a rotation temperature of 238(13) K are found. A few transitions of $^{13}CH_3OH$ were also detected toward the hot core, and the rotation temperature diagram shown in Figure 4.12 yields a total column density of $2.9(5)\times10^{16}$ cm^{-2} with a rotation temperature of 266(43) K. Considering the roughness of the initial analysis the temperatures from the fits of the isotopologues agree rather well.

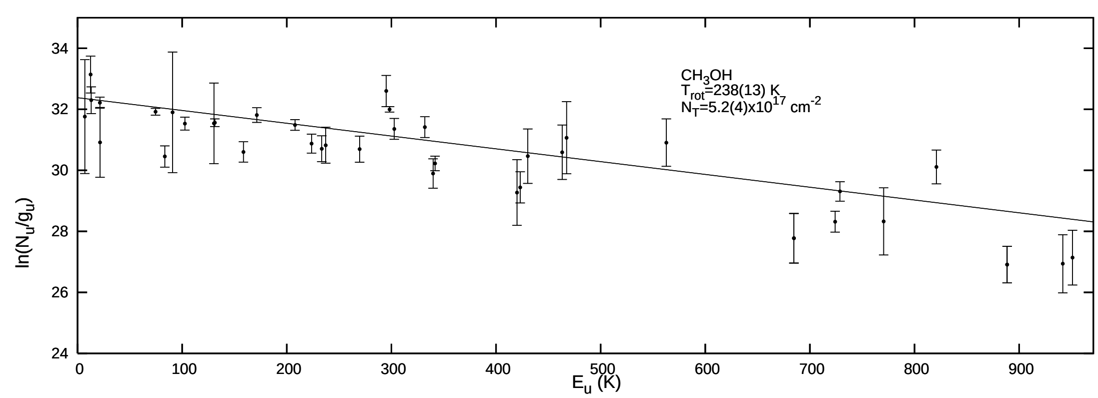

Figure 4.11 Rotation temperature diagram of CH_3OH from the hot core. The abscissa is the upper state energy of the transition in K, and the ordinate is the log of the normalized column density. The line is the weighted least squares fit to the data.

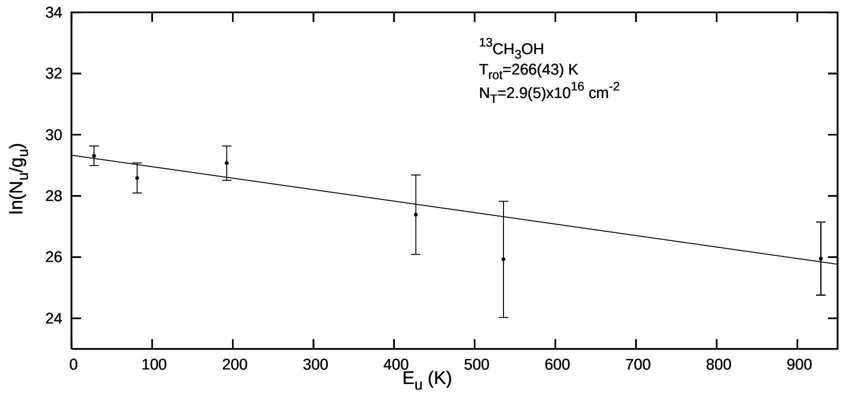

Figure 4.12 Rotation temperature diagram of $^{13}CH_3OH$ from the hot core. The abscissa is the upper state energy of the transition in K, and the ordinate is the log of the normalized column density. The line is the weighted least squares fit to the data.

Compact Ridge

Sixty CH_3OH transitions were detected toward the compact ridge in this survey. Many of these transitions had two linewidth components (one narrow, the other wide). Figure 4.13 shows the rotation temperature diagram for the narrow components. From this a total column density of $4.1(1)\times10^{17}$ cm^{-2} and a rotation temperature of 165(1) K are found. The wide linewidth components yield a total column density of $2.7(1)\times10^{17}$ cm^{-2} and rotation temperature of 171(4) K. The second fit (points denoted by a $\square$) in the diagram are for the $J_{-2,J-1} \rightarrow J_{1,J-1}$ transitions for $J = 2, 4-16$ ($J = 3$ was below 3 σ). These forbidden transitions appear to have a different distribution than the rest of the transitions and give a total column density of $1.0(1)\times10^{18}$ cm^{-2} and a rotation temperature of 52(1) K. Whether these transition are actually not in LTE with the others is not completely clear and further analysis is warranted (e.g., source size and opacity corrections).

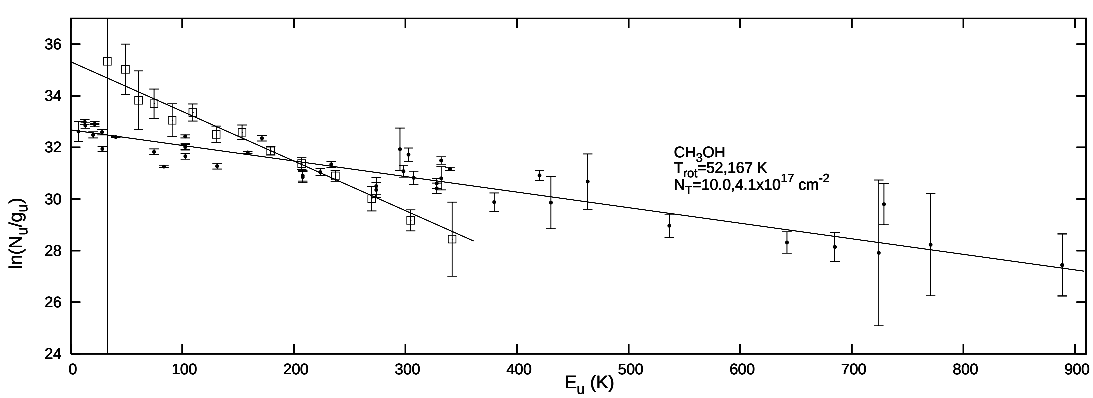

Figure 4.13 Rotation temperature diagram of CH_3OH from the compact ridge. The abscissa is the upper state energy of the transition in K, and the ordinate is the log of the normalized narrow component column density. The line is the weighted least squares fit to the data.

Several transitions of $^{13}CH_3OH$ were also detected toward the compact ridge, and Figure 4.14

shows the rotation temperature diagram, giving a total column density of 1.3(1)$\times 10^{16}$ cm^{-2} and a rotation temperature of 112(3) K.

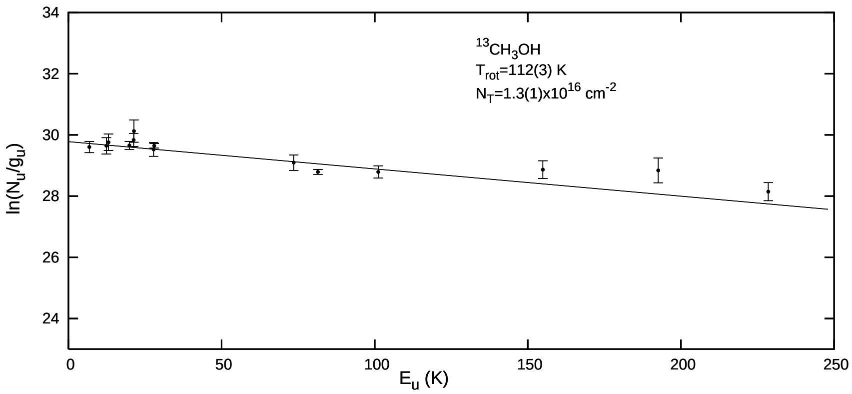

Figure 4.14 Rotation temperature diagram of $^{13}CH_3OH$ from the compact ridge. The abscissa is the upper state energy of the transition in K, and the ordinate is the log of the normalized column density. The line is the weighted least squares fit to the data.

4.4.9 HC_3N (Cyanoacetylene)

Hot Core

Numerous transitions, from both ground and vibrationally excited states, of HC_3N were detected in this survey, toward both the hot core and compact ridge. This molecule appears to have a very complex source structure. The lowest energy (ground state) transitions have three linewidth components (two narrow and one wide), while the lowest vibrationally excited state ($^1\nu_7$) has two linewidth components (one each narrow and wide), and all other vibrationally excited states have only a single narrow linewidth component. Figure 4.15 shows the rotation temperature diagram for all three linewidth components and gives a total column density and rotation temperature of 1.2(1)$\times 10^{16}$ cm^{-2} and 381(11) K for the main (strongest narrow) component ($\bullet$), a total column density and rotation temperature of 5.3(1)$\times 10^{15}$ cm^{-2} and 179(3) K for the wide component ($\square$), and a total column density and rotation temperature of 5.2(1)$\times 10^{14}$ cm^{-2} and 20(1) K for the second narrow component ($\circ$).

All three single-^{13}C isotopomers were also detected, but only toward the hot core. Using the rotation temperature from the main HC_3N, fit total column densities of 4.6(8)$\times 10^{14}$ cm^{-2}, 3.9(5)$\times 10^{14}$ cm^{-2}, and 3.4(4)$\times 10^{14}$ cm^{-2} are found for $H^{13}CCCN$, $HC^{13}CCN$, and $HCC^{13}CN$, respectively.

Compact Ridge

Only transitions of the main HC_3N isotopologue were detected toward the compact ridge. From these ground state and vibrationally excited state transitions a total column density and rotation temperature of 5.6(1)$\times 10^{15}$ cm^{-2} and 1248(201) K are found. Figure 4.16 shows the rotation

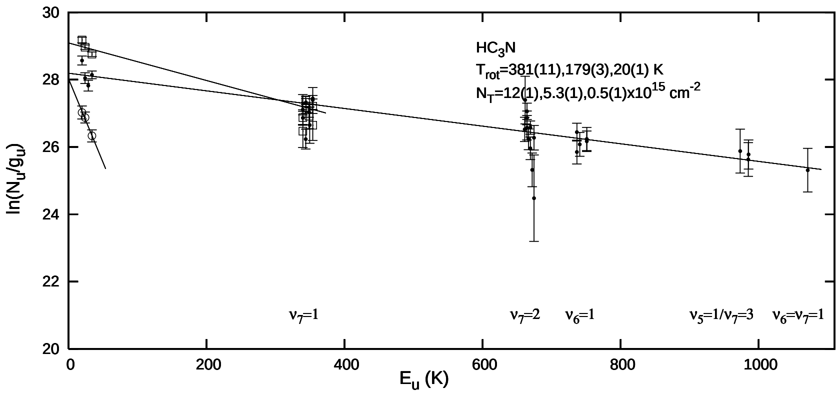

Figure 4.15 Rotation temperature diagram of HC_3N from the hot core. The abscissa is the upper state energy of the transition in K, and the ordinate is the log of the normalized column density. The line is the weighted least squares fit to the data. • denotes the main narrow component, □ denotes the wide component, and ○ denotes the second narrow component.

temperature diagram for HC_3N. This rotation temperature is very high and may be due to the misidentification of weak HC_3N transitions or poor fits due to self absorption of the ground state transitions. One item of note is what appears to be an inverse P-Cygni profile toward the compact ridge in the $J = 10-9$ and $J = 9-8$ ground state transitions. This is discussed further in § 4.4.13.

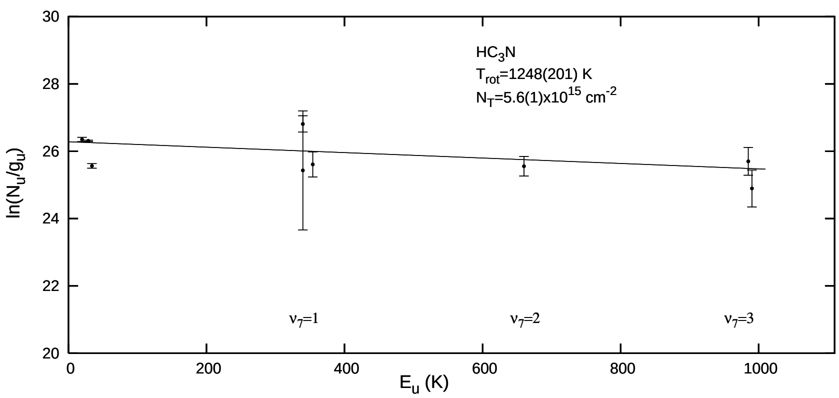

Figure 4.16 Rotation temperature diagram of HC_3N from the compact ridge. The abscissa is the upper state energy of the transition in K, and the ordinate is the log of the normalized column density. The line is the weighted least squares fit to the data.

4.4.10 $HCOOCH_3$ (Methyl Formate)

A total of 177 $HCOOCH_3$ transitions were detected toward the compact ridge (23% of all compact ridge lines and the largest number of lines of any compact ridge species). From the rotation temperature diagram shown in Figure 4.17 a total column density and rotation temperature of $3.3(1)\times10^{17}$ cm^{-2} and 344(55) K are found.

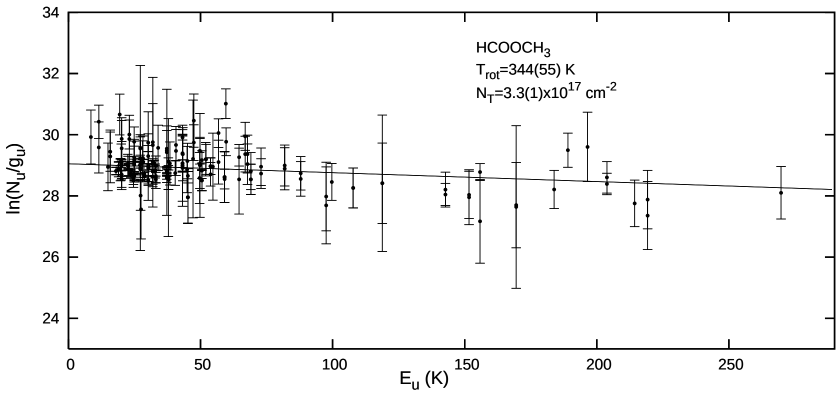

Figure 4.17 Rotation temperature diagram of $HCOOCH_3$ from the compact ridge. The abscissa is the upper state energy of the transition in K, and the ordinate is the log of the normalized column density. The line is the weighted least squares fit to the data.

4.4.11 HNCO (Isocyanic Acid)

Hot Core

A nearly equal number of transitions of HNCO were detected toward both the hot core and compact ridge. From the rotation temperature diagram shown in Figure 4.18 a total column density and rotation temperature of $6.8(12)\times10^{16}$ cm^{-2} and 212(29) K are found for the hot core.

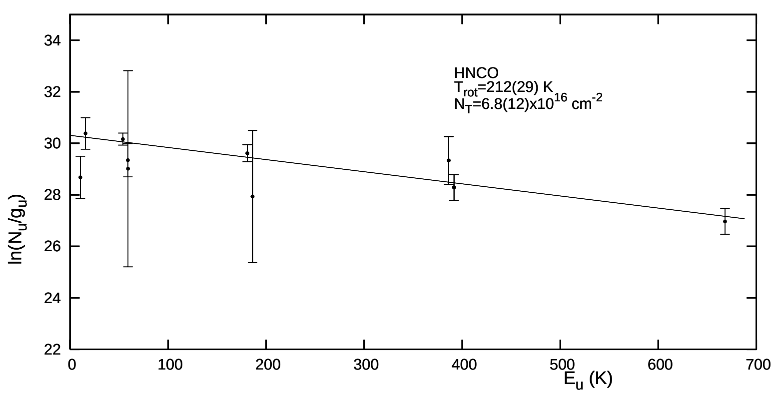

Figure 4.18 Rotation temperature diagram of HNCO from the hot core. The abscissa is the upper state energy of the transition in K, and the ordinate is the log of the normalized column density. The line is the weighted least squares fit to the data.

Compact Ridge

Figure 4.19 shows the rotation temperature diagram from HNCO toward the compact ridge. The data give a total column density of $3.3(3)\times10^{16}$ cm^{-2} and rotation temperature of 282(76) K, which are very similar to the hot core values.

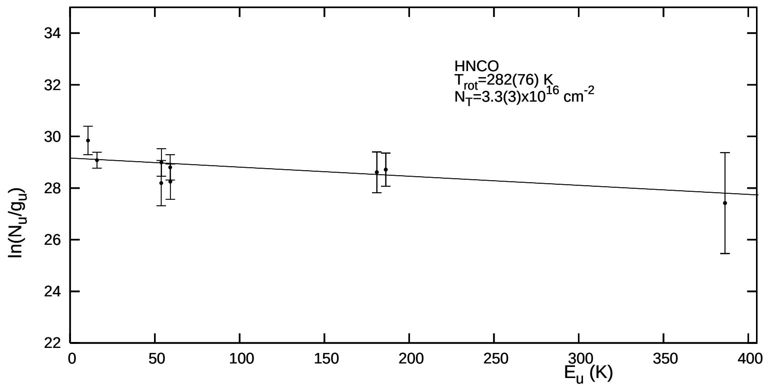

Figure 4.19 Rotation temperature diagram of HNCO from the compact ridge. The abscissa is the upper state energy of the transition in K, and the ordinate is the log of the normalized column density. The line is the weighted least squares fit to the data.

4.4.12 SO_2 (Sulphur Dioxide)

Hot Core

In this survey twenty six SO_2 transitions, including three from the first vibrationally excited state, were detected toward the hot core, while only seven were detected toward the compact ridge. This makes SO_2 the only simple O bearing species with more transitions (factor of ~3.7) detected toward the hot core. This indicates that this species may have a different formation mechanism than other simple O bearing species. Figure 4.20 shows the rotation temperature diagram for SO_2 and gives a total column density of $5.3(4)\times10^{17}$ cm^{-2} and a rotation temperature of 151(6) K. Note that the lowest energy transition was not used in the fit as it appears too strong, possibly from extended or plateau components.

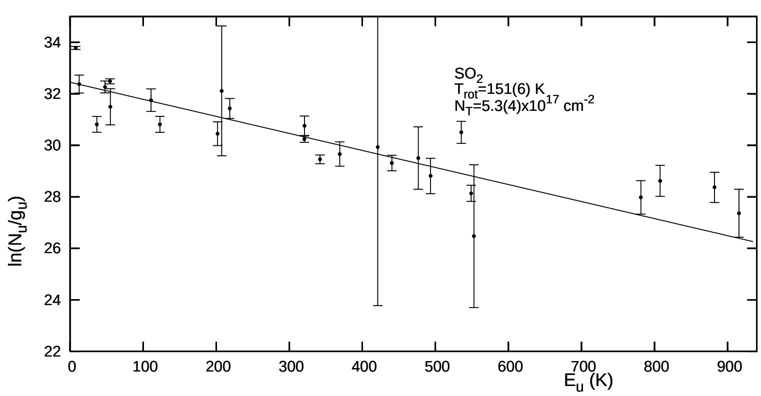

Figure 4.20 Rotation temperature diagram of SO_2 from the hot core. The abscissa is the upper state energy of the transition in K, and the ordinate is the log of the normalized column density. The line is the weighted least squares fit to the data.

Compact Ridge

As can be seen in Figure 4.21 the compact ridge SO_2 points are rather scattered and thus no reliable fit could be obtained. However if a temperature of 150 K is assumed (solid line on diagram) a total column density of 4.4(2)$\times10^{17}$ cm^{-2} is found.

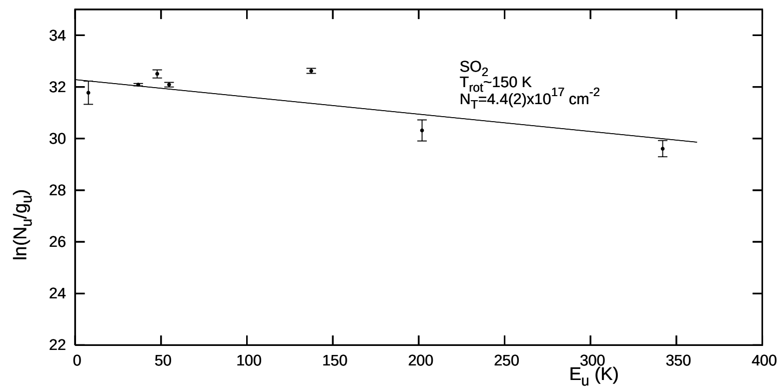

Figure 4.21 Rotation temperature diagram of SO_2 from the compact ridge. The abscissa is the upper state energy of the transition in K, and the ordinate is the log of the normalized column density. The line is the assumed rotation temperature of 150 K.

4.4.13 Non-Gaussian Line Profiles

Several species show peculiar, non-Gaussian line profiles toward the compact ridge. These species include HCO^+, HNC, CH_3CCH, and the two lowest energy HC_3N transitions. All of these show sharp, narrow inverse P-Cygni profiles toward the compact ridge, while having only slight absorption dips toward the hot core. An inverse P-Cygni profile indicates an infall, but if the compact ridge region is the interaction between an outflow and the ambient material an infall would not be expected, unless associated with an extended shell. The narrowness of the feature indicates that the infall motion is very slow (<1.0 km s^{-1}). Other species (HCN, $HC^{15}N$, and CO) do not show this profile but do show significant asymmetries that may be an inverse P-Cygni profile superimposed on a strong emission feature. Another simple species, C_2H, shows a sharp, narrow P-Cygni profile toward the hot core but pure emission toward the compact ridge, indicating a slow expansion away from the hot core. These features need to be investigated and modeled further, possibly with future, higher spatial and spectral resolution observations. These profiles have not been previously reported in the literature and previous line surveys of this region either had too poor spatial or spectral resolution to detect them.

4.4.14 Structural Analysis

In an attempt to examine the observed chemical differences between the hot core and compact ridge, an analysis was carried out on the backbone structure of the larger (>3 atoms) molecules (although OCS was included in the analysis). The backbone structure of a molecule consists of all of the atoms in the molecule with the hydrogens removed (i.e., the backbone of CH_3OH is CO). Figure 4.22 shows the backbone structures of the large species detected in this survey. Red structures indicate backbone structures seen only toward the compact ridge, green only toward the hot core, and black toward both sources. Below each structure, in parenthesis, is an exemplar of the structure. The backbone structures can be categorized onto five groups and each is discussed below.

- **Group 1**: The simple carbon chain (top structure) is present in both sources, and substituting a N for the triply bonded C does not change where it is present. Combining the first two structures into a longer carbon chain with a N at the end still does not change where this structure is seen. However, if this structure is hydrogenated first to C_2H_3CN and then to C_2H_5CN it makes a drastic change, as these species are seen only toward the hot core. Long carbon chain species (e.g., HC_3N) are easily formed in cold dark regions (e.g., Hirota et al., 2004; Kaifu et al., 2004), whereas the distributions of the hydrogenated N bearing carbon chains indicates that the hydrogenation of these chains requires the temperature and/or density of a hot core type source in order to happen. Or these species may require the higher temperatures of a hot core in order to desorb from the grain surface.

- **Group 2**: This group consists of CCO backbone structures. Note that the fully hydrogenated C-C-O structure is present in both sources while all other CCO structures are present only in the compact ridge. Taken in conjunction with the results of group 1, it appears that the hydrogenation/desorption of O bearing carbon chains takes lower temperatures when compared to their N bearing cousins (i.e., weak shocks may be able to desorb the O bearing species but not their N bearing counterparts).

- **Group 3**: This group consists of OCO structures. Note that the C-O-C structure is present in both this group and group 2 because of its similarity to the C-O-C=O structure. The only member of this group that is seen outside of the compact ridge is OCS, the sulphur equivalent to CO_2 (carbon dioxide), which contains no H. S and O are isoelectronic cousins, in other words they have the same structure in their valence shell and have similar chemical properties. All other structures are hydrogenated to some degree. This indicates that OCS may form in the gas phase while the others are formed/released from grains by a shock.

- **Group 4**: This interesting group consists of the CO backbone structure. The fully hydrogenated CO structure (CH_3OH), like the fully hydrogenated member of group 2, is present in both sources. The partially hydrogenated backbone is seen only toward the hot core, and the isoelectronic sulphur version is seen only toward the compact ridge. This indicates that there may be different conditions for the formation/survival of isoelectronic O/S cousins.

- **Group 5**: This is the only group that mixes N, C, and O. The simplest, least hydrogenated structure in this group is present in both sources while the almost completely hydrogenated structure is present only in the hot core. A similar conclusion to that for group 1 can be drawn for this group.

- **$(CH_3)_2O$**: The backbone of acetone is unique when compared to the others shown in the figure, and its presence only in the hot core indicates the need for a warm dense environment in order to form or be released from the grain surface.

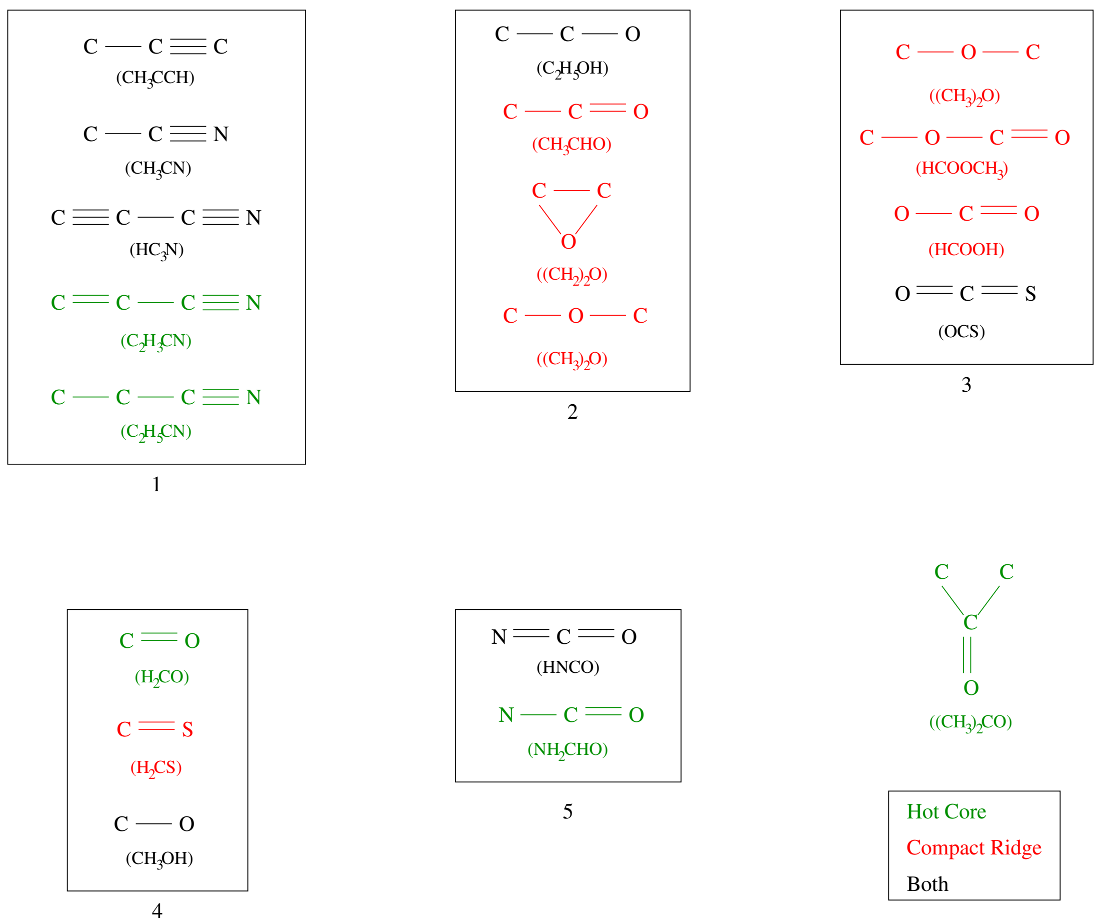

Figure 4.22 Comparison of the backbone (H have been removed) structures of hot core and compact ridge species. Red species are found only toward the compact ridge, green toward the hot core and black toward both sources. Below each backbone structure is an exemplar of the species in parenthesis.

4.4.15 U lines

A total of 627 (355 from the hot core and 272 from the compact ridge) U lines were detected in this survey. Table 4.7[2] lists the U lines from both components. Those that are denoted with a “b” are seen toward both the hot core and compact ridge (these were found by comparing the rest frequency) and may be from the same transition and species in both components. Many of the U lines appear in both the hot core and compact ridge with different rest frequencies for each component. Obviously only one of these frequencies can be correct. However, since it is not currently known which source contains the emission both frequencies are listed.

As with the Sgr B2(N-LMH) survey (see §3.3.20), the U lines from both the hot core and compact ridge were analyzed to determine if any of the frequencies were related (i.e. potentially from the same molecule). Tables 4.3 and 4.4 lists the results from this analysis. The first column lists the match number, the second and third columns list the potentially related U line frequencies, the fourth and fifth columns list the associated J values that relate the lines, and the sixth column lists the B (rotational constant) value for the match. Since the entire region from 80-115.9 GHz was covered, it would be expected that if U lines were related a string of J's would relate several U lines (e.g., there would be connections from J=12 through J=17 for a given U line). From first glance there are only a handful of potential matches that meet this criterion. However, this does not take into account that there may be intervening transitions masking some of the interconnected frequencies nor the fact that the rms noise level is not the same across all bands. Thus a U line that is $\sim$4 σ in a very low noise window may have a missing match (a connecting line that was undetected) that was not detected because it is below 3 σ in a high noise window. Further analysis of all U lines and all "missing" matches is needed.

Table 4.3. Potentially Related U Lines From the Hot Core

Match Number	ν_1 (MHz)	ν_2 (MHz)	(J_1)	(J_2)	B (MHz)
1	80,394.0	87,093.0	12	13	3349.7
2	80,483.1	87,799.3	11	12	3658.3
3	80,631.3	86,834.3	13	14	3101.2
4[a]	80,677.5	93,089.5	13	15	3103.0
5	80,677.5	107,570.8	3	4	13446.3
6	80,677.5	107,570.8	6	8	6723.2
7	80,677.5	107,570.8	9	12	4482.1
8	80,677.5	107,570.8	12	16	3361.6
9	80,677.5	107,570.8	15	20	2689.3
10	80,801.4	89,778.5	9	10	4488.9
11	80,801.4	89,778.5	18	20	2244.5
12	80,803.1	111,882.1	13	18	3107.8
13	81,585.5	89,745.0	10	11	4079.3
14[a]	81,585.5	91,183.7	17	19	2399.6
15	81,585.5	101,981.2	4	5	10198.1
16	81,585.5	101,981.2	8	10	5099.1
17	81,585.5	101,981.2	12	15	3399.4
18	81,585.5	101,981.2	16	20	2549.5
19	82,018.5	104,386.7	11	14	3728.1
20	82,226.0	104,652.1	11	14	3737.6
21	82,226.0	111,592.6	14	19	2936.6
22	82,242.3	92,523.5	8	9	5140.2
23	82,242.3	92,523.5	16	18	2570.1
24	82,242.3	95,948.4	6	7	6853.5
25	82,242.3	95,948.4	12	14	3426.7
26	82,243.7	92,523.5	8	9	5140.2
27	82,243.7	92,523.5	16	18	2570.1
28	82,243.7	99,868.3	14	17	2937.3
29	82,931.6	95,689.8	13	15	3189.7
30	82,936.9	88,861.6	14	15	2962.1
31[a]	82,936.9	107,818.1	10	13	4146.9
32[a]	83,120.5	95,908.6	13	15	3197.0
33[a]	83,120.5	106,869.0	7	9	5937.2
34[a]	83,120.5	106,869.0	14	18	2968.6
35	83,245.0	105,443.2	15	19	2774.8
36	83,728.1	95,689.8	7	8	5980.6
37	83,728.1	95,689.8	14	16	2990.3
38	83,730.3	88,963.1	16	17	2616.6
39[a]	83,730.3	96,612.1	13	15	3220.4
40[a]	84,356.9	109,664.2	10	13	4217.9
41	84,384.2	89,348.8	17	18	2481.9

Table 4.3—Continued

Match Number	ν_1 (MHz)	ν_2 (MHz)	(J_1)	(J_2)	B (MHz)
42	84,384.2	94,312.6	17	19	2481.9
43	84,538.5	103,324.4	9	11	4696.6
44	84,538.5	109,900.9	10	13	4227.0
45	84,807.0	99,772.1	17	20	2494.3
46	84,807.0	100,225.8	11	13	3854.8
47	84,807.0	107,421.6	15	19	2826.9
48	84,807.0	110,250.2	10	13	4240.4
49	85,119.8	90,793.8	15	16	2837.3
50[a]	85,119.8	107,818.1	15	19	2837.3
51	85,360.1	111,625.7	13	17	3283.1
52	86,172.0	97,660.7	15	17	2872.4
53[a]	86,679.5	95,347.3	10	11	4334.0
54	86,679.5	96,311.0	9	10	4815.6
55	86,679.5	96,311.0	18	20	2407.8
56	86,679.5	113,351.3	13	17	3333.9
57	86,679.5	115,572.2	3	4	14446.5
58	86,679.5	115,572.2	6	8	7223.3
59	86,679.5	115,572.2	9	12	4815.5
60	86,679.5	115,572.2	12	16	3611.6
61	86,679.5	115,572.2	15	20	2889.3
62	86,916.0	92,709.5	15	16	2897.2
63	86,923.8	110,104.6	15	19	2897.5
64	86,923.8	113,000.2	10	13	4346.2
65[a]	87,545.8	92,695.6	17	18	2574.9
66[a]	87,566.5	94,863.8	12	13	3648.6
67[a]	87,566.5	97,868.4	17	19	2575.5
68[a]	87,799.3	100,342.4	7	8	6271.4
69[a]	87,799.3	100,342.4	14	16	3135.7
70	88,407.2	93,059.7	19	20	2326.5
71[a]	88,686.1	99,772.1	8	9	5542.9
72[a]	88,686.1	99,772.1	16	18	2771.4
73	88,752.8	100,587.1	15	17	2958.4
74	88,770.1	93,702.1	18	19	2465.8
75[a]	88,805.0	94,725.6	15	16	2960.2
76	88,805.0	98,672.6	9	10	4933.6
77	88,805.0	98,672.6	18	20	2466.8
78	88,805.0	111,006.9	4	5	11100.7
79	88,805.0	111,006.9	8	10	5550.3
80	88,805.0	111,006.9	12	15	3700.2
81	88,805.0	111,006.9	16	20	2775.2
82	88,997.5	97,896.3	10	11	4449.8
83[a]	89,348.8	94,312.6	18	19	2481.9
84[a]	89,479.1	111,848.9	4	5	11184.9

Table 4.3—Continued

Match Number	ν_1 (MHz)	ν_2 (MHz)	(J_1)	(J_2)	B (MHz)
85[a]	89,479.1	111,848.9	8	10	5592.4
86[a]	89,479.1	111,848.9	12	15	3728.3
87[a]	89,479.1	111,848.9	16	20	2796.2
88	89,638.2	95,241.2	16	17	2801.2
89	89,742.2	110,451.2	13	16	3451.6
90	89,768.4	107,721.3	5	6	8976.8
91	89,768.4	107,721.3	10	12	4488.4
92	89,768.4	107,721.3	15	18	2992.3
93	89,768.4	109,005.4	14	17	3206.0
94	90,635.6	106,629.2	17	20	2665.7
95[a]	90,635.6	107,629.4	16	19	2832.4
96	90,793.8	107,818.1	16	19	2837.3
97	90,793.8	110,250.2	14	17	3242.7
98	91,759.6	110,112.1	5	6	9176.0
99	91,759.6	110,112.1	10	12	4588.0
100	91,759.6	110,112.1	15	18	3058.7
101[a]	92,124.4	113,383.6	13	16	3543.2
102	92,124.4	115,156.5	4	5	11515.6
103	92,124.4	115,156.5	8	10	5757.8
104	92,124.4	115,156.5	12	15	3838.5
105	92,124.4	115,156.5	16	20	2878.9
106	92,138.4	97,896.3	16	17	2879.3
107[a]	92,138.4	111,882.1	14	17	3290.6
108[a]	92,141.2	99,229.2	13	14	3543.9
109	92,161.7	103,680.9	8	9	5760.1
110	92,161.7	103,680.9	16	18	2880.0
111	92,695.6	109,054.2	17	20	2726.4
112[a]	92,709.5	98,163.0	17	18	2726.7
113	92,709.5	101,981.2	10	11	4635.5
114	92,725.1	110,112.1	16	19	2897.7
115[a]	93,059.7	109,482.0	17	20	2737.1
116	93,059.7	113,000.2	14	17	3323.5
117	93,066.1	100,225.8	13	14	3579.5
118	93,066.1	101,527.1	11	12	4230.3
119	93,098.2	107,421.6	13	15	3580.7
120	93,264.5	98,750.2	17	18	2743.1
121[a]	93,637.7	99,879.9	15	16	3121.2
122[a]	93,702.1	110,237.8	17	20	2755.9
123	95,247.0	109,900.9	13	15	3663.4
124[a]	95,267.0	114,320.3	5	6	9526.7
125[a]	95,267.0	114,320.3	10	12	4763.3
126[a]	95,267.0	114,320.3	15	18	3175.6
127	95,454.3	113,351.3	16	19	2982.9

Table 4.3—Continued

Match Number	ν_1 (MHz)	ν_2 (MHz)	(J_1)	(J_2)	B (MHz)
128[a]	95,460.2	112,305.9	17	20	2807.6
129	95,480.2	113,383.6	16	19	2983.8
130	95,546.9	109,197.0	7	8	6824.8
131	95,546.9	109,197.0	14	16	3412.4
132	95,709.0	111,659.6	6	7	7975.7
133	95,709.0	111,659.6	12	14	3987.8
134	96,311.0	115,572.2	5	6	9631.0
135	96,311.0	115,572.2	10	12	4815.5
136	96,311.0	115,572.2	15	18	3210.3
137[a]	96,313.1	107,644.4	17	19	2832.7
138[a]	96,382.3	103,796.0	13	14	3707.0
139[a]	96,382.3	107,721.3	17	19	2834.8
140	96,390.3	104,421.8	12	13	4016.2
141	97,868.4	111,848.9	7	8	6990.6
142	97,868.4	111,848.9	14	16	3495.3
143	97,896.3	104,421.8	15	16	3263.2
144	97,896.3	111,882.1	7	8	6992.6
145	97,896.3	111,882.1	14	16	3496.3
146	98,163.0	115,484.9	17	20	2887.1
147[a]	98,194.1	108,013.9	10	11	4909.7
148	98,386.0	105,955.2	13	14	3784.1
149[a]	98,434.9	106,637.7	12	13	4101.5
150[a]	98,672.6	111,006.9	8	9	6167.0
151[a]	98,672.6	111,006.9	16	18	3083.5
152	98,750.2	111,093.2	8	9	6171.8
153	98,750.2	111,093.2	16	18	3085.9
154	98,750.2	111,093.5	8	9	6171.9
155	98,750.2	111,093.5	16	18	3085.9
156	99,229.2	111,633.8	8	9	6201.9
157	99,229.2	111,633.8	16	18	3100.9
158	99,566.9	113,791.7	7	8	7112.0
159	99,566.9	113,791.7	14	16	3556.0
160[a]	99,576.5	104,817.3	19	20	2620.4
161	99,614.6	112,065.6	8	9	6225.9
162	99,614.6	112,065.6	16	18	3112.9
163	99,902.0	107,587.4	13	14	3842.4
164	101,981.2	107,647.7	18	19	2832.8
165	102,911.3	110,261.6	14	15	3675.4
166	103,224.4	111,825.7	12	13	4301.0
167	103,677.6	109,776.9	17	18	3049.4
168	103,680.9	114,048.0	10	11	5184.0
169	103,796.0	109,900.9	17	18	3052.8
170	103,796.0	109,902.6	17	18	3052.9

Table 4.3—Continued

Match Number	ν_1 (MHz)	ν_2 (MHz)	(J_1)	(J_2)	B (MHz)
171	104,619.1	111,592.6	15	16	3487.3
172[a]	105,091.7	111,659.6	16	17	3284.1
173[a]	105,186.9	113,278.0	13	14	4045.6
174	105,186.9	114,750.2	11	12	4781.3
175	105,557.8	115,153.2	11	12	4798.1
176[a]	107,818.1	114,556.9	16	17	3369.3
177[a]	109,013.0	114,750.2	19	20	2868.8

[a]Frequency ratio matches with tolerance of 3.9×10^{-6}, or 1 channel width.

Table 4.4. Potentially Related U Lines From the Compact Ridge

Match Number	ν_1 (MHz)	ν_2 (MHz)	(J_1)	(J_2)	B (MHz)
1[a]	80,520.7	85,553.5	16	17	2516.3
2	80,849.9	110,250.6	11	15	3675.0
3	81,118.1	92,705.9	7	8	5794.1
4	81,118.1	92,705.9	14	16	2897.1
5	81,361.0	89,496.7	10	11	4068.0
6	81,361.0	100,137.1	13	16	3129.3
7	81,370.5	96,165.7	11	13	3698.7
8[a]	81,513.2	89,664.5	10	11	4075.7
9	81,587.4	86,387.3	17	18	2399.6
10	81,653.1	92,539.4	15	17	2721.7
11	81,653.1	115,674.2	12	17	3402.2
12[a]	81,891.4	103,729.4	15	19	2729.7
13	82,421.3	92,724.4	8	9	5151.4
14	82,421.3	92,724.4	16	18	2575.7
15[a]	82,442.7	92,141.7	17	19	2424.8
16[a]	82,445.5	95,129.7	13	15	3171.0
17[a]	83,304.6	92,560.4	9	10	4628.0
18[a]	83,304.6	92,560.4	18	20	2314.0
19[a]	83,949.8	99,690.5	16	19	2623.4
20	84,318.0	110,262.6	13	17	3243.0
21	84,897.9	99,880.7	17	20	2497.0
22	85,120.4	90,795.9	15	16	2837.4
23	85,120.4	93,632.9	10	11	4256.0
24	85,120.4	110,655.4	10	13	4256.0
25	85,360.9	111,626.6	13	17	3283.1
26[a]	85,371.9	109,764.0	7	9	6098.0
27[a]	85,371.9	109,764.0	14	18	3049.0
28	85,442.7	106,804.1	4	5	10680.4
29	85,442.7	106,804.1	8	10	5340.2
30	85,442.7	106,804.1	12	15	3560.1
31	85,442.7	106,804.1	16	20	2670.1
32	86,034.0	90,813.3	18	19	2389.8
33	86,172.8	95,747.0	9	10	4787.4
34	86,172.8	95,747.0	18	20	2393.7
35[a]	86,280.0	91,355.0	17	18	2537.6
36	86,405.9	111,094.2	7	9	6171.9
37	86,405.9	111,094.2	14	18	3086
38	86,668.5	112,668.1	10	13	4333.4
39[a]	87,038.8	110,776.5	11	14	3956.3
40	87,413.5	101,981.4	6	7	7284.4
41	87,413.5	101,981.4	12	14	3642.2

Table 4.4—Continued

Match Number	ν_1 (MHz)	ν_2 (MHz)	(J_1)	(J_2)	B (MHz)
42[a]	88,959.7	115,648.0	10	13	4448.0
43	88,962.3	105,136.8	11	13	4043.7
44	89,095.2	99,577.6	17	19	2620.5
45[a]	89,114.9	96,541.4	12	13	3713.1
46	89,140.7	96,568.4	12	13	3714.2
47	89,363.0	111,703.1	4	5	11170.3
48	89,363.0	111,703.1	8	10	5585.2
49	89,363.0	111,703.1	12	15	3723.4
50	89,363.0	111,703.1	16	20	2792.6
51	89,381.4	95,340.6	15	16	2979.4
52	89,731.9	95,340.6	16	17	2804.1
53	89,965.8	96,391.4	14	15	3213.0
54[a]	90,855.5	96,533.8	16	17	2839.2
55[a]	90,862.6	96,541.4	16	17	2839.5
56[a]	91,093.3	105,108.0	13	15	3503.6
57	92,297.7	106,496.8	13	15	3549.9
58[a]	92,539.4	115,674.2	4	5	11567.4
59[a]	92,539.4	115,674.2	8	10	5783.7
60[a]	92,539.4	115,674.2	12	15	3855.8
61[a]	92,539.4	115,674.2	16	20	2891.9
62	92,542.1	100,253.1	12	13	3855.9
63	92,560.4	109,390.6	11	13	4207.3
64[a]	92,710.4	101,981.4	10	11	4635.5
65	92,717.9	97,597.3	19	20	2439.9
66[a]	92,735.8	99,869.1	13	14	3566.8
67[a]	93,092.1	100,253.1	13	14	3580.5
68	93,107.3	110,035.4	11	13	4232.1
69	93,501.2	105,187.9	8	9	5843.8
70	93,501.2	105,187.9	16	18	2921.9
71	93,756.4	101,568.6	12	13	3906.5
72[a]	93,756.4	113,847.3	14	17	3348.5
73[a]	94,866.5	100,137.1	18	19	2635.2
74	95,129.7	100,137.1	19	20	2503.4
75	95,129.7	109,764.0	13	15	3658.8
76[a]	95,689.6	104,388.5	11	12	4349.5
77	96,819.8	108,921.3	8	9	6051.2
78	96,819.8	108,921.3	16	18	3025.6
79	96,958.2	105,037.3	12	13	4039.9
80[a]	97,739.0	111,701.9	7	8	6981.4
81[a]	97,739.0	111,701.9	14	16	3490.7
82[a]	99,575.7	105,108.0	18	19	2766.0
83	99,880.7	105,136.8	19	20	2628.4
84	100,935.1	106,541.8	18	19	2803.7

Table 4.4—Continued

Match Number	ν_1 (MHz)	ν_2 (MHz)	(J_1)	(J_2)	B (MHz)
85	102,503.3	115,315.2	8	9	6406.4
86	102,503.3	115,315.2	16	18	3203.2

[a]Frequency ratio matches with tolerance of 3.9×10^{-6}, or 1 channel width.

4.4.16 Line Statistics

The 975 lines detected toward the hot core give a spectral line density of 2.72 (1.73 from identified lines and 0.99 from U lines) per 100 MHz. The 790 lines detected toward the compact ridge give a spectral line density of 2.21 (1.45 from identified lines and 0.76 from U lines) per 100 MHz. In order to compare this with the results from the Sgr B2(N-LMH) survey the statistics need to be restricted to the same spectral regions. Doing this gives spectral line densities (per 100 MHz) of 3.87 (3.03 from identified lines and 0.84 from U lines) for the hot core and 3.26 (2.34 from identified lines and 0.93 from U lines) for the compact ridge. Since both regions show distinct chemistry, the best comparison is to combine the spectral line densities from both the hot core and compact ridge (taking into account that some lines are seen toward both sources). This gives a total spectral line density (per 100 MHz) of 6.00 (4.54 from identified lines and 1.46 from U lines). Comparing this to the results from Sgr B2(N-LMH) (6.92 total, 4.31 from identified lines and 2.61 from U lines) indicates that the Orion-KL region has a smaller line density than Sgr B2(N-LMH). However, a larger percentage of the lines in Orion-KL were identified when compared to Sgr B2(N-LMH).

A total of ∼92,000 spectral channels were observed in this survey. Assuming Gaussian statistics and independent channels, one would expect 248 channels to be above 3 σ and 6 channels to be above 4 σ just from random noise. Since many of the line widths of identified lines from the compact ridge are so narrow (< 1.5 km s^{-1}), single channel lines with intensities >3 σ were marked as lines, and thus some of the weak (3-4 σ) lines may be random noise.

4.5 Conclusions and Future Work

This chapter has presented the initial results of the first interferometric $\lambda = 3$ mm spectral line survey of the Orion-KL region. A total of 975 spectral lines (620 identified and 355 unidentified) were detected toward the hot core region, while 790 spectral lines (518 identified and 272 unidentified) were detected toward the compact ridge. The identified transitions are from 60 molecular species and isotopologues.

The simple (∼3 atoms) species, smaller cyanogens (CH_3CN and HC_3N), and alcohols were detected toward both components. More heavily hydrogenated cyanogen species, with the same backbone structure as HC_3N, were detected exclusively toward the hot core, while larger O bearing species were detected only toward the compact ridge. The only exception to this is $(CH_3)_2CO$, the only heavy O bearing species detected only toward the hot core. In general the rotation temperatures found toward the hot core ranged from ∼200-500 K while the rotation temperatures found toward the compact ridge were noticeably lower, ∼80-150 K[4]. These results suggest that larger, highly hydrogenated N bearing species require the higher temperatures of the hot core to form or desorb from the grain surface. Contrary to this the O bearing counterpart (C_2H_5OH) of these N bearing species is widespread, indicating that it is easier to form/desorb the O bearing

[4]There are two exceptions to this. However, due to uncertainties in the data points, these two fits could easily have lower temperatures.

species than the N bearing species. The species with more than one O appear to be the products of grain chemistry, released from the surface by shocks, or they may form in the post shock gas. Source size measurements and close examination of the channel maps will further help to constrain the formation mechanisms of these molecular species.

The spectral line density of the Orion-KL region was found to be lower than that of Sgr B2(N-LMH) (when comparing the same spectral bands). However, a larger percentage of the lines in Orion-KL were identified when compared to the Sgr B2(N-LMH) region. Of the 627 U lines detected toward Orion-KL, 34 (17 each from the hot core and compact ridge) appear at the same frequency in both regions, indicating that they come from a species that exists in both regions. As with the Sgr B2(N-LMH) line survey an analysis of the U lines was carried out to determine if any of the U lines were related (from the same species). A total of 177 pairs were found for the hot core region while 86 pairs were found for the compact ridge region. A more thorough analysis will be carried out to in order to confirm or reject the pairs (are there missing J values, inconsistent line widths or intensities, etc.).

In order to facilitate the publication of the spectra from this survey, a Java based interactive program is being developed to allow for the viewing of the spectra and channel maps over the internet.

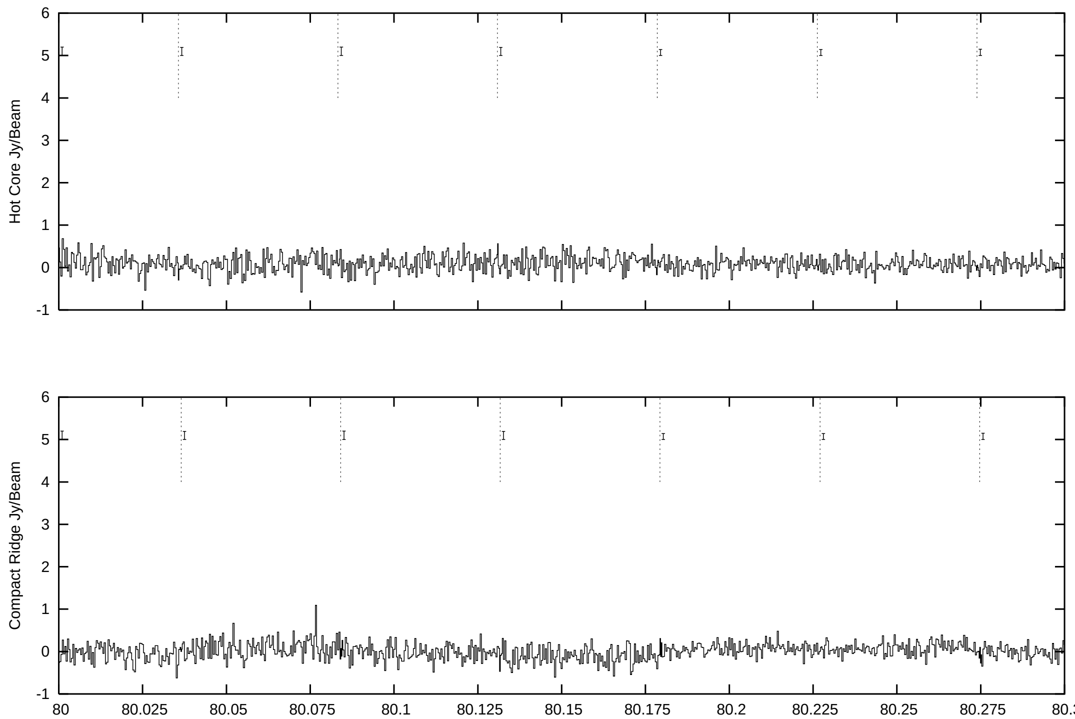

Figure 4.23 Continuum subtracted spectra of Orion-KL from the BIMA Array. The upper panel is the Hot Core and the lower panel is the Compact Ridge.

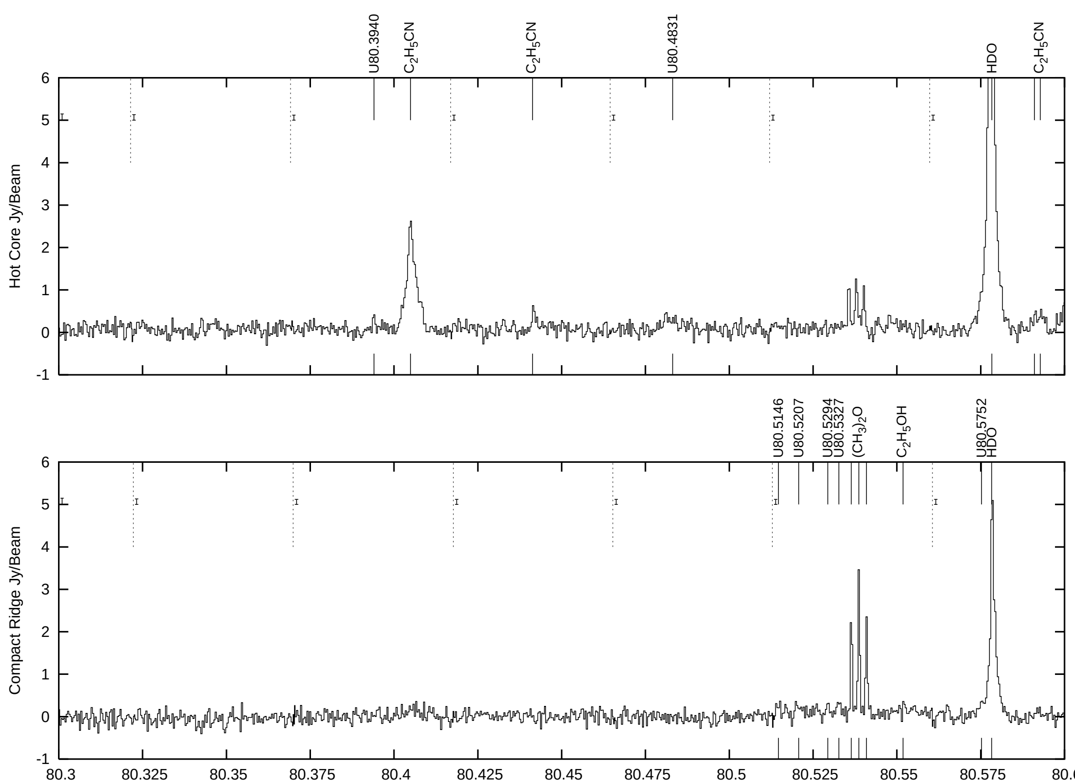

Fig. 4.23b

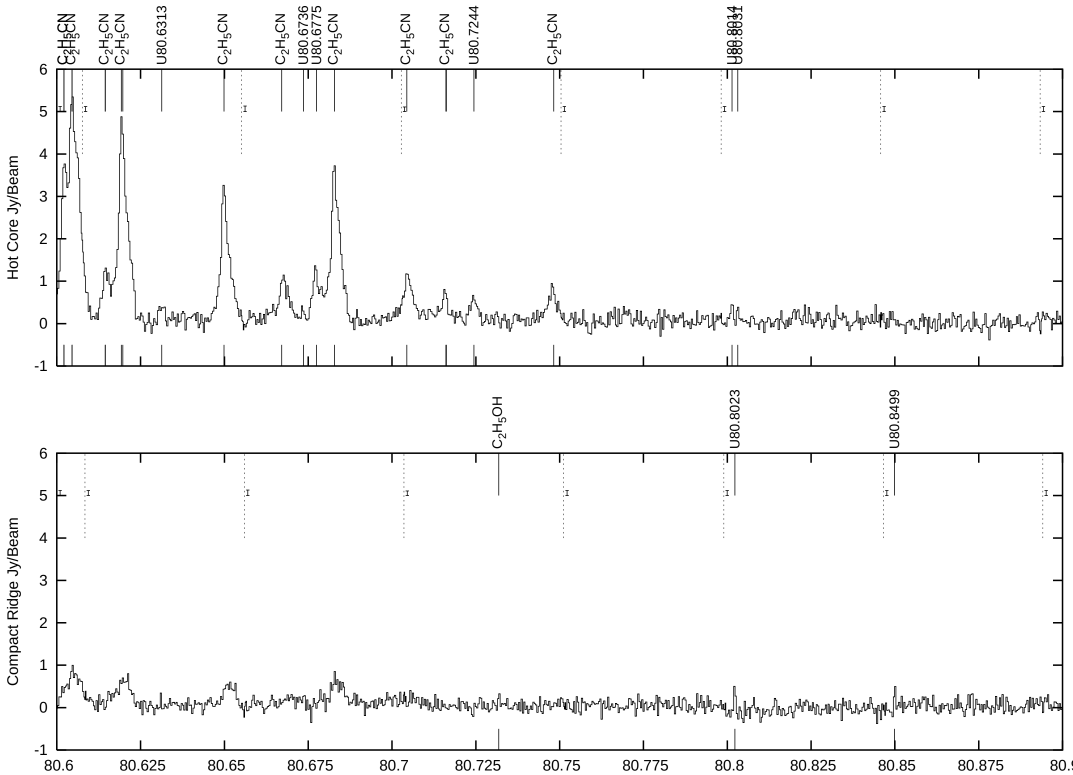

Fig. 4.23c

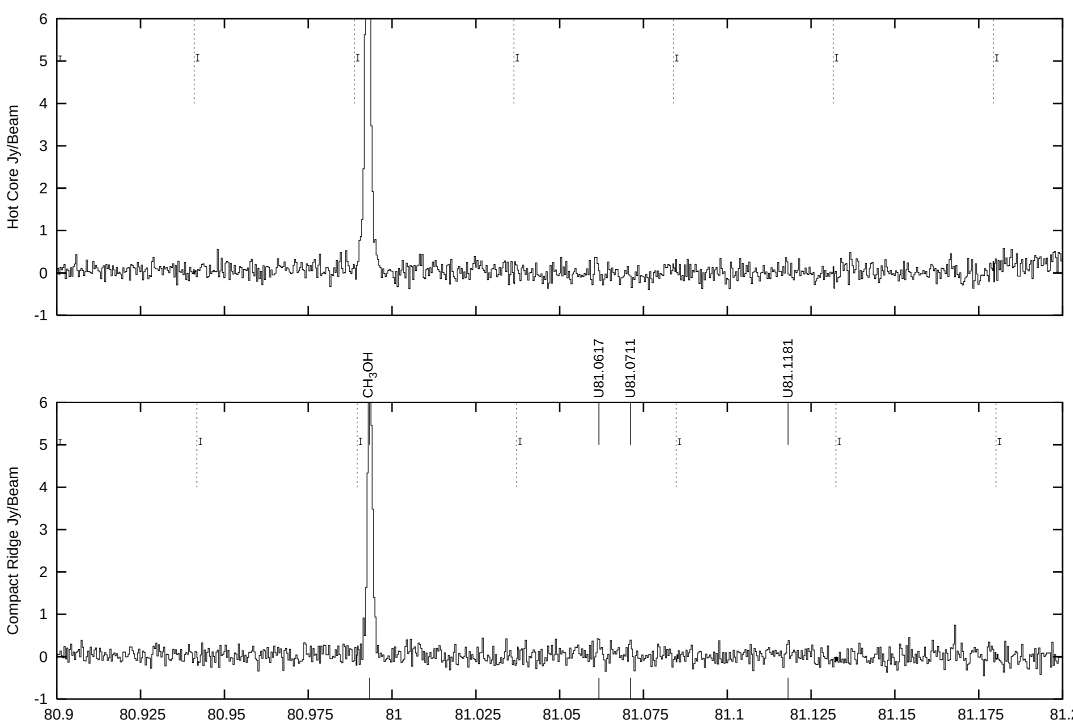

Fig. 4.23d

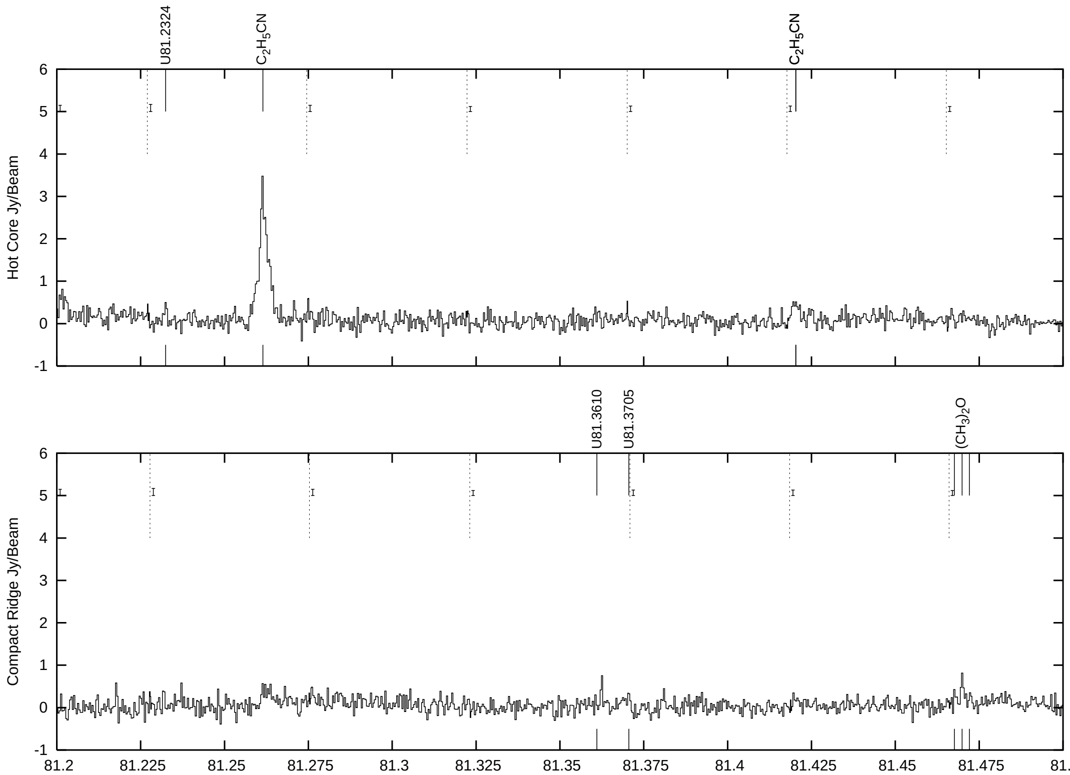

Fig. 4.23e

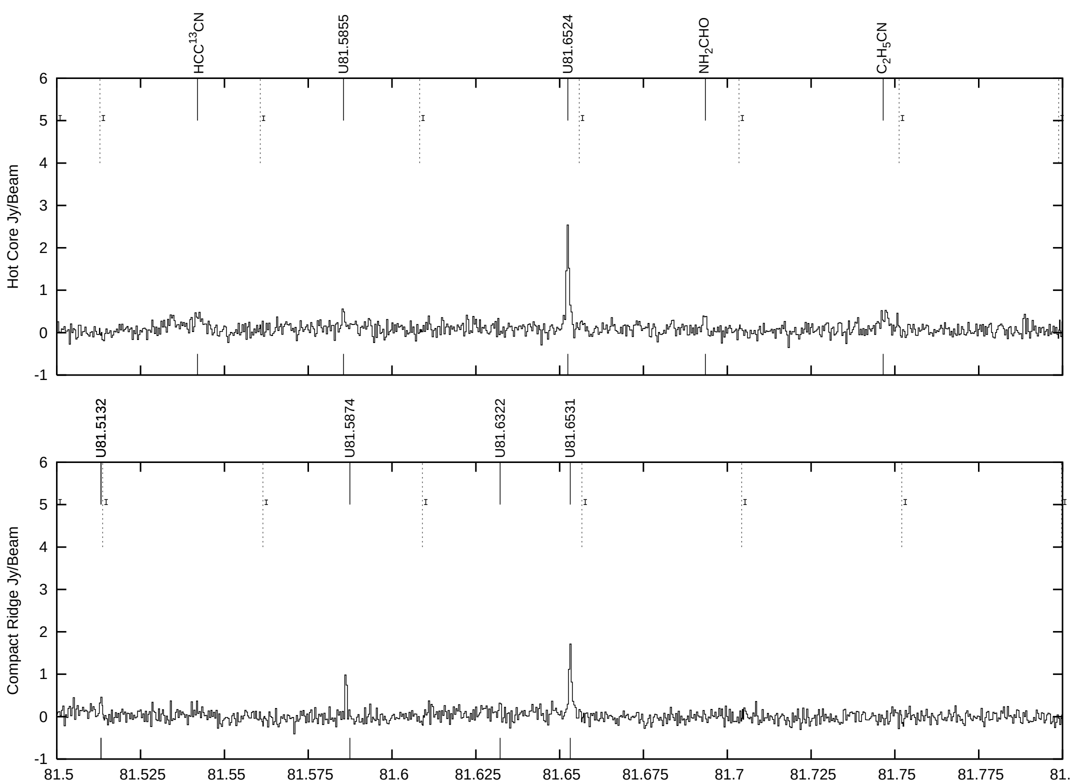

Fig. 4.23f

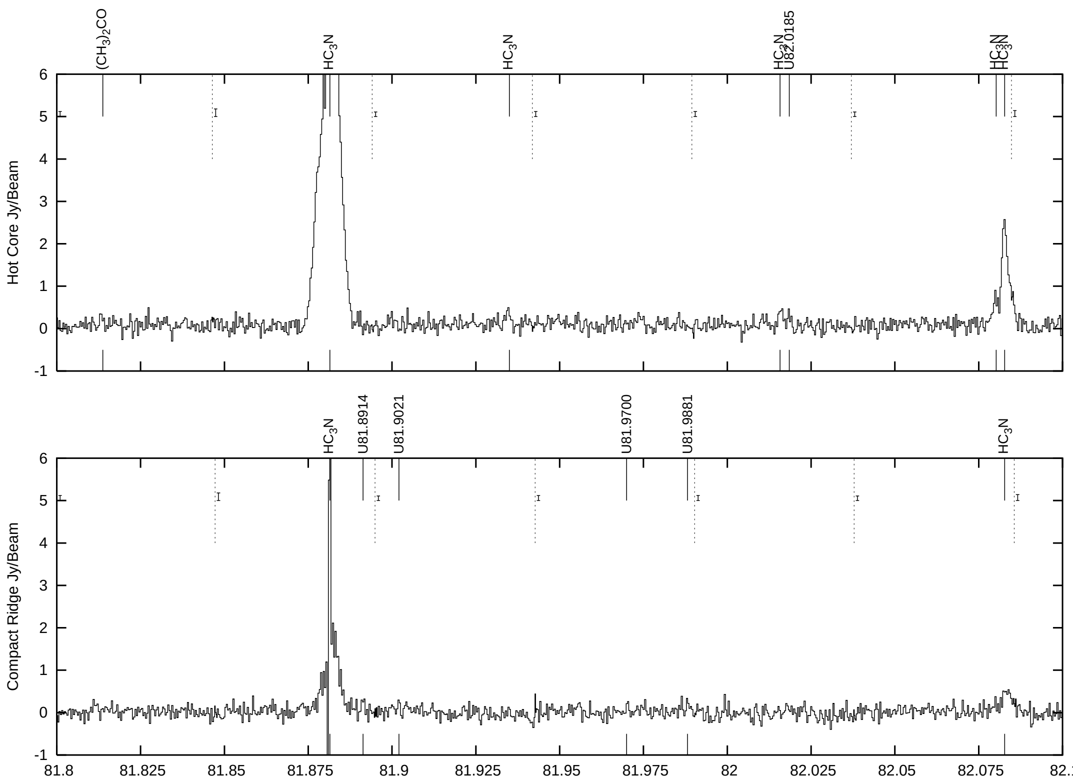

Fig. 4.23g

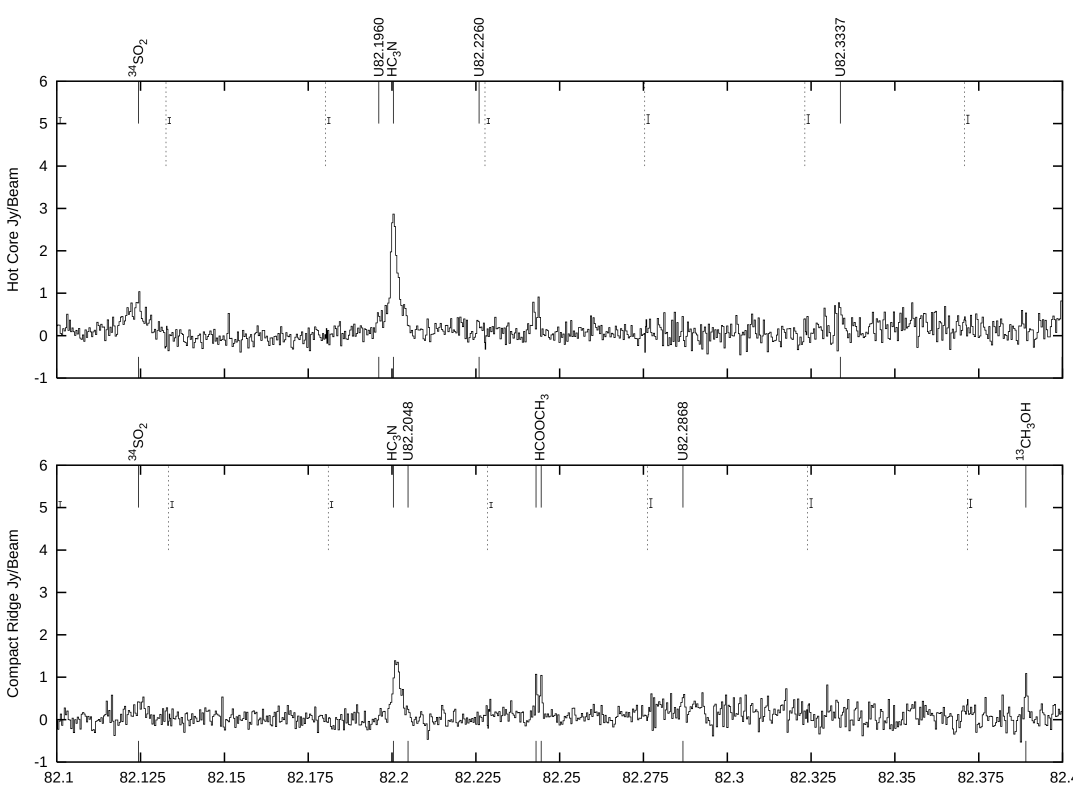

Fig. 4.23h

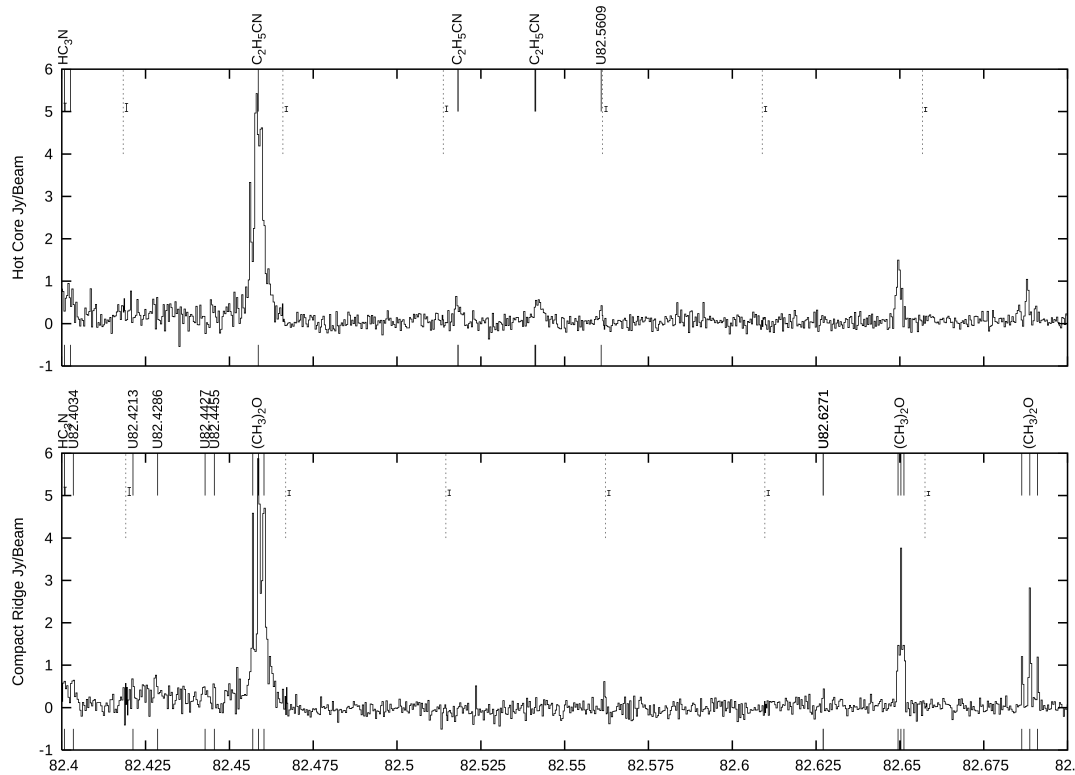

Fig. 4.23i

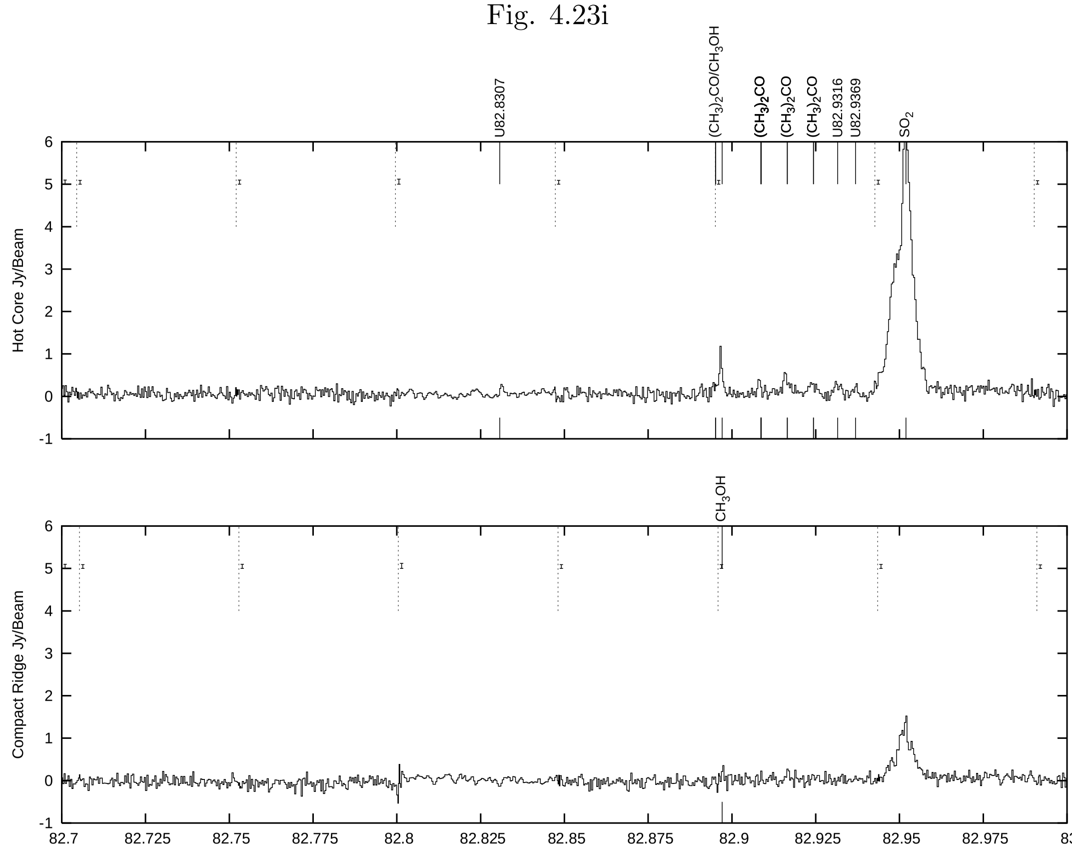

Fig. 4.23j

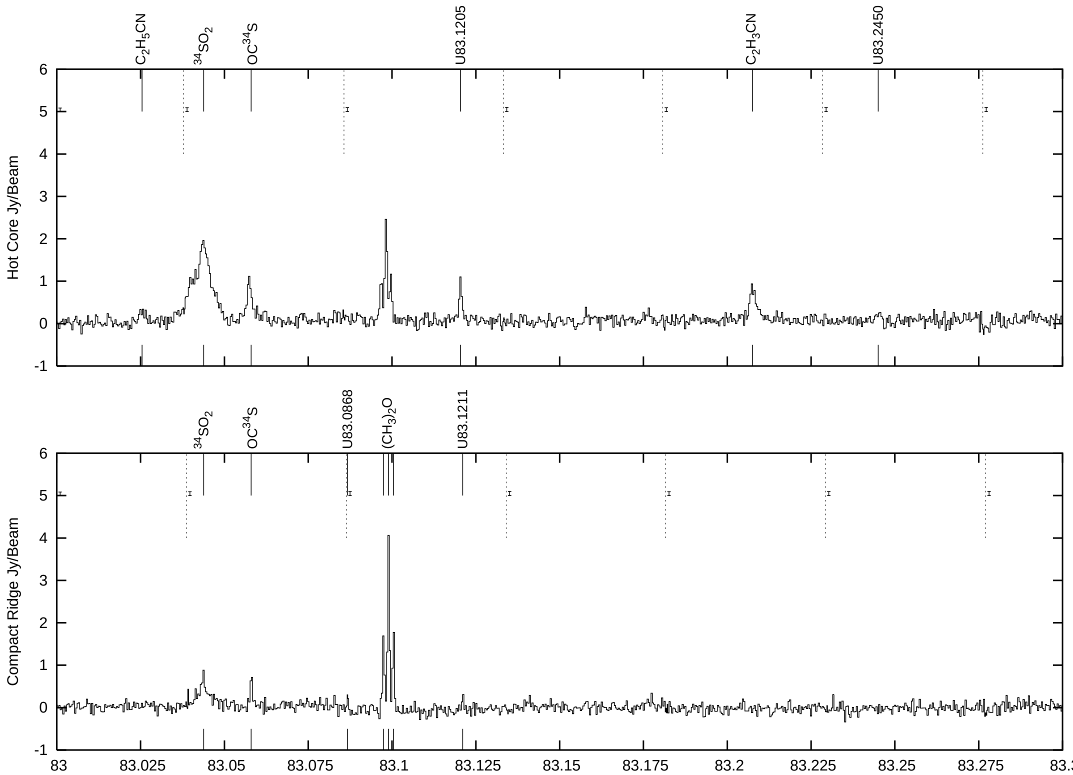

Fig. 4.23k

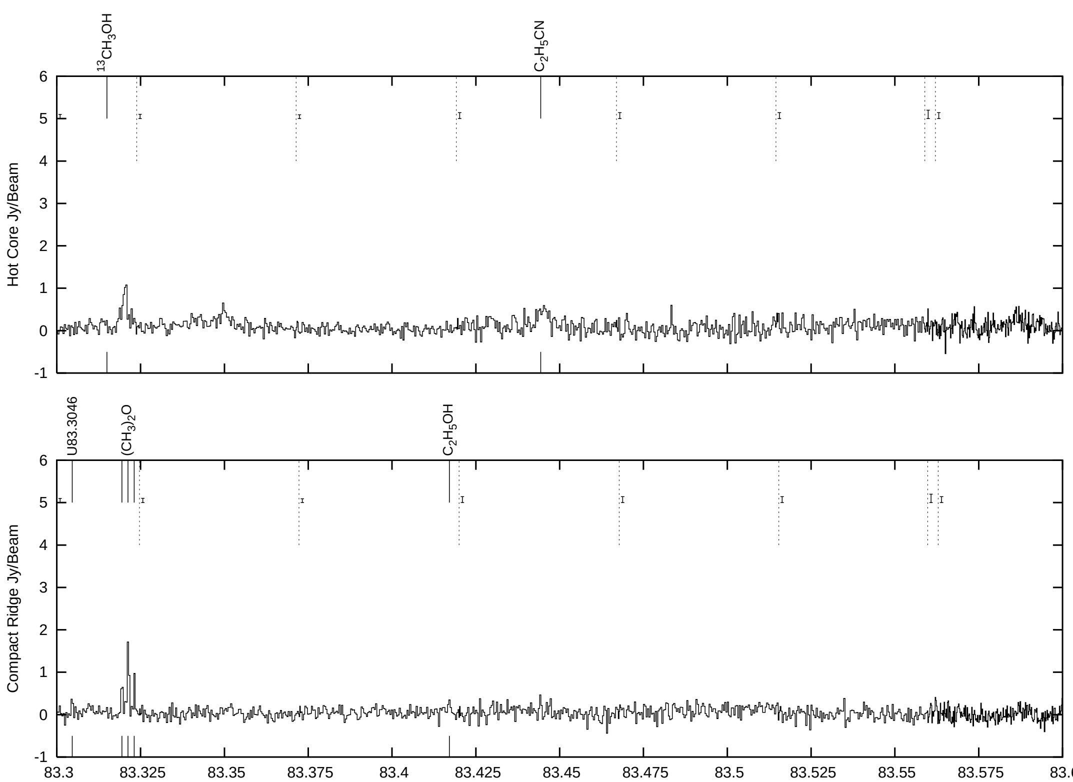

Fig. 4.23l

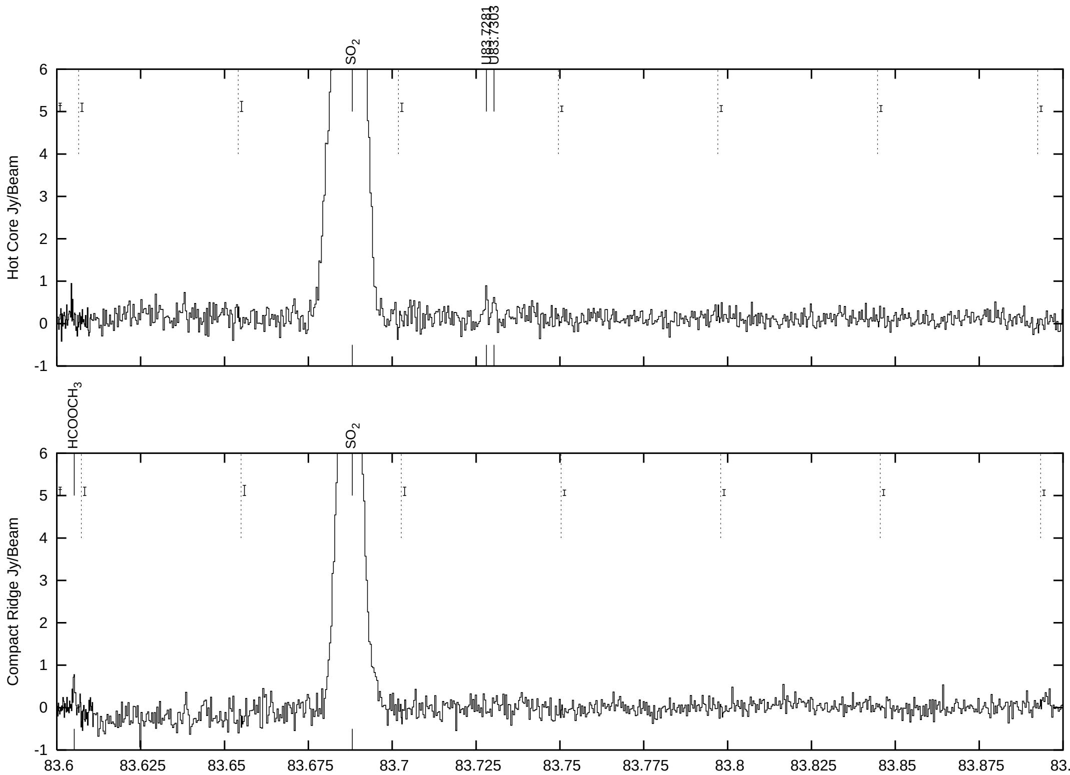

Fig. 4.23m

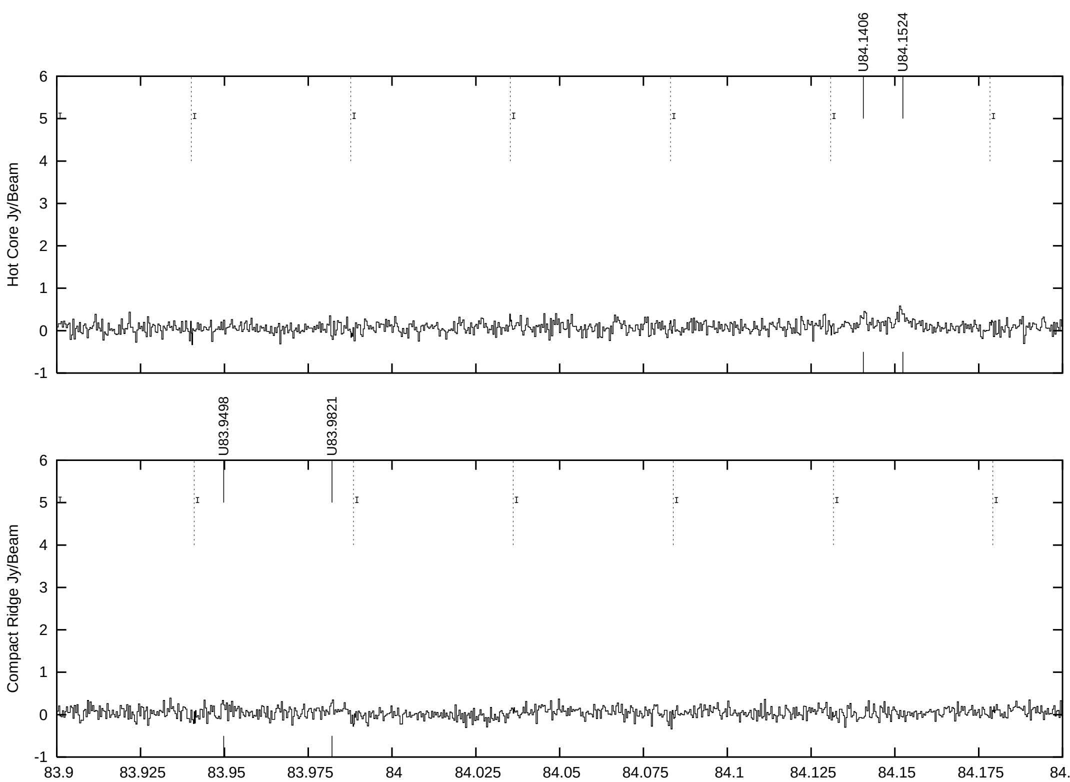

Fig. 4.23n

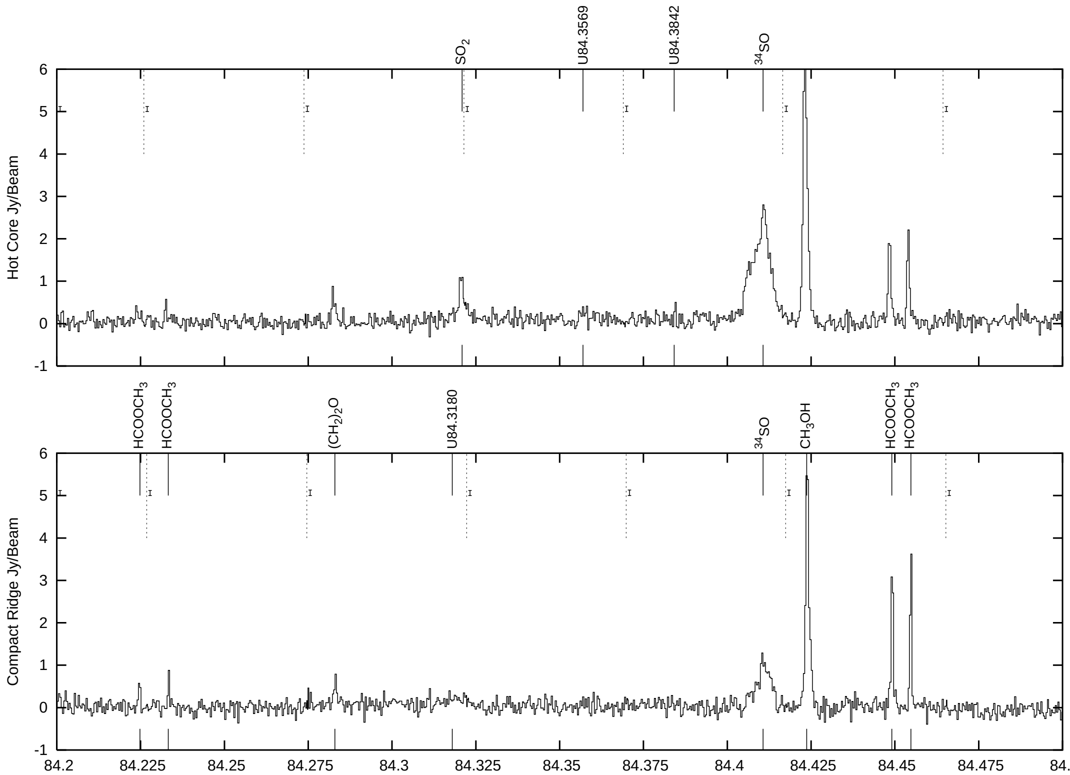

Fig. 4.23o

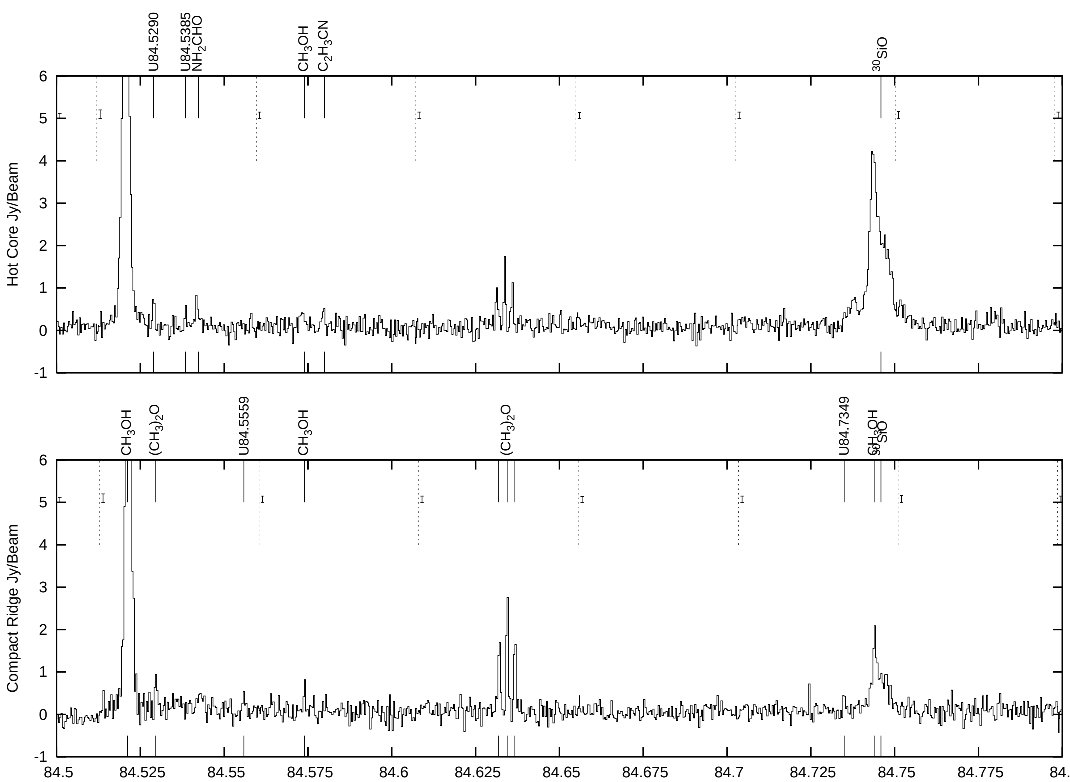

Fig. 4.23p

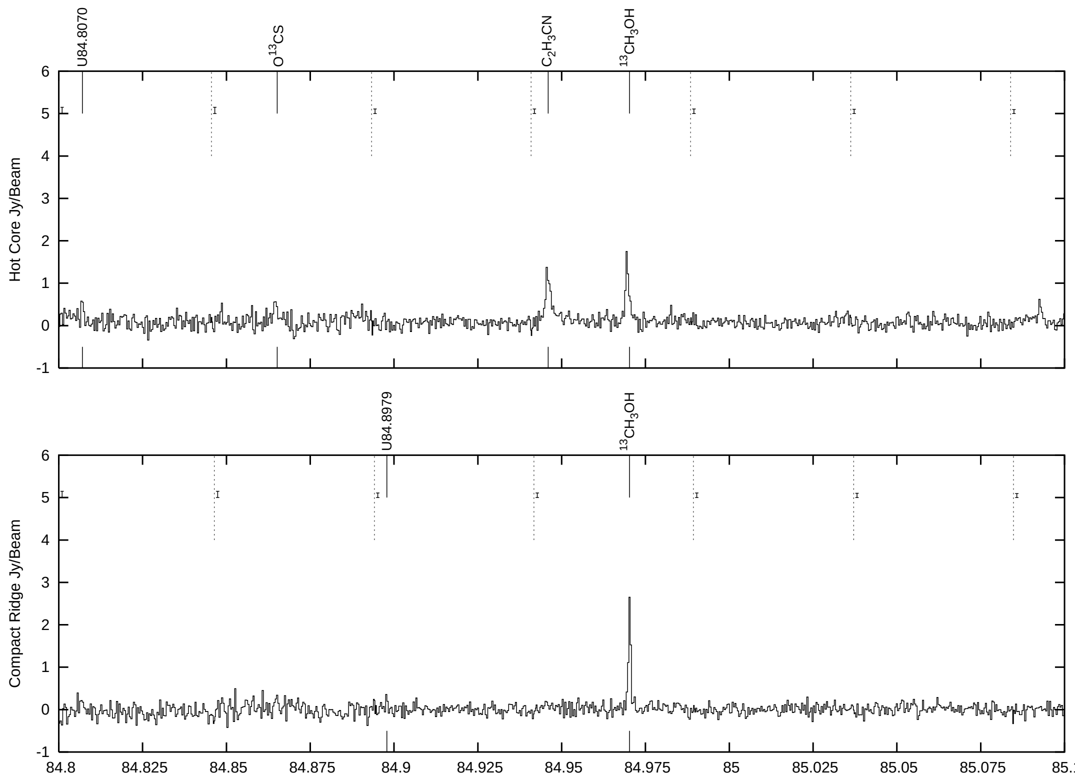

Fig. 4.23q

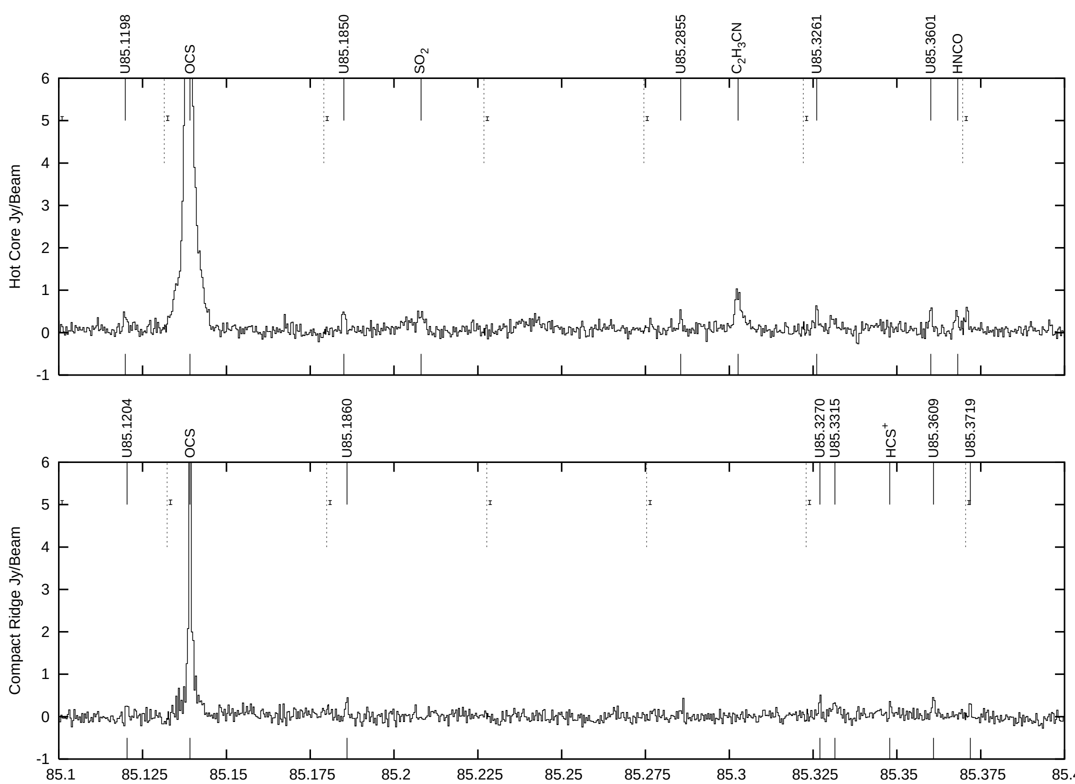

Fig. 4.23r

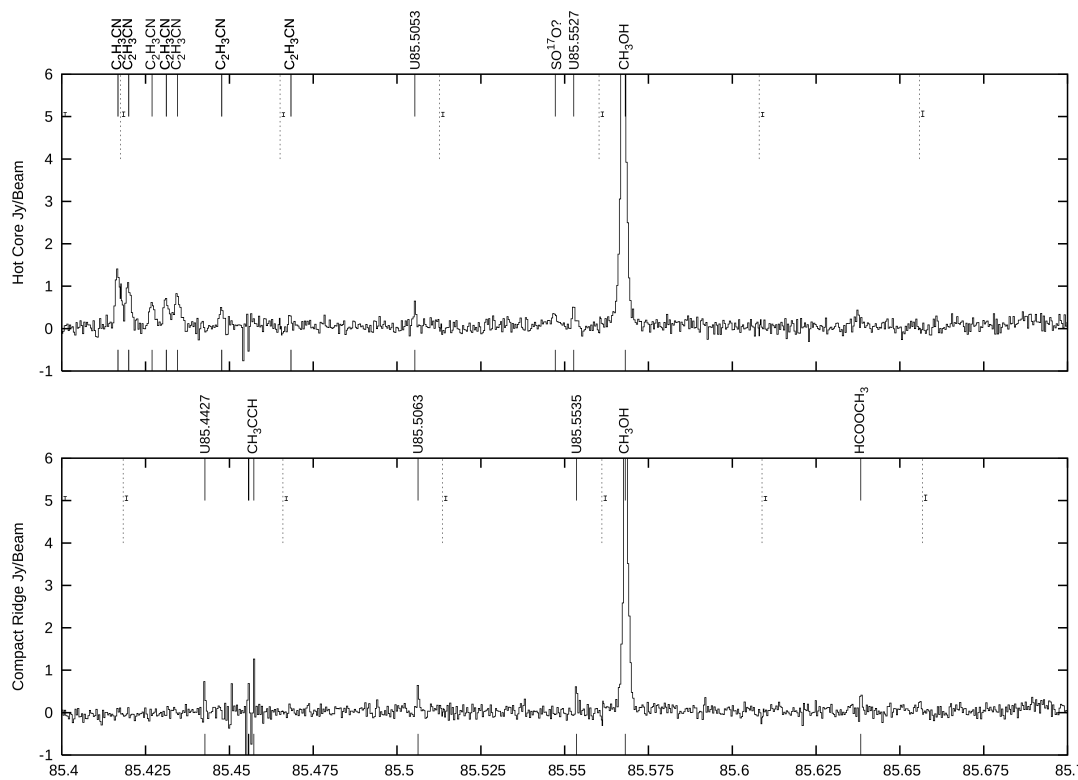

Fig. 4.23s

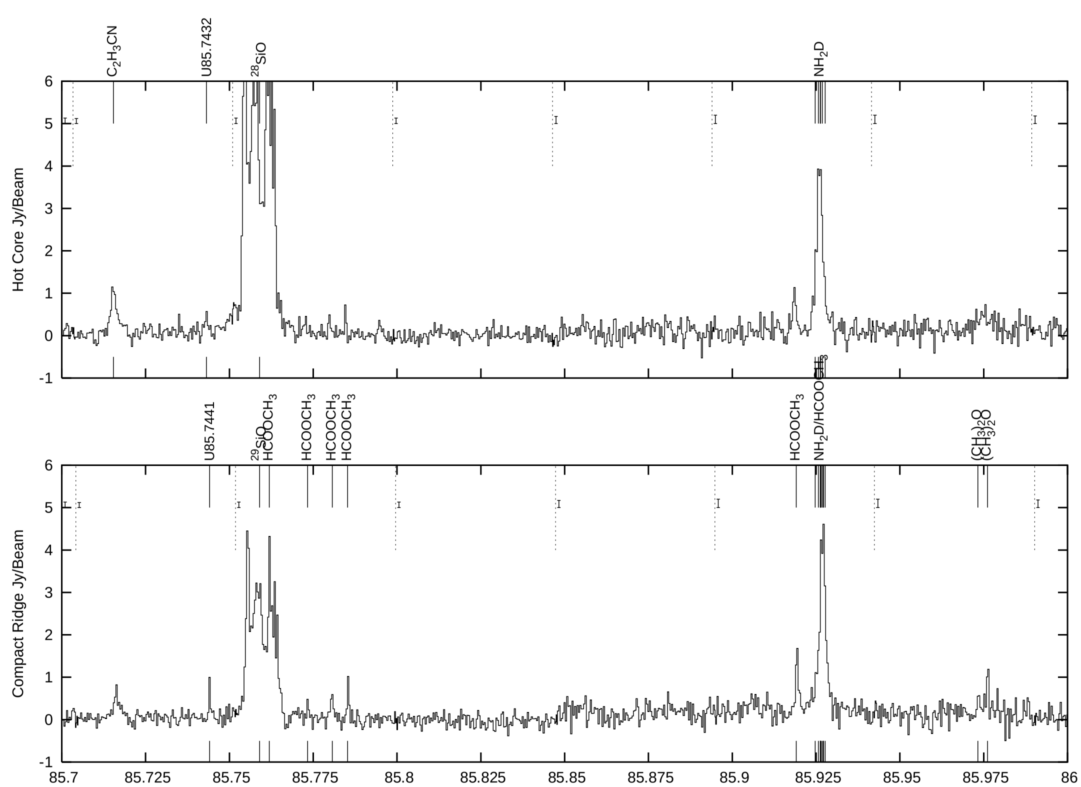

Fig. 4.23t

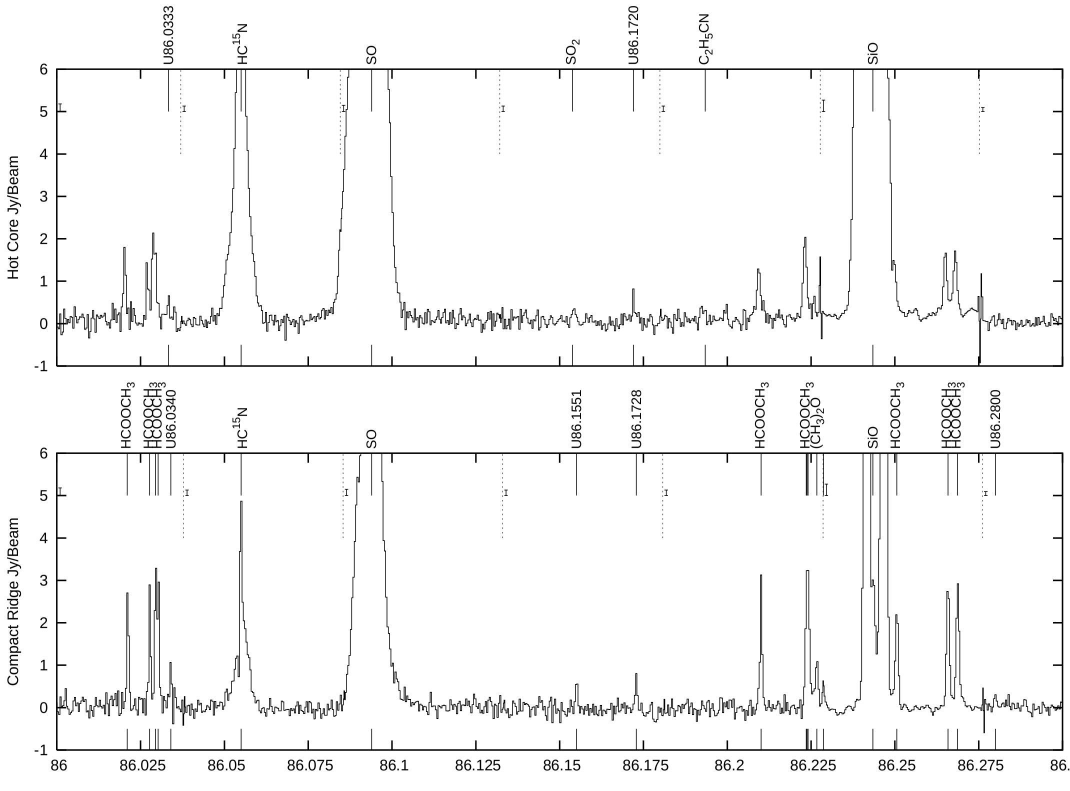

Fig. 4.23u

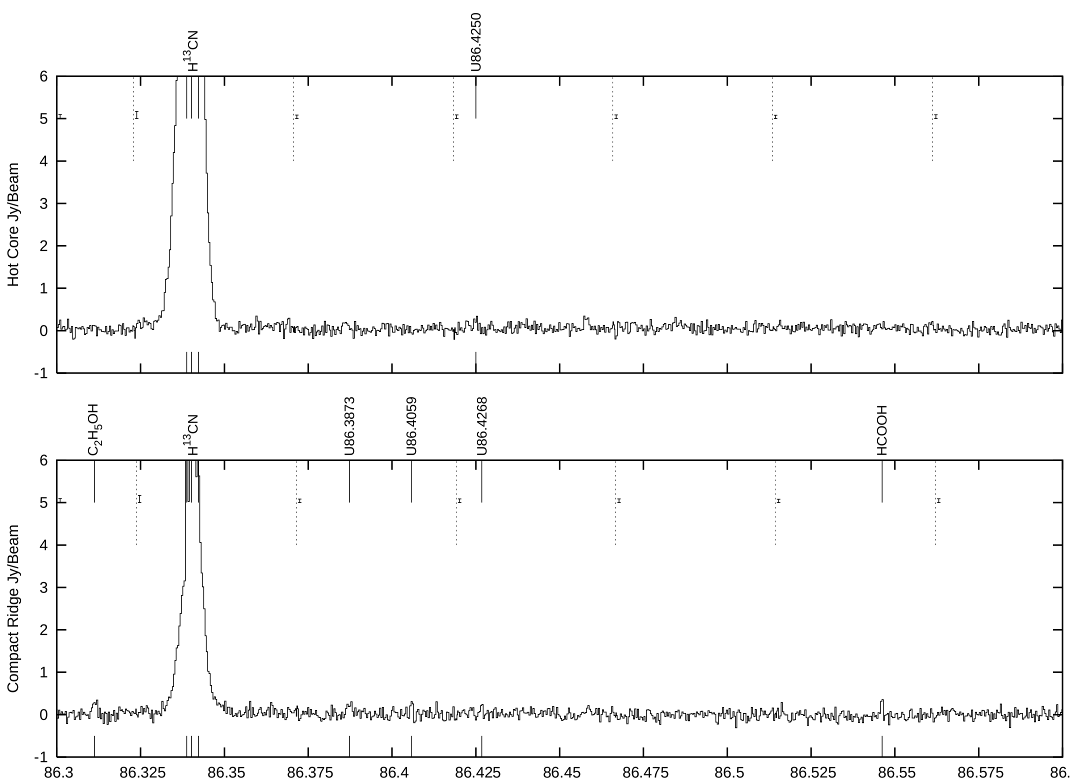

Fig. 4.23v

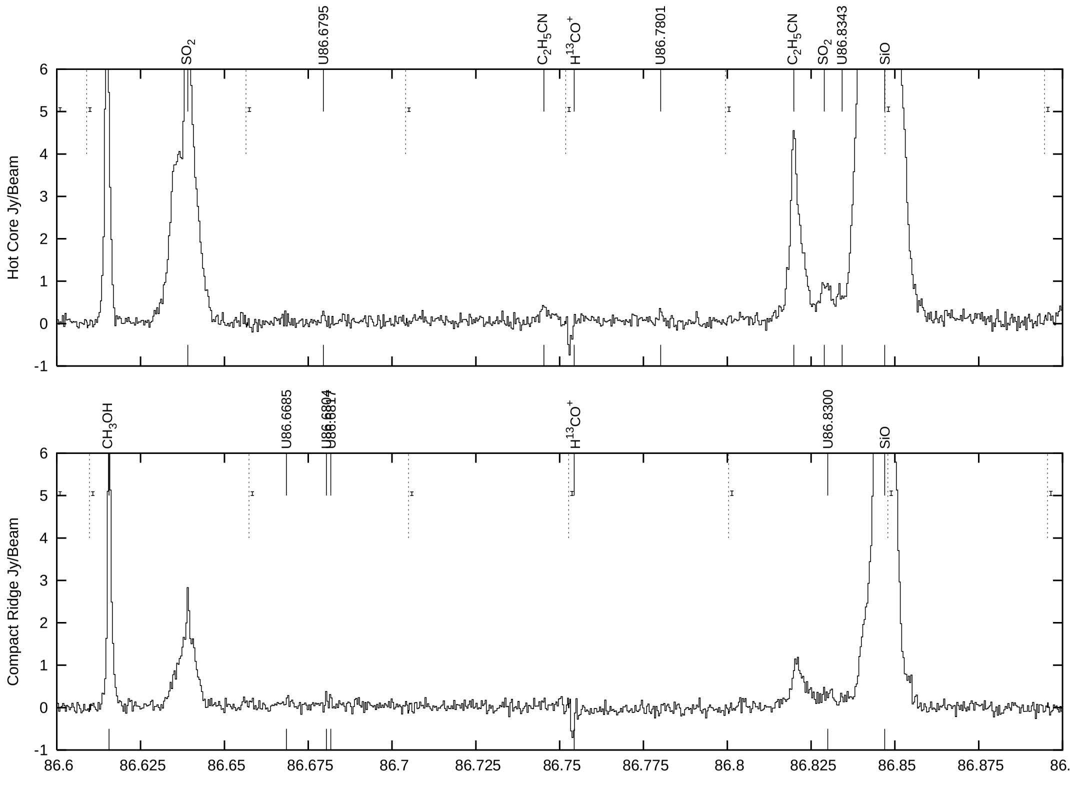

Fig. 4.23w

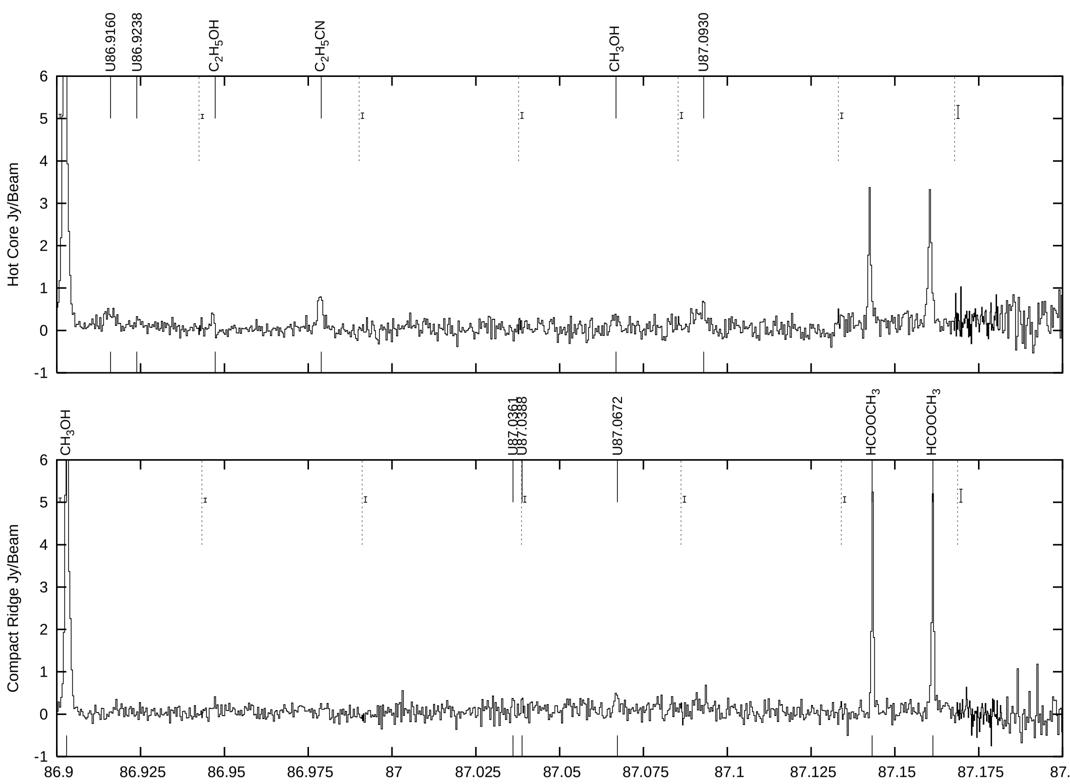

Fig. 4.23x

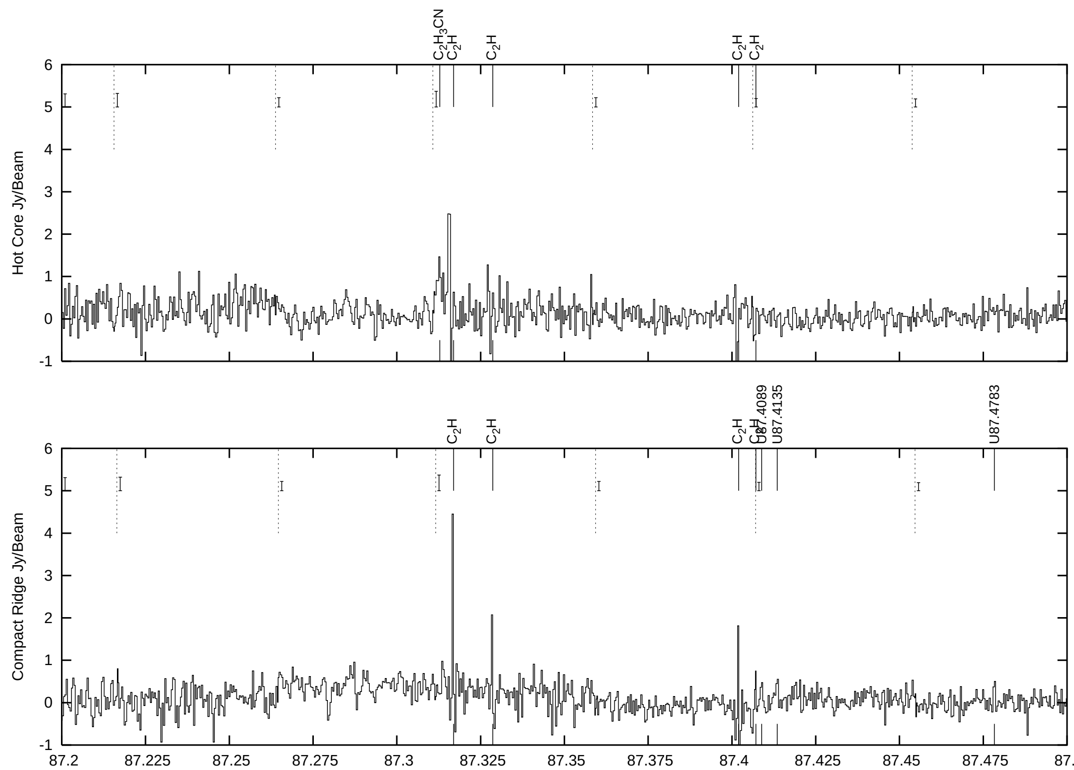

Fig. 4.23y

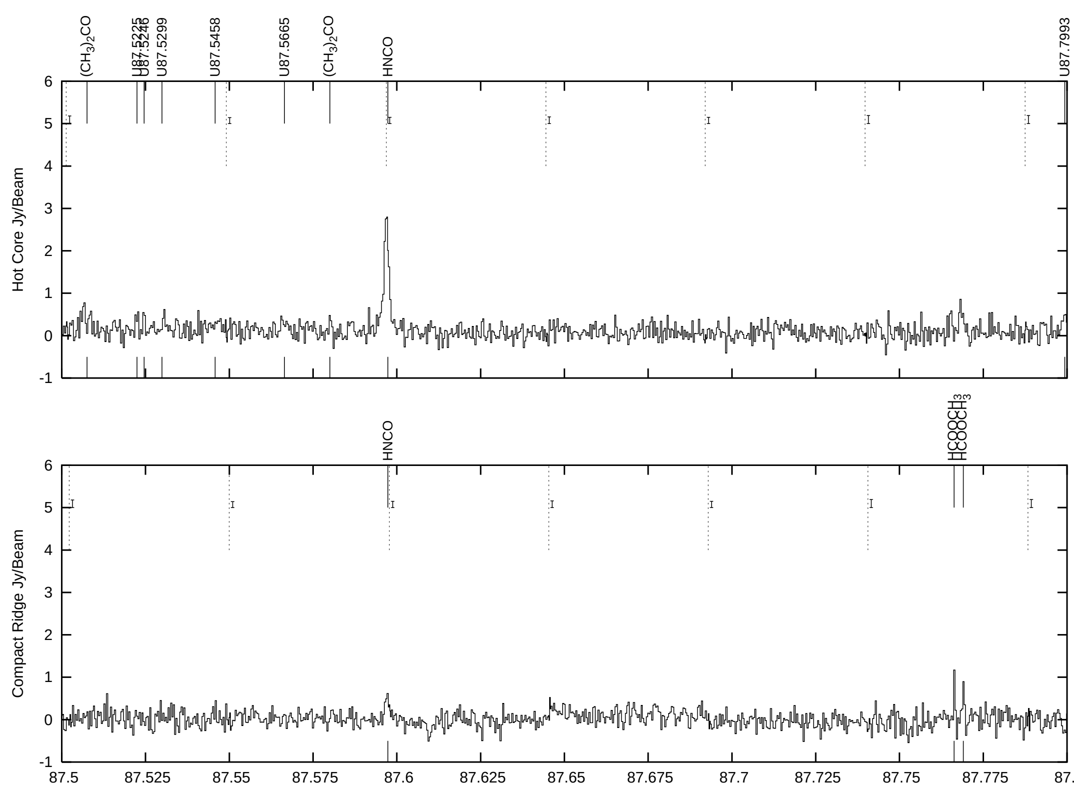

Fig. 4.23z

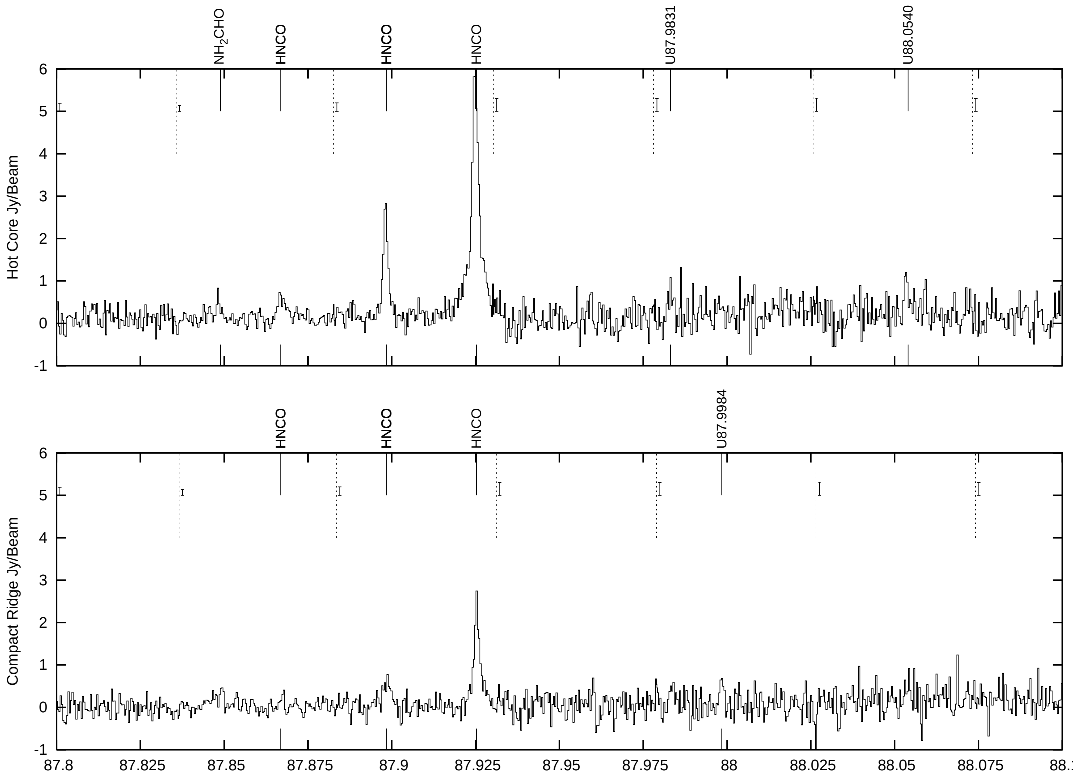

Fig. 4.23aa

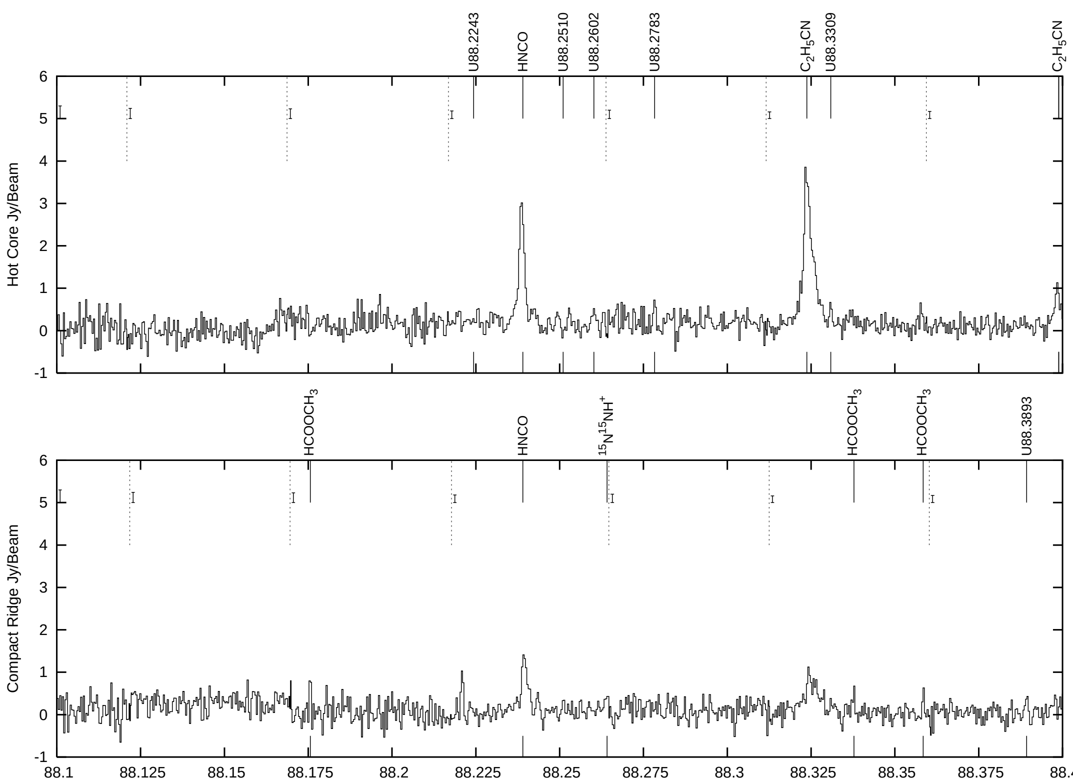

Fig. 4.23ab

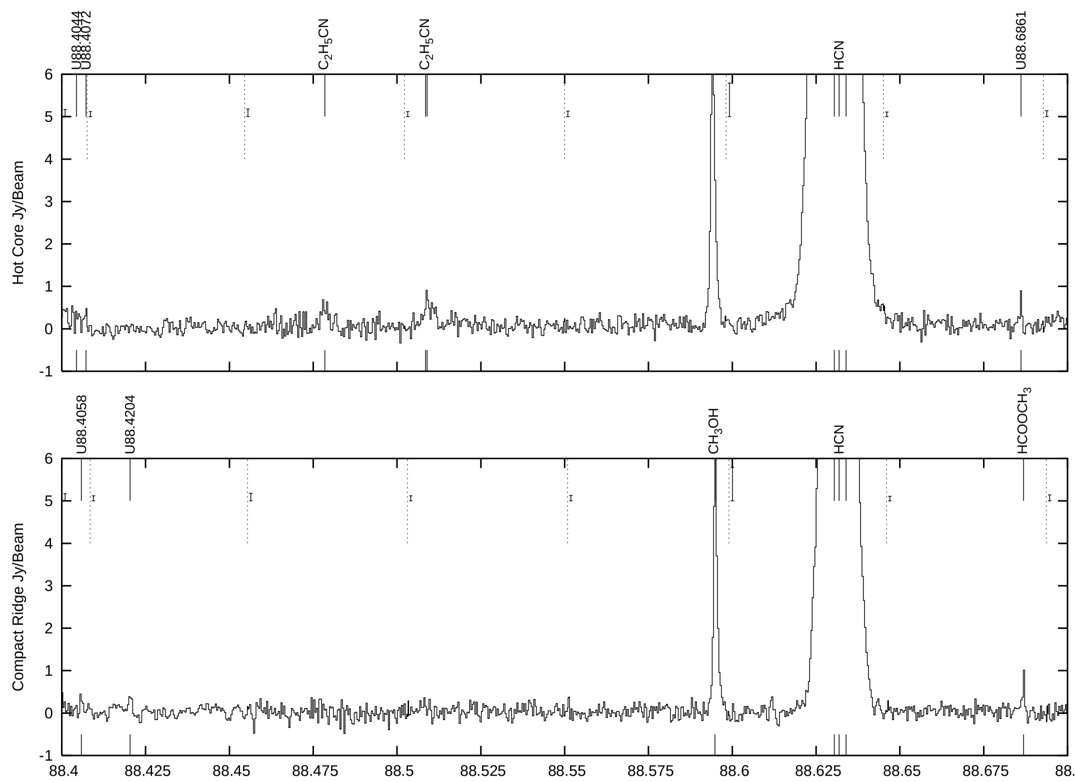

Fig. 4.23ac

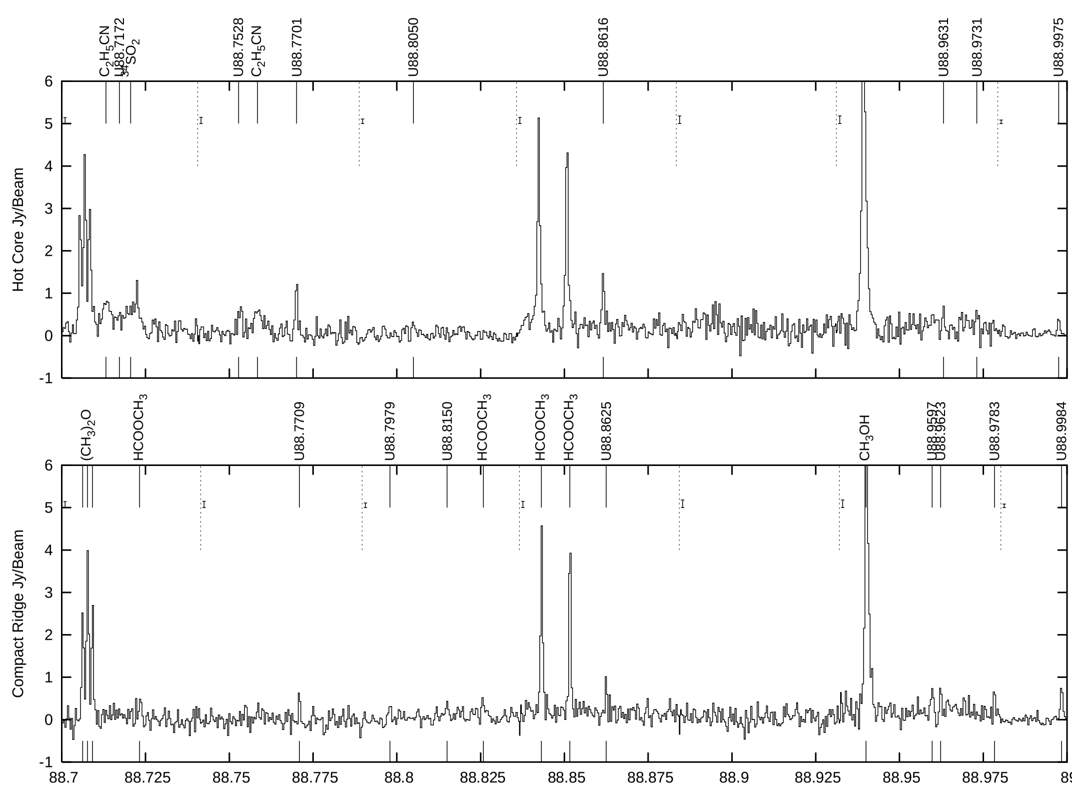

Fig. 4.23ad

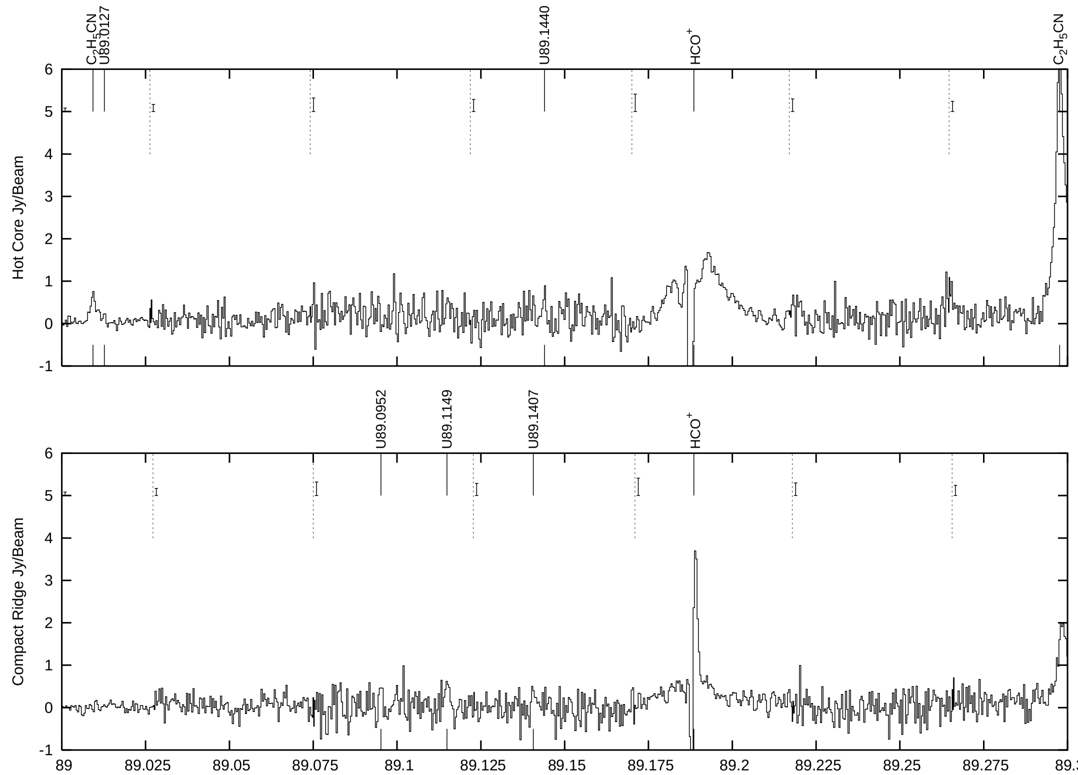

Fig. 4.23ae

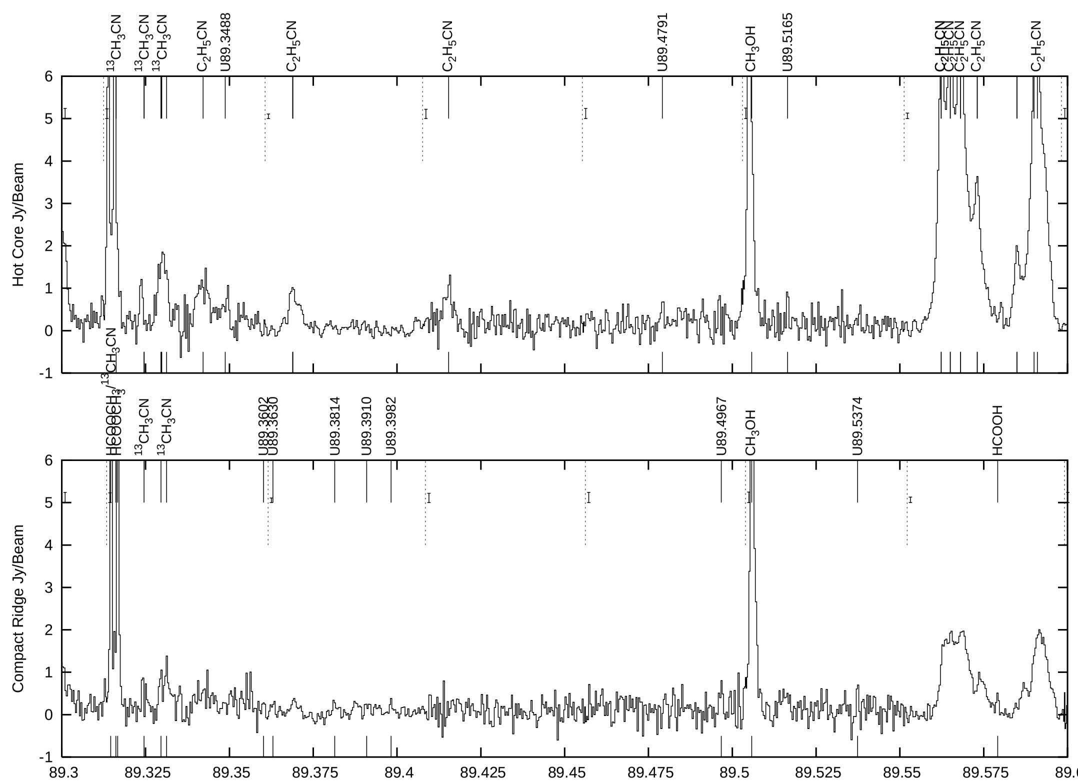

Fig. 4.23af

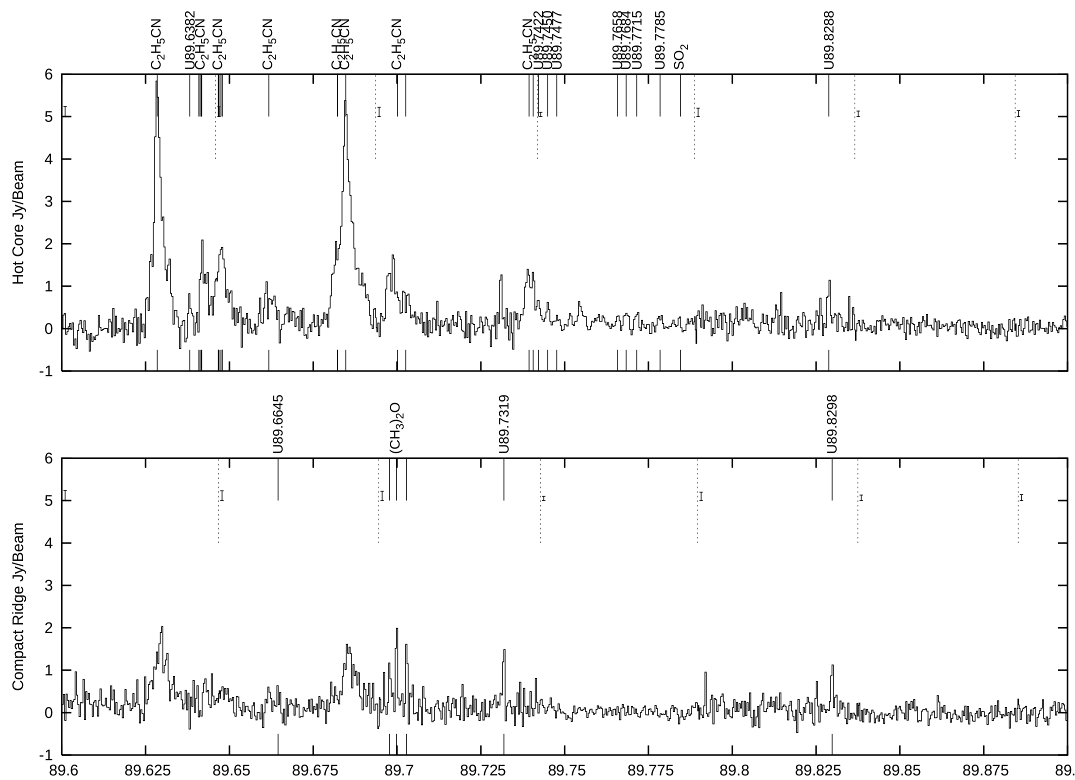

Fig. 4.23ag

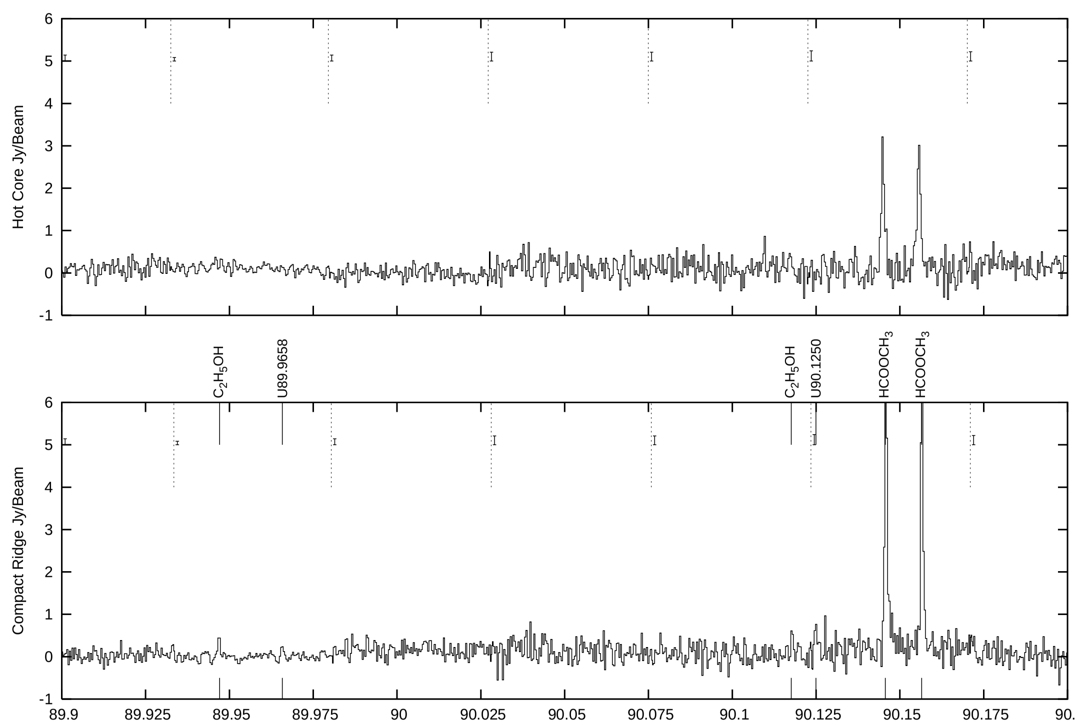

Fig. 4.23ah

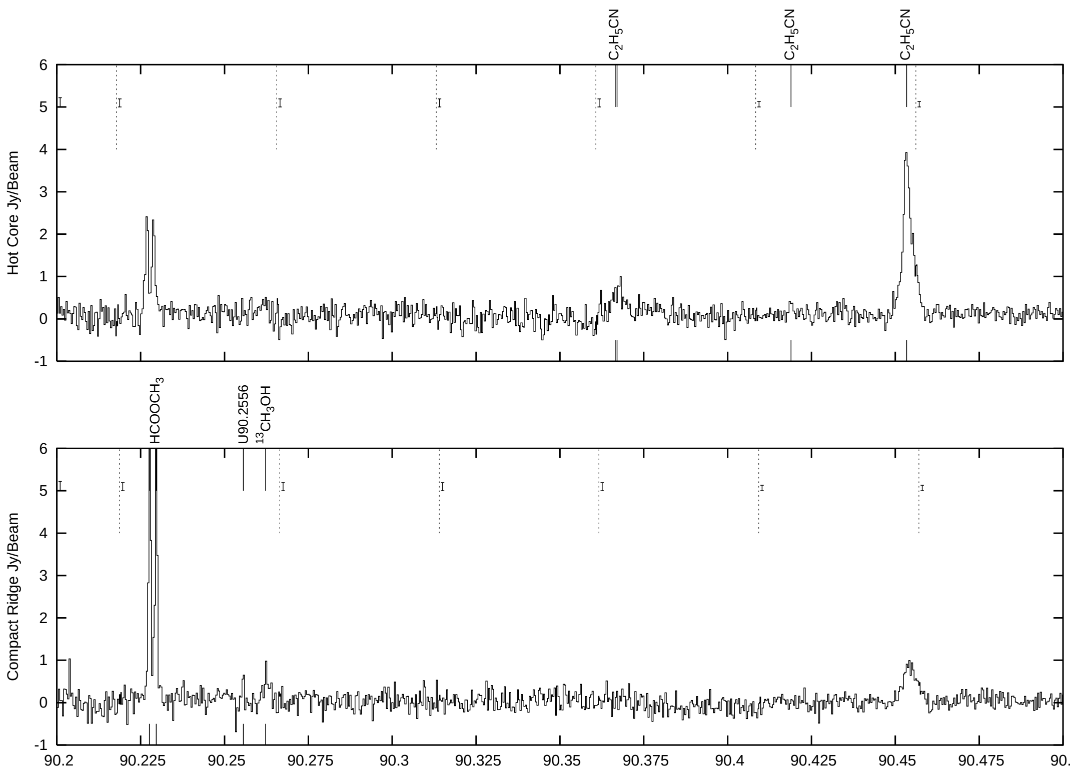

Fig. 4.23ai

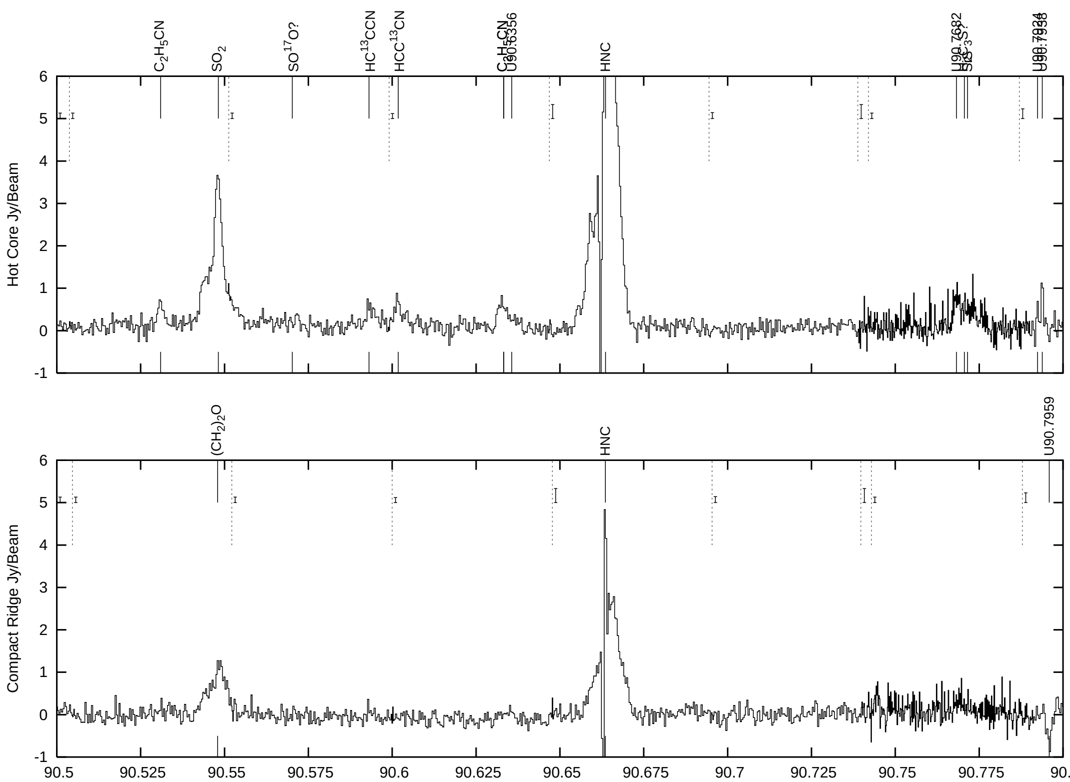

Fig. 4.23aj

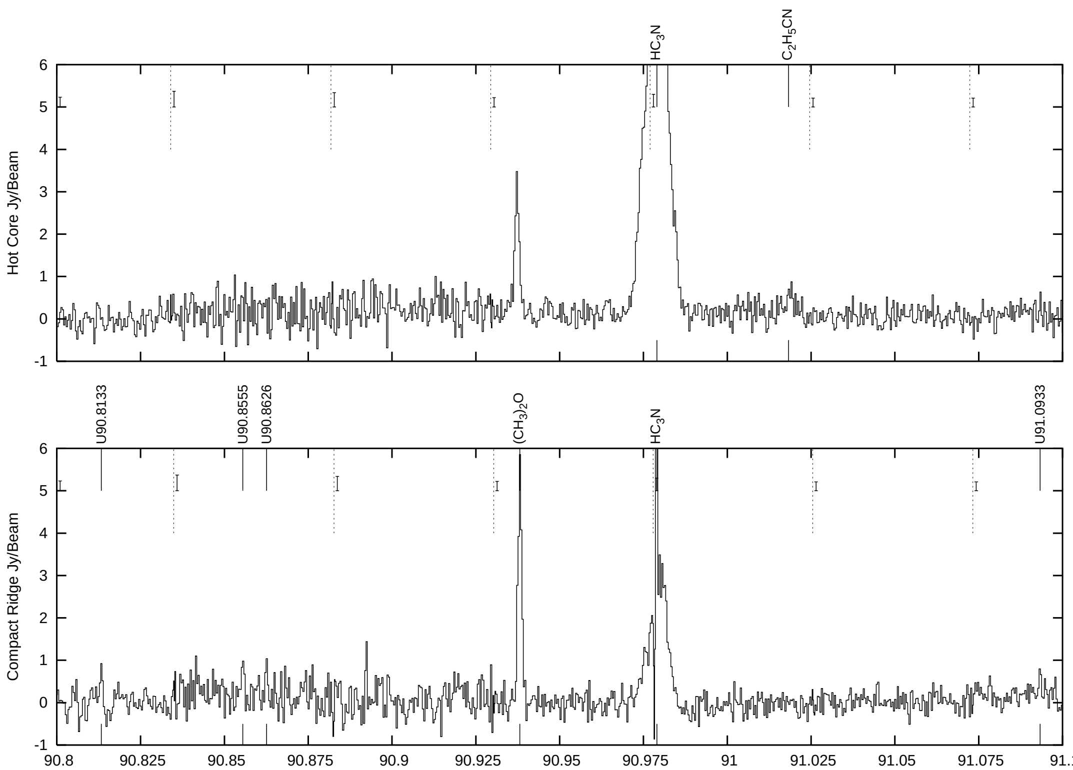

Fig. 4.23ak

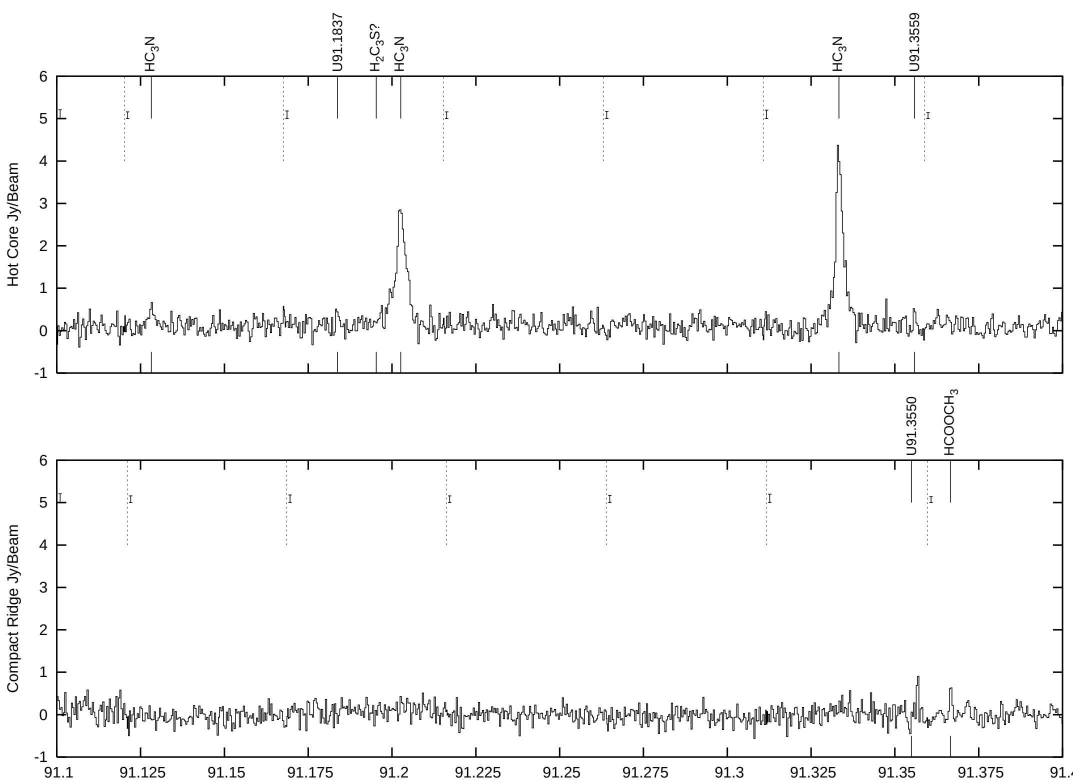

Fig. 4.23al

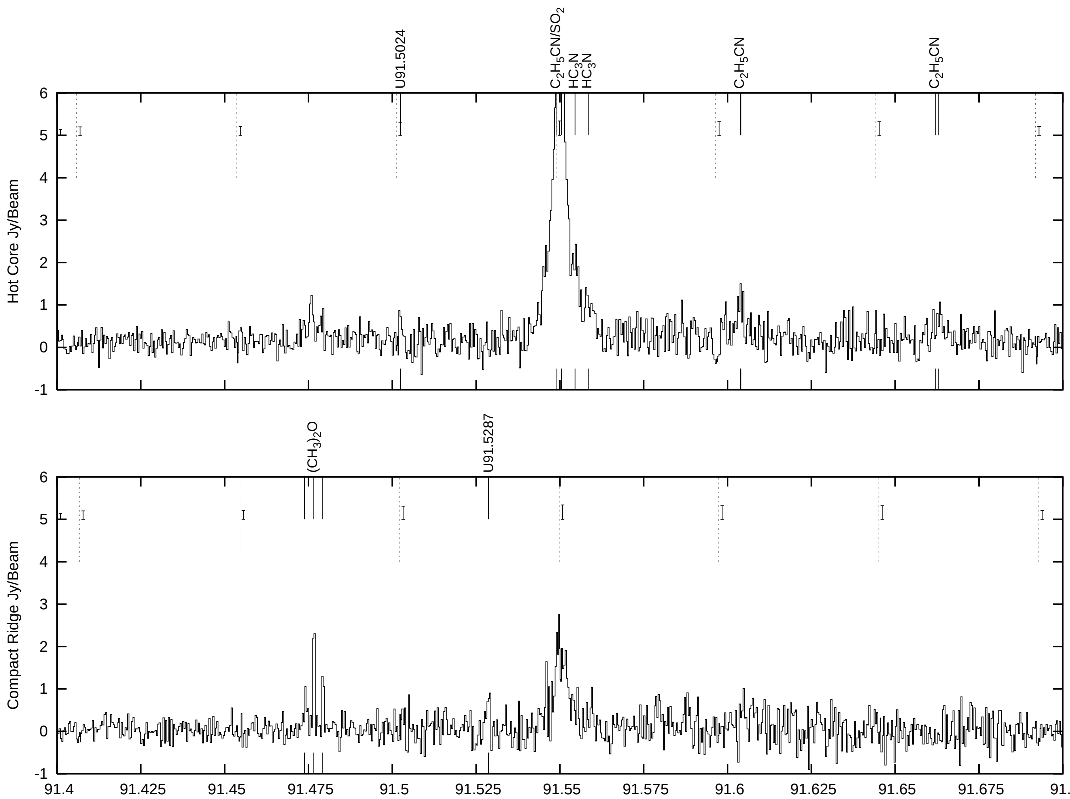

Fig. 4.23am

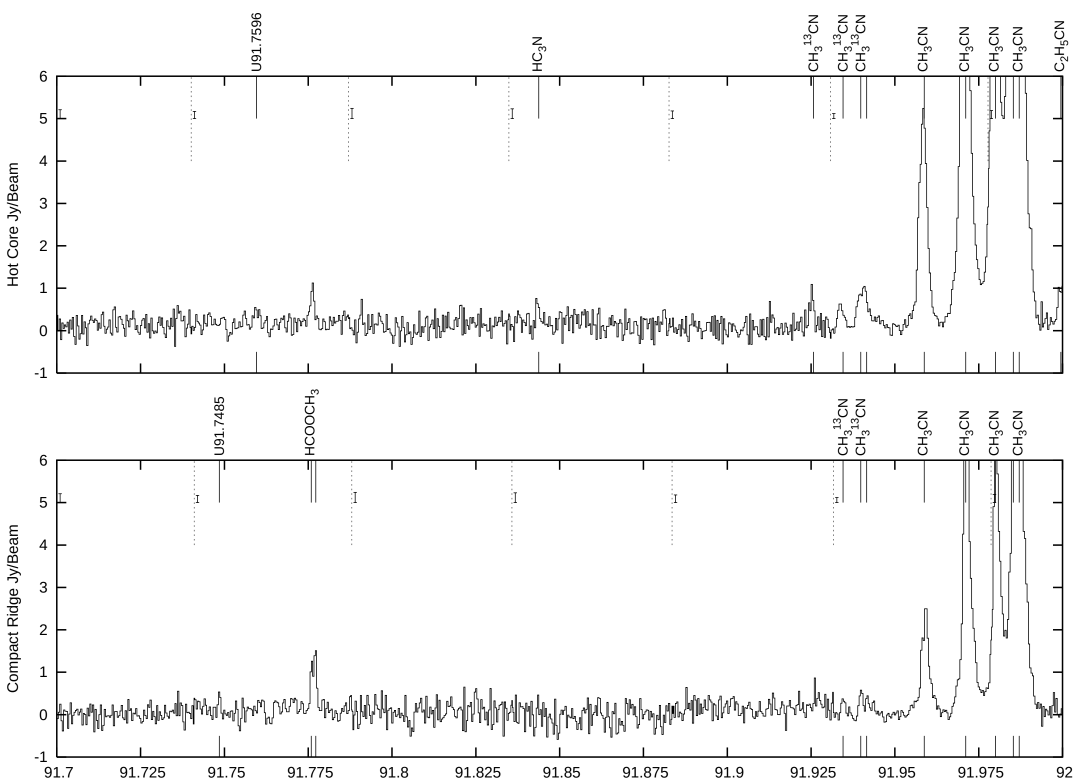

Fig. 4.23an

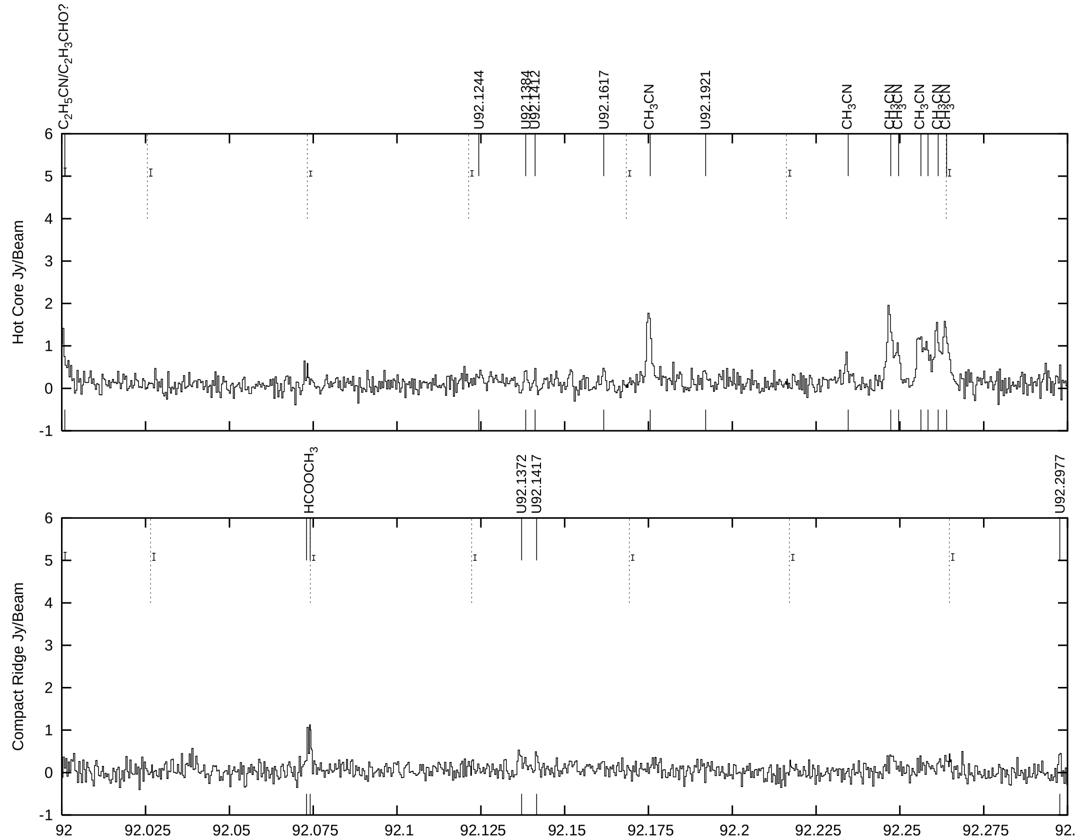

Fig. 4.23ao

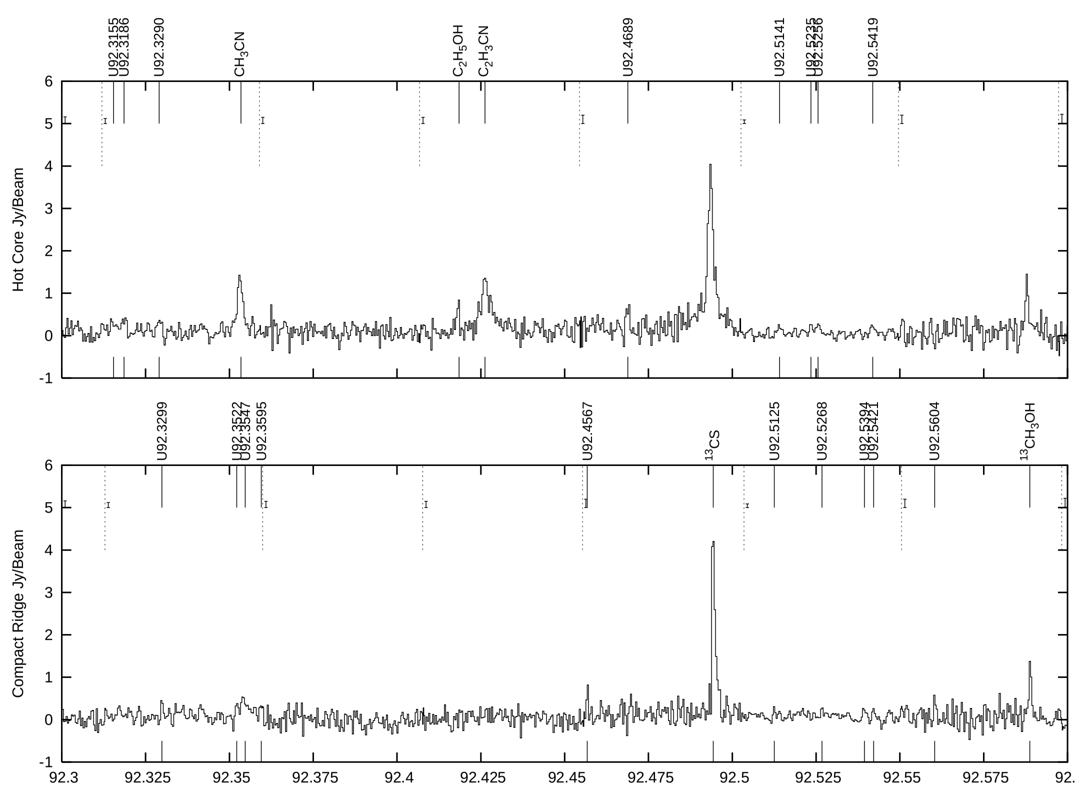

Fig. 4.23ap

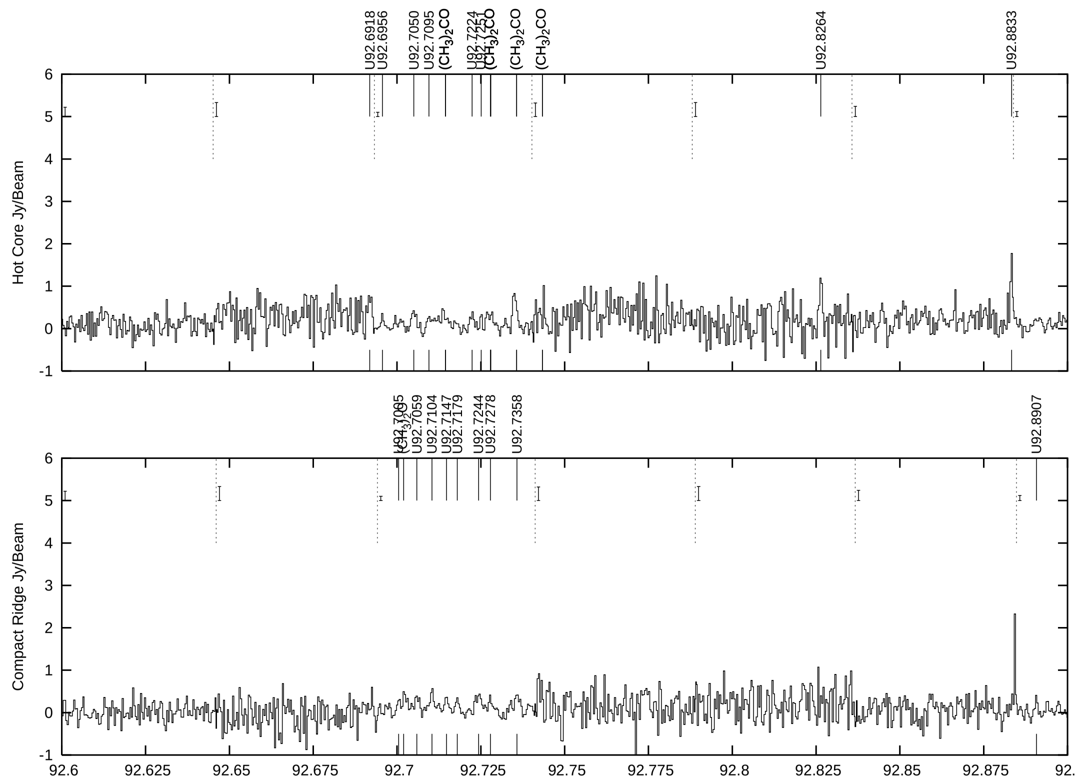

Fig. 4.23aq

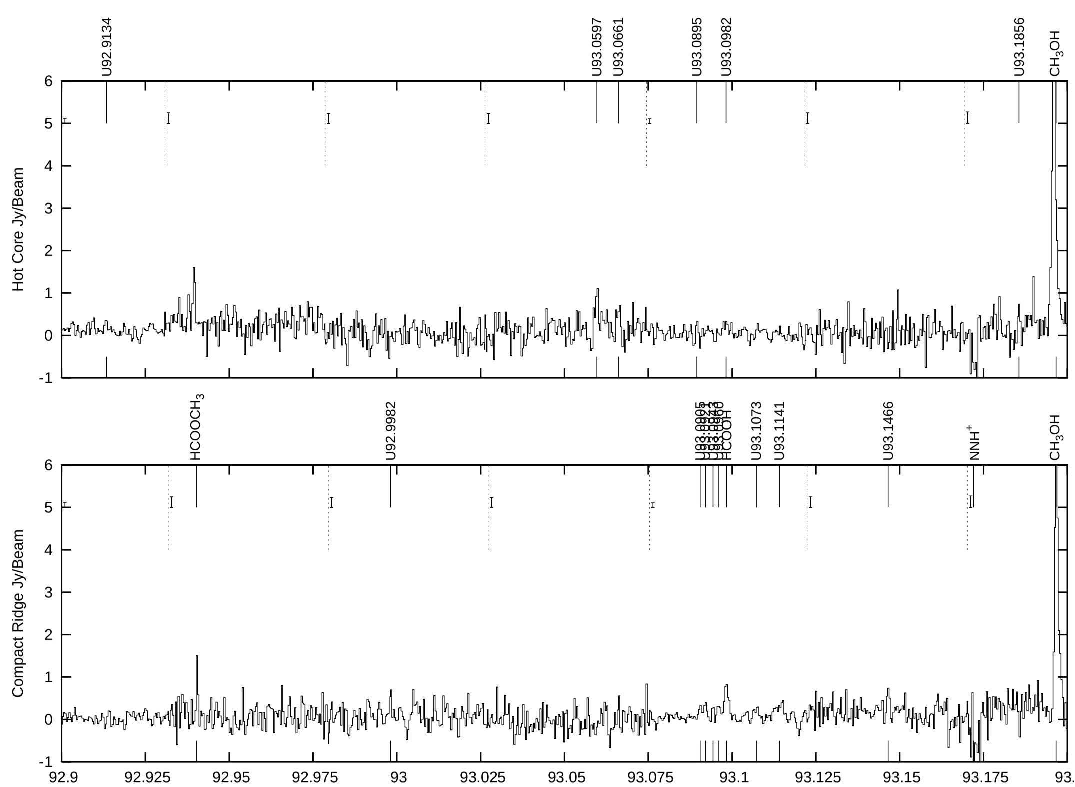

Fig. 4.23ar

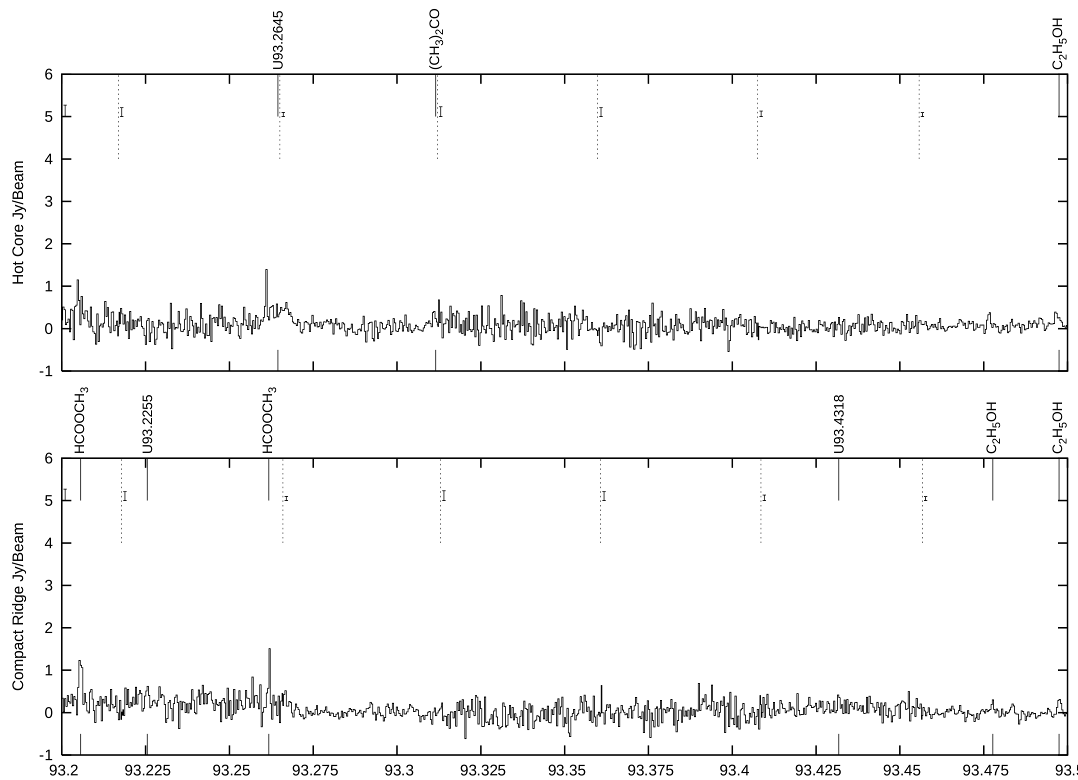

Fig. 4.23as

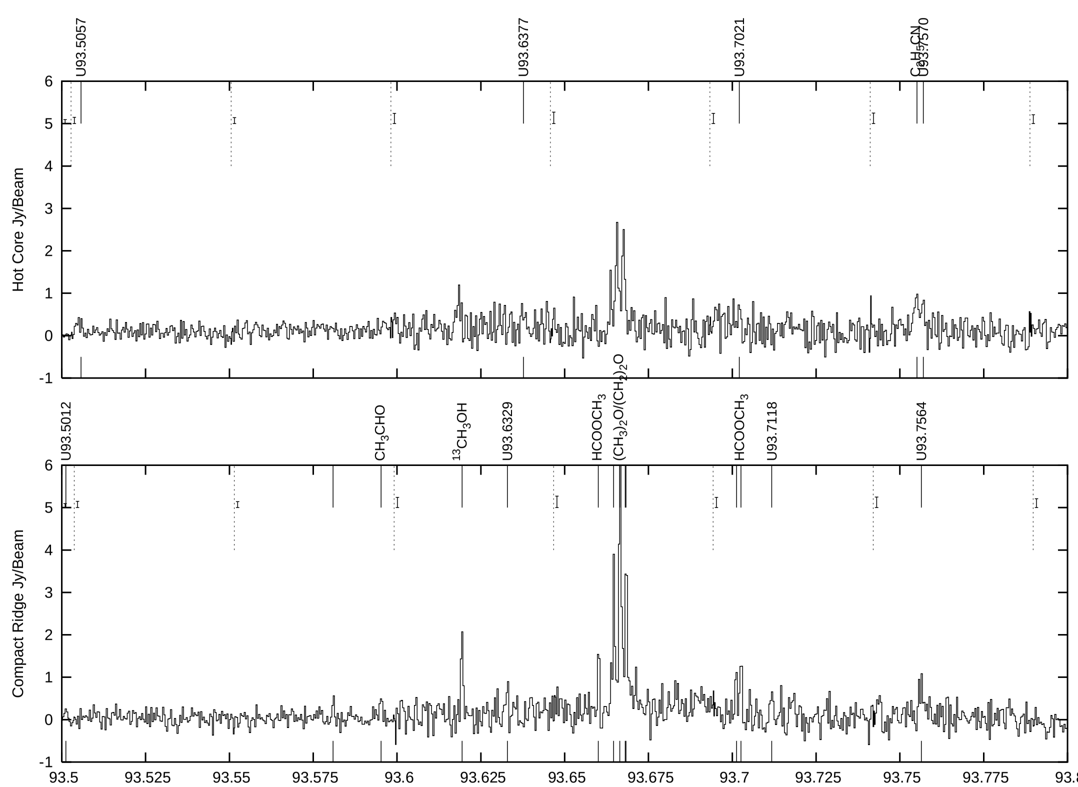

Fig. 4.23at

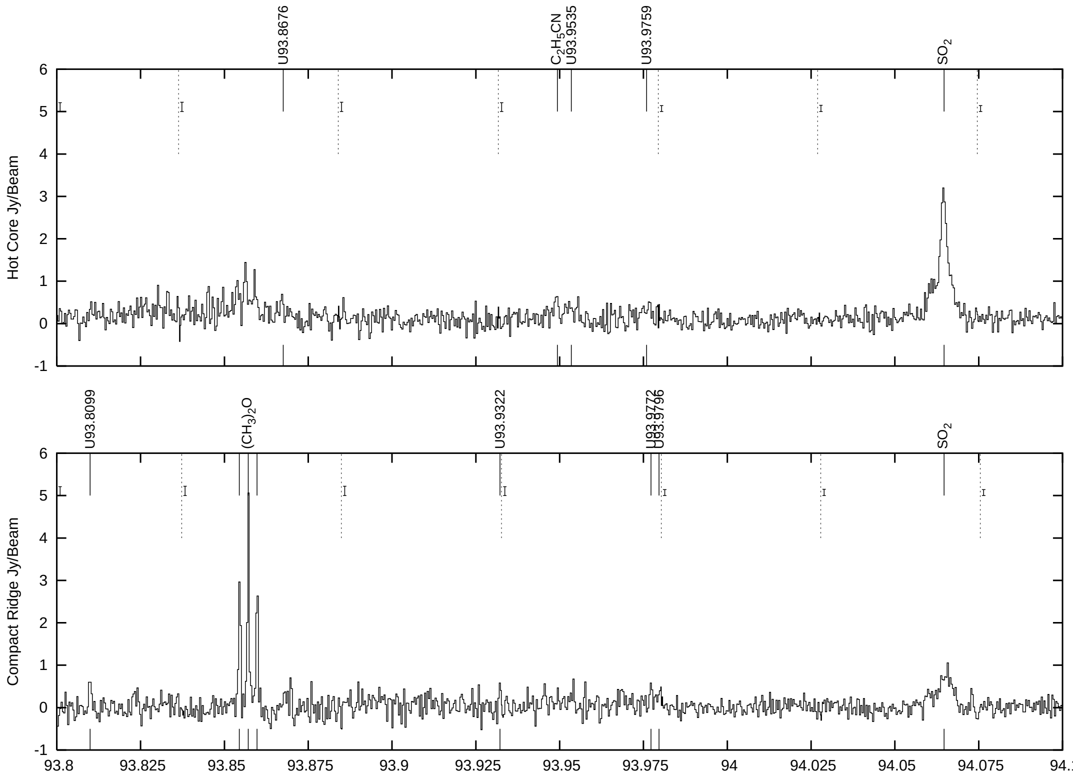

Fig. 4.23au

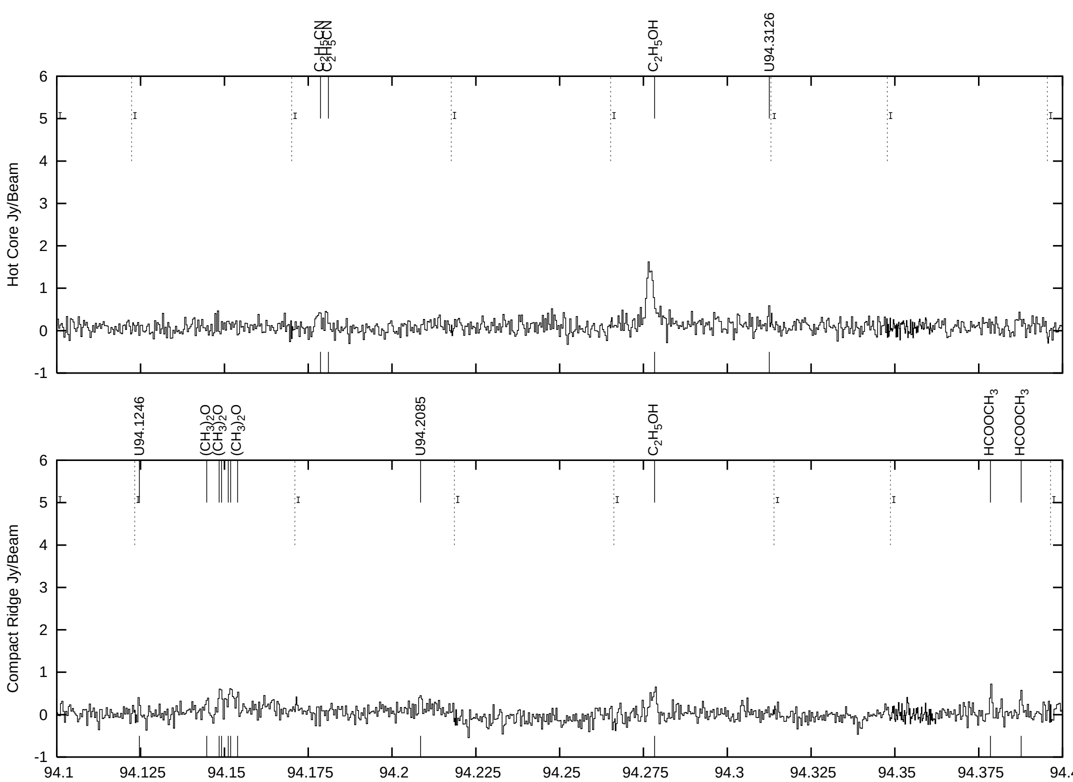

Fig. 4.23av

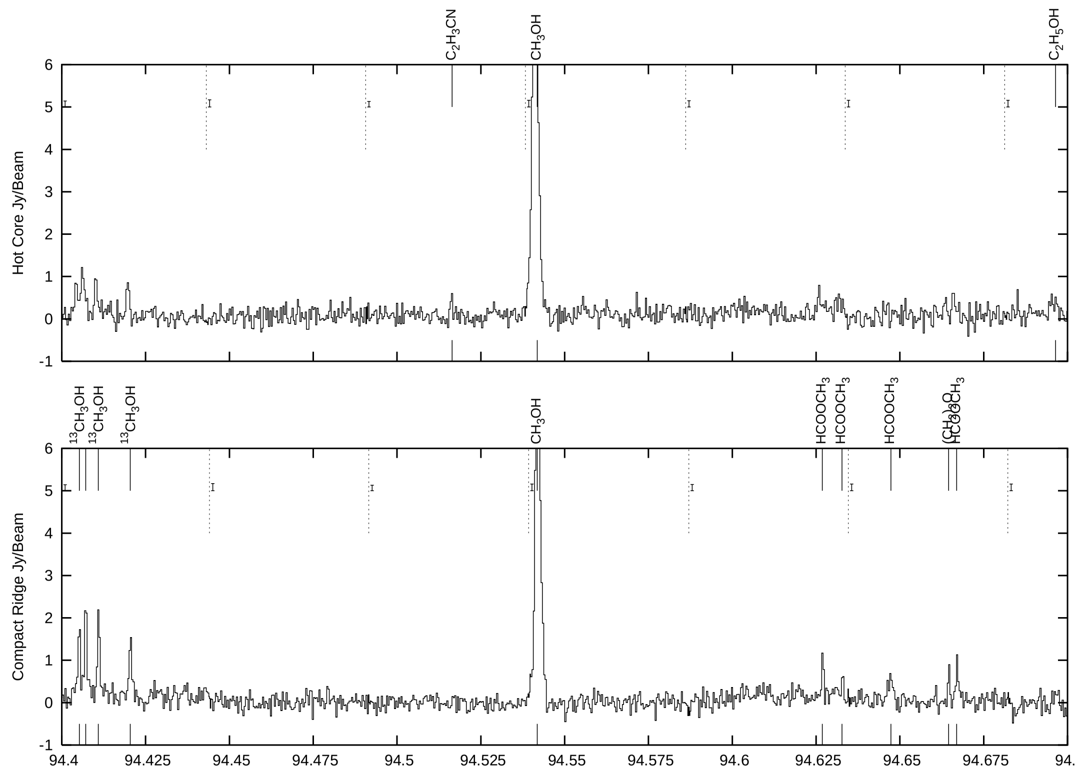

Fig. 4.23aw

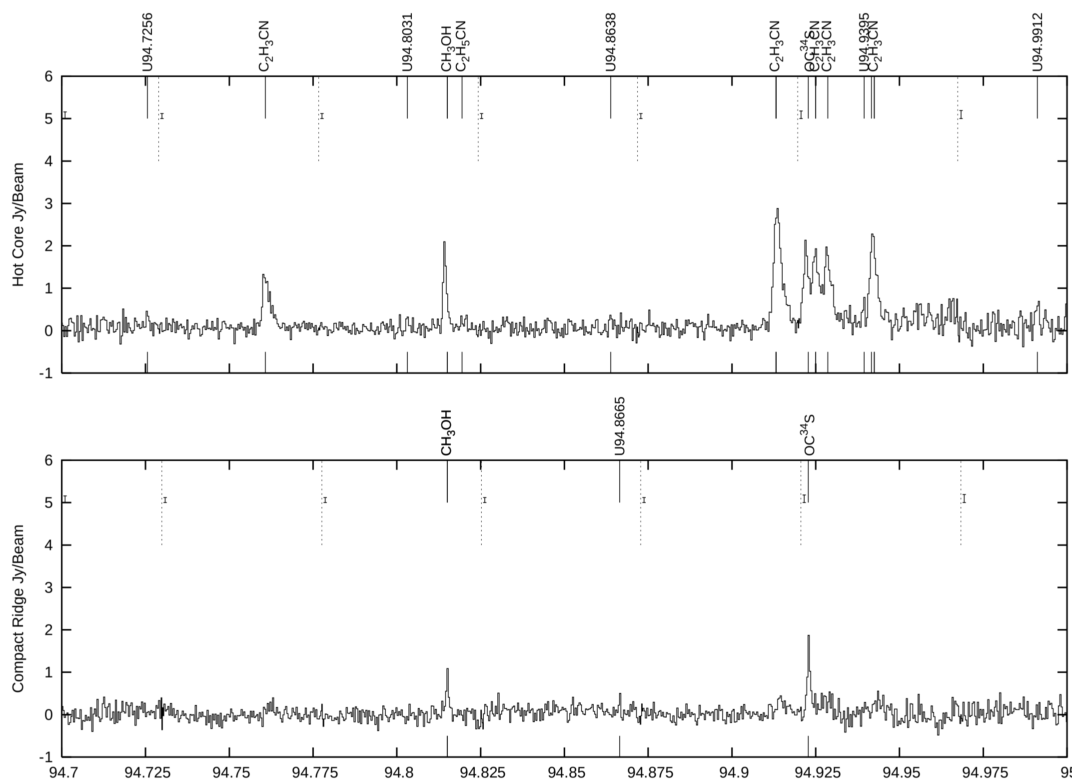

Fig. 4.23ax

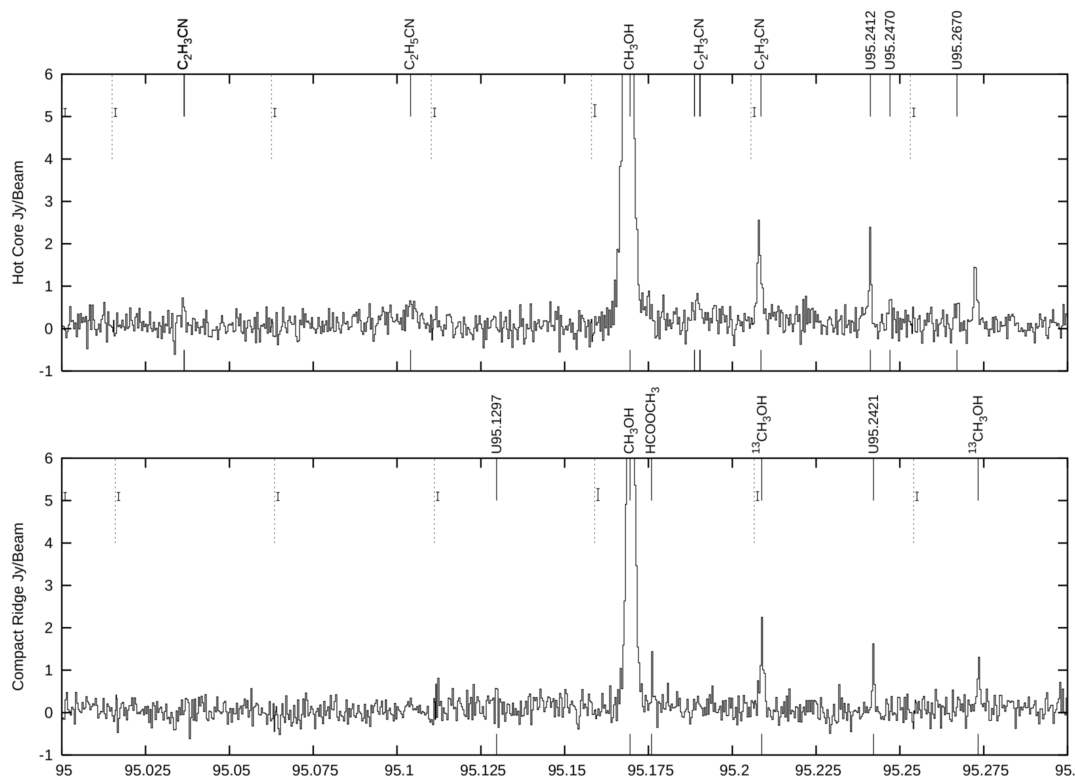

Fig. 4.23ay

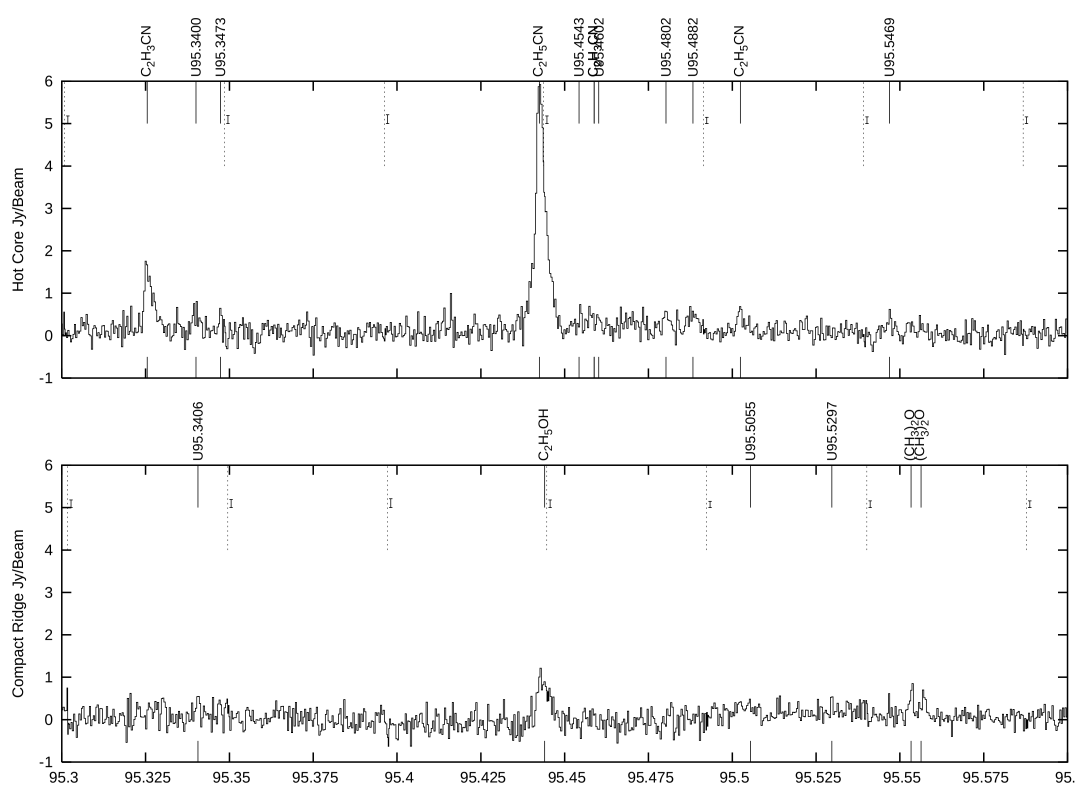

Fig. 4.23az

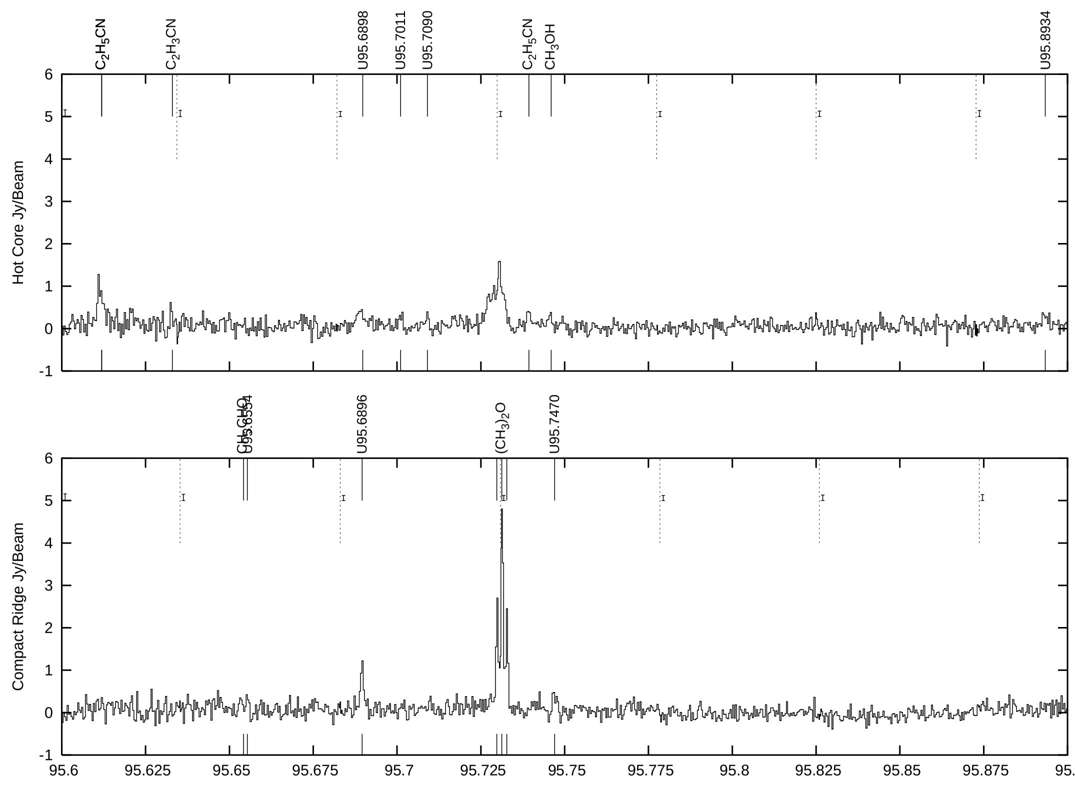

Fig. 4.23ba

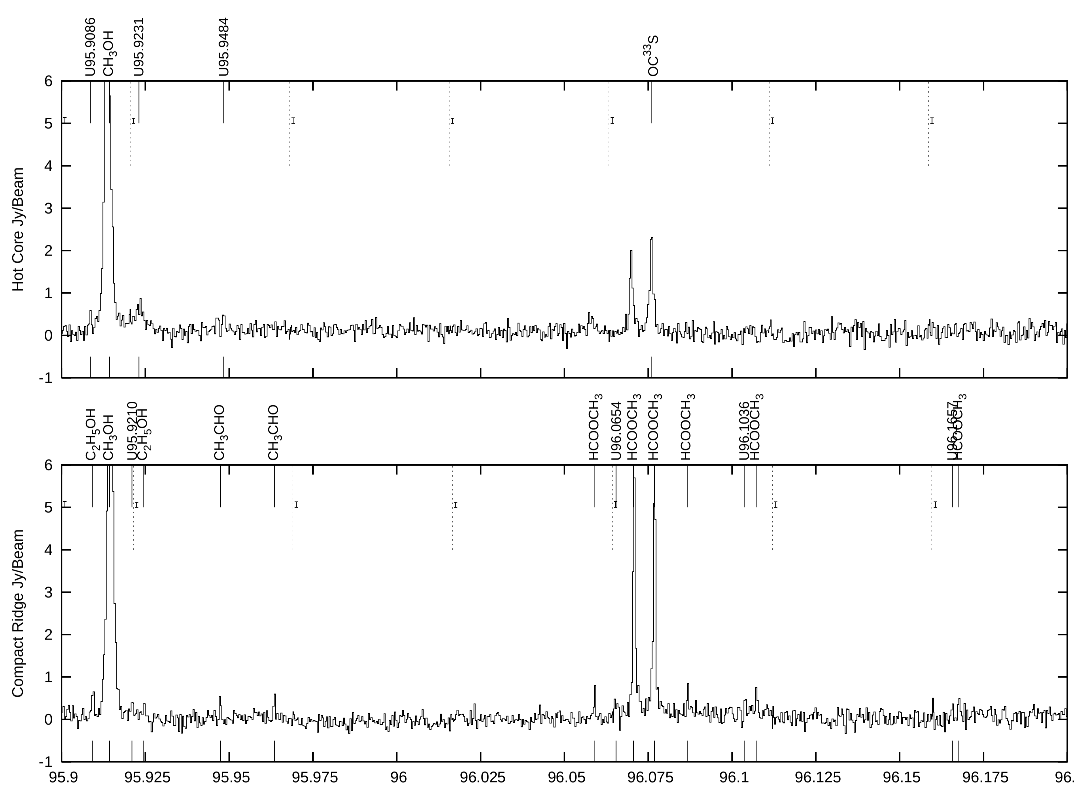

Fig. 4.23bb

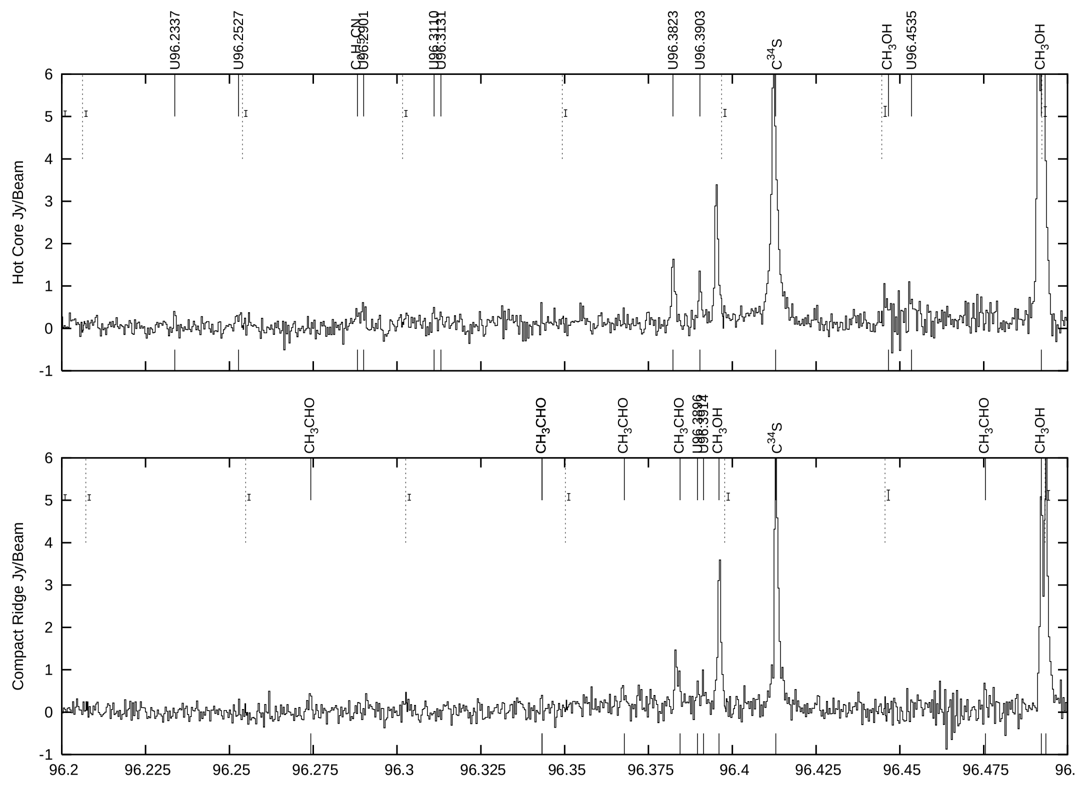

Fig. 4.23bc

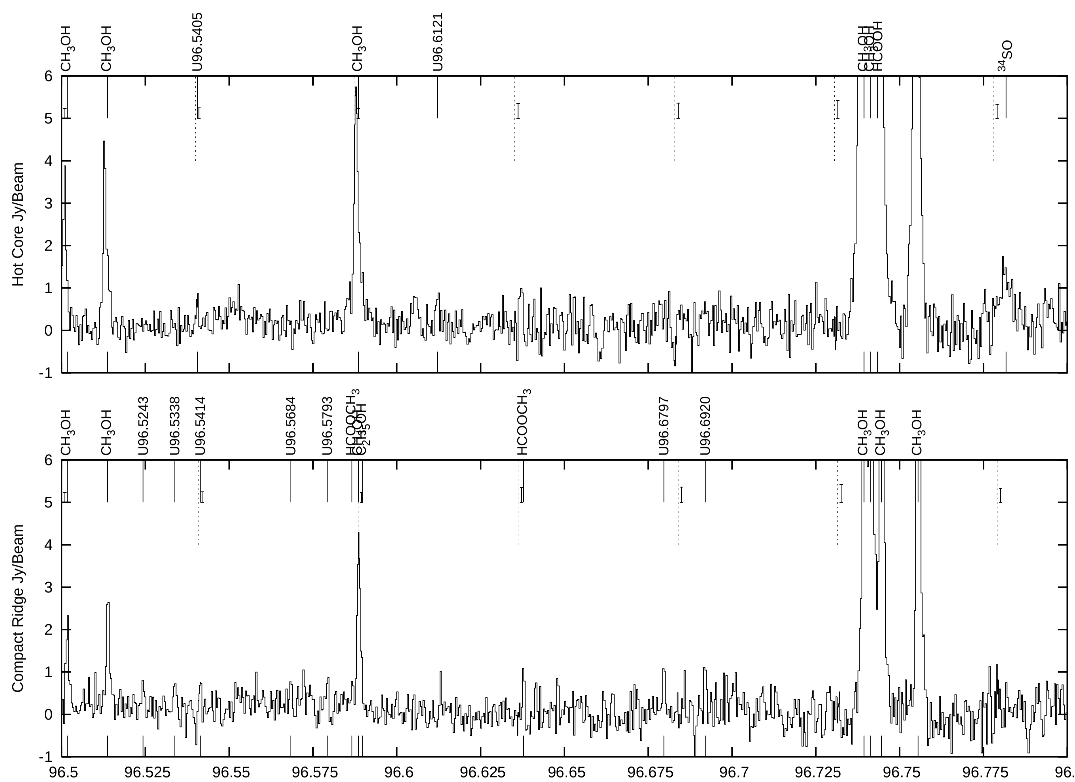

Fig. 4.23bd

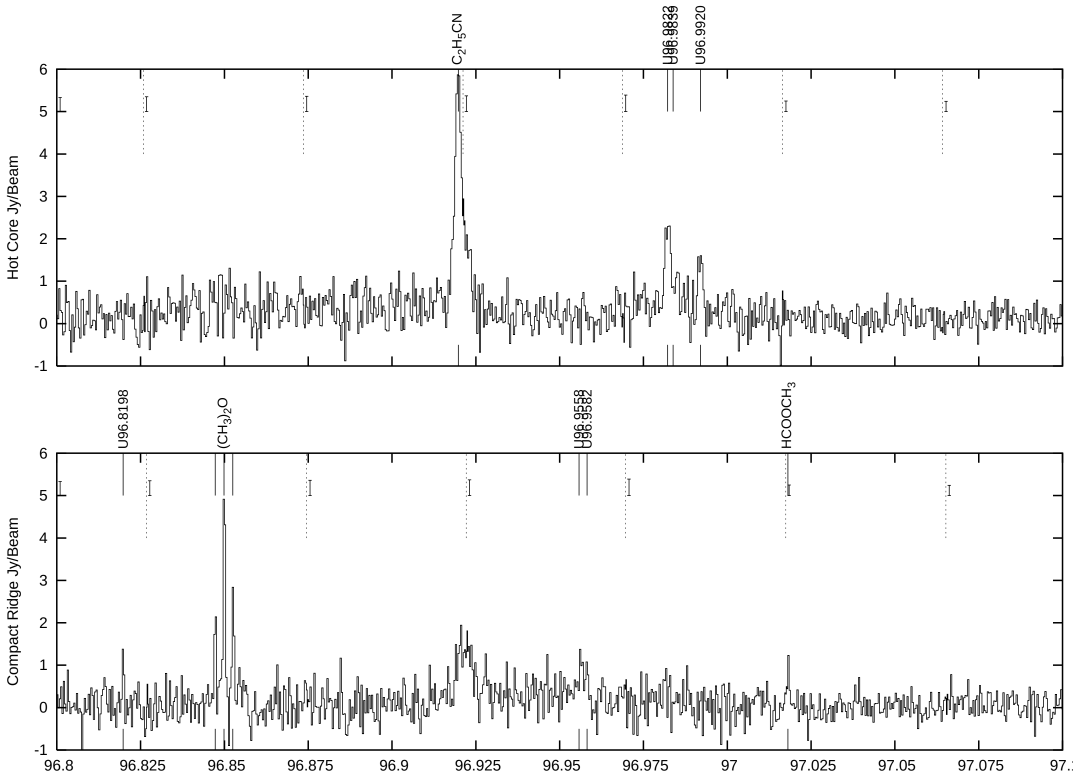

Fig. 4.23be

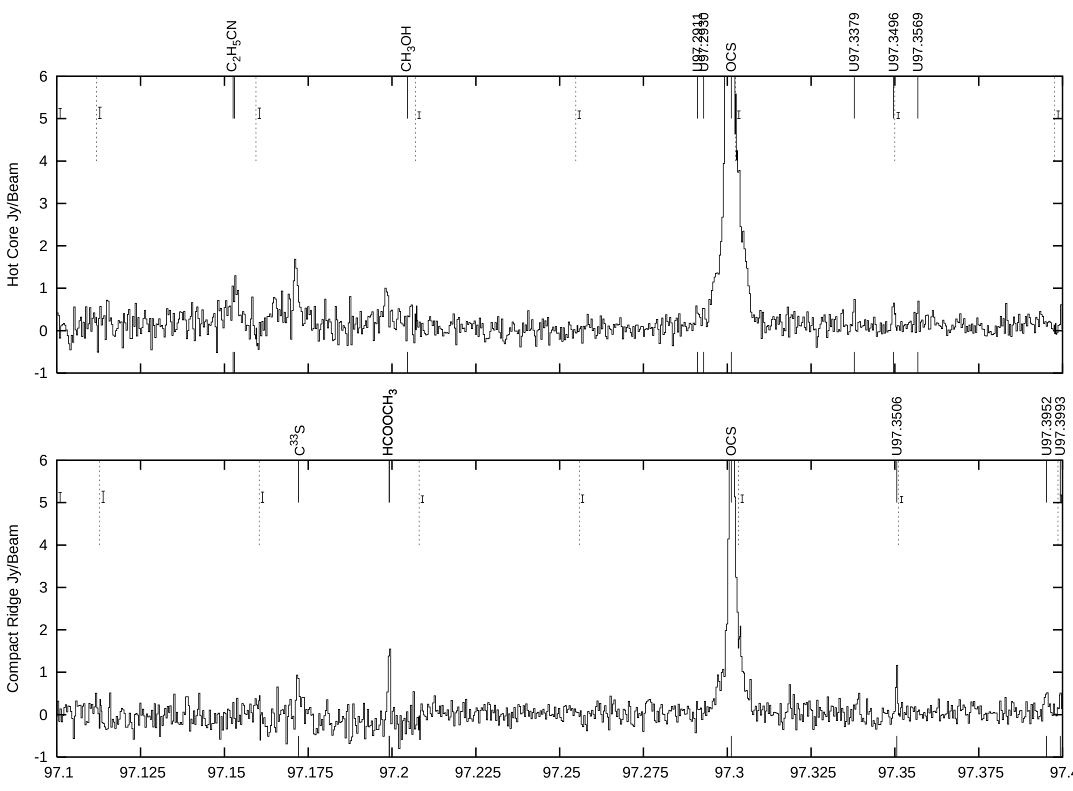

Fig. 4.23bf

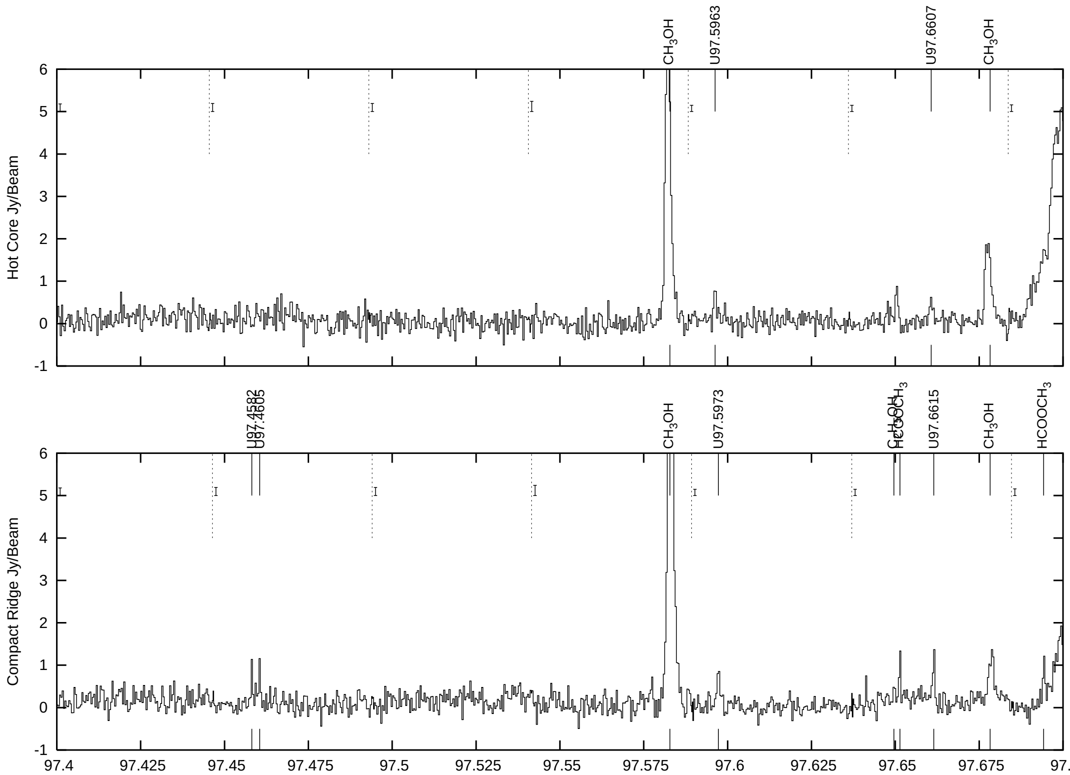

Fig. 4.23bg

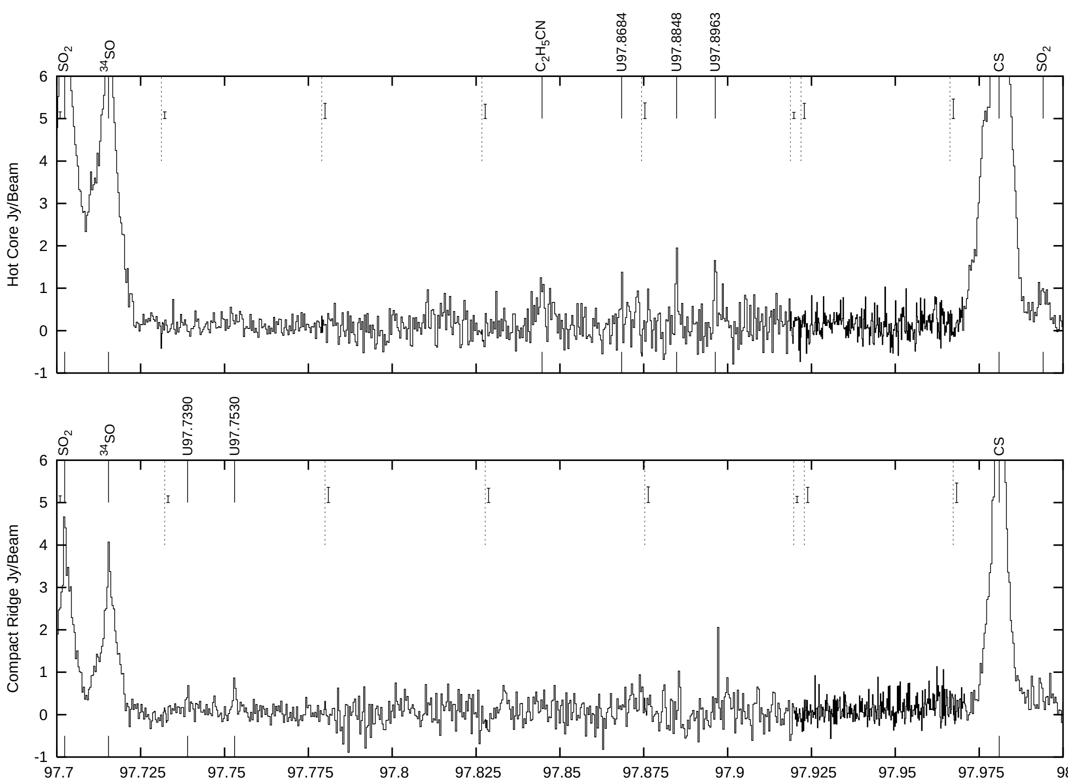

Fig. 4.23bh

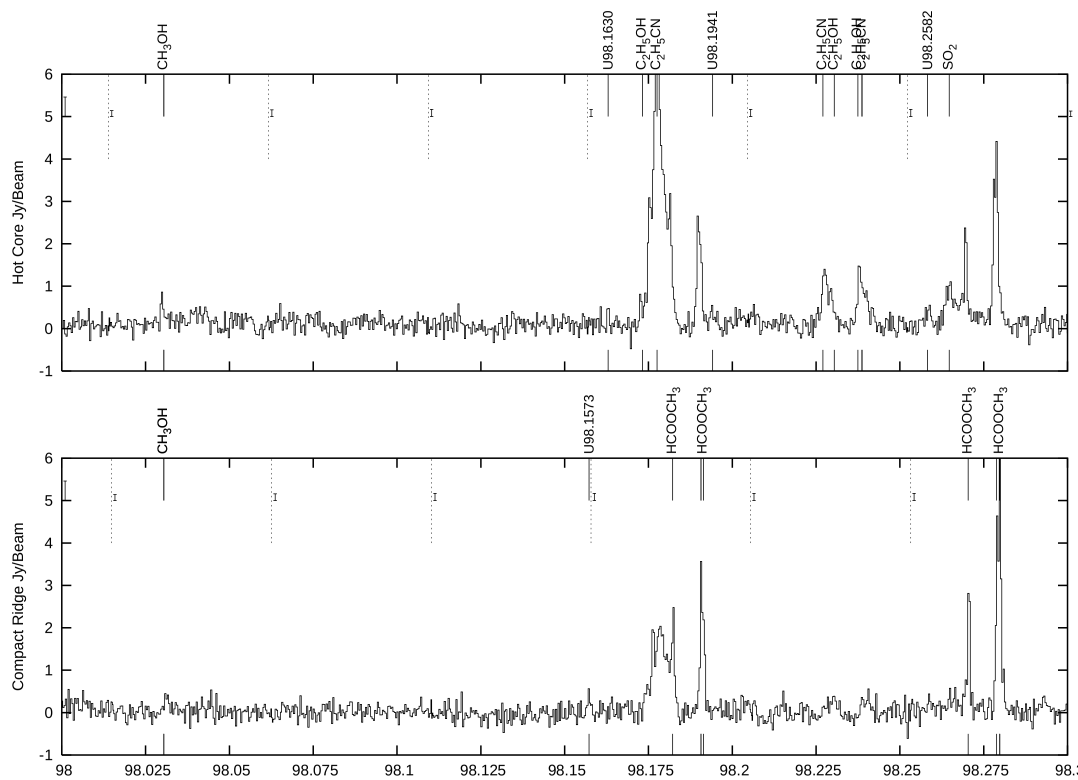

Fig. 4.23bi

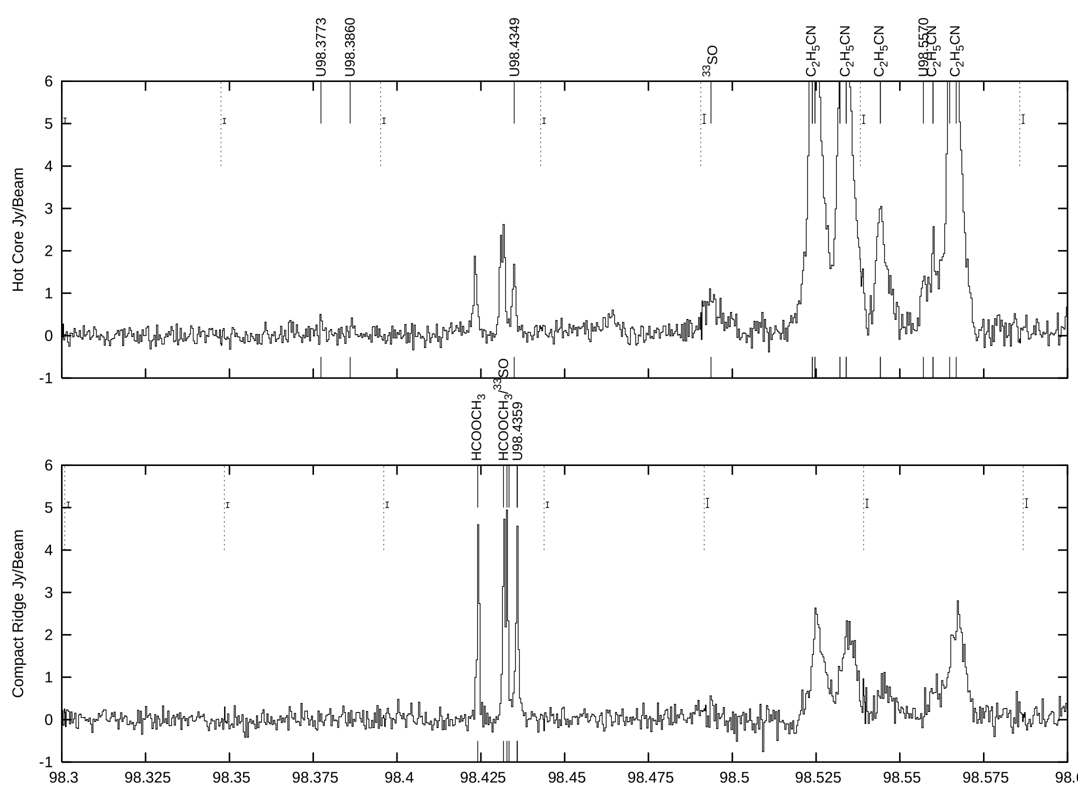

Fig. 4.23bj

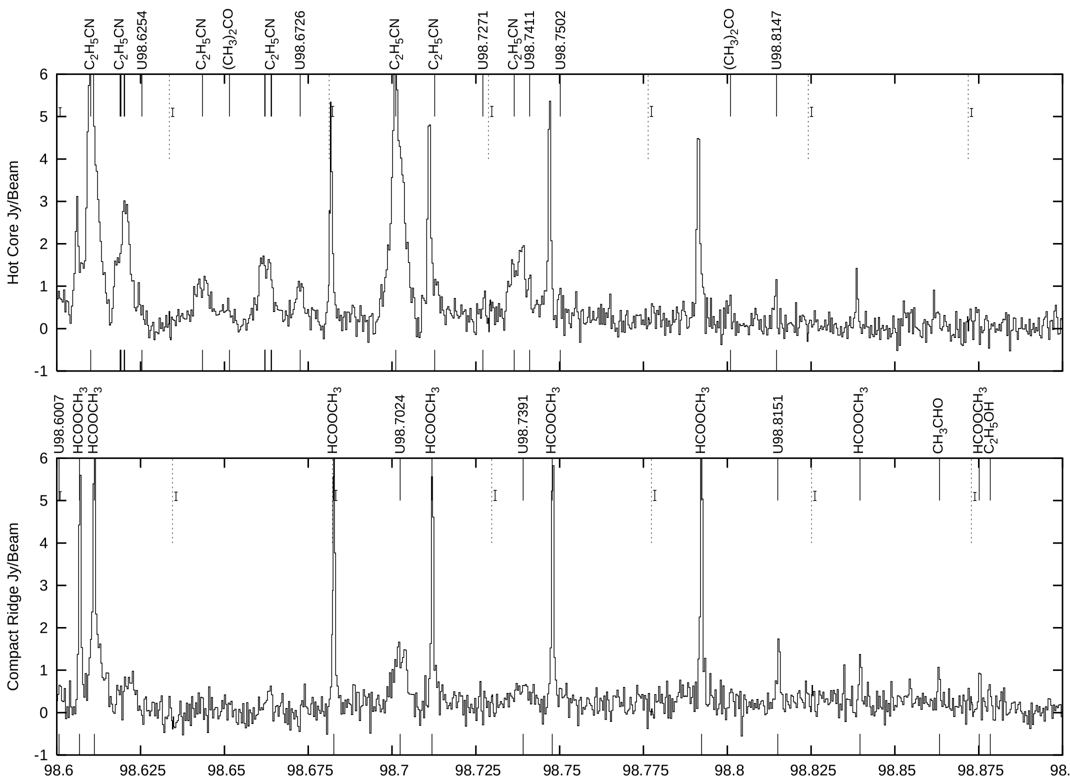

Fig. 4.23bk

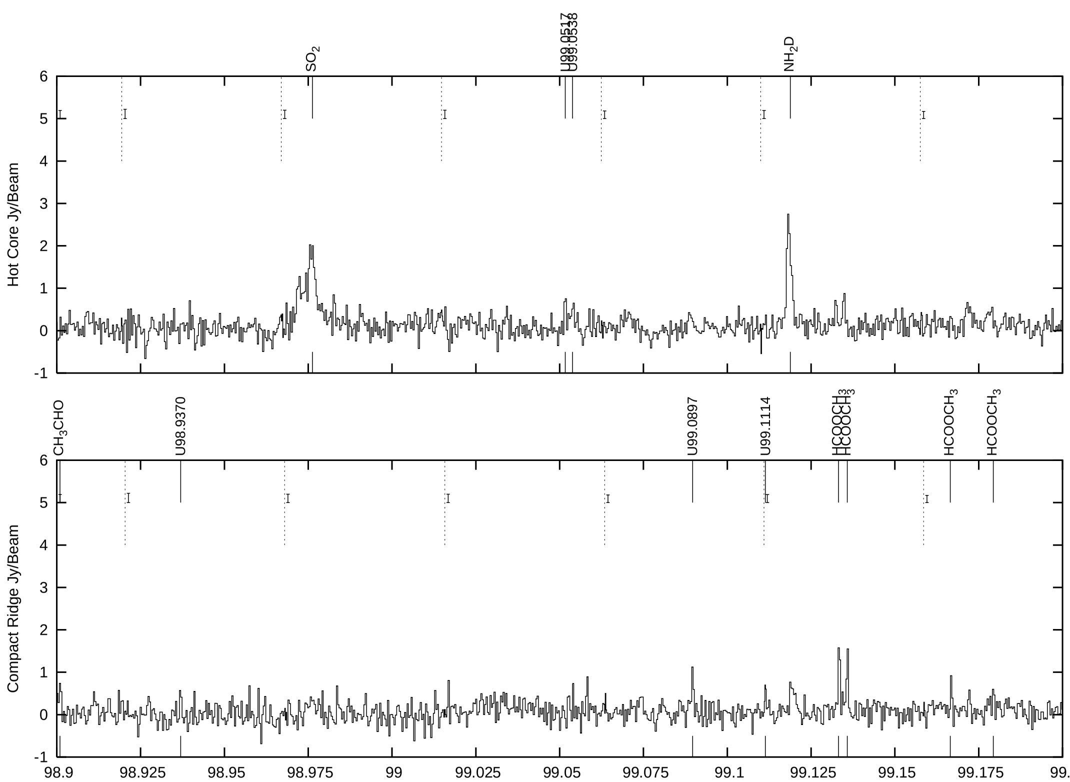

Fig. 4.23bl

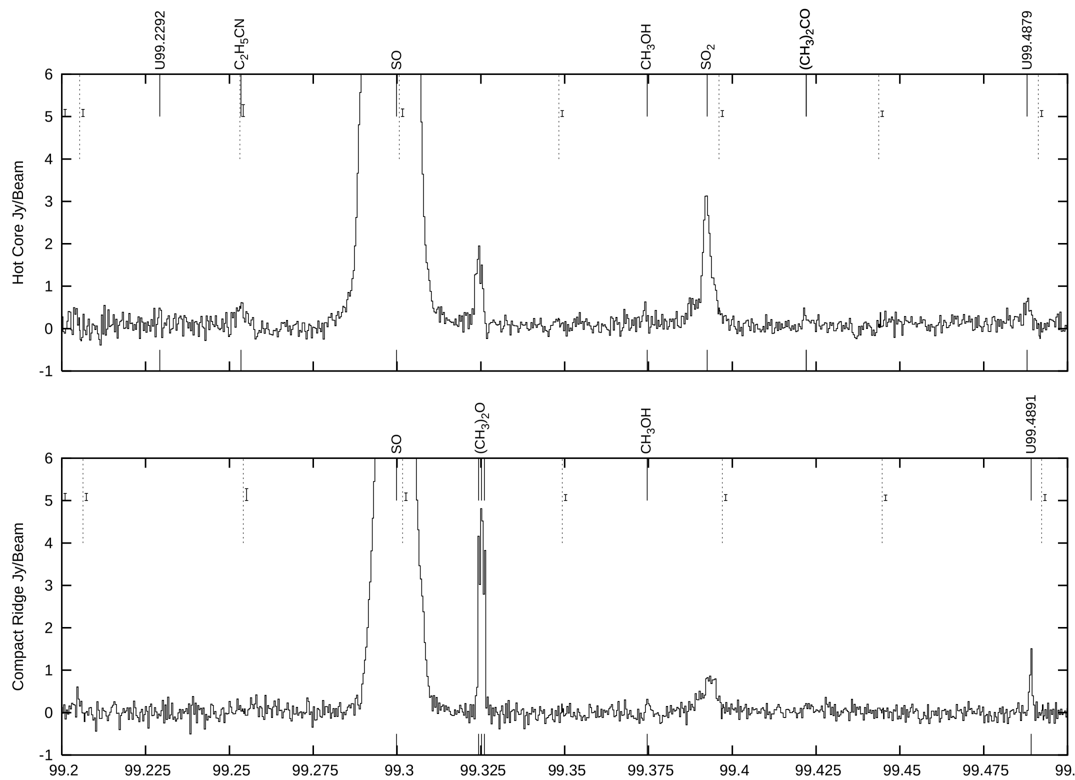

Fig. 4.23bm

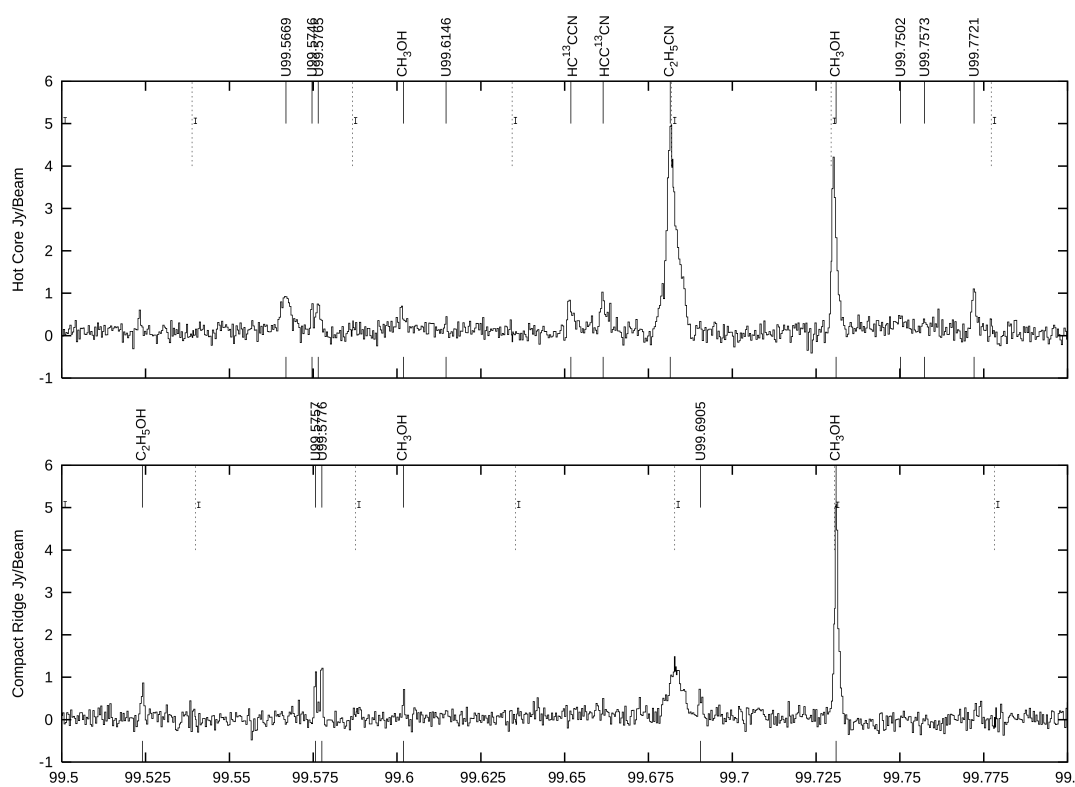

Fig. 4.23bn

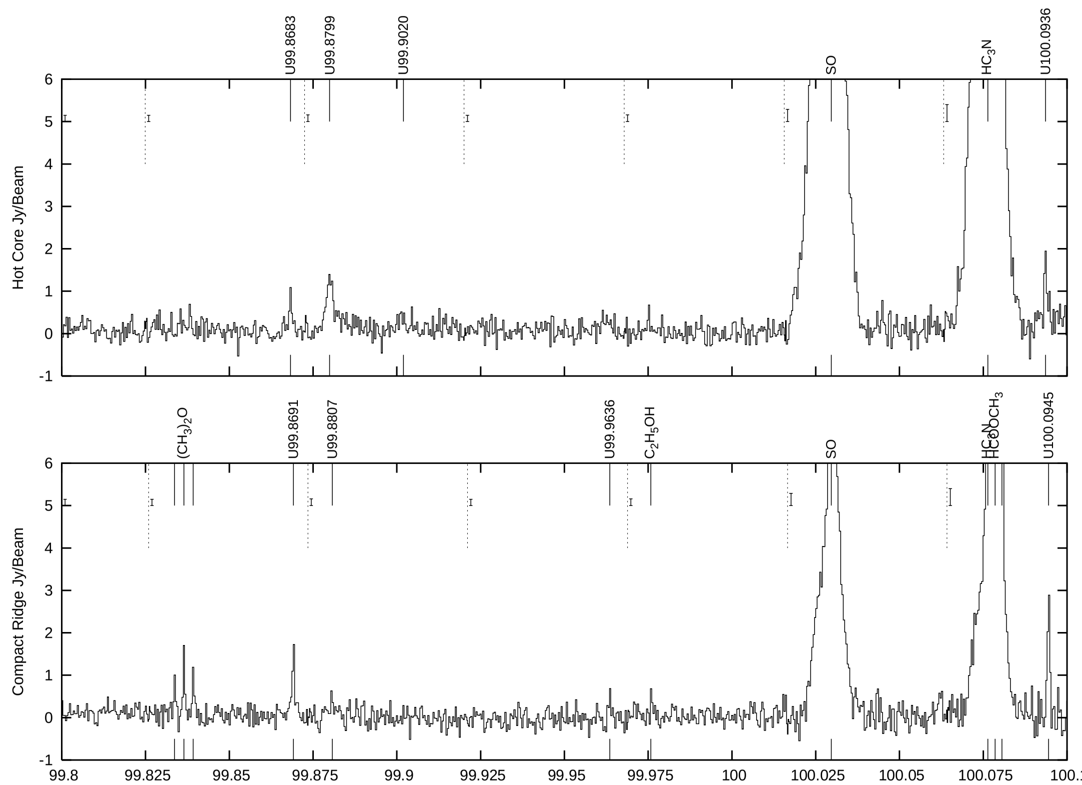

Fig. 4.23bo

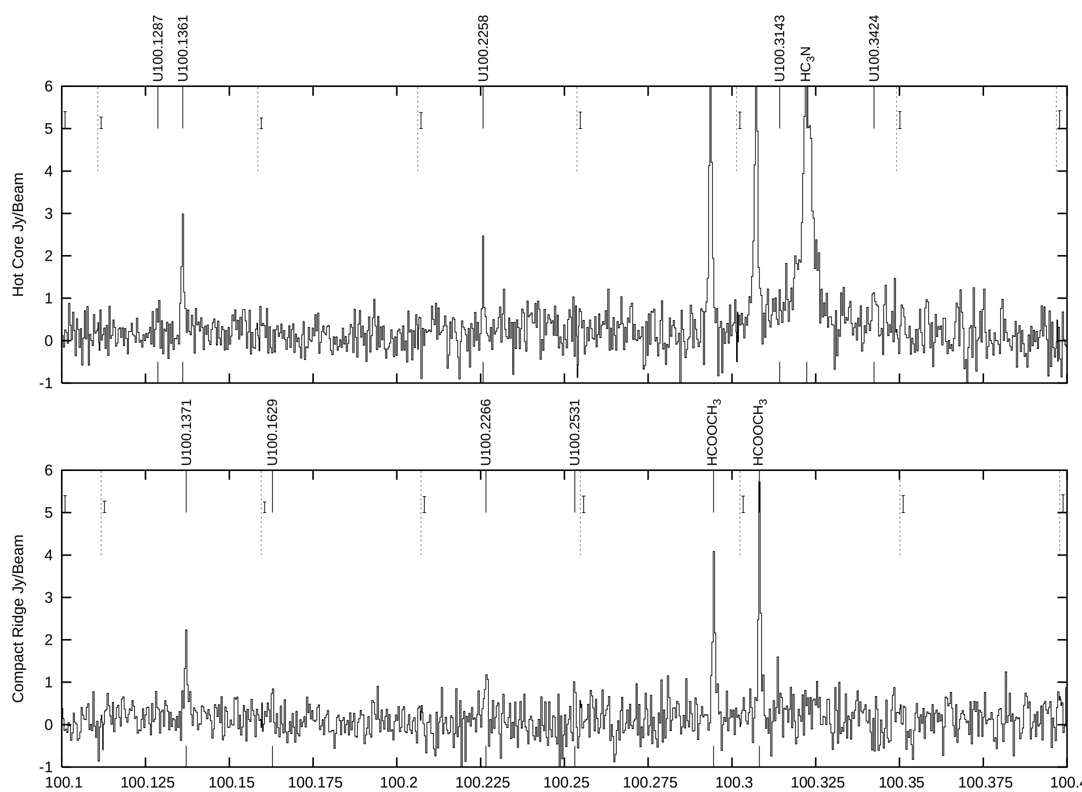

Fig. 4.23bp

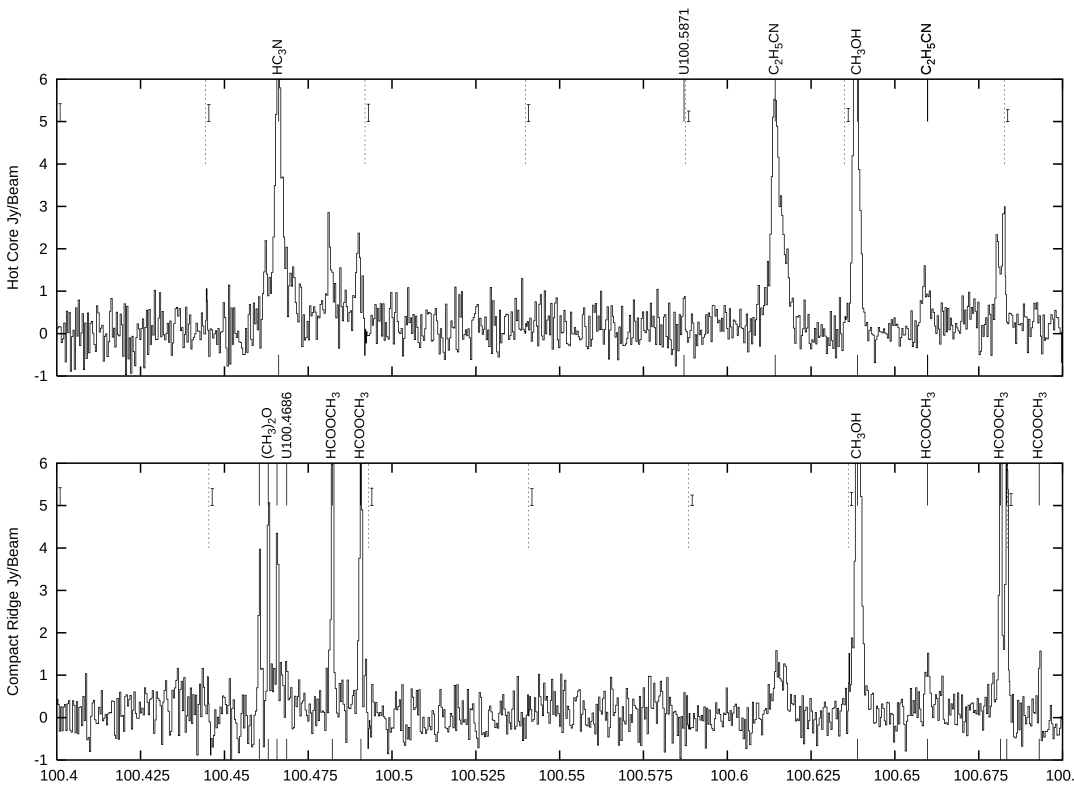

Fig. 4.23bq

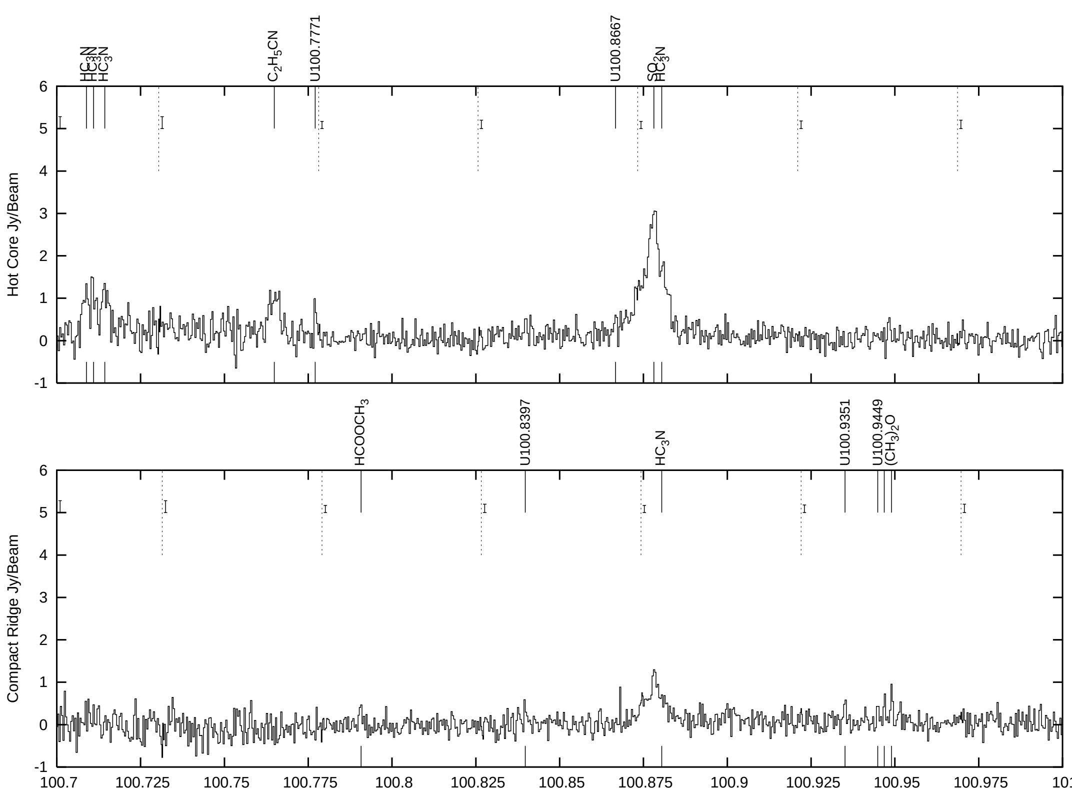

Fig. 4.23br

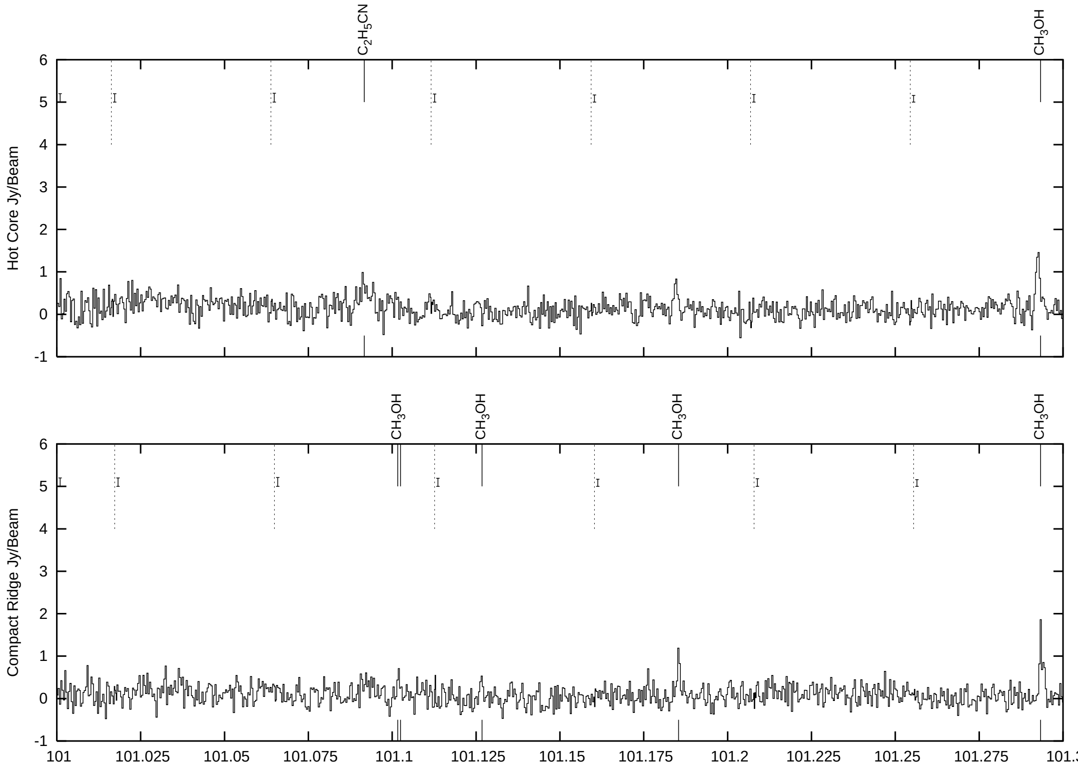

Fig. 4.23bs

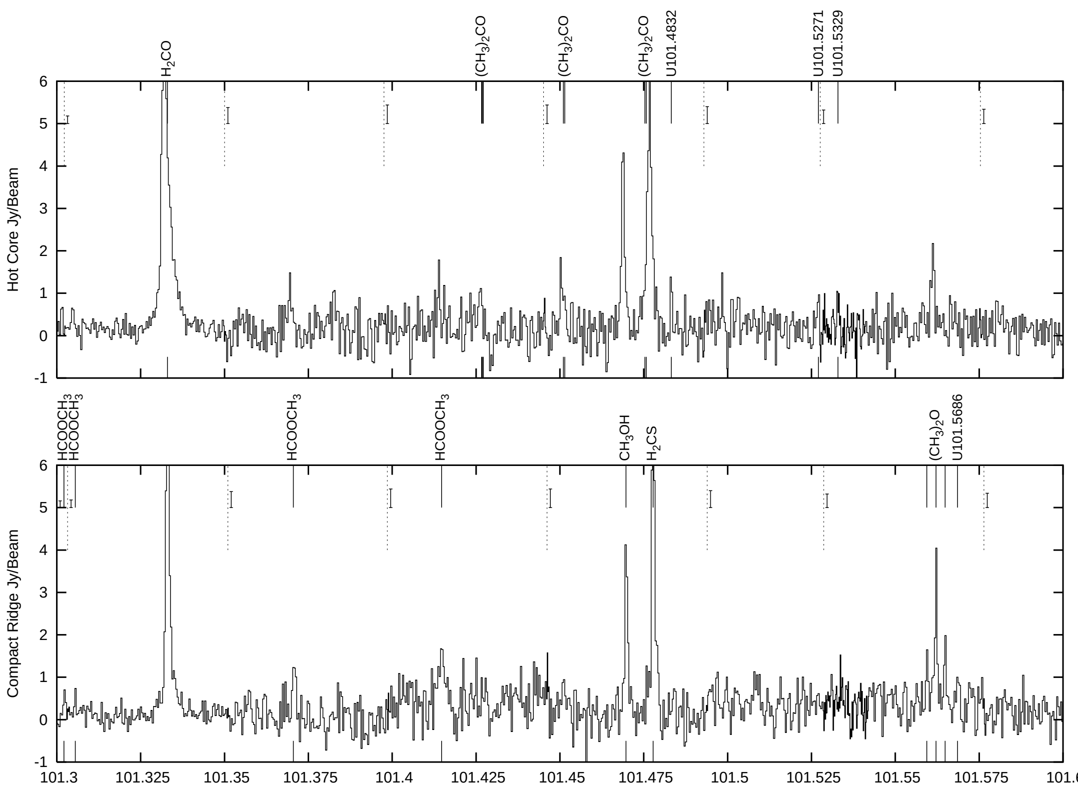

Fig. 4.23bt

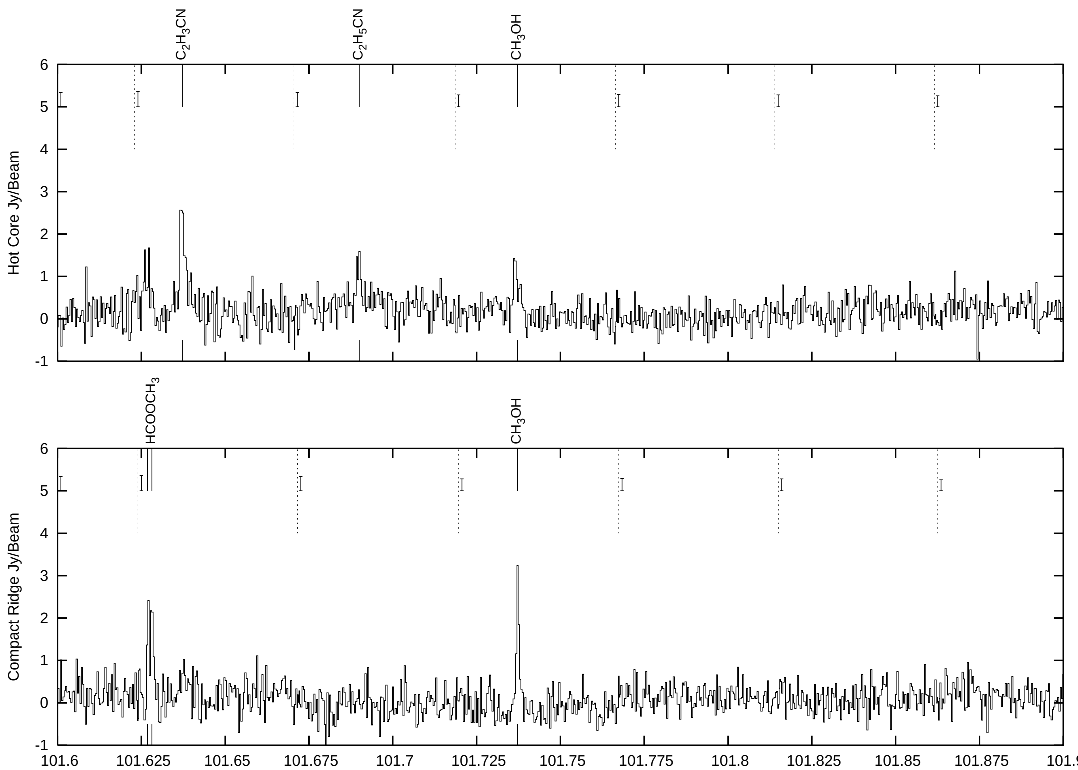

Fig. 4.23bu

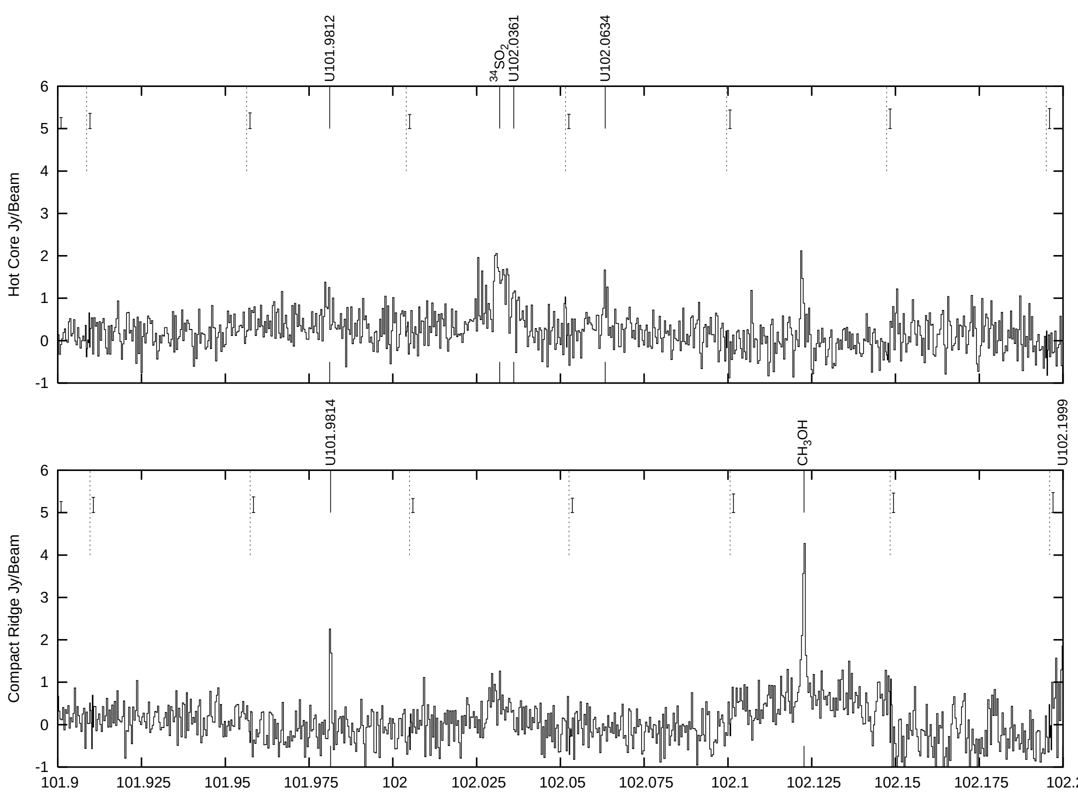

Fig. 4.23bv

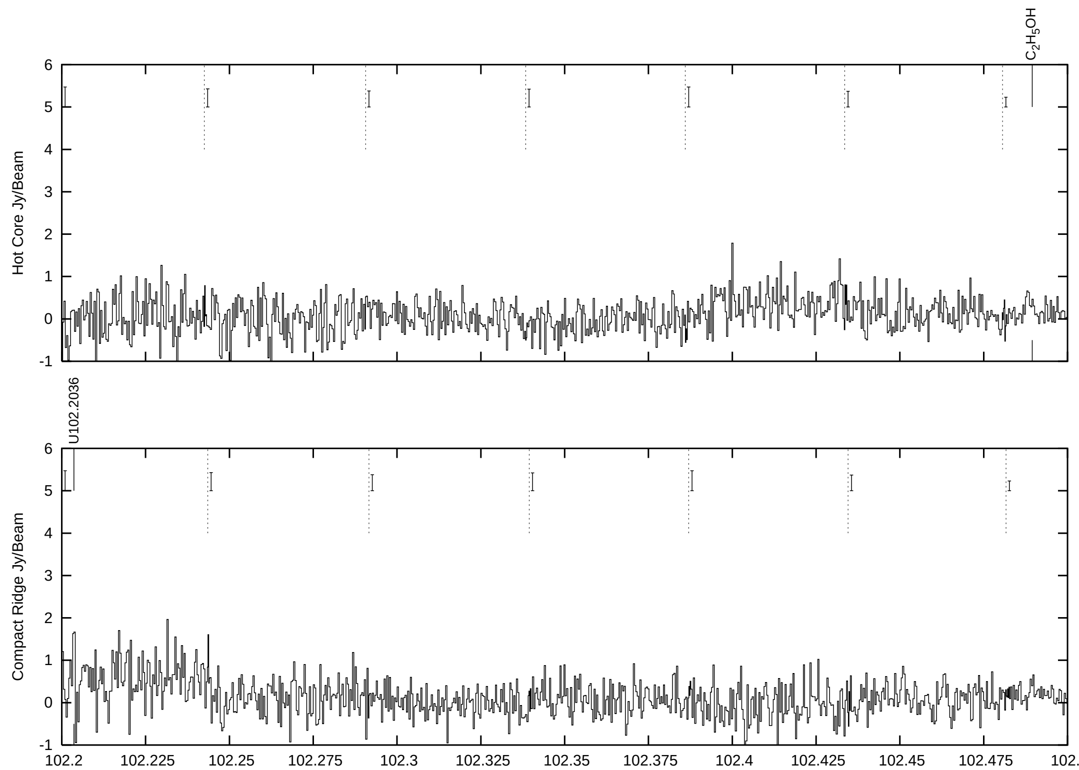

Fig. 4.23bw

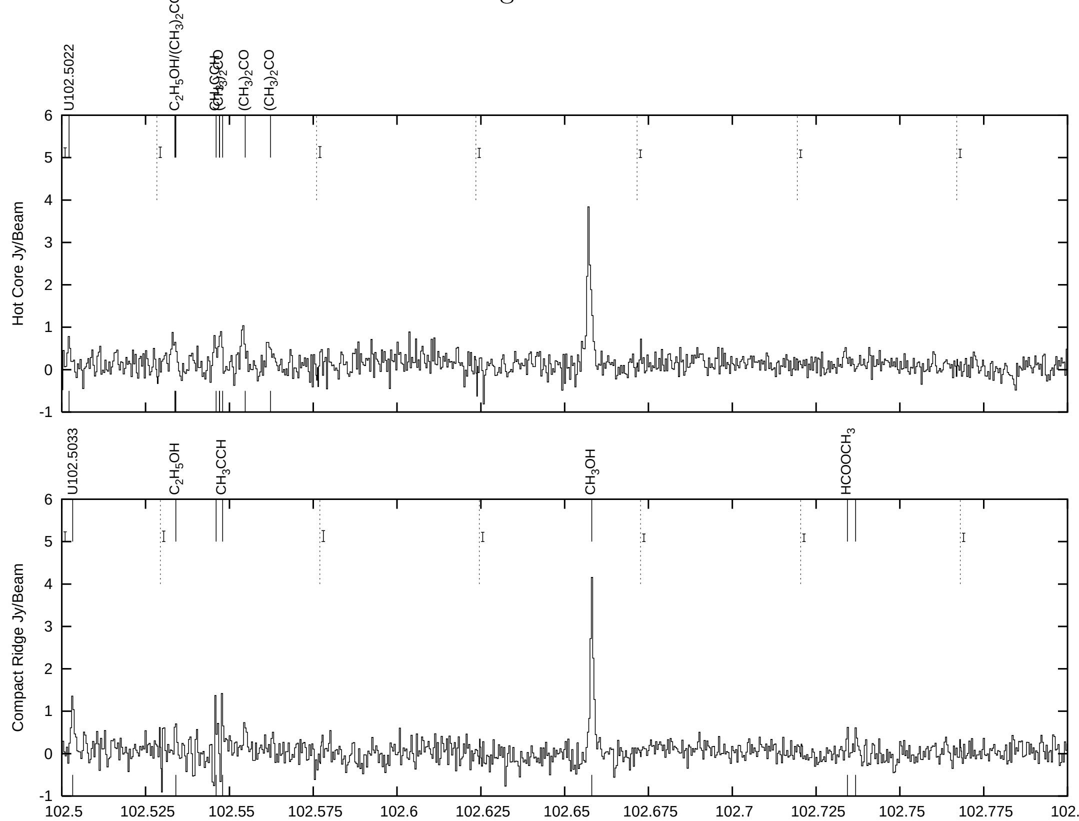

Fig. 4.23bx

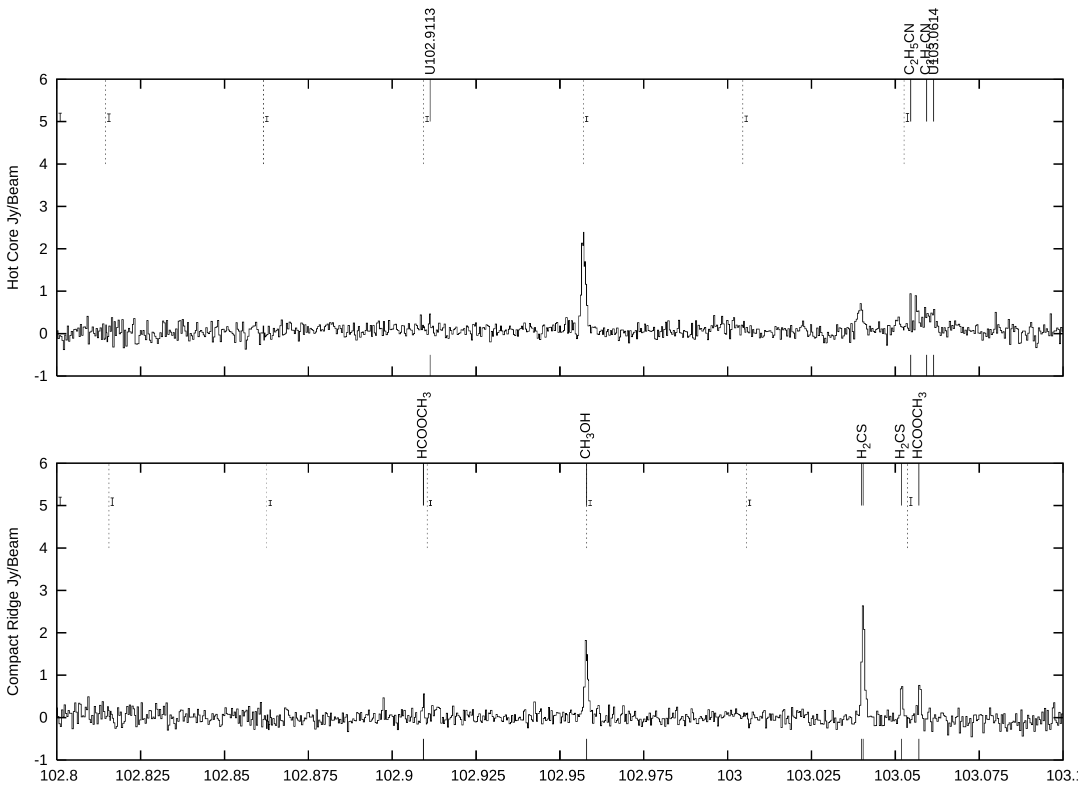

Fig. 4.23by

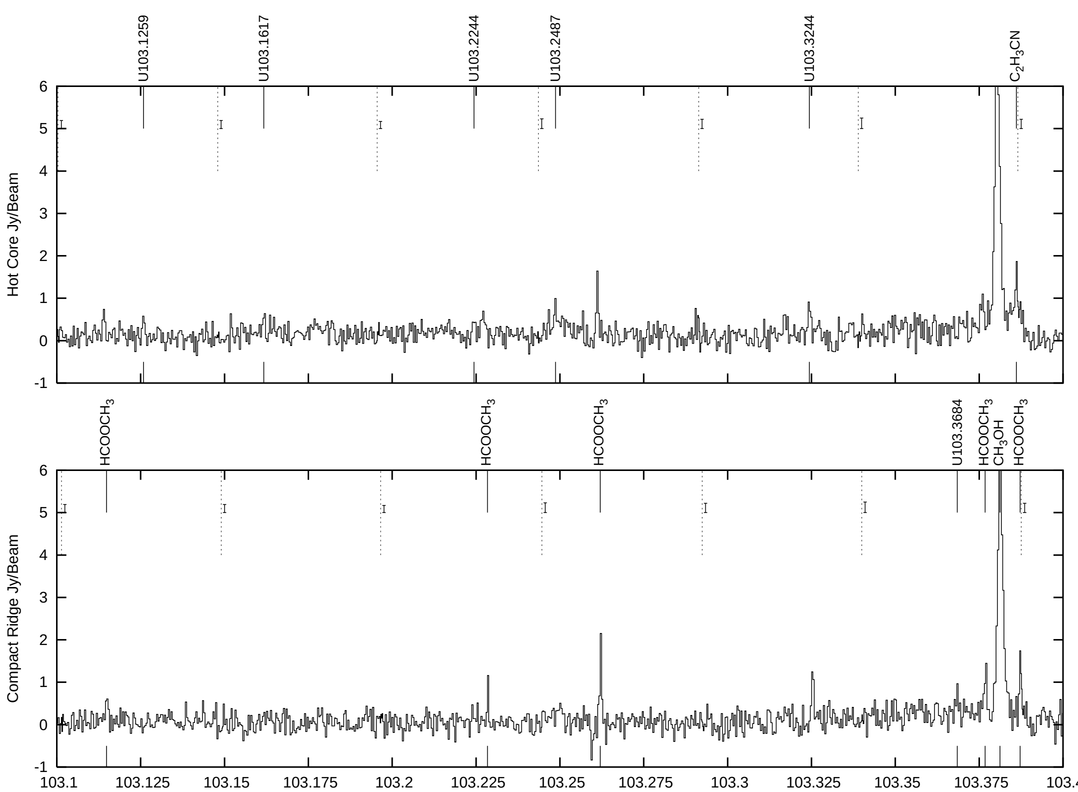

Fig. 4.23bz

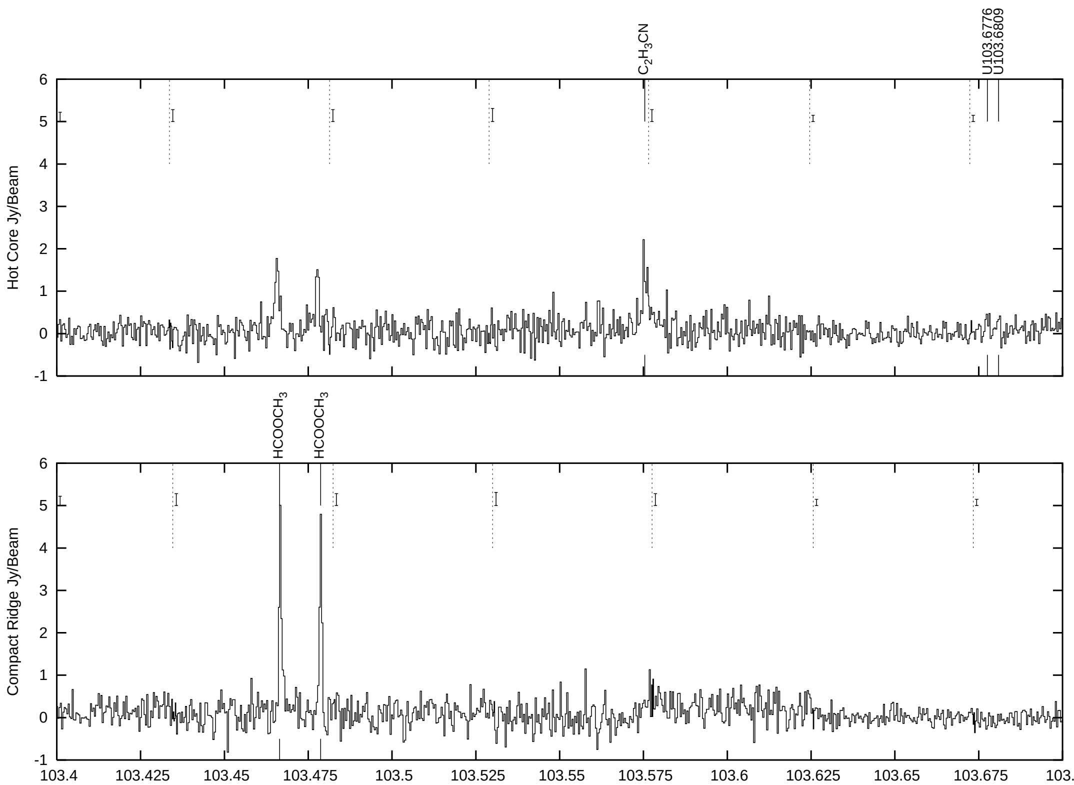

Fig. 4.23ca

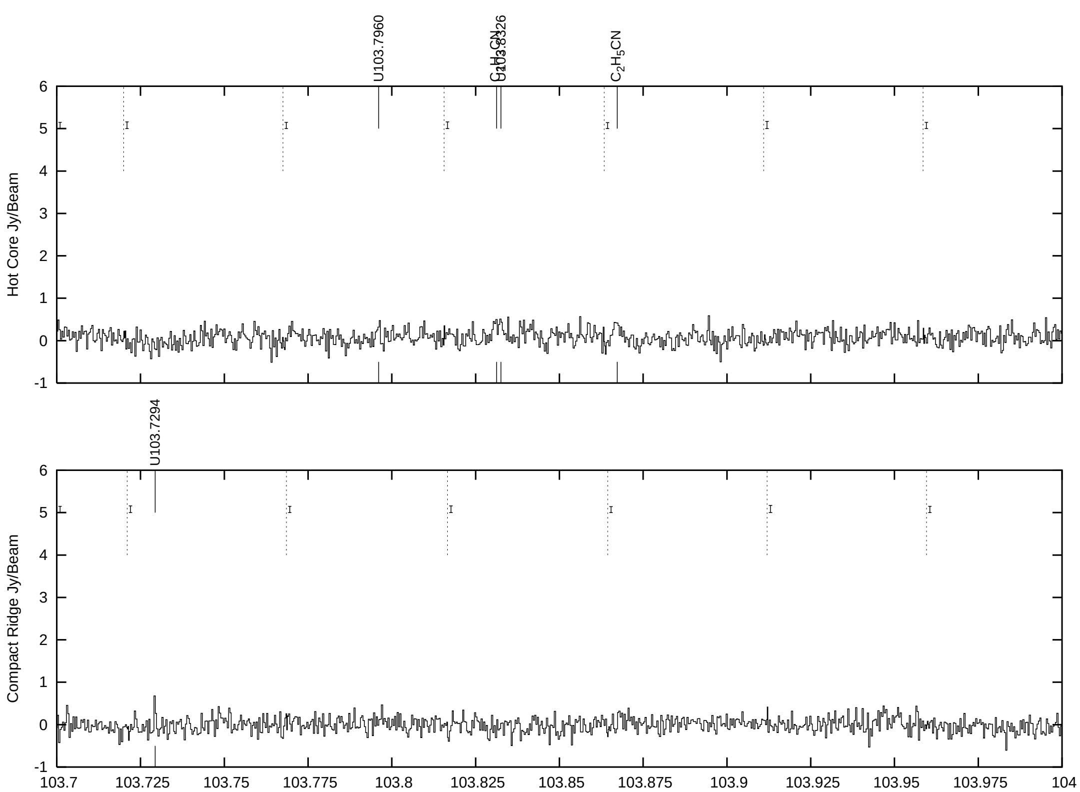

Fig. 4.23cb

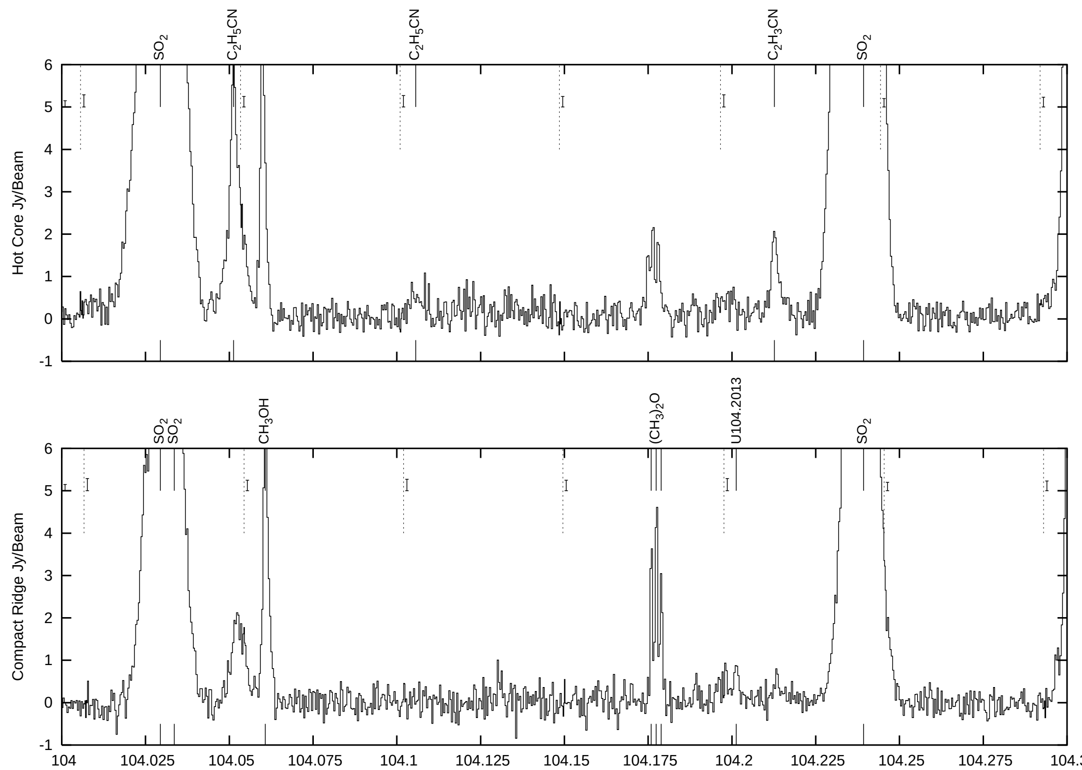

Fig. 4.23cc

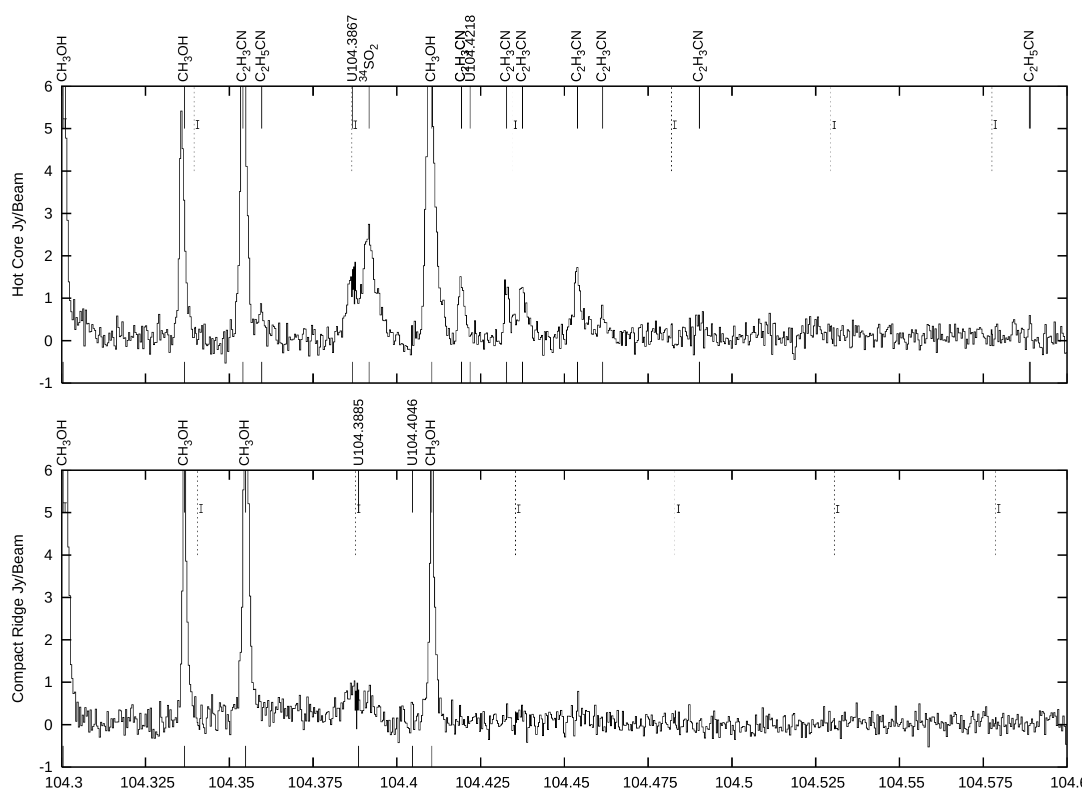

Fig. 4.23cd

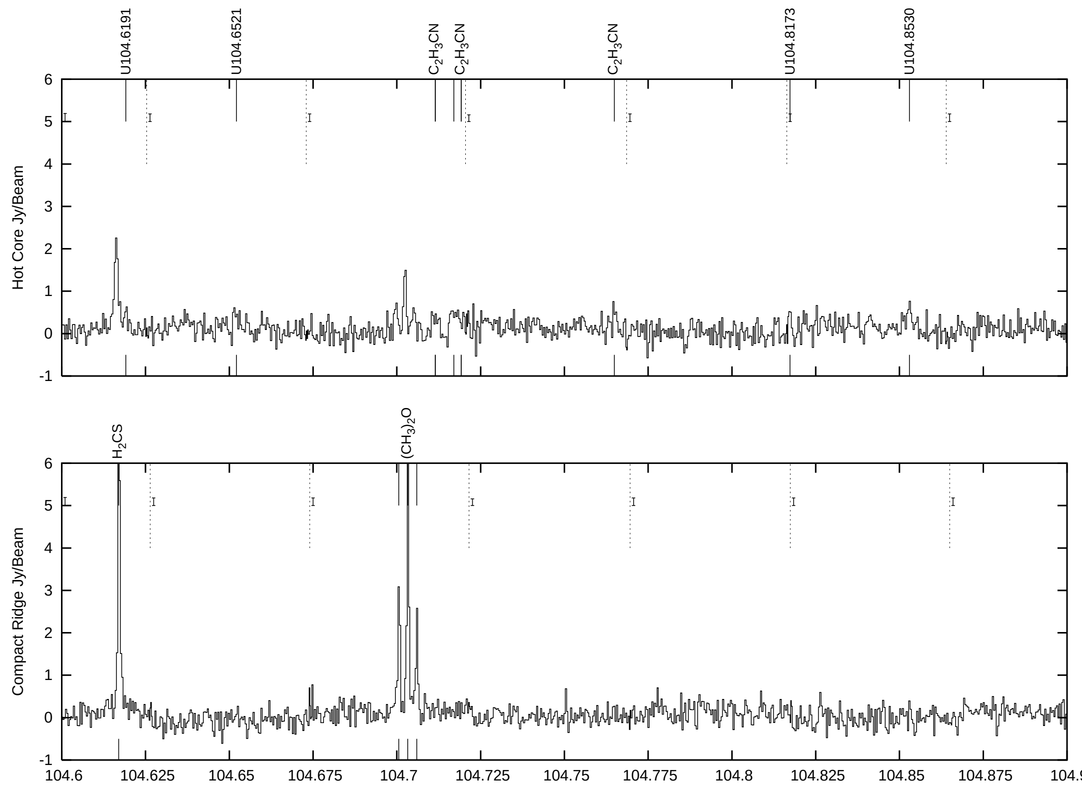

Fig. 4.23ce

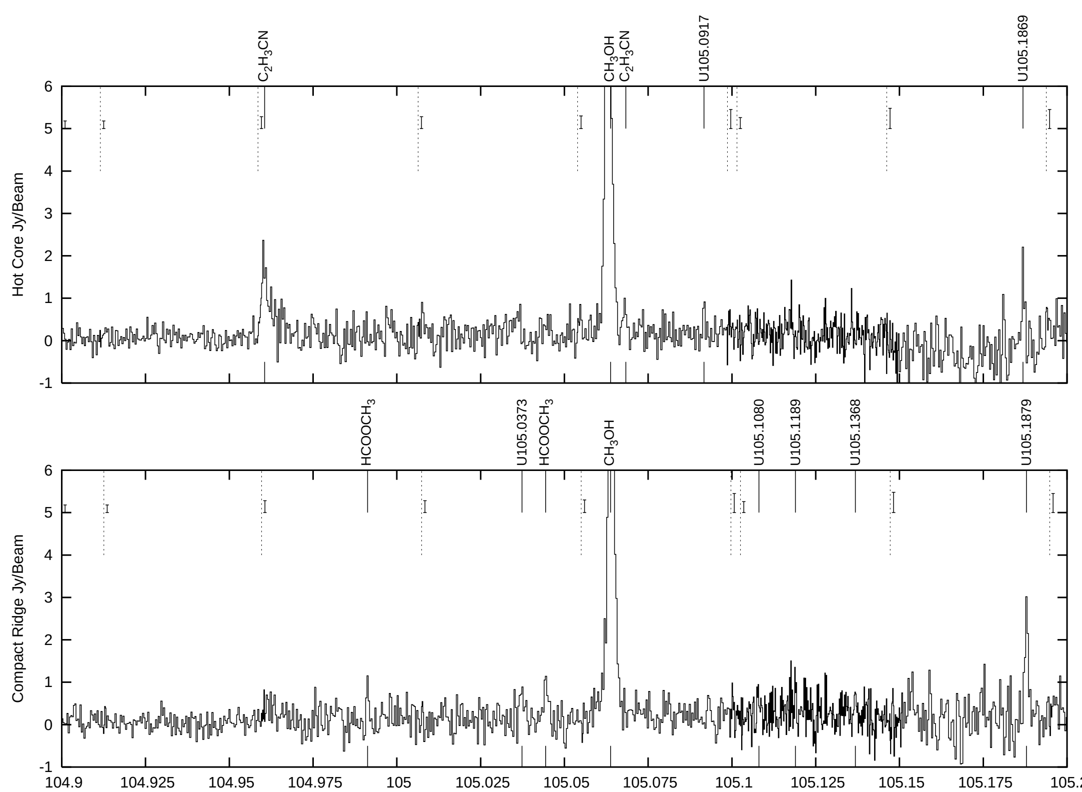

Fig. 4.23cf

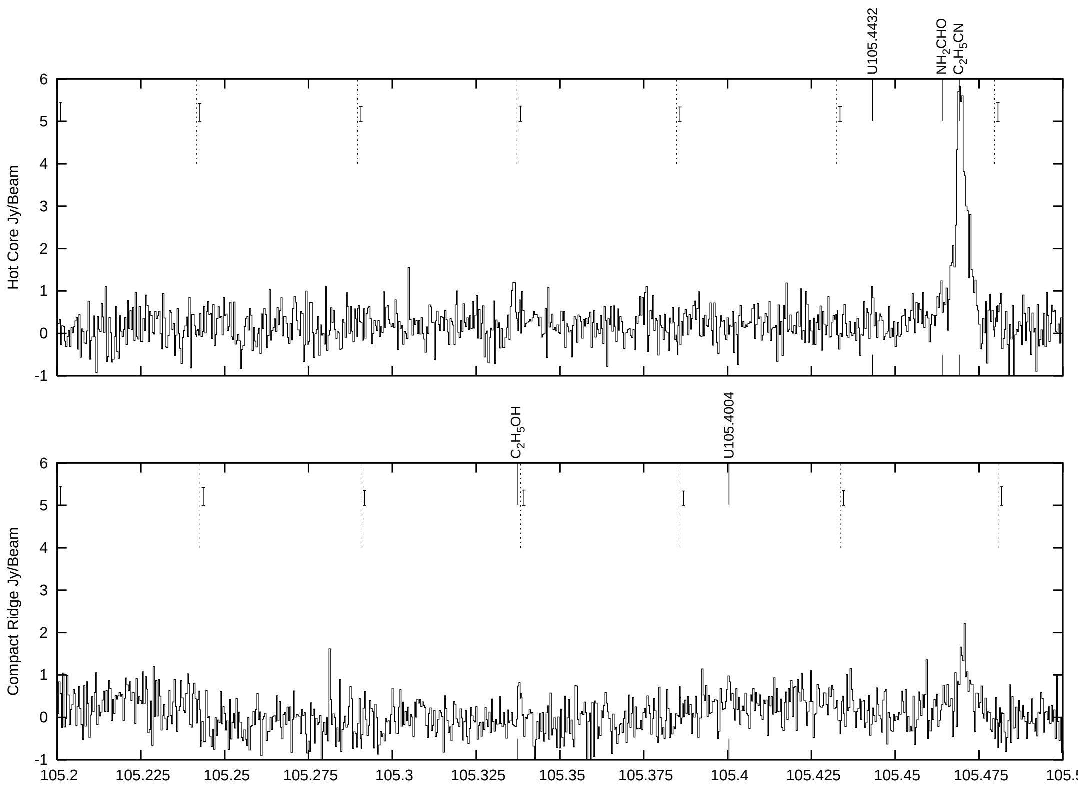

Fig. 4.23cg

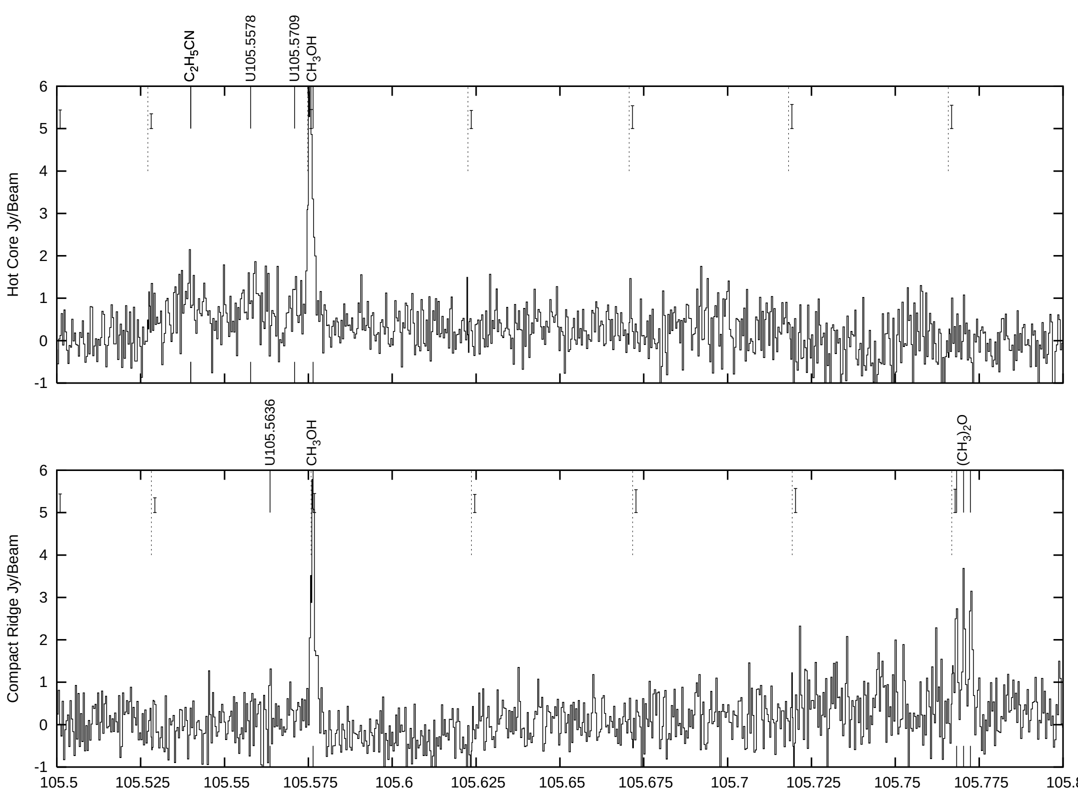

Fig. 4.23ch

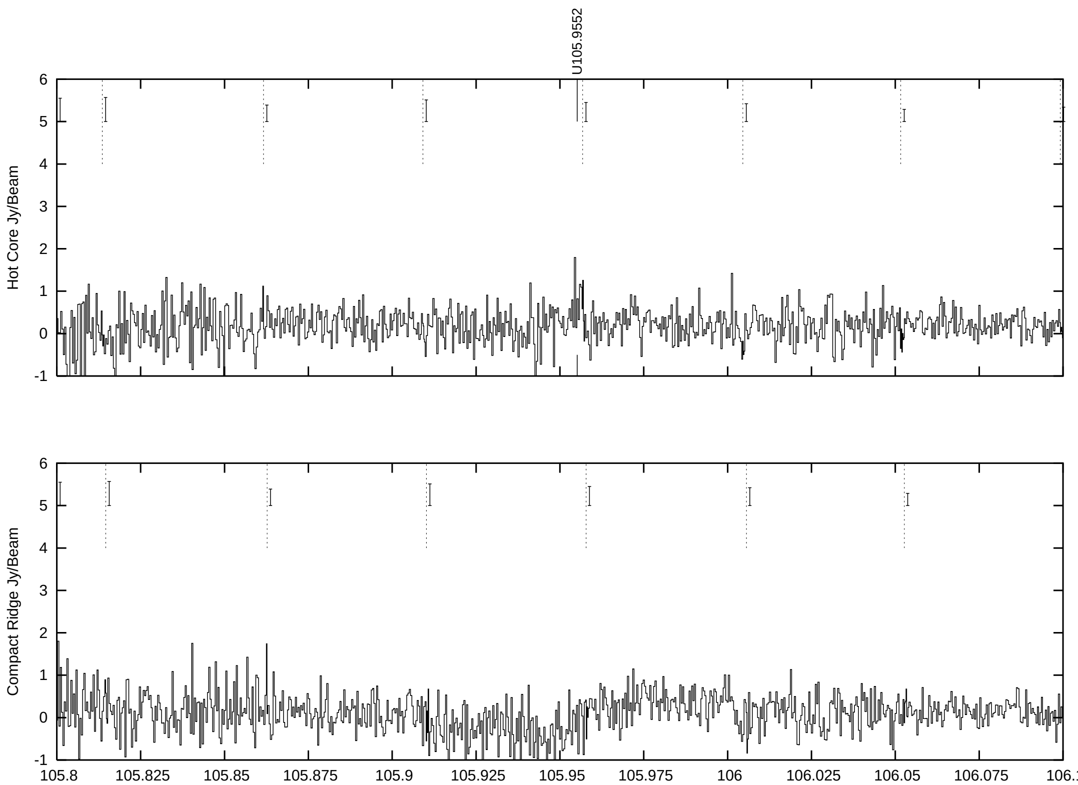

Fig. 4.23ci

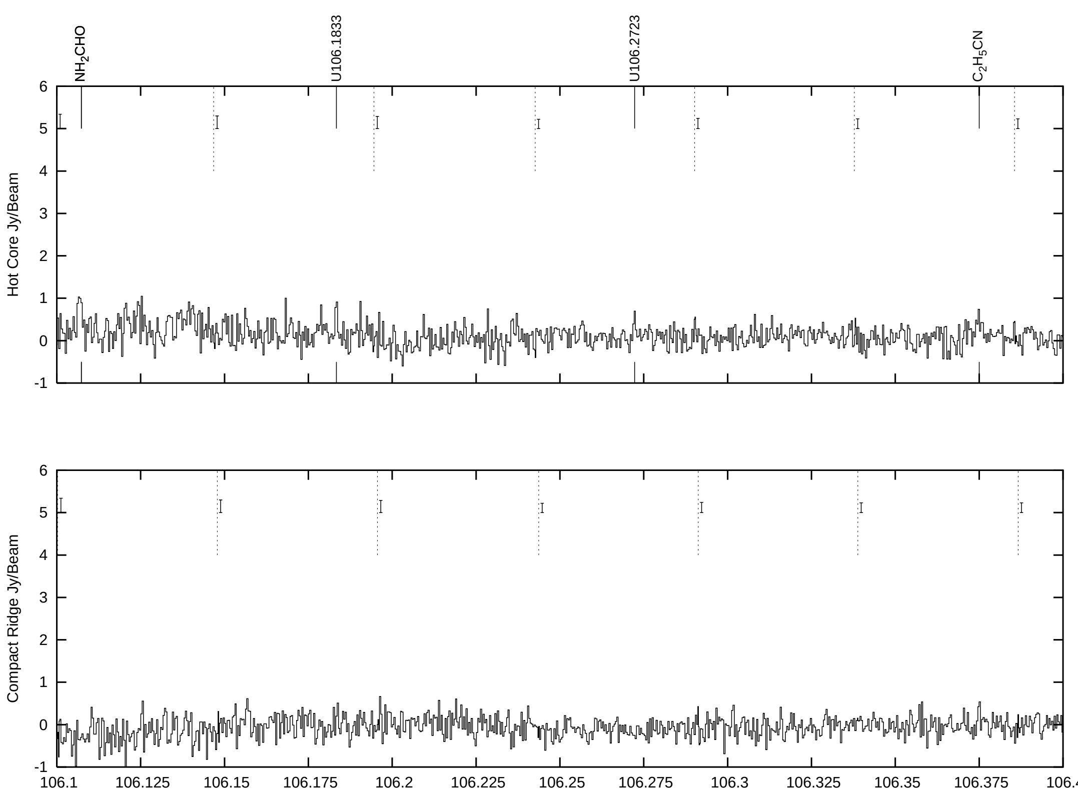

Fig. 4.23cj

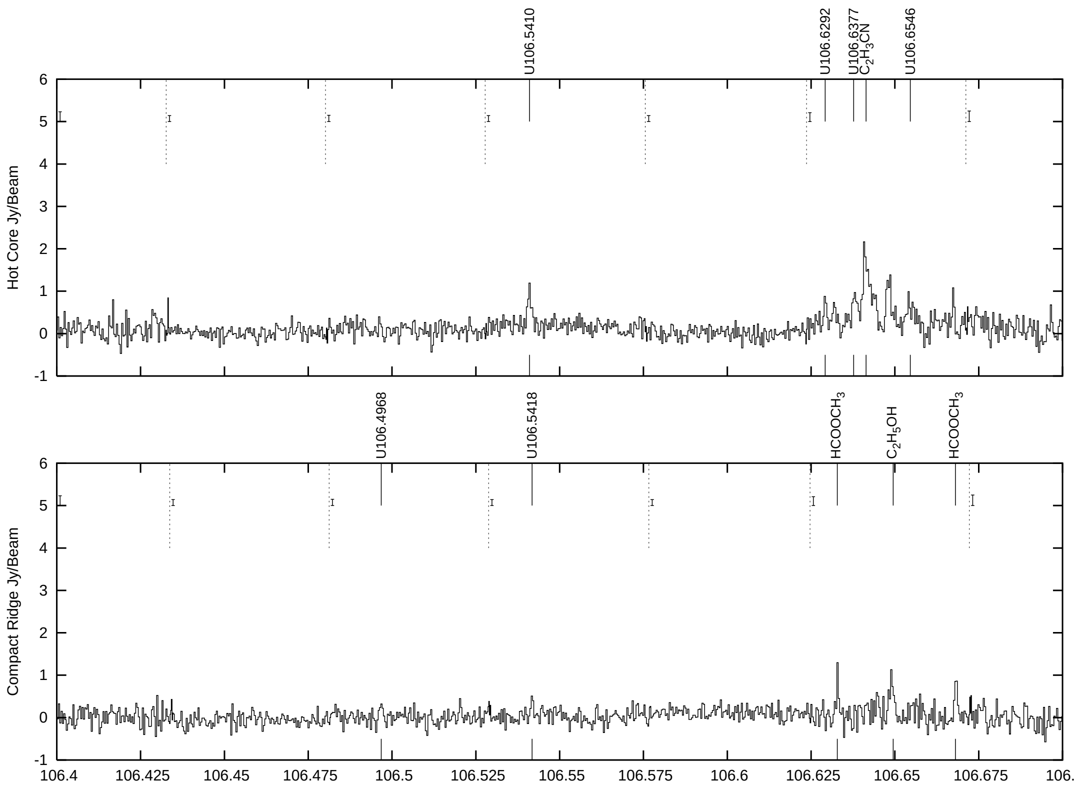

Fig. 4.23ck

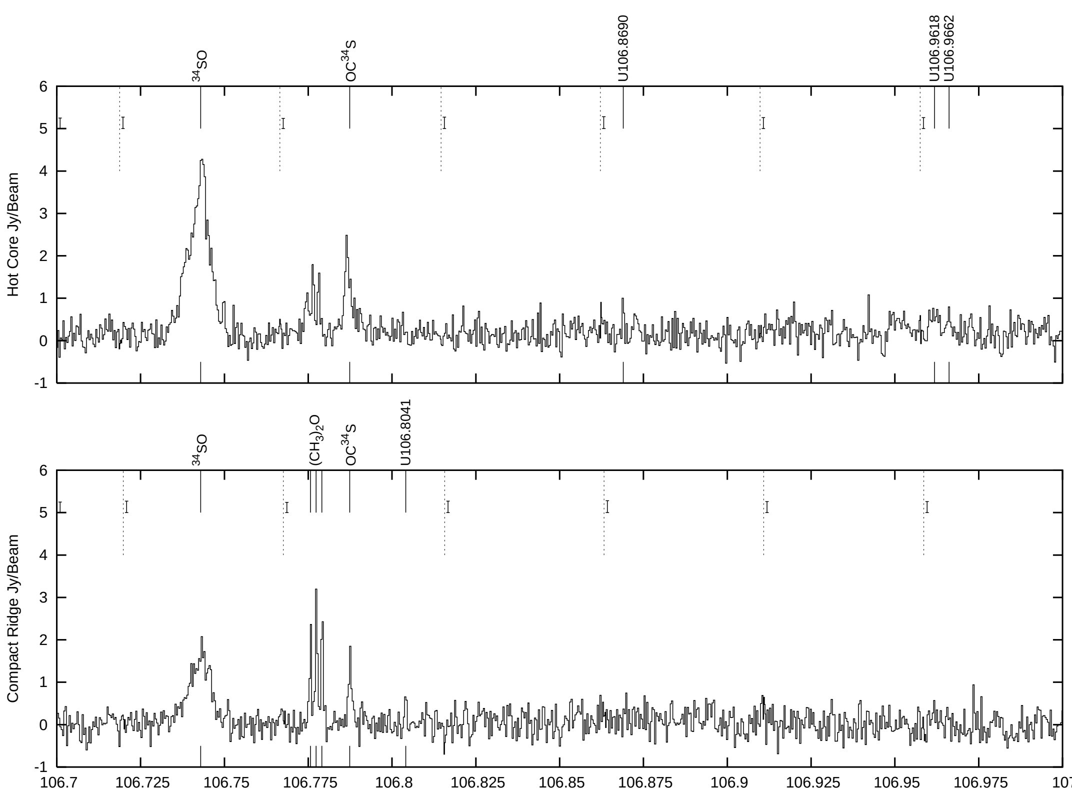

Fig. 4.23cl

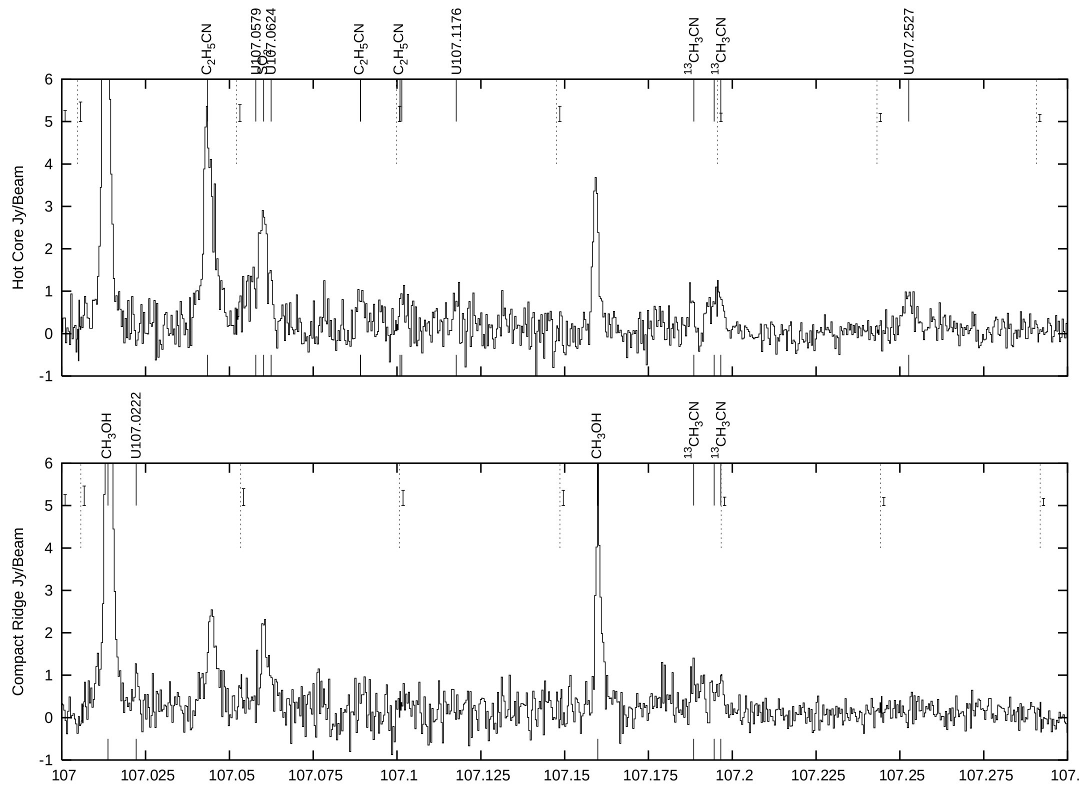

Fig. 4.23cm

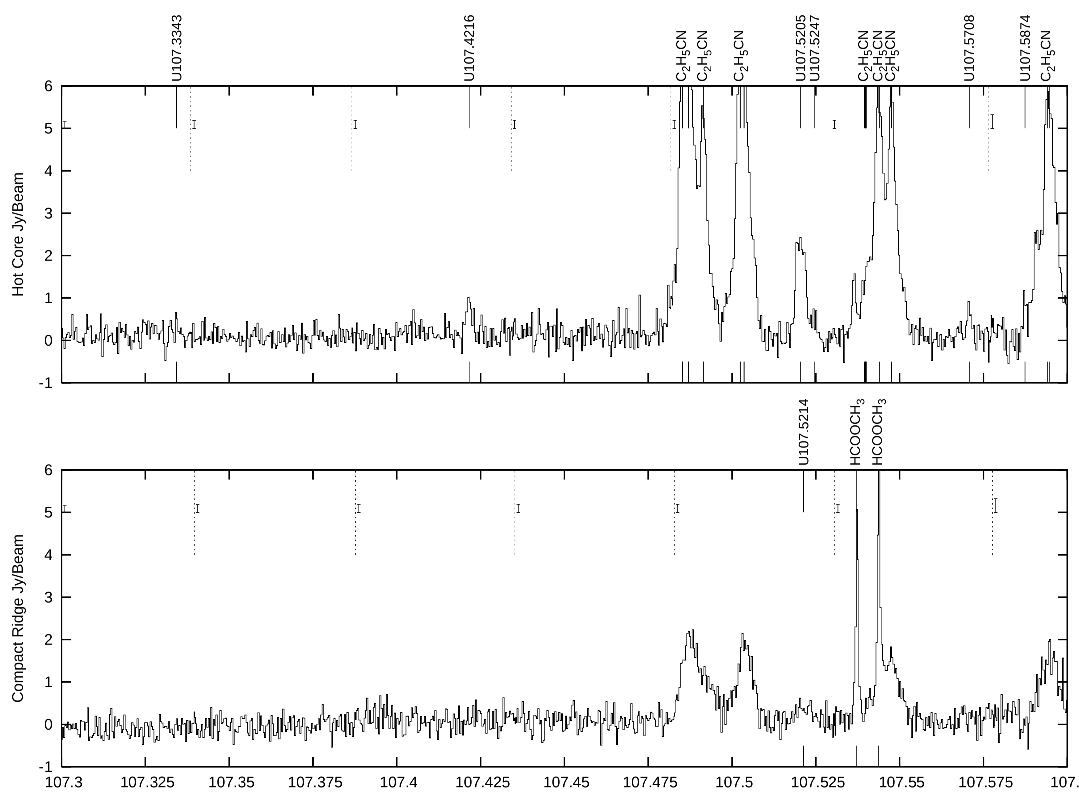

Fig. 4.23cn

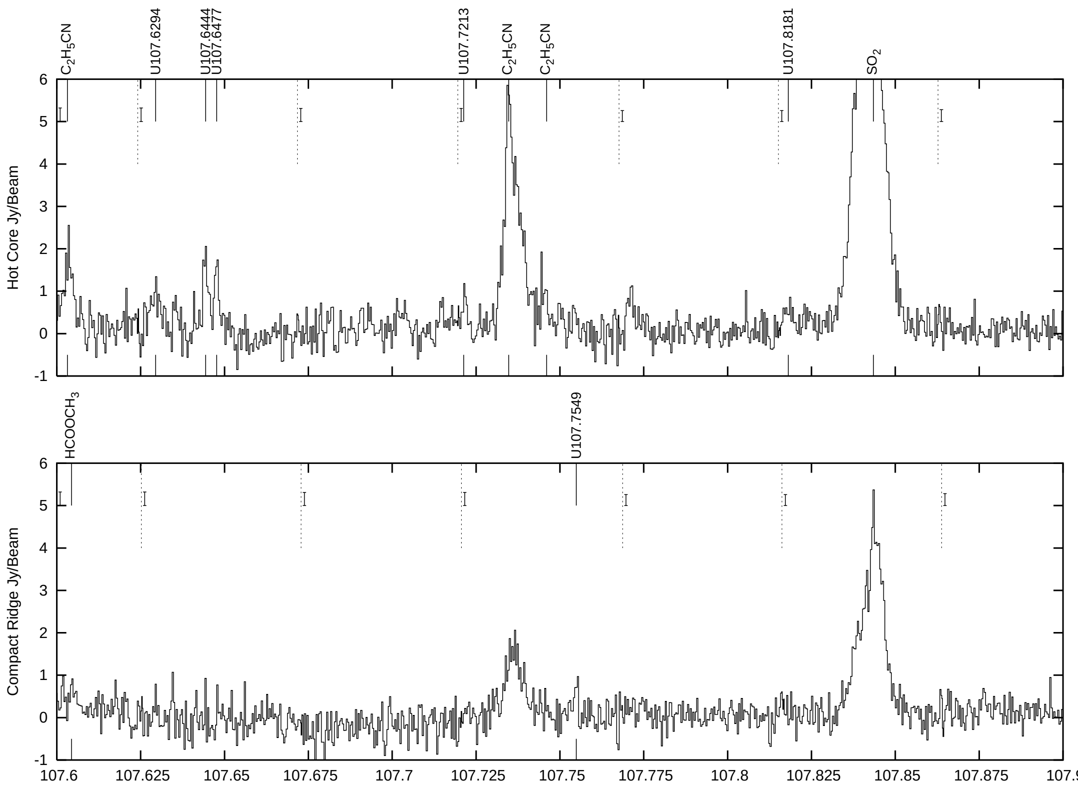

Fig. 4.23co

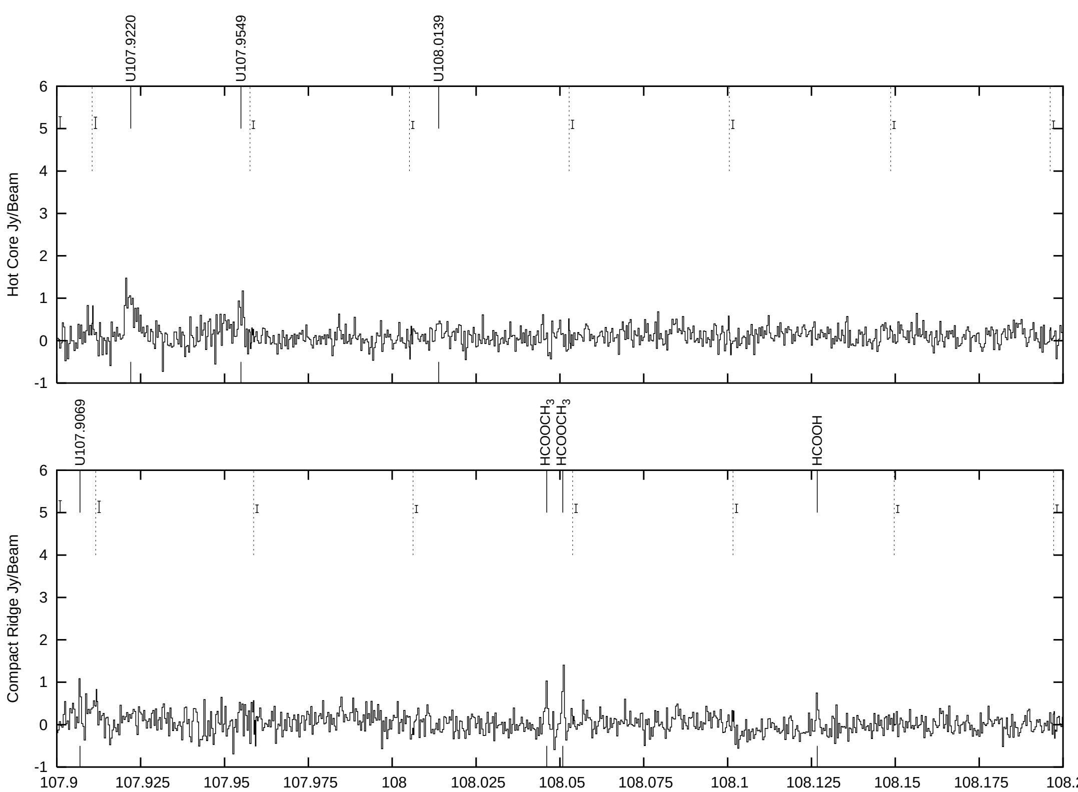

Fig. 4.23cp

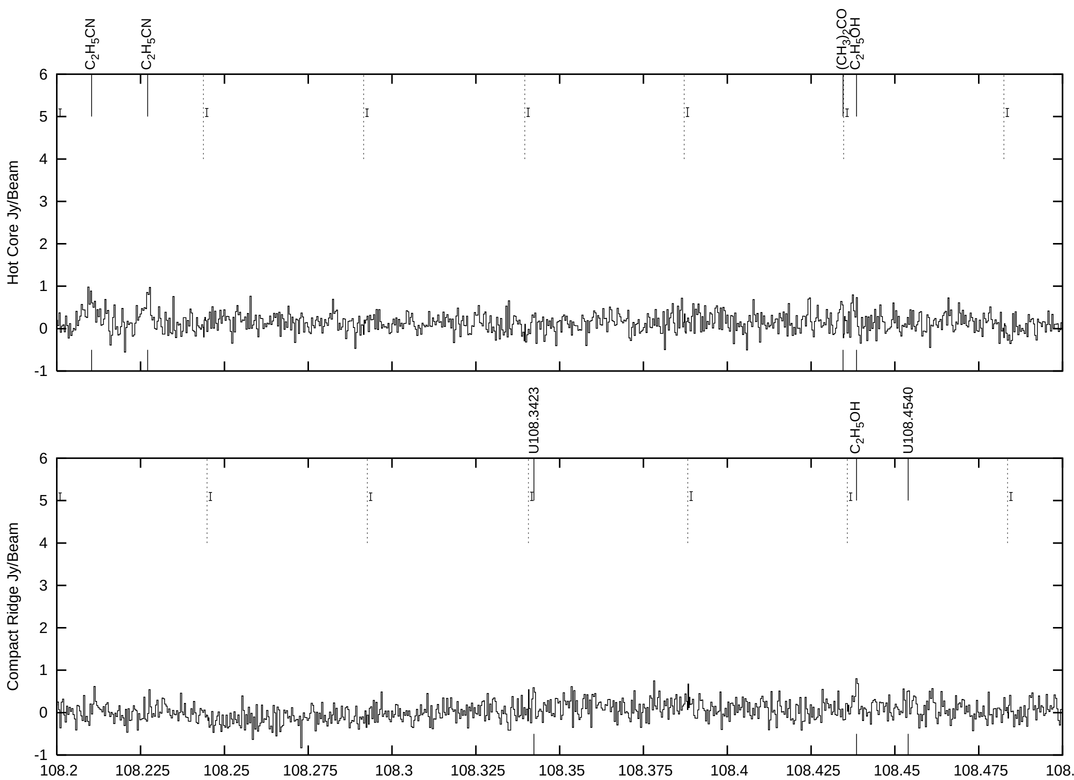

Fig. 4.23cq

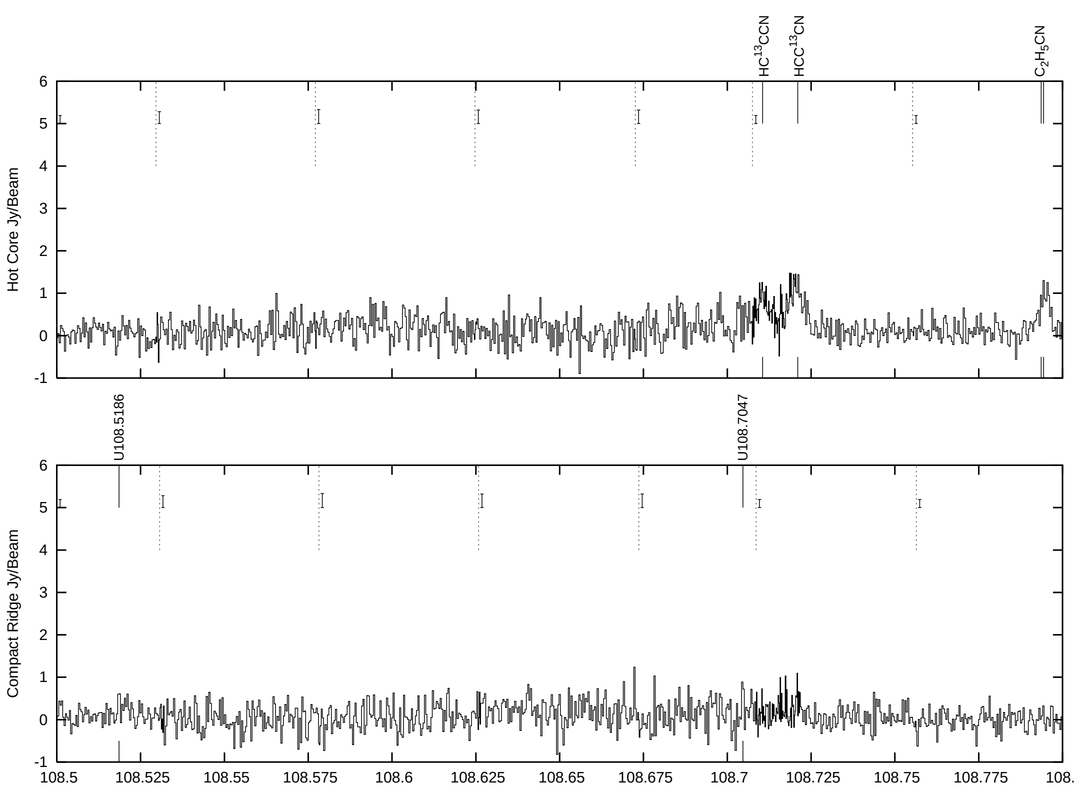

Fig. 4.23cr

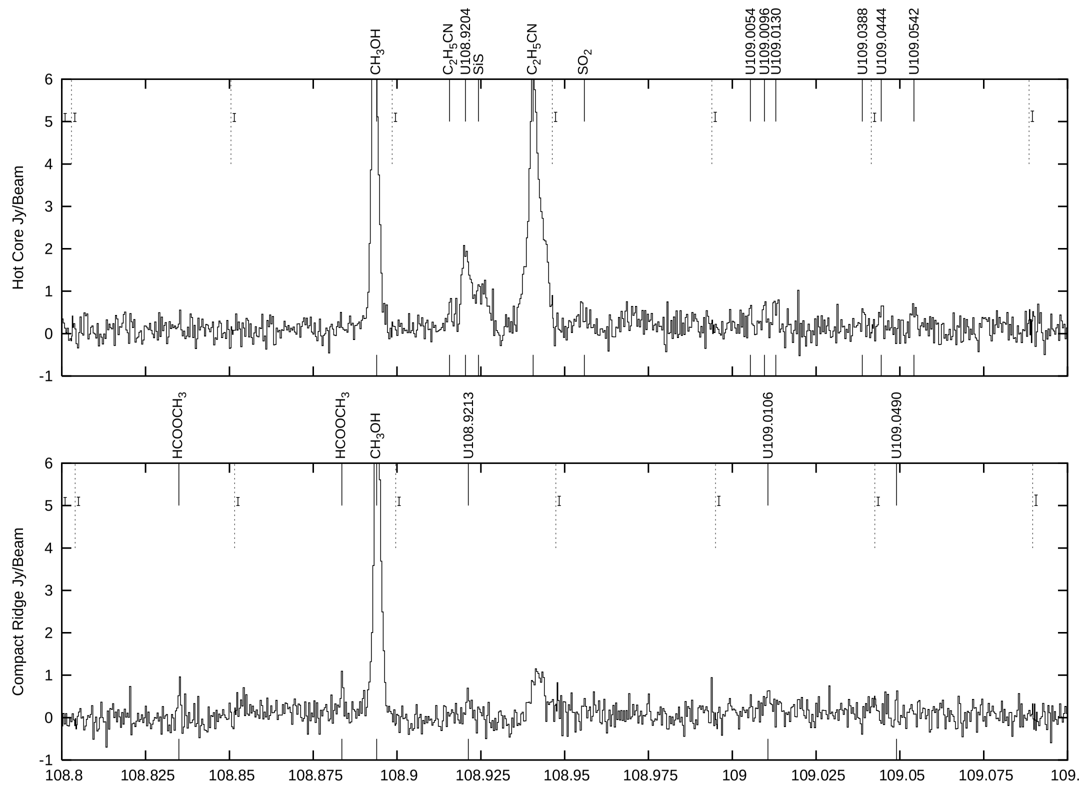

Fig. 4.23cs

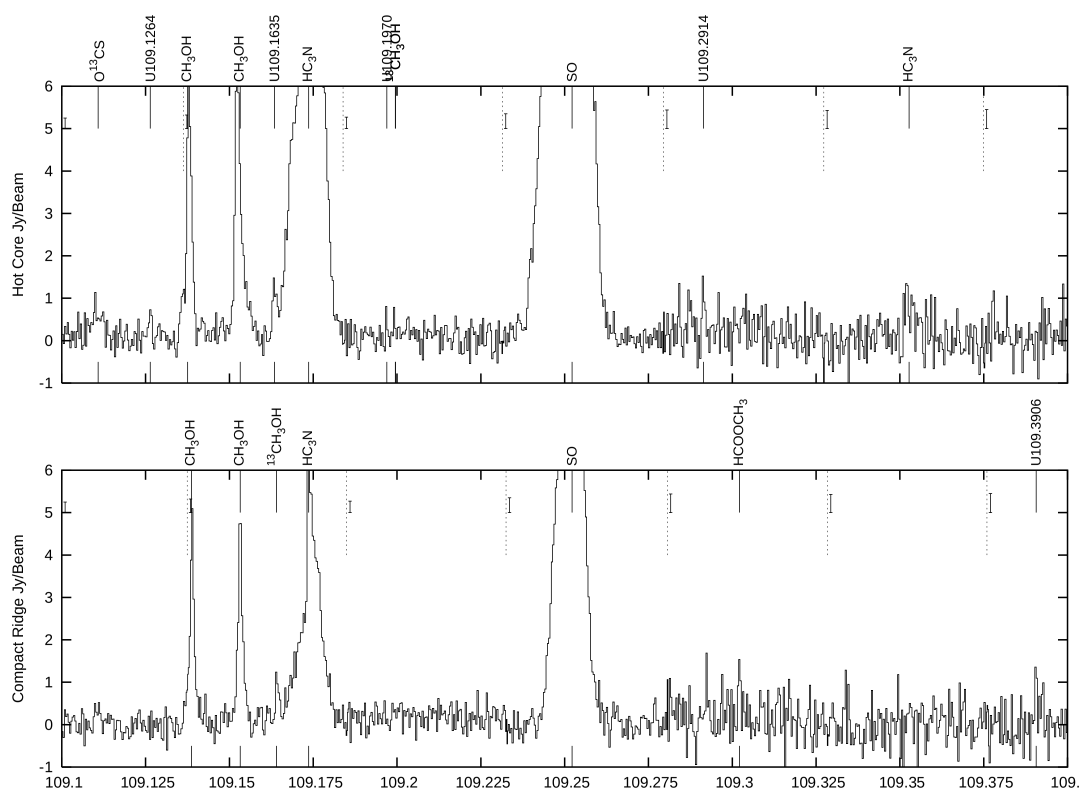

Fig. 4.23ct

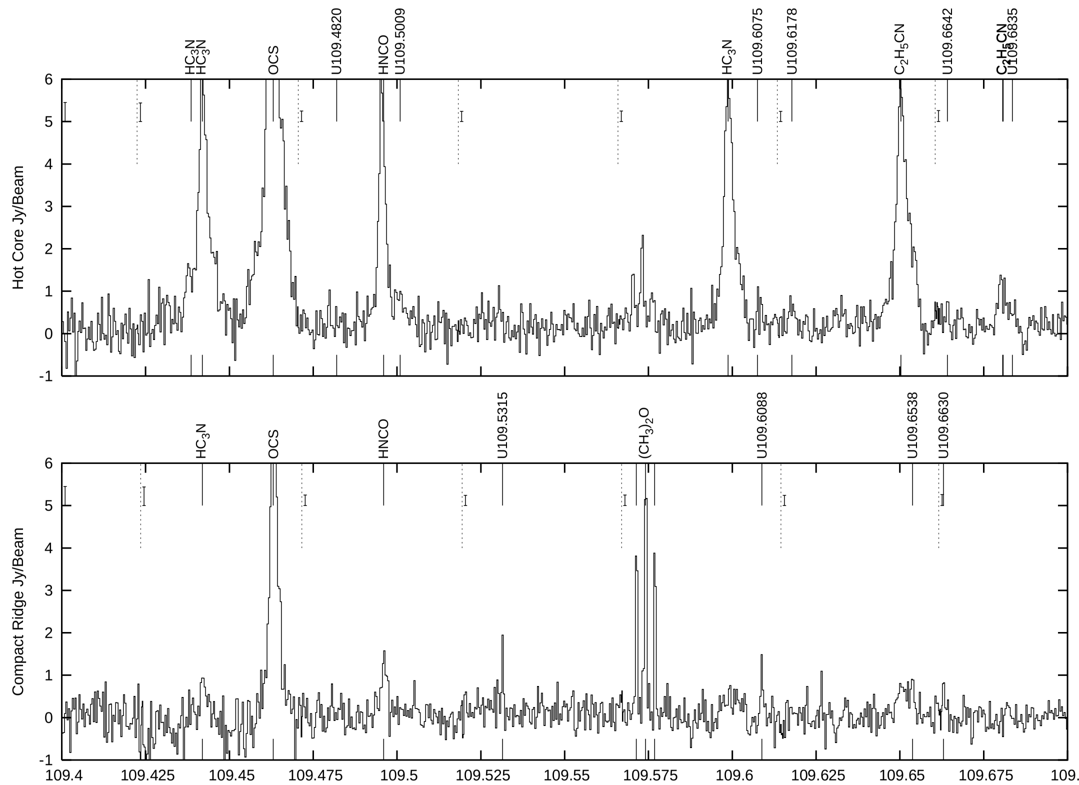

Fig. 4.23cu

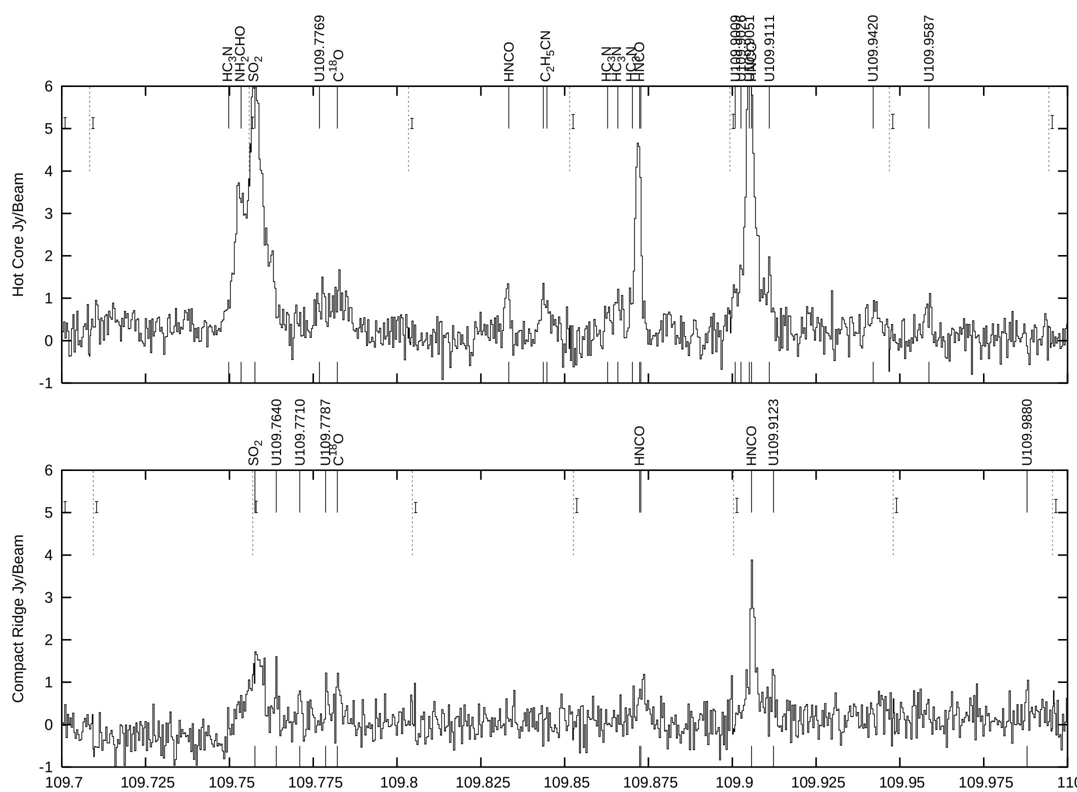

Fig. 4.23cv

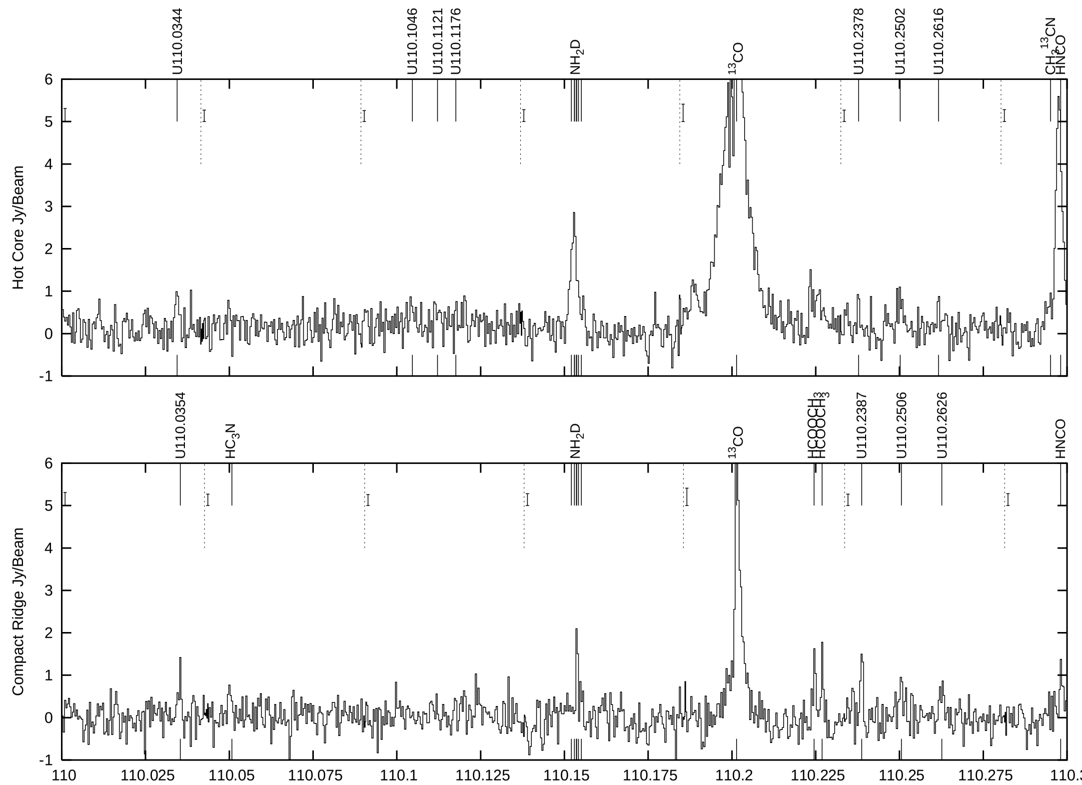

Fig. 4.23cw

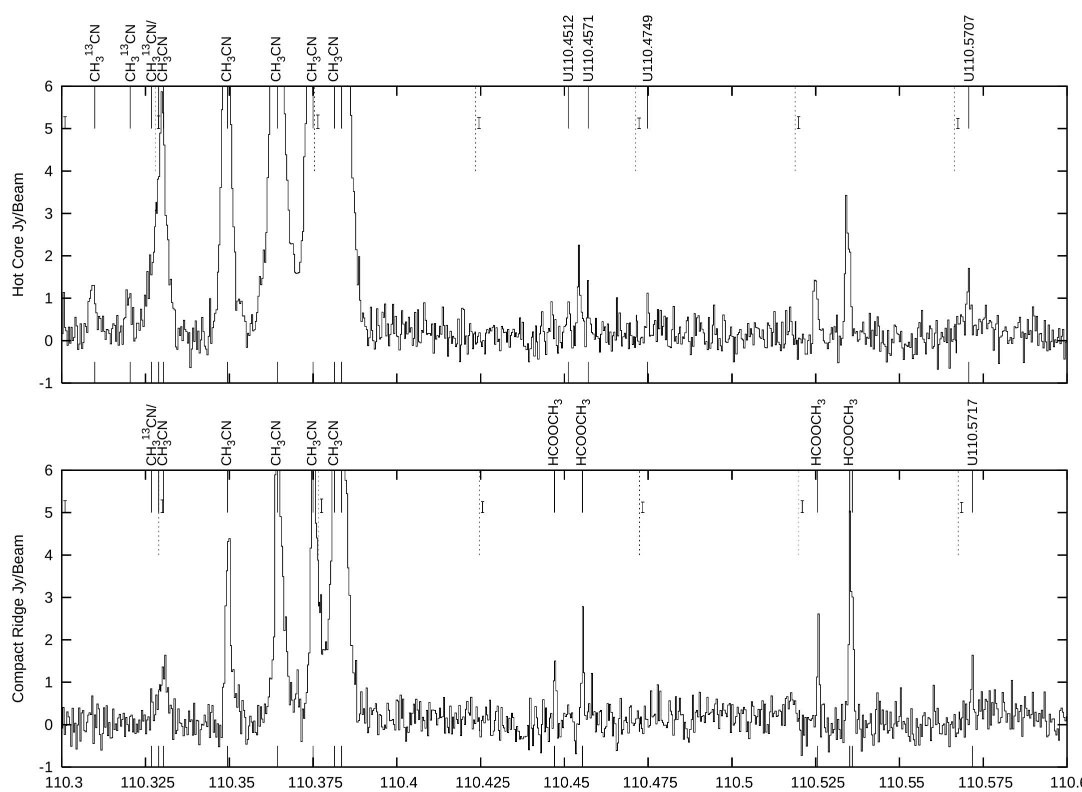

Fig. 4.23cx

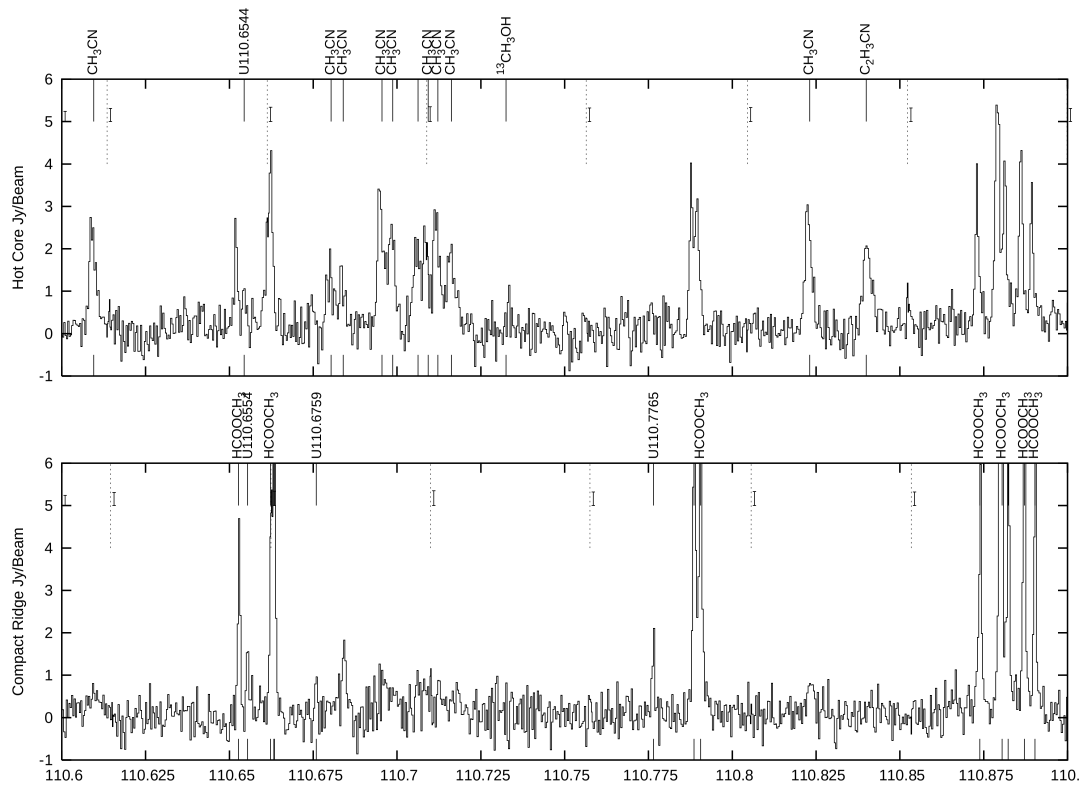

Fig. 4.23cy

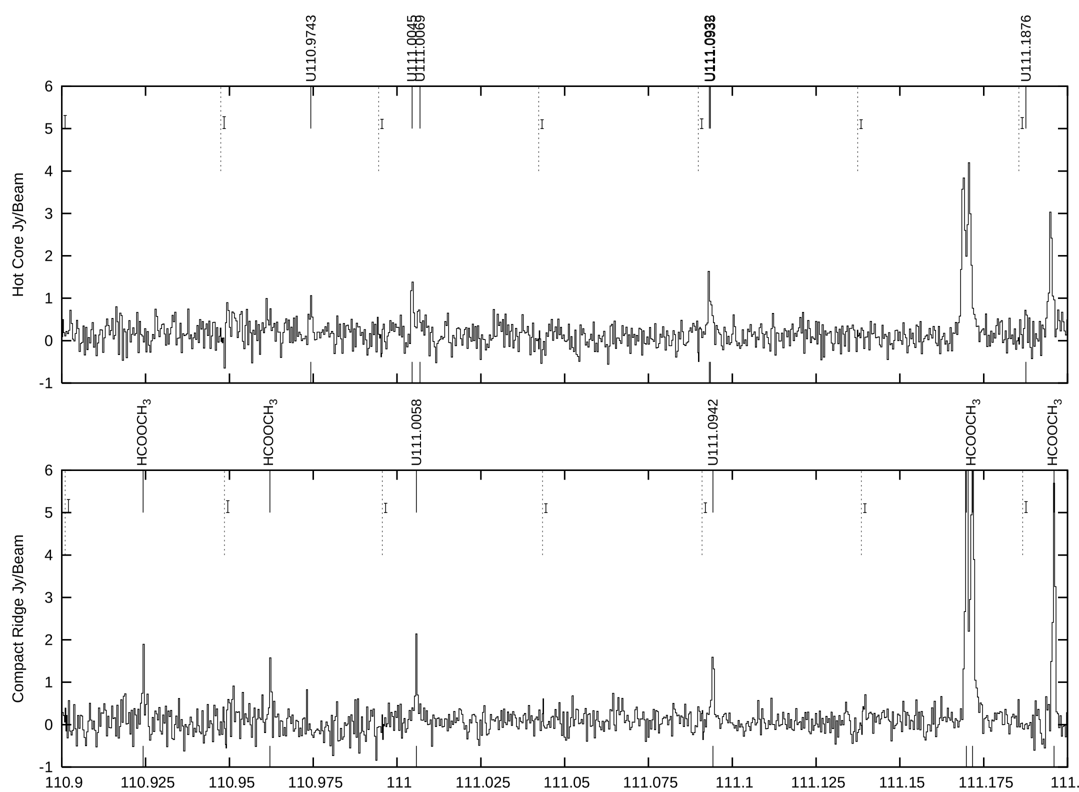

Fig. 4.23cz

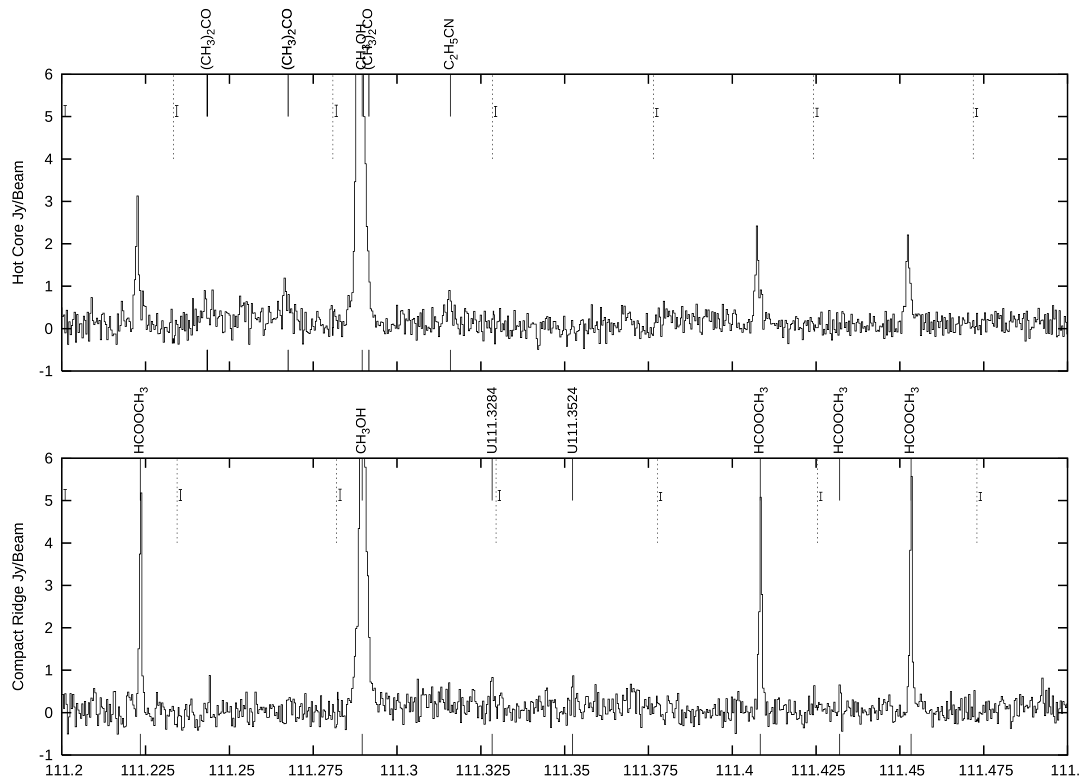

Fig. 4.23da

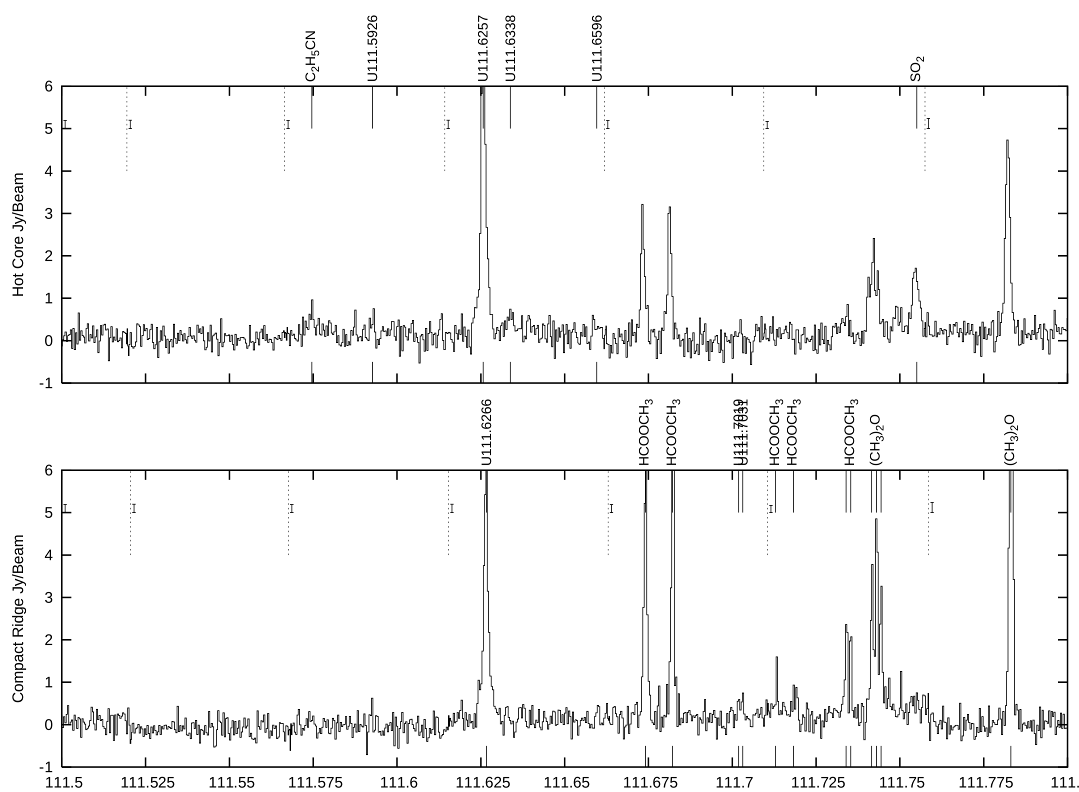

Fig. 4.23db

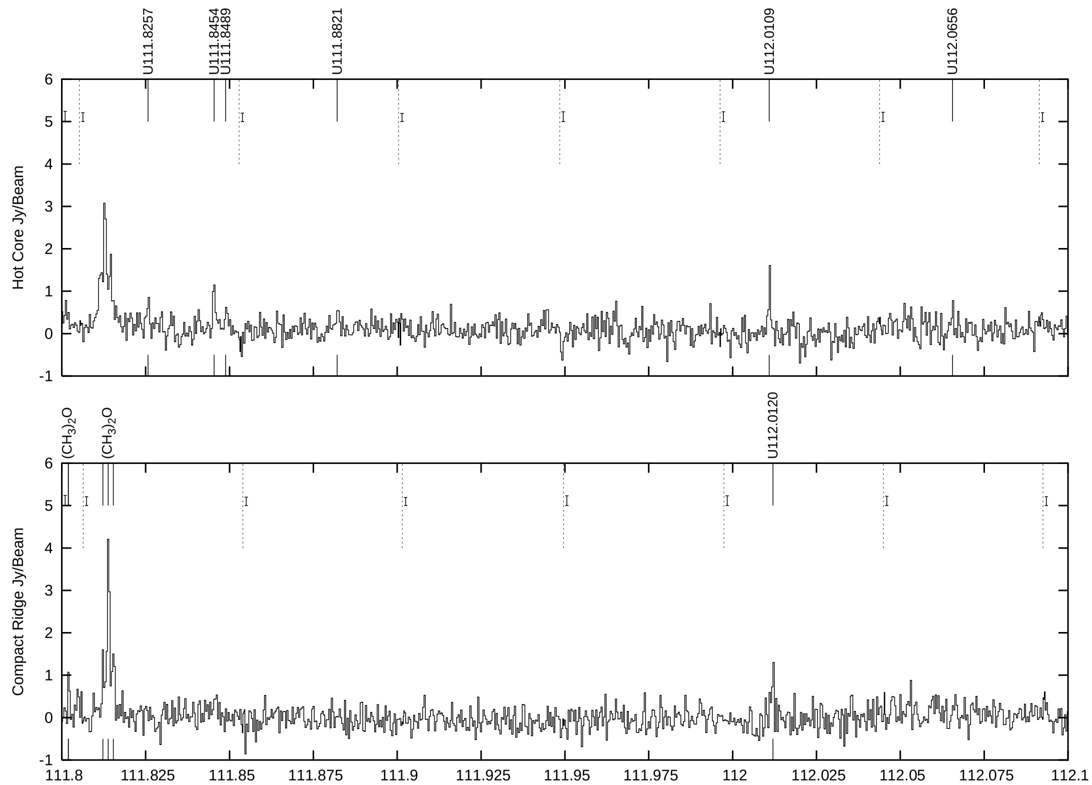

Fig. 4.23dc

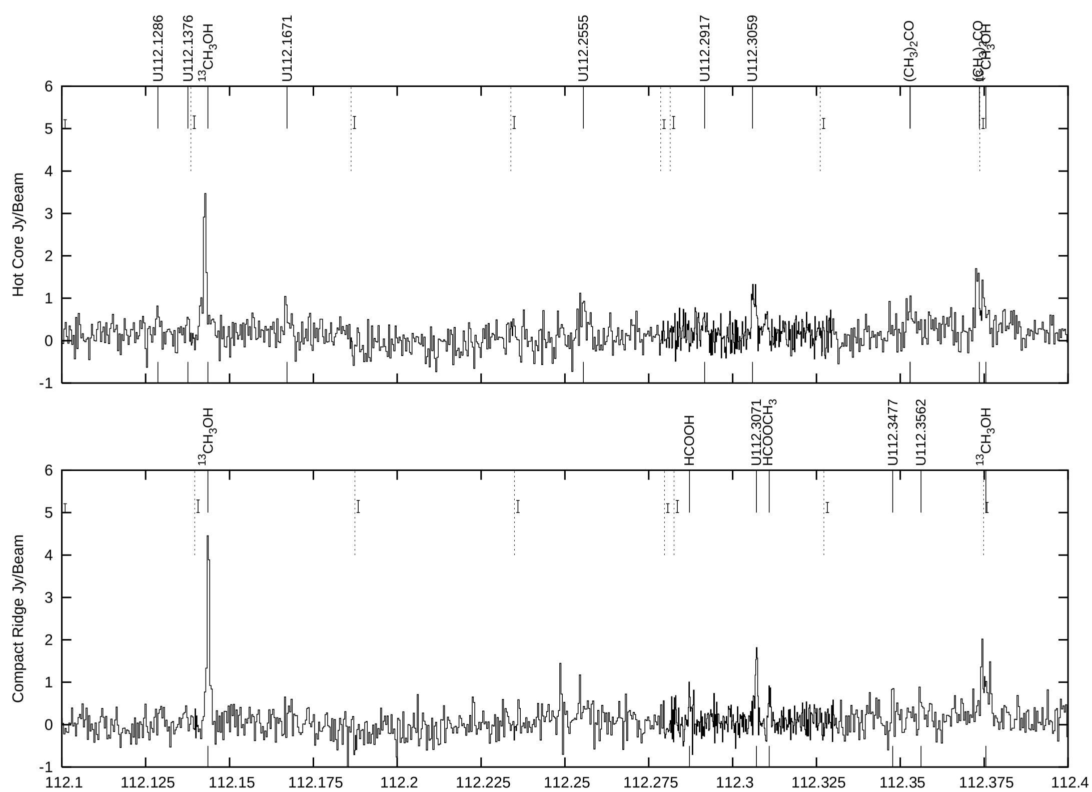

Fig. 4.23dd

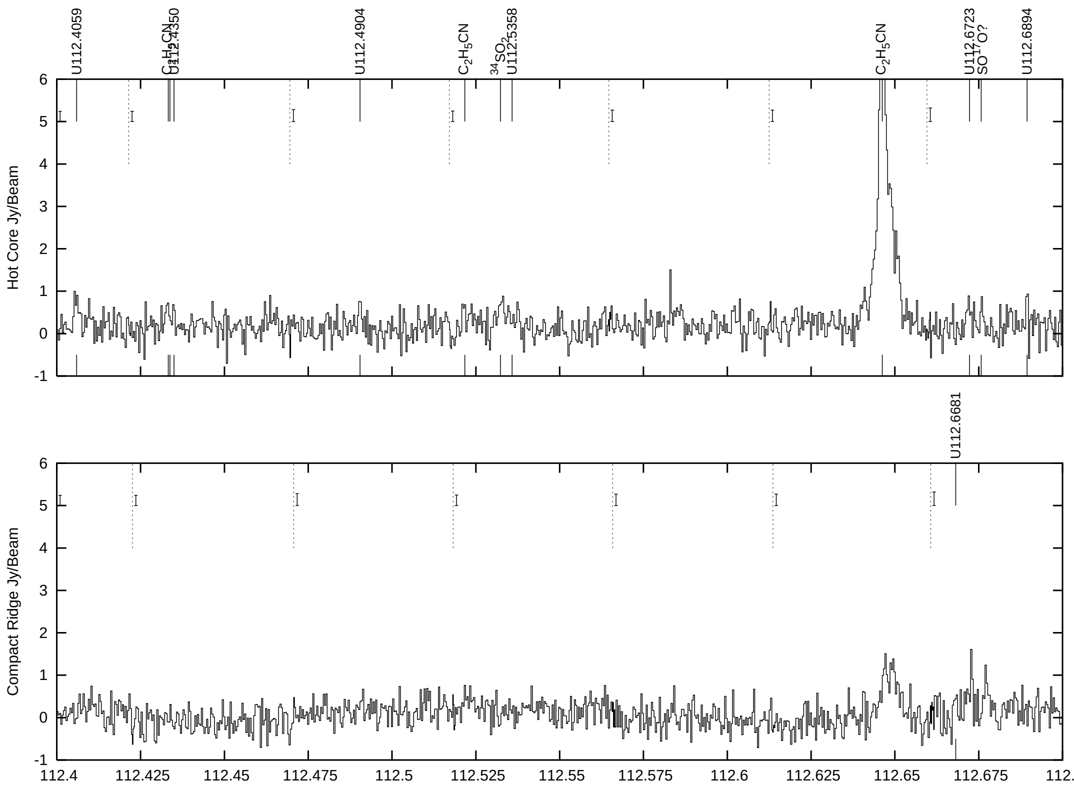

Fig. 4.23de

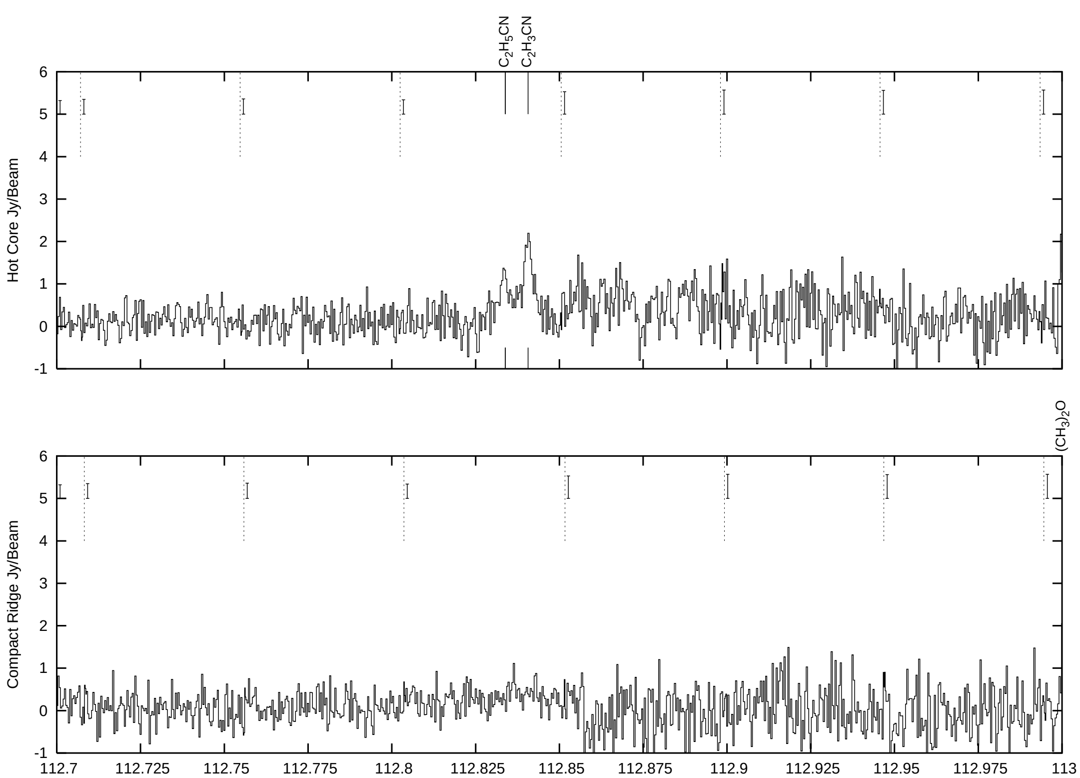

Fig. 4.23df

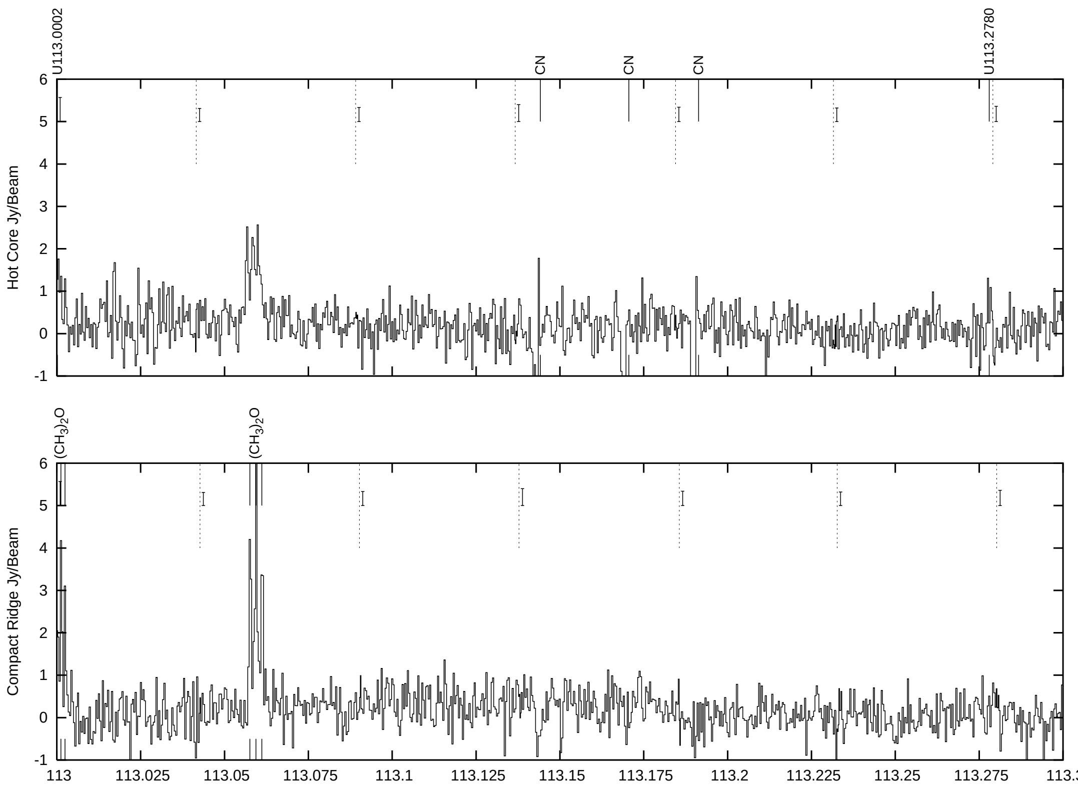

Fig. 4.23dg

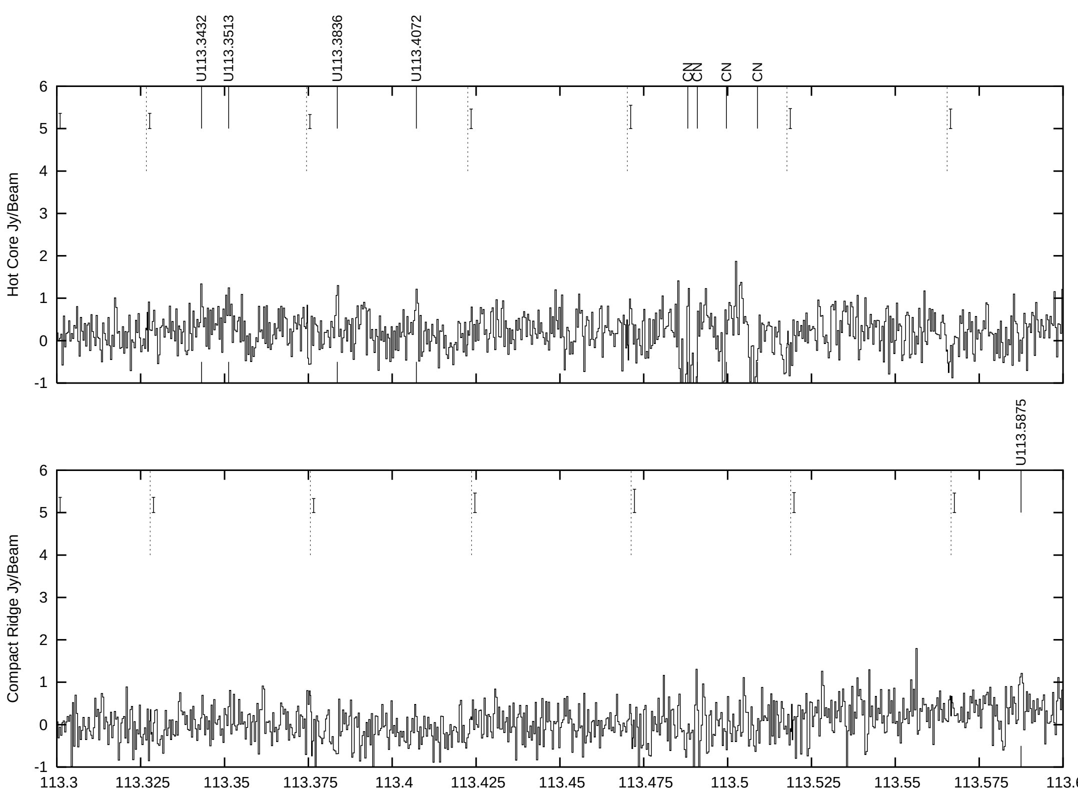

Fig. 4.23dh

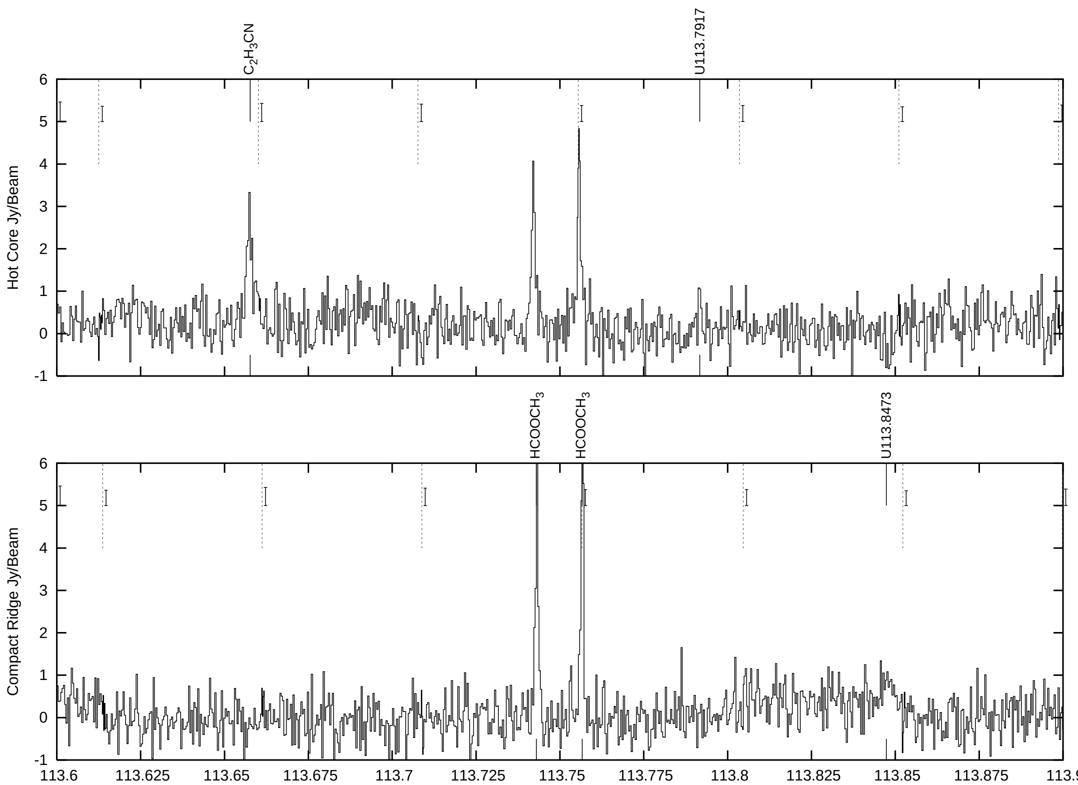

Fig. 4.23di

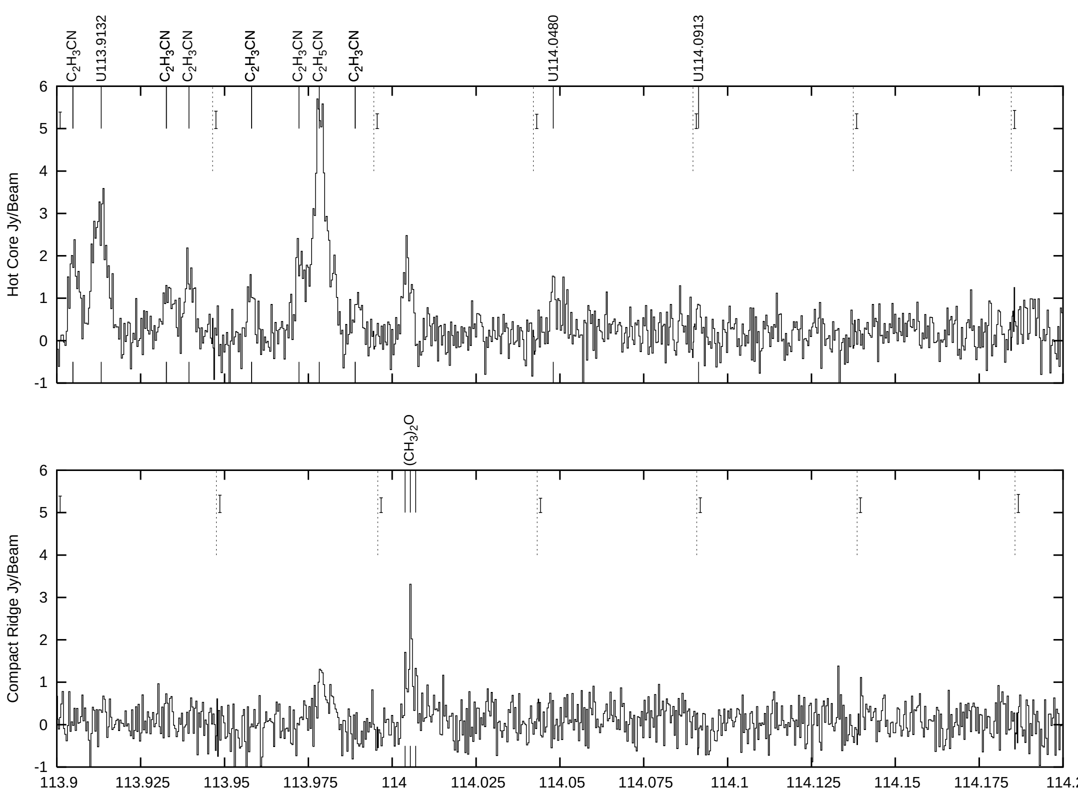

Fig. 4.23dj

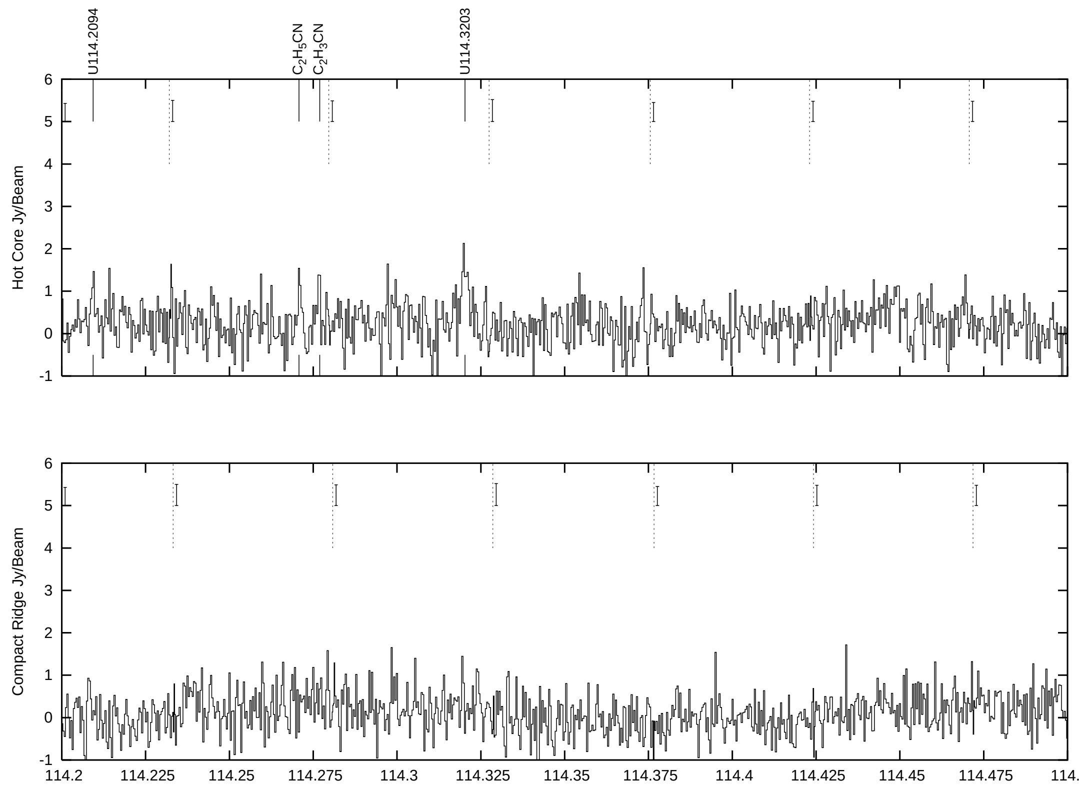

Fig. 4.23dk

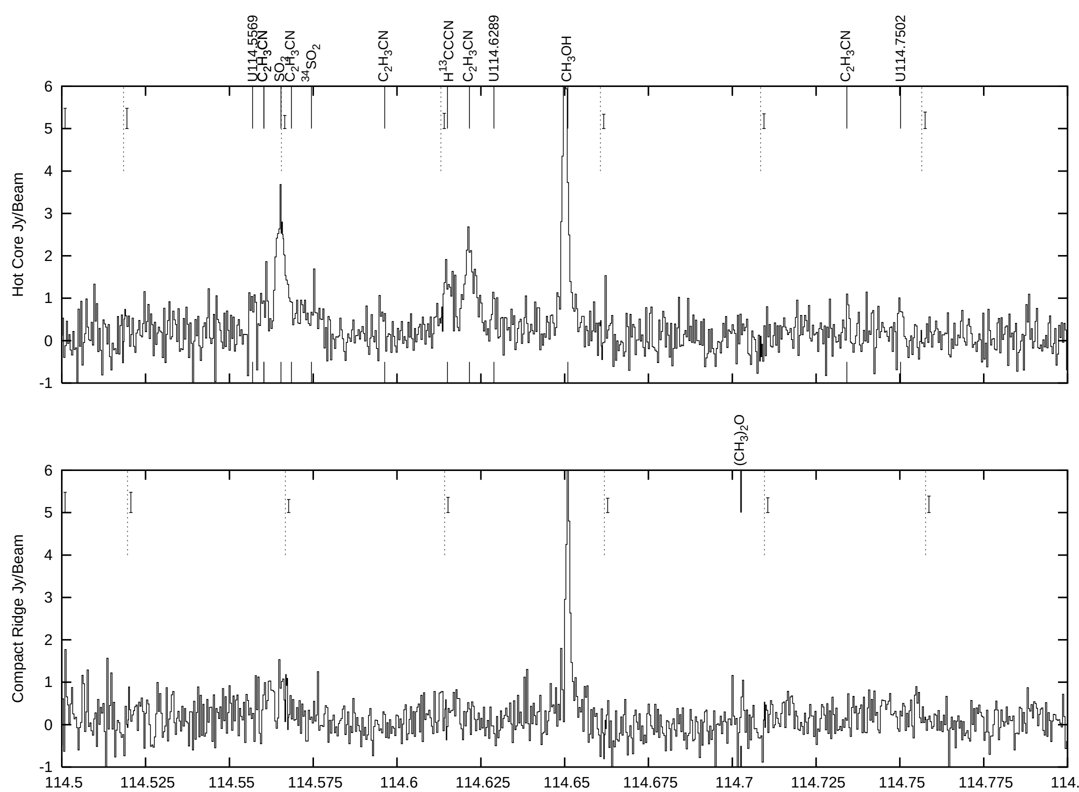

Fig. 4.23dl

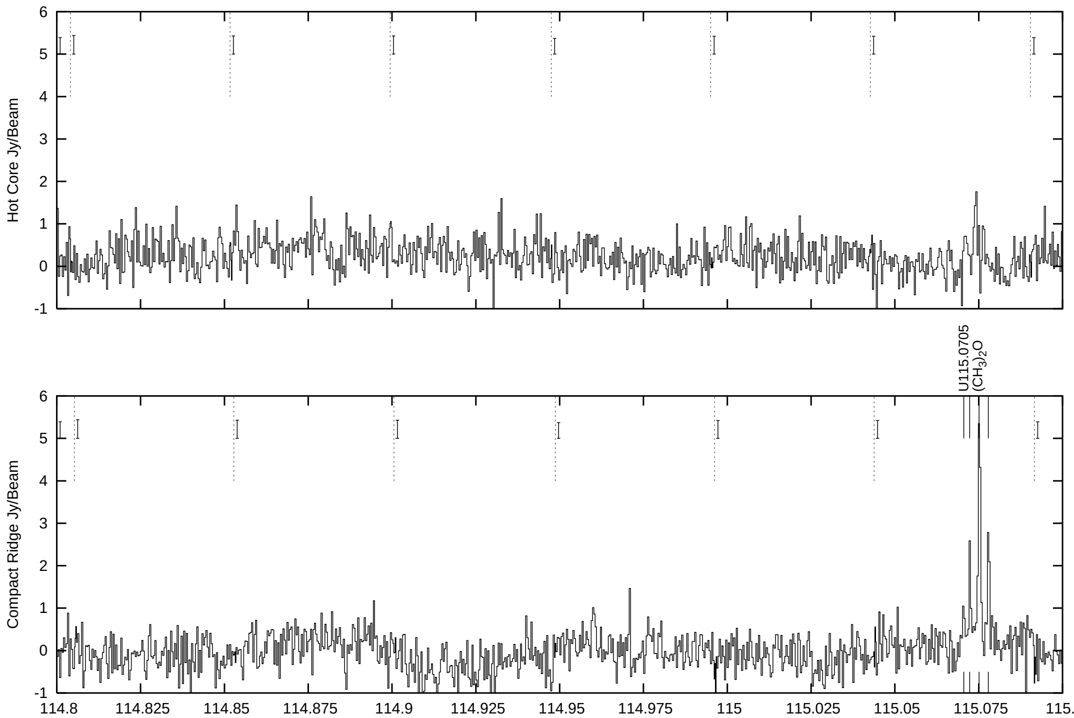

Fig. 4.23dm

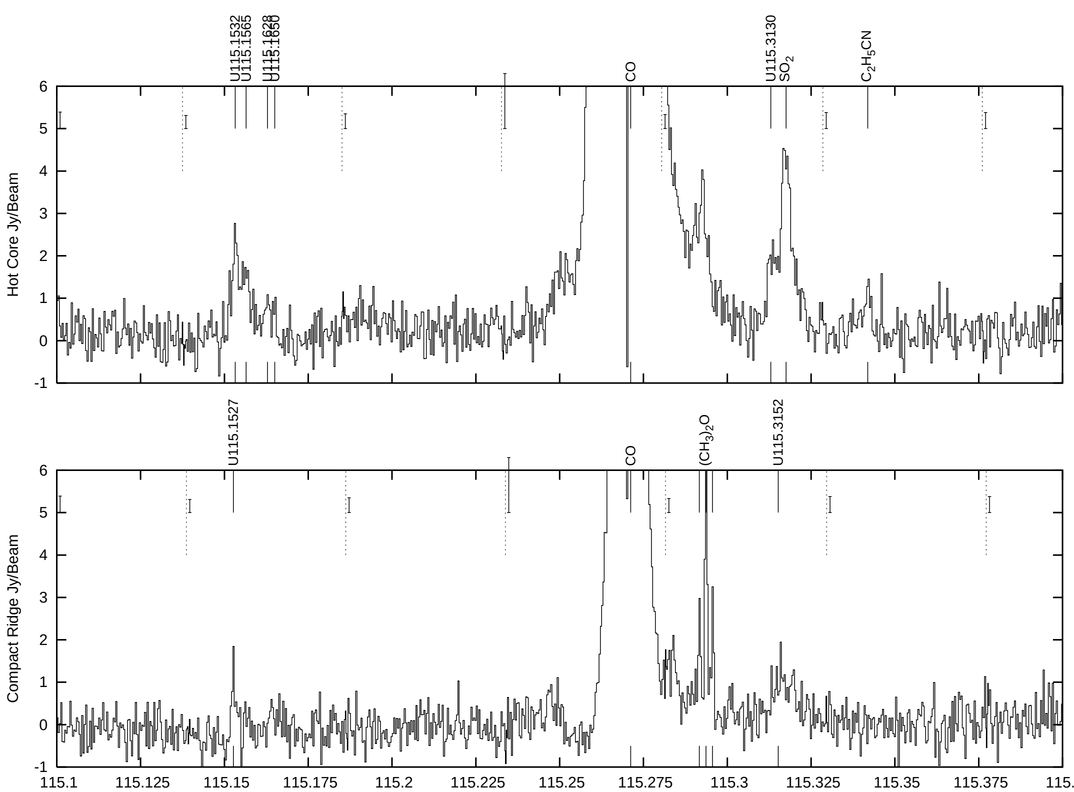

Fig. 4.23dn

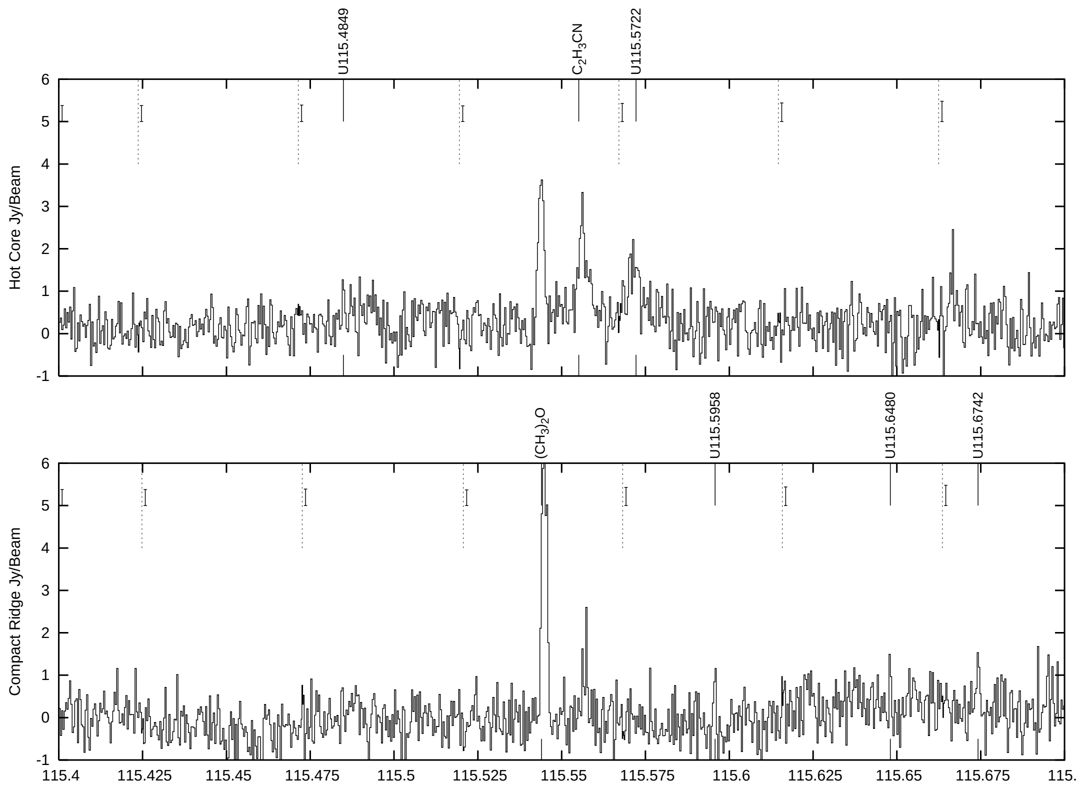

Fig. 4.23do

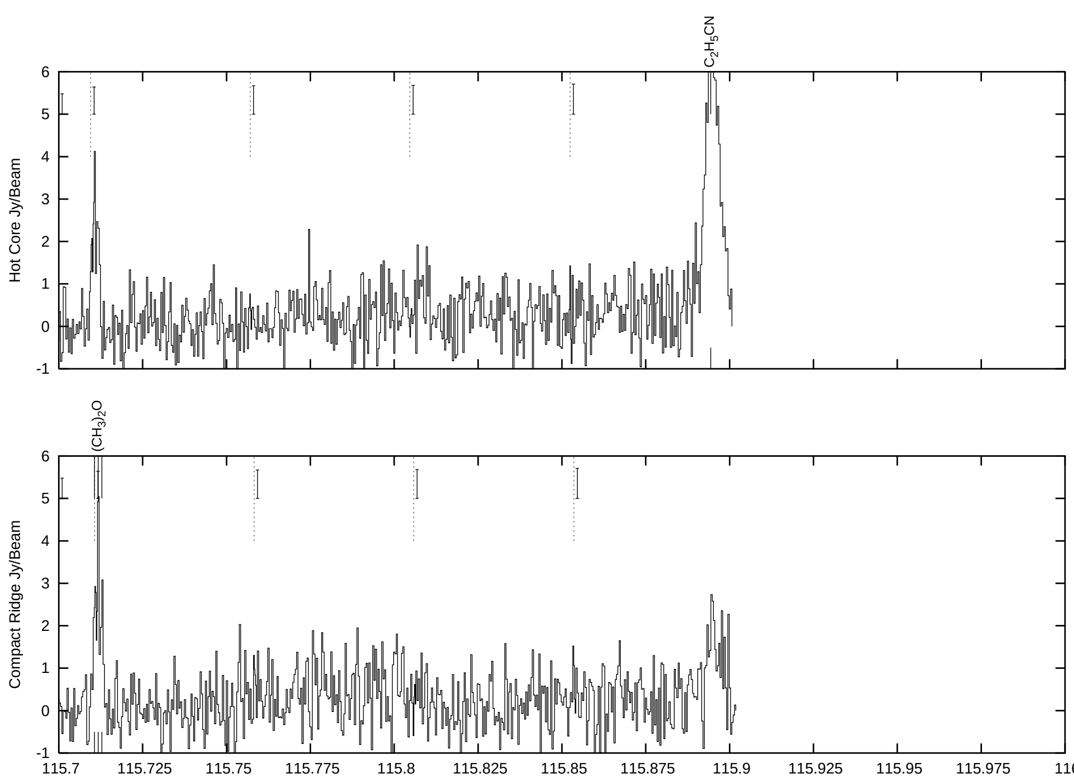

Fig. 4.23dp

Table 4.5. Transitions Detected Toward the Orion-KL Hot Core

Rest Frequency (MHz)[a]	Transition	I_0 (Jy/bm)	Δv (km s^{-1})	Beam Size ($''\times''$)	E_u (K)	$S\mu^2$ (D^2)
		C_2H				
87,316.925(4)	$1_{2,2}-0_{1,1}$	[b]	···	19.2×8.9	4.2	1.06
87,328.624(6)	$1_{2,1}-0_{1,0}$	[b]	···	19.2×8.9	4.2	0.53
87,402.004(5)	$1_{1,1}-0_{1,1}$	[b]	···	12.8×9.1	4.2	0.53
87,407.165(11)	$1_{1,0}-0_{1,1}$	[b]	···	12.8×9.1	4.2	0.21
		C_2H_3CHO?				
92,000.067(9)	$6_{1,6}-5_{0,5}$	[c]	···	13.1×6.9	10.8	3.58
		C_2H_3CN				
83,207.506(1)	$9_{1,9}-8_{1,8}$	0.6(1)	6.0(13)	13.6×8.0	22.1	129.24
		0.3(1)	17.4(13)	13.6×8.0	22.1	129.24
84,579.932(61)	$16_{1,15}-16_{0,16},^2\nu_{11}$	0.5(1)	4.0(13)	18.0×7.8	753.6	158.64
84,946.001(1)	$9_{0,9}-8_{0,8}$	0.9(1)	4.8(9)	13.6×8.3	20.4	130.84
		0.4(1)	18.3(35)	13.6×8.3	20.4	130.84
85,302.648(1)	$9_{2,8}-8_{2,7}$	0.7(1)	5.7(7)	12.5×8.3	29.1	124.44
		0.3(1)	22.1(27)	12.5×8.3	29.1	124.44
85,416.746(1)	$9_{4,6}-8_{4,5}$	0.7(0)	6.8(5)	12.2×7.7	55.1	105.08
85,416.746(1)	$9_{4,5}-8_{4,4}$	0.7(0)	6.8(5)	12.2×7.7	55.1	105.08
85,419.957(1)	$9_{5,5}-8_{5,4}$	0.5(1)	6.7(6)	12.2×7.7	74.5	90.53
85,419.957(1)	$9_{5,4}-8_{5,3}$	0.5(1)	6.7(6)	12.2×7.7	74.5	90.53
85,426.921(1)	$9_{3,7}-8_{3,6}$	0.6(1)	7.0(10)	11.9×7.5	39.9	116.43
85,431.194(1)	$9_{6,4}-8_{6,3}$	0.3(1)	6.4(9)	11.9×7.5	98.2	72.77
85,431.194(1)	$9_{6,3}-8_{6,2}$	0.3(1)	6.4(9)	11.9×7.5	98.2	72.77
85,434.527(1)	$9_{3,6}-8_{3,5}$	0.7(1)	8.4(10)	11.9×7.5	39.9	116.43
85,447.702(1)	$9_{7,3}-8_{7,2}$	0.2(0)	5.4(12)	11.9×7.5	126.2	51.67
85,447.702(1)	$9_{7,2}-8_{7,1}$	0.2(0)	5.4(12)	11.9×7.5	126.2	51.67
85,468.372(1)	$9_{8,2}-8_{8,1}$	0.2(0)	3.0(11)	14.4×7.7	158.4	27.36
85,468.372(1)	$9_{8,1}-8_{8,0}$	0.2(0)	3.0(11)	14.4×7.7	158.4	27.36
85,715.424(1)	$9_{2,7}-8_{2,6}$	0.8(2)	5.0(17)	17.9×7.4	29.2	124.44
		0.4(2)	15.0(50)	17.9×7.4	29.2	124.44
87,312.816(1)	$9_{1,8}-8_{1,7}$	1.2(2)	7.9(15)	19.2×8.9	23.1	129.24
92,426.249(1)	$10_{1,10}-9_{1,9}$	0.9(1)	8.2(14)	15.6×6.1	26.6	143.94
		0.4(1)	38.0(64)	15.6×6.1	26.6	143.94
94,516.445(12)	$10_{0,10}-9_{0,9},^1\nu_{11}$	0.6(2)	2.2(9)	13.8×6.6	368.9	145.40
94,760.782(1)	$10_{2,9}-9_{2,8}$	0.8(2)	4.2(12)	14.8×6.1	33.7	139.57
		0.7(1)	11.7(16)	14.8×6.1	33.7	139.57

Table 4.5—Continued

Rest Frequency (MHz)[a]	Transition	I_0 (Jy/bm)	Δv (km s^{-1})	Beam Size (″×″)	E_u (K)	$S\mu^2$ (D^2)
94,913.117(1)	$10_{4,7}-9_{4,6}$	1.1(1)	6.2(5)	13.6×6.3	59.6	122.25
		0.5(0)	15.6(12)	13.6×6.3	59.6	122.25
94,913.228(1)	$10_{4,6}-9_{4,5}$	1.1(1)	6.2(5)	13.6×6.3	59.6	122.25
		0.5(0)	15.6(12)	13.6×6.3	59.6	122.25
94,925.006(1)	$10_{6,5}-9_{6,4}$	0.5(4)	4.5(18)	14.3×6.4	102.8	93.15
94,925.006(1)	$10_{6,4}-9_{6,3}$	0.5(4)	4.5(18)	14.3×6.4	102.8	93.15
94,928.607(1)	$10_{3,8}-9_{3,7}$	1.3(4)	3.4(7)	14.3×6.4	44.5	132.44
		1.0(3)	6.4(15)	14.3×6.4	44.5	132.44
94,941.631(1)	$10_{3,7}-9_{3,6}$	[c]	⋯	14.3×6.4	44.5000	132.441
94,942.495(1)	$10_{7,3}-9_{7,2}$	[c]	⋯	14.3×6.4	130.7560	74.225
94,942.495(1)	$10_{7,4}-9_{7,3}$	[c]	⋯	14.3×6.4	130.7560	74.225
95,036.458(23)	$10_{4,7}-9_{4,6},^1\nu_{15}$	0.3(1)	3.4(12)	14.1×6.4	549.6	122.25
95,036.558(23)	$10_{4,6}-9_{4,5},^1\nu_{15}$	0.3(1)	3.4(12)	14.1×6.4	549.6	122.25
95,188.704(11)	$10_{5,6}-9_{5,5},^1\nu_{11}$	0.1(0)	12.1(26)	16.1×7.3	422.2	101.88
95,188.705(11)	$10_{5,5}-9_{5,4},^1\nu_{11}$	0.1(0)	12.1(26)	16.1×7.3	422.2	101.88
95,190.317(11)	$10_{4,7}-9_{4,6},^1\nu_{11}$	0.2(0)	12.1(26)	16.1×7.3	403.1	122.25
95,190.446(11)	$10_{4,6}-9_{4,5},^1\nu_{11}$	0.2(0)	12.1(26)	16.1×7.3	403.1	122.25
95,208.548(11)	$10_{3,8}-9_{3,7},^1\nu_{11}$	0.7(3)	4.9(38)	16.1×7.3	388.2	132.44
95,325.475(1)	$10_{2,8}-9_{2,7}$	1.0(2)	4.2(11)	13.9×10.9	33.7	139.57
		0.9(1)	15.6(19)	13.9×10.9	33.7	139.57
95,458.816(29)	$10_{5,6}-9_{5,5},^2\nu_{11}$	0.2(1)	5.1(26)	13.6×10.9	765.5	109.16
95,458.817(29)	$10_{5,5}-9_{5,4},^2\nu_{11}$	0.2(1)	5.1(26)	13.6×10.9	765.5	109.16
95,632.966(11)	$10_{2,8}-9_{2,7},^1\nu_{11}$	0.9(11)	1.4(17)	13.1×7.9	377.6	139.57
101,637.232(2)	$11_{1,11}-10_{1,10}$	2.0(3)	3.4(7)	14.6×6.8	31.4	158.64
		0.9(2)	16.9(31)	14.6×6.8	31.4	158.64
103,386.101(2)	$14_{0,14}-13_{1,13}$	1.1(1)	11.6(14)	13.2×6.3	47.5	121.38
103,575.396(2)	$11_{0,11}-10_{0,10}$	3.5(10)	1.3(7)	11.3×6.5	29.9	159.95
		0.5(1)	18.2(43)	11.3×6.5	29.9	159.95
103,831.233(13)	$11_{0,11}-10_{0,10},^1\nu_{11}$	0.5(1)	3.7(18)	12.6×5.5	373.9	159.95
104,212.647(1)	$11_{2,10}-10_{2,9}$	1.4(2)	4.6(7)	14.3×6.7	38.7	154.71
		0.7(2)	16.0(21)	14.3×6.7	38.7	154.71
104,354.097(26)	$11_{2,10}-10_{2,9},^1\nu_{15}$	4.0(8)	3.3(5)	13.7×6.7	528.1	154.71
104,419.277(1)	$11_{6,6}-10_{6,5}$	0.7(1)	5.6(12)	12.9×5.3	107.8	112.36
		0.1(0)	13.9(161)	12.9×5.3	107.8	112.36
104,419.277(1)	$11_{6,5}-10_{6,4}$	0.7(1)	5.6(12)	12.9×5.3	107.8	112.36
		0.1(0)	13.9(161)	12.9×5.3	107.8	112.36
104,432.781(1)	$11_{3,9}-10_{3,8}$	1.4(1)	4.6(6)	12.9×5.3	49.5	148.16
104,437.479(1)	$11_{7,5}-10_{7,4}$	0.6(0)	9.4(12)	12.8×5.3	135.8	95.19
104,437.479(1)	$11_{7,4}-10_{7,3}$	0.6(0)	9.4(12)	12.8×5.3	135.8	95.19
104,453.915(1)	$11_{3,8}-10_{3,7}$	1.1(2)	4.1(10)	12.8×5.3	49.5	148.16
		0.7(2)	16.3(46)	12.8×5.3	49.5	148.16
104,461.474(1)	$11_{8,3}-10_{8,2}$	0.2(0)	9.2(23)	12.8×5.3	168.0	75.39

Table 4.5—Continued

Rest Frequency (MHz)[a]	Transition	I_0 (Jy/bm)	Δv (km s^{-1})	Beam Size (″×″)	E_u (K)	$S\mu^2$ (D^2)
104,461.474(1)	$11_{8,4} - 10_{8,3}$	0.2(0)	9.2(23)	12.8×5.3	168.0	75.39
104,490.318(2)	$11_{9,2} - 10_{9,1}$	0.2(0)	5.7(16)	14.1×5.0	204.5	52.83
104,490.318(2)	$11_{9,3} - 10_{9,2}$	0.2(0)	5.7(16)	14.1×5.0	204.5	52.83
104,711.455(12)	$11_{5,7} - 10_{5,6},^1\nu_{11}$	0.2(0)	6.4(22)	12.2×5.2	427.2	126.91
104,711.457(12)	$11_{5,6} - 10_{5,5},^1\nu_{11}$	0.2(0)	6.4(22)	12.2×5.2	427.2	126.91
104,716.997(12)	$11_{4,7} - 10_{4,6},^1\nu_{11}$	0.2(0)	14.2(29)	12.2×5.2	408.1	138.94
104,719.198(12)	$11_{6,6} - 10_{6,5},^1\nu_{11}$	0.1(0)	14.2(29)	12.2×5.2	450.6	112.36
104,719.198(12)	$11_{6,5} - 10_{6,4},^1\nu_{11}$	0.1(0)	14.2(29)	12.2×5.2	450.6	112.36
104,764.917(12)	$11_{3,8} - 10_{3,7},^1\nu_{11}$	0.6(2)	3.6(11)	12.1×5.3	393.2	148.16
104,960.541(1)	$11_{2,9} - 10_{2,8}$	1.6(2)	4.2(6)	13.8×6.4	38.8	154.71
		0.6(1)	23.7(34)	13.8×6.4	38.8	154.71
105,068.336(25)	$11_{2,9} - 10_{2,8},^1\nu_{15}$	0.9(3)	4.1(16)	13.1×6.6	528.3	154.71
106,641.390(1)	$11_{1,10} - 10_{1,9}$	1.3(3)	1.7(6)	12.9×5.6	32.9	158.64
		1.3(1)	11.1(22)	12.9×5.6	32.9	158.64
110,839.975(2)	$12_{1,12} - 11_{1,11}$	1.8(5)	7.0(18)	13.3×5.4	36.8	173.34
		0.5(3)	16.4(78)	13.3×5.4	36.8	173.34
112,840.645(2)	$12_{0,12} - 11_{0,11}$	1.0(4)	4.4(19)	12.9×5.7	35.3	174.36
		1.2(4)	13.5(34)	12.9×5.7	35.3	174.36
113,657.636(2)	$12_{2,11} - 11_{2,10}$	1.6(5)	3.2(13)	12.3×5.1	44.1	169.70
		1.3(5)	12.0(27)	12.3×5.1	44.1	169.70
113,904.798(1)	$12_{5,8} - 11_{5,7}$	0.8(2)	5.0(49)	11.4×4.8	89.5	144.23
		0.4(1)	15.0(149)	11.4×4.8	89.5	144.23
113,904.801(1)	$12_{5,7} - 11_{5,6}$	0.8(2)	5.0(49)	11.4×4.8	89.5	144.23
		0.4(1)	15.0(149)	11.4×4.8	89.5	144.23
113,932.670(1)	$12_{7,6} - 11_{7,5}$	0.6(1)	11.2(23)	11.4×4.8	141.2	115.12
113,932.670(1)	$12_{7,5} - 11_{7,4}$	0.6(1)	11.2(23)	11.4×4.8	141.2	115.12
113,939.399(1)	$12_{3,10} - 11_{3,9}$	1.6(2)	8.6(14)	11.4×4.8	55.0	163.59
113,958.051(2)	$12_{8,5} - 11_{8,4}$	0.7(1)	6.3(14)	11.1×4.8	173.5	96.93
113,958.051(2)	$12_{8,4} - 11_{8,3}$	0.7(1)	6.3(14)	11.1×4.8	173.5	96.93
113,972.216(1)	$12_{3,9} - 11_{3,8}$	1.6(3)	6.9(16)	11.1×4.8	55.0	163.59
113,988.975(2)	$12_{9,4} - 11_{9,3}$	0.5(0)	8.4(22)	11.1×4.8	210.0	76.41
113,988.975(2)	$12_{9,3} - 11_{9,2}$	0.5(0)	8.4(22)	11.1×4.8	210.0	76.41
114,276.938(13)	$12_{3,10} - 11_{3,9}$	1.7(5)	1.8(7)	12.0×5.6	398.7	163.59
114,560.280(24)	$12_{5,8} - 11_{5,7},^2\nu_{11}$	0.6(1)	6.1(18)	12.9×5.1	776.7	144.23
114,560.284(24)	$12_{5,7} - 11_{5,6},^2\nu_{11}$	0.6(1)	6.1(18)	12.9×5.1	776.7	144.23
114,568.506(18)	$15_{2,13} - 15_{1,14}$	1.0(40)	9.6(289)	12.9×5.1	63.6	10.92
114,596.321(2)	$15_{0,15} - 14_{1,14}$	0.8(3)	3.7(19)	11.7×5.2	54.2	134.74
114,621.567(1)	$12_{2,10} - 11_{2,9}$	1.9(11)	6.4(18)	11.6×5.2	44.3	169.70
		1.1(4)	9.8(62)	11.6×5.2	44.3	169.70
114,734.194(25)	$12_{2,10} - 11_{2,9}$	1.1(3)	2.3(8)	11.9×5.1	533.8	169.70
115,555.108(2)	$16_{2,14} - 16_{1,15}$	0.9(2)	32.0(69)	11.9×5.1	70.9	9.48

Table 4.5—Continued

Rest Frequency (MHz)[a]	Transition	I_0 (Jy/bm)	Δv (km s^{-1})	Beam Size (″×″)	E_u (K)	$S\mu^2$ (D^2)
			C_2H_5CN			
80,404.893(0)	$9_{2,8} - 8_{2,7}$	2.3(1)	12.1(6)	12.9×8.1	23.7	107.00
80,441.334(2)	$9_{1,8} - 8_{2,6}E, \nu_t = 1$	0.5(1)	6.9(15)	12.9×8.3	330.0	111.70
80,591.013(3)	$9_{2,8} - 8_{2,7}E, \nu_b = 1$	0.2(1)	16.3(28)	12.5×8.0	325.5	107.00
80,592.772(3)	$9_{3,6} - 8_{3,5}A, \nu_b = 1$	0.2(1)	16.3(28)	12.5×8.0	325.5	99.16
80,602.134(0)	$9_{6,3} - 8_{6,2}$	0.8(2)	4.7(6)	12.5×8.0	59.3	58.95
80,602.134(0)	$9_{6,4} - 8_{6,3}$	0.8(2)	4.7(6)	12.5×8.0	59.3	58.95
80,604.575(0)	$9_{5,5} - 8_{5,4}$	2.4(1)	18.8(4)	12.5×8.0	47.1	74.86
80,604.578(0)	$9_{5,4} - 8_{5,3}$	2.4(1)	18.8(4)	12.5×8.0	47.1	74.86
80,614.479(0)	$9_{8,1} - 8_{8,0}$	0.6(1)	11.2(12)	12.7×7.9	90.4	21.14
80,614.479(0)	$9_{8,2} - 8_{8,1}$	0.6(1)	11.2(12)	12.7×7.9	90.4	21.14
80,619.230(0)	$9_{4,6} - 8_{4,5}$	1.1(1)	4.7(5)	12.7×7.9	37.1	88.36
		1.4(1)	15.8(7)	12.7×7.9	37.1	88.36
80,619.685(0)	$9_{4,5} - 8_{4,4}$	1.1(1)	4.7(5)	12.7×7.9	37.1	88.35
		1.4(1)	15.8(7)	12.7×7.9	37.1	88.35
80,649.869(0)	$9_{3,7} - 8_{3,6}$	2.8(4)	8.4(7)	12.7×7.9	29.3	99.16
80,667.076(2)	$9_{4,5} - 8_{4,4}E, \nu_t = 1$	0.9(1)	17.4(15)	13.3×7.9	344.4	88.36
80,682.809(0)	$9_{3,6} - 8_{3,5}$	1.4(2)	3.3(5)	13.3×7.9	29.3	99.15
		2.6(1)	14.7(6)	13.3×7.9	29.3	99.15
80,704.421(2)	$9_{3,6} - 8_{3,5}A, \nu_t = 1$	1.0(1)	15.4(13)	13.6×8.1	336.1	99.16
80,716.073(2)	$9_{3,7} - 8_{3,6}E, \nu_b = 1$	0.2(1)	28.1(44)	13.6×8.1	325.5	99.17
80,716.188(2)	$9_{3,7} - 8_{3,6}A, \nu_b = 1$	0.2(1)	28.1(44)	13.6×8.1	325.5	99.17
80,748.242(2)	$9_{4,5} - 8_{4,4}A, \nu_b = 1$	0.7(1)	15.2(16)	13.6×8.1	332.8	88.36
81,261.436(0)	$9_{2,7} - 8_{2,6}$	2.1(1)	15.4(8)	17.9×8.5	23.9	107.01
81,420.338(2)	$9_{3,6} - 8_{3,5}E, \nu_b = 1$	0.3(1)	10.7(17)	14.2×8.6	320.5	99.16
81,420.346(2)	$9_{2,7} - 8_{2,6}A, \nu_b = 1$	0.3(1)	10.7(17)	14.2×8.6	320.5	107.02
81,746.496(0)	$18_{1,17} - 18_{0,18}$	0.3(1)	20.0(34)	12.5×7.8	75.9	8.80
82,458.610(0)	$9_{1,8} - 8_{1,7}$	1.2(1)	31.1(25)	24.8×8.4	20.9	111.69
82,518.167(2)	$9_{2,7} - 8_{2,6}E, \nu_b = 1$	0.3(1)	8.7(24)	15.2×8.2	317.8	107.02
82,518.238(2)	$9_{1,8} - 8_{1,7}A, \nu_b = 1$	0.3(1)	8.7(24)	15.2×8.2	317.8	111.70
82,541.360(2)	$9_{1,8} - 8_{1,7}A, \nu_t = 1$	[c]	···	15.2×8.2	326.9	111.70
82,541.163(2)	$9_{2,8} - 8_{1,8}E, \nu_t = 1$	[c]	···	15.2×8.2	326.9	111.70
83,025.432(0)	$10_{2,9} - 10_{1,10}$	0.3(1)	10.2(26)	13.3×8.0	28.0	5.74
83,444.345(0)	$24_{2,22} - 24_{1,23}$	0.4(1)	33.2(56)	18.0×8.1	135.6	17.23
86,193.413(53)	$35_{5,31} - 34_{5,30}A, \nu_b = 1$	0.4(1)	6.2(20)	14.5×7.6	594.7	506.33
86,745.313(0)	$8_{1,8} - 7_{0,7}$	0.2(1)	4.3(27)	12.1×7.4	16.1	6.43
86,819.846(0)	$10_{1,10} - 9_{1,9}$	2.5(3)	5.2(7)	14.5×7.7	24.1	123.78
86,978.884(3)	$10_{1,9} - 9_{1,8}E, \nu_b = 1$	0.8(2)	6.4(17)	13.4×7.5	320.9	123.52
88,323.751(0)	$10_{0,10} - 9_{0,9}$	2.1(2)	4.9(6)	13.8×7.1	23.4	124.94
88,398.870(3)	$10_{0,10} - 9_{0,9}E, \nu_b = 1$	0.4(1)	16.8(23)	13.6×7.2	320.4	124.94

Table 4.5—Continued

Rest Frequency (MHz)[a]	Transition	I_0 (Jy/bm)	Δv (km s^{-1})	Beam Size (″×″)	E_u (K)	$S\mu^2$ (D^2)
88,398.891(3)	$10_{0,10} - 9_{0,9}A, \nu_b = 1$	0.4(1)	16.8(23)	13.6×7.2	320.4	124.94
88,478.473(0)	$26_{3,23} - 26_{2,24}$	0.5(1)	9.9(17)	13.5×7.3	162.1	20.97
88,508.534(3)	$10_{0,10} - 9_{0,9}A, \nu_t = 1$	0.4(1)	7.2(19)	13.8×7.3	329.3	124.94
88,508.956(3)	$10_{0,10} - 9_{0,9}E, \nu_t = 1$	0.4(1)	7.2(19)	13.8×7.3	329.3	124.94
88,713.211(0)	$25_{3,22} - 25_{2,23}$	0.7(2)	20.0(80)	16.7×6.4	150.8	20.23
88,758.436(0)	$27_{3,24} - 27_{2,25}$	0.5(2)	14.7(57)	17.1×6.3	174.0	21.57
89,009.308(0)	$25_{2,23} - 25_{1,24}$	0.7(2)	6.4(27)	14.7×6.4	146.5	16.78
		0.3(3)	3.0(39)	14.7×6.4	146.5	16.78
89,297.645(0)	$10_{2,9} - 9_{2,8}$	3.3(3)	4.8(5)	18.3×8.7	28.0	119.26
89,342.132(4)	$10_{2,9} - 9_{2,8}E, \nu_b = 1$	1.0(2)	14.6(19)	17.7×8.9	329.8	119.26
89,368.870(3)	$10_{1,10} - 9_{1,9}E, \nu_b = 1$	0.5(1)	5.9(21)	16.0×8.0	324.6	123.78
89,368.943(3)	$10_{2,9} - 9_{2,8}A, \nu_b = 1$	0.5(1)	5.9(21)	16.0×8.0	324.6	119.26
89,415.375(0)	$24_{3,21} - 24_{2,22}$	0.9(1)	12.4(17)	17.8×8.7	139.8	19.36
89,562.316(0)	$10_{6,4} - 9_{6,3}$	2.5(1)	7.1(5)	15.0×7.1	63.6	74.94
89,562.316(0)	$10_{6,5} - 9_{6,4}$	2.5(1)	7.1(5)	15.0×7.1	63.6	74.94
89,565.032(0)	$10_{7,3} - 9_{7,2}$	2.3(2)	6.7(5)	15.0×7.1	78.1	58.29
89,565.032(0)	$10_{7,4} - 9_{7,3}$	2.3(2)	6.7(5)	15.0×7.1	78.1	58.29
89,568.099(0)	$10_{5,6} - 9_{5,5}$	2.2(1)	7.3(5)	15.0×7.1	51.4	89.64
		1.6(1)	38.9(13)	17.8×8.7	51.4	89.64
89,568.107(0)	$10_{5,5} - 9_{5,4}$	2.2(1)	7.3(5)	15.0×7.1	51.4	89.64
		1.6(1)	38.9(13)	17.8×8.7	51.4	89.64
89,573.055(0)	$10_{8,2} - 9_{8,1}$	0.8(1)	4.7(7)	15.0×7.1	94.7	40.02
89,573.055(0)	$10_{8,3} - 9_{8,2}$	0.8(1)	4.7(7)	15.0×7.1	94.7	40.02
89,584.907(0)	$10_{9,1} - 9_{9,0}$	0.8(1)	8.0(8)	15.0×7.1	113.6	20.46
89,584.907(0)	$10_{9,2} - 9_{9,1}$	0.8(1)	8.0(8)	15.0×7.1	113.6	20.46
89,590.031(0)	$10_{4,7} - 9_{4,6}$	2.6(1)	18.4(5)	15.0×7.1	41.4	102.07
89,591.016(0)	$10_{4,6} - 9_{4,5}$	2.6(1)	18.4(5)	15.0×7.1	41.4	102.07
89,628.447(0)	$10_{3,8} - 9_{3,7}$	3.2(3)	4.2(4)	14.7×7.2	33.6	112.01
89,640.910(2)	$10_{4,7} - 9_{4,6}A, \nu_t = 1$	0.4(1)	3.9(8)	14.7×7.2	348.7	124.50
		0.1(0)	26.3(53)	14.7×7.2	348.7	124.50
89,641.268(2)	$10_{4,7} - 9_{4,6}E, \nu_t = 1$	0.4(1)	3.9(8)	14.7×7.2	348.7	124.50
		0.1(0)	26.3(53)	14.7×7.2	348.7	124.50
89,641.590(2)	$10_{4,6} - 9_{4,5}A, \nu_t = 1$	0.4(1)	3.9(8)	14.7×7.2	348.7	124.50
		0.1(0)	26.3(53)	14.7×7.2	348.7	124.50
89,641.746(2)	$10_{4,6} - 9_{4,5}E, \nu_t = 1$	0.4(1)	3.9(8)	14.7×7.2	348.7	124.50
		0.1(0)	26.3(53)	14.7×7.2	348.7	124.50
89,646.664(3)	$10_{5,6} - 9_{5,5}E, \nu_t = 1$	0.2(1)	7.3(16)	15.7×6.9	359.4	111.20
		0.1(0)	26.3(53)	15.7×6.9	359.4	111.20
89,646.803(3)	$10_{5,6} - 9_{5,5}A, \nu_t = 1$	0.2(1)	7.3(16)	15.7×6.9	359.4	111.20
		0.1(0)	26.3(53)	15.7×6.9	359.4	111.20
89,646.808(3)	$10_{5,5} - 9_{5,4}A, \nu_t = 1$	0.2(1)	7.3(16)	15.7×6.9	359.4	111.20
		0.1(0)	26.3(53)	15.7×6.9	359.4	111.20

Table 4.5—Continued

Rest Frequency (MHz)[a]	Transition	I_0 (Jy/bm)	Δv (km s^{-1})	Beam Size (″×″)	E_u (K)	$S\mu^2$ (D^2)
89,647.218(3)	$10_{5,5} - 9_{5,4}E, \nu_t = 1$	0.2(1)	7.3(16)	15.7×6.9	359.4	111.20
		0.1(0)	26.3(53)	15.7×6.9	359.4	111.20
89,647.833(3)	$10_{6,4} - 9_{6,3}A, \nu_b = 1$	0.1(1)	7.3(16)	15.7×6.9	358.0	94.90
		0.1(0)	26.3(53)	15.7×6.9	358.0	94.90
89,647.833(3)	$10_{6,5} - 9_{6,4}A, \nu_b = 1$	0.1(1)	7.3(16)	15.7×6.9	358.0	94.90
		0.1(0)	26.3(53)	15.7×6.9	358.0	94.90
89,647.835(3)	$10_{6,5} - 9_{6,4}E, \nu_b = 1$	0.1(1)	7.3(16)	15.7×6.9	358.0	94.90
		0.1(0)	26.3(53)	15.7×6.9	358.0	94.90
89,647.865(3)	$10_{6,4} - 9_{6,3}E, \nu_b = 1$	0.1(1)	7.3(16)	15.7×6.9	358.0	94.90
		0.1(0)	26.3(53)	15.7×6.9	358.0	94.90
89,661.742(2)	$10_{3,7} - 9_{3,6}E, \nu_t = 1$	0.7(1)	15.4(23)	15.7×6.9	340.4	112.03
89,682.266(2)	$10_{5,5} - 9_{5,4}A, \nu_b = 1$	0.4(1)	6.3(20)	15.7×6.9	346.4	89.64
89,682.269(2)	$10_{5,6} - 9_{5,5}A, \nu_b = 1$	0.4(1)	6.3(20)	15.7×6.9	346.4	89.64
89,684.713(0)	$10_{3,7} - 9_{3,6}$	3.2(3)	6.6(5)	15.7×6.9	33.6	112.03
89,700.155(2)	$10_{3,8} - 9_{3,7}E, \nu_t = 1$	0.8(8)	0.9(9)	15.2×7.0	340.4	112.02
		0.3(1)	16.9(63)	15.2×7.0	340.4	112.02
89,702.610(2)	$10_{3,7} - 9_{3,6}A, \nu_t = 1$	0.8(8	0.9(9)	15.2×7.0	340.4	112.04
		0.3(1)	16.9(63)	15.2×7.0	340.4	112.04
89,739.381(2)	$10_{4,6} - 9_{4,5}A, \nu_b = 1$	1.3(1)	8.3(17)	15.2×7.0	337.1	102.07
89,740.580(2)	$10_{4,7} - 9_{4,6}E, \nu_b = 1$	1.0(3)	2.2(13)	15.2×7.0	337.1	102.08
90,366.484(2)	$10_{2,8} - 9_{2,7}A, \nu_t = 1$	0.3(1)	20.6(31)	15.7×6.8	334.5	119.24
90,367.030(2)	$10_{2,8} - 9_{2,7}E, \nu_t = 1$	0.3(1)	20.6(31)	15.7×6.8	334.5	119.24
90,418.917(0)	$15_{1,14} - 14_{2,13}$	0.4(1)	6.1(19)	15.4×6.8	53.8	5.47
90,453.353(0)	$10_{2,8} - 9_{2,7}$	2.1(2)	4.8(5)	15.4×6.8	28.2	119.24
90,530.951(0)	$23_{3,20} - 23_{2,21}$	0.6(1)	10.6(17)	14.6×6.7	129.4	18.41
90,633.220(3)	$10_{3,7} - 9_{3,6}E, \nu_b = 1$	0.3(2)	8.4(42)	14.7×6.4	324.8	112.04
90,633.231(3)	$10_{2,8} - 9_{2,7}A, \nu_b = 1$	0.3(2)	8.4(42)	14.7×6.4	324.8	119.24
91,018.259(0)	$29_{3,26} - 29_{2,27}$	[c]	···	14.7×6.4	199.0	22.25
91,549.115(0)	$10_{1,9} - 9_{1,8}$	2.3(7)	30.4(36)	12.8×6.9	25.3	123.52
91,603.913(3)	$10_{2,8} - 9_{2,7}E, \nu_b = 1$	0.5(1)	14.3(20)	12.3×6.9	322.2	119.24
91,603.996(3)	$10_{1,9} - 9_{1,8}A, \nu_b = 1$	0.5(1)	14.3(20)	12.3×6.9	322.2	123.52
91,662.113(2)	$10_{1,9} - 9_{1,8}A, \nu_t = 1$	0.4(1)	14.8(29)	12.0×7.1	331.3	123.52
91,663.009(2)	$10_{2,9} - 9_{2,8}E, \nu_t = 1$	0.4(1)	14.8(29)	12.0×7.1	331.3	119.26
91,999.512(0)	$22_{3,19} - 22_{2,20}$	0.8(1)	12.0(17)	13.1×6.9	119.3	17.39
92,000.904(0)	$13_{2,12} - 13_{1,13}$	[c]	···	13.1×6.9	43.4	6.67
93,755.076(0)	$21_{3,18} - 21_{2,19}$	0.9(2)	6.4(21)	15.6×8.6	109.8	16.34
93,949.314(0)	$9_{1,9} - 8_{0,8}$	0.6(2)	5.1(17)	15.5×6.8	19.9	7.31
94,178.665(0)	$12_{0,12} - 11_{1,11}$	0.4(1)	6.0(18)	13.3×6.3	33.1	9.76
94,181.004(0)	$43_{6,37} - 42_{7,36}$	0.5(2)	2.8(11)	13.3×6.3	447.4	4.50
94,819.445(0)	$9_{2,8} - 9_{0,9}$	0.3(1)	2.2(9)	14.9×5.9	23.7	0.26
95,104.054(0)	$26_{2,24} - 26_{1,25}$	0.6(1)	9.2(22)	13.6×6.5	157.9	16.27
95,442.477(0)	$11_{1,11} - 10_{1,10}$	2.9(5)	5.4(10)	11.7×10.5	28.6	135.40

Table 4.5—Continued

Rest Frequency (MHz)[a]	Transition	I_0 (Jy/bm)	Δv (km s^{-1})	Beam Size (″×″)	E_u (K)	$S\mu^2$ (D^2)
95,502.419(0)	$14_{2,13} - 14_{1,14}$	0.7(1)	6.0(12)	14.8×8.4	49.4	6.88
95,611.898(3)	$11_{1,11} - 10_{1,10}A, \nu_b = 1$	0.3(1)	13.0(16)	13.1×7.9	325.5	135.41
95,611.917(3)	$11_{1,10} - 10_{1,9}E, \nu_b = 1$	0.3(1)	13.0(16)	13.1×7.9	325.5	135.05
95,727.546(0)	$20_{3,17} - 20_{2,18}$	0.8(1)	5.4(21)	14.2×6.9	100.6	15.29
95,739.327(0)	$31_{3,28} - 31_{2,29}$	0.4(1)	5.0(14)	14.1×6.9	225.7	22.22
96,288.182(0)	$20_{1,19} - 20_{0,20}$	0.3(1)	9.1(60)	14.4×6.4	92.8	8.31
96,919.752(0)	$11_{0,11} - 10_{0,10}$	3.8(3)	5.3(5)	16.8×7.0	28.1	136.35
97,152.586(3)	$11_{0,11} - 10_{0,10}A, \nu_t = 1$	0.5(1)	12.5(21)	14.5×6.3	334.0	136.35
97,153.032(3)	$11_{0,11} - 10_{0,10}E, \nu_t = 1$	0.5(1)	12.5(21)	14.5×6.3	334.0	136.35
97,844.674(0)	$19_{3,16} - 19_{2,17}$	0.9(2)	8.3(18)	13.8×7.2	92.0	14.25
98,177.575(0)	$11_{2,10} - 10_{2,9}$	6.8(1)	7.0(4)	15.7×6.8	32.7	131.14
98,227.038(2)	$11_{1,10} - 10_{1,9}E, \nu_t = 1$	0.6(1)	5.6(10)	16.1×6.8	339.0	135.03
98,238.630(3)	$11_{1,11} - 10_{1,10}E, \nu_b = 1$	0.5(1)	10.5(11)	16.1×6.8	329.3	135.03
98,238.727(3)	$11_{2,10} - 10_{2,9}A, \nu_b = 1$	0.5(1)	10.5(11)	16.1×6.8	329.3	135.03
98,523.879(0)	$11_{6,6} - 10_{6,5}$	1.1(11)	13.9(72)	16.1×6.8	68.4	89.81
		1.2(12)	22.8(330)	16.1×6.8	68.4	89.81
98,523.880(0)	$11_{6,5} - 10_{6,4}$	1.1(11)	13.9(72)	16.1×6.8	68.4	89.81
		1.2(12)	22.8(330)	16.1×6.8	68.4	89.81
98,524.661(0)	$11_{7,4} - 10_{7,3}$	1.1(11)	13.9(72)	16.1×6.8	82.8	74.25
		1.2(12)	22.8(330)	16.1×6.8	82.8	74.25
98,524.661(0)	$11_{7,5} - 10_{7,4}$	1.1(11)	13.9(72)	16.1×6.8	82.8	74.25
		1.2(12)	22.8(330)	16.1×6.8	82.8	74.25
98,533.972(0)	$11_{5,7} - 10_{5,6}$	2.6(18)	11.1(14)	13.2×6.3	56.1	103.50
98,533.992(0)	$11_{5,6} - 10_{5,5}$	2.6(18)	11.1(14)	16.1×6.3	56.1	103.50
98,532.072(0)	$11_{8,3} - 10_{8,2}$	1.7(8)	21.4(32)	16.1×6.3	99.4	57.18
98,532.072(0)	$11_{8,4} - 10_{8,3}$	1.7(8)	21.4(32)	16.1×6.3	99.4	57.18
98,544.149(0)	$11_{9,2} - 10_{9,1}$	1.2(3)	7.5(13)	13.6×6.2	118.3	38.88
98,544.149(0)	$11_{9,3} - 10_{9,2}$	1.2(3)	7.5(13)	13.6×6.2	118.3	38.88
98,559.874(0)	$11_{10,1} - 10_{10,0}$	0.9(1)	8.7(13)	13.6×6.2	139.3	19.70
98,559.874(0)	$11_{10,2} - 10_{10,1}$	0.9(1)	8.7(13)	13.6×6.2	139.3	19.70
98,564.831(0)	$11_{4,8} - 10_{4,7}$	5.7(57)	12.2(44)	13.6×6.2	46.1	115.11
98,566.795(0)	$11_{4,7} - 10_{4,6}$	2.9(29)	15.3(149)	13.6×6.2	46.1	115.13
98,610.102(0)	$11_{3,9} - 10_{3,8}$	4.7(3)	4.5(3)	13.9×6.1	38.4	124.38
98,618.874(2)	$11_{4,8} - 10_{4,7}A, \nu_t = 1$	1.2(2)	4.5(3)	13.9×6.1	353.5	115.11
98,619.055(3)	$11_{6,6} - 10_{6,5}A, \nu_b = 1$	0.9(2)	4.5(3)	13.9×6.1	362.7	89.81
98,619.055(3)	$11_{6,5} - 10_{6,4}A, \nu_b = 1$	0.9(2)	4.5(3)	13.9×6.1	362.7	89.81
98,619.057(3)	$11_{6,6} - 10_{6,5}E, \nu_b = 1$	0.9(2)	4.5(3)	13.9×6.1	362.7	89.81
98,619.093(3)	$11_{6,5} - 10_{6,4}E, \nu_b = 1$	0.9(2)	4.5(3)	13.9×6.1	362.7	89.81
98,620.101(3)	$11_{5,6} - 10_{5,5}E, \nu_t = 1$	1.5(1)	9.8(10)	13.9×6.1	364.1	103.50
98,620.230(2)	$11_{4,7} - 10_{4,6}A, \nu_t = 1$	1.5(1)	9.8(10)	13.9×6.1	353.5	115.13
98,643.484(2)	$11_{3,8} - 10_{3,7}E, \nu_t = 1$	1.0(1)	21.1(25)	13.9×6.2	345.1	124.39

Table 4.5—Continued

Rest Frequency (MHz)[a]	Transition	I_0 (Jy/bm)	Δv (km s^{-1})	Beam Size (″×″)	E_u (K)	$S\mu^2$ (D^2)
98,662.048(2)	$11_{5,6}-10_{5,5}A, \nu_b=1$	0.2(1)	12.8(20)	13.9×6.2	351.2	103.50
		0.1(1)	38.9(183)	13.9×6.2	351.2	103.50
98,662.056(2)	$11_{5,7}-10_{5,6}A, \nu_b=1$	0.2(1)	12.8(20)	13.9×6.2	351.2	103.51
		0.1(1)	38.9(183)	13.9×6.2	351.2	103.51
98,662.058(2)	$11_{5,7}-10_{5,6}E, \nu_b=1$	0.2(1)	12.8(20)	13.9×6.2	351.2	103.51
		0.1(1)	38.9(183)	13.9×6.2	351.2	103.51
98,662.103(2)	$11_{5,6}-10_{5,5}E, \nu_b=1$	0.2(1)	12.8(20)	13.9×6.2	351.2	103.50
		0.1(1)	38.9(183)	13.9×6.2	351.2	103.50
98,663.936(3)	$11_{3,9}-10_{3,8}E, \nu_b=1$	0.3(1)	12.8(20)	13.9×6.2	334.5	124.38
		0.1(1)	38.9(183)	13.9×6.2	334.5	124.38
98,664.086(3)	$11_{3,9}-10_{3,8}A, \nu_b=1$	0.3(1)	12.8(20)	13.9×6.2	334.5	124.38
		0.1(1)	38.9(183)	13.9×6.2	334.5	124.38
98,701.104(0)	$11_{3,8}-10_{3,7}$	2.7(1)	3.5(2)	14.6×7.1	38.4	124.39
98,712.742(2)	$11_{3,8}-10_{3,7}A, \nu_t=1$	1.1(1)	10.9(18)	14.6×7.1	345.1	124.39
98,736.443(2)	$11_{4,7}-10_{4,6}A, \nu_b=1$	1.4(1)	9.2(12)	15.2×7.0	341.8	115.13
99,253.452(0)	$15_{2,14}-15_{1,15}$	0.5(1)	12.3(27)	14.2×8.1	55.8	7.06
99,681.510(0)	$11_{2,9}-10_{2,8}$	3.7(6)	6.1(6)	13.3×5.5	33.0	131.11
100,614.288(0)	$11_{1,10}-10_{1,9}$	3.6(15)	5.6(13)	14.1×6.1	30.1	135.05
100,659.702(3)	$11_{2,9}-10_{2,8}E, \nu_b=1$	0.6(1)	9.6(13)	14.0×6.2	327.0	131.12
100,659.801(3)	$11_{1,10}-10_{1,9}A, \nu_b=1$	0.6(1)	9.6(13)	14.0×6.2	327.0	135.03
100,764.860(3)	$11_{2,10}-10_{2,9}E, \nu_t=1$	0.6(1)	12.1(16)	14.0×6.4	336.1	131.15
101,091.658(0)	$10_{1,10}-9_{0,9}$	[c]	⋯	13.2×5.6	24.1	8.25
101,689.984(0)	$27_{2,25}-27_{1,26}$	0.9(10)	3.0(26)	14.1×7.1	169.7	15.73
103,054.589(0)	$21_{2,19}-20_{3,18}$	1.4(14)	0.7(7)	14.7×5.7	105.3	4.89
103,059.344(0)	$33_{3,30}-33_{2,31}$	0.5(1)	6.6(51)	14.7×5.7	254.3	21.54
103,867.269(0)	$21_{1,20}-21_{0,21}$	0.4(1)	7.0(20)	12.5×5.4	101.9	8.09
104,051.275(0)	$12_{1,12}-11_{1,11}$	2.9(3)	4.3(5)	14.3×5.4	33.6	146.70
104,105.635(0)	$13_{0,13}-12_{1,12}$	0.6(1)	16.2(38)	12.0×5.1	38.6	10.89
104,359.690(0)	$16_{3,13}-16_{2,14}$	0.7(1)	9.0(22)	13.7×6.7	68.6	11.37
104,588.756(0)	$26_{8,19}-27_{7,20}$	0.3(2)	2.3(8)	12.7×5.3	221.9	3.20
104,589.004(0)	$26_{8,18}-27_{7,21}$	0.3(2)	2.3(8)	12.7×5.3	221.9	3.20
105,469.297(0)	$12_{0,12}-11_{0,11}$	3.9(16)	5.1(13)	10.7×6.3	33.1	147.52
105,539.918(3)	$12_{0,12}-11_{0,11}E, \nu_b=1$	0.8(1)	9.2(10)	13.2×5.6	330.1	147.52
105,539.941(3)	$12_{0,12}-11_{0,11}A, \nu_b=1$	0.8(1)	9.2(10)	13.2×5.6	330.1	147.52
106,375.014(0)	$15_{3,12}-15_{2,13}$	0.5(1)	6.2(17)	12.9×5.3	61.7	10.50
107,043.518(0)	$12_{2,11}-11_{2,10}$	4.7(19)	4.4(10)	11.8×6.8	37.9	142.65
107,089.029(3)	$12_{1,12}-11_{1,11}E, \nu_b=1$	0.5(1)	8.9(22)	10.9×6.3	334.5	146.71
107,089.155(3)	$12_{2,11}-11_{2,10}A, \nu_b=1$	0.5(1)	8.9(22)	10.9×6.3	334.5	142.65
107,100.886(3)	$12_{2,11}-11_{2,10}A, \nu_t=1$	0.4(1)	9.0(23)	12.3×6.7	344.2	142.65
107,101.413(3)	$12_{1,11}-11_{1,10}E, \nu_t=1$	0.4(1)	9.0(23)	12.3×6.7	344.2	146.71
107,485.179(0)	$12_{7,5}-11_{7,4}$	1.2(1)	7.3(9)	12.3×6.7	87.9	89.08
107,485.179(0)	$12_{7,6}-11_{7,5}$	1.2(1)	7.3(9)	12.3×6.7	87.9	89.08

Table 4.5—Continued

Rest Frequency (MHz)[a]	Transition	I_0 (Jy/bm)	Δv (km s^{-1})	Beam Size (″×″)	E_u (K)	$S\mu^2$ (D^2)
107,486.960(0)	$12_{6,7} - 11_{6,6}$	1.4(1)	7.3(9)	12.0×5.3	73.5	103.74
107,486.961(0)	$12_{6,6} - 11_{6,5}$	1.4(1)	7.3(9)	12.0×5.3	73.5	103.74
107,491.576(0)	$12_{8,4} - 11_{8,3}$	1.4(1)	5.0(5)	12.0×5.3	104.6	72.96
107,491.576(0)	$12_{8,5} - 11_{8,4}$	1.4(1)	5.0(5)	12.0×5.3	104.6	72.96
107,502.424(0)	$12_{5,8} - 11_{5,7}$	3.1(13)	7.6(11)	12.0×5.3	61.3	116.67
107,502.471(0)	$12_{5,7} - 11_{5,6}$	3.1(13)	7.6(11)	12.0×5.3	61.3	116.67
107,503.601(0)	$12_{9,3} - 11_{9,2}$	1.8(6)	12.1(35)	12.0×5.3	123.4	55.68
107,503.601(0)	$12_{9,4} - 11_{9,3}$	1.8(6)	12.1(35)	12.0×5.3	123.4	55.68
107,539.494(3)	$12_{10,3} - 11_{10,2}E, \nu_t = 1$	0.1(0)	10.0(22)	12.2×5.3	456.7	37.55
107,539.832(3)	$12_{10,2} - 11_{10,1}E, \nu_t = 1$	0.1(0)	10.0(22)	12.2×5.3	456.7	37.55
107,539.850(0)	$12_{11,1} - 11_{11,0}$	0.7(1)	10.0(22)	12.2×5.3	167.7	18.87
107,539.850(0)	$12_{11,2} - 11_{11,1}$	0.7(1)	10.0(22)	12.2×5.3	167.7	18.87
107,540.018(3)	$12_{10,2} - 11_{10,1}A, \nu_t = 1$	0.1(0)	10.0(22)	12.2×5.3	456.7	37.55
107,540.018(3)	$12_{10,3} - 11_{10,2}A, \nu_t = 1$	0.1(0)	10.0(22)	12.2×5.3	456.7	37.55
107,543.922(0)	$12_{4,9} - 11_{4,8}$	4.6(6)	6.8(8)	12.2×5.3	51.3	127.60
107,547.597(0)	$12_{4,8} - 11_{4,7}$	2.8(4)	4.6(6)	12.2×5.3	51.3	127.59
107,594.044(0)	$12_{3,10} - 11_{3,9}$	2.0(19)	5.9(24)	13.1×5.5	43.5	136.33
107,594.637(3)	$12_{5,8} - 11_{5,7}E, \nu_t = 1$	0.6(6)	5.9(24)	13.1×5.5	369.3	116.67
107,603.173(3)	$12_{4,8} - 11_{4,7}A, \nu_t = 1$	1.7(1)	10.7(9)	13.1×5.5	358.6	127.59
107,734.736(0)	$12_{3,9} - 11_{3,8}$	5.1(4)	9.5(9)	13.8×5.3	43.5	136.32
107,746.044(3)	$12_{4,9} - 11_{4,8}E, \nu_b = 1$	1.0(2)	9.8(21)	13.8×5.3	347.0	127.60
108,210.384(0)	$11_{1,11} - 10_{0,10}$	0.6(1)	17.6(29)	11.8×5.1	28.6	9.22
108,227.102(0)	$14_{3,11} - 14_{2,12}$	0.6(2)	2.8(15)	11.8×5.1	55.2	9.67
108,793.616(3)	$12_{2,10} - 11_{2,9}A, \nu_t = 1$	0.5(1)	12.0(19)	11.9×5.1	344.5	142.64
108,794.369(3)	$12_{2,10} - 11_{2,9}E, \nu_t = 1$	0.5(1)	12.0(19)	11.9×5.1	344.5	142.64
108,915.656(8)	$12_{3,10} - 12_{2,11}A, \nu_b = 1$	0.7(2)	4.5(13)	12.4×5.2	339.7	7.79
108,940.594(0)	$12_{2,10} - 11_{2,9}$	4.0(5)	5.7(5)	12.4×5.2	38.2	142.64
109,650.298(0)	$12_{1,11} - 11_{1,10}$	5.3(5)	7.3(7)	12.2×5.1	35.4	146.25
109,680.680(3)	$12_{2,10} - 11_{2,9}E, \nu_b = 1$	0.6(1)	7.1(12)	12.6×5.1	332.3	142.64
109,680.797(3)	$12_{1,11} - 11_{1,10}A, \nu_b = 1$	0.6(1)	7.1(12)	12.6×5.1	332.3	146.25
109,843.629(3)	$12_{1,11} - 11_{1,10}A, \nu_t = 1$	0.7(4)	1.7(11)	11.7×5.3	341.4	146.25
109,844.703(3)	$12_{2,11} - 11_{2,10}E, \nu_t = 1$	0.7(2)	13.2(27)	11.7×5.3	341.4	142.66
111,315.872(0)	$12_{3,9} - 12_{2,10}$	0.6(1)	8.5(19)	12.1×5.8	43.5	8.11
111,574.598(0)	$22_{1,21} - 22_{0,22}$	0.7(1)	6.1(12)	12.9×5.0	111.4	7.88
112,433.246(0)	$20_{7,14} - 21_{6,15}$	0.3(1)	6.5(28)	11.7×4.9	144.7	2.60
112,433.731(0)	$20_{7,13} - 21_{6,16}$	0.3(1)	6.5(28)	11.7×4.9	144.7	2.60
112,521.730(0)	$11_{3,8} - 11_{2,9}$	0.7(2)	3.2(12)	11.7×5.0	38.4	7.36
112,646.230(0)	$13_{1,13} - 12_{1,12}$	4.0(3)	4.9(4)	12.0×5.0	39.0	157.70
112,833.876(3)	$13_{1,13} - 12_{1,12}A, \nu_b = 1$	0.6(2)	9.5(33)	12.9×5.7	335.9	157.70
112,833.893(3)	$13_{1,12} - 12_{1,11}E, \nu_b = 1$	0.6(2)	9.5(33)	12.9×5.7	335.9	157.14
113,978.245(0)	$13_{0,13} - 12_{0,12}$	2.3(11)	6.0(19)	11.1×4.8	38.6	158.37
114,270.775(0)	$9_{3,6} - 9_{2,7}$	1.4(4)	3.1(10)	12.0×5.6	29.3	5.90

Table 4.5—Continued

Rest Frequency (MHz)[a]	Transition	I_0 (Jy/bm)	Δv (km s^{-1})	Beam Size ($'' \times ''$)	E_u (K)	$S\mu^2$ (D^2)
115,341.907(0)	$12_{1,12} - 11_{0,11}$	1.0(6)	4.5(33)	11.7×4.9	33.6	10.23
115,894.361(0)	$13_{2,12} - 12_{2,11}$	4.6(46)	9.1(41)	12.5×5.4	43.4	153.82
		3.5(35)	12.7(114)	12.5×5.4	43.4	153.82
			C_2H_5OH			
86,947.257(4)	$15_{2,13} - 15_{1,14}$	0.5(3)	3.1(22)	13.4×7.5	108.0	18.74
92,418.499(15)	$31^{-}_{2,29} - 31^{+}_{3,29}$	0.8(2)	2.8(7)	15.6×6.1	481.9	33.78
93,497.460(8)	$14^{-}_{0,14} - 14^{+}_{1,14}$	0.3(1)	9.3(29)	13.9×6.0	146.3	20.97
94,278.311(6)	$12_{1,11} - 12_{0,12}$	2.6(18)	11.4(14)	13.9×6.0	68.3	8.62
94,696.418(7)	$15^{-}_{0,15} - 15^{+}_{1,15}$	0.5(1)	8.0(18)	15.5×7.4	158.3	24.03
98,173.208(6)	$4^{+}_{3,2} - 3^{-}_{2,2}$	0.6(1)	7.8(22)	15.7×6.8	76.1	2.68
98,230.407(7)	$16^{-}_{1,16} - 16^{+}_{0,16}$	0.7(1)	6.4(20)	16.1×6.8	171.0	26.10
98,237.466(26)	$35^{-}_{1,35} - 35^{+}_{0,35}$	0.9(2)	2.0(7)	16.1×6.8	559.3	52.47
102,489.459(6)	$11^{-}_{1,11} - 11^{+}_{0,11}$	0.5(2)	7.9(31)	12.8×6.3	115.5	16.25
102,534.034(2)	$6^{+}_{0,6} - 5^{+}_{0,5}$	0.8(2)	5.2(18)	12.8×6.2	74.2	7.84
108,438.549(3)	$13_{3,10} - 13_{2,11}$	0.6(2)	4.8(16)	12.5×5.6	88.1	15.11
			CH_3CCH			
102,546.024(1)	$6_1 - 5_1$	0.8(3)	2.6(13)	12.8×6.2	24.4	3.28
102,547.984(1)	$6_0 - 5_0$	[c]	···	12.8×6.2	17.2	3.37
			CH_3CN			
91,958.728(36)	$5_4 - 4_4$	3.5(3)	6.4(2)	13.4×7.0	126.9	27.66
		1.9(2)	15.1(4)	13.4×7.0	126.9	27.66
91,971.132(25)	$5_3 - 4_3$	7.5(4)	6.4(2)	13.4×7.0	77.2	49.17
		6.0(4)	15.1(4)	13.4×7.0	77.2	49.17
91,979.997(17)	$5_2 - 4_2$	7.8(5)	6.4(2)	13.1×6.9	41.6	64.54
		5.5(4)	15.1(4)	13.1×6.9	41.6	64.54
91,985.317(16)	$5_1 - 4_1$	6.9(7)	6.4(2)	13.1×6.9	20.3	73.76
		4.0(9)	15.1(4)	13.1×6.9	20.3	73.76
91,987.090(16)	$5_0 - 4_0$	6.4(7)	6.4(2)	13.1×6.9	13.2	76.83
		7.4(9)	15.1(4)	13.1×6.9	13.2	76.83
92,175.524(120)	$5_{1,1} - 4_{1,1},^{1} \nu_8$	1.7(1)	6.2(2)	13.8×7.0	539.6	73.76
92,234.587(20)	$5_{3,-1} - 4_{3,-1},^{1} \nu_8$	0.6(1)	6.2(2)	13.3×7.0	649.4	49.17
92,247.254(16)	$5_{2,-1} - 4_{2,-1},^{1} \nu_8$	1.7(1)	6.2(2)	13.3×7.0	600.6	64.54
92,249.629(26)	$5_{4,2} - 4_{4,2},^{1} \nu_8$	0.9(1)	6.2(2)	13.3×7.0	599.1	27.66
92,256.278(200)	$5_{1,1} - 4_{1,1},^{1} \nu_8$	1.3(1)	6.2(2)	13.3×7.0	558.6	73.76
92,258.402(20)	$5_{3,1} - 4_{3,1},^{1} \nu_8$	1.0(1)	6.2(2)	13.3×7.0	570.0	49.17
92,261.420(160)	$5_{0,1} - 4_{0,1},^{1} \nu_8$	1.4(1)	6.2(2)	13.3×7.0	545.8	76.83
92,263.938(22)	$5_{2,1} - 4_{2,1},^{1} \nu_8$	1.4(3)	6.2(2)	13.3×7.0	547.7	64.54

Table 4.5—Continued

Rest Frequency (MHz)[a]	Transition	I_0 (Jy/bm)	Δv (km s^{-1})	Beam Size ($''\times''$)	E_u (K)	$S\mu^2$ (D^2)
92,353.434(200)	$5_{1,1}-4_{1,1},^1\nu_8$	1.4(1)	6.2(2)	14.4×7.9	539.7	73.76
110,330.347(46)	6_5-5_5	[c]	...		196.0	28.16
110,349.473(32)	6_4-5_4	8.1(4)	6.9(2)	11.7×4.8	132.2	51.22
		1.9(3)	16.4(5)	11.7×4.8	132.2	51.22
110,364.357(22)	6_3-5_3	10.1(6)	6.9(2)	11.7×4.8	82.5	69.15
		6.6(5)	16.4(5)	11.7×4.8	82.5	69.15
110,374.992(18)	6_2-5_2	8.7(6)	6.9(2)	11.7×4.8	46.9	81.95
		6.3(5)	16.4(5)	11.7×4.8	46.9	81.95
110,381.376(20)	6_1-5_1	8.9(9)	6.9(2)	11.6×4.8	25.6	89.63
		5.7(12)	16.4(5)	11.6×4.8	25.6	89.63
110,383.504(20)	6_0-5_0	7.5(8)	6.9(2)	11.6×4.8	18.5	92.20
		5.9(10)	16.4(5)	11.6×4.8	18.5	92.20
110,609.554(20)	$6_{1,1}-5_{1,1},^1\nu_8$	2.5(2)	6.2(2)	11.5×5.4	544.9	89.13
110,680.350(22)	$6_{3,-1}-5_{3,-1},^1\nu_8$	1.5(2)	6.2(2)	12.6×5.7	654.7	69.15
110,683.959(36)	$6_{5,1}-5_{5,1},^1\nu_8$	1.3(2)	6.2(2)	12.6×5.7	662.4	27.66
110,695.506(18)	$6_{2,-1}-5_{2,-1},^1\nu_8$	3.1(2)	6.2(2)	12.6×5.7	605.9	81.44
110,698.701(26)	$6_{4,1}-5_{4,1},^1\nu_8$	2.5(2)	6.2(2)	12.6×5.7	611.8	50.71
110,706.251(120)	$6_{1,-1}-5_{1,-1},^1\nu_8$	2.0(2)	6.2(2)	12.6×5.7	571.4	89.13
110,709.313(22)	$6_{3,1}-5_{3,1},^1\nu_8$	2.1(2)	6.2(2)	12.6×5.7	575.3	69.15
110,712.166(100)	$6_{0,1}-5_{0,1},^1\nu_8$	2.6(3)	6.2(2)	12.4×5.7	551.1	92.20
110,716.212(34)	$6_{2,1}-5_{2,1},^1\nu_8$	1.3(4)	6.2(2)	12.4×5.7	553.0	81.44
110,823.095(120)	$6_{1,1}-5_{1,1},^1\nu_8$	2.9(1)	6.2(2)	13.3×5.4	545.0	89.13
		$^{13}CH_3CN$				
89,316.213(64)	5_3-4_3	1.3(16)	1.2(9)	17.7×8.9	76.9	49.17
89,324.596(64)	5_2-4_2	1.1(2)	3.0(7)	17.7×8.9	41.5	64.54
89,329.625(64)	5_1-4_1	1.6(1)	10.1(9)	17.7×8.9	20.0	73.76
89,329.827(9)	5_0-4_0	[d] ...		17.7×8.9	12.9	76.83
107,188.545(62)	6_2-5_2	0.9(3)	4.7(15)	12.6×6.7	46.5	81.95
107,194.580(64)	6_1-5_1	0.7(3)	4.1(24)	12.6×6.7	25.1	90.40
107,196.592(64)	6_0-5_0	1.0(2)	9.9(30)	11.5×5.8	18.0	92.20
		$CH_3^{13}CN$				
91,925.729(60)	5_3-4_3	0.9(2)	5.1(13)	13.1×7.0	77.2	49.17
91,934.536(4)	5_2-4_2	0.6(2)	7.1(22)	13.4×7.0	41.6	64.54
91,939.834(4)	5_1-4_1	1.0(1)	11.6(23)	13.4×7.0	20.3	73.76
91,941.600(5)	5_0-4_0	0.3(1)	10.4(80)	13.4×7.0	13.2	76.83
110,295.070(68)	6_4-5_4	0.7(2)	5.5(25)	11.8×4.9	132.1	51.22
110,309.867(58)	6_3-5_3	1.2(1)	8.6(11)	11.8×4.9	82.4	69.15
110,320.435(58)	6_2-5_2	1.1(2)	6.5(11)	11.8×4.9	46.9	81.95
110,326.795(5)	6_1-5_1	[c]	...	11.8×4.9	25.6	89.59

Table 4.5—Continued

Rest Frequency (MHz)[a]	Transition	I_0 (Jy/bm)	Δv (km s^{-1})	Beam Size (″×″)	E_u (K)	$S\mu^2$ (D^2)
110,328.914(5)	$6_0 - 5_0$	[c]	···	11.8×4.9	18.5	92.20
		$(CH_3)_2CO$				
81,813.725(12)	$7_{1,6} - 6_{2,5}EE$	0.3(2)	4.7(30)	13.0×8.3	17.47	5.21
82,895.099(52)	$8_{0,8} - 7_{1,7}EE, \nu = 1$	0.3(1)	6.7(32)	12.5×7.9	133.95	7.38
82,895.124(52)	$8_{1,8} - 7_{0,7}EE, \nu = 1$	[d]	···	12.5×7.9	133.95	7.38
82,908.641(20)	$8_{0,8} - 7_{1,7}AE$	0.4(1)	3.8(11)	12.5×7.9	18.85	7.38
82,908.666(20)	$8_{1,8} - 7_{0,7}AE$	[d]	···	12.5×7.9	18.85	7.38
82,908.690(20)	$8_{0,8} - 7_{1,7}EA$	[d]	···	12.5×7.9	18.85	7.38
82,908.714(20)	$8_{1,8} - 7_{0,7}EA$	[d]	···	12.5×7.9	18.85	7.38
82,916.512(14)	$8_{0,8} - 7_{1,7}EE$	0.6(1)	5.2(8)	12.5×7.9	18.74	7.38
82,916.538(14)	$8_{1,8} - 7_{0,7}EE$	[d]	···	12.5×7.9	18.74	7.38
82,924.311(22)	$8_{0,8} - 7_{1,7}AA$	0.3(1)	8.9(24)	12.5×7.9	18.64	7.38
82,924.338(22)	$8_{1,8} - 7_{0,7}AA$	[d]	···	12.5×7.9	18.64	7.38
87,507.547(46)	$18_{8,10} - 18_{7,11}EE$	0.8(2)	3.3(8)	13.2×9.2	130.6	8.27
87,580.004(44)	$18_{9,10} - 18_{8,11}EE$	0.5(2)	2.7(13)	11.8×7.8	130.6	8.27
92,714.464(54)	$9_{0,9} - 8_{1,8}EE, \nu = 1$	0.3(1)	9.7(69)	13.9×6.2	138.41	8.38
92,714.467(54)	$9_{1,9} - 8_{0,8}EE, \nu = 1$	[d]	···	13.9×6.2	138.41	8.38
92,727.904(22)	$9_{0,9} - 8_{1,8}AE$	0.4(2)	7.8(55)	13.9×6.2	23.3	8.38
92,727.907(22)	$9_{1,9} - 8_{0,8}AE$	[d]	···	13.9×6.2	23.3	8.38
92,727.950(20)	$9_{0,9} - 8_{1,8}EA$	[d]	···	13.9×6.2	23.3	8.38
92,727.953(20)	$9_{1,9} - 8_{0,8}EA$	[d]	···	13.9×6.2	23.3	8.38
92,735.670(16)	$9_{0,9} - 8_{1,8}EE$	0.9(3)	4.3(15)	13.9×6.2	23.19	8.38
92,735.673(16)	$9_{1,9} - 8_{0,8}EE$	[d]	···	13.9×6.2	23.19	8.38
92,743.361(24)	$9_{0,9} - 8_{1,8}AA$	[e]	···	13.9×6.2	23.09	8.38
92,743.364(24)	$9_{1,9} - 8_{0,8}AA$	[e]	···	13.9×6.2	23.09	8.38
93,311.552(90)	$22_{12,11} - 22_{11,12}EE$	0.4(2)	4.2(18)	14.9×6.9	198.48	11.29
98,651.514(20)	$5_{5,1} - 4_{4,1}EE$	0.5(1)	10.5(37)	13.9×6.2	14.09	3.63
98,800.980(14)	$5_{5,0} - 4_{4,0}EE$	0.6(1)	5.8(16)	15.5×7.0	14.09	3.63
99,422.076(24)	$14_{3,11} - 14_{2,12}EE$	0.3(1)	8.5(25)	13.6×6.6	68.11	3.33
99,422.084(24)	$14_{4,11} - 14_{3,12}EE$	[d]	···	13.6×6.6	68.11	3.33
101,426.664(20)	$9_{1,8} - 8_{2,7}AE$	1.1(3)	4.0(12)	12.9×6.7	26.84	7.21
101,426.759(18)	$9_{1,8} - 8_{2,7}EA$	[d]	···	12.9×6.7	26.84	7.21
101,427.041(20)	$9_{2,8} - 8_{1,7}AE$	[d]	···	12.9×6.7	26.84	7.21
101,427.130(18)	$9_{2,8} - 8_{1,7}EA$	[d]	···	12.9×6.7	26.84	7.21
101,451.059(14)	$9_{1,8} - 8_{2,7}EE$	1.3(3)	5.2(12)	13.4×6.9	26.74	7.21
101,451.446(14)	$9_{2,8} - 8_{1,7}EE$	[d]	···	13.4×6.9	26.74	7.21
101,475.332(22)	$9_{1,8} - 8_{2,7}AA$	[c]	···	13.4×6.9	26.64	7.21
101,475.733(22)	$9_{2,8} - 8_{1,7}AA$	[c]	···	13.4×6.9	26.64	7.21
102,533.756(58)	$10_{0,10} - 9_{1,9}EE, \nu = 1$[f]	0.8(2)	3.2(11)	12.8×6.2	143.33	9.37
102,533.756(58)	$10_{1,10} - 9_{0,9}EE, \nu = 1$[f]	[d]	···	12.8×6.2	143.33	9.37

Table 4.5—Continued

Rest Frequency (MHz)[a]	Transition	I_0 (Jy/bm)	Δv (km s^{-1})	Beam Size (″×″)	E_u (K)	$S\mu^2$ (D^2)
102,547.033(24)	$10_{0,10} - 9_{1,9}AE$	[c]	···	12.8×6.2	28.22	9.38
102,547.079(20)	$10_{0,10} - 9_{1,9}EA$	[c]	···	12.8×6.2	28.22	9.38
102,554.696(18)	$10_{0,10} - 9_{1,9}EE$	0.9(2)	4.7(14)	12.8×6.2	28.11	9.38
102,562.281(26)	$10_{0,10} - 9_{1,9}AA$	0.6(2)	7.3(28)	12.8×6.2	28.01	9.38
108,434.511(32)	$14_{2,12} - 14_{1,13}EE$	0.6(2)	3.2(12)	12.2×5.6	63.34	2.29
111,243.339(22)	$10_{1,9} - 9_{2,8}AE$	0.7(2)	4.9(15)	12.4×5.8	32.17	8.21
111,243.388(22)	$10_{2,9} - 9_{1,8}AE$	[d]	···	12.4×5.8	32.17	8.21
111,243.424(20)	$10_{1,9} - 9_{2,8}EA$	[d]	···	12.4×5.8	32.17	8.21
111,243.472(20)	$10_{2,9} - 9_{1,8}EA$	[d]	···	12.4×5.8	32.17	8.21
111,267.514(16)	$10_{1,9} - 9_{2,8}EE$	0.9(1)	5.8(11)	12.4×5.8	32.07	8.21
111,267.565(16)	$10_{2,9} - 9_{1,8}EE$	[d]	···	12.4×5.8	32.07	8.21
111,291.573(24)	$10_{1,9} - 9_{2,8}AA$	[c]	···	12.4×5.8	31.98	8.21
111,291.626(24)	$10_{2,9} - 9_{1,8}AA$	[c]	···	12.4×5.8	31.98	8.21
112,352.908(60)	$11_{0,11} - 10_{1,10}EE, \nu = 1$	[c]	···	12.2×6.0	148.71	10.37
112,352.908(60)	$11_{1,11} - 10_{0,10}EE, \nu = 1$	[c]	···	12.2×6.0	148.71	10.37
112,373.548(18)	$11_{0,11} - 10_{1,10}EE$	[c]	···	11.3×5.0	33.51	10.39
			CH_3OH			
82,897.082(101)	$22_{5,18} - 23_{4,19}A+$	1.0(1)	3.6(5)	12.5×7.9	724.2	7.01
84,574.024(60)	$19_{2,17} - 18_{-3,16}E$	0.3(1)	10.5(31)	18.0×7.8	463.2	0.42
85,568.074(13)	$6_{-2,5} - 7_{-1,7}E$	6.2(3)	6.9(2)	13.8×7.4	74.6	2.01
		0.4(1)	29.6(38)	13.8×7.4	74.6	2.01
87,066.819(67)	$19_{-2,18} - 19_{2,17}E$	0.3(1)	8.4(41)	18.5×7.6	467.4	0.19
89,505.778(17)	$8_{-4,5} - 9_{-3,7}E$	3.7(4)	9.5(5)	14.7×7.1	171.4	1.55
93,196.657(12)	$1_{0,1} - 2_{1,2}E$	2.8(4)	7.5(7)	14.9×6.9	302.7	1.33
94,541.806(19)	$8_{3,5} - 9_{2,7}E$	7.1(4)	7.4(2)	16.5×7.2	131.2	2.24
94,815.075(47)	$19_{7,13} - 20_{6,14}A+$	0.3(1)	6.0(14)	14.9×5.9	684.8	4.55
94,815.080(47)	$19_{7,12} - 20_{6,15}A-$	0.3(1)	6.0(14)	14.9×5.9	684.8	4.55
95,169.516(16)	$8_{0,8} - 7_{1,7}E$	3.2(5)	17.7(13)	16.1×7.3	83.5	7.22
95,745.985(188)	$25_{-6,19} - 26_{-5,21}A$	0.3(1)	5.0(17)	14.1×6.9	941.8	7.70
95,914.310(3)	$2_{1,2} - 1_{1,1}A+$	6.5(5)	6.3(3)	14.1×6.0	21.4	1.21
		0.7(2)	19.9(46)	14.1×6.0	21.4	1.21
96,446.603(112)	$21_{-2,20} - 21_{2,19}E$	0.7(2)	5.3(14)	16.4×7.1	562.9	0.29
96,492.200(100)	$2_{1,2} - 1_{1,1}E$	8.7(2)	5.3(2)	16.4×7.1	298.3	1.21
96,501.698(6)	$2_{-1,1} - 1_{-1,0}E$	3.3(10)	0.9(4)	16.4×7.0	420.1	1.21
96,513.671(8)	$2_{0,2} - 1_{0,1}A+$	2.0(8)	6.5(13)	16.4×7.0	430.4	1.61
96,588.593(5)	$2_{1,1} - 1_{1,0}A-$	1.5(2)	15.2(16)	15.1×6.8	332.0	1.21
96,739.363(3)	$2_{-1,2} - 1_{-1,1}E$	14.1(35)	10.5(18)	12.0×9.9	12.5	1.21
96,741.377(3)	$2_{0,2} - 1_{0,1}A+$	8.4(72)	5.7(21)	16.4×7.0	7.0	1.61
97,204.624(520)	$26_{5,22} - 25_{6,19}A+$	0.6(2)	3.0(9)	14.5×6.3	951.0	7.58
97,582.808(3)	$2_{1,1} - 1_{1,0}A-$	1.1(6)	9.7(17)	13.1×5.9	21.6	1.21

Table 4.5—Continued

Rest Frequency (MHz)[a]	Transition	I_0 (Jy/bm)	Δv (km s^{-1})	Beam Size (″×″)	E_u (K)	$S\mu^2$ (D^2)
97,678.261(100)	$21_{6,16} - 22_{5,17}A-$	1.8(2)	6.2(7)	13.9×6.1	728.9	5.74
98,030.396(118)	$24_{6,19} - 23_{7,16}A-$	0.4(1)	3.0(5)	14.4×6.1	888.5	6.43
98,030.435(118)	$24_{6,18} - 23_{7,17}A+$	0.4(1)	3.0(5)	14.4×6.1	888.5	6.43
99,374.624(264)	$15_{-6,10} - 14_{-7,8}E$	0.5(2)	4.5(17)	13.5×6.6	770.6	2.79
99,601.946(64)	$15_{1,14} - 15_{1,15}A-$	0.5(1)	9.3(15)	13.6×5.8	295.1	0.09
99,730.959(14)	$6_{1,6} - 5_{0,5}E$	1.4(3)	7.4(8)	13.6×5.6	339.9	3.13
100,638.870(24)	$13_{2,11} - 12_{3,9}E$	4.5(9)	7.5(5)	14.0×6.2	233.5	3.84
101,293.328(16)	$7_{-2,6} - 7_{1,6}E$	0.4(2)	2.7(23)	13.4×5.9	90.9	0.04
101,737.211(17)	$9_{-2,8} - 9_{1,8}E$	0.8(3)	3.5(19)	11.1×6.5	130.3	0.16
104,300.396(16)	$11_{-1,11} - 10_{-2,9}E$	0.8(1)	38.8(43)	14.0×6.4	158.6	3.41
104,336.637(20)	$13_{-2,12} - 13_{1,12}E$	1.5(4)	9.0(11)	14.0×6.4	237.2	1.19
104,410.489(17)	$10_{4,6} - 11_{3,9}A+$	3.8(3)	11.0(4)	12.9×5.3	207.9	2.48
105,063.761(30)	$13_{1,13} - 12_{2,10}E$	6.9(10)	7.3(4)	13.1×6.6	223.7	4.27
105,576.385(21)	$14_{-2,13} - 14_{1,13}E$	2.2(4)	9.0(10)	14.9×6.4	269.7	1.79
108,893.929(15)	$0_{0,0} - 1_{-1,1}E$	4.8(10)	7.7(5)	11.5×5.2	13.1	0.97
109,137.566(171)	$26_{0,26} - 26_{-1,26}E$	1.7(4)	10.2(15)	13.1×6.0	821.0	3.07
109,153.210(28)	$16_{-2,15} - 16_{1,15}E$	2.1(2)	11.1(8)	13.1×6.0	341.8	3.68
111,289.601(19)	$7_{2,5} - 8_{1,8}A+$	6.1(6)	8.4(3)	12.1×5.8	102.7	2.33
114,650.932(46)	$18_{-2,17} - 18_{1,17}E$	1.0(2)	17.1(27)	11.6×5.2	423.2	6.75
		$^{13}CH_3OH$				
83,314.934(37)	$9_{1,8} - 10_{2,9}A-$	0.2(1)	7.0(29)	14.5×7.7	426.9	6.04
84,970.232(23)	$8_{0,8} - 7_{1,7}A+$	0.6(1)	9.9(18)	13.6×8.3	81.5	7.20
109,199.495(1279)	$25_{6,20} - 24_{7,17}A-$	0.4(1)	1.5(7)	12.7×6.1	929.2	6.90
109,199.541(1280)	$25_{6,19} - 24_{7,18}A+$	0.4(1)	1.5(7)	12.7×6.1	929.2	6.90
110,732.514(179)	$14_{2,12} - 13_{1,13}A+$	1.1(5)	0.6(5)	12.4×5.7	535.7	8.14
112,143.546(21)	$3_{1,3} - 4_{0,4}A+$	3.6(3)	2.2(3)	13.0×5.8	28.0	3.00
112,375.502(44)	$12_{1,11} - 11_{2,10}A-$	1.0(1)	7.2(19)	11.5×4.9	192.6	4.61
		CN				
113,144.190(50)	$1_{0,1}1 - 0_{0,1}2$	[g]	...	11.9×5.1	5.4	1.24
113,170.535(50)	$1_{0,1}2 - 0_{0,1}1$	[g]	...	11.9×5.1	5.4	1.22
113,191.325(50)	$1_{0,1}2 - 0_{0,1}2$	[g]	...	12.5×5.1	5.4	1.58
113,488.142(50)	$1_{0,2}2 - 0_{0,1}1$	[g]	...	11.6×4.8	5.4	1.24
113,490.985(50)	$1_{0,2}3 - 0_{0,1}2$	[g]	...	11.6×4.8	5.4	1.22
113,499.643(50)	$1_{0,2}1 - 0_{0,1}1$	[g]	...	11.6×4.8	5.4	1.58
113,508.934(50)	$1_{0,2}2 - 0_{0,1}2$	[g]	...	11.6×4.8	5.4	1.58
		CO				
115271.202(1)	$1 - 0$	[g]	...	12.4×4.7	5.3	0.01

Table 4.5—Continued

Rest Frequency (MHz)[a]	Transition	I_0 (Jy/bm)	Δv (km s^{-1})	Beam Size (″×″)	E_u (K)	$S\mu^2$ (D^2)
			$C^{18}O$			
109782.173(6)	$1-0$	[g]	···	11.7×5.3	5.3	0.01
			^{13}CO			
110201.354(5)	$1-0$	[g]	···	12.7×5.4	5.3	0.01
			CS			
97980.950(50)	$2-1$	8.5(51)	3.7(7)	12.4×5.8	7.0	7.71
			^{13}CS			
92,494.310(19)	$2-1$	2.2(3)	5.6(4)	21.3×6.8	6.7	7.71
			$C^{33}S$			
97,172.100(12)	$2-1$	1.0(2)	3.0(8)	14.5×6.3	7.0	7.71
			$C^{34}S$			
96412.940(50)	$2-1$	3.2(5)	8.5(8)	13.6×6.4	6.9	7.71
			HC_3N			
81,881.462(3)	$9-8$	5.4(6)	8.4(6)	13.0×8.6	19.6	124.81
		7.9(6)	21.1(6)	13.0×8.6	19.6	124.81
		1.9(3)	10.2(11)	13.0×8.6	19.6	124.81
81,935.004(58)	$9-8, \nu=?1f$	0.4(2)	7.4(31)	13.8×8.0	973.3	123.15
82,015.723(27)	$9-8,^1\nu_6, 1e$	0.5(1)	6.2(18)	15.2×7.7	736.5	123.15
82,080.199(29)	$9-8,^1\nu_6, 1f$	0.7(1)	8.2(18)	15.1×8.0	736.5	123.15
82,082.730(26)	$9-8,^1\nu_7, 1e$	2.0(8)	5.6(11)	15.1×8.0	339.5	123.15
		1.0(3)	11.8(45)	15.1×8.0	339.5	123.15
82,200.372(26)	$9-8,^1\nu_7, 1f$	1.9(2)	5.5(9)	18.5×7.7	339.5	123.15
		1.1(2)	19.2(27)	18.5×7.7	339.5	123.15
82,399.857(3)	$9-8,^2\nu_7$	0.3(1)	34.9(49)	24.5×8.1	661.1	124.07
82,400.815(3)	$9-8,^2\nu_7, 2e$	0.3(1)	34.9(49)	24.5×8.1	664.4	117.95
82,402.633(3)	$9-8,^2\nu_7, 2f$	0.7(1)	20.0(29)	24.5×8.1	664.4	117.94
90,978.989(3)	$10-9$	4.9(7)	8.4(6)	12.5×9.0	24.0	138.68
		9.8(6)	21.1(6)	12.5×9.0	24.0	138.68
		2.5(3)	10.2(11)	12.5×9.0	24.0	138.68
91,128.186(28)	$10-9,^1\nu_6, 1e$	0.4(1)	11.5(29)	11.9×7.7	740.9	137.29
91,202.607(27)	$10-9,^1\nu_7, 1e$	1.1(2)	4.7(11)	11.5×7.6	343.9	137.29
		1.9(2)	17.2(12)	11.5×7.6	343.9	137.29

Table 4.5—Continued

Rest Frequency (MHz)[a]	Transition	I_0 (Jy/bm)	Δv (km s^{-1})	Beam Size (″×″)	E_u (K)	$S\mu^2$ (D^2)
91,333.308(27)	$10-9,^1\,\nu_7,1f$	2.9(2)	5.5(5)	12.1×7.5	343.9	137.29
		1.5(2)	18.2(17)	12.1×7.5	343.9	137.29
91,554.521(43)	$10-9,^2\,\nu_7$	1.6(11)	10.7(17)	12.8×6.9	661.7	138.68
91,558.432(44)	$10-9,^2\,\nu_7,2f$	1.1(2)	10.7(17)	12.8×6.9	664.3	133.13
91,843.785(35)	$10-9,^3\,\nu_7$	0.7(2)	5.2(17)	11.7×8.8	985.3	126.20
100,076.392(15)	$11-10$	8.9(14)	28.5(12)	24.5×8.1	28.8	457.90
100,322.349(29)	$11-10,^1\,\nu_7,1e$	3.7(4)	6.9(7)	14.7×9.0	348.7	151.16
		2.1(7)	21.6(35)	14.7×9.0	348.7	151.16
100,466.174(3)	$11-10,^1\,\nu_7,1f$	3.0(14)	4.9(13)	16.2×6.9	151.1	349.59
100,708.837(44)	$11-10,^2\,\nu_7$	1.2(2)	6.5(17)	14.1×6.3	666.5	152.55
100,710.972(52)	$11-10,^2\,\nu_7,2e$	1.2(2)	4.8(14)	14.1×6.3	669.2	147.42
100,714.306(46)	$11-10,^1\,\nu_7,1f$	1.1(1)	9.7(17)	14.1×6.3	669.2	147.42
100,880.448(70)	$11-10,^3\,\nu_7,1e$	0.6(2)	6.2(23)	13.1×5.9	984.9	151.16
109,173.638(4)	$12-11$	7.8(7)	8.4(6)	13.1×6.0	34.0	166.42
		11.5(7)	21.1(6)	13.1×6.0	34.0	166.42
		2.1(3)	10.2(11)	13.1×6.0	34.0	166.42
109,244.339(84)	$12-11,^1\,\nu_5,1f$	[c]			987.8	163.37
109,352.726(39)	$12-11,^1\,\nu_6,1e$	0.9(2)	10.6(28)	12.4×6.2	750.9	165.17
109,441.944(30)	$12-11,^1\,\nu_7,1e$	4.9(14)	6.5(10)	12.2×6.3	353.9	165.17
		2.0(5)	14.4(54)	12.2×6.3	353.9	165.17
109,598.751(30)	$12-11,^1\,\nu_7,1f$	4.1(4)	6.1(6)	12.4×5.1	354.0	165.17
		2.1(4)	19.8(20)	12.4×5.1	354.0	165.17
109,870.188(47)	$12-11,^2\,\nu_7,2f$	1.0(7)	1.3(14)	12.3×5.0	674.4	161.70
109,438.572(49)	$12-11,^1\,\nu_6,1f$	1.4(3)	9.2(20)	16.1×6.9	751.0	165.34
109,749.772(0)	$12-11,^1\,\nu_6/^1\nu_7,2e$	0.5(2)	11.0(56)	16.1×6.9	1071.2	165.30
109,752.614(0)	$12-11,^1\,\nu_6/^1\nu_7,2f$	[c]			1071.2	165.30
109,862.828(46)	$12-11,^2\,\nu_7$	0.7(2)	4.4(18)	12.3×5.0	671.8	165.40
109,865.854(55)	$12-11,^2\,\nu_7,2e$	1.0(2)	7.8(24)	12.3×5.0	674.4	160.83
		$H^{13}CCCN$				
114,615.020(18)	$13-12$	1.3(1)	13.3(20)	11.6×5.2	38.5	180.29
		$HC^{13}CCN$				
90,593.061(21)	$10-9$	0.4(1)	22.3(31)	14.6×6.7	23.9	138.68
99,651.865(22)	$11-10$	0.6(1)	9.6(13)	12.9×5.6	28.7	152.55
108,710.525(21)	$12-11$	0.7(1)	26.3(42)	12.1×5.1	33.9	166.42
		$HCC^{13}CN$				
81,541.982(11)	$9-8$	0.3(1)	16.1(39)	12.5×8.3	19.6	124.81

Table 4.5—Continued

Rest Frequency (MHz)[a]	Transition	I_0 (Jy/bm)	Δv (km s^{-1})	Beam Size (″×″)	E_u (K)	$S\mu^2$ (D^2)
90,601.791(12)	$10-9$	0.7(1)	9.1(21)	14.7×6.4	23.9	138.68
99,661.471(12)	$11-10$	0.9(1)	5.2(9)	12.9×5.6	28.7	152.55
108,721.006(7)	$12-11$	1.2(1)	15.3(18)	12.9×5.6	33.9	179.80
		HCN				
88,630.416(1)	$1-0, F=1-1$	[g]	···	13.4×8.9	4.3	8.90
88,631.847(1)	$1-0, F=2-1$	[g]	···	13.4×8.9	4.3	8.90
88,633.936(1)	$1-0, F=0-1$	[g]	···	13.4×8.9	4.3	8.90
		$H^{13}CN$				
86,338.767(30)	$1-0, F=1-1$	[g]	···	12.6×8.0	4.1	8.90
86,340.184(30)	$1-0, F=2-1$	[g]	···	12.6×8.0	4.1	8.90
86,342.274(30)	$1-0, F=0-1$	[g]	···	12.6×8.0	4.1	8.90
		$HC^{15}N$				
86,054.969(6)	$1-0$	[g]	···	15.3×7.8	4.1	8.90
		HCO^+				
89,188.526(21)	$1-0$	[g]	···	14.5×6.5	4.3	10.89
		$H^{13}CO^+$				
86,754.330(50)	$1-0$	-0.8(1)	3.0(4)	11.7×7.6	4.2	10.98
		HCOOH				
96,743.447(7)	$1_{1,1}-0_{0,0}$	15.5(9)	2.6(1)	12.0×9.9	4.6	7.33
		HDO				
80,578.295(20)	$1_{1,0}-1_{1,1}$	7.7(2)	6.5(2)	12.5×8.0	46.7	0.65
		H_2C_3S?				
90,770.584(185)	$18_{1,18}-17_{1,17}$	0.5(0)	32.3(30)	13.7×6.5	58.7	229.42
91,195.279(182)	$18_{1,17}-17_{1,16}$	0.3(1)	10.8(39)	11.5×7.6	58.9	229.43
		H_2CO				
101,332.987(6)	$6_{1,5}-6_{1,6}$	2.5(3)	14.8(17)	13.4×5.9	87.5	5.05

Table 4.5—Continued

Rest Frequency (MHz)[a]	Transition	I_0 (Jy/bm)	Δv (km s^{-1})	Beam Size (″×″)	E_u (K)	$S\mu^2$ (D^2)
			HNC			
90,663.593(9)	$1-0$	[g]	···	14.5×6.3	4.3	9.30
			HNCO			
85,368.158(6)	$34_{1,34}-35_{0,35}$	0.5(1)	4.7(7)	12.5×8.0	668.0	31.90
87,597.341(3)	$4_{1,4}-3_{1,3}$	2.7(1)	6.4(3)	11.8×7.8	53.8	11.76
87,866.894(7)	$4_{3,2}-3_{3,1}$	0.2(1)	14.9(35)	13.0×7.5	386.3	4.49
87,866.894(7)	$4_{3,1}-3_{3,0}$	0.2(1)	14.9(35)	13.0×7.5	386.3	4.49
87,898.341(4)	$4_{2,3}-3_{2,2}$	1.4(2)	6.3(5)	12.5×7.8	180.9	7.69
87,898.473(5)	$4_{2,2}-3_{2,1}$	1.4(2)	6.3(5)	12.5×7.8	180.9	7.69
87,925.222(4)	$4_{0,4}-3_{0,3}$	1.6(5)	2.6(7)	12.5×7.8	10.5	9.60
		1.3(2)	33.7(30)	12.5×7.8	10.5	9.60
88,239.011(3)	$4_{1,3}-3_{1,2}$	3.0(2)	6.2(6)	12.5×7.8	53.8	9.60
109,496.007(4)	$5_{1,5}-4_{1,4}$	0.9(2)	26.4(62)	15.8×7.3	59.0	12.30
		0.9(2)	26.4(62)	11.7×5.3	391.6	8.21
109,833.326(6)	$5_{3,3}-4_{3,2}$	0.7(1)	4.6(9)	11.7×5.3	391.6	8.21
109,872.366(5)	$5_{2,4}-4_{2,3}$	0.5(4)	10.1(81)	11.7×5.3	186.2	7.78
109,872.714(5)	$5_{2,3}-4_{2,2}$	0.5(4)	10.1(81)	11.7×5.3	186.2	7.78
109,905.753(5)	$5_{0,5}-4_{0,4}$	3.2(8)	11.9(21)	11.7×5.3	15.8	12.83
110,298.098(4)	$5_{1,4}-4_{1,3}$	1.0(16)	9.4(97)	11.7×5.3	59.1	12.32
			NH_2CHO			
81,693.444(1)	$4_{1,4}-3_{1,3}$	0.4(1)	4.5(13)	14.3×8.2	12.8	48.90
84,542.328(1)	$4_{0,4}-3_{0,3}$	0.5(1)	7.6(18)	18.1×8.1	10.2	58.07
87,848.871(1)	$4_{1,3}-3_{1,2}$	0.6(2)	6.7(22)	13.0×7.5	13.5	48.90
105,464.216(1)	$5_{0,5}-4_{0,4}$	0.9(1)	10.1(24)	10.7×6.3	15.2	65.24
106,107.300(3)	$5_{4,2}-4_{4,1}$	0.5(1)	5.3(14)	11.1×5.6	62.9	12.29
106,107.326(3)	$5_{4,1}-4_{4,0}$	0.5(1)	5.3(14)	11.1×5.6	62.9	12.29
109,753.499(1)	$5_{1,4}-4_{1,3}$	[c]	···	13.4×5.0	18.8	62.64
			NH_2D			
Ortho	$1_{0,1}-1_{1,1}$					
85,924.747(40)	$F=0-1$	2.5(1)	5.2(3)	12.6×7.6	20.7	3.23
85,925.684(40)	$F=2-1$	2.5(1)	5.2(3)	12.6×7.6	20.7	3.23
85,926.263(20)	$F=0-0$	2.5(1)	5.2(3)	12.6×7.6	20.7	3.23
85,926.263(20)	$F=1-1$	2.5(1)	5.2(3)	12.6×7.6	20.7	3.23
85,926.263(20)	$F=2-2$	2.5(1)	5.2(3)	12.6×7.6	20.7	3.23
85,926.858(40)	$F=1-2$	2.5(1)	5.2(3)	12.6×7.6	20.7	3.23
85,927.721(40)	$F=1-0$	2.5(1)	5.2(3)	12.6×7.6	20.7	3.23

Table 4.5—Continued

Rest Frequency (MHz)[a]	Transition	I_0 (Jy/bm)	Δv (km s^{-1})	Beam Size (″×″)	E_u (K)	$S\mu^2$ (D^2)
99,118.819(10)	$5_{2,4}-5_{1,4}$	2.5(1)	5.2(3)	12.6×7.6	261.3	86.81
Para	$1_{0,1}-1_{1,1}$					
110,152.084(40)	$F=0-1$	2.2(3)	7.1(8)	12.8×5.5	21.2	3.23
110,152.995(40)	$F=2-1$	2.2(3)	7.1(8)	12.8×5.5	21.2	3.23
110,153.599(20)	$F=0-0$	2.2(3)	7.1(8)	12.8×5.5	21.2	3.23
110,153.599(20)	$F=1-1$	2.2(3)	7.1(8)	12.8×5.5	21.2	3.23
110,153.599(20)	$F=2-2$	2.2(3)	7.1(8)	12.8×5.5	21.2	3.23
110,154.222(40)	$F=1-2$	2.2(3)	7.1(8)	12.8×5.5	21.2	3.23
110,155.053(40)	$F=1-0$	2.2(3)	7.1(8)	12.8×5.5	21.2	3.23
			OCS			
85,139.121(10)	$7-6$	4.5(2)	18.7(4)	12.9×8.0	16.3	3.58
97,301.208(0)	$8-7$	3.9(2)	20.3(7)	13.4×6.1	21.0	4.09
109,463.063(5)	$9-8$	2.8(5)	28.2(18)	12.2×6.3	26.3	4.60
			$O^{13}CS$			
84,865.166(10)	$7-6$	0.4(1)	15.9(31)	16.6×7.6	16.3	3.58
109,110.848(3)	$9-8$	0.6(1)	14.3(28)	13.5×6.0	26.2	4.60
			$OC^{33}S$			
96,076.058(3)	$8-7$	1.4(3)	2.2(6)	14.1×5.9	20.7	4.09
			$OC^{34}S$			
83,057.970(1)	$7-6$	0.3(1)	29.0(51)	12.2×8.0	15.9	3.58
94,922.799(1)	$8-7$	1.5(20808)	0.9(4295)	14.3×6.4	20.5	4.09
106,787.389(2)	$9-8$	0.7(2)	18.3(30)	14.2×5.5	25.6	4.60
			SO			
86,093.950(100)	2_2-1_1	10.3(11)	9.7(4)	14.9×8.0	19.3	3.60
99,299.870(100)	2_3-1_2	14.3(23)	9.7(4)	12.9×6.5	9.2	7.05
100,029.640(150)	5_4-4_4	10.5(6)	9.7(4)	14.9×7.0	38.6	0.85
109,252.220(100)	3_2-2_1	13.7(13)	9.7(4)	12.6×6.2	21.0	3.63
			^{33}SO			
98,493.642(60)	2_3-1_2	0.8(1)	23.2(26)	13.2×6.3	9.2	9.88
			^{34}SO			
84,410.690(100)	2_2-1_1	2.4(1)	18.6(12)	14.4×7.5	19.2	3.60

Table 4.5—Continued

Rest Frequency (MHz)[a]	Transition	I_0 (Jy/bm)	Δv (km s^{-1})	Beam Size ($'' \times ''$)	E_u (K)	$S\mu^2$ (D^2)
96,781.760(200)	$5_4 - 4_4$	1.2(1)	18.6(25)	14.9×9.4	38.0	0.85
97,715.390(150)	$2_3 - 1_2$	2.8(3)	6.4(6)	13.5×6.1	9.1	7.05
106,742.920(150)	$3_2 - 2_1$	1.8(15)	4.3(17)	14.0×5.4	20.9	3.62
			SO_2			
82,951.942(2)	$13_{4,10} - 14_{3,11}$	3.1(4)	6.9(6)	16.9×7.8	122.9	5.14
83,688.086(2)	$8_{1,7} - 8_{0,8}$	8.0(11)	9.1(6)	16.9×7.8	36.7	17.01
84,320.887(5)	$32_{5,27} - 31_{6,26}$	0.9(1)	4.5(5)	16.9×7.8	549.1	13.45
85,208.085(2)	$8_{1,7} - 8_{0,8},^1 \nu_2$	0.4(1)	8.2(17)	12.0×8.0	781.3	16.90
86,153.779(3)	$39_{9,31} - 40_{8,32}$	0.4(1)	5.1(20)	14.5×7.8	915.6	15.89
86,639.095(2)	$8_{3,5} - 9_{2,8}$	3.1(10)	7.9(11)	14.5×7.8	55.2	3.01
86,828.940(6)	$20_{2,18} - 21_{1,21}$	0.8(9)	12.5(71)	14.5×7.7	207.6	0.67
89,784.545(327)	$30_{7,23} - 31_{6,26},^1 \nu_2$	0.3(3)	2.4(23)	15.4×7.2	552.8	12.37
90,548.160(3)	$25_{3,23} - 24_{4,20}$	2.8(1)	8.0(4)	15.4×7.2	320.8	8.68
91,550.442(2)	$18_{5,13} - 19_{4,16}$	5.1(8)	12.3(14)	15.4×7.2	218.5	7.16
94,064.686(2)	$23_{6,18} - 24_{5,19}$	2.1(1)	5.8(4)	15.4×7.2	342.0	9.22
97,702.340(2)	$7_{3,5} - 8_{2,6}$	7.6(6)	8.5(7)	16.4×7.1	47.8	2.50
97,994.089(4)	$33_{3,31} - 32_{4,28}$	0.9(1)	16.3(30)	12.4×5.8	535.5	5.35
98,264.705(4)	$16_{2,14} - 15_{3,13},^1 \nu_2$	0.6(1)	6.6(16)	15.9×6.9	882.1	7.89
98,976.278(2)	$28_{7,21} - 29_{6,24}$	1.5(4)	6.0(13)	15.9×6.9	493.4	11.26
99,392.526(3)	$29_{4,26} - 28_{5,23}$	2.7(2)	6.0(8)	13.9×8.2	440.4	11.65
100,878.105(3)	$2_{2,0} - 3_{1,3}$	1.7(2)	7.7(10)	13.9×8.2	12.6	0.42
104,029.410(3)	$3_{1,3} - 2_{0,2}$	18.8(4)	22.2(5)	12.6×5.1	7.7	5.37
		3.4(19)	23.7(85)	12.6×5.1	7.7	5.37
		9.5(33)	10.8(14)	12.6×5.1	7.7	5.37
		11.6(17)	9.9(6)	12.6×5.1	7.7	5.37
104,239.293(3)	$10_{1,9} - 10_{0,10}$	30.5(1)	18.4(9)	14.3×6.5	54.7	17.87
		6.6(4)	13.1(10)	14.3×6.5	54.7	17.87
		18.4(13)	10.4(4)	14.3×6.5	54.7	17.87
		6.6(11)	12.2(7)	14.3×6.5	54.7	17.87
107,060.225(3)	$27_{3,25} - 26_{4,22}$	2.0(3)	6.1(11)	10.9×6.3	369.2	8.27
107,843.478(2)	$12_{4,8} - 13_{3,11}$	7.0(14)	7.9(7)	10.9×6.3	110.9	4.53
108,955.895(4)	$39_{6,34} - 38_{7,31}$	0.5(1)	16.5(37)	12.3×5.2	807.8	16.36
109,757.587(2)	$17_{5,13} - 18_{4,14}$	2.8(5)	7.6(11)	12.3×5.2	202.0	6.60
111,755.028(4)	$31_{3,29} - 30_{4,26}$	1.1(6)	7.6(20)	12.6×4.9	476.6	6.44
114,565.381(4)	$29_{3,27} - 28_{4,24}$	2.5(75)	6.8(47)	12.9×5.1	421.2	7.48
115,317.546(3)	$22_{6,16} - 23_{5,19}$	3.9(4)	10.7(17)	12.5×4.8	320.9	8.65
			$^{34}SO_2$			
82,124.345(3)	$10_{1,9} - 9_{2,8}$	0.6(0)	32.5(27)	16.9×7.8	54.5	6.52
83,043.818(3)	$8_{1,7} - 8_{0,8}$	0.7(1)	7.6(13)	16.9×7.8	36.6	16.69

Table 4.5—Continued

Rest Frequency (MHz)[a]	Transition	I_0 (Jy/bm)	Δv (km s^{-1})	Beam Size ($'' \times ''$)	E_u (K)	$S\mu^2$ (D^2)
88,720.567(3)	$7_{3,5} - 8_{2,6}$	0.5(3)	8.7(114)	16.7×6.4	47.0	2.51
102,031.874(4)	$3_{1,3} - 2_{0,2}$	1.8(2)	13.5(18)	13.7×5.8	7.6	5.37
104,391.703(4)	$10_{1,9} - 10_{0,10}$	1.9(17)	8.0(27)	14.3×6.5	54.5	17.38
112,532.324(3)	$11_{4,8} - 12_{3,9}$	0.7(3)	4.8(25)	11.7×5.0	98.4	3.97
114,574.438(4)	$6_{3,3} - 7_{2,6}$	0.8(2)	21.9(95)	11.7×5.2	40.6	1.89
			$SO^{17}O$?			
85,547.215(5)	$2_{1,2} - 1_{0,1}$	0.2(0)	22.0(48)	14.5×7.4	5.0	?
90,570.223(13)	$9_{1,8} - 9_{0,9}$	0.3(1)	12.4(37)	14.6×6.7	43.9	?
112,675.736(1)	$8_{0,8} - 7_{1,7}$	0.8(3)	2.3(9)	12.1×5.9	31.7	?
			SiO			
86,243.440(41)	$2 - 1, \nu = 1$	[g]	···	13.2×8.2	1775.0	19.20
86,846.960(50)	$2 - 1$	45.8(4)	20.7(3)	14.5×7.7	6.2	19.27
			^{30}SiO			
84,745.900(200)	$2 - 1$	2.1(1)	26.8(15)	17.5×8.1	6.1	19.20
			^{28}SiO			
85,759.000(200)	$2 - 1$	1.0(4)	38.5(78)	17.0×7.3	6.2	19.20
			SiS			
90,771.550(41)	$5 - 4$	0.5(0)	32.3(30)	13.7×6.5	13.1	14.97
108,924.277(82)	$6 - 5$	1.1(1)	15.5(26)	12.4×5.2	18.3	17.96

[a]Frequency uncertainty is 2 σ.

[b]Multiple emission and absorption components seen in spectra.

[c]This transition is highly blended with another(see spectra).

[d]This transition is blended with the previous one(s), and the integrated line intensity and column density are calculated as such.

[e]The AA transition is less than 3 σ and thus is not used for calculations.

[f]This transition of $(CH_3)_2CO$ is coincident with the $6_{0,6} - 5_{0,5}$ transition of ethanol(C_2H_5OH). However, since C_2H_5OH is thought to be a compact ridge species (Schilke et al., 2001) and is only weakly detected toward the compact ridge, we consider the contamination from C_2H_5OH to be minimal.

Table 4.6. Transitions Detected Toward the Orion-KL Compact Ridge

Rest Frequency (MHz)[a]	Transition	I_0 (Jy/bm)	Δv (km s^{-1})	Beam Size (″×″)	E_u (K)	$S\mu^2$ (D^2)
			C_2H			
87,316.925(4)	$1_{2,2}-0_{1,1}$	[b]	⋯	19.2×8.9	4.2	1.06
87,328.624(6)	$1_{2,1}-0_{1,0}$	[b]	⋯	19.2×8.9	4.2	0.53
87,402.004(5)	$1_{1,1}-0_{1,1}$	[b]	⋯	12.8×9.1	4.2	0.53
87,407.165(11)	$1_{1,0}-0_{1,1}$	[b]	⋯	12.8×9.1	4.2	0.21
			C_2H_5OH			
80,551.853(9)	$12^+_{1,11}-12^+_{1,12}$	1.3(13)	1.0(10)	13.7×8.6	124.2	2.51
80,731.826(6)	$3^+_{3,0}-2^-_{2,0}$	0.4(5)	1.8(21)	13.6×8.1	72.8	2.53
83,417.125(5)	$7^-_{0,7}-7^+_{1,7}$	0.3(1)	3.4(15)	15.1×8.1	84.5	8.75
86,311.267(2)	$5^+_{2,4}-4^+_{2,3}$	0.3(2)	5.6(44)	13.0×8.2	74.2	5.37
89,947.097(6)	$10^-_{0,10}-10^+_{1,10}$	0.5(2)	2.5(10)	14.5×6.3	106.4	13.79
90,117.576(2)	$4_{1,4}-3_{0,3}$	0.7(3)	2.2(12)	16.2×8.8	9.3	4.44
93,477.743(8)	$12^-_{0,12}-12^+_{1,12}$	0.3(2)	2.4(15)	13.9×6.0	124.9	15.48
93,497.460(8)	$14^-_{0,14}-14^+_{1,14}$	0.3(1)	3.5(15)	13.9×6.0	146.3	20.97
94,278.311(6)	$12_{1,11}-12_{0,12}$	0.6(1)	6.5(13)	14.0×6.1	68.3	8.62
95,444.024(4)	$16_{2,14}-16_{1,15}$	0.7(1)	11.9(31)	11.7×10.5	121.8	18.63
95,909.189(3)	$7_{2,6}-7_{1,7}$	0.7(1)	2.7(6)	14.1×6.0	28.5	5.41
95,924.513(8)	$17^-_{0,17}-17^+_{1,17}$	0.3(1)	4.2(15)	14.2×5.9	184.4	28.26
96,589.801(9)	$19^-_{0,19}-19^+_{1,19}$	1.2(5)	1.3(8)	15.4×7.2	213.7	32.21
97,649.561(9)	$19^-_{1,19}-19^+_{0,19}$	0.5(1)	3.8(15)	13.9×6.1	213.7	32.17
98,878.429(11)	$13^-_{1,13}-13^+_{0,13}$	0.7(2)	2.9(9)	13.1×10.5	135.3	10.28
99,524.026(2)	$17_{3,14}-17_{2,15}$	0.8(1)	3.1(5)	12.6×5.6	141.3	23.33
99,975.814(2)	$18_{3,15}-18_{2,16}$	3.4(34)	0.7(7)	13.9×6.2	156.8	25.09
102,534.034(2)	$6^+_{0,6}-5^+_{0,5}$	0.8(3)	2.2(11)	12.8×6.2	74.2	7.84
105,337.280(3)	$20_{3,17}-20_{2,18}$	0.8(3)	2.8(13)	10.5×6.2	190.4	27.53
106,649.485(6)	$13_{1,12}-13_{0,13}$	0.9(1)	4.5(8)	12.9×5.6	79.4	8.43
108,438.549(3)	$13_{3,10}-13_{2,11}$	0.8(2)	2.9(9)	12.5×5.6	88.1	15.11
			CH_3CCH			
85,455.622(60)	5_1-4_1	[b]	⋯	11.9×7.5	19.5	2.70
85,457.272(60)	5_0-4_0	[b]	⋯	11.9×7.5	12.3	2.81
102,546.024(1)	6_1-5_1	[b]	⋯	12.8×6.2	24.4	3.28
102,547.984(1)	6_0-5_0	[b]	⋯	12.8×6.2	17.2	3.37
			CH_3CHO			
93,580.914(6)	$5_{1,5}-4_{1,4}A+$	0.6(2)	1.8(8)	14.5×5.5	15.7	30.35
93,595.238(6)	$5_{-1,5}-4_{-1,4}E$	0.6(1)	3.0(9)	14.5×5.5	15.8	30.35

Table 4.6—Continued

Rest Frequency (MHz)[a]	Transition	I_0 (Jy/bm)	Δv (km s^{-1})	Beam Size ($'' \times ''$)	E_u (K)	$S\mu^2$ (D^2)
95,654.204(9)	$5_{1,5} - 4_{1,4} \nu_t = 1$	0.4(1)	3.5(16)	14.8×8.3	219.5	30.07
95,947.439(6)	$5_{0,5} - 4_{0,4} E$	5.8(58)	0.6(6)	14.2×5.9	13.9	31.61
95,963.465(6)	$5_{0,5} - 4_{0,4} A+$	1.0(10)	1.1(11)	14.2×5.9	13.8	31.59
96,274.257(5)	$5_{2,4} - 4_{2,3} A-$	0.5(2)	2.1(10)	14.4×6.4	22.9	26.56
96,343.268(5)	$5_{4,2} - 4_{4,1} A-$	6.7(66)	0.5(5)	14.6×6.3	50.0	11.39
96,343.282(5)	$5_{4,1} - 4_{4,0} A+$	6.7(66)	0.5(5)	14.6×6.3	50.0	11.39
96,367.790(5)	$5_{3,3} - 4_{3,2} A+$	0.5(1)	6.0(13)	14.1×6.2	34.2	20.24
96,384.417(5)	$5_{-3,3} - 4_{-3,2} E$	0.9(2)	2.5(6)	14.1×6.2	34.1	20.24
96,475.523(5)	$5_{2,3} - 4_{2,2} E$	6.1(61)	0.7(7)	16.4×7.1	23.0	26.42
98,863.314(6)	$5_{1,4} - 4_{1,3} E$	1.1(2)	2.9(6)	15.2×7.3	16.6	30.35
98,900.951(6)	$5_{1,4} - 4_{1,3} A-$	0.7(2)	3.3(10)	13.1×10.5	16.5	30.35
			CH_3CN			
91,958.730(1)	$5_4 - 4_4$	1.7(3)	4.2(8)	13.4×7.0	126.9	27.80
		0.9(3)	16.0(31)	13.4×7.0	126.9	27.80
91,971.134(1)	$5_3 - 4_3$	6.7(3)	4.8(2)	13.4×7.0	77.2	46.33
		2.6(2)	15.3(9)	13.4×7.0	77.2	46.33
91,979.997(1)	$5_2 - 4_2$	6.9(3)	2.6(2)	13.1×6.9	41.6	64.86
		4.3(3)	10.0(5)	13.1×6.9	41.6	64.86
91,985.316(2)	$5_1 - 4_1$	8.9(4)	2.3(1)	13.1×6.9	20.3	74.14
		6.8(6)	15.4(7)	13.1×6.9	20.3	74.14
91,987.089(2)	$5_0 - 4_0$	[c]	···	13.1×6.9	13.2	77.22
110,330.352(2)	$6_5 - 5_5$	[d]	···	11.8×4.9	196.0	28.26
110,349.476(2)	$6_4 - 5_4$	4.3(4)	4.4(4)	11.7×4.8	132.2	51.43
		0.7(2)	7.7(45)	11.7×4.8	132.2	51.43
110,364.358(2)	$6_3 - 5_3$	10.6(3)	2.7(1)	11.7×4.8	82.5	69.50
		3.7(3)	11.3(6)	11.7×4.8	82.5	69.50
110,374.992(2)	$6_2 - 5_2$	9.9(4)	2.2(1)	11.7×4.8	46.9	82.32
		4.2(3)	9.2(5)	11.7×4.8	46.9	82.32
110,381.374(2)	$6_1 - 5_1$	9.1(91)	1.7(17)	11.6×4.8	25.6	90.04
110,383.502(2)	$6_0 - 5_0$	11.4(4)	2.0(1)	11.6×4.8	18.5	92.67
		7.0(3)	14.7(4)	11.6×4.8	18.5	92.67
			$^{13}CH_3CN$			
89,316.137(14)	$5_3 - 4_3$	[d]	···	17.7×8.9	76.9	49.17
89,324.542(14)	$5_2 - 4_2$	4.0(40)	0.8(8)	17.7×8.9	41.3	64.54
89,329.586(14)	$5_1 - 4_1$	0.8(2)	3.2(11)	17.7×8.9	20.0	73.76
89,331.267(14)	$5_0 - 4_0$	1.0(1)	9.0(19)	17.7×8.9	12.9	76.83
107,188.495(16)	$6_2 - 5_2$	0.9(1)	12.4(22)	12.6×6.7	46.5	81.85
107,194.580(64)	$6_1 - 5_1$	0.9(1)	9.7(19)	12.6×6.7	25.1	90.40
107,196.564(17)	$6_0 - 5_0$	[c]	···	12.6×6.7	18.0	92.20

Table 4.6—Continued

Rest Frequency (MHz)[a]	Transition	I_0 (Jy/bm)	Δv (km s^{-1})	Beam Size (″×″)	E_u (K)	$S\mu^2$ (D^2)
			$CH_3^{13}CN$			
91,934.536(4)	$5_2 - 4_2$	0.4(2)	4.1(21)	13.4×7.0	41.6	64.54
91,939.834(4)	$5_1 - 4_1$	0.6(2)	3.8(15)	13.4×7.0	20.3	73.76
91,941.600(5)	$5_0 - 4_0$	0.5(2)	3.4(20)	13.4×7.0	13.2	76.83
110,326.795(5)	$6_1 - 5_1$	[d]	···	11.8×4.9	25.6	89.59
110,328.914(5)	$6_0 - 5_0$	[d]	···	11.8×4.9	18.5	92.20
			$(CH_3)_2O$			
80,536.405(3)	$5_{2,3} - 5_{1,4}EA/AE$	2.7(2)	2.1(2)	13.7×8.6	19.3	5.36
80,538.646(2)	$5_{2,3} - 5_{1,4}EE$	3.5(1)	2.3(1)	13.7×8.6	19.3	5.36
80,540.913(4)	$5_{2,3} - 5_{1,4}AA$	2.3(1)	2.4(1)	13.7×8.6	19.3	5.36
81,467.615(6)	$18_{4,15} - 17_{5,12}AA$	0.4(1)	3.7(14)	14.5×8.6	178.4	4.14
81,469.921(4)	$18_{4,15} - 17_{5,12}EE$	0.7(1)	4.1(7)	14.5×8.6	178.4	4.14
81,472.069(6)	$18_{4,15} - 17_{5,12}EA/AE$	0.4(1)	3.7(14)	14.5×8.6	178.4	4.14
82,456.986(3)	$11_{1,10} - 11_{0,11}AE/EA$	[d]	···	24.8×8.4	62.9	14.25
82,458.660(3)	$11_{1,10} - 11_{0,11}EE$	[d]	···	24.8×8.4	62.9	14.25
82,460.334(3)	$11_{1,10} - 11_{0,11}AA$	[d]	···	24.8×8.4	62.9	14.25
82,649.433(2)	$3_{1,3} - 2_{0,2}EA/AE$	1.5(1)	2.9(10)	16.0×8.2	6.7	3.42
82,650.316(1)	$3_{1,3} - 2_{0,2}EE$	3.7(2)	1.9(3)	16.0×8.2	6.7	3.42
82,651.197(2)	$3_{1,3} - 2_{0,2}AA$	1.5(1)	2.6(5)	16.0×8.2	6.7	3.42
82,686.358(3)	$4_{2,2} - 4_{1,3}AE/EA$	1.4(3)	1.7(4)	13.2×8.0	14.7	3.98
82,688.746(2)	$4_{2,2} - 4_{1,3}EE$	2.8(1)	2.2(1)	13.2×8.0	14.7	3.98
82,691.073(4)	$4_{2,2} - 4_{1,3}AA$	1.2(1)	1.9(2)	13.2×8.0	14.7	3.98
83,097.425(2)	$14_{2,12} - 14_{1,13}AE/EA$	1.7(1)	2.2(1)	12.6×7.7	102.8	19.17
83,098.929(2)	$14_{2,12} - 14_{1,13}EE$	4.1(1)	2.2(1)	12.6×7.7	102.8	19.17
83,100.433(2)	$14_{2,12} - 14_{1,13}AA$	1.9(1)	2.0(2)	12.6×7.7	102.8	19.17
83,319.414(4)	$8_{1,7} - 7_{2,6}AA$	0.9(2)	2.0(7)	14.5×7.7	35.0	2.92
83,321.256(3)	$8_{1,7} - 7_{2,6}EE$	1.8(1)	2.1(2)	14.5×7.7	35.0	2.92
83,323.091(3)	$8_{1,7} - 7_{2,6}AE/EA$	1.0(1)	1.7(2)	14.5×7.7	35.0	2.92
84,529.592(4)	$18_{4,14} - 17_{5,13}EE$	1.0(2)	3.2(7)	18.1×8.1	178.6	4.15
84,631.897(3)	$3_{2,1} - 3_{1,2}AE/EA$	1.8(2)	3.0(3)	17.2×7.7	11.1	2.73
84,634.413(2)	$3_{2,1} - 3_{1,2}EE$	3.1(2)	2.2(2)	17.2×7.7	11.1	2.73
84,636.739(5)	$3_{2,1} - 3_{1,2}AA$	1.9(2)	2.4(3)	17.2×7.7	11.1	2.73
85,973.249(4)	$13_{2,12} - 12_{3,9}AA$	0.7(1)	3.1(4)	22.8×7.6	88.0	2.80
85,976.131(4)	$13_{2,12} - 12_{3,9}EE$	1.2(1)	3.1(4)	22.8×7.6	88.0	2.80
86,223.780(3)	$2_{2,0} - 2_{1,1}AE/EA$	[d]	···	14.5×7.6	8.4	1.48
86,226.727(2)	$2_{2,0} - 2_{1,1}EE$	5.4(54)	0.9(9)	14.5×7.6	8.4	1.47
86,228.720(5)	$2_{2,0} - 2_{1,1}AA$	1.1(6)	1.2(5)	14.5×7.6	8.4	1.49
88,706.220(2)	$15_{2,13} - 15_{1,14}AE/EA$	2.6(2)	2.5(2)	16.7×6.4	116.8	19.70
88,707.701(2)	$15_{2,13} - 15_{1,14}EE$	4.0(1)	2.6(1)	16.7×6.4	116.8	19.70

Table 4.6—Continued

Rest Frequency (MHz)[a]	Transition	I_0 (Jy/bm)	Δv (km s^{-1})	Beam Size ($'' \times ''$)	E_u (K)	$S\mu^2$ (D^2)
88,709.181(3)	$15_{2,13} - 15_{1,14}AA$	2.9(2)	2.1(2)	16.7×6.4	116.8	19.70
89,697.737(3)	$2_{2,1} - 2_{1,2}AE$	1.1(1)	3.1(4)	15.2×7.0	8.4	1.41
89,699.797(3)	$2_{2,1} - 2_{1,2}EE$	2.3(2)	2.1(2)	15.2×7.0	8.4	1.39
89,702.809(5)	$2_{2,1} - 2_{1,2}AA$	2.0(3)	1.8(3)	15.2×7.0	8.4	1.41
90,938.103(2)	$6_{0,6} - 5_{1,5}ALL$	5.5(2)	4.4(2)	12.7×8.9	19.0	5.37
91,473.760(3)	$3_{2,2} - 3_{1,3}EA/AE$	1.2(5)	1.5(6)	12.2×7.4	11.1	2.42
91,476.596(2)	$3_{2,2} - 3_{1,3}EE$	3.6(14)	1.5(6)	12.2×7.4	11.1	2.42
91,479.244(5)	$3_{2,2} - 3_{1,3}AA$	1.9(8)	1.5(6)	12.2×7.4	11.1	2.42
92,701.962(8)	$8_{5,3} - 9_{4,5}EE/AA$	0.4(2)	5.3(35)	13.9×6.2	67.9	0.75
93,664.602(3)	$12_{1,11} - 12_{0,12}AE/EA$	3.7(3)	2.4(2)	14.9×8.1	74.0	9.37
93,666.459(3)	$12_{1,11} - 12_{0,12}EE$	8.3(3)	2.3(1)	14.9×8.1	74.0	9.37
93,668.316(4)	$12_{1,11} - 12_{0,12}AA$	3.5(3)	3.6(3)	14.9×8.1	74.0	9.37
93,854.437(3)	$4_{2,3} - 4_{1,4}EA/AE$	3.2(2)	2.2(2)	14.9×6.7	14.7	3.31
93,857.103(2)	$4_{2,3} - 4_{1,4}EE$	5.2(2)	1.8(1)	14.9×6.7	14.7	3.31
93,859.708(5)	$4_{2,3} - 4_{1,4}AA$	3.2(3)	2.0(2)	14.9×6.7	14.7	3.31
94,144.748(17)	$11_{6,5} - 12_{5,7}EA$	0.4(1)	3.6(13)	14.8×6.6	110.7	1.47
94,148.449(13)	$11_{6,5} - 12_{5,7}EE$	0.5(1)	3.5(8)	14.8×6.6	110.7	1.44
94,149.163(14)	$11_{6,5} - 12_{5,8}AE$	0.2(1)	3.5(8)	14.8×6.6	110.7	1.49
94,151.167(14)	$11_{6,6} - 12_{5,7}AA$	0.2(1)	7.8(17)	14.8×6.6	110.7	1.49
94,151.880(13)	$11_{6,6} - 12_{5,8}EE$	0.4(1)	7.8(17)	14.8×6.6	110.7	1.44
94,153.924(14)	$11_{6,5} - 12_{5,8}AA$	0.5(1)	1.7(8)	14.8×6.6	110.7	1.49
95,553.325(32)	$14_{7,8} - 15_{6,9}EE/AE$	0.7(1)	4.8(11)	14.8×8.6	164.4	2.03
95,556.318(33)	$14_{7,7} - 15_{6,10}AA/EE/EA$	0.5(1)	6.8(17)	14.8×8.6	164.4	2.05
95,729.768(3)	$16_{2,14} - 16_{1,15}EA/AE$	2.7(2)	2.5(2)	14.2×6.9	131.8	19.92
95,731.250(2)	$16_{2,14} - 16_{1,15}EE$	5.0(2)	2.4(1)	14.1×6.9	131.8	19.92
95,732.732(3)	$16_{2,14} - 16_{1,15}AA$	2.4(2)	2.4(2)	14.1×6.9	131.8	19.92
96,847.241(3)	$5_{2,4} - 5_{1,5}EA/AE$	2.3(3)	1.9(4)	17.2×7.3	19.3	4.09
96,849.881(2)	$5_{2,4} - 5_{1,5}EE$	5.6(4)	2.3(2)	17.2×7.3	19.3	4.09
96,852.496(4)	$5_{2,4} - 5_{1,5}AA$	2.9(4)	2.3(3)	17.2×7.3	19.3	4.09
99,324.357(2)	$4_{1,4} - 3_{0,3}EA/AE$	4.7(3)	1.8(1)	13.2×6.5	10.2	4.36
99,325.208(2)	$4_{1,4} - 3_{0,3}EE$	6.1(3)	1.8(1)	13.2×6.5	10.2	4.36
99,326.058(2)	$4_{1,4} - 3_{0,3}AA$	4.3(3)	1.8(1)	13.2×6.5	10.2	4.36
99,833.663(4)	$14_{2,13} - 13_{3,10}AA$	1.0(2)	2.1(4)	13.1×6.2	100.6	2.88
99,836.454(4)	$14_{2,13} - 13_{3,10}EE$	1.7(2)	1.8(2)	13.1×6.2	100.6	2.88
99,839.239(4)	$14_{2,13} - 13_{3,10}EA/AE$	1.2(2)	2.0(3)	13.1×6.2	100.6	2.88
100,460.412(3)	$6_{2,5} - 6_{1,6}AE/EA$	[d]	···	16.2×6.9	24.7	4.80
100,463.066(2)	$6_{2,5} - 6_{1,6}EE$	[d]	···	16.2×6.9	24.7	4.80
100,465.708(4)	$6_{2,5} - 6_{1,6}AA$	[d]	···	16.2×6.9	24.7	4.80
100,946.837(6)	$19_{4,16} - 18_{5,13}AA$	0.8(2)	1.7(6)	13.2×5.9	195.8	4.49
100,949.003(4)	$19_{4,16} - 18_{5,13}EE$	1.0(2)	2.1(4)	13.2×5.9	195.8	4.49
101,559.383(5)	$12_{2,10} - 11_{3,9}AA$	1.6(5)	2.8(10)	14.9×7.1	77.6	3.27
101,562.117(4)	$12_{2,10} - 11_{3,9}EE$	3.8(5)	2.3(3)	14.9×7.1	77.6	3.27

Table 4.6—Continued

Rest Frequency (MHz)[a]	Transition	I_0 (Jy/bm)	Δv (km s^{-1})	Beam Size ($''\times''$)	E_u (K)	$S\mu^2$ (D^2)
101,564.832(4)	$12_{2,10} - 11_{3,9}AE/EA$	1.8(4)	3.1(9)	14.9×7.1	77.6	3.27
104,175.867(3)	$17_{2,15} - 17_{1,16}AE/EA$	[d]	···	13.5×5.5	147.6	19.88
104,177.378(3)	$17_{2,15} - 17_{1,16}EE$	5.1(3)	2.3(2)	13.5×5.5	147.6	19.88
104,178.889(3)	$17_{2,15} - 17_{1,16}AA$	3.2(3)	2.3(2)	13.5×5.5	147.6	19.88
104,700.567(3)	$7_{2,6} - 7_{1,7}EA/AE$	3.3(2)	2.1(2)	12.2×5.2	31.1	5.42
104,703.253(2)	$7_{2,6} - 7_{1,7}EE$	5.9(2)	2.0(1)	12.2×5.2	31.1	5.42
104,705.932(4)	$7_{2,6} - 7_{1,7}AA$	2.5(2)	2.1(2)	12.2×5.2	31.1	5.42
105,768.276(4)	$13_{1,12} - 13_{0,13}AE/EA$	2.3(4)	4.4(8)	13.8×6.1	86.0	9.15
105,770.340(3)	$13_{1,12} - 13_{0,13}EE$	3.5(6)	2.4(5)	13.8×6.1	86.0	9.15
105,772.403(5)	$13_{1,12} - 13_{0,13}AA$	3.2(5)	3.2(6)	13.8×6.1	86.0	9.15
106,775.679(4)	$9_{1,8} - 8_{2,7}AA$	2.5(3)	1.5(2)	14.2×5.5	43.4	3.64
106,777.371(3)	$9_{1,8} - 8_{2,7}EE$	3.2(2)	1.9(1)	14.2×5.5	43.4	3.64
106,779.058(3)	$9_{1,8} - 8_{2,7}AE/EA$	2.8(3)	1.9(2)	14.2×5.5	43.4	3.64
109,571.390(3)	$8_{2,7} - 8_{1,8}EA/AE$	5.3(8)	1.5(3)	12.4×5.1	38.3	5.98
109,574.119(2)	$8_{2,7} - 8_{1,8}EE$	6.5(5)	1.8(2)	12.4×5.1	38.3	5.98
109,576.843(4)	$8_{2,7} - 8_{1,8}AA$	5.3(8)	1.3(3)	12.4×5.1	38.3	5.98
111,741.592(4)	$19_{3,16} - 19_{2,17}AE/EA$	3.4(3)	2.2(2)	12.6×4.9	187.4	25.97
111,742.984(3)	$19_{3,16} - 19_{2,17}EE$	5.0(3)	1.9(2)	12.6×4.9	187.4	25.97
111,744.377(5)	$19_{3,16} - 19_{2,17}AA$	2.9(3)	1.8(2)	12.6×4.9	187.4	25.97
111,783.112(2)	$7_{0,7} - 6_{1,6}ALL$	8.8(2)	3.8(1)	12.7×5.0	25.2	6.80
111,801.927(9)	$7_{5,3} - 8_{4,5}EA/AE$	0.5(2)	1.3(3)	12.7×5.0	60.6	0.63
111,801.962(7)	$7_{5,2} - 8_{4,4}EE$	0.8(2)	1.3(3)	12.7×5.0	60.6	0.59
111,812.237(4)	$18_{3,15} - 18_{2,16}AE/EA$	1.6(2)	1.8(3)	12.4×5.0	169.8	24.14
111,813.810(3)	$18_{3,15} - 18_{2,16}EE$	4.3(2)	2.2(1)	12.4×5.0	169.8	24.14
111,815.382(5)	$18_{3,15} - 18_{2,16}AA$	1.6(2)	2.4(4)	12.4×5.0	169.8	24.14
112,999.982(4)	$20_{3,17} - 20_{2,18}AE/EA$	2.2(5)	2.4(9)	12.0×5.9	206.1	27.53
113,001.218(3)	$20_{3,17} - 20_{2,18}EE$	5.0(27)	1.2(8)	12.0×5.9	206.1	27.53
113,002.455(5)	$20_{3,17} - 20_{2,18}AA$	3.3(7)	1.3(3)	12.0×5.9	206.1	27.53
113,057.579(3)	$17_{3,14} - 17_{2,15}AE/EA$	4.5(5)	2.1(3)	11.8×5.0	153.1	22.12
113,059.350(3)	$17_{3,14} - 17_{2,15}EE$	7.4(5)	1.7(1)	11.8×5.0	153.1	22.12
113,061.121(5)	$17_{3,14} - 17_{2,15}AA$	3.9(5)	2.1(3)	11.8×5.0	153.1	22.12
114,003.831(3)	$18_{2,16} - 18_{1,17}AE/EA$	1.8(5)	1.5(5)	11.2×5.2	164.4	19.65
114,005.399(3)	$18_{2,16} - 18_{1,17}EE$	3.1(4)	2.5(3)	11.2×5.2	164.4	19.65
114,006.968(4)	$18_{2,16} - 18_{1,17}AA$	1.6(5)	1.7(7)	11.2×5.2	164.4	19.65
114,702.510(34)	$13_{7,7} - 14_{6,8}AA$	0.2(1)	1.9(7)	11.7×5.2	151.7	1.71
114,702.745(34)	$13_{7,6} - 14_{6,9}EE/AA$	0.9(3)	1.9(7)	11.7×5.2	151.7	1.71
115,072.305(3)	$9_{2,8} - 9_{1,9}EA/AE$	2.6(4)	1.5(3)	11.7×5.0	46.5	6.46
115,075.086(2)	$9_{2,8} - 9_{1,9}EE$	5.6(4)	2.2(2)	11.7×5.0	46.5	6.46
115,077.864(4)	$9_{2,8} - 9_{1,9}AA$	3.1(4)	1.8(3)	11.7×5.0	46.5	6.46
115,291.645(3)	$16_{3,13} - 16_{2,14}EA/AE$	2.2(6)	1.7(5)	12.5×4.8	137.3	20.04
115,293.624(2)	$16_{3,13} - 16_{2,14}EE$	6.4(7)	1.9(2)	12.5×4.8	137.3	20.04
115,295.604(4)	$16_{3,13} - 16_{2,14}AA$	3.0(6)	1.7(4)	12.5×4.8	137.3	20.04

Table 4.6—Continued

Rest Frequency (MHz)[a]	Transition	I_0 (Jy/bm)	Δv (km s^{-1})	Beam Size ($''\times''$)	E_u (K)	$S\mu^2$ (D^2)
115,543.988(2)	$5_{1,5}-4_{0,4}ALL$	7.5(3)	4.3(2)	12.4×5.2	14.6	5.37
115,710.625(4)	$21_{3,18}-21_{2,19}AE/EA$	2.9(4)	2.6(7)	13.2×5.0	225.7	28.77
115,711.736(3)	$21_{3,18}-21_{2,19}EE$	5.3(6)	1.3(3)	11.7×5.6	225.7	28.77
115,712.846(5)	$21_{3,18}-21_{2,19}AA$	3.1(6)	2.1(5)	11.7×5.6	225.7	28.77
		CH_3OH				
80,993.257(19)	$7_{2,6}-8_{1,7}A-$	13.7(2)	3.9(1)	18.0×8.0	102.6	2.52
82,897.082(101)	$22_{5,18}-23_{4,19}A+$	1.2(12)	1.0(10)	12.5×7.9	724.2	7.01
84,423.706(21)	$13_{-3,11}-14_{-2,13}E$	4.1(5)	2.6(3)	13.6×7.5	273.8	4.30
		2.1(5)	7.2(8)	13.6×7.5	273.8	4.30
84,521.206(14)	$5_{-1,5}-4_{0,4}E$	33.6(3)	2.2(0)	18.1×8.1	40.4	3.08
		9.9(3)	7.7(1)	18.1×8.1	40.4	3.08
84,574.024(60)	$19_{2,17}-18_{-3,16}E$	0.9(3)	1.9(8)	18.0×7.8	463.2	0.42
84,743.896(43)	$19_{4,15}-18_{5,14}E$	1.3(2)	3.0(5)	17.5×8.1	536.5	5.19
85,568.074(13)	$6_{-2,5}-7_{-1,7}E$	7.8(3)	2.5(1)	13.8×7.4	74.6	2.00
		4.1(3)	7.6(3)	13.8×7.4	74.6	2.00
86,615.602(14)	$7_{2,6}-6_{3,3}A-$	6.5(2)	2.5(1)	13.1×7.6	102.6	1.35
		2.6(2)	7.3(3)	13.1×7.6	102.6	1.35
86,902.947(14)	$7_{2,5}-6_{3,4}A+$	7.3(3)	2.3(1)	13.9×7.3	102.7	1.35
		3.9(3)	6.7(3)	13.9×7.3	102.7	1.35
88,594.809(19)	$15_{3,13}-14_{4,10}A+$	4.9(3)	2.7(2)	14.1×7.1	328.1	4.20
		2.0(3)	7.4(6)	14.1×7.1	328.1	4.20
88,939.993(20)	$15_{3,12}-14_{4,11}A-$	6.9(4)	2.4(2)	22.7×6.6	328.1	4.20
89,505.778(17)	$8_{-4,5}-9_{-3,7}E$	13.2(4)	2.3(1)	14.7×7.1	171.4	1.55
		4.3(4)	7.8(4)	14.7×7.1	171.4	1.55
93,196.657(12)	$1_{0,1}-2_{1,2}E$	5.8(6)	2.6(2)	14.9×6.9	302.7	1.33
		2.0(5)	6.6(8)	14.9×6.9	302.7	1.33
94,541.806(19)	$8_{3,5}-9_{2,7}E$	8.2(3)	2.4(1)	16.5×7.2	131.2	2.23
		5.9(3)	6.7(2)	16.5×7.2	131.2	2.23
94,815.075(47)	$19_{7,13}-20_{6,14}A+$	0.5(1)	2.6(5)	14.9×5.9	684.8	4.55
94,815.080(47)	$19_{7,12}-20_{6,15}A-$	0.5(1)	2.6(5)	14.9×5.9	684.8	4.55
95,169.516(16)	$8_{0,8}-7_{1,7}A+$	26.3(4)	2.4(0)	16.1×7.3	83.5	7.22
		11.7(4)	7.9(4)	16.1×7.3	83.5	7.22
95,914.310(3)	$2_{1,2}-1_{1,1}A+$	18.7(2)	2.2(0)	14.1×6.0	21.4	1.21
		7.4(2)	7.4(1)	14.1×6.0	21.4	1.21
96,396.055(4)	$2_{1,2}-1_{1,1}A+$	2.5(3)	2.1(4)	14.1×6.2	332.0	1.21
		1.4(4)	6.7(9)	14.1×6.2	332.0	1.21
96,492.164(4)	$2_{1,2}-1_{1,1}E$	4.0(3)	2.3(2)	16.4×7.1	298.3	1.21
96,493.553(4)	$2_{0,2}-1_{0,1}E$	4.1(4)	2.3(2)	16.4×7.1	307.4	1.61
		2.4(4)	9.3(7)	16.4×7.1	307.4	1.61
96,501.698(6)	$2_{-1,1}-1_{-1,0}E$	2.2(1)	3.5(3)	16.4×7.0	420.1	1.21

Table 4.6—Continued

Rest Frequency (MHz)[a]	Transition	I_0 (Jy/bm)	Δv (km s^{-1})	Beam Size (″×″)	E_u (K)	$S\mu^2$ (D^2)
96,513.671(8)	$2_{0,2} - 1_{0,1}A+$	2.1(4)	1.7(8)	16.4×7.0	430.4	1.61
96,588.593(5)	$2_{1,1} - 1_{1,0}A-$	4.1(1)	3.0(2)	15.1×6.8	332.0	1.21
96,739.363(3)	$2_{-1,2} - 1_{-1,1}E$	24.5(6)	2.6(1)	12.0×9.9	12.5	1.21
96,741.377(3)	$2_{0,2} - 1_{0,1}A+$	8.1(11)	7.2(10)	12.0×9.9	7.0	1.61
96,744.549(3)	$2_{0,2} - 1_{0,1}E$	23.3(9)	2.2(1)	12.0×9.9	20.1	1.61
		5.8(9)	6.4(6)	12.0×9.9	20.1	1.61
96,755.507(3)	$2_{1,1} - 1_{1,0}E$	19.1(6)	2.3(1)	12.0×9.9	28.0	1.24
		3.5(6)	7.7(8)	12.0×9.9	28.0	1.24
97,582.808(3)	$2_{1,1} - 1_{1,0}A-$	17.7(5)	2.2(1)	13.1×5.9	21.6	1.21
		7.2(5)	7.0(3)	13.1×5.9	21.6	1.21
97,678.261(100)	$21_{6,16} - 22_{5,17}A-$	0.3(1)	30.4(67)	13.9×6.1	728.9	5.74
98,030.396(118)	$24_{6,19} - 23_{7,16}A-$	0.2(1)	5.1(17)	14.4×6.1	888.5	6.43
98,030.435(118)	$24_{6,18} - 23_{7,17}A+$	0.2(1)	5.1(17)	14.4×6.1	888.5	6.43
99,374.624(264)	$15_{-6,10} - 14_{-7,8}E$	0.3(2)	3.4(25)	13.5×6.6	770.6	2.79
99,601.946(64)	$15_{1,14} - 15_{1,15}A-$	0.7(2)	1.7(5)	13.6×5.8	295.1	0.09
99,730.959(14)	$6_{1,6} - 5_{0,5}E$	5.0(1)	3.7(1)	13.6×5.6	339.9	3.13
100,638.870(24)	$13_{2,11} - 12_{3,9}E$	14.5(5)	2.2(1)	14.0×6.2	233.5	3.84
101,101.654(18)	$4_{-2,3} - 4_{1,3}E$	0.7(2)	2.6(10)	13.2×5.6	49.1	0.00
101,102.472(20)	$2_{-2,1} - 2_{1,1}E$	0.0(2)	2.6(10)	13.2×5.6	32.8	0.00
101,126.774(17)	$5_{-2,4} - 5_{1,4}E$	0.6(2)	2.6(12)	13.2×5.6	60.7	0.01
101,185.367(17)	$6_{-2,5} - 6_{1,5}E$	1.2(2)	2.6(6)	12.5×6.1	74.6	0.02
101,293.328(16)	$7_{-2,6} - 7_{1,6}E$	1.9(3)	1.8(5)	13.4×5.9	90.9	0.04
101,469.719(16)	$8_{-2,7} - 8_{1,7}E$	4.1(4)	3.0(4)	13.3×6.9	109.4	0.09
101,737.211(17)	$9_{-2,8} - 9_{1,8}E$	3.2(3)	2.3(3)	11.1×6.5	130.3	0.16
102,122.701(18)	$10_{-2,9} - 10_{1,9}E$	3.5(3)	5.3(6)	14.5×6.4	153.5	0.29
102,658.096(18)	$11_{-2,10} - 11_{1,10}E$	3.8(2)	3.3(2)	12.3×6.2	179.1	0.48
102,957.986(106)	$15_{-2,13} - 16_{-3,13}E$	1.3(2)	2.9(4)	13.8×5.2	641.9	10.59
		0.3(2)	7.7(1)	13.8×5.2	641.9	10.59
103,381.209(19)	$12_{-2,11} - 12_{1,11}E$	6.5(4)	2.1(2)	13.2×6.3	207.0	0.77
		3.8(4)	7.3(5)	13.2×6.3	207.0	0.77
104,060.717(19)	$13_{-3,11} - 12_{-4,9}E$	4.5(5)	2.2(2)	14.3×5.4	273.8	3.27
		4.1(4)	6.9(4)	14.3×5.4	273.8	3.27
104,300.396(16)	$11_{-1,11} - 10_{-2,9}E$	27.3(5)	1.9(0)	14.0×6.4	158.6	3.41
		10.3(5)	6.0(3)	14.0×6.4	158.6	3.41
104,336.637(20)	$13_{-2,12} - 13_{1,12}E$	5.6(4)	2.6(2)	14.0×6.4	237.2	1.19
		2.0(4)	8.4(9)	14.0×6.4	237.2	1.19
104,354.861(17)	$10_{4,7} - 11_{3,8}A-$	6.8(4)	2.3(2)	13.7×6.7	207.9	2.48
		5.3(4)	7.7(4)	13.7×6.7	207.9	2.48
104,410.489(17)	$10_{4,6} - 11_{3,9}A+$	4.8(3)	2.3(2)	12.9×5.3	207.9	2.48
		3.1(3)	7.7(5)	12.9×5.3	207.9	2.48
105,063.761(30)	$13_{1,13} - 12_{2,10}A+$	13.6(7)	2.2(1)	13.1×6.6	223.7	4.27
		7.9(7)	7.5(4)	13.1×6.6	223.7	4.27

Table 4.6—Continued

Rest Frequency (MHz)[a]	Transition	I_0 (Jy/bm)	Δv (km s^{-1})	Beam Size (″×″)	E_u (K)	$S\mu^2$ (D^2)
105,576.385(21)	$14_{-2,13} - 14_{1,13}E$	4.0(7)	2.5(4)	14.9×6.4	269.7	1.79
		1.7(6)	8.2(19)	14.9×6.4	269.7	1.79
107,013.770(13)	$3_{1,3} - 4_{0,4}A+$	21.1(5)	2.4(1)	11.8×6.8	28.3	3.00
		9.6(4)	7.9(2)	11.8×6.8	28.3	3.00
107,159.915(23)	$15_{-2,14} - 15_{1,14}E$	2.9(4)	2.0(3)	12.6×6.7	304.6	2.60
		3.2(4)	7.0(5)	12.6×6.7	304.6	2.60
108,893.929(15)	$0_{0,0} - 1_{-1,1}E$	13.9(4)	2.3(1)	11.5×5.2	13.1	0.97
		6.1(4)	7.4(3)	11.5×5.2	13.1	0.97
109,138.688(25)	$14_{5,10} - 15_{4,11}E$	3.3(4)	2.3(3)	13.1×6.0	379.5	3.40
		1.8(4)	7.8(10)	13.1×6.0	379.5	3.40
109,153.210(28)	$16_{-2,15} - 16_{1,15}E$	2.8(9)	1.4(9)	13.1×6.0	341.8	3.68
		2.9(5)	6.2(6)	13.1×6.0	341.8	3.68
111,289.601(19)	$7_{2,5} - 8_{1,8}A+$	13.2(4)	2.2(1)	12.1×5.8	102.7	2.33
			$^{13}CH_3OH$			
82,389.079(33)	$13_{2,11} - 12_{3,9}E$	1.1(2)	3.0(7)	24.5×8.1	228.5	3.86
84,970.232(23)	$8_{0,8} - 7_{1,7}A+$	2.6(1)	2.8(2)	13.6×8.3	81.5	7.20
90,262.253(35)	$11_{-1,11} - 10_{-2,9}E$	0.6(1)	7.6(18)	16.1×7.0	154.9	3.45
92,588.759(22)	$7_{2,6} - 8_{1,7}A-$	1.4(2)	2.9(4)	21.7×6.4	101.2	2.51
93,619.431(4)	$2_{1,2} - 1_{1,1}A+$	2.2(3)	2.4(4)	14.0×9.1	21.3	1.21
94,405.223(4)	$2_{-1,2} - 1_{-1,1}E$	1.8(3)	1.9(4)	15.7×6.2	12.4	1.21
94,407.129(4)	$2_{0,2} - 1_{0,1}A+$	2.3(2)	1.9(3)	15.7×6.2	6.8	1.61
94,410.895(4)	$2_{0,2} - 1_{0,1}E$	2.0(2)	2.3(2)	15.7×6.2	19.9	1.61
94,420.439(4)	$2_{1,1} - 1_{1,0}E$	1.3(2)	2.4(4)	15.7×6.2	27.8	1.24
95,208.776(4)	$2_{1,1} - 1_{1,0}A-$	1.0(3)	6.7(14)	15.8×7.3	21.4	1.21
95,273.325(20)	$6_{-2,5} - 7_{-1,7}E$	1.2(2)	3.2(6)	15.1×7.4	73.5	2.01
109,164.048(20)	$0_{0,0} - 1_{-1,1}E$	1.1(2)	3.5(7)	13.1×6.0	13.1	0.97
112,143.546(21)	$3_{1,3} - 4_{0,4}A+$	4.8(3)	2.3(1)	13.0×5.8	28.0	3.00
112,375.502(44)	$12_{1,11} - 11_{2,10}A-$	1.0(2)	5.7(20)	11.5×4.9	192.6	4.61
			$(CH_2)_2O$			
84,282.947(17)	$6_{2,4} - 6_{1,5}$	0.7(1)	4.2(8)	12.0×7.7	40.2	2.11
90,547.942(9)	$2_{2,1} - 1_{1,0}$	0.3(2)	4.4(34)	14.6×6.7	6.6	1.50
93,668.083(12)	$3_{0,3} - 2_{1,2}$	[d]	···	14.9×8.1	9.5	2.35
94,664.552(12)	$3_{1,3} - 2_{0,2}$	0.9(2)	1.9(4)	16.2×7.1	9.5	2.38
			CO			
115,271.202(1)	$1 - 0$	[b]	···	12.4×4.7	5.3	0.01

Table 4.6—Continued

Rest Frequency (MHz)[a]	Transition	I_0 (Jy/bm)	Δv (km s^{-1})	Beam Size (″×″)	E_u (K)	$S\mu^2$ (D^2)
			$C^{18}O$			
109,782.173(6)	$1-0$	[b]	···	11.7×5.3	5.3	0.01
			^{13}CO			
110,201.354(5)	$1-0$	[b]	···	12.7×5.4	5.3	0.01
			CS			
97,980.985(15)	$2-1$	4.0(4)	24.2(13)	12.4×5.8	7.0	7.71
			^{13}CS			
92,494.310(19)	$2-1$	2.2(3)	5.6(4)	21.3×6.8	6.7	7.71
			$C^{33}S$			
97,172.100(12)	$2-1$	1.0(2)	3.0(8)	14.5×6.3	7.0	7.71
			$C^{34}S$			
96,412.993(14)	$2-1$	5.1(2)	2.8(1)	13.6×6.4	6.9	7.71
			HC_3N			
81,881.461(1)	$9-8$	7.8(3)	1.9(1)	13.0×8.6	19.6	374.65
82,082.730(26)	$9-8, 1e,^1\, \nu_7$	0.5(1)	16.6(23)	15.1×8.0	339.5	123.17
82,200.372(26)	$9-8, 1f,^1\, \nu_7$	0.5(7)	5.0(54)	18.5×7.7	339.5	123.17
		1.0(8)	11.9(43)	18.5×7.7	339.5	123.17
82,400.748(46)	$9-8, 2e,^2\, \nu_7$	0.6(1)	6.3(15)	24.5×8.1	659.9	117.95
90,978.989(3)	$10-9$	[e]	···	12.5×9.0	24.0	416.21
100,076.385(3)	$11-10$	15.1(3)	1.8(0)	14.6×6.6	28.8	457.90
100,880.448(70)	$11-10, 1e,^3\, \nu_7$	0.6(1)	6.6(25)	13.1×5.9	984.9	149.58
109,173.638(4)	$12-11$	8.8(3)	1.7(1)	13.1×6.0	34.0	499.53
109,441.944(30)	$12-11, 1e,^1\, \nu_7$	0.9(2)	5.7(17)	12.2×6.3	353.9	165.91
110,050.765(92)	$12-11, 1e,^3\, \nu_7$	0.8(3)	3.0(12)	14.1×5.2	990.2	163.39
			HCN			
88,630.416(1)	$1-0, F=1-1$	[b]	···	13.4×8.9	4.3	8.90
88,631.847(1)	$1-0, F=2-1$	[b]	···	13.4×8.9	4.3	8.90
88,633.936(1)	$1-0, F=0-1$	[b]	···	13.4×8.9	4.3	8.90

Table 4.6—Continued

Rest Frequency (MHz)[a]	Transition	I_0 (Jy/bm)	Δv (km s^{-1})	Beam Size (″×″)	E_u (K)	$S\mu^2$ (D^2)
			$H^{13}CN$			
86,338.767(30)	$1-0, F=1-1$	[b]	···	12.6×8.0	4.1	8.90
86,340.184(30)	$1-0, F=2-1$	[b]	···	12.6×8.0	4.1	8.90
86,342.274(30)	$1-0, F=0-1$	[b]	···	12.6×8.0	4.1	8.90
			$HC^{15}N$			
86,054.969(6)	$1-0$	[b]	···	15.3×7.8	4.1	8.90
			HCO^+			
89,188.526(21)	$1-0$	0.6(1)	64.6(73)	14.5×6.5	4.3	10.89
			$H^{13}CO^+$			
86,754.330(50)	$1-0$	-0.8(1)	3.0(4)	11.7×7.6	4.2	10.98
			$HCOOCH_3$			
82,242.942(13)	$7_{1,7}-6_{0,6}E$	1.2(3)	2.0(7)	18.4×8.0	15.8	2.40
82,244.488(14)	$7_{1,7}-6_{0,6}A$	1.0(2)	2.8(7)	18.4×8.0	15.8	2.40
83,605.193(14)	$10_{3,8}-10_{2,9}E$	0.8(2)	2.4(6)	19.1×8.1	38.4	2.20
84,224.798(15)	$11_{4,7}-11_{3,8}E$	0.7(2)	2.4(7)	12.9×7.6	49.8	3.00
84,233.263(17)	$11_{4,7}-11_{3,8}A$	1.0(6)	1.5(9)	12.3×7.5	49.8	3.00
84,449.102(11)	$7_{2,6}-6_{2,5}E$	3.6(2)	2.4(2)	13.6×7.5	19.0	17.20
84,454.787(12)	$7_{2,6}-6_{2,5}A$	4.2(3)	2.0(2)	13.6×7.5	19.0	17.20
85,638.349(9)	$4_{2,3}-3_{1,2}E$	0.5(1)	2.3(9)	13.1×7.6	8.5	0.80
85,761.879(15)	$21_{5,16}-21_{4,17}E$	2.5(2)	1.8(2)	17.0×7.3	155.8	7.90
85,773.322(16)	$21_{5,16}-21_{4,17}A$	0.5(2)	1.8(10)	17.0×7.3	155.8	7.90
85,780.701(13)	$20_{5,15}-20_{4,16}E$	0.6(1)	3.9(9)	17.0×7.3	142.7	7.30
85,785.258(15)	$20_{5,15}-20_{4,16}A$	1.0(1)	2.0(3)	17.0×7.3	142.7	7.30
85,919.086(14)	$7_{6,1}-6_{6,0}E$	1.5(2)	2.7(4)	23.6×7.7	40.4	5.00
85,926.508(11)	$7_{6,2}-6_{6,1}E$	[d]	···	17.6×8.9	40.4	5.00
85,927.230(12)	$7_{6,2}-6_{6,1}A$	[d]	···	17.6×8.9	40.4	5.00
85,927.236(12)	$7_{6,1}-6_{6,0}A$	[d]	···	17.6×8.9	40.4	5.00
86,021.008(13)	$7_{5,2}-6_{5,1}E$	2.9(2)	2.2(2)	22.3×7.7	33.1	9.20
86,027.674(11)	$7_{5,3}-6_{5,2}E$	2.9(2)	2.1(1)	22.3×7.7	33.1	9.20
86,029.445(12)	$7_{5,3}-6_{5,2}A$	3.4(2)	2.6(4)	22.3×7.7	33.1	9.20
86,030.212(12)	$7_{5,2}-6_{5,1}A$	3.0(3)	1.9(2)	22.3×7.7	33.1	9.20
86,210.079(12)	$7_{4,4}-6_{4,3}A$	3.1(3)	2.3(2)	14.5×7.6	27.2	12.70
86,223.548(13)	$7_{4,3}-6_{4,2}E$	2.0(1)	3.6(3)	14.5×7.6	27.2	12.60
86,224.106(11)	$7_{4,4}-6_{4,3}E$	2.0(1)	3.6(3)	14.5×7.6	27.2	12.60

Table 4.6—Continued

Rest Frequency (MHz)[a]	Transition	I_0 (Jy/bm)	Δv (km s^{-1})	Beam Size (″×″)	E_u (K)	$S\mu^2$ (D^2)
86,250.576(12)	$7_{4,3} - 6_{4,2}A$	3.3(3)	2.5(3)	13.2×8.2	27.2	12.70
86,265.826(12)	$7_{3,5} - 6_{3,4}A$	4.6(5)	2.1(3)	13.2×8.2	22.4	15.30
86,268.659(11)	$7_{3,5} - 6_{3,4}E$	4.0(3)	2.6(2)	13.2×8.2	22.6	15.20
87,143.198(14)	$7_{3,4} - 6_{3,3}E$	5.2(2)	2.2(1)	17.1×7.7	22.6	15.20
87,161.313(12)	$7_{3,4} - 6_{3,3}A$	5.1(2)	2.4(1)	17.1×7.7	22.6	15.30
87,766.301(13)	$8_{0,8} - 7_{1,7}E$	1.2(2)	1.4(5)	12.8×7.7	20.1	2.80
87,769.067(13)	$8_{0,8} - 7_{1,7}A$	0.9(2)	2.1(4)	12.8×7.7	20.0	2.80
88,175.626(15)	$10_{4,6} - 10_{3,7}E$	0.9(3)	2.1(11)	12.3×9.2	43.2	2.50
88,337.802(18)	$22_{5,17} - 22_{4,18}E$	0.8(3)	1.7(10)	13.8×7.1	169.5	8.20
88,358.420(19)	$22_{5,17} - 22_{4,18}A$	0.8(7)	1.6(16)	13.8×7.1	169.5	8.20
88,686.906(15)	$11_{3,9} - 11_{2,10}E$	1.0(2)	1.9(4)	14.8×7.3	45.0	2.40
88,723.239(20)	$11_{3,9} - 11_{2,10}A$	0.5(1)	2.8(9)	16.7×6.4	44.9	2.40
88,825.845(21)	$23_{7,16} - 22_{8,15}A$	0.5(2)	4.0(16)	14.9×8.3	196.5	1.40
88,843.117(11)	$7_{1,6} - 6_{1,5}E$	4.4(2)	2.5(1)	17.2×6.7	18.0	18.20
88,851.641(12)	$7_{1,6} - 6_{1,5}A$	4.6(2)	2.4(1)	17.2×6.7	18.0	18.20
89,314.589(13)	$8_{1,8} - 7_{1,7}E$	7.6(6)	1.8(2)	17.7×8.9	20.1	21.00
89,316.668(13)	$8_{1,8} - 7_{1,7}A$	7.5(3)	2.1(1)	17.7×8.9	20.1	21.00
90,145.634(12)	$7_{2,5} - 6_{2,4}E$	7.2(3)	2.3(1)	15.5×8.4	19.7	17.30
90,156.511(13)	$7_{2,5} - 6_{2,4}A$	6.4(6)	2.0(3)	15.5×8.4	19.7	17.30
90,227.595(13)	$8_{0,8} - 7_{0,7}E$	6.3(2)	2.8(1)	16.1×7.0	20.1	21.00
90,229.647(14)	$8_{0,8} - 7_{0,7}A$	6.3(2)	2.6(1)	16.1×7.0	20.0	21.00
91,366.593(17)	$9_{4,5} - 9_{3,6}E$	0.8(2)	2.5(8)	12.5×7.2	37.3	2.00
91,775.884(13)	$8_{1,8} - 7_{0,7}E$	1.3(3)	2.8(11)	13.1×7.8	20.1	2.90
91,777.248(15)	$8_{1,8} - 7_{0,7}A$	1.6(3)	3.1(9)	13.1×7.8	20.1	2.90
92,073.005(18)	$18_{5,13} - 18_{4,14}A$	1.1(2)	1.9(12)	13.3×6.8	118.8	5.90
92,074.105(15)	$18_{5,13} - 18_{4,14}E$	1.1(4)	1.9(20)	13.3×6.8	118.8	5.90
92,940.284(30)	$17_{3,14} - 17_{2,15}A$	1.6(3)	1.7(4)	17.0×8.6	99.7	4.40
93,205.664(29)	$14_{2,12} - 14_{1,13}E$	1.2(2)	4.5(7)	14.9×6.9	66.9	2.80
93,261.760(39)	$14_{2,12} - 14_{1,13}A$	1.6(3)	1.8(4)	14.0×6.9	66.9	2.80
93,660.027(14)	$8_{4,4} - 8_{3,5}A$	2.3(16)	1.5(12)	14.9×8.1	31.9	1.80
93,701.278(24)	$8_{4,4} - 8_{3,5}E$	1.4(6)	1.9(10)	15.6×8.4	31.9	1.40
93,702.594(23)	$23_{5,18} - 23_{4,19}A$	1.5(3)	2.5(6)	15.6×8.4	183.8	8.40
94,378.491(16)	$9_{1,8} - 8_{2,7}E$	0.7(2)	2.3(5)	15.0×6.5	28.2	1.70
94,387.648(18)	$9_{1,8} - 8_{2,7}A$	0.6(1)	2.4(7)	15.0×6.5	28.1	1.70
94,626.875(17)	$12_{3,10} - 12_{2,11}E$	1.3(2)	2.1(4)	16.7×7.0	52.1	2.50
94,632.718(10)	$5_{2,4} - 4_{1,3}E$	0.7(2)	2.3(7)	16.7×7.0	11.5	1.00
94,647.320(11)	$5_{2,4} - 4_{1,3}A$	0.6(1)	6.1(13)	16.2×7.1	11.5	1.00
94,666.935(23)	$12_{3,10} - 12_{2,11}A$	1.0(2)	2.7(5)	16.2×7.1	51.9	2.50
95,175.924(14)	$7_{4,3} - 7_{3,4}A$	1.4(2)	1.7(3)	16.1×7.3	27.2	1.50
96,059.072(24)	$11_{2,10} - 11_{1,11}E$	0.9(2)	1.5(5)	13.4×6.0	40.7	1.30
96,070.654(12)	$8_{2,7} - 7_{2,6}E$	5.2(2)	1.9(1)	14.1×5.9	23.6	20.00
96,076.878(12)	$8_{2,7} - 7_{2,6}A$	5.1(2)	2.0(1)	14.1×5.9	23.6	20.00

Table 4.6—Continued

Rest Frequency (MHz)[a]	Transition	I_0 (Jy/bm)	Δv (km s^{-1})	Beam Size ($'' \times ''$)	E_u (K)	$S\mu^2$ (D^2)
96,086.660(15)	$6_{4,2} - 6_{3,3}A$	0.8(1)	2.5(5)	14.1×5.9	23.0	1.10
96,107.220(38)	$11_{2,10} - 11_{1,11}A$	0.7(1)	2.4(5)	14.1×5.9	40.7	1.30
96,167.640(26)	$6_{4,2} - 6_{3,3}E$	0.5(1)	2.4(8)	13.7×5.7	23.0	0.80
96,586.624(15)	$5_{4,1} - 5_{3,2}A$	0.6(1)	5.9(17)	15.1×6.8	19.4	0.80
96,637.769(14)	$7_{4,4} - 7_{3,5}A$	1.5(15)	1.5(17)	15.1×9.5	27.2	1.50
97,018.072(13)	$9_{4,6} - 9_{3,7}A$	1.1(2)	2.6(6)	14.5×6.6	37.3	2.10
97,199.129(19)	$17_{5,12} - 17_{4,13}A$	0.9(2)	2.0(5)	14.5×6.3	107.7	5.20
97,199.223(17)	$17_{5,12} - 17_{4,13}E$	0.9(2)	2.0(5)	14.5×6.3	107.7	5.20
97,651.392(13)	$10_{4,7} - 10_{3,8}E$	1.5(3)	1.7(4)	13.9×6.1	43.2	2.40
97,694.197(12)	$10_{4,7} - 10_{3,8}A$	1.1(2)	2.2(5)	13.5×6.1	43.2	2.40
98,182.199(15)	$8_{7,1} - 7_{7,0}E$	1.8(2)	1.9(3)	15.7×6.8	53.8	5.00
98,190.653(14)	$8_{7,1} - 7_{7,0}A$	2.5(2)	1.8(2)	15.7×6.8	53.8	5.00
98,190.653(14)	$8_{7,2} - 7_{7,1}A$	2.5(2)	1.8(2)	15.7×6.8	53.8	5.00
98,191.414(13)	$8_{7,2} - 7_{7,1}E$	2.5(2)	1.8(2)	15.7×6.8	53.8	5.00
98,270.369(15)	$8_{6,2} - 7_{6,1}E$	3.0(2)	2.1(2)	15.9×6.9	45.2	9.40
98,278.870(12)	$8_{6,3} - 7_{6,2}E$	1.3(1)	2.4(10)	15.9×6.9	45.2	9.40
98,279.746(13)	$8_{6,3} - 7_{6,2}A$	1.3(1)	2.4(10)	15.9×6.9	45.2	9.40
98,279.788(13)	$8_{6,2} - 7_{6,1}A$	1.3(1)	2.4(10)	15.9×6.9	45.2	9.40
98,424.082(14)	$8_{5,3} - 7_{5,2}E$	4.7(2)	2.2(1)	14.3×5.7	37.8	13.10
98,431.748(12)	$8_{5,4} - 7_{5,3}E$	2.2(1)	2.6(4)	14.3×5.7	37.8	13.10
98,432.773(13)	$8_{5,4} - 7_{5,3}A$	2.2(1)	2.6(4)	14.3×5.7	37.9	13.10
98,435.820(13)	$8_{5,3} - 7_{5,2}A$	1.7(15)	3.6(14)	14.3×5.7	37.8	13.10
98,606.771(12)	$8_{3,6} - 7_{3,5}E$	5.8(2)	2.4(1)	13.9×6.1	27.2	18.40
98,611.195(13)	$8_{3,6} - 7_{3,5}A$	1.4(2)	17.3(18)	13.9×6.1	27.2	18.40
98,682.635(13)	$8_{4,5} - 7_{4,4}A$	3.4(5)	3.5(3)	14.6×7.1	31.9	16.10
98,711.931(12)	$8_{4,5} - 7_{4,4}E$	5.4(3)	1.8(2)	14.6×7.1	31.9	15.60
98,747.797(16)	$8_{4,4} - 7_{4,3}E$	6.4(2)	2.4(1)	15.2×7.0	31.9	15.60
98,792.314(13)	$8_{4,4} - 7_{4,3}A$	6.4(2)	2.7(1)	15.5×7.0	31.9	16.10
98,839.600(12)	$11_{4,8} - 11_{3,9}E$	1.4(2)	3.0(5)	15.2×7.3	49.8	2.70
98,875.160(12)	$11_{4,8} - 11_{3,9}A$	1.2(3)	1.8(6)	13.1×10.5	49.6	2.70
99,133.188(13)	$9_{0,9} - 8_{1,8}E$	1.9(3)	1.9(4)	12.6×7.6	24.9	3.30
99,135.791(14)	$9_{0,9} - 8_{1,8}A$	1.7(3)	1.7(4)	12.6×7.6	24.9	3.30
99,166.524(24)	$11_{2,9} - 10_{3,8}E$	1.0(3)	1.6(5)	13.9×8.2	43.3	1.10
99,179.361(26)	$11_{2,9} - 10_{3,8}A$	0.6(2)	1.7(9)	13.9×8.2	43.2	1.10
100,078.534(13)	$9_{1,9} - 8_{1,8}E$	7.1(3)	2.1(1)	14.6×6.6	24.9	23.60
100,080.566(14)	$9_{1,9} - 8_{1,8}A$	7.6(3)	1.9(1)	14.6×6.6	24.9	23.60
100,294.508(13)	$8_{3,5} - 7_{3,4}E$	2.6(10)	1.7(5)	11.6×9.5	27.5	18.40
100,308.210(13)	$8_{3,5} - 7_{3,4}A$	4.6(8)	1.8(3)	14.7×9.0	27.3	18.40
100,482.174(12)	$8_{1,7} - 7_{1,6}E$	6.8(4)	2.7(2)	16.1×6.9	22.7	20.80
100,490.715(12)	$8_{1,7} - 7_{1,6}A$	7.5(4)	2.7(2)	16.2×6.9	22.7	20.80
100,659.692(12)	$12_{4,9} - 12_{3,10}E$	1.4(2)	4.9(9)	14.0×6.2	56.8	3.00
100,681.476(13)	$9_{0,9} - 8_{0,8}E$	6.9(3)	3.0(1)	14.0×6.2	24.9	23.70

Table 4.6—Continued

Rest Frequency (MHz)[a]	Transition	I_0 (Jy/bm)	Δv (km s^{-1})	Beam Size (″×″)	E_u (K)	$S\mu^2$ (D^2)
100,683.392(14)	$9_{0,9} - 8_{0,8}A$	7.7(3)	2.5(1)	14.0×6.2	24.9	23.70
100,693.051(13)	$12_{4,9} - 12_{3,10}A$	1.7(3)	1.6(5)	14.1×6.3	56.8	3.00
100,790.768(47)	$12_{1,11} - 12_{0,12}A$	0.5(3)	2.4(18)	12.7×5.9	47.2	1.40
101,302.116(19)	$25_{6,19} - 25_{5,20}A$	0.6(2)	3.8(13)	13.4×5.9	219.2	9.40
101,305.534(17)	$25_{6,19} - 25_{5,20}E$	0.8(3)	1.7(7)	13.4×5.9	219.2	9.40
101,370.518(19)	$13_{3,11} - 13_{2,12}E$	1.4(2)	3.4(6)	12.3×7.3	59.7	2.60
101,414.723(26)	$13_{3,11} - 13_{2,12}A$	1.3(2)	12.3(23)	12.9×6.7	59.6	2.60
101,626.822(14)	$9_{1,9} - 8_{0,8}E$	2.3(3)	1.6(5)	14.6×6.8	24.9	3.30
101,628.167(15)	$9_{1,9} - 8_{0,8}A$	2.3(3)	2.9(6)	14.6×6.8	24.9	3.30
102,734.338(17)	$16_{5,11} - 16_{4,12}E$	0.6(2)	1.5(8)	13.3×5.5	97.5	4.60
102,736.773(19)	$16_{5,11} - 16_{4,12}A$	0.6(2)	2.0(9)	13.3×5.5	97.5	4.60
102,909.292(13)	$6_{2,5} - 5_{1,4}A$	0.5(1)	1.5(5)	13.7×5.3	15.0	1.10
103,057.055(27)	$21_{4,17} - 21_{3,18}E$	1.0(3)	1.8(6)	14.7×5.7	151.6	6.20
103,114.824(28)	$21_{4,17} - 21_{3,18}A$	0.7(2)	2.7(7)	14.5×5.6	151.6	6.20
103,228.415(12)	$13_{4,10} - 13_{3,11}E$	1.2(4)	1.3(6)	13.3×5.8	64.6	3.20
103,262.008(13)	$13_{4,10} - 13_{3,11}A$	2.1(2)	1.8(2)	14.4×6.3	64.6	3.20
103,376.784(19)	$24_{6,18} - 24_{5,19}A$	1.1(2)	4.4(8)	13.2×6.3	203.8	8.70
103,387.227(17)	$24_{6,18} - 24_{5,19}E$	1.7(2)	2.3(3)	13.2×6.3	203.8	8.70
103,466.479(13)	$8_{2,6} - 7_{2,5}E$	4.8(3)	2.5(2)	13.1×6.9	24.6	20.20
103,478.699(13)	$8_{2,6} - 7_{2,5}A$	4.8(3)	2.3(2)	13.1×6.9	24.6	20.20
104,991.284(25)	$12_{2,11} - 12_{1,12}E$	1.2(2)	2.1(5)	13.8×6.4	47.5	1.30
105,044.378(42)	$12_{2,11} - 12_{1,12}A$	1.0(3)	5.1(16)	13.3×6.5	47.5	1.30
106,632.824(13)	$14_{4,11} - 14_{3,12}E$	1.3(2)	1.6(3)	12.9×5.6	72.9	3.40
106,668.054(15)	$14_{4,11} - 14_{3,12}A$	1.0(2)	2.6(6)	12.9×5.6	72.9	3.40
107,537.189(13)	$9_{2,8} - 8_{2,7}E$	5.0(2)	2.5(1)	12.2×5.3	28.8	22.80
107,543.746(13)	$9_{2,8} - 8_{2,7}A$	5.6(2)	2.1(1)	12.2×5.3	28.8	22.80
107,604.399(17)	$23_{6,17} - 23_{5,18}E$	0.6(1)	17.5(39)	13.1×5.5	189.0	7.90
108,046.084(17)	$15_{5,10} - 15_{4,11}E$	1.0(2)	2.0(4)	13.7×4.9	87.9	4.10
108,050.848(19)	$15_{5,10} - 15_{4,11}A$	1.5(3)	1.6(3)	13.7×4.9	87.9	4.10
108,834.940(20)	$14_{3,12} - 14_{2,13}E$	1.0(2)	1.9(5)	11.7×5.2	67.8	2.60
108,883.548(29)	$14_{3,12} - 14_{2,13}A$	1.1(2)	2.4(6)	11.5×5.2	67.8	2.60
109,302.206(17)	$10_{1,9} - 9_{2,8}A$	1.6(4)	2.2(6)	12.8×6.3	33.9	2.10
110,224.485(13)	$10_{0,10} - 9_{1,9}E$	1.7(4)	1.9(4)	12.7×5.4	30.2	3.80
110,226.883(15)	$10_{0,10} - 9_{1,9}A$	1.8(3)	1.7(3)	12.7×5.4	30.2	3.80
110,447.032(16)	$9_{8,1} - 8_{8,0}E$	1.6(3)	2.1(5)	12.4×5.3	69.0	5.10
110,455.358(15)	$9_{8,1} - 8_{8,0}A$	1.4(3)	1.9(2)	12.4×5.3	69.0	5.10
110,455.358(15)	$9_{8,2} - 8_{8,1}A$	1.4(3)	1.9(2)	12.4×5.3	69.0	5.10
110,525.598(16)	$9_{7,2} - 8_{7,1}A$	2.6(3)	1.8(2)	11.7×5.4	59.1	9.60
110,535.182(14)	$9_{7,3} - 8_{7,2}A$	2.6(5)	1.9(7)	11.7×5.4	59.1	9.60
110,535.184(14)	$9_{7,2} - 8_{7,1}A$	2.6(5)	1.9(7)	11.7×5.4	59.1	9.60
110,535.955(13)	$9_{7,3} - 8_{7,2}E$	2.6(5)	1.9(7)	11.7×5.4	59.1	9.60
110,652.678(15)	$9_{6,3} - 8_{6,2}E$	4.6(4)	2.2(2)	12.8×5.7	50.5	13.40

Table 4.6—Continued

Rest Frequency (MHz)[a]	Transition	I_0 (Jy/bm)	Δv (km s^{-1})	Beam Size (″×″)	E_u (K)	$S\mu^2$ (D^2)
110,662.261(13)	$9_{6,4}-8_{6,3}E$	5.2(2)	2.7(4)	12.6×5.7	50.5	13.40
110,663.263(14)	$9_{6,4}-8_{6,3}A$	3.8(6)	1.9(1)	12.6×5.7	50.5	13.40
110,663.456(14)	$9_{6,3}-8_{6,2}A$	3.8(6)	1.9(1)	12.6×5.7	50.5	13.40
110,788.590(14)	$10_{1,10}-9_{1,9}E$	8.0(3)	2.7(1)	12.7×5.7	30.2	26.30
110,790.553(15)	$10_{1,10}-9_{1,9}A$	7.8(3)	2.9(1)	12.7×5.7	30.2	26.30
110,873.828(15)	$9_{5,4}-8_{5,3}E$	5.3(3)	2.7(2)	12.8×5.5	43.2	16.70
110,880.466(13)	$9_{5,5}-8_{5,4}A$	8.7(3)	4.1(1)	12.8×5.5	43.2	16.70
110,882.273(12)	$9_{5,5}-8_{5,4}E$	6.6(3)	2.3(1)	12.8×5.5	43.2	16.70
110,887.127(13)	$9_{3,7}-8_{3,6}A$	7.5(3)	2.6(1)	12.8×5.5	32.5	21.40
110,890.275(13)	$9_{5,4}-8_{5,3}A$	6.1(3)	2.3(2)	12.8×5.5	43.2	16.70
110,924.269(15)	$15_{4,12}-15_{3,13}E$	2.0(4)	1.5(4)	12.3×5.5	81.9	3.60
110,962.074(16)	$15_{4,12}-15_{3,13}A$	1.6(4)	1.7(4)	12.3×5.5	81.9	3.60
111,169.831(14)	$10_{0,10}-9_{0,9}E$	7.2(3)	1.8(1)	11.9×5.3	30.2	26.30
111,171.659(15)	$10_{0,10}-9_{0,9}A$	6.9(3)	1.8(1)	11.9×5.3	30.2	26.30
111,195.990(13)	$9_{4,6}-8_{4,5}A$	5.5(2)	2.3(1)	12.8×5.8	37.3	19.40
111,223.397(14)	$9_{4,6}-8_{4,5}E$	5.3(3)	2.1(1)	12.8×5.8	37.3	18.30
111,408.322(19)	$9_{4,5}-8_{4,4}E$	4.8(2)	2.5(1)	12.4×5.2	37.3	18.30
111,432.033(29)	$13_{1,12}-13_{0,13}E$	0.7(2)	1.5(7)	12.1×5.2	54.7	1.40
111,453.327(13)	$9_{4,5}-8_{4,4}A$	5.7(2)	2.1(1)	12.1×5.2	37.3	19.40
111,674.070(13)	$9_{1,8}-8_{1,7}E$	7.4(2)	2.7(1)	12.7×4.9	28.2	23.40
111,682.224(13)	$9_{1,8}-8_{1,7}A$	8.4(2)	2.4(1)	12.7×4.9	28.1	23.40
111,712.954(35)	$9_{4,5}-8_{4,5}E$	1.2(6)	1.0(9)	12.6×4.9	37.3	1.00
111,718.213(28)	$28_{6,22}-28_{5,23}E$	0.7(2)	4.7(15)	12.6×4.9	269.7	10.30
111,733.936(14)	$10_{1,10}-9_{0,9}E$	2.5(2)	2.5(3)	12.6×4.9	30.2	3.80
111,735.329(15)	$10_{1,10}-9_{0,9}A$	3.1(15)	1.3(7)	12.6×4.9	30.2	3.80
112,310.888(32)	$25_{5,20}-25_{4,21}A$	0.8(2)	2.1(6)	11.2×5.0	214.3	8.10
113,743.007(14)	$9_{3,6}-8_{3,5}E$	6.0(4)	2.5(2)	13.1×4.9	32.8	21.50
113,756.646(14)	$9_{3,6}-8_{3,5}A$	7.2(3)	2.2(2)	13.1×4.9	32.8	21.50
			HCOOH			
86,546.180(1)	$4_{1,4}-3_{1,3}$	2.2(22)	0.8(14)	11.9×7.6	13.6	7.31
89,579.170(1)	$4_{0,4}-3_{0,3}$	0.5(2)	2.7(14)	15.0×7.1	10.8	7.79
93,098.350(1)	$4_{1,3}-3_{1,2}$	0.8(2)	4.9(14)	14.4×6.8	14.3	7.31
108,126.710(1)	$5_{1,5}-4_{1,4}$	0.8(2)	1.6(6)	12.6×5.1	18.7	9.35
112,287.140(1)	$5_{2,4}-4_{2,3}$	0.8(2)	1.7(5)	11.2×5.0	28.9	8.18
			HCS^+			
85,347.878(14)	$2-1$	2.4(24)	0.8(8)	12.5×8.0	6.1	9.16

Table 4.6—Continued

Rest Frequency (MHz)[a]	Transition	I_0 (Jy/bm)	Δv (km s^{-1})	Beam Size (″×″)	E_u (K)	$S\mu^2$ (D^2)
			HDO			
80,578.283(52)	$1_{1,0} - 1_{1,1}$	3.6(5)	1.9(5)	12.5×8.0	46.7	0.65
			H_2CS			
101,477.764(33)	$3_{1,3} - 2_{1,2}$	12.6(6)	2.1(1)	13.3×6.9	22.9	21.70
103,040.416(35)	$3_{0,3} - 2_{0,2}$	2.2(8)	2.4(5)	13.0×5.4	9.9	8.14
103,039.850(34)	$3_{2,2} - 2_{2,1}$	0.6(8)	5.0(25)	13.0×5.4	62.5	4.52
103,051.791(34)	$3_{2,1} - 2_{2,0}$	0.9(2)	2.1(5)	13.0×5.4	62.5	4.52
104,616.988(33)	$3_{1,2} - 2_{1,1}$	6.9(2)	2.3(1)	12.7×5.3	23.2	21.71
			HNC			
90,663.572(4)	$1 - 0$	[f]	···	14.5×6.3	4.3	9.30
			HNCO			
87,597.341(3)	$4(1,4) - 3(1,3)$	0.6(2)	4.9(14)	11.8×7.8	53.8	11.76
87,866.894(7)	$4(3,2) - 3(3,1)$	0.2(1)	2.2(17)	13.0×7.5	386.3	4.49
87,866.894(7)	$4(3,1) - 3(3,0)$	0.2(1)	2.2(17)	13.0×7.5	386.3	4.49
87,898.341(4)	$4(2,3) - 3(2,2)$	0.3(1)	10.4(22)	12.5×7.8	180.9	7.69
87,898.473(5)	$4(2,2) - 3(2,1)$	0.3(1)	10.4(22)	12.5×7.8	180.9	7.69
87,925.222(4)	$4(0,4) - 3(0,3)$	0.9(2)	14.8(24)	12.5×7.8	10.5	9.60
88,239.011(3)	$4(1,3) - 3(1,2)$	1.3(2)	5.1(11)	13.7×8.2	53.8	9.60
109,496.007(4)	$5(1,5) - 4(1,4)$	1.4(2)	5.5(11)	12.5×5.1	59.0	12.30
109,872.366(5)	$5(2,4) - 4(2,3)$	0.4(1)	10.8(22)	12.3×5.0	186.2	7.78
109,872.714(5)	$5(2,3) - 4(2,2)$	0.4(1)	10.8(22)	12.3×5.0	186.2	7.78
109,905.753(5)	$5(0,5) - 4(0,4)$	2.9(3)	3.5(4)	12.2×5.0	15.8	12.83
110,298.098(4)	$5(1,4) - 4(1,3)$	1.2(3)	3.4(8)	11.8×4.9	59.1	12.32
			NH_2D			
Ortho	$1_{0,1} - 1_{1,1}$					
85,924.747(40)	$F = 0 - 1$	[d]	···	12.6×7.6	20.7	3.23
85,925.684(40)	$F = 2 - 1$	[d]	···	12.6×7.6	20.7	3.23
85,926.263(20)	$F = 0 - 0$	[d]	···	12.6×7.6	20.7	3.23
85,926.263(20)	$F = 1 - 1$	[d]	···	12.6×7.6	20.7	3.23
85,926.263(20)	$F = 2 - 2$	[d]	···	12.6×7.6	20.7	3.23
85,926.858(40)	$F = 1 - 2$	[d]	···	12.6×7.6	20.7	3.23
85,927.721(40)	$F = 1 - 0$	[d]	···	12.6×7.6	20.7	3.23
Para	$1_{0,1} - 1_{1,1}$					
110,152.084(40)	$F = 0 - 1$	2.7(8)	1.4(5)	12.8×5.5	21.2	3.23

Table 4.6—Continued

Rest Frequency (MHz)[a]	Transition	I_0 (Jy/bm)	Δv (km s^{-1})	Beam Size ($'' \times ''$)	E_u (K)	$S\mu^2$ (D^2)
110,152.995(40)	$F = 2 - 1$	2.7(8)	1.4(5)	12.8×5.5	21.2	3.23
110,153.599(20)	$F = 0 - 0$	2.7(8)	1.4(5)	12.8×5.5	21.2	3.23
110,153.599(20)	$F = 1 - 1$	2.7(8)	1.4(5)	12.8×5.5	21.2	3.23
110,153.599(20)	$F = 2 - 2$	2.7(8)	1.4(5)	12.8×5.5	21.2	3.23
110,154.222(40)	$F = 1 - 2$	2.7(8)	1.4(5)	12.8×5.5	21.2	3.23
110,155.053(40)	$F = 1 - 0$	2.7(8)	1.4(5)	12.8×5.5	21.2	3.23
			NNH^+			
93,172.053(7)	$1 - 0$	[b]	···	13.7×8.2	4.5	11.56
			$^{15}N^{15}NH^+$			
88,264.120(10)	$1 - 0$	[b]	···	13.7×8.2	4.2	11.56
			OCS			
85,139.121(10)	$7 - 6$	8.8(88)	1.8(18)	12.9×8.0	16.3	3.58
97,301.208(0)	$8 - 7$	12.5(4)	1.9(1)	13.4×6.1	21.0	4.09
109,463.063(5)	$9 - 8$	15.1(5)	2.2(1)	12.2×6.3	26.3	4.60
			$OC^{34}S$			
83,057.970(1)	$7 - 6$	0.8(1)	2.9(4)	12.2×8.0	15.9	3.58
94,922.799(1)	$8 - 7$	1.6(1)	3.5(4)	14.3×6.4	20.5	4.09
106,787.389(2)	$9 - 8$	3.6(36)	0.6(6)	14.2×5.5	25.6	4.60
			SO			
86,093.950(100)	$2_2 - 1_1$	11.2(3)	18.4(6)	14.9×8.0	19.3	3.60
99,299.870(100)	$2_3 - 1_2$	12.1(2)	2.7(1)	12.9×6.5	9.2	7.05
100,029.640(150)	$5_4 - 4_4$	3.3(3)	2.5(3)	14.9×7.0	38.6	0.85
109,252.220(100)	$3_2 - 2_1$	8.1(4)	3.3(2)	12.6×6.2	21.0	3.63
			^{33}SO			
98,433.406(434)	$2_3 - 1_2$	0.4(1)	17.3(40)	14.3×5.7	9.2	0.07
			^{34}SO			
84,410.690(100)	$2_2 - 1_1$	0.4(5)	23.3(79)	14.4×7.5	19.2	3.60
97,715.390(150)	$2_3 - 1_2$	1.2(3)	1.8(4)	13.5×6.1	9.1	7.05
106,742.920(150)	$3_2 - 2_1$	0.6(2)	3.4(14)	14.0×5.4	20.9	3.62

Table 4.6—Continued

Rest Frequency (MHz)[a]	Transition	I_0 (Jy/bm)	Δv (km s^{-1})	Beam Size (″×″)	E_u (K)	$S\mu^2$ (D^2)
			SO_2			
83,688.086(2)	$8_{1,7}-8_{0,8}$	11.9(1)	21.9(5)	16.6×8.0	36.7	17.01
		8.1(3)	2.1(1)	16.6×8.0	36.7	17.01
94,064.686(2)	$23_{6,18}-24_{5,19}$	0.8(1)	14.5(14)	14.1×6.5	342.0	9.22
97,702.340(2)	$7_{3,5}-8_{2,6}$	3.2(1)	18.1(13)	13.5×6.1	47.8	2.50
		2.1(8)	1.5(7)	13.5×6.1	47.8	2.50
104,029.410(3)	$3_{1,3}-2_{0,2}$	6.6(13)	10.2(11)	14.3×5.4	7.7	5.37
		5.5(4)	1.7(2)	14.3×5.4	7.7	5.37
104,033.586(3)	$16_{2,14}-15_{3,13}$	11.7(3)	20.0(8)	14.3×5.4	137.5	7.98
104,239.293(3)	$10_{1,9}-10_{0,10}$	14.4(6)	26.9(3)	14.3×6.7	54.7	17.87
		10.2(3)	1.8(1)	14.3×6.7	54.7	17.87
109,757.587(2)	$17_{5,13}-18_{4,14}$	1.6(1)	11.4(22)	11.7×5.3	202.0	6.60
			$^{34}SO_2$			
82,124.345(3)	$10_{1,9}-9_{2,8}$	0.3(1)	17.2(33)	16.9×7.8	54.5	6.52
83,043.818(3)	$8_{1,7}-8_{0,8}$	0.5(1)	3.4(8)	12.2×8.0	36.6	16.69
			SiO			
86,243.440(41)	$2-1, \nu=1$	[b]	···	13.2×8.2	1775.0	19.20
86,846.960(50)	$2-1$	15.4(32)	17.1(19)	14.5×7.7	6.2	19.27
			^{30}SiO			
84,745.900(200)	$2-1$	0.8(1)	25.1(20)	17.5×8.1	6.1	19.20
			^{29}SiO			
85,759.000(200)	$2-1$	0.9(3)	7.5(24)	17.0×7.3	6.2	19.20

[a]Frequency uncertainty is 2 σ.

[b]Multiple emission and absorption components seen in spectra.

[c]This transition is blended with the previous one(s), and the integrated line intensity and column density are calculated as such.

[d]This transition is highly blended with another(see spectra).

[e]Unable to obtain reliable Gaussian fit. The values given are an estimate.

Table 4.7. Unidentified Lines Detected Toward Orion-KL

Hot Core			Compact Ridge		
Rest Frequency (MHz)[a]	I_0 (Jy/bm)	Δv (km s^{-1})	Rest Frequency (MHz)[a]	I_0 (Jy/bm)	Δv (km s^{-1})
80,394.0	0.5(2)	3.0(12)	80,514.6	0.3(1)	5.1(17)
80,483.1	0.3(0)	38.5(68)	80,520.7	0.3(1)	8.2(25)
80,631.3	0.4(1)	8.0(22)	80,529.4	0.3(1)	4.2(15)
80,673.6	3.5[a]	12.7	80,532.7	0.3(1)	7.7(22)
80,677.5	1.1(1)	12.2(12)	80,575.2	0.3(1)	9.2(33)
80,724.4	0.6(1)	10.7(19)	80,802.3	3.3[a]	0.8
80,801.4	0.5(2)	3.7(16)	80,849.9	3.2[a]	0.8
80,803.1	0.4(2)	2.6(15)	81,061.7	0.4(1)	4.1(15)
81,232.4	0.5(2)	3.5(14)	81,071.1	0.4(2)	2.7(12)
81,585.5	0.5(1)	4.7(11)	81,118.1	2.3[a]	0.9
81,652.4[b]	3.5[a]	12.7	81,361.0	0.3(0)	0.1(1)
82,018.5	0.4(1)	4.2(18)	81,370.5	0.4(2)	2.8(13)
82,196.0	0.4(2)	6.5(32)	81,513.2	0.5(1)	2.8(8)
82,226.0	0.3(2)	5.5(32)	81,513.2	0.5(1)	2.8(8)
82,242.3	0.9(2)	2.8(5)	81,587.4	0.7[a]	0.7
82,243.7	0.9(2)	2.8(5)	81,632.2	0.4(1)	2.5(10)
82,333.7	0.5(1)	9.5(26)	81,653.1[b]	1.3(2)	2.5(4)
82,560.9	0.5(2)	2.7(12)	81,891.4	0.3(2)	3.8(27)
82,830.7	0.4[a]	0.9	81,902.1	0.3(3)	2.3(23)
82,931.6	0.3(1)	9.8(26)	81,970.0	0.4[a]	0.5
82,936.9	0.2(1)	6.6(28)	81,988.1	0.4(3)	2.5(23)
83,120.5[b]	1.0(1)	3.8(4)	82,204.8	0.2(2)	3.1(40)
83,245.0	0.2(1)	8.1(32)	82,286.8	0.6(2)	5.7(19)
83,728.1	0.9(3)	2.9(10)	82,403.4	0.6(1)	6.0(14)
83,730.3	0.6(2)	4.6(18)	82,421.3	0.8(2)	2.4(8)
84,140.6	0.1(0)	8.2(4)	82,428.6	0.5(1)	11.8(18)
84,152.4	0.4(0)	23.8(8)	82,442.7	0.5(1)	8.2(18)
84,356.9	0.3(1)	8.2(19)	82,445.5	4.3[a]	0.8
84,384.2	0.4[a]	0.5	82,627.1	3.2[a]	0.8
84,529.0	0.8(2)	2.6(7)	82,627.1	3.2[a]	0.8
84,538.5	0.6(2)	2.0(8)	83,086.8	0.3(1)	1.2(6)
84,807.0	0.7(1)	3.0(7)	83,121.1[b]	1.9[a]	0.8
85,119.8[b]	0.4(1)	5.4(16)	83,304.6	2.7[a]	0.8
85,185.0	0.5(1)	4.3(11)	83,949.8	0.3(1)	4.7(19)
85,285.5	0.5(1)	2.8(5)	83,982.1	0.3(1)	3.7(16)
85,326.1	0.5(1)	6.8(10)	84,318.0	0.2(0)	42.8(82)
85,360.1	0.6(1)	3.7(5)	84,555.9	0.5(2)	3.5(14)
85,505.3	0.6(1)	3.3(7)	84,734.9	0.6(3)	2.2(13)
85,552.7	0.5(1)	3.7(9)	84,897.9	2.6[a]	0.8
85,743.2	0.5(2)	2.2(11)	85,120.4[b]	0.3(1)	2.9(13)

Table 4.7—Continued

Hot Core			Compact Ridge		
Rest Frequency (MHz)[a]	I_0 (Jy/bm)	Δv (km s^{-1})	Rest Frequency (MHz)[a]	I_0 (Jy/bm)	Δv (km s^{-1})
86,033.3[b]	0.4(1)	9.2(25)	85,186.0	0.5(1)	2.8(9)
86,172.0	0.8(2)	2.0(4)	85,327.0	2.9[a]	0.8
86,425.0	0.3(1)	4.8(15)	85,331.5	0.3(1)	10.0(22)
86,679.5	0.3(1)	3.2(14)	85,360.9	0.5(1)	3.3(7)
86,780.1	0.3(1)	5.3(19)	85,371.9	1.9[a]	0.8
86,834.3	0.6(1)	23.9(560)	85,442.7	4.9[a]	0.7
86,916.0	0.4(1)	13.5(49)	85,506.3	0.7(2)	2.2(6)
86,923.8	0.2(1)	15.8(111)	85,553.5	4.2[a]	0.8
87,093.0	2.4[a]	0.8	85,744.1	1.0(1)	1.8(3)
87,522.5	0.5(2)	3.5(14)	86,034.0[b]	1.1(2)	2.1(3)
87,524.6	0.8[a]	1.6	86,155.1	0.7(2)	2.3(8)
87,529.9	0.3(1)	19.1(67)	86,172.8	0.8(2)	2.2(4)
87,545.8	0.3(1)	17.2(47)	86,280.0	0.3(3)	2.9(31)
87,566.5	0.3(1)	9.8(34)	86,387.3	0.3(2)	6.3(57)
87,799.3	0.5(1)	6.8(19)	86,405.9	0.4(1)	2.6(8)
87,983.1	0.8(2)	7.3(17)	86,426.8	1.5[a]	0.8
88,054.0	0.8(2)	11.3(24)	86,668.5	0.1(0)	17.7(52)
88,224.3	0.3(1)	15.8(51)	86,680.4	0.4(1)	1.9(6)
88,251.0	0.2(1)	28.8(120)	86,681.7	1.6[a]	0.8
88,260.2	0.5(1)	5.8(21)	86,830.0	0.3(0)	75.1(166)
88,278.3	0.8(2)	3.1(9)	87,036.1	0.4(2)	2.5(15)
88,330.9	0.6(2)	3.2(11)	87,038.8	0.4(2)	1.7(11)
88,404.4	0.3(1)	11.8(36)	87,067.2	0.4(1)	9.2(32)
88,407.2	2.5[a]	0.8	87,408.9	0.6(3)	2.1(15)
88,686.1	0.9(4)	2.0(9)	87,413.5	3.5[a]	0.8
88,717.2	1.0[a]	0.9	87,478.3	6.7[a]	0.7
88,752.8	3.5[a]	12.7	87,998.4	0.7(2)	4.4(11)
88,770.1	1.3(4)	2.7(10)	88,389.3	0.5(2)	3.0(14)
88,805.0	0.3(2)	3.4(25)	88,405.8	0.4(1)	2.9(11)
88,861.6	1.4(2)	3.5(6)	88,420.4	0.4(1)	4.0(13)
88,963.1	0.7(2)	2.6(10)	88,770.9	4.1[a]	0.8
88,973.1	0.6(2)	4.3(16)	88,797.9	0.4(1)	2.9(14)
88,997.5	0.4(3)	3.0(21)	88,815.0	0.4(2)	4.3(20)
89,012.7	0.3(3)	2.7(33)	88,862.5	1.1(3)	2.0(5)
89,144.0	0.8(2)	3.4(11)	88,959.7	0.7(2)	3.8(10)
89,348.8	0.6(1)	8.4(23)	88,962.3	0.8(2)	2.4(8)
89,479.1	0.6(2)	5.2(17)	88,978.3	7.0[a]	0.7
89,516.5	1.2(5)	1.9(10)	88,998.4	0.8(2)	2.9(8)
89,638.2	0.8(2)	3.1(10)	89,095.2	0.6(2)	3.3(13)
89,742.2	0.6(2)	5.6(23)	89,114.9	0.6(2)	5.8(17)
89,745.0	0.6(2)	4.3(17)	89,140.7	0.5(2)	3.5(16)

Table 4.7—Continued

Hot Core			Compact Ridge		
Rest Frequency (MHz)[a]	I_0 (Jy/bm)	Δv (km s^{-1})	Rest Frequency (MHz)[a]	I_0 (Jy/bm)	Δv (km s^{-1})
89,747.7	0.3(1)	6.1(42)	89,360.2	0.3(2)	3.0(20)
89,765.8	0.3(2)	3.7(25)	89,363.0	0.3(2)	4.6(29)
89,768.4	0.4(2)	5.0(24)	89,381.4	0.3(1)	5.0(33)
89,771.5	0.4(2)	4.0(22)	89,391.0	0.2(1)	34.0(156)
89,778.5	0.3(2)	5.4(33)	89,398.2	0.4(2)	2.3(16)
89,828.8	1.0(1)	3.9(6)	89,496.7	0.7(2)	3.9(13)
90,635.6	0.3(1)	17.4(168)	89,537.4	1.0(8)	1.7(17)
90,768.2	0.4(1)	5.2(16)	89,664.5	0.4(1)	5.0(12)
90,792.4	0.7(2)	2.0(6)	89,731.9	2.2(10)	1.5(7)
90,793.8	1.4(3)	2.2(5)	89,829.8	1.2(2)	2.4(4)
91,183.7	0.5(2)	4.0(16)	89,965.8	0.3(2)	2.8(18)
91,355.9	0.6(2)	2.5(11)	90,125.0	0.8(2)	3.4(11)
91,502.4	0.9(3)	3.1(10)	90,255.6	4.9[a]	0.7
91,759.6	0.5(2)	7.4(26)	90,795.9	-0.7[a]	4.8
92,124.4	0.3(1)	10.5(25)	90,813.3	0.9(3)	2.6(10)
92,138.4	0.4(1)	3.4(11)	90,855.5	1.0(3)	3.5(11)
92,141.2[b]	0.5(2)	1.7(8)	90,862.6	1.1(3)	2.5(8)
92,161.7	0.5(1)	3.6(10)	91,093.3	0.8(2)	3.2(8)
92,192.1	0.4(1)	5.5(15)	91,355.0	0.6(0)	0.1(1)
92,315.5	0.3(1)	7.4(26)	91,528.7	0.9(2)	4.0(12)
92,318.6	0.4(1)	5.8(18)	91,748.5	0.6(3)	2.5(14)
92,329.0	0.4(1)	5.2(15)	92,137.2	0.4(1)	8.6(24)
92,468.9	0.7(1)	4.2(9)	92,141.7[b]	0.5(1)	3.0(10)
92,514.1	0.2(1)	5.7(35)	92,297.7	0.5(2)	2.2(9)
92,523.5	0.3(2)	2.9(20)	92,329.9	0.5(2)	2.2(10)
92,525.6	0.3(1)	6.0(34)	92,352.2	0.3(2)	2.1(24)
92,541.9[b]	0.2(1)	5.7(32)	92,354.7	0.4(1)	13.4(34)
92,691.8	0.8(3)	4.8(17)	92,359.5	0.4(1)	3.2(13)
92,695.6	0.3(3)	2.6(30)	92,456.7	4.3[a]	0.8
92,705.0	0.4(2)	5.1(35)	92,494.2	21.0[a]	0.7
92,709.5	0.2[a]	3.9	92,512.5	0.3(2)	2.3(15)
92,722.4	0.3(3)	4.6(40)	92,526.8	0.3(2)	2.5(18)
92,725.1[b]	2.0[a]	0.8	92,539.4	0.3(1)	4.2(27)
92,826.4	1.2(3)	3.3(8)	92,542.1[b]	0.3(2)	2.8(21)
92,883.3	1.8(3)	2.6(4)	92,560.4	0.7(5)	1.7(13)
92,913.4	0.2(2)	11.1(84)	92,700.5	0.3(3)	2.9(32)
93,059.7	1.0(2)	4.2(11)	92,705.9	0.4(2)	6.1(37)
93,066.1	0.7(2)	4.2(16)	92,710.4	0.4(2)	7.0(33)
93,089.5	13.6[a]	0.5	92,714.7	0.4(2)	4.5(30)
93,098.2	0.3(2)	8.4(59)	92,717.9	0.3(2)	3.8(30)
93,185.6	0.8(3)	2.2(9)	92,724.4[b]	0.4(2)	7.6(37)

Table 4.7—Continued

Hot Core			Compact Ridge		
Rest Frequency (MHz)[a]	I_0 (Jy/bm)	Δv (km s^{-1})	Rest Frequency (MHz)[a]	I_0 (Jy/bm)	Δv (km s^{-1})
93,264.5	0.4(1)	37.7(59)	92,727.8	0.3(2)	4.3(33)
93,505.7	3.5[a]	12.7	92,735.8	0.4(2)	7.2(37)
93,637.7	0.6(2)	6.6(25)	92,890.7	0.4(3)	2.0(17)
93,702.1	0.7(3)	3.5(14)	92,998.2	0.8(4)	2.1(12)
93,757.0[b]	0.8(3)	3.2(15)	93,090.5	0.3(2)	3.4(35)
93,867.6	0.4(1)	16.5(47)	93,092.1	0.4(2)	3.2(26)
93,953.5	0.4(1)	17.9(56)	93,094.3	2.5[a]	0.7
93,975.9	0.4(1)	10.7(29)	93,096.0	0.4(2)	3.5(28)
94,312.6	0.4(1)	4.0(13)	93,107.3	0.3(2)	5.9(43)
94,725.6	0.4(1)	3.1(11)	93,114.1	0.3(1)	11.4(50)
94,803.1	0.4(1)	2.6(10)	93,146.6	0.8(3)	3.0(11)
94,863.8	0.4(1)	2.7(9)	93,225.5	0.6(2)	4.2(14)
94,939.5	3.5[a]	12.7	93,431.8	0.5(2)	2.4(10)
94,991.2	0.7(1)	4.2(7)	93,501.2	0.3(1)	3.1(19)
95,241.2	2.1(3)	1.9(3)	93,632.9	6.8[a]	0.7
95,247.0	0.7(2)	3.4(10)	93,711.8	0.7(3)	3.5(16)
95,267.0	0.6(1)	4.9(15)	93,756.4[b]	0.8(2)	5.9(18)
95,340.0[b]	0.5(1)	9.5(21)	93,809.9	0.7(2)	2.6(9)
95,347.3	0.7(2)	2.6(9)	93,932.2	0.6(2)	2.0(7)
95,454.3	0.4(1)	15.4(64)	93,977.2	0.6(2)	2.5(10)
95,460.2	0.5(1)	5.1(22)	93,979.6	0.3(1)	6.7(31)
95,480.2	0.4(1)	14.7(33)	94,124.6	3.2[a]	0.7
95,488.2	0.5(1)	14.9(27)	94,208.5	0.5(1)	3.2(10)
95,546.9	0.3(1)	10.5(31)	94,866.5	2.0[a]	0.8
95,689.8[b]	3.5[a]	12.7	95,129.7	5.9[a]	0.7
95,701.1	0.3(1)	4.6(18)	95,242.1	1.6(2)	2.0(3)
95,709.0	0.4(1)	2.7(11)	95,340.6[b]	0.6(2)	3.5(12)
95,893.4	0.3(1)	10.1(31)	95,505.5	0.3(1)	15.0(90)
95,908.6	0.5(2)	1.8(8)	95,529.7	0.6(2)	2.3(9)
95,923.1	0.5(1)	20.9(32)	95,655.4	0.4(2)	2.8(12)
95,948.4	0.5(1)	3.1(9)	95,689.6[b]	1.1(1)	3.8(5)
96,233.7	0.4(1)	1.8(11)	95,747.0	0.4(1)	4.7(14)
96,252.7	0.3(1)	5.6(20)	95,921.0	0.4(1)	4.5(13)
96,290.1	0.4(2)	4.0(23)	96,065.4	0.4(1)	4.4(12)
96,311.0	0.5(2)	2.9(11)	96,103.6	0.7(0)	0.0(0)
96,313.1	0.4(2)	2.8(12)	96,165.7	45.8(0)	0.5(0)
96,382.3	0.9(4)	2.1(10)	96,389.6[b]	0.7(2)	2.6(7)
96,390.3[b]	1.1(2)	2.4(4)	96,391.4	0.7(1)	5.0(11)
96,453.5	0.8(2)	5.5(16)	96,524.3	0.7(1)	3.6(8)
96,540.5	0.8(2)	2.8(9)	96,533.8	0.8(1)	3.7(8)
96,612.1	0.8(3)	4.5(19)	96,541.4	0.8(1)	2.5(5)

Table 4.7—Continued

Hot Core			Compact Ridge		
Rest Frequency (MHz)[a]	I_0 (Jy/bm)	Δv (km s^{-1})	Rest Frequency (MHz)[a]	I_0 (Jy/bm)	Δv (km s^{-1})
96,982.2	1.7(3)	5.2(10)	96,568.4	0.8(2)	2.7(6)
96,983.9	0.9(2)	27.5(47)	96,579.3	0.8(2)	3.1(7)
96,992.0	1.6(2)	5.3(9)	96,679.7	1.2(4)	2.4(9)
97,291.1	0.5(1)	5.0(18)	96,692.0	1.3(4)	2.4(8)
97,293.0	0.6(2)	2.3(11)	96,819.8	1.6(6)	1.7(7)
97,337.9	0.9(7)	1.5(12)	96,955.8	0.8(1)	16.2(36)
97,349.6	0.7(2)	2.9(8)	96,958.2	0.7(5)	1.8(17)
97,356.9	2.1[a]	0.9	97,350.6	1.4(3)	1.5(3)
97,596.3	0.9(2)	2.7(7)	97,395.2	0.5(1)	4.5(14)
97,660.7[b]	0.5(1)	4.3(13)	97,399.3	0.5(2)	2.9(11)
97,868.4	3.9[a]	0.8	97,458.2	1.1(2)	1.7(4)
97,884.8	2.0(4)	2.0(4)	97,460.5	1.1(2)	1.9(4)
97,896.3	1.8(3)	2.5(5)	97,597.3	0.8(2)	3.8(10)
98,163.0	0.5(1)	1.9(8)	97,661.5[b]	1.3(2)	2.7(4)
98,194.1	0.4(1)	8.3(21)	97,739.0	0.6(2)	2.8(9)
98,258.2	0.4(1)	8.4(23)	97,753.0	0.8(2)	3.3(7)
98,377.3	0.6(3)	1.7(10)	98,157.3	0.5(1)	3.0(10)
98,386.0	3.5[a]	12.7	98,435.9	2.6(16)	1.5(6)
98,434.9	1.4(2)	3.0(6)	98,600.7	0.5(1)	9.4(24)
98,557.0	1.3(2)	6.3(12)	98,739.1	0.5(1)	33.1(44)
98,625.4	3.5[a]	12.7	98,815.1[b]	0.7(3)	7.7(18)
98,672.6	0.9(2)	9.2(21)	98,937.0	4.5[a]	0.7
98,727.1	0.6(1)	7.2(10)	99,089.7	1.1(2)	2.0(4)
98,741.1	1.1(2)	2.6(5)	99,111.4	0.7(2)	1.5(5)
98,750.2	0.8(1)	3.9(8)	99,489.1	1.4(1)	2.6(3)
98,814.7[b]	3.5[a]	12.7	99,575.7	1.3(5)	1.7(11)
99,051.7	0.8(2)	1.7(8)	99,577.6	1.8(6)	1.6(6)
99,053.8	0.5(1)	6.9(24)	99,690.5	0.6(1)	4.2(12)
99,229.2	0.6(2)	2.3(11)	99,869.1	1.8(2)	2.2(3)
99,487.9	0.6(1)	8.4(13)	99,880.7	0.3(1)	10.6(34)
99,566.9	0.9(1)	13.8(11)	99,963.6	0.7(3)	1.5(7)
99,574.6	0.8(2)	1.9(6)	100,094.5	2.9(3)	2.6(3)
99,576.5	0.7(1)	5.5(10)	100,137.1	1.8(2)	4.1(6)
99,614.6	0.4(1)	2.6(10)	100,162.9	1.1(6)	1.7(12)
99,750.2	0.4(1)	20.7(36)	100,226.6	1.2(3)	3.4(11)
99,757.3	0.3(1)	5.6(19)	100,253.1	22.2[a]	0.5
99,772.1	1.0(1)	5.3(6)	100,468.6	6.2[a]	0.7
99,868.3	1.0(1)	2.6(4)	100,839.7	2.9[a]	0.7
99,879.9	1.0(1)	5.7(9)	100,935.1	0.6(2)	2.2(8)
99,902.0	0.3(1)	16.7(36)	100,944.9	0.7[a]	1.4
100,093.6	2.0(4)	2.6(6)	101,568.6	0.9(4)	4.7(20)

Table 4.7—Continued

Hot Core			Compact Ridge		
Rest Frequency (MHz)[a]	I_0 (Jy/bm)	Δv (km s^{-1})	Rest Frequency (MHz)[a]	I_0 (Jy/bm)	Δv (km s^{-1})
100,128.7	0.7(3)	4.1(20)	101,981.4[b]	14.8[a]	0.7
100,136.1	2.7(3)	3.0(4)	102,199.9	1.9(4)	2.9(8)
100,225.8	2.4(3)	1.9(3)	102,203.6	14.6[a]	0.6
100,314.3	0.7(1)	33.2(204)	102,503.3	1.3(3)	3.3(8)
100,342.4	1.0(2)	8.0(17)	103,368.4	0.8(2)	4.2(11)
100,587.1	1.0(3)	2.2(7)	103,729.4	4.7[a]	0.6
100,777.1	2.9[a]	0.9	104,201.3	0.9(2)	4.6(10)
100,866.7	0.5(2)	2.2(11)	104,388.5	0.7(1)	28.0(32)
101,483.2	6.7[a]	0.7	104,404.6	7.8[a]	0.6
101,527.1	7.7[a]	0.7	105,037.3	0.7(3)	6.1(24)
101,532.9	1.1(3)	2.2(7)	105,108.0	0.7(2)	4.0(15)
101,981.2[b]	0.8(2)	12.1(27)	105,118.9	1.1(3)	1.8(6)
102,036.1	1.1(4)	2.4(12)	105,136.8	0.7(3)	2.9(12)
102,063.4	1.2(3)	5.0(13)	105,187.9	2.7(3)	3.6(5)
102,502.2	0.7(3)	3.1(14)	105,400.4	0.8(3)	5.6(21)
102,911.3	0.5(1)	2.0(7)	105,563.6	12.2[a]	0.6
103,061.4	0.4(2)	5.5(34)	106,496.8	0.3(1)	2.9(14)
103,125.9	0.6(2)	2.5(8)	106,541.8	0.5(2)	2.2(7)
103,161.7	0.6(2)	3.3(10)	106,804.1	0.8(4)	1.7(10)
103,224.4	0.5(2)	3.3(14)	107,022.2	1.0(2)	5.1(10)
103,248.7	3.5[a]	12.7	107,521.4	0.4(1)	17.5(38)
103,324.4	0.9(2)	3.2(8)	107,754.9	0.9(3)	3.4(11)
103,677.6	0.4(2)	3.7(16)	107,906.9	1.4(10)	1.3(11)
103,680.9	0.4(2)	2.6(13)	108,342.3	0.7(2)	2.0(8)
103,796.0	0.4(2)	3.1(15)	108,454.0	46.5(0)	0.4(0)
103,832.6	0.5(1)	4.3(20)	108,518.6	0.9(6)	1.5(13)
104,386.7	1.4(1)	11.4(16)	108,704.7	6.8[a]	0.6
104,421.8	0.2(1)	13.9(161)	108,921.3	0.5(2)	4.3(15)
104,619.1	0.5(1)	6.4(23)	109,010.6	0.6(1)	7.1(20)
104,652.1	0.5(1)	6.0(18)	109,049.0	3.0[a]	0.7
104,817.3	0.6(2)	2.4(9)	109,390.6	69.4(0)	0.4(0)
104,853.0	0.7(2)	4.1(12)	109,531.5	2.0(4)	1.6(3)
105,091.7	1.2(10)	1.5(16)	109,608.8	1.5(3)	1.9(4)
105,186.9	2.2(4)	1.7(3)	109,653.8	0.8(3)	2.6(13)
105,443.2	1.2(3)	2.4(6)	109,663.0	1.0(4)	1.9(7)
105,557.8	1.2(1)	15.1(15)	109,764.0	1.6(3)	1.7(4)
105,570.9	1.0(1)	11.3(21)	109,771.0	0.9(3)	3.0(11)
105,955.2	0.9(2)	11.3(29)	109,778.7	1.3(3)	7.4(37)
106,183.3	1.0(4)	2.0(10)	109,912.3	1.7[a]	1.2
106,272.3	0.7(2)	2.1(7)	109,988.0	1.1(3)	2.3(8)
106,541.0	1.0(1)	5.0(7)	110,035.4	1.4(3)	1.7(4)

Table 4.7—Continued

Hot Core			Compact Ridge		
Rest Frequency (MHz)[a]	I_0 (Jy/bm)	Δv (km s^{-1})	Rest Frequency (MHz)[a]	I_0 (Jy/bm)	Δv (km s^{-1})
106,629.2	0.9(2)	3.0(8)	110,238.7	1.7(3)	2.3(5)
106,637.7	0.7(1)	9.0(28)	110,250.6[b]	0.7(2)	5.7(19)
106,654.6	0.6(1)	12.7(22)	110,262.6	0.7(2)	4.2(15)
106,869.0	1.4[a]	1.3	110,571.7	1.5(3)	2.1(5)
106,961.8	0.7(1)	9.5(23)	110,655.4	1.8(4)	2.4(6)
106,966.2	0.6(2)	5.8(21)	110,675.9	1.1(4)	2.1(9)
107,057.9	1.1(2)	26.8(38)	110,776.5	1.9(4)	2.3(5)
107,062.4	0.9(4)	2.3(13)	111,005.8	2.1(2)	1.7(2)
107,117.6	0.9(2)	5.7(18)	111,094.2[b]	1.6(2)	2.4(4)
107,252.7	0.8(1)	12.7(16)	111,328.4	0.9(3)	2.0(7)
107,334.3	0.8(3)	1.7(9)	111,352.4	6.4[a]	0.6
107,421.6	0.9(1)	7.1(13)	111,626.6	1.5(3)	10.8(14)
107,520.5	2.5(1)	9.2(6)	111,701.9	0.6(2)	2.6(14)
107,524.7	0.5(2)	5.1(20)	111,703.1	0.8(3)	2.1(10)
107,570.8	0.8(2)	5.0(13)	112,012.0	9.0[a]	0.6
107,587.4	1.1(2)	3.3(8)	112,307.1	1.7(2)	2.4(3)
107,629.4	0.9(1)	13.2(24)	112,347.7	6.3[a]	0.6
107,644.4	1.8(2)	5.4(8)	112,356.2	0.7(2)	3.3(13)
107,647.7	1.7(2)	4.3(7)	112,668.1	0.6(3)	2.8(16)
107,721.3	0.7(2)	8.7(22)	113,587.5	1.3(3)	3.5(11)
107,818.1	0.6(1)	9.2(20)	113,847.3	0.9(1)	15.4(28)
107,922.0	1.0(1)	12.6(16)	115,070.5	0.9(3)	3.1(12)
107,954.9	0.8(2)	5.6(12)	115,152.7[b]	1.8(4)	1.7(4)
108,013.9	0.5(2)	4.1(15)	115,315.2	0.7[a]	10.4
108,920.4	1.9(2)	7.3(9)	115,595.8	4.3[a]	0.7
109,005.4	0.7(2)	3.2(12)	115,648.0	11.0[a]	0.6
109,009.6	0.7(2)	4.2(14)	115,674.2	1.4(5)	3.2(13)
109,013.0	0.7(2)	5.8(16)			
109,038.8	0.3(1)	11.6(46)			
109,044.4	0.6(2)	4.3(16)			
109,054.2	0.6(2)	5.8(18)			
109,126.4	0.7(2)	2.7(10)			
109,163.5	1.3(2)	4.3(8)			
109,197.0	122.2(0)	0.4(0)			
109,291.4	1.4(4)	2.6(8)			
109,482.0	1.7[a]	0.7			
109,500.9	0.5(3)	5.0(59)			
109,607.5	2.5[a]	0.8			
109,617.8	0.7(1)	6.1(12)			
109,664.2	0.8(2)	3.1(8)			
109,683.5	0.6(1)	7.6(28)			

Table 4.7—Continued

Hot Core			Compact Ridge		
Rest Frequency (MHz)[a]	I_0 (Jy/bm)	Δv (km s^{-1})	Rest Frequency (MHz)[a]	I_0 (Jy/bm)	Δv (km s^{-1})
109,776.9	0.7(1)	9.0(20)			
109,900.9	1.0(2)	11.2(52)			
109,902.6	6.7[a]	0.5			
109,905.1	4.9(10)	4.8(7)			
109,911.1	1.4(2)	6.8(14)			
109,942.0	0.6(1)	17.3(34)			
109,958.7	3.5[a]	12.7			
110,034.4	1.0(2)	4.0(10)			
110,104.6	0.7(2)	5.2(16)			
110,112.1	0.6(2)	5.4(18)			
110,117.6	3.8[a]	0.7			
110,237.8	1.2(5)	1.6(8)			
110,250.2[b]	0.8(1)	6.4(14)			
110,261.6	1.1(4)	1.7(8)			
110,451.2	0.8(2)	3.8(10)			
110,457.1	1.4(3)	1.8(4)			
110,474.9	1.1(3)	2.0(5)			
110,570.7	1.5(2)	3.8(6)			
110,654.4	1.0(3)	4.0(12)			
110,974.3	0.9(3)	3.2(11)			
111,004.5	1.4(3)	1.8(5)			
111,006.9	0.5(1)	9.8(32)			
111,093.2	3.6[a]	0.6			
111,093.5[b]	0.6(2)	8.1(20)			
111,187.6	0.8(3)	2.0(7)			
111,592.6	0.5(1)	4.0(12)			
111,625.7	4.8(5)	3.3(3)			
111,633.8	0.7(1)	6.7(16)			
111,659.6	0.4(1)	8.3(27)			
111,825.7	0.8(2)	3.2(9)			
111,845.4	1.2(2)	2.3(5)			
111,848.9	0.4(1)	8.7(32)			
111,882.1	0.4(1)	9.5(32)			
112,010.9	0.6[a]	3.4			
112,065.6	2.5[a]	0.7			
112,128.6	0.7(2)	4.3(13)			
112,137.6	0.6(2)	2.4(10)			
112,167.1	0.7(1)	6.9(17)			
112,255.5	0.7(1)	8.4(16)			
112,291.7	0.5(1)	4.3(11)			
112,305.9	1.2(2)	2.1(6)			

Table 4.7—Continued

Hot Core			Compact Ridge		
Rest Frequency (MHz)[a]	I_0 (Jy/bm)	Δv (km s^{-1})	Rest Frequency (MHz)[a]	I_0 (Jy/bm)	Δv (km s^{-1})
112,405.9	0.8(2)	5.5(13)			
112,435.0	5.8[a]	0.6			
112,490.4	0.8(2)	3.0(10)			
112,535.8	0.4(1)	12.3(77)			
112,672.3	0.6(2)	7.4(24)			
112,689.4	6.2[a]	0.6			
113,000.2	1.8(2)	5.3(8)			
113,278.0	0.9(3)	3.3(11)			
113,343.2	1.0(3)	4.3(14)			
113,351.3	0.9(2)	7.4(19)			
113,383.6	1.3(4)	2.4(7)			
113,407.2	1.2(4)	2.5(9)			
113,791.7	1.2(5)	2.1(9)			
113,913.2	3.5[a]	12.7			
114,048.0	1.6(3)	4.1(9)			
114,091.3	0.9(3)	4.1(14)			
114,209.4	1.2(3)	4.1(13)			
114,320.3	1.8(3)	5.9(11)			
114,556.9	1.1(3)	4.3(15)			
114,628.9	1.0(2)	4.8(13)			
114,750.2	0.9(3)	3.6(12)			
115,153.2[b]	1.6(4)	3.1(11)			
115,156.5	0.5(4)	3.9(44)			
115,162.8	0.9(3)	5.3(23)			
115,165.0	0.9(4)	2.6(15)			
115,313.0	1.6(5)	6.1(28)			
115,484.9	1.3(4)	2.3(9)			
115,572.2	1.3(1)	22.4(30)			

[a]Poor Gaussian fit to profile.

[b]This unidentified line is seen toward both the Hot Core and Compact Ridge.

Chapter 5

Calculating Cometary Production Rates

5.1 Introduction

Comets have long been believed to contain pristine material from the presolar nebula and may yield insight into the formation mechanisms of both simple and complex molecular species. There are two distinct regions where comets are located in the solar system: the Oort cloud and the Kuiper-Edgeworth belt. The Oort cloud is the source of long period (P>200 years) and Halley type (20<P<200 years) comets, and has a spherically symmetric distribution surrounding the solar system out to distances of ∼100,000 AU. The Kuiper-Edgeworth belt is the source of short period (P<20 years) comets, and lies in the ecliptic plane from just beyond the orbit of Pluto out to several hundred AU (Weissman, 1999; Mumma et al., 2005). Recent cometary formation models suggest that Oort cloud comets may have formed in the region between Jupiter and Neptune and been ejected into their current orbits while Kuiper-Edgeworth belt comets formed farther from the Sun, beyond the orbit of Neptune (Weissman, 1999). Thus observations comparing long period and short period comets, since they are believed to have different origins, can give insight into what types of chemistry were happening in different parts of the solar nebula.

Additionally, observations of comets will give insight into whether the molecular diversity (and its formation mechanisms) seen in high and low mass hot molecular cores is transferred to the chemistry of the presolar nebula. The molecular diversity seen in comets may provide the link between the formation mechanisms of complex molecular species seen in high mass cores and low mass young stellar objects to the formation of young solar systems.

A majority of observations of the molecular composition of cometary gas and dust have been done at visible, ultraviolet (Hutsemékers et al., 2005, and references therein), and infrared wavelengths (e.g., Dello Russo et al., 2001; Helbert et al., 2005). A large number of interstellar ices and volatiles were discovered by satellites passing through the coma of Comet Halley (e.g., Mitchell et al., 1992), and there have also been several successful detections of rotational transitions of molecular species at millimeter wavelengths (e.g., Biver et al., 2002; Crovisier et al., 2004a,b). Many of these species (e.g., HCN and CH_3OH) are thought to be parent molecules (originating from the comet nucleus) while others are thought to be the daughter molecules (e.g., CN) of these species, formed as products of photodissociation or gas phase chemistry in the coma.

In the Spring of 2004, the BIMA Array was awarded a rare opportunity to observe two comets passing into the inner solar system and within ~0.3 AU of the Earth. Comet LINEAR (C/2002 T7) reached perigee on 2004 May 19, coming within 0.27 AU, while Comet NEAT (C/2001 Q4) reached perigee on 2004 May 7, coming within 0.32 AU. Both comets were identified as being dynamically new Oort cloud comets[1]; such comets reach a peak of strong activity as they approach perihelion. It was extremely important to observe both comets when they were close to both perihelion and perigee in order to observe them near their peak emission and their maximum signal due to their proximity.

This chapter presents interferometric detections of HCN and CH_3OH (methanol) in both comets and CS in Comet LINEAR and calculates their total beam averaged column densities and production rates. Also presented are upper limits for the molecular species searched for but not detected in the observations.

5.2 Observations

The observations were conducted with the BIMA Array in D-configuration (baselines from ~6m to ~35m), cross-correlation mode, to observe Comets LINEAR (C/2002 T7) and NEAT (C/2001 Q4) during their 2004 apparitions.

The observations of Comet LINEAR, using JPL reference orbit 69, were taken 2004 May 11-15 and were near $\alpha(J2000) = 01^h40^m$, $\delta(J2000) = -09°30'$[2]. The comet was at a heliocentric distance of 0.73-0.77 AU and a geocentric distance of 0.32-0.44 AU ($1''$=319 km at 0.44 AU). W3(OH) was used as the flux density calibrator, for this observation. The quasar 0108+015 was used to calibrate the antenna based gains.

The observations of Comet NEAT, using JPL reference orbit 123, were taken 2004 May 20-24 and were near $\alpha(J2000) = 09^h07^m$, $\delta(J2000) = 34°30'$[2]. The comet was at a heliocentric distance of 0.97 AU and a geocentric distance of 0.55-0.61 AU ($1''$=442 km at 0.61 AU). Mars was used as the flux density calibrator and 0927+390 was used to calibrate the antenna based gains.

The absolute amplitude calibration is accurate to within ~20%. It is noted that the observations may cover a significant amount of the rotation period of Comets LINEAR and NEAT. However, to date no rotation period has been given for either comet; thus any effects rotation may have on the results are unknown at this time. The data were combined and imaged using the MIRIAD software package. Table 5.1 lists the molecular line parameters of the species that were searched for. The first column lists the molecular species, the second lists the transition, the third lists

[1]The identification as Oort cloud comets is from http://stardate.org/nightsky/comets2004.html

[2]Both comets moved substantially across the sky during the observations, thus only approximate coordinates are given.

Table 5.1. Molecular Line Parameters

Species	Quantum Numbers	Frequency (MHz)	E_u (K)	$S\mu^2$ (D^2)	α(1 AU)[a] (s^{-1})
HCN	$1-0$	88,631.847(1)[b]	4.3	4.9[c]	1.3×10^{-5}
CH_3OH	$3_{1,3} - 4_{0,4}A+$	107,013.770(13)	28.3	3.1	1.3×10^{-5}
CS	$2-1$	97,980.985(15)	7.7	7.1	6.7×10^{-6}
^{13}CO	$1-0$	110,201.353(1)	5.3	0.01	1.2×10^{-6}[d]
CH_3CN	$6_K - 5_K$	110,383.502(2)[e]	18.5	91.9	2.9×10^{-6}
C_2H_5CN	$10_{1,10} - 9_{1,9}$	86,819.846(0)	24.1	146.7	$\sim 10^{-5}$
SiO	$2-1$	86,846.960(50)	6.3	19.2	6.7×10^{-6}
$HN^{13}C$	$1-0$	87,090.850(50)[b]	4.2	7.3	1.5×10^{-5}
C_2H_5OH	$4_{1,4} - 3_{0,3}$	90,117.576(2)	9.4	5.4	1.8×10^{-5}
$HCOOCH_3$	$8_{0,8} - 7_{0,7}E$	90,227.595(13)	20.1	21.0	4.7×10^{-5}
	$8_{0,8} - 7_{0,7}A$	90,229.647(14)	20.1	21.0	4.7×10^{-5}
HNC	$1-0$	90,663.572(4)	4.4	9.3	1.5×10^{-5}

[a]Taken or estimated from Crovisier (1994).

[b]Only the frequency of the strongest hyperfine component is given.

[c]The value is based only on the strongest hyperfine component.

[d]Assumed to be the same as for CO.

[e]Only the frequency of the $K = 0$ transition is given.

the transition frequency, the fourth lists the upper energy of the transition, the fifth lists $S\mu^2$, and the last column lists the quiet sun photodissociation rate for each species. Table 5.2 lists the observational parameters. For each comet the heliocentric distance (r_H) in AU, geocentric distance (Δ) in AU, and the synthesized beam size in arcsec are listed for each species. The channel spacing of all observations was 391 kHz, except for CS which had a spacing of 98 kHz.

5.3 Results

5.3.1 HCN

Figure 5.1(a-c) shows the map and spectra of HCN around Comet LINEAR (C/2002 T7). Figure 5.1a shows the map of the $J = 1-0, F = 2-1$ transition of HCN in 1 σ contours, starting at 2 σ. The synthesized beam of $25\farcs4 \times 20\farcs3$ is shown at the bottom left of the map. The line segment in the image shows the projection of the direction toward the sun. The origin of the line segment is anchored at the predicted position of the comet nucleus. The coordinates are given in offset arcseconds centered on the comet nucleus. It is noted that the peak intensity of the HCN

Table 5.2. Observational Parameters

Species	LINEAR			NEAT		
	r_H (AU)	Δ (AU)	$\theta_a \times \theta_b$ ($'' \times ''$)	r_H (AU)	Δ (AU)	$\theta_a \times \theta_b$ ($'' \times ''$)
HCN	0.73	0.44	25.4×20.3	0.97	0.61	21.3×17.5
CH_3OH	0.75	0.38	22.3×16.9	0.97	0.55	16.7×14.3
CS	0.74	0.41	23.7×18.9	0.97	0.55	18.8×15.4
^{13}CO	0.75	0.38	21.8×16.1	0.97	0.55	16.0×14.1
CH_3CN	0.75	0.38	21.6×16.4	0.97	0.55	16.2×14.0
C_2H_5CN	0.77	0.32	28.5×21.3			
SiO	0.77	0.32	28.5×21.3			
$HN^{13}C$	0.77	0.32	28.7×20.0			
C_2H_5OH	0.77	0.32	28.2×19.6			
$HCOOCH_3$	0.77	0.32	27.7×19.3			
HNC	0.77	0.32	27.7×20.4			

emission is offset from the predicted position of the nucleus by $\sim 5''$ along the semi-major axis of the synthesized beam. In general, the positional uncertainty roughly scales as the beamsize/SNR. For Comet LINEAR this uncertainty is 4-5$''$, so the offset is not significant[3]. Figure 5.1b shows the cross-correlation spectrum of this transition. The dashed line corresponds to the rest frequency of the $J = 1-0, F = 2-1$ line for a cometocentric rest velocity of 0 km s^{-1}. The 1 σ rms noise level is seen at the left of the panel. The $F = 2-1$ line for Comet LINEAR was fit with a Gaussian by a least-squares method which gives a peak intensity of 0.59(0.14) Jy beam^{-1}, a FWHM of 2.3(0.56) km s^{-1}, and a cometocentric velocity of -0.29$\pm$0.28 km s^{-1}. Figure 5.1c shows the cross-correlation spectrum (Hanning smoothed over three channels) of this transition.

Figure 5.1(d-f) shows the map and spectra of HCN around Comet NEAT (C/2001 Q4). Figure 5.1d shows the map of the $J = 1-0, F = 2-1$ transition of HCN in 1 σ contours, starting at 2 σ. The synthesized beam of $21''\!.3 \times 17''\!.5$ is shown at the bottom left of the map. As with Comet LINEAR, the HCN peak intensity is offset by $\sim 5''$ along the semi-major axis of the synthesized beam, and there is also some elongation of the source along this axis. Neither the offset nor the elongation is considered to be significant because these are most likely due to the beam size and the low SNR. Figure 5.1e shows the cross-correlation spectrum of this transition. The dashed line is similar to Figure 5.1b for a cometocentric rest velocity of 0 km s^{-1}. The $F = 2-1$ line appears in only a single channel so a FWHM of $\sim$1.3 km s^{-1} is assumed for HCN. Figure 5.1f shows the cross-correlation spectrum (Hanning smoothed over three channels) of this transition.

[3]This does not include any uncertainties in the ephemeris.

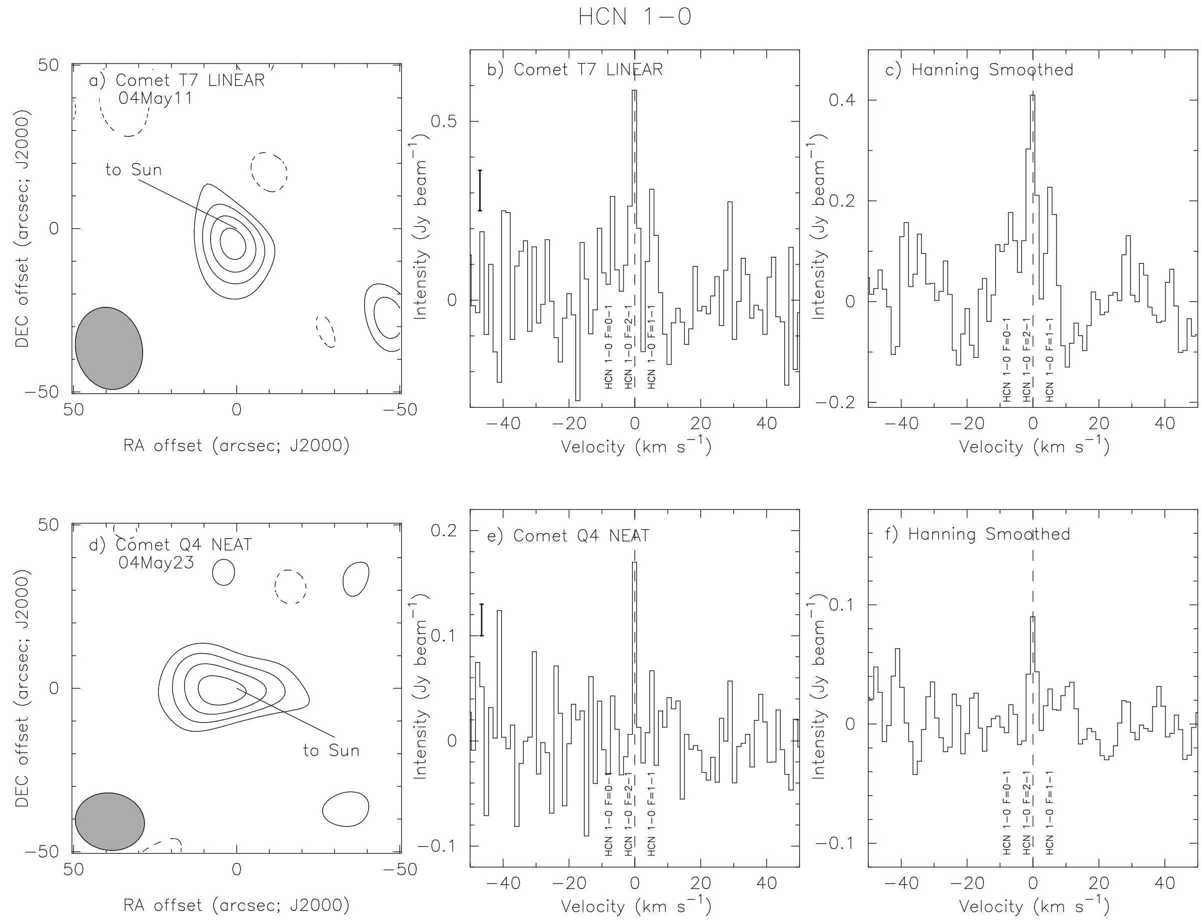

Figure 5.1 Comet LINEAR (C/2002 T7) and NEAT (C/2001 Q4) single field HCN images and spectra. (a) Comet T7 emission contours from the $J = 1 - 0, F = 2 - 1$ transition of HCN at 88.6318 GHz. Contours indicate the HCN emission near its peak centered at a cometocentric velocity of 0 km/s. The contour levels have 1 σ spacing, starting at 2 σ, with a peak of 0.63 Jy/beam. Image coordinates are arcseconds offsets relative to the predicted position of the nucleus. The synthesized beam is in the lower left, and the line segment shows the solar direction. (b) HCN cross-correlation spectra. Abscissa is radial velocity relative to the comet nucleus. Ordinate is flux density per beam, I_ν, in Jy/beam; $\sigma \sim 0.113$ Jy/beam (indicated by the vertical bar at the left). The dashed line is centered on the rest frequency.(c) HCN cross-correlation spectra (Hanning smoothed over 3 channels); labels are the same as in (b). (d) Comet Q4 emission contours of HCN. Contours indicate the HCN emission near its peak centered at a cometocentric velocity of 0 km/s. The contour levels have 1 σ spacing with a peak of 0.17 Jy/beam. Image coordinates are the same as in (a). The synthesized beam is in the lower left, and the line segment shows the solar direction. (e) HCN cross-correlation spectra. Abscissa and ordinate are the same as in (b); $\sigma \sim 0.03$ Jy/beam (indicated by the vertical bar at the left). The dashed line is centered on the rest frequency. (f) HCN cross-correlation spectra (Hanning smoothed over 3 channels). Abscissa and ordinate are the same as in (b).

5.3.2 CH_3OH

Figure 5.2(a-c) shows the map and spectra of CH_3OH around Comet LINEAR. Figure 5.2a shows the map of the $3_{1,3} - 4_{0,4}A+$ transition of CH_3OH in 1 σ contours, starting at 3 σ. The synthesized beam of $22\farcs1 \times 17\farcs2$ is shown at the bottom left of the map. The line segment in the image shows the projection of the direction toward the sun. The origin of the line segment is anchored at the predicted position of the comet nucleus. The coordinates are given in offset arcseconds centered on the comet nucleus. Figure 5.2b shows the cross-correlation spectrum of this transition. The dashed line corresponds to the rest frequency of the $3_{1,3} - 4_{0,4}A+$ line for a cometocentric rest velocity of 0 km s^{-1}. The 1 σ rms noise level is seen at the left of the panel. The line for Comet LINEAR was fit with a Gaussian by a least-squares method which gives a peak intensity of 0.44(0.06) Jy beam^{-1} and a FWHM of 1.74(0.31) km s^{-1}. Figure 5.2c shows the cross-correlation spectrum (Hanning smoothed over three channels) of this transition.

Figure 5.2(d-f) shows the map and spectra of CH_3OH around Comet NEAT. Figure 5.2d shows the map of the $3_{1,3} - 4_{0,4}A+$ transition of CH_3OH in 1 σ contours, starting at 3 σ. The synthesized beam of $16''.9 \times 14''.3$ is shown at the bottom left of the map. Figure 5.2e shows the cross-correlation spectrum of this transition. The dashed line is similar to Figure 5.2b for a cometocentric rest velocity of 0 km s^{-1}. The line for Comet NEAT was fit with a Gaussian by a least-squares method which gives a peak intensity of 0.31(0.13) Jy beam^{-1} and a FWHM of 0.72(0.3) km s^{-1}. Figure 5.2f shows the cross-correlation spectrum (Hanning smoothed over three channels) of this transition.

5.3.3 CS

Figure 5.3(a-c) shows the map and spectra of CS around Comet LINEAR. Figure 5.3a shows the map of the $J = 2 - 1$ transition of CS in 1 σ contours, starting at 2 σ. The synthesized beam of $23''.7 \times 18''.9$ is shown at the bottom left of the map. The line segment in the image shows the projection of the direction toward the sun. The origin of the line segment is anchored at the predicted position of the comet nucleus. The coordinates are given in offset arcseconds centered on the comet nucleus. Figure 5.3b shows the cross-correlation spectrum of this transition. The dashed line corresponds to the rest frequency of the $2 - 1$ line for a cometocentric rest velocity of 0 km s^{-1}. The 1 σ rms noise level is seen at the left of the panel. The line for Comet LINEAR was fit with a Gaussian by a least-squares method which gives a peak intensity of 0.21(0.05) Jy beam^{-1} and a FWHM of 2.45(0.60) km s^{-1}. Figure 5.3c shows the cross-correlation spectrum (Hanning smoothed over three channels) of this transition.

5.3.4 Non-Detections

All other molecules listed in Table 5.1, including CS in Comet NEAT, were not detected above 3 σ. Thus for all calculations an upper limit, based on the 1 σ rms noise level of the associated window, and a line width of 1 channel were assumed. Tables 5.5 and 5.6 list the upper limits of the intensity and line width for each species in columns (1) and (2).

5.4 Excitation Conditions

The analysis of the comet data was done with the Variable Temperature and Outflow Velocity (VTOV) model, detailed in Friedel et al. (2005a) (see Appendix H). This method is dependent

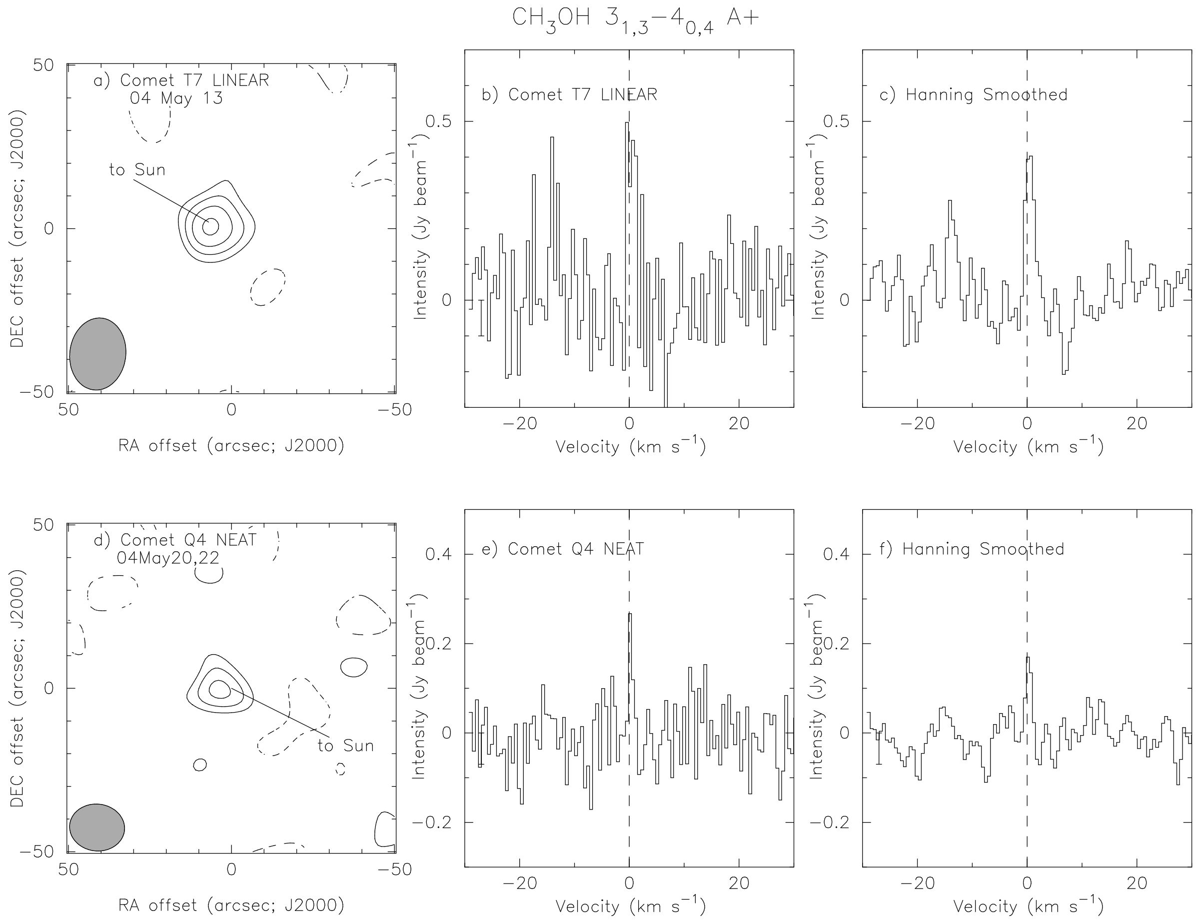

Figure 5.2 Comet LINEAR (C/2002 T7) and NEAT (C/2001 Q4) single field CH_3OH images and spectra. (a) Comet T7 emission contours from the $J = 3_{1,3} - 4_{0,4}A+$ transition of CH_3OH at 107.013 GHz. Image coordinates and labels are the same as in Figure 5.1(a). (b) CH_3OH cross-correlation spectra, labels are the same as in Figure 5.1(b). (c) CH_3OH cross-correlation spectra (Hanning smoothed over 3 channels), labels are the same as in (b). (d) Comet Q4 emission contours from CH_3OH. Contours indicate the CH_3OH emission near its peak centered at a cometocentric velocity of 0 km/s. Image coordinates and labels are the same as in (a). (e) CH_3OH cross-correlation spectra, labels are the same as in (b). (f) CH_3OH cross-correlation spectra (Hanning smoothed over 3 channels), abscissa and ordinate are the same as in (b).

on whether on not each molecular species is in LTE. In the innermost coma, collisions between cold cometary species dominate the rotational population of the gas and keep the gas in LTE, but in the less dense outer coma the collision time becomes longer than the time for absorption of solar photons and the subsequent cascade of emission. In that case, the population can also be determined by solar radiation driven fluorescence. Fluorescence effects could allow LTE to be maintained at a lower density than required in optically thin cases (e.g., Crovisier, 1984; Bockelee-Morvan et al., 1987). Therefore, if the population is determined by collisions, LTE can be assumed, while if the population is determined by fluorescence, LTE cannot necessarily be assumed.

The transition radius (relative to the comet nucleus) is defined as the point where the collisional excitation rate is equal to the radiative excitation rate and is dependent on both the water

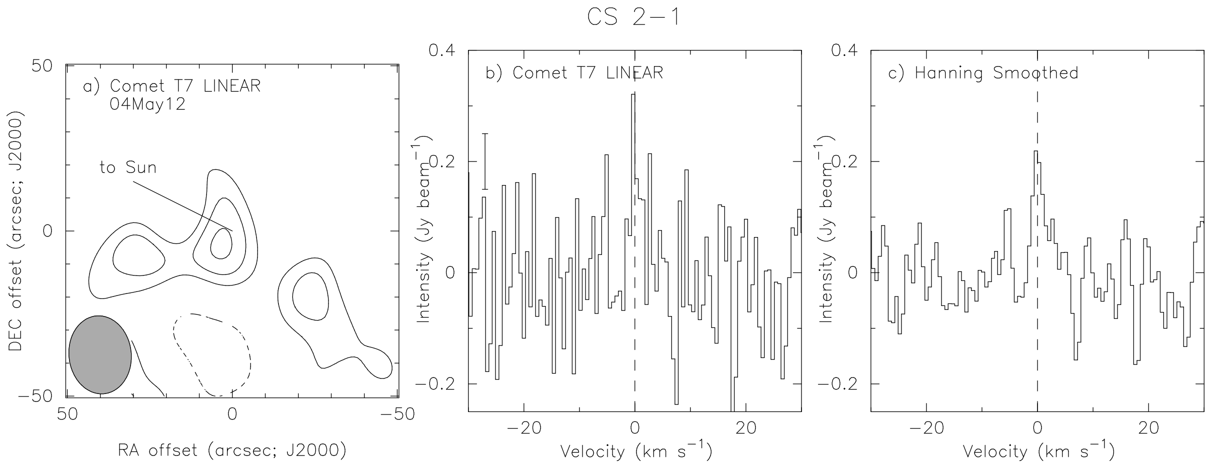

Figure 5.3 Comet LINEAR (C/2002 T7) single field CS image and spectra. (a) Comet T7 emission contours from the $J = 2-1$ transition of CS at 97.980 GHz. Contours indicate the CS emission near its peak centered at a cometocentric velocity of 0 km/s. Image coordinates and labels are the same as in Figure 5.1(a). (b) CS cross-correlation spectra; labels are the same as in Figure 5.1(b). (c) CS cross-correlation spectra (Hanning smoothed over 3 channels); labels are the same as in (b).

production rate and the heliocentric distance of the comet. The transition radius is not known for most molecular species but has previously been investigated for HCN (Lovell et al., 2004) and H_2O (Xie & Mumma, 1992). In this section the transition radius for HCN will be reinvestigated and the transition radii for the other molecular transitions listed in Table 5.1 will be investigated for the first time.

5.4.1 Collisional Excitation

Even though the primary gaseous constituent of cometary outflows is H_2O, it is not the primary collisional partner of many molecular species. This is due to the fact that collision cross sections between H_2O and other molecular species are several orders of magnitude smaller than those between electrons and these other molecules (e.g. Lovell et al., 2004). The H_2O-molecule collisional cross section is comparatively small for most of the molecules studied here because the dipole moment of H_2O is significantly different than its colliding partner's and there is also a lack of resonant interactions between dissimilar species (Bockelee-Morvan et al., 1984). For four of the molecules (CH_3OH, CS, $HCOOCH_3$, and C_2H_5OH) their dipole moments are similar to that of water. However, due to the lack of resonant interactions the cross sections for collisions with H_2O will still be smaller than that of collisions with electrons. In the case of ^{13}CO, which has a very small dipole moment, the collisional cross section with H_2O is most likely roughly equal to that of electrons. Since collisional cross sections between H_2O and the molecules studied here have not been published to date, only collisions with electrons, the primary collider, are considered. The inclusion of collisions with H_2O would increase the transition radii.

The collision rate between electrons and molecule X, $C_{\mathrm{e-X}}$, is defined as

$$C_{\mathrm{e-X}} = n_e \langle \sigma_{\mathrm{e-X}} v \rangle \ \mathrm{s}^{-1} \tag{5.1}$$

where n_e is the electron number density in cm^{-3}, $\sigma_{\mathrm{e-X}}$ is the collisional cross section in cm^2, and v is the velocity of the collision in cm s^{-1}. Lovell et al. (2004) adapted the electron density equations of Xie & Mumma (1992) to be dependent on the gas production rate (since the H_2O production rate is generally orders of magnitude higher than any other species, the total gas production rate is assumed to be equal to the H_2O production rate). Their equations give

$$n_e = \begin{cases} \frac{1.3\times10^7}{r}\left(\frac{Q}{5\times10^{29}}\right)^{1/2} & r < R_{CS} \\ br^m & R_{CS} < r < R_{rec} \\ \frac{5.6\times10^{11}}{r^2}\left(\frac{Q}{5\times10^{29}}\right)^{1/2} & R_{rec} < r < 2\times10^5 \end{cases} \quad \mathrm{cm}^{-3}, \tag{5.2}$$

where r is the radius from the comet nucleus in km, Q is the production rate of H_2O in molecules s^{-1}, R_{CS} is the radius of the contact surface (the point at which the dynamic pressure of the outflowing material is balanced by the dynamic pressure of the solar wind), and R_{rec} is the recombination radius. R_{RC} and R_{rec} are given by (Xie & Mumma, 1992; Lovell et al., 2004)

$$R_{CS} = 7300\left(\frac{Q}{5\times10^{29}}\right)^{3/4} \mathrm{km} \tag{5.3}$$

and

$$R_{rec} = 12,500\left(\frac{Q}{5\times10^{29}}\right)^{1/2} \mathrm{km}. \tag{5.4}$$

The constants b and m are defined such that br^m smoothly connects $n_e(R_{CS})$ and $n_e(R_{rec})$.

The cross section for rotational excitation by electron collisions with linear molecule X is given by (Takayanagi & Itiakawa, 1970)

$$\sigma_{\mathrm{e-X}}(J \to J+1) = \frac{8\pi}{3k^2} D^2 \frac{J+1}{2J+1} \ln\left(\frac{k+k'}{k-k'}\right) \ \mathrm{cm}^2, \tag{5.5}$$

with symmetric top molecule X is given by (Itikawa, 1971)

$$\sigma_{\mathrm{e-X}}(J_K \to J+1_K) = \frac{8\pi}{3k^2} D^2 \frac{(J+1)^2 - K^2}{(J+1)(2J+1)} \ln\left(\frac{k+k'}{k-k'}\right) \ \mathrm{cm}^2, \tag{5.6}$$

and with asymmetric top molecule X is given by (Itikawa, 1972)

$$\sigma_{\mathrm{e-X}}(J \to J') = \frac{8\pi}{3k^2}(2J'+1) D^2 \langle J'|J\rangle^2 \ln\left(\frac{k+k'}{k-k'}\right) \ \mathrm{cm}^2. \tag{5.7}$$

J and J' are the initial and final total angular momentum quantum numbers of the molecule, K is the quantum number for the projection of angular momentum along the axis of symmetry and D

is the dipole moment in atomic units (2.542 debye = 1 atomic unit). k and k' are the initial and final energies of the electron in cm^{-1} and are given by $k = \sqrt{2m_eE/\hbar^2}$ and $k' = \sqrt{k^2 - 2m_e\Delta E/\hbar^2}$ where E is the energy of the electron, m_e is the mass of the electron, and ΔE is the energy of the transition (Sobolev & Makarov, 1984). The quantity $\langle J'|J\rangle^2$ is related to the line strength, S, by (Schwendeman & Laurie, 1958; King et al., 1947)

$$S = (2J' + 1)(2J + 1)\langle J'|J\rangle^2. \tag{5.8}$$

In order to properly calculate the product $\langle\sigma_{\mathrm{e-X}}v\rangle$ the following expression needs to be evaluated

$$\langle\sigma_{\mathrm{e-X}}v\rangle = \frac{\displaystyle\int_{E_{min}}^{\infty} E^{1/2} v\sigma_{\mathrm{e\text{-}X}} e^{-E/T} dE}{\displaystyle\int_{E_{min}}^{\infty} E^{1/2} e^{-E/T} dE}\ \mathrm{cm^3s^{-1}}, \tag{5.9}$$

where E_{min} is the energy of the transition, E is the kinetic energy of the electrons, v is the velocity of the electrons (from $E = m_ev^2/2$), σ is from one of equations (5.5)-(5.7), and T is the electron temperature. The outflow velocity of the electrons is ignored since the thermal velocity of an electron at 20 K is over an order of magnitude larger than the outflow velocity, and the difference will only become larger as the temperature increases. The thermal motion of the molecules is also ignored when calculating v since at any temperature their thermal velocity is orders of magnitude smaller than that of the electrons. The electron temperature is assumed to follow the gas temperature in the inner coma up to R_{CS} where it rises linearly to ∼10,000 K, at about $2R_{CS}$. This is a rough approximation of the *Giotto* spacecraft observations of Comet Haley (Eberhardt & Krankowsky, 1995; Lovell et al., 2004).

Previous calculations along these lines such as Lovell et al. (2004) and Xie & Mumma (1992) do not appear to have performed these integrals. Rather they calculated σv by multiplying the cross section by the mean electron thermal velocity. Thus, the values reported in this section will differ from those reported in previous works. In general, the collision rate in this work is greater for any given heliocentric radius. The C code given in Appendix A was developed to perform the calculations.

5.4.2 Radiative Excitation

The primary method of radiative excitation is the excitation of infrared vibrational bands by solar photons. The radiative excitation rate for each vibrational band is defined as (Crovisier & Encrenaz, 1983)

$$g_{\nu'\nu''} = \frac{\Omega_{bb}}{4\pi} e^{-1.4385\bar{\nu}_{\nu'}/T} A_{\nu''\nu'} \left(e^{hc\bar{\nu}_{\nu'\nu''}/k_bT_{bb}} - 1\right)^{-1}\ \mathrm{s}^{-1}, \tag{5.10}$$

where Ω_{bb} is the solid angle subtended by the sun (1.2×10^{-4} sr. for Comet LINEAR and 7.2×10^{-5} sr. for Comet NEAT), $\bar{\nu}_{\nu'}$ is the energy of the lower vibrational state in cm^{-1} (which is 0 for all cases considered here), T=296 K, $\bar{\nu}_{\nu'\nu''}$ is the frequency of the transition in cm^{-1}, and T_{bb}=5770 K.

The "band spontaneous emission Einstein coefficient" is defined by (Crovisier & Encrenaz, 1983)

$$A_{\nu'\nu''} = 3.080 \times 10^{-8} \bar{\nu}^2_{\nu'\nu''} S_{\nu'\nu''} \text{ s}^{-1}, \tag{5.11}$$

where $S_{\nu'\nu''}$ is the total band strength in cm^{-2} atm^{-1}. The total band excitation rate is given as (Bockelee-Morvan & Crovisier, 1985)

$$g_e = \sum g_{\parallel} + \frac{1}{2} \sum g_{\perp} \text{ s}^{-1}, \tag{5.12}$$

where $g_{\parallel}$ and $g_{\perp}$ are the parallel and perpendicular (doubly degenerate) fundamental vibrational bands. Table 5.3 lists the vibrational transition quantities. The first column lists the vibrational band, the second column lists the band energy, the third column lists $S_{\nu'\nu''}$, the fourth column lists $A_{\nu'\nu''}$, the fifth column denotes whether the band is $\parallel$ or $\perp$, and the sixth column lists $g_{\nu'\nu''}$ in s^{-1}. Only vibrational bands that have a notable contribution to the excitation rate (i.e. within 2 orders of magnitude of the strongest band) are reported. Note that $HCOOCH_3$ is not listed because there were no references which listed reliable $S_{\nu'\nu''}$, $A_{\nu'\nu''}$, or g_e for $HCOOCH_3$.

Figures 5.4 and 5.5 illustrate the results of the calculations for each observed species for Comets LINEAR and NEAT, respectively. The ordinate is the log of the excitation rate, and the abscissa is the log of cometocentric distance. The descending solid line denotes the excitation rate by electron collision for the nominal water production rate (2×10^{29} s^{-1} for Comet LINEAR and 1.2×10^{29} s^{-1} for Comet NEAT) (see §5.5.2). The descending dashed lines are the same as the solid line except for rates of one half (lower dashed line) and twice (upper dashed line) the nominal water production rate. The horizontal lines are the range (denoted by the hatching) of radiative excitation rates for each molecule. The intersection of the electron collision excitation rate and the radiative excitation rate denotes the transition radius for each molecule. Note that the $HCOOCH_3$ plot only gives electron excitation rates because no radiative excitation rates could be found or calculated.

Table 5.4 gives the results of these calculations. The first column lists the molecular species, the second column lists g_e at 1 AU, the third and fifth columns list g_e for Comets LINEAR and NEAT, respectively, and the fourth and sixth columns list the transition radii for Comets LINEAR and NEAT, respectively. The range of radiative excitation rates is because most of the references did not state whether the bands were $\parallel$ or $\perp$. Thus the upper limit on the rate is by assuming all bands are $\parallel$ and the lower limit is from assuming all bands are $\perp$. The actual value is within this range and comprises of a combination of $\parallel$ and $\perp$ bands. Note that the electron excitation rates are transition dependent, thus the transition radii listed here are only applicable to the transitions observed. Also of note is that the radiative excitation rate can also be transition dependent for asymmetric tops. This is because when an asymmetric top is in an excited state it does not have a unique path of radiative de-excitation to the ground state, unlike symmetric tops and linears. Thus the reported radiative excitation rates for the asymmetric top species may be larger than the actual value, making the transition radii reported smaller than the actual value.

Table 5.3. Vibrational Transition Quantities[a]

Band	$\bar{\nu}_{\nu'\nu''}$ (cm^{-1})	$S_{\nu'\nu''}$ (cm^{-2} atm^{-1})	$A_{\nu'\nu''}$ (s^{-1})	$\parallel/\perp$	$g_{\nu'\nu''}$[a] (s^{-1})	Refs.
			HCN			
ν_2	712	200.0	1.70	$\perp$	9.5×10^{-5}	1,2
$^2\nu_2$	1412	$\sim$45	2.76	$\perp$	3.5×10^{-5}	
ν_3	3311	236.0	81.04	$\parallel$	3.6×10^{-4}	
			CH_3OH			
ν_2	2824	130.5	32.07	⋯	1.7×10^{-4}	1,3
ν_4	1026	433.5	14.05	⋯	2.6×10^{-4}	
ν_5	2977	$\sim$120	32.76	⋯	1.6×10^{-4}	
ν_8	1340	$\sim$120	6.64	⋯	9.1×10^{-5}	
Combo.	2564	63.7	12.90	⋯	7.8×10^{-5}	
			CS			
ν_1	1272	⋯	16.10	⋯	2.3×10^{-4}	4
			^{13}CO			
ν_1	2092	⋯	⋯	$\parallel$	2.6×10^{-4}	5,6
			CH_3CN[b]			
ν_1	2960	8.0	3.10	$\parallel$	1.5×10^{-5}	2
ν_2	2272	4.7	1.10	$\parallel$	7.3×10^{-6}	
ν_4	920	5.7	0.21	$\parallel$	3.8×10^{-6}	
ν_5	3028	10.0	2.00	$\perp$	9.8×10^{-6}	
ν_6	1441	230.0	10.6	$\perp$	1.2×10^{-4}	
ν_7	1045	42.0	1.00	$\perp$	1.6×10^{-5}	
ν_8	363	9.0	0.03	$\perp$	1.2×10^{-6}	
			C_2H_5OH			
⋯	880	70.0	1.67	⋯	3.7×10^{-5}	1
⋯	1050	400.0	13.58	⋯	2.5×10^{-4}	
⋯	1250	120.0	5.78	⋯	8.5×10^{-5}	
⋯	1400	150.0	9.06	⋯	1.2×10^{-4}	
⋯	2950	300.0	80.41	⋯	4.0×10^{-4}	

Table 5.3—Continued

Band	$\bar{\nu}_{\nu'\nu''}$ (cm^{-1})	$S_{\nu'\nu''}$ (cm^{-2} atm^{-1})	$A_{\nu'\nu''}$ (s^{-1})	$\parallel/\perp$	$g_{\nu'\nu''}$[a] (s^{-1})	Refs.
			SiO			
ν_1	~800	...	6.61	...	1.6×10^{-4}	7
$^2\nu_1$	~1600	...	0.17	...	1.9×10^{-6}	
			HNC and $HN^{13}C$[c]			
ν_1	3843	1192.0	542.65	...	1.8×10^{-3}	8
ν_2	490	1274.4	9.42	...	3.9×10^{-4}	
ν_3	2067	288.9	38.02	...	3.1×10^{-4}	
			C_2H_5CN			
ν_1/ν_{14}	3005	310.0	86.22	...	4.2×10^{-4}	9
ν_4	2260	11.0	1.73	...	1.2×10^{-5}	
ν_8	1323	17.0	0.92	...	1.3×10^{-5}	
ν_9	1083	37.0	1.34	...	2.3×10^{-5}	
ν_{16}	1463	70.0	4.61	...	5.7×10^{-5}	
ν_{19}	783	9.0	0.17	...	4.3×10^{-6}	

[a]Values of $g_{\nu'\nu''}$ that are two or more orders of magnitude less than the largest value of a molecule are not reported.

[b]Values are for $K = 0$.

[c]No data could be found on $HN^{13}C$. Thus it is assumed to have the same properties as HNC.

References. — (1) Crovisier & Encrenaz (1983); (2) Bockelee-Morvan & Crovisier (1985); (3) Kerkhof et al. (1999); (4) Highberger et al. (2000); (5) Crovisier & Le Bourlot (1983); (6) Bockelee-Morvan et al. (1987); (7) Drira et al. (1997); (8) Rogers & Hillman (1982); (9) Cerceau et al. (1985)

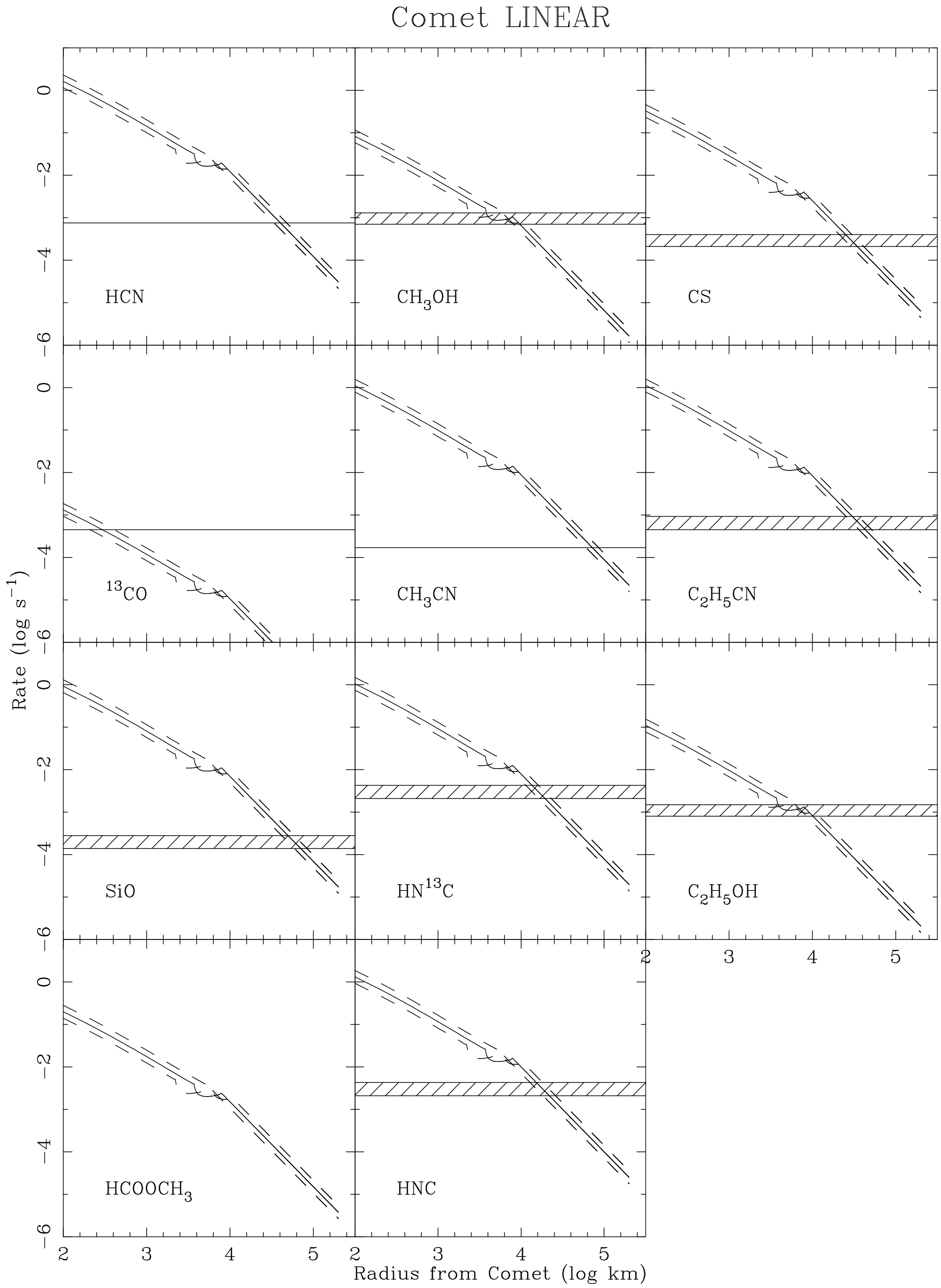

Figure 5.4 Excitation rates for Comet LINEAR for each observed species. The ordinate is the log of the excitation rate, and the abscissa is the log of cometocentric distance. The descending solid line denotes the excitation rate by electron collision for $Q(H_2O)=2\times10^{29}$ s^{-1}. The descending dashed lines are the same as the solid line except for $Q(H_2O)=1\times10^{29}$ s^{-1} (lower dashed line) and $Q(H_2O)=4\times10^{29}$ s^{-1} (upper dashed line). The horizontal line(s) are the range (denoted by the hatching) of the radiative excitation rate for each molecule.

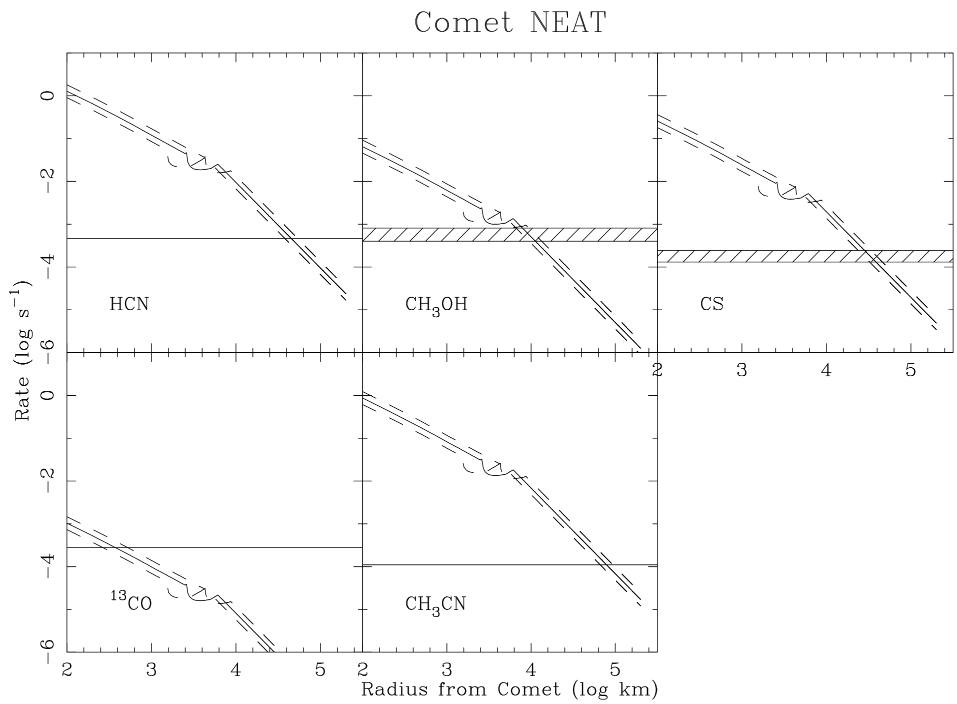

Figure 5.5 Excitation rates for Comet NEAT for each observed species. The ordinate is the log of the excitation rate, and the abscissa is the log of cometocentric distance. The descending solid line denotes the excitation rate by electron collision for $Q(H_2O)=1.2\times10^{29}$ s^{-1}. The descending dashed lines are the same as the solid line except for $Q(H_2O)=0.6\times10^{29}$ s^{-1} (lower dashed line) and $Q(H_2O)=2.4\times10^{29}$ s^{-1} (upper dashed line). The horizontal line(s) are the range (denoted by the hatching) of the radiative excitation rate for each molecule.

5.4.3 Array Response

The synthesized beams sample a cylinder of gas through each comet[4], and because the molecular volume density falls off faster than r^{-2} due to photodissociation, most of the contribution to the integrated line intensity will come from a sample on the order of the size of the projected synthesized beam. Since the synthesized beam is much smaller than the outer radii of the collisionally dominated regions, conditions significantly outside of the beam are not likely to affect the observations.

The contribution from different cometocentric radii (i.e. from different source sizes) is determined by two factors. The first is that sources of differing size but equal total flux do not have equal peak fluxes and thus, when summed together, do not contribute equally to the total peak flux of a map. The second is that the array starts to resolve out flux from sources that are much larger than the synthesized beam. The first effect is dominant for source sizes that are on the order of the synthesized beam while the second becomes more dominant for larger source sizes. These two effects are illustrated in Figure 5.6. The top panel is from the Comet LINEAR observations,

[4]In a small cylinder passing through the cometary gas, only a small fraction of the HCN will be in the less dense fluorescent zone. Hence, unlike the case for some optical molecular observations, here we assume that the HCN in the fluorescence zone can be ignored relative to that in the denser collisional zone.

Table 5.4. Radiative Excitation Rates[a]

Species	g_e(1 AU) (s^{-1})	LINEAR g_e (s^{-1})	LINEAR Trans. Radius (km)	NEAT g_e (s^{-1})	NEAT Trans. Radius (km)
HCN	4.3×10^{-4}	7.5×10^{-4}	33,900-48,000	4.6×10^{-4}	38,100-54,000
CH_3OH	$(3.8\text{-}7.6)\times10^{-4}$	$(0.7\text{-}1.3)\times10^{-3}$	5,900-11,800	$(4.0\text{-}8.1)\times10^{-4}$	6,600-13,400
CS	$(1.2\text{-}2.3)\times10^{-4}$	$(2.1\text{-}4.0)\times10^{-4}$	21,000-41,200	$(1.3\text{-}2.4)\times10^{-4}$	23,900-46,000
^{13}CO	2.6×10^{-4}	4.5×10^{-4}	200-800	2.8×10^{-4}	200-1,000
CH_3CN[b]	1.0×10^{-4}	1.7×10^{-4}	60,500-85,700	1.1×10^{-4}	66,200-93,800
C_2H_5OH	$(4.4\text{-}8.8)\times10^{-4}$	$(0.8\text{-}1.5)\times10^{-3}$	6,200-12,200		
SiO	$(0.8\text{-}1.6)\times10^{-4}$	$(1.4\text{-}2.8)\times10^{-4}$	41,800-83,800		
$HN^{13}C$	$(1.2\text{-}2.5)\times10^{-3}$	$(2.1\text{-}4.3)\times10^{-3}$	11,300-23,100		
C_2H_5CN	$(2.6\text{-}5.3)\times10^{-4}$	$(4.5\text{-}9.2)\times10^{-4}$	25,300-51,300		
$HCOOCH_3$	...	...	...		
HNC	$(1.2\text{-}2.5)\times10^{-3}$	$(2.1\text{-}4.3)\times10^{-3}$	12,800-26,000		

[a]If the type of band ($\parallel$ or $\perp$) is not known then a range of g_e is reported where the minimum is where all bands are $\perp$ and the maximum where all bands are $\parallel$.

[b]Values are for $K = 0$.

and the lower panel is from the Comet NEAT observations. The abscissa is cometocentric radius in arcseconds (lower axis) and in km (upper axis) of a source on the sky, and the ordinate is r_i, the array recovery factor (see Friedel et al. (2005a) and Appendix H for a detailed explanation). The transition radius for each molecular species is denoted by a solid vertical line. Note that for every species but ^{13}CO the BIMA Array is sampling the inner collisionally dominated coma. For C_2H_5OH and CH_3OH the transition radii are small enough that the BIMA Array is sampling a small portion of the fluorescence region. However these transition radii are most likely underestimates, and also the fluorescence may keep these molecules in LTE at these radii (e.g., Crovisier, 1984; Bockelee-Morvan et al., 1987). In the case of ^{13}CO it is unclear whether it will be kept in LTE by the fluorescence and collisions with other molecules, such as H_2O. However since ^{13}CO was not detected in either comet, the calculated column density and production rate upper limits should still be valid limits. In the case of $HCOOCH_3$, where no transition radius can be determined, it is expected that the transition radius would be similar to that of other large highly saturated species. Thus the BIMA Array would be sampling the collisionally dominated region. Therefore, LTE can be assumed for all of the transitions searched for (all CH_3CN calculations are for $K = 0$).

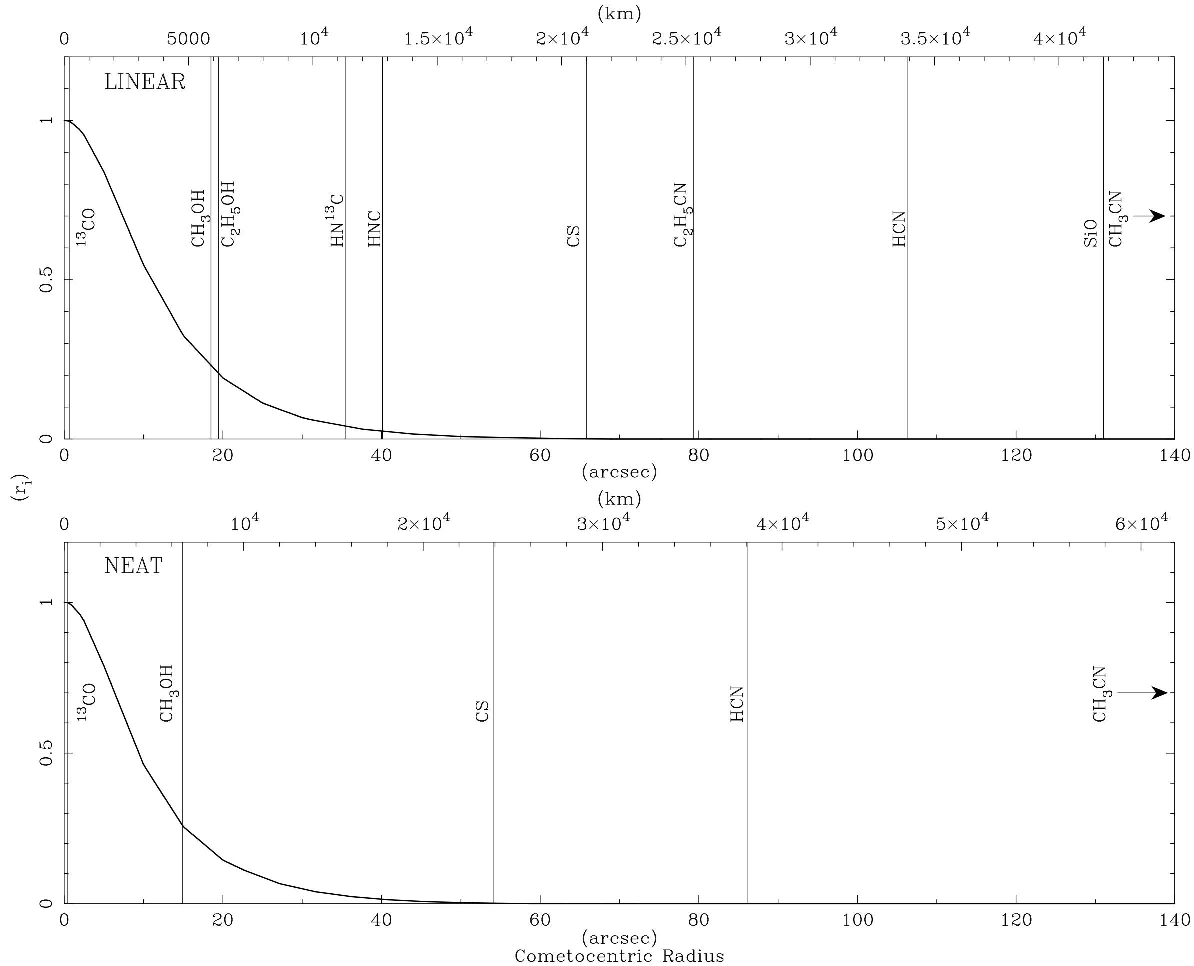

Figure 5.6 BIMA Array response to source size for each comet. The upper panel is from the Comet LINEAR observations, and the lower panel is from the Comet NEAT observations. The abscissa is cometocentric distance in arcseconds (lower axis) and km (upper axis), and the ordinate is the array recovery factor r_i. The transition radius for each molecular species is denoted by a solid vertical line.

Table 5.5. Variable Temperature and Outflow Velocity (VTOV) Results for Comet LINEAR

Species	I_0 (Jy bm^{-1})	Δv km s^{-1})	$\langle N_T \rangle$ (cm^{-2})	Q (s^{-1})	$\frac{Q(X)}{Q(H_2O)}$	$\frac{Q(X)}{Q(CN)}$ [a]
HCN	0.59(0.14)	2.30(0.56)	$6.4(2.1) \times 10^{12}$	$6.5(2.2) \times 10^{26}$	$3.3(1.1) \times 10^{-3}$	4.6(1.5)
CH_3OH	0.44(0.06)	1.74(0.31)	$1.4(0.3) \times 10^{14}$	$7.5(1.5) \times 10^{27}$	$3.8(0.8) \times 10^{-2}$	
CS	0.21(0.05)	2.45(0.60)	$2.3(0.6) \times 10^{12}$	$8.7(3.0) \times 10^{26}$	$4.0(1.0) \times 10^{-3}$	
CH_3CN[b]	< 0.13	1.06	$< 4.6 \times 10^{11}$	$< 2.3 \times 10^{25}$	$< 1.2 \times 10^{-4}$	< 0.16
^{13}CO	< 0.12	1.06	$< 1.5 \times 10^{14}$	$< 7.7 \times 10^{27}$	$< 4.0 \times 10^{-2}$	
$HCOOCH_3$	< 0.09	1.30	$< 2.5 \times 10^{13}$	$< 2.2 \times 10^{27}$	$< 1.0 \times 10^{-2}$	
HNC	< 0.08	1.35	$< 1.8 \times 10^{11}$	$< 1.4 \times 10^{25}$	$< 7.5 \times 10^{-5}$	< 0.10
$HN^{13}C$	< 0.08	1.35	$< 2.8 \times 10^{11}$	$< 2.2 \times 10^{25}$	$< 1.1 \times 10^{-4}$	< 0.16
SiO	< 0.08	1.35	$< 2.2 \times 10^{11}$	$< 1.7 \times 10^{25}$	$< 8.5 \times 10^{-5}$	
C_2H_5CN	< 0.08	1.30	$< 2.3 \times 10^{12}$	$< 1.8 \times 10^{26}$	$< 9.0 \times 10^{-4}$	< 1.3
C_2H_5OH	< 0.08	1.35	$< 1.9 \times 10^{13}$	$< 1.4 \times 10^{27}$	$< 7.0 \times 10^{-3}$	

[a]The ratio is given only for those species which contain a C-N bond.

[b]Values for $K = 0$.

5.5 Discussion

5.5.1 Column Densities and Production Rates

All calculations are made assuming optically thin emission, since the limits on the satellite hyperfine components of HCN show that they are significantly weaker than the main component. The total beam averaged column densities and production rates are given in columns 4 and 5 of Table 5.5 for Comet LINEAR and columns 4 and 5 of Table 5.6 for Comet NEAT.

5.5.2 Relative Production Rates of X to H_2O

Comet NEAT

D. G. Schleicher (2005, private communication) measured H_2O production rates from Comet NEAT and derived a scaling law of Q(H_2O)$\sim r_H^{-4.3}$. From his observations in May and June of 2004 and the scaling law, the H_2O production rates were scaled from the heliocentric distances when they were measured to 0.97 AU for Comet NEAT to match the r_H of the observations. Table 5.7 gives the measurements and their scaled values. Column 1 gives the date of observation, column 2 gives the heliocentric distance of the comet, columns 3 and 4 give the measured production rates of H_2O and CN (see §5.5.3), and columns 5 and 6 give the scaled production rates for H_2O and CN, respectively. The average value for Comet NEAT is Q(H_2O)$\sim 1.2 \times 10^{29}$ s^{-1}, which is very similar to water production rates measured from Comet Hyakutake at similar heliocentric distances to the

Table 5.6. Variable Temperature and Outflow Velocity (VTOV) Results for Comet NEAT

Species	I_0 (Jy bm^{-1})	Δv km s^{-1})	$\langle N_T \rangle$ (cm^{-2})	Q (s^{-1})	$\frac{Q(X)}{Q(H_2O)}$	$\frac{Q(X)}{Q(CN)}$ [a]
HCN	0.17(0.03)	1.32(0.66)	$8.5(4.5) \times 10^{11}$	$8.9(4.7) \times 10^{25}$	$7.4(3.9) \times 10^{-4}$	0.3(0.2)
CH_3OH	0.31(0.13)	0.72(0.30)	$4.6(2.7) \times 10^{13}$	$2.9(1.7) \times 10^{27}$	$2.4(1.4) \times 10^{-2}$	
CS	< 0.14	0.60	$< 3.5 \times 10^{11}$	$< 2.1 \times 10^{24}$	$< 2.0 \times 10^{-3}$	
CH_3CN[b]	< 0.06	1.06	$< 2.0 \times 10^{11}$	$< 1.1 \times 10^{25}$	$< 9.2 \times 10^{-5}$	$< 4.0 \times 10^{-2}$
^{13}CO	< 0.06	1.06	$< 9.8 \times 10^{13}$	$< 8.3 \times 10^{27}$	$< 7.0 \times 10^{-2}$	

[a]The ratio is given only for those species which contain a C-N bond.

[b]Values for $K = 0$.

observations ($\sim 1 \times 10^{29}$ s^{-1} (Lis et al., 1997)).

The relative production rates of each molecular species relative to H_2O are listed in column 6 of Table 5.6. The relative production rate ratios of HCN and CH_3OH to H_2O are most similar to those measured around Comet Hyakutake (C/1996 B2) (1.2×10^{-3} and 1.7×10^{-2}, respectively) (Biver et al., 1999).

Comet LINEAR

H_2O production rates were also measured for Comet LINEAR by D. G. Schleicher (2005, private communication). From his data, he estimated the H_2O production rate to be $\sim 2 \times 10^{29}$ s^{-1} during the observations.

The relative production rates of each molecular species relative to H_2O are listed in column 6 of Table 5.5. The relative production rate ratios of HCN, CH_3OH, and CS to H_2O for Comet LINEAR are most similar to those observed around Comet Hale-Bopp (C/1995 O1) ($(2.1 - 2.6) \times 10^{-3}$, 4×10^{-2}, and $(3.7 - 4.3) \times 10^{-3}$, respectively) (Snyder et al., 2001; Remijan et al., 2004b).

5.5.3 Relative Production Rates of X to CN

Comet NEAT

D. G. Schleicher (2005, private communication) measured CN production rates from Comet NEAT and derived a scaling law of $Q(CN) \sim r_H^{-2.1}$. From his observations in May and June 2004 and the scaling law, these values were scaled from the heliocentric distances when they were measured to the heliocentric distance of Comet NEAT during the observations (see Table 5.7). Averaging these values gives Q(CN) $\sim 2.6 \times 10^{26}$ s^{-1} for Comet NEAT.

The relative production rates of each nitrogen bearing molecular species relative to CN are listed in column 7 of Table 5.6. The relative production rate of HCN to CN is $\sim 0.3 \pm 0.2$ for

Table 5.7. Scaling of H_2O and CN Production Rates From Comet NEAT[a]

Date	r_H (AU)	Q(H_2O) (s^{-1})	Q(CN) (s^{-1})	Scaled Q(H_2O)[b] (s^{-1})	Scaled Q(CN)[c] (s^{-1})
2004 May 11	0.97	1.3×10^{29}	2.6×10^{26}	1.3×10^{29}	2.6×10^{26}
2004 May 12	0.96	1.3×10^{29}	2.5×10^{26}	1.2×10^{29}	2.4×10^{26}
2004 June 09	1.05	8.9×10^{28}	2.4×10^{26}	1.3×10^{29}	2.8×10^{26}
2004 June 10	1.06	7.9×10^{28}	2.1×10^{26}	1.2×10^{29}	2.6×10^{26}

[a]Unscaled data from D. G. Schleicher(private communication).

[b]The H_2O production rates were scaled by $r_H^{-4.3}$ for each comet (see§5.5.2).

[c]The CN production rates were scaled by $r_H^{-2.1}$ for each comet (see§5.5.3).

Comet NEAT. The photodissociative branching ratio of HCN implies that ∼97% of HCN will be photodissociated into H and CN (Huebner, Keady, & Lyon, 1992). Woodney et al. (2002) concluded that HCN is most likely the primary parent species of CN. Thus, one would expect the HCN to CN ratio to be near 1. However, the ratio for Comet NEAT is a factor of ∼3 smaller than the expected ratio.

Comet LINEAR

CN production rates were measured for Comet LINEAR by D. G. Schleicher (2005, private communication). From his data, he estimated the CN production rate to be $\sim 1.4 \times 10^{26}$ s^{-1} during the observations.

The relative production rates of each nitrogen bearing molecular species relative to CN are listed in column 7 of Table 5.5. The Q(HCN)/Q(CN) for Comet LINEAR is $\sim 4.6 \pm 1.5$, which is consistent with HCN being the primary parent of CN.

5.6 Conclusions and Future Work

This chapter reports the detections of HCN and CH_3OH in Comets LINEAR and NEAT and CS in Comet LINEAR. The data were analyzed with the VTOV model, which is considered to be more accurate than the traditional Haser model for interferometric observations because the VTOV model traces the physical conditions of the cometary coma more accurately. Based on the molecular ratios with water, it appears that Comet LINEAR is a Hale-Bopp class of comet while Comet NEAT is a Hyakutake class of comet. It is unclear, due to such a small sample size, whether these are two distinct classes of comets or if there is a range of classes with numerous and different molecular ratios. Future observations, especially those with more sensitivity, of more comets will be able to shed light onto this question. Arrays such as the CARMA Array will be ideal for this type of work, since it offers higher sensitivity and better u-v coverage than the BIMA Array. Also of importance is observing comets that pass very close to the sun because comets become very productive at such small heliocentric radii. An example of such a comet is Comet Bradfield (C/2004 F4) which passed only 0.17 AU from the sun in April 2004. Unfortunately, observations of these comets can be difficult as they may not be identified until they are very close to perihelion, giving little time to prepare for observations. Future observations will also be able to shed more light onto the chemistry of the presolar nebula and possibly be able to link this chemistry with that happening in hot cores and young stellar objects.

Chapter 6

Conclusions and Future Prospects

This dissertation presents the results and analysis of a partial $\lambda = 3$ mm spectral line survey of the high mass star forming region Sgr B2(N-LMH) and the initial results from a full $\lambda = 3$ mm spectral line survey of the high mass star forming region Orion-KL.

The Sgr B2(N-LMH) survey detected a total of 331 spectral lines of which 205 have been identified as coming from 40 molecular species and isotopologues. The Orion-KL survey detected a total of 975 spectral lines from the hot core region and 790 spectral lines from the compact ridge region. These lines are from 60 molecular species and isotopologues. These line counts give spectral line densities (per 100 MHz) of 6.92 (4.31 from identified lines and 2.61 from U lines) for the Sgr B2(N-LMH) survey and 2.72 (1.73 from identified lines and 0.99 from U lines) from the hot core and 2.21 (1.45 from identified lines and 0.76 from U lines) from the compact ridge for the Orion-KL survey. However, the Orion-KL survey has a spectral line density (per 100 MHz) of 6.00 (4.54 from identified lines and 1.46 from U lines) if only the frequency bands covered by the Sgr B2(N-LMH) survey are considered. Thus, Orion-KL appears to have fewer spectral lines, but a higher percentage of these lines are identified toward Orion-KL.

The Sgr B2(N-LMH) survey presents the first source size measurements for most of the species detected. The source sizes indicate that the large highly saturated molecular species occupy a region only a few tens of kAU across. The single exception to this is the lowest energy transition of C_2H_5OH detected in the survey. This transition has a source size of at least $70''$ indicating that C_2H_5OH can be formed and desorbed from grain surfaces in the low temperature region surrounding the hot cores of Sgr B2(N). Observations of low temperature (< 10 K) transitions of other large saturated species should be carried out to determine if they too are present in this low temperature region. This has been done for glycolaldehyde (CH_2OHCHO), which has been found to be highly extended (Hollis et al., 2004).

Additionally, simple species ($\sim$3 atoms), CH_3OH, and HC_3N were also found to have extended components around the Sgr B2(N-LMH) region. Similarly the simple species plus CH_3OH, CH_3CN, C_2H_5OH, and HC_3N in Orion-KL also appear to have a larger distribution since they were detected toward both the hot core and compact ridge. In contrast, the hydrogenated species with the HC_3N backbone structure appear only toward the hot core region of Orion-KL, while the larger O bearing species (with the exception of C_2H_5OH and $(CH_3)_2CO$) appear exclusively toward the compact ridge region. $(CH_3)_2CO$ is the only large O bearing species seen exclusively toward the hot core region, indicating a formation mechanism similar to that of the large N bearing species.

Several of the simple species and HC_3N exhibit inverse P-Cygni profiles toward the Orion-KL compact ridge. These features are very sharp and narrow, indicating infall at <1 km s^{-1}. This infall profile has not been previously observed toward the compact ridge and needs to be investigated further by examining the channel maps and possibly higher spatial and spectral resolution observations.

An analysis of the frequencies of the U lines for each source was carried out. This analysis searched for potential relations between the U line frequencies (i.e., were they from the same molecular species). Nine potential pairs were found for the Sgr B2(N-LMH) survey, 179 potential pairs were found for the Orion-KL hot core, and 86 potential pairs were found for the Orion-KL compact ridge. A more thorough analysis of the Orion-KL pairs will be carried out in order to confirm or reject them (are there missing J values, inconsistent line widths or intensities, etc.). However, for the Sgr B2(N-LMH) pairs, further observations of the frequency bands not covered in this survey will be needed in order to confirm or reject the pairs.

The U lines from both surveys were compared in order to see if they were seen in more than one source. Six U lines appear in both Sgr B2(N-LMH) and the Orion-KL hot core and four U lines appear in both Sgr B2(N-LMH) and the Orion-KL compact ridge. Also of the 631 U lines detected toward Orion-KL 34 (17 each from the hot core and compact ridge) appear at the same frequency in both regions, indicating that they come from species that exists in both regions. Only two of these lines appear in all three sources. Additionally, four of the Sgr B2(N-LMH) U lines have been identified as potential methyl glycolate transitions, and three other U lines from Sgr B2(N-LMH) appear to follow the pattern of double rotor species and may be related.

Many of the U lines are likely to be vibrationally excited transitions of known molecular species such as $HCOOCH_3$, $(CH_3)_2O$, C_2H_5OH, and CH_3OH. Laboratory experiments which observed a mixture of "weed" species (e.g., $HCOOCH_3$, C_2H_5CN, and C_2H_3CN) show a forest of lines in the 3 mm window, indicating that a tremendous number of lines can be formed by the ground and vibrationally excited states of a small number of species (Eric Herbst, private communication, 2005). Catalogs of transitions from vibrationally excited states for most species do not yet exist, and those that do are only for the lowest few vibrationally excited states. As these catalogs and catalogs of new species become available they will be compared to the U lines from these surveys to search for identifications.

In Sgr B2(N) many species, both simple and complex, have emission components at velocities other than the systemic velocity of Sgr B2(N-LMH). Emission components were seen in complex species at $\sim$72 and $\sim$52 km s^{-1}. The $\sim$72 km s^{-1} component originates from a second core 5$''$ north of the main core. This second core may be at a different evolutionary stage than the main core, as indicated by the much higher carbon chain molecule abundance in this secondary core. The origin of the $\sim$52 km s^{-1} velocity component is much less clear and may require higher spatial resolution observations in order to see its origins. Most simple species show absorption (emission in the case of ^{13}CO) lines from large scale cooler clouds both around the Sgr B2 complex and along the line of sight. Most of the local components surround both the Sgr B2(N-LMH) and Sgr B2(M) cores, while one component at ~85-90 km s^{-1} appears to only be around Sgr B2(N-LMH).

The analysis of the Orion-KL survey is not complete. Source size measurements and analysis of the channel maps are planned, and the results will further help to constrain the formation mechanisms of the observed species. Additionally, in order to facilitate the publication of the spectra from this survey, a Java based interactive program is being developed to allow for the viewing of the spectra and channel maps over the internet.

In an attempt to connect chemistry in high mass star forming regions with chemistry around forming low mass stars, observations of two comets (C/2002 T7 LINEAR and C/2001 Q4 NEAT) were conducted. The data were analyzed with the VTOV model, which tracks the physical conditions in the cometary coma. The results indicated that Comet LINEAR is a Hale-Bopp class of comet while Comet NEAT is a Hyakutake class of comet. However, due to the small sample size of observed comets, it is unclear whether these are two distinct classes of comet or if there is a range of classes with numerous and different molecular ratios.

In order to complete the chemistry picture, further observations of comets and low mass star forming regions should be conducted. This will allow for the comparison of molecular species and formation mechanisms across a wide range of physical conditions (hot core, both high and low mass, to presolar nebula). These observations will be best carried out by both single element radio telescopes and arrays such as CARMA and ALMA, which will offer a tremendous gain in sensitivity when compared to previous observations.

Appendix A

Collision Rate Code

The following is a C code that models the rotational excitation of molecules in cometary comae by collisions with electrons. The user only needs to modify the top block in order to customize the code for any molecule. A file containing the temperature profile of the comet is required, as are qromb.c, trapzd.c, polint.c, nrutil.c, and nr.h from Press et al. (1992). These routines cannot be supplied with this code due to copyright restrictions.

```
/*******************************************************************************/
//  Program: collision.c                                                       /
//  By: Douglas N. Friedel                                                     /
//                                                                             /
//  Program collision.c calculates the radial profile of the electron number   /
//   density and collision rate with linear, symmetric top, and asymmetric top /
//   molecules. The number densities equations are from Xie & Mumma (1992) and /
//   Lovell et al. (2004). Collisional cross sections are from  Takayanagi &   /
//   Itikawa (1970) (linear), Itikawa (1971) (symmetric tops) and Itikawa      /
//   (1972) (asymmetric tops). The collision rate (C) is calculated as         /
//   C=n*<sigma*v>, where the quantity <sigma*v> is derived from the integral  /
//   across all energies of sigma*v. The integral is done in units of eV.      /
//   The output is put in a file named comet.out the columns are the radius    /
//   (in km), log of the radius, electron number density (cm^-3), log of the   /
//   electron number density, collision rate (s^-1), and log of the collision  /
//   rate. If the radiative excitation rate is given in radr then the program  /
//   will output the radius (within a step size) at which the primary          /
//   excitation mechanism switches from collisions to photons.                 /
//                                                                             /
// Only the values in the top section should be changed for different molecules./
// The following files are also required but are not supplied due to copyright: /
//   qromb.c, trapzd.c, polint.c, nrutil.c, and nr.h.                          /
```

```
//  These are the standard Numerical Recipes files.                           /
// In Linux the program can be compiled with the command:                     /
//  gcc qromb.o trapzd.o polint.o nrutil.o collision.c -lm -o collision.e     /
/*****************************************************************************/
#include <stdio.h>
#include <math.h>
#include "nr.h"

/*****************************************************************************/
//  Users should only change values in the next section                       /
/*****************************************************************************/
#define frequency  88631.8470    //frequency of transition in MHz
#define Q 2.*pow(10.,29.)        //produxtion rate x*10^29
#define D 3.36                   //dipole moment in debye
#define S 1.                     //line strength
#define J 0.                     //lower J state
#define Jp 1.                    //upper J state (J')
#define K 1.                     //K quant. num. (only used for symmetric tops)
#define Tmax 10000.              //maximum emectron temperature in K
#define radr (4.1*pow(10.,-4.))  //radiative excit. rate, set to 0. if not using
//only one of the following can be chosen
//#define choice 0                 //linear molecule
//#define choice 1                 //symmetric top
#define choice 2                 //asymmetric top

/*****************************************************************************/
//  Do not change values below this point                                     /
//                                                                            /
//  Constants and conversion factors                                          /
/*****************************************************************************/
#define PI 3.141592654                  //Pi
#define KteV (8.6173*pow(10.0,-5.0))    //convert K to eV
#define eVtK (1.1605*pow(10,4))         //convert eV to K
#define me (9.1093897*pow(10,-28.0))    //mass of electron in g
#define meeV 510999.06                  //mass of electron in eV
#define eVterg (1.6021772*pow(10,-12)) //convert eV to ergs
#define hb (6.582122*pow(10,-16))       //h-bar in eV
#define Hzticm (3.335641*pow(10,-11.0))//convert Hz to cm^-1
#define Dtau 2.542                      //convert debye to a.u.
```

```
//Global variables
double rcs;                       //contact surface radius in km
double rrec;                      //recombination radius in km
double a;                         //variable for joining sections of n_e curve
double b;                         //variable for joining sections of n_e curve
double profile[2000][3];          //output profile(radius, e density, C rate)
int len;                          //length of the radial temperature profile array
double temp[1000][2];             //radial temperature profile (radius,temp)
double T;                         //current electron temperature in eV
int first;                        //first time through
double ta;                        //for temperature profile above rcs
double tb;                        //for temperature profile above rcs
double energy;                    //energy of transition in eV
float Z;                          //constant multiplyer for integral

//function that contains the lower integral x is energy in eV and T is temp in eV
float lowfunc(float x){
  return (float)sqrt(x)*exp(-(x/T));
}

//function that contains the upper integral
//x is in eV
//T is in eV
float func(float x){
  double sigma;                     //cross section
  double E;                         //initial energy of electron
  double Ep;                        //final energy of electron
  E=sqrt(2*meeV*x/(pow(hb,2.0)));
  Ep=sqrt(pow(E,2.0)-2*meeV*energy/(pow(hb,2.0)))*Hzticm;
  E=E*Hzticm;
  sigma=log((E+Ep)/(E-Ep))/pow(E,2.0);
  return (float)(Z*x*sigma*exp(-(x/T)));
}

//function to set up temperature profile
//reads in radial temperature profile from temp.dat
//column 1 is radius in km
//column 2 is temperature in K
```

```
void setup(void){
  FILE *f;
  int i=0;
  int j;
  f=fopen("temp.dat","r");
  if(f){
    while(fscanf(f,"%lf %lf",&temp[i][0],&temp[i][1])!=EOF){
      i++;
    }
    len=i;
    fclose(f);
  }
  else{
    fprintf(stderr,"Cannot open temp.dat\n");
    exit(1);
  }
//calculate the multiplyer depending on type of molecule
  if(choice==0){                         //linear
    Z=(float)(sqrt(2.*eVterg/me)*8.*PI*pow((D/Dtau),2.)*(J+1.)/(3.*(2.*J+1.)));
  }
  else if(choice==1){                    //symmetric top
    Z=(float)(sqrt(2.*eVterg/me)*8.*PI*pow((D/Dtau),2.)*
              (pow(J+1.,2.)-pow(K,2.))/(3.*(J+1.)*(2.*J+1.)));
  }
  else{                                  //asymmetric top
    Z=(float)(sqrt(2.*eVterg/me)*8.*PI*pow((D/Dtau),2.)*(2.*Jp+1.)*
              S/(3.*(2.*Jp+1.)*(2.*J+1.)));
  }
}

//fits function of type a*x^b by solving a+bx
void fitter(void){
  double min,max,diff,diffb;
  min=log10(1.3*pow(10,7.0)*sqrt(Q/(5.0*pow(10,29)))/rcs);
  max=log10(5.6*pow(10,11.0)*sqrt(Q/(5.0*pow(10,29)))/pow(rrec,2.0));
//solve for b then a
  diff=max-min;
  diffb=log10(rrec)-log10(rcs);
  b=diff/diffb;
```

```
  a=pow(10,min-(log10(rcs)*b));
}

//fits function of type ta+tbx
void Tfitter(double radius){
  double diff,diffb;
  diff=Tmax-(T*eVtK);
//solve for b then a
  diffb=2*rcs-radius;
  tb=diff/diffb;
  ta=Tmax-(tb*2*rcs);
}

//function to calculate the electron number density at each radius
void density(int j){
  if(profile[j][0] <= rcs){              //inside contact surface
    profile[j][1]=1.3*pow(10.,7.)*sqrt(Q/(5.*pow(10.,29.)))/profile[j][0];
  }
  else if(profile[j][0] < rrec){         //between rce and rrec
    profile[j][1]=a*pow(profile[j][0],b);
  }
  else{                                 //beyond recombination radius
    profile[j][1]=5.6*pow(10.,11.)*
            sqrt(Q/(5.*pow(10.,29.)))/pow(profile[j][0],2.);
  }
}


//function which calculates the temperature of the electrons in eV
//linearly interpolates between given points
//at radii larger than rcs the temp climbs linearly to Tmax at 2rcs
double gettemp(double radius){
  int i,indx;
  indx=-1;
  if(radius <= rcs){
    for(i=0;i<len-1;i++){               //find the index of the bracketing radii
      if(radius>temp[i][0] && radius<=temp[i+1][0]){
        indx=i;
      }
```

```
    }
    if(indx == -1){                    //if there is no interpolation
      fprintf(stderr,"Error in interpolating temperature profile.\n");
      exit(1);
    }
    T=(((temp[indx+1][1]-temp[indx][1])/(temp[indx+1][0]-temp[indx][0]))*
              (radius-temp[indx][0])+temp[indx][1])*KteV;
  }
  else if(radius <= 2.*rcs){
    if(first==1){
      Tfitter(radius);
    }
    T=(ta+(tb*radius))*KteV;
    first=0;
  }
  else{
    T=Tmax*KteV;
  }
}

//function to calculate the collision rate at each radius
//calculates 2 integrals by calling qromb from Numerical Recipes
void collision(int i, double cutoff,double temperature){
  float top,bottom;
  top=qromb(func,(float)cutoff,20.*(float)T);
  bottom=qromb(lowfunc,(float)cutoff,20.*(float)T);
  profile[i][2]=profile[i][1]*((double)(top/bottom));
}

int main(void){
  int i;
  double temperature;
  FILE *f;
  first=1;
  setup();
  rcs=7300*pow((Q/(5.0*pow(10,29))),0.75);
  rrec=12500*sqrt(Q/(5.0*pow(10,29)));
  fitter();
  energy=frequency*4.1357*pow(10,-9);            //energy of the transition in eV
```

```
  f=fopen("comet.out","w+");                   //output file, will overwrite
  if(f){
    for(i=0;i<2000;i++){
      profile[i][0]=(i+1)*100.;                //set radius
      density(i);                              //set electron number density
      temperature=gettemp(profile[i][0]);      //set electron temperature
      collision(i,(energy*1.00001),temperature); //calculate C
//announce when the transition from collisional to radiative excit. is reached
      if(radr != 0. && radr <= profile[i-1][2] && radr >= profile[i][2]){
        printf("Excitation transition between %i and %i km\n",
               (int)profile[i-1][0],(int)profile[i][0]);
      }
      fprintf(f,"%11.6g  %11.6g  %11.6g  %11.6g  %11.6g  %11.6g\n",profile[i][0],
              log10(profile[i][0]),profile[i][1],log10(profile[i][1]),
              profile[i][2],log10(profile[i][2]));
    }
  }
  else{
    fprintf(stderr,"Cannot open comet.out\n");
    exit(1);
  }
  fclose(f);
}
```

Appendix B

A Survey of Acetic Acid Toward Hot Molecular Cores

By
Anthony Remijan, Lewis E. Snyder, Douglas N. Friedel, Sheng-Yuan Liu & Ronak Y. Shah
2003 ApJ 590 314

The Astrophysical Journal, 590:314–332, 2003 June 10

A SURVEY OF ACETIC ACID TOWARD HOT MOLECULAR CORES

A. Remijan,[1] L. E. Snyder,[1] D. N. Friedel,[1] S.-Y. Liu,[2,3] and R. Y. Shah[1,4]
Received 2002 December 30; accepted 2003 February 21

ABSTRACT

We have surveyed 12 Galactic hot molecular cores for interstellar acetic acid (CH_3COOH). This is the most extensive search for acetic acid to date. We have detected a new source of acetic acid toward the high-mass hot molecular core source G34.3+0.2. Using a temperature range between 70 and 185 K, we find a CH_3COOH column density range of (0.77–1.64) $\times 10^{15}$ cm^{-2} toward G34.3+0.2. This gives a relative $CH_3COOH/HCOOCH_3$ abundance ratio of $\sim 3.3 \times 10^{-2}$, which is comparable to the abundance ratio of (3–6) $\times 10^{-2}$ found toward Sgr B2(N-LMH) and W51e2 by Remijan and colleagues. All currently known acetic acid sources are within 7 kpc of the Galactic center. Furthermore, our survey suggests that hot molecular cores that have a mass range between 200 and 2000 $M_\odot$ and do not show a distinct differentiation between O and N chemistry may be the best places to search for acetic acid and the structurally similar biologically important molecule glycine.

Subject headings: astrochemistry — ISM: abundances — ISM: individual (G34.3+0.2, IRAS 16293−2422, L1448-C, M17-SW, NGC 1333 IRAS 4, NGC 2024 FIR 5, Orion KL, Serpens SMM 1, W3, W49 A) — ISM: molecules

1. INTRODUCTION

There has been great interest in searching a variety of star-forming regions for interstellar acetic acid because it shares common structural elements with glycine (NH_2CH_2COOH), the simplest amino acid, and because it is an isomer to both methyl formate ($HCOOCH_3$) and glycolaldehyde (CH_2OHCHO) (Remijan et al. 2002). The first detection of interstellar acetic acid (CH_3COOH) was made by Mehringer et al. (1997) toward the star-forming region Sgr B2(N-LMH). They successfully detected four transitions of acetic acid at 3 mm wavelengths. Remijan et al. (2002) followed up the initial detection of Mehringer et al. (1997) by detecting two new acetic acid transitions toward Sgr B2(N-LMH) and eight transitions of acetic acid toward the star-forming region W51e2. To extend our survey of acetic acid sources, we carried out observations toward 12 Galactic hot molecular cores that sample both high-mass ($\geq 10\ M_\odot$) and low-mass ($< 10\ M_\odot$) star-forming regions with the Berkeley-Illinois-Maryland Association (BIMA) array.[5]

Two features that identify regions of high-mass star formation are ultracompact (UC) H II regions and H_2O masers (Watt & Mundy 1999). In order to drive the high luminosity of the UC H II region or the pumping for the H_2O maser emission, these regions are believed to lie very close to high-mass (O and B) stars in formation. Dense regions of hot molecular gas are associated with these UC H II regions and H_2O masers. These so-called hot molecular cores (HMCs) have typical molecular hydrogen densities of $n \sim 10^7$ cm^{-3} and temperatures of 100–200 K. To date, the only detections of acetic acid have been toward high-mass star-forming regions [Sgr B2(N-LMH) and W51e2]. Recent observations of low-mass star-forming regions suggest that, like their more massive counterparts, they also contain HMCs where dust and gas temperatures exceed 100 K. These low-mass star-forming regions may also produce complex molecules either at a similar abundance or even in greater abundance than their high-mass counterparts (Ceccarelli et al. 2000b). However, there has been no reported acetic acid detection toward any low-mass star-forming region. Clearly, both the high-mass and low-mass hot, dense regions of molecular gas are ideal sites to search for large molecular species for the following two reasons: first, the high density shields the large molecules from photodissociating UV flux, and second, the high temperatures permit a warm gas-phase chemistry to take place that ordinarily would not occur in cold dark clouds (Ehrenfreund & Charnley 2000).

2. OBSERVATIONS

The acetic acid survey took place from 2000 May to 2002 June utilizing the B, C, and D configurations of the BIMA array. The minimum baseline for these observations was 8 m, and the maximum baseline was 150 m, providing angular resolutions of $\sim 2''$–$15''$. Table 1 lists the observational parameters of our survey. Column (1) lists the sources observed. Column (2) lists the sources used to calibrate the antenna based gains. The absolute amplitude calibration of these sources was based on planetary observations and is accurate to within ~20%. Column (3) lists the observation date. Columns (4) and (5) give the array configuration and corresponding beam size. Column (6) lists the approximate 1 σ channel rms noise level in the window containing our acetic acid transition. In § 2.1, we describe the sources surveyed for acetic acid. The sources are listed in order of increasing right ascension. In § 2.2, we describe the spectral parameters of our observations.

[1] Department of Astronomy, University of Illinois, Urbana, IL 61801; aremijan@astro.uiuc.edu, snyder@astro.uiuc.edu, friedel@astro.uiuc.edu.
[2] Department of Astronomy, California Institute of Technology, Pasadena, CA 91125.
[3] Current address: Institute of Astronomy and Astrophysics, Academia Sinica, P.O. Box 23-141, Taipei 106, Taiwan, Republic of China; syliu@asiaa.sinica.edu.tw.
[4] Current address: Boston University and the Institute for Astrophysical Research, Boston, MA 02215; ronak@bu.edu.
[5] Operated by the University of California, Berkeley, the University of Illinois, and the University of Maryland with support from the National Science Foundation.

TABLE 1
Observational Parameters

Source (1)	Gain Calibrator (2)	Observation Date (3)	Array (4)	Beam (arcsec) (5)	Channel rms (Jy beam^{-1}) (6)
W3(H_2O)	0228+673	2000 May 22	D	21.5 × 15.3	0.35
		2000 May 28	D	16.2 × 14.7	0.10
		2000 Jun 2	D	18.8 × 14.6	0.15
		2001 Nov 9	C	6.9 × 6.3	0.10
L1448-C	0237+288	2002 Apr 1	C	7.5 × 6.2	0.05
NGC 1333 IRAS 4	0237+288	2002 Mar 17	B	3.0 × 2.0	0.07
		2002 Apr 20	C	7.2 × 6.0	0.07
Orion KL	0530+135	2001 Mar 25	C	11.5 × 8.5	0.15
		2001 May 25	C	11.1 × 6.3	0.14
		2001 Apr 17	C	9.6 × 5.6	0.20
NGC 2024 FIR 5	0609−157	2000 Jun 11	D	20.0 × 15.1	0.06
		2002 Mar 18	B	3.9 × 2.0	0.10
		2002 Apr 21	C	9.6 × 6.1	0.13
IRAS 16293−2422	1625−254	2002 Mar 20	B	5.8 × 1.8	0.40
		2002 Apr 11	C	14.6 × 5.5	1.00
		2002 May 05	C	14.3 × 5.6	0.50
M17-SW	1733−130	2000 May 18	D	24.3 × 16.7	0.35
Serpens SMM 1	1733−130	2002 Mar 25	B	3.8 × 1.9	0.10
		2002 Apr 28	C	8.7 × 6.3	0.08
		2002 Jun 11	D	18.7 × 15.8	0.10
G34.3+0.2	1830+063	2000 May 26	D	18.9 × 15.2	0.20
		2000 Jun 5	D	18.7 × 15.2	0.20
		2000 Jun 19	D	18.8 × 15.3	0.35
		2000 Jun 27	D	19.1 × 15.0	0.40
		2001 Nov 26	C	8.8 × 6.6	0.14
W49 A	1830+063	2000 Jun 18	D	17.9 × 15.8	0.21

2.1. *Sources*

Table 2 lists the 12 sources surveyed for acetic acid in column (1). Columns (2) and (3) list the pointing center for each observation. Columns (4) and (5) list the distance to each source from the Sun and the distance to each source from the Galactic center (Galactocentric), respectively. The Galactocentric distance to each source was calculated using the accepted distance to the Galactic center (8.5 kpc; Reid 1993), the measured distance to each source, and finally, the Galactic longitude of the source. Galactic longitude can be found from the source's right ascension. Finally, columns (6) and (7) list the kinetic temperature and mass of each star-forming region. The criteria for selecting the sources were (1) they represent a sample of both high-mass and low-mass star-forming regions; (2) many have been searched for small molecular species; (3) they have a large amount of dust continuum emission; and (4) a few have molecular species that are possible precursor species to the formation of acetic acid. We discuss each source in detail below.

2.1.1. *W3*(H_2O) *and W3*(OH)

The two most prominent components toward W3, where large molecular species have primarily been found, are coincident with OH and H_2O maser emission, respectively: W3(OH) ($\alpha = 2^h27^m03\overset{s}{.}9$, $\delta = 61°52'24\overset{''}{.}6$ [J2000.0]) and W3(H_2O) ($\alpha = 2^h27^m04\overset{s}{.}6$, $\delta = 61°52'25\overset{''}{.}5$ [J2000.0]). The W3(H_2O) source is often referred as the "hot core" source in this region (Wyrowski et al. 1999). It contains an order-of-magnitude higher abundance of organic molecules such as methanol (CH_3OH), dimethyl ether (CH_3OCH_3), and methyl formate ($HCOOCH_3$) than any other source within W3 (Helmich & van Dishoeck 1997). From aperture synthesis, it was found that there was a very compact core (<1″) centered on H_2O. It was further argued that the heating of H_2O could not be provided by W3(OH). Thus, it must itself be a site of star formation (Turner & Welch 1984).

2.1.2. *L1448-C*

L1448-C ($\alpha = 3^h25^m38\overset{s}{.}9$, $\delta = 30°44'05\overset{''}{.}1$ [J2000.0]) is the very young stellar object that is the powering source of the highly collimated bipolar outflow L1448. In previous large molecule surveys, we have included only high-mass HMCs, such as Sgr B2(N-LMH) or W51e2. However, the environment around low-mass protostars and young stellar objects is favorable for the formation and survival of complex species (see § 1). The L1448 outflow is located in a region traced by H_2O masers, four compact radio continuum sources, three *IRAS* sources, several high-velocity CO outflows, and regions of ammonia (NH_3) condensations (Curiel et al. 1999). Recently, Liu et al. (2002) showed that formic acid (HCOOH), a possible precursor for the formation of acetic acid, was present in shocked regions near the boundary of dense molecular gas. Therefore, the regions around the bipolar outflows also appear to be good locations to search for complex molecular species.

2.1.3. *NGC 1333 IRAS 4*

NGC 1333 IRAS 4 ($\alpha = 3^h29^m10\overset{s}{.}3$, $\delta = 31°13'31\overset{''}{.}7$ [J2000.0]) is a well-studied star-forming region in the L1450 dark cloud located at a distance of 350 pc. There are at least five young stellar objects observed in the dust continuum with IRAS 4 driving a well-collimated bipolar outflow. An

TABLE 2

Hot Cores and Their Physical Parameters

Source Name (1)	R.A. (J2000.0) (2)	Decl. (J2000.0) (3)	Distance (kpc) (4)	Galactocentric Distance (kpc) (5)	T_e (K) (6)	Mass ($M_\odot$) (7)
High-Mass Star-forming Regions						
$W3(H_2O)$[a]	02 27 04.6	61 52 25.5	2.20	10.2	150–200	15
W3(OH)[b]	02 27 03.9	61 52 24.6	2.20	10.2	150	~30[c]
Orion hot core[d]	05 35 14.5	-05 22 30.0	0.45	8.9	250	580[e]
Orion compact ridge[f]	05 35 14.2	−05 22 41.0	0.45	8.9	90	580[e]
M17-SW	18 20 27.6	−16 12 00.9	1.60[g]	7.0	200[g]	~11500[h]
G34.3+0.2[i]	18 53 18.6	01 14 58.0	3.80	5.8	70–185[j]	1400
W49 A[k]	19 07 50.0	9 01 20.0	11.4	7.8	150	$\sim 10^5$
Low-Mass Star-forming Regions						
L1448C[l]	03 25 38.9	30 44 05.1	0.30	8.8	25	0.8
NGC 1333 IRAS4[m]	03 29 10.3	31 13 31.7	0.35	8.9	40	1.0
NGC 2024 FIR5[n]	05 41 44.3	−01 22 40.7	0.42	8.9	30	5.1
IRAS 16293−2422[o]	16 32 22.8	−24 28 33.0	0.16	8.3	40	5.4
Serpens SMM 1[p]	18 29 49.6	01 15 27.8	0.22	8.3	30	3–5

Note.—Units of right ascension are hours, minutes, and seconds, and units of declination are degrees, arcminutes, and arcseconds.

[a] Wyrowski et al. 1999.
[b] Sutton et al. 2001.
[c] E. Sutton 2003, private communication.
[d] Wilner et al. 1994.
[e] The calculated mass is for the entire Orion KL region.
[f] Blake et al. 1987.
[g] Nielbock et al. 2001.
[h] Goldsmith, Bergin, & Lis 1997.
[i] Kurtz et al. 2000.
[j] Garay & Rodriguez 1990.
[k] Buckley & Ward-Thompson 1996.
[l] Barsony et al. 1998.
[m] DiFrancesco et al. 2001.
[n] Visser et al. 1998.
[o] Schöier et al. 2002.
[p] McMullin et al. 2000.

extensive survey of this region was performed by Blake et al. (1995) at 1 mm wavelengths. Their observations detected several molecular species including CO, CS, SiO, SO, HCN, DCN, HNC, HCO^+, DCO^+, N_2H^+, CH_3OH, and formaldehyde (H_2CO). Thus, the IRAS 4 region is rich in molecular species. In fact, the measured abundances of CH_3OH and H_2CO were 10–100 times higher than the abundances measured in the Orion plateau region.

2.1.4. *Orion KL*

Orion KL is the nearest (~450 pc) massive star-forming region observed in our survey. Early infrared (IR) studies (Wynn-Williams et al. 1984; Genzel & Stutzki 1989) and molecular line surveys (Johansson et al. 1984; Sutton et al. 1985; Turner 1989, 1991) revealed numerous structures that possessed a complex interstellar chemistry. Recent interferometric observations showed that most of the large molecular line detections have come either from the "hot core" ($\alpha = 5^{\mathrm{h}}35^{\mathrm{m}}14^{\mathrm{s}}.5$, $\delta = -5^\circ 22' 30''$ [J2000.0]; Blake et al. 1995) or the "compact ridge" ($\alpha = 5^{\mathrm{h}}35^{\mathrm{m}}14^{\mathrm{s}}.2$, $\delta = -5^\circ 22' 41''$ [J2000.0]; Liu, Mehringer, & Snyder 2001; Liu et al. 2002). Recently, Liu et al. (2002) mapped HCOOH toward the Orion compact ridge. The distribution of HCOOH emission traces a layer that delineates the surface of interaction between the outflow material and the ambient quiescent cloud. HCOOH was also detected toward the hot core.

2.1.5. *NGC 2024 FIR 5*

NGC 2024 FIR 5 ($\alpha = 5^{\mathrm{h}}41^{\mathrm{m}}44^{\mathrm{s}}.3$, $\delta = -01^\circ 22' 40''.7$ [J2000.0]) is a well-studied star-forming region located about 415 pc away. High-resolution measurements show a string of seven high-density cores, labeled FIR 1–FIR 7, embedded in a ridge of molecular emission (Mangum, Wootten, & Barsony 1999). There have been many surveys of simple molecules, such as CO, CS, H_2CO, HCN, HCS, NH_3, and methyl cyanide (CH_3CN) (Schulz et al. 1991; Mauersberger et al. 1992; Chandler & Carlstrom 1996; Mangum et al. 1999), which show peaks close to the dust emission peaks. However, there has not been any survey of large complex molecules toward this region despite its large abundance of dust.

2.1.6. *IRAS 16293−2422*

IRAS 16293−2422 ($\alpha = 16^{\mathrm{h}}32^{\mathrm{m}}22^{\mathrm{s}}.8$, $\delta = -24^\circ 28' 33''$ [J2000.0]) was searched recently for interstellar glycine (Ceccarelli et al. 2000b). The observations of IRAS 16293 indicate that it is chemically similar to more massive hot cores (Ceccarelli et al. 2000a, 2000c; Boogert et al. 2000). Schöier et al. (2002) found the molecular abundances toward IRAS 16293 were an order of magnitude smaller than what was found in most interstellar ices but are comparable to what is observed toward high-mass hot cores. Specifically, the fractional abundances of molecular species such as HC_3N, HNCO, and CH_3OH are similar to what is found toward the Orion hot core. In addition, many species are more abundant in low-mass protostars than in their high-mass counterparts. For example, deuterated formaldehyde (D_2CO) and H_2CO are 20 and 100 times more abundant, respectively, in IRAS 16293 than in the high-mass cores of Orion (Ceccarelli et al. 2000b).

2.1.7. *M17-SW*

M17-SW ($\alpha = 18^h20^m27^s.6$, $\delta = -16°12'00''.9$ [J2000.0]) was extensively studied by Bergin et al. (1997). Their observations determined the abundances of over 20 different molecules and isotopic variants in the cores of Orion A, M17, and Cepheus A. Their molecular survey included molecules such as CS, CN, C_2H, HCO^+, methyl acetylene (CH_3C_2H), cyanoacetylene (HC_3N), SO, CH_3OH, HCN, HNC, and cyclopropenylidene (C_3H_2) (Bergin et al. 1997). The M17-SW core is a site of ongoing star formation as evidenced by IR emission from embedded stars. Recently, there have been observations of the 3–12 μm dust emission features and possible features from polycyclic aromatic hydrocarbons (PAHs) (Crété et al. 1999).

2.1.8. *Serpens SMM 1*

The Serpens SMM 1 ($\alpha = 18^h29^m49^s.6$, $\delta = 01°15'27''.8$ [J2000.0]) region was studied extensively by McMullin et al. (2000). They utilized both single-element radio telescope data and interferometric data in order to sample spatial scales between 10′ and 10″; the detected molecular species included DCO^+, DCN, H_2CO, SO, SO_2, HCN, HCO, SiO, CO, and CH_3OH. The results show strong emission lines of CH_3OH and H_2CO, suggesting a strong similarity between the Serpens cores and IRAS 16293−2422.

2.1.9. *G34.3+0.2*

G34.3+0.2 ($\alpha = 18^h53^m18^s.6$, $\delta = 01°14'58''$ [J2000.0]) was the first discovered UC H II region with a "cometary" morphology (Reid & Ho 1985). It is believed that the cometary morphology is shaped by O- and B-type stars moving supersonically through the ambient molecular gas. The G34.3+0.2 region contains a cluster of OH masers that are located at the "head" of the UC H II cometary region (Zheng, Moran, & Reid 2000). Just to the east of the UC H II region and the OH maser emission lies a hot, compact molecular core. This hot core was studied extensively by Mehringer & Snyder (1996). Their study showed an array of complex molecular species including vinyl cyanide (CH_2CHCN), CH_3OH, $HCOOCH_3$, ethanol (CH_3CH_2OH), CH_3OCH_3, and ethyl cyanide (CH_3CH_2CN) (Mehringer & Snyder 1996). Nummelin et al. (1998) made observations of ethylene oxide (c-C_2H_4O) and its structural isomer CH_3CHO. They also detected and analyzed several transitions of CH_3OH, CH_3OCH_3, CH_3CH_2OH, and HCOOH.

2.1.10. *W49 A*

W49 A ($\alpha = 19^h07^m50^s.0$, $\delta = 9°01'20''.0$ [J2000.0]) has been identified as an active star-forming region (Dickel & Goss 1990). The large abundance of molecular and ionized gas makes it a prime target to investigate the interaction between a newly forming star and its environment. There have been extensive studies of the continuum emission, recombination lines, molecular lines, H_2O masers, and OH masers in this region. The molecular line surveys toward this region include small molecules such as CS, CO, and NH_3 (Scoville & Solomon 1973; de Pree, Mehringer, & Goss 1997). However, there has never been any survey of this region for large molecules such as CH_3COOH.

2.2. *Spectral Parameters*

Table 3 lists the molecular parameters of all the 25 observed transitions in our survey. Column (1) lists the transition, and column (2) lists the calculated rest frequency and its 2 σ standard deviation; column (3) lists the product of the line strength and the square of the relevant dipole moment, and column (4) lists the upper-state energy level of each transition. Except for the Orion KL region, each correlator configuration included the two strongest ($10_{*,10}$–$9_{*,9}$ *A* and *E*) acetic acid transitions at 111.5 GHz, the methyl formate ($HCOOCH_3$) transitions at 107.5 and 111.5 GHz, and the ethyl cyanide (CH_3CH_2CN), formic acid (HCOOH), and deuterated methanol (CH_3OD) transitions in the passband. The spectral window containing these transitions had a bandwidth of 50 MHz and was divided into 128 channels for a spectral resolution of 0.39 MHz per channel. Toward Orion KL, we were able to use a single pointing to search both the compact ridge and the hot core region for the $8_{*,8}$–$7_{*,7}$ (90.2 GHz), $9_{*,9}$–$8_{*,8}$ (100.9 GHz), and the $10_{*,10}$–$9_{*,9}$ (111.5 GHz) *A* and *E* lines of CH_3COOH; the $8_{0,8}$–$7_{0,7}$ (90.2 GHz) *A* and *E* lines of $HCOOCH_3$; and the C_2H, CH_3OH, and CH_2CHCN lines in the passband. The spectral windows containing the CH_3COOH lines had a bandwidth of 25 MHz and were divided into 256 channels for a spectral resolution of 0.098 MHz per channel. We also used a wider bandwidth of 50 MHz divided into 128 channels for a spectral resolution of 0.39 MHz per channel. This was done to identify an approximate baseline for the continuum subtraction. All data were combined, imaged, and self-calibrated using the MIRIAD software package (Sault, Teuben, & Wright 1995). To include all the data from a source with multiple tracks or in multiple arrays, the data were inverted in *u*-*v* space. The resulting synthesized beam size was determined using the largest baseline of the combined data set. The 1 σ rms noise level of the final maps was used to set upper limits to the column densities of the molecular species searched for in our survey.

3. RESULTS

The 12 sources in Table 2 were surveyed for acetic acid, as well as selected molecular transitions of other large molecular species listed in Table 3 (see § 2.2). Only G34.3+0.2 has an acetic acid detection. Furthermore, only this source, the Orion hot core and the compact ridge, and W3(H_2O) and W3(OH) were detectable sources of any of the other molecular transitions listed in Table 3. In § 3.1, we discuss the spectral lines detected toward G34.3+0.2 including the first detection of acetic acid and formic acid. In §§ 3.2 and 3.3, we discuss the spectral lines detected toward Orion KL and W3, respectively. We were able to set acetic acid column density upper limits for all the sources, except G34.3+0.2, on the basis of the 1 σ rms noise level and using the rest

TABLE 3
Molecular Line Parameters

Transition (1)	Frequency (MHz) (2)	$\langle S_{i,j}\mu^2\rangle$ (Debye^2) (3)	E_u (K) (4)
CH_3COOH[a]			
$8_{*,8}$–$7_{*,7}$ E	90,203.444(40)[b]	43.2	20.3
$8_{*,8}$–$7_{*,7}$ A	90,246.250(40)	43.2	20.3
$9_{*,9}$–$8_{*,8}$ E	100,855.437(40)	48.9	25.2
$9_{*,9}$–$8_{*,8}$ A	100,897.459(40)	48.9	25.2
$10_{*,10}$–$9_{*,9}$ E	111,507.270(40)	54.8	30.5
$10_{*,10}$–$9_{*,9}$ A	111,548.533(40)	54.8	30.5
$HCOOCH_3$[c]			
$8_{0,8}$–$7_{0,7}$ E	90,227.595(24)	21.0	20.0
$8_{0,8}$–$7_{0,7}$ A	90,229.647(26)	21.0	20.0
$9_{2,8}$–$8_{2,7}$ E	107,537.189(24)	22.8	28.8
$9_{2,8}$–$8_{2,7}$ A	107,543.746(26)	22.8	28.8
$9_{4,5}$–$8_{4,4}$ A	111,453.327(24)	19.4	37.3
$13_{1,12}$–$13_{0,13}$ A	111,492.462(100)	1.4	54.7
CH_3CH_2CN[d]			
$12_{8,5}$–$11_{8,4}$	107,491.573(28)	98.8	104.7
$12_{8,4}$–$11_{8,3}$	107,491.573(28)	98.8	104.7
$12_{5,8}$–$11_{5,7}$	107,502.426(26)	147.0	61.4
$12_{5,7}$–$11_{5,6}$	107,502.474(26)	147.0	61.4
$12_{4,9}$–$11_{4,8}$	107,543.926(26)	158.1	51.4
$12_{4,8}$–$11_{4,7}$	107,547.601(26)	158.1	51.4
$12_{3,10}$–$11_{3,9}$	107,594.049(28)	166.8	43.6
C_2H[e]			
$N = 1$–0 $(3/2,2$–$1/2,1)$	87,317.05(36)	0.6	4.2
$N = 1$–0 $(3/2,1$–$1/2,0)$	87,328.70(38)	0.6	4.2
HCOOH[f]			
$5_{1,5}$–$4_{1,4}$	108,126.710(160)	9.3	18.8
CH_3OH[g]			
24_6–23_7 $A+/-$	98,030.396(236)	6.4	889.8
CH_3OD[h]			
4_1–4_0 $E1$	110,950.750(2382)	5.1	30.8
CH_2CHCN[i]			
$9_{1,8}$–$8_{1,7}$	87,312.821(34)	120.3	23.2

[a] Each of the CH_3COOH lines consists of two *a*-type and two *b*-type degenerate transitions. The listed $\langle S_{i,j}\mu^2\rangle$ value is the sum of all four transitions in each group. This degeneracy is indicated by the asterisk substituted for the *K* quantum numbers (Ilyushin et al. 2001; F. J. Lovas 2001, private communication; I. Kleiner 2001, private communication); $Q_r = 14.10T_r^{3/2}$.

[b] The error in the frequency is 2 σ uncertainty for the calculated frequency in MHz. This holds for all transitions.

[c] Rest frequencies of methyl formate taken from Oesterling et al. 1999; $Q_r = 12.45T_r^{3/2}$.

[d] Rest frequencies of ethyl cyanide taken from Lovas 1982; $Q_r = 7.17T_r^{3/2}$.

[e] Rest frequencies of C_2H taken from Tucker, Kutner, & Thaddeus 1974.

[f] Rest frequencies of formic acid taken from Willemot et al. 1980; $Q_r = 1.71T_r^{3/2}$.

[g] Rest frequencies of CH_3OH taken from Xu & Lovas 1997; $Q_r = 1.23T_r^{3/2}$.

[h] Rest frequencies of CH_3OD taken from Anderson et al. 1988; $Q_r = 0.71T_r^{3/2}$.

[i] Rest frequencies of vinyl cyanide taken from Gerry, Yamada, & Winnewisser 1979; $Q_r = 5.05T_r^{3/2}$.

frequency of the $10_{*,10}$–$9_{*,9}$ A acetic acid line (111.5485 GHz). Table 4 summarizes our results. Column (1) lists the source, and column (2) lists the 1 σ rms noise level of the combined data set in each window. We used this value as an upper limit to the line intensity (Jy beam^{-1}) of the acetic acid transition for the sources with no detectable acetic acid. Column (3) is the upper limit to the line intensity of the acetic acid transition in temperature units (K) (see Appendix). Columns (4) and (5) list the excitation temperatures (K) and corresponding specific intensities (Jy beam^{-1}) of each source. Column (6) lists the specific intensity (Jy beam^{-1}) of the total background continuum contribution from each source. Column (7) lists line widths (km s^{-1}) used in our column density determinations. Columns (8) and (9) list the major and minor axes of the synthesized beam (arcseconds) of the combined data sets. Columns (10) and (11) list the optical depths and optical depth correction factors of each transition, respectively. Finally, column (12) lists the acetic acid column density (cm^{-2}) results for all our sources. The discussion of how the optical depths, the optical depth correction factors, and column densities for all the molecular species were determined is in § 4.1 and in the Appendix.

3.1. *G34.3+0.2*

Figure 1*a* shows the first detection of CH_3COOH (AcA) toward G34.3+0.2 (Hanning-smoothed over three channels). The spectral line labels located in the upper left of each window correspond to the rest frequency for a v_{LSR} of 57 km s^{-1}. The 1 σ rms noise level is seen at the left of each spectral window. Also included in the spectra are several unidentified features as well as the 111.509 GHz $H^{13}COOH$ $5_{0,5}$–$4_{0,4}$ transition. Many of these features were also seen in the spectra toward Sgr B2(N-LMH) and W51e2 (Remijan et al. 2002). Figures 1*b* and 1*c* show the maps of the $10_{*,10}$–$9_{*,9}$ E and A lines of acetic acid in contours, respectively. The gray scale in each figure is the 111.5 GHz continuum emission of the G34.3+0.2 region. The offset in emission peaks of the acetic acid emission is not significant given the size of the synthesized beam (seen at the bottom left of Fig. 1*c*). Figure 2*a* shows the first detection of HCOOH toward G34.3+0.2. The spectral line labels are similar to Figure 1*a*. Figure 2*b* shows the map of the $5_{1,5}$–$4_{1,4}$ transition of formic acid (*contours*) on top of the 108.1 GHz continuum emission (*gray scale*). Figures 3*a*–3*d* show the detection of several transitions of CH_3CH_2CN (EtCN) and $HCOOCH_3$ (MeF). The spectral line labels are similar to Figure 1*a*. Figure 3*e* shows the distribution of the 107.502 GHz CH_3CH_2CN (EtCN) emission (*contours*) on the 3 mm continuum emission (*gray scale*) toward the G34.3+0.2 region. Similarly, Figure 3*f* shows the distribution of the 107.537 GHz $HCOOCH_3$ (MeF) emission. Finally, Figure 3*g* shows the first detection of deuterated methanol (CH_3OD) toward G34.3+0.2. The relative agreement in peak positions (within one synthesized beam of the 3 mm continuum emission) of CH_3COOH, $HCOOCH_3$, HCOOH, and CH_3CH_2CN strongly indicates that all the molecular emission is coming from a common source. Table 5 lists the molecular species that were detected toward G34.3+0.2 at or near the systemic velocity (57 km s^{-1}). Least-squares Gaussian fits were made for each spectral line in order to obtain the radial velocities, peak intensities, and line widths for the detected transitions. In Table 5, column (1) lists either the calculated rest frequencies of previously

TABLE 4

ACETIC ACID (CH_3COOH) COLUMN DENSITIES

Source Name	ΔI (Jy beam^{-1})	T_L (K)	T_e (K)	$I(T_e)$ (Jy beam^{-1})	I_b (Jy beam^{-1})	dv (km s^{-1})	θ_a (arcsec)	θ_b (arcsec)	τ ($\times 10^{-3}$)	C_τ	N_T[a] ($\times 10^{15}$cm^{-2})
High-Mass Star-forming Regions											
$W3(H_2O)$	0.05	0.23	150–200	33.2–44.3[b]	3.5	6	6.9	6.3	2–1[b]	1.00	<0.66–0.93[b]
W3(OH)	0.05	0.23	150	33.2	3.5	4	6.9	6.3	2	1.00	<0.44
Orion (HC)[c]	0.1	0.37	250	68.5	1.0	6	9.6	5.6	1	1.00	<1.91
Orion (CR)[d]	0.1	0.37	90	24.7	1.0	4	9.6	5.6	4	1.00	<0.35
M17-SW	0.3	0.14	200	413.9	1.6	6	24.3	16.7	0.7	1.00	<0.56
G34.3+0.2	0.3	0.95	70–185	20.7–54.8[b]	9.3	2.5	8.8	6.6	27–10[b]	1.02–1.00[b]	0.77–1.64[b]
W49 A	0.2	0.14	150	216.3	1.1	6	17.9	15.8	0.9	1.00	<0.36
Low-Mass Star-forming Regions											
L1448C	0.06	0.25	25	5.9	0.08	2	7.5	6.2	10	1.01	<0.04
NGC 1333 IRAS4	0.05	1.63	40	1.2	0.20	2	3.0	2.0	50	1.03	<0.42
NGC 2024 FIR5	0.09	2.26	30	1.2	0.26	2	3.9	2.0	101	1.05	<0.53
IRAS 16293−2422	0.3	5.63	40	2.1	0.70	2	5.8	1.8	236	1.12	<1.97
Serpens SMM 1	0.05	1.36	30	1.1	0.19	2	3.8	1.9	56	1.03	<0.30

[a] All CH_3COOH (AcA) abundances are upper limits based on the 1 σ rms noise level in the window where the AcA transition was located except for G34.3+0.2, where the AcA lines were detected (Table 5).

[b] The upper and lower bounds of the specific intensities, opacities, optical depth correction factors, and column densities are based on the upper and lower limits of the given temperature range.

[c] Orion hot core.

[d] Orion compact ridge.

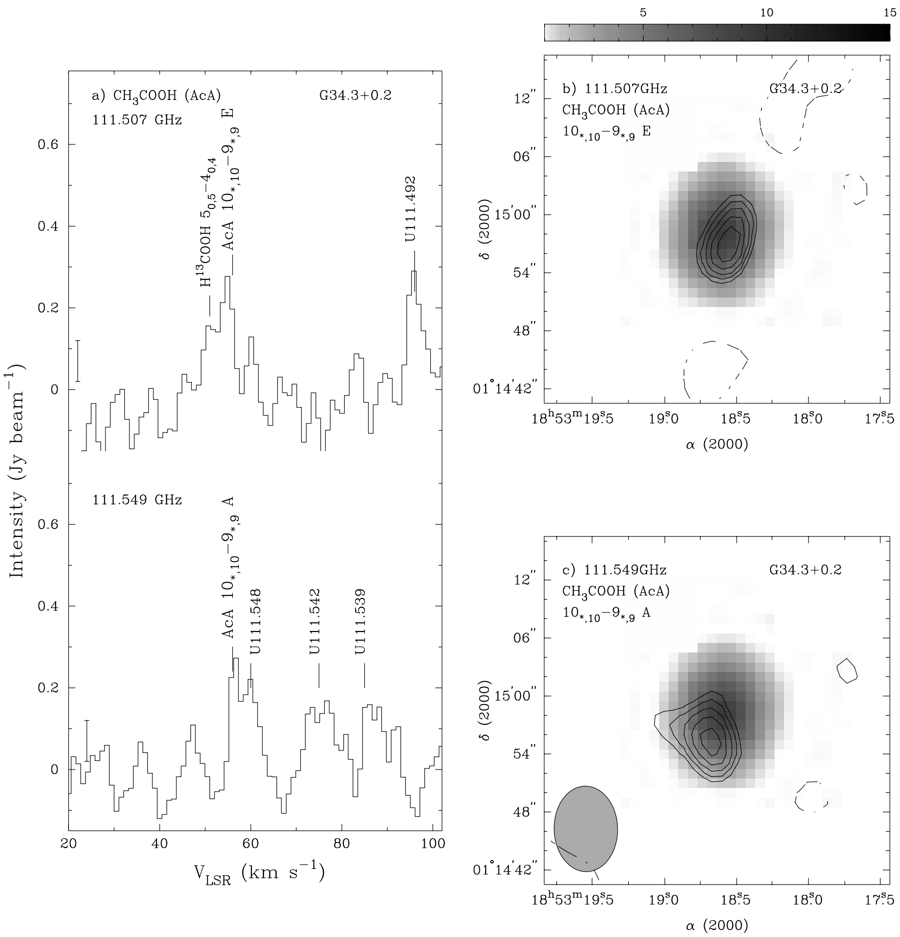

FIG. 1.—(*a*) CH_3COOH (AcA) spectra toward G34.3+0.2 (Hanning-smoothed over three channels). The rms noise level is ~80 mJy beam^{-1} (indicated by the vertical bar at the left of each spectrum). The spectral line labels correspond to the rest frequency located at the top left of each spectral window for a v_{LSR} of 57 km s^{-1}. (*b*) Emission contours from the $10_{*,10}$–$9_{*,9}$ *E* transition of CH_3COOH at 111.507 GHz overlaid on the G34.3+0.2 continuum emission at 111.5 GHz (*gray scale*). The numbers on the gray-scale wedge are in units of Jy beam^{-1}. Contours indicate the location of the CH_3COOH emission averaged between 56 and 58 km s^{-1}. At 111.507 GHz, the contour levels are −0.300, 0.225, 0.250, 0.275, 0.300, and 0.325 Jy beam^{-1}. (*c*) Emission contours from the $10_{*,10}$–$9_{*,9}$ *A* transition of CH_3COOH at 111.549 GHz overlaid on the G34.3+0.2 continuum emission at 111.5 GHz, as in (*b*). The CH_3COOH contour levels are −0.200, 0.225, 0.250, 0.275, 0.300, and 0.325 Jy beam^{-1}. The synthesized beam of 8″.8 × 6″.6 is indicated at the bottom left corner.

identified species or the observed frequencies of unidentified species. Columns (2) and (3) list the molecular species and associated transitions, respectively. Columns (4) and (5) list the fitted line intensities in units of specific intensity and temperature, respectively. Column (6) lists the full power line widths at half-maximum intensities. Finally, columns (7) and (8) list the calculated optical depth of each transition and the optical depth correction factor for $T_e = 70$ and 185 K, respectively.

3.2. *Orion KL*

Figures 4*a* and 4*b* show the spectra for the six transitions of acetic acid outlined in Table 3 toward the Orion compact ridge and the Orion hot core, respectively. Even though no acetic acid transition was detected beyond our 1 σ detection limit, the spectra show the dangers of identifying a new molecular species with a single transition. If several transitions were not observed toward the compact ridge, one might have mistaken U90.203 as the $8_{*,8}$–$7_{*,7}$ *E* transition of acetic acid. This unidentified emission feature was also seen by Mehringer et al. (1997) and Remijan et al. (2002) toward Sgr B2(N-LMH) and W51e2, respectively. Figure 5 shows the spectra of CH_2CHCN (VyCN), C_2H, $HCOOCH_3$ (MeF), and CH_3OH taken toward the Orion hot core and the corresponding maps of CH_2CHCN (VyCN) and CH_3OH. Figure 5*a* shows the detection of CH_2CHCN (VyCN) toward the Orion hot core. The spectral line labels located in the upper left of each window correspond to the rest frequency for a v_{LSR} of 9 km s^{-1} (*dashed line*). The 1 σ rms noise level is seen at the left of each spectral

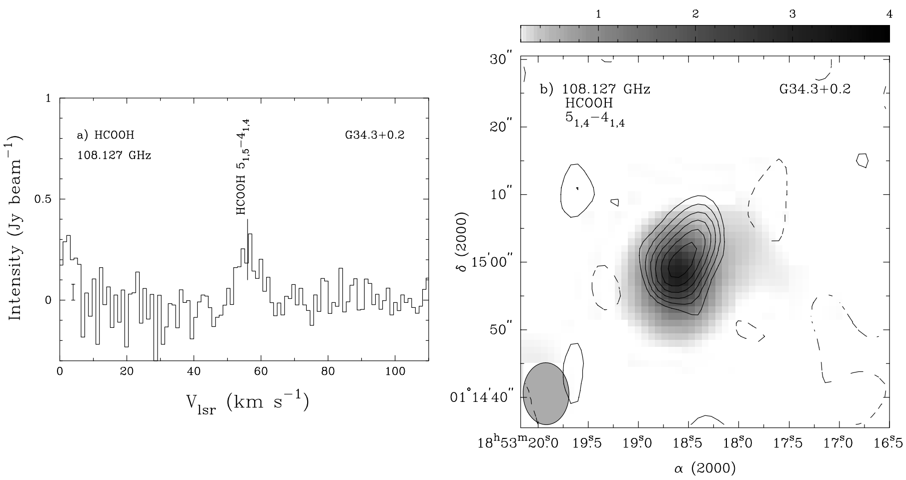

Fig. 2.—(*a*) HCOOH spectrum toward G34.3+0.2. The rms noise level is ~70 mJy beam^{-1} (indicated by the vertical bar at the left of the spectrum). The spectral line label corresponds to the rest frequency located at the top left of the spectral window for a v_{LSR} of 57 km s^{-1}. (*b*) Emission contours from the $5_{1,5}$–$4_{1,4}$ transition of HCOOH at 108.127 GHz overlaid on the G34.3+0.2 continuum emission at 108.1 GHz (*gray scale*). The numbers on the gray-scale wedge are in units of Jy beam^{-1}. Contours indicate the location of the HCOOH emission averaged between 56 and 58 km s^{-1}. The contour levels are −0.08, 0.12, 0.16, 0.20, 0.24, 0.28, and 0.32 Jy beam^{-1}. The synthesized beam of 9."2 × 6."8 is indicated at the bottom left corner.

window. Also seen in this passband are two transitions of C_2H in absorption toward the hot core. The corresponding map of the CH_2CHCN transition (Fig. 5*d*) shows that the emission contours are centered on the Orion hot core. Figure 5*b* shows the detection of $HCOOCH_3$ toward the Orion hot core, and Figure 5*c* shows a methanol (CH_3OH) transition with its corresponding map (Fig. 5*e*) centered also near the hot core.

TABLE 5
G34.3+0.2 Molecular Line Identifications

						$T_e = 70$ K		$T_e = 185$ K	
ν (MHz)	Species	Transition	ΔI (Jy beam^{-1})	T_L (K)	dv (km s^{-1})	τ ($\times 10^{-3}$)	C_τ	τ ($\times 10^{-3}$)	C_τ
107,491.6....	EtCN[a]	$12_{8,*}$–$11_{8,*}$	1.6	5.82	4.8	180	1.09	40	1.02
107,502.4....	EtCN	$12_{5,*}$–$11_{5,*}$	2.4	8.72	7.1	280	1.15	60	1.03
107,520	U107.520		0.8		7.8				
107,537.2....	MeF[b]	$9_{2,8}$–$8_{2,7}$ E	1.4	5.09	4.2	160	1.08	40	1.02
107,543.7....	MeF	$9_{2,8}$–$8_{2,7}$ A	1.6	5.81	5.6[c]	170	1.06	40	1.02
107,543.9....	EtCN	$12_{4,9}$–$11_{4,8}$	1.0	3.63	4.9[c]	160	1.08	20	1.01
107,547.6....	EtCN	$12_{4,8}$–$11_{4,7}$	1.5	5.45	4.2	160	1.08	40	1.02
107,594.1....	EtCN	$12_{3,10}$–$11_{3,9}$	1.3	4.72	8.9[c]	140	1.07	30	1.02
107,604	U107.604		0.6		6.2				
108,126.7....	HCOOH	$5_{1,5}$–$4_{1,4}$	0.3	1.08	5.7	20	1.01	10	1.00
110,950.8....	CH_3OD	4_1–4_0 E1	0.3	1.02	3.7	30	1.01	10	1.00
111,453.3....	MeF	$9_{4,5}$–$8_{4,4}$ A	1.7	5.75	6.0	160	1.08	40	1.02
111,492	U111.492		0.3		3.1				
111,507.3....	AcA[d]	$10_{*,10}$–$9_{*,9}$ E	0.3	1.01	2.5	30	1.02	6	1.00
111,508.6[e] ..	$H^{13}COOH$	$5_{0,5}$–$4_{0,4}$	0.2	0.83	2.5	30	1.01	10	1.00
111,539	U111.539		0.2		4.2				
111,542	U111.542		0.2		4.1				
111,548	U111.548		0.2		2.2				
111,548.5....	AcA	$10_{*,10}$–$9_{*,9}$ A	0.3	1.01	2.2	30	1.02	6	1.00

[a] EtCN = ethyl cyanide (CH_3CH_2CN).
[b] MeF = methyl formate ($HCOOCH_3$).
[c] Blended line.
[d] AcA = acetic acid (CH_3COOH).
[e] The rest frequency coincides with the $5_{0,5}$–$4_{0,4}$ transition of $H^{13}COOH$ at a frequency of 100,508.63 MHz (Pickett et al. 1998).

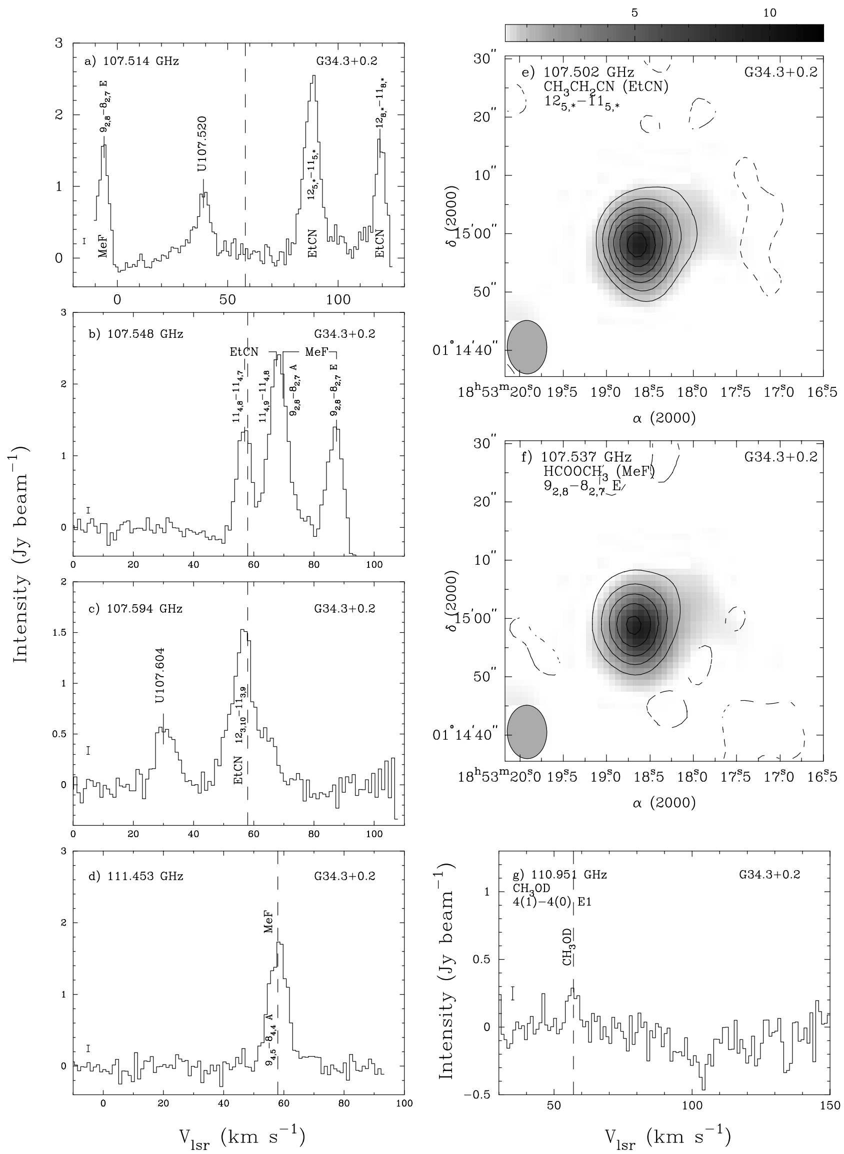

FIG. 3.—(*a–d*) Spectra taken toward G34.3+0.2 showing several detections of $HCOOCH_3$ (MeF) and CH_3CH_2CN (EtCN). The rms noise level is indicated by the vertical bar at the left of each spectrum. The spectral line labels correspond to the rest frequency located at the top left of each spectral window for a v_{LSR} of 57 km s^{-1} (*dashed line*). (*e*) Emission contours from the $12_{5,*}$–$11_{5,*}$ transition of EtCN at 107.502 GHz averaged between 82 and 95 km s^{-1} overlaid on the G34.3+0.2 continuum emission at 107.5 GHz (*gray scale*). The numbers on the gray-scale wedge are in units of Jy beam^{-1}. The EtCN contour levels are −0.05, 0.30, 0.50, 0.70, 0.90, 1.10, and 1.30 Jy beam^{-1}. The synthesized beam of 9″.2 × 6″.8 is indicated at the bottom left corner. (*f*) Emission contours from the $9_{2,8}$–$8_{2,7}$ *E* transition of MeF at 107.537 GHz averaged between −10 and −2 km s^{-1} overlaid on the G34.3 continuum emission at 107.5 GHz. The $HCOOCH_3$ contour levels are −0.05, 0.20, 0.40, 0.60, 0.80, and 1.00 Jy beam^{-1}. (*g*) Spectrum showing the first detection of CH_3OD toward G34.3+0.2.

Figure 6 shows the spectra of CH_2CHCN (VyCN), C_2H, $HCOOCH_3$ (MeF), and several unidentified lines taken toward the Orion compact ridge and the corresponding map of $HCOOCH_3$ (MeF). Figures 6*a* and 6*b* are similar to Figures 5*a* and 5*b* except that the spectra are taken toward the Orion compact ridge. The corresponding map of the $HCOOCH_3$ (MeF) lines (Fig. 6*d*) shows that the emission contours are centered closer to the Orion compact ridge. Finally, Figure 6*c* shows the spectrum of all unidentified lines taken toward the compact ridge. There are no molecular transitions that correspond to those frequencies in either the JPL (Pickett et al. 1998) or Lovas line lists (F. J. Lovas 2002, private communication). Table 6 lists the molecular species that we detected at or

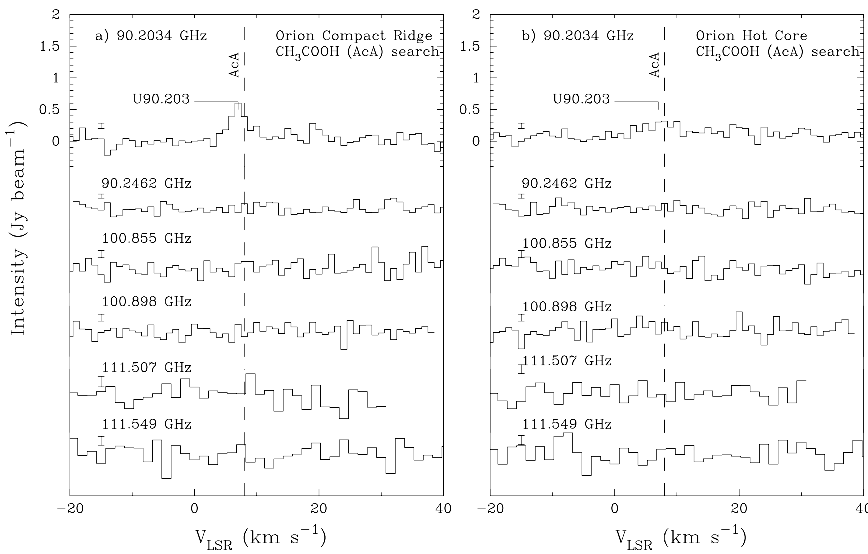

FIG. 4.—(*a*) CH_3COOH (AcA) spectral window toward the Orion compact ridge. The rms noise level is ~80 mJy beam^{-1} (indicated by the vertical bar at the left of each spectrum). The spectral line labels correspond to the rest frequencies in Table 3 for a v_{LSR} of 9 km s^{-1}. The dashed line is centered on the v_{LSR} of the Orion KL region (9 km s^{-1}). The ordinate of each spectrum ranges from 0 to 2 Jy beam^{-1}. (*b*) Spectra toward the Orion hot core. The spectral line labels and rms noise level are the same as in (*a*).

TABLE 6
ORION KL MOLECULAR LINE IDENTIFICATIONS

ν (MHz)	Species	Transition	ΔI (Jy beam^{-1})	T_L (K)	dv (km s^{-1})	τ ($\times 10^{-3}$)	C_τ
Hot Core ($T_e = 250$ K)							
87,312.8	VyCN[a]	$9_{1,8}$–$8_{1,7}$	1.2	7.14	5.4	30	1.01
87,317.1	C_2H	$N = 1$–$0\ (3/2,2$–$1/2,1)$	ab[b]				
87,328.7	C_2H	$N = 1$–$0\ (3/2,1$–$1/2,0)$	ab[b]				
90,227.6	MeF[c]	$8_{0,8}$–$7_{0,7}\ E$	1.7	9.48	3.1	40	1.02
90,229.6	MeF[c]	$8_{0,8}$–$7_{0,7}\ A$	1.6	8.92	3.1	40	1.02
98,030.4	CH_3OH	24_6–$23_7\ A+/-$	1.2	4.36	2.3	20	1.01
98,031	U98.031		0.5		2.3		
98,060	U98.060		0.4		4.4		
Compact Ridge ($T_e = 90$ K)							
87,312.8	VyCN	$9_{1,8}$–$8_{1,7}$	0.5	2.98	7.7	30	1.02
87,317.1	C_2H	$N = 1$–$0\ (3/2,2$–$1/2,1)$	ab[b]				
87,328.7	C_2H	$N = 1$–$0\ (3/2,1$–$1/2,0)$	ab[b]				
90,203	U90.203		0.5		3.1		
90,227.6	MeF	$8_{0,8}$–$7_{0,7}\ E$	6.9	38.5	2.4	610	1.33
90,229.6	MeF	$8_{0,8}$–$7_{0,7}\ A$	7.1	39.6	2.4	630	1.35
107,629	U107.629		2.1		7.2[d]		
107,631	U107.631		2.5		4.6		
107,636	U107.636		1.8		4.3		
107,647	U107.647		1.4		11.5[d]		
107,650	U107.650		0.6		9.7[d]		

[a] VyCN = vinyl cyanide (CH_2CHCN).
[b] This line was seen in absorption in our passband. Because of the small line width and our spectral resolution (~1.39 km s^{-1}), a Gaussian fit was not possible.
[c] MeF = methyl formate ($HCOOCH_3$).
[d] Blended line.

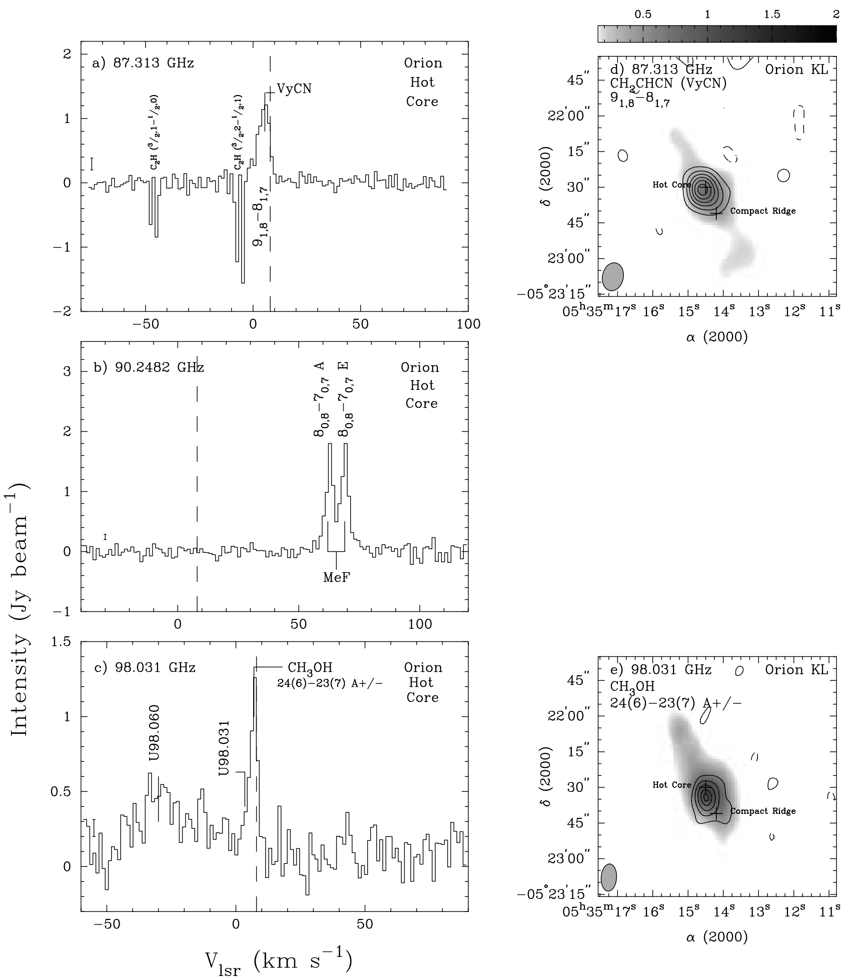

FIG. 5.—(*a*) CH_2CHCN (VyCN) spectrum toward the Orion hot core. Also included in the passband are two transitions of C_2H (Table 3). The rms noise level is indicated by the vertical bar at the left of the spectrum. The spectral line label corresponds to the rest frequency located at the top left of the spectral window for a v_{LSR} of 9 km s^{-1} (*dashed line*). (*b*) $HCOOCH_3$ (MeF) spectrum toward the Orion hot core. The spectral line labels and rms noise level are the same as in (*a*). (*c*) CH_3OH spectrum toward the Orion hot core. The spectral line labels and rms noise level are the same as in (*a*). (*d*) Emission contours from the $9_{1,8}$–$8_{1,7}$ transition of VyCN at 87.312 GHz taken in the direction of the Orion hot core. The emission from CH_2CHCN is averaged between 0 and 10 km s^{-1}. The emission is overlaid on the Orion KL continuum emission at 87.3 GHz (*gray scale*). The numbers on the gray-scale wedge are in units of Jy $beam^{-1}$. The VyCN contour levels are −0.10, 0.10, 0.20, 0.30, 0.40, 0.50, and 0.60 Jy $beam^{-1}$. The synthesized beam of $11''.9 \times 8''.8$ is indicated at the bottom left corner. (*e*) Emission contours of the 24_6–23_7 $A+-$transition of CH_3OH at 98.031 GHz averaged between 6 and 9 km s^{-1} taken toward the Orion hot core. The emission is overlaid on the Orion KL continuum emission at 98.03 GHz (*gray scale*). The CH_3OH contour levels are −0.20, 0.20, 0.40, 0.60, 0.80, and 0.92 Jy $beam^{-1}$.

near the systemic velocity ($v_{LSR} = 9$ km s^{-1}) of Orion KL. The column labels are the same as in Table 5.

3.3. *W3*(H_2O) *and W3*(OH)

Figures 7*a* and 7*b* show the spectra for the 111.5 GHz lines of acetic acid toward W3(H_2O) and W3(OH), respectively. The spectral line labels located at the upper left of each spectral window correspond to the rest frequency for a v_{LSR} of −47 km s^{-1} (*dashed line*). The 1 σ rms noise level is seen at the left of each spectrum. Even though no acetic acid transitions were detected beyond our 1 σ detection limit, we were able to give an upper limit to the column density of acetic acid toward W3(H_2O) and W3(OH) (Table 4). Figures 8*a*–8*d* show the detection of several transitions of CH_3CH_2CN (EtCN) and $HCOOCH_3$ (MeF) at 3 mm wavelength toward W3(H_2O). The spectral line labels are similar to Figure 7*a*. Figure 8*e* shows the map of the distribution of the 107.502 GHz CH_3CH_2CN (EtCN) (*contours*) on the 3 mm continuum emission (*gray scale*) toward the W3 complex. It is apparent that CH_3CH_2CN (EtCN) peaks toward the hot core source W3(H_2O). Figures 9*a*–9*c* are similar to Figures 8*a*-8*d* except that the spectra are taken toward W3(OH) and there are no detected transitions of CH_3CH_2CN (EtCN). Figure 9*d* shows the map of the distribution of the 107.537 GHz $HCOOCH_3$ (MeF) transition. In

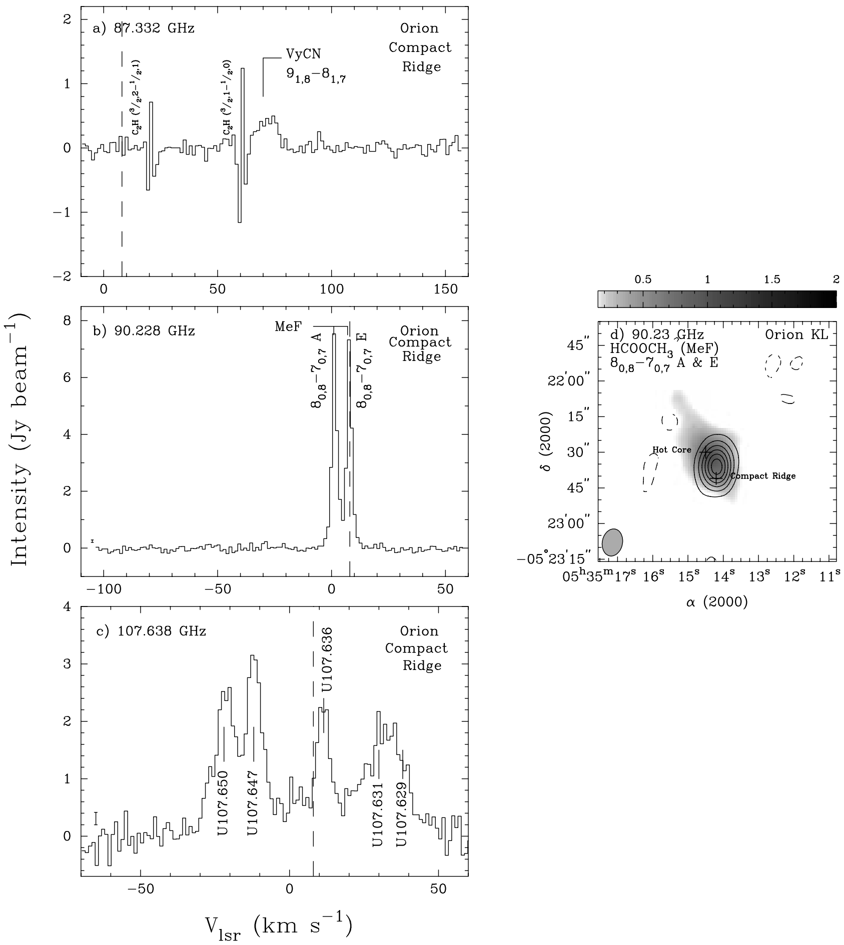

FIG. 6.—(*a*) CH_2CHCN (VyCN) spectrum toward the Orion compact ridge. Also included in the passband are two transitions of C_2H (Table 3). The rms noise level is indicated by the vertical bar at the left of the spectrum. The spectral line label corresponds to the rest frequency located at the top left of the spectral window for a $v_{\rm LSR}$ of 9 km s^{-1} (*dashed line*). (*b*) $HCOOCH_3$ (MeF) spectrum toward the Orion compact ridge. The spectral line labels and rms noise level are the same as in (*a*). (*c*) Lower sideband spectrum taken toward the Orion compact ridge that shows several unindentified transitions. The spectral line labels and rms noise level are the same as in (*a*). (*d*) Emission contours of MeF at 90.223 GHz averaged between −3 and 13 km s^{-1} taken toward the Orion compact ridge. The emission from MeF is overlaid on the Orion KL continuum emission at 90.2 GHz (*gray scale*). The numbers on the gray-scale wedge are in units of Jy beam^{-1}. The MeF contour levels are −0.1, 0.4, 0.8, 1.2, 1.6, 2.0, and 2.4 Jy beam^{-1}. The synthesized beam of 11."9 × 8."8 is indicated at the bottom left corner.

this case, $HCOOCH_3$ (MeF) is distributed toward W3(OH). Table 7 lists the molecular species that we detected at or near the systemic velocity ($v_{\rm LSR} = -47$ km s^{-1}) toward W3(H_2O) and W3(OH). The column labels are the same as in Table 5.

4. DISCUSSION

4.1. *Column Densities*

Clearly, determining the best column density estimates for the complex molecules studied in this paper is very important because these species may be central to the problem of understanding the role of grains in molecular formation and the related astrochemistry. With the assumption of LTE, we have

$$N_T = 2.04 C_\tau \frac{\int \Delta I \, dv}{\theta_a \theta_b} \left[\frac{I(T_e)}{I(T_e) - I_b} \right] \frac{Q_{\rm rot} e^{(E_u/T_e)}}{\nu^3 \langle S_{ij} \mu^2 \rangle} \times 10^{20} \ {\rm cm}^{-2}$$
$$= C_\tau N_T^{\rm thin} \ {\rm cm}^{-2} \ . \quad (1)$$

In equation (1), N_T is the total column density for any optical depth and $N_T^{\rm thin}$ is the total column density for the optically thin case from Miao et al. (1995); C_τ is the optical depth correction factor from Goldsmith & Langer (1999), which is discussed in the Appendix. The integrated line intensity $\int \Delta I \, dv$ (Jy beam^{-1} km s^{-1}) may be found from the product of ΔI and dv given in Tables 4–7; θ_a and θ_b are the FWHM beam sizes (arcseconds), $I(T_e)$ is the specific

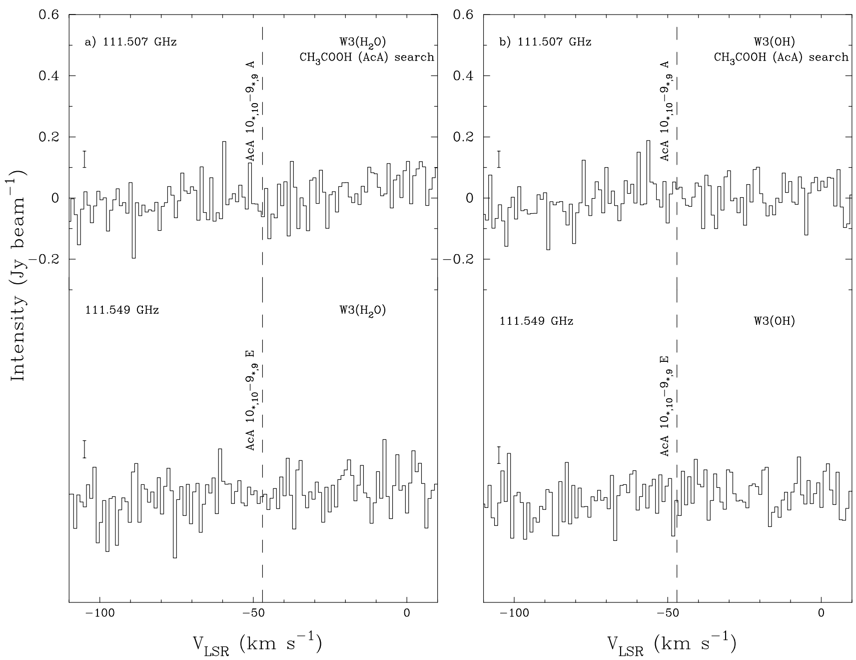

FIG. 7.—(*a*) CH_3COOH (AcA) search spectral window toward W3(H_2O). The rms noise level is ∼60 mJy beam^{-1} (indicated by the vertical bar at the left of each spectrum). The spectral line labels correspond to the rest frequencies in Table 3 for a v_{LSR} of −47 km s^{-1}. The dashed line is centered on the v_{LSR} of the W3(OH) region (−47 km s^{-1}). The ordinate of each spectrum ranges from −0.2 to 0.6 Jy beam^{-1}. (*b*) Search spectra toward W3(OH). The spectral line labels and rms noise levels are the same as in (*a*).

TABLE 7

W3 MOLECULAR LINE IDENTIFICATIONS

ν (MHz)	SPECIES	TRANSITION	ΔI (Jy beam^{-1})	T_L (K)	dv (km s^{-1})	$T_e = 70$ K: τ ($\times10^{-3}$)	$T_e = 70$ K: C_τ	$T_e = 185$ K: τ ($\times10^{-3}$)	$T_e = 185$ K: C_τ
				W3(H_2O)					
107,491.6.............	EtCN[a]	$12_{8,*}$–$11_{8,*}$	0.15	0.73	6.0	5	1.00	4	1.00
107,502.4.............	EtCN	$12_{5,*}$–$11_{5,*}$	0.22	1.07	6.8	8	1.00	6	1.00
107,520	U107.520		0.10		3.2				
107,537.2.............	MeF[b]	$9_{2,8}$–$8_{2,7}$ *E*	0.20[c]	0.97	4.0	7	1.00	5	1.00
107,543.7.............	MeF	$9_{2,8}$–$8_{2,7}$ *A*	0.20[c]	0.97	4.0	7	1.00	5	1.00
107,543.9.............	EtCN	$12_{4,9}$–$11_{4,8}$	0.20[c]	0.97	4.0	7	1.00	5	1.00
107,547.6.............	EtCN	$12_{4,8}$–$11_{4,7}$	0.20[c]	0.97	4.0	7	1.00	5	1.00
107,594.1.............	EtCN	$12_{3,10}$–$11_{3,9}$	0.20[c]	0.97	4.0	7	1.00	5	1.00
111,453.3.............	MeF	$9_{4,5}$–$8_{4,4}$ *A*	0.20	0.90	8.1[d]	7	1.00	5	1.00
				W3(OH)					
107,537.2.............	MeF[b]	$9_{2,8}$–$8_{2,7}$ *E*	0.36	1.75	2.0	10	1.01		
107,543.7.............	MeF	$9_{2,8}$–$8_{2,7}$ *A*	0.35	1.70	2.0	10	1.01		
111,453.3.............	MeF	$9_{4,5}$–$8_{4,4}$ *A*	0.27	1.22	3.9	10	1.00		

[a] EtCN = ethyl cyanide (CH_3CH_2CN).
[b] MeF = methyl formate ($HCOOCH_3$).
[c] The intensity and line width were approximated because the least-squares Gaussian fitting routine did not give a satisfactory fit.
[d] Blended line.

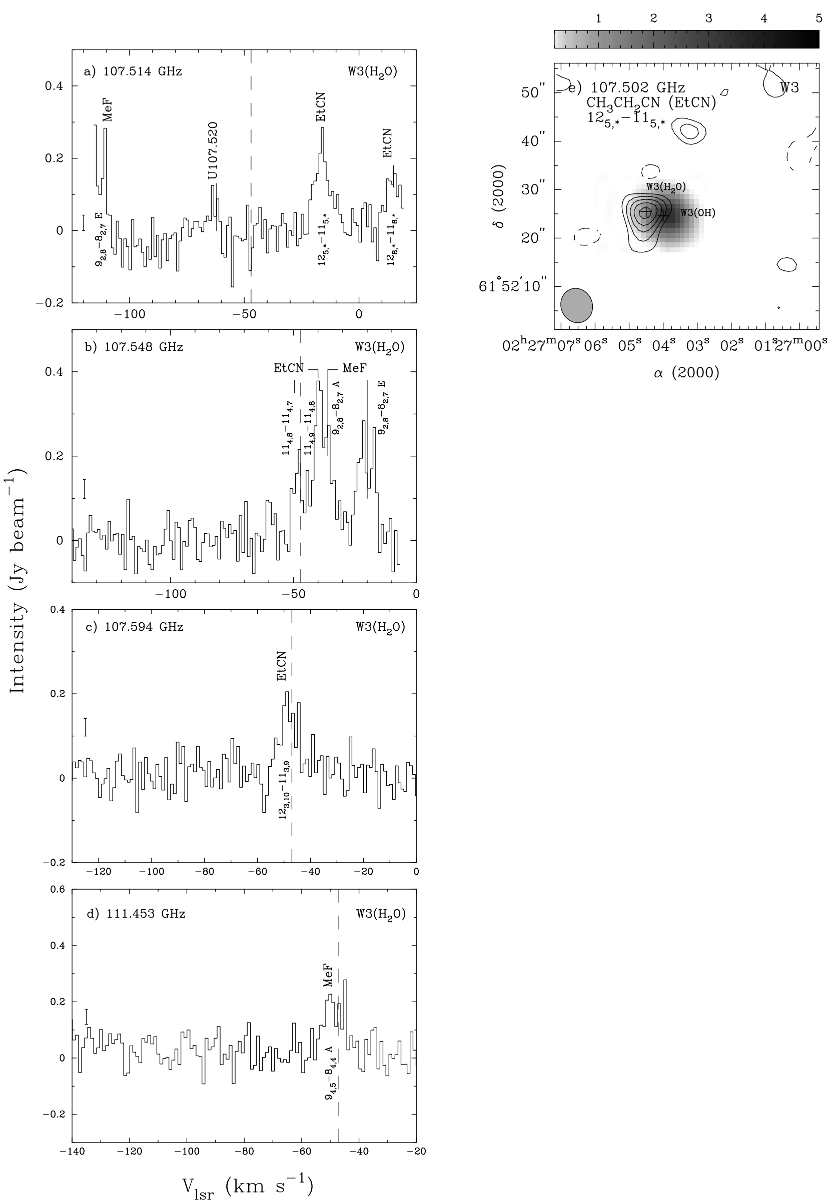

FIG. 8.—(*a–d*) Spectra taken toward W3(H_2O) showing several detections of $HCOOCH_3$ (MeF) and CH_3CH_2CN (EtCN). The rms noise level is indicated by the vertical bar at the left of each spectrum. The spectral line labels correspond to the rest frequency located at the top left of each spectral window. The dashed line is centered on this rest frequency at the v_{LSR} of W3(H_2O) (-47 km s^{-1}). (*e*) Emission contours from the $12_{5,*}$–$11_{5,*}$ transition of EtCN at 107.502 GHz averaged between -17 and -15 km s^{-1} overlaid on the W3(OH) continuum emission at 107.5 GHz (*gray scale*). The numbers on the gray-scale wedge are in units of Jy beam^{-1}. The EtCN contour levels are -0.090, 0.090, 0.135, 0.180, 0.225, and 0.270 Jy beam^{-1}. The synthesized beam of $7\farcs2 \times 6\farcs5$ is indicated at the bottom left corner.

intensity of the source at T_e (Jy beam^{-1}), and I_b is the specific intensity of the total background continuum contribution (Jy beam^{-1}). The beam size and specific intensity for each source are given in Table 4. Any uncertainty in the specific intensity will be dominated by calibration uncertainties (§ 2); $Q_{\rm rot}$ is the rotational partition function, E_u is the upper-state energy level (K), T_e is the excitation temperature (K), ν is the rest frequency (GHz), and $S_{ij}\mu^2$ is the product of the transition line strength and the square of the electric dipole moment (debye^2). Because CH_3COOH is an asymmetric rotor, its rotational partition function is approximated by $Q_r = CT_r^{3/2}$, where $C = 14.10$ K$^{-3/2}$

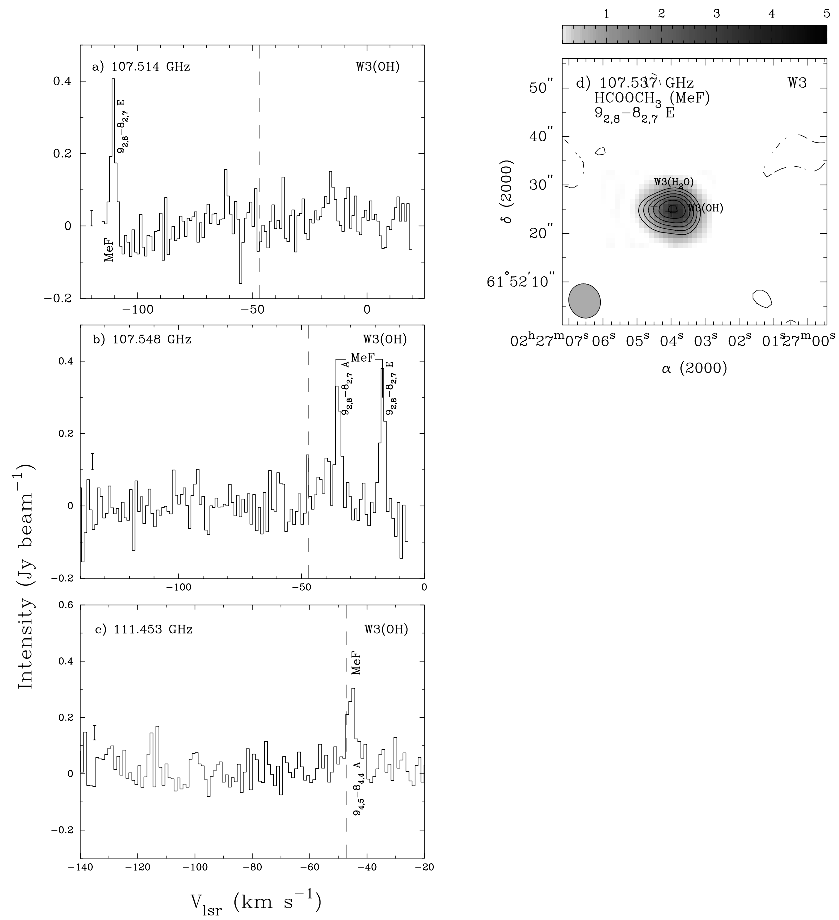

FIG. 9.—(*a–c*) Same as in Fig. 8, except the spectra were taken toward W3(OH). (*d*) Emission contours from the $9_{2,8}$–$8_{2,7}$ *E* transition of $HCOOCH_3$ (MeF) at 107.537 GHz averaged between −110 and −112 km s^{-1} overlaid on the W3(OH) continuum emission at 107.5 GHz. The MeF contour levels are −0.10, 0.15, 0.20, 0.25, 0.30, 0.35, and 0.40 Jy beam^{-1}. The synthesized beam of $7''.2 \times 6''.5$ is indicated at the bottom left corner.

(Mehringer et al. 1997). Other rotational partition functions for the observed molecular species are given in Table 3. Table 8 summarizes the total column densities of all the large molecular species found toward each hot molecular core. The source for each column density measurement is given in column (1). The other columns list the values for $HCOOCH_3$ (col. [2]), CH_3CH_2CN (col. [3]), and CH_3COOH (col. [4]), which are discussed in §§ 4.2–4.5.

4.2. *Column Densities of Large Molecular Species in G34.3+0.2*

We observed two transitions of CH_3COOH, five transitions of CH_3CH_2CN, three transitions of $HCOOCH_3$, one transition of HCOOH, and one transition of CH_3OD. Because all the transitions of a single species were so close in upper-state energy level (Table 3), a rotational temperature diagram was not meaningful. Mehringer & Snyder (1996) used the VLA observations of NH_3 by Garay & Rodriguez (1990) to estimate the temperature structure toward G34.3+0.2. They estimated that T_e increases from 70 K near the edges of the core to 185 K at its center. Since our synthesized beam ($8''.8 \times 6''.6$) lies within the source size measured by the VLA observations, we used this temperature range to calculate the total column density. Assuming that the temperature range between 70 and 185 K is close to the kinetic temperature of the gas, for CH_3COOH we find an average total column density range of 7.7×10^{14} cm^{-2} $\leq N_{CH_3COOH} \leq 1.6 \times 10^{15}$ cm^{-2}. For $HCOOCH_3$, we find an average total column density range of 2.4×10^{16} cm^{-2} $\leq N_{HCOOCH_3} \leq 4.8 \times 10^{16}$ cm^{-2}. This gives a relative $CH_3COOH/HCOOCH_3$ abundance ratio of $\sim 3.3 \times 10^{-2}$ for G34.3+0.2. This is comparable to the abundance ratio found toward Sgr B2(N-LMH) and W51e2 [$(3–6) \times 10^{-2}$; Remijan et al. 2002]. For CH_3CH_2CN, we find an average total column density range of 2.8×10^{15} cm^{-2} $\leq N_{CH_3CH_2CN} \leq 4.1 \times 10^{15}$ cm^{-2}, and for HCOOH we find 1.2×10^{15} cm^{-2} $\leq N_{HCOOH} \leq 2.9 \times 10^{15}$ cm^{-2}. Finally, for CH_3OD, we find a total column density range of 6.6×10^{14} cm^{-2} $\leq N_{CH_3OD} \leq 1.4 \times 10^{15}$ cm^{-2}. Mehringer & Snyder (1996) measured a total column

TABLE 8

Column Densities

Source	N_{HCOOCH_3} ($\times 10^{15}$ cm^{-2})	$N_{CH_3CH_2CN}$ ($\times 10^{15}$ cm^{-2})	N_{CH_3COOH} ($\times 10^{15}$ cm^{-2})
High-Mass Star-forming Regions			
$W3(H_2O)$	5.85–8.29	0.42–0.56	<0.66–0.93
W3(OH)	4.47	<0.11	<0.44
Orion hot core	69.1	...	<1.91
Orion compact ridge	76.4	...	<0.35
M17-SW	<1.44	<0.13	<0.56
G34.3+0.2	23.8–48.4	2.78–4.12	0.77–1.64
W49 A	<0.95	<0.09	<0.36
Low-Mass Star-forming Regions			
L1448-C	<0.14	<0.13	<0.04
NGC 1333 IRAS4	<1.24	<0.43	<0.42
NGC 2024 FIR5	<1.67	<1.02	<0.53
IRAS 16293−2422	<5.85	<2.10	<1.97
Serpens SMM 1	<0.93	<0.56	<0.30
Previous Detections			
Sgr B2(N-LMH)	100–200[a]	46.3[b]	6.10[a]
W51e2	300–1500[a]	29.9[b]	17.5[a]

Note.—All upper limits were calculated from the 1 σ rms noise in the spectral window, the beam size, and dv given in Table 4. For the upper limit of $HCOOCH_3$, we used a frequency of 111.453 GHz, for CH_3CH_2CN we used 107.492 GHz, and for CH_3COOH we used 111.549 GHz. The upper and lower bounds of the column densities are based on the upper and lower limits of the given temperature range.

[a] Remijan et al. 2002.

[b] The column densities were taken from Liu et al. 2001, and for W51e2 we assumed a source size of 2''.4 as in Remijan et al. 2002.

density range of 1.7×10^{17} cm$^{-2} \leq N_{CH_3OH} \leq 2.6 \times 10^{17}$ cm^{-2} for CH_3OH. This gives a CH_3OD/CH_3OH abundance ratio range of $(3.9–5.4) \times 10^{-3}$.

4.3. *Column Densities of Large Molecular Species in Orion KL*

In order to determine the total column densities of the species found toward the Orion compact ridge and the Orion hot core, we used the temperature of 90 K found by Blake et al. (1987) for the compact ridge and 250 K for the hot core based on the Wilner, Wright, & Plambeck (1994) observations. In total, we observed two transitions of $HCOOCH_3$, one transition of CH_2CHCN, and one transition of CH_3OH. For the compact ridge, we find a total column density of 1.1×10^{15} cm^{-2} for CH_2CHCN and an average total column density of 7.6×10^{16} cm^{-2} for $HCOOCH_3$. For the hot core, we find a total column density of 6.9×10^{15} cm^{-2} for CH_2CHCN, an average total column density of 6.9×10^{16} cm^{-2} for $HCOOCH_3$, and a total column density of 2.3×10^{17} cm^{-2} for CH_3OH. Using the 1 σ value of 0.1 Jy beam^{-1} in our window containing the CH_3COOH lines, we find a column density upper limit using a typical line width of 4 km s^{-1} at 90 K of less than 3.5×10^{14} cm^{-2}, and using a typical line width of 6 km s^{-1} at 250 K of less than 1.9×10^{15} cm^{-2}. This gives a relative $CH_3COOH/HCOOCH_3$ abundance ratio of less than 4.6×10^{-3} for the Orion compact ridge and less than 2.8×10^{-2} for the Orion hot core.

4.4. *Column Densities of Large Molecular Species in W3(H_2O) and W3*(OH)

In order to determine the column densities of the large molecular species we observed toward W3, we used the temperature measurements from the high-resolution observations of Wyrowski et al. (1999). They determined temperatures of 200(40), 150(15), and 190(15) K for their A, B, and C continuum peaks toward $W3(H_2O)$, respectively. For the W3(OH) region, Sutton et al. (2001) constrained the kinetic temperature of this region to greater than 110 K with a best-fit value of 150 K from their models of methanol masers. Thus, we used the temperature range of 150–200 K for $W3(H_2O)$ and 150 K for W3(OH) for our calculations of the total column density of CH_3CH_2CN and $HCOOCH_3$ and to set an upper limit for CH_3COOH. For the $W3(H_2O)$ region, we find an average total column density range of 5.9×10^{15} cm$^{-2} \leq N_{HCOOCH_3} \leq 8.3 \times 10^{15}$ cm^{-2} for $HCOOCH_3$. For CH_3CH_2CN, we find an average total column density range of 4.2×10^{14} cm$^{-2} \leq N_{CH_3CH_2CN} \leq 5.6 \times 10^{14}$ cm^{-2}. This is comparable to what Liu et al. (2001) measured from their survey (2.1×10^{15} cm^{-2}). Using 150 K for the W3(OH) region, we find an average column density of 4.5×10^{15} cm^{-2} for $HCOOCH_3$ and an upper limit of less than 1.1×10^{14} cm^{-2} for CH_3CH_2CN. The column density of $HCOOCH_3$ is comparable to that measured toward $W3(H_2O)$ and is also the first column density measurement of $HCOOCH_3$ toward W3(OH) with an interferometer. Finally, using the rms noise level (~0.05 Jy beam^{-1}) in the CH_3COOH window and using a typical line width of

6 km s^{-1}, we set an upper limit of CH_3COOH toward W3(H_2O) of less than 6.6×10^{14} cm^{-2} at 150 K. For W3(OH), using a typical line width of 4 km s^{-1}, we find the upper limit of the CH_3COOH column density to be less than 4.4×10^{14} cm^{-2}. This gives a relative $CH_3COOH/HCOOCH_3$ abundance ratio of less than 1.1×10^{-1} for W3(H_2O) and less than 9.8×10^{-2} for W3(OH).

4.5. *Column Densities in Other Sources*

No other source showed emission from any of the large molecular species given in Table 3. The most probable reason why no features were detected toward these other sources is that currently, the spectral features lie below our detection limit. However, from the 1 σ rms noise level in the spectral window containing these species, we were able to set upper limits to the total column density. These upper limits are given in Table 8.

5. POSSIBLE CONSTRAINTS ON ACETIC ACID SOURCES

The observations discussed here and in Remijan et al. (2002) place some constraints on the detection of interstellar acetic acid sources. In § 2.1, we described each source in detail and why each was considered as a possible source of acetic acid. For example, some sources, such as W3(H_2O), Orion KL, and G34.3+0.2, already had detections of large molecular species such as $HCOOCH_3$ and CH_3OCH_3. Other sources showed a considerable amount of dust continuum emission, and since acetic acid is thought to be formed in the warm regions surrounding dust grains (Remijan et al. 2002), these regions seemed like good places to search for acetic acid. However, our observations showed that a detectable amount of acetic acid is present only in regions that follow certain constraints. The three known acetic acid sources are within 7 kpc of the Galactic center (Fig. 10), but more extensive observations will be necessary to determine whether Galactocentric distances really are a factor in the chemical abundance of acetic acid. On the other hand, it is apparent that mass has an influence on whether acetic acid is detectable toward star-forming regions. This is significant because the only acetic acid detections that have been made are in star-forming regions with masses between 200 and 2000 $M_\odot$ (Fig. 11).

It was also relevant to compare the acetic acid column density to other large molecular species. The $CH_3COOH/HCOOCH_3$ abundance ratio ranges from 0.01 to 0.06 in those sources with detectable amounts of both species. The $CH_3COOH/HCOOH$ abundance ratio is about 10 times larger, ranging from ~0.1 in Sgr B2(N-LMH) and W51e2 to ~0.6 in G34.3+0.2. Finally, the CH_3COOH/CH_3CH_2CN is comparable to the $CH_3COOH/HCOOH$ ratio ranging from ~0.1 in Sgr B2(N-LMH) to ~0.4 in G34.3+0.2, where both acetic acid and ethyl cyanide are detected. For those sources where methyl formate was detected but acetic acid was not, the upper limit to the abundance ratio was less than 0.1. Also, those sources where ethyl cyanide or vinyl cyanide was detected and acetic acid was not, the upper limit to the abundance ratio of CH_3COOH/CH_3CH_2CN was less than 1.7, and the upper limit to the abundance ratio of CH_3COOH/CH_2CHCN was less than 0.4. Hence, in a typical acetic acid source, the column density of acetic acid appears to be ~15–100 times below the abundance of methyl formate, ~2–10 times below the abundance of formic acid, and ~2–10 times below the abundance of ethyl cyanide. In those sources where acetic acid was not detected, such as W3(H_2O) and W3(OH), we did not reach these detection limits. Toward the Orion hot core and the compact ridge, we did reach these detection limits yet did not

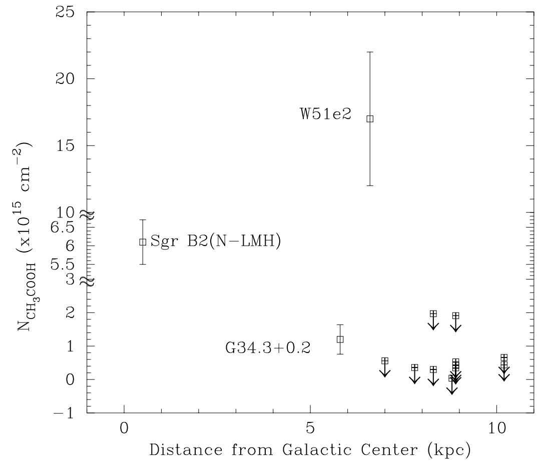

Fig. 10.—Plot of the CH_3COOH (AcA) column densities (ordinate: N_{CH_3COOH} [$\times 10^{15}$ cm^{-2}]) vs. distance from the Galactic center (abscissa: Galactocentric distance [kpc]) toward the 12 sources present in this survey (Table 2), Sgr B2(N-LMH), and W51e2. The AcA detections have associated error bars on the column density. The remaining points are upper limits. The only detections occur between 0 and 7 kpc from the Galactic center. (To calculate the distance each HMC is from the Galactic center, we used a distance of 8.5 kpc from the Sun to the Galactic center, Sgr A*; Reid 1993.)

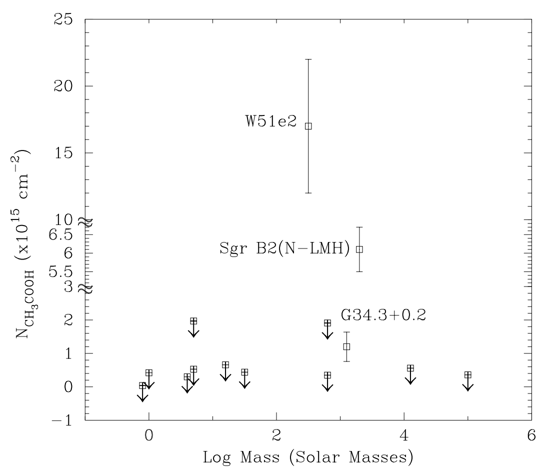

Fig. 11.—Plot of the CH_3COOH (AcA) column densities (ordinate: N_{CH_3COOH} [$\times 10^{15}$ cm^{-2}]) vs. hot molecular core mass (abscissa: log mass [$M_\odot$]) toward the 12 sources present in this survey (Table 2), Sgr B2(N-LMH), and W51e2. The AcA detections have associated error bars on the column density. The remaining points are upper limits. The only detections occur between 200 and 2000 $M_\odot$.

detect acetic acid. However, the W3 sources and Orion KL may differ from the other sources. For example, our observations reveal no detection of acetic acid in any HMC that shows a chemical differentiation of the O-bearing and N-bearing species, such as Orion KL, where Blake et al. (1987) characterized the hot core and compact ridge as N-rich and O-rich molecular sources, respectively. Our observations clearly show this chemical differentiation toward both Orion KL and W3(OH). While the spectra toward W3(H_2O) show several strong transitions of CH_3CH_2CN, no transitions are seen toward W3(OH) (see Figs. 8 and 9). Therefore, it is possible that the formation of acetic acid may depend strongly on a mix of nitrogen and oxygen chemistry. Regions that do not have significant O and N chemistry occurring cospatially may not produce acetic acid in detectable quantities.

6. SUMMARY

We have surveyed 12 galactic hot molecular cores for interstellar acetic acid (CH_3COOH) with the BIMA array. To date, this is the most extensive search for interstellar CH_3COOH. From our observations, we have detected a new source of acetic acid toward the high-mass hot molecular core source G34.3+0.2. Using a temperature range between 70 and 185 K, we find a CH_3COOH column density range of $(0.77\text{–}1.64) \times 10^{15}$ cm^{-2} toward G34.3+0.2. This gives a relative $CH_3COOH/HCOOCH_3$ abundance ratio of $\sim 3.3 \times 10^{-2}$, which is comparable to the abundance ratio found toward Sgr B2(N-LMH) and W51e2 [$(3\text{–}6) \times 10^{-2}$] by Remijan et al. (2002). In addition to CH_3COOH, we also detected several transitions of other large molecular species such as ethyl cyanide (CH_3CH_2CN), vinyl cyanide (CH_2CHCN), and methyl formate ($HCOOCH_3$), and we made the first interferometric detection of formic acid (HCOOH) and deutrated methanol (CH_3OD) toward G34.3+0.2. The maps and beam-averaged column densities indicate that the emission is coming from a very compact source toward these regions. Furthermore, our survey suggests that hot molecular cores that have a mass range between 200 and 2000 $M_\odot$ and do not show a distinct differentiation between O and N chemistry are the strongest sources of interstellar acetic acid. The three known acetic acid sources are within 7 kpc of the Galactic center, but more extensive survey observations will be required to determine whether Galactocentric distance is a significant factor in the chemical abundance of acetic acid.

We thank F. J. Lovas for the use of his new line list of identified molecular species to identify spectral features in our passbands. We appreciate helpful comments from D. Meier. We are indebted to B. E. Turner for pointing out the potential significance of optical depth effects in large molecules. We acknowledge support from the Laboratory for Astronomical Imaging at the University of Illinois and NSF AST 99-81363. S.-Y. Liu acknowledges support from NSF AST 99-81546, which supports research at the Caltech Owens Valley Millimeter Array.

APPENDIX

OPTICAL DEPTH CORRECTIONS

There is ample evidence going back for more than a decade that certain large molecules have abundance values that may have been underestimated as a result of optical depth effects (e.g., Turner 1991). With single-element telescope observations, enough spectral line data may be available to check the relative intensities of related series of lines and thus ascertain whether low optical depths are consistent with the data. However, all data in this paper were obtained with the BIMA array in the 3 mm wavelength range; data for related line series at adjacent wavelengths observed with similar beam sizes usually are not available. Under these circumstances, the best approach is to apply the optical depth method of Goldsmith & Langer (1999) using C_τ, the optical depth correction factor, where

$$C_\tau = \frac{\tau}{1 - e^{-\tau}} . \tag{A1}$$

The optical depth τ usually will be different for each transition. If the spectral line intensity is given by T_L, the gas excitation temperature is given by T_e, and the background continuum temperature is given by T_b, then the optical depth is given by

$$\tau = \ln\left(\frac{T_e - T_b}{T_e - T_b - T_L}\right) . \tag{A2}$$

Figures 1–3 and 5–9 show that the source emission generally fills the synthesized beam. In this case, the source brightness temperature T_S is given by the main beam brightness temperature multiplied by 2 (Rohlfs & Wilson 2000), where

$$T_S = 2.44 \frac{I_\nu}{\theta_a \theta_b \nu^2} \times 10^6 \text{ K} , \tag{A3}$$

I_ν is the specific intensity measured by the interferometer in units of Jy beam^{-1}, θ_a and θ_b are the major and minor axes of the synthesized beam measured in arcseconds, and ν is the frequency of the transition in GHz. Equation (A3) may be used to derive both T_L and T_b for use in equations (A2) and (A1). Since the array resolves out the uniform 2.7 K microwave background, T_b can be calculated from the continuum brightness values for each source (Table 4). Tables 5–7 list the line brightness values used to calculate T_L for each spectral line. The excitation temperature T_e can be taken from the source gas temperature T_k, although sometimes $T_k > T_e$ (Goldsmith & Langer 1999). The resulting values of τ and C_τ for the detected molecular transitions toward G34.3+0.2, Orion KL, and W3 are listed in Tables 5–7.

REFERENCES

Anderson, T., Crownover, R. L., Herbst, E., & de Lucia, F. C. 1988, ApJS, 67, 135
Barsony, M., Ward-Thompson, D., André, P., & O'Linger, J. 1998, ApJ, 509, 733
Bergin, E. A., Ungerechts, H., Goldsmith, P. F., Snell, R. L., Irvine, W. M., & Schloerb, F. P. 1997, ApJ, 482, 267
Blake, G. A., Sandell, G., van Dishoeck, E. F., Groesbeck, T. D., Mundy, L. G., & Aspin, C. 1995, ApJ, 441, 689
Blake, G. A., Sutton, E. C., Masson, C. R., & Phillips, T. G. 1987, ApJ, 315, 621
Boogert, A. C. A., Tielens, A. G. G. M., Ceccarelli, C., Boonman, A. M. S., van Dishoeck, E. F., Keane, J. V., Whittet, D. C. B., & de Graauw, T. 2000, A&A, 360, 683
Buckley, H. D., & Ward-Thompson, D. 1996, MNRAS, 281, 294
Ceccarelli, C., Castets, A., Caux, E., Hollenbach, D., Loinard, L., Molinari, S., & Tielens, A. G. G. M. 2000a, A&A, 355, 1129
Ceccarelli, C., Loinard, L., Castets, A., Faure, A., & Lefloch, B. 2000b, A&A, 362, 1122
Ceccarelli, C., Loinard, L., Castets, A., Tielens, A. G. G. M., & Caux, E. 2000c, A&A, 357, L9
Chandler, C. J., & Carlstrom, J. E. 1996, ApJ, 466, 338
Crété, E., Giard, M., Joblin, C., Vauglin, I., Léger, A., & Rouan, D. 1999, A&A, 352, 277
Curiel, S., Torrelles, J. M., Rodríguez, L. F., Gómez, J. F., & Anglada, G. 1999, ApJ, 527, 310
de Pree, C. G., Mehringer, D. M., & Goss, W. M. 1997, ApJ, 482, 307
Dickel, H. R., & Goss, W. M. 1990, ApJ, 351, 189
Di Francesco, J., Myers, P. C., Wilner, D. J., Ohashi, N., & Mardones, D. 2001, ApJ, 562, 770
Ehrenfreund, P., & Charnley, S. B. 2000, ARA&A, 38, 427
Garay, G., & Rodriguez, L. F. 1990, ApJ, 362, 191
Genzel, R., & Stutzki, J. 1989, ARA&A, 27, 41
Gerry, M. C. L., Yamada, K., & Winnewisser, G. 1979, J. Phys. Chem. Ref. Data, 8, 107
Goldsmith, P. F., Bergin, E. A., & Lis, D. C. 1997, ApJ, 491, 615
Goldsmith, P. F., & Langer, W. D. 1999, ApJ, 517, 209
Helmich, F. P., & van Dishoeck, E. F. 1997, A&AS, 124, 205
Ilyushin, V. V., et al. 2001, J. Mol. Spectrosc., 205, 286
Johansson, L. E. B., et al. 1984, A&A, 130, 227
Kurtz, S., Cesaroni, R., Churchwell, E., Hofner, P., & Walmsley, C. M. 2000, in Protostars and Planets IV, ed. V. Manning, A. P. Boss, & S. Russell (Tucson: Univ. Arizona Press), 299
Liu, S.-Y., Girart, J. M., Remijan, A. J., & Snyder, L. E. 2002, ApJ, 576, 255
Liu, S.-Y., Mehringer, D. M., & Snyder, L. E. 2001, ApJ, 552, 654
Lovas, F. J. 1982, J. Phys. Chem. Ref. Data, 11, 251
Mangum, J. G., Wootten, A., & Barsony, M. 1999, ApJ, 526, 845
Mauersberger, R., Wilson, T. L., Mezger, P. G., Gaume, R., & Johnston, K. J. 1992, A&A, 256, 640
McMullin, J. P., Mundy, L. G., Blake, G. A., Wilking, B. A., Mangum, J. G., & Latter, W. B. 2000, ApJ, 536, 845
Mehringer, D. M., & Snyder, L. E. 1996, ApJ, 471, 897
Mehringer, D. M., Snyder, L. E., Miao, Y., & Lovas, F. J. 1997, ApJ, 480, L71
Miao, Y., Mehringer, D. M., Kuan, Y.-J., & Snyder, L. E. 1995, ApJ, 445, L59
Nielbock, M., Chini, R., Jutte, M., & Manthey, E. 2001, A&A, 377, 273
Nummelin, A., Dickens, J. E., Bergman, P., Hjalmarson, Å., Irvine, W. M., Ikeda, M., & Ohishi, M. 1998, A&A, 337, 275
Oesterling, L. C., Sieghard, A., de Lucia, F. C., Sastry, K. V. L. N., & Herbst, E. 1999, ApJ, 521, 255
Pickett, H. M., Poynter, R. L., Cohen, E. A., Delitsky, M. L., Pearson, J. C., & Muller, H. S. P. 1998, J. Quant. Spectrosc. Radiat. Transfer, 60, 883
Reid, M. J. 1993, ARA&A, 31, 345
Reid, M. J., & Ho, P. T. P. 1985, ApJ, 288, L17
Remijan, A. J., Liu, S. Y., Snyder, L. E., Mehringer, D. M., & Kuan, Y. J. 2002, ApJ, 576, 264
Rohlfs, K. & Wilson, T. L. 2000, Tools of Radio Astronomy (New York: Springer)
Sault, R. J., Teuben, P. J., & Wright, M. C. H. 1995, in ASP Conf. Ser. 77, Astronomical Data Analysis Software and Systems IV, ed. R. A. Shaw, H. E. Payne, & J. J. E. Hayes (San Francisco: ASP), 433
Schöier, F. L., Jorgensen, J. K., van Dishoeck, E. F., & Blake, G. A. 2002, A&A, 390, 1001
Schulz, A., Güesten, R., Zylka, R., & Serabyn, E. 1991, A&A, 246, 570
Scoville, N. Z., & Solomon, P. M. 1973, ApJ, 180, 31
Sutton, E. C., Blake, G. A., Masson, C. R., & Phillips, T. G. 1985, ApJS, 58, 341
Sutton, E. C., Sobolev, A. M., Ellingsen, S. P., Cragg, D. M., Mehringer, D. M., Ostrovskii, A. B., & Godfrey, P. D. 2001, ApJ, 554, 173
Tucker, K. D., Kutner, M. L., & Thaddeus, P. 1974, ApJ, 193, L115
Turner, B. E. 1989, ApJS, 70, 539
———. 1991, ApJS, 76, 617
Turner, J. L., & Welch, W. J. 1984, ApJ, 287, L81
Visser, A. E., Richer, J. S., Chandler, C. J., & Padman, R. 1998, MNRAS, 301, 585
Watt, S., & Mundy, L. G. 1999, ApJS, 125, 143
Willemot, E., Dangoisse, D., Monnanteuil, N., & Bellet, J. 1980, J. Phys. Chem. Ref. Data, 9, 59
Wilner, D. J., Wright, M. C. H., & Plambeck, R. L. 1994, ApJ, 422, 642
Wynn-Williams, C. G., Genzel, R., Becklin, E. E., & Downes, D. 1984, ApJ, 281, 172
Wyrowski, F., Schilke, P., Walmsley, C. M., & Menten, K. M. 1999, ApJ, 514, L43
Xu, L. H., & Lovas, F. J. 1997, J. Phys. Chem. Ref. Data, 26, 17
Zheng, X. W., Moran, J. M., & Reid, M. J. 2000, MNRAS, 317, 192

Appendix C

A Spectral Line Survey of Selected 3 Millimeter Bands Toward Sagittarius B2(N-LMH) Using the National Radio Astronomy 12 Meter Radio Telescope and the Berkeley-Illinois-Maryland Association Array I. The Observational Data

By

Douglas N. Friedel, Lewis E. Snyder, Barry E. Turner & Anthony Remijan

2004 ApJ 600, 234

The Astrophysical Journal, 600:234–253, 2004 January 1

A SPECTRAL LINE SURVEY OF SELECTED 3 MILLIMETER BANDS TOWARD SAGITTARIUS B2(N-LMH) USING THE NATIONAL RADIO ASTRONOMY OBSERVATORY 12 METER RADIO TELESCOPE AND THE BERKELEY-ILLINOIS-MARYLAND ASSOCIATION ARRAY. I. THE OBSERVATIONAL DATA

D. N. Friedel,[1] L. E. Snyder,[1] B. E. Turner,[2] and A. Remijan[1]

Received 2003 May 20; accepted 2003 September 10

ABSTRACT

We have initiated a spectral line survey, at a wavelength of 3 mm, toward the hot molecular core Sgr B2(N-LMH). This is the first spectral line survey of the Sgr B2(N) region utilizing data from both an interferometer (Berkeley-Illinois-Maryland Association [BIMA] array) and a single-element radio telescope (NRAO 12 m). In this survey, covering 3.6 GHz in bandwidth, we detected 218 lines (97 identified molecular transitions, one recombination line, and 120 unidentified transitions). This yields a spectral line density (lines per 100 MHz) of 6.06, which is much larger than any previous 3 mm line survey. We also present maps from the BIMA array that indicate that most highly saturated species (three or more H atoms) are products of grain chemistry or warm gas-phase chemistry. Because of the nature of this survey, we are able to probe each spectral line on multiple spatial scales, yielding information that could not be obtained by either instrument alone.

Subject headings: ISM: individual (Sagittarius B2) — ISM: molecules — radio lines: ISM — surveys

On-line material: machine-readable tables

1. INTRODUCTION

Sgr B2 is a massive star-forming region at a distance of 7.1 kpc and within 300 pc of the Galactic center (Reid et al. 1988). It is well known for its abundance of molecular species and has been the target of many searches for complex molecules (e.g., Mehringer et al. 1997; Liu, Mehringer, & Snyder 2001; Martín-Pintado et al. 2001) and several spectral line surveys (e.g., Cummins, Thaddeus, & Linke 1986; Turner 1989, 1991). The region is made up of several individual sources. Table 1 contains a list of the main sources in the region, along with their coordinates. The first column gives the source name. The second and third columns give the right ascension and declination of each source, respectively. The dense molecular core toward Sgr B2(N) has been called the "Large Molecule Heimat" [Sgr B2(N-LMH)], since it is the source of all of the large molecules observed in that region (Snyder, Kuan, & Miao 1994; Mehringer et al. 1997). Sgr B2(N-LMH) has the most detected and identified molecular species and the strongest spectral emission lines of any source in the complex.[3] Within the 3 mm synthesized beam of the Berkeley-Illinois-Maryland Association (BIMA) array[4] in its C configuration toward Sgr B2(N), there are at least four H II regions (de Pree et al. 1995). This is unlike Sgr B2(M), which has over 21 H II regions in the same size beam (Gaume et al. 1995; de Pree et al. 1996).

Spectral line surveys provide powerful tools to analyze the coupled dynamical and chemical evolution of molecular clouds. In a survey, many lines of a single species are observed at similar sensitivities, diminishing the errors associated with derived quantities. For example, a particular problem arises in deriving accurate abundances because of overlapping identifications of molecular species. Surveys provide the best means of avoiding this problem by revealing intensity changes in lines of a given species. The first line surveys of the Sgr B2 source complex were aimed at Sgr B2(OH). Sgr B2(OH) is an OH and H_2O maser source [$\sim 30''$ south of Sgr B2(M)] that is not a main site of molecular concentration in the region (Snyder, Kuan, & Pratap 1991) and furthermore has little or no millimeter continuum emission (≤ 0.1 Jy beam^{-1}; Kuan & Snyder 1994; Kuan, Mehringer, & Snyder 1996). However, the main beams of these surveys were large enough to encompass Sgr B2(M) and, in the case of Cummins et al. 1986), possibly even Sgr B2(N) at some frequencies. Thus, many of the molecular transitions detected by these surveys may have come not from Sgr B2(OH) but from Sgr B2(M) or Sgr B2(N). More recent surveys covering 330–355 GHz (Sutton et al. 1991) and 218–263 GHz (Nummelin et al. 1998, 2000) did use Sgr B2(N) and Sgr B2(M) as the primary sources. Figure 1 shows the pointing centers and average beams from this and previous spectral line surveys of the Sgr B2 region. The five cores of Sgr B2 are labeled (north, northwest, main, south, and OH). The beams from this survey have bold outlines, centered on Sgr B2(N). The dashed beams around Sgr B2(N), Sgr B2(M), and Sgr B2(NW) are from Nummelin et al. (1998, 2000). The two gray beams around Sgr B2(N) and Sgr B2(M) are from Sutton et al. (1991). The beams centered on Sgr B2(OH) are from Turner (1989, 1991) and Cummins et al. (1986).

This survey uses both the BIMA array (10 6.1 m elements) and the single-element NRAO[5] 12 m radio telescope. Unlike previous surveys that only used single-element telescopes, we are able to sample several spatial scales for this source. A

[1] Department of Astronomy, University of Illinois, Urbana, IL 61801; friedel@astro.uiuc.edu, snyder@astro.uiuc.edu, aremijan@astro.uiuc.edu.

[2] National Radio Astronomy Observatory, Charlottesville, VA 22903; bturner@nrao.edu.

[3] With the exception of SO and SO_2, which are strongest toward Sgr B2(M) (Sutton et al. 1991).

[4] Operated by the University of California, Berkeley, the University of Illinois, and the University of Maryland, with support from the National Science Foundation.

[5] The National Radio Astronomy Observatory is a facility of the National Science Foundation, operated under cooperative agreement by Associated Universities, Inc.

TABLE 1
COORDINATES OF SOURCES

Source	α(J2000.0)	δ(J2000.0)
Sgr B2(N-LMH)[a]	17 47 20.0	−28 22 17.3
Sgr B2(M)[b]	17 47 20.3	−28 23 07.3
Sgr B2(OH)[b]	17 47 20.8	−28 23 32.2
Sgr B2(S)[b]	17 47 20.3	−28 23 46.3
Sgr B2(NW)[c]	17 47 16.4	−28 22 22.5

NOTE.—Units of right ascension are hours, minutes, and seconds, and units of declination are degrees, arcminutes, and arcseconds.

[a] Taken from Miao & Snyder 1997.
[b] Taken from Sutton et al. 1991.
[c] Taken from Nummelin et al. 1998.

single-element telescope is best for detecting large-scale, extended emission but is poor at detecting compact sources because of beam dilution. An array is insensitive to structures larger than an angular size determined by the minimum spacing of its elements and thus resolves out large-scale structure. For the BIMA array, this is ∼10 times the size of the synthesized beam (Wright 1996).[6] This feature is very important in astrochemistry, because the location of a particular molecular species may indicate its formation mechanism. Molecules formed by low-temperature gas-phase reactions will be primarily extended in emission. On the other hand, molecules formed on grains, while they may form anywhere in the cloud, will evaporate from the grains and be detected in the warmer compact cores of the sources (Caselli, Hasegawa, & Herbst 1993). Similarly, molecules formed by warm gas-phase reactions will also be detected in the warmer cores. Thus, a

[6] The BIMA Memoranda Series (Wright 1996) is available at http://bima.astro.umd.edu/memo/memo45.ps.

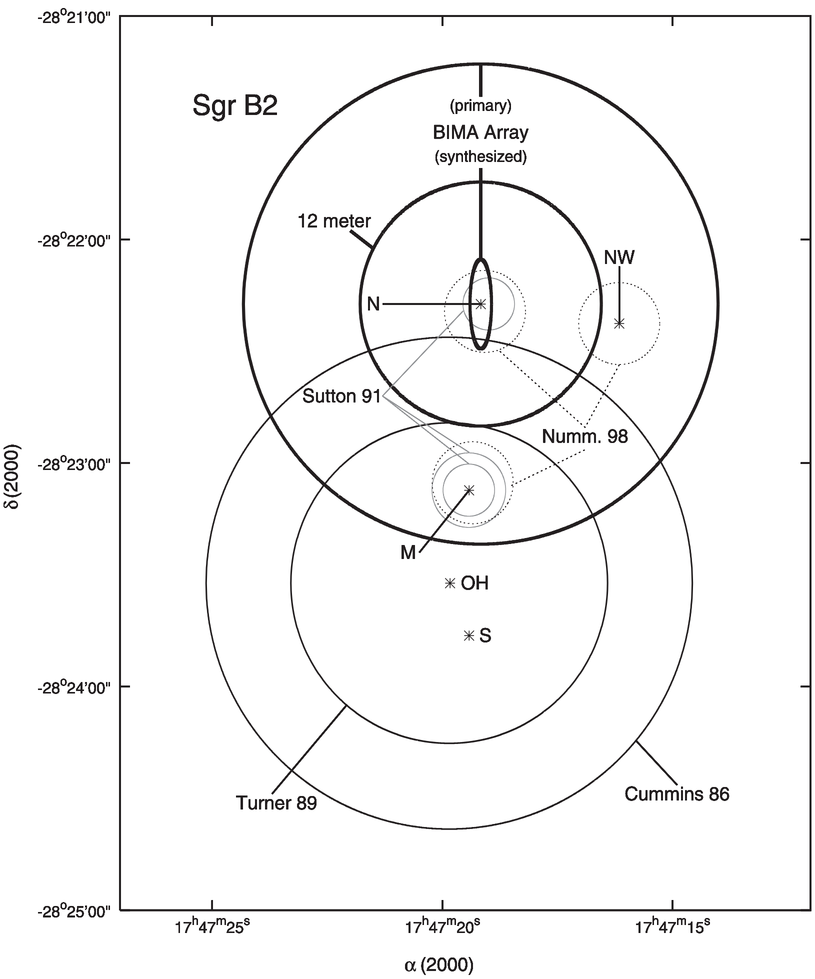

FIG. 1.—Pointing centers and average beams from this and previous spectral line surveys of the Sgr B2 region. The five cores of Sgr B2 are labeled (north, main, south, northwest, and OH). The beams from this survey have bold outlines centered on Sgr B2(N). The dashed beams around Sgr B2(N), Sgr B2(M), and Sgr B2(NW) are from Nummelin et al. (1998, 2000). The gray beams around Sgr B2(N) and Sgr B2(M) (two beams) are from Sutton et al. (1991). The beams centered on Sgr B2(OH) are from Turner (1989, 1991) and Cummins et al. 1986).

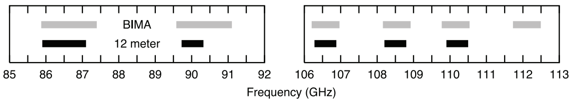

Fig. 2.—Frequency coverage of the line survey. Twelve-meter telescope coverage is in black. BIMA array coverage is in gray. Some frequencies are covered by the BIMA array and not the 12 m telescope because of the dual sidebands of the BIMA array receiver and correlator systems. Only frequencies that have been observed by both instruments are presented in this paper.

single element telescope would be most sensitive to molecules formed in extended, low-temperature gas clouds, while an array would be most sensitive to molecules formed in warm cores (either in warm gas-phase reactions or initially on a grain and then desorbed from the surface).

Our spectral line survey is the first to use both interferometric data and single-element telescope data from Sgr B2(N-LMH) and is also the first 3 mm survey of this source. Here we present the results of a line survey toward Sgr B2(N-LMH) of six 600 MHz wide spectral bands (Fig. 2). All bands were observed with both the BIMA array and the NRAO 12 m radio telescope.

2. OBSERVATIONS AND DATA

The pointing center of our survey was Sgr B2(N-LMH).[7] The spectral bands surveyed (Fig. 2) were centered on 86.2, 86.8, 90.025, 106.58, 108.5, and 110.2 GHz.[8] We chose these bands because each contains at least one previously identified molecular transition. In most cases, the spectral bands contained many well-known molecular species, including silicon monoxide (SiO), sulfur monoxide (SO), deuterated ammonia (NH_2D), methyl formate ($HCOOCH_3$, or MeF), cyanogen (^{13}CN), carbon monoxide (^{13}CO), methyl cyanide (CH_3CN), and formamide (NH_2CHO).

2.1. *NRAO* 12 m *Telescope Observations*

The NRAO 12 m telescope observations were carried out in 2000 July. The spectra observed with the 12 m telescope utilized the dual-channel Superconductor-Insulator-Superconductor mixer receiver operating in a single-sideband mode with the image sideband rejected at a typical level of 20 dB. The Millimeter Autocorrelator spectrometer was used in its 600 MHz bandwidth mode with a channel spacing of 195 kHz per channel. This gives a frequency resolution of 391 kHz per channel, owing to internal Hanning weighting, and a velocity resolution of $\sim$1.4, 1.4, 1.3, 1.1, 1.1, and 1.1 km s^{-1} for the 86.2, 86.8, 90.025, 106.58, 108.5, and 110.2 GHz bands, respectively. The two receivers provided orthogonal linear polarizations and integrated on source for 1.75–2.5 hr. Calibration of the intensity scale made use of the chopper wheel method, with the resulting data on the T_A^* scale. This was converted to the T_R^* scale by applying the main-beam efficiency, which varies between 0.68 at 86 GHz and 0.62 at 110 GHz and is accurate to within $\sim$5% (Kutner & Ulich 1981). This scale corrects for atmospheric extinction and telescope spillover losses but not for error-beam losses or the forward beam coupling to the source. Data were taken using position switching, with the reference position 30′ west in azimuth in order to avoid any extended structure. The passbands were calibrated by baseline-fitting to the data with a polynomial on the order of 4 or less. The passbands were checked before and after calibration for spurious features; none was found. The 12 m telescope data were analyzed with the UniPOPS software package (Salter, Maddalena, & Garwood 1995).[9]

2.2. *BIMA Array Observations*

Observations with the BIMA array were carried out in C configuration (minimum baseline of 8 m and maximum baseline of 61 m) between 2001 March and 2002 April. The array was operating in cross-correlation mode (double sideband), with a sideband rejection of better than 20 dB. The correlator configuration was four 50 MHz spectral windows set side by side with the edges overlapping by three channels, giving an effective bandwidth of just under 200 MHz in each sideband. Each window had 128 channels, resulting in a spectral resolution of 390 kHz per channel and a velocity resolution of $\sim$1.4, 1.4, 1.3, 1.1, 1.1, and 1.1 km s^{-1} for the 86.2, 86.8, 90.025, 106.58, 108.5, and 110.2 GHz bands, respectively. This set of four windows was set up to start at the lower end of each of the 600 MHz wide spectral bands and integrated on source for 50 minutes. Next, the observing frequency was shifted by 197 MHz, and the integration was continued. This process was repeated until the entire 600 MHz band was observed. Neptune and Mars were used as flux density calibrators, and 1733−130 was used to calibrate the antenna-based gains. The absolute amplitude calibration of 1733−130 from the flux density calibrators is accurate to within $\sim$20%. The passbands were automatically calibrated on-line during data acquisition.[10] In the past, this method has been quite satisfactory and has not generated spurious features. The BIMA array data were calibrated and imaged using the MIRIAD software package (Sault, Teuben, & Wright 1995).

2.3. *Data*

Table 2 contains a list of beam sizes and rms noise levels for the observations. The first column lists the central frequency of the observed band (in GHz). The second and third columns

[7] While this is the pointing center of all observations, the beams of both telescopes also encompassed other sources within Sgr B2(N).

[8] While the BIMA array observed a wider spectral band than the 12 m telescope in several instances, these data are not being presented in this paper, since there is no 12 m data to compare it to, but they will be presented in future papers.

[9] UniPOPS information is available at: http://info.gb.nrao.edu/~rmaddale/140ft/unipops/unipops_toc.html.

[10] A technical description of this can be found at http://astron.berkeley.edu/~plambeck/technical.html.

TABLE 2
Beam Sizes[a] and rms Noise Levels of Observations

Frequency (GHz)	Bima Array		12 m Telescope	
	Beam[b] (arcsec)	rms[b] (Jy beam^{-1})	Beam (arcsec)	rms (Jy beam^{-1})
86.200	27.2 × 6.6	0.216	74	0.613
86.800	32.2 × 6.5	0.231	73	0.569
90.025	25.2 × 6.3	0.197	71	0.700
106.580	23.2 × 5.2	0.462	60	0.628
108.500	21.0 × 5.3	0.586	59	0.941
110.200	23.2 × 5.1	0.679	57	0.598

[a] Synthesized beam for BIMA array observations and main diffraction beamwidth (FWHM) for 12 m telescope observations.
[b] Average of all scans.

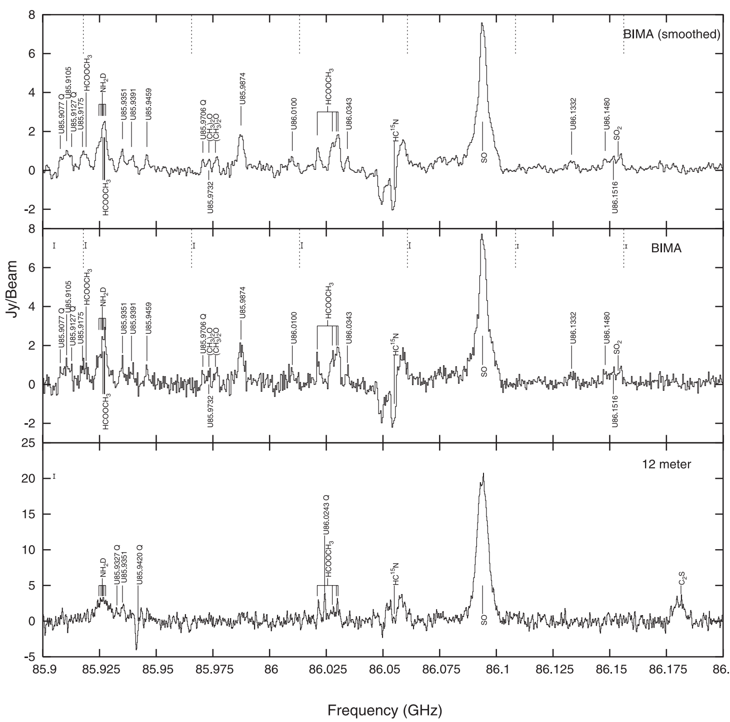

FIG. 3*a*

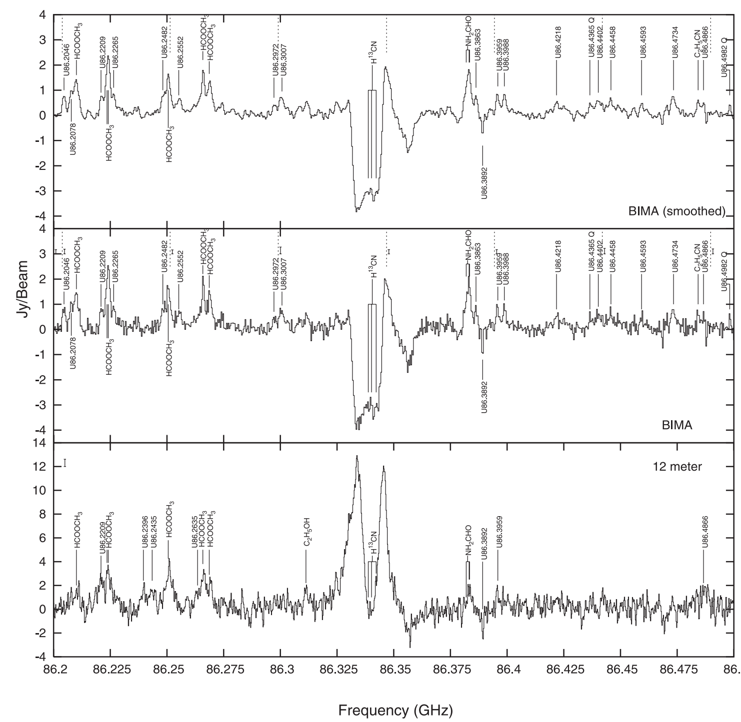

FIG. 3*b*

FIG. 3.—Top spectra are from the BIMA array. Vertical dashed lines denote where two spectral windows meet. Bars next to the window edges denote the rms noise level of each window. The bottom spectra are from the NRAO 12 m and match the BIMA array frequency range. The 12 m telescope intensity scale was converted from T_R^* to Jy beam^{-1} using 30.5, 30.6, 30.8, 31.6, 31.8, and 32.0 Jy K^{-1} as conversion factors for the 86.2, 86.8, 90.025, 106.58, 108.5, and 110.2 GHz bands, respectively. Detected transitions of known lines are noted, as are lines from unknown transitions (denoted as "U").

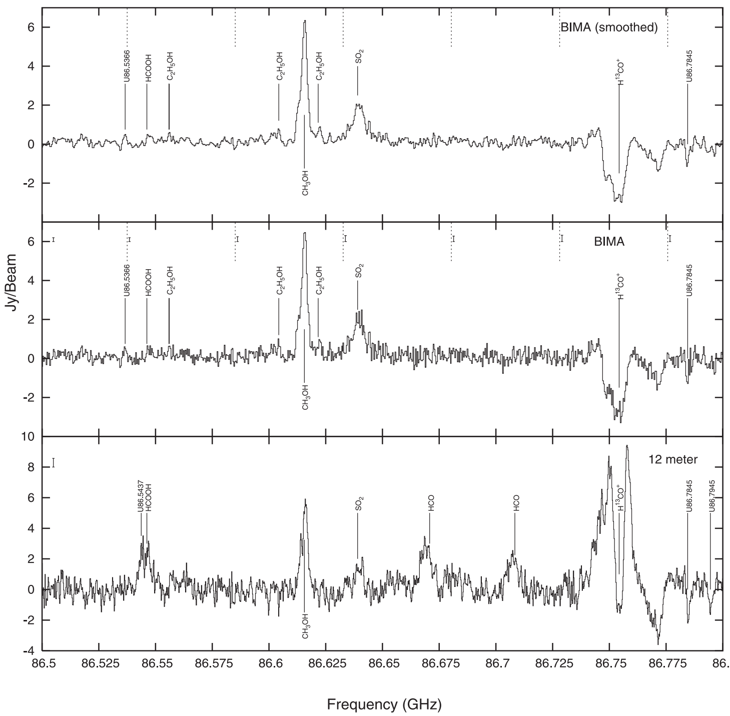
BIMA (smoothed)
BIMA
12 meter
Jy/Beam
Frequency (GHz)
U86.5366
HCOOH
C_2H_5OH
CH_3OH
SO_2
$H^{13}CO^+$
U86.7845
U86.5437
HCO
U86.7945
86.5
86.525
86.55
86.575
86.6
86.625
86.65
86.675
86.7
86.725
86.75
86.775
86.8

FIG. 3*c*

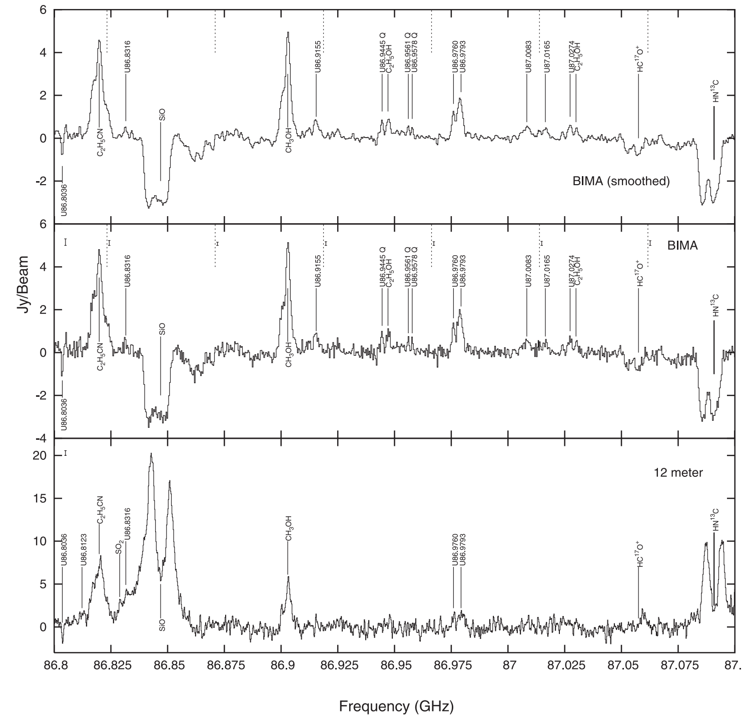
BIMA (smoothed)
BIMA
12 meter
Jy/Beam
Frequency (GHz)
U86.8036
C_2H_5CN
U86.8316
SiO
CH_3OH
U86.9155
U86.9445 Q
C_2H_5OH
U86.9561 Q
U86.9578 Q
U86.9760
U86.9793
U87.0083
U87.0165
U87.0274
$HC^{17}O^+$
$HN^{13}C$
U86.8123
SO_2
86.8
86.825
86.85
86.875
86.9
86.925
86.95
86.975
87
87.025
87.05
87.075
87.1

FIG. 3*d*

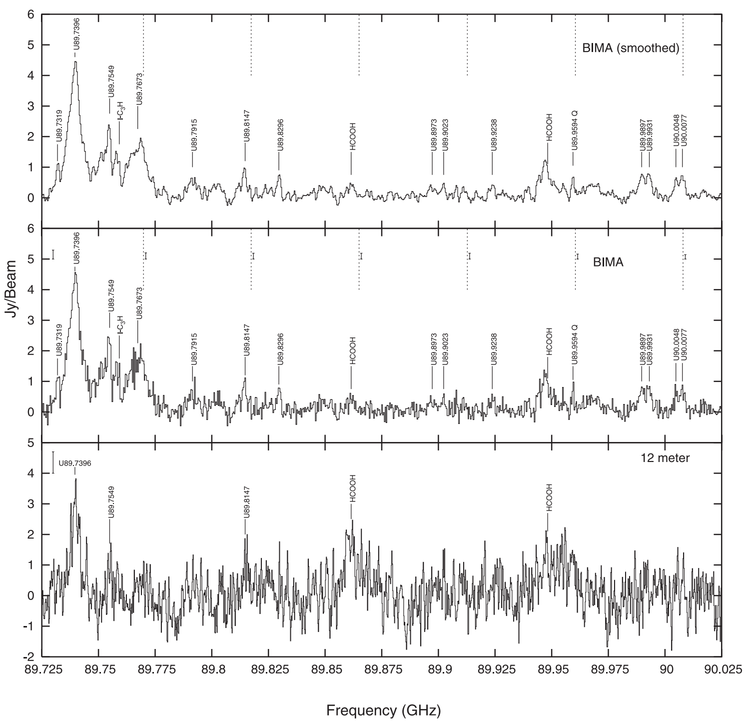
BIMA (smoothed)
BIMA
12 meter
Jy/Beam
Frequency (GHz)
U89.7319
U89.7396
U89.7549
C₂H
U89.7673
U89.7915
U89.8147
U89.8296
HCOOH
U89.8973
U89.9023
U89.9238
HCOOH
U89.9594
U89.9897
U89.9931
U90.0048
U90.0077

FIG. 3e

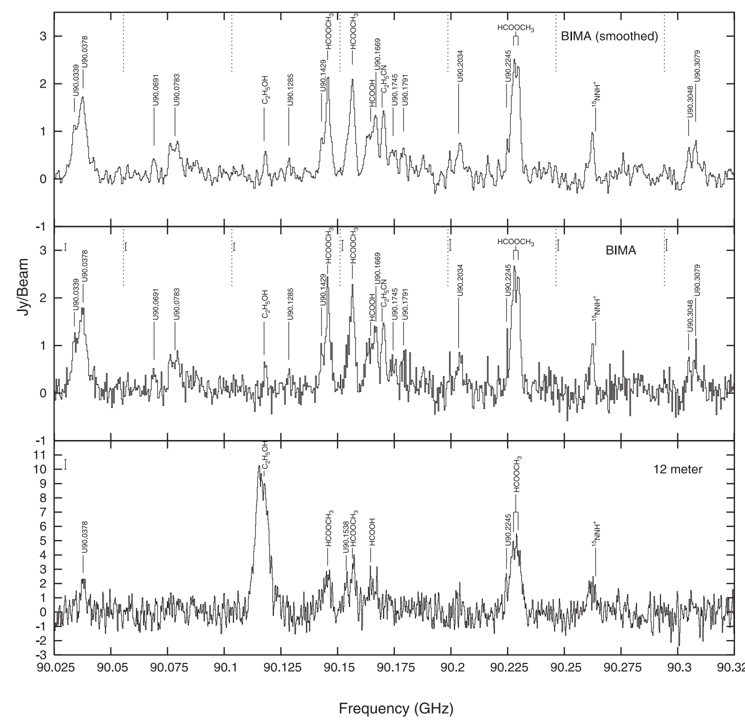
BIMA (smoothed)
BIMA
12 meter
Jy/Beam
Frequency (GHz)
U90.0339
U90.0378
U90.0691
U90.0783
C₂H₅OH
U90.1285
U90.1429
HCOOCH₃
HCOOCH₃
HCOOH
U90.1669
C₂H₅CN
U90.1745
U90.1791
U90.2034
U90.2245
HCOOCH₃
¹⁵NNH⁺
U90.3048
U90.3079
U90.1538

FIG. 3f

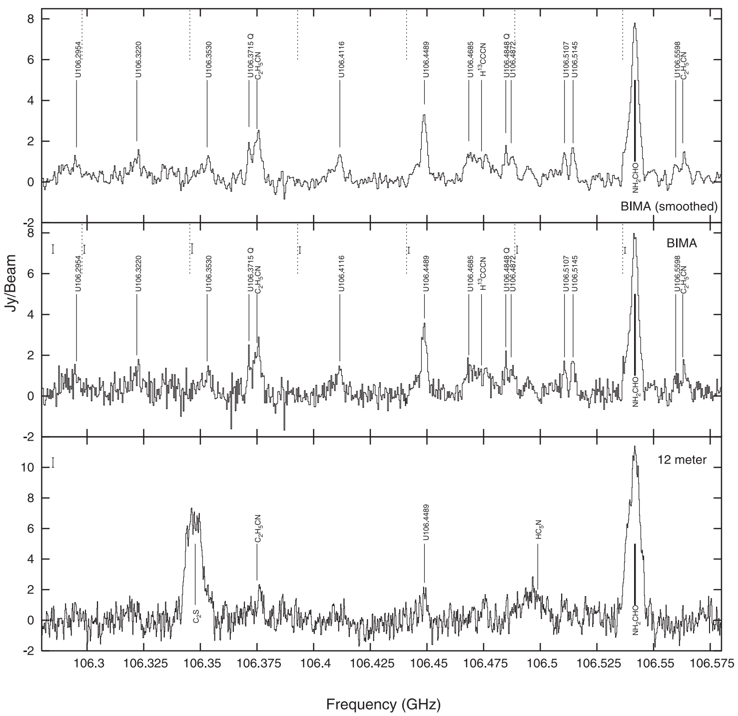
BIMA (smoothed)
BIMA
12 meter
Jy/Beam
Frequency (GHz)

Fig. 3g

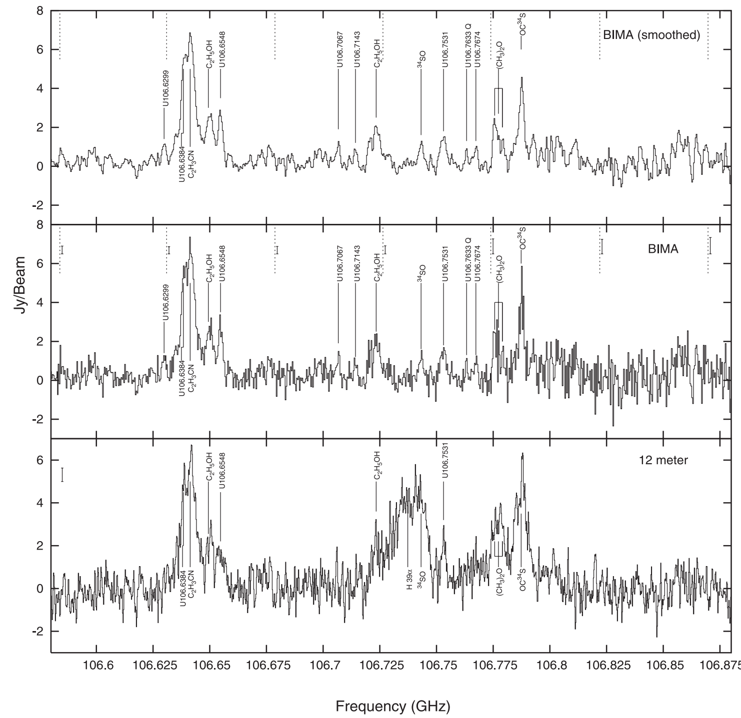
BIMA (smoothed)
BIMA
12 meter
Jy/Beam
Frequency (GHz)

Fig. 3h

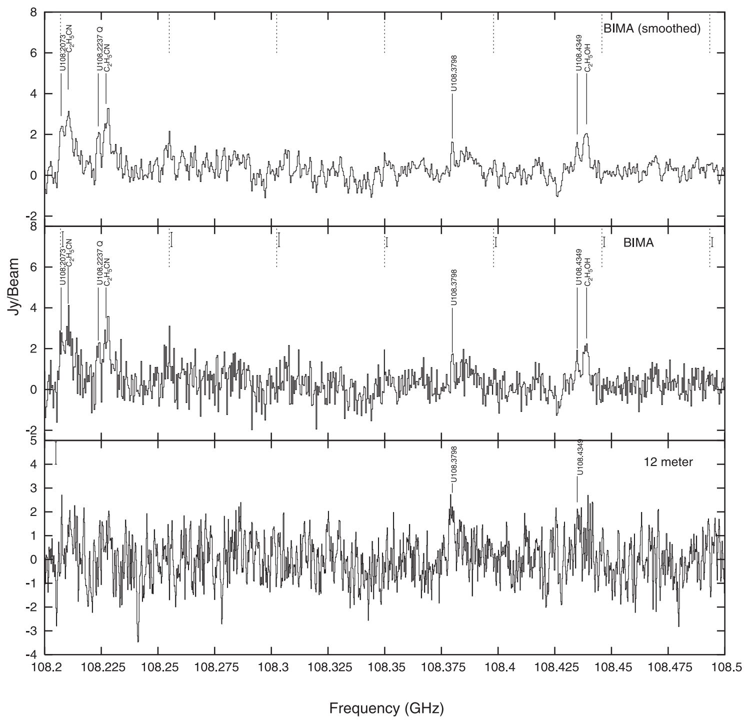
BIMA (smoothed)
BIMA
12 meter
Jy/Beam
Frequency (GHz)
U108.2073
U108.2237 Q
U108.3798
U108.4349
C2H5OH

FIG. 3*i*

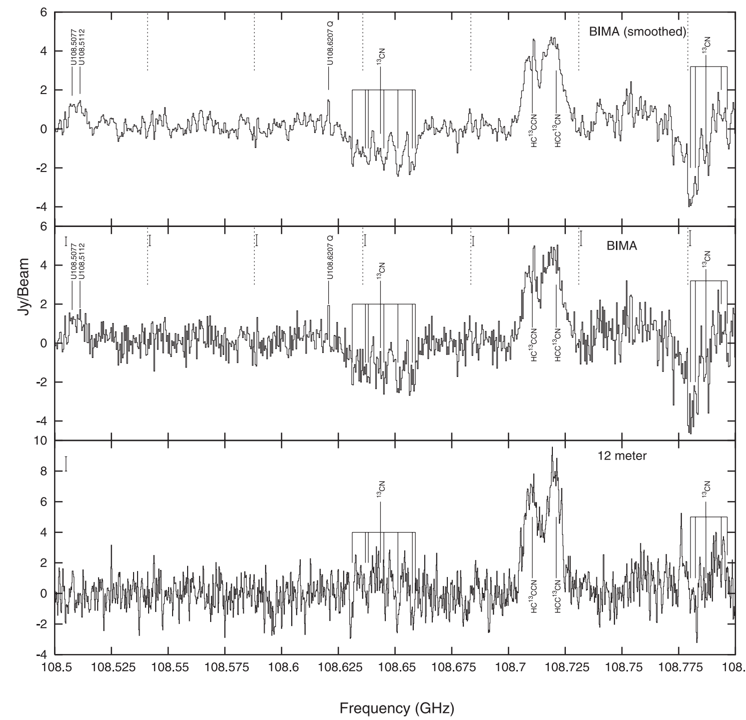
BIMA (smoothed)
BIMA
12 meter
Jy/Beam
Frequency (GHz)
U108.5077
U108.5112
U108.6207 Q
13CN
HC13CCN
HCC13CN

FIG. 3*j*

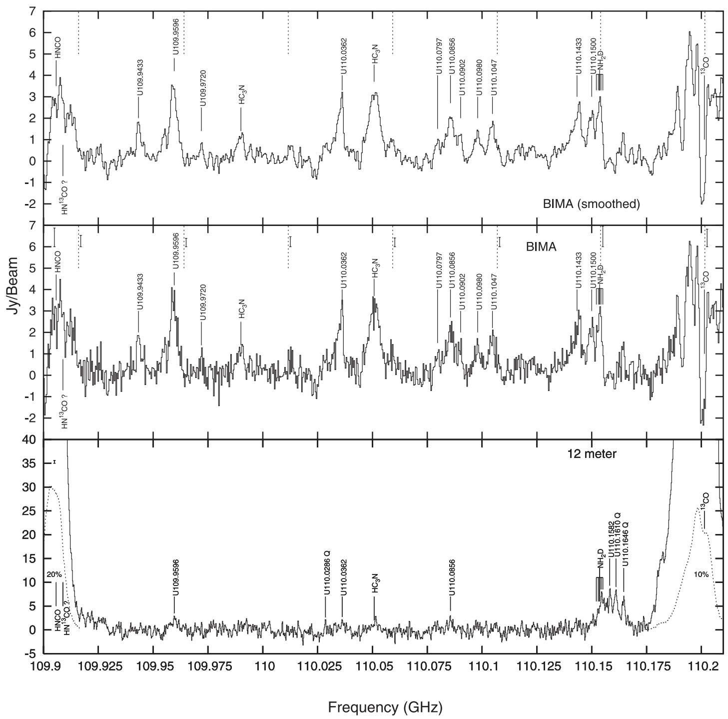
BIMA (smoothed)
BIMA
12 meter
Jy/Beam
Frequency (GHz)
HNCO
HN^{13}CO ?
U109.9433
U109.9596
U109.9720
HC$_3$N
U110.0362
U110.0797
U110.0856
U110.0902
U110.0980
U110.1047
U110.1433
U110.1500
NH$_2$D
^{13}CO
U110.0286 Q
U110.1582
U110.1610 Q
U110.1646 Q
20%
10%

FIG. 3*k*

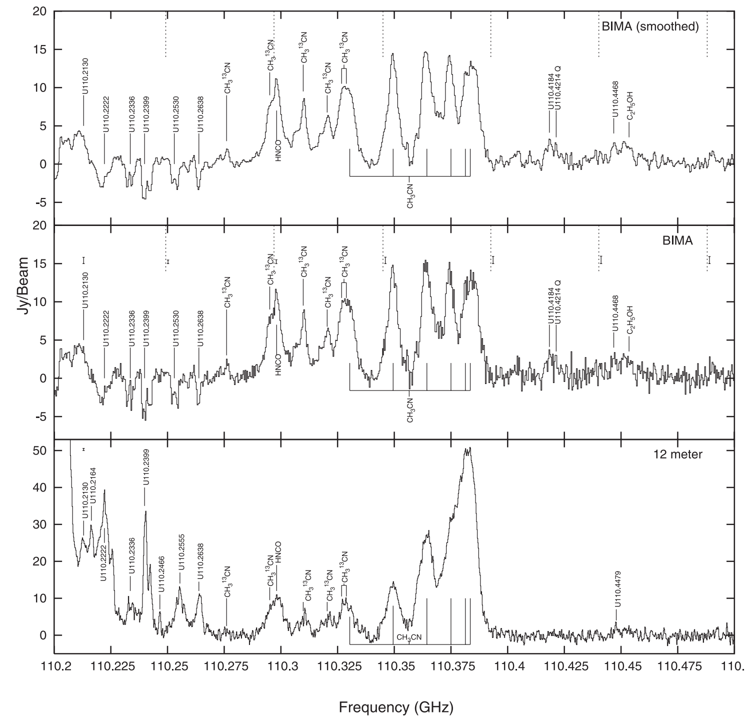
BIMA (smoothed)
BIMA
12 meter
Jy/Beam
Frequency (GHz)
U110.2130
U110.2164
U110.2222
U110.2336
U110.2399
U110.2466
U110.2530
U110.2555
U110.2638
CH$_3$^{13}CN
HNCO
CH$_3$CN
U110.4184
U110.4214 Q
U110.4468
U110.4479
C$_2$H$_5$OH

FIG. 3*l*

list the synthesized beam size (in arcsec) and the 1 σ channel rms noise level (in Jy beam^{-1}) for the BIMA array observations, which have been averaged over all windows. The last two columns list the FWHM beam size (in arcsec) and the 1 σ channel rms noise level (in Jy beam^{-1}) of the 12 m telescope observations. The 1 σ rms noise levels from the BIMA array were determined by taking the rms over all channels from a spatial region that was free from continuum emission. The 1 σ rms noise levels from the 12 m telescope were determined by calculating the rms in sections of line-free channels.

The spectra are presented in Figures 3*a*–3*l*. In order to derive the frequency scale for the BIMA array, $V_{\rm LSR} = 64$ km s^{-1} was used (Mehringer et al. 1997). For the 12 m telescope, $V_{\rm LSR} = 65$ km s^{-1} was used, because it is the value in a standard 12 m catalog. In the figures, the two upper panels show BIMA array data, and the lower panel shows 12 m telescope data. The top panel in each figure shows BIMA array data, which are Hanning-weighted to bring out weaker features by reducing the noise level. The middle panel in each figure shows the BIMA array data, which are unsmoothed (not Hanning-weighted) in order to preserve narrow features that are also seen in the 12 m telescope data. The 12 m telescope data were automatically Hanning-smoothed as part of the internal data acquisition routine. The spectral resolution of the unsmoothed BIMA array data matches that of the smoothed 12 m telescope data to within 1 kHz. The 12 m telescope intensity scale was converted from T_R^* to Jy beam^{-1} using 30.5, 30.6, 30.8, 31.6, 31.8, and 32.0 Jy K^{-1} as conversion factors for the 86.2, 86.8, 90.025, 106.58, 108.5, and 110.2 GHz bands, respectively. The dashed lines on the BIMA array spectra denote spectral window edges, and the "*I*" bars, in both the 12 m telescope and BIMA array data (unsmoothed), denote 1 σ rms noise levels. The threshold for defining a line is as follows: it must have a signal-to-noise ratio of at least 3 σ and have a line width of at least 4 km s^{-1} (unless a notable feature is seen at the same frequency with both instruments). Unidentified lines labeled with "Q" are questionable detections due to their narrow line width.

Table 3 summarizes the molecular detections of the survey. The first column lists the molecule; the second and third columns list the number of detected transitions by the BIMA array and the 12 m telescope, respectively. The fourth column lists the reference for the molecular information for each species. Table 4 lists the molecular transitions, grouped by molecule. The first column lists the rest frequency of the transition, along with the 2 σ standard deviation. The second column lists the quantum numbers of the transition. The third and fourth columns list the intensity and line width,[11] with the 2 σ standard deviation, of each line observed by the BIMA array. Fits to the BIMA array data were on the unsmoothed spectra. If the transition was not detected, a 1 σ upper limit has been set for the intensity. The fifth and sixth columns list the intensity and line width, with the 2 σ standard deviation, of each line observed by the 12 m telescope. In a single case from the BIMA array, the blend of MeF and NH_2D at 85.92 GHz (see Fig. 3*a*), the MeF lines were modeled using the fits to the other detected MeF transitions, in order to obtain a satisfactory fit to all components. The seventh column lists the upper energy level of each transition. The eighth column lists the product of the line strength and the square of the relevant dipole moment. Table 5 lists the detected unidentified (U) lines. The first column lists the rest frequency [based on the LSR velocity of Sgr B2(N-LMH)]. The second and third columns list the peak intensity and line width, with the 2 σ standard deviation, of each line from the BIMA array. The fourth and fifth columns list the peak intensity and line width, with the 2 σ standard deviation, of each line from the 12 m telescope. If a line was undetected by one of the telescopes, a 1 σ upper limit has been set for the intensity. In order to find potential identi-

TABLE 3

Summary of Molecules Detected by the BIMA Array and NRAO 12 m Radio Telescope

	Detected Transitions		
Species	BIMA Array	12 m Telescope	References
l–C_3H[a]	1	0	1, 2, 3
C_2H_3CN	1	1	4
C_2H_5CN	7	2	5
C_2H_5OH	11	4	5, 6
C_2S	0	2	7, 8
CH_3CN	6	6	9
$CH_3^{13}CN$	6	6	9
$(CH_3)_2O$	6	4	10
CH_3OH	2	2	11
^{13}CN[a]	4	4	12
^{13}CO	1	1	13
$H39\alpha$	0	1	14
HC_5N	0	1	3, 15
HC_3N	2	1	15, 16, 17
$H^{13}CCCN$	1	0	15, 17
$HC^{13}CCN$	1	1	16
$HCC^{13}CN$	1	1	16
$H^{13}CN$[a]	1	1	18
$HC^{15}N$	1	1	18
HCO[a]	0	1	3, 19
$H^{13}CO^+$	1	1	20
$HC^{17}O^+$	1	1	21
$HCOOCH_3$	18	14	22
HCOOH	4	4	23
$HN^{13}C$[a]	1	1	3, 24
HNCO	2	2	3, 25
$HN^{13}CO$	1	1	26
NH_2CHO[a]	2	2	26
NH_2D[a]	2	2	3, 27, 28
$^{15}NNH^+$	1	1	3, 15
$OC^{34}S$	1	1	3, 18
SiO	1	1	29
SO	1	1	30
^{34}SO	1	1	30
SO_2	2	2	31
U	108	41	
Total	199	116	

[a] Number of detected lines does not include hyperfine components.

References.—(1) Gottlieb et al. 1986; (2) Yamamoto et al. 1990b; (3) Pickett et al. 1998; (4) Gerry, Yamada, & Winnewisser 1979; (5) Lovas 1982; (6) J. C. Pearson, private communication; (7) Yamamoto et al. 1990a; (8) Murakami 1990; (9) Boucher et al. 1980; (10) Groner et al. 1998; (11) Xu & Lovas 1997; (12) Bogey, Demuynck, & Destombles 1984; (13) Lovas & Tiemann 1974; (14) Lilley & Palmer 1968; (15) Lovas 2004; (16) Lafferty & Lovas 1978; (17) Wyrowski, Schilke, & Walmsley 1999; (18) Lovas 1978; (19) Snyder, Schenewerk, & Hollis 1985; (20) Woods et al. 1981; (21) Guélin, Cernicharo, & Linke 1982; (22) Oesterling et al. 1999; (23) Willemot et al. 1980; (24) Frerking, Wilson, & Langer 1979; (25) Winnewisser, Hocking, & Gerry 1976; (26) Johnson, Lovas, & Kirchhoff 1972; (27) Bester et al. 1983; (28) Shah & Wootten 2001; (29) Lovas & Krupenie 1974; (30) Tiemann 1974; (31) Lovas 1985.

[11] Intensities and line widths were obtained by a Gaussian least-squares fit to the line profiles.

TABLE 4

DETECTED TRANSITIONS

Rest Frequency (MHz)[a]	Transition[b]	BIMA Array I_0 (Jy beam^{-1})	BIMA Array Δv (km s^{-1})	12 m Telescope I_0 (Jy beam^{-1})	12 m Telescope Δv (km s^{-1})	E_u (K)	$\langle S_{i,j}\mu^2 \rangle$ (D^2)
			l–C_3H ($\nu_4^2\Sigma^\mu$)				
89,759.3280 (480)[c]	$N_J = 4_{7/2}-3_{5/2},\ F = 4-3$	1.0(8)	7.0(56)	<0.7	...	49.9	18.45
89,759.8490 (480)[c]	$F = 3-2$	...	...	<0.7	...	49.9	13.74
			C_2H_3CN (VyCN)				
106,641.3940 (170).........	$11_{1,10}-10_{1,9}$	6.7(4)	11.7(38)	6.1(4)	10.7(18)	32.9	147.71
			C_2H_5CN (EtCN)				
86,484.2300 (400)[d]	$29_{3,27}-28_{4,24}$	0.5(2)	5.9(38)	<0.6	...	197.1	6.20
86,819.8510 (130)[e]	$10_{1,10}-9_{1,9}$	4.6(2)	11.4(10)	7.5(2)	13.8(14)	24.1	146.68
90,169.6330 (260)[d]	$20_{2,18}-19_{3,17}$	1.5(2)	6.6(18)	<0.7	...	96.4	6.09
106,375.0030 (200).........	$15_{3,12}-15_{2,13}$	2.4(4)	10.9(26)	2.0(4)	7.6(28)	61.7	13.24
106,562.9160 (320)[d]	$27_{3,24}-26_{4,23}$	1.3(4)	9.6(28)	<0.6	...	174.1	7.23
108,210.3860 (170)[d]	$11_{1,11}-10_{0,10}$	2.7(6)	13.8(70)	<0.9	...	28.6	11.01
108,227.0930 (200)[d]	$14_{3,11}-14_{2,12}$	2.6(8)	13.0(52)	<0.9	...	55.2	12.07
			C_2H_5OH[f] (EtOH)				
86,311.2673 (32)[d]	$5^+_{2,4}-4^+_{2,3}$	<0.3	...	1.8(2)	6.0(10)	73.7	5.03
86,555.9124 (28)[c,d]	$5^+_{4,2}-4^+_{4,1}$	0.7(4)	4.4(26)	<0.6	...	88.3	4.20
86,556.0115 (28)[c,d]	$5^+_{4,1}-4^+_{4,0}$	...	...	<0.6	...	88.3	4.20
86,604.2917 (28)[d]	$5^+_{3,3}-4^+_{3,2}$	0.9(2)	4.3(16)	<0.6	...	79.8	4.07
86,621.7341 (28)[d]	$5^+_{3,2}-4^+_{3,1}$	0.9(2)	7.5(24)	<0.6	...	79.8	4.07
86,947.1200 (270)[d]	$15_{2,13}-15_{1,14}$	0.9(4)	7.2(30)	<0.6	...	108.1	22.56
87,029.9919 (30)[d]	$5^+_{2,3}-4^+_{2,2}$	0.6(2)	4.2(22)	<0.6	...	73.8	5.02
90,117.6000 (90).............	$4_{1,4}-3_{0,3}$	0.6(2)	4.7(22)	9.9(4)	21.5(10)	9.4	5.35
106,649.4400 (310)[d]	$13_{1,12}-13_{0,13}$	2.7(4)	11.4(32)	2.5(4)	7.8(26)	79.4	10.14
106,723.4100 (180).........	$9_{2,8}-9_{1,9}$	1.9(4)	11.3(44)	1.7(4)	10.4(34)	42.7	7.66
108,439.0700 (800)[d]	$13_{3,10}-13_{2,11}$	2.2(2)	7.8(12)	<0.6	...	88.2	18.19
110,453.5300 (3990)[d]	$21_{3,18}-21_{2,19}$	2.7(6)	15.4(48)	<0.6	...	208.7	33.93
			C_2S				
86,181.4130 (100)...........	$J_N = 6_7-5_6$	<0.2	...	2.8(4)	18.7(24)	23.3	41.03
106,347.7420 (100).........	$J_N = 9_8-8_7$	<0.5	...	7.1(4)	22.4(12)	24.5	63.01
			CH_3CN				
110,330.3470 (23)[g]	$J_K = 6_5-5_5$	6.0(12)	19.8(10)	3.1(10)	20.9(6)	196.1	28.07
110,349.4730 (16)...........	$J_K = 6_4-5_4$	13.1(10)	15.8(14)	12.5(12)	20.9(6)	132.2	51.03
110,364.3570 (11)...........	$J_K = 6_3-5_3$	14.1(10)	17.7(16)	26.8(12)	20.9(6)	82.5	68.90
110,374.9920 (9).............	$J_K = 6_2-5_2$	12.6(10)	18.0(22)	27.1(18)	20.9(6)	47.0	81.66
110,381.3760 (10)...........	$J_K = 6_1-5_1$	10.7(18)	12.0(16)	16.1(42)	20.9(6)	25.7	89.31
110,383.5040 (10)...........	$J_K = 6_0-5_0$	10.9(18)	12.0(16)	36.5(42)	20.9(6)	18.5	91.87
			$CH_3^{13}CN$				
110,276.0470 (460)[d]	$J_K = 6_5-5_5$	1.2(4)	17.2(4)	0.6(4)	15.4(8)	197.5	28.07
110,295.0700 (340)[d]	$J_K = 6_4-5_4$	3.2(18)	17.2(4)	5.3(4)	15.4(8)	133.1	51.03
110,309.8670 (290).........	$J_K = 6_3-5_3$	6.8(4)	17.2(4)	4.5(4)	15.4(8)	83.0	68.90
110,320.4350 (290)[d]	$J_K = 6_2-5_2$	5.4(4)	17.2(4)	4.4(4)	15.4(8)	47.2	81.66
110,326.7770 (300)[g]	$J_K = 6_1-5_1$	1.6(12)	17.2(4)	1.5(8)	15.4(8)	25.7	89.31
110,328.8900 (310)[g]	$J_K = 6_0-5_0$	4.3(22)	17.2(4)	4.9(16)	15.4(8)	18.5	91.87
			$(CH_3)_2O$				
85,973.2490 (80).............	$13_{2,12}-12_{3,9}$AA	0.3(2)	5.6(30)	<0.6	...	88.0	2.81
85,976.1310 (80).............	$13_{2,12}-12_{3,9}$EE	0.8(4)	5.6(30)	<0.6	...	88.0	2.81
106,775.6790 (80)...........	$9_{1,8}-8_{2,7}$AA	0.9[h]	7.0	1.1(2)	15.7(26)	43.4	3.66
106,777.3710 (60)...........	$9_{1,8}-8_{2,7}$EE	1.4[h]	7.0	1.7(2)	15.7(26)	43.4	3.66
106,779.0580 (60)...........	$9_{1,8}-8_{2,7}$AE	0.5[h]	7.0	0.6(1)	15.7(26)	43.4	3.66

TABLE 4—*Continued*

Rest Frequency (MHz)[a]	Transition[b]	BIMA Array I_0 (Jy beam^{-1})	BIMA Array Δv (km s^{-1})	12 m Telescope I_0 (Jy beam^{-1})	12 m Telescope Δv (km s^{-1})	E_u (K)	$\langle S_{i,j}\mu^2\rangle$ (D^2)
			$(CH_3)_2O$				
106,779.0660 (60)..........	$9_{1,8}-8_{2,7}$EA	0.4[h]	7.0	0.4(1)	15.7(26)	43.4	3.66
			CH_3OH				
86,615.6020 (140)[e]	$7_{2,6}-6_{3,3}$A−	6.3(4)	10.2(8)	5.8(4)	8.3(10)	102.7	1.36
86,902.9470 (140)[e]	$7_{2,5}-6_{3,4}$A+	5.0(2)	8.9(6)	5.2(4)	8.9(8)	102.7	1.36
			^{13}CN				
108,631.1210 (1000)[d]	$N_{J,F} = 1_{1,0}-0_{0,1}$	[i]	...	[i]	...	5.2	2.10
108,636.9230 (1000)[d]	$N_{J,F} = 1_{1,1}-1_{0,1}$	[i]	...	[i]	...	5.2	2.10
108,638.2120 (1000)[d]	$N_{J,F} = 1_{1,1}-0_{1,0}$	[i]	...	[i]	...	5.2	2.10
108,643.5900 (1000)[d]	$N_{J,F} = 1_{1,2}-0_{1,1}$	[i]	...	[i]	...	5.2	2.10
108,645.0640 (2000)[d]	$N_{J,F} = 1_{1,1}-0_{1,1}$	[i]	...	[i]	...	5.2	2.10
108,645.0640 (2000)[d]	$N_{J,F} = 1_{1,0}-0_{1,1}$	[i]	...	[i]	...	5.2	2.10
108,651.2970 (1000).......	$N_{J,F} = 1_{1,2}-0_{0,1}$	[i]	...	[i]	...	5.2	2.10
108,657.6460 (1000).......	$N_{J,F} = 1_{1,2}-0_{1,2}$	[i]	...	[i]	...	5.2	2.10
108,658.9480 (1000).......	$N_{J,F} = 1_{1,1}-0_{1,2}$	[i]	...	[i]	...	5.2	2.10
108,780.2010 (1000).......	$N_{J,F} = 1_{2,3}-0_{1,2}$	[i]	...	[i]	...	5.2	4.21
108,782.3740 (1000).......	$N_{J,F} = 1_{2,2}-0_{1,1}$	[i]	...	[i]	...	5.2	4.21
108,786.9820 (1000).......	$N_{J,F} = 1_{2,1}-0_{1,0}$	[i]	...	[i]	...	5.2	4.21
108,793.7530 (1000)[d]	$N_{J,F} = 1_{2,1}-0_{1,1}$	[i]	...	[i]	...	5.3	4.21
108,796.4000 (1000)[d]	$N_{J,F} = 1_{2,2}-0_{1,2}$	[i]	...	[i]	...	5.3	4.21
			^{13}CO				
110,201.3700 (200).........	$J = 1-0$	[i]	...	123.5(132)[j]	12.1(10)	5.3	0.01
				105.8(122)[j]	10.8(6)		
				156.2(64)[j]	34.5(16)		
			$H^{39}\alpha$				
106,737.3630..................	Recombination Line	<0.4	...	4.0(2)	43.2(54)	...	...
			HC_5N				
106,498.9110 (80)..........	$J = 40-39$	<0.4	...	1.7(2)	34.1(52)	103.6	749.96
			HC_3N				
109,990.0000 (2000).......	$J = 12-11,\ \nu_6^1,\ \nu_7^1, \ell = 1e-$	1.3(2)	10.0(26)	<0.6	...	1391.0	166.00[k]
110,050.7650 (184).........	$J = 12-11, 3\nu_7^1, \ell = 1e$	3.1(4)	18.2(26)	1.6(6)	8.3(40)	990.7	165.27
			$H^{13}CCCN$				
106,474.1000 (10000).....	$J = 12-11,\ \nu_7^2$	1.1(2)	33.0(116)	<0.6	...	673.0	166.00[k]
			$HC^{13}CCN$				
108,710.5230 (240).........	$J = 12-11$	3.5(2)	17.9(32)	6.9(4)	20.3(18)	33.9	166.42
			$HCC^{13}CN$				
108,721.0077 (144).........	$J = 12-11$	4.6(4)	27.7(36)	8.1(4)	19.2(14)	33.9	166.42
			$H^{13}CN$				
86,338.7670 (600)...........	$J = 1-0\ F = 1-1$	[i]	...	[i]	...	4.0	8.91
86,340.1840 (600)...........	$J = 1-0\ F = 2-1$	[i]	...	[i]	...	4.0	8.91
86,342.2740 (600)...........	$J = 1-0\ F = 0-1$	[i]	...	[i]	...	4.0	8.91
			$HC^{15}N$				
86,054.9610 (600)...........	$J = 1-0$	[i]	...	[i]	...	4.1	8.91

TABLE 4—*Continued*

REST FREQUENCY (MHz)[a]	TRANSITION[b]	BIMA ARRAY I_0 (Jy beam^{-1})	BIMA ARRAY Δv (km s^{-1})	12 m TELESCOPE I_0 (Jy beam^{-1})	12 m TELESCOPE Δv (km s^{-1})	E_u (K)	$\langle S_{i,j}\mu^2\rangle$ (D^2)
			HCO				
	$N_{K_a,K_c} = 1_{0,1}-0_{0,0},\ J = (3/2)-(1/2)$						
86,670.8200 (800)..........	$F = 2-1$	<0.3	...	2.8(4)	19.7(26)	4.2	1.86
86,708.3500 (800)..........	$F = 1-0$	<0.3	...	2.1(2)	17.8(28)	4.2	1.86
			$H^{13}CO^+$				
86,754.3290 (780)..........	$J = 1-0$	[i]	...	[i]	...	4.2	10.89
			$HC^{17}O^+$				
87,057.5000 (10000).......	$J = 1-0$	[i]	...	[i]	...	4.2	10.89
			$HCOOCH_3$ (MeF)				
85,919.0860 (280)..........	$7_{6,1}-6_{6,0}$E	0.7(3)[l]	6.8(23)	<0.6	...	40.4	5.00
85,926.5080 (220)..........	$7_{6,2}-6_{6,1}$E	0.7(3)[l]	6.8(23)	<0.6	...	40.4	5.00
85,927.2300 (240)..........	$7_{6,2}-6_{6,1}$A	0.7(3)[l]	6.8(23)	<0.6	...	40.4	5.00
85,927.2360 (240)..........	$7_{6,1}-6_{6,0}$A	0.7(3)[l]	6.8(23)	<0.6	...	40.4	5.00
86,021.0080 (260)..........	$7_{5,2}-6_{5,1}$E	1.2(4)	5.6(22)	2.6(8)	3.6(12)	33.1	9.20
86,027.6740 (220)..........	$7_{5,3}-6_{5,2}$E	1.5(4)	7.8(40)	1.2(6)	5.9(20)	33.1	9.20
86,029.4450 (240)..........	$7_{5,3}-6_{5,2}$A	1.2(4)	4.2(28)	1.2(6)	5.9(20)	33.1	9.20
86,030.2120 (240)..........	$7_{5,2}-6_{5,1}$A	1.8(6)	4.4(18)	1.2(8)	5.9(20)	33.1	9.20
86,210.0790 (240)..........	$7_{4,4}-6_{4,3}$A	1.3(2)	8.2(20)	1.7(4)	8.3[m]	27.2	12.70
86,223.5480 (260)..........	$7_{4,3}-6_{4,2}$E	1.5(2)	7.1(32)	1.2(6)	8.3[m]	27.2	12.60
86,224.1060 (220)..........	$7_{4,4}-6_{4,3}$E	1.3(2)	3.7(16)	1.7(4)	8.3[m]	27.2	12.60
86,250.5760 (240)..........	$7_{4,3}-6_{4,2}$A	1.5(2)	7.8(26)	3.1(4)	14.4(20)	27.2	12.70
86,265.8260 (240)..........	$7_{3,5}-6_{3,4}$A	1.7(4)	6.3(24)	2.9(4)	8.4(14)	22.4	15.30
86,268.6590 (220)..........	$7_{3,5}-6_{3,4}$E	1.3(4)	8.6(40)	2.5(4)	5.2(40)	22.6	15.20
90,145.6340 (240)..........	$7_{2,5}-6_{2,4}$E	2.0(2)	9.1(18)	2.3(4)	13.6(28)	19.7	17.30
90,156.5110 (260)..........	$7_{2,5}-6_{2,4}$A	1.9(2)	11.1(16)	3.3(6)	8.2(20)	19.7	17.30
90,227.5950 (260)..........	$8_{0,8}-7_{0,7}$E	2.2(4)	7.7(10)	2.8(30)	14.0(18)	20.1	21.00
90,229.6470 (280)..........	$8_{0,8}-7_{0,7}$A	2.2(4)	7.7(10)	3.0(26)	14.0(18)	20.0	21.00
			HCOOH				
86,546.1800 (200)..........	$4_{1,4}-3_{1,3}$	0.5(2)	9.4(44)[h]	2.4(4)	10.8(44)	13.6	7.26
89,861.4800 (200)..........	$4_{2,3}-3_{2,2}$	0.4(2)	14.1(48)	2.3(8)	8.5(33)[h]	23.5	5.80
89,948.2100 (200)[d]	$4_{3,2}-3_{3,1}$	1.3(2)	9.2(36)	1.8(2)	7.2(14)	39.4	3.39
90,164.6200 (200)[d]	$4_{2,2}-3_{2,1}$	0.9(2)	13.5(80)	1.9(4)	17.8(42)	23.5	5.80
			$HN^{13}C$				
87,090.7350 (920)..........	$J = 1-0\ F = 0-1$	[i]	...	[i]	...	4.2	7.28
87,090.8590 (920)..........	$J = 1-0\ F = 2-1$	[i]	...	[i]	...	4.2	7.28
87,090.9420 (920)..........	$J = 1-0\ F = 1-1$	[i]	...	[i]	...	4.2	7.28
			HNCO				
109,905.7530 (100)[j]........	$5_{0,5}-4_{0,4}$	2.9(4)	24.4(74)	151.2(12)	26.5(2)	15.8	12.40
		1.7(12)	6.3(56)	23.6(22)	6.8(8)		
110,298.0980 (80)[h]	$5_{1,4}-4_{1,3}$	8.5(8)	17.6(14)	8.4(6)	15.0(10)	59.0	11.91
			$HN^{13}CO$				
109,908.8710 (440)[d]	$5_{0,5}-4_{0,4}$	???	...	???	...	15.8	12.40
			NH_2CHO				
86,381.9540 (80)[d]	$7_{1,6}-7_{0,7}, F = 7-7$	0.7[h]	7.5(40)	0.4[h]	7.2(56)	32.5	1.46[n]
86,383.2490 (30)[c,d]	$7_{1,6}-7_{0,7}, F = 8-8$	1.5(6)	7.5(40)	1.6(6)	7.2(56)	32.5	1.69[n]
86,383.4350 (50)[c,d]	$7_{1,6}-7_{0,7}, F = 6-6$	...	...	...	...	32.5	1.28[n]
106,541.8110 (800).........	$5_{2,3}-4_{2,2}$[e]	7.4(4)	12.5(8)	10.6(4)	17.8(6)	27.2	54.92

TABLE 4—*Continued*

Rest Frequency (MHz)[a]	Transition[b]	BIMA Array I_0 (Jy beam^{-1})	BIMA Array Δv (km s^{-1})	12 m Telescope I_0 (Jy beam^{-1})	12 m Telescope Δv (km s^{-1})	E_u (K)	$\langle S_{i,j}\mu^2\rangle$ (D^2)
			NH_2D				
Ortho	$1_{0,1}-1_{1,1}$						
85,924.7470 (400)	$F=0-1$	0.1(0)	18.0(48)	0.3(0)	26.0(28)	20.7	0.36[n]
85,925.6840 (400)	$F=2-1$	0.2(0)	18.0(48)	0.4(0)	26.0(28)	20.7	0.45[n]
85,926.2630 (200)	$F=0-0$	0.0(0)	18.0(48)	0.0(0)	26.0(28)	20.7	0.00[n]
85,926.2630 (200)	$F=1-1$	0.5(1)	18.0(48)	1.2(1)	26.0(28)	20.7	1.34[n]
85,926.2630 (200)	$F=2-2$	0.1(0)	18.0(48)	0.2(0)	26.0(28)	20.7	0.27[n]
85,926.8580 (400)	$F=1-2$	0.2(0)	18.0(48)	0.4(0)	26.0(28)	20.7	0.45[n]
85,927.7210 (400)	$F=1-0$	0.1(0)	18.0(48)	0.3(0)	26.0(28)	20.7	0.36[n]
Para	$1_{0,1}-1_{1,1}$						
110,152.0840 (400)	$F=0-1$	0.5(2)	4.4(20)	0.7(3)	2.3(11)	21.2	0.36[n]
110,152.9950 (400)	$F=2-1$	0.6(2)	4.4(20)	0.9(4)	2.3(11)	21.2	0.45[n]
110,153.5990 (200)	$F=0-0$	0.0(0)	4.4(20)	0.0(0)	2.3(11)	21.2	0.00[n]
110,153.5990 (200)	$F=1-1$	1.8(6)	4.4(20)	2.8(12)	2.3(11)	21.2	1.34[n]
110,153.5990 (200)	$F=2-2$	0.3(1)	4.4(20)	0.5(2)	2.3(11)	21.2	0.27[n]
110,154.2220 (400)	$F=1-2$	0.6(2)	4.4(20)	0.9(4)	2.3(11)	21.2	0.45[n]
110,155.0530 (400)	$F=1-0$	0.5(2)	4.4(20)	0.7(3)	2.3(11)	21.2	0.36[n]
			$^{15}NNH^+$				
90,263.8330 (600)	$J=1-0$	1.0(2)	6.3(20)	1.9(2)	14.2(28)	4.5	11.56
			$OC^{34}S$				
106,787.3800 (1600)	$J=9-8$	3.8(10)	10.1(28)	4.8(4)	19.2(18)	26.3	4.60
			SiO				
86,846.8910 (560)	$J=2-1$	[i]	...	[i]	...	6.3	19.20
			SO				
86,093.9380 (340)	$J_K=2_2-1_1$[e]	7.6(4)	14.3(10)	19.8(2)	20.6(4)	19.3	3.60
			^{34}SO				
106,743.2440 (1400)	$J_N=2_3-1_2$	1.2(6)	6.7(32)	2.0(8)	14.3(54)	20.9	3.63
			SO_2				
86,153.7090 (250)	$39_{9,31}-40_{8,32}$	0.8(4)	4.0(26)	<0.6	...	916.1	15.91
86,639.0400 (1000)	$8_{3,5}-9_{2,8}$	2.0(2)	20.7(38)	1.5(4)	13.0(34)	55.2	3.02
86,828.8820 (590)[d]	$20_{2,18}-21_{1,21}$	<0.2	...	1.9[h]	6.8	207.8	0.07

[a] Uncertainty is 95% (2 σ) confidence level.
[b] Transitions are J_{K_a,K_c} unless otherwise noted.
[c] These transitions were blended and were fitted with a single Gaussian.
[d] Previously undetected transition.
[e] Multiple emission components are visible. Only the intensity and line width of the main component are given.
[f] For EtOH a "+" = gauche+ and a "−"=gauche− state.
[g] These transitions were highly blended, and thus the intensity and line widths were approximated because the least-squares Gaussian fitting did not give a satisfactory fit.
[h] Intensity and line width were approximated because the least-squares Gaussian fitting did not give a satisfactory fit.
[i] Multiple emission and absorption components detected.
[j] Multiple strong components are apparent in the data (see Fig. 3); each component is listed on a separate line in this table.
[k] Estimated value, since the dipole moment μ was not stated in the reference.
[l] Because of confusion from transitions from NH_2D, the intensity and line width of this transition of MeF were extrapolated from the other detected MeF transitions.
[m] Line width was fixed in order to get an adequate intensity fit.
[n] In order to calculate the line strength of these hyperfine components, the line strength for the entire transition was multiplied by the relative intensity of the hyperfine component.

TABLE 5
Detected Unidentified Lines

Rest Frequency (MHz)	BIMA Array I_0 (Jy beam^{-1})	BIMA Array Δv (km s^{-1})	12 m Telescope I_0 (Jy beam^{-1})	12 m Telescope Δv (km s^{-1})	Potential Identification Transition, Frequency in MHz, and Species
85,907.7[a]	0.7[b]	3.4	<0.6	...	
85,910.5	1.0(4)	10.9(68)	<0.6	...	$9_{4,6}-8_{4,5}$, 85,910.564, C_2H_3CN $\nu2 = 11$ (FJL) $9_{4,5}-8_{4,4}$, 85,910.632, C_2H_3CN $\nu2 = 11$ (FJL)
85,912.7[a]	0.9[b]	1.7	<0.6	...	
85,917.5	0.9(4)	6.9(36)	<0.6	...	$9_{6,*}-8_{6,*}$, 85,917.187, C_2H_3CN $\nu2 = 11$ (FJL)
85,932.7[a]	<0.3	...	1.2(6)	3.9(28)	
85,935.1	1.0(4)	6.9(28)	2.1(4)	6.9(20)	
85,939.1	0.7(2)	10.5(54)	<0.6	...	
85,942.0[a]	<0.3	...	−4.2(8)	3.1(6)	
85,945.9	0.9(4)	5.0(26)	<0.6	...	$9_{8,*}-8_{8,*}$, 85,945.968, C_2H_3CN $\nu2 = 11$ (FJL)
85,970.6[a]	0.7(6)	3.3(30)	<0.6	...	
85,973.2	0.4[b]	5.7	<0.6	...	$13_{2,12}-12_{3,9}$AA, 85,973.249, $(CH_3)_2O$ (Groner et al. 1998)
85,987.4	1.9(4)	10.5(24)	<0.6	...	$9_{2,7}-8_{2,6}$, 85,987.176, C_2H_3CN $\nu1 = 11$ (FJL)
86,010.0	0.8(4)	5.1(32)	<0.6	...	
86,024.3[a]	<0.3	...	4.1(8)	2.7(6)	
86,034.3	0.8(4)	5.1(32)	<0.6	...	
86,133.2	0.5(2)	10.0(72)	<0.6	...	$18^{+}_{4,14}-18^{-}_{3,16}$[c], 86,132.920, EtOH (JCP) $6_{3,3}-6_{3,4}$ $J = 11/2-11/2$, 86,129.608–86,133.000[d], c-$CC^{13}CH$ (Pickett et al. 1998)
86,148.0	0.5(4)	5.3(48)	<0.6	...	$6_{3,3}-6_{3,4}$ $J = 11/2-11/2$, 86,147.719–86,150.854[d], c-$CC^{13}CH$ (Pickett et al. 1998)
86,151.6	0.6(2)	17.3(140)	<0.6	...	
86,204.6	0.9(2)	5.4(20)	<0.6	...	
86,207.8	0.9(2)	7.4(28)	<0.6	...	
86,220.9	0.9(2)	4.7(24)	2.1(4)	14.9(40)	
86,226.5	0.7(2)	13.2(74)	<0.6	...	$2_{2,0}-2_{1,1}$EE, 86,226.727, $(CH_3)_2O$ (Groner et al. 1998)
86,239.6	<0.2	...	1.7(4)	8.1(34)	
86,243.5	<0.2	...	1.6(4)	10.6(46)	$2-1$, $\nu = 1$, 86,243.440, SiO[e] (Lovas 2004; Snyder & Buhl 1974)
86,248.2	0.8(2)	6.6(34)	<0.6	...	
86,255.2	0.6(2)	12.2(54)	<0.6	...	$9_{2,7}-8_{2,6}$, 86,254.848, C_2H_3CN $\nu2 = 11$ (FJL)
86,263.5	<0.2	...	1.4(4)	10.0(56)	
86,297.2	0.4(2)	5.0(38)	<0.6	...	
86,300.7	0.7(2)	12.5(40)	<0.6	...	29−28, 86,300.430, $^{30}SiC_4$ (FJL)
86,386.3	0.9(4)	4.6(24)	<0.6	...	
86,389.2	−1.1(4)	2.2(12)	−2.7(8)	2.4(8)	
86,395.9[f]	0.9(2)	5.2(18)	1.9(6)	3.3(14)	
86,398.8	0.8(2)	7.4(26)	<0.6	...	
86,421.8	0.6(2)	6.7(32)	<0.6	...	
86,436.5[a]	0.6(4)	1.9(12)	<0.6	...	
86,440.2	0.5(2)	17.8(76)	<0.6	...	
86,445.8	0.6(2)	9.9(46)	<0.6	...	
86,459.3	0.5(4)	5.2(46)	<0.6	...	$6_{3,3}-6_{3,4}$ $J = 13/2-13/2$, 86,458.768–86,459.831[d], c-$CC^{13}CH$ (Pickett et al. 1998)
86,473.4[f]	0.7(2)	8.9(26)	<0.6	...	
86,486.6	0.6[b]	3.2	1.3(2)	24.2(72)	
86,498.2[a]	0.7[b]	1.9	<0.6	...	
86,536.6	0.6(2)	4.8(28)	<0.6	...	
86,543.7	<0.2	...	2.4(6)	8.3(30)	
86,784.5	−1.4(6)	3.7(20)	−2.2(8)	3.8(14)	
86,794.5	<0.3	...	−1.4(4)	5.1(20)	
86,803.6	−1.2(6)	2.2(18)	−2.0(8)	2.2(12)	
86,812.3	<0.3	...	1.6(2)	10.7(34)	
86,831.6	0.8[b]	2.5	1.7[b]	6.0	13_3-14_2A+, 86,831.480, CH_3SH (FJL)
86,915.5	0.8(2)	9.5(30)	<0.6	...	
86,944.5[a]	1.0(4)	3.7(20)	<0.6	...	
86,956.1[a]	0.7(2)	3.6(12)	<0.6	...	
86,957.8[a]	0.8(2)	2.2(10)	<0.6	...	
86,976.0	1.3(4)	4.4(16)	1.5(6)	3.9(20)	
86,979.3[f]	1.9(2)	9.5(18)	1.6(4)	10.1(32)	$10_{1,10}-9_{1,9}$A, 86,978.865, EtCN (JCP) $10_{1,9}-9_{1,8}$E, 86,978.884, EtCN (JCP)
87,008.3	0.5(2)	14.5(40)	<0.6	...	
87,016.5	0.5(2)	8.5(28)	<0.6	...	$4_{3,2}-3_{3,1}$, 87,016.896, HCOOD (Pickett et al. 1998)

TABLE 5—*Continued*

Rest Frequency (MHz)	BIMA Array I_0 (Jy beam^{-1})	BIMA Array Δv (km s^{-1})	12 m Telescope I_0 (Jy beam^{-1})	12 m Telescope Δv (km s^{-1})	Potential Identification Transition, Frequency in MHz, and Species
87,027.4	0.7(2)	6.7(24)	< 0.6	...	$5^{-}_{2,3}-4^{-}_{2,2}$[c], 87,027.093, EtOH (JCP)
89,731.9	0.9(4)	7.1(36)	< 0.7	...	
89,739.6	4.1(2)	22.6(20)	2.9(4)	15.7(22)	$10_{4,6}-9_{4,5}$A, 89,739.381, EtCN (JCP)
					$10_{4,6}-9_{4,5}$E, 89,739.935, EtCN (JCP)
89,754.9	1.6(8)	4.8(26)	1.2(6)	5.3(32)	
89,767.3	1.7(2)	32.6(54)	< 0.7	...	
89,791.5	0.6(2)	18.4(82)	< 0.7	...	
89,814.7	0.8(2)	11.9(40)	1.1(4)	8.8(32)	$33_{1,32}-33_{1,33}$, 89,814.7342–89,816.2485[g], HNCO (Pickett et al. 1998)
89,829.6	0.8(4)	5.9(26)	< 0.7	...	
89,897.3	0.3(2)	15.4(14)	< 0.7	...	
89,902.3	0.5(4)	5.4(42)	< 0.7	...	
89,923.8	0.4(2)	9.1(60)	< 0.7	...	
89,959.4[a]	0.8(4)	3.4(20)	< 0.7	...	
89,989.7	0.8(2)	10.3(36)	< 0.7	...	
89,993.1	0.8(2)	7.5(26)	< 0.7	...	$33_{1,32}-33_{1,33}$, 89,992.9883–89,993.4035[g], $HN^{13}CO$ (Pickett et al. 1998)
90,004.8	0.6(2)	5.5(30)	< 0.7	...	
90,007.7	0.7(2)	8.8(38)	< 0.7	...	$13^{+}_{0,13}-13^{+}_{1,13}$[c], 90,007.693, EtOH (JCP)
90,033.9	1.0(2)	11.6(50)	< 0.7	...	
90,037.8[f]	1.7(2)	12.1(40)	2.2(4)	8.2(20)	
90,069.1	0.5(2)	6.3(34)	< 0.7	...	
90,078.3	0.8(2)	18.5(38)	< 0.7	...	$17_{2,15}-17_{2,16}$, 90,077.914, HCOOH (Pickett et al. 1998)
90,128.5	0.5(2)	4.8(32)	< 0.7	...	
90,142.9	0.8(4)	4.1(26)	< 0.7	...	
90,153.8	< 0.2	...	2.3(6)	5.3(22)	
90,166.9	1.2(6)	6.8(32)	< 0.7	...	
90,174.5	0.6(2)	11.8(62)	< 0.7	...	
90,179.1	0.7(2)	7.4(36)	< 0.7	...	$24^{+}_{4,21}-23^{-}_{5,19}$[c], 91,178.955, EtOH (JCP)
90,203.4[f]	0.7(2)	13.2(36)	< 0.7	...	
90,224.5	1.3(4)	1.6(6)	2.2(8)	2.2(10)	
90,304.8	0.6(4)	4.1(34)	< 0.7	...	
90,307.9	0.6(2)	12.0(66)	< 0.7	...	$23_{3,21}-22_{4,19}$, 90,307.778, C_2H_5OOCH (Pickett et al. 1998)
106,295.4	1.0(4)	9.1(56)	< 0.6	...	
106,322.0	1.0(2)	22.9(84)	< 0.6	...	$18^{+}_{2,16}-18^{+}_{1,17}$[c], 106,322.066, EtOH (JCP)
106,353.0	0.9(2)	17.3(66)	< 0.6	...	$22_{3,19}-21_{4,18}$, 106,352.655–106,353.379[d], $SO^{17}O$ (FJL)
					$32_{3,29}-33_{2,32}$, 106,351.742–106,353.062[d], $SO^{17}O$ (FJL)
					$11_{1,10}-10_{2,9}$, 106,352.528–106,352.878[d], DNO (Pickett et al. 1998)
106,371.5[a]	1.9(6)	3.9(16)	< 0.6	...	
106,411.6	1.4(4)	7.3(30)	< 0.6	...	$5_{2,3}-4_{2,2}$, 106,411.010–106,411.461[d], $NH_2^{13}CHO$ (FJL)
					$35_{22,14}-35_{21,15}$AA, 106,411.273, $(CH_3)_2CO$ (Groner et al. 2002; Snyder et al. 2002)
106,448.9	3.4(4)	7.7(14)	1.8(6)	5.5(20)	
106,468.5	0.8(6)	10.6(74)	< 0.6	...	
106,484.8[a]	1.5(8)	1.9(10)	< 0.6	...	$5_{1,5}-4_{1,4}$, 106,484.610, $HO^{13}CO^+$ (Pickett et al. 1998)
					$15^{-}_{6,10}-16^{+}_{5,12}$[c], 106,484.991, EtOH (JCP)
106,487.2	1.1(2)	13.9(46)	< 0.6	...	
106,510.7	1.5(4)	5.7(22)	< 0.6	...	
106,514.5	1.8(4)	5.9(18)	< 0.6	...	
106,559.8	0.9(4)	5.8(38)	< 0.6	...	
106,629.9	1.2(4)	6.6(30)	< 0.6	...	
106,638.4	4.3(18)	6.6(24)	4.0(8)	6.6(14)	4_5-3_4, 106,638.559, $HC_2^{15}N$ (FJL)
					$11_{2,12}-10_{2,11}$, 106,638.577, C_4H (Müller et al. 2001)
106,654.8	2.8(4)	6.4(14)	1.7(4)	12.2(42)	
106,706.7	1.2(6)	5.4(32)	< 0.6	...	
106,714.3	1.0(6)	4.5(36)	< 0.6	...	
106,753.1	1.5(4)	8.8(26)	2.2(6)	6.1(18)	$11_{1,10}-10_{1,9}$ $vt = 2$, 106,753.070, C_2H_3CN (Pickett et al. 1998)
106,763.3[a]	1.3(8)	2.2(16)	< 0.6	...	
106,767.4	1.0(4)	5.2(28)	< 0.6	...	$6^{-}_{1,5}-5^{-}_{1,4}$[c], 106,767.176, EtOH (JCP)
108,207.3	1.8(16)	4.3(46)	< 0.9	...	$2_{2,0}-3_{1,3}$, 108,207.399, VyCN (Pickett et al. 1998)
108,223.7[a]	2.1(14)	3.9(32)	< 0.9	...	
108,379.8	1.9(12)	3.5(24)	2.3(6)	6.6(20)	
108,434.9	1.6(4)	5.0(12)	1.6(8)	7.7(40)	$14_{2,12}-14_{1,13}$EE, 108,434.511, $(CH_3)_2CO$ (Groner et al. 2002; Snyder et al. 2002)
					26−25, $J = 49/2-49/2$, 108,435.7053, l–HC_4N (Müller et al. 2001)

TABLE 5—*Continued*

Rest Frequency (MHz)	BIMA Array I_0 (Jy beam^{-1})	BIMA Array Δv (km s^{-1})	12 m Telescope I_0 (Jy beam^{-1})	12 m Telescope Δv (km s^{-1})	Potential Identification Transition, Frequency in MHz, and Species
108,507.7	1.3(4)	9.1(68)	<0.9	...	
108,511.2	1.3(6)	7.4(62)	<0.9	...	$31_{3,29}-30_{4,26}$, 108,511.262–108,511.299[d], $^{33}SO_2$ (Müller et al. 2001)
108,620.7[a]	2.2(8)	1.8(10)	<0.9	...	
109,943.3	2.0(4)	5.0(16)	<0.6	...	
109,959.6	3.5(4)	10.5(16)	2.1(6)	8.1(44)	$33_{1,33}-34_{0,34}$, 109,959.100, HNCO (Winnewisser et al. 1976)
					$22_{1,21}-22_{1,22}$, 109,958.699, EtCN (Lovas 1982)
					$16_{8,9}-15_{8,8}$, 109,960.360, NH_2CH_2COOH–I (glycine)[h] (FJL)
109,972.0	0.9(6)	4.1(30)	<0.6	...	
110,028.6[a]	<0.5	...	2.4(16)	1.3(10)	
110,036.2	3.5[b]	3.3	1.5(8)	5.9(36)	
110,079.7	0.9(4)	6.7(40)	<0.6	...	
110,085.6	2.0(4)	13.3(38)	1.9(8)	6.3(26)	$4_{2,3}-3_{1,2}$A $vt = 1$, 110,085.727, EtCN (JCP)
110,090.2	1.2(6)	4.7(28)	<0.6	...	$6_{5,2}-5_{4,1}$AE, 110,089.569, $(CH_3)_2CO$ (Groner et al. 2002; Snyder et al. 2002)
					$7_{5,3}-6_{4,2}$, 110,089.998, NH_2CH_2COOH–I[i] (FJL)
					$4_{2,2}-3_{1,3}$E $vt = 1$, 110,090.695, EtCN (JCP)
110,098.0	1.2(4)	10.8(28)	<0.6	...	
110,104.7	1.7(4)	10.8(38)	<0.6	...	$4_{4,0}-3_{2,1}$, 110,104.847, NH_2CH_2COOH–I[i] (FJL)
110,143.3	2.5[b]	16.7	<0.6	...	
110,150.0	2.2(6)	7.8(26)	<0.6	...	$9_{2,7}-8_{3,6}$EA, 110,149.102, $(CH_3)_2CO$ (Groner et al. 2002; Snyder et al. 2002)
					$9_{2,7}-8_{3,6}$AE, 110,148.838, $(CH_3)_2CO$ (Groner et al. 2002; Snyder et al. 2002)
110,158.2	<1.0	...	5.1[j]	31.8	$26_{21,6}-26_{20,7}$EA, 110,158.590, $(CH_3)_2CO$ (Groner et al. 2002; Snyder et al. 2002)
			3.6[j]	1.9	
110,161.0[a]	<1.0	...	3.5(14)	2.6(12)	
110,164.6[a]	<1.0	...	4.5(12)	3.1(12)	$5_{1,4}-4_{1,3}$, 110,164.245, HNCO ν_6[k] (Lovas 2004; Wyrowski et al. 1999)
110,213.0	[l]	...	[l]	...	
110,216.4	<0.8	...	[l]	...	$5_{4,1}-4_{4,0}$, 110,216.85, DCOOH (Willemot et al. 1980)
					$5_{4,2}-4_{4,1}$, 110,216.64, DCOOH (Willemot et al. 1980)
110,222.2	[l]	...	[l]	...	
110,233.6	[l]	...	[l]	...	
110,239.9[f]	[l]	...	[l]	...	
110,246.6	<0.8	...	[l]	...	
110,253.0	[l]	...	<0.6	...	$15_{15}-14_{14}$, 110,252.932, $C^{13}CS$ (Pickett et al. 1998)
110,255.5	<0.5	...	[l]	...	$4_{4,1}-5_{3,2}$AA, 110,256.338, $(CH_3)_2O$ (Groner et al. 1998)
110,263.8	[l]	...	[l]	...	
110,418.4	2.9(10)	9.4(46)	<0.6	...	$22_{20,2}-22_{19,3}$EA, 110,417.969, $(CH_3)_2CO$ (Groner et al. 2002; Snyder et al. 2002)
110,421.4[a]	2.8(18)	2.9(24)	<0.6	...	36−35, 110,420.724, SiC_4 (Pickett et al. 1998)
110,446.8	2.6(8)	6.4(26)	<0.6	...	$9_{8,1}-8_{8,0}$E, 110,447.032, MeF (Oesterling et al. 1999)
110,447.9	<1.0	...	2.6(10)	4.9(20)	$14_{3,12}-14_{2,13}$A, 110,447.595, EtCN (JCP)

[a] This feature is a questionable detection because its line width is less than 4 km s−1; hence, it may be due to interference.
[b] Intensity and line width were approximated because the least-squares Gaussian fitting did not give a satisfactory fit.
[c] For EtOH a "+"= gauche+ and a "−"= gauche− states.
[d] Large frequency spread due to hyperfine components.
[e] The transition has been previously reported as a masing transition in Orion by Snyder & Buhl 1974. However, because of its large line width combined with its very high E_u (∼1760 K), it is unlikely that this identification is correct for this source.
[f] Previously detected U-line.
[g] Large frequency spread due to multiple J components.
[h] It is not likely that this line is from glycine, since it is detected strongly with both instruments and glycine is expected to be very compact in distribution.
[i] It is not likely that this line is from glycine, since this transition has an unfavorable line strength.
[j] Multiple components were necessary to get an approximate least-squares Gaussian fit. Each component is listed on a separate line.
[k] This transition has been previously reported as an HNCO transition toward G10.47+0.03 by Wyrowski et al. 1999. However, because of its narrow line width we are reporting it as a questionable detection for Sgr B2(N-LMH).
[l] Multiple emission and absorption components detected.

fications for the U-lines, we searched the JPL database (Pickett et al. 1998), the Cologne Database for Molecular Spectroscopy (Müller et al. 2001), and the Lovas List, a compilation of observed molecular transitions from the interstellar medium (Lovas 2004). Potential identifications were also given by F. J. Lovas (2003, private communication, hereafter FJL) and J. C. Pearson (2003, private communication, hereafter JCP). The sixth column gives these potential identifications, which were made on the basis of the rest frequency of the transition. Any transition having a 2 σ standard deviation frequency greater than 1 MHz (3 km s^{-1} at 3 mm) and any molecule containing astrophysically unlikely elements was excluded. Three of these transitions are labeled as potentially coming from NH_2CH_2COOH-I (glycine), although the likelihood of this identification is small (an explanation is given with each label). There are 21 U-lines listed in Table 5 (denoted with footnote a) that do not meet both of the threshold criteria, 15 from the BIMA array and six from the 12 m telescope. While the origin of these lines is unknown, those detected by the BIMA array are most likely coming from the warmest and most compact parts of the core and could be vibrationally excited transitions of unidentified species. Those detected by the 12 m telescope are most likely coming from the extended cool gas around the core. These lines are not included in any of the line counts or statistics.

3. RESULTS

3.1. *Statistics*

In this survey, we detected a total of 218 lines (97 identified molecular transitions from 18 molecular species and 16 isotopomers, one recombination line, and 120 U-lines). The BIMA array detected 199 lines (91 from 15 molecular species and 16 isotopomers and 108 U-lines), and the 12 m telescope detected 116 lines (74 from 17 molecular species and 15 isotopomers, one recombination line, and 41 U-lines). Note that the number of detected lines does not include hyperfine transitions. Of the lines detected by the BIMA array, 21 are previously undetected transitions of known molecules, 102 are previously undetected U-lines, and 102 (23 transitions of known molecules and 79 U-lines) were only detected by the BIMA array. The 12 m telescope detected 12 previously undetected transitions of known molecules and 37 new U-lines, and 19 (seven transitions of known molecules and 12 U-lines) were only detected by the 12 m telescope.

The above line counts yield a spectral line density (average number of lines per 100 MHz) of 6.06 from all observed lines (2.72 from identified lines and 3.34 from U-lines). This is a large increase over previous 3 mm surveys of the Sgr B2 region. Table 6 compares the line counts and densities from this survey to previous 3 mm surveys of this source and to Lovas (2004). The first column gives the source of the data. The second and third columns give the line counts and densities (from the same frequency bands covered in this survey) of identified transitions from each source. The fourth and fifth columns give the line counts and density of U-lines from each source. The sixth and seventh columns give the total line counts and densities from each source. The total line density from this survey is greater than that from either of the previous line surveys and from Lovas (2004). The largest increase is the number of U-lines detected; a total of $\sim$55% of the lines we detected are unidentified. This demonstrates that with higher sensitivity and smaller beams, more spectral features will be detected.

Because of the relatively large line widths (typically 5–10 km s^{-1}) and the large number of molecular species in the region, many spectral features are unresolved. In cases of very strong emission from a single transition, nearby weaker transitions may not have been observed. Thus, if a specific transition was not detected, it may either currently lie below our detection limit or be blended in the wings of stronger lines.

3.2. *Maps*

Figure 4 shows maps from the BIMA array toward Sgr B2(N-LMH) of NH_2CHO (formamide), C_2H_5OH (ethanol, or EtOH), SO, and $H^{13}CN$. In each map, the continuum is mapped in gray scale, with the transition averaged over the FWHM of the line mapped in contours. The central continuum peak is Sgr B2(N), and the lower continuum peak is Sgr B2(M). The BIMA array and 12 m telescope spectra of each mapped transition are below their respective maps. The vertical axis shows intensity in units of Jy $beam^{-1}$, and the horizontal axis shows frequency in GHz. The synthesized beam is given in the lower left-hand corner of each map. The numbers on the gray-scale wedge are in units of Jy $beam^{-1}$.

4. DISCUSSION

The higher (>90 K) upper state energy (E_u) transitions of all species will map toward the core, since these transitions are only populated to detectable levels in the warmer regions. But the lower E_u transitions can be excited in both the warm core and the cooler surrounding gas. Thus, the lower E_u transitions trace a truer distribution of each molecular species and are an indicator of that molecule's formation mechanism. Since hydrogenation of atoms heavier than H and molecules happens with very high efficiency on grains (Watson & Salpeter 1972), all transitions of highly saturated (three or more H atoms) molecules should map toward the core in which the molecules are desorbing from the grain surfaces. Similarly, any molecule formed by reactions by ions or other heavier atoms and molecules on grain surfaces should map toward the core. We also expect that any molecules formed in warm gas-phase reactions will map primarily toward the hot core, since this is where the temperatures are warm enough for the reactions to proceed. The lower E_u transitions of species that are produced by cool gas-phase reactions should have a large, extended component in their distribution, since these reactions do not require the higher temperatures of the core to proceed.

Figure 4*a* shows the BIMA array map of the 106.541 GHz, $5_{2,3}-4_{2,2}$ transition of NH_2CHO, which has an $E_u = 27.2$ K. The contours are 3, 6, 9, 12, 15, 18, and 21 σ. The average

TABLE 6
COMPARISON OF LINE STATISTICS

SOURCE	IDENTIFIED		UNIDENTIFIED		TOTAL	
	Lines	Density[a]	Lines	Density[a]	Lines	Density[a]
Cummins et al. (1986).....	49	1.36	3	0.08	52	1.44
Turner (1989)..................	57	1.58	10	0.28	67	1.86
Lovas (2004)....................	151	4.19	38	1.06	189	5.25
This survey......................	98	2.72	120	3.34	218	6.06

[a] Lines per 100 MHz.

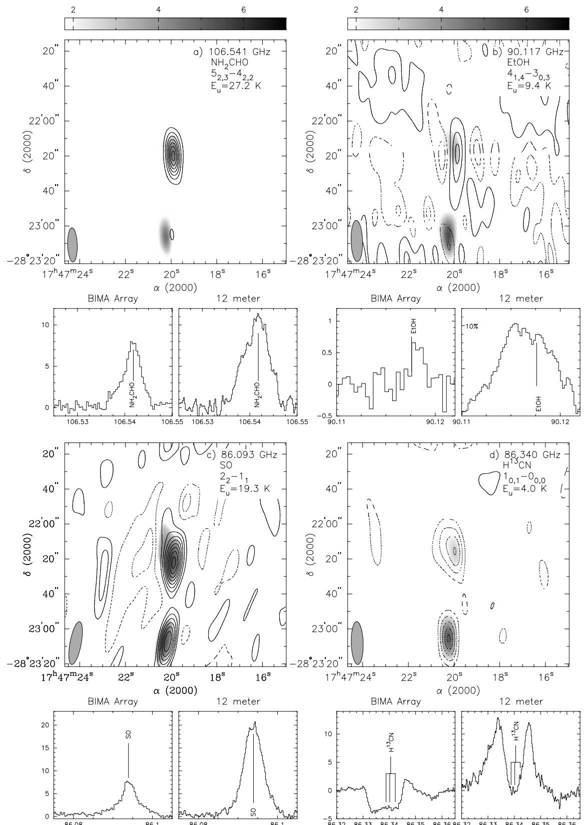

FIG. 4.—Maps from the BIMA array toward Sgr B2(N-LMH) of four representative molecular species. In each map the continuum is mapped in gray scale with the transition, averaged over the FWHM of the line, mapped in contours. The central continuum peak shows Sgr B2(N-LMH), and the lower continuum peak shows Sgr B2(M). The BIMA array and 12 m telescope spectra of each mapped transition are below their respective maps. The vertical axis shows intensity in Jy beam^{-1}, and the horizontal axis shows frequency in GHz. The synthesized beam is given in the lower left-hand corner of each map. The numbers on the gray-scale wedge are in Jy beam^{-1}. (*a*) Map of the 106.541 GHz, $5_{2,3}-4_{2,2}$ transition of NH_2CHO (formamide). The contours are 3, 6, 9, 12, 15, 18, and 21 σ. (*b*) The 90.117 GHz, $4_{1,4}-3_{0,3}$ transition of C_2H_5OH (ethanol, EtOH). The contours are −2, −1, 1, 3, and 4.5 σ. (*c*) Map of the 86.093 GHz, 2_2-1_1 transition of SO. The contours are −6, −3, 3, 6, 9, 12, 15, 18, 21, and 24 σ. (*d*) Map of the 86.340 GHz, $1_{0,1}-0_{0,0}$ transition of $H^{13}CN$. The contours are −14, −12, −9, −6, −3, and 3 σ.

(across the FWHM of the line) flux detected by the BIMA array is 6.27(29)[12] Jy beam^{-1}, while the average flux detected by the 12 m telescope is 8.61(63) Jy beam^{-1}. This map and the difference in flux indicate that NH_2CHO has a compact distribution toward the core with few extended components and is most likely the product of grain chemistry or warm gas-phase chemistry. The observations by Schilke et al. (1991) agree with this view of the NH_2CHO distribution. With a 17″ beam, they found unresolved NH_2CHO emission toward Sgr B2(N), with much weaker emission toward the Sgr B2(M) region. This map is indicative of most of the highly saturated species we have observed.

One of the exceptions is shown in Figure 4*b*, which is the BIMA array map of the 90.117 GHz, $4_{1,4}-3_{0,3}$ transition of EtOH with an $E_u = 9.4$ K. The contours are −2, −1, 1, 3, and 4.5 σ. This transition has peaks and valleys throughout the map and an average flux of 0.60(15) Jy beam^{-1} from the BIMA array and 8.20(68) Jy beam^{-1} from the 12 m telescope. The 12 m telescope spectrum has a much wider line, as well as several more velocity components than the BIMA array spectrum. This indicates that EtOH has a highly extended distribution and suggests a cooler gas-phase formation mechanism. The 106.775 GHz, $9_{1,8}-8_{2,7}$ AA ($E_u = 43.4$ K) transition of $(CH_3)_2O$ (dimethyl ether) (see Fig. 3*h*), the other exception, maps similarly to this transition of EtOH. While there is no great intensity difference between the BIMA array spectrum and 12 m telescope spectrum of this transition, the 12 m telescope spectrum has wider lines and several velocity components, indicating an extended distribution and a cool gas-phase formation mechanism.

Figure 4*c* shows the BIMA array map of the 86.093 GHz, 2_2-1_1 transition of SO, which has an $E_u = 19.3$ K. The contours are −6, −3, 3, 6, 9, 12, 15, 18, 21, and 24 σ. The average flux detected by the BIMA array is 6.69(28) Jy beam^{-1}, and the average flux detected by the 12 m telescope is 16.30(61) Jy beam^{-1}. This transition show the distinction between sulfurated species and highly saturated organic species in the region. It has strong peaks toward both Sgr B2(N-LMH) and Sgr B2(M), as well as strong peaks and valleys throughout the rest of the map. While most of the flux is coming from the hot core regions, the flux difference between the two instruments, along with the map, indicated that SO has significant extended structure.

Figure 4*d* shows the BIMA array map of the 86.340 GHz, $1_{0,1}-0_{0,0}$ transition of $H^{13}CN$, which has an $E_u = 4.0$ K. The contours are −14, −12, −9, −6, −3, and 3 σ. The map of this transition is indicative of the other species that also show strong absorption. This map, across the FWHM of the absorption, does not show any of the emission components seen in the 12 m telescope spectrum. This is because these components are very extended and are being resolved out by the BIMA array.

These maps show that the highly saturated species,[13] such as EtCN, CH_3CN, MeF, NH_2CHO, and VyCN, map toward the Sgr B2(N-LMH) core, indicating that these species are products of grain or warm gas-phase chemistry. In contrast to this, two other highly saturated species, EtOH and $(CH_3)_2O$, show highly extended distributions, indicating a cooler gas-phase formation mechanism.

5. SUMMARY

We have presented the spectra and line fits from the first 3 mm spectral line survey, using both an interferometer and a single-element radio telescope of the Sgr B2(N-LMH) hot molecular core. We detected 218 lines (97 identified molecular transitions from 18 molecular species and 16 isotopomers, one recombination line, and 120 unidentified transitions). The survey has a spectral line density of 6.06 lines per 100 MHz from all observed lines (2.72 from identified lines and 3.34 from -lines), which is much greater than any previous 3 mm survey of this source. The high density of U-lines that we detected (∼55% of all detected lines) indicates that as Sgr B2(N-LMH) is observed with increasing sensitivity and smaller beams, more spectral features will be seen.

[12] Errors quoted are 1 σ rms noise level for the associated transition.

[13] No conclusion about the spatial distribution of CH_3OH can be made from our data, since both detected transitions have a higher E_u of 102 K.

Because of the nature of this survey, we are able to probe each spectral line on multiple spatial scales, yielding information that could not be obtained by either instrument alone. From this spatial information we can constrain potential formation mechanisms for the identified molecular species. Products of cool gas-phase reactions will show extended distributions, while products of warm gas-phase reactions or grain surface reactions will show compact distributions. The BIMA array maps show that the observed highly saturated species, such as EtCN, CH_3CN, MeF, NH_2CHO, and VyCN, show compact emission from the Sgr B2(N-LMH) core, indicating a grain chemistry or warm gas-phase chemistry formation mechanism. Contrasting this, two other highly saturated species, EtOH and $(CH_3)_2O$, show very extended distributions, indicating a cooler gas-phase chemistry formation mechanism. A detailed analysis of selected data sets, including temperature determinations, column densities, and comparison of results with existing chemical models will be presented in a subsequent paper.

We thank D. S. Meier for many helpful discussions. F. J. Lovas, J. C. Pearson, and J. M. Hollis helped us identify U-lines. We thank A. Apponi for help with information on the 12 m telescope and J. R. Forster for help with information on the BIMA array. We also thank an anonymous referee for many helpful comments that improved this manuscript. We acknowledge support from the Laboratory for Astronomical Imaging at the University of Illinois and grants NSF AST 99-81363 and AST 02-28953.

REFERENCES

Bester, M., Yamada, K., Winnewisser, G., & Urban, S. 1983, A&A, 121, L13
Bogey, M., Demuynck, C., & Destombles, J. L. 1984, Canadian J. Phys., 62, 1248
Boucher, D., Burie, J., Bauer, A., Dubrulle, A., & Demaison, J. 1980, J. Phys. Chem. Ref. Data, 9, 659
Caselli, P., Hasegawa, T. I., & Herbst, E. 1993, ApJ, 408, 548
Cummins, S. E., Thaddeus, P., & Linke, R. A. 1986, ApJS, 60, 819
de Pree, C. G., Gaume, R. A., Goss, W. M., & Claussen, M. J. 1995, ApJ, 451, 284
———. 1996, ApJ, 464, 788
Frerking, M. A., Wilson, R. W., & Langer, W. D. 1979, ApJ, 232, L65
Gaume, R. A., Claussen, M. J., de Pree, C. G., Goss, W. M., & Mehringer, D. M. 1995, ApJ, 449, 663
Gerry, M. C. L., Yamada, K., & Winnewisser, G. 1979, J. Phys. Chem. Ref. Data, 8, 107
Gottlieb, C. A., Gottlieb, E. W., Thaddeus, P., & Vrtilek, J. M. 1986, ApJ, 303, 446
Groner, P., Albert, S., Herbst, E., & de Lucia, F. C. 1998, ApJ, 500, 1059
Groner, P., Albert, S., Herbst, E., de Lucia, F. C., Lovas, F. J., Drouin, B. J., & Pearson, J. C. 2002, ApJS, 142, 145
Guélin, M., Cernicharo, J., & Linke, R. A. 1982, ApJ, 263, L89
Johnson, D. R., Lovas, F. J., & Kirchhoff, W. H. 1972, J. Phys. Chem. Ref. Data, 1, 1011
Kuan, Y., Mehringer, D. M., & Snyder, L. E. 1996, ApJ, 459, 619
Kuan, Y., & Snyder, L. E. 1994, ApJS, 94, 651
Kutner, M. L., & Ulich, B. L. 1981, ApJ, 250, 341
Lafferty, W. J., & Lovas, F. J. 1978, J. Phys. Chem. Ref. Data, 7, 441
Lilley, A. E., & Palmer, P. 1968, ApJS, 16, 143
Liu, S., Mehringer, D. M., & Snyder, L. E. 2001, ApJ, 552, 654
Lovas, F. J. 1978, J. Phys. Chem. Ref. Data, 7, 1445
———. 1982, J. Phys. Chem. Ref. Data, 11, 251
———. 1985, J. Phys. Chem. Ref. Data, 14, 395
———. 2004, J. Phys. Chem. Ref. Data, 33, 1
Lovas, F. J., & Krupenie, P. H. 1974, J. Phys. Chem. Ref. Data, 3, 259
Lovas, F. J., & Tiemann, E. 1974, J. Phys. Chem. Ref. Data, 3, 609
Martín-Pintado, J., Rizzo, J. R., de Vicente, P., Rodríguez-Fernández, N. J., & Fuente, A. 2001, ApJ, 548, L65
Mehringer, D. M., Snyder, L. E., Miao, Y., & Lovas, F. J. 1997, ApJ, 480, L71
Miao, Y., & Snyder, L. E. 1997, ApJ, 480, L67
Müller, H. S. P., Thorwirth, S., Roth, D. A., & Winnewisser, G. 2001, A&A, 370, L49
Murakami, A. 1990, ApJ, 357, 288
Nummelin, A., Bergman, P., Hjalmarson, A., Friberg, P., Irvine, W. M., Millar, T. J., Ohishi, M., & Saito, S. 1998, ApJS, 117, 427
Nummelin, A., Bergman, P., Hjalmarson, A., Friberg, P., Irvine, W. M., Millar, T. J., Ohishi, M., & Saito, S. 2000, ApJS, 128, 213
Oesterling, L. C., Albert, S., de Lucia, F. C., Sastry, K. V. L. N., & Herbst, E. 1999, ApJ, 521, 255
Pickett, H. M., Poynter, R. L., Cohen, E. A., Delitsky, M. L., Pearson, J. C., & Müller, H. S. P. 1998, J. Quant. Spectrosc. Radiat. Transfer, 60, 883
Reid, M. J., Schneps, M. H., Moran, J. M., Gwinn, C. R., Genzel, R., Downes, D., & Rönnäng, B. 1988, ApJ, 330, 809
Salter, C., Maddalena, R. J., & Garwood, B. 1995, The UniPOPS Cookbook (Greenbank: NRAO)
Sault, R. J., Teuben, P. J., & Wright, M. C. H. 1995, in ASP Conf. Ser. 77, Astronomical Data Analysis Software and Systems IV, ed. R. A. Shaw, H. E. Payne, & J. J. E. Hayes (San Francisco: ASP), 443
Schilke, P., Walmsley, C. M., Henkel, C., & Millar, T. J. 1991, A&A, 247, 487
Shah, R. Y., & Wootten, A. 2001, ApJ, 554, 933
Snyder, L. E., & Buhl, D. 1974, ApJ, 189, L31
Snyder, L. E., Kuan, Y.-J., & Miao, Y. 1994, The Structure and Content of Molecular Clouds: 25 Years of Molecular Radioastronomy, ed. T. L. Wilson & K. J. Johnston (New York: Springer), 187
Snyder, L. E., Kuan, Y.-J., & Pratap, P. 1991, in ASP Conf. Ser. 16, Atoms, Ions, and Molecules: New Results in Spectral Line Astrophysics, ed. A. D. Haschick & P. T. P. Ho (San Francisco: ASP), 191
Snyder, L. E., Lovas, F. J., Mehringer, D. M., Miao, N. Y., Kuan, Y., Hollis, J. M., & Jewell, P. R. 2002, ApJ, 578, 245
Snyder, L. E., Schenewerk, M. S., & Hollis, J. M. 1985, ApJ, 298, 360
Sutton, E. C., Jaminet, P. A., Danchi, W. C., & Blake, G. A. 1991, ApJS, 77, 255
Tiemann, E. J. 1974, J. Phys. Chem. Ref. Data, 3, 259
Turner, B. E. 1989, ApJS, 70, 539
———. 1991, ApJS, 76, 617
Watson, W. D., & Salpeter, E. E. 1972, ApJ, 174, 321
Willemot, E., Dangoisse, D., Monnanteuil, N., & Bellet, J. 1980, J. Phys. Chem. Ref. Data, 9, 59
Winnewisser, G., Hocking, W. H., & Gerry, M. C. L. 1976, J. Phys. Chem. Ref. Data, 5, 79
Woods, R. C., Saykally, R. J., Anderson, T. G., Dixon, T. A., & Szanto, P. G. 1981, J. Chem. Phys., 75, 4256
Wright, M. C. H. 1996, BIMA Memo. Ser. 45 (College Park: Univ. Maryland)
Wyrowski, F., Schilke, P., & Walmsley, C. M. 1999, A&A, 341, 882
Xu, L.-H., & Lovas, F. J. 1997, J. Phys. Chem. Ref. Data, 26, 17
Yamamoto, S., Saito, S., Kawaguchi, K., Chikada, Y., Suzuki, H., Kaifu, N., Ishikawa, S., & Ohishi, M. 1990, ApJ, 361, 318
Yamamoto, S., Saito, S., Suzuki, H., Deguchi, S., Kaifu, N., Ishikawa, S., & Ohishi, M. 1990, ApJ, 348, 363

Appendix D

High Resolution Observations of Methyl Cyanide (CH_3CN) Toward the Hot Core Regions W51e1/e2

By
Anthony Remijan, Edmund C. Sutton, Lewis E. Snyder, Douglas N. Friedel, Sheng-Yuan Liu &
C.-C. Pei
2004 ApJ 606, 917

The Astrophysical Journal, 606:917–928, 2004 May 10

HIGH-RESOLUTION OBSERVATIONS OF METHYL CYANIDE (CH_3CN) TOWARD THE HOT CORE REGIONS W51e1/e2

A. Remijan,[1,2] E. C. Sutton,[1] L. E. Snyder,[1] D. N. Friedel,[1] S.-Y. Liu,[1,3] and C.-C. Pei[1,4]
Received 2003 October 15; accepted 2004 January 22

ABSTRACT

We have detected strong methyl cyanide (CH_3CN) emission lines from the hot core regions W51e1 and W51e2, using the BIMA Array. This is the first survey of CH_3CN toward W51 to utilize both 3 mm (J = 5–4 and 6–5) and 1 mm (J = 12–11, 13–12, and 14–13) transitions as probes of the physical and chemical conditions present in these regions. The emission reveals molecular clumps centered on the ultracompact H II regions found by Zhang and colleagues. The CH_3CN lines show large optical depths in the lower K transitions toward both regions in W51. To determine the true kinetic temperatures, densities, and column densities of the emitting regions W51e1 and e2, statistical equilibrium models were used to calculate the relative populations of each energy level. The best fit to the observed spectra toward W51e1 is given by a temperature of 123(11) K, a hydrogen density of $5(1) \times 10^5$ cm^{-3}, and a total methyl cyanide column density of $1.4(1) \times 10^{16}$ cm^{-2}. The uncertainties describe a nominal 90% confidence interval for the last digit given. The best fit to the observed spectra toward W51e2 is given by a temperature of 153(21) K, a hydrogen density of $5(2) \times 10^5$ cm^{-3}, and a total methyl cyanide column density of $3.8(7) \times 10^{16}$ cm^{-2}. Our observations indicate that CH_3CN can be used as a good probe of the physical conditions present in hot molecular cores and as a tracer of hard-to-detect large molecular species. Despite the differences in molecular structure and chemical formation mechanisms, methyl cyanide (CH_3CN), ethyl cyanide (CH_3CH_2CN), and acetic acid (CH_3COOH) are found to have similar abundances toward the W51e1 and e2 regions. In contrast, for a column density of CH_3CN more than 15 times smaller than the column density of $HCOOCH_3$ the integrated line flux is more than 7 times larger. Thus, because CH_3CN lines are easy to detect, it appears to be a much better tracer of CH_3CH_2CN and CH_3COOH than $HCOOCH_3$.

Subject headings: ISM: abundances — ISM: individual (W51) — ISM: molecules — radio lines: ISM — stars: formation

1. INTRODUCTION

W51 is a complex of H II regions located about 7 kpc away in the Sagittarius spiral arm. Since the 1960s it has been a prime target for radio astronomy observations because of its large continuum emission and its abundance of molecular emission lines. The centimeter emission from the W51 region was shown by Martin (1972) to consist of eight distinct components, W51a–h. The strongest of the eight components, W51e and W51d, were studied by Scott (1978), who found W51e to be divided into two compact continuum components: e1 and e2. Because both e1 and e2 are thought to be important star-forming cores, their magnetic fields were mapped interferometrically by Lai et al. (2001). In addition, W51e1 and e2 have been primary targets in surveys for large molecules. At 2 mm, Zhang, Ho, & Ohashi (1998) imaged dimethyl ether (CH_3OCH_3), methyl formate ($HCOOCH_3$; MeF), and methyl cyanide (CH_3CN). Furthermore, they noted asymmetric line profiles, especially for CH_3CN, near the location of the W51e2 continuum peak. While the central velocity coincided with the systemic velocity of W51e2 ($\sim$55.0 km s^{-1}), a prominent blueshifted peak showed up 2–3 km s^{-1} lower than the systemic velocity. At their spectral (0.5 km s^{-1}) and spatial ($\sim 1''$) resolution, they inferred this asymmetric profile to be evidence of infall. At 3 mm, Liu, Mehringer, & Snyder (2001) imaged four formic acid (HCOOH) transitions and detected transitions of ethyl cyanide (CH_3CH_2CN) and MeF. Recently, Remijan et al. (2002) observed additional transitions of MeF and made the first detection of acetic acid (CH_3COOH) toward the hot core region W51e2. Thus, it is apparent that there is an active chemistry taking place toward the hot core regions W51e1 and W51e2 that favors the formation of these large molecular species. However, it has been difficult to get a good understanding of the location of large molecular species, as well as the physical and chemical conditions present in these regions. Often, when large molecular species, such as CH_3CH_2CN, MeF, and CH_3COOH, are observed, the rotational transitions are distributed across a large frequency range. A large frequency range is required for a complete analysis, in order to cover a wide range of upper-state energy levels. However, comparing observations covering many different frequencies can be problematic because of calibration errors in the relative flux density scales at each frequency.

Thus, in order to get a better understanding of the physical and chemical conditions present in the W51e1 and e2 regions, we used the symmetric-top species methyl cyanide (CH_3CN) to probe the temperature and density in these regions. Symmetric tops have properties that make them ideal probes of hot molecular cores. In a symmetric top, the rotational levels are labeled by J, the total angular momentum quantum number, and K, the quantum number for the projection of angular momentum along the symmetry axis (Cummins et al. 1983).

[1] Department of Astronomy, University of Illinois, Urbana, IL 61801; aremijan@astro.uiuc.edu, sutton@astro.uiuc.edu, snyder@astro.uiuc.edu, friedel@astro.uiuc.edu.
[2] Current address: NASA Goddard Space Flight Center, Earth and Space Data Computing Center, Code 930, Greenbelt, MD 20771.
[3] Current address: Institute of Astronomy and Astrophysics, Academia Sinica, P.O. Box 23-141, Taipei 106, Taiwan, Republic of China; syliu@asiaa.sinica.edu.tw.
[4] Current address: Purple Mountain Observatory, National Astronomical Observatories, Chinese Academy of Sciences, China; ccpei@nj.col.com.cn.

TABLE 1
W51 Observational Parameters

Observation Date	Frequency (GHz)	Beam (arcsec)	Channel rms (Jy beam^{-1})
1998 Jun 2	110.383	8.7 × 5.7	0.20
1998 Jun 3	91.987	10.1 × 6.7	0.50
2001 May 11	220.747	3.6 × 2.7	0.21
2001 May 28	257.527	3.3 × 2.6	0.74
2001 Jun 4	239.138	3.2 × 2.6	0.30

By selection rules, radiative transitions do not change the value of K. Thus, radiative transitions can occur only within a K-ladder. However, collisional transitions are permitted across K-ladders. Therefore, the population of one K-ladder relative to another is largely determined by collisions and, hence, is closely related to the kinetic temperature and density of the region (Solomon et al. 1971). The relative intensities of the K-components across several $\Delta J = 1$ transitions can be then be used to determine the kinetic temperature, density, and total beam-averaged column density. In addition, the $K = 0$ to J components are closely spaced in frequency for each rotational band $J + 1 \rightarrow J$ (Pankonin et al. 2001). Thus, many lines can be observed simultaneously at similar sensitivities. This also helps to minimize the effects of calibration errors. Therefore, using symmetric-top species, such as methyl cyanide (CH_3CN), we can obtain measurements that constrain the physical conditions present in these regions and give a better understanding of the chemistry that is capable of forming large molecular species.

2. OBSERVATIONS

The W51 CH_3CN observations were made between 1998 June and 2001 June utilizing the C configuration of the Berkeley-Illinois-Maryland Association (BIMA) Millimeter Array.[5] Table 1 summarizes the observational parameters. The first column lists the observation date. The second column lists the rest frequency of the $K = 0$ component of each band. The third column lists the beam size. Finally, the fourth column lists the approximate 1 σ channel noise level in the CH_3CN passbands. The passbands were calibrated automatically during data acquisition.[6] In the past, this method has been quite satisfactory and has not generated spurious features. The phase center for the 3 mm observations was coincident with the continuum source W51 IRS 1, at α(J2000.0) = $19^h23^m41\overset{s}{.}87$, δ(J2000.0) = $14°30'36\overset{''}{.}2$. The phase center

[5] Operated by the University of California, Berkeley, the University of Illinois, and the University of Maryland, with support from the National Science Foundation.

[6] A technical description of this can be found at http://astron.berkeley.edu/~plambeck/technical.html.

TABLE 2
CH_3CN Molecular Line Parameters

Transition $J+1 \rightarrow J$	K	Frequency[a] (MHz)	Line Strength $S(J, K)$	E_u
5–4	0	91,987.054 (120)	5.00	13.25
	1	91,985.284 (120)	4.80	20.38
	2	91,980.000 (500)	4.20	41.70
	3	91,971.374 (120)	3.20	77.27
	4	91,959.206 (400)	1.80	127.04
6–5	0	110,383.494 (120)	6.00	18.56
	1	110,381.376 (120)	5.83	25.68
	2	110,374.986 (120)	5.33	47.02
	3	110,364.470 (100)	4.50	82.57
	4	110,349.760 (200)	3.33	132.34
12–11	0	220,747.263 (40)	12.00	68.92
	1	220,743.013 (40)	11.92	76.03
	2	220,730.263 (100)	11.67	97.37
	3	220,709.020 (100)	11.25	132.93
	4	220,679.291 (140)	10.67	182.69
	5	220,641.088 (200)	9.92	246.66
	6	220,594.428 (66)	9.00	324.81
	7	220,539.330 (68)	7.92	417.11
	8	220,475.815 (62)	6.67	523.58
13–12	0	239,137.914 (40)	13.00	80.41
	1	239,133.311 (40)	12.92	87.52
	2	239,119.503 (40)	12.69	108.86
	3	239,096.496 (100)	12.31	144.42
	4	239,064.299 (140)	11.77	194.17
14–13	0	257,527.374 (40)	14.00	92.78
	1	257,522.418 (40)	13.93	99.89
	2	257,507.553 (100)	13.71	121.22
	3	257,482.784 (100)	13.36	156.77
	4	257,448.122 (160)	12.86	206.54

[a] Errors are 2 σ standard deviations.

TABLE 3
$CH_3{}^{13}CN$ Molecular Line Parameters

Transition $J+1 \rightarrow J$	K	Frequency [a] (MHz)	Line Strength $S(J, K)$	E_u (K)
12–11	0	220,637.992 (314)	12.00	68.89
	1	220,633.765 (310)	11.92	76.05
	2	220,621.082 (300)	11.67	97.55
	3	220,599.945 (288)	11.25	133.37

[a] Errors are 2 σ standard deviations.

for the 1 mm observations was coincident with the hot core source W51e2, at α(J2000.0) = 19^{h}23^{m}43^s.50, δ(J2000.0) = 14°30′34″.0. The spectral windows containing the 3 mm CH_3CN lines had bandwidths of 50 MHz and were divided into 128 channels, for a spectral resolution of 0.39 MHz per channel. The spectral windows containing the 1 mm CH_3CN lines had bandwidths of 100 MHz and were divided into 64 channels, for a spectral resolution of 1.56 MHz per channel. Jupiter and Uranus were used as the flux density calibrators for these observations. The quasar 1925+211 was used to calibrate the antenna-based gains. The absolute amplitude calibration of this source, based on the planetary observations, is thought to be accurate to within ~20%. The data were combined, imaged, and self-calibrated using the MIRIAD software package (Sault, Teuben, & Wright 1995). Table 2 lists the molecular parameters of the CH_3CN transitions searched for in our survey. The first two columns list the transition; the third, the calculated rest frequency and its 2 σ standard deviation; the fourth, the line strength of each transition; and the fifth, the upper-state energy of each transition. Table 3 lists the molecular parameters of the $CH_3{}^{13}CN$ transitions that were detected in the 220 GHz frequency band. The column labels are the same as in Table 2. All the molecular parameters of CH_3CN were taken from Boucher et al. (1980).

3. RESULTS

Figure 1 shows the averaged intensity maps of the $J = 6$–5 CH_3CN emission lines. The gray scale in Figure 1*a* is for the 110.4 GHz continuum of the W51 region. In each panel, the given *K*-ladder transition averaged over the FWHM of the line is mapped in contours. The region to the northwest, IRS 2, has CH_3CN emission offset from the continuum. The region to the east contains two distinct regions, e1 and e2, which are unresolved in our 9″ × 6″ beam in this 110 GHz band. Figure 2 shows the averaged intensity maps of the $J = 12$–11 CH_3CN emission lines. The gray scale in Figure 2*a* is for the 220.6 GHz continuum of the W51e1/e2 region. In each panel, the given *K*-ladder transition averaged over the FWHM of the line is mapped in contours. In these higher resolution maps with a 3″ × 2″ beam (seen at the bottom left of each panel), the hot core regions surrounding the locations of W51e1 and W51e2 are resolved.

Figure 3 shows the CH_3CN spectra toward region W51e1 at 3 and 1 mm wavelengths in order of increasing frequency. The rest frequency listed in the upper left of each panel corresponds to the $K = 0$ component, except for the 220 GHz transitions. In Figure 3*c*, the rest frequency is for the $K =$ 3 component; in Figure 3*d*, the rest frequency is for the $K =$ 5 component; and finally, in Figure 3*e*, the rest frequency is for the $K = 8$ component. We measure a v_{LSR} of 56(2) km s^{-1} for the W51e1 region.[7] The ±1 σ noise level is seen at the left in each panel. The ±1 σ noise levels were determined by taking the rms over all channels from a spatial region that was free from both line and continuum emission. Regions e1 and e2 are unresolved in the 3 mm beam of ~9″ × 6″ (Fig. 1). At 1 mm, however, regions e1 and e2 are resolved with a ~3″ × 2″ beam (Fig. 2). We determined the peak positions and source sizes of regions e1 and e2 using Gaussian-distributed sources for regions e1 and e2 in the 1 mm data. The peak positions were then used to estimate the amount of flux contributed by e1 and e2 in the 3 mm data. We

[7] The uncertainty is shown in parentheses, with the number of digits referring to the last digit(s) given. The uncertainties describe a nominal 90% confidence interval.

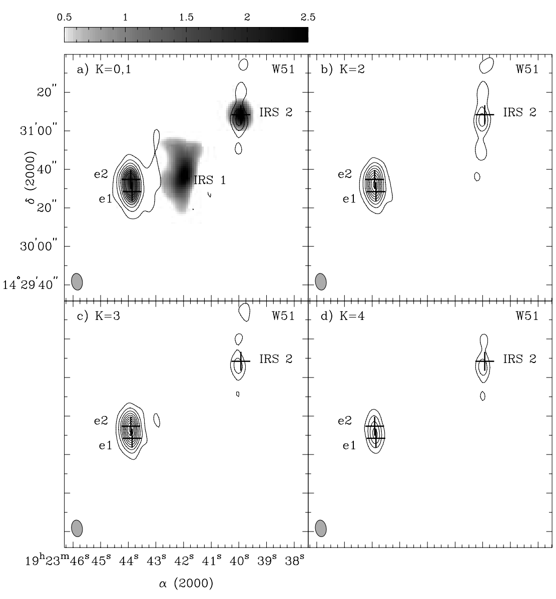

Fig. 1.—Averaged intensity maps of the $J = 6$–5 CH_3CN emission lines. The gray scale in (*a*) is for the 110.4 GHz continuum of the W51 region. The numbers on the gray-scale wedge are in units of Jy beam^{-1}. In each panel, the given *K*-ladder transition averaged over the FWHM of the line is mapped in contours. The contour levels are 0.6, 1.2, 1.8, 2.4, 3.0, 3.6, 4.2, and 4.8 Jy beam^{-1}. In addition, we have labeled the positions of the UC H II regions e1, e2, IRS 1, and IRS 2, as given by Zhang et al. (1998). The region to the northwest, IRS 2, has CH_3CN emission offset from the continuum. The region to the east contains two distinct regions, e1 and e2. Region e2 is north of e1. However, regions e1 and e2 are unresolved in our 9″ × 6″ beam (*bottom left corner of each panel*).

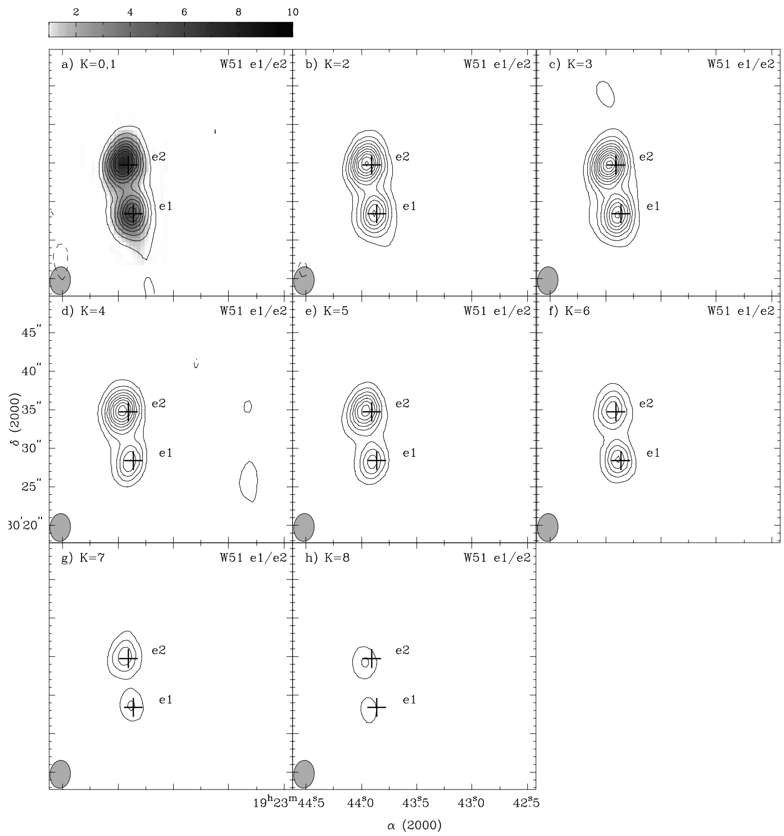

FIG. 2.—Averaged intensity maps of the $J = 12-11$ CH_3CN emission lines. The gray scale in (*a*) is for the 220.6 GHz continuum of the W51 region. The numbers on the gray-scale wedge are in units of Jy beam^{-1}. In each panel, the given *K*-ladder transition averaged over the FWHM of the line is mapped in contours. The contour levels are 1.0, 2.0, 3.0, 4.0, 5.0, 6.0, 7.0, and 8.0 Jy beam^{-1}. In addition, we have labeled the positions of the UC H II regions e1 and e2, as given by Zhang et al. (1998). Regions e1 and e2 are resolved in our $\sim 3'' \times 2''$ beam (*bottom left corner of each panel*).

found from the 1 mm data that region e1 subtends an area of 7.9(6) arcsec^2, that e2 subtends an area of 6.0(9) arcsec^2, and that ~45% of the total flux originates from the e1 core. However, we note that the source sizes may be underestimated because of the errors in the fitting routine. We distributed the total flux in the 3 mm data in the same proportions: e1 (45%) and e2 (55%). In Figures 3*a* and 3*b*, the dashed spectra are taken over the entire W51e1/e2 region. The solid spectra are for the amount of flux attributed to the e1 region (Table 4).

Table 4 lists the fitted CH_3CN line parameters toward the W51e1 region. Least-squares Gaussian fits were made for each spectral line in order to obtain the radial velocities (in units of km s^{-1}) and integrated line fluxes (in units of Jy km s^{-1}) for the detected transitions. In Table 4, the first and second columns list the calculated rest frequencies and associated transitions of the CH_3CN lines, respectively. The third column lists the integrated line fluxes and their 1 σ errors (in units of Jy km s^{-1}). In order to constrain the number of free parameters in the Gaussian fits, we fixed the frequency spacing between the *K*-components and constrained the line widths of the transitions to be the same in each spectral window. Finally, the last column lists a calculated optical depth of each transition for a $T_{\rm rot} = 141$ K and an $N_{\rm tot}/Q_{\rm rot}$ of 1.0×10^{13} cm^{-2} (§ 4.1, eq. [3]).

Figure 4 shows the CH_3CN spectra toward region W51e2 at the 3 and 1 mm wavelengths in order of increasing frequency. The spectral line labels are the same as in Figure 3. We measure a $v_{\rm LSR}$ of 53(2) km s^{-1} for the W51e2 region. The ± 1 σ noise level is seen at the left in each panel. In Figures 4*a* and 4*b*, the dashed spectra are taken over the entire W51e1/e2 region. The solid spectra are for the amount of flux attributed to the e2 region. Table 5 lists the fitted CH_3CN line parameters toward the W51e2 region. Least-squares Gaussian fits were made as before for each spectral line in order to obtain the radial velocities (in units of km s^{-1}) and integrated line fluxes (in units of Jy km s^{-1}) for the detected transitions. For the $J = 5$–4 and 6–5 lines, the flux listed is that attributable to e2. The column labels are the same as in Table 4, except the optical depths in the last column were calculated for a $T_{\rm rot} = 149$ K and an $N_{\rm tot}/Q_{\rm rot}$ of 1.8×10^{13} cm^{-2} (§4.1, eq. [3]).

A major problem in determining the intensities and widths of spectral lines has been interference from lines of other molecular species or from unidentified features. For example, in a recent spectral line survey toward Sgr B2(N-LMH), Friedel et al. (2004) detected 218 lines covering ~3.6 GHz in bandwidth. This yielded a spectral line density (average number of lines per 100 MHz) of 6.06 from all observed lines (2.72 from identified lines and 3.34 from unidentified lines).

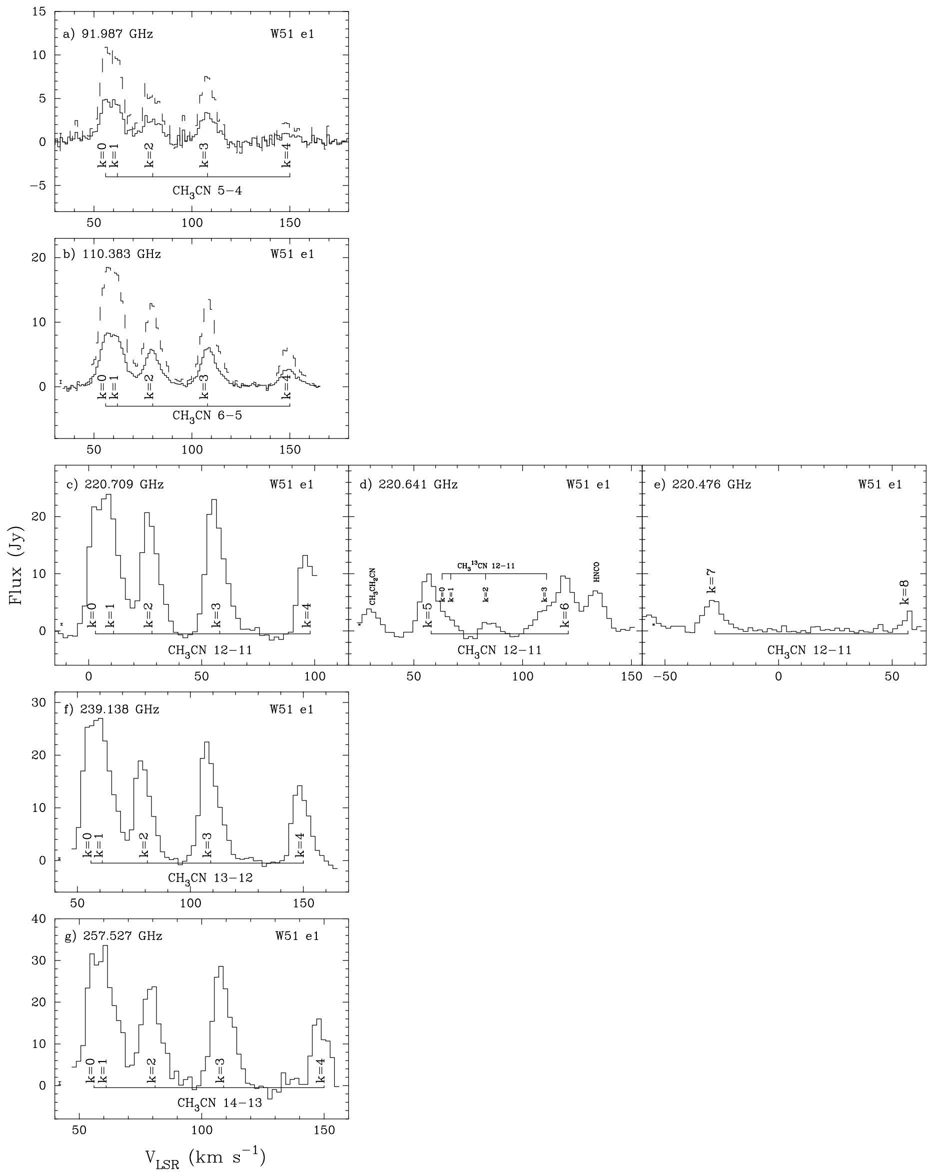

Fig. 3.—Spectra toward W51e1 for the five observed spectral bands, in order of increasing frequency. The rest frequency listed in the upper left corner of each panel corresponds to the $K = 0$ component (except in the 220 GHz band; § 3). We measured a v_{LSR} of 56 km s^{-1} for the W51e1 region. Note the change in intensity scale for each frequency band.

Therefore, contamination from other spectral features in our passbands of CH_3CN is quite possible, and we list possible interfering features below. We have checked the standard line lists from the Lovas database (Lovas 2004), the JPL database (Pickett et al. 1998), and the Cologne Database for Molecular Spectroscopy (Müller et al. 2001) for interference from other lines. At 91,958 MHz, very close in frequency to the 5(4)–4(4) transition of CH_3CN, there is the $7_{2,6}$–$7_{1,6}$ transition of CH_3CH_2OH (ethanol, EtOH). This spectral line has an upper-state energy level of ~89 K and may be blended with the CH_3CN feature. In addition, at 91,984 MHz, very close in frequency to the 5(1)–4(1) transition of CH_3CN, there is the 10–9 transition of $C^{13}CCCH$. This feature has an upper-state energy level of ~27 K and may be blended with the CH_3CN feature. At 110,368 MHz, there is the $8_{1,8}$–$8_{0,8}$ transition of EtOH. This feature lies between the 6(3)–5(3) transition at 110,364 MHz and the 6(2)–5(2) transition at 110,374 MHz of CH_3CN. The EtOH spectral line has an upper-state energy level of ~91 K but does not appear to interfere with the detection of any CH_3CN feature. At 220 GHz, there appear to be several features that may interfere with the CH_3CN lines, including interference from its isotopomer $CH_3{}^{13}CN$ (Table 3). This is further complicated by the coarser spectral resolution at 1 mm wavelengths. Near the 12(3)–11(3) transition at 220,709 MHz, there is the $10_{4,7}$–$9_{3,7}$ E transition of MeF at 220,702 MHz. This MeF

TABLE 4

W51e1 CH_3CN Molecular Line Identifications

ν (GHz)	Transition	$\int \Delta I\, dv$[a] (Jy km s^{-1})	τ[b]
91.987	5(0)–4(0)	30.8 (2.3)	0.28
91.985	5(1)–4(1)	35.3 (2.6)	0.26
91.980	5(2)–4(2)	30.1 (1.4)	0.19
91.971	5(3)–4(3)	34.1 (1.4)	0.23
91.958	5(4)–4(4)	9.8 (1.1)	0.05
110.384	6(0)–5(0)	63.7 (2.0)	0.39
110.381	6(1)–5(1)	58.2 (2.0)	0.36
110.375	6(2)–5(2)	56.3 (1.3)	0.28
110.364	6(3)–5(3)	60.0 (1.3)	0.37
110.350	6(4)–5(4)	27.5 (1.1)	0.10
220.747	12(0)–11(0)	176.5 (13.4)	1.09
220.743	12(1)–11(1)	169.0 (12.7)	1.03
220.730	12(2)–11(2)	185.2 (0.7)	0.86
220.709	12(3)–11(3)	209.8 (11.2)	1.30
220.679	12(4)–11(4)	122.9 (9.3)	0.43
220.641	12(5)–11(5)	85.2 (4.8)	0.25
220.594	12(6)–11(6)	87.3 (4.5)	0.27
220.539	12(7)–11(7)	52.2 (6.2)	0.06
220.476	12(8)–11(8)	19.0 (5.6)	0.02
239.138	13(0)–12(0)	193.6 (16.6)	1.18
239.133	13(1)–12(1)	194.0 (16.4)	1.11
239.120	13(2)–12(2)	177.8 (11.9)	0.94
239.097	13(3)–12(3)	206.4 (12.6)	1.42
239.064	13(4)–12(4)	127.9 (10.4)	0.48
257.527	14(0)–13(0)	227.0 (14.2)	1.25
257.522	14(1)–13(1)	211.7 (13.8)	1.18
257.508	14(2)–13(2)	235.6 (12.4)	1.00
257.483	14(3)–13(3)	267.9 (13.2)	1.52
257.448	14(4)–13(4)	138.3 (10.6)	0.51

[a] Errors are 1 σ.

[b] The optical depth for W51e1 is calculated for a rotational temperature of 141 K and $N_{\rm tot}/Q_{\rm rot} = 1.0 \times 10^{13}$ cm^{-2}.

spectral line has an upper-state energy level of ~44 K and may interfere with the detection of the CH_3CN feature. In addition, there is the $7_{3,5}$–$6_{3,3}$ transition of EtOH at 220,707 MHz, which may also interfere with the same CH_3CN feature. In fact, in Figures 3*c* and 4*c*, there is a noticeable wing on the lower frequency end of the $K = 3$ emission feature. These interfering lines may lead to an enhancement of this CH_3CN feature. However, the asymmetric profile in these lines may also be due to the infall measured by Zhang et al. (1998). Between the 12(1)–11(2) transition at 220,730 MHz and the 12(1)–11(1) transition at 220,742 MHz there are two spectral features of MeF: the $8_{5,3}$–$8_{3,6}$ A-transition at 220,736 MHz and the $9_{5,4}$–$9_{3,7}$ A-transition at 220,739 MHz. These transitions have very low upper-state energy levels (~41 K) and may interfere with the CH_3CN transitions. At 220,594 MHz, the 12(6)–11(6) line may have some interference from the $10_{1,9}$–$9_{1,8}$ transition of $HN^{13}CO$ at 220,592 MHz. This transition has an upper-state energy level of ~102 K and may add to the intensity of the CH_3CN line. It is apparent that between the 12(5)–11(5) and 12(6)–11(6) transitions of CH_3CN, there is interference from the $J = 12$–11, $K = 0$–3 lines of $CH_3{}^{13}CN$ (Table 3). These transitions are labeled in the spectrum in Figures 3*d* and 4*d*. Thus, obtaining accurate line intensities and line widths of the $K = 5$ and 6 CH_3CN transitions is very difficult in this frequency band. However, this is the only frequency band we observed where the $CH_3{}^{13}CN$ lines are causing interference. In the 239 GHz band, there may be interference due to another symmetric-top species, propyne (CH_3CCH). The 14(6)–13(6) and 14(5)–13(5) lines lie very close to the 13(3)–12(3) and 13(0)–12(0) transitions of CH_3CN, respectively. However, to date, these transitions have not been detected in the interstellar medium. Finally, at 257,448 MHz, the 14(4)–13(4) transition may have some interference from the $9_{4,5}$–$8_{4,5}$ transition of EtOH at 257,450 MHz. This transition has an upper-state energy level of ~117 K and may add to the intensity of the CH_3CN line. However, none of the lines outlined above, except for the $CH_3{}^{13}CN$ lines, have ever been detected as possible interlopers affecting the detection of the CH_3CN lines. Higher spectral resolution measurements are needed to determine whether the EtOH or MeF emission contributes to the CH_3CN emission. For now, we assume that the emission from the EtOH and MeF transitions are negligible and that we can measure the contribution coming from the $CH_3{}^{13}CN$ emission.

4. ANALYSIS

4.1. *Rotational Temperature Diagram Method*

Determining the best column density estimates for complex molecules is important because they may be central to the problem of understanding the role of grains in molecular formation, the importance of warm-gas–phase chemistry, or where cold-gas–phase chemistry becomes important. In order to estimate the temperatures and column densities of the regions that contain the CH_3CN emission, we used two different methods to analyze the data. The first is the conventional treatment of forming a rotational temperature diagram (a plot of the logarithm of normalized column density vs. upper-state energy). However, included in this formalism are many assumptions. First, we assume that each region has uniform physical conditions and that the populations of the energy levels can be characterized by a Boltzmann distribution. However, we have no a priori knowledge that this is an accurate representation of the distribution of the level populations, and, in fact, this may not be true. Second, we assume optically thin conditions. We may be able to correct for this assumption later in the analysis. Third, it is important that we are able to measure a source size of the emitting region. If we are not able to measure a source size, we assume that the source fills the synthesized beam of our observation. Finally, we assume that the background radiation is negligible. So if the population distribution can be adequately described by a single rotational temperature and if all the lines are optically thin, the measured fluxes are proportional to the column densities in the upper levels of the transitions being observed. They also vary exponentially with the energies of the upper states. This can be written as

$$\frac{N_u}{g_u} = \frac{3c^2}{\Omega_s 16\pi^3\nu^3}\frac{\int \Delta I\, dv}{S_{ij}\mu^2} \quad (1)$$

and

$$\frac{N_u}{g_u} = \frac{N_{\rm tot}}{Q(T_{\rm rot})}e^{-(E_u/kT_{\rm rot})}. \quad (2)$$

One can thereby obtain a temperature (the "rotational" temperature) and an estimate of the total molecular column

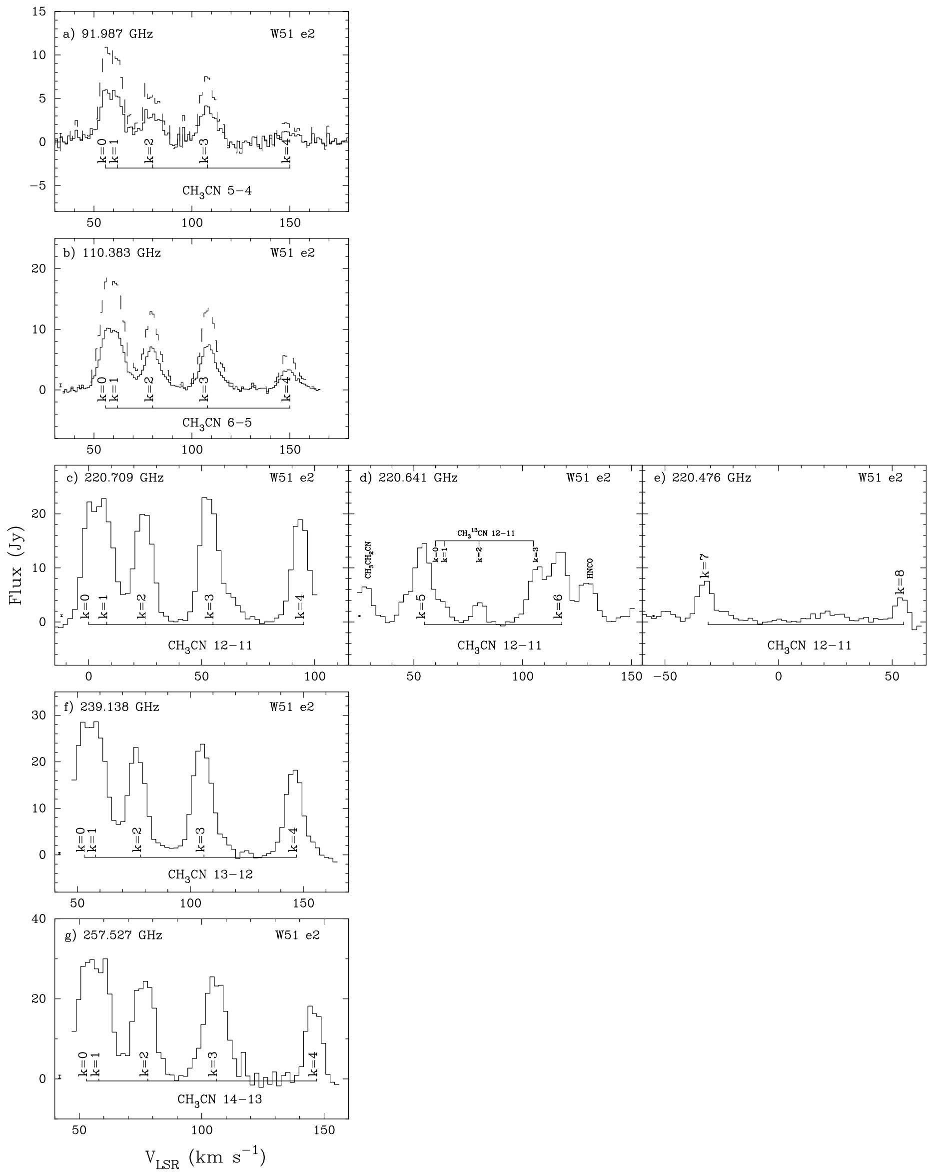

FIG. 4.—Same as Fig. 3, but toward W51e2. We measured a v_{LSR} of 53 km s^{-1} for W51e2. Note the change in intensity scale for each frequency band.

density. The temperature obtained would be equal to the kinetic temperature only at sufficiently high densities. However, symmetric-top molecules like CH_3CN form a special case, since radiative processes across K-ladders are forbidden. Therefore, the populations in the different K-ladders can be used to estimate the kinetic temperature even if the levels are not fully thermalized. If the emission is not optically thin, the finite opacity produces an underestimate in the upper-level column density of the observed transition, and it can also produce an error in the rotational temperature that is determined (Goldsmith & Langer 1999). If the opacity can be calculated, iterative corrections can be made to the rotational temperature and total column density derived from this analysis.

From Turner (1991), we find that the optical depth at the line center is given by

$$\tau = \frac{8\pi^3}{3k} \frac{S_{ij}\mu^2\nu}{\Delta v T_{\rm rot}} \frac{N_u}{g_u}. \tag{3}$$

In equation (1), N_u is the upper-level column density and g_u is the statistical weight of the upper level $(2J+1)$, Ω_s is the solid angle subtended by the source, $\int \Delta I\, dv$ is the integrated line flux, ν is the rest frequency, and $S_{ij}\mu^2$ is the product of the total torsion-rotational line strength and the square of the electric dipole moment. In equation (2), $N_{\rm tot}$ is the total column density, $Q(T_{\rm rot})$ is the rotational partition function, E_u is the upper state energy level, and $T_{\rm rot}$ is the rotational

TABLE 5
W51e2 CH_3CN Molecular Line Identifications

ν (GHz)	Transition	$\int \Delta I\, dv$[a] (Jy km s^{-1})	τ[b]
91.987	5(0)–4(0)	37.6 (2.3)	0.42
91.985	5(1)–4(1)	43.1 (2.7)	0.38
91.980	5(2)–4(2)	36.7 (1.4)	0.29
91.971	5(3)–4(3)	41.7 (1.4)	0.35
91.958	5(4)–4(4)	11.9 (1.1)	0.07
110.384	6(0)–5(0)	77.8 (2.0)	0.63
110.381	6(1)–5(1)	71.2 (2.0)	0.58
110.375	6(2)–5(2)	68.8 (1.3)	0.46
110.364	6(3)–5(3)	73.4 (1.3)	0.60
110.350	6(4)–5(4)	33.6 (1.1)	0.16
220.747	12(0)–11(0)	174.2 (13.8)	1.88
220.743	12(1)–11(1)	171.0 (13.1)	1.78
220.730	12(2)–11(2)	204.6 (10.6)	1.51
220.709	12(3)–11(3)	236.6 (11.3)	2.29
220.679	12(4)–11(4)	185.3 (9.9)	0.78
220.641	12(5)–11(5)	139.4 (6.1)	0.55
220.594	12(6)–11(6)	118.4 (5.0)	0.59
220.539	12(7)–11(7)	64.3 (7.5)	0.15
220.476	12(8)–11(8)	33.0 (5.0)	0.06
239.138	13(0)–12(0)	221.2 (13.8)	1.98
239.133	13(1)–12(1)	227.1 (13.6)	1.88
239.120	13(2)–12(2)	232.1 (11.6)	1.60
239.097	13(3)–12(3)	252.5 (11.7)	2.44
239.064	13(4)–12(4)	183.4 (9.9)	0.84
257.527	14(0)–13(0)	225.8 (13.3)	2.13
257.522	14(1)–13(1)	228.0 (14.0)	2.02
257.508	14(2)–13(2)	269.0 (12.5)	1.72
257.483	14(3)–13(3)	277.3 (13.2)	2.65
257.448	14(4)–13(4)	162.4 (10.1)	0.91

[a] Errors are 1 σ.
[b] The optical depth for W51e2 is calculated for a rotational temperature of 149 K and $N_{tot}/Q_{rot} = 1.8 \times 10^{13}$ cm^{-2}.

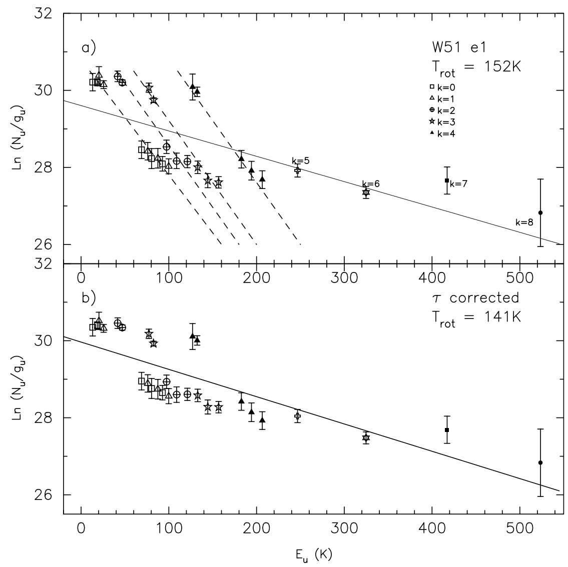

Fig. 5.—(*a*) Rotational temperature diagram for the observed CH_3CN transitions toward W51e1. *Ordinate*: ln (N_u/g_u). *Abscissa*: $E_u(K)$. The least-squares fit across *K*-levels is shown as a solid line. The least-squares fits in a given *K*-ladder are shown as dashed lines. The resulting rotational temperature is 152 K. (*b*) Rotational temperature diagram for the observed CH_3CN transitions that have been corrected for optical depth. The resulting rotational temperature is 141(20) K.

temperature. Finally, in equation (3), Δv is the FWHM line width. Because CH_3CN is a symmetric-top molecule, its rotational partition function is approximated by $Q(T_{rot}) = CT_{rot}^{3/2}$, where $C = 0.98K^{-3/2}$. By combining equations (1) and (2) with a single rotational temperature and a single total column density, one finds that ln (N_u/g_u) is a linear function of E_u, with the slope of the line equal to $-1/T_{rot}$. Thus, a plot of ln (N_u/g_u) versus E_u will yield an initial rotational temperature and a total beam-averaged column density. We can then calculate the optical depth of each transition (eq. [3]) and iteratively correct each observation by multiplying N_u/g_u by the optical depth correction factor: $C_\tau = \tau/(1 - e^{-\tau})$ (Goldsmith & Langer 1999).

In order to combine the 3 and 1 mm data into one rotational temperature diagram, the data had to be analyzed assuming a similar source size. Using the procedure outlined in § 3, we found that W51e1 subtends an area of 7.9(6) $arcsec^2$, that e2 subtends an area of 6.0(9) $arcsec^2$, and that ~55% of the total flux originates from the e2 core. Using these source sizes and distributing the total flux between regions e1 (45%) and e2 (55%) in the 3 mm data, the plot of ln (N_u/g_u) versus E_u showed good correlation but still some scatter at the lower *K*-values toward each region. Part of this scatter may be due to the uncertainties in fitting the blended $K = 0$, 1 components. Other scatter may be due to high opacities, particularly in the $K = 0$, 1, and 3 lines. Figure 5*a* shows the result of this analysis toward W51e1. The solid line shows the least-squares fit to the data across all *K*-ladders. The dashed lines are for fits to the data within a *K*-ladder. All the 3 mm data points lie above the solid line. The error bars on the data are 3 σ errors based on the rms noise level in the spectral window and the errors due to the Gaussian fit routine to the line intensity and line width. Furthermore, because of the extra factor of 2 in degeneracy of the $K = 3n$ ($n = 1$, 2) levels, those data were divided by 2 and included in the fit. From the fit we estimated a rotational temperature of 152 K and $N_{tot}/Q_{rot} = 7.2 \times 10^{12}$ cm^{-2}. We then applied the C_τ correction described above and iterated until the temperature and column density converged. The optical depths in Table 4 were calculated from the final temperature and total CH_3CN column density (Table 4). After we corrected for optical depth effects, the scatter in the lower *K*-values in Figure 5*a* was reduced; however, there was still a definite separation between the 3 and 1 mm data. Figure 5*b* shows the result of this analysis. From the optical depth–corrected data, we derived a rotational temperature of 141(20) K and a total beam-averaged column density of $2.5(5) \times 10^{16}$ cm^{-2} for the W51e1 region. We performed the same analysis toward region W51e2. Figure 6 shows the result of this analysis. The derived optical depth of each CH_3CN transition toward W51e2 is given in Table 5. From the optical depth–corrected data, we derived a rotational temperature of 149(22) K and a total beam-averaged column density of $5(1) \times 10^{16}$ cm^{-2} for the W51e2 region.

4.2. *Statistical Equilibrium Analysis*

A major problem arises if the molecule level populations are not thermalized and cannot be approximated by a Boltzmann-like distribution. In that case, it is harder to determine the total column density of the species, because the fractional population of a given level can be greater or less than that in LTE. So, it is difficult to make a general statement about how

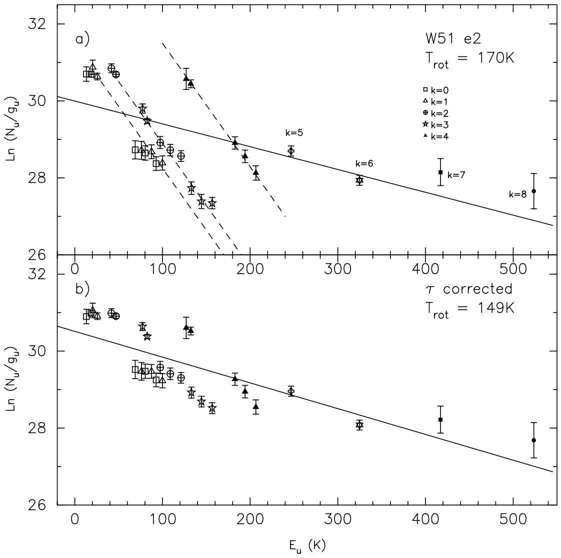

Fig. 6.—(*a*) Same as Fig. 5*a*, but toward W51e2. The resulting rotational temperature is 170 K. (*b*) Same as Fig. 5*b*, but toward W51e2. The resulting rotational temperature is 149(22) K.

the determination of the total column density is affected (Goldsmith & Langer 1999). In this case of non-LTE excitation, the assumption that all the levels are thermalized is valid only for the case of high density ($n \geq 10^6$ cm^{-3}). In the lower density case ($n \leq 10^6$ cm^{-3}), the kinetic temperature is generally underestimated, and so is the total beam-averaged column density of the observed species. Improvements can be made in the rotational temperature diagram method (RTDM) to better estimate the temperature and column density in these regions (Goldsmith & Langer 1999). However, the RTDM may still either overestimate or underestimate the total column density and temperature.

Therefore, in an attempt to determine the true kinetic temperatures, densities, and column densities of the emitting regions W51e1 and W51e2, we made statistical equilibrium calculations based on the radiative and collisional transition rates of the CH_3CN molecule (Green 1986; Cummins et al. 1983). Applying this technique to our data, we calculated the fractional population of each energy level up to $J = 25$ and $K = 21$. There are several competing factors that will determine the population of any given level. First, spontaneous emission will be the primary radiative process in causing the de-excitation of the higher energy levels. Second, collisions will play a major role in the population of a given level, because they cause both upward and downward transitions. In addition, collisional transitions obey different selection rules than radiative transitions. Therefore, obtaining a detailed set of collision rates at several different temperatures is important in this analysis. Finally, in optically thick conditions, stimulated processes are also important in determining a level population, because radiative trapping of the emitted photons may occur. Taking all these processes into account, we can input values of density and kinetic temperature and calculate an equilibrium set of level populations. The equilibrium populations of the model can then be compared with the observational data. For our purpose, the statistical equilibrium code from Sutton et al. (1986) was used to analyze the data.

In a first attempt, the data were compared to a model that did not contain radiative trapping, that is, an optically thin model. It was quickly realized that certain characteristics of the data were not matched by the model. For example, there was a definite decrease in the fractional level population in the $K = 3$ level that the model did not account for. We saw the same effect in the $K = 6$ level, although not as pronounced as in the lower energy $K = 3$ level. We also noticed an enhancement of the fractional level population going from $K = 0$ to 2. This trend was also not seen in the model. However, errors in the Gaussian fits of the spectral features may account for this trend. Overall, however, the data did not fit the optically thin models.

A second attempt was made that did include radiative trapping. This was done by specifying a source-averaged column density of CH_3CN, and thus several transitions became optically thick. To account for radiative trapping in the model, the rate of spontaneous emission from each level (the Einstein *A*-coefficient) was modified by multiplying it by the photon escape probability β. The value of β was determined in the usual way for a spherical geometry with a velocity field proportional to the radius: $\beta = (1 - e^{-\tau})/\tau$, where τ is the optical depth of the appropriate transition. Furthermore, in this model, the fractional level populations (f) calculated from the model were multiplied by the escape probabilities (β) to give quantities directly proportional to the integrated line fluxes (Sutton et al. 1986). Figure 7 shows the results of the model with radiative trapping for a temperature of 123 K toward W51e1. In Figure 7, the model data (*circles*) are labeled by their corresponding *J*-values and are connected by solid lines. The observational data (*open symbols*) are plotted, along with their corresponding *J*-values. The error bars on the observational data represent 3 σ errors based on the noise level in the spectral window and the errors due to the Gaussian fit routine to the line intensity and line width. As can be seen, the model nearly matches all the features seen in the data. For example, the model correctly predicts a depletion in the intensities of the $K = 3$ and 6 lines. There still remains the enhancement of the fractional level population from $K = 0$–2, especially in the higher J transitions. However, as was

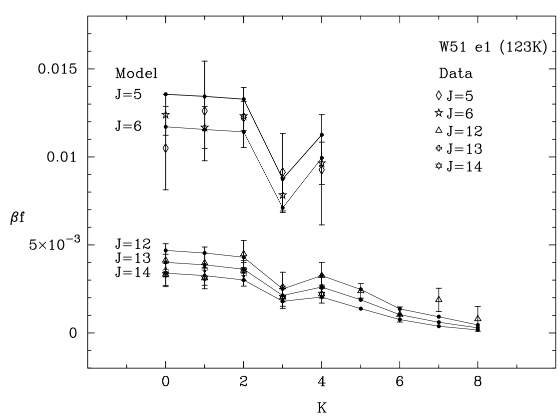

Fig. 7.—Fractional populations of (J, K) levels of CH_3CN toward W51e1. *Ordinate*: βf (fractional level population multiplied by escape probability). *Abscissa*: *K*. In all models the $K = 3$ and 6 values have been divided by 2 to correct for the extra degeneracy of those levels. The data toward W51e1 are plotted alongside each model. The best fit to the observed spectra toward W51e1 is given by a temperature of 123(11) K, a hydrogen density of $5(1) \times 10^5$ cm^{-3}, and a total column density of $1.4(1) \times 10^{16}$cm^{-2}.

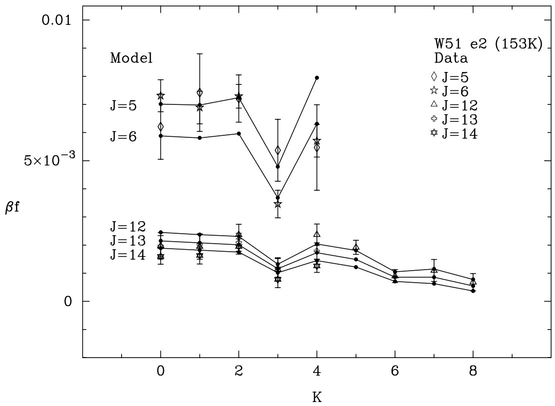

FIG. 8.—Same as Fig. 7, but toward W51e2. The best fit to the observed spectra toward W51e2 is given by a temperature of 153(21) K, a hydrogen density of $5(2) \times 10^5$ cm^{-3}, and a total column density of $3.8(7) \times 10^{16}$ cm^{-2}.

previously stated, errors in the Gaussian fits of the spectral features may account for this trend. Still, the radiative trapping model fits the data better than the optically thin case. Figure 8 shows the results of the statistical equilibrium analysis for the region W51e2. Toward W51e2, the data were much harder to fit to the model because of the high opacity of the CH_3CN lines. Furthermore, the model predicts a much higher population in the $K = 4$ ladder that is not seen in our data.

In order to find the best-fit model of the observed spectra, a variety of models with different kinetic temperatures (T_k = 100–400 K), densities ($n = 10^{4.0}$–$10^{5.8}$ cm^{-3}), and column densities ($N_{\rm tot} = 10^{15.7}$–$10^{18.0}$ cm^{-2}) were constructed. The χ^2 hypersurface appeared to have only a single minimum within the range searched. The best-fit model to the data was determined using the standard technique of inversion of the 3×3 Hessian (curvature) matrix (Press et al. 1992). Values of χ^2 at minimum were of the order of 100–400, greater than the number of degrees of freedom (26), indicating either that the observational uncertainties were underestimated or that factors in the model, such as uncertainties in the assumed collisional rates, contributed significantly to χ^2. Therefore, the values of χ^2 were rescaled so that the quoted uncertainties in the parameters were based on the actual discrepancies between the model and the data and not on a presumed knowledge of the origin and magnitude of the uncertainties. Nominal confidence limits were then determined for each parameter directly from the formal covariance matrix on the basis of an assumed normal distribution of errors (lognormal in the cases of hydrogen and methyl cyanide column densities).

The best fit to the observed spectra toward W51e1 is given by a temperature of 123(11) K, a hydrogen density of $5(1) \times 10^5$ cm^{-3}, and a total column density of $1.4(1) \times 10^{16}$ cm^{-2}. The uncertainties describe a nominal 90% confidence interval. The best fit to the observed spectra toward W51e2 is given by a temperature of 153(21) K, a hydrogen density of $5(2) \times 10^5$ cm^{-3}, and a total column density of $3.8(7) \times 10^{16}$ cm^{-2}. The best-fit values of temperature, density and total column density were used to generate Figures 7 and 8.

5. DISCUSSION

Our observations indicate that CH_3CN can be used as a good probe of the physical conditions present in hot molecular cores and as a tracer of hard-to-detect large molecular species. We discuss both points in detail below.

First, our analysis utilizing both the RTDM and the statistical equilibrium method (SEM) shows that CH_3CN is a good probe of the physical conditions present in hot molecular cores. However, there are still some discrepancies that need to be accounted for. In the RTDM, we see that the 3 mm data lie above the 1 mm data (Figs. 5 and 6). Initially, we corrected for optical depth effects, which reduced the separation between the 3 and 1 mm data (§ 4.1) but could not remove it completely. Furthermore, errors due to flux calibration or the line-fitting routine also cannot account for the difference between the 3 and 1 mm data. Thus, we need another explanation to account for this separation. It is possible to interpret such diagrams not only by drawing a best-fit line across the K-values (Figs. 5 and 6, *solid lines*), but also by fitting the values in a given K-ladder (Figs. 5 and 6, *dashed lines*). The temperature determined from such an analysis is referred to as the "excitation" temperature ($T_{\rm ex}$) and measures the temperature that can account for the population between adjacent J-levels of the same K-ladder (Loren & Mundy 1984; Hollis 1982). If we fit a line through a K-ladder, we find that the temperature is much lower than what is found across K-ladders (~31 K for e1 and e2). This is due to the fact that radiative relaxation processes are important in determining the population distribution within a given K-ladder. If, in fact, the temperature in a K-ladder were similar to the derived rotational temperature, this would imply that radiative transitions were negligible and that collisional processes dominate. In the RTDM, the derived rotational temperature ($T_{\rm rot}$) is believed to be a better estimate of the kinetic temperature (T_k) (Loren & Mundy 1984). Even though the derived rotational temperatures are higher than the excitation temperatures, they still may not represent the true kinetic temperatures of the regions. The SEM, which include collisional processes and radiative processes, gives a much better interpretation of the kinetic temperature in these regions.

The temperatures derived from the SEM (~125 K for e1 and ~150 K for e2) were similar to the temperatures determined from the RTDM (~150 K). In addition, the total beam-averaged column density of CH_3CN determined from the SEM was very similar to that from the RTDM: $N_{\rm tot}({\rm RTDM})/N_{\rm tot}({\rm SEM}) = 1.8$ for W51e1 and 1.3 for e2. Finally, the results from the SEM indicate that the hydrogen densities in these regions are very similar. In general, the statistical equilibrium model provides a much better physical interpretation of the data and a better measure of the temperature and total column density of a molecular species. However, by correcting for optical depth effects, it is possible to get a good understanding of the temperature and total beam-averaged column density of a molecular species using the RTDM. The limitation of the statistical equilibrium model is that it is only applicable to molecular species whose collision rates are either known or can be estimated to obtain a physically reasonable model. If these rates are not known or cannot be determined, the RTDM may be the only way to estimate temperature and total column density. We also note that the derived uncertainties from each method should be considered lower limits. The real errors may be much larger because of the inherent properties of the sources (i.e., clumping) and not our analysis technique.

Second, our observations indicate that CH_3CN is a good tracer of hard-to-detect large molecular species. To be a good tracer, a molecule needs to be easily detectable and have a column density similar to that of the molecular species that is harder to detect. Because of its large line strength and dipole moment ($\mu = 3.9$ D), CH_3CN is easily detectable in many hot core regions and low-temperature dark clouds (Pankonin et al. 2001). Furthermore, the column density of CH_3CN from this survey was very similar to the measured column densities of CH_3CH_2CN and CH_3COOH toward W51e1 and e2 (Remijan et al. 2002; Liu et al. 2001). In order to obtain an accurate column density comparison, we needed to compare the column densities of the other species for our determined source sizes (§ 3). Once this was done, we compared the CH_3CN column density with the column density of CH_3CH_2CN and CH_3COOH[8] toward W51e1 and e2. The CH_3CN/CH_3CH_2CN abundance ratio toward W51e1, using a source size of 7.9(6) arcsec^2, is $\sim$0.6. The upper limit of the CH_3CN/CH_3COOH abundance ratio is 2 times larger, at $\sim$1.2. The CH_3CN/CH_3CH_2CN abundance ratio toward W51e2, using a source size of 6.0(9) arcsec^2, is $\sim$1.3. The CH_3CN/CH_3COOH abundance ratio is slightly larger, at $\sim$2.3. We can also obtain a fractional abundance of CH_3CN using the density of H_2 from the SEM. If we assume that W51e1 and e2 are spherical at a distance of 7 kpc, we derive an H_2 column density of $\sim 1.1 \times 10^{23}$ cm^{-2} for W51e1 and $\sim 8.3 \times 10^{22}$ cm^{-2} for W51e2. Thus, the best estimates for the CH_3CN fractional abundances are $X_{CH_3CN} = 1.3 \times 10^{-7}$ for W51e1 and $X_{CH_3CN} = 4.6 \times 10^{-7}$ for W51e2. We can compare these values to previous measurements of the fractional abundance of CH_3CN toward other high-mass hot molecular cores. Wilner, Wright, & Plambeck (1994) observed CH_3CN emission toward Orion. Their observations indicated that the CH_3CN abundance was at least 2 orders of magnitude larger toward the Orion hot core and 1 order of magnitude larger toward the Orion southern ridge than toward the Orion compact ridge. This gives a CH_3CN fractional abundance of 10^{-8}, 10^{-9}, and 10^{-10} toward the hot core, southern ridge, and compact ridge, respectively. Such large abundances are not predicted by the gas phase formation models (Huntress & Mitchell 1979). Nummelin et al. (2000) also measured a fractional abundance of CH_3CN as high as 3×10^{-8} toward the hot core region Sgr B2(N). Therefore, our derived values are very similar to previously observed values and may indicate that grain surface chemistry is leading to an enhancement of CH_3CN relative to H_2 toward W51e1 and e2.

Finally, one molecular species that has been used to try to detect elusive large molecular species is MeF. MeF is considered an important biomolecule because it is an isomer to both CH_3COOH and glycolaldehyde (CH_2OHCHO) (Remijan et al. 2002). MeF is easily detectable in many hot molecular cloud cores, such as OMC-1, G34.3+0.2, Sgr B2(N-LMH), and W51 (e1, e2, and d). We find that the CH_3CN/MeF abundance ratio is $\sim$0.02 toward the W51e1 region and $\sim$0.04 toward the W51e2 region, from the column density measurements of Remijan et al. (2002). From these observations, it is possible to determine that CH_3CN would be a much better tracer of large molecular species than MeF. To determine this, we compared the integrated line flux to total column density of CH_3CN and MeF on the basis of the spectroscopic parameters of each molecule and the measured column densities toward the W51e2 region. Correcting for temperature and source size, we find an MeF column density of 5.7×10^{17} cm^{-2} (Remijan et al. 2002). From the SEM, we find a CH_3CN column density

[8] Because CH_3COOH was not detected toward W51e1, the column density ratio is an upper limit.

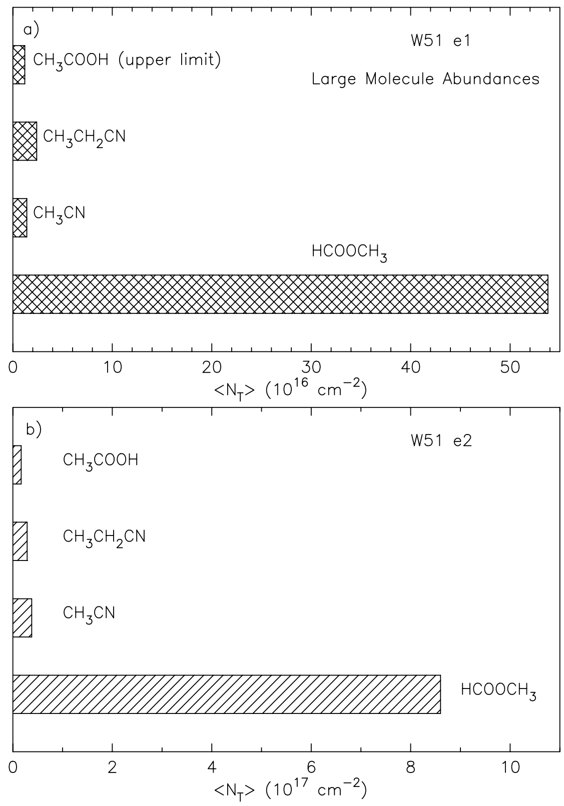

Fig. 9.—(*a*) Beam-averaged column densities determined from W51e1 interferometric measurements, assuming a source size of 7.9(6) arcsec^2 for acetic acid (CH_3COOH), ethyl cyanide (CH_3CH_2CN), methyl cyanide (CH_3CN), and MeF . (*b*) Beam-averaged column densities determined from W51e2 interferometric measurements assuming a source size of 6.0(9) arcsec^2.

of 3.8×10^{16} cm^{-2}. Comparing the MeF line parameters at 90 and 228 GHz (Remijan et al. 2002) with the CH_3CN line parameters at 91 and 220 GHz, we find that the integrated line flux of the CH_3CN lines is more than 7 times larger than that of the MeF lines. Thus, for a column density more than 15 times smaller, the integrated line flux is more than 7 times larger. The column densities of all these molecular species toward W51e1 and e2 are illustrated in Figure 9. A similar figure was shown by Snyder et al. (2002, their Fig. 7) toward Sgr B2(N-LMH). From Figure 9, it is clear that the abundance of CH_3CN is closer than that of the MeF to the abundances of CH_3CH_2CN and CH_3COOH. Furthermore, both figures indicate that the MeF abundance is larger than that of any other large molecular species—larger by more than an order of magnitude in several cases. Thus, because lines of CH_3CN are easy to detect, it appears to be a much better tracer of CH_3CH_2CN and CH_3COOH than MeF. Further observations are needed to determine whether this hypothesis applies to other large molecular species.

6. CONCLUSIONS

We have detected strong CH_3CN emission lines from the hot core regions W51e1 and W51e2. Furthermore, the regions of emission reveal molecular clumps centered on the ultracompact H II regions found by Zhang et al. (1998). The CH_3CN

lines show large optical depths in the lower *K* transitions toward both regions in W51. A first attempt to calculate temperatures and total beam-averaged column densities of CH_3CN toward these regions was made by rotational temperature diagrams. From the optical depth–corrected data, we derived a rotational temperature of 141(20) K and a total beam-averaged column density of $2.5(5) \times 10^{16}$ cm^{-2} for the W51e1 region (Fig. 5). From the optical depth–corrected data, we derived a rotational temperature of 149(22) K and a total beam-averaged column density of $5(1) \times 10^{16}$ cm^{-2} for the W51e2 region (Fig. 6). To determine the true kinetic temperatures, densities, and column densities of the emitting regions W51e1 and e2, statistical equilibrium models were used to calculate the relative populations of each energy level. The best fit to the observed spectra toward W51e1 is given by a temperature of 123(11) K, a hydrogen density of $5(1) \times 10^5$ cm^{-3}, and a total column density of $1.4(1) \times 10^{16}$ cm^{-2}. The uncertainties describe a nominal 90% confidence interval. The best fit to the observed spectra toward W51e2 is given by a temperature of 153(21) K, a hydrogen density of $5(2) \times 10^5$ cm^{-3}, and a total column density of $3.8(7) \times 10^{16}$ cm^{-2}. Finally, our observations indicate that CH_3CN can be used as a good probe of the physical conditions present in hot molecular cores and as a tracer of hard-to-detect large molecular species. For a column density of CH_3CN more than 15 times smaller than the column density of MeF, the integrated line flux is more than 7 times larger. Finally, Figure 9 illustrates the column densities of large molecules toward the W51e1 and e2 regions. From this figure, it is clear that the abundance of CH_3CN is closer to the abundances of CH_3CH_2CN and CH_3COOH. Thus, because lines of CH_3CN are easy to detect, it appears to be a much better tracer of CH_3CH_2CN and CH_3COOH than MeF.

We appreciate the help given by D. S. Meier in numerous discussions. We also thank an anonymous referee for useful suggestions. Research at the Laboratory for Astronomical Imaging is supported by NSF grants AST 99-81363 and AST 02-28953 and by the University of Illinois.

REFERENCES

Boucher, D., Burie, J., Bauer, A., Dubrulle, A., & Demaison, J. 1980, J. Phys. Chem. Ref. Data, 9, 659
Cummins, S. E., Green, S., Thaddeus, P., & Linke, R. A. 1983, ApJ, 266, 331
Friedel, D. N., Snyder, L. E., Turner, B. E., & Remijan, A. 2004, ApJ, 600, 234
Goldsmith, P. F., & Langer, W. D. 1999, ApJ, 517, 209
Green, S. 1986, ApJ, 309, 331
Hollis, J. M. 1982, ApJ, 260, 159
Huntress, W. T., Jr., & Mitchell, G. F. 1979, ApJ, 231, 456
Lai, S.-P., Crutcher, R. M., Girart, J. M., & Rao, R. 2001, ApJ, 561, 864
Liu, S.-Y., Mehringer, D. M., & Snyder, L. E. 2001, ApJ, 552, 654
Loren, R. B., & Mundy, L. G. 1984, ApJ, 286, 232
Lovas, F. J. 2004, J. Phys. Chem. Ref. Data, in press
Martin, A. H. M. 1972, MNRAS, 157, 31
Müller, H. S. P., Thorwirth, S., Roth, D. A., & Winnewisser, G. 2001, A&A, 370, L49
Nummelin, A., Bergman, P., Hjalmarson, Å., Friberg, P., Irvine, W. M., Millar, T. J., Ohishi, M., & Saito, S. 2000, ApJS, 128, 213
Pankonin, V., Churchwell, E., Watson, C., & Bieging, J. H. 2001, ApJ, 558, 194
Pickett, H. M., Poynter, R. L., Cohen, E. A., Delitsky, M. L., Pearson, J. C., & Müller H. S. P. 1998, J. Quant. Spectrosc. Radiat. Transfer, 60, 883
Press, W. H., Teukolsky, S. A., Vetterling, W. T., & Flannery, B. P. 1992, Numerical Recipes in FORTRAN 77: The Art of Scientific Computing (2nd ed.; Cambridge: Cambridge Univ. Press)
Remijan, A. J., Snyder, L. E., Liu, S.-Y., Mehringer, D. M., & Kuan, Y.-J. 2002, ApJ, 576, 264
Sault, R. J., Teuben, P. J., & Wright, M. C. H. 1995, in ASP Conf. Ser. 77, Astronomical Data Analysis Software and Systems IV, ed. R. A. Shaw, H. E. Payne, & J. J. E. Hayes (San Francisco: ASP), 433
Scott, P. F. 1978, MNRAS, 183, 435
Snyder, L. E., Lovas, F. J., Mehringer, D. M., Miao, N, Y., Kuan, Y.-J., Hollis, J. M., & Jewell, P. R. 2002, ApJ, 578, 245
Solomon, P. M., Jefferts, K. B., Penzias, A. A., & Wilson, R. W. 1971, ApJ, 168, L107
Sutton, E. C., Blake, G. A., Genzel, R., Masson, C. R., & Phillips, T. G. 1986, ApJ, 311, 921
Turner, B. E. 1991, ApJS, 76, 617
Wilner, D. J., Wright, M. C. H., & Plambeck, R. L. 1994, ApJ, 422, 642
Zhang, Q., Ho, P. T. P., & Ohashi, N. 1998, ApJ, 494, 636

Appendix E

A Survey of Large Molecules of Biological Interest Toward Selected High-Mass Star-Forming Regions

By

A. Remijan, Y.-S. Shiao, D. N. Friedel, D. S. Meier, & L. E. Snyder

2004 ApJ 617, 384

The Astrophysical Journal, 617:384–398, 2004 December 10

A SURVEY OF LARGE MOLECULES OF BIOLOGICAL INTEREST TOWARD SELECTED HIGH-MASS STAR-FORMING REGIONS

A. Remijan,[1,2,3] Y.-S. Shiao,[1] D. N. Friedel,[1] D. S. Meier,[1] and L. E. Snyder[1]
Received 2004 August 6; accepted 2004 August 20

ABSTRACT

We have surveyed the high-mass Galactic star-forming regions G19.61−0.23, G45.47+0.05, and W75N for interstellar methanol (CH_3OH), formic acid (HCOOH), acetic acid (CH_3COOH), methyl formate ($HCOOCH_3$), methyl cyanide (CH_3CN), and ethyl cyanide (CH_3CH_2CN) with the Berkeley-Illinois-Maryland Association Array. From our observations, we have detected two new sources of interstellar HCOOH toward the hot core regions G19.61−0.23 and W75N. We have also made the first detections of CH_3CH_2CN and $HCOOCH_3$ toward G19.61−0.23. The relative HCOOH/$HCOOCH_3$ abundance ratio toward G19.61−0.23 is 0.18, which is comparable to the abundance ratios found by Liu and colleagues toward Sgr B2(N-LMH), Orion, and W51 (∼0.10). We have made the first detection of $HCOOCH_3$ toward W75N. The relative HCOOH/$HCOOCH_3$ abundance ratio toward W75N is 0.26, which is more than twice as large as the abundance ratios found by Liu and colleagues. Furthermore, the hot core regions around W75N show a chemical differentiation between the O and N cores similar to what is seen toward the Orion Hot Core and Compact Ridge and W3(OH) and W3(H_2O). It is also apparent from our observations that the high-mass star-forming region G45.47+0.05 does not contain any compact hot molecular core (HMC), and as a consequence its chemistry may be similar to that of cold dark clouds. Finally, the formation of CH_3COOH appears to favor HMCs with well-mixed N and O, despite the fact that CH_3COOH does not contain a N atom. If proved to be true, this is an important constraint on CH_3COOH formation and possibly other structurally similar biomolecules.

Subject headings: ISM: abundances — ISM: individual (G19.61−0.23, G45.47+0.05, W75N) — ISM: molecules

1. INTRODUCTION

Recently, there has been great interest in searching a variety of star-forming regions (SFRs) for biologically interesting molecules (biomolecules), including formic acid (HCOOH) and acetic acid (CH_3COOH), because they share common structural elements with glycine (NH_2CH_2COOH), the simplest amino acid (Remijan et al. 2003; Liu et al. 2001, 2002). By measuring the abundance and distribution of these structurally similar species, we are helping to constrain the number of sources that may contain interstellar glycine. Furthermore, large molecules such as CH_3COOH and methyl formate ($HCOOCH_3$) may provide important clues to the formation chemistry of large biomolecules. CH_3COOH, $HCOOCH_3$, and glycolaldehyde (CH_2OHCHO) are all isomers. However, $HCOOCH_3$ and CH_3COOH are detectable in the high-mass SFRs W51e2, G34.3+0.24, and Sgr B2(N-LMH) and show a very compact (∼2–10 arcsec^2) distribution, while CH_2OHCHO has only been detected toward Sgr B2(N-LMH) and shows a distribution extended over 1′ (Hollis et al. 2001). The different distributions demonstrate that these isomers form in different ways. The question remains as to why CH_3COOH and $HCOOCH_3$ have such a different distribution compared to CH_2OHCHO despite their identical atoms and atomic composition. By further investigating the sources where large biomolecules may be found, a better understanding of the chemistry under which these species are formed can be achieved.

There have been a number of molecular line surveys using single-element radio telescopes over the last several years that have detected many large molecules in various SFRs (see, e.g., Nummelin et al. 2000; Ikeda et al. 2001; Gibb et al. 2000; Hatchell et al. 1998; Helmich & van Dishoeck 1997; Helmich et al. 1994). However, to date, the only interferometric detections of HCOOH and CH_3COOH have been toward high-mass (>10 $M_\odot$) SFRs (Remijan et al. 2002, 2003; Liu et al. 2001). Two features that identify regions of high-mass star formation are ultracompact (UC) H II regions and H_2O masers. Dense regions of hot molecular gas are often associated with these regions, and these "hot molecular cores" (HMCs) have typical molecular hydrogen densities of $n \sim 10^5$–10^7 cm^{-3} and temperatures of 100–200 K. It is toward these regions in and surrounding HMCs that the bulk of large biomolecules are found. Therefore, to extend our database of sources that contain large biomolecules, we carried out observations toward three high-mass SFRs with the Berkeley-Illinois-Maryland Association (BIMA) Array.[4] Because arrays typically have better angular resolution than single-element radio telescopes and have larger fields of view, they are more suitable for determining the detailed distributions of the various molecular emissions, including the sizes and positions of compact emission sources. For species with compact distributions, this property will also lead to higher intensity lines and larger beam-averaged column densities.

Remijan et al. (2003) carried out an extensive survey of CH_3COOH toward both high-mass and low-mass SFRs. As a result of their survey, they detected a new source of interstellar

[1] Department of Astronomy, University of Illinois, Urbana, IL 61801; aremijan@astro.uiuc.edu, shaw2@astro.uiuc.edu, friedel@astro.uiuc.edu, meierd@astro.uiuc.edu, snyder@astro.uiuc.edu.
[2] Current address: NASA Goddard Space Flight Center, Earth and Space Data Computing Division, Code 930, Greenbelt, MD 20771.
[3] National Research Council Resident Research Associate.

[4] Operated by the University of California, Berkeley, the University of Illinois, and the University of Maryland with support from the National Science Foundation.

TABLE 1
COMBINED MAP PARAMETERS

Source (1)	Gain Calibrator (2)	Beam (arcsec × arcsec) (3)	Frequency (GHz) (4)	Channel rms[a] (Jy beam^{-1}) (5)
G19.61−0.23	1733−130	4.5 × 1.9	111.5	0.05
		16.9 × 5.4	110.3	0.60
G45.47+0.05	1925+211	3.3 × 1.9	111.5	0.04
		9.3 × 5.8	110.3	0.10
W75N [b]	2025+337	2.7 × 2.2	110.3	0.07
	2013+370	4.4 × 3.7	111.5	0.06

[a] The stated channel rms is given for the window containing the transitions of AcA at 111.5 GHz or the CH_3CN transitions at 110.3 GHz.
[b] Data toward W75N at 110.3 GHz used with permission from C. Watson (2003 Oct 16).

CH_3COOH toward the high-mass HMC G34.3+0.2. Furthermore, that survey suggested HMCs that have a mass range between 200 and 2000 $M_\odot$ and do not show differentiation between O and N chemistries are sources of interstellar CH_3COOH. In addition, the three known CH_3COOH sources are within 7 kpc of the Galactic center. Therefore, it appears galactocentric distance could be a factor in the abundance of CH_3COOH. Finally, Remijan et al. (2004) found that methyl cyanide (CH_3CN) is a better tracer of the large molecules ethyl cyanide (CH_3CH_2CN) and CH_3COOH than is $HCOOCH_3$ toward the HMCs W51 e1 and e2. In order to investigate these hypotheses, we observed CH_3CN, CH_3CH_2CN, methanol (CH_3OH), HCOOH, CH_3COOH, and $HCOOCH_3$ toward a sample of massive SFRs selected based on the above criteria.

2. OBSERVATIONS

The large molecule survey took place from 1999 October to 2003 November utilizing the B and C configurations of the BIMA Array. The minimum baseline for these observations was ~8 m, and the maximum baseline was ~150 m, providing angular resolutions of ~2″–13″. Table 1 lists the parameters of the combined data sets of our survey.[5] To include all the data from a source with multiple tracks or in multiple arrays, the data were inverted in *u-v* space. The resulting synthesized beam size was determined by the region of heaviest *u-v* coverage. Column (1) lists the sources observed. Column (2) lists the sources used to calibrate the antenna-based gains. Saturn and Uranus were used as the flux density calibrators for these observations. The absolute amplitude calibration of these sources is accurate to within ~20%. Column (3) lists the corresponding beam size, column (4) lists the rest frequency of each observation, and column (5) lists the approximate 1 σ channel rms noise level in the CH_3COOH or CH_3CN windows of the combined data sets. The passbands were calibrated automatically during data acquisition.[6] In the past, this method has been quite satisfactory and has not generated spurious features. In § 2.1 we describe the sources included in our large biomolecule survey.

Table 2 lists the molecular parameters of all the 41 observed transitions in our survey. Column (1) lists the species; column (2) lists the transition. Column (3) lists the calculated rest frequency and its 2 σ standard deviation. Column (4) lists the product of the line strength and the square of the relevant dipole moment; column (5) lists the upper state energy level of each transition. The estimated rotational partition functions are given in the footnotes. Each correlator configuration included the full *K* structure of CH_3CN, the two strongest ($10_{*,10}$–$9_{*,9}$ A and E) CH_3COOH transitions near 111.5 GHz, a HCOOH transition at 108 GHz, and several strong transitions of $HCOOCH_3$ and CH_3CH_2CN. The spectral windows containing these transitions had a bandwidth of 50 MHz and were divided into 128 channels for a spectral resolution of 0.39 MHz per channel. All data were combined, imaged, and self-calibrated using the MIRIAD software package (Sault et al. 1995). The 1 σ rms noise level of the final maps was used to set upper limits to the column densities of the undetected molecular species searched for in our survey.

2.1. *Sources*

Table 3 lists the three sources surveyed for CH_3CN, CH_3CH_2CN, CH_3OH, HCOOH, CH_3COOH, and $HCOOCH_3$ in column (1). Columns (2) and (3) list the pointing center for each observation. Columns (4) and (5) list the distance to each source from the Sun and from the Galactic center (galactocentric),[7] respectively. Finally, column (6) lists the mass of each SFR, and column (7) lists the systemic local standard of rest velocity (v_{LSR}). Each source was selected based on the conclusions of Remijan et al. (2003) that regions containing detectable amounts of the large biomolecule CH_3COOH are HMCs (1) between 200 and 2000 $M_\odot$, (2) within 7 kpc of the Galactic center, and (3) that are not known to show chemical differentiation between O and N chemistry. We discuss each source in detail below.

2.1.1. *G19.61−0.23*

G19.61−0.23 ($\alpha = 18^h27^m38\overset{s}{.}1$, $\delta = -11°56'39''$ [J2000.0]) is a well-studied high-mass SFR. Some of the earliest observations of G19.61−0.23 were performed by Matthews et al. (1977) as they identified radio continuum emission toward regions containing OH maser sources. They interpreted the large amount of extended structure as containing several H II regions. This region has been extensively studied for OH masers (Garay et al. 1985; Forster & Caswell 1989), H_2O masers (Forster &

[5] For a complete description of the observations taken between 1999 October and 2000 April toward W75N, see Watson et al. (2002).
[6] A technical description of this can be found at http://astron.berkeley.edu/~plambeck/technical.html.
[7] For a description of how galactocentric distance was determined, see Remijan et al. (2003).

TABLE 2

MOLECULAR LINE PARAMETERS

Species (1)	Transition (2)	Frequency[a] (MHz) (3)	$\langle S_{i,j}\mu^2 \rangle$ (debye^2) (4)	E_u (K) (5)
CH_3CN[b]	6(5)–5(5)	110,329.608 ± 120	28.1	196.3
	6(4)–5(4)	110,349.760 ± 200	51.0	132.3
	6(3)–5(3)	110,364.470 ± 100	68.9	82.6
	6(2)–5(2)	110,374.986 ± 120	81.6	47.0
	6(1)–5(1)	110,381.376 ± 120	89.3	25.7
	6(0)–5(0)	110,383.494 ± 120	91.9	18.6
$CH_3^{13}CN$[b]	6(3)–5(3)	110,309.847 ± 10	68.9	83.0
	6(2)–5(2)	110,320.438 ± 10	81.6	47.2
	6(1)–5(1)	110,326.795 ± 10	89.3	25.7
	6(0)–5(0)	110,328.914 ± 10	91.9	18.5
CH_3OH[c]	3(1)–4(0) A^+	107,013.850 ± 100	3.0	28.4
	15(−2)–15(1) E2	107,159.790 ± 100	2.6	305.0
CH_3OD[d]	3(1)–3(0) E1	110,475.760 ± 1826	3.8	22.2
	4(1)–4(0) E1	110,950.750 ± 2382	5.1	30.8
CH_3COOH[e]	$10_{*,10}-9_{*,9}$ E	111,507.270 ± 40	54.8	30.5
	$10_{*,10}-9_{*,9}$ A	111,548.533 ± 40	54.8	30.5
CH_3CH_2CN[f]	$17_{2,16}-17_{1,17}$	107,481.468 ± 46	91.5	70.0
	$12_{7,6}-11_{7,5}$	107,485.178 ± 26	117.3	88.1
	$12_{7,5}-11_{7,4}$	107,485.178 ± 26	117.3	88.1
	$12_{6,7}-11_{6,6}$	107,486.961 ± 26	133.4	73.6
	$12_{6,6}-11_{6,5}$	107,486.962 ± 26	133.4	73.6
	$12_{8,5}-11_{8,4}$	107,491.573 ± 28	98.8	104.7
	$12_{8,4}-11_{8,3}$	107,491.573 ± 28	98.8	104.7
	$12_{5,8}-11_{5,7}$	107,502.426 ± 26	147.0	61.4
	$12_{5,7}-11_{5,6}$	107,502.474 ± 26	147.0	61.4
	$12_{4,9}-11_{4,8}$	107,543.926 ± 26	158.1	51.4
	$12_{4,8}-11_{4,7}$	107,547.601 ± 26	158.1	51.4
	$12_{3,10}-11_{3,9}$	107,594.049 ± 28	166.8	43.6
HCOOH[g]	$5_{1,5}-4_{1,4}$	108,126.710 ± 160	9.3	18.8
$HCOOCH_3$[h]	$9_{2,8}-8_{2,7}$ E	107,537.189 ± 24	22.8	28.8
	$9_{2,8}-8_{2,7}$ A	107,543.746 ± 26	22.8	28.8
	$9_{8,2}-8_{8,1}$ A	110,455.358 ± 30	69.1	5.1
	$9_{8,1}-8_{8,0}$ A	110,455.358 ± 30	69.1	5.1
	$9_{8,2}-8_{8,1}$ E	110,457.971 ± 28	69.1	5.1
	$9_{7,2}-8_{7,1}$ E	110,525.598 ± 32	59.2	9.6
	$9_{7,3}-8_{7,2}$ A	110,535.182 ± 28	59.2	9.6
	$9_{7,2}-8_{7,1}$ A	110,535.184 ± 28	59.2	9.6
	$9_{7,3}-8_{7,2}$ E	110,535.955 ± 26	59.2	9.6
	$7_{2,6}-6_{1,5}$ E	110,550.217 ± 28	1.4	19.0
	$7_{2,6}-6_{1,5}$ A	110,560.053 ± 30	1.4	19.0
	$9_{4,5}-8_{4,4}$ A	111,453.327 ± 24	19.4	37.3

[a] Errors are 2 σ.
[b] Boucher et al. (1980); $Q_{\rm rot} = 0.98T_{\rm rot}^{3/2}$.
[c] Xu & Lovas (1997); $Q_{\rm rot} = 1.23T_{\rm rot}^{3/2}$.
[d] Anderson et al. (1988); $Q_{\rm rot} = 0.71T_{\rm rot}^{3/2}$.
[e] Ilyushin et al. (2001); $Q_{\rm rot} = 14.10T_{\rm rot}^{3/2}$.
[f] Lovas (1982); $Q_{\rm rot} = 7.17T_{\rm rot}^{3/2}$.
[g] Willemot et al. (1980); $Q_{\rm rot} = 1.71T_{\rm rot}^{3/2}$.
[h] Oesterling et al. (1999); $Q_{\rm rot} = 12.45T_{\rm rot}^{3/2}$.

Caswell 1989; Comoretto et al. 1990; Hofner & Churchwell 1996), and CH_3OH masers (Kalenskii et al. 1994; Larionov et al. 1999). Recently, one of the most extensive studies of the structure and molecular environments of the G19.61−0.23 region was performed by Garay et al. (1998). Using high-resolution (2″–3″) Very Large Array[8] observations, they mapped the ionized gas of this region using the H66α recombination line and the 1.6 GHz continuum, as well as the molecular gas using the (2, 2) inversion transition of NH_3. The ionized gas observations indicated at least five distinct H II regions, implying the presence of an OB association. The NH_3 observations showed molecular emission from three distinct clumps, one of which lies very near the center of the cluster of H II regions (Garay et al. 1998). Since these observations, the G19.61−0.23 region has been observed in other molecular species such as CS (Shirley et al. 2003; Wu & Evans 2003; Larionov et al. 1999), HCN (Wu & Evans 2003), and CO (Hofner et al. 2000). However, the largest molecular species observed toward this region is methyl acetylene (CH_3C_2H; Fontani

[8] The VLA is operated by the National Radio Astronomy Observatory, which is a facility of the National Science Foundation, operated under cooperative agreement by Associated Universities, Inc.

TABLE 3

HOT CORES AND THEIR PHYSICAL PARAMETERS

Source Name (1)	R.A. (J2000.0) (2)	Decl. (J2000.0) (3)	Distance (kpc) (4)	Galactocentric[a] (kpc) (5)	Mass ($M_\odot$) (6)	v_{LSR} (km s^{-1}) (7)
G19.61−0.23[b]	18 27 38.1	−11 56 39	3.5	4.8	450	40
G45.47+0.05[b]	19 14 25.6	11 09 26	8.3	6.3	250	62
W75N	20 38 36.6	42 37 32	2.0[c]	8.0	∼440[d]	10

NOTE.—Units of right ascension are hours, minutes, and seconds, and units of declination are degrees, arcminutes, and arcseconds.

[a] Galactocentric distance was determined using the procedure outlined in Remijan et al. (2003).

[b] Kurtz et al. (2000).

[c] Hunter et al. (1994).

[d] Watson et al. (2002).

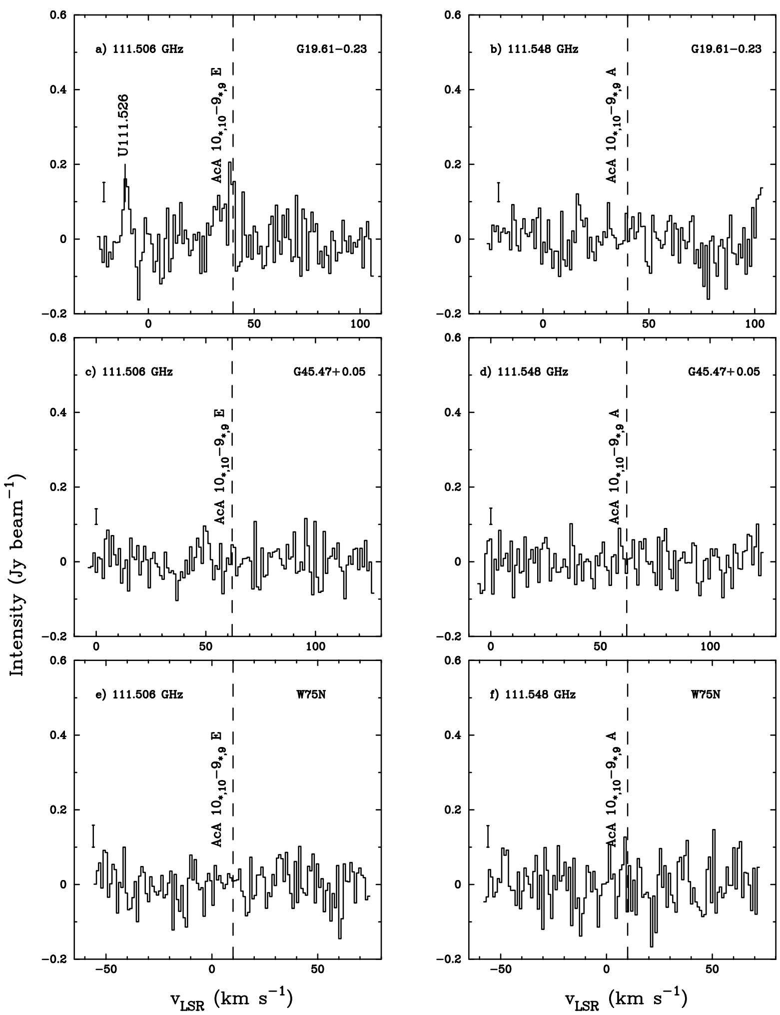

FIG. 1.—(*a*, *b*) Acetic acid (CH_3COOH, marked AcA) survey lines toward G19.61−0.23. The noise level is ∼60 mJy beam^{-1} (indicated by the vertical bar at the left of each panel). The spectral line labels correspond to the rest frequency located at the top left of each panel for a v_{LSR} of 40 km s^{-1} (*dashed line*). (*c*, *d*) Same as (*a*, *b*) except toward G45.47+0.05; rms ∼40 mJy beam^{-1}; v_{LSR} = 62 km s^{-1}. (*e*, *f*) Same as (*a*, *b*) except toward W75N; rms ∼50 mJy beam^{-1}; v_{LSR} = 10 km s^{-1}.

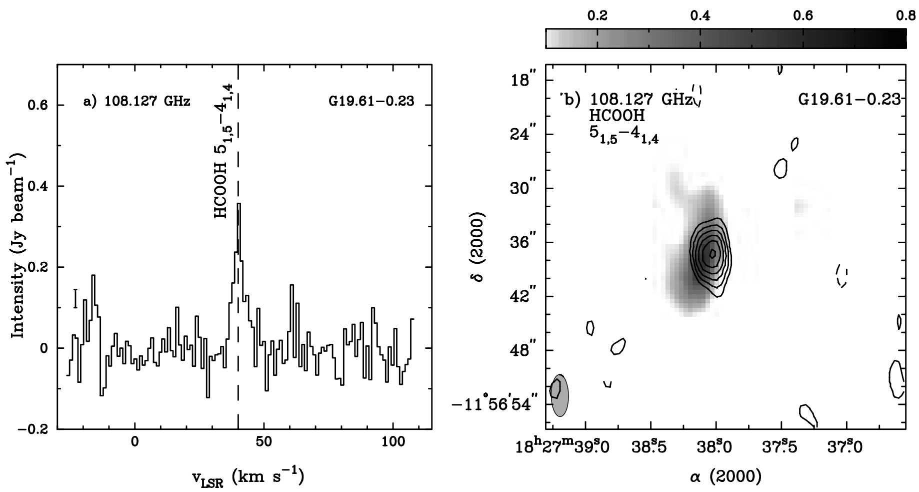

FIG. 2.—(*a*) HCOOH spectrum toward G19.61−0.23. The noise level is ∼40 mJy beam^{-1} (indicated by the vertical bar at the left of the spectrum). The spectral line label corresponds to the rest frequency located at the top left of the panel for a v_{LSR} of 40 km s^{-1} (*dashed line*). (*b*) Emission contours from the $5_{1,5}-4_{1,4}$ transition of HCOOH at 108.127 GHz overlaid on the G19.61−0.23 continuum emission at 108.1 GHz (*gray scale*). The numbers on the gray scale wedge are in units of Jy beam^{-1}. Contours indicate the location of the HCOOH emission near its peak at 40 km s^{-1}. The contour levels are −0.10, 0.10, 0.15, 0.20, 0.25, 0.30, and 0.35 Jy beam^{-1}. The synthesized beam of 5″.5 × 2″.9 is indicated at the bottom left corner.

et al. 2002) with the IRAM 30 m and FCRAO 14 m radio telescopes. Using an angular size of 30″ measured by Hofner et al. (2000) from $C^{17}O$ emission, Fontani et al. (2002) measured a rotational temperature of $T_{rot} = 56 \pm 7$ K and a total CH_3C_2H source-averaged column density of $N_{tot} = (1.1 \pm 3) \times 10^{15}$ cm^{-2}. They concluded from the rotation temperature diagram of the G19.61−0.23 region that the molecular gas was very close to LTE, and thus the measured rotational temperature is a good estimate of the kinetic temperature of the molecular gas. However, this region has never been surveyed at high resolution for large nitrogen-bearing species such as CH_3CH_2CN or oxygen-bearing molecules such as $HCOOCH_3$ and CH_3COOH. Therefore, our observations not only further constrain the detectability of CH_3COOH toward high-mass HMCs but also obtain information on the N and O chemistry present toward G19.61−0.23.

2.1.2. *G45.47+0.05*

G45.47+0.05 ($\alpha = 19^h14^m25^s.6$, $\delta = 11°09′26″$ [J2000.0]) is a high-mass SFR that has been extensively studied for OH masers (Matthews et al. 1977; Forster & Caswell 1989), H_2O masers (Forster & Caswell 1989; Churchwell et al. 1990), and CH_3OH masers (Zheng & Ling 1997; Larionov et al. 1999). Churchwell et al. (1992) searched this region for emission from CS, ^{13}CO, and CH_3CN. Using an excitation temperature of 100 K, they derived a total ^{13}CO column density of $N_{tot} = 3.6 \times 10^{17}$ cm^{-2} and a CS column density of $N_{tot} = 1.3 \times 10^{13}$ cm^{-2}. Initially, CH_3CN was not detected in this region. However, Olmi et al. (1993) conducted a survey of NH_3 and CH_3CN using the IRAM 30 m radio telescope. From their observations, they were able to construct rotational temperature diagrams (RTDs) and measured an approximate kinetic temperature of $T_k = 44 \pm 1$ K and a total CH_3CN beam-averaged column density of $N_{tot} = (2.5 \pm 5) \times 10^{13}$ cm^{-2}. For NH_3, they measured a rotational temperature of $T_{rot} = 39$ K and a total NH_3 beam-averaged column density of $N_{tot} = 4.4 \times 10^{14}$ cm^{-2}. One of the most extensive molecular line surveys done toward this source was performed by Hatchell et al. (1998) using the James Clerk Maxwell Radio Telescope. Their survey included lines of $C^{17}O$, SO, SO_2, CH_3OH, $^{13}CH_3OH$, CH_3CCH, CH_3CN, CH_3CH_2CN, CH_3OCH_3, $HCOOCH_3$, HC_3N, OCS, and CCH. From their survey, they detected lines of CH_3CN, CH_3C_2H, CH_3OH, $C^{17}O$, CO, and CCH and possibly $HCOOCH_3$ and HC_3N. However, they concluded from their survey that the hot core region toward G45.47+0.05 must be very small (<1″) or low in density (<10^8 cm^{-3}). Most recently, Fontani et al. (2002) observed transitions of CH_3C_2H and measured a source size of 35″ ± 8″ and from that, a rotational temperature of $T_{rot} = 39 \pm 7$ K and a total source-averaged CH_3C_2H column density of $N_{tot} = (5.0 \pm 3) \times 10^{14}$ cm^{-2}. Our observations investigated this region at high resolution (<10 arcsec^2) for large, biologically interesting molecules including HCOOH and CH_3COOH, in an attempt to detect any molecular emission associated with a compact HMC.

2.1.3. *W75N*

W75N ($\alpha = 20^h38^m36^s.6$, $\delta = 42°37′32″$ [J2000.0]) is a massive SFR containing several UC H II regions that has been a target of many surveys since its detection by Westerhout (1958). Primarily, this region has been extensively studied for OH masers (e.g., Palmer et al. 2003, 2004; Gasiprong et al. 2002), H_2O masers (e.g., Valdetto et al. 2002; Lekht & Krasnov 2000; Torelles et al. 1997), CH_3OH masers (Voronkov et al. 2002; Lekht et al. 2002; Minier et al. 2001), and H_2CO masers (Mehringer et al. 1995). There have been very few surveys of this source for large molecules. The most recent was performed by Kalenskii et al. (2002). In that survey, they searched for thermal CH_3OH lines as well as lines of CH_3CN, HC_3N, $HCOOCH_3$, and SO_2 with the IRAM 30 m radio telescope. They successfully detected the CH_3OH transitions but no emission from any of the other molecular species. However, Pankonin et al. (2001) successfully detected emission from CH_3CN using the Heinrich Hertz Telescope. From their observations, they measured a rotational temperature $T_{rot} = 135 \pm 33$ K and a total CH_3CN beam-averaged column density of $N_{tot} = (2.3 \pm 3) \times 10^{14}$ cm^{-2} within the 35″ beam. More recently, Watson et al. (2002) followed up the observations of Pankonin et al. (2001) toward W75N using the BIMA Array. They concluded that the CH_3CN emission coming

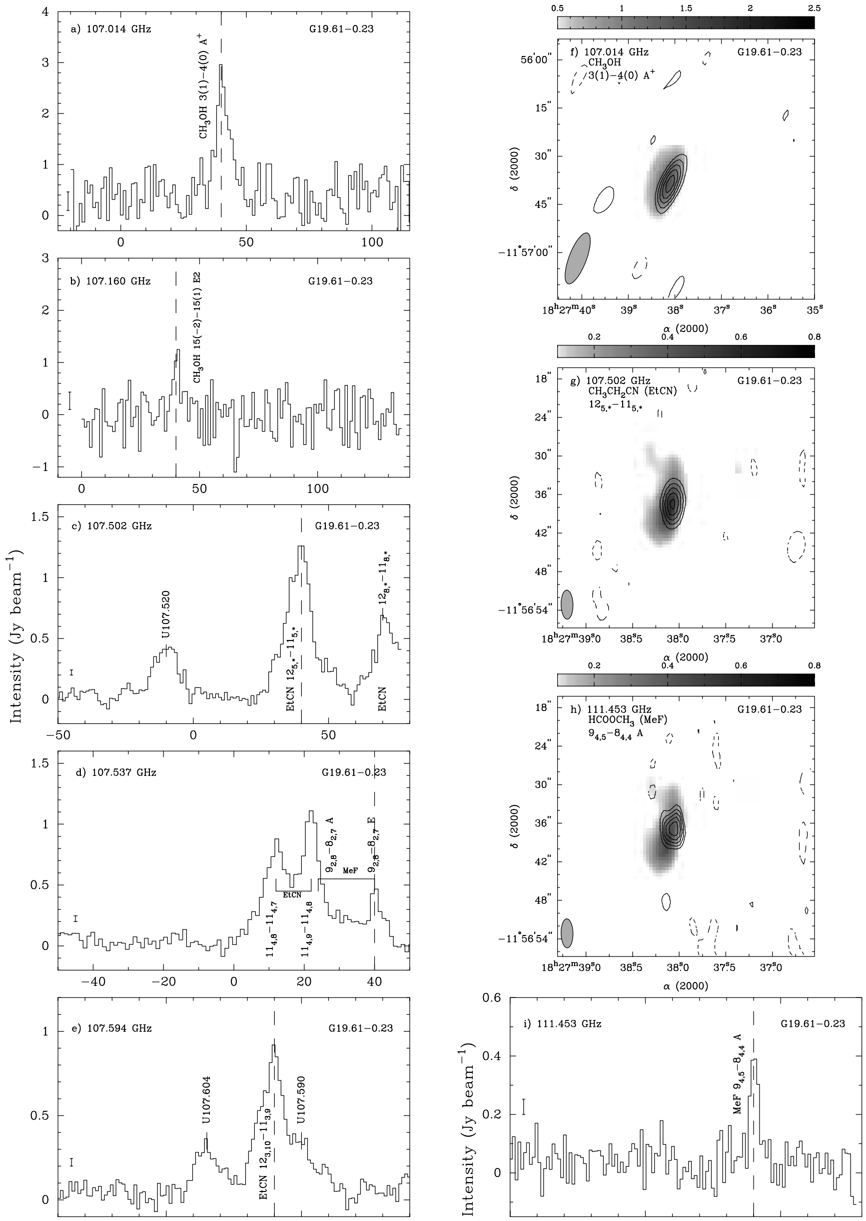

FIG. 3.—(*a–e*) Spectrum taken toward G19.61−0.23 showing several detections of CH_3OH, CH_3CH_2CN (EtCN), and $HCOOCH_3$ (MeF). The rms noise level is indicated by the vertical bar at the left of the spectrum. The spectral line labels correspond to the rest frequency located at the top left of each panel for a v_{LSR} of 40 km s^{-1} (*dashed line*). (*f*) Emission contours from the 3(1)−4(0) A^+ transition of CH_3OH at 107.014 GHz at the emission peak of 40 km s^{-1} overlaid on the G19.61−0.23 continuum emission at 107.0 GHz (*gray scale*). The numbers on the gray scale wedge are in units of Jy $beam^{-1}$. The CH_3OH contour levels are −0.10, 0.10, 0.15, 0.20, 0.25, 0.30, and 0.35 Jy $beam^{-1}$. The synthesized beam of $16''.9 \times 5''.5$ is indicated at the bottom left corner. (*g*) Emission contours from the $12_{5,*}-11_{5,*}$ transition of CH_3CH_2CN at 107.502 GHz at the emission peak of 40 km s^{-1} overlaid on the G19.61−0.23 continuum emission at 107.5 GHz (*gray scale*). The CH_3CH_2CN contour levels are −0.1, 0.4, 0.6, 0.8, 1.0, and 1.2 Jy $beam^{-1}$. The synthesized beam of $4''.7 \times 1''.9$ is indicated at the bottom left corner. (*h*) Emission contours from the $9_{4,5}-8_{4,4}$ A transition of $HCOOCH_3$ at 111.453 GHz at the emission peak of 40 km s^{-1} overlaid on the G19.61−0.23 continuum emission at 111.5 GHz (*gray scale*). The $HCOOCH_3$ contour levels are −0.10, 0.15, 0.20, 0.25, 0.30, and 0.35 Jy $beam^{-1}$. The synthesized beam of $4''.7 \times 1''.9$ is indicated at the bottom left corner. (*i*) Spectrum showing the 111.453 GHz transition of $HCOOCH_3$. The labels are the same as in (*a*).

from the hot core region was optically thick and that corrections needed to be made in order to more accurately determine T_{rot} and N_{tot}. Remijan et al. (2004) made an extensive study of CH_3CN toward the hot core regions W51 e1 and e2. In that analysis, they corrected for optical depth, and the results from the RTD analysis closely matched the statistical equilibrium analysis. Furthermore, they found CH_3CN is a good tracer of large hard-to-detect species such as CH_3COOH. In this analysis, we reexamined the CH_3CN data from Watson et al. (2002) and investigated how well CH_3CN traces larger molecular species.

3. RESULTS

The three sources in Table 3 were surveyed for CH_3COOH, as well as the selected transitions of other large molecular species listed in Table 2. Figure 1 summarizes the CH_3COOH (acetic acid [AcA]) survey toward each region. The spectral line labels located at the upper left of each panel correspond to the rest frequency for the v_{LSR} of each source (40 km s^{-1} for G19.61−0.23, 62 km s^{-1} for G45.47+0.05, and 10 km s^{-1} for W75N). The 1 σ noise level is shown at the left of each spectrum. No new sources of CH_3COOH were detected. We did make the first detections of HCOOH, $HCOOCH_3$, and CH_3CH_2CN toward G19.61−0.23 and HCOOH and $HCOOCH_3$ toward W75N. Finally, we detected CH_3CN emission from all the sources and were able to measure the column density of the detected molecular species and, based on the 1 σ detection limit, place upper limits on the species that were not detected. In § 3.1, we discuss the spectral lines detected toward G19.61−0.23. In §§ 3.2 and 3.3, we discuss the spectral lines detected toward G45.47+0.05 and W75N, respectively.

3.1. *G19.61−0.23*

Figure 2*a* shows the first detection of HCOOH toward G19.61−0.23. The spectral line label located in the upper left of Figure 2*a* corresponds to the rest frequency for a v_{LSR} of 40 km s^{-1}. The 1 σ noise level is shown at the left of the spectral window. Figure 2*b* shows the map of the $5_{1,5}$–$4_{1,4}$ transition of formic acid (*contours*) on top of the 108.1 GHz continuum emission (*gray scale*). Note that the emission peak of HCOOH is offset from the continuum emission. The offset in emission peaks is significant, given the size of the synthesized beam (shown at the bottom left of Fig. 2*b*). Figure 3 shows the detection and distribution of several large molecular species toward the G19.61−0.23 region, including CH_3OH, CH_3CH_2CN (EtCN), and $HCOOCH_3$ (MeF). Figures 3*a* and 3*b* show the detection of CH_3OH at 107.014 and 107.160 GHz, respectively. The spectral line labels are similar to those of Figure 2*a*. Figure 3*f* shows the distribution of the 107.014 GHz CH_3OH emission (*contours*) on the 3 mm continuum emission (*gray scale*) toward G19.61−0.23. Figures 3*c*–3*e* show the detections of several transitions of CH_3CH_2CN. Figure 3*g* shows the distribution of the 107.502 GHz CH_3CH_2CN emission. Finally, Figures 3*d* and 3*i* show the detections of three transitions of $HCOOCH_3$. Figure 3*h* shows the distribution of the 111.453 GHz $HCOOCH_3$ emission. Figure 4 shows the detection and distribution of CH_3CN toward the G19.61−0.23 region. In Figure 4*f* we show the predicted locations of the $J = 6$–5, $K = 0$, 1, 2 and 3 $CH_3^{13}CN$ emission lines. While the $K = 3$ line is clearly seen near v_{LSR} of 148 km s^{-1}, the lower *K*-value transitions are not as clearly seen. However, we note that as much as 50% of the emission from the $K = 5$ CH_3CN line may be due to the $K = 0$ and 1 $CH_3^{13}CN$ lines. Higher signal-to-noise ratio observations are needed to confirm the amount of contamination from $CH_3^{13}CN$. The peak positions of CH_3CN, CH_3OH, HCOOH, CH_3CH_2CN, and $HCOOCH_3$ agree, strongly indicating that all the molecular emission is coming from a common source. Table 4 lists the molecular species that were detected toward G19.61−0.23 at or near the systemic velocity (40 km s^{-1}). Least-squares Gaussian fits were made for each spectral line in order to obtain the radial velocities and integrated line intensities for the detected transitions. In Table 4, column (1) lists either the calculated rest frequencies of previously identified species or the observed frequencies of unidentified transitions. Columns (2) and (3) list the molecular species and associated transitions, respectively. Finally, column (4) lists the fitted integrated line intensity of each detected transition.

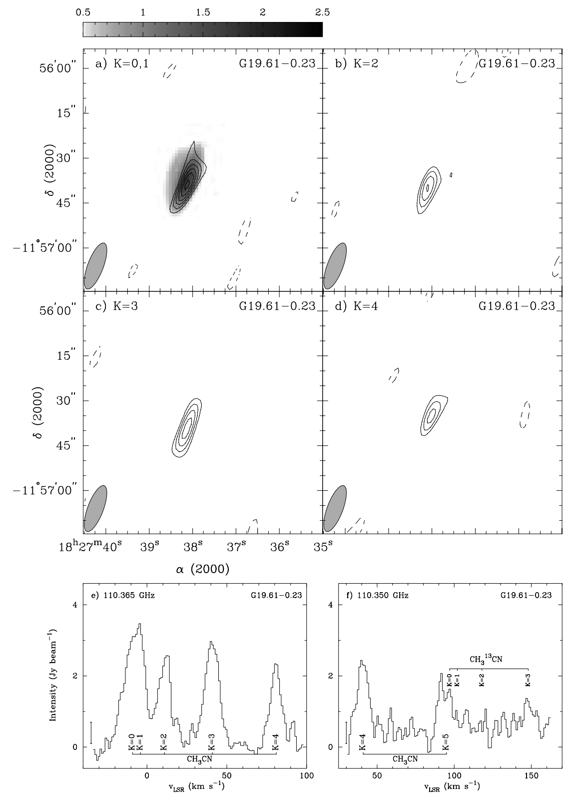

FIG. 4.—(*a*–*d*) Averaged intensity maps of the $J = 6$−5 CH_3CN emission lines. The gray scale in (*a*) is for the 110.4 GHz continuum of the G19.61−0.23 region. The numbers on the gray scale wedge are in units of Jy $beam^{-1}$. In each panel, the given *K*-ladder transition taken at the peak velocity of the line is mapped in contours. The contour levels are −1.0, 1.5, 2.0, 2.5, 3.0, 3.5, and 4.0 Jy $beam^{-1}$. The synthesized beam of 16″.4 × 5″.3 is indicated at the bottom left of each panel. (*e*) CH_3CN spectrum taken toward the G19.61−0.23 region. The rest frequency located in the top left corner corresponds to the $K = 3$ component for a v_{LSR} of 40 km s^{-1}. The noise level is ∼0.6 Jy $beam^{-1}$ (indicated by the vertical bar at the left of the spectrum). (*f*) Same as (*e*) except the rest frequency corresponds to the $K = 4$ component. Also shown are the predicted locations of the $J = 6$−5, $K = 0$, 1, 2, and 3 $CH_3^{13}CN$ emission lines. The $K = 3$ line is clearly seen near v_{LSR} of 148 km s^{-1}.

3.2. *G45.47+0.05*

Figure 5 shows the results of our survey toward G45.47+0.05. Of the seven molecular species searched for, we only

TABLE 4

G19.61−0.23 Molecular Line Identifications

Frequency[a] (MHz) (1)	Species (2)	Transition (3)	$\int \Delta I\, dv$[b] (Jy beam^{-1} km s^{-1}) (4)
107,013.850 ± 100	CH_3OH	3(1)–4(0) A^+	24.1 ± 3.9
107,159.790 ± 100	CH_3OH	15(−2)–15(1) E2	4.5 ± 1.7
107,491.573 ± 28	EtCN[c]	$12_{8,*}-11_{8,*}$	7.8 ± 6
107,502.426 ± 26	EtCN	$12_{5,*}-11_{5,*}$	14.7 ± 8
107,520.0	U107.520		5.3 ± 5
107,537.189 ± 24	MeF[d]	$9_{2,8}-8_{2,7}$ E	3.1 ± 3
107,543.746 ± 26	MeF	$9_{2,8}-8_{2,7}$ A	3.1 ± 1.0[e]
107,543.926 ± 26	EtCN	$12_{4,9}-11_{4,8}$	5.5 ± 1.0[e]
107,547.601 ± 26	EtCN	$12_{4,8}-11_{4,7}$	6.6 ± 4
107,590.0	U107.590		3.2 ± 5[e]
107,594.049 ± 28	EtCN	$12_{3,10}-11_{3,9}$	10.0 ± 6[e]
107,604.0	U107.604		3.9 ± 4
108,126.710 ± 160	HCOOH	$5_{1,5}-4_{1,4}$	1.5 ± 3
110,309.847 ± 10	$CH_3^{13}CN$	6(3)–5(3)	13.1 ± 3.0
110,329.608 ± 120	CH_3CN	6(5)–5(5)	16.3 ± 2.1[e]
110,349.760 ± 200	CH_3CN	6(4)–5(4)	22.5 ± 2.0
110,364.470 ± 100	CH_3CN	6(3)–5(3)	33.8 ± 2.3
110,374.986 ± 120	CH_3CN	6(2)–5(2)	26.4 ± 2.1
110,381.376 ± 120	CH_3CN	6(1)–5(1)	23.8 ± 3.0[e]
110,383.494 ± 120	CH_3CN	6(0)–5(0)	25.8 ± 3.0[e]
111,453.327 ± 24	MeF	$9_{4,5}-8_{4,4}$ A	1.8 ± 3
111,526.0	U111.526		0.5 ± 2

[a] Errors are 2 σ.
[b] Errors are 1 σ.
[c] EtCN = ethyl cyanide (CH_3CH_2CN).
[d] MeF = methyl formate ($HCOOCH_3$).
[e] Blended line.

detected emission from one transition of CH_3OH and four transitions of CH_3CN. Figure 5*a* shows the detection of the 3(1)–4(0) A^+ transition of CH_3OH toward G45.47+0.05. The spectral line label located in the upper left of Figure 5*a* corresponds to the rest frequency for a v_{LSR} of 62 km s^{-1}. The 1 σ noise level is shown at the left of the spectral window. Figure 5*b* shows the map of the 3(1)–4(0) A^+ transition of CH_3OH (*contours*) on top of the 107.0 GHz continuum emission (*gray scale*). In this case, significant differences between the continuum peak and the CH_3OH emission peak are not seen. Figures 5*c*–5*f* show the average intensity maps and spectrum of the four detected transitions of the $J = 6-5$ CH_3CN emission lines. Once again, no offsets are seen between the CH_3CN emission peak and the 110.5 GHz continuum peak. However, from Figure 5*c* there appears to be at least two additional emission peaks of CH_3CN, one to the southeast and one to the northwest. The peaks also appear in the $K = 1$ window; however, we also see emission coming from the southwest. In the $K = 3$ window, only the CH_3CN emission peak near the continuum is present. From the fitting routine to measure source sizes (§ 4.1), we found that this region may contain several molecular cores. Higher signal-to-noise ratio observations are necessary to identify the number of individual cores toward this region. Table 5 lists the molecular species that were detected toward G45.47+0.05 at or near the systemic velocity (62 km s^{-1}). The column labels are the same as in Table 4.

3.3. *W75N*

Figure 6 shows the first detections of $HCOOCH_3$ and HCOOH toward W75N. Figure 6*a* shows the detection of the $9_{2,8}-8_{2,7}$ A and E transitions of $HCOOCH_3$ near 107.5 GHz. The spectral line labels correspond to the rest frequency located at the upper left of the panel for a v_{LSR} of 10 km s^{-1}. The 1 σ noise level is shown at the left of the spectrum. Figure 6*b* shows the map of the $9_{2,8}-8_{2,7}$ E transition of $HCOOCH_3$ (*contours*) on top of the 107.5 GHz continuum emission (*gray scale*). Note that the emission peak of $HCOOCH_3$ is offset from the continuum emission. The offset in emission peaks is significant, given the size of the synthesized beam (seen at the bottom left of Fig. 6*b*). Figure 6*c* shows the detection of the $5_{1,5}-4_{1,4}$ transition of HCOOH at 108.1 GHz. This is the first time any large oxygen-bearing molecule has been detected toward W75N. Furthermore, we do not detect any large nitrogen-bearing molecules, such as CH_3CH_2CN, in this region. Figure 7 shows the average intensity maps and spectrum of the $J = 6-5$ CH_3CN emission lines. From these maps, we see the CH_3CN emission is extended beyond the 2.″7 × 2.″2 synthesized beam (*shown at the bottom left of each panel*) but peaks near the continuum. The peaks of the emission contours of CH_3CN and $HCOOCH_3$ are offset by ∼2.″7, indicating that the molecular emission is coming from at least two distinct sources. Table 6 lists the molecular species that were detected toward W75N at or near the systemic velocity (10 km s^{-1}). The column labels are the same as in Table 4.

4. DISCUSSION

4.1. *Rotational Temperature Diagrams of* CH_3CN

One of the most difficult factors to determine is the column densities of large biomolecules in the interstellar medium. By measuring the column densities of biomolecules in many different regions with various physical conditions, we can get a

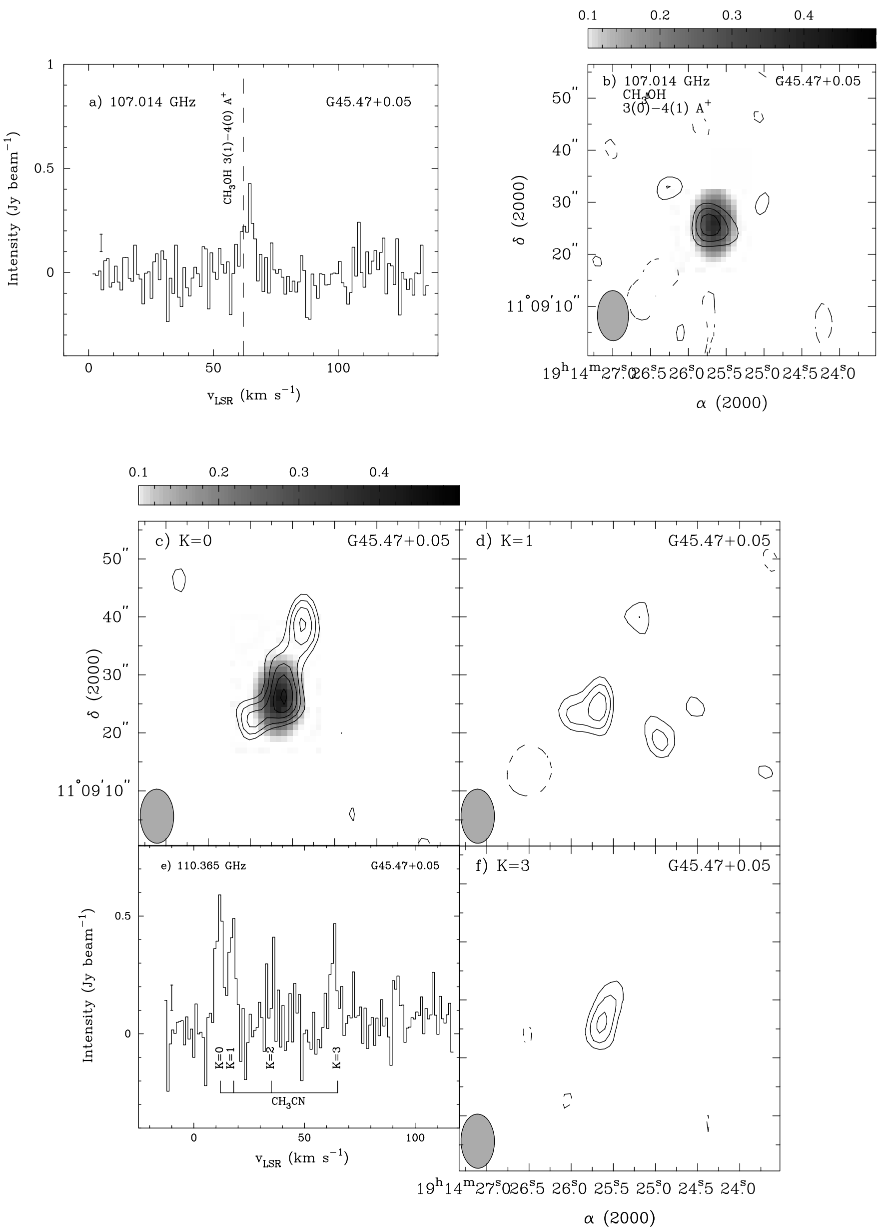

FIG. 5.—(*a*) CH_3OH spectrum toward G45.47+0.05. The noise level is ~84 mJy beam^{-1} (indicated by the vertical bar at the left of the spectrum). The spectral line label corresponds to the rest frequency located at the top left of the panel for a v_{LSR} of 62 km s^{-1} (*dashed line*). (*b*) Emission contours from the 3(1)–4(0) A$^+$ transition of CH_3OH at 107.014 GHz overlaid on the G45.47+0.05 continuum emission at 107.0 GHz (*gray scale*). The numbers on the gray scale wedge are in units of Jy beam^{-1}. Contours indicate the location of the CH_3OH emission near its peak at 65 km s^{-1}. The contour levels are −0.15, 0.225, 0.30, 0.375, 0.45, and 0.525 Jy beam^{-1}. The synthesized beam of 9″.6 × 6″.1 is indicated at the bottom left corner. (*c*–*f*) Averaged intensity maps and spectrum of the $J = 6-5$ CH_3CN emission lines. The gray scale in (*c*) is for the 110.4 GHz continuum of the G45.47+0.05 region. The numbers on the gray scale wedge are in units of Jy beam^{-1}. In each panel, the given *K*-ladder transition taken at the peak velocity of the line is mapped in contours. The contour levels are −0.3, 0.3, 0.375, 0.45, 0.525, 0.60, and 0.75 Jy beam^{-1}. The synthesized beam of 9″.3 × 5″.8 is indicated at the bottom left of each panel.

better understanding of their formation mechanism, distribution, and relative abundance compared with other large molecular species.

There are three primary procedures used in calculating the total beam-averaged column density of a particular molecular species. They are the rotational temperature diagram method (RTDM; Goldsmith & Langer 1999), the statistical equilibrium method (SEM), and the assumption of LTE. The methods are outlined in detail in Remijan et al. (2004). With the exception of CH_3CN, not enough transitions with a wide spread of upper-state energy levels have been observed to utilize the RTDM. Furthermore, because many of our species are asymmetric top molecules, detailed collision rates are not known, so we cannot utilize the SEM. In the case of CH_3CN, we can use the RTDM

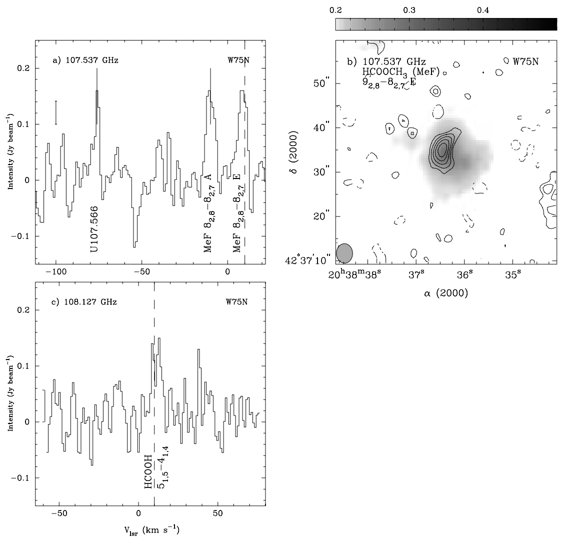

FIG. 6.—(*a*) $HCOOCH_3$ spectrum toward W75N. The noise level is $\sim$40 mJy beam^{-1} (indicated by the vertical bar at the left of the spectrum). The spectral line label corresponds to the rest frequency located at the top left of the panel for a v_{LSR} of 10 km s^{-1} (*dashed line*). (*b*) Emission contours from the $9_{2,8}-8_{2,7}$ E transition of $HCOOCH_3$ at 107.537 GHz overlaid on the W75N continuum emission at 107.5 GHz (*gray scale*). The numbers on the gray scale wedge are in units of Jy beam^{-1}. Contours indicate the location of the $HCOOCH_3$ emission near its peak at 10 km s^{-1}. The contour levels are −0.1, 0.1, 0.15, 0.20, 0.25, and 0.30 Jy beam^{-1}. The synthesized beam of 4.″4 × 3.″7 is indicated at the bottom left corner. (*c*) HCOOH spectrum toward W75N. The spectral line labels are the same as in (*a*).

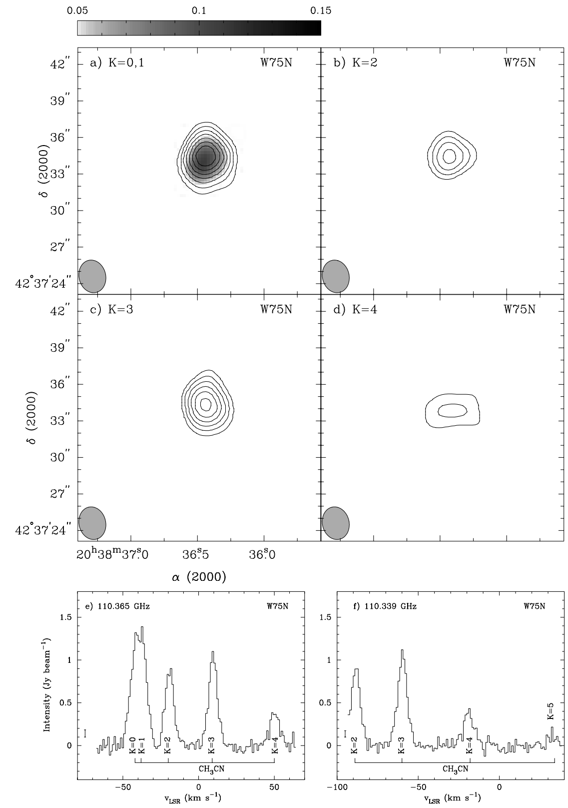

FIG. 7.—Same as Fig. 4, but toward W75N. The contour levels are 0.4, 0.5, 0.6, 0.7, 0.8, and 1.0 Jy beam^{-1} except in (*d*), where the contour levels are 0.2 and 0.3 Jy beam^{-1}. The synthesized beam of 2.″7 × 2.″2 is indicated at the bottom left corner of each panel.

to determine a rotational temperature and the column density. If the CH_3CN population can be described by a single rotational temperature and if all the lines are optically thin, the measured intensities are proportional to the column densities in the upper levels of the transitions being observed. From Remijan et al. (2004), we have

$$\frac{N_u}{g_u} = 2.04\frac{\int \Delta I\, dv}{\Omega_s \nu^3 S_{ij}\mu^2} \times 10^{20}\ \mathrm{cm}^{-2}, \tag{1}$$

$$\frac{N_u}{g_u} = \frac{N_{\mathrm{tot}}}{Q(T_{\mathrm{rot}})} e^{-\left(E_u/kT_{\mathrm{rot}}\right)}, \tag{2}$$

where N_u is the upper level column density, g_u is the statistical weight of the upper level, Ω_s is the solid angle subtended by the source (arcsec^2), $\int \Delta I\, dv$ is the integrated line intensity (Jy beam^{-1} km s^{-1}), ν is the rest frequency (GHz), $S_{ij}\mu^2$ is the product of the total torsional-rotational line strength and the square of the electric dipole moment (D^2), and, in equation (2), N_{tot} is the total source-averaged column density, $Q(T_{\mathrm{rot}})$ is the rotational partition function, E_u is the upper-state energy level, and T_{rot} is the rotational temperature. One can thereby determine the rotational temperature from the slope of the fit and

TABLE 5

G45.47+0.05 MOLECULAR LINE IDENTIFICATIONS

Frequency[a] (MHz)	Species	Transition	$\int \Delta I\, dv$[b] (Jy beam^{-1} km s^{-1})
107,013.850 ± 100........	CH_3OH	3(1)–4(0) A$^+$	1.7 ± 7
110,364.470 ± 100........	CH_3CN	6(3)–5(3)	1.6 ± 3
110,374.986 ± 120........	CH_3CN	6(2)–5(2)	0.9 ± 3
110,381.376 ± 120........	CH_3CN	6(1)–5(1)	1.9 ± 3
110,383.494 ± 120........	CH_3CN	6(0)–5(0)	2.3 ± 4

[a] Errors are 2 σ.
[b] Errors are 1 σ.

TABLE 6

W75N MOLECULAR LINE IDENTIFICATIONS

Frequency[a] (MHz)	Species	Transition	$\int \Delta I\, dv$[b] (Jy beam^{-1} km s^{-1})
107,537.189 ± 24.......	MeF[c]	$9_{2,8}-8_{2,7}$ E	0.8 ± 1[d]
107,543.746 ± 26.......	MeF	$9_{2,8}-8_{2,7}$ A	0.7 ± 1[d]
107,566.0....................	U107.566	. . .	0.5 ± 1[d]
108,126.710 ± 160.....	HCOOH	$5_{1,5}-4_{1,4}$	0.6 ± 1[d]
110,329.608 ± 120.....	CH_3CN	6(5)–5(5)	0.8 ± 2[e]
110,349.760 ± 200.....	CH_3CN	6(4)–5(4)	2.9 ± 2
110,364.470 ± 100.....	CH_3CN	6(3)–5(3)	7.6 ± 3
110,374.986 ± 120.....	CH_3CN	6(2)–5(2)	6.4 ± 2
110,381.376 ± 120.....	CH_3CN	6(1)–5(1)	7.6 ± 4[e]
110,383.494 ± 120.....	CH_3CN	6(0)–5(0)	7.6 ± 4[e]

[a] Errors are 2 σ.
[b] Errors are 1 σ.
[c] MeF: methyl formate ($HCOOCH_3$).
[d] The intensity and line width were approximated because the least-squares Gaussian fitting routine did not give a satisfactory fit.
[e] Blended line.

TABLE 7
SOURCE SIZE MEASUREMENTS

Source (1)	Species (2)	Transition (3)	Size (arcsec^2) (4)
G19.61−0.23..................	CH_3CN	6(0)–5(0)	60.9 ± 6.0[a]
	CH_3CN	6(1)–5(1)	60.9 ± 6.0[a]
	CH_3CN	6(2)–5(2)	31.8 ± 3.2
	CH_3CN	6(3)–5(3)	15.5 ± 3.0
	CH_3CN	6(4)–5(4)	64.8 ± 15.1
	EtCN	$12_{8,*}-11_{8,*}$	2.9 ± 2
	EtCN	$12_{5,*}-11_{5,*}$	1.7 ± 3
	EtCN	$12_{4,8}-11_{4,7}$	3.6 ± 2
	EtCN	$12_{3,10}-11_{3,9}$	2.6 ± 1
	EtCN	$12_{4,9}-11_{4,8}$	2.2 ± 1[a]
	MeF	$9_{2,8}-8_{2,7}$ A	2.2 ± 1[a]
	MeF	$9_{2,8}-8_{2,7}$ E	2.4 ± 5
	MeF	$9_{4,5}-8_{4,4}$ A	3.8 ± 6
	HCOOH	$5_{1,5}-4_{1,4}$	Point source
	CH_3OH	3(1)–4(0) A^+	Point source
G45.47+0.05	CH_3CN	6(0)–5(0)	243.1 ± 35.5
	CH_3CN	6(1)–5(1)	294.2 ± 151.2
	CH_3CN	6(3)–5(3)	189.4 ± 43.4
	CH_3OH	3(1)–4(0) A^+	65.4 ± 6.0
W75N............................	CH_3CN	6(0)–5(0)	11.3 ± 3[a]
	CH_3CN	6(1)–5(1)	11.3 ± 3[a]
	CH_3CN	6(2)–5(2)	8.8 ± 3
	CH_3CN	6(3)–5(3)	8.8 ± 3
	CH_3CN	6(4)–5(4)	10.1 ± 1.1
	CH_3CN	6(4)–5(4)	12.7 ± 5.0
	MeF	9(2,8)–8(2,7) A	19.8 ± 2
	MeF	9(2,8)–8(2,7) E	7.2 ± 2

[a] Blended line.

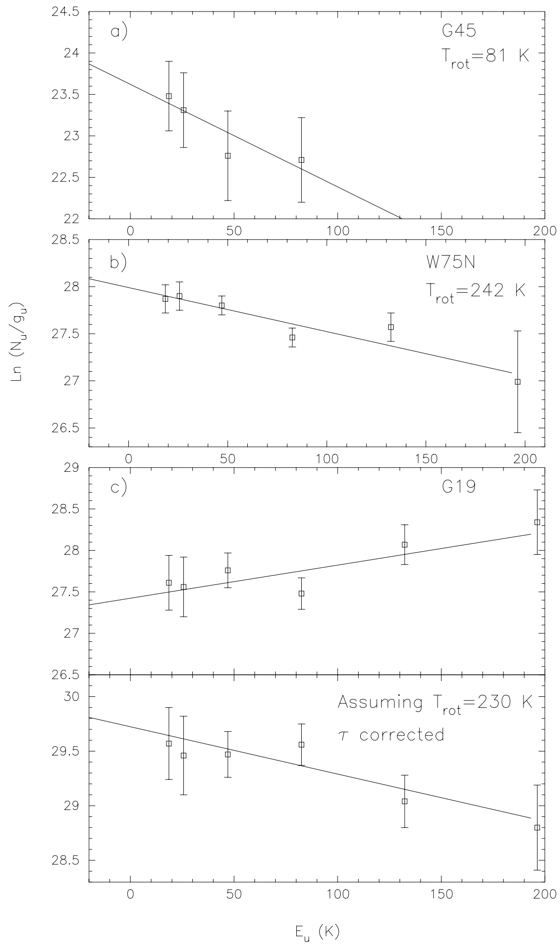

FIG. 8.—(*a*) Rotational temperature diagram for the observed CH_3CN transitions toward G45.47+0.05. *Ordinate*: $\ln(N_u/g_u)$. *Abscissa*: $E_u(K)$. The least-squares fit across *K*-levels is shown as a solid line. The resulting rotational temperature is 81 K. (*b*) Rotational temperature diagram for the observed CH_3CN transitions toward W75N. The resulting rotational temperature is 242 K. (*c*) Rotational temperature diagram for the observed CH_3CN transitions toward G19.61−0.23. In this case, the diagram gives a nonphysical rotational temperature. Below, the rotational temperature diagram assuming a temperature of 230 K and correcting for optical depth effects.

an estimate of the total molecular column density from the *y*-intercept. In order to measure Ω_s and construct accurate RTDs, we need a CH_3CN source size for each region. Source sizes are determined for the detected transitions assuming a Gaussian distribution and are summarized in Table 7. In column (1) we list the source. Columns (2) and (3) list the molecular species and associated transition, respectively. Column (4) lists the source size deconvolved from the synthesized beam determined from that transition along with its 1 σ error. From this analysis, we find an average source size of 43.3 ± 8.4 arcsec^2 for CH_3CN, 2.6 ± 2 arcsec^2 for CH_3CH_2CN, and 2.8 ± 4 arcsec^2 for $HCOOCH_3$ toward G19.61−0.23. Toward G45.47+0.05, we find an average source size of 242.2 ± 80.6 arcsec^2 for CH_3CN and 65.4 ± 6.0 arcsec^2 for CH_3OH. Toward W75N, we find an average source size of 10.3 ± 2.6 arcsec^2 for CH_3CN and 13.5 ± 2.0 arcsec^2 for $HCOOCH_3$. Using these values, we constructed RTDs using CH_3CN for each source. The results are shown in Figure 8. In each diagram, optical depth corrections were made using the procedure outlined in Remijan et al. (2004).

Figure 8*a* shows the RTD of CH_3CN toward G45.47+0.05. We were only able to detect four *K*-components in the $J = 6$–5 ladder. From the RTD, we find a rotational temperature of 81 ± 63 K and a total source-averaged column density of $N_{tot} = (1.9 \pm 2.3) \times 10^{13}$ cm^{-2}. It is apparent from the spectrum shown in Figure 5 that the CH_3CN emission is optically thin ($\tau < 0.003$). Given the lower rotational temperature and the highly extended (>240 arcsec^2) nature of the emission, it appears that CH_3CN may contain several individual cores that trace a cooler component of molecular gas. Figure 8*b* shows the RTD for all six *K*-components in the $J = 6$–5 ladder toward W75N. From the diagram, we find a rotational temperature of 242 ± 84 K and a total source-averaged column density of $N_{tot} = (7.5 \pm 3.9) \times 10^{15}$ cm^{-2}. Furthermore, the emission is very compact (∼10 arcsec^2); however, the optical depth of these lines is no greater than 0.06. Toward W75N, we are clearly detecting a HMC region unlike that seen toward G45.47+0.05. Finally, Figure 8*c* shows the RTD toward G19.61−0.23. In this case, we see the CH_3CN emission is optically thick, and we obtain a nonphysical rotational temperature. Therefore, the standard procedure of iteratively making corrections to the RTD cannot be applied in this case. However, if we assume $T_{rot} = 230$ K (Kurtz et al. 2000), we can make optical depth corrections by changing the column density until the slope of the RTD gives a temperature of 230 K. Using this method, we find a total source-averaged column density of $N_{tot} = 1.6 \times 10^{18}$ cm^{-2} and optical depth values as large as

8.0 in the $K = 3$ transition. This opacity-corrected rotation diagram assuming a temperature of 230 K is also shown in Figure 8*c*. However, the total column density value should only be considered an approximation, and in order to truly measure the temperature, the column density of CH_3CN, and H_2 density toward this region, a full statistical equilibrium analysis needs to be applied.

4.2. *Column Densities of Large Molecular Species in G19.61−0.23*

In order to determine the column densities of the remaining large molecules, we adopted the temperature reported by Kurtz et al. (2000) of 230 K and assumed LTE excitation. Figure 9 and Table 8 summarize the total source-averaged column densities, fractional abundances, and upper limits of all the large molecular species toward each high-mass SFR. In Table 8, the source for each column density measurement is given in column (1). Columns (2), (3), (4), and (5) list the total source-averaged column densities for HCOOH, $HCOOCH_3$, CH_3CH_2CN, and CH_3COOH, respectively. Assuming a temperature of 230 K, we find an average total source-averaged column density of $N_{tot} = 9.3 \times 10^{16}$ cm^{-2} for CH_3CH_2CN and $N_{tot} = 3.4 \times 10^{17}$ cm^{-2} for $HCOOCH_3$. For HCOOH, we find a total source-averaged column density of $N_{tot} = 6.0 \times 10^{16}$ cm^{-2}. Using this same procedure for our CH_3CN lines, we find a total source-averaged column density of $N_{tot} = 6.8 \times 10^{15}$ cm^{-2}. Finally, using the 1 σ noise level of our combined data set, we were able to set an upper limit to the total column density of $N_{tot} = 3.0 \times 10^{16}$ cm^{-2} for CH_3COOH. This gives a relative $CH_3COOH/HCOOCH_3$ abundance ratio of less than 9×10^{-2} for G19.61−0.23. This is higher than the abundance ratio found toward Sgr B2(N-LMH), W51e2, and G34.3+0.2 [(3–7) $\times 10^{-2}$], but this is still an upper limit (Remijan et al. 2003). The relative $HCOOH/HCOOCH_3$ abundance ratio is 0.18, which is comparable to the abundance ratios found by Liu et al. (2001) toward Sgr B2(N-LMH), Orion, and W51 ($\sim$0.10). For the two transitions of CH_3OH, we can use the same procedure to calculate an average CH_3OH total source-averaged column density of $N_{tot} = 2.0 \times 10^{18}$ cm^{-2}. However, both are maser transitions of CH_3OH, so the column density determined from equation (1) is not valid in this case and should be considered only as an upper limit. From our observations, it appears that the hot core regions toward the G19.61−0.23 region are very similar to the hot cores in G34.3+0.2. In fact, the measured column densities of $HCOOCH_3$ and CH_3CH_2CN are higher toward G19.61−0.23 than G34.3+0.2 (Remijan et al. 2003). We conclude that the nondetection of CH_3COOH toward this region is signal-to-noise limited and that a deeper survey should detect emission of CH_3COOH. In fact, in Figure 1*a*, there is a suggestion that the 111.507 GHz line of CH_3COOH is starting to be resolved out of the noise.

4.3. *Column Densities of Large Molecular Species in W75N and G45.47+0.05*

In total, we observed two transitions of $HCOOCH_3$ toward W75N, one transition of HCOOH toward W75N, and one transition of CH_3OH toward G45.47+0.05. For the transition of CH_3OH toward G45.47+0.05 using the rotational temperature of 81 K from the RTDM of CH_3CN, we find a CH_3OH total source-averaged column density of $N_{tot} = 1.8 \times 10^{15}$ cm^{-2}. However, this is a maser transition of CH_3OH, so the column density determined should once again only be considered an upper limit. For $HCOOCH_3$ toward W75N using the rotational temperature of 242 K from the RTDM of CH_3CN, we find an average total source-averaged column density of $N_{tot} = 2.1 \times 10^{16}$ cm^{-2}, and for HCOOH, we find a total source-averaged column density of $N_{tot} = 5.4 \times 10^{15}$ cm^{-2}. The relative $HCOOH/HCOOCH_3$ abundance ratio is 0.26, which is more than twice as large as the abundance ratios found by Liu et al. (2001). Figure 9 graphically summarizes the column densities and upper limit column densities of CH_3COOH, CH_3CH_2CN, HCOOH, CH_3CN, and $HCOOCH_3$ toward G19.61−0.23, G45.47+0.05, and W75N. Toward G45.47+0.05, we did not detect emission from any other large molecular species except for CH_3OH and CH_3CN. The emission from both species is highly extended, greater than 60 arcsec^2 for CH_3OH and greater than 240 arcsec^2 for CH_3CN, and the temperature determined from the RTDM is only 81 K with a large error (63 K). Thus, it appears that G45.47+0.05 does not contain a compact HMC that contains the physical conditions suitable to form large molecular species. In fact, the G45.47+0.05 region may contain a chemistry similar to that of cold dark clouds. Further observations that compare the chemistry of these regions are necessary to confirm this hypothesis.

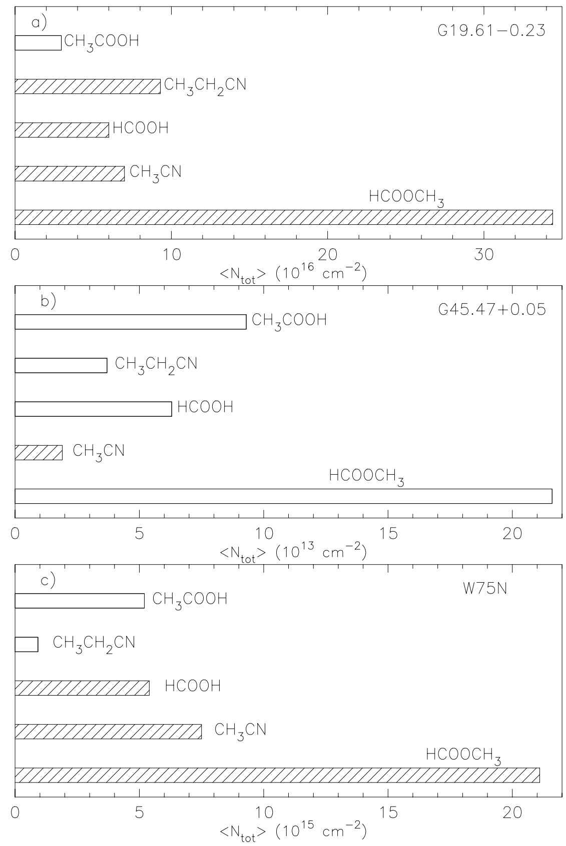

FIG. 9.—(*a*) Beam-averaged column densities determined from G19.61−0.23 interferometric measurements. The unhatched bars indicate upper limits to the column density measurements; the hatched bars indicate measured column densities based on optically thin emission assuming LTE excitation. (*b*) Beam-averaged column densities determined from G45.47+0.05 interferometric measurements. (*c*) Beam-averaged column densities determined from W75N interferometric measurements.

W75N does contain hot cores, but these observations suggest for the first time that there is a differentiation between the O and N cores toward this region. The emission from

TABLE 8
Column Densities and Fractional Abundances

Source (1)	N_{HCOOH} (10^{15} cm^{-2}) (2)	N_{HCOOCH_3} (10^{15} cm^{-2}) (3)	$N_{CH_3CH_2CN}$ (10^{15} cm^{-2}) (4)	N_{CH_3COOH} (10^{15} cm^{-2}) (5)
G19.61−0.23................	60.2	344.5	93.3	<29.6
G45.47+0.05................	<0.06	<0.22	<0.04	<0.09
W75N...........................	5.4	21.1	<0.92	<5.17
Source	X_{HCOOH} ($\times10^{-8}$)	X_{HCOOCH_3} ($\times10^{-8}$)	$X_{CH_3CH_2CN}$ ($\times10^{-8}$)	X_{CH_3COOH} ($\times10^{-8}$)
G19.61−0.23[a]	7.5	43.1	11.7	>3.7
G45.47+0.05[a]...............	>0.01	>0.04	>0.007	>0.02
W75N[b]	2.7	10.6	>0.5	>2.6

Note.—All upper limits were calculated from the 1 σ rms noise in the spectral window, the source sizes, and temperatures of 230, 81, and 242 K for G19.61−0.23, G45.47+0.05, and W75N, respectively (see §§ 4.2–4.3). For the upper limit of $HCOOCH_3$, we used a frequency of 111.453 GHz; for CH_3CH_2CN, 107.492 GHz; for HCOOH, 108.126 GHz; and for CH_3COOH, 111.549 GHz.

[a] H_2 column density taken from Fontani et al. (2002).

[b] H_2 column density taken from Zinchenko et al. (2000).

$HCOOCH_3$ and HCOOH is located ~2″.7 to the east of the CH_3CN peak and has a cometary morphology similar to that seen by Liu et al. (2002) toward Orion. The CH_3CN emission, on the other hand, falls very close to the continuum emission, which is offset from the $HCOOCH_3$ and HCOOH emission. Indeed, the W75N region is more similar to the hot core regions surrounding W3 and Orion that show a differentiation between the O and N cores than to the W51e2 or Sgr B2(N-LMH) HMCs. Further high-resolution observations are necessary to investigate the O and N cores toward this region.

4.4. *Implications for Future Acetic Acid* (CH_3COOH) *Surveys*

Recalling the conclusions reached by Remijan et al. (2003) that CH_3COOH sources are HMCs located within 7 kpc of the Galactic center, have a mass range between 200 and 2000 $M_\odot$, and did not show a differentiation between O and N bearing cores, we discuss the validity of these criteria in light of the new nondetections. The distances and mass requirements are met as a result of source selection (except for W75N, which at a galactocentric distance of 8 kpc is outside the 7 kpc limit; however, given the mass and size of this source and the errors involved in distance determination, we believed W75N would be a good source to survey for CH_3COOH). We determined that G45.47+0.05 does not contain a hot compact core. The implication from the CH_3CN rotation diagram is that the molecular emission is extended and may contain several distinct sources. Because we believe CH_3COOH is formed in warm HMCs, we would not expect to detect it toward this region. We find that W75N has different O and N cores similar to W3(OH)/W3(H_2O) or the Orion Compact Ridge/Hot Core. With this discovery, we would not expect to detect CH_3COOH in this region. We can also rule out the O and N differentiation is due to our ability to resolve out the individual O and N cores in these sources. While it is true that each source in which O and N chemical differentiation has been seen is at a heliocentric distance of less than 3 kpc, we note that G19.61−0.23 does not show such a distinction at a heliocentric distance of 3.6 kpc. This leaves G19.61−0.23 as the lone remaining suitable CH_3COOH source. G19.61−0.23 seemed to fit all the selection criteria, and, in fact, there is an indication of an CH_3COOH transition at 111.507 GHz; however, the corresponding A transition at 111.549 GHz is not seen (Fig. 1). It appears that the chemistry present toward G19.61−0.23 is similar to G34.3+0.2. If you compare our Figure 3 and Figure 3 from Remijan et al. (2003), it is clear that all the same transitions of each molecular species are detected; however, the spectral lines toward G19.61−0.23 are all weaker by a factor of ~2–3. If we apply the same reduction to the acetic acid lines, we find the acetic acid transitions should have a peak line intensity between 0.07 and 0.1 Jy $beam^{-1}$. The noise level in the acetic acid windows toward G19.61−0.23 was ~0.05 Jy $beam^{-1}$, so we would only expect to detect these lines at the 1–2 σ level. Thus, to be confident in a detection, we would need to decrease the noise level to ~0.02 Jy $beam^{-1}$ for a 3–5 σ detection. We expect that further observations with a better signal-to-noise ratio should detect these lines. Therefore, in summary, our new results remain consistent with the conclusions of Remijan et al. (2003). Apparently, the formation of CH_3COOH favors HMCs with well-mixed N and O, despite the fact that CH_3COOH does not contain a N atom. If proved to be true, this is an important constraint on CH_3COOH formation and possibly other structurally similar biomolecules.

CH_3CN appears to be a good proxy in the search for hard-to-detect large molecular species, particularly in light of the potential importance of N chemistry. This is because CH_3CN is easily detectable and has a column density similar to the hard-to-detect large molecules (Remijan et al. 2003). Figure 10 illustrates this toward each of our SFRs, along with the previously observed sources Sgr B2(N-LMH) and W51e2 (Remijan et al. 2004, 2002; Snyder et al. 2002). In this case, each molecular species is plotted as a fractional abundance relative to CH_3CN. In nearly every case, we note that the CH_3CN column density is similar to the column densities of CH_3COOH, HCOOH, and CH_3CH_2CN. However, the measured relative abundances of $HCOOCH_3$ are often several times larger than those of any other molecular species. Thus, while CH_3CN appears to have a column density closer to that of the large molecular species, it is still not clear how CH_3CN is related to the chemistry that forms these large molecules, especially in those regions that have O- and N-rich cores. The only analysis trying to explain the formation of O- and N-rich cores was performed by Rodgers & Charnley (2001). They determined that the

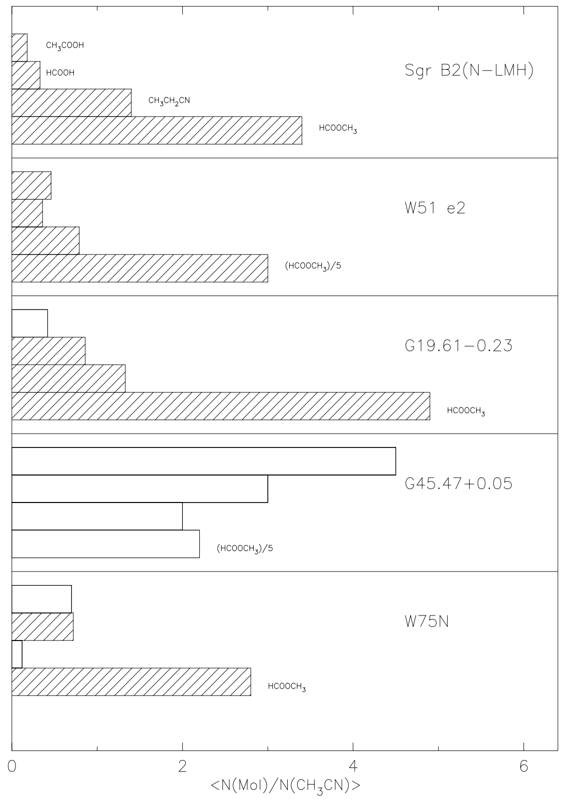

FIG. 10.—Beam-averaged fractional abundances relative to methyl cyanide (CH_3CN) for Sgr B2(N-LMH), W51e2, G19.61−0.23, G45.47+0.05, and W75N interferometric measurements. The hatching scheme is the same as in Fig. 9. The first bar corresponds to the fractional abundance of CH_3COOH, the second bar corresponds to the fractional abundance of HCOOH, the third bar corresponds to the fractional abundance of CH_3CH_2CN, and the fourth bar corresponds to the fractional abundance of $HCOOCH_3$ toward each source. Toward W51e2 and G45, note that the fractional abundance of $HCOOCH_3$ is divided by a factor of 5 for purposes of this display.

O- and N-rich cores are formed as a result of the abundance (or lack) of ammonia (NH_3) on grain mantles and the timescale of the core formation: O-rich cores form first, then they become N-rich. However, our observations indicate that large molecules are found in regions in which the formation of O- and N-rich cores is occurring simultaneously in the interstellar environment. Because CH_3CN lines are easy to detect, by first observing a source for CH_3CN, one can obtain information about the column densities of the larger molecules and, from that, an approximate line intensity. This will undoubtedly influence future surveys and at the same time help to gain an understanding of the physical conditions present toward future surveyed sources.

5. SUMMARY

We have surveyed three high-mass Galactic SFRs for interstellar methanol (CH_3OH), formic acid (HCOOH), acetic acid (CH_3COOH), methyl formate ($HCOOCH_3$), methyl cyanide (CH_3CN), and ethyl cyanide (CH_3CH_2CN) with the BIMA Array. From our observations, we have detected two new sources of interstellar HCOOH toward the hot core regions G19.61−0.23 and W75N. We have also made the first detections of CH_3CH_2CN and $HCOOCH_3$ toward G19.61−0.23. The relative HCOOH/$HCOOCH_3$ abundance ratio is 0.18, which is comparable to the abundance ratios found by Liu et al. (2001) toward Sgr B2(N-LMH), Orion, and W51 (~0.10). We have made the first detection of $HCOOCH_3$ toward W75N. The relative HCOOH/$HCOOCH_3$ abundance ratio is 0.26, which is more than twice as large as the abundance ratios found by Liu et al. (2001). Furthermore, the hot core regions around W75N show for the first time a chemical differentiation between the O and N cores similar to that seen toward the Orion Hot Core and Compact Ridge and W3(OH) and W3(H_2O). It is also apparent from our observations that the high-mass SFR G45.47+0.05 does not contain any compact HMC, and its chemistry may be more similar to cold dark clouds. Finally, it appears that CH_3CN is a good tracer for harder to detect biomolecules. CH_3CN was detected toward all three sources, and, as Figures 9 and 10 illustrate, the total source-averaged CH_3CN column density is similar to the larger molecular species. Because CH_3CN lines appear easy to detect by first observing a source for CH_3CN, one can obtain information about the column densities of the larger biomolecules and, from that, an approximate line intensity. This will undoubtedly influence future surveys and at the same time help to gain an understanding of the physical conditions present toward future surveyed sources.

We are indebted to C. Watson for use of his BIMA data toward W75N. We thank F. J. Lovas for the use of his new line list of identified molecular species to identify spectral features in our passbands. We appreciate helpful comments from J. M. Hollis and E. C. Sutton. We thank an anonymous referee for some very useful comments. We acknowledge support from the Laboratory for Astronomical Imaging at the University of Illinois and NSF AST 99-81363 and AST 02-28953.

REFERENCES

Anderson, T., Crownover, R. L., Herbst, E., & de Lucia, F. C. 1988, ApJS, 67, 135
Boucher, D., Burie, J., Bauer, A., Dubrulle, A., & Demaison, J. 1980, J. Phys. Chem. Ref. Data, 9, 659
Churchwell, E., Walmsley, C. M., & Cesaroni, R. 1990, A&AS, 83, 119
Churchwell, E., Walmsley, C. M., & Wood, D. O. S. 1992, A&A, 253, 541
Comoretto, G., et al. 1990, A&AS, 84, 179
Fontani, F., Cesaroni, R., Caselli, P., & Olmi, L. 2002, A&A, 389, 603
Forster, J. R., & Caswell, J. L. 1989, A&A, 213, 339
Garay, G., Moran, J. M., Rodríguez, L. F., & Reid, M. J. 1998, ApJ, 492, 635
Garay, G., Reid, M. J., & Moran, J. M. 1985, ApJ, 289, 681
Gasiprong, N., Cohen, R. J., & Hutawarakorn, B. 2002, MNRAS, 336, 47
Gibb, E., Nummelin, A., Irvine, W. M., Whittet, D. C. B., & Bergman, P. 2000, ApJ, 545, 309
Goldsmith, P. F., & Langer, W. D. 1999, ApJ, 517, 209
Hatchell, J., Thompson, M. A., Millar, T. J., & MacDonald, G. H. 1998, A&AS, 133, 29
Helmich, F. P., Jansen, D. J., de Graauw, Th., Groesbeck, T. D., & van Dishoeck, E. F. 1994, A&A, 283, 626
Helmich, F. P., & van Dishoeck, E. F. 1997, A&AS, 124, 205
Hofner, P., & Churchwell, E. 1996, A&AS, 120, 283
Hofner, P., Wyrowski, F., Walmsley, C. M., & Churchwell, E. 2000, ApJ, 536, 393
Hollis, J. M., Vogel, S. N., Snyder, L. E., Jewell, P. R., & Lovas, F. J. 2001, ApJ, 554, L81
Hunter, T. R., Taylor, G. B., Felli, M., & Tofani, G. 1994, A&A, 284, 215
Ikeda, M., Ohishi, M., Nummelin, A., Dickens, J. E., Bergman, P., Hjalmarson, Å., & Irvine, W. M. 2001, ApJ, 560, 792
Ilyushin, V. V., et al. 2001, J. Mol. Spectrosc., 205, 286

Kalenskii, S. V., Berulis, I. I., Val'tts, I. E., Dzura, A. M., Slysh, V. I., & Vasil'kov, V. I. 1994, AZh, 71, 51

Kalenskii, S. V., Slysh, V. I., & Val'tts, I. E. 2002, Astron. Rep., 46, 96

Kurtz, S., Cesaroni, R., Churchwell, E., Hofner, P., & Walmsley, C. M. 2000, in Protostars and Planets IV, ed. V. Manning, A. P. Boss, & S. Russell (Tucson: Univ. Arizona Press), 299

Larionov, G. M., Val'tts, I. E., Winnberg, A., Johansson, L. E. B., Booth, R. S., & Golubev, V. V. 1999, A&AS, 139, 257

Lekht, E. E., & Krasnov, V. V. 2000, Astron. Lett., 26, 38

Lekht, E. E., Silant'ev, N. A., Mendoza-Torres, J. E., & Tolmachev, A. M. 2002, Astron. Lett., 28, 89

Liu, S.-Y., Girart, J. M., Remijan, A. J., & Snyder, L. E. 2002, ApJ, 576, 255

Liu, S.-Y., Mehringer, D. M., & Snyder, L. E. 2001, ApJ, 552, 654

Lovas, F. J. 1982, J. Phys. Chem. Ref. Data, 11, 251

Matthews, H. E., Goss, W. M., Winnberg, A., & Habing, H. J. 1977, A&A, 61, 261

Mehringer, D. M., Goss, W. M., & Palmer, P. 1995, ApJ, 452, 304

Minier, V., Conway, J. E., & Booth, R. S. 2001, A&A, 369, 278

Nummelin, A., Bergman, P., Hjalmarson, Å., Friberg, P., Irvine, W. M., Millar, T. J., Ohishi, M., & Saito, S. 2000, ApJS, 128, 213

Oesterling, L. C., Sieghard, A., de Lucia, F. C., Sastry, K. V. L. N., & Herbst, E. 1999, ApJ, 521, 255

Olmi, L., Cesaroni, R., & Walmsley, C. M. 1993, A&A, 276, 489

Palmer, P., Goss, W. M., & Devine, K. E. 2003, ApJ, 599, 324

Palmer, P., Goss, W. M., & Whiteoak, J. B. 2004, MNRAS, 347, 1164

Pankonin, V., Churchwell, E., Watson, C., & Bieging, J. H. 2001, ApJ, 558, 194

Remijan, A., Snyder, L. E., Friedel, D. N., Liu, S.-Y., & Shah, R.-Y. 2003, ApJ, 590, 314

Remijan, A., Snyder, L. E., Liu, S.-Y., Mehringer, D. M., & Kuan, Y.-J. 2002, ApJ, 576, 264

Remijan, A., Sutton, E. C., Snyder, L. E., Friedel, D. N., Liu, S.-Y., & Pei, C.-C. 2004, ApJ, 606, 917

Rodgers, S. D., & Charnley, S. B. 2001, ApJ, 546, 324

Sault, R. J., Teuben, P. J., & Wright, M. C. H. 1995, in ASP Conf. Ser. 77, Astronomical Data Analysis Software and Systems IV, ed. R. A. Shaw, H. E. Payne, & J. J. E. Hayes (San Francisco: ASP), 433

Shirley, Y. L., Evans, N. J., Young, K. E., Knez, C., & Jaffe, D. T. 2003, ApJS, 149, 375

Snyder, L. E., Lovas, F. J., Mehringer, D. M., Miao, Y., Kuan, Y.-J., Hollis, J. M., & Jewell, P. R. 2002, ApJ, 578, 245

Torelles, J. M., Gomez, J. F., Rodríguez, L. F., & Ho, P. T. P. 1997, ApJ, 489, 744

Valdetto, R., Palla, F., Brand, J., Cesaroni, R., Comoretto, G., & Felli, M. 2002, A&A, 383, 244

Voronkov, M. A., Austin, M. C., & Sobolev, A. M. 2002, A&A, 387, 310

Watson, C., Churchwell, E., Pankonin, V., & Bieging, J. H. 2002, ApJ, 577, 260

Westerhout, G. 1958, Bull. Astron. Inst. Netherlands, 14, 215

Willemot, E., Dangoisse, D., Monnanteuil, N., & Bellet, J. 1980, J. Phys. Chem. Ref. Data, 9, 59

Wu, J., & Evans, N. J. 2003, ApJ, 592, L79

Xu, L. H., & Lovas, F. J. 1997, J. Phys. Chem. Ref. Data, 26, 17

Zheng, X.-W., & Ling, Z.-F. 1997, Acta Astron. Sinica, 38, 135

Zinchenko, I., Henkel, C., & Mao, R. Q. 2000, A&A, 361, 1079

Appendix F

A Rigorous Attempt to Verify Interstellar Glycine

By

L. E. Snyder, F. J. Lovas. J. M. Hollis, D. N. Friedel, P. R. Jewel, A. Remijan, V. V. Ilyushin,
E. A. Alekseev, & S. F. Dyubko

2005 ApJ 619, 914

The Astrophysical Journal, 619:914–930, 2005 February 1

A RIGOROUS ATTEMPT TO VERIFY INTERSTELLAR GLYCINE

L. E. Snyder,[1] F. J. Lovas,[2] J. M. Hollis,[3] D. N. Friedel,[1] P. R. Jewell,[4] A. Remijan,[1,3,5]
V. V. Ilyushin,[6] E. A. Alekseev,[6] and S. F. Dyubko[6]
Received 2004 May 25; accepted 2004 October 7

ABSTRACT

In 2003, Kuan and coworkers reported the detection of interstellar glycine (NH_2CH_2COOH) based on observations of 27 lines in 19 different spectral bands in one or more of the sources Sgr B2(N-LMH), Orion KL, and W51 e1/e2. They supported their detection report with rotational temperature diagrams for all three sources. In this paper we present essential criteria that can be used in a straightforward analysis technique to confirm the identity of an interstellar asymmetric rotor such as glycine. We use new laboratory measurements of glycine as a basis for applying this analysis technique, both to our previously unpublished 12 m telescope data and to the previously published Swedish-ESO Submillimetre Telescope (SEST) data of Nummelin and colleagues. We conclude that key lines necessary for an interstellar glycine identification have not yet been found. We identify some common molecular candidates that should be examined further as more likely carriers of several of the lines reported as glycine. Finally, we illustrate that a rotational temperature diagram used without the support of correct spectroscopic assignments is not a reliable tool for the identification of interstellar molecules.

Subject headings: ISM: abundances — ISM: clouds —
ISM: individual (Sagittarius B2(N-LMH), Orion Kleinmann-Low, W51 e1/e2) —
ISM: molecules — radio lines: ISM

1. INTRODUCTION

Interstellar glycine (NH_2CH_2COOH) has been unsuccessfully sought using both single-element telescopes (Brown et al. 1979; Hollis et al. 1980; Snyder et al. 1983; Berulis et al. 1985; Guelin & Cernicharo 1989; Combes et al. 1996; Ceccarelli et al. 2000) and interferometric arrays (Snyder 1997; Hollis et al. 2003a, 2003b). Recently, Kuan et al. (2003) reported the identification of interstellar glycine (NH_2CH_2COOH) in the direction of the hot molecular cores Sgr B2(N-LMH), Orion KL, and W51 e1/e2.

We note several unusual aspects about the Kuan et al. (2003) reported glycine results. First, their glycine report was based on the detection of 27 spectral line features in the sources Orion KL, W51 e1/e2, and Sgr B2(N-LMH). They used the NRAO[7] 12 m radio telescope operating in the range of 130–242 GHz. The 27 independent spectral line features detected in three different sources might seem to be reasonable evidence. Certainly the detection of the same ensemble of spectral lines in multiple sources is a characteristic of interstellar molecules with structural components similar to those of glycine, such as formic acid (HCOOH) and acetic acid (CH_3COOH; see, e.g., Liu et al. 2001; Remijan et al. 2002). However, each of the three glycine sources was observed to contain no more than 13–16 of the 27 independent spectral line features, and only three of the 27 spectral line features were found to be common to all three sources. Second, 16 of the 27 reported glycine features are not the fourfold degenerate rotational transitions that should be the most likely to be detected for *R*-branch asymmetric rotor transitions. Third, the glycine rest frequencies used in their observations were based on a Hamiltonian calculation that was extrapolated over 100 GHz. This method can yield potentially large uncertainties in the frequency predictions. Fourth, the glycine column densities derived from rotational temperature diagrams were surprisingly high. In fact, Orion KL was reported to have the highest glycine column density, but the interstellar molecule with structure closest to glycine, acetic acid, has never been detected there (Remijan et al. 2003).

In this paper we investigate the above concerns by starting from new laboratory measurements of glycine that improve the Hamiltonian fit and thereby result in highly reliable interpolated frequency predictions that provide the foundation for our discussion. We list and explain rigorous and essential criteria for identifying a new interstellar molecule such as glycine. Then we use these criteria on key glycine spectral lines reported by Kuan et al. (2003) to interpret independent observational data for Orion KL, W51 e1/e2, and Sgr B2(N-LMH) and show that their key lines fail the tests required for a correct glycine identification. In investigating alternative identifications, we find that the carriers of several important spectral lines that have been assigned to glycine are more logically assigned to other, more common species. Finally, we find that random choices of unidentified spectral lines can be used to generate a reasonable glycine rotational temperature diagram similar to those published by Kuan et al. (2003).

2. GLYCINE SPECTRAL LINE ANALYSIS AND PREDICTED REST FREQUENCIES

The microwave spectrum of conformer I of glycine was first recorded by Suenram & Lovas (1980) from 82 to 113 GHz in a

[1] Department of Astronomy, University of Illinois, 1002 West Green Street, Urbana, IL 61801; snyder@astro.uiuc.edu, friedel@astro.uiuc.edu, aremijan@pop900.gsfc.nasa.gov.
[2] Optical Technology Division, National Institute of Standards and Technology, Gaithersburg, MD 20899-8441; lovas@nist.gov.
[3] Earth and Space Data Computing Division, NASA Goddard Space Flight Center, Code 930, Greenbelt, MD 20771; jan.m.hollis@gsfc.nasa.gov.
[4] National Radio Astronomy Observatory, Green Bank, WV 24944-0002; pjewell@nrao.edu.
[5] National Research Council Resident Research Associate.
[6] Institute of Radio Astronomy, National Academy of Sciences of Ukraine, Krasnoznamennaya 4, 61002 Kharkow, Ukraine; ilyushin@rian.ira.kharkov.ua, alekseev@rian.ira.kharkov.ua.
[7] The National Radio Astronomy Observatory (NRAO) is a facility of the National Science Foundation operated under cooperative agreement by Associated Universities, Inc.

heated parallel plate Stark cell. This study provided rotational analysis and a rough dipole moment determination. Additional measurements of the ^{14}N quadrupole coupling hyperfine structure and the Stark effect on low-J transitions between 16 and 24.5 GHz were subsequently reported by Lovas et al. (1995). While these literature data provided a firm basis for predicting transitions up to about 150 GHz for guiding past interstellar searches, the 2 σ (standard deviation) uncertainties[8] ranged from 1.5 MHz at 206 GHz to 2.8 MHz at 240 GHz for the main interstellar transitions reported by Kuan et al. (2003). Recently, at Kharkow, Ukraine, a heated quartz absorption cell was used to provide new measurements between 75 and 260 GHz utilizing an automated synthesizer-based spectrometer described by Ilyushin et al. (2001). New glycine search frequencies could then be predicted by incorporating both the previously reported transitions and the new measurements into a rotational analysis that employed the Watson A-reduction Hamiltonian with quartic centrifugal distortion terms included (Watson 1977). The details of these laboratory measurements and Hamiltonian calculations will be reported in a future paper. For this paper it is important to note that for the majority of the calculated transitions the uncertainties have been reduced by a factor of 10 or more from those used by Kuan et al. (2003). Thus, we are starting our analysis with highly accurate glycine rest-frequency predictions.

Table 1 summarizes the reported glycine line detections in the direction of the hot molecular cores Sgr B2(N-LMH), Orion KL, and W51 e1/e2. The first column lists a number that Kuan et al. (2003) introduced to represent a particular glycine line. For the convenience of the reader, we adopt this shorthand notation, hereafter referred to as the "glycine line number." The second column gives the rotational quantum numbers of the associated transitions, and the third identifies each reported transition as an a-type or a b-type. The fourth column lists our newly calculated glycine rest frequencies, and the fifth and sixth columns give the associated line strengths and upper energy levels. The final six columns in Table 1 list the observed LSR velocity and brightness temperature of each glycine line reported for each source. We have marked with asterisks the LSR velocity and brightness temperature values for the lines that were displayed by Kuan et al. (2003).

3. ESSENTIAL CRITERIA FOR ESTABLISHING THE IDENTIFICATION OF A NEW INTERSTELLAR MOLECULE

The task of establishing the identification of a new interstellar molecule in a dense interstellar cloud is made more complicated by high spectral line densities. For example, at the 3 mm wavelength Sgr B2(N-LMH) has a spectral line density of 6.06 lines per 100 MHz, half of which are unidentified (Friedel et al. 2004). This is the highest reported line density in radio astronomy. Hence, the detection of spectral lines with frequencies close to those of a new species is not in itself sufficient evidence for a correct assignment. Consequently, there are several criteria to consider in securing the correct identification of a new interstellar molecule such as glycine.

Rest frequencies.—The most important criterion for establishing the identification of a new interstellar molecule is that the rest frequencies must be established to a high degree of accuracy. Preferably, the spectral line astronomical rest frequencies to be used in the interstellar search should have been directly measured in the laboratory. If such direct measurements are not available, interpolation fitting of the available laboratory data from other frequencies should allow the construction of a high-precision Hamiltonian model that can be used to predict search frequencies with uncertainties on the order of 1 part in 10 million.

Frequency agreement.—There must be frequency agreement among all detected transitions. This means that an accurate astronomical rest frequency of the assigned transition must be in reasonable agreement with the frequency corresponding to the LSR velocity of the source. Variations in the LSR velocity of a given molecular species can occur when regions with different kinematics contribute to the emission or absorption spectrum. However, it is evident that emission lines from a given molecular species that emanate from a region with no large kinematic variance will have a well-defined velocity field. Examples are the Very Large Array (VLA) measurements of the kinematics of methyl formate ($HCOOCH_3$) toward OMC-1 by Hollis et al. (2003b) and of ethyl cyanide (CH_3CH_2CN) toward Sgr B2(N-LMH) by Hollis et al. (2003a). If there is a source velocity gradient, as established from observed transitions of known molecules, it cannot be a random function of transition frequency or energy level.

Furthermore, it is not uncommon to have an interstellar spectral line from one species blend with another line of either the same or another species. In order to correctly assign or confirm a line identification, a common standard is that the lines should be at least resolved by the Rayleigh criterion. That is, the minimum distance between two spectral lines in frequency space must be such that the maximum intensity of one line falls on the first null of the other (see, e.g., Jenkins & White 1957, p. 300; Sommerfeld 1964, p. 290). This is approximately equivalent to requiring that overlapping lines be separated by their FWHM intensity (assuming identical line profiles). In practice, a more stringent criterion based on the signal-to-noise ratio is often needed, whereby two overlapping lines can be considered to be resolved if they are at least separated at the half-maximum intensity of the weakest line.

Beam dilution.—Suppose one uses a single-element radio telescope with a circular aperture of diameter D (such as the NRAO 12 m telescope) to observe separate transitions of some molecule at 50, 100, and 150 GHz. The full half-power beamwidth (HPBW) of the telescope is approximately given by $1.22\lambda/D$ rad (Born & Wolf 1980, p. 397; see also Rohlfs & Wilson 2000, p. 141), so in this case the telescope HPBW changes by a factor of 3 over the range of observations. As we discuss below, beam dilution scales with source size squared and beam size squared. To examine the required correction for beam dilution, we can start with $\langle N_T \rangle$, the beam-averaged molecular column density determined from the integrated intensity of a rotational transition observed by a single-element radio telescope. In autocorrelation mode, with the assumptions of LTE and low optical depth[9] (see, e.g., Snyder et al. 2001; Dickens et al. 1997), $\langle N_T \rangle$ is given by

$$\langle N_T \rangle = \frac{1.67 W_T Z e^{E_u/T_{\rm rot}}}{S\mu^2\nu} \times 10^{14}\ {\rm cm}^{-2}. \qquad (1)$$

[8] Unless otherwise noted, all uncertainties quoted in this paper are 2 σ or coverage factor $k = 2$ as described by Taylor & Kuyatt (1994).

[9] The corrections to apply when the optical depth is not low and when the excitation is subthermal have been discussed in detail by Goldsmith & Langer (1999) and are mentioned in the Appendix. The aspects of maser excitation have been examined by Reid & Moran (1988). Because we are following the assumptions of Kuan et al. (2003) that their reported glycine lines are optically thin and in LTE, we confine our discussion to this particular case.

TABLE 1

Summary of Reported Glycine Line Detections

						Sgr B2(N-LMH)		Orion KL		W51 e1/e2	
Line Number (1)	Transition (2)	Type (3)	Rest Frequency[a] (MHz) (4)	Line Strength S (5)	E_u (K) (6)	V_{LSR}[b] (km s^{-1}) (7)	T_R^*[c] (mK) (8)	V_{LSR}[b] (km s^{-1}) (9)	T_R^*[c] (mK) (10)	V_{LSR}[b] (km s^{-1}) (11)	T_R^*[c] (mK) (12)
1............................	$21_{1,20}-20_{2,19}$	*b*	130346.775(13)	16.7	72.3	66.3(1.2)	26.0(5.9)	8.0(3.1)	9.0(2.0)	U interloper[d]	
2............................	$21_{2,20}-20_{2,19}$	*a*	130354.371(13)	20.5	72.3	66.3(1.2)	30.0(5.9)	U interloper		U interloper	
3............................	$21_{1,20}-20_{1,19}$	*a*	130360.890(13)	20.5	72.3	U interloper		U interloper		60.0(3.1)	7.5(2.2)
4............................	$21_{2,20}-20_{1,19}$	*b*	130368.485(13)	16.7	72.3	ID interloper[e]		ID interloper		60.0(3.1)	6.4(2.1)
5............................	$19_{3,16}-18_{3,15}$	*a*	131423.627(13)	18.1	67.6	Not observed[f]		8.5(1.1)*	15.0(4.1)*	60.0(3.0)	15.0(4.0)
6............................	$12_{5,8}-11_{4,7}$	*b*	142225.340(120)	4.6	34.0	64.0(5.6)	22.0(2.0)	7.8(2.8)	5.2(1.4)	Not detected[g]	
7............................	$21_{3,18}-20_{3,17}$	*a*	142301.054(13)	20.0	81.0	64.0(2.1)	38.0(2.2)	ID interloper		60.0(2.8)	6.6(2.8)
8............................	$21_{9,12}-20_{9,11}$	*a*	144841.736(22)	17.2	102.9	Not observed		5.0(2.8)	20.9(3.8)	56.0(2.8)	20.7(2.9)
9............................	$21_{5,17}-20_{5,16}$	*a*	144847.191(16)	19.7	84.8	Not observed		8.0(1.4)	17.9(5.2)	60.0(1.4)	15.5(4.2)
10..........................	$24_{1,23}-23_{2,22}$	*b*	147812.030(17)	19.7	92.7	64.0(1.0)	20.0(5.0)	Not observed		Not observed	
	$24_{2,23}-23_{2,22}$	*a*	147813.168(17)	23.5	92.7						
	$24_{1,23}-23_{1,22}$	*a*	147814.186(17)	23.5	92.7						
	$22_{3,19}-21_{3,18}$	*a*	147815.031(14)	21.0	88.0						
	$24_{2,23}-23_{1,22}$	*b*	147815.324(17)	19.7	92.7						
11..........................	$25_{0,25}-24_{1,24}$	*b*	148268.007(18)	23.6	94.0	U interloper		5.0(2.0)	11.0(2.1)	U interloper	
	$25_{1,25}-24_{1,24}$	*a*	148268.016(18)	24.8	94.0						
	$25_{0,25}-24_{0,24}$	*a*	148268.024(18)	24.8	94.0						
	$25_{1,25}-24_{0,24}$	*b*	148268.033(18)	23.6	94.0						
12..........................	$22_{12,11}-21_{12,10}$	*a*	150909.703(20)	15.5	130.8	68.0(2.7)	18.0(2.5)	Not detected (S/N)[h]		58.0(2.0)	8.0(1.5)
	$22_{12,10}-21_{12,9}$	*a*	150909.703(20)	15.5	130.8						
13..........................	$23_{6,18}-22_{6,17}$	*a*	160153.431(30)	21.4	103.5	U interloper		U interloper		60.0(2.5)	37.0(4.1)
14..........................	$26_{2,24}-25_{3,23}$	*b*	164851.728(30)	18.8	113.7	Not observed		7.5(1.2)*	21.2(4.5)*	U interloper	
15..........................	$26_{3,24}-25_{3,23}$	*a*	164862.039(30)	25.2	113.7	Not observed		7.5(1.2)*	25.0(4.5)*	60.0(1.2)	14.6(4.0)
16..........................	$26_{2,24}-25_{2,23}$	*a*	164870.438(30)	25.2	113.7	Not observed		7.5(1.2)*	20.0(4.5)*	Not detected	
17..........................	$26_{3,24}-25_{2,23}$	*b*	164880.749(30)	18.8	113.7	Not observed		7.5(1.2)*	17.7(4.5)*	Not detected (S/N)	
18..........................	$24_{12,13}-23_{12,12}$	*a*	164886.068(33)	18.0	146.4	Not observed		7.5(1.2)	21.6(4.5)	Not detected	
	$24_{12,12}-23_{12,11}$	*a*	164886.071(33)	18.0	146.4						
19..........................	$27_{1,26}-26_{2,25}$	*b*	165270.666(22)	22.7	115.7	64.8(0.9)*	60.0(4.6)*	Not detected		58.2(2.4)*	8.0(2.1)*
	$27_{2,26}-26_{2,25}$	*a*	165270.829(22)	26.5	115.7						
	$27_{1,26}-26_{1,25}$	*a*	165270.979(22)	26.5	115.7						
	$27_{2,26}-26_{1,25}$	*b*	165271.142(22)	22.7	115.7						
20..........................	$33_{2,31}-32_{3,30}$	*b*	205560.595(67)	25.7	176.8	67.0(0.7)*	95.0(11.9)*	Not detected		58.6(3.9)*	17.0(4.1)*
	$33_{3,31}-32_{3,30}$	*a*	205560.730(67)	32.2	176.8						
	$33_{2,31}-32_{2,30}$	*a*	205560.849(67)	32.2	176.8						
	$33_{3,31}-32_{2,30}$	*b*	205560.984(67)	25.7	176.8						
21..........................	$35_{0,35}-34_{1,34}$	*b*	206468.453(17)	33.6	180.5	66.0(1.9)*	210.0(8.9)*	7.3(0.7)*	230.0(10.0)*	60.5(0.7)*	65.0(9.7)*
	$35_{1,35}-34_{1,34}$	*a*	206468.453(17)	34.8	180.5						
	$35_{0,35}-34_{0,34}$	*a*	206468.453(17)	34.8	180.5						
	$35_{1,35}-34_{0,34}$	*b*	206468.453(17)	33.6	180.5						

TABLE 1—*Continued*

Line Number (1)	Transition (2)	Type (3)	Rest Frequency[a] (MHz) (4)	Line Strength S (5)	E_u (K) (6)	Sgr B2(N-LMH) V_{LSR}[b] (km s^{-1}) (7)	Sgr B2(N-LMH) T_R^*[c] (mK) (8)	Orion KL V_{LSR}[b] (km s^{-1}) (9)	Orion KL T_R^*[c] (mK) (10)	W51 e1/e2 V_{LSR}[b] (km s^{-1}) (11)	W51 e1/e2 T_R^*[c] (mK) (12)
22	$36_{0,36}$–$35_{1,35}$	*b*	212286.829(18)	34.6	190.7	66.0(0.7)	58.0(15.6)	ID interloper		ID interloper	
	$36_{1,36}$–$35_{1,35}$	*a*	212286.829(18)	35.8	190.7						
	$36_{0,36}$–$35_{0,35}$	*a*	212286.829(18)	35.8	190.7						
	$36_{1,36}$–$35_{0,35}$	*b*	212286.829(18)	34.6	190.7						
23	$36_{2,34}$–$35_{3,33}$	*b*	223004.375(88)	28.9	208.2	67.3(1.8)*	40.0(10.5)*	Not detected		Not observed	
	$36_{3,34}$–$35_{3,33}$	*a*	223004.395(88)	35.2	208.2						
	$36_{2,34}$–$35_{2,33}$	*a*	223004.413(88)	35.2	208.2						
	$36_{3,34}$–$35_{2,33}$	*b*	223004.432(88)	28.9	208.2						
24	$36_{3,33}$–$35_{4,32}$	*b*	228419.435(104)	25.9	216.3	65.0(1.3)	70.0(7.6)	4.9(3.5)*	40.0(2.0)*	57.0(1.8)	40.0(5.1)
	$36_{4,33}$–$35_{4,32}$	*a*	228420.029(104)	34.9	216.3						
	$36_{3,33}$–$35_{3,32}$	*a*	228420.526(104)	34.9	216.3						
	$36_{4,33}$–$35_{3,32}$	*b*	228421.120(104)	25.9	216.3						
25	$33_{6,27}$–$32_{6,26}$	*a*	230348.993(64)	31.3	202.5	ID interloper		8.0(3.5)	26.0(3.9)	58.7(3.5)	19.0(6.0)
26	$40_{1,39}$–$39_{2,38}$	*b*	240900.647(76)	35.8	244.2	63.2(0.6)*	94.0(11.0)*	5.0(1.7)*	35.0(7.2)*	57.0(1.7)*	17.0(5.5)*
	$40_{2,39}$–$39_{2,38}$	*a*	240900.647(76)	39.5	244.2						
	$40_{1,39}$–$39_{1,38}$	*a*	240900.647(76)	39.5	244.2						
	$40_{2,39}$–$39_{1,38}$	*b*	240900.647(76)	35.8	244.2						
27	$41_{0,41}$–$40_{1,40}$	*b*	241373.340(32)	39.6	245.9	U/ID interloper		Not detected		57.0(1.7)*	26.0(6.4)*
	$41_{1,41}$–$40_{1,40}$	*a*	241373.340(32)	40.8	245.9						
	$41_{0,41}$–$40_{0,40}$	*a*	241373.340(32)	40.8	245.9						
	$41_{1,41}$–$40_{0,40}$	*b*	241373.340(32)	39.6	245.9						

[a] The 2 σ frequency uncertainty is given in parentheses. These numbers refer to the last digits shown. For example, 130346.775(13) would be read as 130346.775 $\pm$ 0.013.
[b] This is the V_{LSR} and uncertainty listed by Kuan et al. (2003).
[c] This is the T_R^* and rms noise level listed by Kuan et al. (2003).
[d] "U interloper" indicates that there was an unidentified interloper.
[e] "ID interloper" indicates that there was an identified interloper.
[f] "Not observed" indicates that no observations were made toward this source for this transition.
[g] "Not detected" indicates that this line toward this source was not detected but should have been (the predicted signal should have been more than 3 σ).
[h] "Not detected (S/N)" indicates that this line toward this source was not detected because its predicted strength should have been below 3 σ.

In equation (1), $W_T = \int T_R\, dv$ in K km s^{-1}, where T_R is the radiation temperature of the source and dv is the FWHM line width. The value of T_R is related to the measured antenna temperature T_R^* (corrected for atmospheric attenuation, rear spillover, blockage, ohmic losses, and forward spillover) by $T_R = T_R^*/\eta_C$, where η_C is the source-beam coupling efficiency (Kutner & Ulich 1981). Other terms in equation (1) are the rotational partition function Z, the upper rotational energy level E_u, the rotational temperature $T_{\rm rot}$, the line strength S, the square of the dipole moment μ^2 in debye^2, and the frequency ν in GHz. If the source is comparable to or smaller than the main beam, $\eta_C = \eta_M^* B$, where η_M^* is the corrected main-beam efficiency, the fraction of power in the main beam relative to the power in the main beam plus the error beam (Jewell 1990). Here B is the geometric coupling efficiency between the main beam and the source, often called the beam filling factor. Note that η_M^* is related to the phase errors of the reflector surface and is thus a function of frequency. For example, for the NRAO 12 m telescope, $\eta_M^* = 0.83$ at 113 GHz and 0.45 at 240 GHz. The above formalism is applicable to sources with angular extent smaller than or on the order of the main beam. Highly extended sources may couple with some or all of the error beam and require a different source-beam convolution.

For a circular Gaussian telescope beam size Θ_b centered on the peak of a circular Gaussian source of size Θ_s, the resulting convolution yields a beam filling factor B given by (e.g., see eq. [28] of Ulich & Haas 1976)

$$B = \frac{\Theta_s^2}{\Theta_b^2 + \Theta_s^2}. \qquad (2)$$

If $\Theta_s \gg \Theta_b$, then $B \sim 1$. When $\Theta_s \sim \Theta_b$, $B \sim 0.5$, but if $\Theta_s \ll \Theta_b$, then $B \sim \Theta_s^2/\Theta_b^2$.

Relative intensities.—Once several molecular transition assignments have been made, their relative intensities must be tested for consistency. For a source comparable to or smaller in angular size than the main beam of the telescope, the relative intensity of two single lines is determined by the corrected beam efficiencies, beam filling factors, dipole moments, line strengths, frequencies, energy levels, and rotational temperature according to equation (1) as

$$\frac{T_R^*(i)}{T_R^*(j)} = \left[\frac{\eta_M^*(i)}{\eta_M^*(j)}\right]\left(\frac{B_i}{B_j}\right)\left(\frac{\nu_i}{\nu_j}\right)\left(\frac{S_i}{S_j}\right)\left(\frac{\mu_i^2}{\mu_j^2}\right)e^{-(E_{u,i}-E_{u,j})/T_{\rm rot}}. \qquad (3)$$

Conformer I glycine has an a-type dipole moment of $\mu_a = 0.911(6)$ D [$3.039(20)\times10^{-30}$ C m] and a b-type one of $\mu_b = 0.697(10)$ D [$2.325(34)\times10^{-30}$ C m; Lovas et al. 1995]. Therefore, for a given frequency, the product $S\mu^2$ dictates that a-type transitions are stronger than b-type ones when the S-values are comparable.

A typical property of prolate asymmetric rotors such as glycine is that two low-K_{-1} a-type and two b-type transitions become degenerate as the transition frequencies increase. In this fourfold degeneracy, all four transitions have the same rest frequency and energy levels but different line strengths for the a-type and the b-type. This effect begins at $\sim$107 GHz for glycine, and it is important because the lines with this degeneracy are the most likely to be detected. The total intensity of a fourfold degenerate line at frequency ν_i is given by the sum of the four individual unresolved components, $\left[\sum_{k=1}^4 T_R^*(k)\right]_i$, and the ratio of the ith degenerate line to the jth degenerate line is given by equation (1) as

$$\frac{\left[\sum_{k=1}^4 T_R^*(k)\right]_i}{\left[\sum_{k=1}^4 T_R^*(k)\right]_j} = \left[\frac{\eta_M^*(i)}{\eta_M^*(j)}\right]\left(\frac{B_i}{B_j}\right)\left(\frac{\nu_i}{\nu_j}\right) \times \left(\frac{S_{a,i}\mu_a^2 + S_{b,i}\mu_b^2}{S_{a,j}\mu_a^2 + S_{b,j}\mu_b^2}\right)e^{-(E_{u,i}-E_{u,j})/T_{\rm rot}}. \qquad (4)$$

Similar expressions can be derived for comparing the intensity of a single glycine line to either a twofold or a fourfold degenerate glycine line.

Confirming transitions.—Once a candidate line is assigned, the assumption of optical thinness under LTE conditions allows predictions of intensities of additional confirming transitions, unless line self-absorption, maser activity, or some other mitigating effect is evident. Hence, a key test of the correctness of the assignment of a transition is that any other transitions connected by favorable transition probabilities must also be present if the relative intensity predictions lead to detectable signal levels.

The maximum line strength for a-type asymmetric rotor R-branch transitions of a molecule like glycine occurs when S approaches J', the upper level value of J. For a-type transitions, this means that the strongest transitions in a series will be those for which $J'_{K'_{-1},K'_1}$–$J_{K_{-1},K_1} = J'_{0,J'}$–$(J'-1)_{0,J'-1}$ or $J'_{1,J'}$–$(J'-1)_{1,J'-1}$. The next strongest in this series will be $J'_{1,J'-1}$–$(J'-1)_{1,J'-2}$ or $J'_{2,J'-1}$–$(J'-1)_{2,J'-2}$. For b-type transitions, the maximum line strength occurs when S approaches $J'-1$. Here the strongest transitions will be $J'_{0,J'}$–$(J'-1)_{1,J'-1}$ or $J'_{1,J'}$–$(J'-1)_{0,J'-1}$. The next strongest will be $J'_{1,J'-1}$–$(J'-1)_{2,J'-2}$ or $J'_{2,J'-1}$–$(J'-1)_{1,J'-2}$. Note that a-type transitions follow radiative selection rules in which the parity change of the quantum numbers K_{-1}, K_1 in a transition is $e,e \leftrightarrow e,o$ (even, even $\leftrightarrow$ even, odd) or $o,o \leftrightarrow o,e$, while the b-type transitions obey $e,e \leftrightarrow o,o$ or $e,o \leftrightarrow o,e$ (see, e.g., Townes & Schawlow 1975, p. 94).

4. AN EXAMINATION OF THE DATA

Kuan et al. (2003) state that their 27 glycine lines (Table 1) are detected in one or more hot molecular cores (HMCs). We note that HMCs are compact objects in which interferometric measurements have shown that structurally similar but simpler large molecules are concentrated with diameters <10″. For example, the diameter of the HMC of one of their sources, Sgr B2(N-LMH), is $\sim$4″ as measured in ethyl cyanide (CH_3CH_2CN) and vinyl cyanide (CH_2CHCN) by Liu & Snyder (1999). On the other hand, Kuan et al. (2003) assume that their HMC glycine lines are optically thin and in LTE and do not correct for beam dilution in their rotational temperature diagrams—a tacit assumption that their glycine sources are extended enough to at least fill their beam. In the case of Orion KL, they speculated that the glycine emission is extended because the rotational temperature diagram has a "tight fit" and, in addition, perhaps the emission is not perfectly centered at the nominal compact ridge position. They used this scenario to reject the Orion glycine negative results found by Combes et al. (1996) with the IRAM 30 m telescope, because the narrower 30 m beam might have missed a significant portion of the glycine emission observed by the wider NRAO 12 m beam.

We note that equation (1) of Kuan et al. (2003) is basically the same as equation (23) of Goldsmith & Langer (1999) if the gas is assumed to be optically thin in LTE. The resulting column density is called the "beam-averaged total column density." However, equation (38) of Goldsmith & Langer (1999) shows that equation (1) is actually based on the further assumption that each glycine source fills the beam at each of the reported glycine frequencies. Otherwise, the derived glycine beam-averaged total column densities and rotational excitation temperatures have little physical meaning; they just become numerical parameters of a least-squares fit with little predictive value. How can the condition that the reported glycine sources fill each beam be satisfied? Kuan et al. (2003) state that their HPBWs are $\sim 30''$, $45''$, and $60''$ at 1.3, 2, and 3 mm, respectively. Table 1 of Kuan et al. (2003) lists the 2 mm lines (starting with glycine line 1) as the lowest frequency glycine lines that they claim. Thus, these lines would determine the smallest extent ($\sim 45''$) that the reported glycine could have in equation (1) of Kuan et al. (2003) without suffering from beam dilution. Consequently, in our analysis we used $45''$ as our upper limit for our trial source size. In the following sections, we apply the criteria from § 3 to examine available observational data for the possibility that the spectral lines assigned to glycine have been misidentified. In order to address the ambiguities introduced by the glycine source sizes, we assume two cases: (1) the glycine emission sources are HMCs with core diameters typically $<10''$; or (2) glycine fills the beam of the 12 m telescope and hence is extended over at least $45''$ in each source. For our analysis we use our newly determined astronomical rest frequencies listed in Table 1.

4.1. *VLA Searches for Glycine in Compact Sources: Orion and Sgr B2(N-LMH)*

In 2001, Hollis et al. (2003b) conducted a deep Q-band ($\lambda \sim$ 7 mm) search with the VLA toward OMC-1 in four rotational transitions of conformer I glycine. The J2000.0 phase center for their observations was $\alpha = 5^{\rm h}35^{\rm m}14\overset{\rm s}{.}25$, $\delta = -5°22'35\overset{''}{.}5$, which is midway between the Orion hot core source and the peak formic acid position from Liu et al. (2002). The Kuan et al. (2003) pointing position precessed from B1950.0 to J2000.0 was $\alpha = 5^{\rm h}35^{\rm m}14\overset{\rm s}{.}48$, $\delta = -5°22'36\overset{''}{.}6$ toward Orion KL. The average 12 m telescope HPBW for the Orion observations by Kuan et al. (2003) was $\sim 41''$, and the VLA primary beam is $\sim 45''$, so the difference in pointing positions is not significant. The best VLA upper limits of Hollis et al. (2003b) were for the $7_{0,7}$–$6_{0,6}$ transition at 47753.841(28) MHz with $S = 6.851$, $E_u = 8.657$ K, and synthesized telescope beam size $\Theta_b = 6''$: $\langle N_T \rangle < 8.0 \times 10^{14}$ cm^{-2} for $T_{\rm rot} = 43$ K, and $\langle N_T \rangle < 25.2 \times 10^{14}$ cm^{-2} for $T_{\rm rot} = 100$ K. Kuan et al. (2003) found $\langle N_T \rangle = 4.37 \times 10^{14}$ cm^{-2} for $T_{\rm rot} = 141$ K, which is below the upper limits of Hollis et al. (2003b) only if there is no significant beam dilution in the 12 m results for Orion KL. However, if the glycine source size is $6''$ in diameter (suggested by Hollis et al. 2003b), then the 12 m glycine column density $\langle N_T \rangle$ becomes 2.08×10^{16} cm^{-2}, which is far above the VLA upper limits.

In 2003, Hollis et al. (2003a) repeated their VLA Q-band glycine search toward Sgr B2(N-LMH). Again the results were negative, and the best upper limits were for the $7_{0,7}$–$6_{0,6}$ transition observed with a synthesized beam $1\overset{''}{.}5 \times 1\overset{''}{.}4$ in the direction of the K2 position. They reached an upper limit of $\langle N_T \rangle < 1.4 \times 10^{17}$ cm^{-2} for $T_{\rm rot} = 170$ K. In this same source, Kuan et al. (2003) reported $\langle N_T \rangle = 4.16 \times 10^{14}$ cm^{-2} for $T_{\rm rot} = 76$ K from observations with an average HPBW of $38''$. If the glycine source size is comparable to the VLA synthesized beam, then the 12 m glycine column density $\langle N_T \rangle$ becomes 2.67×10^{17} cm^{-2}, which is again above the VLA upper limits.

In summary, the VLA glycine negative results (Hollis et al. 2003b, 2003a) contradict the glycine detection reports only if the glycine sources in Orion and Sgr B2(N-LMH) are compact. However, as discussed previously, Kuan et al. (2003) assumed that their glycine emission sources are extended and at least $45''$ in diameter. In the following sections, we examine this assumption.

4.2. *Search for Glycine in Extended Sources: Orion KL*

A direct way to examine the assumption by Kuan et al. (2003) that their reported glycine line sources are extended is to use their reported results to generate predicted intensities for other glycine lines that they did not observe. These predictions can be checked against other single-element telescope observations that would be sensitive to glycine emission from extended sources. In particular, we observed interstellar acetone [$(CH_3)_2CO$] in 1995 March with the NRAO 12 m radio telescope toward Sgr B2(N) (Snyder et al. 2002). During Orion time, we searched for the nearly fourfold degenerate $J = 19$–18 glycine transitions around 113336 MHz. Our Orion KL pointing position was essentially identical to that used by Kuan et al. (2003): exactly the same right ascension and within $9''$ in declination. The NRAO 3 mm single-sideband SIS receiver had a sideband rejection of ≥ 25 dB and an effective system temperature (referenced to above the atmosphere and including rear and forward spillover efficiencies) of ~ 300 K. Chopper calibration corrected for atmospheric extinction and telescope losses, and the resulting data are on the T_R^* temperature scale (Kutner & Ulich 1981). Data were taken while position switching $30'$ in azimuth, while Kuan et al. (2003) switched by $20'$. The HPBW (FWHM) was $\sim 56''$ at 113.3 GHz. The spectrometer was the NRAO hybrid spectrometer with two 256 channel filter banks used as a backup. The hybrid spectrometer was operated with two polarization intermediate frequencies (IFs) in parallel, with 300 MHz bandwidth and 768 Hanning-smoothed channels per IF, giving an effective spectral resolution of 0.781 MHz. The filter banks were operated with two IFs in parallel, with 250 kHz resolution in one bank and 500 kHz in the other. Therefore, this system was exactly the same as that used by Kuan et al. (2003), except that they chose to use wider filters for their observations. The NRAO 12 m data were reduced using the NRAO data reduction package UniPOPS (Salter et al. 1995).[10]

The Kuan et al. (2003) pointing position toward Orion KL was $\alpha({\rm B1950.0}) = 5^{\rm h}32^{\rm m}47\overset{\rm s}{.}0$, $\delta({\rm B1950.0}) = -5°24'30\overset{''}{.}0$. Our pointing position was $\alpha({\rm B1950.0}) = 5^{\rm h}32^{\rm m}47\overset{\rm s}{.}0$, $\delta({\rm B1950.0}) = -5°24'21\overset{''}{.}0$, which in our $\sim 56''$ beam was only a negligible $9''$ difference. Table 2 summarizes our Orion KL search frequencies for the $J = 19$–18 glycine transitions and for the test lines used to check the operation of the system. The first column lists rest frequencies; the second and third list molecular identifications (when known) and rotational quantum numbers; the fourth, fifth, and sixth columns give the transition types, line strengths, and upper energy levels; and the next two columns give intensities and line widths for Orion KL. Figure 1 shows the Orion KL spectra from 113323 to 113354 MHz (centered at 113339 MHz) observed with the hybrid spectrometer on the NRAO 12 m telescope. The spectral positions of the negative results for the nearly fourfold degenerate $J = 19$–18 glycine lines (listed in Table 2) are marked by the four vertical lines. The unidentified line U113326 is on the left, and the 6_1–6_0 E_1 transition of CH_3OD is

[10] UniPOPS information is available at http://www.gb.nrao.edu/~rmaddale/140ft/unipops/unipops_toc.html.

TABLE 2

113 GHz Search Frequencies for Orion KL and W51

Rest Frequency[a] (MHz)	Molecule	Transition	Type	Line Strength S	E_u (K)	Orion KL T_R^* (mK)	Orion KL Δv (km s^{-1})	W51 e1/e2 T_R^* (mK)	W51 e1/e2 Δv (km s^{-1})
113326	U113326	...	...	...	...	36	1.6	23	2.9
113335.700 (18)	NH_2CH_2COOH	$19_{0,19}$–$18_{1,18}$	*b*	17.6	55.5	<3.7	...	<6.4	...
113336.209 (18)	NH_2CH_2COOH	$19_{1,19}$–$18_{1,18}$	*a*	18.8	55.5	<3.7	...	<6.4	...
113336.696 (18)	NH_2CH_2COOH	$19_{0,19}$–$18_{0,18}$	*a*	18.8	55.5	<3.7	...	<6.4	...
113337.205 (18)	NH_2CH_2COOH	$19_{1,19}$–$18_{0,18}$	*b*	17.6	55.5	<3.7	...	<6.4	...
113250.80 (10)[b]	CH_3OD	6_1–6_0E_1	*b*	7.8[c]	54.8	74	1.4	11	3.6

[a] The 2 σ frequency uncertainty is given in parentheses. These numbers refer to the last digits shown.
[b] Rest frequency from Kaushik et al. (1980).
[c] This is the product $S\mu^2$ in debye^2.

on the right; these two lines served as system checks. We note that U113326 is very close in frequency to the $6_{1,6}$–$6_{0,6}$ transition of ground state g-CH_3CH_2OH (gauche ethanol), which is listed in the JPL Catalog (Pickett et al. 1998) at 113325.5088 MHz.

Kuan et al. (2003) reported the detection of 15 optically thin glycine lines in the direction of Orion KL. If they were glycine, lines 1, 5, 6, 8, 9, 14, 15, 16, 17, 18, and 25 in Table 1 would be single transitions. Lines 11, 21, 24, and 26 would be fourfold degenerate. Of these 15 lines, none contained connecting confirming transitions, which would be a key test of the correctness of the glycine assignment, as discussed in § 3. Among these, we note that lines 5, 14, 15, 16, and 26 marginally meet the Rayleigh criterion for spectral resolution. By applying the discussion in § 3 and adapting equation (4) to *each* of the reported Orion glycine lines, we can use each reported line to make an independent prediction of the intensity of the nearly fourfold degenerate $J = 19$–18 glycine lines that we did not detect, as shown in Figure 1. Figure 2 shows the range of predicted intensities that we should have observed with the NRAO 12 m telescope for each of the 15 reported Orion glycine transitions emanating from a 45″ extended source. For each prediction, three different points are labeled to denote the Kuan et al. (2003) rotational temperature and its uncertainties, $T_{\rm rot} = 141^{+76}_{-37}$ K. The uncertainties for each rotational temperature point are based on the rms noise level given for each reported glycine line by Kuan et al. (2003; see Table 1). The dotted line in Figure 2 shows the 3.7 mK noise level from Figure 1. For example, Orion line 21 has a peak intensity $T_R^* = 230 \pm 10.0$ mK as observed with a 30″ beam. In Table 1, it is assigned as a degenerate quartet of two *a*-type and two *b*-type glycine lines at 206468 MHz: $35_{0,35}$–$34_{0,34}$, $35_{1,35}$–$34_{1,34}$, $35_{0,35}$–$34_{1,34}$, and $35_{1,35}$–$34_{0,34}$. If line 21 is an optically thin glycine line in LTE with a rotational temperature of 141 K, then the nearly blended $J = 19$–18 quartet would appear in Figure 1 with a peak

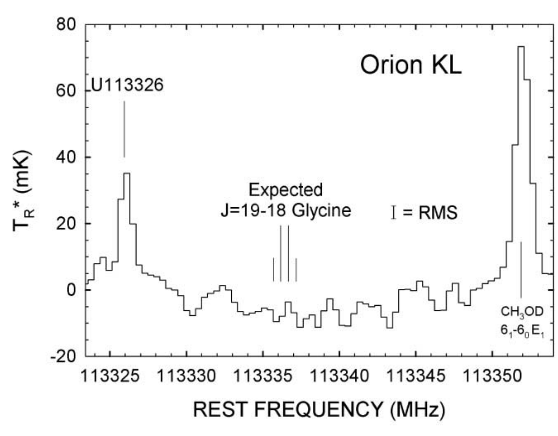

Fig. 1.—Orion KL spectra from 113323 to 113355 MHz (centered at 113339 MHz) observed with the hybrid spectrometer on the NRAO 12 m telescope. The spectral positions of the negative results for the nearly fourfold degenerate $J = 19$−18 glycine lines are marked by the four vertical lines centered at 113336 MHz. U113326 is on the left, and CH_3OD is on the right. The ordinate is in units of mK on the T_R^* scale. The abscissa is rest frequency calculated with respect to $V_{\rm LSR} = 9$ km s^{-1} (for the Orion compact ridge), except for the CH_3OD rest frequency, which is with respect to $V_{\rm LSR} = 5.6$ km s^{-1} (representative of the Orion hot core). The rms noise level for the spectral region between U113326 and CH_3OD is 3.7 mK.

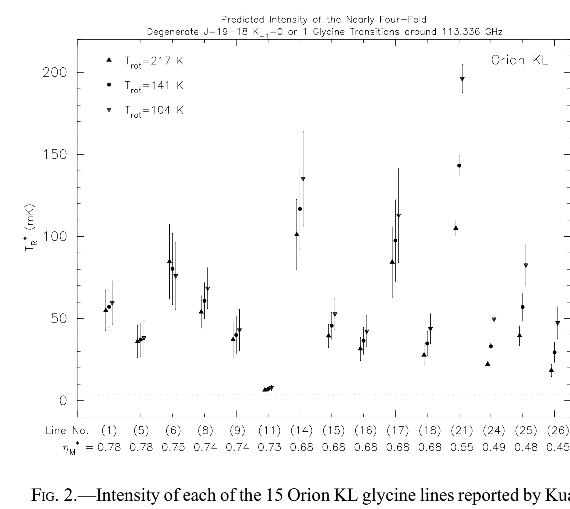

Fig. 2.—Intensity of each of the 15 Orion KL glycine lines reported by Kuan et al. (2003) was used to independently predict the intensity of the nearly fourfold degenerate $J = 19$−18 glycine lines at 113.366 GHz. A 45″ extended source of glycine was assumed. As in Fig. 1, the ordinate is in units of mK based on the T_R^* scale. The upper label for the abscissa lists the glycine line number from Table 1, and the lower one gives the corresponding main-beam efficiency η_M^* for the NRAO 12 m telescope. Each predicted intensity is calculated for the Orion rotational temperature and its uncertainties, $T_{\rm rot} = 141^{+76}_{-37}$ K, derived by Kuan et al. (2003; 217 K: *upright triangles*; 141 K: *circles*; 104 K: *inverted triangles*). The uncertainties for each rotational temperature point are based on the rms noise level given for each glycine line reported by Kuan et al. (2003; see Table 1). The dotted line shows the 3.7 mK noise level from Fig. 1. The intensities predicted from all 15 reported glycine lines show that the 19–18 glycine lines should have been detected in Orion KL, but they were not (see Fig. 1).

intensity of $T_R^* \sim 143 \pm 7$ mK for an extended source size of $\Theta_s = 45''$. All the predictions plotted in Figure 2 are above the 3.7 mK noise level from Figure 1. Hence, if the Orion reported glycine detection were correct, we should have detected a blended line with an intensity of 5 mK $\leq T_R^* \leq$ 205 mK for the $J = 19-18$ glycine quartet. Since we did not, we conclude that glycine has not been detected in an extended source in Orion KL. In § 4.1 we ruled out the detection of glycine in a compact source in Orion. Consequently, we conclude that the presence of interstellar glycine has not been verified in Orion KL.

4.3. *Search for Glycine in Extended Sources: W51*

During the 1995 March observations with the NRAO 12 m telescope, we also searched for the fourfold nearly degenerate $J = 19-18$ glycine transitions in the direction of W51. The Kuan et al. (2003) pointing position toward W51 e1/e2 was α(B1950.0) = $19^{h}21^{m}26\overset{s}{.}3$, δ(B1950.0) = $+14^\circ24'39\overset{''}{.}0$. Our W51 pointing position was α(B1950.0) = $19^{h}21^{m}26\overset{s}{.}3$, δ(B1950.0) = $+14^\circ24'43\overset{''}{.}0$, which in our $\sim 56''$ beam was only a negligible $4''$ difference. As with the Orion KL observations, our W51 data were taken while position switching $30'$ in azimuth, while Kuan et al. (2003) switched $20'$. Again, the system was exactly the same as that used by Kuan et al. (2003), except that they used wider filters. In Table 2 the last two columns give intensities and line widths for the W51 search frequencies for the $J = 19-18$ glycine transitions and for the test lines used to check the operation of the system; they are the same transitions used for the Orion KL search. Figure 3 shows the W51 spectra from 113323 to 113354 MHz (centered at 113339 MHz) observed with the hybrid spectrometer on the NRAO 12 m telescope. As in the case of Orion KL, the spectral positions of the negative results for the nearly fourfold degenerate $J = 19-18$ glycine lines (listed in Table 2) are marked by the four vertical lines centered at 113336 MHz. As in Figure 1, the system checks are the unidentified line U113326 on the left and the weak $6_1-6_0\ E_1$ transition of CH_3OD on the right.

Kuan et al. (2003) reported the detection of 16 optically thin glycine lines in the direction of W51. If these lines were glycine, lines 3, 4, 5, 7, 8, 9, 13, 15, and 25 in Table 1 would be single

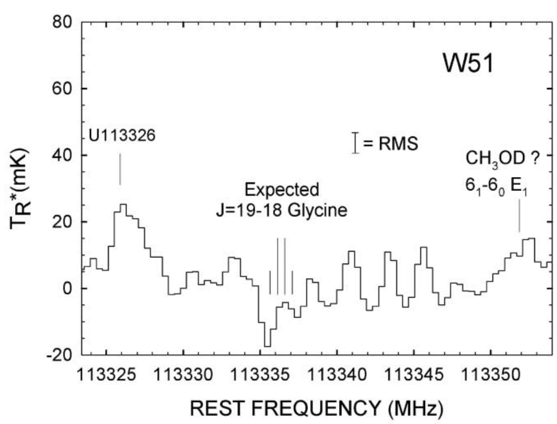

FIG. 3.—W51 spectra from 113323 to 113355 MHz (centered at 113339 MHz) observed with the hybrid spectrometer on the NRAO 12 m telescope. The spectral positions of the negative results for the nearly fourfold degenerate $J = 19-18$ glycine lines are marked by the four vertical lines centered at 113336 MHz. U113326 is on the left, and a weak emission feature from CH_3OD is on the right. As in Fig. 1, the ordinate is in units of mK on the T_R^* scale. The abscissa is rest frequency calculated with respect to $V_{LSR} = 57.1$ km s^{-1}. The rms noise level for the spectral region between U113326 and CH_3OD is 6.4 mK.

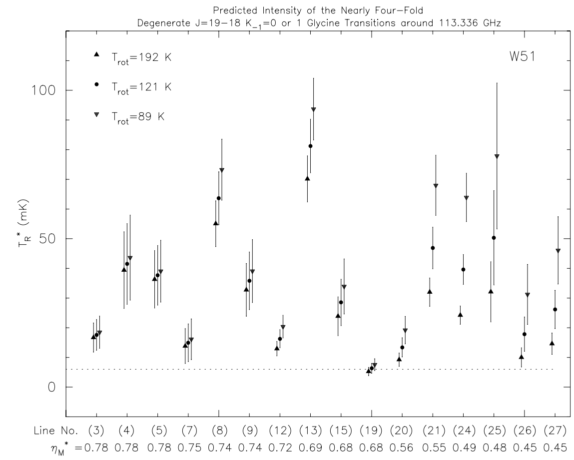

FIG. 4.—Intensity of each of the 16 W51 glycine lines reported by Kuan et al. (2003) was used to independently predict the intensity of the nearly fourfold degenerate $J = 19-18$ glycine lines at 113.366 GHz. A $45''$ extended source of glycine was assumed. As in Fig. 1, the ordinate is in units of mK based on the T_R^* scale. The upper label for the abscissa lists the glycine line number from Table 1, and the lower one gives the corresponding main-beam efficiency η_M^* for the NRAO 12 m telescope. Each predicted intensity is calculated for the W51 rotational temperature and its uncertainties, $T_{rot} = 121^{+71}_{-32}$ K, derived by Kuan et al. (2003; 192 K: *upright triangles*; 121 K: *circles*; 89 K: *inverted triangles*). The uncertainties for each rotational temperature point are based on the rms noise level given for each glycine line reported by Kuan et al. (2003; see Table 1). The dotted line shows the 6.4 mK noise level from Fig. 3. The intensities predicted from 15 of the 16 reported glycine lines show that the 19−18 glycine lines should have been detected in W51, but they were not (see Fig. 3).

transitions. Line 12 would be twofold degenerate, and lines 19, 20, 21, 24, 26, and 27 would be fourfold degenerate. Of these 16 lines, none contained connecting confirming transitions, which would be a key test of the correctness of the glycine assignment, as discussed in § 3. Among the displayed spectra, line 27 does not meet the Rayleigh criterion for spectral resolution. As with the Orion KL data, we can use the intensity of each of the reported glycine lines to independently predict the intensity of the nearly fourfold degenerate $J = 19-18$ glycine lines at 113366 MHz that we did not detect, as shown in Figure 3. Figure 4 shows the range of predicted intensities that we should have observed with the NRAO 12 m telescope for each of the 16 reported W51 glycine transitions emanating from a $45''$ extended source. As in Figure 2, three different points are labeled for each prediction to denote the Kuan et al. (2003) rotational temperature and its uncertainties, $T_{rot} = 121^{+71}_{-32}$ K. The uncertainties for each rotational temperature point are based on the rms noise level given for each reported glycine line by Kuan et al. (2003; see Table 1). The dotted line in Figure 4 shows the 6.4 mK noise level from Figure 3. All the predictions plotted in Figure 4, except those from line 19, are above this noise level. Hence, the intensities of 15 out of the 16 glycine lines predict that we should have detected a blended $J = 19-18$ glycine line quartet with an intensity of 10 mK $\leq T_R^* \leq$ 105 mK if the reported W51 glycine detection were correct. Since we did not, we conclude that the presence of interstellar glycine has not been verified in W51.

4.4. *Search for Glycine in Extended Sources: Sgr B2(N-LMH)*

Kuan et al. (2003) assigned glycine transitions to 13 emission lines in the direction of Sgr B2(N-LMH) at α(B1950.0) = $17^{h}44^{m}10\overset{s}{.}20$, δ(B1950.0) = $-28^\circ21'15\overset{''}{.}0$. Their rest frequencies were calculated with respect to $V_{LSR} = 64$ km s^{-1}. Their

TABLE 3

CONNECTED $K_{-1} = 1$ OR 2 GLYCINE TRANSITIONS IN THE NUMMELIN ET AL. (1998) SURVEY RANGE

Transition	Type	Rest Frequency[a] (MHz)	Line Strength S	E_u (K)	Predicted T_{mb} (mK)	Observed T_{mb} (mK)	Comments
$43_{2,42}$–$42_{2,41}$	*a*	258346.029 (96)	42.5	276.8	...	...	Masked by CH_3NH_2 at 258349 MHz[b]
$43_{2,42}$–$42_{1,41}$	*b*	258346.029 (96)	38.8	276.8			
$43_{1,42}$–$42_{2,41}$	*b*	258346.029 (96)	38.8	276.8			
$43_{1,42}$–$42_{1,41}$	*a*	258346.029 (96)	42.5	276.8			
$42_{2,41}$–$41_{2,40}$	*a*	252531.295 (89)	41.5	268.2	233^{+65}_{-55}	<100	
$42_{1,41}$–$41_{2,40}$	*b*	252531.295 (89)	37.8	268.2			
$42_{2,41}$–$41_{1,40}$	*b*	252531.295 (89)	37.8	268.2			
$42_{1,41}$–$41_{1,40}$	*a*	252531.295 (89)	41.5	268.2			
$41_{2,40}$–$40_{2,39}$	*a*	246716.164 (82)	40.5	256.1	265^{+58}_{-53}	<100	
$41_{2,40}$–$40_{1,39}$	*b*	246716.164 (82)	36.8	256.1			
$41_{1,40}$–$40_{2,39}$	*b*	246716.164 (82)	36.8	256.1			
$41_{1,40}$–$40_{1,39}$	*a*	246716.164 (82)	40.5	256.1			
$40_{2,39}$–$39_{2,38}$	*a*	240900.647 (76)	39.5	244.3	Standard[c]	300	Line 26[d]
$40_{1,39}$–$39_{2,38}$	*b*	240900.647 (76)	35.8	244.3			
$40_{2,39}$–$39_{1,38}$	*b*	240900.647 (76)	35.8	244.3			
$40_{1,39}$–$39_{1,38}$	*a*	240900.647 (76)	39.5	244.3			
$39_{2,38}$–$38_{2,37}$	*a*	235084.758 (70)	38.5	232.7	338^{+73}_{-68}	250	Line U235085 at 235085 MHz[b]
$39_{2,38}$–$38_{1,37}$	*b*	235084.758 (70)	34.8	232.7			
$39_{1,38}$–$38_{2,37}$	*b*	235084.758 (70)	34.8	232.7			
$39_{1,38}$–$38_{1,37}$	*a*	235084.758 (70)	38.5	232.7			
$38_{2,37}$–$37_{2,36}$	*a*	229268.511 (65)	37.5	221.4	...	...	Masked by CH_3CH_2CN at 229262 MHz[b]
$38_{1,37}$–$37_{2,36}$	*b*	229268.511 (65)	33.8	221.4			
$38_{2,37}$–$37_{1,36}$	*b*	229268.511 (65)	33.8	221.4			
$38_{1,37}$–$37_{1,36}$	*a*	229268.511 (65)	37.5	221.4			
$37_{2,36}$–$36_{2,35}$	*a*	223451.918 (60)	36.5	210.4	...	...	Masked by NH_2CHO at 223449 MHz[b]
$37_{2,36}$–$36_{1,35}$	*b*	223451.918 (60)	32.8	210.4			
$37_{1,36}$–$36_{2,35}$	*b*	223451.918 (60)	32.8	210.4			
$37_{1,36}$–$36_{1,35}$	*a*	223451.918 (60)	36.5	210.4			

[a] The 2 σ frequency uncertainty is given in parentheses. These numbers refer to the last digits shown.
[b] See Nummelin et al. (1998).
[c] The intensity of this line is the standard on which all other Table 3 and Table 4 predictions are based.
[d] Kuan et al. (2003) list this as glycine line 26.

emission lines 1, 2, 6, and 7 in Table 1 were assigned to single glycine transitions. Line 10 would have a fivefold degeneracy, and line 12, a twofold degeneracy, if they were glycine. Lines 19, 20, 21, 22, 23, 24, and 26 would be fourfold degenerate. Of these 13 lines, only lines 21 and 22 would contain connecting confirming transitions, a key test of the correctness of the assignment, as discussed in § 3. Only lines 19, 20, 21, 23, and 26 were displayed by Kuan et al. (2003); of these, lines 19, 21, and 23 marginally meet the Rayleigh criterion for spectral resolution. Fortunately, Nummelin et al. (1998) surveyed Sgr B2(N) in the direction $\alpha(\mathrm{B1950.0}) = 17^{\mathrm{h}}44^{\mathrm{m}}10^{\mathrm{s}}.10$, $\delta(\mathrm{B1950.0}) = -28°21'17''.0$ between 218.3 and 263.55 GHz with the 15 m Swedish ESO-Submillimetre Telescope (SEST). Their position coincided with the Sgr B2(N-LMH) position used by Kuan et al. (2003). Their beamwidth was $\sim 20''$ (adequate for extended sources), and their spectral resolution was $\sim$1.4 MHz, which corresponds to $\sim$1.8 km s^{-1} at 230 GHz. Their frequency range covered several important glycine transitions, which we discuss below. Rest frequencies were calculated with respect to $V_{\mathrm{LSR}} = 62$ km s^{-1}.

By applying the discussion in § 3 to predict the expected glycine intensities, it is straightforward to use the Nummelin et al. (1998) data to examine the Sgr B2(N-LMH) glycine assignments of Kuan et al. (2003). If lines 26 and 27 were glycine, for any reasonable temperature their line strengths would make them the two strongest glycine lines listed in Table 1. Line 26 was observed by Kuan et al. (2003) with the NRAO 12 m telescope to have $T_R^* = 94$ mK. It was assigned to a degenerate glycine quartet consisting of two *a*-type and two *b*-type transitions with $J = 40$–39, $K_{-1} = 1$ or 2 at 240899.5 MHz. Nummelin et al. (1998) detected this line with SEST; it has a main-beam brightness temperature $T_{\mathrm{mb}} = 300$ mK. Kuan et al. (2003) assigned line 27 to a degenerate glycine quartet with $J = 41$–40, $K_{-1} = 0$ or 1 at 241373.3 MHz. While line 27 would be expected to be slightly stronger than line 26, it was reported by Kuan et al. (2003) to be masked by unidentified interlopers in their Sgr B2(N-LMH) 12 m data, and the spectrum was not displayed. However, this interloper masking argument is not supported by the data from Nummelin et al. (1998), which show not only that the line 27 frequency falls in a relatively clear spectral region in Sgr B2(N-LMH) but also that line 27 was not detected (as we discuss below).

Nummelin et al. (1998) reported all their data in kelvins on the main-beam brightness temperature (T_{mb}) scale. Hence, η_M^*, the main-beam efficiency, has already been taken into account, and equation (4) can be used for intensity predictions with T_{mb} substituted for T_R^*/η_M^*. To conduct our analysis, we used the $T_{\mathrm{mb}} = 300$ mK intensity (with an estimated 50 mK rms noise level uncertainty) of line 26 from Nummelin et al. (1998) as a basis for predicting the intensities of those $K_{-1} = 1$ or 2 degenerate glycine quartet lines connected to line 26 via two *a*-type and two *b*-type transitions. By confining our predictions to the Nummelin et al. (1998) data set, we eliminated any problems caused by calibration differences between the NRAO 12 m and

TABLE 4

Connected $K_{-1} = 0$ or 1 Glycine Transitions in the Nummelin et al. (1998) Survey Range

Transition	Type	Rest Frequency[a] (MHz)	Line Strength S	E_u (K)	Predicted $T_{\rm mb}$ (mK)	Observed $T_{\rm mb}$ (mK)	Comments
$44_{1,44}$–$43_{1,43}$	a	258820.597 (46)	43.8	282.3	210^{+72}_{-57}	<200	Dominated by narrow noise spikes[b]
$44_{1,44}$–$43_{0,43}$	b	258820.597 (46)	42.6	282.3			
$44_{0,44}$–$43_{1,43}$	b	258820.597 (46)	42.6	282.3			
$44_{0,44}$–$43_{0,43}$	a	258820.597 (46)	43.8	282.3			
$43_{1,43}$–$42_{1,42}$	a	253005.255 (41)	42.8	269.9	240^{+68}_{-57}	<50	
$43_{0,43}$–$42_{1,42}$	b	253005.255 (41)	41.6	269.9			
$43_{1,43}$–$42_{0,42}$	b	253005.255 (41)	41.6	269.9			
$43_{0,43}$–$42_{0,42}$	a	253005.255 (41)	42.8	269.9			
$42_{1,42}$–$41_{1,41}$	a	247189.500 (36)	41.8	257.7	273^{+62}_{-57}	<100	
$42_{1,42}$–$41_{0,41}$	b	247189.500 (36)	40.6	257.7			
$42_{0,42}$–$41_{1,41}$	b	247189.500 (36)	40.6	257.7			
$42_{0,42}$–$41_{0,41}$	a	247189.500 (36)	41.8	257.7			
$41_{1,41}$–$40_{1,40}$	a	241373.340 (32)	40.8	245.9	310^{+54}_{-53}	<100	Line 27[c]; not masked by interlopers[b]
$41_{0,41}$–$40_{1,40}$	b	241373.340 (32)	39.6	245.9			
$41_{1,41}$–$40_{0,40}$	b	241373.340 (32)	39.6	245.9			
$41_{0,41}$–$40_{0,40}$	a	241373.340 (32)	40.8	245.9			
$40_{1,40}$–$39_{1,39}$	a	235556.787 (29)	39.8	234.3	...	...	Masked by CH_3CH_2CN at 235562 MHz[b]
$40_{1,40}$–$39_{0,39}$	b	235556.787 (29)	38.6	234.3			
$40_{0,40}$–$39_{1,39}$	b	235556.787 (29)	38.6	234.3			
$40_{0,40}$–$39_{0,39}$	a	235556.787 (29)	39.8	234.3			
$39_{1,39}$–$38_{1,38}$	a	229739.850 (26)	38.8	223.0	...	...	Masked by CH_3OH at 229756 MHz[b]
$39_{0,39}$–$38_{1,38}$	b	229739.850 (26)	37.6	223.0			
$39_{1,39}$–$38_{0,38}$	b	229739.850 (26)	37.6	223.0			
$39_{0,39}$–$38_{0,38}$	a	229739.850 (26)	38.8	223.0			
$38_{1,38}$–$37_{1,37}$	a	223922.537 (23)	37.8	211.9	...	...	Masked by CH_3CH_2CN at 223932 MHz[b]
$38_{1,38}$–$37_{0,37}$	b	223922.537 (23)	36.6	211.9			
$38_{0,38}$–$37_{1,37}$	b	223922.537 (23)	36.6	211.9			
$38_{0,38}$–$37_{0,37}$	a	223922.537 (23)	37.8	211.9			

[a] The 2 σ frequency uncertainty is given in parentheses. These numbers refer to the last digits shown.
[b] See Nummelin et al. (1998).
[c] Kuan et al. (2003) list this as glycine line 27.

SEST telescopes. Table 3 lists all the $K_{-1} = 1$ or 2 degenerate glycine lines that fall in the 218.3–263.55 GHz range of the Nummelin et al. (1998) survey that would be radiatively connected to line 26 if its assignment to the degenerate glycine quartet of two a-type and two b-type transitions with $J = 40$–39, $K_{-1} = 1$ or 2 were correct. The first column lists the individual quantum numbers of each degenerate frequency group, the second lists the transition type, and the third lists the rest frequency of each degenerate glycine line. Note that the line quartets are arranged in descending order of frequency. The top transition in each degenerate quartet feeds directly into the top transition in the next lower frequency degenerate quartet, the second transition in each degenerate quartet feeds directly into the second transition in the next lower degenerate quartet, etc. The fourth column in Table 3 gives the line strengths, and the fifth, the upper state energy levels. The next column gives the predicted values of $T_{\rm mb}$ for each line if the assignment of line 26 to the $J = 40$–39, $K_{-1} = 1$ or 2 degenerate glycine transition at 240899.5 MHz were correct. These predicted $T_{\rm mb}$ values (as well as the values for the upper and lower error bars) were calculated for a gas rotational temperature of 75 K with an uncertainty ranging from 59 to 104 K (Kuan et al. 2003) in addition to the 50 mK rms noise level uncertainty for line 26. The next column lists what was observed by Nummelin et al. (1998) at each frequency: the peak $T_{\rm mb}$ value for any clearly resolved line, the upper limit to the noise level if no line is present, or an ellipsis indicating that the line is masked by the wings of an interloper line. The final column in Table 3 lists relevant comments, if any, for each observed frequency. Table 4 follows the format of Table 3 for the stronger $K_{-1} = 0$ or 1 degenerate glycine lines that fall in the same range as the Nummelin et al. (1998) survey. Again, the predicted intensities in Table 4 are based on the observed intensity of $T_{\rm mb} = 300$ mK for line 26 (with an estimated 50 mK rms noise level uncertainty) and the assumption that it can be assigned to glycine.

An examination of Table 3 shows that the $K_{-1} = 1$ or 2 frequencies of the degenerate glycine quartets $J = 43$–42, 38–37, and 37–36 are obscured by the wings of lines previously identified by Nummelin et al. (1998). U235.085 at 235085 MHz would be a possible candidate for the $J = 39$–38, $K_{-1} = 1$ or 2 degenerate glycine transition at 235084.8 MHz, but the peak intensity is too low. Finally, the glycine lines missing from the Nummelin et al. (1998) data at the $\sim$100 mK level are the $K_{-1} =$ 1 or 2 frequencies of the degenerate glycine quartets $J = 42$–41 at 252531.295 MHz and 41–40 at 246716.164 MHz. The data for these missing lines and for line 26 at 240900.647 MHz are shown in Figures 5a, 5b, and 5c, adapted from the Sgr B2(N) data and molecular assignments of Nummelin et al. (1998).

Table 4 shows that the $K_{-1} = 0$ or 1 frequencies of the degenerate glycine quartets $J = 40$–39, 39–38, and 38–37 are obscured by the wings of lines previously identified by Nummelin et al. (1998). In addition, the spectral region around the degenerate glycine transition $J = 44$–43 at 258820.597 MHz is dominated by what appear to be narrow, weak interference spikes in the Nummelin et al. (1998) data for Sgr B2(N), Sgr B2(M), and Sgr B2(NW). The $K_{-1} = 0$ or 1 glycine lines missing from the

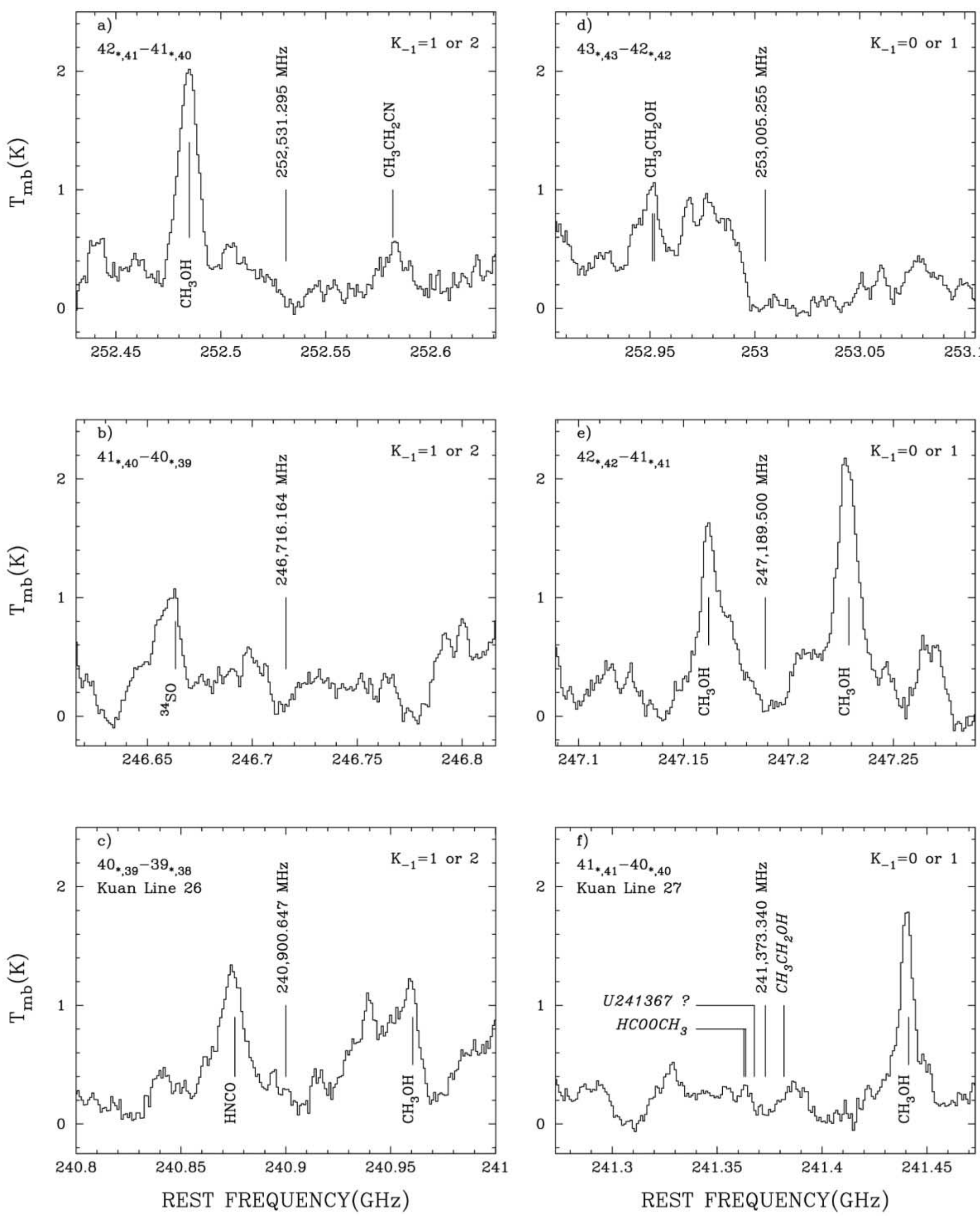

FIG. 5.—This figure is adapted from the Sgr B2(N) data and molecular assignments given by Nummelin et al. (1998). (*a*) Nummelin et al. (1998) data for the missing glycine lines for the $K_{-1} = 1$ or 2 frequencies of the fourfold degenerate glycine quartet $J = 42-41$ at 252531.295 MHz. (*b*) Missing fourfold degenerate glycine quartet $J = 41-40$ at 246716.164 MHz. (*c*) Data for line 26 of Kuan et al. (2003), which is reported to be the fourfold degenerate glycine quartet $J = 40-39$ at 240900.647 MHz. (*d*) Data for the missing glycine lines for the $K_{-1} = 0$ or 1 frequencies of the fourfold degenerate glycine quartet $J = 43-42$ at 253005.255 MHz. (*e*) Missing fourfold degenerate glycine quartet $J = 42-41$ at 247189.500 MHz. (*f*) Missing fourfold degenerate glycine quartet $J = 41-40$ at 241373.340 MHz (line 27 of Kuan et al. 2003).

Nummelin et al. (1998) data at the $\sim$50 mK level are the $J =$ 43–42 degenerate quartet at 253005.255 MHz. Furthermore, the $J = 42$–41 degenerate quartet at 247189.500 MHz and the $J = 41$–40 degenerate quartet at 241373.340 MHz (line 27 of Kuan et al. 2003) are missing at the $\sim$100 mK level. The data for these missing lines are shown in Figures 5*d*, 5*e*, and 5*f*. Because of the five missing key quartets summarized in Tables 3 and 4 and shown in Figure 5, we conclude that glycine has not been detected in an extended source in Sgr B2(N). In § 4.1 we ruled out the detection of glycine in a compact source in Sgr B2(N-LMH). Thus, we conclude that the presence of interstellar glycine has not been verified in Sgr B2(N).

4.5. *Alternative Identifications*

Now that we have shown that the carriers of key spectral lines assigned to glycine by Kuan et al. (2003) cannot be verified

TABLE 5

Other Candidates for Some of the Reported Glycine Lines

Line Number	Search Frequency[a] (MHz)	Glycine Frequency[a] (MHz)	Possible Carrier	Transition	Carrier Rest Frequency[a] (MHz)
		Lines Reported in Sgr B2(N-LMH), Orion KL, and W51 e1/e2			
21	206468.023(1694)	206468.453(17)	CH_3CH_2CN	$23_{6,18}$–$22_{6,17}$ A $\nu_b = 1$	206467.172(7)[b]
21	206468.023(1694)	206468.453(17)	CH_3CH_2CN	$23_{6,17}$–$22_{6,16}$ A $\nu_b = 1$	206467.307(7)[b]
24	228418.243(1100)	228419.435(104)	CH_2CHCN	$24_{11,13/14}$– $23_{11,12/13}$ $\nu_{15} = 1$	228418.10(17)[c]
24	228418.836(1100)	228420.029(104)			
24	228419.333(1100)	228420.526(104)			
24	228419.927(1100)	228421.120(104)			
26	240899.571(1908)	240900.647(76)	Compact source (see text)		
		Lines Reported in Both Sgr B2(N-LMH) and W51 e1/e2			
12	150909.783(166)	150909.703(20)	CH_2DCH_2CN	$4_{3,1}$–$3_{2,2}$	150910.45(12)[d]
12	150909.784(166)	150909.703(20)			
		Lines Reported Only in Sgr B2(N-LMH)			
10	147811.758(304)	147812.030(17)	g-CH_3CH_2OH	$21_{4,17}$–$20_{5,16}$	147815.83(2)[d]
10	147812.896(304)	147813.168(17)			
10	147813.913(304)	147814.186(17)			
10	147814.763(316)	147815.031(14)			
10	147815.051(304)	147815.324(17)			
		Lines Reported Only in Orion KL			
16	164870.010(394)	164870.438(30)	$(CH_3)_2CO$	$31_{12/13,19}$–$31_{11/12,20}$ EE	164870.14(18)[e]
		Lines Reported Only in W51 e1/e2			
13	160153.458(266)	160153.431(30)	H_2C_2O	$8_{1,8}$–$7_{1,7}$	160142.1[d, f]
13	160153.458(266)	160153.431(30)	CH_2CHCN	$35_{6,29}$–$36_{5,32}$ $\nu_{15} = 1$	160154.8(52)[g]
13	160153.458(266)	160153.431(30)	$(CH_3)_2CO$	$21_{3,18}$–$21_{2,19}$ AE, EA	160155.80(10)[e]

[a] The 2 σ frequency uncertainty is given in parentheses. These numbers refer to the last digits shown.
[b] Rest frequency from J. C. Pearson (2003, private communication).
[c] Rest frequency from Lovas (2004).
[d] Rest frequency from Pickett et al. (1998).
[e] Rest frequency from Groner et al. (2002).
[f] Identified in Orion by Lee & Cho (2002).
[g] Rest frequency from F. J. Lovas (2004, private communication).

as interstellar glycine, in this section we suggest some logical assignments to other, more common species. Our proposed carriers, listed in Table 5, are presented to underline the impact of line confusion on the growing and difficult problem of identifying new interstellar species. The first and second columns in Table 5 list the line number and rest frequency for glycine taken from Kuan et al. (2003). We list these older, less accurate glycine frequencies because they were the only rest frequencies reported by Kuan et al. (2003) for their detected lines. They reported that for most of their observations, filter bank spectrometers with 1 and 2 MHz resolution were used in parallel mode, but filter banks of 1 MHz and 500 kHz resolution were used for all observations taken from 2000 December to 2001 March. However, it is not always clear which spectral resolution applies to each reported glycine line, since most of their data were not displayed. Therefore, unless otherwise stated, we assume a minimum uncertainty of 1 MHz on top of the 2 σ computational uncertainty in the reported rest frequency of each line. For convenient comparison, the third column in Table 5 lists our newer, more accurate glycine frequencies taken from Table 1 of this paper. The fourth, fifth, and sixth columns list the possible molecular candidates, their quantum numbers, and the rest frequencies of their transitions, respectively. In § 1 we pointed out that one of the peculiarities in the glycine detection report by Kuan et al. (2003) was that each of their three glycine sources [Orion KL, W51 e1/e2, and Sgr B2(N-LMH)] was observed to contain no more than 13–16 of the 27 independent spectral line features and that only three of the 27 spectral line features were found to be common to all three sources: lines 21, 24, and 26 in Table 1. Consequently, we begin with a discussion of these lines. Line 21 was observed with the NRAO 12 m telescope with a 30″ beam and was misassigned to the four-fold degenerate glycine quartet $35_{0,35}$–$34_{1,34}$, $35_{1,35}$–$34_{1,34}$, $35_{0,35}$–$34_{0,34}$, and $35_{1,35}$–$34_{0,34}$ at 206468 MHz. In all three sources, line 21 is anomalously strong relative to all other purported glycine transitions that were observed. This suggests that even in the unlikely event that all the other lines reported by Kuan et al. (2003) belong to the same species, line 21 most likely belongs to another molecular species altogether. Recently, vibrationally excited ethyl cyanide (CH_3CH_2CN) has been shown to be a common constituent of Sgr B2(N-LMH) (Mehringer et al. 2004). Furthermore, the $23_{6,18}$–$22_{6,17}$ A and E and $23_{6,17}$–$22_{6,16}$ A and E transitions of vibrationally excited ethyl cyanide ($\nu_b = 1$) span the range of 206466.6–206467.3 MHz (J. C. Pearson 2003, private communication). Of particular interest are the

$23_{6,18}$–$22_{6,17}$ *A* and $23_{6,17}$–$22_{6,16}$ *A* transitions listed in Table 1, because they are at most only 0.85 MHz (1.3 km s^{-1}) away from the assumed glycine search frequency of Kuan et al. (2003). Therefore, we suggest that a possible carrier of line 21 is vibrationally excited ethyl cyanide. If this suggestion is correct, the slightly weaker ethyl cyanide $23_{6,18}$–$22_{6,17}$ *E* and $23_{6,17}$–$22_{6,16}$ *E* ($\nu_b = 1$) transitions at 206466.623(8) MHz and 206466.939(7) MHz, respectively, are blended into the low-frequency shoulder of line 21 in Sgr B2(N-LMH), Orion KL, and W51 e1/e2 (see Figs. 1*a*, 1*b*, and 1*c* of Kuan et al. 2003).

Line 24 was misassigned to the nearly fourfold degenerate glycine quartet $36_{3,33}$–$35_{4,32}$, $36_{4,33}$–$35_{4,32}$, $36_{3,33}$–$35_{3,32}$, and $36_{4,33}$–$35_{3,32}$ at an average observed frequency of 228419.1 MHz. Kuan et al. (2003) dismissed the frequency coincidence of the $J = 24$–23, $K_{-1} = 11$ transition doublet of vinyl cyanide (CH_2CHCN) as an "unlikely" $\nu = 2$ state of the molecule. However, these transitions are actually in the out-of-plane bending mode, $\nu_{15} = 1$, which Nummelin & Bergman (1999) have shown to be the carrier of 45 lines of vinyl cyanide in Sgr B2(N) (including the vinyl cyanide doublet, which was misassigned as line 24 of glycine). In their Table 40, Nummelin et al. (1998) list the rest frequency of the vinyl cyanide doublet as 228417.8 MHz, but a new calculation by Lovas (2004) gives 228418.10(17) MHz. As shown in Table 5, the new vinyl cyanide rest frequency is only ~1 MHz away from the search frequency that was used by Kuan et al. (2003) for glycine, but it is ~2 MHz away from the new average glycine rest frequency.

The third key line, line 26, was misassigned to the fourfold degenerate glycine quartet $40_{1,39}$–$39_{2,38}$, $40_{2,39}$–$39_{2,38}$, $40_{1,39}$–$39_{1,38}$, and $40_{2,39}$–$39_{1,38}$ at an average observed frequency of 240899.6 MHz, whereas the actual glycine frequency is 1.1 MHz higher (see Table 5). The Sgr B2(N) data for line 26 have been published by both Kuan et al. (2003) in their Figure 1*d* and by Nummelin et al. (1998) in their Figure 1. We note that line 26 has the same flux (~6 Jy) in the ~20″ beam of Nummelin et al. (1998) as it has in the ~26″ beam of Kuan et al. (2003). This suggests that the carrier of line 26 could also be a constituent of a somewhat compact source, such as a hot molecular core.

In addition to lines 21, 24, and 26, there are potential carriers for other reported glycine lines that were detected in only one or two of the three reported glycine sources. Several potentially viable alternative identifications were listed by Kuan et al. (2003) as possible line carrier candidates but dismissed without further consideration. These worthy candidates are discussed in order by source and are listed in the remaining sections of Table 5.

Line 12, reported in Sgr B2(N-LMH) and W51 e1/e2, was misassigned to the degenerate glycine pair $22_{12,11}$–$21_{12,10}$ and $22_{12,10}$–$21_{12,9}$ at an observed frequency of 150909.8 MHz. CH_2DCH_2CN (Table 5) was considered and dismissed by Kuan et al. (2003) because of the combination of rare isotopic species (D) and an unlikely transition. However, because of the close frequency coincidence, it cannot be completely eliminated from consideration without further observation of comparable transitions of that species. Line 10, observed only in Sgr B2(N-LMH), was misassigned to the cluster of glycine lines $24_{1,23}$–$23_{2,22}$, $24_{2,23}$–$23_{2,22}$, $24_{1,23}$–$23_{1,22}$, $22_{3,19}$–$21_{3,18}$, and $24_{2,23}$–$23_{1,22}$ at an average center frequency of 147813.7 MHz (Table 5). Kuan et al. (2003) recognized the possibility of overlap with the $21_{4,17}$–$20_{5,16}$ transition of CH_3CH_2OH (ethanol), but they misidentified it as a $\nu = 1$ vibrationally excited state of ethanol and hence removed it from consideration as a possible identification. The correct assignment is to g-CH_3CH_2OH (gauche ethanol) in the ground state (Table 5), so ethanol should remain in consideration as a possible carrier of line 10.

Line 16, reported only in Orion KL, was misassigned to the $26_{2,24}$–$25_{2,23}$ transition of glycine at 164870.0 MHz (Table 5). This line is shown to be barely above the noise level by Kuan et al. (2003) in their Figure 3. They recognized that the frequency of line 16 agrees almost perfectly with the degenerate transitions of $(CH_3)_2CO$ (acetone) listed in Table 5, but dismissed this possibility because the transitions are unfavorable. However, because of the close frequency agreement and the low intensity of line 16, there is no strong basis for ignoring acetone without further observations.

Line 13, reported only in W51 e1/e2, was misassigned to the $23_{6,18}$–$22_{6,17}$ transition of glycine at 160153.458(266) MHz (Table 5). Line 13 was not reported in either Sgr B2(N-LMH) or Orion, but the detection of U160144 was listed instead. No spectra of line 13 or U160144 were displayed by Kuan et al. (2003). Thus, it is fortunate that Lee & Cho (2002) used the Taeduk Radio Astronomy Observatory (TRAO) 14 m telescope to conduct an Orion survey over this frequency range. They detected and identified the $8_{1,8}$–$7_{1,7}$ transition of H_2C_2O (ketene) at 160142 MHz, with a high-frequency shoulder. An examination of their published spectra leaves no doubt that U160144 in Orion is ketene, and the high-frequency shoulder (which extends to almost 160160 MHz) includes the frequency of line 13. A further complication is that line 13 is almost coincident with transitions of both vinyl cyanide (CH_2CHCN) and acetone [$(CH_3)_2CO$; see Table 5]. The vinyl cyanide line was considered and ruled out by Kuan et al. (2003) because it appeared to be an unfavorable transition in the $\nu = 2$ vibrational state. However, it is actually in the $\nu_{15} = 1$ state. Thus, we have listed several possibilities for line 13: it could be a velocity component of ketene, it could be acetone, it could be vinyl cyanide, or it could be a partial mixture of these and unknown components. An observational check on these possibilities would be straightforward.

There are probably other good alternative identifications for the additional lines reported by Kuan et al. (2003), because of the plethora of transitions from ground and excited states of many common interstellar molecules. For example, deep searches for acetone have only been conducted in Sgr B2(N) (Snyder et al. 2002), but acetone may well be detectable in Orion KL and W51 e1/e2 at the levels cited by Kuan et al. (2003). Certainly most of the good alternative candidates for lines reported as glycine are more likely to be detectable than glycine, and the identification of these candidates can be checked by further observational work on other favorable transitions.

5. ROTATIONAL TEMPERATURE DIAGRAM LIMITATIONS

In a given spectral range for a given source, it is our intention to demonstrate that one can use random unidentified (U) line data that are nearly frequency coincident with glycine transitions to obtain a reasonable-looking rotational diagram. The results of the rotation diagram are then used to show that the most likely glycine transitions (particularly *a*-type with large transition strengths) are either severely lacking in predicted intensity or altogether missing in the given spectral range.

Kuan et al. (2003) used rotation temperature diagrams constructed from Sgr B2(N-LMH), Orion KL, and W51 e1/e2 data to bolster their arguments for the identification of glycine. In the Appendix, we have noted that rotational temperature diagrams cannot be used as independent tools to verify interstellar spectral line identifications, because the frequency parameter in equation (A4) or (A5) will dominate the integrated intensity, line strength, and dipole moment terms for typical spectral line data in the millimeter or submillimeter range. In the following

TABLE 6

Incorrectly Assigned Glycine Transitions Used to Create the Rotational Temperature Diagram

Calculated Glycine Frequency[a] (MHz) (1)	Corresponding Glycine Transition (2)	$S\mu^2$ (debye^2) (3)	E_u (K) (4)	Nearly Frequency Coincident U Line (MHz) (5)	U Line[b] $\int \Delta I\,dv$ (Jy beam^{-1} km s^{-1}) (6)	Beam $\theta_a \times \theta_b$ (arcsec × arcsec) (7)
86210.408(367)........	$19_{7,13}$–$19_{6,14}$	5.1	79.0	U86207.8	7.1(16)	23.9 × 6.6
86440.861(1000)......	$32_{9,23}$–$32_{8,24}$	10.4	202.5	U86440.2	9.5(28)	24.1 × 7.0
86885.889(19)..........	$12_{3,9}$–$11_{3,8}$	9.4	29.4	. . .	<1.9[c]	25.7 × 6.5
89735.673(344)........	$26_{7,20}$–$26_{6,21}$	7.4	132.9	U89731.9	6.8(23)	30.9 × 6.3
89831.975(10)..........	$14_{1,13}$–$13_{1,12}$	11.2	34.4	U89829.6	5.0(17)	23.8 × 6.2
89875.703(14)..........	$13_{5,9}$–$12_{5,8}$	9.2	38.3	. . .	<2.4[d]	24.5 × 6.2
90035.981(16)..........	$15_{0,15}$–$14_{1,14}$	6.6	35.4	U90033.9	12.3(29)	23.4 × 6.6
90043.198(16)..........	$15_{1,15}$–$14_{1,14}$	12.3	35.4	. . .	<1.8[e]	23.4 × 6.6
90049.762(16)..........	$15_{0,15}$–$14_{0,14}$	12.3	35.4	. . .	<1.8[e]	23.4 × 6.6
90056.979(16)..........	$15_{1,15}$–$14_{0,14}$	6.6	35.4	. . .	<2.0[f]	23.8 × 6.6
90303.355(12)..........	$14_{2,13}$–$13_{1,12}$	4.6	34.4	U90304.8	2.6(14)	27.1 × 6.2
106559.495(497)......	$24_{6,18}$–$23_{7,17}$	1.6	112.8	U106559.8	5.6(22)	19.4 × 5.7
106767.076(788)......	$31_{8,24}$–$30_{9,21}$	1.7	186.2	U106763.3	3.0(15)	20.7 × 5.3
109960.322(11)........	$16_{8,9}$–$15_{8,8}$	10.0	65.9			
				U109959.6	39.1(37)	22.0 × 5.0
109961.001(11)........	$16_{8,8}$–$15_{8,7}$	10.0	65.9			
110089.888(121)......	$7_{5,3}$–$6_{4,2}$	2.2	17.5	U110085.6	28.3(49)	18.9 × 5.3
110106.688(121)......	$7_{5,2}$–$6_{4,3}$	2.2	17.5	U110104.7	19.5(41)	18.9 × 5.3

[a] The 2 σ frequency uncertainty is given in parentheses. These numbers refer to the last digits shown.
[b] Derived from data in Table 5 of Friedel et al. (2004). Limits are 1 σ; integrated intensity uncertainties are 1 σ.
[c] The $T_{\rm rot}$ diagram predicts at least a 13 σ glycine line; none detected.
[d] The $T_{\rm rot}$ diagram predicts at least a 9 σ glycine line; none detected.
[e] The $T_{\rm rot}$ diagram predicts at least a 18 σ glycine line; none detected.
[f] The $T_{\rm rot}$ diagram predicts at least a 9 σ glycine line; none detected.

discussion, we illustrate this important point. As a database, we used the 123 U lines detected in a millimeter wavelength spectral line survey conducted by Friedel et al. (2004) toward Sgr B2(N-LMH) with the Berkeley-Illinois-Maryland Association (BIMA) Array. We searched this U-line database for near frequency coincident transitions of glycine with the following criteria for matching lines:

1. The 2 σ frequency uncertainty of each calculated glycine transition had to be less than 2.82 MHz (equivalent to twice the largest 1 σ uncertainty from Kuan et al. 2003). This uncertainty turned out to be less than 1.84 MHz.
2. Friedel et al. (2004) established the rest frequency of each U line by assuming a $V_{\rm LSR}$ of 64 km s^{-1}. Kuan et al. (2003) states that an acceptable velocity range for Sgr B2(N-LMH) is between 58 and 75 km s^{-1}. Therefore, we allowed a tolerance in our U-line frequencies that corresponded to a $V_{\rm LSR}$ of 64^{+11}_{-6} km s^{-1}, with an additional uncertainty of ±390 kHz due to the spectral resolution used by Friedel et al. (2004) for the U-line observations.
3. The width of each matched U line had to be between 2.8 and 12.7 km s^{-1}, which is the spread in line widths from the data in Kuan et al. (2003) toward Sgr B2(N). There were two exceptions, but the uncertainties easily reached into this range.
4. We selected only U lines whose intensity was not too great for the associated transition. If the U line appeared to be a blend of transitions from several species, it was not used.

Table 6 lists the glycine and U-line frequencies that are used in our rotational temperature diagram discussion. The first two columns list the calculated glycine rest frequencies and corresponding transitions. The third and fourth columns list the product of the line strength and dipole moment squared ($S\mu^2$) and the upper energy (E_u) for each glycine transition. The fifth column lists U lines that were selected using the criteria listed above. The sixth and seventh columns list the U-line integrated intensity derived from Friedel et al. (2004) and the synthesized beam size employed in the observations. Table 6 shows that the frequencies of 11 U lines (col. [5]) nearly match the frequencies of 12 degenerate and nondegenerate glycine transitions (col. [1]). Under the assumption of no beam dilution, the glycine rotational temperature diagram in Figure 6 was constructed by using the glycine frequencies calculated in equation (A4). The Figure 6 data points were fitted with a straight line by a least-squares method that weighted each integrated intensity by

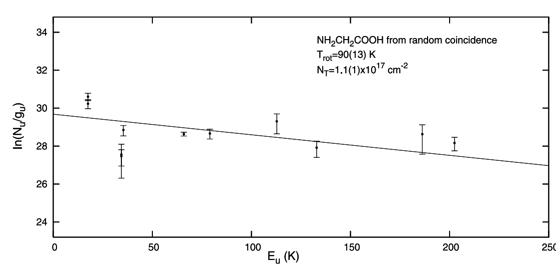

Fig. 6.—Pseudo glycine rotational temperature diagram based on U lines incorrectly assigned to glycine transitions. Table 6 U-line data (Friedel et al. 2004) were taken with the BIMA array toward Sgr B2(N-LMH) and are approximately frequency coincident with glycine transitions. The ordinate is the Naperian logarithm of the beam-averaged upper level column density, $\langle N_u \rangle$, divided by g_u, the statistical weight of the upper level $(2J+1)$; the abscissa E_u is the upper state rotational energy level for each transition. As discussed in the text, this diagram may appear to be reasonable and yield a rotation temperature in a range characteristic of the source, but it has no power to predict intensities of glycine lines, as shown in Table 6. Such a diagram cannot be used as evidence of interstellar glycine (see text).

its uncertainty, which generally resulted in smaller uncertainties in slope and intercept when compared to an unweighted least-squares fit (Bevington & Robinson 1992, p. 106). The resulting weighted fit[11] produced a rotational temperature of 90(13) K and a total column density $\langle N_T \rangle$ of $1.1(1) \times 10^{17}$ cm^{-2}. The derived rotational temperature and column density are similar to those of other molecules detected toward Sgr B2(N-LMH) at a high spatial resolution. If Figure 6 were a valid glycine rotational diagram, then the derived rotational temperature and column density parameters could be used to predict other likely (i.e., large $S\mu^2$) glycine lines in the frequency range of the Friedel et al. (2004) survey. Five such glycine transitions were contained within the survey, but none was detected. The 1 σ integrated intensity upper limits are given in column (6) of Table 6. The integrated intensity upper limits are the product of the rms noise level in units of Jy beam^{-1} and an assumed line width of 12.7 km s^{-1} (the largest line width reported by Kuan et al. 2003). Predictions for the minimum expected intensity of these five lines are included in footnotes to column (6) and range from 9 to 18 σ. These missing lines demonstrate that the Figure 6 rotational diagram purported to be glycine is based on incorrectly identified and misassigned lines.

We have produced a rotational temperature diagram that looks reasonable and gives reasonable results for U lines assumed to be glycine, but we have also demonstrated that these rotational temperature diagram results have no power to predict the intensities of other likely glycine lines. We conclude that this particular rotational diagram is the result of misassigned U lines and cannot be used as reliable independent evidence to support the interstellar molecular identification of glycine. We note that equation (A4) or (A5) will be dominated by the frequency parameter, and as a result, one can almost always construct a reasonable-looking rotational temperature diagram from any forest of weak lines spread across a large enough range in energy of a complicated asymmetric rotor molecule like glycine.

6. CONCLUSIONS

As we discussed in § 1, there are several peculiarities if the lines reported by Kuan et al. (2003) in Sgr B2 (N-LMH), Orion KL, and W51 el/e2 belong to interstellar glycine. Therefore, we examined their assignments of key glycine transitions to the spectral lines listed in Table 1. We noted that their lack of correction for beam dilution amounted to the tacit assumption that their glycine sources have an extended source size with $\Theta_s \geq 45''$. In Orion KL, we found that none of the 15 glycine line assignments could be verified, because the reported intensities of all 15 lines predict that a major glycine quartet ($J = 19$–18, $K_{-1} = 0$ or 1) should have been detected in our Orion data from the NRAO 12 m telescope (Figs. 1 and 2). Therefore, we can conclude that the Orion spectral lines reported by Kuan et al. (2003; Table 1, cols. [9] and [10]) are not glycine. Previously, the VLA data from Hollis et al. (2003b) established upper limits in Orion for compact glycine sources. Therefore, glycine has not been verified in either extended or in compact sources in Orion. In W51 el/e2, 16 lines were assigned to glycine. Fifteen of the 16 line intensities lend strength to the predictions that the $J = 19$–18, $K_{-1} = 0$ or 1 glycine quartets should have been detected in our W51 data from the NRAO 12 m telescope (Figs. 3 and 4). Since our spectra show a negative result, we can conclude that the reported W51 spectral lines are also not glycine (Table 1, cols. [11] and [12]). In the direction of Sgr B2(N-LMH), only 13 lines were assigned to glycine, but the situation is slightly more complicated by the high spectral line density. However, it can be simplified by recognizing that, on the basis of both line strength values and intensity calculations, the two strongest glycine lines should be those assigned to lines 26 and 27 in columns (7) and (8) of Table 1. Line 26 appears with a peak intensity of 300 mK in the Sgr B2(N) band scan data from Nummelin et al. (1998), but the important connected lines, $J = 42$–41 and 41–40 in the $K_{-1} = 1$ or 2 series, are missing altogether (Table 3). Furthermore, line 27 should be stronger than line 26, but it, too, is missing, along with the connected $J = 43$–42 and 42–41 lines in the $K_{-1} = 0$ or 1 series (Table 4). All of these key glycine lines strongly connect major $K_{-1} = 0$, 1, or 2 rotational levels, so their absence is not possible if the other Sgr B2(N-LMH) glycine lines are assigned correctly. Therefore, we conclude that the Sgr B2(N-LMH) spectral lines reported by Kuan et al. (2003; Table 1, cols. [7] and [8]) are not glycine. In addition, the VLA data from Hollis et al. (2003a) established upper limits for compact glycine sources in Sgr B2(N-LMH). Consequently, glycine has not been verified in Sgr B2(N-LMH) either in extended or in compact sources.

If the 27 lines reported by Kuan et al. (2003) in Orion KL, W51 el/e2, and Sgr B2(N-LMH) are not glycine, what are they? Lines 21, 24, and 26 in Table 1 are the three lines reported to be common to all three sources. We have argued that vibrationally excited ethyl cyanide (CH_3CH_2CN) is a logical assignment for line 21, and vibrationally excited vinyl cyanide (CH_2CHCN) for line 24. Line 26 could also be a constituent of a somewhat compact source. Four other reported glycine lines could be possibly assigned to more common species listed in Table 5. Beyond this, it is difficult to comment on other possible line carrier candidates, because Kuan et al. (2003) only published sample spectra for 11 of their 27 lines. Finally, we have demonstrated that rotational temperature diagrams cannot by themselves be used to identify interstellar molecules.

We are indebted to A. Nummelin for providing data from Sgr B2(N). We thank E. B. Churchwell, P. Schilke, E. C. Sutton, and W. D. Watson for helpful assistance. We appreciate the useful comments from two referees. J. M. H. gratefully acknowledges research support from H. A. Thronson, Technology Director of the NASA Office of Space Science. We acknowledge support from the Laboratory for Astronomical Imaging at the University of Illinois and NSF grants AST 99-81363 and AST 02-28953. The laboratory measurements of the glycine spectrum were supported by the Science and Technology Center in Ukraine under contract 2132.

[11] Kuan et al. (2003) constructed rotation temperature diagrams based on fits that were not weighted by the uncertainties in the integrated intensities.

APPENDIX

SOME COMMENTS ABOUT ROTATIONAL TEMPERATURE DIAGRAMS

The conventional method for forming a rotational temperature diagram is to plot the logarithm of the normalized column density versus the upper state rotational energy level. However, this approach incorporates several assumptions. First, it is assumed that each region in the interstellar cloud has uniform physical conditions and that the populations of the energy levels can be characterized by a Boltzmann distribution. Second, optically thin conditions are assumed, but it may be possible to correct for this assumption later in the analysis. Third, if it is not possible to measure the source size, it must be assumed that the source fills the observational beam. Therefore, if the population distribution can be described adequately by a single rotational temperature, and if all the lines are optically thin, the measured fluxes are proportional to the column densities in the upper levels of the transitions being observed.

For autocorrelation (single-element telescope) observations, we can start with equation (1) in § 3. For cross-correlation (interferometric array) observations, we can use (see, e.g., Snyder et al. 2001)

$$\langle N_T \rangle = \frac{2.04 W_I Z e^{E_u/T_{\rm rot}}}{B\theta_a\theta_b S\mu^2\nu^3} \times 10^{20}\ {\rm cm^{-2}}. \tag{A1}$$

In equation (A1), $W_I = \int I_\nu \, dv$ in Jy beam^{-1} km s^{-1}, and I_ν is the flux density per beam. Here Z is the rotational partition function, B is the beam filling factor, θ_a and θ_b are the FWHM synthesized beam dimensions in arcseconds, S is the line strength, μ^2 is the square of the dipole moment in debye^2, and ν is the frequency in GHz. The beam-averaged upper level column density $\langle N_u \rangle$ is defined by

$$\frac{\langle N_u \rangle}{g_u} = \frac{\langle N_T \rangle}{Z} e^{-E_u/T_{\rm rot}}, \tag{A2}$$

where g_u is the statistical weight of the upper level $(2J+1)$. A standard approach is to take the Naperian (base e) logarithm of equation (A2),

$$\ln\left(\frac{\langle N_u \rangle}{g_u}\right) = -\frac{E_u}{T_{\rm rot}} + \ln\left(\frac{\langle N_T \rangle}{Z}\right). \tag{A3}$$

Then for cross-correlation data equations (A1) and (A3) give

$$\ln\left(\frac{\langle N_u \rangle}{g_u}\right) = \ln\left(\frac{2.04 W_I \times 10^{20}}{B\theta_a\theta_b S\mu^2\nu^3}\right) = -\frac{E_u}{T_{\rm rot}} + \ln\left(\frac{\langle N_T \rangle}{Z}\right). \tag{A4}$$

A linear least-squares fit to equation (A4) can be used to construct a rotational temperature diagram in which the slope gives the negative reciprocal of the rotational temperature. This temperature can be used to estimate the total molecular column density $\langle N_T \rangle$. The rotational temperature will be equal to the kinetic temperature only at sufficiently high densities. A similar approach can be followed with equations (1) and (A2) to construct a rotational temperature diagram from autocorrelation (single-element telescope) data:

$$\ln\left(\frac{\langle N_u \rangle}{g_u}\right) = \ln\left(\frac{1.67 W_T \times 10^{14}}{S\mu^2\nu}\right) = -\frac{E_u}{T_{\rm rot}} + \ln\left(\frac{\langle N_T \rangle}{Z}\right). \tag{A5}$$

There are two more important caveats about rotational temperature diagrams that must be noted. First, if common (Briggsian) base 10 logarithms are used, the result is

$$\log_{10}\left(\frac{\langle N_u \rangle}{g_u}\right) = -\frac{E_u \log_{10} e}{T_{\rm rot}} + \log_{10}\left(\frac{\langle N_T \rangle}{Z}\right). \tag{A6}$$

This approach slightly complicates the rotational temperature term. However, it makes the data scatter appear to be smaller, since $\log_{10}(\langle N_u \rangle / g_u) = 0.434 \ln_e(\langle N_u \rangle / g_u)$. The second important caveat is that in either equation (A4) or equation (A5), the frequency parameter will dominate the integrated intensity, line strength, and dipole moment terms for typical spectral line data in the millimeter or submillimeter range. Hence, rotational temperature diagrams cannot be used as independent tools to verify interstellar spectral line identifications. This point is illustrated in § 5.

If the emission is not optically thin, the finite opacity produces an underestimate in the upper level column density of the observed transition, and it can also produce an error in the rotational temperature. Based on the discussion presented by Goldsmith & Langer (1999), the optical depth τ can be used to define an optical depth correction factor C_τ, where

$$C_\tau = \frac{\tau}{1 - e^{-\tau}} = \frac{\langle N_u \rangle}{\langle N_u^{\rm thin} \rangle}. \tag{A7}$$

From equations (A1) and (A2), we find for cross-correlation data

$$\langle N_u^{\rm thin} \rangle = \left(\frac{2.04 g_u W_I \times 10^{20}}{B\theta_a\theta_b S\mu^2\nu^3}\right)\ {\rm cm^{-2}}. \tag{A8}$$

Since $C_\tau \geq 1$, it has been described by Goldsmith & Langer (1999) as the factor by which $\langle N_u^{\rm thin} \rangle$ (derived directly from W_I) can appear to be too small because of a finite optical depth. Note that C_τ can be different for each independent transition, because τ is proportional to $S\mu^2$. For finite optical depths, we find

$$\ln\left(\frac{\langle N_u^{\rm thin}\rangle}{g_u}\right) = \ln\left(\frac{2.04 W_I \times 10^{20}}{B\theta_a\theta_b S\mu^2\nu^3}\right) = \ln\left(\frac{\langle N_T\rangle}{Z}\right) - \ln C_\tau - \frac{E_u}{T_{\rm rot}}, \tag{A9}$$

which is analogous to equation (24) of Goldsmith & Langer (1999). Clearly, $\ln C_\tau$ lowers the ordinate intensity from the optically thin value for each point on the rotational intensity diagram. We cannot calculate a realistic value of $\ln C_\tau$ for glycine, as no interstellar glycine line identification has been confirmed. However, Goldsmith & Langer (1999) modeled τ-values for methanol (an established interstellar asymmetric rotor) that ranged from 0.25 to 30. If $\tau = 30$ for a given glycine line, that point on the rotational temperature diagram would be depressed by 3.4, a significant amount. On the other hand, $\tau = 1$ would reduce the ordinate intensity by only 0.5.

REFERENCES

Berulis, I. I., Winnewisser, G., Krasnov, V. V., & Sorochenko, R. L. 1985, Soviet Astron. Lett., 11, 251
Bevington, P. R., & Robinson, D. K. 1992, Data Reduction and Error Analysis for the Physical Sciences (2d ed.; New York: McGraw-Hill)
Born, M., & Wolf, E. 1980, Electromagnetic Theory of Propagation Interference and Diffraction of Light (6th ed.; New York: Pergamon)
Brown, R. D., et al. 1979, MNRAS, 186, 5P
Ceccarelli, C., Loinard, L., Castets, A., Faure, A., & Lefloch, B. 2000, A&A, 362, 1122
Combes, F., Nguyen-Q-Rieu, & Wlodarczak, G. 1996, A&A, 308, 618
Dickens, J. E., Irvine, W. M., Ohishi, M., Ikeda, M., Ishikawa, S., Nummelin, A., & Hjalmarson, Å. 1997, ApJ, 489, 753
Friedel, D. N., Snyder, L. E., Turner, B. E., & Remijan, A. 2004, ApJ, 600, 234
Goldsmith, P. F., & Langer, W. D. 1999, ApJ, 517, 209
Groner, P., Albert, S., Herbst, E., DeLucia, F. C., Lovas, F. J., Drouin, B. J., & Pearson, J. C. 2002, ApJS, 142, 145
Guelin, M., & Cernicharo, J. 1989, in The Physics and Chemistry of Interstellar Molecules, ed. G. Winnewisser & T. Armstrong (Berlin: Springer), 337
Hollis, J. M., Pedelty, J. A., Boboltz, D. A., Liu, S.-Y., Snyder, L. E., Palmer, P., Lovas, F. J., & Jewell, P. R. 2003a, ApJ, 596, L235
Hollis, J. M., Pedelty, J. A., Snyder, L. E., Jewell, P. R., Lovas, F. J., Palmer, P., & Liu, S.-Y. 2003b, ApJ, 588, 353
Hollis, J. M., Snyder, L. E., Suenram, R. D., & Lovas, F. J. 1980, ApJ, 241, 1001
Ilyushin, V. V., et al. 2001, J. Mol. Spectrosc., 205, 286
Jenkins, F. A., & White, H. E. 1957, Fundamentals of Optics (3rd ed.; New York: McGraw-Hill)
Jewell, P. R. 1990, Users Manual for the NRAO 12 m Millimeter-Wave Telescope (Greenbank: NRAO)
Kaushik, V. K., Takagi, K., & Matsumura, C. 1980, J. Mol. Spectrosc., 82, 418
Kuan, Y.-J, Charnley, S. B., Huang, H.- C., Tseng, W.-L., & Kisiel, Z. 2003, ApJ, 593, 848
Kutner, M. L., & Ulich, B. L. 1981, ApJ, 250, 341
Lee, C. W., & Cho, S.-H. 2002, J. Korean Astron. Soc., 35, 187
Liu, S.-Y., Girart, J. M., Remijan, A., & Snyder, L. E. 2002, ApJ, 576, 255
Liu, S.-Y., Mehringer, D. M., & Snyder, L. E. 2001, ApJ, 552, 654
Liu, S.-Y., & Snyder, L. E. 1999, ApJ, 523, 683
Lovas, F. J. 2004, J. Phys. Chem. Ref. Data, 33, 177
Lovas, F. J., Kawashima, Y., Grabow, J.-U., Suenram, R. D., Fraser, G. T., & Hirota, E. 1995, ApJ, 455, L201
Mehringer, D. M., Pearson, J. C., Keene, J., & Phillips, T. G. 2004, ApJ, 608, 306
Nummelin, A., & Bergman, P. 1999, A&A, 341, L59
Nummelin, A., Bergman, P., Hjalmarson, Å., Friberg, P., Irvine, W. M., Millar, T. J., Ohishi, M., & Saito, S. 1998, ApJS, 117, 427
Pickett, H. M., Poynter, R. L., Cohen, E. A., Delitsky, M. L., Pearson, J. C., & Muller, H. S. P. 1998, J. Quant. Spectrosc. Radiat. Transfer, 60, 883
Reid, M. J., & Moran, J. M. 1988, in Galactic and Extragalactic Radio Astronomy, ed. G. L. Verschuur & K. I. Kellerman (Berlin: Springer), 255
Remijan, A., Snyder, L. E., Friedel, D. N., Liu, S.-Y., & Shah, R. Y. 2003, ApJ, 590, 314
Remijan, A., Snyder, L. E., Liu, S.-Y., Mehringer, D., & Kuan, Y.-J. 2002, ApJ, 576, 264
Rohlfs, K., & Wilson, T. L. 2000, Tools of Radio Astronomy (3rd ed.; Berlin: Springer)
Salter, C., Maddalena, R. J., & Garwood, B. 1995, The UniPOPS Cookbook (Greenbank: NRAO)
Snyder, L. E. 1997, Origins Life Evol. Biosphere, 27, 115
Snyder, L. E., Hollis, J. M., Suenram, R. D., Lovas, F. J., Brown, L. W., & Buhl, D. 1983, ApJ, 268, 123
Snyder, L. E., Lovas, F. J., Mehringer, D. M., Miao, N. Y., Kuan, Y.-J., Hollis, J. M., & Jewell, P. R. 2002, ApJ, 578, 245
Snyder, L. E., et al. 2001, AJ, 121, 1147
Sommerfeld, A. 1964, Optics (New York: Academic Press)
Suenram, R. D., & Lovas, F. J. 1980, J. Am. Chem. Soc., 102, 7180
Taylor, B. N., & Kuyatt, C. E. 1994, NIST Tech. Note 1297 (Washington: GPO)
Townes, C. H., & Schawlow, A. L. 1975, Microwave Spectroscopy (New York: Dover)
Ulich, B. L., & Haas, R. W. 1976, ApJS, 30, 247
Watson, J. K. G. 1977, in Vibrational Spectra and Structure, Vol. 6, ed. J. R. Durig (Amsterdam: Elsevier), 19

Appendix G

A Survey of Large Molecules Toward the Proto-Planetary Nebula CRL 618

By

Anthony J. Remijan, Friedrich Wyrowski, Douglas N. Friedel, David S. Meier, & Lewis E. Snyder

2005 ApJ 626, 233

The Astrophysical Journal, 626:233–244, 2005 June 10

A SURVEY OF LARGE MOLECULES TOWARD THE PROTO–PLANETARY NEBULA CRL 618

Anthony J. Remijan,[1,2,3] Friedrich Wyrowski,[4] Douglas N. Friedel,[1] David S. Meier,[1] and Lewis E. Snyder[1]
Received 2005 January 11; accepted 2005 February 17

ABSTRACT

We present the results of our survey toward the proto–planetary nebula CRL 618 for several large, highly saturated, oxygen-bearing organic molecules of biological importance including acetaldehyde (CH_3CHO), acetic acid (CH_3COOH), dimethyl ether (CH_3OCH_3), ethanol (CH_3CH_2OH), formic acid ($HCOOH$) and methyl formate ($HCOOCH_3$); large carbon chain molecules including methyl cyanide (CH_3CN), methylcyanoacetylene (CH_3C_3N), cyanoacetylene (HC_3N), cyanodiacetylene (HC_5N), and C_6H; and, finally, smaller molecules including ^{34}SO, SO_2, $OC^{34}S$, and MgNC. No biologically important organic molecules were detected. However, we report the first interferometric detections of CH_3CN and vibrationally excited HC_3N and HC_5N toward this source. The temperature and distribution of CH_3CN toward CRL 618 indicates that it is formed in the outer envelope surrounding the ultracompact H II region. Furthermore, the P Cygni line profile and corresponding channel maps of vibrationally excited HC_5N support its distribution in the extended envelope expanding radially from the central star. The detection of vibrationally excited HC_3N confirmed the temperature structure and column density of HC_3N in the inner envelope found by Wyrowski and colleagues. Finally, our observations clearly indicate that CRL 618 is a good source of large carbon chain species but a very poor source for detecting or producing organic species of biological importance.

Subject headings: line: identification — radio lines: stars — stars: AGB and post-AGB — stars: individual (CRL 618)

1. INTRODUCTION

Recently, there have been several surveys for complex molecular species toward massive star-forming regions including W75N, G45.47+0.05, G19.61−0.23 (Remijan et al. 2004a), and Sgr B2(N-LMH) (Hollis et al. 2004; Friedel et al. 2004; Snyder et al. 2002). These massive star-forming regions all have very similar physical conditions. First, they are rich in interstellar dust. Many molecular species, even H_2, appear to have their origins on the icy surfaces of dust grains (Hollenbach & Salpeter 1971). Dust becomes more important as more complex molecules are found in the interstellar medium (ISM). The abundances of large molecules in several regions are much larger than the predicted abundances from ion-molecule gas-phase chemistry models (Remijan et al. 2002; Mehringer & Snyder 1996). Thus, grain surface chemistry has been invoked to account for the large abundance of complex interstellar molecules. Second, the high density of gas and dust limit the amount of UV flux. This is important because UV photons destroy complex molecules (Ehrenfreund et al. 2001). Finally, the hot-core regions have high temperatures. It is generally believed that molecules formed via grain surface reactions in a cold-collapse phase are then evaporated by thermal heating and thereafter deposited into the gas phase. Typically, if the temperature of dust grains exceeds 100 K, the mantles evaporate, and species that were frozen on the grain can now escape into the gas phase (Tielens & Hagen 1982; Hasegawa et al. 1992). Furthermore, an interesting warm gas-phase chemistry may take place after the molecules are evaporated, leading to the production of even more complex molecules. Thus, these regions appear to be ideal environments for complex interstellar chemistry. It is logical to assume that similar regions rich in dust, with high density and near a source of high temperature, i.e., O and B stars or ultracompact (UC) H II regions, should also contain the necessary chemistry to synthesize large molecular species.

Another astronomical environment that appears to fit the above selection criteria is the extended envelope of proto–planetary nebulae (PPNe). The PPN phase of stellar evolution occurs at the end of the asymptotic giant branch (AGB) stage, in which substantial mass loss is taking place, and before the formation of the white dwarf, after which the temperature becomes high enough to ionize the extended envelope and start the formation of a planetary nebula. This phase of stellar evolution is typically very short, lasting only about 10 thousand years. However, during that time a very interesting chemistry may take place in the extended envelope of the post-AGB star. Thus, the extended envelopes of PPNe may be ideal chemical factories to produce large molecules and molecules of biological importance.

CRL 618 (AFGL 618, IRAS 04395+3601) is a carbon-rich, evolved PPN with a thick molecular envelope surrounding a B0 star and an UC H II region (Cernicharo et al. 2001b). However, the complete physical structure of CRL 618 is very complex. CRL 618 has been observed in several molecular species at different resolutions and wavelengths. Some of its distinct structures include optical high-velocity bipolar outflows (Trammell 2000), a central UC H II region, a low-velocity, expanding torus of molecular emission, and an extended, expanding AGB envelope (Sanchez Contreras & Sahai 2004). In addition to several individual structures, the circumstellar envelope (CSE) itself also shows a complex structure and is predicted to exhibit a complex distribution of several different molecular species (Woods et al. 2003). Thus, by observing the molecular envelope in several different molecular species at different excitation temperatures, we can obtain a better understanding of the temperature and density structure of the CSE. Furthermore, the interactions of the

[1] Department of Astronomy, 103 Astronomy Building, 1002 West Green Street, University of Illinois, Urbana, IL 61801; friedel@astro.uiuc.edu, meierd@astro.uiuc.edu, snyder@astro.uiuc.edu.
[2] Current address: NASA Goddard Space Flight Center, Earth and Space Data Computing Division, Code 930, Greenbelt, MD 20771; aremijan@pop900.gsfc.nasa.gov.
[3] National Research Council Resident Research Associate.
[4] Max-Planck-Institut für Radioastronomie, Auf dem Hügel 69, D-53121 Bonn, Germany; wyrowski@mpifr-bonn.mpg.de.

TABLE 1
Observational Parameters

Observation Date (1)	Gain Calibrator (2)	Flux Calibrator (3)	Frequency (GHz) (4)	Array (5)	Beam (arcsec × arcsec) (6)
2002 Oct 11	0359+509	Saturn	111.5	C	7.18 × 6.59
2002 Oct 19	0359+509	Saturn	111.5	C	6.97 × 6.50
2002 Nov 4	0359+509	Jupiter	110.3	C	6.91 × 6.43
2002 Nov 18	0359+509	Saturn	111.5	C	7.46 × 6.66
2003 Jan 28................	0359+509	Jupiter	110.3	B	2.90 × 1.84
2003 Jan 31................	0359+509	Jupiter	111.5	B	3.72 × 1.90
2003 Feb 1	0359+509	Jupiter	111.5	B	2.75 × 1.96
2003 Feb 3	0359+509	Jupiter	111.5	B	3.48 × 2.04

high- and low-velocity outflows from the embedded evolved star may also contribute significantly to the chemistry in the CSE. For example, within the high-velocity bipolar outflow, Ueta et al. (2001) discovered distinct near-IR "microstructures." They note that the positions of these microstructures occur in shocked regions where the molecular clumps are interfacing with the ambient circumstellar shell. Shocked regions also often trace areas of interesting interstellar chemistry that lead to the formation of complex molecular species. For example, Liu et al. (2002) detected formic acid (HCOOH) emission from shocked gas toward the Orion Compact Ridge. Also, Hollis et al. (2004) detected emission from propenal (CH_2CHCHO) and propanal (CH_3CH_2CHO) toward Sgr B2(N). The formation and widespread distribution of these species are most likely due to shocks in the Sgr B2(N) region that provided the energy necessary for the endothermic reactions to form these species and eventually distribute them into the gas phase. Thus, it appears that CRL 618 contains the physical conditions necessary to produce complex molecules.

Two recent surveys were performed toward CRL 618 using the *Infrared Space Observatory* (*ISO*) and the IRAM 30 m radio telescope (Cernicharo et al. 2001a, 2001b). These observations made the first detections in the circumstellar medium of the polyacetylenic chains C_4H_2 and C_6H_2 and the first detection of circumstellar benzene (C_6H_6). They also detected the infrared bands of NH_3 and C_2H_4 and made the first detection in the circumstellar medium of the methylpolyynes CH_3C_2H and CH_3C_4H. Obviously, there is a rich chemistry available to form large carbon chain molecular species, including HC_3N and HC_5N (Fukasaku et al. 1994). Bujarrabal et al. (1988) compared the column densities of several molecular species measured toward CRL 618 to those measured toward other PPNe, specifically IRC +10216 and CRL 2688, as well as interstellar molecular clouds, specifically Orion A and TMC-1. What they found was that the abundances of many molecular species, including nitrogen-bearing species (e.g., HC_3N and HC_5N) and oxygen-bearing species (HCO^+ in particular), were more similar to the abundances found in the ISM rather than those in other PPNe. Furthermore, this was the first time HCO^+ was detected in a carbon-rich object. Thus, they suggested that CRL 618 was at a particular point in its evolution at which the chemistry occurring in the CSE was more similar to the chemistry in the ISM than to the chemistry of other PPNe (§ 4.5). There have also been detections of small oxygen-bearing molecules toward CRL 618, including CO, H_2O, and H_2CO (Cernicharo et al. 1989). However, there has not been any survey to fully investigate the extent of the chemistry present toward CRL 618 that may form larger oxygen-bearing molecules, although it appears to be the ideal environment to produce oxygen-bearing organic molecules, as well as other large molecular species.

Thus, to investigate whether the chemistry present toward CRL 618 can produce large oxygen-bearing organic molecules, we used the Berkeley-Illinois-Maryland Association (BIMA) Array[5] to carry out a large-molecule survey toward this region. Included in the survey were transitions of formic acid (HCOOH), acetic acid (CH_3COOH), methyl formate ($HCOOCH_3$), and acetaldehyde (CH_3CHO), as well as methyl cyanide (CH_3CN), cyanoacetylene (HC_3N), and cyanodiacetylene (HC_5N). The observations of these large molecules helped constrain not only the chemistry present toward CRL 618 but also the temperature and column density of large molecular species in the surrounding circumstellar environment.

2. OBSERVATIONS

The large-molecule survey took place from 2002 October to 2003 February using the B and C configurations of the BIMA Array. The minimum baseline for these observations was ~8 m, and the maximum baseline was ~150 m, providing angular resolutions of ~2″–13″. Table 1 lists the observational parameters of our survey toward CRL 618. Column (1) lists the observation date. Column (2) lists the source used to calibrate the antenna-based gains, and column (3) lists the flux density calibrator. The absolute amplitude calibration of these sources is accurate to within ~20%. We find a flux density of the source of 1.86 Jy at the continuum emission peak of our observations at 108 GHz, which is very similar to the flux density measured by Wyrowski et al. (2003) of 1.8 Jy with the IRAM 30 m radio telescope at 109.2 GHz. Column (4) lists the observing frequency of the upper sideband, and column (5) lists the array configuration of the observation. Finally, column (6) lists the corresponding beam size. To obtain the best signal-to-noise ratio at each observing frequency, all the data from the source with multiple tracks and in multiple arrays were inverted in *u-v* space. The resulting synthesized beam size (5.″8 × 5.″1, near 108 GHz) was determined by the region of densest *u-v* coverage, and the 1 σ rms noise level of the final maps was determined by selecting a region free from line and continuum emission. The passbands were calibrated automatically during data acquisition;[6] this method has been quite satisfactory and has not generated spurious features.

Table 2 lists the molecular parameters of the 44 transitions of the 15 molecular species searched for in our survey. Column (1)

[5] Operated by the University of California, Berkeley, the University of Illinois, and the University of Maryland with support from the National Science Foundation.
[6] A technical description of this can be found at http://astron.berkeley.edu/~plambeck/technical.html.

TABLE 2

Molecular Line Parameters

Species (1)	Transition (2)	Frequency[a] (MHz) (3)	$\langle S_{i,j}\mu^2\rangle$ (D^2) (4)	E_u (K) (5)	Q_r (6)
C_6H[b]	$^2\Pi_{3/2} J = 77/2-75/2$ f	106,762.470(90)	1340.2	101.2	$89.8T$
^{34}SO[c]	2(3)–1(2)	106,743.374(18)	3.6	21.0	$2.9T$
$OC^{34}S$[d]	9–8	106,787.380(80)	4.6	25.7	$3.4T$
SO_2[b]	$27_{3,25}-26_{4,22}$	107,060.209(3)	8.3	370.5	$1.1T^{3/2}$
MgNC[b]	9–8	107,399.800(400)	245.2	25.9	$7.0T$
CH_3CN[e]	6(4)–5(4)	110,349.760(200)	51.0	132.3	$1.0T^{3/2}$
	6(3)–5(3)	110,364.470(100)	68.9	82.6	...
	6(2)–5(2)	110,374.986(120)	81.6	47.0	...
	6(1)–5(1)	110,381.376(120)	89.3	25.7	...
	6(0)–5(0)	110,383.494(120)	91.9	18.6	...
$(CH_3)_2O$[f]	$9_{1,8}-8_{2,7}$ *AA*	106,775.679(80)	3.66	43.4	$91.6T^{3/2}$
	$9_{1,8}-8_{2,7}$ *EE*	106,777.371(80)	3.66	43.4	...
	$9_{1,8}-8_{2,7}$ *AE*	106,779.058(80)	3.66	43.4	...
	$9_{1,8}-8_{2,7}$ *EA*	106,779.066(80)	3.66	43.4	...
CH_3CHO[b,g]	$3_{1,2}-2_{0,2}$ *E*	107,887.477(1598)	0.02	8.07	$2.3T^{3/2}$
CH_3COOH[h]	$10_{*,10}-9_{*,9}$ *E*	111,507.270(40)	54.8	30.5	$14.1T^{3/2}$
	$10_{*,10}-9_{*,9}$ *A*	111,548.533(40)	54.8	30.5	...
CH_3C_3N[i]	27(6)–26(6)	111,503.905(3)	579.1	345.3	$8.7T^{3/2}$
	27(5)–26(5)	111,515.692(3)	588.3	262.8	...
	27(1)–26(1)	111,541.424(4)	608.4	82.7	...
	27(0)–26(0)	111,542.497(4)	609.2	75.2	...
CH_3CH_2OH[j]	$12_{7,6}-13_{6,7}$	111,510.340(31)	1.7	127.4	$6.5T^{3/2}$
	$12_{7,5}-13_{6,8}$	111,510.550(31)	1.7	127.4	...
	$8_{2,7}-8_{0,8}$	111,738.020(19)	0.1	35.3	...
HCOOH[k]	$5_{0,5}-4_{0,4}$	111,746.780(10)	10.0	16.2	$1.7T^{3/2}$
$HCOOCH_3$[l]	$9_{7,2}-8_{7,1}$ *E*	110,525.598(32)	59.2	9.6	$12.4T^{3/2}$
	$9_{7,3}-8_{7,2}$ *A*	110,535.182(28)	59.2	9.6	...
	$9_{7,2}-8_{7,1}$ *A*	110,535.184(28)	59.2	9.6	...
	$9_{7,3}-8_{7,2}$ *E*	110,535.955(26)	59.2	9.6	...
	$7_{2,6}-6_{1,5}$ *E*	110,550.217(28)	19.0	1.4	...
	$7_{2,6}-6_{1,5}$ *A*	110,560.053(30)	19.0	1.4	...
	$9_{1,8}-8_{1,7}$ *E*	111,674.070(13)	22.8	28.9	...
	$9_{1,8}-8_{1,7}$ *A*	111,682.224(13)	22.8	28.9	...
	$10_{1,10}-9_{0,9}$ *E*	111,733.936(14)	3.8	30.3	...
	$10_{1,10}-9_{0,9}$ *A*	111,735.329(15)	3.8	30.3	...
HC_3N[m]	$J = 12-11$ $(0, 0, 0, 4)^0$	110,543.700(130)	169.4	1314.4	$13.7T$
	$J = 12-11$ $(0, 0, 0, 4)^{2-}$	110,549.013(1594)	169.3	1314.4	...
	$J = 12-11$ $(0, 0, 0, 4)^4$	110,554.377(42)	169.3	1314.4	...
	$J = 12-11$ $(0, 1, 0, 3)^{1+}$	110,366.474(337)	169.0	994.4	...
HC_5N[n]	$J = 40-39$ $(0, 0, 0, 1)^{1+}$	106,767.4842(44)	749.96	259.4	$15.7T$
	$J = 40-39$ $(0, 0, 0, 3)^{1-}$	107,068.1920(300)	750.0	568.2	...
	$J = 40-39$ $(0, 0, 0, 3)^{1+}$	107,254.3370(300)	750.0	568.4	...
	$J = 40-39$ $(0, 0, 0, 4)^{4-}$	107,394.3161(50)	750.0	726.2	...
	$J = 40-39$ $(0, 0, 0, 4)^{4+}$	107,394.3435(50)	750.0	726.2	...

[a] Errors are 2 σ.
[b] Pickett et al. (1998).
[c] Tiemann (1974).
[d] Maki (1974).
[e] Boucher et al. (1980).
[f] Groner et al. (1998).
[g] Bauder et al. (1976).
[h] Iluyshin et al. (2001).
[i] Müller et al. (2001).
[j] Lovas (1982).
[k] Willemot et al. (1980).
[l] Oesterling et al. (1999).
[m] Wyrowski et al. (1999); Yamada & Creswell (1986).
[n] Yamada et al. (2004); Müller et al. (2001).

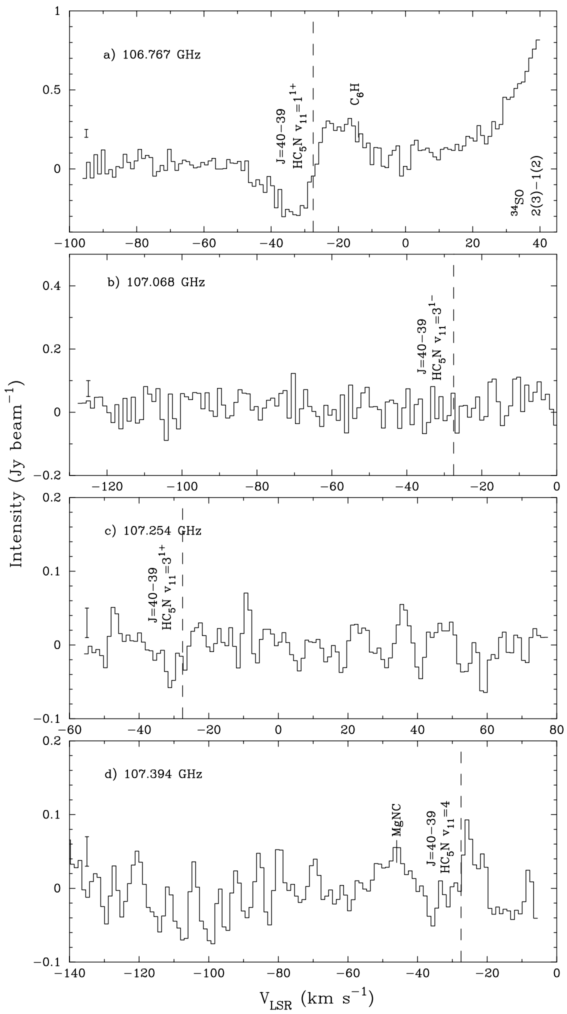

FIG. 1.—Spectra of the four transitions of vibrationally excited HC_5N located in the passbands of our survey. (*a*) First detection the HC_5N $J = 40–39$, (0, 0, 0, 1)$^{1+}$ transition toward CRL 618 seen in absorption and emission. The emission peaks near a v_{LSR} of −24 km s^{-1}. The spectral line label in the upper left of each panel is the rest frequency of each HC_5N transition for a v_{LSR} of −27.5 km s^{-1}. The dashed line is centered on the v_{LSR} of CRL 618 (−27.5 km s^{-1}). Near 40 km s^{-1} we begin to detect the ^{34}SO 2(3)–1(2) transition in emission. We also label the location of the C_6H $^2\Pi_{3/2} J = 77/2–75/2$ f transition. The 1 σ rms noise level is ~40 mJy beam^{-1} (*vertical bar at the left of each spectrum*). (*b*) Passband containing the HC_5N $J = 40–39$, (0, 0, 0, 3)$^{1-}$ transition toward CRL 618. No spectral feature is detected beyond the 1 σ rms noise level. (*c*) Passband containing the HC_5N $J = 40–39$, (0, 0, 0, 3)$^{1+}$ transition toward CRL 618. No spectral feature is detected beyond the 1 σ rms noise level. (*d*) Passband containing the HC_5N $J = 40–39$, (0, 0, 0, 4) transition toward CRL 618. We also label the location of the MgNC $N = 9–8$ transition. No spectral feature is detected beyond the 1 σ rms noise level; however, the MgNC transition is beginning to be resolved out of the noise (§ 4.4).

lists the species; Column (2) lists the transition. Column (3) lists the calculated rest frequency and its 2 σ standard deviation. Column (4) lists the product of the line strength and the square of the relevant dipole moment, and column (5) lists the upper state energy level of each transition. Finally, the estimated rotational partition functions for each molecular species are given in column (6). The spectral windows containing these transitions had a bandwidth of 50 MHz and were divided into 128 channels for a spectral resolution of 0.39 MHz per channel. All data were combined, imaged, and self-calibrated using the MIRIAD software package (Sault et al. 1995). The 1 σ rms noise level of the final maps was used to set upper limits on the column densities of the undetected molecular species searched for in our survey (§ 4.4).

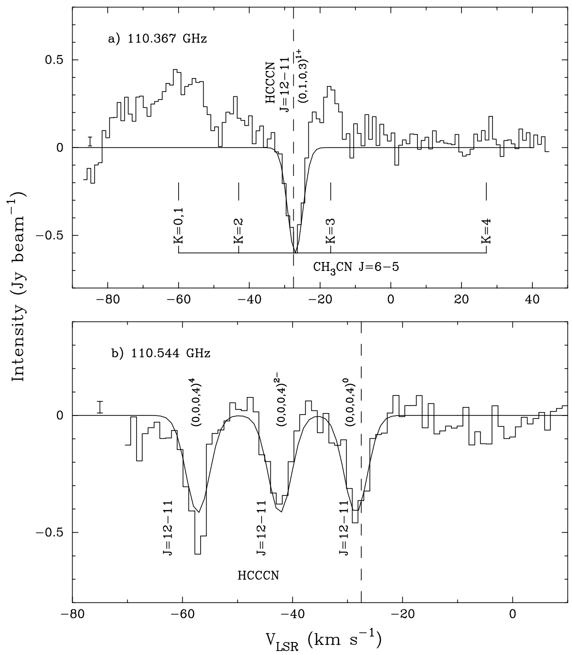

FIG. 2.—Spectra of the detected transitions of CH_3CN and HC_3N found from our survey toward CRL 618. (*a*) First detection of the $J = 6–5$ rotational transitions of CH_3CN seen entirely in emission. Between the $K = 2$ and 3 lines of CH_3CN lies the $J = 12–11$ (0, 1, 0, 3)$^{1+}$ vibrational transition of HC_3N seen in absorption. The measured v_{LSR} of the absorption trough of HC_3N is −27.5 km s^{-1}. The spectral line label in the upper left of the panel is the rest frequency of the HC_3N transition. The 1 σ rms noise level is ~40 mJy beam^{-1} (*vertical bar at the left of each spectrum*). (*b*) Spectrum of three vibrationally excited transitions of HC_3N. Each of these transitions lies at a v_{LSR} of −27.5 km s^{-1}. The spectral line labels located in the upper left of each panel correspond to the rest frequency of the HC_3N $J = 12–11$ (0, 0, 0, 4)^0 transition.

3. RESULTS

Figure 1 shows the four transitions of vibrationally excited HC_5N located in the passbands of our survey. The HC_5N transitions and corresponding rest frequencies were taken from a new survey by Yamada et al. (2004) and the Cologne Database for Molecular Spectroscopy (Müller et al. 2001). In Figure 1*a* we show the first interferometric detection of vibrationally excited ($v_{11} = 1$) HC_5N toward CRL 618. The spectral line labels located in the upper left of each panel correspond to the rest frequency of each HC_5N transition for a v_{LSR} of −27.5 km s^{-1} (*dashed line*). The 1 σ noise level is seen at the left of each panel. The classic P Cygni line profile indicates that HC_5N is present in an expanding envelope of material. Also included in Figure 1*a* are the spectral line labels of C_6H and ^{34}SO. These features will be discussed in more detail (§§ 4.4 and 4.5). Figures 1*b*–1*d* show the spectra of higher vibrational transitions ($v_{11} = 3$ and 4) that were not detected beyond our 1 σ detection limit. From these nondetections, we were able to set an upper limit on the temperature of this species in this region. Finally, in Figure 1*d*, we label the location of MgNC. The nondetection of this feature will also be discussed in more detail (§ 4.4).

TABLE 3
LINE DETECTIONS

Frequency (MHz) (1)	Species (2)	Transition (3)	v_{LSR} (km s^{-1}) (4)	$\int \Delta I\, dv$ (Jy beam^{-1} km s^{-1}) (5)
106,767.4842(44).............	HC_5N	$J = 40–39$ (0, 0, 0, 1)$^{1+}$	−24	4.74(1.9)
	...	...	−34	−4.15(1.7)
106,743.374(18)................	^{34}SO	2(3)–1(2)	...	[a]
110,349.760(200).............	CH_3CN	6(4)–5(4)	−27.5	0.58(42)
110,364.470(100).............	CH_3CN	6(3)–5(3)	−27.5	2.77(18)
110,366.742(337).............	HC_3N	12–11 (0, 1, 0, 3)$^{1+}$	−27.5	−2.69(30)
110,374.986(120).............	CH_3CN	6(2)–5(2)	−27.5	1.85(17)
110,381.376(120).............	CH_3CN	6(1)–5(1)	...	[b]
110,383.494(120).............	CH_3CN	6(0)–5(0)	−27.5	7.63(24)[b]
110,543.508(130).............	HC_3N	12–11 (0, 0, 0, 4)^0	−27.5	−1.56(3)
110,550.328(1594)...........	HC_3N	12–11 (0, 0, 0, 4)$^{2-}$	−27.5	−1.38(3)
110,554.742(42)...............	HC_3N	12–11 (0, 0, 0, 4)^4	−27.5	1.92(3)[c]

[a] Because we did not see the line peak, no attempt was made to fit this transition.
[b] Because the $K = 0$ and 1 components could not be fitted with separate Gaussians, a one-Gaussian fit was applied to both lines.
[c] This line may be blended with the $15_{4,2}–14_{5,2}$ transition of c–C_3H_2 at 110.558(9) GHz (Pickett et al. 1998).

Figure 2 shows the spectra of the CH_3CN and vibrationally excited HC_3N detected in our survey. Figure 2*a* shows the first detection of the $J = 6–5$ rotational transitions of CH_3CN. All the CH_3CN transitions are seen in emission. Between the $K = 2$ and 3 lines of CH_3CN lies the $J = 12–11$, (0, 1, 0, 3)$^{1+}$ vibrational transition of HC_3N seen in absorption. The measured v_{LSR} of the absorption trough is −27.5 km s^{-1}, which is consistent with previous detections of vibrationally excited HC_3N (Wyrowski et al. 2003). Finally, Figure 2*b* shows the spectrum of three vibrationally excited transitions of HC_3N. Once again, each of these transitions lies at a v_{LSR} of −27.5 km s^{-1}. The spectral line labels located at upper left in Figures 2*a* and 2*b* correspond to the rest frequency of the HC_3N $J = 12–11$, (0, 1, 0, 3)$^{1+}$ and the HC_3N $J = 12–11$, (0, 0, 0, 4)^0 transitions,[7] respectively. Table 3 lists the molecular species that were detected toward CRL 618 at or near the systemic velocity (−27.5 km s^{-1}). Least-square Gaussian fits were made for each spectral line to obtain the radial velocities and integrated line intensities for the detected transitions. In Table 3, column (1) lists the calculated rest frequencies of the identified species. Columns (2) and (3) list the molecular species and associated transitions, respectively. Column (4) lists the v_{LSR} corresponding to the emission or absorption components of each spectral feature. Finally, column (5) lists the fitted integrated line intensity of each detected transition and the associated 1 σ uncertainty.

Figure 3 shows the HC_5N velocity channel maps toward CRL 618. The spectral line channel maps displayed are a combination of the B- and C-array data. The v_{LSR} intervals are indicated in km s^{-1} units at the top right of each panel. The synthesized beam of $5''.8 \times 5''.1$ is shown at the bottom left of each velocity channel map. The lowest contour plotted is 0.08 Jy beam^{-1} which corresponds to 2 σ. The absorption peaks near a v_{LSR} of −34 km s^{-1}, and the emission peaks near −24 km s^{-1}. Both the absorption and emission peaks are coincident with the high-resolution B-array 3 mm continuum shown in the bottom right panel of the figure (synthesized beam of $3''.0 \times 1''.9$). Thus, it is apparent from both the P Cygni profile and velocity channel maps that HC_5N is contained in an expanding envelope and not in the bipolar outflows.

Figure 4 shows the HC_3N velocity channel maps toward CRL 618. As in Figure 3, the data displayed are a combination of the B- and C-array data, and the v_{LSR} intervals are indicated at top right in each panel. In this case, we see no emission features of HC_3N. This is not unexpected because all the high-energy, high vibrational state transitions (i.e., $v_5 = 1$ and $v_7 = 3$) detected by Wyrowski et al. (2003) were seen primarily in absorption. The transitions detected in our survey were at a higher vibrational state ($v_7 = 3$ or 4) than the transitions of the Wyrowski et al. (2003) survey, but the upper state energy levels were comparable to some of the higher energy transitions detected in their survey. In contrast, the ground state and first vibrational states in the Wyrowski et al. (2003) survey were seen primarily in emission. Once again, we see that the absorption is coincident with the 3 mm continuum, and presumably all the vibrationally excited HC_3N is contained in the CSE.

Finally, we note that we did not detect any emission or absorption features from any of the other molecular species listed in Table 2 beyond our 1 σ detection limit. These include all the oxygen-bearing organic molecules, as well as CH_3C_3N, C_6H, and all the smaller molecular species. However, it does appear that we are starting to detect the $N = 9–8$ transition of MgNC in Figure 1*d*. Higher signal-to-noise ratio interferometric observations are necessary to confirm this detection. Based on the 1 σ detection limit, we were able to place upper limits on the species that were not detected. All column densities and upper limits are listed in Table 4 (§ 4.4). In § 4.5 we discuss these upper limits, along with the predicted fractional abundances based on the gas-phase formation models of Woods et al. (2003) and in the UMIST database (Le Teuff et al. 2000).

4. ANALYSIS AND DISCUSSION

One of the most important physical parameters to determine in either an interstellar or circumstellar environment is the total beam-averaged column density of a molecular species. There are three primary procedures used in calculating the total beam-averaged column density of a particular molecular species, each of which is described in detail in Remijan et al. (2004b). For our purposes, we use the rotational temperature diagram method

[7] The notation given for the vibrational excited transitions of HC_3N is defined as (v_4, v_5, v_6, v_7)^l, where v is the vibrational quantum number and l is the l-type–doubling quantum number (Thorwirth et al. 2003).

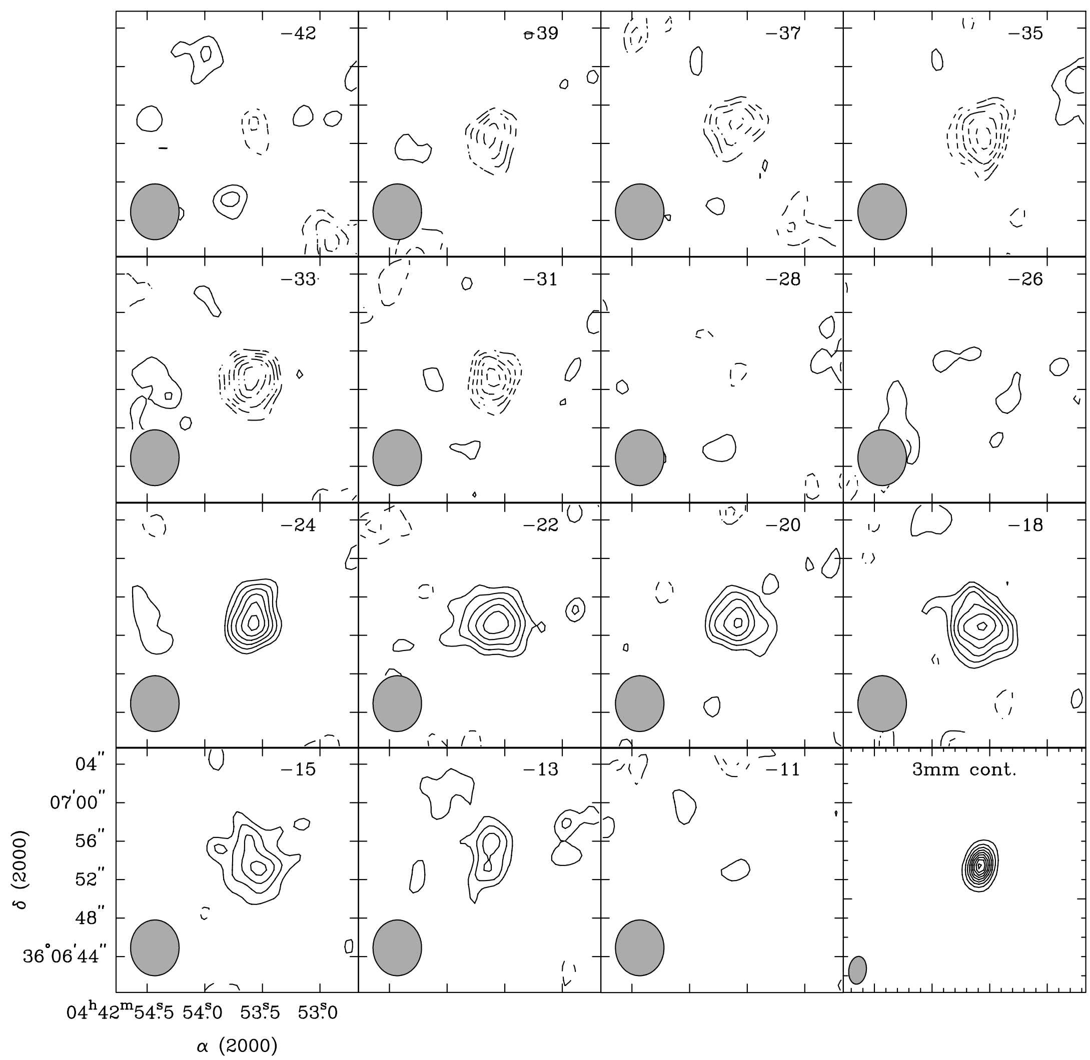

FIG. 3.—HC_5N velocity channel maps toward CRL 618. The data displayed are a combination of those from the B- and C-array data. The LSR velocities of the absorption and emission features are indicated in km s^{-1} at the top right of each panel. The contour level ranges are −0.24, −0.20, −0.16, −0.12, −0.08, 0.08, 0.12, 0.16, 0.20, 0.24 and 0.28 Jy $beam^{-1}$. The synthesized beam of $5''.8 \times 5''.1$ is shown at the lower left of each panel. *Bottom right*: Continuum emission at 3 mm toward CRL 618 in the BIMA B array. The synthesized beam of $3''.0 \times 1''.9$ is shown at lower left, The continuum emission peaks at an intensity of 1.86 Jy $beam^{-1}$ at a frequency near 108 GHz.

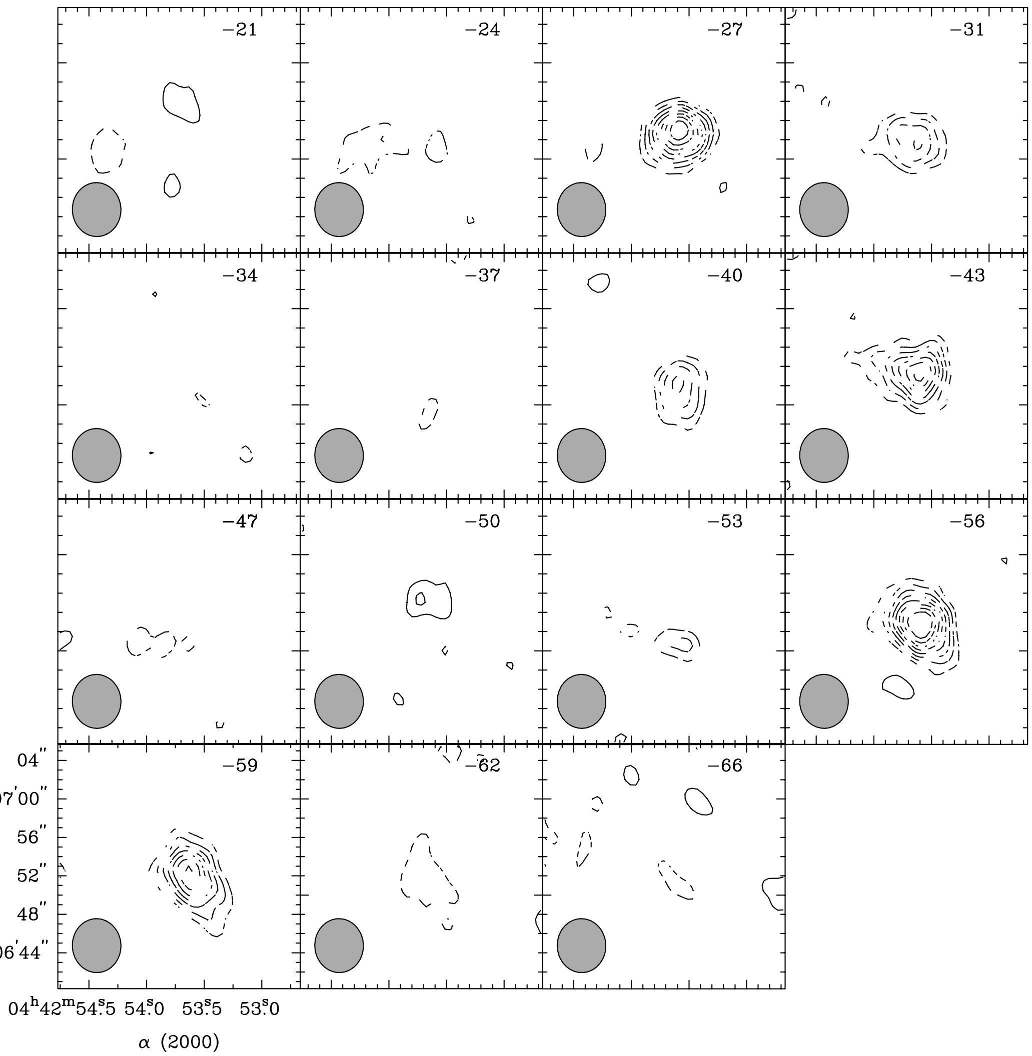

FIG. 4.—HC_3N $v_7 = 4$ velocity channel maps toward CRL 618. The data displayed are a combination of those from the B- and C-array data. The panel labels and beam sizes are the same as in Fig. 3. The contour level ranges are −0.36, −0.32, −0.28, −0.24, −0.20, −0.16, −0.12, −0.08, 0.08, and 0.12 Jy beam^{-1}.

TABLE 4
COLUMN DENSITIES

Species (1)	Frequency (MHz) (2)	N_{tot} (cm^{-2}) (3)	$X(H_2)$ (4)
Detections			
HC_5N[a]	106,767.484	9.9×10^{14}	7.6×10^{-9}
HC_3N	[b]	$4.7 (6) \times 10^{17}$	$3.6 (5) \times 10^{-6}$
CH_3CN	[b]	$3.2 (3) \times 10^{14}$	$2.4 (3) \times 10^{-9}$
Upper Limits			
C_6H	106,762.470	2.5×10^{13}	1.9×10^{-10}
$OC^{34}S$	106,787.380	1.2×10^{14}	9.1×10^{-10}
SO_2	107,060.209	1.0×10^{16}	7.8×10^{-8}
MgNC	107,399.800	4.4×10^{12}	3.4×10^{-11}
$HCOOCH_3$	110,550.217	1.1×10^{16}	8.5×10^{-8}
$(CH_3)_2O$	106,777.371	1.0×10^{17}	7.9×10^{-7}
CH_3CHO	107,887.477	1.4×10^{17}	1.1×10^{-6}
CH_3COOH	111,548.533	3.5×10^{14}	2.7×10^{-9}
CH_3C_3N	111,542.497	3.3×10^{13}	2.5×10^{-10}
CH_3CH_2OH	111,738.020	9.4×10^{16}	7.3×10^{-7}
HCOOH	111,746.780	2.0×10^{14}	1.5×10^{-9}

[a] Column density based on the emission-line detection (§ 4.3).
[b] All lines were used to calculate the total column density of this molecule.

(RTDM) for the CH_3CN and HC_5N emission and assume local thermodynamic equilibrium (LTE) for all other molecular species. From Remijan et al. (2003), the total beam-averaged column density is given as

$$N_T = 2.04 C_\tau \frac{\int \Delta I\, dv}{\theta_a \theta_b} \frac{I(T_e)}{I(T_e) - I_b} \frac{Q_{\rm rv} e^{(E_u/T_e)}}{\nu^3 \langle S_{ij}\mu^2 \rangle} \times 10^{20}\ {\rm cm}^{-2}$$
$$= C_\tau N_T^{\rm thin}\ {\rm cm}^{-2}, \qquad (1)$$

where N_T is the total column density for any optical depth and $N_T^{\rm thin}$ is the total column density for the optically thin case, C_τ is the optical depth correction factor from Goldsmith & Langer (1999), $\int \Delta I\, dv$ (in Jy beam^{-1} km s^{-1}) is the integrated line intensity given in Table 3, θ_a and θ_b are the FWHM beam sizes (in arcseconds), $I(T_e)$ is the specific intensity of the source at T_e (in Jy beam^{-1}), I_b is the specific intensity of the total background continuum contribution (in Jy beam^{-1}), and $Q_{\rm rv}$ is a combination of the rotational and vibrational partition functions. The vibrational part of the partition function needs to be applied to both the HC_5N (Müller et al. 2001) and the the HC_3N (Wyrowski et al. 2003) column density calculations. E_u is the upper state energy level (in K), T_e is the rotational temperature (in K), ν is the rest frequency (in GHz), and $S_{ij}\mu^2$ is the product of the total torsional-rotational line strength and the square of the electric dipole moment (debye^2).

4.1. *Methyl Cyanide* (CH_3CN)

Methyl cyanide (CH_3CN) has been used as an excellent tracer of the physical and chemical conditions toward high-mass star-forming regions of the ISM (Remijan et al. 2004b; Sutton et al. 1986). CH_3CN is a symmetric top molecule whose properties make it an ideal probe of kinetic temperature and column density. In a symmetric top, the rotational levels are labeled by J, the total angular momentum quantum number, and K, the quantum number for the projection of the angular momentum vector along the symmetry axis (Cummins et al. 1983). By selection rules, radiative transitions do not change the value of K. However, collisional transitions are permitted across K ladders. Therefore, the population of one K ladder relative to another is largely determined by collisions and hence is closely related to the kinetic temperature and density (Solomon et al. 1971). The first reported detection of CH_3CN toward CRL 618 was by Bujarrabal et al. (1988) using the IRAM 30 m radio telescope. Also with the IRAM 30 m, Guelin & Cernicharo (1991) used several millimeter transitions of CH_3CN to examine the physical conditions toward IRC +10216. From their observations, they found a rotation temperature of $T_{\rm rot} = 16$ K and a column density of 6×10^{12} cm^{-2} toward IRC +10216 (Guelin & Cernicharo 1991). Figure 5 shows the results of the RTDM toward CRL 618 using the $J = 6$–5 transitions. Because the $K = 0$ and 1 transitions are severely blended, we could not resolve the lines into two separate Gaussians; thus, we included the pair as one point on the rotational temperature diagram by separating the intensities by their appropriate statistical weights and then averaging. Using the procedures outlined in Remijan et al. (2004b), we found a best-fit rotational temperature of 88 (44) K and a total beam-averaged column density of $3.2(3) \times 10^{14}$ cm^{-2}. Assuming an H_2 column density of $\sim 1.3 \times 10^{23}$ cm^{-2} (Woods et al. 2003), we find a fractional abundance of $X_{\rm CH_3CN} = 2.4(3) \times 10^{-9}$. This value is very close to the predicted peak value of $\sim 10^{-8}$ from the Woods et al. (2003) model at a radial distance of $\sim 9.1 \times 10^{15}$ cm from the exciting star. Thus, it is clear from our observations that CH_3CN appears to reside in the outer regions of the expanding envelope. Furthermore, transitions of vibrationally excited CH_3CN $v_8 = 1$ are below our 1 σ detection limit, which again may imply that CH_3CN exists in the outer envelope.

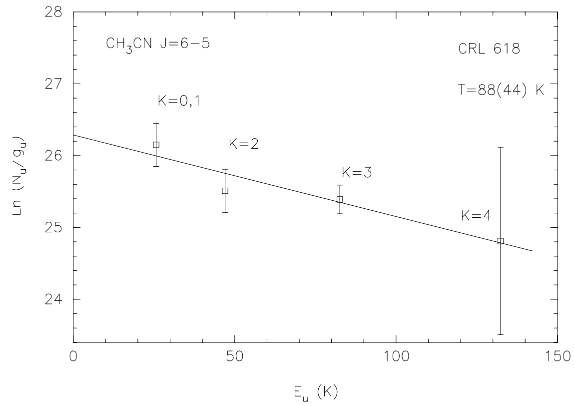

FIG. 5.—Rotational temperature diagram for the observed CH_3CN transitions toward CRL 618. *Ordinate*, ln (N_u/g_u); *abscissa*, E_u(in K). The least-squares fit is shown as a solid line. The resulting rotational temperature is 88 (44) K in a beam size of 5."8 × 5."1.

4.2. *Cyanoacetylene* (HC_3N)

Cyanoacetylene (HC_3N) is a carbon chain molecule that has been extensively studied toward CRL 618 in both the ground and excited vibrational states (see, e.g., Pardo et al. 2004; Wyrowski et al. 2003 and references therein). So, from our data, we were able to check the previously measured physical conditions and help further constrain the physical and chemical models of CRL 618. In Figure 2, we show the detections of four vibrationally excited transitions of HC_3N. Also shown in these spectra are the best-fit modeled spectra to the data (*solid line*). To calculate the best-fit spectra, we used the spectral line parameters given in Table 2 and used an FWHM line width of $\Delta v = 5$ km s^{-1} based on the fits in Table 3. Models were constructed using the temperature and upper state column density as input parameters. We varied the temperature between 400 and 600 K and the upper state column density between 10^{16} and 10^{18} cm^{-2}. We then calculated the χ^2 between the model and the data and found the minimum χ^2. The best-fit models (*solid lines*) are shown in Figure 2 for a temperature of 580 (150) K and a total HC_3N beam-averaged column density of $4.7(6) \times 10^{17}$ cm^{-2}. The errors given for the temperature and total column density are 3 σ errors based on the fit, thus giving a 99% confidence interval. The only line that does not seem to fit the model very well is the $J = 12$–11 (0, 0, 0, 4)^4 transition at 110.555 GHz (Table 2). This line may be blended with the $15_{4,2}$–$14_{5,2}$ transition of c–C_3H_2 at 110.558(9) GHz (Pickett et al. 1998) or possibly a transition from another unknown circumstellar species. The values of $T_{\rm rot}$ and N_T are very similar to the values determined by Wyrowski et al. (2003) of $T = 520(80)$ K and a total HC_3N column density between $(3–6) \times 10^{17}$ cm^{-2}. To find the total HC_3N column density, we need to include the vibrational part of the partition function. Using Figure 9 in Wyrowski et al. (2003) and a temperature of 580 K, we find $Q_{\rm rv} = 1.8 \times 10^5$. Also in equation (1) we need to account for the optical depth and the intensity of the background continuum. For the HC_3N lines, we find $\tau = \ln(T_c/T_c–T_L) = 0.25$, which gives an optical depth correction factor of $C_\tau = 1.13$, and if we use the continuum temperature and the excitation temperature of 580 K, the column density correction due to $I(T_{\rm ex})/[I(T_{\rm ex}) - I_b]$ is $\sim$1.06, which gives a total correction of $\sim$1.20 for a temperature of 580 K. Assuming an H_2 column density of $\sim 1.3 \times 10^{23}$ cm^{-2} (Woods et al. 2003), we find a fractional abundance of $X_{\rm HC_3H} = 3.6(5) \times 10^{-6}$, which matches that of the models of Woods et al. (2003). The average value of the HC_3N fractional abundance in the envelope predicted by the model is $\sim 10^{-6}$, and the model predicts a peak value of 1.6×10^{-6} at a radial distance of $\sim 10^{16}$ cm from the central star. Thus, it appears that the models are predicting the relative abundance of this species very well toward CRL 618.

4.3. *Cyanodiacetylene* (HC_5N)

The first reported detection of HC_5N in a PPN was by Winnewisser & Walmsley (1978) toward IRC +10216. They observed the $J = 9$–8 rotational transition near 24 GHz. From their observations, they found the HC_5N emission to be quite extended over their 40″ beam and measured an HC_5N column density of 4×10^{14} cm^{-2}. However, they did not detect any emission from the $v_{11} = 1$ vibrational mode. These observations were later followed up by Jennings & Fox (1982), who determined an HC_5N rotational temperature of 13^{+12}_{-4} K, which was in agreement with the determined HC_3N rotational temperature of 12 K measured at the time. The first detection of HC_5N in CRL 618 was by Bujarrabal et al. (1988). In this case, they assumed the HC_5N emission to be much smaller than their beam of $\sim$15″. From that, they found an HC_5N rotational temperature of $\sim$81 K. Since then, several other transitions of HC_5N have been observed toward other PPNe (see, e.g., Fukasaka et al. 1994). The first detection of vibrationally excited transitions of HC_5N reported in CRL 618 was by Thorwirth (2001). Later observations followed by Cernicharo et al. (2001b) and Wyrowski et al. (2003). However, ours are the first data of vibrationally excited HC_5N taken with an interferometer and the first maps of vibrationally excited HC_5N toward CRL 618. In Figure 1, we showed the first interferometric detection of the $J = 40$–39, $v_{11} = 1$ transition of HC_5N. No higher vibrational states ($v_{11} = 3$ or 4) were detected (Figs. 1*b*–1*d*). However, from the 1 σ noise levels, we were able to plot the upper limits on a rotational temperature diagram of HC_5N. Plotting these data on a rotational temperature diagram, we were able to determine an upper limit on the HC_5N rotational temperature of $T_{\rm rot} = 114$ K. Using the measured vibrationally excited partition function from Müller et al. (2001) for HC_5N, we were able to calculate the total rotational-vibrational HC_5N partition function for 114 K. We find $Q_{\rm rv} \simeq 950$. From the rotational temperature diagram, we find a total beam-averaged column density of HC_5N of $\sim 10^{15}$ cm^{-2} and a fractional abundance of $X_{\rm HC_5H} = 7.6 \times 10^{-9}$. This column density is about an order of magnitude lower than the predicted value of 1.7×10^{16} cm^{-2} from the Woods et al. (2003) model. However, the column density is in the range of measured values toward this source from previous observations (Fukasaku et al. 1994; Cernicharo et al. 2001b).

Also, looking at the velocity channel maps in Figure 3, we see that the HC_5N emission is coincident with the 3 mm continuum and that no HC_5N emission is seen in the bipolar outflow above our 3 σ detection limit cutoff. The classic P Cygni line profile indicates a spherically symmetric expansion with an expansion velocity of $\sim$5–7 km s^{-1}. The slow expansion velocity would occur at the outer edges of the envelope as the expanding material begins to interact with the remnant AGB wind. Also, the expansion velocity of HC_5N is close to the measured expansion velocity of HC_3N ($\sim$10 km s^{-1}) found by Pardo et al. (2004), and it matches the expansion velocity used by Woods et al. (2003) in their formation models. Thus, from the spectral line profile and mapping data it appears that HC_5N is found in the extended CSE.

To summarize, all the detected species are found in the extended envelope. In the case of CH_3CN, the observed transitions are low in upper state energy and are optically thin. Thus, we are probing the gas in the very extended envelope and should see only emission features. On the other hand, the HC_3N transitions have high upper state energies. The gas sampled in this case must lie deeper in the envelope, where the column density is high, which leads to a high opacity, and the lines are seen primarily in absorption. Transitions of HC_3N at a lower energy state with respect to the transitions we observed are seen by other authors in emission and as P Cygni profiles. This implies that these authors are sampling the outer envelope where the gas is at a lower temperature but the column density is high enough that there are competing effects of emission and absorption (see, e.g., Pardo et al. 2004). Finally, for HC_5N, the temperature implies that the gas resides in the outer envelope, intermediate between the vibrational HC_3N and lower energy CH_3CN transitions, and that the column density is high enough that, once again, there are competing effects of emission and absorption. The hypothesis based on the formation models of each species (Woods et al. 2003) is that CH_3CN, HC_3N, and HC_5N are probably contained throughout the CSE of CRL 618. To fully investigate that assumption, observations of transitions that sample a wide range of upper state energy levels of each species are necessary.

4.4. *Column Density Upper Limits of the Remaining Molecular Species*

Of the remaining species listed in Table 2, we detected emission from ^{34}SO only (Fig. 1*a*). Because this line was near the edge of the spectral window, we were not able to make a Gaussian fit or a calculation of the total ^{34}SO beam-averaged column density. However, this is the first detection of this isotopic species of SO in a PPN. Further observations of ^{34}SO and ^{32}SO will be needed to determine the isotopic ratio and compare the column densities with those of other detected O-bearing species, including CO and H_2O toward CRL 618 (Herpin & Cernicharo 2000).

We also note that we did not reliably detect any emission from the $N = 9–8$ transition of magnesium isocyanide (MgNC). This species was recently detected using the Arizona Radio Observatory (ARO) 12 m and the IRAM 30 m telescopes via five rotational transitions at 95.4, 131.2, 143.2, 151.1, and 167.0 GHz. The column density of MgNC from that survey was found from a rotational temperature diagram to be 2.4×10^{12} cm^{-2} with a $T_{rot} = 21$ K (Highberger & Ziurys 2003). They note that the derived rotational temperature is consistent with the kinetic temperature of ~50 K (Herpin et al. 2002). Using this column density, we can predict the expected line intensity for our observations. Using a rotational temperature of 21 K, we predict an intensity of ~0.035 Jy beam^{-1} for our BIMA observations. If the temperature is closer to the CH_3CN temperature of 88 K, the predicted intensity drops to ~0.022 Jy beam $^{-1}$. The average rms noise of the combined B- and C-array data set containing the MgNC transition is ~0.04 Jy beam^{-1}. Thus, even with the highest predicted line intensity, we would have detected this transition only at the ~1 σ level. In Figure 1*d*, we labeled the position of the MgNC transition, and it appears the line is beginning to be resolved out of the noise. However, higher signal-to-noise ratio interferometric observations are necessary to claim this as a detection.

No other molecular species were detected toward CRL 618 beyond the 1 σ detection limit. However, we were able to set upper limits on the column densities of those species based on the 1 σ rms noise level (~0.04 Jy beam^{-1}) and an average line width of ~5 km s^{-1}, assuming a temperature of 88 K found from the CH_3CN data. Table 4 summarizes the column densities of all molecular species, including upper limits. Column (1) lists the molecular species observed toward CRL 618. Column (2) lists the frequency of the transition used to calculate the upper limit on the total column density (MHz). Using equation (1), an average beam of 25 arcsec^2, and the spectroscopic parameters and partition functions in Table 2, we were able to calculate the total beam-averaged column densities of each molecular species. Column (3) lists the total beam-averaged column density (in cm^{-2}). Finally, column (4) lists the fractional abundance of each molecular species with respect to H_2, assuming an H_2 column density of 1.3×10^{23} cm^{-2}.

4.5. *Formation and Detection of Oxygen-bearing Organic Biomolecules in Proto–Planetary Nebulae*

Our detections of CH_3CN, HC_3N, and HC_5N strongly suggest that the chemistry present toward CRL 618 is conducive to producing large carbon chain molecules and that the formation models that predict the abundance of these species also match the measured abundances very well. The only large carbon chain molecule that was predicted to be present in a large abundance toward CRL 618 but was not detected was C_6H. Woods et al. (2003) predict a total column density of 2.5×10^{15} cm^{-2}, and our measured upper limit was 2 orders of magnitude lower, at 2.5×10^{13} cm^{-2}. Also, there is no formation model that takes into account methylcyanoacetylene (CH_3C_3N), and our measured upper limit is 3.3×10^{13} cm^{-2}. However, the models of Woods et al. (2003) predict the column densities of CH_3C_4H and C_6H_5CN, which are presumed to be more complex species than either C_6H or CH_3C_3N, to be 1.5×10^{15} cm^{-2}. Thus, if the formation models are correct, we should have easily detected C_6H. If the predicted column density of CH_3C_3N is similar to either CH_3C_4H or C_6H_5CN, we should have also easily detected CH_3C_3N. The fact that neither species was detected beyond our 1 σ detection limit implies that the calculated upper limit of ~10^{13} cm^{-2} for both C_6H and CH_3C_3N must be taken into account in future formation models.

In addition to large carbon chain molecules, there have been several detections of simple, singly oxygenated species detected in the CSE and in the bipolar outflows of CRL 618. These molecules include CO, H_2O, H_2CO (Cernicharo et al. 1989), and HCO^+ (Bujarrabal et al. 1988). The hypothesis of Bujarrabal et al. (1988) was that the CSE was at a particular point in its evolution at which the opacity was low enough to allow UV photons from the central star to act on existing molecules in the CSE. In fact, only PPNe younger than ~300 yr are seen to be molecule-rich. In older PPNe, such as NGC 2346 and the Red Rectangle, photodissociation by UV photons can explain the lack of molecular emission seen toward these objects. In contrast, objects younger than CRL 618, including CRL 2688 and IRC +10216, show an abundance of molecular emission from large carbon chain species, such as HC_3N; however, the chemistry involving photodissociation has not evolved to the point of forming larger molecules from simply oxygenated species. CRL 618 is unique in that it has evolved enough to begin an interesting circumstellar chemistry but not to the point at which a large number of molecules are being quickly dissociated. The high abundance of HCO^+ with respect to younger objects supports this hypothesis. In fact, the abundance of many oxygen-bearing molecules in CRL 618 is very similar to the abundances found in oxygen-rich PPNe, including OH 231.8+4.2. HCO^+, and other small singly oxygenated molecules, including atomic oxygen (Herpin & Cernicharo 2000), are used in gas chemistry models to produce more complex and organic molecules of biological importance.

The nondetections of very favorable transitions of oxygen-bearing organic molecules such as HCOOH, $HCOOCH_3$, and CH_3COOH, however, imply that the chemistry of PPNe may not be conducive to form large organic molecules of biological interest (biomolecules). In fact, the only biomolecules that have been detected toward a PPN are formaldehyde (H_2CO; Cernicharo et al. 1989), toward CRL 618, and, in a tentative but unverified detection, methanol (CH_3OH), toward IRC +10216 (Latter & Charnley 1996). Numerous chemical models have been used to try to explain the formation and measured abundances of oxygen-bearing organic molecules in the ISM and CSE. These models include many different types of energetics, including shocks and thermal heating to drive the predicted chemistry. For our purposes, we include only a brief overview of some models and how they may apply to CSEs.

In the case of forming CH_3OH and H_2CO in a CSE, shock chemistry is invoked to explain the formation of H_2CO and CH_3OH. It is believed that both species would form in the postshock gas after CO dissociates. For CH_3OH, CH_4+OH or CH_3+ H_2O could form CH_3OH in the postshock gas (Latter & Charnley 1996; Hartquist et al. 1995). H_2CO would form in a similar manner, with the reaction of O+CH_3 and then the release of a H atom (Cernicharo 2004). Another possible formation mechanism is H addition after the dissociation of CO in the postshock gas.

Grain surface reactions are also proposed to account for the abundance of oxygen-bearing molecules. For example, Watanabe et al. (2004 and references therein) have shown that H_2CO and CH_3OH can form from both CO and CO-H_2O ice sprayed with cold H. From this experiment they concluded that for an ISM environment with 1 H atom cm^{-3} and a temperature of 10 K, a timescale of 10^6 yr would be necessary to match observed CO/CH_3OH and H_2CO/CH_3OH ratios in molecular clouds. Subsequent H addition has also been theorized to produce complex oxygen-bearing organic molecules, including propenal (CH_2CHCHO) and propanal (CH_3CH_2CHO) (Hollis et al. 2004). To date, however, CH_3OH has not been detected toward

CRL 618, and the timescale of the PPN phase is only about 10 thousand years. It is apparent that this formation mechanism would be too slow to produce detectable amounts of CH_3OH in CRL 618.

Finally, there are also gas-phase reaction schemes that attempt to predict the abundance of oxygen-bearing organic molecules. To investigate whether gas-phase reactions may be responsible for the formation of oxygen-bearing organic molecules in the CSE of CRL 618, we used the gas-phase reactions of the UMIST database (Le Teuff et al. 2000) and compared the predicted fractional abundance to the upper limits measured from our survey. The limitation that we found on this procedure is the limited number of reactions to form the larger oxygen-bearing organic molecules. However, we can discuss two molecular formation models and how they compare to our measured upper limits. Furthermore, as a constraint on our analysis, we included only formation models that contained molecules already detected toward CRL 618 or molecules that are structurally similar to other species but have not yet been detected.

We adopt a measured UV flux of $\sim 3 \times 10^6$ photons s^{-1}, a n_{H_2} abundance of 10^7 cm^{-3}, and a temperature of 100 K (Herpin & Cernicharo 2000). The proposed gas-phase reaction formation of HCOOH is $HCO^+ + H_2O \rightarrow HCOOH_2^+$ and the destruction mechanism is $HCOOH + h\nu \rightarrow HCO + OH$. HCO^+ and H_2O have been detected in the CSE of CRL 618, and their fractional abundances have also been measured. The calculated fractional abundance of HCOOH based on the formation model is $\sim 5 \times 10^{-11}$. The calculated upper limit based on our observations is $X_{HCOOH} \sim 2 \times 10^{-9}$. Thus, the combination of a lower abundance of H_2O and HCO^+ and a higher UV ionization rate suggests that doubly oxygenated molecules have abundances that are still too low to detect. No other oxygen-bearing organic molecule that we searched for had any formation mechanism based on species already found in the CSE of CRL 618 or formation models listed in the UMIST database.

However, the situation is less clear for the singly oxygenated species such as CH_3CHO. The proposed gas-phase reaction formation of CH_3CHO is $O + C_2H_5 \rightarrow CH_3CHO + H$, and the destruction mechanism is $CH_3CHO + h\nu \rightarrow CO + CH_4$. C_2H_5 has not yet been detected in the CSE of CRL 618; however, C_2H_4 has been detected, and the fractional abundance has been measured as $\sim 10^{-4}$. The calculated fractional abundance of CH_3CHO based on the formation model is $\sim 5 \times 10^{-6}$. The calculated upper limit based on our observations is below this value, $X_{CH_3CHO} \sim 10^{-6}$. The implication for the formation and detection of CH_3CHO is that if the abundance of C_2H_5 is similar to that of C_2H_4, gas-phase reactions like those listed above are not important to the formation of this molecule.

One obvious difference between PPNe and molecular cores that may account for the difference in grain surface reactions is their different grain properties. In the cold-collapse phase of molecular cores, molecules are depleted onto ices, where hydrogenation then slowly changes the chemical composition of the mantles. The mantles are then evaporated during the hot-core phase, and the subsequent release of these mantle species into the gas phase can then drive the complex chemistry observed in hot molecular cores. The envelopes of AGB stars and PPNe, on the other hand, are the actual sites of the formation of carbon dust via the formation of polycyclic aromatic hydrocarbons (PAHs). Hence, grain properties are very different from star-forming cores, and the cold-collapse phase is completely lacking. Therefore, if grain chemistry and the subsequent processing of the grain mantle products in a hot-gas phase constitute the main route to produce large organic biomolecules in a large abundance, they cannot be expected to exist in PPNe. For further reviews of the chemistry leading to organic molecules, see Tielens & Charnley (1997) and Ehrenfreund & Charnley (2000). Indeed, while a complex chemistry is taking place toward PPNe, including CRL 618, it appears that the physical conditions and chemistry may not be efficient enough for large organic biomolecules to be produced and detected.

5. SUMMARY

We have presented the results of our survey toward the proto−planetary nebula CRL 618 for several large, highly saturated organic molecules of biological importance including acetaldehyde (CH_3CHO), acetic acid (CH_3COOH), dimethyl ether (CH_3OCH_3), ethanol (CH_3CH_2OH), formic acid (HCOOH), and methyl formate ($HCOOCH_3$); large carbon chain molecules including methyl cyanide (CH_3CN), methylcyanoacetylene (CH_3C_3N), cyanoacetylene (HC_3N), cyanodiacetylene (HC_5N), and C_6H; and, finally, smaller molecules including ^{34}SO, SO_2, $OC^{34}S$, and MgNC. No biologically important organic molecules were detected. However, based on the 1 σ rms noise level in the spectral windows containing our large molecular species, we were able to place upper limits on the column density and fractional abundances relative to H_2 (Table 4). We made the first interferometric detection of CH_3CN toward CRL 618. Using a rotational temperature diagram of the $J = 6$–5 rotational transitions, we found a temperature of 88 (44) K, and from the temperature and distribution of CH_3CN toward CRL 618, we find that CH_3CN is formed in the outer envelope surrounding the UC H II region. We also made the first interferometric detection of vibrationally excited HC_5N toward this source, as well as detections of transitions of the $\nu_7 = 3$ and 4 states of HC_3N. The P Cygni line profile and corresponding channel maps of vibrationally excited HC_5N supports its distribution in the extended CSE expanding away from the central star. The detection of vibrationally excited HC_3N confirmed the temperature structure and column density of HC_3N in the extended envelope found by Wyrowski et al. (2003). Finally, our observations clearly indicate that CRL 618 is a good source of large carbon chain species but a very poor source for detecting or producing organic species of biological importance.

We acknowledge support from the Laboratory for Astronomical Imaging at the University of Illinois and NSF AST 99-81363 and AST 02-28953. We also greatly thank an anonymous referee, whose comments and suggestions provided additional insight to this manuscript.

REFERENCES

Bauder, A., Lovas, F. J., & Johnson, D. R. 1976, J. Phys. Chem. Ref. Data, 5, 53
Boucher, D., Burie, J., Bauer, A., Dubrulle, A., & Demaison, J. 1980, J. Phys. Chem. Ref. Data, 9, 659
Bujarrabal, V., Bachiller, R., Alcolea, J., & Martin-Pintado, J. 1988, A&A, 206, L17
Cernicharo, J. 2004, ApJ, 608, L41
Cernicharo, J., Guelin, M., Martin-Pintado, J., Penalver, J., & Mauersberger, R. 1989, A&A, 222, L1
Cernicharo, J., Heras, A. M., Pardo, J. R., Tielens, A. G. G. M., Guelin, M., Dartois, E., Neri, R., & Waters, L. B. F. M. 2001a, ApJ, 546, L127
Cernicharo, J., Heras, A. M., Tielens, A. G. G. M., Pardo, J. R., Herpin, F., Guelin, M., & Waters, L. B. F. M. 2001b, ApJ, 546, L123
Cummins, S. E., Green, S., Thaddeus, P., & Linke, R. A. 1983, ApJ, 266, 331
Ehrenfreund, P., Bernstein, M. P., Dworkin, J. P., Sandford, S. A., & Allamandola, L. J. 2001, ApJ, 550, L95

Ehrenfreund, P., & Charnley, S. B. 2000, ARA&A, 38, 427
Friedel, D. N., Snyder, L. E., Turner, B. E., & Remijan, A. 2004, ApJ, 600, 234
Fukasaku, S., Hirahara, Y., Masuda, A., Kawaguchi, K., Ishikawa, S., Kaifu, N., & Irvine, W. M. 1994, ApJ, 437, 410
Goldsmith, P. F., & Langer, W. D. 1999, ApJ, 517, 209
Groner, P., Albert, S., Herbst, E., & de Lucia, F. C. 1998, ApJ, 500, 1059
Guelin, M., & Cernicharo, J. 1991, A&A, 244, 21L
Hartquist, T. W., Menten, K. M., Lepp, S., & Dalgarno, A. 1995, MNRAS, 272, 184
Hasegawa, T. I., Herbst, E., & Leung, C. M. 1992, ApJS, 82, 167
Herpin, F., & Cernicharo, J. 2000, ApJ, 530, L129
Herpin, F., Goicoechea, J. R., Pardo, J. R., & Cernicharo, J. 2002, ApJ, 577, 961
Highberger, J. L., & Ziurys, L. M. 2003, ApJ, 597, 1065
Hollenbach, D., & Salpeter, E. E. 1971, ApJ, 163, 155
Hollis, J. M., Jewell, P. R., Lovas, F. J., Remijan, A., & Møllendal, H. 2004, ApJ, 610, L21
Ilyushin, V. V., et al. 2001, J. Mol. Spectrosc., 205, 286
Jennings, D. E., & Fox, K. 1982, ApJ, 254, 111
Latter, W. B., & Charnley, S. B. 1996, ApJ, 463, L37
Le Teuff, Y. H., Millar, T. J., & Markwick, A. J. 2000, A&AS, 146, 157
Liu, S.-Y., Girart, J. M., Remijan, A., & Snyder, L. E. 2002, ApJ, 576, 255
Lovas, F. J. 1982, J. Phys. Chem. Ref. Data, 11, 251
Maki, A. G. 1974, J. Phys. Chem. Ref. Data, 3, 221
Mehringer, D. M., & Snyder, L. E. 1996, ApJ, 471, 897
Müller, H. S. P., Thorwirth, S., Roth, D. A., & Winnewisser, G. 2001, A&A, 370, L49
Oesterling, L. C., Albert, S., de Lucia, F. C., Sastry, K. V. L. N., & Herbst, E. 1999, ApJ, 521, 255
Pardo, J. R., Cernicharo, J., Goicoechea, J. R., & Phillips, T. G. 2004, ApJ, 615, 495
Pickett, H. M., Poynter, R. L., Cohen, E. A., Delitsky, M. L., Pearson, J. C., & Muller, H. S. P. 1998, J. Quant. Spectrosc. Radiat. Transfer, 60, 883
Remijan, A., Shiao, Y.-S., Friedel, D. N., Meier, D. S., & Snyder, L. E. 2004a, ApJ, 617, 384
Remijan, A., Snyder, L. E., Friedel, D. N., Liu, S.-Y., & Shah, R. Y. 2003, ApJ, 590, 314
Remijan, A., Snyder, L. E., Liu, S.-Y., Mehringer, D. M., & Kuan, Y.-J. 2002, ApJ, 576, 264
Remijan, A., Sutton, E. C., Snyder, L. E., Friedel, D. N., Liu, S.-Y., & Pei, C. C. 2004b, ApJ, 606, 917
Sanchez Contreras, C., & Sahai, R. 2004, ApJ, 602, 960
Sault, R. J., Teuben, P. J., & Wright, M. C. H. 1995, in ASP Conf. Ser. 77, Astronomical Data Analysis Software and Systems IV, ed. R. A. Shaw, H. E. Payne, & J. J. E. Hayes (San Francisco: ASP), 433
Snyder, L. E., Lovas, F. J., Mehringer, D. M., Miao, N. Y., Kuan, Y.-J., Hollis, J. M., & Jewell, P. R. 2002, ApJ, 578, 245
Solomon, P. M., Jefferts, K. B., Penzias, A. A., & Wilson, R. W. 1971, ApJ, 168, L107
Sutton, E. C., Blake, G. A., Genzel, R., Masson, C. R., & Phillips, T. G. 1986, ApJ, 311, 921
Thorwirth, S. 2001, Ph.D. thesis, Univ. Köln
Thorwirth, S., Wyrowski, F., Schilke, P., Menten, K. M., Brünken, S., Müller, H. S. P., & Winnewisser, G. 2003, ApJ, 586, 338
Tielens, A. G. G. M., & Charnley, S. B. 1997, Origins Life Evolution Biosphere, 27, 23
Tielens, A. G. G. M., & Hagen, W. 1982, A&A, 114, 245
Tiemann, E. J. 1974, J. Phys. Chem. Ref. Data, 3, 259
Trammell, S. R. 2000, in ASP Conf. Ser. 199, Asymmetrical Planetary Nebulae II: From Origins to Microstructures, ed. J. Kastner, N. Soker, & S. Rappaport (San Francisco: ASP), 147
Ueta, T., Fong, D., & Meixner, M. 2001, ApJ, 557, L117
Watanabe, N., Nagaoka, A., Shiraki, T., & Kouchi, A. 2004, ApJ, 616, 638
Willemot, E., Dangoisse, D., Monnanteuil, N., & Bellet, J. 1980, J. Phys. Chem. Ref. Data, 9, 59
Winnewisser, G., & Walmsley, C. M. 1978, A&A, 70, 37L
Woods, P. M., Millar, T. J., Herbst, E., & Zijlstra, A. A. 2003, A&A, 402, 189
Wyrowski, F., Schilke, P., Thorwirth, S., Menten, K. M., & Winnewisser, G. 2003, ApJ, 586, 344
Wyrowski, F., Schilke, P., & Walmsley, C. M. 1999, A&A, 341, 882
Yamada, K. M. T., & Creswell, R. A. 1986, J. Mol. Spectrosc. 116, 384
Yamada, K. M. T., Degli Esposti, C., Botschwina, P., Förster, P., Bizzocchi, L., Thorwirth, S., & Winnewisser, G. 2004, A&A, 425, 767

Appendix H

BIMA Array Detections of HCN in Comets LINEAR (C/2002 T7) and NEAT (C/2001 Q4)

By
D. N. Friedel, Anthony J. Remijan, L. E. Snyder, M. F. A'Hearn, Geoffrey A. Blake, Imke de Pater, H. R. Dickel, J. R. Forster, M. R. Hogerheijde, C. Kraybill, L. W. Looney, Patrick Palmer & M. C. H. Wright
2005 ApJ 630, 623

The Astrophysical Journal, 630:623–630, 2005 September 1

BIMA ARRAY DETECTIONS OF HCN IN COMETS LINEAR (C/2002 T7) AND NEAT (C/2001 Q4)

D. N. Friedel,[1] Anthony J. Remijan,[2,3] L. E. Snyder,[1] M. F. A'Hearn,[4] Geoffrey A. Blake,[5] Imke de Pater,[6] H. R. Dickel,[1] J. R. Forster,[6] M. R. Hogerheijde,[7] C. Kraybill,[6] L. W. Looney,[1] Patrick Palmer,[8] and M. C. H. Wright[6]

Received 2004 August 18; accepted 2005 May 24

ABSTRACT

We present interferometric detections of HCN in comets LINEAR (C/2002 T7) and NEAT (C/2001 Q4) with the Berkeley-Illinois-Maryland Association (BIMA) array. With a $25''.4 \times 20''.3$ synthesized beam around comet LINEAR and using a variable temperature and outflow velocity (VTOV) model, we found an HCN column density of $\langle N_T \rangle = (6.4 \pm 2.1) \times 10^{12}$ cm^{-2} and a production rate of $Q(\mathrm{HCN}) = (6.5 \pm 2.2) \times 10^{26}$ s^{-1}, giving a production rate ratio of HCN relative to H_2O of $\sim(3.3 \pm 1.1) \times 10^{-3}$ and relative to CN of $\sim 4.6 \pm 1.5$. With a $21''.3 \times 17''.5$ synthesized beam around comet NEAT and using a VTOV model, we found an HCN column density of $\langle N_T \rangle = (8.5 \pm 4.5) \times 10^{11}$ cm^{-2} and a production rate of $Q(\mathrm{HCN}) = (8.9 \pm 4.7) \times 10^{25}$ s^{-1}, giving a production rate ratio of HCN relative to H_2O of $\sim(7.4 \pm 3.9) \times 10^{-4}$ and relative to CN of $\sim 0.3 \pm 0.2$. For both comets, the production rates relative to H_2O are similar to those found in previous comet observations. For comet LINEAR, the production rate relative to CN is consistent with HCN being the primary parent species of CN, while for comet NEAT it is too low for this to be the case.

Subject headings: comets: individual (C/2002 T7 (LINEAR), NEAT (C/2001 Q4)) — molecular processes — radio lines: solar system — techniques: interferometric

1. INTRODUCTION

HCN has been extensively studied around several comets, including comet P/Halley (Despois et al. 1986), comet Hyakutake (C/1996 B2) (e.g., Mumma et al. 1996; Lis et al. 1997; Womack et al. 1997; Biver et al. 1999a), comet Hale-Bopp (C/1995 O1) (e.g., Fitzsimmons & Cartwright 1996; Wright et al. 1998; Hirota et al. 1999; Irvine et al. 1999; Magee-Sauer et al. 1999; Ziurys et al. 1999; Veal et al. 2000; Snyder et al. 2001; Woodney et al. 2002), and comet LINEAR (C/1999 S4) (Bockelée-Morvan et al. 2001; Hogerheijde et al. 2004). Veal et al. (2000) made some of the first interferometric observations of HCN in comet Hale-Bopp. From the distribution and temporal behavior of the HCN emission, they were able to make very accurate calculations of the HCN production rate, as well as model its distribution in the coma using a spherical Haser model (Haser 1957). The deviations from the Haser model were explained by the existence of jets releasing HCN gas, a conclusion directly supported by high spatial resolution interferometric imaging of comet Hale-Bopp by Blake et al. (1999). Snyder et al. (2001) followed up the observations of Veal et al. (2000) and found the measured HCN scale length to be very similar to the theoretical predictions of Huebner et al. (1992) and Crovisier (1994).

In the spring of 2004, we were awarded a rare opportunity to observe two comets passing into the inner solar system and within ∼0.3 AU of the Earth. Comet LINEAR (C/2002 T7) reached perigee on 2004 May 19, coming within 0.27 AU, while comet NEAT (C/2001 Q4) reached perigee on 2004 May 7, coming within 0.32 AU. Both comets were identified as being dynamically new; such comets reach a peak of strong activity as they approach perihelion. It was extremely important to observe both comets when they were close to both perihelion and perigee in order to observe them near their peak emission and their maximum signal due to their proximity.

This paper describes the results of an effort to observe HCN in both comets LINEAR and NEAT with the Berkeley-Illinois-Maryland Association (BIMA) array[9] near Hat Creek, California (§ 2). We present interferometric detections of HCN in both comets and calculate the total beam-averaged HCN column densities and production rates by two methods. The first assumes the realistic scenario of a temperature and an outflow velocity that vary with cometocentric distance, and the second model assumes constant temperature and outflow velocity throughout the coma.

2. OBSERVATIONS

We used the BIMA array at Hat Creek, California (121°28′23″.9 west, 40°49′4″.1 north; altitude 1043 m) in D configuration (baselines from ∼6 to ∼35 m) cross-correlation mode to observe HCN in comets LINEAR (C/2002 T7) and NEAT (C/2001 Q4) during their 2004 apparitions.

The HCN observations of comet LINEAR, using JPL reference orbit 69, were taken on 2004 May 11 toward the topocentric

[1] Department of Astronomy, University of Illinois, 1002 West Green Street, Urbana IL 61801; friedel@astro.uiuc.edu, snyder@astro.uiuc.edu, lanie@astro.uiuc.edu, lwl@astro.uiuc.edu.

[2] NASA Goddard Space Flight Center, Computational and Information Sciences and Technologies Office, Code 606, Greenbelt, MD 20771; aremijan@pop900.gsfc.nasa.gov.

[3] National Research Council Resident Research Associate.

[4] Department of Astronomy, University of Maryland, College Park, MD 20742-2421; ma@astro.umd.edu.

[5] Division of Geological and Planetary Sciences and Division of Chemistry and Chemical Engineering, California Institute of Technology, MS 150-21, Pasadena, CA 91125; gab@gps.caltech.edu.

[6] Department of Astronomy, University of California, Berkeley, CA 94720; imke@floris.berkeley.edu, rforster@astro.berkeley.edu, ckraybill@astro.berkeley.edu, wright@astro.berkeley.edu.

[7] Leiden Observatory, PO Box 9513, 2300 RA, Leiden, Netherlands; michiel@strw.leidenuniv.nl.

[8] Department of Astronomy and Astrophysics, University of Chicago, Chicago, IL 60637; ppalmer@oskar.uchicago.edu.

[9] Operated by the University of California, Berkeley, the University of Illinois, and the University of Maryland with support from the National Science Foundation.

TABLE 1
HCN Molecular Line Parameters

Quantum Numbers	Frequency (MHz)	E_u (K)	$\langle S_{i,j}\mu^2 \rangle$ (D^2)
J = 1–0, F = 1–1	88,630.4157 (10)	4.3	3.0
J = 1–0, F = 2–1	88,631.8473 (10)	4.3	4.9
J = 1–0, F = 0–1	88,633.9360 (10)	4.3	1.0

coordinates $\alpha = 01^h15^m59\overset{s}{.}06$, $\delta = -07°39'16\overset{''}{.}5$ (J2000.0)[10] at the beginning of our observations (16:54 UT) and that moved to $\alpha = 01^h18^m20\overset{s}{.}56$, $\delta = -07°52'33\overset{''}{.}9$ (J2000.0) by the end of our observations (20:58 UT). The comet was at a heliocentric distance of 0.73 AU and a geocentric distance of 0.44 AU ($1'' = 319$ km at 0.44 AU). The spectral window containing the HCN hyperfine components had a bandwidth of 50 MHz and was divided into 128 channels, giving a channel spacing of 0.39 MHz (1.321 km s^{-1}). W3(OH) was used as the flux density calibrator for this observation. The quasar 0108+015 was used to calibrate the antenna-based gains.

The HCN observations of comet NEAT, using JPL reference orbit 123, were taken on 2004 May 23 toward the topocentric coordinates $\alpha = 09^h13^m54\overset{s}{.}67$, $\delta = 36°46'30\overset{''}{.}7$ (J2000.0) at the beginning of our observations (20:58 UT) and that moved to $\alpha = 09^h15^m23\overset{s}{.}16$, $\delta = 37°18'34\overset{''}{.}9$ (J2000.0) by the end of our observations (06:51 May 24 UT). The comet was at a heliocentric distance of 0.97 AU and a geocentric distance of 0.61 AU ($1'' = 442$ km at 0.61 AU). The spectral resolution was the same as for comet LINEAR. Mars was used as the flux density calibrator, and 0927+390 was used to calibrate the antenna-based gains.

The absolute amplitude calibration is accurate to within ∼20%. We note that our observations may cover a significant amount of the rotation period of comets LINEAR and NEAT. However, to date no rotation period has been given for either comet; thus, we are unable to comment on any effects this may have on our results. The data were combined and imaged using the MIRIAD software package (Sault et al. 1995). Table 1 lists the HCN molecular line parameters. The HCN spectroscopic constants were taken from Maki (1974). In the following, our analysis is for the strongest component, the $J = 1$–0, $F = 2$–1 transition.

3. RESULTS

Figures 1*a*–1*c* show our map and spectra of HCN around comet LINEAR (C/2002 T7). Figure 1*a* shows the map of the $J = 1$–0, $F = 2$–1 transition of HCN in 1 σ contours, starting at 2 σ. The synthesized beam of $25\overset{''}{.}4 \times 20\overset{''}{.}3$ is shown at the bottom left of the map. The line segment in the image shows the projection of the direction toward the Sun. The origin of the line segment is anchored at the predicted position of the comet nucleus. The coordinates are given in offset arcseconds centered on the comet nucleus. We note that the peak intensity of the HCN emission is offset from the predicted position of the nucleus by ∼5″ along the semimajor axis of the synthesized beam. In general, the positional uncertainty roughly scales as the beam size and signal-to-noise ratio (S/N). For comet LINEAR this uncertainty is 4″–5″, so the offset is not significant.[11] Figure 1*b* shows the cross-correlation spectrum of this transition. The dashed line corresponds to the rest frequency of the $J = 1$–0, $F = 2$–1 line for a cometocentric rest velocity of 0 km s^{-1}. The 1 σ rms noise level is seen at the left of the panel. The $F = 2$–1 line for comet LINEAR was fit with a Gaussian by a least-squares method, which gives a peak intensity of 0.59 ± 0.14 Jy $beam^{-1}$, a FWHM of 1.38 ± 0.34 km s^{-1}, and a cometocentric velocity of -0.29 ± 0.28 km s^{-1}. Figure 1*c* shows the cross-correlation spectrum (Hanning-smoothed over three channels) of this transition.

Figures 1*d*–1*f* show our map and spectra of HCN around comet NEAT (C/2001 Q4). Figure 1*d* shows the map of the $J = 1$–0, $F = 2$–1 transition of HCN in 1 σ contours, starting at 2 σ. The synthesized beam of $21\overset{''}{.}3 \times 17\overset{''}{.}5$ is shown at the bottom left of the map. We note, as with comet LINEAR, that the HCN peak intensity is offset by ∼5″ along the semimajor axis of our synthesized beam and that there is also some elongation of the source along this axis. We consider neither the offset nor the elongation to be significant because these are most likely due to the beam size and the low S/N. Figure 1*e* shows the cross-correlation spectrum of this transition. The dashed line is similar to Figure 1*b* for a cometocentric rest velocity of 0 km s^{-1}. The $F = 2$–1 line appears in only a single channel, so we assume a FWHM of ∼1.3 km s^{-1} for HCN. Figure 1*f* shows the cross-correlation spectrum (Hanning-smoothed over three channels) of this transition.

4. DISCUSSION

4.1. *Column Densities and Production Rates*

In the innermost coma, collisions between cold cometary species dominate the rotational population of the gas, but in the less dense outer coma the collision time becomes longer than the time for absorption of solar photons and the subsequent cascade of emission. In that case, the population can also be determined by solar radiation–driven fluorescence. Fluorescence effects could allow local thermodynamic equilibrium (LTE) to be maintained at a lower density than that required in optically thin cases (e.g., Crovisier 1984; Bockelée-Morvan et al. 1987). Lovell et al. (2004) determined that for the $J = 1$–0 transition of HCN for comet Hyakutake (C/1996 B2), the transition between collisionally dominated and fluorescence-dominated emission is between 26,000 and 38,000 km from the nucleus. Since both comet LINEAR and comet NEAT have similar water production rates relative to comet Hyakutake (D. G. Schleicher 2005, private communication; see § 4.2) at comparable heliocentric distances, we assume that their transition radii are also comparable. On the sky this translates to 82″–119″ for comet LINEAR and 59″–86″ for comet NEAT.

The synthesized beams sample a cylinder of gas through each comet,[12] and because the HCN volume density falls off faster than r^{-2} due to photodissociation, most of the contribution to the integrated line intensity will come from a sample on the order of the size of the projected synthesized beam. Since the synthesized beam is much smaller than the outer radii of the collisionally dominated regions, conditions significantly outside the beam are not likely to affect our observations.

The contribution from different cometocentric radii (i.e., from different source sizes) is determined by two factors. The first is that sources of differing size but equal total flux do not have equal peak fluxes and thus, when summed together, do not contribute equally to the total peak flux of a map. The second is that the array starts to resolve out flux from sources that are much

[10] We believe the positional accuracy to be good to a few arcseconds for our observations. This error is insignificant relative to the size of the synthesized beams (see § 3).

[11] This does not include any uncertainties in the ephemeris.

[12] In a small cylinder passing through the cometary gas, only a small fraction of the HCN will be in the less dense fluorescence zone. Hence, unlike the case for some optical molecular observations, here we assume that the HCN in the fluorescence zone can be ignored relative to that in the denser collisional zone.

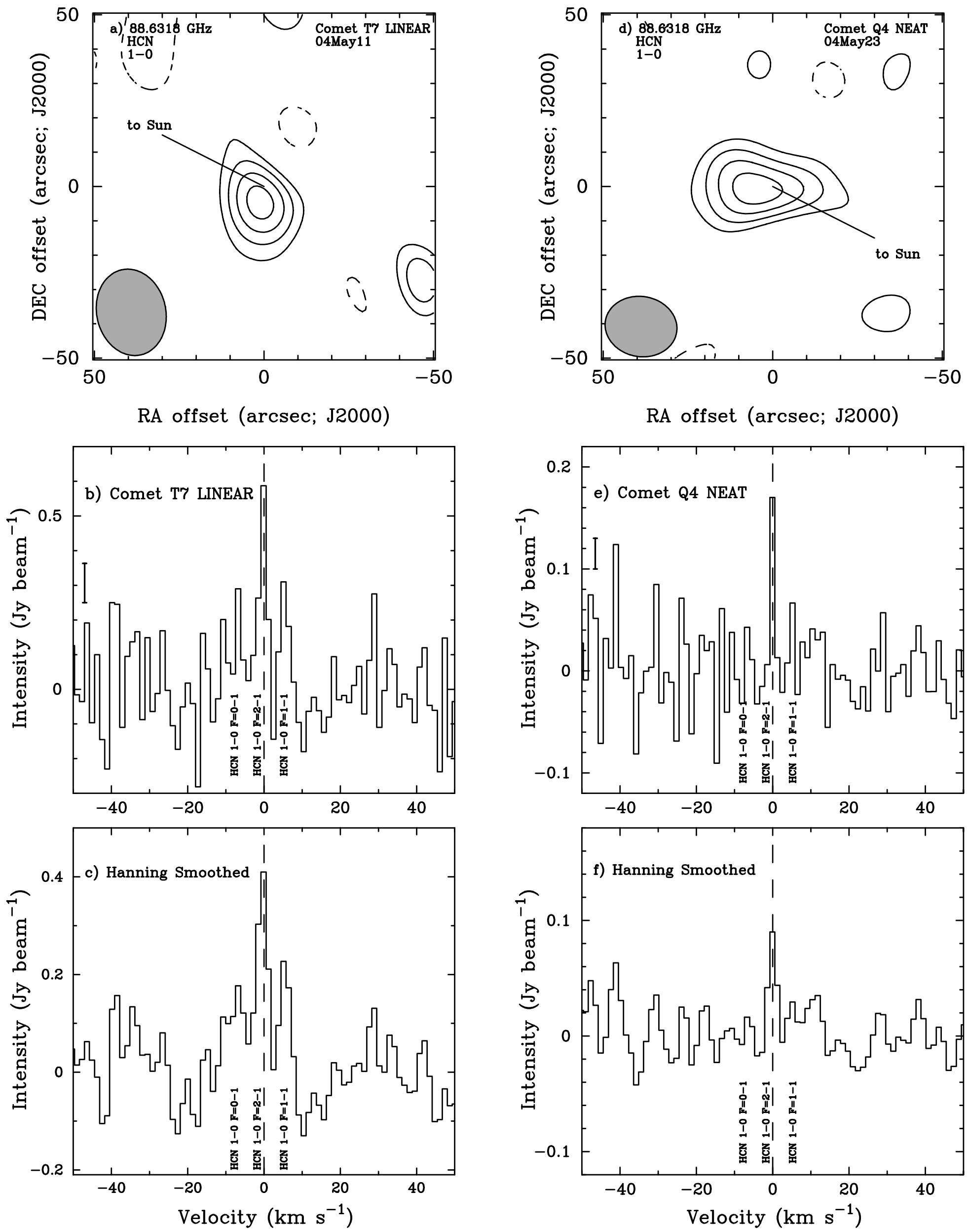

FIG. 1.—Comets LINEAR (C/2002 T7) and NEAT (C/2001 Q4) single-field HCN images and spectra. (*a*) Comet LINEAR emission contours from the $J = 1$–0, $F = 2$–1 transition of HCN at 88.6318 GHz. Contours indicate the HCN emission near its peak, centered at a cometocentric velocity of 0 km s^{-1}. The contour levels are −0.226, 0.226, 0.339, 0.452, and 0.565 Jy beam^{-1} (1 σ spacing). The peak is 0.63 Jy beam^{-1}. Image coordinates are offsets in arcseconds relative to the predicted position of the nucleus. The synthesized beam of 25.″41 × 20.″34 is in the lower left, and the line segment shows the solar direction. (*b*) HCN cross-correlation spectra. The abscissa is radial velocity relative to the comet nucleus. The ordinate is flux density per beam, I_ν, in janskys per beam; $\sigma \sim 0.113$ Jy beam^{-1} (indicated by the vertical bar at the left). The dashed line is centered on the rest frequency (88.6318 GHz). (*c*) HCN cross-correlation spectra (Hanning-smoothed over three channels). Labels are the same as in (*b*). (*d*) Comet NEAT emission contours from the $J = 1$–0, $F = 2$–1 transition of HCN. Contours indicate the HCN emission near its peak, centered at a cometocentric velocity of 0 km s^{-1}. The contour levels are −0.06, 0.06, 0.09, 0.12 and 0.15 Jy beam^{-1} (1 σ spacing). The peak is 0.17 Jy beam^{-1}. Image coordinates are the same as in (*a*). The synthesized beam of 21.″27 × 17.″53 is in the lower left, and the line segment shows the solar direction. (*e*) HCN cross-correlation spectra. The abscissa and ordinate are the same as in (*b*); $\sigma \sim 0.03$ Jy beam^{-1} (indicated by the vertical bar at the left). The dashed line is centered on the rest frequency (88.6318 GHz). (*f*) HCN cross-correlation spectra (Hanning-smoothed over three channels). The abscissa and ordinate are the same as in (*b*).

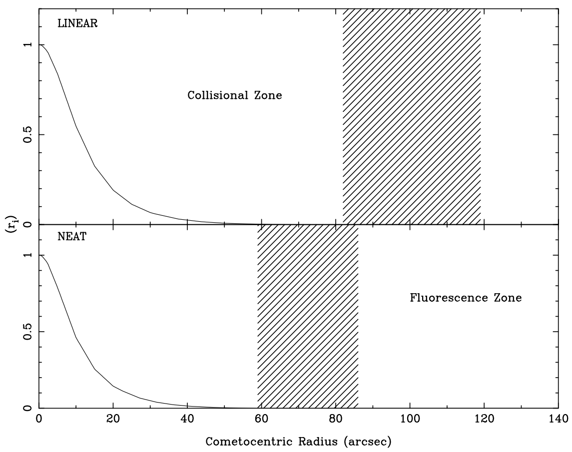

FIG. 2.—BIMA array response to source size for each comet. The top panel is from our comet LINEAR observations, and the bottom panel is from our comet NEAT observations. The abscissa is the cometocentric distance in arcseconds, and the ordinate is the array recovery factor r_i. The region of the cometary coma that is dominated by collisions is labeled "Collisional Zone." The hatched area denotes the region of the transition between collisionally dominated and fluorescence-dominated regions. The region of the coma that is dominated by fluorescence is labeled "Fluorescence Zone." The solid line shows r_i for each source size. The array response to different source sizes shows that we are sampling the inner, collisionally dominated region of the coma.

larger than the synthesized beam. The first effect is dominant for source sizes that are on the order of the synthesized beam, while the second becomes more dominant for larger source sizes. These two effects are illustrated in Figure 2. The top panel is from our comet LINEAR observations, and the bottom panel is from our comet NEAT observations. The abscissa is cometocentric radius in arcseconds of a source on the sky, and the ordinate is r_i, the array recovery factor (see the Appendix for a detailed explanation). The collisionally dominated region of the coma is labeled "Collisional Zone," the transition between the collisionally dominated and fluorescence-dominated regions is denoted by the hatching, and the fluorescence-dominated region is labeled "Fluorescence Zone." The solid line shows the peak flux detected by the array from each source size as a percentage of the peak flux of a point source of equal total flux. Thus, both from this figure and the above argument, it is clear that we are sampling the collisionally dominated region and are insensitive to fluorescence effects.

Our calculations are made assuming optically thin emission, since the limits on the satellite hyperfine components show that they are significantly weaker than the main component. For cross-correlation observations, $\langle N_T \rangle$, the beam-averaged molecular column density, is

$$\langle N_T \rangle = \frac{2.04 W_I Z e^{E_u/T_{\rm rot}}}{\theta_a \theta_b S \mu^2 \nu^3} \times 10^{20}\ {\rm cm}^{-2}, \qquad (1)$$

where $W_I = \int I_\nu\, dv$ in Jy beam^{-1} km s^{-1}, I_ν is the flux density per beam, Z is the rotational partition function ($Z = 0.47 T_{\rm rot}$), E_u is the upper state energy of the transition, $T_{\rm rot}$ is the rotation temperature, θ_a and θ_b are the FWHM synthesized beam dimensions in arcseconds, S is the line strength, μ is the dipole moment in Debye, and ν is the frequency in GHz.

From the least-squares fit to the comet LINEAR spectrum, we find an integrated line intensity of 1.46 ± 0.49 Jy beam^{-1} km s^{-1} for the $J = 1$–0, $F = 2$–1 HCN line around comet LINEAR.[13] From Figure 1*e*, we find an integrated line intensity of 0.22 ± 0.11 Jy beam^{-1} km s^{-1} for the $J = 1$–0, $F = 2$–1 HCN line around comet NEAT.[14]

4.1.1. *Model 1: Assuming Variable Temperatures and Outflow Velocities*

We consider the case in which the temperature and outflow velocity vary with cometocentric distance, as has been observed and modeled in previous comets (e.g., comets Hyakutake and Hale-Bopp; Combi et al. 1999a, 1999b). We label this the variable temperature and outflow velocity (VTOV) model. In order to do this, we modeled the HCN emission as concentric shells (of thickness 100 km out to a radius of 10,000 km and a thickness of 2000 km for radii of 10,000–30,000 km) around the nucleus and calculated the total column density and production rate. Since we consider both comets to be similar to comet Hyakutake, we used the velocity profiles from Figure 3 of Combi et al. (1999a) or the fit to those data from Lovell et al. (2004) to give velocities to each shell. The April 9 profile was used for comet LINEAR, and the March 30 profile and fit were used for comet NEAT, since on these dates comet Hyakutake was at similar heliocentric distances. These velocities were scaled to match the observed velocity profile of the spectral line, taking into account thermal broadening. Similarly, the temperature profiles for each comet were also taken from Combi et al. (1999a). Our VTOV model is explained in detail in the Appendix and gives total beam-averaged column densities of $\langle N_T \rangle = (6.4 \pm 2.1) \times 10^{12}$ cm^{-2} for comet LINEAR and $\langle N_T \rangle = (8.5 \pm 4.5) \times 10^{11}$ cm^{-2} for comet NEAT and production rates of Q(HCN) $= (6.5 \pm 2.2) \times 10^{26}$ s^{-1} for comet LINEAR and Q(HCN) $= (8.9 \pm 4.7) \times 10^{25}$ s^{-1} for comet NEAT.

4.1.2. *Model 2: Assuming Constant Temperatures and Outflow Velocities*

In the case of assuming constant $T_{\rm rot}$, the calculation of total beam-averaged column density is straightforward, using equation (1). For comet LINEAR we assume a rotation temperature of 115 K (DiSanti et al. 2004; Magee-Sauer et al. 2004; Küppers et al. 2004), and for comet NEAT we assume a rotation temperature of 52 K. The temperature for comet NEAT was derived from Figure 3 of Combi et al. (1999a) by averaging across the section of their March 30 curve that we are sensitive to, when comet Hyakutake was at a similar heliocentric distance. Using the above temperature for comet LINEAR, we find a total beam-averaged HCN column density (corrected for the other hyperfine components) of $\langle N_T \rangle = (9.5 \pm 3.2) \times 10^{12}$ cm^{-2}. Using the above temperature for comet NEAT, we find a total beam-averaged HCN column density (corrected for the other hyperfine components) of $\langle N_T \rangle = (9.6 \pm 5.1) \times 10^{11}$ cm^{-2}.

To calculate Q_p, the parent molecule production rate, we use the total beam-averaged column densities with the Haser model (Haser 1957). Since the Haser model assumes a constant outflow velocity, it is better suited for the fluorescence region than for the inner, collisionally dominated coma. However, we compare the Haser model results with our model, since the Haser model has been commonly used by previous cometary observations (Hogerheijde et al. 2004; Snyder et al. 2001; Veal et al. 2000; Wright et al. 1998).

[13] To convert this to integrated main-beam brightness temperature, multiply by 0.30 K (Jy beam^{-1})$^{-1}$.

[14] To convert this to integrated main-beam brightness temperature, multiply by 0.42 K (Jy beam^{-1})$^{-1}$.

TABLE 2

Comparison of Constant Temperature and Velocity Results with Variable Temperature and Outflow Velocity (VTOV) Results

Comet (1)	$\langle N_T \rangle$ (cm^{-2}) (2)	Q(HCN) (s^{-1}) (3)	$Q(HCN)/Q(H_2O)$ (4)	Q(HCN)/Q(CN) (5)
Constant Temperature and Outflow Velocity (Haser Model)				
LINEAR	$(9.5 \pm 3.2) \times 10^{12}$	$(5.1 \pm 1.7) \times 10^{26}$	$(2.6 \pm 0.9) \times 10^{-3}$	3.6 ± 1.2
NEAT	$(9.6 \pm 5.1) \times 10^{11}$	$(5.7 \pm 3.0) \times 10^{25}$	$(4.7 \pm 2.5) \times 10^{-4}$	0.2 ± 0.1
Variable Temperature and Outflow Velocity (VTOV Model)				
LINEAR	$(6.4 \pm 2.1) \times 10^{12}$	$(6.5 \pm 2.2) \times 10^{26}$	$(3.3 \pm 1.1) \times 10^{-3}$	4.6 ± 1.5
NEAT	$(8.5 \pm 4.5) \times 10^{11}$	$(8.9 \pm 4.7) \times 10^{25}$	$(7.4 \pm 3.9) \times 10^{-4}$	0.3 ± 0.2

For a photodissociation scale length λ_p, nuclear radius r_n, and constant radial outflow velocity v_0, the density as a function of r, $n_p(r)$, is given by Snyder et al. (2001),

$$n_p(r) = \frac{Q_p}{4\pi r^2 v_0} e^{-(r-r_n)/\lambda_p}. \tag{2}$$

For comets LINEAR and NEAT, we assume a nuclear radius of $r_n = 5$ km. We use a radial outflow velocity of $v_0 = 0.62$ km s^{-1} for comet LINEAR, based on the half-width at half-maximum (HWHM) of the Gaussian fit and taking into account the 10% increase in line width due to thermal broadening (Biver et al. 1999b), and $v_0 = 0.59$ km s^{-1} for comet NEAT, based on the single-channel half-width of the line and taking into account thermal broadening.

Consider a point on the line of sight that passes a projected distance, p, in the plane of the sky from the nucleus. For a given value of z, measured along the line of sight, this will correspond to a radial distance $r = (p^2 + z^2)^{1/2}$ from the nucleus. The column density, N_p, is given by (Snyder et al. 2001),

$$N_p(p) = \frac{Q_p}{4\pi v_0} e^{r_n/\lambda_p} \int_{-\infty}^{\infty} \frac{\exp\left\{-\left[(p^2+z^2)^{1/2}/\lambda_p\right]\right\}}{(p^2+z^2)} dz. \tag{3}$$

Finally, N_p from equation (3) may be averaged over the synthesized beam and equated to $\langle N_T \rangle$, the beam-averaged molecular column density, in order to obtain Q_p, the parent molecule production rate from the Haser model.

The quiet-Sun HCN photodissociation rate in the solar UV field at $r_H = 1$ AU is given by Huebner et al. (1992) as $\alpha(1 \text{ AU}) = 1.3 \times 10^{-5}$ s^{-1} and by Crovisier (1994) as 1.5×10^{-5} s^{-1}. The expected accuracy is 10%–20% (Crovisier 1994), so this is a reasonable agreement. Thus, we assume $\alpha(1 \text{ AU}) = 1.3 \times 10^{-5}$ s^{-1} (equivalent to $\sim 3.7 \times 10^4$ km for comet NEAT and $\sim 2.2 \times 10^4$ km for comet LINEAR). We find that the May 11 data around comet LINEAR give a production rate, Q(HCN), of $(5.1 \pm 1.7) \times 10^{26}$ s^{-1} and that the May 23 data around comet NEAT give a production rate of $(5.7 \pm 3.0) \times 10^{25}$ s^{-1}.

4.1.3. *Comparison of Models*

The column densities calculated with the VTOV model (model 1) are 11%–33% lower than those calculated with model 2. However, the production rates calculated with the VTOV model are 22%–36% higher than those calculated with the Haser model (see model 2 in § 4.1.2). These differences are not large. However, the VTOV model provides a better approximation than the Haser model for the physical conditions in the cometary collisional regions that the BIMA array sampled. Consequently, for the interferometric observations discussed in this paper, the VTOV model should produce more realistic results than the Haser model. Table 2 gives a comparison of the two methods. Column (1) gives the comet name, column (2) gives the total column density, column (3) gives the production rate, column (4) gives the HCN/H_2O ratio (see § 4.2), and column (5) gives the HCN/CN ratio (see § 4.3).

4.2. *Relative Production Rates of* HCN *to* H_2O

4.2.1. *Comet NEAT*

D. G. Schleicher (2005, private communication) measured H_2O production rates from comet NEAT and derived a scaling law of $Q(H_2O) \sim r_H^{-4.3}$, where r_H is the heliocentric distance of the comet. From his observations in 2004 May and June and the scaling law, we scaled the H_2O production rates from the heliocentric distances when they were measured to 0.97 AU for comet NEAT to match the r_H of our observations. Table 3 gives the measurements and their scaled values. Column (1) gives the

TABLE 3

Scaling of H_2O and CN Production Rates From Comet NEAT

Date (1)	r_H (AU) (2)	$Q(H_2O)$ (s^{-1}) (3)	Q(CN) (s^{-1}) (4)	Scaled $Q(H_2O)$[a] (s^{-1}) (5)	Scaled Q(CN)[b] (s^{-1}) (6)
2004 May 11	0.97	1.3×10^{29}	2.6×10^{26}	1.3×10^{29}	2.6×10^{26}
2004 May 12	0.96	1.3×10^{29}	2.5×10^{26}	1.2×10^{29}	2.4×10^{26}
2004 Jun 09	1.05	8.9×10^{28}	2.4×10^{26}	1.3×10^{29}	2.8×10^{26}
2004 Jun 10	1.06	7.9×10^{28}	2.1×10^{26}	1.2×10^{29}	2.6×10^{26}

Note.—Unscaled data are from D. G. Schleicher (2005, private communication).

[a] The H_2O production rates were scaled by $r_H^{-4.3}$ for each comet (see § 4.2).

[b] The CN production rates were scaled by $r_H^{-2.1}$ for each comet (see § 4.3).

date of observation, column (2) gives the heliocentric distance of the comet, columns (3) and (4) give the measured production rates of H_2O and CN (see § 4.3), respectively, and columns (5) and (6) give the scaled production rates for H_2O and CN, respectively. The average value for comet NEAT is $Q(H_2O) \sim 1.2 \times 10^{29}$ s^{-1}, which is very similar to water production rates measured from comet Hyakutake at similar heliocentric distances to those of our observations ($\sim 1 \times 10^{29}$ s^{-1}; Lis et al. 1997). If we assume constant temperature and outflow velocity, we find the production rate of HCN relative to H_2O for comet NEAT to be $\sim(4.7 \pm 2.5) \times 10^{-4}$. On the other hand, if we assume the more realistic VTOV model, we find the production rate of HCN relative to H_2O to be $\sim(7.4 \pm 3.9) \times 10^{-4}$ for comet NEAT. This is similar to the ratios observed around previous comets such as comet Hyakutake (1×10^{-3}; Lis et al. 1997).

4.2.2. *Comet LINEAR*

H_2O production rates were also measured for comet LINEAR by D. G. Schleicher (2005, private communication). From his data, he estimated the H_2O production rate to be $\sim 2 \times 10^{29}$ s^{-1} during our May 11 observations. If we assume constant temperature and outflow velocity, we find the production rate of HCN relative to H_2O to be $\sim(2.6 \pm 0.9) \times 10^{-3}$ for comet LINEAR. On the other hand, if we assume the more realistic VTOV model, we find the production rate of HCN relative to H_2O to be $\sim(3.3 \pm 1.1) \times 10^{-3}$. This is similar to the ratio observed around comet Hale-Bopp [$(2.1-2.6) \times 10^{-3}$; Snyder et al. 2001].

4.3. *Relative Production Rates of* HCN *to* CN

4.3.1. *Comet NEAT*

D. G. Schleicher (2005, private communication) measured CN production rates from comet NEAT and derived a scaling law of $Q(\mathrm{CN}) \sim r_H^{-2.1}$. From his observations in 2004 May and June and the scaling law, we scaled these values from the heliocentric distances where they were measured to the heliocentric distance of comet NEAT during our observations (see Table 3). Averaging these values gives $Q(\mathrm{CN}) \sim 2.6 \times 10^{26}$ s^{-1} for comet NEAT. If we assume constant temperature and outflow velocity, we find the production rate of HCN relative to CN to be $\sim 0.2 \pm 0.1$ for comet NEAT. On the other hand, if we assume the more realistic VTOV model, we find the production rate of HCN relative to CN to be $\sim 0.3 \pm 0.2$ for comet NEAT. The photodissociative branching ratio of HCN implies that $\sim$97% of HCN will be photodissociated into H and CN (Huebner et al. 1992). Woodney et al. (2002) concluded that HCN is most likely the primary parent species of CN. Thus, one would expect the HCN-to-CN ratio to be near 1. However, the ratio for comet NEAT is a factor of $\sim$3 smaller than the expected ratio.

4.3.2. *Comet LINEAR*

CN production rates were measured for comet LINEAR by D. G. Schleicher (2005, private communication). From his data, he estimated the CN production rate to be $\sim 1.4 \times 10^{26}$ s^{-1} during our May 11 observations. If we assume constant temperature and outflow velocity, we find the production rate of HCN relative to CN to be $\sim 3.6 \pm 1.2$ for comet LINEAR. On the other hand, if we assume the more realistic VTOV model, we find the production rate of HCN relative to CN to be $\sim 4.6 \pm 1.5$.

5. SUMMARY

We have detected the $J = 1-0$ transition of HCN in comets NEAT (C/2001 Q4) and LINEAR (C/2002 T7). We have calculated the total column density and production rates by two different models. The first (VTOV) model assumes the realistic scenario of temperature and outflow velocity that vary with cometocentric distance. We compare this model to one in which the temperature and outflow velocity are constant throughout the coma (Haser model). The differences between the outcomes of the models are $\sim$11%–33% for N_T and $\sim$22%–36% for Q. However, for the interferometric observations described in this paper, more realistic results will be obtained using the VTOV model outlined in § 4.1.1 and the Appendix. This model gives production rates of $Q(\mathrm{HCN}) = (6.5 \pm 2.2) \times 10^{26}$ s^{-1} and ratios of HCN/H_2O and HCN/CN of $\sim(3.3 \pm 1.1) \times 10^{-3}$ and $\sim 4.6 \pm 1.5$, respectively, for comet LINEAR and $Q(\mathrm{HCN}) = (8.9 \pm 4.7) \times 10^{25}$ s^{-1} and ratios of HCN/H_2O and HCN/CN of $\sim(7.4 \pm 3.9) \times 10^{-4}$ and $\sim 0.3 \pm 0.2$, respectively, for comet NEAT.

The HCN production rate relative to H_2O for comet NEAT is similar to that found previously for comet Hyakutake (Lis et al. 1997), while the ratio for comet LINEAR is similar to that observed from the highly productive comet Hale-Bopp (Snyder et al. 2001). The HCN production rate relative to CN for comet LINEAR is consistent with HCN being the primary parent of CN, as was suggested in Woodney et al. (2002). However, for comet NEAT the value is too low.

We thank J. R. Dickel for assisting with the observations, an anonymous referee for many helpful comments, and D. G. Schleicher for providing H_2O and CN production rates. This work was partially funded by NSF grants AST 02-28953, AST 02-28963, AST 02-28974, and AST 02-28955, and the Universities of Illinois, Maryland, and California, Berkeley, and Caltech.

APPENDIX

DESCRIPTION OF THE VTOV MODEL

The variable temperature and outflow velocity (VTOV) model consists of concentric spherical shells centered on a cometary nucleus of radius 5 km. The shells had a thickness of 100 km (with the exception of the first shell, which was 95 km thick) out to a cometocentric radius of 10,000 km and a thickness of 2000 km for radii from 10,000 to 30,000 km. Thirty thousand kilometers is equivalent to a cometocentric radius of 94″on the sky for comet LINEAR and 67.″9 for comet NEAT. This distance was chosen as the outer limit of our model because structures of this size contribute less than 0.1% to the peak flux, and the population of HCN at this radius is less than 40% of that of the central shell due to photodissociation. Thus, by the combination of these factors the contribution from any shells beyond 30,000 km would be negligible.

While quantities such as the outflow velocity and temperature vary in a very nonlinear way across the coma of each comet, the changes across any given shell are small enough to be considered linear. Thus, the quantities calculated for each shell, unless otherwise specified, are calculated at the average radius of each shell, since they are very close to the average value for the entire shell.

For the model we calculate the following quantities for each shell i.

1. The time, t_i, each molecule spends in the shell is given by

$$t_i = \frac{(R_i - R_{i-1})}{V_i}, \tag{A1}$$

where R_i and R_{i-1} are the outer and inner radii of shell i, respectively, and V_i is the average velocity of the molecule across the shell (from Combi et al. 1999a).

2. The total time, $t_{i,\mathrm{tot}}$, it takes a molecule to travel from the nucleus to midway between R_{i-1} and R_i is given by

$$t_{i,\mathrm{tot}} = \left(\sum_{j=1}^{i-1} t_j\right) + \frac{t_i}{2}. \tag{A2}$$

3. The number of molecules, n_i, in each shell is given by

$$n_i = Qt_i e^{-\alpha t_{i,\mathrm{tot}}/r_H^2}, \tag{A3}$$

where Q is the production rate, α is the photodissociation rate [assumed to be $\alpha(1\ \mathrm{AU}) = 1.3 \times 10^{-5}\ \mathrm{s}^{-1}$], and r_H is the heliocentric radius of the comet. Note that at this point it does not matter what value we give Q, since it does not vary from shell to shell and thus is a constant for this part of the model.

4. The BIMA array's flux recovery factor for the projected size of the shell on the sky is defined as the peak flux of a shell compared to that of a point source. This is a combination of a geometric effect (i.e., the flux is spread out over larger areas for larger shells), which is dominant for source sizes comparable to our synthesized beam size, and the fact that the array resolves out flux from sources that are much larger than the synthesized beam (array-filtering effect). The recovery factor is found in the following way.

A. Each source size (or shell) is modeled by first creating a Gaussian[15] source image for each concentric shell, of the appropriate FWHM and at the position on the sky of the comet, with the MIRIAD task `imgen`.[16] Every Gaussian shell is assumed to contribute equally to the flux recovery for a uniformly extended source.

B. In order to remove geometric and filtering effects, each image is run through `uvmodel` to produce a u-v data set that is the array's response to the input source based on the u-v tracks of our actual observations.

C. Each data set is then `inverted`, `cleaned`, and `restored` as usual to produce the final output map.

D. The peak intensity (p_i) of each map is compared to that of a point-source (p_{ps}) model of equal integrated intensity to give the array's recovery factor, r_i, where

$$r_i = \frac{p_i}{p_{\mathrm{ps}}}. \tag{A4}$$

Note that $r_i \to 0$ for an infinitely extended source, $r_i \to 1$ for a point source, and $r_i = 0.5$ if the source just fills the beam.

The array's recovery factor is illustrated in Figure 2. The top panel is for comet LINEAR, and the bottom panel is for comet NEAT. The abscissa is the cometocentric radius, and the ordinate is r_i. The solid line shows r_i for all shells.

5. The production rate Q of the comet is found by modifying equation (1),

$$\frac{4\ln(2) n_i r_i}{\pi ab} = \langle N_i \rangle = \frac{2.04 W_i Z_i e^{E_u/T_i}}{\theta_a \theta_b S \mu^2 \nu^3} \times 10^{20}\ \mathrm{cm}^{-2}. \tag{A5}$$

We note that $4\ln(2)/\pi ab$ is the projected area on the sky of our Gaussian synthesized beam (in square centimeters), N_i is the beam-averaged column density of the shell, W_i is the integrated line intensity of the shell, and T_i is the rotation temperature for the shell (from Combi et al. 1999a). Rearranging equation (A5) and incorporating the fact that

$$W = \sum_i W_i \tag{A6}$$

gives

$$W = \frac{1.36\theta_a \theta_b S \mu^2 \nu^3}{\pi ab} \sum_i \frac{n_i r_i}{Z_i e^{E_u/T_i}} \times 10^{-20}. \tag{A7}$$

[15] In this step we approximate the shells as Gaussian sources rather than as actual shells because any structure on the sky that has sharp edges, such as a shell, will produce ringing in the u-v plane and artifacts in the final map. Since the actual observations of the comets observed continuous distributions on the sky with no sharp edges, approximating the shell by a Gaussian is reasonable.

[16] Detailed descriptions of all MIRIAD tasks can be found at http://bima.astro.umd.edu/miriad/ref.html.

Incorporating equation (A3) and rearranging equation (A7) gives

$$Q = \frac{0.736 W \pi ab}{\theta_a \theta_b S \mu^2 \nu^3} \left(\sum_i \frac{r_i t_i e^{-\alpha t_{i,\mathrm{tot}}/r_H^2}}{Z_i e^{E_u/T_i}} \right)^{-1} \times 10^{20}. \tag{A8}$$

Since all factors on the right-hand side of equation (A8) are known, Q can be found. Note that in equation (A5) we divided n_i by the projected beam area rather than the projected area of the shell, even for those shells with a projected area larger than our beam. This is done because although there are some molecules outside the synthesized beam, they are contributing flux to the area inside the synthesized beam.

6. Now that Q has been found, we use it in equation (A3) to find n_i. Then we use each n_i in equation (A5) to find N_i for each shell. Then the total beam-averaged column density, $\langle N_T \rangle$, is given by the sum over all shells,

$$\langle N_T \rangle = \sum_i \langle N_i \rangle. \tag{A9}$$

REFERENCES

Biver, N., et al. 1999a, AJ, 118, 1850
———. 1999b, Earth Moon Planets, 78, 5
Blake, G. A., Qi, C., Hogerheijde, M. R., Gurwell, H. A., & Muhleman, D. O. 1999, Nature, 398, 213
Bockelée-Morvan, D., Crovisier, J., Despois, D., Forveille, T., Gerard, E., Schraml, J., & Thum, C. 1987, A&A, 180, 253
Bockelée-Morvan, D., et al. 2001, Science, 292, 1339
Combi, M. R., Cochran, A. L., Cochran, W. D., Lambert, D. L., & Johns-Krull, C. M. 1999a, ApJ, 512, 961
Combi, M. R., Kabin, K., DeZeeuw, D. L., Gombosi, T. I., & Powell, K. G. 1999b, Earth Moon Planets, 79, 275
Crovisier, J. 1984, A&A, 130, 361
———. 1994, J. Geophys. Res., 99, 3777
Despois, D., Crovisier, J., Bockelee-Morvan, D., Gerard, E., & Schraml, J. 1986, A&A, 160, L11
DiSanti, M. A., Reuter, D. C., Mumma, M. J., Dello Russo, N., Magee-Sauer, K., Gibb, E. L., Bonev, B., & Anderson, W. M. 2004, DPS Meeting 36, 23.08
Fitzsimmons, A., & Cartwright, I. M. 1996, MNRAS, 278, L37
Haser, L. 1957, Acad. R. Belgique Bull. Cl. Sci. Ser. 5, 43, 740
Hirota, T., Yamamoto, S., Kawaguchi, K., Sakamoto, A., & Ukita, N. 1999, ApJ, 520, 895
Hogerheijde, M. R., et al. 2004, AJ, 127, 2406
Huebner, W. F., Keady, J. J., & Lyon, S. P. 1992, Ap&SS, 195, 1
Irvine, W. M., Dickens, J. E., Lovell, A. J., Schloerb, F. P., Senay, M., Bergin, E. A., Jewitt, D., & Matthews, H. E. 1999, Earth Moon Planets, 78, 29
Küppers, M., Hartogh, P., & Villanueva, G. 2004, DPS Meeting 36, 25.05
Lis, D. C., et al. 1997, Icarus, 130, 355
Lovell, A. J., Kallivayalil, N., Schloerb, F. P., Combi, M. R., Hansen, K. C., & Gombosi, T. I. 2004, ApJ, 613, 615
Magee-Sauer, K., Dello Russo, N., DiSanti, M. A., Bonev, B., Gibb, E. L., & Mumma, M. J. 2004, DPS Meeting 36, 25.03
Magee-Sauer, K., Mumma, M. J., DiSanti, M. A., Russo, N. D., & Rettig, T. W. 1999, Icarus, 142, 498
Maki, A. G. 1974, J. Phys. Chem. Ref. Data, 3, 221
Mumma, M. J., Disanti, M. A., dello Russo, N., Fomenkova, M., Magee-Sauer, K., Kaminski, C. D., & Xie, D. X. 1996, Science, 272, 1310
Sault, R. J., Teuben, P. J., & Wright, M. C. H. 1995, in ASP Conf. Ser. 77, Astronomical Data Analysis Software and Systems IV, ed. R. A. Shaw, H. E. Payne, & J. J. E. Hayes (San Francisco: ASP), 433
Snyder, L. E., et al. 2001, AJ, 121, 1147
Veal, J. M., et al. 2000, AJ, 119, 1498
Womack, M., Festou, M. C., & Stern, S. A. 1997, AJ, 114, 2789
Woodney, L. M., et al. 2002, Icarus, 157, 193
Wright, M. C. H., et al. 1998, AJ, 116, 3018
Ziurys, L. M., Savage, C., Brewster, M. A., Apponi, A. J., Pesch, T. C., & Wyckoff, S. 1999, ApJ, 527, L67

Appendix I

Detection of Interstellar Acetone Toward the Orion-KL Hot Core

By

D. N. Friedel, L. E. Snyder, Anthony J. Remijan, and B. E. Turner

2005 ApJL 632, L95

The Astrophysical Journal, 632:L95–L98, 2005 October 20

DETECTION OF INTERSTELLAR ACETONE TOWARD THE ORION-KL HOT CORE

D. N. Friedel,[1] L. E. Snyder,[1] Anthony J. Remijan,[1,2,3] and B. E. Turner[4]
Received 2005 August 17; accepted 2005 September 12; published 2005 October 10

ABSTRACT

We present the first detection of interstellar acetone [$(CH_3)_2CO$] toward the high-mass star-forming region Orion-KL and the first detection of vibrationally excited $(CH_3)_2CO$ in the interstellar medium (ISM). Using the BIMA array, 28 emission features that can be assigned to 54 acetone transitions were detected. Furthermore, 37 of these transitions have not been previously observed in the ISM. The observations also show that the acetone emission is concentrated toward the hot core region of Orion-KL, contrary to the distribution of other large oxygen-bearing molecules. From our rotational temperature diagram, we find a beam-averaged $(CH_3)_2CO$ column density of $[2.0(0.3)–8.0(1.2)] \times 10^{16}$ cm^{-2} and a rotational temperature of 176(48)–194(66) K.

Subject headings: ISM: individual (Orion-KL) — ISM: molecules — radio lines: ISM

The first detection of interstellar acetone [$(CH_3)_2CO$] was reported by Combes et al. (1987) and later confirmed by Snyder et al. (2002), toward the hot molecular core source Sagittarius B2(N-LMH). Previous to this Letter, acetone had yet to be reported in any other high-mass or low-mass star-forming region despite being structurally similar to dimethyl ether [$(CH_3)_2O$]. Conversely, $(CH_3)_2O$ has been detected both in low-mass star-forming regions, including IRAS 16293−2422 (Cazaux et al. 2003), and high-mass star-forming regions, including Sgr (Winnewisser & Gardner 1976) and Orion (Snyder et al. 1974). It seemed therefore likely that acetone may be prevalent in other star-forming regions such as Orion-KL.

The Orion-KL region is the closest (~480 pc) site of massive star formation (Genzel et al. 1981). There are several cloud components (e.g., hot core, compact ridge, extended ridge, and plateau) that are associated with Orion-KL, each with different chemical and physical properties (see, e.g., Blake et al. 1987). The two most chemically interesting components, the hot core and compact ridge, are separated by only ~5800 AU. Large oxygen-bearing species (such as methyl formate [$HCOOCH_3$], dimethyl ether [$(CH_3)_2O$], and formic acid [HCOOH]) are observed primarily toward the compact ridge (e.g., Liu et al. 2002), while large nitrogen-bearing species (i.e., vinyl cyanide [C_2H_3CN] and ethyl cyanide [C_2H_5CN]) are located toward the hot core (e.g., Blake et al. 1987).

In this Letter, we present the first detection of interstellar $(CH_3)_2CO$ toward the high-mass star-forming region Orion-KL and the first detection of vibrationally excited $(CH_3)_2CO$ in the interstellar medium (ISM). Using the Berkeley-Illinois-Maryland Association (BIMA) array,[5] 28 emission features that can be assigned to 54 acetone transitions were detected toward the Orion hot core. The detection of $(CH_3)_2CO$ toward the Orion hot core is unusual, since it is a complex oxygen-bearing species, structurally similar to $(CH_3)_2O$, a compact-ridge species. This indicates that the formation of $(CH_3)_2CO$ may be very different from that of $(CH_3)_2O$ and may invoke N-bearing species or grain surface reactions. Finally, since acetone is prevalent toward the Orion hot core region, it is most likely that a spectral line assigned as interstellar glycine (NH_2CH_2COOH) toward the Orion-KL region can be assigned instead to interstellar $(CH_3)_2CO$.

The data presented were taken between 2002 and 2003 November as part of a 3 mm spectral line survey of the Orion-KL region by the BIMA array (D. N. Friedel et al. 2006, in preparation) in its C configuration. The phase center of our observations was $\alpha = 5^h35^m14^s.3$, $\delta = -5°22'27''.6$ (J2000), which is near the hot core ($\alpha = 5^h35^m14^s.5$, $\delta = -5°22'30''$) and the compact ridge ($\alpha = 5^h35^m14^s.2$, $\delta = -5°22'41''$). The array was operating in cross-correlation (double sideband) mode, with a sideband rejection of better than 20 dB. The correlator was configured to have four 50 MHz wide windows in each sideband with 128 channels per window. This resulted in a channel spacing of 391 kHz (~1.4–1.1 km s^{-1}), for all observations. Saturn was used as the flux density calibrator, and 0423−013 and 0609−157 were used to calibrate the antenna-based gains. The absolute amplitude calibration of 0423−013 and 0609−157 from the flux density calibrators is accurate to within ~20%. The passbands were automatically calibrated during data acquisition. The data were calibrated, continuum-subtracted, and imaged using the MIRIAD software package (Sault et al. 1995). The ground-state $(CH_3)_2CO$ molecular parameters were taken from Groner et al. (2002), and the vibrational $(CH_3)_2CO$ molecular parameters were taken from Groner et al. (2005).

Table 1 lists the molecular parameters and observational results for the detected acetone lines. Column (1) lists the rest frequency in MHz, column (2) lists the quantum numbers, column (3) lists the upper state energy (E_u) in K, column (4) lists the line strength (S_{ij}), column (5) lists the spin weight, column (6) lists the integrated line intensity (W) in Jy beam^{-1} km s^{-1}, column (7) lists the rest velocity of the transitions (V_{LSR}) in km s^{-1}, column (8) lists the synthesized beam size in arcseconds, and column (9) lists the figure in which the associated spectra appear. We detected a total of 28 spectral features that can be assigned to 54 $(CH_3)_2CO$ transitions, 37 of which have not been previously observed in the ISM, toward the Orion hot core. Of these 54 transitions, 46 are from the ground state and eight are from the first vibrationally excited state, which lies at 115 K above ground. No $(CH_3)_2CO$ transitions were seen, above our 3 σ limit, toward the Orion compact ridge.

[1] Department of Astronomy, 1002 West Green Street, University of Illinois, Urbana, IL 61801; friedel@astro.uiuc.edu, snyder@astro.uiuc.edu.

[2] Computational and Information Sciences and Technologies Office, Code 606, NASA Goddard Space Flight Center, Greenbelt, MD 20771; aremijan@pop900.gsfc.nasa.gov.

[3] National Research Council Resident Research Associate.

[4] National Radio Astronomy Observatory, 520 Edgemont Road, Charlottesville, VA 22903; bturner@nrao.edu.

[5] Operated by the University of California, Berkeley, the University of Illinois, and the University of Maryland with support from the National Science Foundation.

TABLE 1

ACETONE [$(CH_3)_2CO$] MOLECULAR LINE AND OBSERVATIONAL PARAMETERS[a]

Frequency[b] (MHz) (1)	Quantum Numbers (2)	E_u (K) (3)	S_{ij} (4)	Spin Weight (5)	W (Jy beam^{-1} km s^{-1}) (6)	V_{LSR} (km s^{-1}) (7)	$\theta_a \times \theta_b$ (arcsec) (8)	Fig. (9)
81,813.725 (12)	$7_{1,6}-6_{2,5}$ *EE*	17.47	5.21	16	1.5(1.0)	6.6(2.5)	12.99 × 8.33	[c]
82,895.112 (52)	$8_{*,8}-7_{*,7}$ *EE*, $\nu = 1$[d,e]	133.95	7.38	32	2.1(0.6)	6.0(2.3)	12.54 × 7.86	1*a*
82,908.654 (20)	$8_{*,8}-7_{*,7}$ *AE*	18.85	7.38	8	1.7(0.3)	6.9(0.9)	12.54 × 7.86	1*a*
82,908.702 (20)	$8_{*,8}-7_{*,7}$ *EA*	18.85	7.38	8	[f]	...	...	1*a*
82,916.525 (14)	$8_{*,8}-7_{*,7}$ *EE*	18.74	7.38	32	3.0(0.3)	7.3(0.4)	12.54 × 7.86	1*a*
82,924.325 (22)	$8_{*,8}-7_{*,7}$ *AA*	18.64	7.38	16	2.8(0.5)	7.5(1.1)	12.54 × 7.86	1*a*
87,507.547 (46)	$18_{8,10}-18_{7,11}$ *EE*[d,e]	130.60	8.27	16	2.8(0.3)	6.6(2.4)	13.16 × 9.21	1*b*
87,580.004 (44)	$18_{9,10}-18_{8,11}$ *EE*[d,e]	130.60	8.27	16	1.4(0.7)	4.5(0.5)	11.82 × 7.81	[c]
92,714.466 (54)	$9_{*,9}-8_{*,8}$ *EE*, $\nu = 1$[d,e]	138.41	8.38	32	3.1(0.8)	8.3(6.9)	13.89 × 6.20	1*c*
92,727.906 (22)	$9_{*,9}-8_{*,8}$ *AE*	23.30	8.38	8	3.3(0.9)	5.8(0.8)	13.89 × 6.20	1*c*
92,727.952 (20)	$9_{*,9}-8_{*,8}$ *EA*	23.30	8.38	8	[f]	...	...	1*c*
92,735.672 (16)	$9_{*,9}-8_{*,8}$ *EE*	23.19	8.38	32	4.1(0.5)	6.9(1.9)	13.89 × 6.20	1*c*
92,743.363 (24)	$9_{*,9}-8_{*,8}$ *AA*	23.09	8.38	16	[g]	...	...	1*c*
93,311.552 (90)	$22_{12,11}-22_{11,12}$ *EE*[d,e]	198.48	11.29	16	1.8(0.7)	6.5(1.7)	14.86 × 6.91	1*d*
98,651.514 (20)	$5_{5,1}-4_{4,1}$ *EE*[d,e]	14.09	3.63	16	5.6(0.4)	7.0(3.0)	13.86 × 6.19	1*e*
98,800.980 (14)	$5_{5,0}-4_{4,0}$ *EE*[d,e]	14.09	3.63	16	3.7(0.3)	6.2(1.3)	15.54 × 7.03	1*f*
99,422.080 (24)	$14_{*,11}-14_{*,12}$ *EE*[d,e]	68.11	3.33	32	2.7(0.5)	4.7(2.1)	13.64 × 6.61	1*g*
101,426.716 (19)	$9_{1,8}-8_{2,7}$ *AE/EA*[d]	26.84	7.21	10	4.7(0.4)	6.3(0.5)	12.91 × 6.74	1*h*
101,427.090 (19)	$9_{2,8}-8_{1,7}$ *AE/EA*[d]	26.84	7.21	6	[f]	...	...	1*h*
101,451.059 (14)	$9_{1,8}-8_{2,7}$ *EE*[d]	26.74	7.21	16	7.2(0.3)	6.7(1.0)	13.35 × 6.94	1*h*
101,451.446 (14)	$9_{2,8}-8_{1,7}$ *EE*[d]	26.74	7.21	16	[f]	...	...	1*h*
101,475.332 (22)	$9_{1,8}-8_{2,7}$ *AA*[d]	26.64	7.21	10	[h]	...	...	1*h*
101,475.733 (22)	$9_{2,8}-8_{1,7}$ *AA*[d]	26.64	7.21	6	[h]	...	...	1*h*
102,533.756 (58)	$10_{*,10}-9_{*,9}$ *EE*, $\nu = 1$[d,e,i]	143.33	9.37	32	2.7(0.5)	6.3(1.5)	12.80 × 6.17	1*i*
102,547.058 (22)	$10_{0,10}-9_{1,9}$ *AE/EA*[d]	28.22	9.38	16	[j]	...	...	1*i*
102,554.696 (18)	$10_{0,10}-9_{1,9}$ *EE*[d]	28.11	9.38	32	4.5(0.4)	6.9(1.9)	12.80 × 6.17	1*i*
102,562.281 (26)	$10_{0,10}-9_{1,9}$ *AA*[d]	28.01	9.38	16	4.7(0.5)	6.8(2.4)	12.80 × 6.17	1*i*
108,434.511 (32)	$14_{2,12}-14_{1,13}$ *EE*[d,e]	63.34	2.29	32	2.0(0.5)	6.9(1.1)	12.22 × 5.64	1*j*
111,243.359 (22)	$10_{*,9}-9_{*,8}$ *AE*[d]	32.17	8.21	8	3.6(0.4)	7.1(1.2)	12.44 × 5.77	1*k*
111,243.448 (20)	$10_{*,9}-9_{*,8}$ *EA*[d]	32.17	8.21	8	[f]	...	...	1*k*
111,267.540 (16)	$10_{*,9}-9_{*,8}$ *EE*[d]	32.07	8.21	32	5.6(0.2)	6.6(0.9)	12.44 × 5.77	1*k*
111,291.600 (24)	$10_{*,9}-9_{*,8}$ *AA*[d]	31.98	8.21	16	[k]	...	...	1*k*
112,352.908 (60)	$11_{*,11}-10_{*,10}$ *EE*, $\nu = 1$[d,e]	148.71	10.37	32	[l]	...	...	1*l*
112,373.548 (18)	$11_{0,11}-10_{1,10}$ *EE*[d,e]	33.51	10.39	32	[m]	...	...	1*l*

[a] Degenerate pairs of transitions are denoted with an asterisk in the quantum numbers or list two torsional states (i.e., *AE/EA*). The reported frequency is the average frequency of the transitions, and the reported spin weight is the sum from the transitions. See Groner et al. (2002, 2005) for a complete listing.

[b] Frequency uncertainty is 2 σ.

[c] Transition will be shown in D. N. Friedel et al. (2006, in preparation).

[d] Not previously observed in the ISM.

[e] The *AA*, *AE*, and *EA* transitions were below the 3 σ detection limit.

[f] This transition is blended with the previous one(s), and the integrated line intensity and column density are calculated as such.

[g] The *AA* transitions are less than 3 σ and thus are not used in the calculations.

[h] This transition is blended with the $18_{3,15}-18_{3,16}$ *E* transition of methyl formate ($HCOOCH_3$).

[i] This transition of $(CH_3)_2CO$ is coincident with the $6_{0,6}-5_{0,5}$ transition of ethanol (C_2H_5OH); however, since C_2H_5OH is thought to be a compact-ridge species (Schilke et al. 1997) and is only weakly detected toward the compact ridge, we consider the contamination from C_2H_5OH to be minimal.

[j] This transition is blended with the 6_0-5_0 transition of propyne (CH_3CCH).

[k] This transition is blended with the $7_{2,5}-8_{1,8}$ A^- transition of methanol (CH_3OH).

[l] This transition is blended with the $11_{1,11}-10_{0,10}$ *A*, $\nu_t = 1$ transition of ethyl cyanide (C_2H_5CN).

[m] This transition may be blended with the $8_{1,8}-7_{0,7}$ ${}^1\nu_{11}$ transition of vinyl cyanide (C_2H_3CN) and is not used in the calculations.

Figure 1 shows the spectra of each of our detected transitions and nearby identified and unidentified lines. All spectra are Hanning smoothed over three channels, and the spectral line fiducials are for a V_{LSR} of 5 km s^{-1}. The "I" bar in the upper left corner of each panel denotes the 1 σ rms noise level for the plot. In Figures 1*c* and 1*d*, the dotted line and second "I" bar denote where a second spectral window was located and the associated 1 σ rms noise level of that window.

Figure 2 shows the map of the $8_{*,8}-7_{*,7}$ *EE* degenerate transitions of $(CH_3)_2CO$ ($E_u = 19$ K) in heavy contours. Contours are $\pm 3\ \sigma$ and $\pm 5\ \sigma$ ($\sigma = 0.09$ Jy beam^{-1}). The light contours are the $7_{0,7}-6_{1,6}$ fourfold-degenerate transition of $(CH_3)_2O$ ($E_u = 25$ K, $\nu = 111.783112$ GHz). Contour spacing is 4 σ starting at 4 σ ($\sigma = 0.24$ Jy beam^{-1}). The hot core and compact ridge are labeled and indicated by the plus signs. Note that the $(CH_3)_2CO$ emission traces closer to the hot core, while the $(CH_3)_2O$ emission traces closer to the compact ridge. The synthesized beams for each species are in the lower left corner of the map. The average V_{LSR} for the detected $(CH_3)_2CO$ transitions is 6.4(1.3)[6] km s^{-1}, which is between the V_{LSR} for the hot core (~5 km s^{-1}) and the compact ridge (~8 km s^{-1}). Yet it is consistent with the V_{LSR} of other molecular species (Blake et al. 1987). The maps of the transitions, however, indicate that $(CH_3)_2CO$ is more closely associated with the hot core than the compact ridge (Blake et al. 1987).

For interferometric observations, the total column density $\langle N_T \rangle$ can be calculated from

$$\frac{\langle N_T \rangle}{q_{rv}} e^{-E_u/T_{rot}} = \frac{\langle N_u \rangle}{g_u} = \frac{2.04}{B\theta_a\theta_b S\mu^2\nu^3}\left(\frac{W}{g}\right) \times 10^{20}\ \mathrm{cm}^{-2} \quad (1)$$

[6] All uncertainties are 1 σ unless otherwise noted.

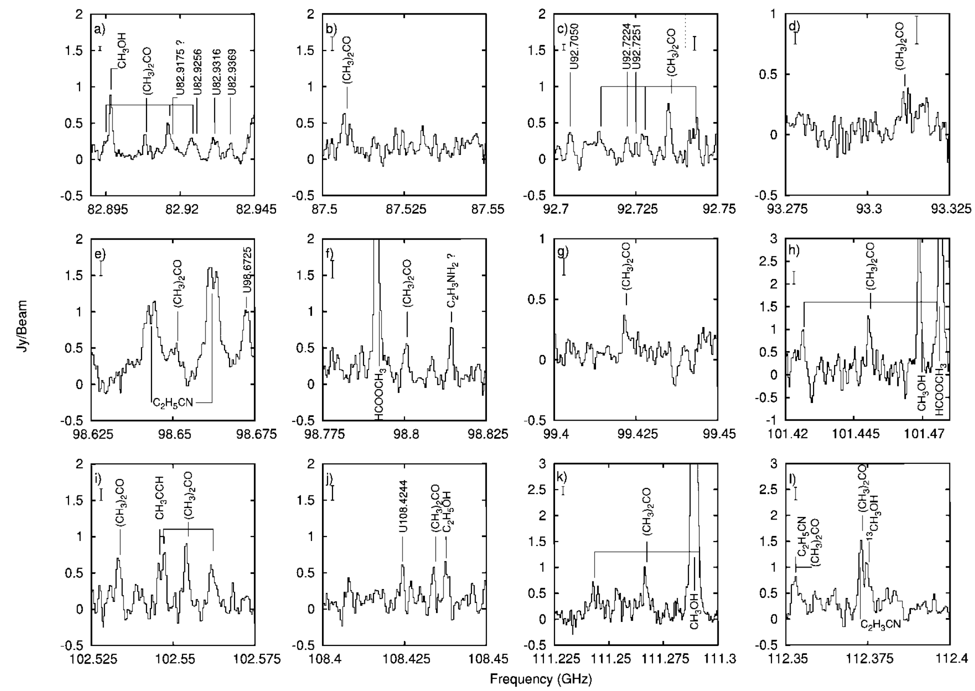

FIG. 1.—Spectra of each of the detected acetone [$(CH_3)_2CO$] transitions toward the Orion hot core, along with nearby identified and unidentified transitions. All spectra have been Hanning smoothed over three channels. The "I" bar in the upper left corner of each panel denotes the 1 σ rms noise level for the respective panel. The dotted line and second "I" bar in (*c*) and (*d*) indicate where a second window is located and its associated 1 σ rms noise level.

(Snyder et al. 2002, 2005), where $\langle N_u \rangle / g_u$ is the beam-averaged upper level column density over the statistical weight, B is the beam filling factor, g is the spin weight, μ is the dipole moment (μ_b = 2.93 D), ν is the transition frequency in GHz, $T_{\rm rot}$ is the rotational temperature, and E_u is the upper level energy of the transition in K. The rotational-vibrational partition function, $q_{\rm rv}$, is defined as

$$q_{\rm rv} \approx \sum_{i=0}^{2} e^{-E_i/T_{\rm rot}} q_r, \tag{2}$$

where E_i are the energies above ground for the ground state and the first two vibrational states (0, 115, and 180 K, respectively) and q_r is the rotational partition function[7] ($261.7 T_{\rm rot}^{3/2}$) (Groner et al. 2002, 2005; Widicus Weaver et al. 2005). Even though we did not detect any transitions from the second vibrationally excited state, it lies only 180 K above ground and thus will have a significant population at temperatures above 100 K. For a set of degenerate transitions, g is the sum of the spin weights of the blended states. By plotting $\ln(\langle N_u \rangle / g_u)$ for each integrated line intensity in Table 1 versus E_u, we can obtain the total beam-averaged column density and rotational temperature of $(CH_3)_2CO$. Figure 3 shows the rotational temperature diagram (assuming the source fills our synthesized beams, B = 0.5, as discussed in Snyder et al. 2005) and yields $\langle N_T \rangle$ = 2.0(0.3) × 10^{16} $\rm cm^{-2}$ and $T_{\rm rot}$ = 176(48) K. If instead we assume a source size similar to the hot core continuum size seen by Liu et al. (2002) of 5″ × 3″, the diagram yields $\langle N_T \rangle$ = 8.0(1.2) × 10^{16} $\rm cm^{-2}$ and $T_{\rm rot}$ = 194(66) K. Both temperatures are reasonable considering the range in temperatures observed toward the hot core (~100 K [C_2H_5CN; White et al. 2003] to ~300 K [HC_3N; Wright et al. 1996]). From these column densities, rotation temperatures, and Turner

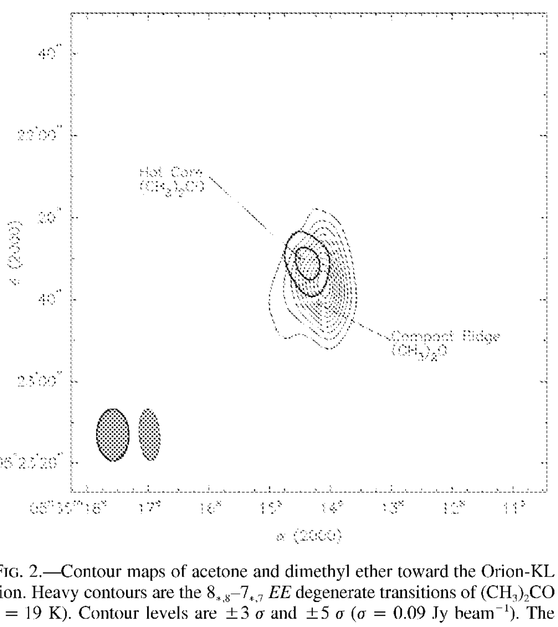

FIG. 2.—Contour maps of acetone and dimethyl ether toward the Orion-KL region. Heavy contours are the $8_{*,8}$–$7_{*,7}$ *EE* degenerate transitions of $(CH_3)_2CO$ (E_u = 19 K). Contour levels are ±3 σ and ±5 σ (σ = 0.09 Jy $\rm beam^{-1}$). The light contours are the $7_{0,7}$–$6_{1,6}$ degenerate transitions of $(CH_3)_2O$ (E_u = 25 K, ν = 111.783112 GHz). Contour spacings are 4 σ starting at 4 σ (σ = 0.24 Jy $\rm beam^{-1}$). The hot core and compact ridge are labeled with plus signs. The synthesized beams for the respective maps are in the lower left corner.

[7] The rotational part of the partition function is approximated by the ground-state q_r, since q_r for the first vibrational state differs from the ground state by less than 1 part in 1000 and q_r for the second vibrational state has not been reported.

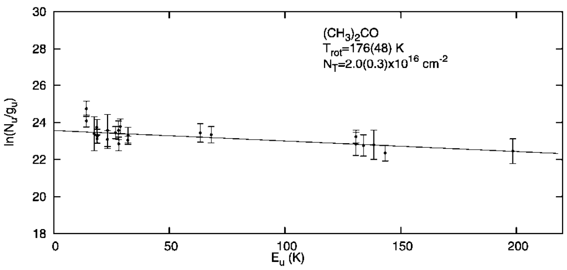

FIG. 3.—Rotational temperature diagram for detected acetone transitions. The ordinate is ln $(\langle N_u \rangle / g_u)$, the abscissa is E_u in K, and the uncertainties are 1 σ. The weighted least-squares fit is shown by the line. The resulting rotational temperature and column density are shown.

(1991), we calculated the opacity to be less than 0.02 for all transitions. For an H_2 column density of $\sim 5 \times 10^{24}$ cm^{-2} (Kaufman et al. 1998 and references therein), we find a fractional abundance of $[4.0(0.6)\text{–}16.0(2.4)] \times 10^{-9}$, which is higher than the fractional abundance of $(CH_3)_2CO$ toward Sgr B2(N-LMH) $[(4\text{–}30) \times 10^{-10}$; Snyder et al. 2002]. The difference however can be attributed our use of the vibrational part of the partition function. If we recalculate the abundances from Sgr B2(N-LMH) including the vibrational part of the partition function, it agrees with our abundance toward Orion.

The detection of $(CH_3)_2CO$ toward the hot core and the nondetection (above 3 σ) toward the compact ridge make $(CH_3)_2CO$ the only known highly saturated O species that is seen only toward the hot core. This suggests a formation mechanism such as high-temperature gas-phase reactions (i.e., neutral-neutral) or grain surface reactions, as was suggested by Herbst et al. (1990), rather than formation in or behind a shock front (i.e., ion-molecule chemistry or liberation from the grain surface).

Finally, the detection of acetone toward the Orion hot core is also very significant because it shows that a spectral feature previously identified as glycine may in fact be due to interstellar acetone. Kuan et al. (2003) noted that one of the lines assigned to glycine was coincident with the $31_{*,19}\text{–}31_{*,20}$ *EE* degenerate $(CH_3)_2CO$ pair. The identification of a transition of $(CH_3)_2CO$ was dismissed as unlikely because of its unfavorable quantum numbers. However, we can calculate the expected integrated intensity for these degenerate acetone transitions using the $(CH_3)_2CO$ column densities from this work and from equations (1) and (2) of Snyder et al. (2005). Solving equations (1) and (2) of Snyder et al. (2005) for the integrated line intensity (W), we find

$$W = \frac{\langle N_T \rangle g S \mu^2 \nu B^*}{1.67 q_{rv} e^{E_u/T_{rot}}} \times 10^{-14} \text{ K km s}^{-1}, \qquad (3)$$

where, for these transitions, $g = 16 + 16 = 32$, $S = 12.555$, $\nu = 164.870$ GHz, and $E_u = 364$ K. Also, $B^* = \eta_M^* B$, where η_M^* is the corrected main-beam efficiency for the NRAO 12 m telescope ($\eta_M^* \sim 0.7$ at 164 GHz). If we use the $5'' \times 3''$ source size and associated $\langle N_T \rangle$ and T_{rot}, we calculate an integrated line intensity of 0.218(0.031) K km s^{-1}. Comparing this value with that reported by Kuan et al. (2003) of 0.091(0.035) K km s^{-1}, we see that the integrated line intensity overlaps with the reported value at the 2 σ level. Because of the detection of 54 transitions of interstellar $(CH_3)_2CO$ toward the Orion hot core, it is most likely that the transition attributed to glycine by Kuan et al. is due to $(CH_3)_2CO$.

We have reported the detection of 54 $(CH_3)_2CO$ transitions toward the Orion-KL hot core region with a column density of $[2.0(0.3)\text{–}8.0(1.2)] \times 10^{16}$ cm^{-2} and a rotational temperature of 176(48)–194(66) K. We also have reported the first detection of vibrationally exited $(CH_3)_2CO$ in the ISM. The detection of a large O-bearing species purely toward the hot core suggests that the formation of $(CH_3)_2CO$ may be very different from that of $(CH_3)_2O$ and may invoke N-bearing species or grain surface reactions.

We thank P. Groner and B. Drouin for supplying useful data. We also thank an anonymous referee for a very favorable review of this work. This work was partially funded by grant NSF AST 02-28953 and the University of Illinois.

REFERENCES

Blake, G. A., Sutton, E. C., Masson, C. R., & Phillips, T. G. 1987, ApJ, 315, 621
Cazaux, S., Tielens, A. G. G. M., Ceccarelli, C., Castets, A., Wakelam, V., Caux, E., Parise, B., & Teyssier, D. 2003, ApJ, 593, L51
Combes, F., Gerin, M., Wootten, A., Wlodarczak, G., Clausset, F., & Encrenaz, P. J. 1987, A&A, 180, L13
Genzel, R., Reid, M. J., Moran, J. M., & Downes, D. 1981, ApJ, 244, 884
Groner, P., Albert, S., Herbst, E., De Lucia, F. C., Lovas, F. J., Drouin, B. J., & Pearson, J. C. 2002, ApJS, 142, 145
Groner, P., Herbst, E., De Lucia, F. C., Drouin, B. J., & Mäder, H. 2005, in Proc. 60th Ohio State Univ. Intl. Symp. on Molecular Spectroscopy (Columbus: Ohio State Univ.), 206
Herbst, E., Giles, K., & Smith, D. 1990, ApJ, 358, 468
Kaufman, M. J., Hollenbach, D. J., & Tielens, A. G. G. M. 1998, ApJ, 497, 276
Kuan, Y.-J., Charnley, S. B., Huang, H.-C., Tseng, W.-L., & Kisiel, Z. 2003, ApJ, 593, 848
Liu, S.-Y., Girart, J. M., Remijan, A., & Snyder, L. E. 2002, ApJ, 576, 255
Sault, R. J., Teuben, P. J., & Wright, M. C. H. 1995, in ASP Conf. Ser. 77, Astronomical Data Analysis Software and Systems IV, ed. R. A. Shaw, H. E. Payne, & J. J. E. Hayes (San Francisco: ASP), 433
Schilke, P., Groesbeck, T. D., Blake, G. A., & Phillips, T. G. 1997, ApJS, 108, 301
Snyder, L. E., Buhl, D., Schwartz, P. R., Clark, F. O., Johnson, D. R., Lovas, F. J., & Giguere, P. T. 1974, ApJ, 191, L79
Snyder, L. E., Lovas, F. J., Mehringer, D. M., Miao, N. Y., Kuan, Y.-J., Hollis, J. M., & Jewell, P. R. 2002, ApJ, 578, 245
Snyder, L. E., et al. 2005, ApJ, 619, 914
Turner, B. E. 1991, ApJS, 76, 617
White, G. J., Araki, M., Greaves, J. S., Ohishi, M., & Higginbottom, N. S. 2003, A&A, 407, 589
Widicus Weaver, S. L., Butler, R. A. H., Drouin, B. J., Petkie, D. T., Dyl, K. A., De Lucia, F. C., & Blake, G. A. 2005, ApJS, 158, 188
Winnewisser, G., & Gardner, F. F. 1976, A&A, 48, 159
Wright, M. C. H., Plambeck, R. L., & Wilner, D. J. 1996, ApJ, 469, 216

References

Allen, M., & Robinson, G. W. 1975, ApJ, 195, 81

Bernath, P. F. 1995, Spectra of Atoms and Molecules (Oxford University Press:New York)

Bester, M., Yamada, K., Winnewisser, G., & Urban, S. 1983, A&A, 121, L13

Biver, N., Bockelée-Morvan, D., Crovisier, J., Davies, J. K., Matthews, H. E., Wink, J. E., Rauer, H., Colom, P., Dent, W. R. F., Despois, D., Moreno, R., Paubert, G., Jewitt, D., & Senay, M. 1999, AJ, 118, 1850

Biver, N., Bockelée-Morvan, D., Crovisier, J., Colom, P., Henry, F., Moreno, R., Paubert, G., Despois, D., & Lis, D. C. 2002, Earth Moon and Planets, 90, 323

Blake, G. A., Mundy, L. G., Carlstrom, J. E., Padin, S., Scott, S. L., Scoville, N. Z., & Woody, D. P. 1996, ApJ, 472, L49

Blake, G. A., Sutton, E. C., Masson, C. R., & Phillips, T. G. 1987, ApJ, 315, 621

Bockelee-Morvan, D., & Crovisier, J. 1985, A&A, 151, 90

Bockelee-Morvan, D., Crovisier, J., Baudry, A., Despois, D., Perault, M., Irvine, W. M., Schloerb, F. P., & Swade, D. 1984, A&A, 141, 411

Bockelee-Morvan, D., Crovisier, J., Despois, D., Forveille, T., Gerard, E., Schraml, J., & Thum, C. 1987, A&A, 180, 253

Bogey, M., Demuynck, C., & Destombes, J. L. 1984, Canadian Journal of Physics, 62, 1248

Boucher, D., Burie, J., Bauer, A., Dubrulle, A., & Demaison, J. 1980, J. Phys. Chem. Ref. Data, 9, 659

Cazaux, S., & Tielens, A. G. G. M. 2002, ApJ, 575, L29

Cerceau, F., Raulin, F., Courtin, R., & Gautier, D. 1985, Icarus, 62, 207

Charnley, S. 2001, in The Bridge Between the Big Bang and Biology: Stars, Planetary Systems, Atmospheres, Volcanoes: Their Link to Life, 139

Charnley, S. B. 1997, in IAU Colloq. 161: Astronomical and Biochemical Origins and the Search for Life in the Universe, 89

Charnley, S. B., Kress, M. E., Tielens, A. G. G. M., & Millar, T. J. 1995, ApJ, 448, 232

Charnley, S. B., Tielens, A. G. G. M., & Millar, T. J. 1992, ApJ, 399, L71

Crovisier, J. 1984, A&A, 130, 361

—. 1994, J. Geophys. Res., 99, 3777

Crovisier, J., Bockelée-Morvan, D., Biver, N., Colom, P., Despois, D., & Lis, D. C. 2004a, A&A, 418, L35

Crovisier, J., Bockelée-Morvan, D., Colom, P., Biver, N., Despois, D., Lis, D. C., & the Team for target-of-opportunity radio observations of comets. 2004b, A&A, 418, 1141

Crovisier, J., & Encrenaz, T. 1983, A&A, 126, 170

Crovisier, J., & Le Bourlot, J. 1983, A&A, 123, 61

Cuppen, H., & Herbst, E. 2005, in 60^{th} International Symposium on Molecular Spectroscopy

D. R. Lide, J., ed. 2004, CRC Handbook of Chemistry and Physics, eighty-fourth edn. (New York:CRC Press), 6–8

de Pree, C. G., Gaume, R. A., Goss, W. M., & Claussen, M. J. 1995, ApJ, 451, 284

—. 1996, ApJ, 464, 788

de Vicente, P., Martín-Pintado, J., Neri, R., & Colom, P. 2000, A&A, 361, 1058

de Vicente, P., Martin-Pintado, J., & Wilson, T. L. 1997, A&A, 320, 957

Dello Russo, N., Mumma, M. J., DiSanti, M. A., & Magee-Sauer, K. 2001, Bulletin of the American Astronomical Society, 33, 1076

Doeleman, S. S., Lonsdale, C. J., & Pelkey, S. 1999, ApJ, 510, L55

Drira, I., Hure, J. M., Spielfiedel, A., Feautrier, N., & Roueff, E. 1997, A&A, 319, 720

Duley, W. W. 1996, MNRAS, 279, 591

Duley, W. W., & Williams, D. A. 1985, Interstellar Chemistry (Academic Press: London)

Eberhardt, P., & Krankowsky, D. 1995, A&A, 295, 795

Fischer, G., & Ross, I. G. 2003, Journal of Physical Chemistry A, 107, 10631

Frerking, M. A., Wilson, R. W., & Langer, W. D. 1979, ApJ, 232, L65

Friedel, D. N., Remijan, A. J., Snyder, L. E., A'Hearn, M. F., Blake, G. A., de Pater, I., Dickel, H. R., Forster, J. R., Hogerheijde, M. R., Kraybill, C., Looney, L. W., Palmer, P., & Wright, M. C. H. 2005a, ApJ, 630, 623

Friedel, D. N., Snyder, L. E., Remijan, A. J., & Turner, B. E. 2005b, ApJ, 632, L95

Friedel, D. N., Snyder, L. E., Turner, B. E., & Remijan, A. 2004, ApJ, 600, 234

Gaume, R. A., Claussen, M. J., de Pree, C. G., Goss, W. M., & Mehringer, D. M. 1995, ApJ, 449, 663

Genzel, R., Reid, M. J., Moran, J. M., & Downes, D. 1981, ApJ, 244, 884

Gerry, M. C. L., Yamada, K., & Winnewisser, G. 1979, J. Phys. Chem. Ref. Data, 8, 107

Goldsmith, P. F., & Langer, W. D. 1999, ApJ, 517, 209

Gottlieb, C. A., Gottlieb, E. W., Thaddeus, P., & Vrtilek, J. M. 1986, ApJ, 303, 446

Gould, R. J., & Salpeter, E. E. 1963, ApJ, 138, 393

Greaves, J. S. 1995, MNRAS, 273, 918

Greaves, J. S., & Nyman, L.-A. 1996, A&A, 305, 950

Greaves, J. S., & Williams, P. G. 1994, A&A, 290, 259

Groner, P., Albert, S., Herbst, E., & de Lucia, F. C. 1998, ApJ, 500, 1059

Groner, P., Albert, S., Herbst, E., De Lucia, F. C., Lovas, F. J., Drouin, B. J., & Pearson, J. C. 2002, ApJS, 142, 145

Groner, P., Herbst, E., De Lucia, F. C., Drouin, B. J., & Mäder, H. 2005, in 60^{th} International Symposium on Molecular Spectroscopy

Guelin, M., Cernicharo, J., & Linke, R. A. 1982, ApJ, 263, L89

Halverson, F., Stamm, R. F., & Whalen, J. J. 1948, The Journal of Chemical Physics, 16, 808

Hartquist, T. W., Menten, K. M., Lepp, S., & Dalgarno, A. 1995, MNRAS, 272, 184

Hasegawa, T. I., & Herbst, E. 1993, MNRAS, 261, 83

Hasegawa, T. I., Herbst, E., & Leung, C. M. 1992, ApJS, 82, 167

Helbert, J., Rauer, H., Boice, D. C., & Huebner, W. F. 2005, A&A, 442, 1107

Highberger, J. L., Apponi, A. J., Bieging, J. H., Ziurys, L. M., & Mangum, J. G. 2000, ApJ, 544, 881

Hiraoka, K., Miyagoshi, T., Takayama, T., Yamamoto, K., & Kihara, Y. 1998a, ApJ, 498, 710

Hiraoka, K., Yamashita, A., Miyagoshi, T., Oohashi, N., Kihara, Y., & Yamamoto, K. 1998b, ApJ, 508, 423

Hirota, T., Maezawa, H., & Yamamoto, S. 2004, ApJ, 617, 399

Hollenbach, D., & Salpeter, E. E. 1971, ApJ, 163, 155

Hollis, J. M., Jewell, P. R., Lovas, F. J., & Remijan, A. 2004, ApJ, 613, L45

Hollis, J. M., Pedelty, J. A., Boboltz, D. A., Liu, S.-Y., Snyder, L. E., Palmer, P., Lovas, F. J., & Jewell, P. R. 2003, ApJ, 596, L235

Horiuchi, S., & Kameya, O. 2000, PASJ, 52, 545

Horn, A., Møllendal, H., Sekiguchi, O., Uggerud, E., Roberts, H., Herbst, E., Viggiano, A. A., & Fridgen, T. D. 2004, ApJ, 611, 605

Huebner, W. F., Keady, J. J., & Lyon, S. P. 1992, Ap&SS, 195, 7

Hutsemékers, D., Manfroid, J., Jehin, E., Arpigny, C., Cochran, A., Schulz, R., Stüwe, J. A., & Zucconi, J.-M. 2005, A&A, 440, L21

Huttemeister, S., Wilson, T. L., Henkel, C., & Mauersberger, R. 1993, A&A, 276, 445

Itikawa, Y. 1971, J. Phys. Soc. Japan, 30, 835

—. 1972, J. Phys. Soc. Japan, 32, 217

Jacox, M. E. 2005, Vibrational and Electronic Energy Levels of Polyatomic Transient Molecules in NIST Chemistry WebBook, NIST Standard Reference Database Number 69 (Gaithersburg MD, 20899 (http://webbook.nist.gov): National Institute of Standards and Technology)

Johansson, L. E. B., Andersson, C., Ellder, J., Friberg, P., Hjalmarson, A., Hoglund, B., Irvine, W. M., Olofsson, H., & Rydbeck, G. 1984, A&A, 130, 227

Johnson, D. R., Lovas, F. J., & Kirchhoff, W. H. 1972, J. Phys. Chem. Ref. Data, 1, 1011

Kaifu, N., Ohishi, M., Kawaguchi, K., Saito, S., Yamamoto, S., Miyaji, T., Miyazawa, K., Ishikawa, S.-I., Noumaru, C., Harasawa, S., Okuda, M., & Suzuki, H. 2004, PASJ, 56, 69

Kerkhof, O., Schutte, W. A., & Ehrenfreund, P. 1999, A&A, 346, 990

King, G. W., Hainer, R. M., & Cross, P. C. 1947, Physical Review, 71, 433

Kleinmann, D. E., & Low, F. J. 1967, ApJ, 149, L1

Kuan, Y., Mehringer, D. M., & Snyder, L. E. 1996, ApJ, 459, 619

Lafferty, W. J., & Lovas, F. J. 1978, J. Phys. Chem. Ref. Data, 7, 441

Latter, W. B., & Charnley, S. B. 1996, ApJ, 463, L37+

Lilley, A. E., & Palmer, P. 1968, ApJS, 16, 143

Lis, D. C., Keene, J., Young, K., Phillips, T. G., Bockelee-Morvan, D., Crovisier, J., Schilke, P., Goldsmith, P. F., & Bergin, E. A. 1997, Icarus, 130, 355

Liu, S., Girart, J. M., Remijan, A., & Snyder, L. E. 2002, ApJ, 576, 255

Liu, S., Mehringer, D. M., & Snyder, L. E. 2001, ApJ, 552, 654

Lovas, F. J. 1978, J. Phys. Chem. Ref. Data, 7, 1445

—. 1982, J. Phys. Chem. Ref. Data, 11, 251

—. 1985, J. Phys. Chem. Ref. Data, 14, 395

Lovas, F. J., & Krupenie, P. H. 1974, J. Phys. Chem. Ref. Data, 3, 259

Lovas, F. J., & Tiemann, E. 1974, J. Phys. Chem. Ref. Data, 3, 609

Lovell, A. J., Kallivayalil, N., Schloerb, F. P., Combi, M. R., Hansen, K. C., & Gombosi, T. I. 2004, ApJ, 613, 615

Lucas, R., & Liszt, H. S. 1993, A&A, 276, L33+

Müller, H. S. P., Thorwirth, S., Roth, D. A., & Winnewisser, G. 2001, A&A, 370, L49

Martín-Pintado, J., Rizzo, J. R., de Vicente, P., Rodríguez-Fernández, N. J., & Fuente, A. 2001, ApJ, 548, L65

McNaughton, D., Evans, C. J., Lane, S., & Nielsen, C. J. 1999, Journal of Molecular Spectroscopy, 193, 104

McQuarrie, D. A. 2000, Statistical Mechanics (University Science Books:Sausalito, CA)

Mehringer, D. M., Pearson, J. C., Keene, J., & Phillips, T. G. 2004, ApJ, 608, 306

Mehringer, D. M., Snyder, L. E., Miao, Y., & Lovas, F. J. 1997, ApJ, 480, L71

Miao, Y., Mehringer, D. M., Kuan, Y., & Snyder, L. E. 1995, ApJ, 445, L59

Miao, Y., & Snyder, L. E. 1997, ApJ, 480, L67

Mitchell, D. L., Lin, R. P., Carlson, C. W., Korth, A., Reme, H., & Mendis, D. A. 1992, Icarus, 98, 125

Mizushima, M. 1975, The Theory of Rotating Diatomic Molecules (New York:John Wiley and Sons)

Mumma, M. J., DiSanti, M. A., Magee-Sauer, K., Bonev, B. P., Villanueva, G. L., Kawakita, H., Dello Russo, N., Gibb, E. L., Blake, G. A., Lyke, J. E., Campbell, R. D., Aycock, J., Conrad, A., & Hill, G. M. 2005, Science, 310, 270

Murakami, A. 1990, ApJ, 357, 288

Nakajima, M., Sumiyoshi, Y., & Endo, Y. 2002, Journal of Chemical Physics, 117, 9327

Nummelin, A., & Bergman, P. 1999, A&A, 341, L59

Nummelin, A., Bergman, P., Hjalmarson, Å., Friberg, P., Irvine, W. M., Millar, T. J., Ohishi, M., & Saito, S. 2000, ApJS, 128, 213

Oesterling, L. C., Albert, S., de Lucia, F. C., Sastry, K. V. L. N., & Herbst, E. 1999, ApJ, 521, 255

O'Neill, P. T., Viti, S., & Williams, D. A. 2002, A&A, 388, 346

Parneix, P., & Brechignac, P. 1998, A&A, 334, 363

Pickett, H. M., Poynter, R. L., Cohen, E. A., Delitsky, M. L., Pearson, J. C., & Muller, H. S. P. 1998, J. Quant. Spectrosc. & Rad. Transfer, 60, 883

Pirronello, V., Liu, C., Shen, L., & Vidali, G. 1997, ApJ, 475, L69+

Press, W. H., Teukolsky, S. A., Vetterling, W. T., & Flannery, B. P. 1992, Numerical Recipes in C: The Art of Scientific Computing (Cambridge University Press: New York)

Rao, R., Crutcher, R. M., Plambeck, R. L., & Wright, M. C. H. 1998, ApJ, 502, L75

Remijan, A., Shiao, Y.-S., Friedel, D. N., Meier, D. S., & Snyder, L. E. 2004a, ApJ, 617, 384

Remijan, A., Snyder, L. E., Friedel, D. N., Liu, S.-Y., & Shah, R. Y. 2003, ApJ, 590, 314

Remijan, A., Snyder, L. E., Friedel, D. N., Veal, J. M., Palmer, P., Woodney, L. M., A'Hearn, M. F., Forster, J. R., Wright, M. C. H., & de Pater, I. 2004b, AAS/Division for Planetary Sciences Meeting Abstracts, 36

Remijan, A., Sutton, E. C., Snyder, L. E., Friedel, D. N., Liu, S.-Y., & Pei, C.-C. 2004c, ApJ, 606, 917

Remijan, A. J., Wyrowski, F., Friedel, D. N., Meier, D. S., & Snyder, L. E. 2005, ApJ, 626, 233

Rogers, J. D., & Hillman, J. J. 1982, J. Chem. Phys., 77, 3615

Rohlfs, K., & Wilson, T. L. 2000, Tools of Radio Astronomy (Springer-Verlag:New York)

Ruffle, D. P., & Herbst, E. 2000, MNRAS, 319, 837

—. 2001, MNRAS, 322, 770

Sault, R. J., Teuben, P. J., & Wright, M. C. H. 1995, in Astronomical Data Analysis Software and Systems IV, ed. R. A. Shaw, H. E. Payne, & J. J. E. Hayes, ASP Conference Series 77, 443

Schilke, P., Benford, D. J., Hunter, T. R., Lis, D. C., & Phillips, T. G. 2001, ApJS, 132, 281

Schwendeman, R. H., & Laurie, V. W. 1958, Tables of Line Strengths for Rotational Transitions of Asymmetric Rotor Molecules (Pergamon:London)

Senent, M. L., Smeyers, Y. G., Domínguez-Gómez, R., & Villa, M. 2000, The Journal of Chemical Physics, 112, 5809

Shah, R. Y., & Wootten, A. 2001, ApJ, 554, 933

Shalabiea, O. M., & Greenberg, J. M. 1994, A&A, 290, 266

Snyder, L. E., Lovas, F. J., Hollis, J. M., Friedel, D. N., Jewell, P. R., Remijan, A., Ilyushin, V. V., Alekseev, E. A., & Dyubko, S. F. 2005, ApJ, 619, 914

Snyder, L. E., Schenewerk, M. S., & Hollis, J. M. 1985, ApJ, 298, 360

Snyder, L. E., Veal, J. M., Woodney, L. M., Wright, M. C. H., Palmer, P., A'Hearn, M. F., Kuan, Y.-J., de Pater, I., & Forster, J. R. 2001, AJ, 121, 1147

Sobolev, A. M., & Makarov, S. V. 1984, Soviet Astronomy, 28, 720

Sutton, E. C., Blake, G. A., Masson, C. R., & Phillips, T. G. 1985, ApJS, 58, 341

Sutton, E. C., Jaminet, P. A., Danchi, W. C., & Blake, G. A. 1991, ApJS, 77, 255

Takahashi, J. 1999, Earth, Planets, and Space, 51, 1215

Takayanagi, K., & Itiakawa, K. 1970, Advances in Atomic and Molecular Physics, Vol. 6, The Rotational Excitation of Molecules by Slow Electrons (Academic Press: New York), 105

Tieftrunk, A., Pineau des Forets, G., Schilke, P., & Walmsley, C. M. 1994, A&A, 289, 579

Tiemann, E. J. 1974, J. Phys. Chem. Ref. Data, 3, 259

Turner, B. E. 1989, ApJS, 70, 539

—. 1991, ApJS, 76, 617

Ulich, B. L., & Haas, R. W. 1976, ApJS, 30, 247

Vastel, C., Polehampton, E. T., Baluteau, J.-P., Swinyard, B. M., Caux, E., & Cox, P. 2002, ApJ, 581, 315

Watson, W. D., & Salpeter, E. E. 1972, ApJ, 174, 321

Weissman, P. R. 1999, Space Science Reviews, 90, 301

Welch, W. J., Wright, M. C. H., Plambeck, R. L., Bieging, J. H., & Baud, B. 1981, ApJ, 245, L87

Widicus Weaver, S. L. 2005a, Ph.D. Thesis

Widicus Weaver, S. L. 2005b, in 60^{th} International Symposium on Molecular Spectroscopy

Widicus Weaver, S. L., Butler, R. A. H., Drouin, B. J., Petkie, D. T., Dyl, K. A., De Lucia, F. C., & Blake, G. A. 2005, ApJS, 158, 188

Willemot, E., Dangoisse, D., Monnanteuil, N., & Bellet, J. 1980, J. Phys. Chem. Ref. Data, 9, 59

Winnewisser, G., Hocking, W. H., & Gerry, M. C. L. 1976, J. Phys. Chem. Ref. Data, 5, 79

Woodney, L. M., A'Hearn, M. F., Schleicher, D. G., Farnham, T. L., McMullin, J. P., Wright, M. C. H., Veal, J. M., Snyder, L. E., de Pater, I., Forster, J. R., Palmer, P., Kuan, Y.-J., Williams, W. R., Cheung, C. C., & Smith, B. R. 2002, Icarus, 157, 193

Woods, R. C., Saykally, R. J., Anderson, T. G., Dixon, T. A., & Szanto, P. G. 1981, J. Chem. Phys., 75, 4256

Wright, M. C. H. 1996, BIMA Memoranda Ser. 45

Wright, M. C. H., Plambeck, R. L., & Wilner, D. J. 1996, ApJ, 469, 216

Xie, X., & Mumma, M. J. 1992, ApJ, 386, 720

Xu, L.-H., & Lovas, F. J. 1997, J. Phys. Chem. Ref. Data, 26, 17

Yamamoto, S., Saito, S., Kawaguchi, K., Chikada, Y., Suzuki, H., Kaifu, N., Ishikawa, S., & Ohishi, M. 1990a, ApJ, 361, 318

Yamamoto, S., Saito, S., Suzuki, H., Deguchi, S., Kaifu, N., Ishikawa, S., & Ohishi, M. 1990b, ApJ, 348, 363

Curriculum Vitae

Douglas N. Friedel

Department of Astronomy
103 Astronomy Building
1002 W. Green Street
Urbana, IL 61801

Office: (217)244-5470
E-mail: friedel@astro.uiuc.edu

Education

University of Illinois Urbana, IL
PhD., Astronomy 1999-2005
Thesis: *3mm Spectral Line Surveys of the High Mass Star Forming Regions Sagittarius B2(N-LMH) and Orion-KL*

Clarkson University Potsdam, NY
B.S., Physics 1995-1999
B.S., Mathematics 1995-1999
Graduated with Distinction

Professional Experience

BIMA/CARMA Research Assistant 1999-present
Department of Astronomy, University of Illinois
BIMA Proposal Processor 1999-2004
Department of Astronomy, University of Illinois
BIMA Operator 2000-2004
Department of Astronomy, University of Illinois
MIRIAD System Manager 2004-present
Department of Astronomy, University of Illinois
CARMA Observer 2005-present
Department of Astronomy, University of Illinois

Awards

Sigurds Arajas Memorial Award for Experimental Physics 1996
Clarkson University, Potsdam, NY

Professional Societies

American Astronomical Society (Junior Member) 2003-present
Division of Planetary Science, American Astronomical Society (Junior Member) 2004-present

Conferences Attended

60th International Symposium on Molecular Spectroscopy 2005
Oral presentation

36th Division of Planetary Sciences Meeting of the American Astronomical Society 2004
Oral presentation

59th International Symposium on Molecular Spectroscopy 2004
Oral presentation

58th International Symposium on Molecular Spectroscopy 2003
Oral presentation

Refereed Publications

Detection of Interstellar Acetone Toward the Orion-KL Hot Core, **Friedel, D. N.**, Snyder, L. E., Remijan, Anthony J., & Turner, B. E., 2005, *Astrophysical Journal Letters*, 632, L95

BIMA Array Detections of HCN in Comets LINEAR (C/2002 T7) and NEAT (C/2001 Q4), **Friedel, D. N.**, Remijan, Anthony J., Snyder, L. E., A'Hearn, M. F., Blake, Geoffrey A., de Pater, Imke, Dickel, H. R., Forster, J. R., Hogerheijde, M. R., Kraybill, C., Looney, L. W., Palmer, Patrick, & Wright, M. C. H., 2005, *Astrophysical Journal*, 630, 623

A Survey of Large Molecules toward the Protoplanetary Nebula CRL 618, Remijan, Anthony J., Wyrowski, Friedrich, **Friedel, D. N.**, Meier, D. S., and Snyder, L. E., 2005, *Astrophysical Journal*, 626, 233

A Rigorous Attempt to Verify Interstellar Glycine, Snyder, L. E., Lovas, F. J., Hollis, J. M., **Friedel, D. N.**, Jewell, P. R., Remijan, A., Ilyushin, V. V., Alekseev, E. A., & Dyubko, S. F., 2005, *Astrophysical Journal*, 619, 914

A Survey of Large Molecules of Biological Interest Toward Selected High Mass Star Forming Regions, Remijan, A., Shiao, Y.-S., **Friedel, D. N.**, Meier, D. S., Snyder, L. E., 2004, *Astrophysical Journal*, 617, 384

High-Resolution Observations of Methyl Cyanide (CH_3CN) toward the Hot Core Regions W51e1/e2, Remijan, A., Sutton, E. C., Snyder, L. E., **Friedel, D. N.**, Liu, S.-Y., & Pei, C.-C., 2004, *Astrophysical Journal*, 606, 917

A Spectral Line Survey of Selected 3 Millimeter Bands toward Sagittarius B2(N-LMH) Using the National Radio Astronomy Observatory 12 Meter Radio Telescope and the Berkeley-Illinois-Maryland Association Array. I. The Observational Data, **Friedel, D. N.**, Snyder, L. E., Turner, B. E., & Remijan, A., 2004, *Astrophysical Journal*, 600, 243

A Survey of Acetic Acid toward Hot Molecular Cores, Remijan, A., Snyder, L. E., **Friedel, D. N.**, Liu, S.-Y., & Shah, R. Y., *Astrophysical Journal*, 2003, 590, 314

Conference Proceedings

BIMA Array observations of Comets LINEAR (C/2002 T7) and NEAT (C/2001 Q4), **Friedel, D. N.**, Remijan, A., Snyder, L. E., A'Hearn, M. F., Blake, G. A., de Pater, I., Dickel, H. R., Forster, J. R., Hogerheijde, M. R., Kraybill, C., Looney, L. W., Palmer, P., & Wright, M. C. H., *60^{th} Ohio State University Symposium on Molecular Spectroscopy*, 2005

BIMA Array 3mm Spectral Line Survey of Orion-KL, **Friedel, D. N.**, Snyder, L. E., Turner, B. E., & Remijan A. *60^{th} Ohio State University Symposium on Molecular Spectroscopy*, 2005

Survey of Large Molecules Toward the Protoplanetary Nebula CRL 618, Remijan, A. J., Wyrowski, F, **Friedel, D. N.**, Meier, D. S., and Snyder, L. E.,*60^{th} Ohio State University Symposium on Molecular Spectroscopy*, 2005

BIMA Array observations of Comets LINEAR (C/2002 T7) and NEAT (C/2001 Q4), **Friedel, D. N.**, Remijan, A., Snyder, L. E., A'Hearn, M. F., Blake, G. A., de Pater, I., Dickel, H. R., Forster, J. R., Hogerheijde, M. R., Kraybill, C., Looney, L. W., Palmer, P., & Wright, M. C. H., 2004, *36^{th} Meeting of the Division of Planetary Sciences, American Astronomical Society*, 36, 2506

A BIMA Array Search for Biomolecules in Comet Hale-Bopp(C/1995 O1), Remijan, A., Snyder, L. E., **Friedel, D. N.**, Veal, J. M., Palmer, Patrick, Woodney, L. M., A'Hearn, Michael F., Forster, J. R., Wright, M. C. H., & de Pater, I., 2004, *36^{th} Meeting of the Division of Planetary Sciences, American Astronomical Society*, 36, 3202

Molecular Outflows from Massive Protostars, Kim, K.-T., Churchwell, E., **Friedel, D. N.**, & Sewilo, M., *59^{th} Ohio State University Symposium on Molecular Spectroscopy*, 2004, RI02, 241

High-Resolution Observations of Methyl Cyanide (CH_3CN) toward the Hot Core Regions W51e1/e2, Remijan, A., Sutton, E. C., Snyder, L. E., **Friedel, D. N.**, Liu, S.-Y., & Pei, C.-C., *59^{th} Ohio State University Symposium on Molecular Spectroscopy*, 2004, RI03, 242

A Spectral Line Survey of Selected 3 Millimeter Bands toward Sagittarius B2(N-LMH) Using the National Radio Astronomy Observatory 12 Meter Radio Telescope and the Berkeley-Illinois-Maryland Association Array. II. Data Analysis, **Friedel, D. N.**, Snyder, L. E., Turner, B. E., & Remijan, A., *59^{th} Ohio State University Symposium on Molecular Spectroscopy*, 2004, RI02, 242

High-Resolution Observations of Methyl Cyanide (CH_3CN) toward the Hot Core Regions W51e1/e2, Remijan, A., Sutton, E. C., Snyder, L. E., **Friedel, D. N.**, Liu, S.-Y., & Pei, C.-C., 2004, *204^{th} Meeting of the American Astronomical Society*, 204, 6116

A λ=3 mm Spectral Line Survey of Sagittarius B2(N-LMH) with the BIMA Array and NRAO 12 Meter Radio Telescope, **Friedel, D. N.**, Snyder, L. E., Turner, B. E., & Remijan, A. J., *58^{th} Ohio State University Symposium on Molecular Spectroscopy*, 2003, FA03, 243

Interstellar Urea [$(NH_2)_2CO$], Snyder, L. E., Remijan, A. J., Lovas, F. J., **Friedel, D. N.**, & Liu, S.-Y., *58^{th} Ohio State University Symposium on Molecular Spectroscopy*, 2003, WE05, 164